

THE MINISTRY OF SCIENCE AND HIGHER EDUCATION OF THE RUSSIAN FEDERATION



ST. PETERSBURG STATE
POLYTECHNICAL UNIVERSITY
JOURNAL

Physics
and Mathematics

**VOLUME 16, No.1.1,
2023**

Peter the Great St. Petersburg
Polytechnic University
2023

ST. PETERSBURG STATE POLYTECHNICAL UNIVERSITY JOURNAL. PHYSICS AND MATHEMATICS

JOURNAL EDITORIAL COUNCIL

A.I. Borovkov – vice-rector for perspective projects;
V.A. Glukhikh – full member of RAS;
D.A. Indeitsev – corresponding member of RAS;
V.A.I. Rudskoy – full member of RAS;
R.A. Suris – full member of RAS;
A.E. Zhukov – corresponding member of RAS.

JOURNAL EDITORIAL BOARD

V.K. Ivanov – Dr. Sci. (phys.-math.), prof., SPbPU, St. Petersburg, Russia, – editor-in-chief;
A.E. Fotiadi – Dr. Sci. (phys.-math.), prof., SPbPU, St. Petersburg, Russia, – deputy editor-in-chief;
V.M. Kapralova – Candidate of Phys.-Math. Sci., associate prof., SPbPU, St. Petersburg, Russia, – executive secretary;
V.I. Antonov – Dr. Sci. (phys.-math.), prof., SPbPU, St. Petersburg, Russia;
I.B. Bezprozvanny – Dr. Sci. (biology), prof., The University of Texas Southwestern Medical Center, Dallas, TX, USA;
A.V. Blinov – Dr. Sci. (phys.-math.), prof., SPbPU, St. Petersburg, Russia;
A.S. Cherepanov – Dr. Sci. (phys.-math.), prof., SPbPU, St. Petersburg, Russia;
D.V. Donetski – Dr. Sci. (phys.-math.), prof., State University of New York at Stony Brook, NY, USA;
V.V. Dubov – Dr. Sci. (phys.-math.), prof., SPbPU, St. Petersburg, Russia;
D.A. Firsov – Dr. Sci. (phys.-math.), prof., SPbPU, St. Petersburg, Russia;
P.A. Karasev – Dr. Sci. (phys.-math.), prof., SPbPU, St. Petersburg, Russia;
A.S. Kheifets – Ph.D., prof., Australian National University, Canberra, Australia;
O.S. Loboda – Candidate of Phys.-Math. Sci., associate prof., SPbPU, St. Petersburg, Russia;
J.B. Malherbe – Dr. Sci. (physics), prof., University of Pretoria, Republic of South Africa;
V.M. Ostryakov – Dr. Sci. (phys.-math.), prof., SPbPU, St. Petersburg, Russia;
V.E. Privalov – Dr. Sci. (phys.-math.), prof., SPbPU, St. Petersburg, Russia;
E.M. Smirnov – Dr. Sci. (phys.-math.), prof., SPbPU, St. Petersburg, Russia;
A.V. Solov'yov – Dr. Sci. (phys.-math.), prof., MBN Research Center, Frankfurt am Main, Germany;
A.K. Tagantsev – Dr. Sci. (phys.-math.), prof., Swiss Federal Institute of Technology, Lausanne, Switzerland;
I.N. Toptygin – Dr. Sci. (phys.-math.), prof., SPbPU, St. Petersburg, Russia.

The journal is included in the List of leading peer-reviewed scientific journals and other editions to publish major findings of theses for the research degrees of Doctor of Sciences and Candidate of Sciences.

The publications are presented in the VINITI RAS Abstract Journal and Ulrich's Periodical Directory International Database.

The journal is published since 2008 as part of the periodical edition 'Nauchno-tekhnicheskie vedomosti SPb-GPU'.

The journal is registered with the Federal Service for Supervision in the Sphere of Telecom, Information Technologies and Mass Communications (ROSKOMNADZOR). Certificate ПИ № ФС77-52144 issued December 11, 2012.

The journal is distributed through the CIS countries catalogue, the «Press of Russia» joint catalogue and the «Press by subscription» Internet catalogue. The subscription index is 71823.

The journal is in the **Web of Science** (Emerging Sources Citation Index), **Scopus**, the **Russian Science Citation Index** (RSCI) and the **Directory of Open Access Journals** (DOAJ) databases.

© Scientific Electronic Library (<http://www.elibrary.ru>).

No part of this publication may be reproduced without clear reference to the source.

The views of the authors may not represent the views of the Editorial Board.

Address: 195251 Politekhnicheskaya St. 29, St. Petersburg, Russia.

Phone: (812) 294-22-85.

<http://ntv.spbstu.ru/physics>

© Peter the Great St. Petersburg Polytechnic University, 2023

PREFACE



International Conference PhysicA.SPb/2022

The International Conference PhysicA.SPb took place in Saint Petersburg, Russia, from October 17 to 21, 2022. The Conference continues the tradition of St. Petersburg Seminars on Physics and Astronomy originating from mid-90s. Since then PhysicA.SPb maintains both scientific and educational quality of contributions delivered to the audience. This is the main feature of the Conference that makes it possible to present the whole spectrum of modern Physics and Astronomy within one event.

PhysicA.SPb/2022 has brought together over 400 academics from many universities and research institutes across Russia as well as from United Kingdom, South Africa, Kazakhstan, Belarus, Azerbaijan, South Korea, Armenia, Germany and France. Oral and poster presentations were organized into well-defined categories among which one should name Astronomy and Astrophysics, Optics and spectroscopy, Physics of ferroics, Nuclear and elementary particle physics, and many others.

This is the first issue of the St. Petersburg State Polytechnical University Journal: Physics and Mathematics presenting the extended contributions from participants of PhysicA.SPb/2022 that were peer-reviewed by expert referees through processes administered by the Presidents of the Organizing and Program Committees to the highest professional and scientific standards. This became possible due to the efforts of the Sectional and Technical Editors of this Issue: Prof. Petr Arseev (Lebedev Physical Institute), Prof. Alexander Ivanchik (Ioffe Institute), Prof. Polina Ryabochkina (Ogarev Mordova State University), Prof. Yuri Kusraev (Ioffe Institute), Dr. Sergey Nekrasov (Ioffe Institute), Prof. Igor Sokolov (Ioffe Institute), Dr. Natalia Teplova (Ioffe Institute), Dr. Nikolay Bert (Ioffe Institute), Dr. Nikita Gordeev (Ioffe Institute), Dr. Grigorii Savchenko (Ioffe Institute), Dr. Prokhor Alekseev (Ioffe Institute), Dr. Mikhail Dunaevskii (Ioffe Institute), Prof. Mikhail Nestoklon (Ioffe Institute), Prof. Andrey Dunaev (Orel State University), Dr. Vadim Evtikhiev (Ioffe Institute), Prof. Alexey Ustinov (St.Petersburg State Electrotechnical University "LETI"), Dr. Alexandra Kalashnikova (Ioffe Institute), Prof. Ivan Mitropolsky (NRC Kurchatov Institute – PNPI), Dr. Evgenia Cherotchenko (Ioffe Institute) and Prof. Dmitry Khokhlov (Moscow State University).

The Editors: **Nikita S. Averkiev**, **Sergey A. Poniaev** and **Grigorii S. Sokolovskii**

Contents

Condensed matter physics

Gerega V.A., Suslov A.V., Komarov V.A., Grabov V.M., Demidov E.V., Stepanov R.S., Rodionov A.V., Kolobov A.V. <i>Size effects in the galvanomagnetic and thermoelectric properties of ultrathin bismuth-antimony films</i>	9
Myasoedov A.V., Pavlov I.S., Pechnikov A.I., Stepanov S.I., Nikolaev V.I. <i>TEM study of the defect structure of α-Ga₂O₃ layers grown by HVPE</i>	16
Melnichenko I.A., Nadtochiy A.M., Ivanov K.A., Makhov I.S., Maksimov M.V., Mintairov S.A., Kalyuzhnyy N.A., Kryzhanovskaya N.V., Zhukov A.E. <i>Time-resolved photoluminescence study of InGaAs/GaAs quantum well-dots with upconversion method</i>	22
Korolev R.I., Antonets I.V., Golubev E.A. <i>Complex permittivity of graphene-containing shungite within 0.05 – 15 MHz</i>	28
Il'inskiy A.V., Castro R.A., Pashkevich M.E., Popova I.O., Sidorov A.I., Shadrin E.B. <i>Dielectric spectroscopy of Ag₂S nanowires synthesized in porous silicate glasses</i>	33
Milinskiy A.Yu., Baryshnikov S.V., Zeeva A.A. <i>Dielectric properties of ferroelectric composite (KNO₃)_(1-x)/(RbNO₃)_x</i>	38
Kondratev V.M., Vyacheslavova E.A., Morozov I.A., Nalimova S.S., Moshnikov V.A., Gudovskikh A.S., Bolshakov A.D. <i>Study of quasi 1D silicon nanostructures adsorption properties via impedance spectroscopy</i>	43
Agekyan V.F., Filosofov N.G., Karczewski G., Resnitsky A.N., Serov A.Yu., Smirnov A.S., Shtrom I.V., Verbin S.Yu. <i>Photoluminescence and energy transfer between CdTe/CdMnTe quantum wells separated by thick barriers</i>	49
Castro Arata R.A., Kononov A.A., Nikonorova N.A. <i>Charge transfer in thin layers of polymer nanocomposites based on aromatic thermoplastic polyimide and cerium dioxide</i>	54
Damaskinskaya E.E., Hilarov V.L., Nosov Yu.G., Podurets K.M., Kaloyan A.A., Korost D.V., Damaskinskii D.K. <i>Specific features of defect structure of a quartz single crystal at early stages of deformation</i>	60
Guryev V.V., Irodova A.V., Chumakov N.K., Shavkin S.V. <i>Low-field magnetization features of superconducting tapes with strong pinning anisotropy</i>	67
Valeeva A.R., Pronin I.P., Kaptelov E.Yu., Senkevich S.V., Nemov S.A., Staritsyn M.V. <i>Microstructure and ferroelectric properties of submicron polycrystalline lead zirconate titanate films with a gradient composition distribution over the thickness</i>	74
Mynbaeva M.G., Lebedev S.P. <i>Self-organization of the structure of porous silicon carbide under external influences</i>	79
Gureva S.A., Marikhin V.A., Vlasova E.N. <i>Conformational disorder and its effect on structural phase transitions in tricosane C₂₃H₄₈</i>	84
Borisov A.K., Egorov V.M., Marikhin V.A., Myasnikova L.P. <i>Dimensional effect of nanocrystalline elements of the polyethylene structure</i>	90

Golubev Ye.A., Antonets I.V., Korolev R.I. <i>Frequency and concentration dependences of the electrical properties of natural disordered carbon in the high-frequency region.....</i>	97
Shmargilov S.A., Galutskiy V.V., Puzanovskiy K.V., Stroganova E.V. <i>Influence of the refractive index gradient on the transmission coefficient in the 1.5-micron range in an electro-optical converter based on lithium niobate.....</i>	102
Dunaevskiy M.S. <i>Study of mechanical resonance frequencies in tapered nanowires.....</i>	109
Eremeev I.A., Vorobev M.G., Grashchenko A.S., Pirogov E.V., Andreeva V.D., Osipov A.V., Kukushkin S.A. <i>Evolution of the crystal microstructure of hybrid SiC/Si substrates grown by the method of atomic substitution.....</i>	113
Lukhmyrina T.S., Klimov A.A., Kunkov R.E., Lebedeva N.M., Matveev B.A., Cheryakov A.E. <i>Temperature distribution in InAsSbP/InAsSb/InAs double heterostructure on-chip sensors.....</i>	119
Puchkov N.I., Solovyev V.G., Cvetkov A.V., Yanikov M.V. <i>Propagation of surface plasmon-polaritons in metal-dielectric structures based on opals.....</i>	126
Babkina A.N., Zyryanova K.S., Kulpina E.V., Gavrilov R.R. <i>Alkali ion effect on phase transition temperatures of CuCl nanocrystals in potassium-alumina-borate glass.....</i>	131
Vasilyev Yu.B. <i>Two-dimensional plasmon excitations in a random array of quantum antidots.....</i>	137
Chikurov D.S., Volkov M.P. <i>Study of the anisotropy of critical currents in 2G-HTSC tapes by a non-contact method.....</i>	142
Argunova T.S., Kohn V.G., Krymov V.M. <i>Study of defects in shaped sapphire crystals by synchrotron X-ray phase contrast imaging.....</i>	146
Reznik R.R., Gridchin V.O., Kotlyar K.P., Dragunova A.S., Kryzhanovskaya N.V., Samsonenko Yu.B., Soshnikov I.P., Khrebtov A.I., Cirilin G.E. <i>Features of MBE growth of AlGaAs nanowires with InAs quantum dots on the silicon surface.....</i>	153
Kaveev A.K. <i>Formation of a dielectric sublayer heterostructure of lead-tin telluride.....</i>	158
Korolev D.S., Tereshchenko A.N., Nikolskaya A.A., Mikhaylov A.N., Belov A.I., Tetelbaum D.I. <i>Dislocation-related photoluminescence in self-implanted silicon with different surface orientation.....</i>	162
Ivanov A.E., Chernyakov A.E., Zakgeim A.L. <i>Comprehensive study of power capabilities of UV-C LEDs in pulsed and continuous modes.....</i>	167
Ionov A.N., Volkov M.P., Nikolaeva M.N., Smyslov R.Y., Bugrov A.N. <i>Magnetization of different types of reduced graphene oxide in composites based on polystyrene.....</i>	172
Conyuh D.A., Beltukov Ya.M. <i>Quasi-local vibrations of amorphous solids in correlated random matrix theory.....</i>	178
Martyshkin A.A., Gubanova Y.A., Beginin E.N., Sadovnikov A.V. <i>Interconnect elements of magnonic networks based on controlled meander 3D magnonic structures.....</i>	185
Cherednichenko A.I., Zakharov P.V., Eremin A.M., Starostenkov M.D., Korznikova E.A., Dmitriev S.V. <i>Effect of surface curvature of an FCC crystal on the characteristics of localized vibrations of atoms.....</i>	191

Simkin I.V., Yakovlev E.V., Kryuchkov N.P., Korsakova S.A., Yurchenko S.O. <i>Calculation of correlation lengths in 2D Lennard-Jones fluids.....</i>	197
Libet P.A., Shirokova A.A., Simkin I.V., Yakovlev E.V., Yurchenko S.O. <i>Application of conical magnetic rotating fields for controlled colloidal self-assembly.....</i>	205
Fedorov V.A., Balybin D.V., Pluzhnikova T.N., Boitsova M.V., Fedotov D.Yu., Berezner A.D., Yakovlev A.V. <i>Features of electrochemical behavior of an amorphous iron-based alloy in acidic solutions containing potassium rhodanide.....</i>	211

Simulation of physical processes

Belyaev K.V., Garbaruk A., Golubkov V.D., Strelets M.Kh. <i>Application of global stability analysis to predicting characteristics of Tollmien-Schlichting waves.....</i>	218
Myasnichenko V.S., Sokolov D.N., Sdobnyakov N.Yu., Ershov P.M., Nepsha N.I., Veselov A.D., Mikhailov R., Kirilov L. <i>Adaptation of the Monte-Carlo method for modeling layer-by-layer growth of clusters and nanoalloys.....</i>	225
Hilarov V.L., Damaskinskaya E.E. <i>Fracture modeling with the discrete elements method.....</i>	231
Matyushenko A.A., Golubkov V.D., Garbaruk A.V., Strelets M.Kh., <i>Application of machine learning approach for turbulence model improvement for flow around airfoil near stall conditions.....</i>	236
Marakueva O.V., Duben A.P. <i>Accuracy of flow simulation in a low-pressure turbine using a laminar-turbulent transition model.....</i>	243
Ivanchenko G.S., Ten A.V. <i>Simulation of vibrations in hydrogenated diamond-like nanofilms.....</i>	250
Guseva E.K., Shur M.L., Stabnikov A.S., Ströer S.P., Travin A.K. <i>Zonal RANS-IDDES of asymmetric curved wake subjected to adverse pressure gradient.....</i>	255
Kamalova N.S., Matveev N.N., Evsikova N.Yu., Lisitsyn V.I., Vnukova S.V., Nguyen H.T. <i>Formalized model of cellulose thermopolarization processes in natural wood in a non-uniform temperature field.....</i>	262
Mukhutdinova A.A., Kireev V.N., Urmancheev S.F. <i>Influence of variable thermophysical properties on the flow of fluids in an annular channel under intensive heat exchange.....</i>	269
Charykov N.A., Kuznetsov V.V., Sadowski W., Semenov K.N., Keskinov V.A., Blokhin A.A., Letenko D.G., Shamardanov Z.K., Shaymardanova B.K., Kulenova N.A., Sadenova M.A. <i>Equilibrium shift in chemical reactions.....</i>	275
Fatkullina N.B., Solnyshkina O.A., Bulatova A.Z., Andryuschenko V.A. <i>3D simulation of deformable particle dynamics in channel with hydrodynamic traps.....</i>	281
Bulatova A.Z., Solnyshkina O.A., Fatkullina N.B. <i>Numerical study of the rheological characteristics of dispersed systems in shear flow using the boundary element method.....</i>	288
Pigusov E.A., Pavlenko O.V., Kornushenko A.V., Vinogradov O.N., Reslan M.G. <i>Effect of running propellers on flow and hinge moments of trailing edge mechanization of high aspect ratio.....</i>	295
Tashayev Yu.N. <i>Working process calculation of the control circuit for pulsed operation regime of the MPD accelerator.....</i>	301

Lebedev S.P., Priobrazhenskii S.Iu., Plotnikov A.V., Mynbaeva M.G., Lebedev A.A. Numerical simulation of the temperature field distribution in the epitaxial graphene growth setup.....	309
Pigusov E.A., Golovkin M.A., Pavlenko O.V. Flow modelling of slotted slit on spin model.....	315
Lytaev A.A., Popov I.Yu. Numerical simulation of waveguide couplers using the coupled mode theory for quantum gates implementation.....	320
Klikunova A.Yu., Khoperskov A.V. Calculation of hydrological connection between the Volga river and the Akhtuba river using numerical hydrodynamic modeling.....	326
Khavin V.E., Popov A.Yu., Teplova N.V., Troshin G.A., Gusakov E.Z. One dimensional Fokker-Planck equation with relativistic effects for numerical simulations.....	331
Ignatenko V.A., Smirnovsky A.A. Study of the effect of dynamic and temperature inhomogeneities on epitaxial processes in a horizontal CVD reactor.....	336
Atom physics and physics of clusters and nanostructures	
Ilkivi.V., Kotlyar P., Kirilenko D.A., Sharov V.A., Reznik R.R., Ciril G.E. Formation of Ge quantum dots on GaN nanowires by molecular beam epitaxy.....	341
Sachkov Yu.I., Yunin P.A., Travkin V.V. Conductivity in nanostructured films of paramagnetic manganese phthalocyanine.....	346
Levina S.A., Emelyanov V.M., Filimonov E.D., Shvarts M.Z. Determination of subcell parameters for multijunction solar cells at radiation exposure.....	351
Nelson D.K., Starukhin A.N., Kurdyukov D.A., Stovpyaga E.Yu. Thermally induced depolarization of fluorescence of matrix-isolated MoS₂ nanodots.....	356
Krichevtsov B.B., Korovin A.M., Suturin S.M., Sokolov N.S. Nanoscale layers of hexaferrite BaFe₁₂O₁₉ grown by laser molecular beam epitaxy: growth, crystal structure and magnetic properties.....	363
Bogdanov A.A., Gavrish S.V., Martsinovsky A.M., Stolyarov I.I. Application of cesium lamps for indoor lighting and preventive ultraviolet irradiation.....	369
Lubyankina E. A., Babich E.S., Lipovskii A.A. Pesticide detection by SERS using dendritic structures grown in glass.....	374
Arteev D.S., Sakharov A.V., Nikolaev A.E., Zavarin E.E., Tsatsulnikov A.F. 2DEG-based multilayer AlGa₁₂/Ga₁₉ heterostructures with lowered sheet resistance.....	380
Vaulin N.V., Afonicheva P.K., Lebedev D.V., Bukatin A.S., Mukhin I.S. Study of ion transport in single solid-state nanopores formed by optical and ion lithography.....	385
Afonicheva P.K., Vaulin N.V., Lebedev D.V., Bukatin A.S., Mukhin I.S., Evstrapov A.A. Investigation of ion transport in solid-state nanopores upon optical radiation.....	389
Khalugarova K., Kondratev V.M., Spivak Yu.M., Shomakhov Z.V., Moshnikov V.A. Compositions based on porous silicon and nickel oxide obtained by cooperative synthesis.....	393
Gromov I.A., Kuleshova T.E., Kuznetsov Yu.A., Lapushkin M.N., Samsonova N.S. Electron-stimulated desorption of lithium and potassium atoms in the adsorption of lithium and potassium atoms on gold.....	398

Aksenova V.V., Smirnova I.P., Markov L.K., Pavluchenko A.S., Kolokolov D.S., Volkov D.Yu. Wet- tability of transparent conductive nanostructured ITO and ITO/Al₂O₃ coatings.....	404
Salii R.A., Mintairov M.A., Mintairov S.A., Nakhimovich M.V., Shvarts M.Z., Kalyuzhnyy N.A. Infl- ence of GaP compensating layers on the characteristics of GaAs photovoltaic converters with InGaAs quantum dot arrays.....	411
Mitina M.D., Verbitskaya V.E., Fadeeva N.N., Eremin I.V. Bragg peak effect on the electrical characteristics of Si detectors irradiated with medium energy ⁴⁰Ar ions.....	416
Nikolskaia A.B., Kozlov S.S., Alexeeva O.V., Vildanova M.F., Karyagina O.K., Almjasheva O.V., Gu- sarov V.V., Shevaleevskiy O.I. New inorganic materials for electron transport layers in perovskite so- lar cells.....	422
Experimental technique and devices	
Filimonov E.D., Levina S.A., Shvarts M.Z. Temperature effect on spectral irradiance blurring of solar radiation by Fresnel lens sunlight concentrators.....	428
Barinov Yu.A. Determination of discharge gas temperature with liquid non-metallic electrodes using the BOS method.....	433
Tuboltsev Yu.V., Chichagov Yu.V., Bodganov A.A., Kantor M.Yu., Sidorov A.V. Shaping amplifier for soft X-ray spectrometer with a silicon drift detector.....	438
Popov P.A., Monakhov N.A. Analysis of thermal and thermoelectric processes in heat flux sensors based on layered metal structures.....	444
Monakhov N.A., Sakharov V. A., Popov P.A. Heat flux measurements of high speed flow around an axisymmetric body using sensors based on anisotropic thermoelements.....	450
Rochas S.S., Blokhin S.A., Babichev A.V., Karachinsky L.Ya., Novikov I.I., Blokhin A.A., Bobrov M.A., Maleev N.A., Andryushkin V. V., Bougrov V.E., Gladyshev A.G., Melnichenko I.A., Voropaev K.O., Zhumaeva I.O., Ustinov V.M., Li H., Tian S., Han S.Y., Sapunov G.A., Egorov A.Yu., Bimberg D.H. 1550 nm high-speed VCSELS based on compressively strained In(Al)GaAs QWs.....	456
Mosharov V.E., Radchenko V.N., Senuev I.V., Kotov M.A. Application of temperature-sensitive paint with two channels for studying thermal processes in short duration gas dynamic facilities...	463
Kotov M.A., Solovyev N.G., Glebov V.N., Dubrova G.A., Malyutin A.M. Pulse thermal load for thermoelectric detector calibration.....	472
Shvarts M.Z., Malevskiy D.A., Nakhimovich M.V., Pokrovskiy P.V., Sadchikov N.A., Soluyanov A.A. Estimation of optical diffuse properties in Fresnel lenses.....	478
Kantor M.Yu., Sidorov A.V., Bogdanov A.A., Tuboltsev Yu.V., Chichagov Yu.V. A soft X-ray spec- trometer with enhanced output count rate.....	484
Kuleshov D.O., Solovieva A.V., Gromov I.A., Pikovskoi I.I., Ul'yanovskii N.V., Belesov A.V., Sypalov S.A., Mazur D.M. Application of a liquid electrode for collecting products of chemical reactions carried out in charged microdroplets of an electrospray torch.....	491

CONDENSED MATTER PHYSICS

Conference materials

UDC 538.935

DOI: <https://doi.org/10.18721/JPM.161.101>

Size effects in the galvanomagnetic and thermoelectric properties of ultrathin bismuth-antimony films

V.A. Gerega¹✉, A.V. Suslov¹, V.A. Komarov¹, V.M. Grabov¹, E.V. Demidov¹,
R.S. Stepanov¹, A.V. Rodionov², A.V. Kolobov¹

¹ Herzen University, Saint Petersburg, Russia;

² Bunin Yelets State University, Yelets, Russia

✉gerega.vasilisa96@gmail.com

Abstract. The paper presents the results of a study of the electrical, galvanomagnetic, and thermoelectric properties of Bi and Bi_{1-x}Sb_x ($x = 0.03, 0.05, \text{ and } 0.12$) thin films (10–50 nm) on a mica substrate. All samples are characterized by an increase in conductivity with a decrease in film thickness, which can be associated with the presence of topologically protected surface states. It has been found that the band structure of the alloys significantly affects the appearance of the metallic type of conductivity in films with $a \leq 18$ nm thickness. It was found that the resistivity of Bi_{0.97}Sb_{0.03} films ≤ 17 nm thick is almost independent of temperature. Despite the increase in the conductivity of the samples, with a decrease in the thickness, the thermoelectric power factor decreases, which casts doubt on the fact that surface states have a positive effect on the thermoelectric figure of merit of thin Bi_{1-x}Sb_x films. However, the detection of a positive thermoelectric power in Bi_{0.88}Sb_{0.12} samples may be of interest in the development of the p branch of thermoelectric converters.

Keywords: bismuth, bismuth-antimony alloys, galvanomagnetic properties, thermoelectric properties, thin films, thermoelectric power factor

Funding: This work has been supported by the Russian Science Foundation (grant No. 22-22-00850, <https://rscf.ru/project/22-22-00850/>).

Citation: Gerega V.A., Suslov A.V., Komarov V.A., Grabov V.M., Demidov E.V., Stepanov R.S., Rodionov A.V., Kolobov A.V. Size effects in the galvanomagnetic and thermoelectric properties of ultrathin bismuth-antimony films, St. Petersburg State Polytechnical University Journal. Physics and Mathematics. 16 (1.1) (2023) 9–15. DOI: <https://doi.org/10.18721/JPM.161.101>

This is an open access article under the CC BY-NC 4.0 license (<https://creativecommons.org/licenses/by-nc/4.0/>)

Материалы конференции

УДК 538.935

DOI: <https://doi.org/10.18721/JPM.161.101>

Размерные эффекты в гальваномагнитных и термоэлектрических свойствах сверхтонких пленок растворов висмут-сурьмы

В.А. Гергега¹✉, А.В. Суслов¹, В.А. Комаров¹, В.М. Грабов¹, Е.В. Демидов¹,
Р.С. Степанов¹, А.В. Родионов², А.В. Колобов¹

¹ РГПУ им. А.И. Герцена, Санкт-Петербург, Россия;

² ЕГУ им. И.А. Бунина, г. Елец, Россия

✉gerega.vasilisa96@gmail.com

Аннотация. В работе представлены результаты исследования электрических, гальваномагнитных и термоэлектрических свойств тонких пленок (10–50 нм) Вi и Вi_{1-x}Сb_x ($x = 0,03, 0,05 \text{ и } 0,12$) на слюдяной подложке. Для всех образцов характерно

увеличение проводимости при уменьшении толщины пленки, что может быть связано с наличием топологически защищенных поверхностных состояний. Установлено, что зонная структура сплавов существенно влияет на появление металлического типа проводимости в пленках толщиной ≤ 18 нм. Установлено, что удельное сопротивление пленок $\text{Bi}_{0.97}\text{Sb}_{0.03}$ толщиной ≤ 17 нм практически не зависит от температуры. Несмотря на увеличение проводимости образцов, с уменьшением толщины коэффициент термоэдс уменьшается, что ставит под сомнение положительное влияние поверхностных состояний на термоэлектрическую эффективность тонких пленок $\text{Bi}_{1-x}\text{Sb}_x$. Однако обнаружение положительной термоэдс в образцах $\text{Bi}_{0.88}\text{Sb}_{0.12}$ может представлять интерес для разработки p-ветви термоэлектрических преобразователей.

Ключевые слова: висмут, висмут-сурьмяные сплавы, гальваномагнитные свойства, термоэлектрические свойства, тонкие пленки, термоэлектрический фактор мощности

Финансирование: Исследование выполнено за счет Российского научного фонда (грант № 22-22-00850).

Ссылка при цитировании: Герега В.А., Суслов А.В., Комаров В.А., Грабов В.М., Демидов Е.В., Степанов Р.С., Родионов А.В., Колобов А.В. Размерные эффекты в гальваномагнитных и термоэлектрических свойствах сверхтонких пленок растворов висмут-сурьмы // Научно-технические ведомости СПбГПУ. Физико-математические науки. 2023. Т. 16. № 1.1. С. 9–15. DOI: <https://doi.org/10.18721/JPM.161.101>

Статья открытого доступа, распространяемая по лицензии CC BY-NC 4.0 (<https://creativecommons.org/licenses/by-nc/4.0/>)

Introduction

Theoretical and practical interest in the study of bismuth and bismuth-antimony alloys is due to the peculiarities of their physical properties: strong anisotropy of Fermi surfaces, small effective masses, large values of the mean free path and de Broglie wavelength of charge carriers, strong spin-orbit interaction, etc. In this regard, many works are devoted to the study of the transport properties of bismuth and bismuth-antimony crystals and thin films, in particular, their thermoelectric properties [1, 2]. In addition, it is of interest to study classical and quantum size effects on this class of materials [3, 4]. Theoretical works predict that the quantum size effect leads to the transition of bismuth thin films from a semimetallic state to a semiconductor one [5]. However, in ultrathin films of pure bismuth, a transition of the temperature dependence of resistivity to a metallic form is experimentally observed [6, 7], which is associated with the presence of metallic surface states [8]. According to various sources, the thickness of the films at which the transition is observed is different [9, 10]. In [7] we also observed the transition of the temperature dependence of the resistance of the ultrathin films of the $\text{Bi}_{0.88}\text{Sb}_{0.12}$ to a metallic form. Thus, a comprehensive investigation of the electrical, galvanomagnetic, and thermoelectric properties of bismuth and bismuth-antimony thin films is topical.

Bismuth-antimony alloys are of interest because the properties of a topological insulator in bulk crystals were experimentally confirmed for the first time on this material [11]. It is assumed that $\text{Bi}_{1-x}\text{Sb}_x$ have a nontrivial topological structure starting from $x > 0.04$, which corresponds to band inversion. In addition, recent ARPES and scanning electron microscopy studies of thin bismuth films have shown manifestations of the Rashba effect in the surface states of pure bismuth [12–14]. The nontrivial nature of the pure bismuth band structure is associated with an increase in the gap at the L point, which can be caused by the quantum size effect or in-plane deformation of the crystal lattice [15].

In this regard, of particular practical interest is the study of the thermoelectric power of thin films of bismuth and bismuth-antimony alloys. The high mobility of charge carriers of surface states can make it possible to increase the electrical conductivity without affecting the thermal conductivity of the material. This would make it possible to achieve an increase in thermoelectric figure of merit, which requires a combination of high electrical conductivity and low thermal conductivity.



Materials and Methods

The samples were produced by thermal evaporation in a vacuum $\sim 10^{-5}$ Torr on a mica substrate. The thickness of the samples was 10–50 nm. The material for producing samples was 99.999% purity bismuth and bismuth–antimony solid solutions with 3, 5, and 12 at.% Sb. Sample preparation parameters: deposition temperature is 393 K; annealing temperature is 473 K, and annealing time is 1 hour. Manganin contact pads were deposited on the samples by thermal evaporation in a vacuum. In addition, to measure the thermoelectric properties, a film thermistor and heater structure was formed on the reverse side of the substrate by a similar method.

The samples surface structure was studied by atomic-force microscopy (AFM). The samples thickness and the crystallites size were measured using the AFM method in combination with the method of selective chemical etching, described in [16]. The etching time was chosen depending on the sample thickness, calculated from the mass of the evaporated substance, and was 5–30 s. The thickness measurement accuracy with this method is about 10%.

As shown in our previous work [17], the transport properties of thin films of bismuth and alloys based on it are significantly affected by mechanical deformations. Therefore, the classical techniques for measuring thermoelectric power, in which the temperature gradient in the sample is created using a rigid mechanical contact of the sample with a copper plate, are not suitable. A significant difference in the coefficients of thermal expansion (CTE) of the gradient plate, heat transfer paste and substrate leads to a distortion of the deformed state of the film–substrate system so the measurement result, especially in the low temperature region, may be ambiguous.

In this regard, to measure the temperature dependences of the Seebeck coefficient, a method was used that excludes the appearance of additional mechanical stresses in the film substrate system, which is described in detail in [18]. To do this, a copper film resistance temperature sensor and a film heater were formed on the reverse side of the substrate relative to the film. Since the mica substrate is fairly thin (5–40 μm), the temperature of the resistance thermometer and the film in the contact zone can be considered the same. Measurements on the setup are carried out at a constant current in a constant magnetic field up to 0.7 T in the temperature range of 77–300 K.

Results and Discussion

AFM images of the samples surface structure indicate that the crystals trigonal axis is perpendicular to the substrate plane. The films are polycrystalline; the average crystallite size is 0.3–1 μm . Both the addition of antimony and a decrease in thickness on average reduces the size of crystallites, however, it always significantly exceeds the thickness of the samples. This is essential for the appearance of a metallic type of conductivity [19].

It should be noted that the conductivity of all investigated ultrathin films is greater in absolute value than the conductivity of thicker films studied earlier [20].

The type of temperature dependences on the resistivity of the samples strongly depends on their thickness. Pure bismuth films are characterized by a sharp change in the form of resistivity dependence at a thickness of ≤ 18 nm (Fig. 1). The resistivity of films with a thickness of ≥ 20 nm increases with decreasing temperature, while the resistivity of the investigated films of smaller thickness decreases with decreasing temperature, i. e., it has the form of the metals. A similar sharp change in the form of the resistivity temperature dependence is observed for $\text{Bi}_{0.88}\text{Sb}_{0.12}$ samples. In absolute value, the resistivity of $\text{Bi}_{0.88}\text{Sb}_{0.12}$ samples ≤ 18 nm thick turns out to be lower than the resistivity of pure bismuth films of this thickness, even though bulk crystals of this alloy are semiconductors and don't have band overlap, as in pure bismuth.

Bulk solid solutions with a 3 and 5 at.% Sb characterize the transition from a semimetallic to a semiconductor state, so they are of interest in the context of this study. The resistivity temperature dependences of these two compositions increase with decreasing temperature over the entire thickness range. However, the resistivity of $\text{Bi}_{0.97}\text{Sb}_{0.03}$ ≤ 17 nm films changes insignificantly, i. e., it practically doesn't depend on temperature. The absolute value of the resistivity of the $\text{Bi}_{0.97}\text{Sb}_{0.03}$ and $\text{Bi}_{0.95}\text{Sb}_{0.05}$ samples is higher than that of pure bismuth samples of the corresponding thickness, which is associated with smaller crystallite sizes, and a decrease and disappearance of band overlap at the L - and T -points.

In Bi and $\text{Bi}_{0.97}\text{Sb}_{0.03}$ films with a thickness of > 20 nm, the magnetoresistance depends on temperature non-monotonically, while in films with a thickness of 10–18 nm, the magnetoresistance

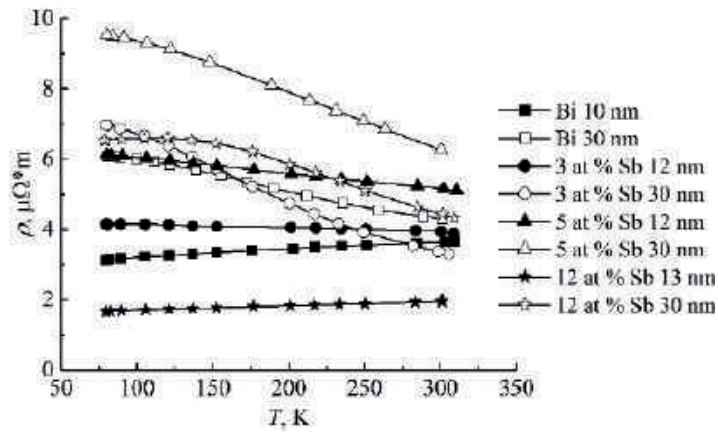


Fig. 1. Temperature dependence of the resistivity of films ~10 and 30 nm thick

is small and weakly depends on temperature. The relative magnetoresistance of the $\text{Bi}_{0.95}\text{Sb}_{0.05}$ and $\text{Bi}_{0.88}\text{Sb}_{0.12}$ films is close to zero, and doesn't depend on temperature over the entire investigated thickness range. A small or not observed magnetoresistance indicates a decrease in the mobility of charge carriers with a decrease in the film thickness. The combination of a decrease in resistivity and magnetoresistance qualitatively indicates an increase in the concentration of charge carriers with a decrease in the film thickness.

The Hall coefficient of Bi films is positive, which is also observed in polycrystalline films on a mica substrate $\sim 1 \mu\text{m}$ thick, the crystallite sizes of which exceed the thickness of the film itself. In such films the limitation of the electron mobility by the thickness manifests itself more significantly than the limitation of the hole mobility by the size of the crystallites [17]. The Hall coefficient of $\text{Bi}_{0.97}\text{Sb}_{0.03}$ and $\text{Bi}_{0.95}\text{Sb}_{0.05}$ bulk crystals and thicker films has a negative value (Fig. 2). However, for all studied samples $< 40 \text{ nm}$ thick, it is positive. Crystals and thicker $\text{Bi}_{0.88}\text{Sb}_{0.12}$ films are also characterized by a negative value of the Hall coefficient, which is observed in the studied films $> 20 \text{ nm}$ thick. However, as the thickness decreases below 18 nm, the sign of the Hall coefficient changes from negative to positive. The temperature dependences of the Hall coefficient of Bi, $\text{Bi}_{0.97}\text{Sb}_{0.03}$, and $\text{Bi}_{0.95}\text{Sb}_{0.05}$ films exhibit a maximum, which shifts to higher temperatures with decreasing film thickness.

The value of the Hall coefficient strongly depends on the ratio of the electron and hole mobilities. The component of the Hall coefficient tensor in the trigonal plane of Bi and $\text{Bi}_{1-x}\text{Sb}_x$ crystals is negative and rather small, so it is sensitive to various factors. In bismuth, due to anisotropy, the lowest hole mobility is observed along the trigonal axis, and electrons in the trigonal plane; therefore, when interpreting the measurement results, it is necessary to take into account the different limitations of charge carrier mobility on the film surface and crystallite boundaries [17]. In addition, the change in the ratio of the contributions of electrons and holes

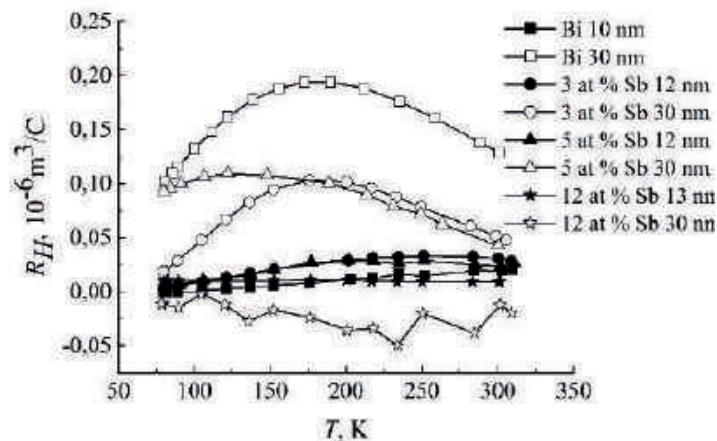


Fig. 2. Temperature dependence of the Hall coefficient of films ~10 and 30 nm thick



to the Hall coefficient can also be due to other factors, including the influence of surface states and deformations.

The Seebeck coefficient of the studied films decreases in absolute value with decreasing temperature. Thicker $\text{Bi}_{1-x}\text{Sb}_x$ films are characterized by an increase in thermoelectric power with decreasing temperature. In absolute value, the Seebeck coefficient is, on average, less than for samples with a thickness of 0.1–1 μm , i. e., with a decrease in the thickness of the samples, the thermoelectric power also decreases (Fig. 3).

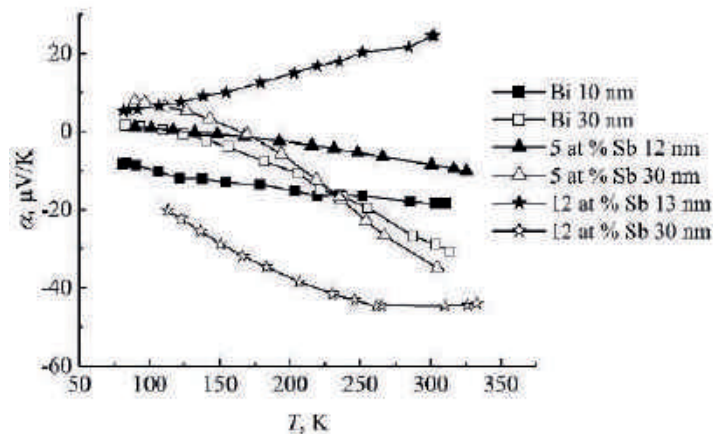


Fig. 3. Temperature dependence of the Seebeck coefficient of films ~ 10 and 30 nm thick

The temperature dependences of the Seebeck coefficient of the $\text{Bi}_{0.88}\text{Sb}_{0.12}$ films exhibit a sign reversal at thicknesses corresponding to the sign reversal of the Hall coefficient (18 nm). With an increase in the antimony concentration in the bismuth-antimony solid solution, the extremum of heavy holes at the H -point becomes actual. Therefore, the change in the sign of the thermopower in $\text{Bi}_{0.88}\text{Sb}_{0.12}$, in the case of ultrathin films, can be due not only to a significant limitation of the electron mobility but also to the manifestation of the contribution of holes at the H -point of the Brillouin zone.

Based on the results of measuring the thermopower and resistivity, the dependences of the power factor ($P = \alpha^2/\rho$) on temperature were calculated. It has been established that the power factor decreases with decreasing film thickness. I. e., an increase in the conductivity of ultrathin films with a decrease in thickness is insufficient to increase the thermoelectric power factor.

Conclusion

It has been found that all samples are characterized by a decrease in resistivity with decreasing thickness, which may be due to the contribution of the conductivity of surface states. A sharp change in the shape of the temperature dependence of the resistivity from a semiconductor type to a metallic one was found for films of pure bismuth and $\text{Bi}_{0.88}\text{Sb}_{0.12}$ films ≤ 18 nm thick. For $\text{Bi}_{0.97}\text{Sb}_{0.03}$ and $\text{Bi}_{0.95}\text{Sb}_{0.05}$ films no such transition was found. Interestingly, the resistivity of $\text{Bi}_{0.97}\text{Sb}_{0.03} \leq 17$ nm films is practically independent of temperature.

The Seebeck coefficient of all studied samples is lower in absolute value than that of films of 0.1–1 μm thickness. In this case, an increase in conductivity with decreasing sample thickness does not lead to an increase in the power factor. This casts doubt on the assumption that the contribution of surface states leads to an increase in the thermoelectric figure of merit of materials based on ultrathin films of bismuth-antimony. However, the detected positive thermoelectric power in $\text{Bi}_{0.88}\text{Sb}_{0.12}$ thin films may be of interest for creating a thermoelectric converter, the p - and n -branches of which will be films of the same composition but different thicknesses.

Acknowledgments

This work has been supported by the Russian Science Foundation (grant No 22-22-00850, <https://rscf.ru/project/22-22-00850/>).

REFERENCES

1. Yuan J., Cai Yo., Shen L., Xiao Ya., Ren J.-Ch., Wang Ai., Feng Yu.P., Yan X., One-dimensional thermoelectrics induced by Rashba spin-orbit coupling in two-dimensional BiSb monolayer, *Nano Energy*. 52 (2018) 163–70.
2. Nikolaeva A.A., Konopko L.A., Huber T.E., Bodiul P.P., Popov I.A., Moloshnik E.F., Size-quantization semimetal-semiconductor transition in Bi_{0.98}Sb_{0.02} nanowires: Thermoelectric properties, *Journal of Electronic Materials*. 41(9) (2012) 2313–2316.
3. Boffouï M.O., Lenoir B., Jacquot A., Scherrer H., Dauscher A., Stulzer M., Structure and transport properties of polycrystalline Bi films, *Journal of Physics and Chemistry of Solids*. 61(12) (2000) 1979–1983.
4. Condrea E., Gilewski A., Quantum oscillations of resistivity in bismuth nanowires, *Low Temperature Physics*. 36(3) (2010) 250–253.
5. Meriuts A., Rogacheva E., Dresselhaus M., On semimetal-semiconductor transition in thin Bi films, *AIP Conference Proceedings*. 1449(1) (2012) 29–32.
6. Demidov E.V., Grabov V.M., Komarov V.A., Krushelnitskii A.N., Suslov A.V., Suslov M.V., Specific features of the quantum-size effect in transport phenomena in bismuth thin films on mica substrates, *Semiconductors*. 53(6) (2019) 727–731.
7. Gerega V.A., Suslov A.V., Komarov V.A., Grabov V.M., Demidov E.V., Kolobov A.V., On the galvanomagnetic properties and thermoelectric power of ultrathin films of the bismuth-antimony system on a mica substrate, *Semiconductors*. 56(1) (2022) 42–47.
8. Hofmann Ph., The surfaces of bismuth: Structural and electronic properties, *Progress in Surface Science*. 81(5) (2006) 191–245.
9. Rogacheva E.I., Lyubchenko S.G., Dresselhaus M.S., Semimetal-semiconductor transition in thin Bi films, *Thin Solid Films*. 516(10) (2008) 3411–3415.
10. Wang N., Dai Y.X., Wang T.L., Yang H.Z., Qia Y., Investigation of growth characteristics and semimetal-semiconductor transition of polycrystalline bismuth thin films. *IUCrJ* 7 (2020) 49–57.
11. Hsieh D., Qian D., Wray L., Xia Y., Hor Y.S., Cava R.J., Hasan M.Z., A topological Dirac insulator in a quantum spin Hall phase, *Nature*. 452 (2008) 970–974.
12. Takayama A., Sato T., Souma S., Oguchi T., Takahashi T., One-dimensional edge states with giant spin splitting in a bismuth thin film, *Physical Review Letters*. 114 (2015) 066402.
13. Hirahara T., Fukui N., Shirasawa T., Yamada M., Aitani M., Miyazaki H., Matsunami M., Kimura S., Takahashi T., Hasegawa S., Kobayashi K., Atomic and electronic structure of ultrathin Bi(111) films grown on Bi₂Te₃(111) substrates: Evidence for a strain induced topological phase transition, *Physical Review Letters*. 109 (2012) 227401.
14. Ito S., Feng B., Arita M., Takayama A., Liu R.-Y., Someya T., Chen W.C., Iimori T., Namatame H., Taniguchi M., Cheng C.-M., Tang S.-J., Komori F., Kobayashi K., Chiang T.-C., Matsuda I., Proving non-trivial topology of pure bismuth by quantum confinement, *Physical Review Letters*. 117 (2016) 236402.
15. Chang T.R., Lu Q., Wang X., Lin H., Miller T., Chiang T.-C., Bian G., Band topology of bismuth quantum films, *Crystals*. 9 (2019) 510.
16. Demidov E.V., Komarov V.A., Krushelnitskii A.N., Suslov A.V., Measurement of the thickness of block-structured bismuth films by atomic-force microscopy combined with selective chemical etching, *Semiconductors*. 51(7) (2017) 840–842.
17. Suslov A.V., Grabov V.M., Komarov V.A., Demidov E.V., Senkevich S.V., Suslov M.V., The thermoelectric power of Bi_{1-x}Sb_x films ($0 \leq x \leq 0.15$) on mica and polyimide substrates in the temperature range of 77–300 K, *Semiconductors*. 53(5) (2019) 589–592.
18. Demidov E.V., Grabov V.M., Komarov V.A., Suslov A.V., Suslov M.V., The method of measuring the thermoelectric power in the thin films of the semimetals and narrow gap semiconductors formed on the thin substrates, *Journal of Physics. Conf. Series* 857 (2017) 012006.
19. Demidov E., Gerega V., Grabov V., Komarov V., Suslov A., Topological insulator's state in bismuth thin films, *AIP Conference Proceedings*. 2308 (2020) 050007.
20. Komarov V.A., Grabov V.M., Suslov A.V., Kablukova N.S., Suslov M.V., The Hall and Seebeck effects in bismuth thin films on mica substrates in the temperature range of 77–300 K, *Semiconductors*. 53(5) (2019) 593–598.



THE AUTHORS

GEREGA Vasilisa

gerega.vasilisa96@gmail.com
ORCID: 0000-0003-4235-7713

SUSLOV Anton

a.v_suslov@mail.ru
ORCID: 0000-0003-1934-245X

KOMAROV Vladimir

va-komar@yandex.ru
ORCID: 0000-0002-2482-0885

GRABOV Vladimir

vmgrabov@yandex.ru
ORCID: 0000-0003-0215-6474

DEMIDOV Evgenii

demidov_evg@mail.ru
ORCID: 0000-0002-1190-0376

STEPANOV Roman

frid.rom.serg@gmail.com
ORCID: 0000-0003-2559-7598

RODIONOV Arkadi

arkadijfirst3@gmail.com
ORCID: 0000-0002-2169-983X

KOLOBOV Aleksandr

akolobov@ Herzen.spb.ru
ORCID: 0000-0002-8125-1172

Received 27.09.2022. Approved after reviewing 08.11.2022. Accepted 08.11.2022.

Conference materials

UDC 538.9

DOI: <https://doi.org/10.18721/JPM.161.102>

TEM study of the defect structure of α -Ga₂O₃ layers grown by HVPE

A.V. Myasoedov ¹✉, I.S. Pavlov ², A.I. Pechnikov ^{1,3},

S.I. Stepanov ^{1,3}, V.I. Nikolaev ^{1,3}

¹ Ioffe Institute, Saint Petersburg, Russia;

² National Research Centre "Kurchatov Institute", Shubnikov Institute of Crystallography of Federal Scientific Research Centre "Crystallography and Photonics" of RAS, Moscow, Russia;

³ Perfect Crystals LLC, Saint Petersburg, Russia

✉ amyasoedov88@gmail.com

Abstract. Prismatic stacking faults in α -Ga₂O₃ films on (0001) Al₂O₃ substrates are investigated using transmission electron microscopy (TEM). The studied films are grown by halide vapor phase epitaxy (HVPE) up to 1.3 μ m in thickness. The initial growth stage results in threading dislocations (TDs) of an average density of 10^{10} cm⁻². The majority of the TDs are identified as $1/3 \langle 1\bar{1}00 \rangle$ partial edge and $1/3 \langle 1\bar{1}01 \rangle$ perfect mixed types using $g \cdot b = 0$ invisibility criterion under two-beam diffraction conditions. The edge component of Burgers vector is determined by the Burgers circuit procedure using high-resolution TEM images of dislocation cores. It is suggested that $1/3 \langle 1\bar{1}01 \rangle$ partial dislocations may arise as a result of dissociation of $1/3 \langle 2\bar{1}10 \rangle$ perfect dislocations which leads to the emergence of prismatic stacking faults in the films.

Keywords: gallium oxide, TEM, dislocations

Funding: This research was supported by the Russian Foundation for Basic Research (RFBR), grant No. 19-29-12041mk.

Citation: Myasoedov A.V., Pavlov I.S., Pechnikov A.I., Stepanov S.I., Nikolaev V.I. TEM study of the defect structure of α -Ga₂O₃ layers grown by HVPE, St. Petersburg State Polytechnical University Journal. Physics and Mathematics. 16 (1.1) (2023) 16–21. DOI: <https://doi.org/10.18721/JPM.161.102>

This is an open access article under the CC BY-NC 4.0 license (<https://creativecommons.org/licenses/by-nc/4.0/>)

Материалы конференции

УДК 538.9

DOI: <https://doi.org/10.18721/JPM.161.102>

ПЭМ-исследование дефектной структуры пленок α -Ga₂O₃, выращенных методом хлоридной эпитаксии

А.В. Мясоедов ¹✉, И.С. Павлов ², А.И. Печников ^{1,3},

С.И. Степанов ^{1,3}, В.И. Николаев ^{1,3}

¹ Физико-технический институт им. А.Ф. Иоффе РАН, Санкт-Петербург, Россия;

² Национальный исследовательский центр «Курчатовский институт», Институт кристаллографии им. А.В. Шубникова ФНИЦ «Кристаллография и фотоника» РАН, Москва, Россия;

³ ООО «Совершенные кристаллы», Санкт-Петербург, Россия

✉ amyasoedov88@gmail.com

Аннотация. Методом просвечивающей электронной микроскопии (ПЭМ) исследованы призматические дефекты упаковки в пленках α -Ga₂O₃ на (0001) Al₂O₃. Исследуемые пленки толщиной до 1,3 мкм были выращены методом хлоридной эпитаксии (ХЭ). Начальный этап эпитаксии сопровождается образованием высокой плотности проникающих дислокаций (ПД) на уровне 10^{10} см⁻². С помощью применения крите-



рия невидимости $g \cdot b = 0$ при двухлучевых дифракционных условиях большинство ПД были определены как частичные $1/3 \langle 1\bar{1}00 \rangle$ краевые и $1/3 \langle 1\bar{1}01 \rangle$ дислокации смешанного типа. Краевая компонента была определена с помощью построения контура Бюргерса на изображениях высокого разрешения ядер дислокаций. Предполагается, что $1/3 \langle 1\bar{1}00 \rangle$ частичные дислокации могут возникать в результате диссоциации $1/3 \langle 2\bar{1}\bar{1}0 \rangle$ полных дислокаций, которая приводит к появлению призматических дефектов упаковки в пленке.

Ключевые слова: оксид галлия, ПЭМ, дислокации

Финансирование: Работа выполнена при поддержке РФФИ. Грант № 19 29 12041мк.

Ссылка при цитировании: Мясоедов А.В., Павлов И.С., Печников А.И., Степанов С.И., Николаев В.И. ПЭМ-исследование дефектной структуры пленок α -Ga₂O₃, выращенных методом хлоридной эпитаксии // Научно-технические ведомости СПбГПУ. Физико-математические науки. 2023. Т. 16. № 1.1. С. 16–21. DOI: <https://doi.org/10.18721/JPM.161.102>

Статья открытого доступа, распространяемая по лицензии CC BY-NC 4.0 (<https://creativecommons.org/licenses/by-nc/4.0/>)

Introduction

Gallium oxide (Ga₂O₃), a wide bandgap semiconductor, is an attractive material for applications in power and optoelectronic devices [1]. In recent years, much attention has been given to various polymorphs of Ga₂O₃. Among all polymorphic forms, α -Ga₂O₃ has the widest direct bandgap of 5–5.3 eV at room temperature. α -Ga₂O₃ devices have the potential to outperform current GaN devices [2]. This polymorph has the corundum crystal structure which allows to grow α -Ga₂O₃ on (0001) Al₂O₃ substrates by various techniques such as halide vapor phase epitaxy (HVPE) [3, 4]. However, the large lattice mismatch ($\sim 4.7\%$) between the epilayer and the substrate results in a high density of threading dislocations (TDs) in the order of 10^{10} – 10^{11} cm⁻² [5]. TDs propagate along the film growth direction $\langle 0001 \rangle$. Numerous reports provided evidence that edge-type dislocations comprise the great majority of TDs in thin films of about 2 μ m thickness [3, 5, 6]. TDs act as non-radiative and charged scattering centers, and negatively affect recombination efficiency and carrier mobility [7].

Revealing dislocations of different types is important for the optimization of the growth process and device design. In previous studies of monoclinic β -Ga₂O₃ single crystals, several possible slip systems, and more than 10 possible Burgers vectors of dislocations were characterized [8, 9]. It was determined by TEM analysis that, in addition to perfect dislocations, partial dislocations exist in β -Ga₂O₃ [9]. However, the character of dislocations in trigonal α -Ga₂O₃ is poorly described in the literature.

In this work, we investigate the dislocation structure in up to 1.3 μ m thick α -Ga₂O₃ films grown by HVPE on (0001) sapphire substrates.

Materials and Methods

Single crystalline α -Ga₂O₃ films were grown on c-plane sapphire substrates by HVPE in an atmospheric pressure horizontal quartz reactor developed by Perfect Crystals LLC [10]. Gallium chloride (GaCl) and high-purity grade oxygen (O₂) were used as precursors. GaCl was synthesized in situ by passing gaseous hydrogen chloride (HCl) over metallic gallium (Ga) at 600 °C. The purity of HCl and Ga precursors was greater than 99.999%. The GaCl vapor was then mixed with O₂ in the deposition zone of the reactor to produce α -Ga₂O₃. The rate of deposition on a (0001) sapphire substrate varied from 8 to 12 μ m·h⁻¹. The deposition duration was chosen to produce a layer with the desired thickness. The films were transparent, mirror like, and crack-free. Samples with a thickness of 0.8–1.3 μ m were selected for the TEM study. According to our results, samples with different thicknesses showed similar results.

The TEM studies were carried out using an FEI Tecnai Osiris transmission electron microscope operated at 200 kV. Cross-sectional and plan-view lamellas were prepared using a conventional (lift-out) focused ion beam technique.

Results and Discussion

Typically, α -Ga₂O₃ films on Al₂O₃ substrates exhibit a high density of TDs. Fig. 1 shows dark-field (DF) cross-sectional TEM images, taken at different diffraction conditions. TDs are visible as line-shaped features that produce a diffraction contrast. According to earlier studies [5, 6], the great majority of TDs consist of edge-type dislocations. Moreover, edge dislocations are represented by two types, appearing in a ratio of 95 to 3.5%, has been recently described [11].

Our analysis of the dislocation structure in α -Ga₂O₃ films is mostly based on the geometry of slip systems determined for sapphire single crystals [12]. Table 1 summarizes the shortest Burgers vectors **b** and slip planes, available in sapphire crystals. The extension of this analysis to α -Ga₂O₃ is valid, because **b** values are similar to those of the established Burgers vectors of dislocations in α -Ga₂O₃ crystals. For the sake of convenience, we consider the Burgers vector to consist of two components lying perpendicular (*c*) and parallel (*a*) to the basal plane of the hexagonal lattice. It allows identifying dislocations using geometrically simply interpretable images.

Table 1

Shortest Burgers vectors and dislocation slip systems in Al₂O₃ and α -Ga₂O₃

Burgers vector	α -Ga ₂ O ₃ , Å	Al ₂ O ₃ , Å	Slip planes [12]
$1/3 \langle 11\bar{2}0 \rangle$	4.98	4.75	(0001), (1 $\bar{1}$ 00), (1 $\bar{1}$ 01), (1 $\bar{1}$ 02)
$1/3 \langle 1\bar{1}01 \rangle$	5.32	5.12	{11 $\bar{2}0$ }, {1 $\bar{1}$ 01}, {1 $\bar{1}$ 02}, {2 $\bar{1}$ 13}
$\langle 1\bar{1}00 \rangle$	8.63	8.22	{0001}, {11 $\bar{2}0$ }, {11 $\bar{2}2$ }, {11 $\bar{2}3$ }
$1/3 \langle 1\bar{1}00 \rangle^*$	2.88	2.74	* Partial dislocation

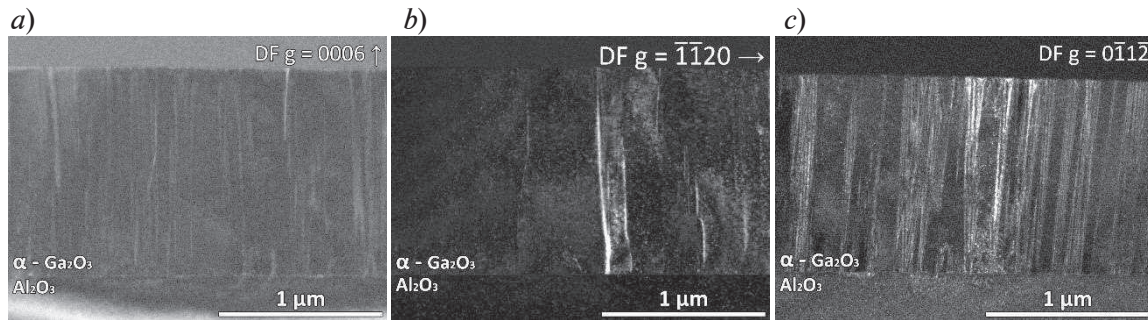


Fig. 1. Dark field TEM images of the cross-sectional area of α -Ga₂O₃ film with a thickness of 1.3 μ m, acquired in two-beam diffraction conditions. The diffraction vector equals: $\mathbf{g} = 0006$ (a); $\mathbf{g} = \bar{1}120$ (b); $\mathbf{g} = 0\bar{1}12$ (c)

An edge-type TD has a non-zero *a*-component and zero *c*-component. In crystals with the corundum structure, there are two possible Burgers vectors that satisfy these conditions for perfect dislocations. They are indicated as $\mathbf{b}_1 = \langle 11\bar{2}0 \rangle$ and $\mathbf{b}_2 = \langle 1\bar{1}00 \rangle$ in Table 1. We note that the latter vector \mathbf{b}_2 is about twice the magnitude of the former. Therefore, the vector \mathbf{b}_2 can be disregarded from further consideration because it is unlikely to occur in α -Ga₂O₃. In addition, dislocations with the Burgers vector $\mathbf{b} = \langle 0001 \rangle$ have not been reported for sapphire crystals. Similarly, one could hardly expect to find a perfect screw TD in α -Ga₂O₃. At the same time, perfect mixed TDs that have non-zero *a*- and *c*-components are likely to be found in α -Ga₂O₃. The lowest magnitude of the Burgers vector, which satisfies this condition is $\mathbf{b} = 1/3 \langle 1\bar{1}00 \rangle$ (Table 1). It is consistent with experimental observations made for GaN. Perfect screw TDs with $\mathbf{b} = \langle 0001 \rangle$ are rare in GaN thin films, while mixed ones with $\mathbf{b} = 1/3 \langle 11\bar{2}3 \rangle$ are more common.

Lattice defects can be identified using the diffraction contrast. Variations in the dislocation visibility can be interpreted using the well-known invisibility criteria. A screw dislocation is invisible when $\mathbf{g} \cdot \mathbf{b} = 0$. An edge dislocation is invisible when $\mathbf{g} \cdot \mathbf{b} = 0$, and a residual contrast depends upon the angle between \mathbf{g} and $\mathbf{b} \times \mathbf{l}$, where \mathbf{l} is dislocation line direction. For a mixed dislocation, visibility is the lowest under the same conditions as for edge one, and the contrast corresponding to the $\mathbf{g} \cdot \mathbf{b}_e = 0$ criterion, where \mathbf{b}_e – edge component of the mixed dislocation, is usually negligible.



The DF images shown in Fig. 1 were acquired under two-beam conditions with the diffraction vector $\mathbf{g} = 0006$ (a), $\mathbf{g} = \bar{1}\bar{1}20$ (b) and $\mathbf{g} = 0\bar{1}12$ (c). It can be seen that strong contrast is generated at the lowest number of TDs when $\mathbf{g} = \bar{1}\bar{1}20$ (Fig. 1, b). This result is inconsistent with previously published reports [5, 6, 11]. Furthermore, we classify the TDs imaged with the diffraction vector $\mathbf{g} = 0006$ (Fig. 1, a) as mixed perfect dislocations having non-zero c -component and Burgers vector of $1/3 \langle 1\bar{1}00 \rangle$. The majority of dislocations, observed at $\mathbf{g} = 0\bar{1}12$ (Fig. 1, c), should have a Burgers vector of $1/3 \langle 1\bar{1}00 \rangle$, because we do not observe so many TDs under $\mathbf{g} = 0006$. It is more likely that this contrast is caused by the many flat boundaries located in the layer.

Plan-view specimens were prepared to analyze the density and spatial distribution of dislocations. The specimens were taken not from the surface but from the volume of the film, since the lift-out method requires some space to prepare a lamella. The dislocation density was found to be not higher than 10^{10} cm^{-2} . Fig. 2 clearly shows images of plan-view specimens that contained dislocations and a large number of boundaries. The images were acquired along the $[0001]$ zone axis, using a bright-field (BF) scanning TEM (STEM). To determine the location and shape of boundaries, each sample was tilted with respect to the incident electron beam. As a result, the inclined projections allowed us to reveal that a flat boundary was located perpendicular to the basal plane and terminated at dislocations. Most of the TDs are localized at the boundaries.

The presence of inclusion of 60° -rotational domains was also found out, but these inclusions could not form open boundaries. These inclusions should be bounded by prismatic domain boundaries, thus they can only explain the presence of closed boundaries.

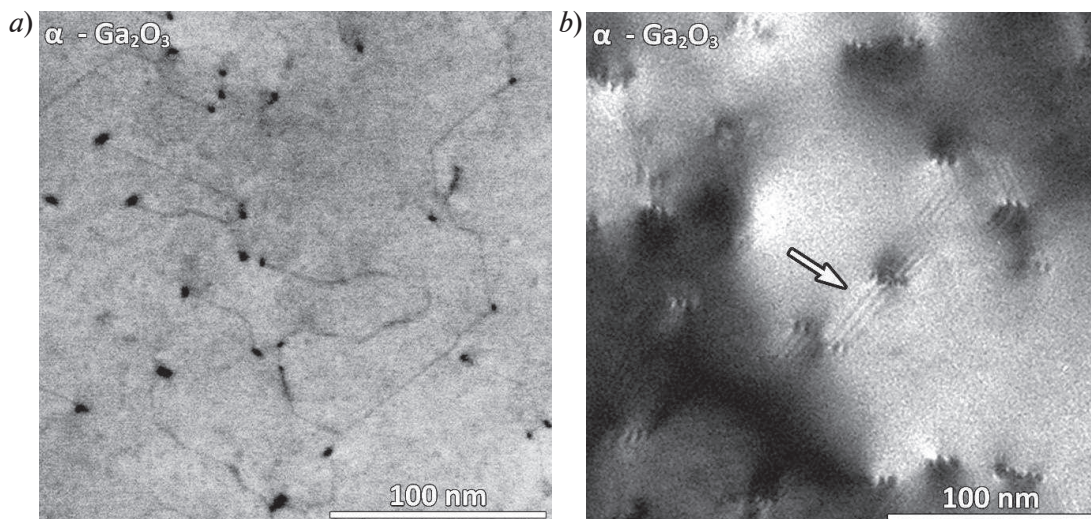


Fig. 2. Plan-view STEM-BF images taken along $[0001]$ zone axis. Projections of the TD lines onto the basal plane. The occurrence and distribution of planar defects (located on prismatic planes) can be seen between the dislocations (a). A sample is tilted with respect to the incident electron beam.

Multiple fringes that appeared on the image confirm the presence of prismatic faults (b)

It is known that perfect dislocation can dissociate into two partial dislocations because it lowers total energy. Such reactions have been studied for sapphire [13–15]. Below we consider stacking faults (SF), located at prismatic planes and terminated by partials. According to the images, shown in Fig. 2, the separation between the stacking faults is up to a few tens of nanometers.

The Burgers vectors of TDs were determined by a Burgers circuit procedure. Images of dislocation cores were acquired along the zone axis $[0001]$ using high-resolution electron microscopy (HREM). Fig. 3, a shows two dislocation cores. Small Burgers circuits are drawn around each core. The core regions are associated with partial dislocations having the Burgers vectors $\mathbf{b}_2 = 1/3 \langle 1\bar{1}00 \rangle$ and $\mathbf{b}_3 = 1/3 \langle 10\bar{1}0 \rangle$. The inset of Fig. 3, a represents magnified fragments of a large Burgers circuit drawn around the pair of dislocations. It is seen that the extra atom-to-atom path corresponds to the Burgers vector $\mathbf{b}_1 = 1/3 \langle 2\bar{1}\bar{1}0 \rangle$ of the perfect dislocation. This result is similar to earlier findings of the dislocation structures of low angle grain boundaries in sapphire [14]. The following dissociation reaction can be proposed: $1/3 \langle 2\bar{1}\bar{1}0 \rangle \rightarrow 1/3 \langle 1\bar{1}00 \rangle + 1/3 \langle 10\bar{1}0 \rangle + \text{SF}$, suggesting that the stacking fault on $\{2\bar{1}\bar{1}0\}$ prismatic plane is

formed between partial dislocations. The plane of SF does not coincide with the slip plane of the perfect dislocation $1/3 \langle 2\bar{1}\bar{1}0 \rangle$, as it is pointed out in [14]. Therefore, one should conclude that the self-climb mechanism takes place.

Our data show that neither inclusions of 60° rotational domains nor prismatic SFs appear against the background of the matrix in HREM-images along the $[0001]$ zone axis. The large separation of stacking faults makes it difficult to trace and compare the paths between two partial dislocations.

The HREM-image in Fig. 3, *b* represents the core of either mixed perfect $1/3 \langle 1\bar{1}01 \rangle$ or partial $1/3 \langle 1\bar{1}00 \rangle$ TD. It should be noted that mixed perfect $1/3 \langle 1\bar{1}01 \rangle$ dislocations also have a $1/3 \langle 1\bar{1}00 \rangle$ component of the Burgers vector. We identified ten $1/3 \langle 1\bar{1}00 \rangle$ cores throughout the investigations of the HREM-images acquired along the $[0001]$ zone axis.

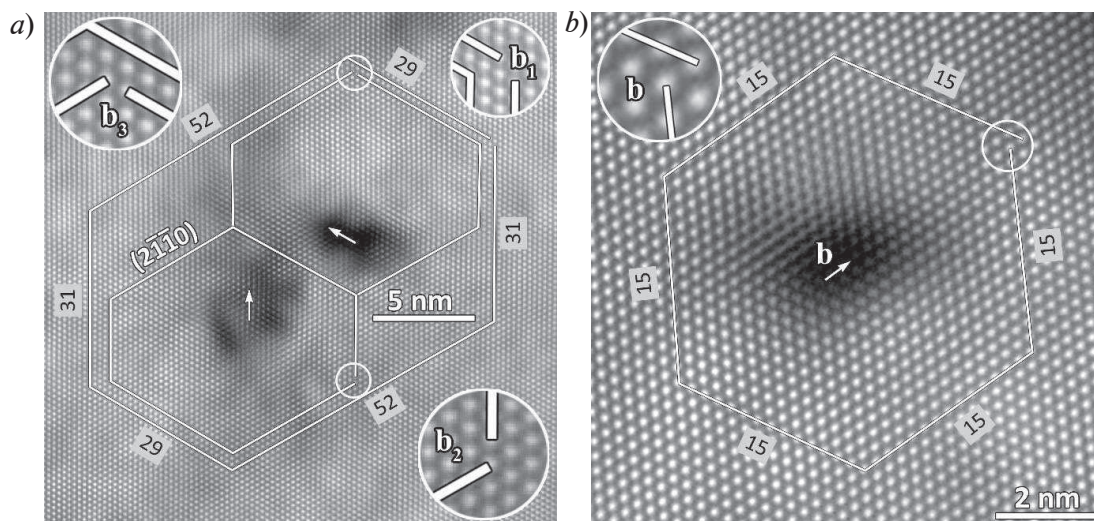


Fig. 3. Fourier-filtered HREM-images of dislocation cores were acquired along the zone axis $[0001]$. Two dislocation cores are located next to each other. A large Burgers circuit shows the edge component of $b_1 = 1/3 \langle 2\bar{1}\bar{1}0 \rangle$. A small Burgers circuits show the edge components of $b_2 = 1/3 \langle 1\bar{1}00 \rangle$ and $b_3 = 1/3 \langle 10\bar{1}0 \rangle$ (*a*). Single dislocation core with Burgers vector $b = 1/3 \langle 01\bar{1}0 \rangle$. The inserts show enlarged areas of the extra atom-to-atom path of the Burgers circuit drawn around dislocation cores (*b*)

Conclusion

The dislocation structure of α - Ga_2O_3 films grown on Al_2O_3 (0001) substrates by HVPE has been investigated using conventional and high-resolution TEM methods. The films contained a very large quantity of TDs with a density of about 10^{10} cm^{-2} . The density of mixed-type dislocations was not much less than that of edge TDs. The Burgers vector of the majority of dislocations were identified as $1/3 \langle 1\bar{1}00 \rangle$. Furthermore, our study revealed that edge TDs tend to dissociate into partial dislocations bounding prismatic stacking faults. High strain resulted in the formation of flat boundaries, rotational domains, and stacking faults, which deteriorated the crystalline quality.

REFERENCES

1. Zhang J., Shi J., Qi D.-C., Chen L., Zhang K.H.L., Recent progress on the electronic structure, defect, and doping properties of Ga_2O_3 , *APL Mater.* 8 (2) (2020) 020906.
2. Ahmadi E., Oshima Y., Materials issues and devices of α - and β - Ga_2O_3 , *J. Appl. Phys.* 126 (16) (2019) 160901.
3. Oshima Y., Vñllora E.G., Shimamura K., Halide vapor phase epitaxy of twin-free α - Ga_2O_3 on sapphire (0001) substrates, *Appl. Phys. Express.* 8 (5) (2015) 4–8.
4. Stepanov S.I., Nikolaev V.I., Almaev A.V., Pechnikov A.I., Scheglov M.P., Chikiryaka A.V., Kushnarev B.O., Polyakov A.Y., HVPE growth of corundum-structured α - Ga_2O_3 on sapphire substrates with α - Cr_2O_3 buffer layer, *Cryst. Growth Des.* 47 (2021) 577–581.



5. Kaneko K., Kawanowa H., Hiroshi I., Fujita S., Evaluation of misfit relaxation in α -Ga₂O₃ epitaxial growth on α -Al₂O₃ substrate, Appl. Phys. 51 (2012) 020201.
6. Ma T.C., Chen X.H., Kuang Y., Li L., Li J., Kremer F., Ren F.-F., Gu S.L., Zhang R., Zheng Y.D., Tan H.H., Jagadish C., Ye J.D., On the origin of dislocation generation and annihilation in α -Ga₂O₃ epilayers on sapphire, Appl. Phys. Lett. 115 (18) (2019) 182101.
7. Fujita S., Oda M., Kaneko K., Hitora T., Evolution of corundum-structured III-oxide semiconductors: Growth, properties, and devices, Jpn. J. Appl. Phys. 55 (12) (2016) 1202A3.
8. Yamaguchi H., Kuramata A., Masui T., Slip system analysis and X-ray topographic study on β -Ga₂O₃, Superlattices Microstruct. 130 (2019) 232.
9. Yao Y., Sugawara Y., Ishikawa Y., Observation of dislocations in β -Ga₂O₃ single crystal substrates by synchrotron X-ray topography, chemical etching, and transmission electron microscopy, Jpn. J. Appl. Phys. 59 (4) (2020) 045502.
10. Pechnikov A.I., Stepanov S.I., Chikiryaka A.V., Scheglov M.P., Odnobludov M.A., Nikolaev V.I., Thick α -Ga₂O₃ layers on sapphire substrates, grown by halide epitaxy, Semiconductors. 53 (6) (2019) 780–783.
11. Oshima Y., Yagyu S., Shinohe T., Visualization of threading dislocations in an α -Ga₂O₃ epilayer by HCl gas etching, J. Cryst. Growth. 576 (2021) 126387.
12. Snow J. D., Heuer A. H., Slip Systems in Al₂O₃, J. Am. Ceram. Soc. 56 (3) (1973) 153–157.
13. Lagerluf K.P., Mitchell T.E., Heuer A.H., TEM of dislocations in sapphire (c-Al₂O₃), 31 (1984) 303–315.
14. Tochigi E., Nakamura A., Shibata N., Ikuhara Y., Dislocation structures in low angle grain boundaries of α -Al₂O₃, Crystals. 8 (3) (2018) 1–14.
15. Tsuruta K., Tochigi E., Kezuka Y., Takata K., Shibata N., Nakamura A., Ikuhara Y., Core structure and dissociation energetics of basal edge dislocation in α -Al₂O₃: A combined atomistic simulation and transmission electron microscopy analysis, Acta Mater. 65 (2014) 76–84.

THE AUTHORS

MYASOEDOV Alexander V.
amyasoedov88@gmail.com
ORCID: 0000-0003-2706-7240

STEPANOV Sergey I.
s.i.stepanov@gmail.com
ORCID: 0000-0003-1324-3055

PAVLOV Ivan S.
win8765495@gmail.com
ORCID: 0000-0001-9366-0101

NIKOLAEV Vladimir I.
Nikolaev.V@mail.ioffe.ru
ORCID: 0000-0002-5630-0833

PECHNIKOV Aleksey I.
pechnikovai@gmail.com
ORCID: 0000-0003-4604-1935

Received 28.09.2022. Approved after reviewing 10.11.2022. Accepted 17.11.2022.

Conference materials

UDC 538.9

DOI: <https://doi.org/10.18721/JPM.161.103>

Time-resolved photoluminescence study of InGaAs/GaAs quantum well-dots with upconversion method

I.A. Melnichenko ¹✉, A.M. Nadtochiy ¹, K.A. Ivanov ¹, I.S. Makhov ¹, M.V. Maximov ²,
S.A. Mintairov ³, N.A. Kalyuzhnyy ³, N.V. Kryzhanovskaya ¹, A.E. Zhukov ¹

¹HSE University, St. Petersburg, Russia;

²Alferov University, St. Petersburg, Russia;

³Ioffe Institute, St. Petersburg, Russia

✉ imelnichenko@hse.ru

Abstract. For the first time we show time-resolved photoluminescence dependencies with 0.2 ps resolution for the novel type of InGaAs/GaAs quantum-sized heterostructures, referred to as quantum well-dots (QWDs). Photoluminescence upconversion method, that allows achieving time resolution up to 0.2 ps, was used to obtain time-resolved spectra for light (*lh*) and heavy hole (*hh*) optical transitions of QWDs. We concluded that the capture of charge carriers to the *lh* and *hh* states of QWDs occurs simultaneously in the time range of ~ 10 ps and is probably limited by carrier diffusion in the matrix. The characteristic time of photoluminescence decay for the *hh* state (3 ns) was found to be greater than that of *lh* one (2 ns).

Keywords: time-resolved photoluminescence, InGaAs heterostructures, quantum well-dots

Funding: This work was supported by the Russian Science Foundation (grant No. 18 12 00287, <https://rscf.ru/project/18-12-00287/>). Support of optical measurements from the Basic Research Program of the National Research University Higher School of Economics is gratefully acknowledged.

Citation: Melnichenko I.A., Nadtochiy A.M., Ivanov K.A., Makhov I.S., Maksimov M.V., Mintairov S.A., Kalyuzhnyy N.A., Kryzhanovskaya N.V., Zhukov A.E. Time-resolved photoluminescence study of InGaAs/GaAs quantum well-dots with upconversion method, St. Petersburg State Polytechnical University Journal. Physics and Mathematics. 16 (1.1) (2023) 22–27. DOI: <https://doi.org/10.18721/JPM.161.103>

This is an open access article under the CC BY-NC 4.0 license (<https://creativecommons.org/licenses/by-nc/4.0/>)

Материалы конференции

УДК 538.9

DOI: <https://doi.org/10.18721/JPM.161.103>

Исследование фотолуминесценции InGaAs/GaAs квантовых яма-точек с временным разрешением методом АП-конверсии

И.А. Мельниченко ¹✉, А.М. Надточий ¹, К.А. Иванов ¹, И.С. Махов ¹, М.В. Максимов ²,
С.А. Минтаиров ³, Н.А. Калюжный ³, Н.В. Крыжановская ¹, А.Е. Жуков ¹

¹Национальный исследовательский университет «Высшая школа экономики», Санкт-Петербург, Россия;

²Академический университет им. Ж.И. Алфёрова, Санкт-Петербург, Россия;

³Физико-технический институт им. А.Ф. Иоффе РАН, Санкт-Петербург, Россия

✉ imelnichenko@hse.ru

Аннотация. Впервые показана зависимость сигнала фотолуминесценции (ФЛ) от времени для нового типа квантоворазмерных гетероструктур InGaAs/GaAs, называемых квантовыми яма-точками (КЯТ). Был использован метод ап-конверсии фотолуминесценции, позволивший достичь временного разрешения до 0,2 пс и получить временные зависимости сигнала ФЛ для оптических переходов легких (*lh*) и тяжелых

дырок (hh) в КЯТ. Было показано, что захват носителей заряда в lh и hh состояния КЯТ происходит одновременно в диапазоне времени ~ 10 пс, и, вероятно, ограничивается диффузией носителей в матрице. Характерное время затухания фотолюминесценции для состояния hh (3 нс) оказалось больше, чем для lh (2 нс).

Ключевые слова: время-разрешенная фотолюминесценция, InGaAs гетероструктуры, квантовые яма-точки

Финансирование: Работа выполнена при поддержке Российского научного фонда (грант № 18-12-00287, <https://rscf.ru/project/18-12-00287/>). Выражается благодарность за поддержку оптических измерений из программы фундаментальных исследований НИУ ВШЭ.

Ссылка при цитировании: Мельниченко И.А., Надточий А.М., Иванов К.А., Махов И.С., Максимов М.В., Минтаиров С.А., Калюжный Н.А., Крыжановская Н.В., Жуков А.Е. Исследование фотолюминесценции InGaAs/GaAs квантовых яма-точек с временным разрешением методом АП-конверсии // Научно-технические ведомости СПбГПУ. Физико-математические науки. 2023. Т. 16. № 1.1. С. 22–27. DOI: <https://doi.org/10.18721/JPM.161.103>

Статья открытого доступа, распространяемая по лицензии CC BY-NC 4.0 (<https://creativecommons.org/licenses/by-nc/4.0/>)

Introduction

A lot of modern optoelectronic devices, such as microlasers [1] or solar cells [2], widely use an active area based on quantum wells (QWs) or quantum dots (QDs). Both types of quantum-sized heterostructures have their advantages and disadvantages determined by their structural and optical properties. For example, QD structures are less affected by the structural defects during growth process, have comparatively wide range of emission wavelength and suppressed lateral carrier diffusion. QWs, on the other hand, have much higher optical gain/absorption than QDs, but due to long diffusion length of charge carriers in lateral plane its application in microdevices is limited. The need to further optimize the properties of modern devices, as well as the need to develop new applications, leads researchers to look for a new configuration of the quantum-sized active region.

Recently developed quantum well-dots (QWDs) are attractive, because they combine properties of both QD and QW structures. QWDs can be described as a dense array of small QDs or QW with quasi regular variation in its composition and width. Such structures have suppressed formation of defects due to partial relaxation of elastic strain and allow achieving maximum material gain at $1.1 \cdot 10^4 \text{ cm}^{-1}$ [3]. InGaAs/GaAs QWDs used as an active medium in microlasers with a diameter of 20–50 μm made it possible to obtain continuous wave (CW) lasing with a wavelength of $\sim 1.1 \mu\text{m}$ at room temperature and at temperatures as high as 110 $^\circ\text{C}$ [4].

However, the studies of processes of relaxation and recombination of charge carriers in QWDs remain relevant. In this work we studied optical properties of InGaAs/GaAs QWDs with time-resolved photoluminescence to provide a deeper understanding of charge carriers' kinetics in the QWDs. The results obtained are in demand for the realization of ultrahigh-frequency electrooptical devices based on QWDs.

Experimental

The InGaAs/GaAs heterostructure with QWDs was grown by MOVPE epitaxy on a slightly misoriented GaAs (100) substrate. After deposition of the GaAs buffer layer, the 200 nm thick $\text{Al}_{0.39}\text{Ga}_{0.61}\text{As}$ layer was grown to prevent carrier leakage from quantum-confined active region to the substrate. The active region was formed by a 1 layer of $\text{In}_{0.4}\text{Ga}_{0.6}\text{As}$ with deposited thickness of 8 monolayers and placed in the middle of a 600 nm thick GaAs layer [5]. The structure was terminated with a 50 nm thick $\text{Al}_{0.39}\text{Ga}_{0.61}\text{As}$ layer and 5 nm GaAs cap.

Photoconductivity spectrum was measured using a conventional lock-in technique with a halogen lamp in a combination with a monochromator as a light source in the geometry of normal light incidence. Indium contacts were soldered onto the surface of the structure as described in [6]. Photoluminescence spectrum in CW regime was recorded using 532 nm YAG:Nd laser and cooled Ge photodiode in combination with monochromator.

Time-resolved photoluminescence (TRPL) spectra of the InGaAs/GaAs heterostructure were investigated at room temperature with subpicosecond time resolution using the upconversion method. The source of femtosecond radiation was the mode-locked Ti:Sapphire “Coherent Mira 900” laser with a pulse duration of ~ 130 fs, repetition rate of 76 MHz, and tunable wavelength from 700 to 980 nm. PL signal was registered with FOG-100 spectrometer (CDP Systems). The laser pulse with wavelength of 780 nm was divided into two beams using a beamsplitter. First of them was passed through the delay line, while the second one was used to excite the PL in the sample. PL signal was collected by the optical system and mixed with the first beam on a nonlinear optical BBO crystal. Resulted upconverted signal was registered using a monochromator and a photomultiplier tube. This setup configuration provided TRPL spectra in the wavelength range of 850...1200 nm with optical resolution of 10–15 nm and up to 8 ns of time delay with time resolution of ~ 0.2 ps.

Results and Discussion

In Fig. 1 we demonstrate the scheme of the grown structure and transition electron microscopy (TEM) cross-section of QWD layer as insert. The formation of “islands” with variable In content is caused by misoriented substrate orientation (from 2° to 15° tilt degree). Atomic steps, caused by vicinal surface, facilitate creation of such islands of variable In content. Misoriented substrate also allows growing bigger QD (~ 20 – 30 nm) that cover many atomic steps [7].

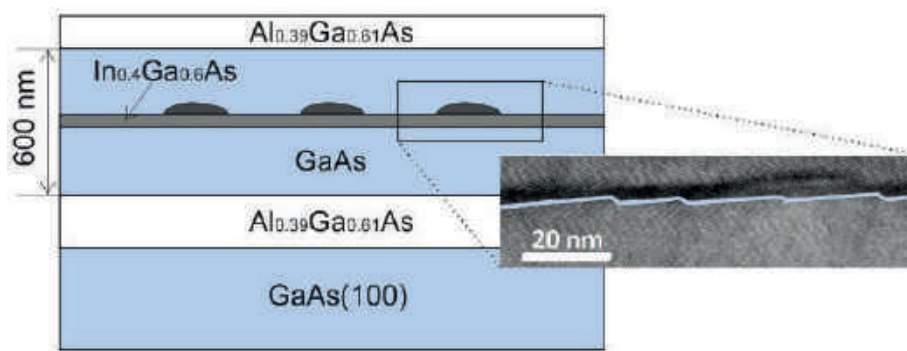


Fig. 1. Scheme of grown structure with QWD region. Inset shows a TEM cross-section of misoriented sample with QWDs

Photoluminescence (PL) and photoconductivity (PC) spectra are shown in Fig. 2. We observe PC plateau below ~ 870 nm, which corresponds to the GaAs matrix, and two peaks at 980 nm and 1040 nm. According to previous discussions [8, 9], these two peaks are attributed to radiative transitions between electron level $e1$ and two hole levels: heavy and light holes ($e1-hh1$ and $e1-lh1$). In contrast to PC, PL spectrum in Fig. 2 demonstrates Stokes-shifted peaks for GaAs matrix and $e1-hh1$ transition, and only a shoulder for $e1-lh1$. This could be explained by step-shaped density of states for QWDs, leading to overlay of PL signal of $e1-lh1$ with continuance of $e1-hh1$.

Fig. 3 demonstrates TRPL spectra taken at different delays. One can see pronounced GaAs peak decaying with time and one broad QWD peak at ~ 1020 nm, remaining its intensity during the period of 2 ns. Even though TRPL spectra do not evidence different QWD states, we found it reasonable to analyze in details kinetics for wavelength corresponding to light and heavy hole states, as well as GaAs.

PL kinetics of QWD structure taken at room temperature and different wavelength of GaAs matrix (~ 875 nm), $e1-lh1$ (~ 980 nm), and $e1-hh1$ transitions of QWD (~ 1040 nm) are shown in Fig. 4. Pumping power was on an average level of 85 mW, which corresponds to fluence ~ 10 $\mu\text{J}/\text{cm}^2$. GaAs curve demonstrates picosecond risetime, relatively fast decay at initial part (Fig. 4, *b*) and after that monoexponential decay (Fig. 4, *a*) with $\tau \sim 1.4$ ns. We attribute fast decay in GaAs peak to the effect of filling of QWD states with carriers resulting in relatively fast decrease in carrier concentration in GaAs.

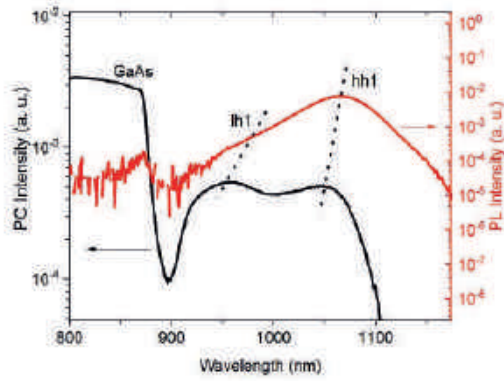


Fig. 2. PL and PC spectra of the sample, obtained in CW regime, room temperature

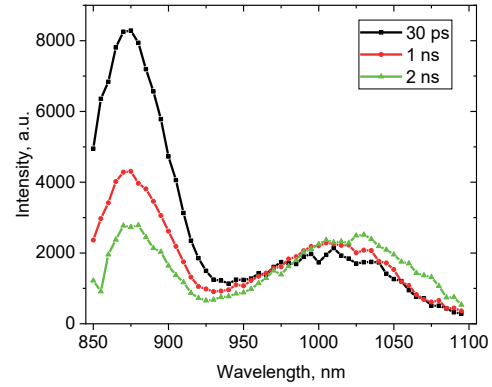


Fig. 3. Evolution of TRPL spectrum with time after excitation, room temperature

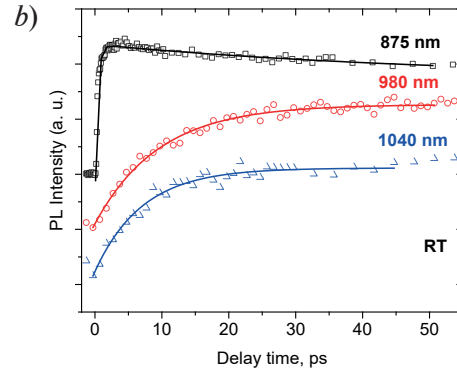
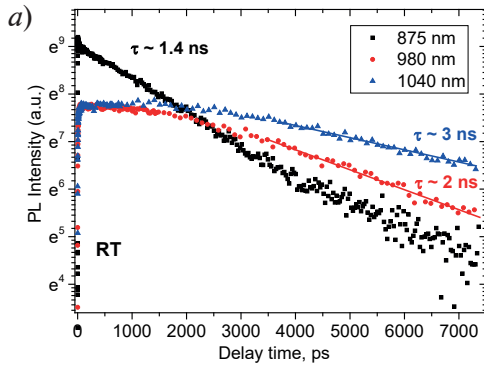


Fig. 4. PL kinetics taken at different wavelengths at room temperature, full time range (a), risetime range (b). The curves are normalized and shifted on (b) for clarity of presentation. Symbols show experimental data, lines — fitting

Initial part of GaAs curve may be fitted well with empirical equation (given $\tau_{\text{rise}} \ll \tau_{\text{decay}}$):

$$I_{\text{PL}}(t) = A(e^{-t/\tau_{\text{decay}}} - e^{-t/\tau_{\text{rise}}} + C),$$

giving characteristic risetime, $\tau_{\text{rise}} \sim 0.4 \pm 0.02$ ps, and decay one, $\tau_{\text{decay}} \sim 40 \pm 20$ ps.

At the same time initial parts of QWDs' curves show typical 1st order step response and fitted well with:

$$I_{\text{PL}}(t) = A(1 - e^{-t/\tau_{\text{rise}}}),$$

resulting in $\tau_{\text{rise}} \sim 9.5$ ps and ~ 7 ps for 980 nm and 1040 nm, correspondingly. It seems clear, that both hh and lh states are filling with charge carriers simultaneously due to their comparable risetime, and there is no cascade relaxation in QWDs over their states. However, comparison to results from Aleshkin *et al.* [10] shows, that risetime values of QWD peaks several times higher than that of InGaAs QW of similar optical range (7–9 ps vs 1–3 ps). Such difference can be caused by longer diffusion time of charge carriers in larger GaAs reservoir to single QWD layer comparing to the much smaller GaAs regions in case in [10]. Also note comparable or even longer decay of GaAs peak at initial part than risetime of QWD peaks (~ 40 ps vs ~ 10 ps). This fact may indicate predominant exciton diffusion and capture in QWDs, rather than separate electron or hole capture, because otherwise, one must see decay in GaAs faster than increase in QWDs.

Further time kinetics of QWD PL could be characterized by several sequential processes. After the initial filling of states with charge carriers, hh and lh transitions remain the same intensity for ~ 1 ns (Fig. 4, a). As long as GaAs matrix remains filled with charge carriers, they migrate to QWDs and provide stable source of carriers' reproduction instead of those which have recombined. When carrier density in GaAs decreases, we observe beginning of PL decaying of lh state. Depletion of lh state starts at delay ~ 1 ns, while hh state stays filled until 2.5–3 ns. This probably illustrates general dynamic of charge carrier concentration of QWDs (Fig. 5).

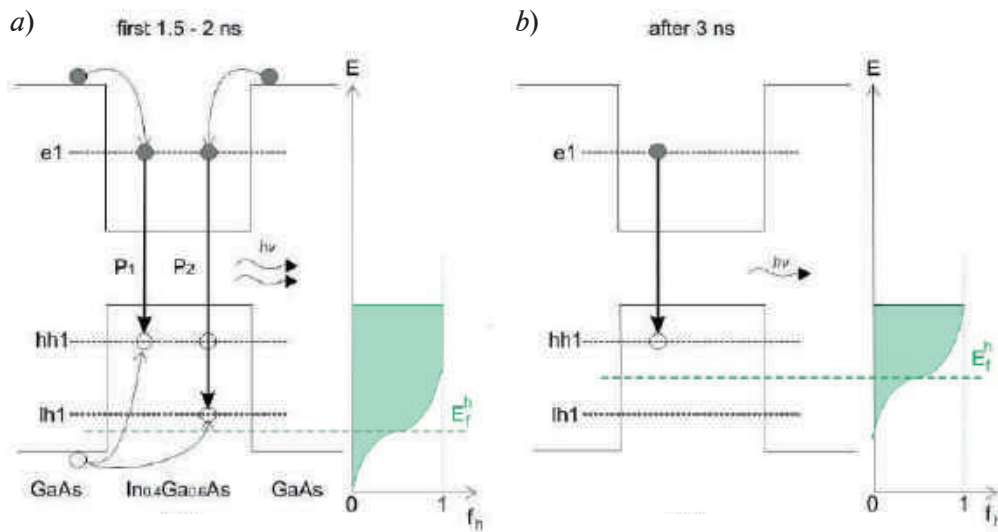


Fig. 5. Schematic presentation of QWD band structure and probable time evolution of carrier dynamics during (a) first 2 ns of laser excitation and (b) after first 1.5–2 ns with quasi Fermi functions

According to Aleshkin *et al.* [10] carrier relaxation rate in InGaAs QW, which is close in properties to QWDs, reaches 100 meV/ps at room temperature. This means that during the time range of approximately 5 ps charge carriers are thermalized and distributed over QWD states according to Fermi-Dirac statistic with quasi-Fermi levels (Fig. 5). As the rate of carrier recombination in QWDs is much slower than nanoseconds, according to Fig. 4, *b* all QWD states may be considered as the united system (Fig. 5), meaning that eliminating or adding carrier to any QWD state influences the others. As concentration of charge carriers is decreasing in QWDs and quasi-Fermi level in the valence band shifts upward (is opposite for electrons), PL signal of *lh* state (Fig. 5, *a*), first, and then *hh* one (Fig. 5, *b*) is starting to decay.

According to above, relatively fast decay of PL for *lh* state ($\tau_{\text{decay}} \sim 2$ ns at delays 4–7 ns (Fig. 4, *a*) reflects high rate of carrier loss in heavily filled QWDs, when the carriers recombine both from *lh* and *hh* states (Fig. 5, *a*). Switching to more moderate QWDs' carrier filling (Fig. 5, *b*) results in a weak PL of *lh* state and, correspondingly, slower PL decay of *hh* state ($\tau_{\text{decay}} \sim 3$ ns), as the carriers recombine primarily through *hh* state.

Overall PL lifetime at a level of e^{-1} for *hh* state reaches 6–8 ns (Fig. 4, *a*) and correlates well with the previous results [5], proving that non-radiative recombination rate is relatively low due to high quality of the sample.

Conclusion

The results obtained allow us to conclude that the capture of charge carriers from the GaAs matrix to the QWD *lh* and *hh* states occurs simultaneously and relatively slow (~ 10 ps). Long capture time can be explained by a long time of carrier diffusion through large GaAs reservoir. According to the GaAs fast decay time, we assume that different charge carriers (electrons and holes) diffuse and capture in QWDs simultaneously. Charge carriers form inside QWDs united system of thermalized carriers with Fermi-Dirac distribution and quasi-Fermi level. The characteristic time PL decay for the *hh* state (3 ns) was found to be greater than that of *lh* one (2 ns). The values of rise and decay times possess great importance for the design of high-speed devices based on QWDs and the estimation of their potentially achievable characteristics.

REFERENCES

1. Michler P., Kiraz A., Zhang L., Becher C. Hu E., and Imamoglu A., Laser emission from quantum dots in microdisk structures, *Applied Physics Letters*. 77 (2) (2000) 184.
2. Luque A., Martí A. Increasing the efficiency of ideal solar cells by photon induced transitions at intermediate levels, *Physical review letters*. 78 (26) (1997) 5014.



3. Gordeev N.Y., Maximov M.V., Payusov A.S., Serin A.A., Shernyakov Y.M., Mintairov S.A., Kalyuzhnyy N.A., Nadtochiy A.M., and Zhukov A.E., Material gain of InGaAs/GaAs quantum well-dots, *Semiconductor Science and Technology*. 36 (1) (2020) 015008.
4. Moiseev E., Kryzhanovskaya N., Maximov M., Zubov F., Nadtochiy A., Kulagina M., Zadiranov Y., Kalyuzhnyy N., Mintairov S., and Zhukov A., Highly efficient injection microdisk lasers based on quantum well-dots, *Optics Letters*. 43 (19) (2018) 4554.
5. Nadtochiy A.M., Mintairov S.A., Kalyuzhnyy N.A., Maximov M.V., Sannikov D.A., Yagafarov T.F., and Zhukov A.E., Time-resolved photoluminescence of InGaAs nanostructures different in quantum dimensionality, *Semiconductors*. 53 (11) (2019) 1489.
6. Nadtochiy A.M., Maximov M.V., Mintairov S.A., Kalyuzhnyy N.A., Nevedomskiy V.N., Rouvimov S.S., and Zhukov A.E., Gradual evolution from quantum-well-like to quantum-dot-like characteristics in InGaAs/GaAs nanostructures, *Physica status solidi*. 255 (9) (2018) 1800123.
7. Maximov M.V. et al., Light emitting devices based on quantum well-dots, *Applied Sciences*. 10 (3) (2020) 1038.
8. Mintairov S.A. et al., Experimental and theoretical examination of the photosensitivity spectra of structures with In_{0.4}Ga_{0.6}As quantum well-dots of the optical range (900–1050 nm), *Technical Physics Letters*. 46 (3) (2020) 203–206.
9. Kharchenko A.A. et al., Study of waveguide absorption in InGaAs “quantum well-dots” heterostructures, *Nano-Structures and Nano-Objects*. 25 (2021) 100628.
10. Aleshkin V.Y. et al., Picosecond photoluminescence dynamics of InGaAs/GaAs heterostructure with quantum wells, *Fizika I Technika Poluprovodnikov (Semiconductors)*. 46 (7) (2012) 940-943.

THE AUTHORS

MELNICHENKO Ivan A.

imelnichenko@hse.ru

ORCID: 0000-0003-3542-6776

NADTOCHIY Alexey M.

al.nadtochy@mail.ioffe.ru

ORCID: 0000-0003-0982-907X

IVANOV Konstantin I.

kivanov1992@gmail.com

ORCID: 0000-0003-2165-1067

MAKHOV Ivan S.

makhoviv@gmail.com

ORCID: 0000-0003-4527-1958

MAXIMOV Mikhail V.

maximov.mikh@gmail.com

ORCID: 0000-0002-9251-226x

MINTAIROV Sergey A.

mintairov@scell.ioffe.ru

ORCID: 0000-0002-6176-6291

KALYUZHNYIY Nikolay A.

nickk@mail.ioffe.ru

ORCID: 0000-0001-8443-4663

KRYZHANOVSKAYA Natalia V.

nataliakryzh@gmail.com

ORCID: 0000-0002-4945-9803

ZHUKOV Alexey E.

zhukale@gmail.com

ORCID: 0000-0002-4579-0718

Received 30.10.2022. Approved after reviewing 08.11.2022. Accepted 08.11.2022.

Conference materials

UDC 538.956

DOI: <https://doi.org/10.18721/JPM.161.104>

Complex permittivity of graphene-containing shungite within 0.05–15 MHz

R.I. Korolev ¹✉, I.V. Antonets ¹, E.A. Golubev ²

¹ Department of Radiophysics, Pitirim Sorokin Syktyvkar State University, Syktyvkar, Russia;

² Institute of Geology of Komi SC, RAS, Syktyvkar, Russia

✉ korolev36a@gmail.com

Abstract. The paper presents the results of experimental studies of changes in the complex permittivity of natural graphene-containing shungites with different carbon content. A technique for determining the real and imaginary parts of the permittivity for conducting samples is presented. The dependences of the dielectric loss tangent and the real part of the permittivity on the carbon concentration for three resonant frequencies in the range of 0.05–15 MHz are studied.

Keywords: shungite, permittivity, carbon concentration

Funding: This study was funded by RSF, according to the research project No. 21 47 00019.

Citation: Korolev R.I., Antonets I.V., Golubev E.A. Complex permittivity of graphene containing shungite within 0.05–15 MHz, St. Petersburg State Polytechnical University Journal. Physics and Mathematics. 16 (1.1) (2023) 28–32. DOI: <https://doi.org/10.18721/JPM.161.104>

This is an open access article under the CC BY-NC 4.0 license (<https://creativecommons.org/licenses/by-nc/4.0/>)

Материалы конференции

УДК 538.956

DOI: <https://doi.org/10.18721/JPM.161.104>

Комплексная диэлектрическая проницаемость графенсодержащего шунгита в диапазоне 0,05–15 МГц

Р.И. Королев ¹✉, И.В. Антонец ¹, Е.А. Голубев ²

¹ Кафедра радиофизики и электроники, Сыктывкарский государственный университет имени Питирима Сорокина, г. Сыктывкар, Россия;

² Институт геологии Коми НЦ УрО РАН, г. Сыктывкар, Россия

✉ korolev36a@gmail.com

Аннотация. В работе представлены результаты экспериментальных исследований изменения комплексной диэлектрической проницаемости в природных графенсодержащих шунгитах с различным содержанием углерода. Представлена методика определения действительной и мнимой частей диэлектрической проницаемости проводящих образцов. Исследованы зависимости тангенса угла диэлектрических потерь и действительной части диэлектрической проницаемости от концентрации углерода для трех резонансных частот в диапазоне 0,05–15 МГц.

Ключевые слова: шунгит, диэлектрическая проницаемость, концентрация углерода

Финансирование: Исследование выполнено при финансовой поддержке РФФ, в соответствии с исследовательским проектом № 21-47-00019.

Ссылка при цитировании: Королев Р.И., Антонец И.В., Голубев Е.А. Комплексная диэлектрическая проницаемость графенсодержащего шунгита в диапазоне 0,05–15 МГц // Научно-технические ведомости СПбГПУ. Физико-математические науки. 2023. Т. 16. № 1.1. С. 28–32. DOI: <https://doi.org/10.18721/JPM.161.104>

Статья открытого доступа, распространяемая по лицензии CC BY-NC 4.0 (<https://creativecommons.org/licenses/by-nc/4.0/>)



Introduction

In modern technologies, materials with improved and new functional properties are used. Obtaining such materials is often costly from an economic point of view. Therefore, the study of natural objects in order to identify such properties has great prospects. Conductive and high frequency properties are among the most demanded. In this regard, the electrically conductive properties (with emphasis on the determination of the complex permittivity) of the unique natural disordered carbon of shungites from Karelia were studied. A technique for measuring the dielectric constant of conducting samples is presented.

Materials and Methods

The parallelepiped samples were made from natural shungite by cutting and subsequently grinding the faces. The sample height was 1.5 mm, and the side length was 6.0 mm. Two opposite surfaces were metallized by magnetron sputtering of a thin layer of gold in vacuum using argon as a working gas. The total impedance and phase shift at frequencies of 0.05–15 MHz were measured using an E7-29 immittance meter. The specific conductivity for calculating the dielectric loss tangent was determined from the reciprocal value of the electrical resistivity measured at the studied current frequency by the two-probe method [1–3]. To obtain resonance characteristics, a parallel oscillatory circuit with replaceable inductors in a shielded case was used, connected to UP-5. The air condenser for the oscillatory circuit was made of FR-4 foil fiberglass by milling square-shaped plates with an area of $37.4 \pm 0.1 \text{ mm}^2$. To arrange the plates at a fixed distance and ensure plane-parallelism, 4 spacers were used at the corners of the fiberglass. The distance between the plates was $1.95 \pm 0.01 \text{ mm}$. The plate leads were located on opposite sides to reduce the effect on the capacitance. To determine the interturn capacitance of the inductor and the screen capacitance, tubular ceramic capacitors with a capacitance of $3.23 \pm 0.05 \text{ pF}$ and $6.25 \pm 0.02 \text{ pF}$ were connected in parallel to the oscillatory circuit with an empty air capacitor. Based on the obtained resonant frequencies, the additional capacitance caused by the interturn capacitance of the coil and the screen capacitance was calculated. The resonant frequencies were determined by the method of approximation of the Lorentz function from the graphic dependences of the impedance on the frequency [3, 4]. The estimate of the accuracy of calculating the permittivity by the method of standard deviations was 16%.

Consider an oscillatory circuit consisting of a coil with inductance L and an interturn capacitance C_L and an air plane-parallel capacitor connected in parallel with a capacitance C_0 . The inductor is placed in a metal shield to reduce the influence of external electromagnetic field. The resonant frequency of an empty circuit is determined by the formula [5]:

$$f_0 = \frac{1}{2\pi[L(C_0 + C_L)]^{1/2}}, \quad (1)$$

where the capacitance of the capacitor is:

$$C_0 = \frac{\varepsilon_0 S_0}{d_0}, \quad (2)$$

S_0 is condenser area, d_0 is distance between plates, ε_0 is vacuum permittivity.

When a sample is introduced into the gap between the capacitor plates, the circuit frequency will change:

$$f_x = \frac{1}{2\pi[L(C_x + C_L)]^{1/2}}, \quad (3)$$

where C_x is capacitance of a capacitor with installed sample.

The location of the sample in the measuring capacitor of the oscillatory circuit is shown in Fig. 1. Due to the complexity of manufacturing the dimensions of the sample equal to the dimensions of the measuring capacitor, as well as the high conductivity of the sample, it becomes

necessary to take into account the capacitance associated with incomplete filling of the area of the sample measuring capacitor lining C_δ :

$$C_\delta = \frac{\varepsilon_0(S_0 - S_1)}{d_0}, \quad (4)$$

and capacitance due to incomplete filling of the capacitor volume:

$$C_{10} = \frac{\varepsilon_0 S_1}{d_0 - d_1}, \quad (5)$$

where S_1 is sample area, d_1 is sample thickness.

The measuring oscillatory circuit can be represented as an equivalent electrical circuit in Fig. 2, and the capacitance of the measuring capacitor C_x is defined as:

$$C_x = \frac{C_1 C_{10}}{C_1 + C_{10}} + C_\delta, \quad (6)$$

where C_1 is capacitance of the capacitor, formed by the sample:

$$C_1 = \frac{\varepsilon \varepsilon_0 S_1}{d_1}. \quad (7)$$

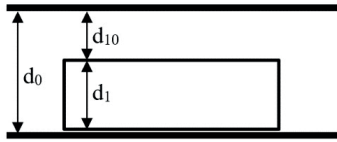


Fig. 1. Cross section of measuring capacitor with sample

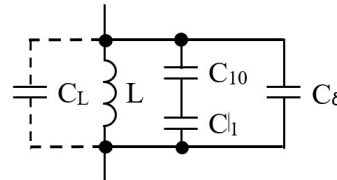


Fig. 2. Equivalent electrical circuit of a parallel oscillatory circuit with a sample

We introduce the following notation:

$$\Delta F = \frac{f_0}{f_x}, \quad (8)$$

$$A = \Delta F^2 - 1 \quad (9)$$

$$B = S_0 A + S_1 \quad (10)$$

Solving Equations (1) and (3) together, taking into account (8–10), we obtain an expression for the real part of the permittivity ε' [5–7]:

$$\varepsilon' = \frac{\varepsilon_0 B + d_0 C_L A}{\varepsilon_0 (S_0 d_0 A - d_1 B) + d_0 C_L A (d_0 - d_1)} d_1, \quad (11)$$

To determine the interturn capacitance we jointly solve Equations (1, 2, 8) with respect to C_L , we obtain:

$$C_L = \frac{-\Delta F^2 C_1 + C_2}{\Delta F^2 - 1}, \quad (12)$$

In this case, C_1 and C_2 are the capacitances of additional capacitors, connected to an unfilled measuring capacitor, ΔF is the ratio of the resonant frequencies of the circuit with these additional capacitances. The dielectric loss tangent is determined by the formula:

$$\tan \delta = \frac{\sigma}{2\pi f_0 \varepsilon_0 \varepsilon'}, \quad (13)$$



where σ — sample conductivity:

$$\sigma = \frac{1}{\rho} = \frac{d_1}{S_1 Z \cos \varphi}, \quad (14)$$

where Z — sample impedance, φ — angle of phase shift between the current and voltage of the probing signal.

The imaginary part of the permittivity is related to the loss tangent by the expression:

$$\varepsilon'' = \varepsilon' \tan \delta, \quad (15)$$

The desired complex permittivity:

$$\varepsilon = \varepsilon' - i\varepsilon''. \quad (16)$$

Results and Discussion

Figures 3 and 4 show the dependences of the permittivity (Fig. 3) and the dielectric loss tangent (Fig. 4) on the carbon concentration of shungites at three different resonant frequencies of the oscillatory circuit: 2.6, 8.7, and 14.36 MHz. As it can be seen from the figures, at the same carbon content, the permittivity somewhat increases with increasing frequency, and the dielectric loss tangent decreases, which corresponds to the behavior of ionic relaxation at the indicated frequencies.

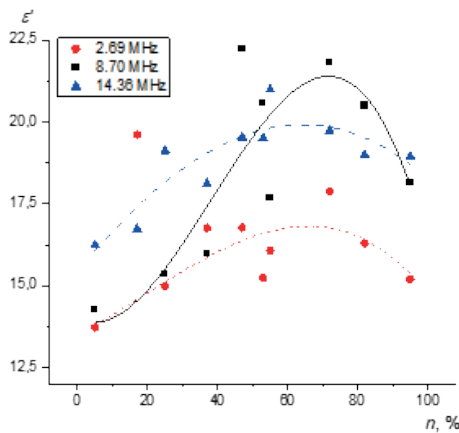


Fig. 3. Dependences of the real part of the permittivity on the carbon concentration at different frequencies

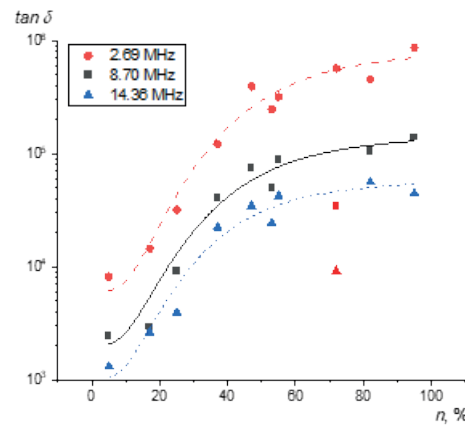


Fig. 4. Dependences of the dielectric loss tangent on the carbon concentration at different frequencies

Shungites have rather high electrical conductivity (hundreds–thousands of S/m) even at low carbon content (from 17% and higher) [1, 2]. Therefore, the dielectric loss tangent of the samples is also very significant, but it decreases with increasing frequency (Fig. 4). Thus, at a carbon concentration of 5%, with an increase in frequency from 2.6 to 8.7 MHz, $\tan \delta$ decreases by a factor of three, and with an increase in frequency from 8.7 to 14.4 MHz, by one and a half times. For high-carbon shungites with a carbon concentration of 90%, with increasing frequency, the dielectric loss tangent decreases by 5 and 2 times, respectively. The qualitative behavior of the dependences of the loss tangent on the carbon concentration is preserved for all frequencies. According to Fig. 4, at a carbon content of 60–70%, the loss tangent begins to saturate and is only weakly dependent on concentration. In this case, due to the smallness of the real part of the permittivity in comparison with the imaginary one, the qualitative behavior ε'' of the carbon content is almost coincident with the dependence of $\tan \delta$.

As can be seen from Fig. 3, the real part of the dielectric constant of shungites varies depending on the frequency in the range of 0.05–15 MHz and the carbon concentration n in the range from 13.5 to 22.5, which corresponds to the values presented in [8]. An increase in the carbon concentration leads to a gradual increase in the real permittivity ε' up to $n = 60$ –70%, at which the dielectric loss tangent saturates. With a further increase in n , the real part of the permittivity sharply decreases. This behavior ε' is associated with an increase in the conductivity of shungite

due to the formation of conductive channels from carbon, which leads to a decrease in the volume of dielectric inclusions and the area of interboundary regions with the dielectric phase. At low carbon content, the main contribution to the dielectric permittivity is made by the ionic and dipole nature of the dielectric permittivity; at high carbon concentrations, the dipole nature begins to transform into atomic one. The peak at the resonant frequency of 8.70 MHz at $n = 70\%$ can be associated with the resonant dispersion of the permittivity, which indicates the ionic nature of the polarization.

Conclusion

In this paper, the dependences of the dielectric loss tangent and the real part of the dielectric constant as a function of carbon concentration for three resonant frequencies in the range of 0.05–15 MHz are studied. The dielectric permittivity in shungite grows with an increase in the carbon content up to $n = 60\text{--}70\%$. In this range of carbon concentration, there is a peak in the dielectric constant. A further sharp decrease in the permittivity with an increase in the carbon content occurs due to an increase in conductivity. The peak at the resonant frequency of 8.70 MHz at $n = 70\%$ indicates the ionic nature of the polarization.

REFERENCES

1. Antonets I.V., Golubev E.A., Shavrov V.G., Shcheglov V.I., Application of the independent channel method for determining the electrical conductivity of graphene-containing shungite, Journal of radio electronics. 7 (2021). <http://jre.cplire.ru/jre/jul21/6/text.pdf>
2. Golubev E.A., Antonets I.V., Shcheglov V.I., Static and dynamic conductivity of nanostructured carbonaceous shungite geomaterials, Materials chemistry and physics. 226 (2019) 195–203.
3. Antonets I.V., Golubev E.A., Korolev R.I., Electrophysical parameters of shungite, AIP Conf. Proc. 2467 (2022) 020026.
4. Antonets I.V., Golubev E.A., Korolev R.I., St. Petersburg Polytechnic University Journal: Physics and Mathematics. (2023) (in press).
5. Keysight, Basics of Measuring the Dielectric Properties of Materials Application Note. (2017).
6. Hewlett-Packard Company, Dielectric constant measurement of solid materials using the 16451B dielectric test fixture Application Note 308–1. (1998).
7. GOST 22372-77 Dielectric materials. Methods of determination of permittivity and powerfactor with in a frequency range of 100 to 5 MHz.
8. Moshnikov I.A., Kovalevsky V.V., Lazareva T.N., Petrov A.V., The use of shungite rocks in the creation of radio shielding composite materials, Petrozavodsk: Geodynamics, magmatism, sedimentogenesis and minerageny of the North-West of Russia. (2007) 272–274.

THE AUTHORS

KOROLEV Roman I.
korolev36a@gmail.com
ORCID: 0000-0002-5091-1385

GOLUBEV Evgeniy A.
yevgenyGolubev74@mail.ru
ORCID: 0000-0001-5354-937X

ANTONETS Igor V.
aiv@mail.ru
ORCID: 0000-0003-1103-4313

Received 29.09.2022. Approved after reviewing 06.12.2022. Accepted 06.12.2022.

Conference materials

UDC 537.9

DOI: <https://doi.org/10.18721/JPM.161.105>

Dielectric spectroscopy of Ag₂S nanowires synthesized in porous silicate glasses

A.V. Il'inskiy¹, R.A. Castro², M.E. Pashkevich³,

I.O. Popova^{2✉}, A.I. Sidorov⁴, E.B. Shadrin¹

¹ Ioffe Institute, St. Petersburg, Russia;

² Herzen Russian State Pedagogical University, St. Petersburg, Russia;

³ Peter the Great St. Petersburg Polytechnic University, St. Petersburg, Russia;

⁴ ITMO University, St. Petersburg, Russia

✉ timof-ira@yandex.ru

Abstract. We have studied the frequency dielectric spectra of silver sulfide nanowires synthesized in porous silicate glasses. A possible mechanism of the thermal superionic phase transition in the samples is discussed. In this work, based on the analysis of the DS, the following conclusion was made. After the superionic phase transition occurs, the octa coordinated Ag⁺ ions become mobile, representing the elements of a “viscous liquid”, while the tetra-coordinated Ag⁺ ions, remaining immobile (up to phonon vibrations), stabilize the crystal lattice of the material.

Keywords: superionic phase transition, nanowires silver iodide, nanoporous silicate glasses, dielectric spectroscopy

Citation: Il'inskiy A.V., Castro R.A., Pashkevich M.E., Popova I.O., Sidorov A.I., Shadrin E.B. Dielectric spectroscopy of Ag₂S nanowires synthesized in porous silicate glasses, St. Petersburg State Polytechnical University Journal. Physics and Mathematics. 16 (1.1) (2023) 33–37. DOI: <https://doi.org/10.18721/JPM.161.105>

This is an open access article under the CC BY-NC 4.0 license (<https://creativecommons.org/licenses/by-nc/4.0/>)

Материалы конференции

УДК 537.9

DOI: <https://doi.org/10.18721/JPM.161.105>

Диэлектрическая спектроскопия нанонитей, синтезированных в пористых силикатных стеклах

А.В. Ильинский¹, Р.А. Кастро², М.Э. Пашкевич³,

И.О. Попова^{2✉}, А.И. Сидоров⁴, Е.Б. Шадрин¹

¹ Физико-технический институт им. А.Ф. Иоффе РАН, Санкт-Петербург, Россия;

² РГПУ им. А.И. Герцена, Санкт-Петербург, Россия;

³ Санкт-Петербургский политехнический университет Петра Великого, Санкт-Петербург, Россия;

⁴ Университет ИТМО, Санкт-Петербург, Россия

✉ timof-ira@yandex.ru

Аннотация. В работе изучены частотные диэлектрические спектры нанонитей сульфида серебра, синтезированных в пористых силикатных стеклах. Обсуждается возможный механизм термического суперионного фазового перехода в таких образцах. На базе анализа ДС сделан следующий вывод. После совершения суперионного ФП окта координированные ионы Ag⁺ становятся подвижными, представляя собой элементы «вязкой жидкости», а тетра-координированные ионы Ag⁺, оставаясь неподвижными (с точностью до фононных колебаний), стабилизируют кристаллическую решетку материала.

Ключевые слова: суперионный фазовый переход, нанонити сульфида серебра, нанопористые силикатные стекла, диэлектрическая спектроскопия

Ссылка при цитировании: Ильинский А.В., Кастро Арата Р., Пашкевич М.Э., Попова И.О., Сидоров А.И., Шадрин Е.Б. Диэлектрическая спектроскопия нанонитей, синтезированных в пористых силикатных стеклах // Научно-технические ведомости СПбГПУ. Физико-математические науки. 2023. Т. 16. № 1.1. С. 33–37. DOI: <https://doi.org/10.18721/JPM.161.105>

Статья открытого доступа, распространяемая по лицензии CC BY-NC 4.0 (<https://creativecommons.org/licenses/by-nc/4.0/>)

Introduction

Superionic materials, in particular silver sulfide, are used as the working medium of various sensors with combined electron-ion conductivity, as miniature capacitors of ultrahigh capacitance [1]. Along with applied research, it is also important to study the fundamental physical properties of superionics and, in particular, the semiconductor superionic phase transition, which expands the possibilities of superionic materials application [2].

Silver sulfide has two types of phase transitions: $\alpha \rightarrow \beta$ transition with the transition temperature $T_c = 176$ °C and $\beta \rightarrow \gamma$ transition (transition temperature $T_c = 592$ °C) [3]. The dielectric spectroscopy (DS) research method, presented in this paper, opens up new possibilities for studying the physical properties of Ag_2S nanocrystallites embedded in nanoporous silicate glasses (NSG). The purpose of this work is to demonstrate the peculiarities of the semiconductor-superionic phase transition mechanism in Ag_2S nanowires synthesized inside NSG channels.

Materials and Methods

NSG samples were made at the National Research University ITMO in St. Petersburg. They were silicon dioxide structures with branched through filamentous tubes 17 nm in diameter. The sample size was $10 \times 10 \times 1$ mm. The inner space of the tubes was half filled with Ag_2S nanocrystals. The samples were warmed up to 110 °C immediately before measurements of the DS to remove water that penetrated into the pores of the NSG during long-term storage of the samples in air.

The impedance measurements were performed on a Concept 81 dielectric spectrometer from Novocontrol Technologies. The sample was placed in the spectrometer cell between flat electrodes. The electrical capacitance of the empty cell was $C_0 = 1.7$ pF. DS were measured in the frequency range 10^{-1} – 10^6 Hz. The sample temperature T was varied with a step of 10 °C in the range of 0–250 °C.

Results and Discussion

The frequency dependences of the $\text{tg}\delta(f)$ (dielectric loss tangent) and the Cole-Cole diagrams $\varepsilon''(\varepsilon')$ of the NSG + Ag_2S samples are shown in Figure 1. Here $\varepsilon'(f)$ is the real part of the permittivity ε , and $\varepsilon''(f)$ is its imaginary part. The maximum of the function $\text{tg}\delta(f)$ was located by $T = 0$ °C at a frequency 0.5 Hz, and its value was $\text{tg}\delta(f_{\text{max}}) = 0.35$. The maximum of the $\text{tg}\delta(f)$ function shifted with increasing temperature towards higher frequencies, while its value increased from 0.35 to 0.6. At $T > 160$ °C the frequency shift stopped. With a temperature decreasing, the frequency position of this maximum on the frequency scale was reproduced within the measurement error, that is, the temperature hysteresis of the frequency position of the maximum was not recorded.

Nevertheless, the temperature hysteresis of the numerical value of $\text{tg}\delta(f)$ at the frequency $f = 0.1$ Hz was registered (Fig. 2). The point is that at such a low frequency, with increasing T , a “slope” of the second, even lower frequency, maximum of the function $\text{tg}\delta(f)$ began to appear, the position of which at low temperatures went beyond the frequency range of the spectrometer measurements. The temperature hysteresis loop was located in the region of 160–220 °C and had a width of 60 °C. This indicates that in this temperature range a phase transition occurs, which has a thermal hysteresis.

Since there are two maxima $\text{tg}\delta(f)$ in the DS and also two semicircles on the Cole-Cole diagram take place, the 2-circuit equivalent electrical circuit of the sample should be used to simulate

the physical processes under study (inset in Fig. 1). Calculations of circuit parameters were performed with such modeling by the symbolic method.

At temperatures of 0–110 °C the Ag_2S nanowires, filling the filamentous tubes of the NSG sample, are in the semiconductor phase. Therefore, it was sufficient to use one electrical circuit to simulate the DS. In it, in parallel with the resistance R_I of the semiconductor Ag_2S , the capacitance C_I is included the capacitance of the NSG. Capacitance C_{II} was the capacitance of a thin dielectric layer between the cell electrodes and the NPS sample. The thermal variation of the frequency position of the first maximum of the function $\text{tg}\delta(f)$ in the temperature range 0–110 °C is determined from general physical considerations mainly only by changing the resistance value R_I with temperature because the thermal constancy of the capacitance.

At temperatures of 110–250 °C in Ag_2S nanowires the semiconductor superionic phase transition occurs. Therefore, to describe the DS at temperatures above T_c , but in the immediate vicinity of it, the simulation requires the use of both electrical circuits, although at higher temperatures far from the phase transition, only the second circuit can be used for modeling. Significant differences in the parameters of electrical circuits come down to the fact that $C_{IV} \gg C_{II}$ and $R_{II} \gg R_I$. The point is that at high temperatures after the phase transition, free Ag^+ ions appear which increase the conductivity of the sample at low frequencies. In this case, the former high value of the ohmic resistance R_{II} decreases. A thin layer of metallic silver with a high electric capacitance appears inside the NSG sample in the region close to the electrodes. This contributes to the appearance of the second maximum of the function $\text{tg}\delta(f)$ in the DS at low frequencies. The results of the calculation of the equivalent electrical circuit are shown in Fig. 1 by dotted lines. The calculated curves are in good agreement with the experimental data.

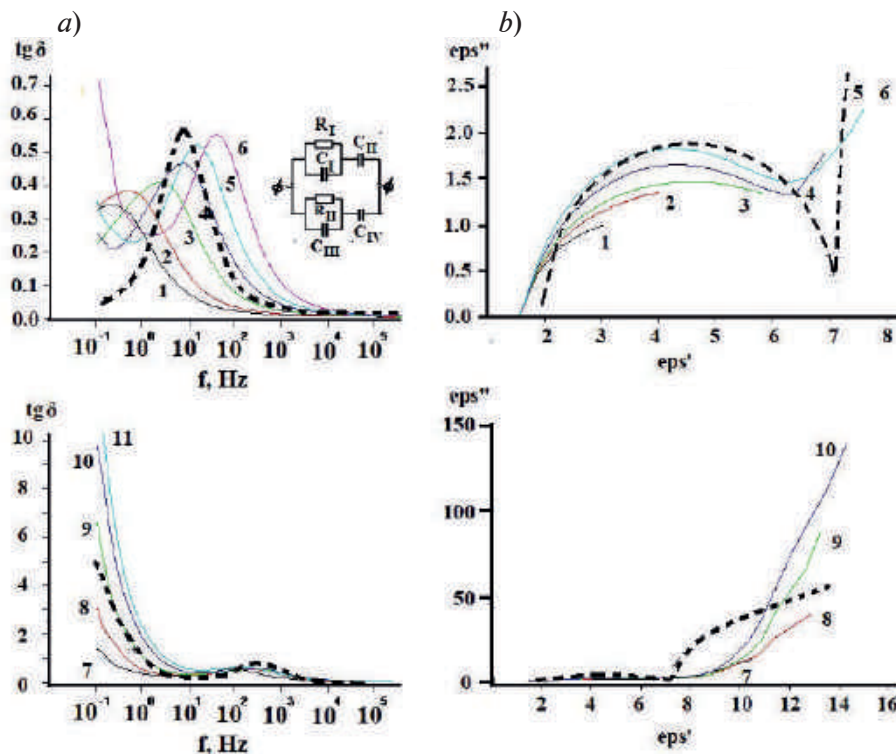


Fig. 1. Frequency dependences $\text{tg}\delta(f)$ (a), and Cole-Cole diagrams (b), obtained experimentally at temperatures $T = 0$ (1), 20 (2), 40 (3), 60 (4), 80 (5), 100 (6), 120 (7), 140 (8), 160 (9), 180 (10) °C for NSG samples with pores, filled with Ag_2S . Dashed curves are calculation results

With an increase in T , the $\text{tg}\delta$ maximum first moves towards high frequencies (curves 1–6, a), then at $T > 100$ °C the second maximum $\text{tg}\delta$ appears in the low-frequency region (curves 7–11, a). At the same time, a semicircle is formed in the region of high frequencies (curves 1–6, b), then at $T > 100$ °C a second semicircle appears in the region of low frequencies (curves 7–10, b).

The shift of the maximum of the dielectric loss tangent towards higher frequencies with increasing T is explained by a decrease in the resistance of the Ag_2S semiconductor nanowire

due to an increase in the rate of thermal generation of free electrons. In addition, since a phase transition ($\alpha \rightarrow \beta$) occurs at high temperature at $T_c = 176 \text{ }^\circ\text{C}$, a “liquid” fraction of Ag^+ ions appears, and the electrical conductivity acquires a predominantly ionic character. As a result, the total electrical resistance of the NSG sample decreases significantly and the numerical value of $\text{tg}\delta(f)$ increases many times over. The semiconductor superionic phase transition demonstrates the presence of temperature hysteresis, which is shown in Fig. 2, where the temperature hysteresis loop of $\text{tg}\delta$ at frequency of 0.1 Hz can be seen.

To explain the results obtained, we propose the following microscopic model of the superionic phase transition. Ag_2S undergoes a transition from the monoclinic crystalline α modification to the cubic β -modification at $T_c = 176 \text{ }^\circ\text{C}$. The details of the phase transition are explained with the help of Fig. 3, which shows a fragment of the Ag_2S crystal lattice [4].

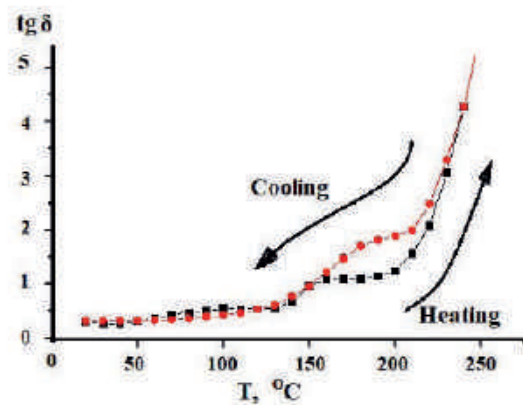


Fig.2. Temperature hysteresis of the $\text{tg}\delta$ value for dehydrated NSG + Ag_2S samples at frequency $f = 0.1 \text{ Hz}$

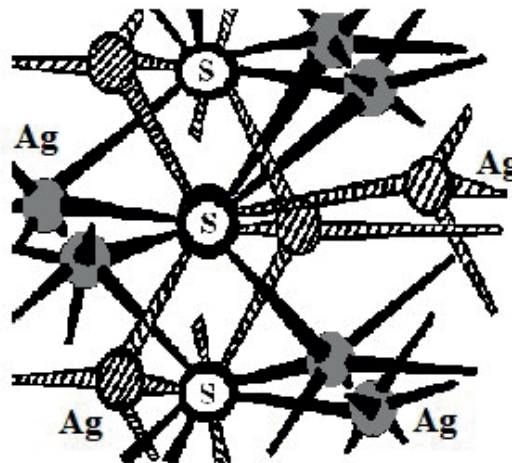


Fig.3. Fragment of the Ag_2S lattice with tetra-coordinated (shaded circles) and octa-coordinated (unshaded circles) Ag^+ ions

As the temperature rises, the bonds of the octa-coordinated Ag^+ ions break, while the tetra-coordinated Ag^+ ions retain their integrity, remaining unaffected by heating. The released octa-coordinated Ag^+ ions behave like a liquid with a high degree of viscosity [3]. When the critical concentration of broken bonds is reached, the symmetry of the crystal lattice changes from monoclinic to cubic and a structural superionic phase transition of the first order occurs, which has a temperature hysteresis. At the same time, the crystal lattice itself remains stable due to the preservation of the integrity of strong tetra- $\text{Ag-S-}\sigma$ -bonds.

The band gap of the low-temperature semiconductor phase is $E_g = 0.9 \text{ eV}$ [5]. We point out that at $T_c = 176 \text{ }^\circ\text{C}$ the thermal energy is much less than this value: $kT = 40 \text{ meV}$. In spite of this, octa-coordinated Ag^+ ions still break, as was mentioned above. The reason for this is that



the band gap sharply decreases as the conduction band is thermally populated by electrons as T_c is approached. This means that the Ag_2S semiconductor inherits the strong correlation properties of the neutral silver atom. This process leads to a strong “metallization” of the crystal immediately before the structural superionic phase transition. Thus, before the superionic structural phase transition, a purely electronic Mott transition of the second order, which is extended in temperature, takes place. From what has been said, it follows that the temperature-extended Mott correlation transition [6] initiates a structural phase transition (superionic in the case of Ag_2S).

Conclusion

Thus, in this work, based on the analysis of the DS, the following conclusion was made. After the superionic phase transition occurs, the octa-coordinated Ag^+ ions become mobile, representing the elements of a “viscous liquid”, while the tetra-coordinated Ag^+ ions, remaining immobile (up to phonon vibrations), stabilize the crystal lattice of the material.

REFERENCES

1. Liu Z.K, Jiang J., Zhou B., Wang Z.J., Zhang Y., Weng H.M., Prabhakaran D., Mo S-K., Peng H., Dudin P., Kim T., Hoesch M., Fang Z., Dai X., Shen Z.X., Feng D.L., Hussain Z., Chen Y.L., A stable three-dimensional topological Dirac semimetal Cd_3As_2 , Nature Materials. 13 (2014) 677–681.
2. Ukshe E.A., Bukun N.G., Solid electrolytes, M.: Nauka (1977).
3. Wang Z., Luo K., Yu R., Large Fermi arc and robust Weyl semimetal phase in Ag_2S , Physical Review B. 100 (20) (2019) 205117–1.
4. Il'inskii A.V., Castro R.A., Pashkevich M.E., Popova I.O., Shadrin E.B., Semiconductor-superionic phase transition in silver sulfide films, Physics of the Solid State. 62 (2020) 2403–2411.
5. Bletskan D.I., Vakul'chak V.V., Lukach A.V., Studenyak I.P., Electronic structure of Ag_2S and Ag_2CeS_3 , Nauch.Vestn. Uzhgor. Univ. Ser. Fiz. (2016) 30–40.
6. Il'inskii A.V., Kvashenkina O.E., Shadrin E.B., Protonic metallization of the monoclinic phase in VO_2 films, Semiconductors. 45(9) (2011) 1153–1157.

THE AUTHORS

IL'INSKIY Aleksandr V.

E-mail: ilinskiy@mail.ioffe.ru
ORCID: 0000-0002-1548-1180

CASTRO Rene Arata A.

E-mail: recastro@mail.ru
ORCID: 0000-0002-1902-5801

PASHKEVICH Marina E.

E-mail: marpash@yandex.ru
ORCID: 0000-0002-3373-4129

POPOVA Irina O.

E-mail: timof-ira@yandex.ru
ORCID: 0000-0002-0822-985X

SIDOROV Aleksandr I.

E-mail: sidorov@oi.itmo.ru
ORCID: 0000-0001-5024-6728

SHADRIN Evgenii B.

E-mail: Shadr.solid@mail.ioffe.ru
ORCID: 0000-0002-1423-2852

Received 29.09.2022. Approved after reviewing 08.11.2022. Accepted 06.12.2022.

Conference materials

UDC 537.226

DOI: <https://doi.org/10.18721/JPM.161.106>

Dielectric properties of ferroelectric composite $(\text{KNO}_3)_{3(1-x)}/(\text{RbNO}_3)_x$

A.Yu. Milinskiy ¹✉, S.V. Baryshnikov ¹, A.A. Zeeva ¹

¹ Blagoveshchensk State Pedagogical University, Blagoveshensk, Russia

✉ a.milinskiy@mail.ru

Abstract: The temperature dependences of the permittivity, the amplitude of the third harmonic and the differential thermal analysis signal for the $(\text{KNO}_3)_{3(1-x)}/(\text{RbNO}_3)_x$ composite were studied. To obtain $(\text{KNO}_3)_{3(1-x)}/(\text{RbNO}_3)_x$ samples, KNO_3 and RbNO_3 powders with particle size of 5–10 μm were used. The powders were mixed in appropriate proportions, after that the tablets were made at a pressure of $8 \cdot 10^3$ kg/cm². The samples with x from 0.05 to 0.5 were examined (x is the volume fraction of RbNO_3). Before measurements, the obtained samples were heated to 593 K, which is higher than the melting point of RbNO_3 , but lower than that of KNO_3 . It has been found that an increase in the RbNO_3 content leads to the appearance of additional phase transitions and the expansion of the temperature region of the ferroelectric phase. The transition temperatures for potassium nitrate do not shift along the temperature axis. For rubidium nitrate, the phase transition at 437 K decreases by 4–5 K, and the temperature hysteresis of this transition increases. The expansion of the ferroelectric phase upon cooling is explained by the superposition of the ferroelectric phases of potassium nitrate and the $\text{Rb}_x\text{K}_{(1-x)}\text{NO}_3$ solid solution.

Keywords: composite, ferroelectric, potassium nitrate, rubidium nitrate

Citation: Milinskiy A.Yu., Baryshnikov S.V., Zeeva A.A. Dielectric properties of ferroelectric composite $(\text{KNO}_3)_{3(1-x)}/(\text{RbNO}_3)_x$. St. Petersburg State Polytechnical University Journal: Physics and Mathematics. 16 (1.1) (2023) 49–53. DOI: <https://doi.org/10.18721/JPM.161.106>

This is an open access article under the CC BY-NC 4.0 license (<https://creativecommons.org/licenses/by-nc/4.0/>)

Материалы конференции

УДК 537.226

DOI: <https://doi.org/10.18721/JPM.161.106>

Диэлектрические свойства сегнетоэлектрических композитов $(\text{KNO}_3)_{3(1-x)}/(\text{RbNO}_3)_x$

А.Ю. Милинский ¹✉, С.В. Барышников ¹, А.А. Зеева ¹

¹ Благовещенский государственный педагогический университет, г. Благовещенск, Россия

✉ a.milinskiy@mail.ru

Аннотация. Исследованы температурные зависимости диэлектрической проницаемости, амплитуды третьей гармоники и сигнала ДТА для композита $(\text{KNO}_3)_{3(1-x)}/(\text{RbNO}_3)_x$. Установлено, что увеличение содержания RbNO_3 приводит к возникновению дополнительных фазовых переходов и расширению температурного интервала существования сегнетоэлектрической фазы.

Ключевые слова: композит, сегнетоэлектрик, нитрат калия, нитрат рубидия

Ссылка при цитировании: Милинский А.Ю., Барышников С.В., Зеева А.А. Диэлектрические свойства сегнетоэлектрических композитов $(\text{KNO}_3)_{3(1-x)}/(\text{RbNO}_3)_x$ // Научно-технические ведомости СПбГПУ: Физико-математические науки. 2023. Т. 16. № 1.1. С. 49–53. DOI: <https://doi.org/10.18721/JPM.161.106>

Статья открытого доступа, распространяемая по лицензии CC BY-NC 4.0 (<https://creativecommons.org/licenses/by-nc/4.0/>)



Introduction

Potassium nitrate is widely known as a material with a rectangular hysteresis loop, and it is a convenient material for creating a non-volatile ferroelectric memory [1]. However, the ferroelectric phase in KNO_3 appears only upon cooling in a narrow temperature range. A number of works reported attempts to expand the range of existence of the ferroelectric phase by creating composites and solid solutions, based on potassium nitrate [2–5]. For the ferroelectric composites $(\text{KNO}_3)_{(1-x)}/(\text{BaTiO}_3)_x$ [2] and $(\text{KNO}_3)_{(1-x)}/(\text{KNbO}_3)_x$ [3] an expansion of the region of existence of the ferroelectric phase of potassium nitrate is observed. It was reported about the expansion of the region of existence of KNO_3 ferroelectric phase in double salt systems of

$(\text{KNO}_3)_{(1-x)}/(\text{NaNO}_3)_x$ [4] and $(\text{KNO}_3)_{(1-x)}/(\text{AgNO}_3)_x$ [5]. As far as we know from publications, studies of potassium nitrate with other nitrate additives were not carried out. In this work, we study the effect of RbNO_3 on the formation of the ferroelectric state in KNO_3 .

Materials and Methods

Potassium nitrate at room temperature has an orthorhombic structure ($Pmcn$ space group) [6]. This phase is often referred to as phase II. When the sample is heated to about 401 K, a transition occurs to phase I, which has a disordered trigonal calcite-like structure $R3m$. Upon cooling, phase II does not directly transfer into phase I, but instead at $T = 397$ K it transfers into another trigonal phase III, which is ferroelectric with spontaneous polarization along the c axis. Spontaneous polarization is about $8\text{--}10 \mu\text{C}/\text{cm}^2$ at a temperature of 393 K. It was found that the temperature range of the existence of the ferroelectric state in KNO_3 depends on the thermal prehistory and cooling rate [7, 8] and upon preliminary heating of the sample to 473 K for the first heating-cooling cycle is about 22–24 K.

Rubidium nitrate has four stable forms. At room temperature, RbNO_3 has a trigonal space group $P3_1$ (phase IV) and crystallizes from an aqueous solution in the form of needles along the c axis [9]. This phase is stable up to 437 K and is pyroelectric with the formation of 180-degree pyroelectric domains. In the temperature range of 437–492 K rubidium nitrate exists in the cubic pyroelectric phase $Pm3m$ (phase III). According to [10], at the phase transition of 437 K the conductivity of RbNO_3 increases by two orders of magnitude, and this phase has superionic conductivity. In the range from 492 to 564 K [9] (or, according to [11], 558 K), RbNO_3 is in the rhombohedral phase $R3m$ (phase II). This phase is defined as antiferroelectric [12]. Above the phase transition at 564 K, RbNO_3 again transfers into a cubic phase $Fm3m$ (phase I), which exists up to the melting point of 587 K.

To obtain $(\text{KNO}_3)_{(1-x)}/(\text{RbNO}_3)_x$ samples, KNO_3 and RbNO_3 powders with a particle size of $5\text{--}10 \mu\text{m}$ were used. The powders were mixed in appropriate proportions, after which pellets with a diameter of 10 mm and a thickness of 1.5 mm were obtained by a pressure of $8 \cdot 10^3 \text{ kg}/\text{cm}^2$. Samples with x from 0.05 to 0.5 were used for the study (x is RbNO_3 volume fraction). The prepared samples were heated to a temperature of 593 K, which is higher than the melting point of RbNO_3 , but lower than that of KNO_3 . A photograph of the $(\text{KNO}_3)_{0.75}/(\text{RbNO}_3)_{0.25}$ sample surface is shown in Figure 1.

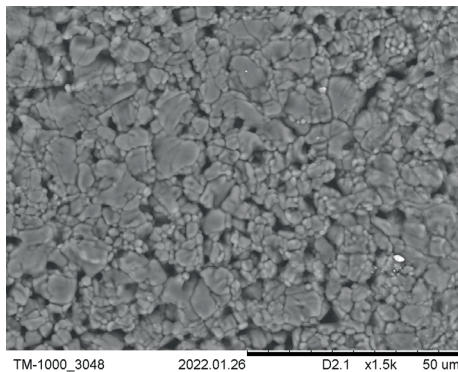


Fig. 1. Electron photograph of the $(\text{KNO}_3)_{0.75}/(\text{RbNO}_3)_{0.25}$ surface

To measure the dielectric permittivity of the samples, E7-25 digital immittance meter with a frequency range of 25–10⁶ Hz was used. In-Ga paste was used as electrodes. The measurements were carried out at a heating-cooling rate of ~ 1 K/min in the temperature range of 290–450 K. The temperature was recorded by a Center 340 electronic thermometer with a chromel-alumel thermocouple. The data was automatically recorded on a computer.

The setup for studying the nonlinear dielectric properties of the samples included a generator of harmonic oscillations with an operating frequency of 2 kHz. The electric field strength on the samples during the measurement was 50 V/mm. The signal was taken from a resistor connected in series with the sample and fed to a digital spectrum analyzer, which was a computer with analog to-digital converter ZET 230. To determine the region of existence of the ferroelectric phase we studied the coefficients of the third ($\gamma_{3\omega} = U_{3\omega}/U_{\omega}$) or fifth ($\gamma_{5\omega} = U_{5\omega}/U_{\omega}$) harmonics. The technique for studying ferroelectrics by using nonlinear dielectric spectroscopy is described in more detail in [13].

To study the samples by the method of differential thermal analysis (DTA), a Linseis STA PT 1600 synchronous thermal analyzer was used. The studies were carried out in the heating cooling mode at a rate of 1 K/min in the same temperature range as for dielectric measurements.

Results and Discussion

The temperature dependences of the permittivity $\epsilon'(T)$ and the third harmonic coefficient $\gamma_{3\omega}(T)$ for polycrystalline potassium nitrate are shown in Figure 2. If the sample is heated to 450 K, two anomalies are observed on the $\epsilon'(T)$ curve upon cooling. At $T = 397$ K, potassium nitrate transfers from phase I into a ferroelectric phase III, and at $T = 375$ K, a transition occurs from phase III to phase II, which is stable at room temperature. According to the data on the third harmonic coefficient $\gamma_{3\omega}(T)$ (see Fig. 1), the ferroelectric phase in potassium nitrate, which appears upon cooling, occupies a temperature range of approximately 22 K, which corresponds to the known data [6]. The third harmonic coefficient at its maximum is ~ 0.04 at $E = 50$ V/mm.

Figure 3 shows the temperature dependences of the permittivity $\epsilon'(T)$ and the third harmonic coefficient $\gamma_{3\omega}(T)$ for rubidium nitrate. As RbNO_3 is a pyroelectric, the third harmonic coefficient is ~ 0.01, however, it has a minimum at the phase transition, which is probably due to the vanishing of the pyroelectric polarization or a change of the piezoelectric coefficient.

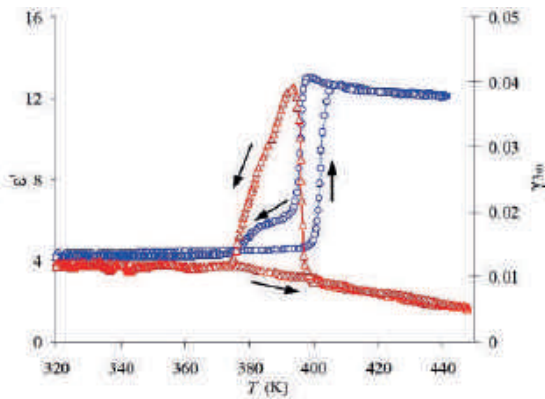


Fig. 2. Dependences $\epsilon'(T)$ at a frequency of 500 kHz (circles) and the coefficient of the third harmonic $\gamma_{3\omega}$ (triangles) for KNO_3 at a field strength of 50 V/mm

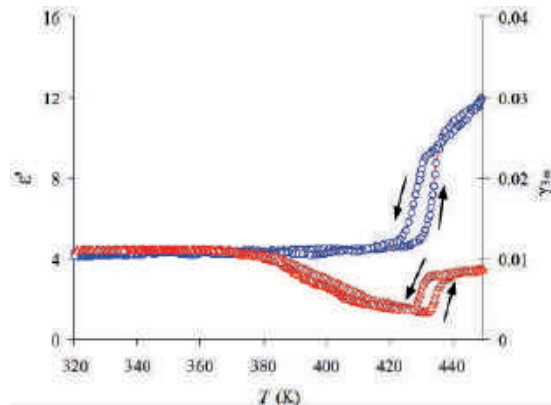


Fig. 3. Dependences $\epsilon'(T)$ at a frequency of 500 kHz (circles) and the third harmonic coefficient $\gamma_{3\omega}$ (triangles) for RbNO_3 at a field strength of 50 V/mm

For $(\text{KNO}_3)_{(1-x)}/(\text{RbNO}_3)_x$ composite samples, an increase in x is accompanied by an increase in the permittivity and expansion of the region of existence of the ferroelectric phase. The dielectric loss tangent in the ferroelectric phase at $T = 391$ K at a frequency of 20 kHz is: $\text{tg}\delta \approx 0.11$ for KNO_3 ; $\text{tg}\delta \approx 0.35$ for $x = 0.1$; $\text{tg}\delta \approx 0.6$ for $x = 0.3$; $\text{tg}\delta \approx 0.51$ for $x = 0.5$; and $\text{tg}\delta \approx 0.06$ for pure RbNO_3 . The range of existence of the ferroelectric state in $(\text{KNO}_3)_{(1-x)}/(\text{RbNO}_3)_x$ composite samples, determined from DTA diagrams, has a maximum at $x = 0.05$ (Fig. 4). In this case, as x increases, the amplitude of the third harmonic decreases (Fig. 5), which can be explained by a decrease in spontaneous polarization.

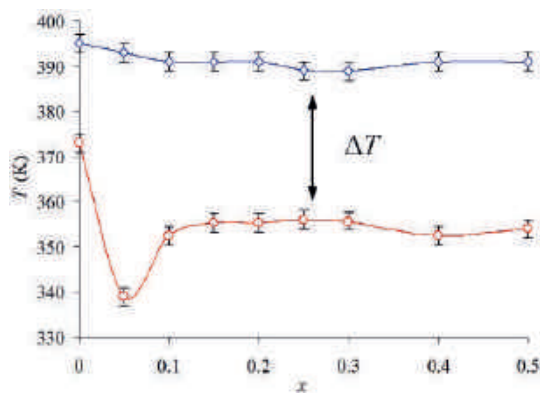


Fig. 4. Dependences of the temperature range of existence of the KNO_3 ferroelectric phase on the content of RbNO_3 in $(\text{KNO}_3)_{(1-x)}/(\text{RbNO}_3)_x$

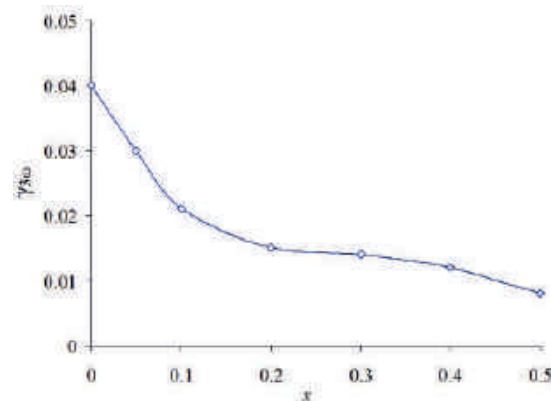


Fig. 5. Dependences of the amplitude $\gamma_{3\omega}$ on the content of rubidium nitrate in $(\text{KNO}_3)_{(1-x)}/(\text{RbNO}_3)_x$

To understand the results obtained, we compared them with the dielectric properties of $\text{K}_{(1-x)}\text{Rb}_x\text{NO}_3$ solid solutions, smelted from RbNO_3 and KNO_3 at a temperature of 530 K. Figure 6 shows the permittivities of the $(\text{KNO}_3)_{(1-x)}/(\text{RbNO}_3)_x$ composite and $\text{K}_{(1-x)}\text{Rb}_x\text{NO}_3$ solid solution for $x = 0.4$.

Analyzing the graphs, we can conclude that the $(\text{KNO}_3)_{0.6}/(\text{RbNO}_3)_{0.4}$ composite contains KNO_3 , RbNO_3 , and the $\text{RbK}_{(1-x)}\text{NO}_3$ solid solution, each having its own phase transition temperatures. In this case, the transition temperatures for potassium nitrate practically do not shift. For rubidium nitrate, the phase transition at $T = 437$ K decreases by 4–5 K, and the temperature hysteresis of this transition increases. The expansion of the ferroelectric phase upon cooling probably occurs due to the superposition of the ferroelectric phases of potassium nitrate and the $\text{K}_{(1-x)}\text{Rb}_x\text{NO}_3$ solid solution, which follows from the graphs, shown in Figures 6 and 7. The ferroelectric properties of $\text{K}_{(1-x)}\text{Rb}_x\text{NO}_3$ solid solution were studied in [14], where it was shown that the polar phase exists in the range of $x = 0$ to 0.56. In this case, P_s changes from 8.6 to 0.8 $\mu\text{C}/\text{cm}^2$. Hence, it follows that it is unlikely to obtain an interval of existence of a polar state greater than 40–55 K in the $(\text{KNO}_3)_{0.6}/(\text{RbNO}_3)_{0.4}$ composite.

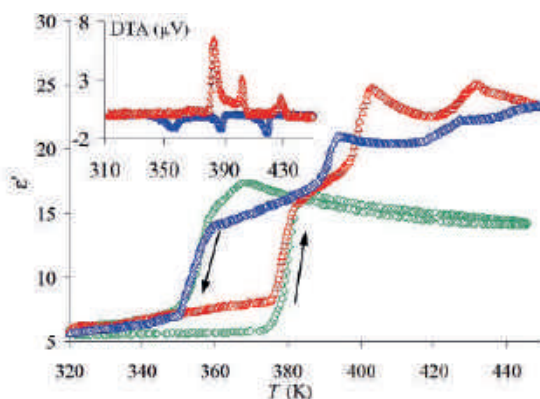


Fig. 6. Dependences $\varepsilon'(T)$ for the $(\text{KNO}_3)_{0.6}/(\text{RbNO}_3)_{0.4}$ composite (triangles) and $\text{RbK}_{(1-x)}\text{NO}_3$ solid solution (diamonds) at a frequency of 500 kHz. The inset shows the DTA signal for the same composite

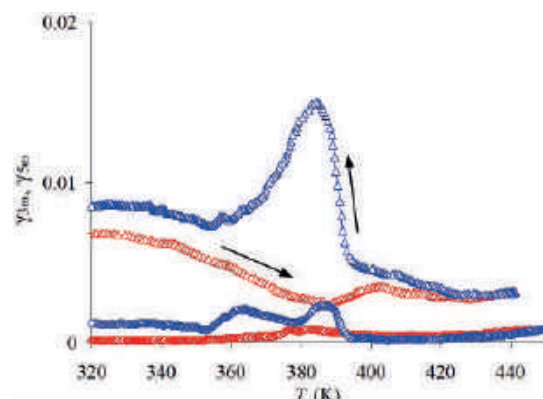


Fig. 7. Dependences $\gamma_{3\omega}(T)$ (triangles) and $\gamma_{5\omega}(T)$ (rhombuses) for $(\text{KNO}_3)_{0.6}/(\text{RbNO}_3)_{0.4}$ at a field strength of 50 V/mm

Conclusion

Thus, as shown by studies of $(\text{KNO}_3)_{(1-x)}/(\text{RbNO}_3)_x$ composites, the presence of RbNO_3 increases the temperature range of the ferroelectric state existence. The expansion of the polar state occurs due to the partial formation of the $\text{K}_{(1-x)}\text{Rb}_x\text{NO}_3$ solid solution, for which the temperature region of the polar phase is lower than that for pure KNO_3 .

REFERENCES

1. **Scott J.F.**, Ferroelectric Memories, Springer Series in Advanced Microelectronics. 2000.
2. **Stukova E.V., Baryshnikov S.V.**, Stabilization of the ferroelectric phase in $(\text{KNO}_3)_{1-x}(\text{BaTiO}_3)_x$ composites, Inorganic materials: applied research. 2 (2011) 434–438.
3. **Stukova E.V., Baryshnikov S.V.**, Expansion of the ferroelectric phase temperature interval in the composites $(\text{KNO}_3)_{1-x}(\text{BaTiO}_3)_x$ and $(\text{KNO}_3)_{1-x}(\text{PbTiO}_3)_x$, World Journal of Engineering. 3 (2010) 1055–1057.
4. **Shimada S., Aoki T.**, Stabilization of the ferroelectric γ -phase of KNO_3 by doping with Na^+ , determined by the acoustic emission method, Chemistry Letters. 25 (1996) 393–394.
5. **Rysiakiewicz-Pasek E., Antropova T., Polyakova I., Pshenko O., Cizman A.**, New insight into phase transitions of porous glass-based ferroelectric nanocomposites, Materials. 13 (2020) 3698.
6. **Chen A., Chernow A.**, Nature of Ferroelectricity in KNO_3 , Phys. Rev. 154 (1967) 493–505.
7. **Deshpande V.V., Karkhanavala M.D., Rao U.R.K.**, Phase transitions in potassium nitrate, J. of Therm. Anal. and Cal. 6 (1974) 613–621.
8. **Nimmo J.K., Lucas B.W.**, The crystal structures of γ - and β - KNO_3 and the $\alpha \leftarrow \gamma \leftarrow \beta$ phase transformations, Acta Cryst. B32 (1976) 1968–1971.
9. **Bury P.C., McLaren A.C.**, Pyroelectric Properties of Rubidium, Cesium, and Thallium Nitrates, Phys. Stat. Sol. 31 (1969) 799–806.
10. **Salhotra P.P., Subbarao A.C., Venkateswarlu P.**, Polymorphism of Rubidium Nitrate, Phys. Stat. Sol. 31 (1968) 859–854.
11. **Fujimoto S., Yasuda N., Shimizu H., Tsuboi S., Kawabe K., Takagi Y., Midorikawa M.**, Dielectric properties of rubidium nitrate under hydrostatic pressure, J. Phys. Soc. Jpn. 42 (1977) 911–915.
12. **Yamamoto S., Suematsu Y., Shinnaka Y.**, X-Ray study of phase transition in RbNO_3 , J. Phys. Soc. Jpn. 7 (1977) 1962–1967.
13. **Ikeda S., Kominami H., Koyama K., Wada Y.**, Nonlinear dielectric constant and ferroelectric-to-paraelectric phase transition in copolymers of vinylidene fluoride and trifluoroethylene, J. Appl. Phys. 62 (1987) 3339–3342.
14. **Kawabe U., Yanagi T., Sawada S.**, Dielectric and X-ray studies of KNO_3 -series mixed crystal, J. Phys. Soc. Japan 20 (1965) 2059–2073.

THE AUTHORS

MILINSKIY Alexey Yu.
a.milinskiy@mail.ru
ORCID: 0000-0001-7525-4396

ZEEVA Anna A.
anutka_2010.1997@mail.ru
ORCID: 0000-0001-7216-3931

BARYSHNIKOV Sergey V.
svbar2003@list.ru
ORCID: 0000-0002-3362-8975

Received 01.10.2022. Approved after reviewing 22.11.2022. Accepted 23.11.2022.

Conference materials

UDC 538.9

DOI: <https://doi.org/10.18721/JPM.161.107>

Study of quasi 1D silicon nanostructures adsorption properties via impedance spectroscopy

V.M. Kondratev^{1,4}✉, E.A. Vyacheslavova^{1,2}, I.A. Morozov^{1,2}, S.S. Nalimova²,
V.A. Moshnikov², A.S. Gudovskikh^{1,2}, A.D. Bolshakov^{1,3,4}

¹ Alferov University, Saint Petersburg, Russia;

² Saint Petersburg Electrotechnical University "LETI", Saint Petersburg, Russia;

³ ITMO University, Saint Petersburg, Russia;

⁴ Moscow Institute of Physics and Technology, Dolgoprudny, Russia

✉ kvm_96@mail.ru

Abstract. The work is aimed at study of correlation between quasi 1D silicon nanostructures adsorption properties and their electrical characteristics in terms of change in Si nanowires impedance under action of different environments with a target adsorbate. Here we fabricate silicon nanowires based gas sensor and demonstrate the possibility of qualitative and quantitative gaseous media analysis for the presence of ammonia. The equivalent electric circuits of the sensor under action of air, water vapour and water ammonia solutions are considered. The sensor response under action of the different adsorbates and optimal impedance spectroscopy parameters are discussed.

Keywords: silicon, nanowires, 1D, electrical impedance spectroscopy

Funding: Ministry of Science and Higher Education of the Russian Federation (Grant FSRM-2023-0009); Ministry of Science and Higher Education of the Russian Federation (agreement 075-03-2023-106, project FSMG-2021-0005).

Citation: Kondratev V.M., Vyacheslavova E.A., Morozov I.A., Nalimova S.S., Moshnikov V.A., Gudovskikh A.S., Bolshakov A.D., Study of quasi 1D silicon nanostructures adsorption properties via impedance spectroscopy, St. Petersburg State Polytechnical University Journal: Physics and Mathematics. 16 (1.1) (2023) 43–48. DOI: <https://doi.org/10.18721/JPM.161.107>

This is an open access article under the CC BY-NC 4.0 license (<https://creativecommons.org/licenses/by-nc/4.0/>)

Материалы конференции

УДК 538.9

DOI: <https://doi.org/10.18721/JPM.161.107>

Исследование адсорбционных свойств квазиодномерных наноструктур кремния методом спектроскопии электрического импеданса

В.М. Кондратьев^{1,4}✉, Е.А. Вячеславова^{1,2}, И.А. Морозов^{1,2}, С.С. Налимова²,
В.А. Мошников², А.С. Гудовских^{1,2}, А.Д. Большаков^{1,3,4}

¹ Академический университет им. Ж.И. Алфёрова, Санкт-Петербург, Россия;

² Санкт-Петербургский государственный электротехнический университет «ЛЭТИ» имени В.И. Ульянова (Ленина), Санкт-Петербург, Россия;

³ Университет ИТМО, Санкт-Петербург, Россия;

⁴ Московский физико-технический институт, г. Долгопрудный, Россия

✉ kvm_96@mail.ru

Аннотация. Работа направлена на изучение адсорбционных свойств нанонитей кремния методом спектроскопии электрического импеданса. Продемонстрирована корреляция между адсорбционными свойствами и электрическими характеристиками нанонитей.

© Kondratev V.M., Vyacheslavova E.A., Morozov I.A., Nalimova S.S., Moshnikov V.A., Gudovskikh A.S., Bolshakov A.D. (2023) Published by Peter the Great St. Petersburg Polytechnic University.

Ключевые слова: кремний, нанонити, сенсор, спектроскопия импеданса

Финансирование: Министерство науки и высшего образования Российской Федерации (грант № FSRM-2023-0009); Министерство науки и высшего образования Российской Федерации (Соглашение 075-03-2023-106 от 13.01.2023, проект FSMG-2021-0005).

Ссылка при цитировании: Кондратьев В.М., Вячеславова Е.А., Морозов И.А., Налимова С.С., Мошников В.А., Гудовских А.С., Большаков А.Д., Исследование адсорбционных свойств квазиодномерных наноструктур кремния методом спектроскопии электрического импеданса // Научно-технические ведомости СПбГПУ: Физико-математические науки. 2023. Т. 16. № 1.1. С. 43–48. DOI: <https://doi.org/10.18721/JPM.161.107>

Статья открытого доступа, распространяемая по лицензии CC BY-NC 4.0 (<https://creativecommons.org/licenses/by-nc/4.0/>)

Introduction

There are many research activities in the field of modern electronics, based on nanomaterials, especially nanowires. The possibility of development of efficient light-emitting [1], resonator [1–2], and waveguide [2] structures, based on III–V and II–VI nanowires [3–4], as well as sensor elements [5–9], are widely presented. Despite the possibilities these highly crystalline nanostructures bring, their synthesis protocols are rather expensive and incompatible with modern CMOS processes.

As such, development of devices, based on silicon-cheap and technologically feasible material, and study of adsorption properties of quasi 1D Si nanowires is an important field being the subject of this work.

Synthesis

Silicon nanowires with a length of 10–12 μm and thickness of about 350 nm were obtained using cryogenic plasmachemical etching of Si (001) substrate in Oxford PlasmaLab System 100 ICP380 (Oxford instruments, Abingdon, UK). Anisotropic etching occurs on Si surface under flow of oxygen and etcher (O_2/SF_6) mixture. Primarily etched Si islands on the surface are passivated by non-volatile SiO_xF_y compound, which prevents lateral etching. An increase in temperature after the etching interruption leads to volatilization of F and conversion of SiO_xF_y into the native oxide. Typical parameters, growth conditions and result of the structural characterization via Raman spectroscopy are reposted previously [10–11]. The nanowires morphology and geometry were investigated by scanning electron microscopy (SEM) Zeiss Supra25 (Carl Zeiss AG, Jena, Germany) (Fig. 1, *a*).

As-synthesized Si nanowires were separated from Si (001) substrate by ultrasonication and transferred to an auxiliary substrate with concentric interdigital gold contacts (contact step of 10 μm) (Fig. 1, *b*). Gold-nanowires contacts are found to be of the Schottky type, which is proven by the voltage-current characterization, obtained using Keithley 2400 source-meter (Tektronix, Beaverton, USA) (Fig. 1, *c*).

The current-voltage (I-V) characteristic of the sensor demonstrates symmetry and a diode shape with a knee voltage of about 5 V, which indicates the barrier nature of the sensor conductivity. The phenomenon of barrier conductivity at the nanowire-gold interfaces can be effectively used for ammonia detection as shown below via electric impedance spectroscopy of sensor under exposure of analyte vapour at 100 mV bias in the frequency range from 100 Hz to 500 kHz (by impedance meter Z500P (Elins, Chernogolovka, Russia)). The impedance spectra were represented in Nyquist's plots — in the form of a dependence of the imaginary part of the sensor impedance on the real one, and analyzed for a shift followed by the change in the sensor environment. Impedance spectrum of the sensor in a reference medium, air, is shown in Figure 1, *d*.

Study

Vapour media with adsorbates were delivered to the sensor by natural evaporation of water and aqueous ammonia solutions (room temperature, atmospheric pressure) from a reservoir 4 cm

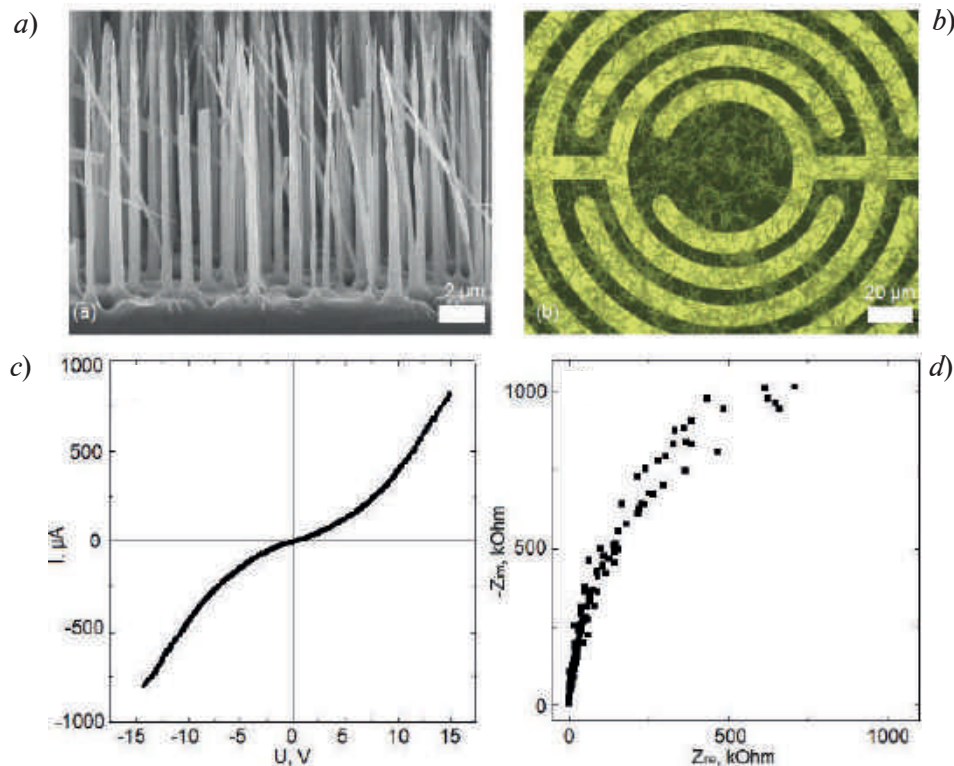


Fig. 1. SEM image of the vertically oriented structures based on plasma chemically etched Si nanowires (a); typical optical image of the Si nanowires on the surface of an auxiliary substrate with concentric interdigital gold contacts (further — sensor) (b); current-voltage characteristic of the sensor (c); measured sensor impedance spectrum in ambient conditions (d)

(1.6 in) in diameter, located at a distance of about 5 cm (2.0 in) below the sensor. A change in the sensor electrical impedance under action of the target adsorbates (vapours of NH_3 , aqua solutions with concentrations of 0.125, 0.250, and 0.500 $\text{mmol}\cdot\text{l}^{-1}$) (Fig. 2, *b–d*) was measured and compared with the impedance in the water vapours medium (Fig. 2, *a*).

Analysis of the dependencies in Figure 2 showed presence of characteristic plot regions, typical for impedance spectra of semiconductor materials — semicircular at frequencies of the order of 10–500 kHz and quasi-linear at frequencies of the order of 100 Hz–10 kHz. The first of these regions is associated with the contribution to the sensor impedance from the electrical resistance and capacitance of silicon nanowires, connected in parallel by interdigital contacts. The second region is largely determined by barrier phenomena at Schottky contacts between nanowires and gold [12–15].

Discussion

The conductivity of nanowires is determined by the cross section of the conducting channel inside the nanowire, the width of which varies depending on the adsorption processes on the surface, which leads to the formation of depleted or enriched regions that act on the conduction channel [12, 16]. In this work the sensitive element of the sensor is an array of conducting nanowires, connected in parallel through a Schottky contact, and the sensor impedance spectra carry information about the correlation between the adsorption properties and electrical characteristics of silicon NWs (semicircular region of the spectrum), as well as about contact phenomena at the NW-gold interface (quasi-linear region).

As follows from Figure 2, the projection of the semicircular part of the sensor impedance spectrum (the active resistance of silicon nanowires) decreases, when the sensor passes from air to unsaturated water vapour and vapours of aqueous ammonia solutions.

The oxidation of nanowires surface occur due to increase in temperature after the cryogenic plasmachemical etching interruption and volatilization of F with subsequent conversion of SiO_xF_y into the native oxide [10–11]. The adsorption interaction presumably proceeds through two main mechanisms [16]:

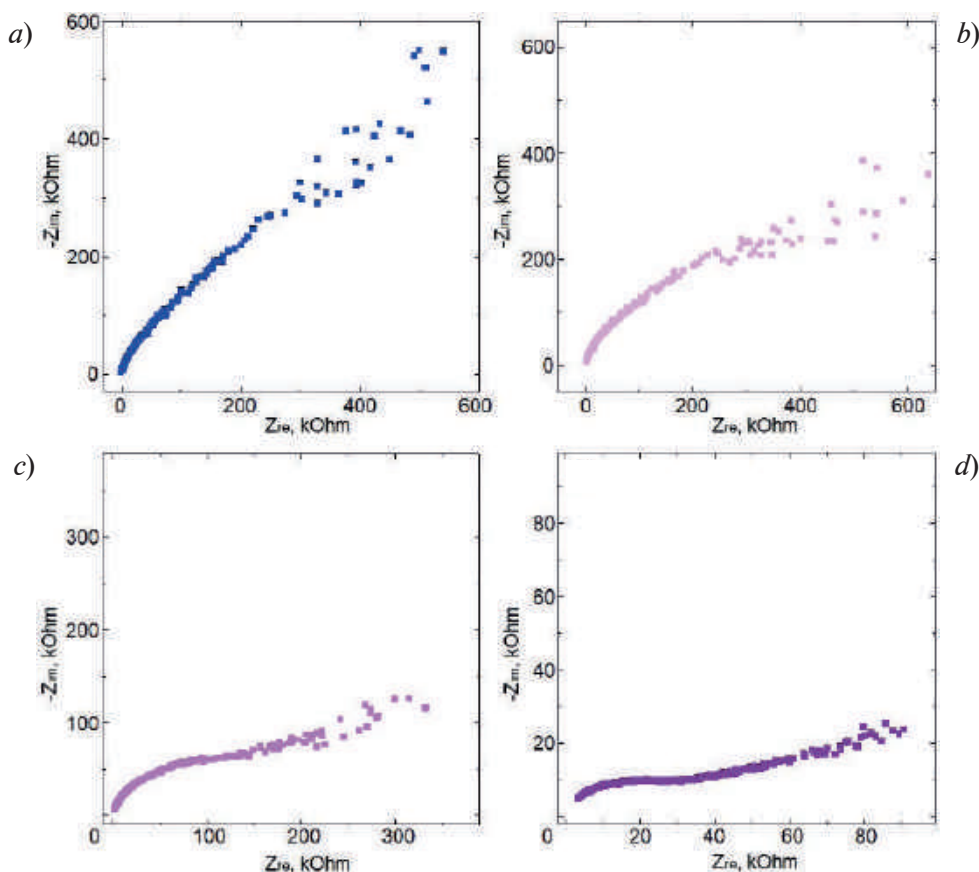


Fig. 2. Measured impedance spectra exposed under vapours of H_2O (a), and 0.125 (b), 0.250 (c), and 0.500 (d) $\text{mmol}\cdot\text{l}^{-1}$ of NH_3

1) hydration of the silicon oxidized surface by OH^- molecules (breaking the bond between oxygen and silicon in the near-surface native oxide and its replacement with a more energetically advantageous one);

2) protonation of the hydrated surface of the nanowire by NH_3 molecules (separation of the proton H^+ from the OH molecule on the surface of the nanowire) with formation of the NH_4^+ ion.

In both cases described, conduction electrons enter silicon, which affect the resistance and impedance of nanowires.

In addition, it is necessary to take into account the small transverse dimensions of single nanowires and the huge ratio of the surface area to the volume of NWs, as a result of which there is a strong bending of the energy bands in the axial direction of the NWs. In the case of quasi 1D silicon nanostructures such effects lead to an inversion of conductivity from p-type (substrate) to n-type (NWs), as well as a predominant effect on the conductivity of silicon NWs from adsorbates [16].

The estimation of the projection of the semicircular part of the sensor impedance spectrum (the active resistance of silicon nanowires) value makes it possible to estimate the total resistance of the nanowire array (sensitive element of the sensor). This resistance under action of ammonia less than resistance of the sensor in the air (2250 kOhm) and water vapour environment (200 kOhm) and decreases with increasing ammonia concentration (150, 55, and 12 kOhm for 0.125, 0.250, and 0.500 $\text{mmol}\cdot\text{l}^{-1}$, respectively).

The optimal frequency of the measuring voltage is in the range from 10 to 500 kHz, at which there is no significant contribution to the sensor impedance spectrum from the Schottky contacts between nanowires and gold, and the sensor impedance is determined mainly due to the active and reactive resistance of silicon nanowires, which correlates with the composition of the environment.



Conclusion

Correlation between silicon nanowires adsorption properties and their electrical characteristics demonstrate the possibility of qualitative and quantitative gaseous (vapour) media analysis for the presence of ammonia in extra low concentration with the fabricated sensor.

The semicircular part of the sensor impedance spectrum corresponds to the resistance of the sensor is used to analyze change in the resistance under the vapour adsorption. The resistance of the sensor changes, when water vapour is replaced by vapour of an aqueous solution of ammonia to 25, 73, and 94% (for 0.125, 0.250, and 0.500 mmol·l⁻¹, respectively).

The optimal frequencies of the measuring voltage at which there is no significant contribution to the sensor impedance spectrum from the Schottky contacts are shown. These frequencies can be used to perform real-time detection.

REFERENCES

1. Kuznetsov A., Roy P., Kondratev V.M., Fedorov V.V., Kotlyar K.P., Reznik R.R., Vorobyev A.A., Mukhin I.S., Cirlin G.E., Bolshakov A.D., Anisotropic radiation in heterostructured emitter in a cavity, *Nanowire. Nanomaterials*. 12 (2022) 241.
2. Kuznetsov A., Fominykh N., Kondratev V., and Fedina S.V., GaP nanowire waveguides, 2022 Conference of Russian Young Researchers in Electrical and Electronic Engineering (EIConRus). (2022) 1126–1129.
3. Kadinskaya S.A., Kondratev V.M., Kindyushov I.K., Kuznetsov A., and Punegova K.N., Hydrothermal ZnO-based nanostructures: Geometry control and narrow band UV emission, 2022 Conference of Russian Young Researchers in Electrical and Electronic Engineering (EIConRus). (2022) 958–961.
4. Kadinskaya S.A., Kondratev V.M., Kindyushov I.K., Labzovskaya M.E., Novikov B.V., Shtrom I.V., Lihachev A.I., Nashchekin A.V., and Bolshakov A.D., Hydrothermal zinc oxide nanostructures: Geometry control and narrow band UV emission, *J. Phys.: Conf. Ser.* (2022) 2227 012007.
5. Kondratev V.M. et al., Gallium phosphide nanowires for biological concentrations ammonia detection, *J. Phys.: Conf. Ser.* (2022) 2172 012006.
6. Kondratev V.M., Kuznetsov A., Gridchin V.O., Fedina S.V., and Aubekero K., III–V nanowires for biological ammonia concentrations detection, 2022 Conference of Russian Young Researchers in Electrical and Electronic Engineering (EIConRus). (2022) 970–974.
7. Kondratev V.M. et al., III–V nanowires for ammonia detection, *J. Phys.: Conf. Ser.* (2021) 2086 012186.
8. Kondratev V.M., Bolshakov A.D., and Nalimova S.S., Technologically feasible ZnO nanostructures for carbon monoxide gas sensing, 2021 IEEE Conference of Russian Young Researchers in Electrical and Electronic Engineering (EIConRus). (2021) 1163–1166.
9. Nalimova S.S., and Kondratev V.M., Study of surface acid-base properties of gas sensitive metal oxides, 2020 IEEE Conference of Russian Young Researchers in Electrical and Electronic Engineering (EIConRus). (2020) 987–990.
10. Kondratev V.M. et al., Silicon nanowires based adsorption sensors for CO and NH₃ detection, *J. Phys.: Conf. Ser.* (2021) 2103 012229.
11. Kondratev V.M. et al., Silicon nanowires as multi-environment sensor elements for carbon monoxide and ammonia detection, *J. Phys.: Conf. Ser.* (2021) 2015 012068.
12. Schipani F. et al., Conduction mechanisms in SnO₂ single-nanowire gas sensors: An impedance spectroscopy study. *Sensors and actuators, B Chemical*. (2017) 241.
13. Chen Y.-M. et al., Application of impedance spectroscopy and surface analysis to obtain oxide film thickness, *Journal of the Electrochemical Society*. 164 (9) (2017).
14. Lin Y.F. et al., Nanocontact disorder in nanoelectronics for modulation of light and gas sensitivities, *Scientific Reports*. 5 (2015).
15. Mei B.A. et al., Physical interpretations of nyquist plots for EDLC electrodes and devices, *Journal of Physical Chemistry C*. 122 (1) (2018).
16. Li C. et al., Impact of ammonia on the electrical properties of p-type Si nanowire arrays, *Journal of Applied Physics*. 114 (17) (2013).

THE AUTHORS

KONDRATEV Valeriy M.

kvm_96@mail.ru

ORCID: 0000-0002-3469-5897

VYACHESLAVOVA Ekaterina A.

cate.viacheslavova@yandex.ru

ORCID: 0000-0001-6869-1213

MOROZOV Ivan A.

morivan@mail.ru

ORCID: 0000-0001-8505-0864

NALIMOVA Svetlana S.

sskarpova@list.ru

ORCID: 0000-0003-3065-3961

MOSHNIKOV Vyacheslav A.

vamoshnikov@mail.ru

ORCID: 0000-0001-6500-5492

GUDOVSKIKH Alexander S.

gudovskikh@spbau.ru

ORCID: 0000-0002-7632-3194

BOLSHAKOV Alexey D.

acr1235@mail.ru

ORCID: 0000-0001-7223-7232

Received 08.10.2022. Approved after reviewing 08.11.2022. Accepted 08.11.2022.

Conference materials

UDC 538.935

DOI: <https://doi.org/10.18721/JPM.161.108>

Photoluminescence and energy transfer between CdTe/CdMnTe quantum wells separated by thick barriers

V.F. Agekyan¹, N.G. Filosofov¹✉, G. Karczewski², A.N. Resnitsky³,
A.Yu. Serov¹, A.S. Smirnov³, I.V. Shtrom¹, S.Yu. Verbin¹

¹ St. Petersburg State University, St. Petersburg, Russia;

² Institute of Physics PAN, Warsaw, Poland;

³ Ioffe Institute, St. Petersburg, Russia

✉ n.filosofov@spbu.ru

Abstract. Reflection, luminescence (PL), and luminescence excitation (PLE) spectra of a CdTe/CdMnTe heterostructure with quantum wells of different thicknesses are studied. It has been found that at low temperatures light emission comes from localized exciton states of quantum wells. The PLE spectra show that the contributions of excitons and free carriers to the population of quantum well depend on its thickness. The ratio of these contributions affects the dependence of the quantum well luminescence intensity on the level of optical excitation. It has been established that the coupling of quantum wells, separated by thick barrier layers, occurs through exciton excited states.

Keywords: exciton, heterostructures, coupling quantum wells

Funding: Grant No. 75746688 (V. Agekyan, A. Serov, and N. Filosofov) of St. Petersburg SU and UMO-2021/41/B/ST3/03651 (G. Karczewski).

Citation: Agekyan V.F., Filosofov N.G., Karczewski G., Resnitsky A.N., Serov A.Yu., Smirnov A.S., Shtrom I.V., Verbin S.Yu., Photoluminescence and energy transfer between CdTe/CdMnTe quantum wells separated by thick barriers, St. Petersburg State Polytechnical University Journal: Physics and Mathematics. 16 (1.1) (2023) 49–53. DOI: <https://doi.org/10.18721/JPM.161.108>

This is an open access article under the CC BY-NC 4.0 license (<https://creativecommons.org/licenses/by-nc/4.0/>)

Материалы конференции

УДК 538.935

DOI: <https://doi.org/10.18721/JPM.161.108>

Фотолуминесценция и перенос энергии между квантовыми ямами CdTe/CdMnTe, разделенными широкими барьерами

В.Ф. Агемян¹, Н.Г. Философов¹✉, Г. Карчевский², А.Н. Резницкий³,
А.Ю. Серов¹, А.С. Смирнов³, И.В. Штром¹, С.Ю. Вербин¹

¹ Санкт-Петербургский государственный университет, Санкт-Петербург, Россия;

² Институт физики ПАН, г. Варшава, Польша;

³ Физико-технический институт им. А.Ф. Иоффе РАН, Санкт-Петербург, Россия

✉ n.filosofov@spbu.ru

Аннотация. Исследованы спектры отражения, люминесценции (PL) и спектры возбуждения люминесценции (PLE) гетероструктур CdTe/CdMnTe, содержащих квантовые ямы различной толщины. Было обнаружено, что низкотемпературная люминесценция обусловлена локализованными состояниями экситона в квантовой яме. Анализ PLE позволяет сделать вывод, что вклад экситонов и свободных носителей в заселение состояний квантовой ямы зависит от ее толщины. Показано, что соотношение этих вкладов в интенсивность люминесценции локализованного экситона квантовой ямы

зависит от уровня оптического возбуждения. Установлено, что квантовые ямы, разделенные широким барьером, взаимодействуют друг с другом посредством возбужденных состояний экситона.

Ключевые слова: экситон, гетероструктуры, связанные квантовые ямы

Финансирование: Грант № 75746688 (В. Агемян, А. Серов и Н. Философов) СПбГУ и УМО-2021/41/В/ST3/03651 (Г. Карчевский).

Ссылка при цитировании: Агемян В.Ф., Философов Н.Г., Карчевский Г., Резницкий А.Н., Серов А.Ю., Смирнов А.С., Штром И.В., Вербин С.Ю., Фотолюминесценция и перенос энергии между квантовыми ямами CdTe/CdMnTe, разделенными широкими барьерами // Научно-технические ведомости СПбГПУ: Физико-математические науки. 2023. Т. 16. № 1.1. С. 49–53. DOI: <https://doi.org/10.18721/JPM.161.108>

Статья открытого доступа, распространяемая по лицензии CC BY-NC 4.0 (<https://creativecommons.org/licenses/by-nc/4.0/>)

Introduction

The energy transfer process between quantum wells separated by barriers is of fundamental interest in semiconductor physics. One might expect that the quantum wells separated by a thick barrier would be independent at low temperature, because the energy transfer is inefficient by both tunneling and thermal excitation. In this paper, however, we present quantum well luminescence results that show evidence of efficient energy transfer between wells separated by thick (20 nm) barrier at low temperature.

Materials and Methods

We have studied reflection, photoluminescence (PL) and photoluminescence excitation (PLE) spectra of a CdTe/Cd_{1-x}Mn_xTe heterostructure, containing three CdTe quantum wells (QWs) 16, 8, and 4 monolayers (ML) thick (QW-1, QW-2, and QW-3, respectively), separated by 62 ML thick Cd_{1-x}Mn_xTe barrier layers (Fig. 1). The heterostructure is grown on GaAs-CdTe substrate, the QW-1 is separated from the substrate by a Cd_{1-x}Mn_xTe layer 150 ML thick, the Cd_{1-x}Mn_xTe cap layer have a thickness of 62 ML. A nominal value of x is 0.45, and 1 ML thicknesses are 0.324 and 0.320 nm for CdTe and Cd_{0.55}Mn_{0.45}Te, respectively.

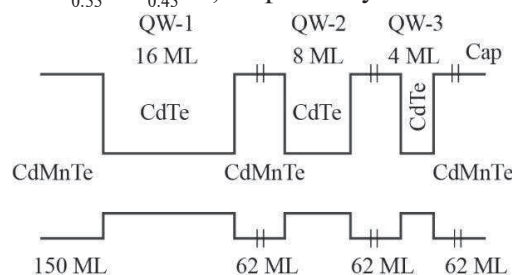


Fig. 1. Energy profile scheme of the CdTe/Cd_{1-x}Mn_xTe heterostructure with three quantum wells QW-1, QW-2, and QW-3

The He-Cd laser with 442 nm wavelength was used to excite a photoluminescence. The samples were placed in the closed-cycle He cryostat, and the spectrometer MDR-204 and photoelectron multiplier Hamamatsu R928 were used to record the low-temperature PL spectra. Micro-PL spectra were excited with Nd-YAG laser ($\lambda_{exc} = 532$ nm) and recorded using the optical complex based on spectrometer LabRAM HR Evolution (Horiba, France) equipped with a confocal microscope.

Results and Discussions

Under above barrier excitation three emission bands of QW-1, QW-2, and QW-3 are observed in the PL spectrum (Fig. 2), the QW-3 band overlaps with a broad band of Mn²⁺ intracenter luminescence. The FWHM of QW bands are 4.5, 10, and 45 meV, respectively, which is in agreement with the estimates of the inhomogeneous broadening of exciton levels due to one ML fluctuations of the QW thicknesses [1, 2].

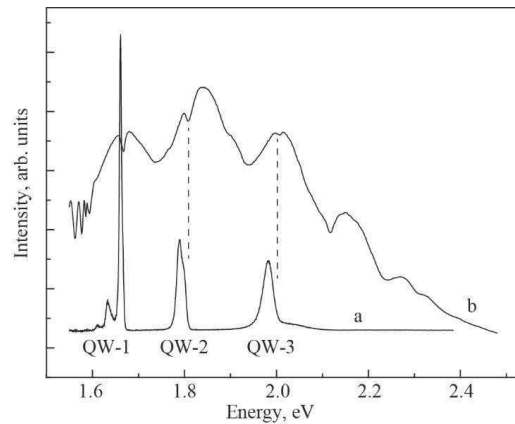


Fig. 2. Photoluminescence (*a*) and reflection (*b*) spectra of the CdTe/Cd_{1-x}Mn_xTe heterostructure at $T = 5$ K. The dashed lines show the features of the reflection spectrum, corresponding to the energies of free excitons (FE) of quantum wells

In the reflection spectrum against the background of interference fringes, features are observed, their energies corresponding to the energy levels of free excitons (FE) of three QWs (Fig. 2). At $T = 5$ K the maxima of QW bands are shifted towards low energy relative to the features of the reflection spectrum. This suggests that luminescence comes mainly from localized exciton states (LE) at low temperatures.

As the excitation level increases, the low-energy component of the doublet saturates, while the high-energy component relatively enhances (Fig. 3). This makes it possible to interpret these components as LE and free exciton (FE) emission, respectively. As the temperature increases, the LE component weakens, while the FE component increases, which confirms their origin (Fig. 4). In the QW-2 spectrum the doublet structure appears to be less distinct, in QW-3 spectrum it is not resolved at all. However, the temperature behavior of FWHM and maximum energy position of QW-3 PL band (Fig. 5) indicate the redistribution of the light emission intensity in favor of FE, when the sample is heated [3].

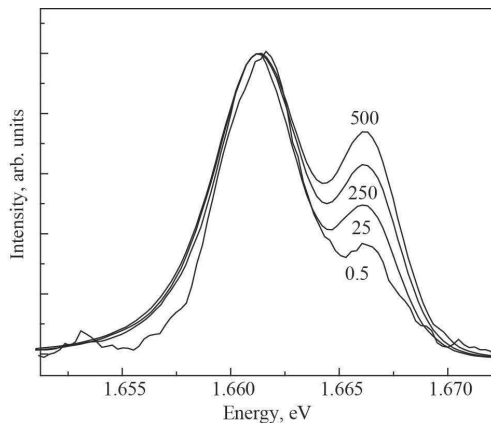


Fig. 3. QW-1 PL spectra at different excitation levels (from 0.5 up to $5 \cdot 10^2$ W/cm²). The spectra are normalized to the maximum

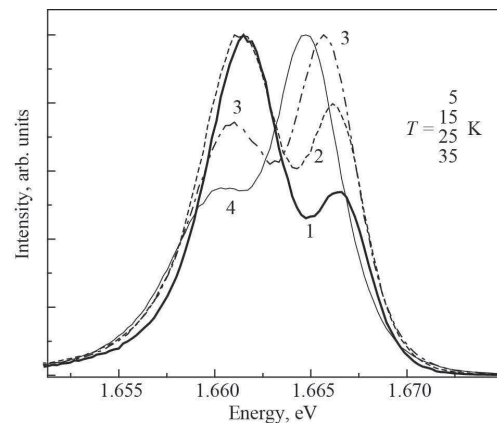


Fig. 4. Spectra of QW-1 PL at various temperatures (free FE and localized LE excitons). The spectra are normalized to the maximum

An anomalous dependence of QW-1 PL on the excitation level was revealed (Fig. 6). At an excitation level of less than 1 W/cm² the QW-1 PL band practically does not stand out distinctly against the noise. However, at an excitation level of more than 100 W/cm² the intensity of QW-1 PL band already exceeds the intensities of QW-2 and QW-3 PL. Such behavior of the QW-1 PL can be explained by the presence of a non-radiative channel near QW-1, which saturates as the excitation increases. In the heterostructure under study QW-1 is significantly removed from the substrate and the surface, so the actual non-radiative centers are most likely located at the QW-1 interfaces.

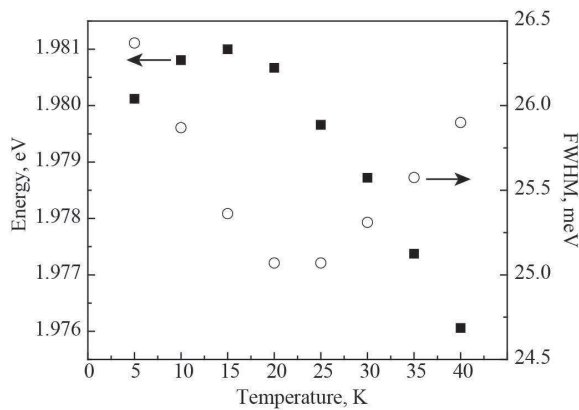


Fig. 5. Temperature dependences of FWHM and maximum energy of the QW-3 PL band

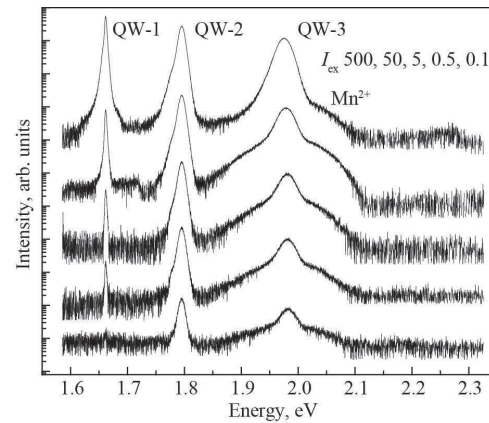


Fig. 6. PL spectra (shifted for clarity) of the CdTe/Cd_{1-x}Mn_xTe heterostructure at different excitation levels from 0.1 up to 5·10² W/cm² (lowest to upper spectra, respectively), T = 10 K

The question arises, why non-radiative centers affect QW-1 PL much stronger as compared to QW-2 and QW-3. The answer is provided by the study of the PLE spectra in the above-barrier region. As can be seen from Figure 7, in this spectral region the PLE QW-2 and QW-3 spectra have a distinct maximum at the region of 2.34 eV, which corresponds to the exciton states of the barrier. At the same time, in the PLE QW-1 spectrum the exciton maximum in this region is completely blurred and “the center of gravity” of the PLE spectrum is noticeably shifted to the short-wave region. This result means that the QW-1 states are filled mainly with free carriers, while the filling of the QW-2 and QW 3 states dominates by the exciton mechanism. Under weak excitation a carrier captured in QW-1, can relax to non-radiative center without waiting for a carrier of the opposite sign [4, 5]. When the exciton is captured, its relaxation as a whole to a non-radiative center is less probable. Moreover, the relaxation is limited by the fast exciton radiative recombination. In addition, it should be also taken into account that the higher mobility of carriers in thick QW increases the probability of their capture by the non-radiative centers.

Thus, the PLE spectra indicate that the narrower is the QW, the less efficiently it is filled through the free carrier mechanism. The reason may be a weak localization of carriers, the holes especially, in the narrow QWs. The exciton localization turns out to be more efficient, since the electron holds the hole with its Coulomb field.

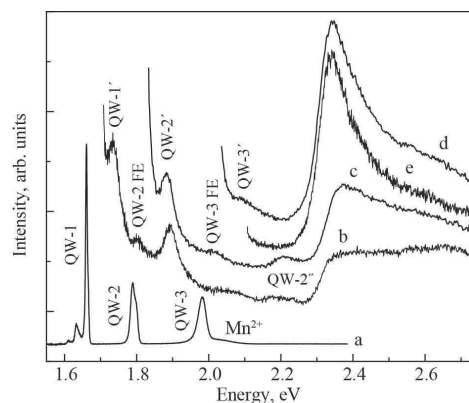


Fig. 7. PL spectrum (a) and PLE spectra of QW-1 (b), QW-2 (c), QW-3 (d) and Mn²⁺ (e), T = 5 K

Additional information, concerning to the interaction of QWs, is provided by the PLE spectra in the below-barrier region. The structure of the PLE spectra suggests that the QW-1, QW-2, and QW-3 are coupled to each other. Indeed, the QW-2 PLE spectrum has a maximum at 2.020 eV, coinciding with the energy of the QW-3 excited state; the QW-1 PLE maximum at 1.891 eV coincides with the QW-2 FE excited state, the weaker maximum at 1.810 eV corresponds to the QW-2 FE ground state (Fig.7).



It should be also seen from Figure 7 that the transfer of the above-barrier excitation to Mn^{2+} 3d-shell occurs through the exciton mechanism, so that the shape of the PLE spectrum of manganese intracenter luminescence makes it possible to refine the exciton energy of $Cd_{1-x}Mn_xTe$ barriers. The maximum at 2.34 eV of PLE spectrum of manganese intracenter luminescence corresponds to the FE position in $Cd_{1-x}Mn_xTe$ for $x = 0.47$ [6], which is close to the nominal of $x = 0.45$.

Conclusion

The features, corresponding to the ground and excited exciton states, were found in the PLE spectra of all QW, studied in this work. We can conclude that in the case of QWs, separated by thick barriers, when there is no connection between the ground states of QWs, energy transfer may occur through the excited states.

Acknowledgments

The spectra, shown in Figure 6, were excited with Nd-YAG laser ($\lambda_{exc} = 532$ nm) and recorded using an optical complex, based on spectrometer LabRAM HR Evolution (Horiba, France), equipped with a confocal microscope.

REFERENCES

1. Waag A., Schmeusser S., Bicknell-Tassius R.N., Yakovlev D.R., Ossau W., Landwehr G., Molecular beam epitaxial growth of ultrathin CdTe-CdMnTe quantum wells and their characterization, Appl. Phys. Lett. 59(23) (1991) 2995–2997.
2. Kutrowski M., Kopalko K., Karczewski G., Wojtowicz T., Kossut J., Luminescence study of CdTe/Cd_{1-x}Mn_xTe quantum wells, grown by MBE, Thin Solid Films. 267(1–2) (1995) 64–68.
3. Klochikhin A., Reznitsky A., Dal Don B., Priller H., Kalt H., Klingshirn C., Permogorov S., Ivanov S., Temperature dependence of photoluminescence bands in Zn_{1-x}Cd_xSe/ZnSe quantum wells with planar CdSe islands, Phys. Rev. B. 69 (8) (2004) 085308.
4. Budkin G.V., Eremenko M.V., Reznitsky A.N., Charge and energy transfer in double asymmetric quantum wells with quantum dots, J. Exp. Theor. Physics. 124 (5) (2017) 740.
5. Agekyan V., Filosofov N., Karczewski G., Serov A.Yu., Shtrom I., Reznitsky A., Spectroscopic evidence of tunnel coupling between CdTe quantum wells in the CdTe/ZnTe heterostructures, J. Phys. Conf. Ser. 2103 (1) (2021) 012102.
6. Goede O., Heimbrodt W., Optical properties of (Zn, Mn) and (Cd, Mn) chalcogenide mixed crystals and superlattices, PSS(b). 146 (1) (1988) 11–62.

THE AUTHORS

AGEKYAN Vadim

v.agekyan@spbu.ru

ORCID 0000-0002-5508-6660

FILOSOFOV Nikolai

n.filosofov@spbu.ru

ORCID 0000-0001-6004-3553

KARCZEWSKI Grzegorz

carcz@ifpan.edu.pl

ORCID 0000-0003-3441-1425

RESNITSKY Alexander

alexander.reznitsky@mail.ioffe.ru

ORCID 0000-0001-7876-4279

SEROV Alexey

a.serov@spbu.ru

ORCID 0000-0003-1122-9014

SMIRNOV Alexander

Alex.Smirnov@mail.ioffe.ru

ORCID 0000-0001-9709-5138

SHTROM Igor

i.shtrom@spbu.ru

ORCID 0000-0001-8912-2570

VERBIN Sergey

s.verbin@spbu.ru

ORCID 0000-0001-5791-7707

Received 11.10.2022. Approved after reviewing 15.11.2022. Accepted 15.11.2022.

Conference materials

UDC 538.935

DOI: <https://doi.org/10.18721/JPM.161.109>

Charge transfer in thin layers of polymer nanocomposites based on aromatic thermoplastic polyimide and cerium dioxide

R.A. Castro¹, A.A. Kononov¹✉, N.A. Nikonorova²

¹ Herzen State Pedagogical University of Russia, Saint Petersburg, Russia;

² Institute of Macromolecular Compounds of RAS, Saint Petersburg, Russia

✉ kononovaa@herzen.spb.ru

Abstract. The results of the study of the electric charge transfer processes in R-OOD polyimide films and in nanocomposite based on it with cerium dioxide are presented. Using the existing model of charge barrier hopping (CBH), the values of the charge transfer parameters, such as the carrier concentration N , free path length R_ω , and potential barrier height W_M are calculated. The activation energy of conductivity processes is determined for all samples. The experimental results made it possible to draw following conclusions about the effect of the filler on the polymer matrix: the power-law nature of the frequency dependence of the specific conductivity $\sigma'(\omega)$ and the decrease in the exponent s with an increase in temperature in a wide range of frequencies and temperatures indicate the existence of a hopping mechanism of conductivity in the R-OOD + CeO₂ composite;

charge transfer is a thermally activated process with an activation energy of $E = 0.077$ eV for R-OOD and $E = 0.070$ eV for R-OOD + CeO₂;

the introduction of 3% CeO₂ filler into the R-OOD matrix leads to an increase in the specific conductivity in the low-frequency region and a change in the nature of the hopping mechanism of conduction.

Keywords: electric charge transfer, polyimide, cerium dioxide, charge barrier hopping

Funding: The research was supported by the Ministry of Education of the Russian Federation as part of State task (Project No. FSZN-2020-0026).

Citation: Castro R.A., Kononov A.A., Nikonorova N.A., Charge transfer in thin layers of polymer nanocomposites based on aromatic thermoplastic polyimide and cerium dioxide, St. Petersburg State Polytechnical University Journal: Physics and Mathematics. 16 (1.1) (2023) 54–59 DOI: <https://doi.org/10.18721/JPM.161.109>

This is an open access article under the CC BY-NC 4.0 license (<https://creativecommons.org/licenses/by-nc/4.0/>)

Материалы конференции

УДК 538.935

DOI: <https://doi.org/10.18721/JPM.161.109>

Перенос заряда в тонких слоях полимерных нанокмполитов на основе ароматического термопластичного полиимида и диоксида церия

Р.А. Кастро¹, А.А. Кононов¹✉, Н.А. Никонорова²

¹ Российский государственный педагогический университет имени А.И. Герцена, Санкт Петербург, Россия;

² Институт высокомолекулярных соединений РАН, Санкт-Петербург, Россия

✉ kononovaa@herzen.spb.ru

Аннотация. Представлены результаты исследования процессов переноса электрического заряда в полиимидных пленках Р-ООД и в нанокмполите на основе с диоксидом церия. С использованием существующей модели прыжков через потенциальный барьер рассчитаны значения параметров переноса заряда, такие как концентрация носителей

заряда, длина свободного пробега и высота потенциального барьера. Для всех образцов определена энергия активации процессов проводимости. Результаты экспериментов позволили сделать некоторые выводы о влиянии наполнителя на полимерную матрицу.

Ключевые слова: перенос электрического заряда, полиимид, диоксид церия, прыжковый перенос заряда

Финансирование: Работа выполнена при поддержке Министерства просвещения Российской Федерации в рамках Государственного задания (проект № FSZN-2020-0026).

Ссылка при цитировании: Кастро Р.А., Кононов А.А., Никонорова Н.А., Перенос заряда в тонких слоях полимерных нанокомпозитов на основе ароматического термопластичного полиимида и диоксида церия // Научно-технические ведомости СПбГПУ: Физико-математические науки. 2023. Т. 16. № 1.1. С. 54–59. DOI: <https://doi.org/10.18721/JPM.161.109>

Статья открытого доступа, распространяемая по лицензии CC BY-NC 4.0 (<https://creativecommons.org/licenses/by-nc/4.0/>)

Introduction

Polymer composite materials are widely used in almost all areas of human life. Particular attention is paid to the study of polymer composite materials based on polyimides (PI), as they are characterized by their exceptional mechanical, dielectric, and thermal properties. The possibilities of using these materials are extensive — from industry to microelectronics, medicine, etc. [1–5]. Nevertheless, the issue of using one or another PI-based nanocomposite requires separate studies and detailed analysis.

Various fillers, including nanofibers of metal oxides, which can improve the mechanical and electrical properties of compositions, are used for modifying PI [6–9]. Thus, in composites based on PI and cerium dioxide nanoparticles a number of important results have been obtained concerning thermal stability and mechanical properties [9]. However, no attention has been paid in these studies to the study of charge transfer processes in these materials. That is why the purpose of this work was to establish the features of charge transfer processes in polymer composites based on aromatic polyimide R-OOD with cerium dioxide as a filler by the dielectric spectroscopy method.

Materials and Methods

The objects of study in present work were the initial R-OOD and the nanocomposite R-OOD + 3% CeO₂. In these PIs the anhydride part of the macromolecule was 1,3 bis (3',4 dicarboxyphenoxy)benzene dianhydride, and 4,4'-bis-(4"-aminophenoxy)diphenyl oxide (R-OOD) was used as the diamine. Polyimide films were obtained in Institute of Macromolecular Compounds of the Russian Academy of Sciences by a standard two-stage method [1, 10]. Cerium dioxide CeO₂ (3%) was used as a nanofiller. The films of 25–50 μm thick were pressed between brass electrodes and additionally heated to 250 K.

To study the surface structure and determine the elemental composition of the samples, a Carl Zeiss EVO 40 scanning electron microscope was used. This measuring system is designed to obtain images of objects in “forward” and backscattering electrons with a maximum resolution of several nanometers.

The dielectric response of the samples was obtained using a Concept-81 broadband dielectric spectrometer (NOVOCONTROL Technologies GmbH&Co) with an ALPHA-ANB high-resolution automatic frequency analyzer (core shared research facilities “Modern physical and chemical methods for the formation and study of materials for the needs of industry, science, and education”/Herzen University). To study the transfer processes in R-OOD and R-OOD + CeO₂, an alternating electric field with a frequency $f = 10^{-1}–10^7$ Hz was applied to the samples in the temperature range $T = 173–253$ K.

Results and Discussion

The frequency dependences of the specific conductivity for R-OOD and R-OOD + CeO₂ at various temperatures are shown in Figures 1 and 2, respectively.

As follows from the figure, the dispersion σ' complies with the law:

$$\sigma'(\omega) = A\omega^s \quad (1)$$

here ω is the angular frequency, A is a frequency-independent constant, and s is the exponent.

This type of dependence is characteristic for many disordered systems, such as glassy and amorphous semiconductors, polymer systems and composite materials based on them [11]. The values of the power dependence parameter were determined by approximating the experimental data using a linear function (the relative error did not exceed 3% over the entire temperature range).

The temperature dependence of the parameter s is shown in Figure 3 for R-OOD and R-OOD + CeO₂. Qualitative differences in the temperature dependences of the parameter s indicate a change in the conductivity mechanism in samples with 3% CeO₂ nanoparticles.

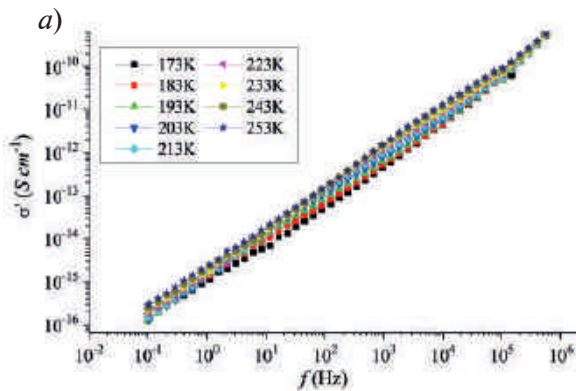


Fig. 1. Frequency dependence of specific conductivity σ' at different temperatures for R-OOD

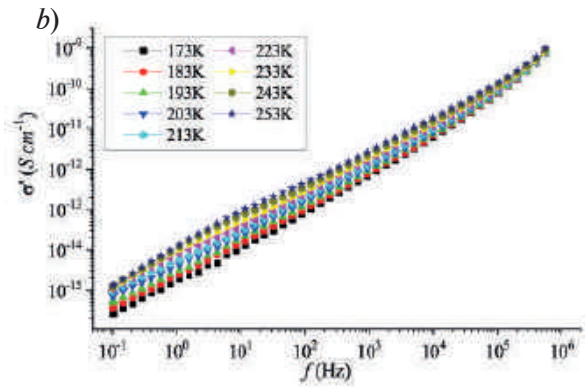


Fig. 2. Frequency dependence of specific conductivity σ' at different temperatures for R-OOD + CeO₂

The temperature dependence of the parameter s is shown in Figure 3 for R-OOD and R-OOD + CeO₂. Qualitative differences in the temperature dependences of the parameter s indicate a change in the conductivity mechanism in samples with 3% CeO₂ nanoparticles.

The existence of an exponential dependence of specific conductivity σ' on temperature (Fig. 4 and 5) allows us to conclude that charge transfer in the systems under study is a thermally activated process obeying the Arrhenius law [12]. The activation energy E was calculated from the slope of the curves $\ln\sigma' = f(10^3/T)$. The E values for R-OOD and R-OOD + CeO₂ are 0.077 and 0.070 eV, respectively (the relative calculation error did not exceed 3%). The introduction of 3% CeO₂ into the R-OOD polyimide matrix leads to an increase in the specific conductivity in the low-frequency region. This can be associated with structural changes in the polymer matrix (Fig. 6).

For R-OOD + CeO₂, the power dependence of conductivity on frequency (Fig. 6, curve 1), as well as the decrease in the functional parameter s with temperature from 0.94 to 0.79 (Fig. 3, curve 2), are apparently associated with the manifestation of the hopping mechanism of conductivity. There are several models for hopping charge transfer; the linear drop in the temperature dependence of s can be explained in terms of the CBH model (correlated barrier hopping model) [13]. It is assumed that the charge transfer is carried out by electrons jumping between energy states, overcoming the potential barrier W between two localized states (equilibrium centers). In this case, the height of the barrier between two localization centers is determined by the Coulomb interaction between neighboring defect (impurity) states, which can be charged formations in the structure that form a dipole.

According to the authors of [14], the expression for alternating current is as follows:

$$\sigma'(\omega) = \frac{\pi^3 N^2 \epsilon \epsilon_0 \omega R_0^6}{24}, \quad (2)$$

here N is the density of the pairs of states, R_0 is jump length, ω is angular frequency.

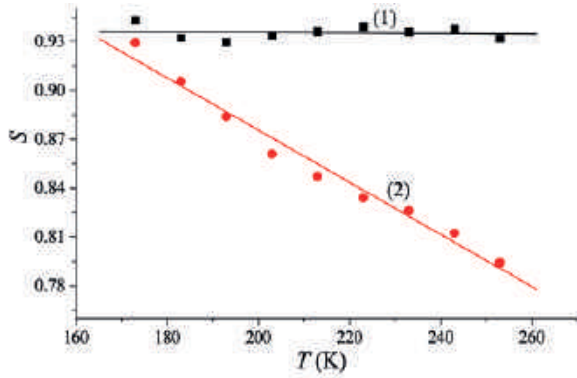


Fig. 3. Temperature dependence of the exponent s from Equation (3) for samples R-OOD — (1), and R-OOD + CeO₂ — (2)

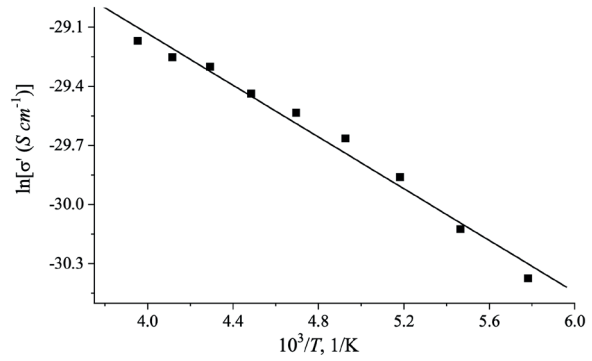


Fig. 4. Temperature dependence of specific conductivity σ' for R-OOD

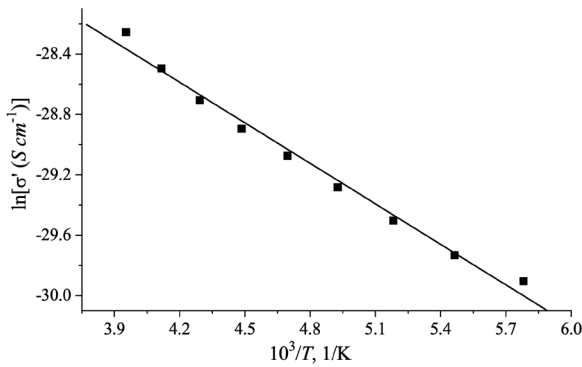


Fig. 5. Temperature dependence of specific conductivity σ' for R-OOD + CeO₂

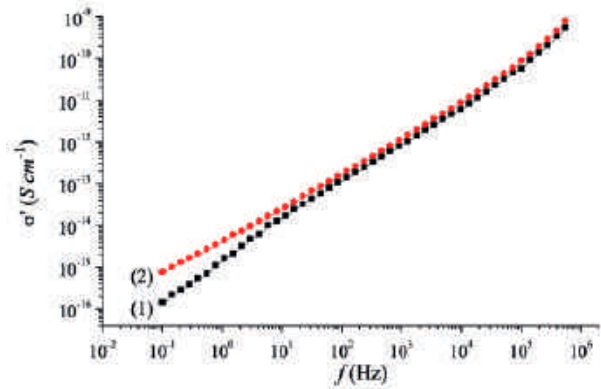


Fig. 6. Frequency dependence of specific conductivity at $T = 203$ K. (1) — R-OOD ($s = 0.94$); (2) — R-OOD + CeO₂ ($s = 0.86$)

The relationship between R_ω and the height of the potential barrier W_M can be expressed by the equation:

$$R_\omega = \frac{e^2}{\pi \epsilon \epsilon_0} \left[W_M - kT \ln \left(\frac{1}{\omega \tau_0} \right) \right]^{-1}, \quad (3)$$

here τ_0 is the characteristic relaxation time (the reciprocal of the phonon frequency ν_{ph}).

Theoretically, it is shown that the exponent s is related to the barrier height W_M by the expression:

$$s = 1 - \frac{6kT}{W_M}. \quad (4)$$

Equations (2–4) can be used to calculate the microparameters N , R_ω , and W_M for the systems under study over the entire temperature range (Table 1).

The observed patterns of charge transfer processes in the R-OOD + CeO₂ nanocomposite, the change in the nature of the hopping mechanism of the charge transfer, and the increase in conductivity are associated with the introduction of a filler — cerium dioxide nanoparticles.

X-ray study (EDX — energy-dispersive X-ray) of PI + CeO₂ nanocomposites showed that if in the initial R-OOD there is a uniform distribution of particles in the sample, then in the R-OOD + CeO₂ nanocomposite the formation of CeO₂ aggregates of various sizes is observed [9]. The appearance of intrinsic structures of cerium dioxide in the polymer matrix can lead to the formation of continuous conducting channels, which in turn leads to an increase in conductivity. A similar situation was observed in a nanocomposite based on polyphenylene oxide with fullerene [15].

Table 1

Values of microparameters of R-OOD polyimide calculated within the framework of the CBH model

T (K)	s	N (m ⁻³)	R_{ω} (nm)	W_M (eV)
173	0.94	$2.10 \cdot 10^{23}$	2.20	1.27
183	0.91	$7.51 \cdot 10^{22}$	3.19	1.00
193	0.88	$3.48 \cdot 10^{22}$	4.28	0.86
203	0.86	$1.54 \cdot 10^{22}$	5.84	0.75
213	0.85	$1.02 \cdot 10^{22}$	6.92	0.72
223	0.83	$6.63 \cdot 10^{21}$	8.23	0.70
233	0.82	$5.51 \cdot 10^{21}$	9.04	0.69
243	0.81	$3.18 \cdot 10^{21}$	11.12	0.67
253	0.79	$1.23 \cdot 10^{21}$	16.08	0.64
Error	$\leq 3.0\%$	$\leq 5.0\%$	$\leq 5.0\%$	$\leq 5.0\%$

Conclusion

In this work the dielectric method is used for the first time to study the features of charge transfer processes in R-OOD polyimides films and a nanocomposite based on it with cerium dioxide as a filler. Conductivity parameters were calculated within the framework of the CBH conductivity model. The main conclusions of the work are as follows:

1. The power-law nature of the frequency dependence of the specific conductivity $\sigma'(\omega)$ and the decrease in the exponent s with an increase in temperature in a wide range of frequencies and temperatures indicate the existence of a hopping mechanism of conductivity in the R-OOD + CeO₂ composite.

2. Charge transfer is a thermally activated process with an activation energy of $E = 0.077$ eV for R-OOD and $E = 0.070$ eV for R-OOD + CeO₂.

3. The introduction of 3% CeO₂ filler into the R-OOD matrix leads to an increase in the specific conductivity in the low-frequency region and a change in the nature of the hopping mechanism of conduction.

REFERENCES

1. Bryant R.G., Polyimides, Encyclopedia of Polymer Science and Technology, John Wiley & Sons. New York, 2002.
2. Sroog C.E., Encyclopedia of Polymer Science and Technology, John Wiley & Sons. New York, 1969.
3. Kase Y., Advanced Membrane Technology Applications, John Wiley & Sons. New York, 2008.
4. Yudin V.E., Otaigbe J.U., Gladchenko S., Olson B.G., Nazarenko S., Korytkova E.N., Gusarov V.V., New polyimide nanocomposites based on silicate type nanotubes: Dispersion, processing and properties, Polymer. 48 (5) (2007) 1306–1315.
5. Avico-Salvado O., Sabbah W., Buttay C., Morel H., Bevilacqua P., Evaluation of printed-circuit board materials for high-temperature operation, Journal of Microelectronics and Electronic Packaging. 14 (4) (2017) 166–171.
6. Sang X., Li K., Wang P., Jia K., Lei X., Liu X., Fabrication and microwave absorption properties of size-controlled polymer/Fe₃O₄ hybrid microsphere based on aggregation-induced emission active polyarylene ether nitrile, Journal of Polymer Research. 25 (9) (2018) 207.
7. Shah P., Pandey K., Advancement in packaging film using microcrystalline cellulose and TiO₂, American Journal of Polymer Science and Technology. 3 (6) (2017) 97–102.
8. Mallakpour S., Darvishzadeh M., Ultrasonic treatment as recent and environmentally friendly route for the synthesis and characterization of polymer nanocomposite having PVA and biosafe BSA-modified ZnO nanoparticles, Polymers for Advanced Technologies. 29 (8) (2018) 2174–2183.
9. Gofman I., Nikolaeva A., Yakimansky A., Ivanova O., Baranchikov A., Ivanov V., Unexpected



selective enhancement of the thermal stability of aromatic polyimide materials by cerium dioxide nanoparticles, *Polymers for Advanced Technologies*. 30 (6) (2019) 1518–1524.

10. **Bessonov M.I.**, Polyimides are a class of heat-resistant polymers, Nauka. Leningrad, 1983.

11. **Mott N.F., Davis E.A.**, Electronic processes in non-crystalline materials, Clarendon Press. Oxford, 1979.

12. **Kremer K.**, Broadband dielectric spectroscopy, Springer. Berlin Heidelberg, 2003.

13. **Elliott S.R.**, AC conduction in amorphous chalcogenide and pnictide semiconductors, *Advances in Physics*. 36 (2) (1987) 135–217.

14. **Austin I.G., Mott N.F.**, Polarons in crystalline and non-crystalline materials, *Advances in Physics*. 18 (71) (1969) 41–102.

15. **Kononov A.A., Castro Arata R.A., Nikonorova N.A.**, Effect of quasi-stationary electric field on charge transfer in poly(phenylene oxide) based composites, *Physics of Complex Systems*. 1 (2) (2020) 52–55.

THE AUTHORS

CASTRO Rene Alejandro

recastro@mail.ru

ORCID: 0000-0002-1902-5801

NIKONOROVA Natalia A.

n_nikonorova2004@mail.ru

ORCID: 0000-0002-7928-9227

KONONOV Alexey A.

rakot1991@mail.ru

ORCID: 0000-0002-5553-3782

Received 13.10.2022. Approved after reviewing 08.11.2022. Accepted 25.11.2022.

Conference materials

UDC 539.421

DOI: <https://doi.org/10.18721/JPM.161.110>

Specific features of defect structure of a quartz single crystal at early stages of deformation

E.E. Damaskinskaya ¹✉, V.L. Hilarov ¹, Yu.G. Nosov ¹, K.M. Podurets ²,

A.A. Kaloyan ², D.V. Korost ³, K.A. Damaskinskii ⁴

¹ Ioffe Institute, St. Petersburg, Russia;

² NRC Kurchatov Institute, Moscow, Russia;

³ Lomonosov Moscow State University, Moscow, Russia;

⁴ Peter the Great St. Petersburg Polytechnic University, St. Petersburg, Russia

✉ Kat.Dama@mail.ioffe.ru

Abstract. The paper is concerned with studies of the fracture process in a synthetic quartz single crystal under uniaxial compression at early stages of deformation by three independent techniques, i.e., acoustic emission, X-ray computed tomography and topography using a synchrotron radiation source. The most intense crack formation was observed in the region of higher internal deformations in the original crystal which were detected by topography. The energy of acoustic emission signals and the volume of the defects formed have been found to be linearly related. This result is of practical significance, since it allows estimation of sizes of fracture regions *in situ* merely by analyzing acoustic emission data in the cases, when other control techniques are inapplicable (for example, during the operation of industrial facilities).

Keywords: acoustic emission, X-ray computed tomography, synchrotron radiation topography (X-ray diffraction imaging), quartz single crystal, defects volume

Funding: This work was performed within the framework of the State assignment of the Ioffe Institute (0040-2014-0008).

Citation: Damaskinskaya E.E., Hilarov V.L., Nosov Yu.G., Podurets K.M., Kaloyan A.A., Korost D.V., Damaskinskii K.A., Specific features of defect structure of a quartz single crystal at early stages of deformation, St. Petersburg State Polytechnical University Journal: Physics and Mathematics. 16 (1.1) (2023) 60–66. DOI: <https://doi.org/10.18721/JPM.161.110>

This is an open access article under the CC BY-NC 4.0 license (<https://creativecommons.org/licenses/by-nc/4.0/>)

Материалы конференции

УДК 539.421

DOI: <https://doi.org/10.18721/JPM.161.110>

Особенности дефектной структуры монокристалла кварца, сформировавшейся на ранних этапах деформирования

Е.Е. Дамаскинская ¹✉, В.Л. Гиляров ¹, Ю.Г. Носов ¹, К.М. Подурец ²,

А.А. Калоян ², Д.В. Корост ³, К.А. Дамаскинский ⁴

¹ Физико-технический институт им. А.Ф. Иоффе РАН, Санкт-Петербург, Россия;

² НИЦ «Курчатовский институт», Москва, Россия;

³ Московский государственный университет им. М.В. Ломоносова, Москва, Россия;

⁴ Санкт-Петербургский политехнический университет Петра Великого, Санкт-Петербург, Россия

✉ Kat.Dama@mail.ioffe.ru

Аннотация. С помощью трех независимых неразрушающих методов — акустической эмиссии, рентгеновской компьютерной томографии, топографии с использованием источника синхротронного излучения — проведено исследование процесса разрушения

в синтетическом монокристалле кварца при одноосном сжатии на ранних этапах деформирования. Наиболее интенсивное образование трещин наблюдалось в области повышенных внутренних деформаций в исходном кристалле, обнаруженной с помощью топографии. Установлена линейная зависимость между энергией сигналов акустической эмиссии и объемом образовавшихся дефектов. Данный результат имеет практическое значение, поскольку позволяет в дальнейшем оценивать размеры областей разрушения *in situ* только по анализу данных акустической эмиссии в тех случаях, когда применение других методов контроля невозможно (например, при эксплуатации промышленных объектов).

Ключевые слова: акустическая эмиссия, рентгеновская компьютерная томография, рентгеновская дифракционная топография, объем дефектов, монокристалл кварца

Финансирование: Работа выполнена в рамках Государственного задания ФТИ им. А.Ф. Иоффе «Проблемы физики прочности: процессы разрушения твердых тел, принципы упрочнения материалов и повышения динамической прочности материалов, создание трещиностойких, износостойких материалов, разработка технологий легкой прозрачной брони» (код темы [0040-2014-0008]).

Ссылка при цитировании: Дамаскинская Е.Е., Гиляров В.Л., Носов Ю.Г., Подурец К.М., Калоян А.А., Корост Д.В., Дамаскинский К.А., Особенности дефектной структуры монокристалла кварца, сформировавшейся на ранних этапах деформирования // Научно-технические ведомости СПбГПУ. Физико-математические науки. 2023. Т. 16. № 1.1. С. 60–66. DOI: <https://doi.org/10.18721/JPM.161/110>

Статья открытого доступа, распространяемая по лицензии CC BY-NC 4.0 (<https://creativecommons.org/licenses/by-nc/4.0/>)

Introduction

The fracture process caused by the formation of single submicro- and micro-cracks and their further evolution up to a macro-crack under the action of mechanical stresses is still not fully understood. This is due to the complexity of the experimental observation of defects in the material bulk during deformation without violating the integrity of the object of study.

One of the techniques that make it possible to control material damage *in situ* is the recording of acoustic emission (AE) signals that accompany the formation and development of submicro-, micro-, and macrocracks [1, 2]. It has been shown that acoustic emission in quartz occurs under high pressures, at heating and phase transformations [3–6].

The goal of our study was to trace the evolution of defects in a synthetic quartz single crystal by using complementary techniques, i.e., acoustic emission (AE), computed microtomography (CT), and X-ray diffraction imaging (XDI) or topography.

Experimental

We used a synthetic Z-oriented quartz crystal grown by hydrothermal synthesis at the All Union Research Institute for the Synthesis of Mineral Raw Materials [7]. Cylindrical samples ($d = 10$ mm, $h = 20$ – 24 mm) were cut from the crystal perpendicular to the $\{0001\}$ pinacoid faces, the sample axis was in the $\langle 0001 \rangle$ direction.

The samples were subjected to uniaxial quasi-static compression at a loading rate (displacement of loading plates) of $5 \mu\text{m}/\text{min}$ on an AGX-Plus electromechanical machine (Shimadzu, Japan, maximum force 30 tons). The force was applied parallel to the cylinder axis. The compression was carried out up to a force equal to 6 kN, which corresponded to 0.08 of F_{max} (F_{max} is the breaking load, determined in preliminary experiments). The sample was then kept under constant strain until the AE activity dropped to zero (Fig. 2).

Acoustic emission signals were recorded in real time during sample loading by using the Amsy-5 Vallen system (Germany). Two AE105A piezoelectric transducers (frequency range 450–1150 kHz) were mounted at the sample ends. The accuracy of determining the coordinates of the AE signals hypocenters was not poorer than 2 mm. Each AE signal was characterized by the emission time, source coordinate along the sample height, and energy. The details of the experiment were described earlier; see, for example, [8].

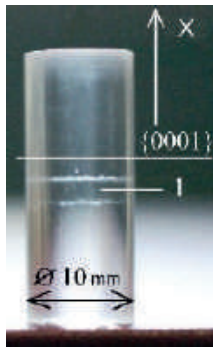


Fig. 1. Sample of a quartz single crystal (number 1 indicates the region of the sample where the seed is located; the white dots are the initial surfaces of the seed)

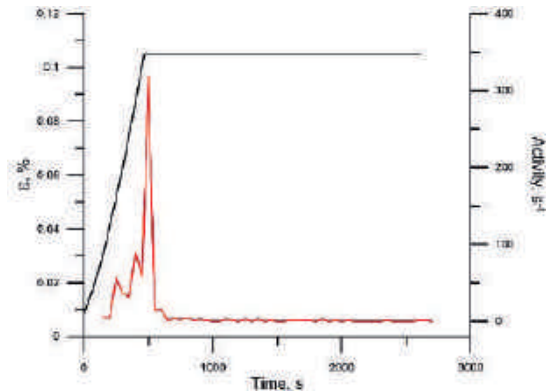


Fig. 2. Changes in strain (black line) and AE activity (red line) during the experiment

The study of the defects, characterized by a variation in the electron density of the material (in this case, pores or cracks), was performed by using X-ray computed microtomography (CT). Tomographic imaging before and after mechanical tests was carried out by a SkyScan 1172 tomograph (Bruker, Belgium) equipped with a Hamamatsu 100/250 microfocus X-ray tube and a detector (CCD — charge-coupled device 11-megapixel). For reconstruction the SkyScan's Nrecon software was used.

The selected sample size made it possible to achieve a spatial resolution of computed tomography of $\sim 3 \mu\text{m}$.

Tomographic imaging of the samples performed before mechanical testing revealed defects that were left from the seed surface. Figure 3 shows that the defects are located randomly inside the sample in the region with coordinates 11–14 mm in height. It was in this area that the seed was located (as can be seen in Figure 1). No defects such as cracks (discontinuities) were found outside the region of the seed plane.

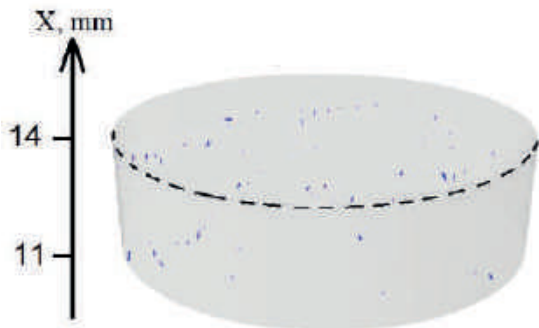


Fig. 3. Three-dimensional visualization of original defects (that were left from the seed) (blue objects)

To reveal the defects in the crystal structure and their aggregates, which did not affect the material density, but caused internal stresses, X-ray topography (XDI) was used. XDI made it possible to obtain an image of long-range strain fields in the form of a change in diffracted beam intensity (due to extinction contrast) [9]. Extinction contrast is a contrast, caused by local changes in the degree of crystal perfection.

Topographic studies were carried out at station “Median” of the Kurchatov specialized source of synchrotron radiation “KISI-Kurchatov”. Images (topographs) were recorded by using a two-coordinate detector based on a 4008×2672 CCD matrix, a GdOS:Tb scintillator, with a pixel size of $8.9 \mu\text{m}$. For image processing the ImageJ software was used [10].

Results and Discussion

The distribution of AE signal hypocenters along the sample height (Fig. 4) shows that the largest number of sources (in 7–10 times more than in other areas) is present in the 16–20 mm region. This implies that the most intense defect formation occurs in this region.

According to the data, described earlier in Section 2, there are no defects, associated with the seed in this region. A tomographic survey of the loaded specimen showed that the crack (black surface in Figure 5, a) was formed outside the original defects (red objects in Figure 5, b). Comparison of tomographic sections, obtained before and after loading, suggests that the initial defects at a given load level did not undergo any changes, i.e., neither germination of defects nor their closure was observed.

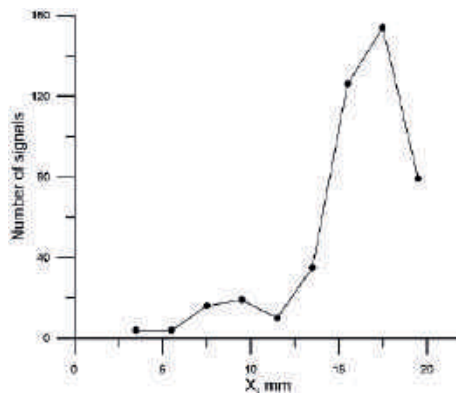


Fig. 4. Distribution of AE signals along the sample height

Figure 6 shows the change in the volume of defects in 2 mm high layers, determined from the CT data by using the CTan software. The largest volume of defects was detected in the 16–20 mm region. It is in this area that the fracture has a branched structure, which is demonstrated by the tomographic slices (Fig. 5, *c*).

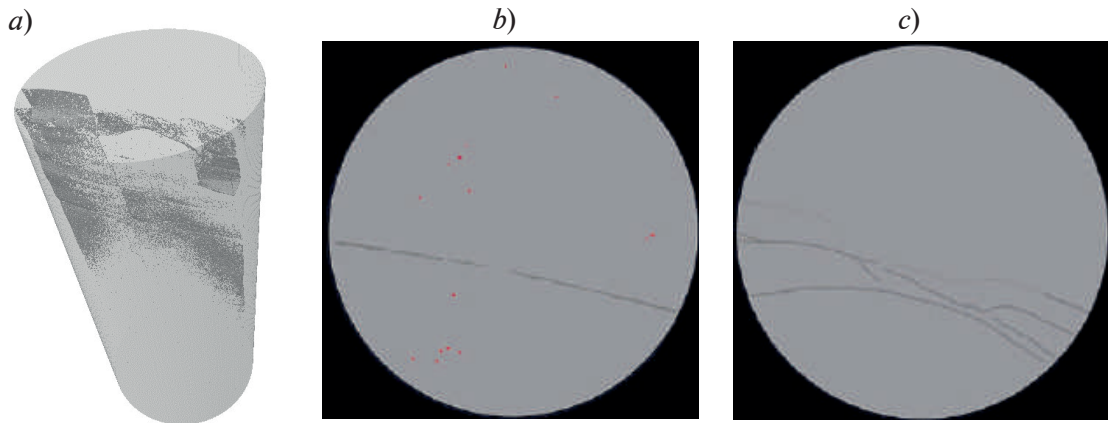


Fig 5. 3D visualization of the defect structure built from the X-ray tomography data using specialized CTan and CTvol softwares (*a*), and examples of tomographic sections: *b* — a slice of the area near the seed (the original defects are in red, the crack is in black); *c* — slice of the area with the most branched crack (black lines) far from the seed

A correlation between the mean signal energy AE and the volume of defects (Fig. 7) has been established. The dependence is approximated by a linear function (determination coefficient $R^2 = 0.89$). This result allows estimation of the volume of defects from the AE signals parameters.

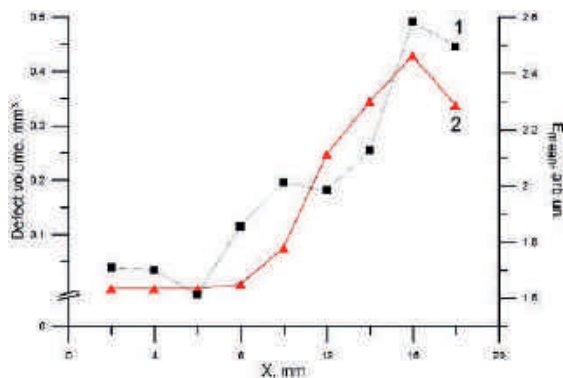


Fig. 6. Variations in the mean signal energy AE (gray curve 1) and defect volume (red curve 2) along the coordinate (sample height)

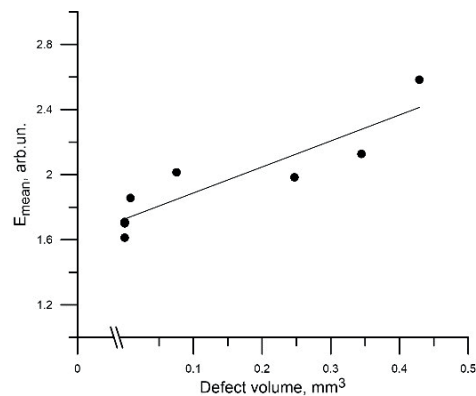


Fig. 7. Dependence of the mean signal energy AE on the volume of defects

X-ray topography revealed that the main “motif” of the defect structure was the presence of linear formations in the form of wavy fibers, extending along the sample height, i.e., in the direction of crystal growth (Fig. 8). The “fibers” are not an image of individual linear defects (dislocations), because in many cases they are observed to be broken, which is not typical of dislocations.

No elementary defects, such as dislocations, low-angle boundaries, etc., are detected on topographs. The observed imperfections are not discontinuities. It can be supposed that the fibrous structure is the manifestation of the assemblies of defects, mainly dislocations, the density of which is constant along the fiber and varies significantly in the transverse direction. There is the region in the crystal, in which the density of fibrous assemblies is higher as compared to the average density in the crystal (indicated by the arrow in Fig. 8, *a* and *b*).

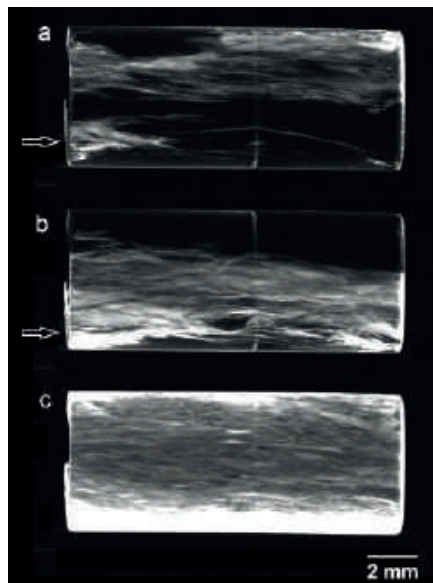


Fig. 8. Two topographs of the quartz crystal with an angular interval of 9.4° , taken before application of a mechanical load (*a*, *b*), and a map of maximum intensity (*c*). A border of simultaneous reflection is observed in the middle of the image

Topographs of the quartz crystal were obtained after it was subjected to mechanical action. Analysis of the AE and CT data showed that the most developed crack (the largest amount of defects) was formed in the area with coordinates 16–20 mm. The topographs (Fig. 9) reveal a higher intensity in the same spatial region.

Thus, XDI allowed detection of a region of higher strains in the original sample. It is in this area that where the most intense cracking occurred after mechanical impacts, as evidenced by computed tomography.

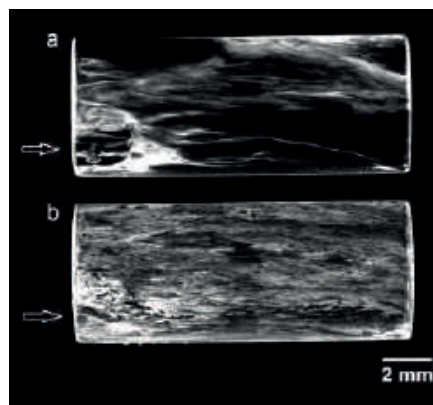


Fig. 9. A topograph of the quartz crystal, taken after application of a mechanical load (*a*), and a map of the rocking curve widths (*b*). The arrow indicates the region of fracture



The topographic pattern of fibers in the crystal bulk, obtained in our experiments, coincides with the pattern of structural defects in quartz, i.e, striations caused by assemblies of growth dislocations, which has been repeatedly described [7, 11]. The formation of cracks was observed in the region of higher densities of striae (fibrous formations) suggests that the primary structural defect, which gives rise to the formation of cracks under loading, are “bundle-like” dislocation clusters along the striae boundaries.

Conclusion

The accumulation of defects in a synthetic single crystal of quartz under uniaxial compression at early stages of deformation has been studied. A simultaneous application of three independent non-destructive techniques — acoustic emission, X-ray computed tomography, and the topography using a synchrotron radiation source — has given a more complete information on the development of fracture.

XDI allowed detection of the region of higher internal deformations in the original crystal.

Computed tomography visualized the cracks that were formed after load application and gave the data on the shape, size and volume of defects.

Analysis of parameters of acoustic emission signals allowed identification of the spatial region of the sample, in which defect formation was most intense.

Thus, the results obtained with the three techniques are consistent with each other and allowed detection of the region of the most intense defect formation in the sample bulk, and, what is especially important, allowed comparison of the parameters of the AE signals with those of the defects.

REFERENCES

1. **Xinglin Lei, Shengli Ma.**, Laboratory acoustic emission study for earthquake generation process, *Earthquake Science*. 27 (2014) 627–646.
2. **Voznesenskii A.S., Krasilov M.N., Kutkin Ya.O., Tavostin M.N., and Osipov Yu.V.**, Features of interrelations between acoustic quality factor and strength of rock salt during fatigue cyclic loadings, *International Journal of Fatigue*. 97 (2017) 70–78.
3. **Schmidt-Mumm A.**, Low frequency acoustic emission from quartz upon heating from 90 to 610 °C, *Physics and Chemistry of Minerals*. 17 (1991) 545–553.
4. **Glover P.W.J., Baud P., Darot M., Meredith P.G., Boon S.A., LeRavalec M., Zoussi S., Reuschlé T.**, α/β phase transition in quartz monitored using acoustic emissions, *Geophysical Journal International*. 120(3) (1995) 775–782.
5. **Gasc J., Schubnel A., Brunet F., Guillon S., Mueller H.-J., Lathe C.**, Simultaneous acoustic emissions monitoring and synchrotron X-ray diffraction at high pressure and temperature: Calibration and application to serpentinite dehydration, *Physics of the Earth and Planetary Interiors*. 189 (3–4) (2011) 121–133.
6. **Vettegren V.I., Kuksenko V.S., and Shcherbakov I. P.**, Dynamics of fractoluminescence, and electromagnetic, and acoustic emission upon an impact against the marble surface, *Technical Physics*. 58 (1) (2013) 136–139.
7. **Dorogovin B.A. ed, et al.**, *Sintez mineralov*, Vol. 1 (2000). VNIISIMS, 2000 (in Russian).
8. **Damaskinskaya E.E., Hilarov V.L., Pantelev I.A., Gafurova D.R., and Frolov D.I.**, Statistical regularities of formation of a main crack in a structurally inhomogeneous material under various deformation conditions, *Physics of the Solid State*. 60(9) (2018) 1821–1826.
9. **Shul’pina I.L., Prokhorov I.A.**, X-ray diffraction topography for materials science, *Crystallography Reports*. 57 (2012) 661–669.
10. **Schneider C.A., Rasband W.S., Eliceiri K.W.**, NIH image to ImageJ: 25 years of image analysis, *Nature Methods*. 9 (7) (2012) 671–675.
11. **Kleshchev G.V., Kabanovich I.V., Chernyi L.N.**, On the nature of the optical inhomogeneity of quartz, *Doklady AN SSSR*. 174 (3) (1967) 585–586.

THE AUTHORS

DAMASKINSKAYA Ekaterina E.
Kat.Dama@mail.ioffe.ru
ORCID: 0000-0001-6328-0917

HILAROV Vladimir L.
Vladimir.Hilarov@mail.ioffe.ru
ORCID: 0000-0002-9211-6144

NOSOV Yuri G.
yu.nosov@mail.ioffe.ru

PODURETS Konstantin M.
Podurets_KM@nrcki.ru
ORCID: 0000-0003-2215-3692

KALOYAN Aleksandr A.
alexander.kaloyan@gmail.com

KOROST Dmitrii V.
dkorost@mail.ru
ORCID: 0000-0001-8957-6871

DAMASKINSKII Konstantin A.
damaskinsk@mail.ru
ORCID: 0000-0002-6692-2644

Received 13.10.2022. Approved after reviewing 08.11.2022. Accepted 08.11.2022.

Conference materials

UDC 537.9

DOI: <https://doi.org/10.18721/JPM.161.111>

Low-field magnetization features of superconducting tapes with strong pinning anisotropy

V.V. Guryev ¹✉, A.V. Irodova ¹, N.K. Chumakov ¹, S.V. Shavkin ¹

¹ National Research Centre "Kurchatov Institute", Moscow, Russia

✉ Gurev_VV@nrcki.ru

Abstract. The electrodynamic behavior of II-type superconductors is determined by the physics of the vortex matter, for which the superconducting material is the medium of existence. It is noteworthy that for all practical superconductors this medium is both anisotropic and inhomogeneous. On the basis of data on the degree of inhomogeneity and anisotropy, some features of magnetization in low external field, comparable to self-field, can be explained. Namely: 1) an anomalous shift of the central magnetization peak, and 2) the fishtail shape in inclined magnetic fields. In this paper, we present an experimental study of the low-field magnetization of Nb-Ti tapes. The degree of anisotropy was varied by heat treatment of the original cold-rolled tape and by slicing the samples along and across the rolling direction. The obtained results are discussed in comparison with the features of the magnetization loops of other practical superconductors.

Keywords: vortex matter, magnetization, fishtail, pinning anisotropy

Citation: Guryev V.V., Irodova A.V., Chumakov N.K., Shavkin S.V., Low-field magnetization features of superconducting tapes with strong pinning anisotropy, St. Petersburg State Polytechnical University Journal: Physics and Mathematics. 16 (1.1) (2023) 67–73. DOI: <https://doi.org/10.18721/JPM.161.111>

This is an open access article under the CC BY-NC 4.0 license (<https://creativecommons.org/licenses/by-nc/4.0/>)

Материалы конференции

УДК 537.9

DOI: <https://doi.org/10.18721/JPM.161.111>

Особенности низкополевой намагниченности сверхпроводящих лент с сильной анизотропией пиннинга

В.В. Гурьев ¹✉, А.В. Иродова ¹, Н.К. Чумаков ¹, С.В. Шавкин ¹

¹ Национальный исследовательский центр «Курчатовский институт», Москва, Россия

✉ Gurev_VV@nrcki.ru

Аннотация. Электродинамика сверхпроводников II рода определяется физикой ансамбля вихрей, для которых сверхпроводящий материал является средой существования. Примечательно, что для всех технических сверхпроводников эта среда одновременно анизотропна и неоднородна. На основании данных о степени неоднородности и анизотропии можно объяснить некоторые особенности намагниченности в слабом внешнем поле, сравнимом с собственным. А именно: 1) аномальный сдвиг центрального пика намагниченности, и 2) форма «fishtail» в наклонных магнитных полях. В этой статье мы представляем экспериментальное исследование низкополевой намагниченности сверхпроводящих Nb-Ti лент. Степень анизотропии варьировалась с помощью термической обработки исходной холоднокатаной ленты и путем нарезки образцов вдоль и поперек направления прокатки. Полученные результаты обсуждаются в сравнении с особенностями петель намагничивания других технических сверхпроводников.

Ключевые слова: ансамбль вихрей, намагниченность, fishtail, анизотропия пиннинга

Ссылка при цитировании: Гурьев В.В., Иродова А.В., Чумаков Н.К., Шавкин С.В., Особенности низкополевой намагниченности сверхпроводящих лент с сильной анизотропией пиннинга // Научно-технические ведомости СПбГПУ: Физико-математические науки. 2023. Т. 16. № 1.1. С. 67–73. DOI: <https://doi.org/10.18721/JPM.161.111>

Статья открытого доступа, распространяемая по лицензии CC BY-NC 4.0 (<https://creativecommons.org/licenses/by-nc/4.0/>)

Introduction

Quite a long time has passed from the prediction by A.A. Abrikosov of magnetic flux quantization in type II superconductors [1] to the acceptance by the scientific community of vortex matter as a new state of condensed matter. It turned out that in practically important cases anisotropy plays an essential role in the physics of vortex matter [2]. It is customary to distinguish between external and internal causes of anisotropy. Internal with respect to vortex matter or intrinsic anisotropy is the anisotropy of the thermodynamic critical fields H_{c1} and H_{c2} , which leads through the coherence length ξ and the penetration length λ to the anisotropy of the vortices spatial dimensions. This type of anisotropy is typical for HTS, in which the structural unit cell itself is strongly anisotropic [3]. The external anisotropy is due to the anisotropy of the pinning center morphology, which takes place in all practical superconductors, both in HTS and in traditional ones such as Nb₃Sn and Nb-Ti. Vortices, unlike particles, are essentially elongated objects. Therefore, generally one should distinguish between anisotropy with respect to the direction of the magnetic field \mathbf{B} , and anisotropy with respect to the direction of the driving force $\mathbf{F} = [\mathbf{j} \times \mathbf{B}]$, which, for a fixed direction of the magnetic field, is determined by the direction of the transport current density \mathbf{j} [4].

This is a fairly exhaustive classification of anisotropy types. Note that even in an isotropic superconductor a tensor relationship between current density and electric field has been predicted [4]. Therefore, the mismatch of the directions of these vectors cannot serve as a criterion for the presence of anisotropy.

The distinction between the causes of anisotropy becomes important when interpreting the features in the low-field parts of the magnetization curves $M(H)$, which arise in planar superconductors in tilted magnetic fields. Magnetization measurements have been proven to be a useful tool for estimating critical current density [5]. Models have been developed and widely used to estimate the in-plane anisotropy of the critical current in perpendicular magnetic field [6, 7], which is a special case of anisotropy with respect to the driving force, and to estimate the angular dependence of the critical current in the configuration of the maximum driving force (the vectors of the magnetic field and current density are always perpendicular to each other) [8, 9]. However, with rare exceptions, such as [10], the low-field part of magnetization is not analyzed. This is mainly due to the fact that the analysis is difficult, since the combined influence of the self-field and anisotropy leads to a non-uniform current distribution over the cross-section [11, 12]. At the same time, there are intriguing effects, such as a low-field fishtail in tilted magnetic fields [13, 14] and an anomalous shift of the central magnetization peak [15, 16, 17]. The latter effect is especially important, because, on the one hand, it allows one to estimate the degree of granularity [18]; on the other hand, its presence may indicate that the models mentioned above for critical current estimating are not applicable [15].

In this paper, we present the studies of the low-field magnetization of a 10 μm thick Nb-Ti tape heat-treated at 385 °C/25 h in comparison with the original cold-rolled one. In cold-rolled single-phase β -Nb-Ti tape, the pinning centers are the grain boundaries. The heat treatment led to the precipitation of 6% volume α -Ti particles, acting as strong pinning centers [19]. In accordance with previous transport measurements, the presence of α -Ti particles significantly increases the volume pinning force and reduces its anisotropy [20].



Materials and Methods

For magnetic studies 4 samples were selected, sliced along (RD-samples) and across the rolling (TD-samples) (Table 1). Slicing samples with an optimal length-to-width ratio can significantly reduce the edge effect in tilted magnetic fields [8]. The parameters of our measuring system are close to those, used in [8], and therefore the optimal aspect ratio is also about 5. Previously, samples prepared in a similar way were investigated by the transport method in a liquid helium environment at 4.2 K [4, 20, 21]. Table 1 provides descriptions, dimensions, and transport method data for the tested samples. In the series of samples from № 1 to № 4, the value of the critical current density measured at 1 T in perpendicular geometry (the external magnetic field \mathbf{H} is co-directed with the normal of the tape \mathbf{n} : $\mathbf{H}\parallel\mathbf{n}$) increases. At the same time, the ratio of the critical current densities when the field, lies in the plane of the tape ($\mathbf{H}\perp\mathbf{n}$) to the current density in the perpendicular geometry ($\mathbf{H}\parallel\mathbf{n}$) decreases. This ratio can serve as a rough estimate of the anisotropy degree in the maximum driving force configuration. The critical currents were measured not only at 1 T, but in a much wider range of magnetic fields up to the upper critical field. The obtained field dependencies were approximated by the frequently used scaling law [22]:

$$j_c H = C \left(\frac{H}{H_{irr}} \right)^p \left(1 - \frac{H}{H_{irr}} \right)^q, \quad (1)$$

where j_c is the critical current density, H is the applied magnetic field, H_{irr} is the irreversibility field $\mu_0 H_{irr} \approx 10.6$ T [23, 24], C , p , q are fitting parameters. For magnetic fields $\mu_0 H < 1$ T, p is the key fitting parameter. This parameter does not exceed unity and shows how fast the critical current density increases with decreasing magnetic field: $j_c \sim H^{p-1}$. These values are also given in Table 1.

Table 1

Description of samples and their current carrying capacity, obtained by transport measurements

Sample	Condition	Slicing	Size, mm × mm	$j_c(1\text{T}, \mathbf{H}\parallel\mathbf{n})$, kA/mm ²	$j_c(\mathbf{H}\perp\mathbf{n})/j_c(\mathbf{H}\parallel\mathbf{n})$, at 1T	p , $\mathbf{H}\perp\mathbf{n}$
№ 1	cold-worked	TD	11.7 × 2.1	0.24	13	0.8
№ 2		RD	11.4 × 1.9	0.58	6	0.7
№ 3	heat-treated	TD	11.6 × 2.1	0.83	6	0.6
№ 4		RD	11.3 × 1.9	1.33	4	0.4

The magnetization curves were measured with the Vibrating Sample Magnetometer “LakeShore 7400 series VSM System” with the magnet field of up to 1 T. The sample oscillated perpendicular to the magnetic field lines. Each magnetization curve was recorded at different orientations of the sample to the magnetic field, at certain rotating angle around the axis passing through the central line of the sample. A component of the magnetization vector parallel to the external magnetic field direction was recorded. The measurements were carried out at 5 K in a helium gas medium. The experiment consisted of the following steps. The magnetization was measured on a sample cooled in a zero magnetic field. Then the system was heated to 20 K (far above the critical temperature of Nb-Ti ~ 9 K), the orientation angle of the sample was changed, and the sample was again cooled down in a zero magnetic field.

Results and Discussion

Figure 1 shows the magnetization loops of the tested samples at 5 K and at different orientations of the magnetic field. Usually plane samples are examined in perpendicular geometry, so it is convenient to begin discussions with this orientation. Remarkable that for transverse samples № 1 and № 3 an anomalous shift of the central magnetization peak is observed, while it is not the case for longitudinal samples № 2 and № 4. This effect was considered in detail in [15] and is related to the inhomogeneous penetration of the flux into the sample due to variations in the tape thickness

in the transverse direction. Please note that the scale on the vertical axes is different. The width of the hysteresis loop increases for samples from 1 to 4, which corresponds to known trends for such heat treatment [25, 26, 27]. This is also consistent with transport measurements (Table 1) since the loop width ΔM is proportional to the critical current density j_c [7]:

$$\Delta M = \frac{j_{cl} w}{2} \left(1 - \frac{w j_{cw}}{3l j_{cl}} \right), \quad (2)$$

where l and w are the length and width of the rectangular sample; j_{cl} and j_{cw} are the critical current density along the length and width, respectively. Formula (2) can be used for quantitative estimates (Table 2). Clearly, if an anomalous shift of the central magnetization peak is observed, then (2) gives an overestimated value of the critical current density. Here two things must be noted. First, transport measurements were carried out at 4.2 K while magnetic measurements — at 5 K, so the critical current should be lower in the latter case. Second, the electric field criterion for magnetic measurements is lower than for transport measurements [8]. Consequently, the estimate of the critical current, obtained from magnetic measurements, should be lower than for transport measurements, which is not the case for transverse samples №1 and №3. This confirms the conclusions of the work [15] that the anomalous central peak shift indicates an inhomogeneous flux penetration. This leads to the fact that Formula (2), obtained in the framework of the critical state model, gives an overestimated value compared to transport measurements.

Table 2

Comparison of transport measurements and magnetic estimates at 1 T

Sample	Slicing	Anomalous central peak shift	j_c (1 T, 4.2 K), kA/mm ² transport	j_c (1 T, 5 K), kA/mm ² magnetization
№ 1	TD	Yes	0.24	0.27
№ 2	RD	No	0.58	0.48
№ 3	TD	Yes	0.83	0.84
№ 4	RD	No	1.33	1.16

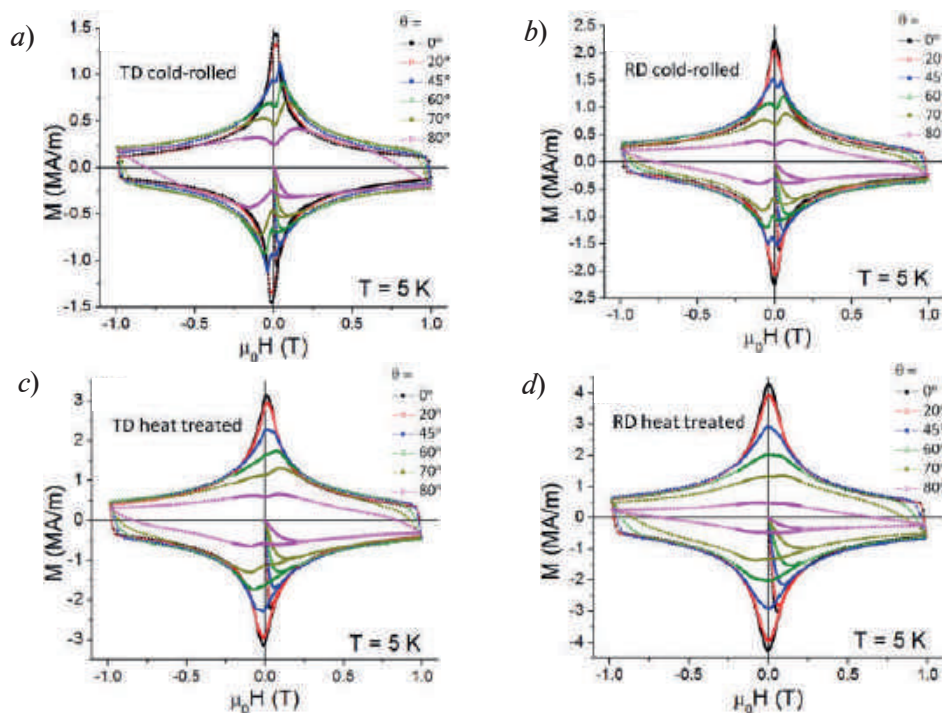


Fig. 1. Magnetization curves for samples № 1 (a), № 2 (b), № 3 (c) and № 4 (d). The angle between the normal to the tape and the magnetic field is indicated in the legend

As for tilted magnetic fields, there are several theoretical works, predicting interesting phenomena [28, 29, 30]. A low-field fishtail for superconductors with anisotropic pinning has been predicted [14]. The essence of this effect is as follows. When the self-field of screening currents is comparable to the external field, there are locations in the cross-section of the sample, where the direction of magnetic induction deviates significantly from the direction of the external magnetic field. If the critical current density has a pronounced anisotropy, then this leads to a sharply non-uniform distribution of the current over the cross section and may lead to a non-monotonic dependence of the total magnetization on the external field. This effect was actually observed in inclined magnetic fields on cold-rolled Nb-Ti tape [13]. Figure 1 shows the evolution of this effect at different angles of the magnetic field for samples with different degrees of anisotropy (Table 1). The low-field fishtail effect occurs on stationary hysteresis loops, when the direction of the external magnetic field differs from normal direction ($\theta \neq 0^\circ$) and manifests itself initially as a violation of the symmetry of the central peak (see loops at $\theta = 20^\circ$ in Figures 1, *a* and 1, *b*) with subsequent splitting of the central peak into two smaller ones (at angles $\theta = 45^\circ, 60^\circ, 70^\circ, 80^\circ$ in Figures 1, *a* and 1, *b*). Moreover, these features appear only on the stationary hysteresis magnetization curve, while the virgin curves are free of any features. This is an important fact, because it allows one to distinguish between intrinsic and external anisotropy. Intrinsic anisotropy is characterized by the appearance of an additional peak on the virgin curve and the absence of any features on the stationary hysteresis curve [31, 32]. When a sample with intrinsic anisotropy is magnetized in an inclined magnetic field, it is energetically favorable for the vortices to turn, so that the dimensions of the vortex become smaller. If the pinning is sufficiently weak and the rotation of the vortices is not hindered, then this appears as a double peak on the virgin branch of the magnetization curve: the first peak corresponds to the penetration of the vortices into the whole sample cross section, and the second corresponds to the full rotation of vortices in the direction of the external field [33]. In terms of the generalized critical state model, this corresponds to successive penetration of magnetic field components [34].

Qualitatively, with a decrease in the anisotropy degree the severity of the low-field fishtail effect reduces with almost complete disappearance for sample № 4 with a minimum degree of anisotropy. It is interesting to compare the hysteretic loops for samples № 2 and № 3, the anisotropy of which has the similar value (Table 1), but the fishtail effect for sample № 3 is much less pronounced. Such a significant difference may seem especially strange, since the critical current, and hence the self-field of sample № 3, is higher than of sample № 2, which means that the effect, associated with the curvature of magnetic lines by the self-field, should be more pronounced. However, it turns out that not only the ratio $j_c(\mathbf{H} \perp \mathbf{n})/j_c(\mathbf{H} \parallel \mathbf{n})$ is important for the occurrence of the low-field fishtail effect, but also the details of the critical current angular dependence. It was shown [21] that the critical current angular dependence of the Nb-Ti tape is well described by the two-parametric dependence:

$$j_c(\theta) = j_c(90^\circ) \sqrt{\frac{(k^L \cos \theta)^2 + (\sin \theta)^2}{(k^U \cos \theta)^2 + (\sin \theta)^2}}, \quad (3)$$

where θ is the angle between the tape normal \mathbf{n} and the magnetic field \mathbf{H} , k^L and k^U — the parameters of the angular dependence.

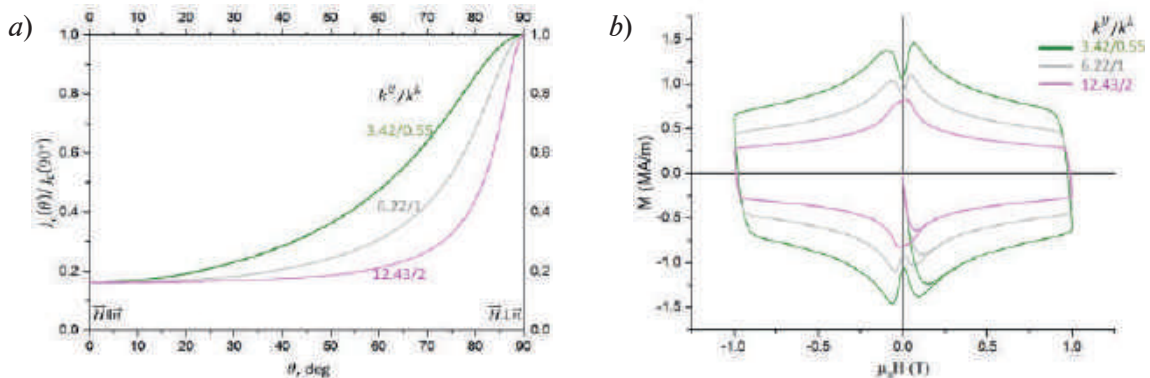


Fig. 2. Model angular dependencies with a different values of the parameters k^U and k^L at a constant ratio k^U/k^L (a). Corresponding simulated magnetization curves at $\theta = 70^\circ$ (b)

From (3) it follows that $j_c(\mathbf{H}\perp\mathbf{n})/j_c(\mathbf{H}\parallel\mathbf{n}) = j_c(90^\circ)/j_c(0^\circ) = k^u/k^l$. Thus, the details of the angular dependencies are described by different sets of the parameters (Fig. 2). Using the angular dependence (3), the magnetization loops of a long flat sample with a width-to-thickness ratio $w/t = 10$ were calculated using the program, developed in [13]. The results are shown in Figure 2. For the same ratio $j_c(\mathbf{H}\perp\mathbf{n})/j_c(\mathbf{H}\parallel\mathbf{n})$, the low-field fishtail can have a different degree of severity, depending on the sharpness of the peak near $\theta = 90^\circ$.

Conclusion

The low-field fishtail effect has been experimentally studied on samples with different degrees of external anisotropy. In contrast to intrinsically anisotropic superconductors, the magnetization curves of Nb-Ti samples in tilted magnetic fields do not show peculiarities on the virgin magnetization curve, while features are observed on the stationary hysteresis loops. Increasing the degree of anisotropy enhances the low-field fishtail effect. In addition, the manifestation of the low-field fishtail effect is sensitive to the details of the critical current angular dependence.

An anomalous shift in the central magnetization peak was observed for the transverse samples. It is shown that the estimation of the critical current density over the width of the magnetization loop, performed within the framework of the critical state model, yields overestimated values compared to the transport measurements.

Acknowledgments

The work was supported by NRC “Kurchatov Institute”. The work was partially performed on the equipment of the resource center Electrophysics of the NRC “Kurchatov Institute”.

REFERENCES

1. **Abrikosov A.A.**, The magnetic properties of superconducting alloys, *Journal of Physics and Chemistry of Solids*. 2 (3) (1957) 199–208.
2. **Blatter G., Feigel'man M.V., Geshkenbein V.B., Larkin A.I., Vinokur V.M.**, Vortices in high-temperature superconductors, *Reviews of Modern Physics*. 66 (1125) (1994).
3. **Vlasko-Vlasov V.K., Glatz A., Koshelev A.E., Welp U., Kwok W.K.**, Anisotropic superconductors in tilted magnetic fields, *Phys. Rev. B*. 91 (224505) (2015).
4. **Klimenko E.Yu., Shavkin S.V., Volkov P.V.**, Anisotropic pinning in macroscopic electrodynamics of superconductors, *J. Exp. Theor. Phys.* 85 (1997) 573–587.
5. **Caplin A.D., Cohen L.F., Perkins G.K., Zhukov A.A.**, The electric field within high temperature superconductors: mapping the E-J-B surface, *Supercond. Sci. Technol.* 7 (412) (1994).
6. **Gyorgy E.M., van Dover R.B., Jackson K.A., Schneemeyer L.F., Waszczak J.V.**, Anisotropic critical currents in $\text{Ba}_2\text{YCu}_3\text{O}_7$, analyzed using an extended Bean model, *Appl. Phys. Lett.* 55 (283) (1989).
7. **Sauerzopf F.M., Wiesinger H.P., Weber H.W.**, Anisotropic current flow and demagnetization corrections in the Bean model, *Cryogenics*. 30(7), 650–655 (1990).
8. **Hengstberger F., Eisterer M., Weber H.W.**, Magnetic measurement of the critical current anisotropy in coated conductors, *Supercond. Sci. Technol.* 24 (045002) (2011).
9. **Thompson J.R., Sinclair J.W., Christen D.K., Zhang Y., Zuev Y.L., Cantoni C., Chen Y., Selvamanickam V.**, Field, temperature, and angle dependent critical current density $j_c(H, T, \theta)$ in coated conductors, obtained via contact-free methods, *Supercond. Sci. Technol.* 23 (014002) (2010).
10. **Kapolka M., Pardo E.**, 3D modelling of macroscopic force-free effects in superconducting thin films and rectangular prisms, *Supercond. Sci. Technol.* 32 (054001) (2019).
11. **Mikitik G.P.**, Critical states in thin planar type-II superconductors in a perpendicular or inclined magnetic field (Review), *Low Temperature Physics*. 36 (13) (2010).
12. **Pardo E., Vojenciak M., Gomory F., Souc L.**, Low-magnetic-field dependence and anisotropy of the critical current density in coated conductors, *Supercond. Sci. Technol.* 24 (065007) (2011).
13. **Guryev V., Shavkin S., Kruglov V., Chumakov N., Emelyanov A.**, Magnetization of a superconducting Nb-Ti tape with anisotropic current-carrying capacity in an inclined magnetic field, *AIP Conference Proceedings*. 2163 (020004) (2019).
14. **Babich I.M., Mikitik G.P.**, On the nature of the fishtail effect in the magnetic hysteresis loop of high- T_c -superconductors, *Jetp. Lett.* 64 (1996) 586–591.



15. **Shavkin S.V., Guryev V.V., Chumakov N.K., Irodova A.V., Kruglov V.S.**, Anomalous magnetization central peak shift of Nb-Ti tapes with high in-plane critical current anisotropy, *J. Supercond. Nov. Magn.* 35 (2022) 2119–2125.
16. **Palau A., Puig T., Obradors X., Pardo E., Navau C., Sanchez A., Usoskin A., Freyhardt H.C., Fernandez L., Holzapfel B., Feenstra R.**, Simultaneous inductive determination of grain and intergrain critical current densities of $\text{YBa}_2\text{Cu}_3\text{O}_{7-x}$ coated conductors, *Appl. Phys. Lett.* 84 (230) (2004).
17. **Johansen T.H., Shantsev D.V., Koblischka M.R., Galperin Y.M., Nalevka P., Jirsa M.**, The low-field peak in magnetization loops of uniform and granular superconductors in perpendicular magnetic fields, *Physica C*. P3(341–348) (2000) 1443–1444.
18. **Bonura M., Cayado P., Konstantopoulou K., Alessandrini M., Senatore C.**, Heating-induced performance degradation of $\text{REBa}_2\text{Cu}_3\text{O}_{7-x}$ coated conductors: An oxygen out diffusion scenario with two activation energies, *ACS Appl. Electron. Mater.* 4 (3) (2022) 1318–1326.
19. **Shavkin S., Guryev V., Kruglov V., Ovcharov A., Likhachev I., Vasiliev A., Veligzhanin A., Zubavichus Y.**, Features of microstructure and magnetic flux dynamics in superconducting Nb-Ti tapes with strong anisotropic pinning. *EPJ Web of Conferences*. 185 (08007) (2018).
20. **Guryev V., Shavkin S., Kruglov V.**, Guided vortex motion in dilute strong pinning environment: Models and experiment, *Physica C*. 599(13540802021) (2022).
21. **Guryev V.V., Shavkin S.V., Kruglov V.S.**, Method for critical current angular dependencies analysis of superconducting tapes, *J. Phys.: Conf. Ser.* 2103(012096) (2021).
22. **Dew-Hughes D.**, Flux pinning mechanisms in type II superconductors, *Phil. Mag.* 30 (2) (1974).
23. **Guryev V., Shavkin S., Kruglov V.**, Inhomogeneity and irreversibility field of superconducting Nb-Ti tapes, *EPJ Web of Conferences*. 185 (08004) (2018).
24. **Guryev V.V., Shavkin S.V., Kruglov V.S.**, Irreversibility field and anisotropic δl pinning in type II superconductors, *J. Phys.: Conf. Ser.* 1697 (012202) (2020).
25. **Baker C., Sutton J.**, Correlation of superconducting and metallurgical properties of a Ti-20 at.% Nb alloy, *Philosophical Magazine*, 19(1969) 1223–1255.
26. **Matsushita T., Kupfer H.**, Enhancement of the superconducting critical current from saturation in Nb-Ti wire. I, *Journal of Applied Physics*. 63 (5048) (1988).
27. **Kupfer H., Matsushita T.**, Superconducting critical current of Nb-Ti wire with anisotropic defect structure. II, *Journal of Applied Physics*. 63 (5060) (1988).
28. **Huang Chen-Guang, Liu Jun.**, Magnetic and mechanical properties of a finite thickness superconducting strip with a cavity in oblique magnetic fields, *Journal of Applied Physics*. 121 (023905) (2017).
29. **Pompeo N., Silva E.**, Analysis of the measurements of anisotropic AC vortex resistivity in tilted magnetic fields, *IEEE Transactions on Applied Supercond.* 28 (2) (2018).
30. **Yokoji H., Kato M.**, Structures of vortices in a superconductor under a tilted magnetic field, *J. Phys.: Conf. Ser.* 1975 (012001) (2021).
31. **Voloshin I.F., Kalinov A.V., Fisher L.M., Derevyanko S.A., Yampol'ski V.A.**, A new type of peak effect in the magnetization of anisotropic superconductors, *Jetp Lett.* 73 (2001) 285–288.
32. **Bugoslavsky Yu.V., Ivanov A.L., Minakov A.A., Vasyurin S.I.**, Fishtails and anisotropy in underdoped LaSrCuO single crystals, *Physica C*. 233(1-2) 67–76.
33. **Buzdin A.I., Simonov A.Yu.**, Magnetization of anisotropic superconductors in the tilted magnetic field, *Physica C*. 175 (1991) 143–155.
34. **Romero-Salazar C., Perez-Rodriguez F.**, Critical state of anisotropic hard superconductors, *Supercond. Sci. Technol.* 16 (2003) 1273–1281.

THE AUTHORS

GURYEV Valentin V.
Gurev_VV@nrcki.ru
ORCID: 0000-0003-4946-2559

CHUMAKOV Nikolai K.
Chumakov_NK@nrcki.ru

IRODOVA Alla V.
Irodova_AV@nrcki.ru

SHAVKIN Sergey V.
Shavkin_SV@nrcki.ru

Received 17.10.2022. Approved after reviewing 22.11.2022. Accepted 22.11.2022.

© Peter the Great St. Petersburg Polytechnic University, 2023

Conference materials

UDC 537.266.4

DOI: <https://doi.org/10.18721/JPM.161.112>

Microstructure and ferroelectric properties of submicron polycrystalline lead zirconate titanate films with a gradient composition distribution over the thickness

A.R. Valeeva ¹✉, I.P. Pronin ¹, E.Yu. Kaptelov ¹, S.V. Senkevich ^{1,2}

S.A. Nemov ³, M.V. Staritsyn ⁴

¹ Ioffe Institute, St. Petersburg, Russia;

² Herzen State Pedagogical University of Russia, St. Petersburg, Russia;

³ Peter the Great St. Petersburg Polytechnic University, St. Petersburg, Russia;

⁴ NRC "Kurchatov Institute", CRISM "Prometey", St. Petersburg, Russia

✉ ValeevaAR@mail.ioffe.ru

Abstract. The paper presents the results of two-layer thin ferroelectric PZT films studies with a change in the lead content over the thickness of the films, obtained by RF magnetron deposition at various pressures of the working gas mixture. The microstructure and elemental composition were investigated by scanning electron microscopy and electron probe X-ray spectral microanalysis. It is shown that the elemental composition and dielectric properties depend on the sequence of layers deposition. The results obtained make it possible to characterize the physical mechanism of self-polarization formation in thin PZT films.

Keywords: thin ferroelectric films, lead zirconate titanate, RF magnetron sputtering, non uniform distribution of lead over the thickness

Citation: Valeeva A.R., Pronin I.P., Kaptelov E.Yu., Senkevich S.V., Nemov S.A., Staritsyn M.V., Microstructure and ferroelectric properties of submicron polycrystalline lead zirconate titanate films with a gradient composition distribution over the thickness, St. Petersburg State Polytechnical University Journal: Physics and Mathematics. 16 (1.1) (2023) 74–78. DOI: <https://doi.org/10.18721/JPM.161.112>

This is an open access article under the CC BY-NC 4.0 license (<https://creativecommons.org/licenses/by-nc/4.0/>)

Материалы конференции

УДК 537.266.4

DOI: <https://doi.org/10.18721/JPM.161.112>

Микроструктура и сегнетоэлектрические свойства субмикронных поликристаллических пленок цирконата титаната свинца с градиентным распределением состава по толщине

А.Р. Валеева ¹✉, И.П. Пронин ¹, Е.Ю. Каптелов ¹, С.В. Сенкевич ^{1,2}

С.А. Немов ³, М.В. Старицын ⁴

¹ Физико-технический институт им. А.Ф. Иоффе РАН, Санкт-Петербург, Россия;

² Российский государственный педагогический университет им. А.И. Герцена, Санкт-Петербург, Россия;

³ Санкт-Петербургский политехнический университет Петра Великого, Санкт-Петербург, Россия;

⁴ НИЦ «Курчатовский институт», ЦНИИ КМ «Прометей», Санкт-Петербург, Россия

✉ ValeevaAR@mail.ioffe.ru

Аннотация. В работе представлены результаты исследований двухслойных тонких сегнетоэлектрических пленок ЦТС с изменением содержания свинца по толщине пленок, полученных ВЧ-магнетронным напылением при различных давлениях рабочей газовой смеси. Микроструктуру и элементный состав исследовали методами сканирующей электронной микроскопии и электронно-зондового рентгеновского микроанализа.

Показано, что элементный состав диэлектрические свойства зависят от последовательности нанесения слоев. Полученные результаты позволяют охарактеризовать физический механизм формирования самополяризации в тонких пленках ЦТС.

Ключевые слова: тонкие сегнетоэлектрические пленки, цирконат титаната свинца, высокочастотное магнетронное распыление, неоднородное распределение свинца по толщине

Ссылка при цитировании: Валеева А.Р., Пронин И.П., Каптелов Е.Ю., Сенкевич С.В., Немов С.А., Старицын М.В., Микроструктура и сегнетоэлектрические свойства субмикронных поликристаллических пленок цирконата титаната свинца с градиентным распределением состава по толщине // Научно-технические ведомости СПбГПУ: Физико-математические науки. 2023. Т. 16. № 1.1. С. 74–78. DOI: <https://doi.org/10.18721/JPM.161.112>

Статья открытого доступа, распространяемая по лицензии CC BY-NC 4.0 (<https://creativecommons.org/licenses/by-nc/4.0/>)

Introduction

Thin ferroelectric films with a perovskite structure are increasingly used in dynamic and static memory elements, microelectromechanical (MEMS) devices, infrared devices, energy harvesters, magnetoelectric converters, and other devices [1–5]. Of greatest interest are polycrystalline thin films of $\text{Pb}(\text{Zr},\text{Ti})\text{O}_3$ solid solutions (PZT), whose composition corresponds to the region of a morphotropic phase boundary (MPB), where extremely high values of dielectric, electromechanical, pyroelectric, and a number of other physical characteristics are observed [6].

A serious obstacle to achieving the maximum parameters, which leads to smearing of the MPB, is the elemental inhomogeneity of the PZT films over the thickness, associated with both the inhomogeneous distribution of Zr/Ti atoms and of superstoichiometric lead presented in the form of its oxide [7–9]. The reasons for the elemental inhomogeneity may be caused by a number of reasons, related to the methods of forming thin films, the mechanisms of perovskite phase crystallization, as well as a number of parameters, such as the material of the lower electrode, deposition and synthesis temperatures, film thickness, and so on [8, 10, 11]. In [8], in order to reduce the inhomogeneity in the distribution of Zr(Ti) atoms in sol-gel PZT films, each of the precursor sublayers (about 250 nm thick) was formed with a given change (gradient) in the Zr/Ti elemental ratio over the thickness. This approach made it possible to reduce the Zr/Ti gradient by a factor of three (from ~ 15% to ~ 5%) within each layer and significantly increase the dielectric permittivity. In [12, 13] two-layer PZT structures with different compositions were formed by ion-plasma deposition and characterized. It was shown that the phase state, dielectric properties, and such an important characteristic for MEMS as the magnitude of self-polarization (or internal field) [14, 15] depend on the order of the layers in thickness. In contrast to the previous study, bi-layer structures are characterized by the equality of the thicknesses of each of the layers, the reduced total thickness of the two-layer structure, slight variation in the composition (elemental ratio of Zr/Ti) and increased sintering temperatures of the layers.

Materials and Methods

Two-layer structures were fabricated by RF magnetron sputtering of ceramic PZT target with composition, corresponding to MPB, at two pressures (4 and 8 Pa) of the working gas [16]. Thus, the bi-layer PZT structures consisted of two layers, each 300 nm thick, deposited sequentially at 8 and 4 Pa (sample I) or 4 and 8 Pa (sample II). To form perovskite phase, the samples were then annealed at conventional furnace at 600 °C in air. The platinumized silicon substrate with an adhesive sublayer of titanium dioxide ($\text{Pt}/\text{TiO}_2/\text{SiO}_2/\text{Si}$) used as a substrate. Upper platinum $120 \times 120 \mu\text{m}$ contact pads were applied to study dielectric properties.

LYRA 3 scanning electron microscope (Tescan) with the X-Max 80 energy dispersive attachment (energy of the probe beam was 12 keV) used for microstructure and elemental analyses. To control the phase state, X-ray diffraction and optical microscopy were attracted. E7-20 immittance meter used to diagnose the dielectric properties. Dielectric hysteresis loops were studied at modified Sawyer-Tower circuit at 1 kHz.

Results and Discussion

Table 1 shows the elemental analysis data for amorphous structures and structures annealed at 600 °C. It can be seen that the lead content in the PZT layer, deposited at 4 Pa, is slightly lower than the stoichiometric ($Pb/(Zr + Ti) \sim 0.99$) and nearly 17% less than in the layer deposited at 8 Pa ($Pb/(Zr + Ti) \sim 1.16$), and Ti/Zr ratio is closed to 45/55. Structure annealing resulted in invariability of Pb content and decrease in Ti of about 1% in the top layer of sample I and in essential decrease of Pb content and increase in Ti of about 1% in the top layer of sample II.

The composition changes (Ti/Zr ratio) on depth in annealed structures are defined by the changes in perovskite phase formation. In sample I perovskite nucleation occurs near the lower interface of the structure, while in sample II it occurs near its upper surface. Since the synthesis temperature of the perovskite phase is lower for lead titanate than for lead zirconate, this leads to the migration of Ti atoms in the direction of the nucleation centers of the perovskite phase and, as a consequence, to partial segregation of titanium and zirconium atoms [8]. Nevertheless, estimates show that in the sintered structures, the total inhomogeneity in the Ti/Zr distribution of atoms over the thickness does not exceed 5%.

Table 1

The data of elemental analysis of the amorphous and high temperature annealed PZT structures and dielectric parameters of perovskite capacitor

Samples I and II	Pb/(Zr + Ti)		Ti/Zr		ϵ_{max} , 10 kHz	$(P_r^+ + P_r^-)/2$, $\mu C/cm^2$
	Amorphous phase	Perovskite phase	Amorphous phase	Perovskite phase		
$\frac{4Pa}{8Pa}$	0.99	0.99	44.7/55.3	43.6/56.4	1000	16
$\frac{8Pa}{4Pa}$	1.16	1.05	45.1/54.9	45.9/54.1	880	13

A comparison of the dielectric properties of bi-layer structures showed that in structure I the dielectric permittivity (ϵ_{max}), obtained from the reversible dependences of $\epsilon(V)$ (Fig. 1 and Table 1), noticeably exceeds the analogous value characteristic of structure II. An even greater difference was observed for the values of the remanent polarization P_r (Fig. 2, a, b, Table 1).

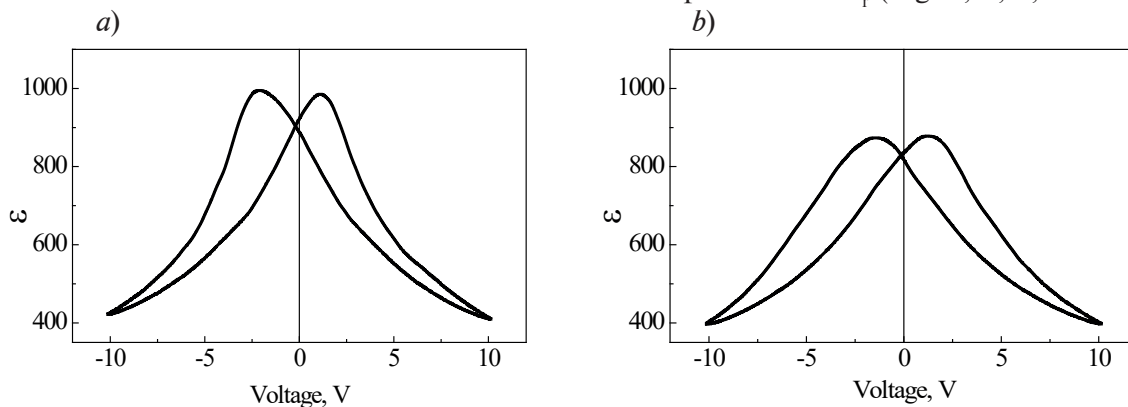


Fig. 1. The reversible dependences of dielectric permittivity ($\epsilon-V$) of samples I (a) and II (b).

Such differences are likely related to the fact that during the nucleation of the perovskite phase in the lower part of structure I excess lead is squeezed upwards and enriches the upper layer, which leads to almost complete crystallization of the structure into the perovskite phase [10, 16]. In structure II the nucleation of the perovskite phase in the upper layer leads to both extrusion of lead into the lower part of the structure and migration to the surface, where oxidized lead evaporates into the atmosphere. In this case, we assume that when lead is deficient, local microregions of the nonferroelectric pyrochlore phase remain near the lower interface, which are



characterized by a low (~ 30 – 40) dielectric permittivity. This leads both to a decrease in the effective dielectric permittivity of the two-layer structure and to a redistribution of the applied external voltage between the regions of the pyrochlore and perovskite phases and to a decrease in the switchable polarization.

Figures 2, *c* and 2, *d* reflect the difference in the behavior of the internal field values, obtained from the hysteresis loops in structures I and II with an increase of applied voltage amplitude. The presence of an internal field (E_{int}), whose vector in both cases is oriented towards the free surface of the structure, reflects the inhomogeneous distribution of charged oxygen vacancies over the thickness of the structure. The observed difference in the behavior of E_{int} (V) in structures I and II still remains unclear and requires further research.

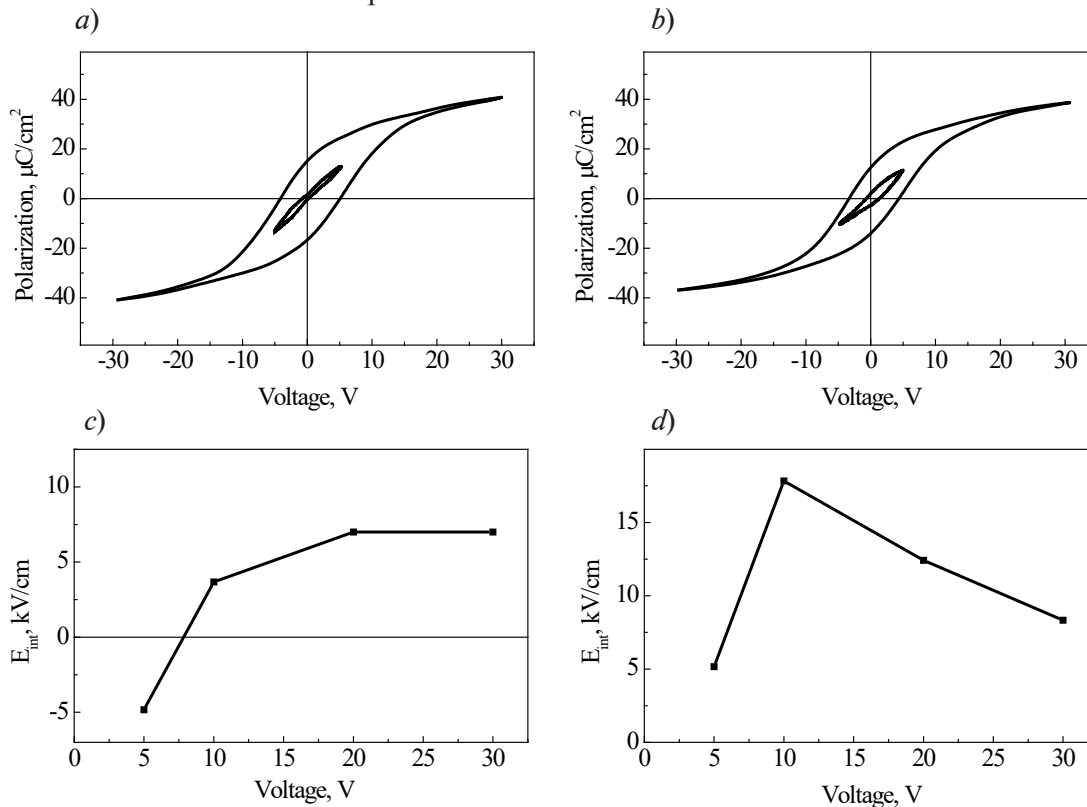


Fig. 2. Variations of hysteresis loops and internal field (E_{int}) depending on the applied voltage of samples I (*a*, *c*) and II (*b*, *d*), correspondingly

Conclusion

Two bi-layer ferroelectric PZT structures with a highly inhomogeneous distribution of lead over the thickness were formed, the difference between which was in the sequence of layer deposition at working gas pressures of 4 and 8 Pa. The thickness of each of the layers was 300 nm. Crystallization of the perovskite phase was carried out at 600 °C. It is shown that a change in the sequence of deposition leads to a difference in the composition and a change in the mechanism of the perovskite phase crystallization, which, in turn, leads to a difference in the values of the dielectric permittivity, remanent polarization and internal field.

Acknowledgments

Experimental studies were carried out on the equipment of the Core shared research facilities “Composition, structure, and properties of structural and functional materials” of the NRC “Kurchatov Institute”, CRISM “Prometey”, with the financial support of the state, represented by the Ministry of Education and Science of the Russian Federation, under agreement No. 13.CKP.21.0014 (075-11-2021-068). The unique identifier is RF----2296.61321X0014.

REFERENCES

1. **Muralt P.**, Micromachined infrared detectors based on pyroelectric thin films, Reports on Progress in Physics. 64 (10) (2001) 1339–1388.
2. **Martin L.W., Rappe A.M.**, Thin-film ferroelectric materials and their applications, Nature Reviews Materials. 2 (2016) 16087.
3. **Bukharaev A.A., Zvezdin A.K., Pyatakov A.P., Fetisov Y.K.**, Straintronics: a new trend in micro- and nanoelectronics and materials science, Physics-Uspekhi. 61 (12) (2018) 1175.
4. **Ma Y., Son J., Wang X., Liu Y., Zhou J.**, Synthesis, microstructure and properties of magnetron sputtered lead zirconate-titanate (PZT) thin film coatings, Coatings. 11(8) (2021) 944.
5. **Song L., Glinsek S., Defay E.**, Toward low-temperature processing of lead zirconate titanate thin films: Advances, strategies, and applications, Applied Physics Reviews. 8 (2021) 041315.
6. **Jaffe B., Cook W., Jaffe H.**, Piezoelectric ceramics, London, New York: Academic Press. 1971.
7. **Ledermann N., Muralt P., Baborowski J., Gentil S., Mukati K., Cantoni M., Seifert A., Setter N.**, {100}-textured, piezoelectric $\text{Pb}(\text{Zr}_x, \text{Ti}_{1-x})\text{O}_3$ thin films for MEMS: Integration, deposition, and properties, Sensors and Actuators A: Physical. 105 (2) (2003) 162–170.
8. **Calamea F., Muralt P.**, Growth and properties of gradient free sol-gel lead zirconate titanate thin films, Appl. Phys. Lett.. 90 (2007) 062907.
9. **Afanasjev V.P., Mosina G.N., Petrov A.A., Pronin I.P., Sorokin L.M., Tarakanov E.A.**, Specific properties of the PZT-based thin-film capacitor structures with excess lead oxide, Tech. Phys. Lett. 27 (2001) 467–469.
10. **Pronin V.P., Senkevich S.V., Kaptelov E.Yu., Pronin I.P.**, Anomalous losses of lead in crystallization of the perovskite phase in thin PZT films, Physics of the Solid State. 55 (2013) 105–108.
11. **Mukhin N., Chigirev D., Bakhchova L., Tumarkin A.**, Microstructure and properties of PZT films with different PbO content-ionic mechanism of built-in fields formation, Materials. 12 (18) (2019) 2926.
12. **Pronin V.P., Dolgintsev D.M., Volpyas V.A., Staritsyn M.V., Kaptelov E.Yu., Senkevich S.V., Pronin I.P.**, Structure and properties of thin PZT films with inhomogeneous composition distribution, IOP Conf. Series: Journal of Physics. Conference Series 1281 (2019) 012063.
13. **Valeeva A.R., Pronin I.P., Senkevich S.V., Kaptelov E.Yu., Staritsyn M.V., Dolgintsev D.M., Nemov S.A.**, Microstructure and dielectric properties of thin polycrystalline PZT films with inhomogeneous distribution of the composition over thickness, Journal of Surface Investigation: X-ray, Synchrotron and Neutron Techniques. 15 (1) (2021) S12–S17.
14. **Kholkin A.L., Brooks K.G., Taylor D.V., Hiboux S., Setter N.**, Self-polarization effect in $\text{Pb}(\text{Zr}, \text{Ti})\text{O}_3$ thin films, Integrated Ferroelectrics. 22 (1-4) (1998) 525–533.
15. **Balke N., Bdikin I., Kalinin S.V., Kholkin A.L.**, Electromechanical imaging and spectroscopy of ferroelectric and piezoelectric materials: State of the art and prospects for the future, Journal of the American Ceramic Society. 92 (8) (2009) 1629.
16. **Pronin I.P., Kukushkin S.A., Spirin V.V., Senkevich S.V., Kaptelov E.Yu., Dolgintsev D.M., Pronin V.P., Kiselev D.A., Sergeeva O.N.**, Formation mechanisms and the orientation of selfpolarization in PZT polycrystalline thin films, Materials Physics and Mechanics. 30 (1) (2017) 20–34.

THE AUTHORS

VALEEVA Alsu R.

ValeevaAR@mail.ioffe.ru
ORCID: 0000-0002-8826-8938

SENKEVICH Stanislav V.

SenkevichSV@mail.ioffe.ru
ORCID: 0000-0002-4503-1412

PRONIN Igor P.

Petrovich@mail.ioffe.ru
ORCID: 0000-0003-3749-8706

NEMOV Sergey A.

nemov_s@mail.ru
ORCID: 0000-0001-7673-6899

KAPTELOV Eugeneiy Yu.

kaptelov@mail.ioffe.ru
ORCID: 0000-0002-7423-6943

STARITSYN Mikhail V.

ms_145@mail.ru
ORCID: 0000-0002-0088-4577

Received 18.10.2022. Approved after reviewing 08.11.2022. Accepted 08.11.2022.

Conference materials

UDC 538.911

DOI: <https://doi.org/10.18721/JPM.161.113>

Self-organization of the structure of porous silicon carbide under external influences

M.G. Mynbaeva ¹✉, S.P. Lebedev ¹

¹Ioffe Institute, St. Petersburg, Russia

✉ mgm@mail.ioffe.ru

Abstract. This paper presents the results of a study of the effect of external influences on the structure and phase composition of porous SiC layers obtained by anodization. It is shown how carrying out of standard technological operations makes it possible to control the properties of porous structures and significantly expands the variety of their morphological forms. The conditions facilitating the occurrence of phase-structural and polytype transformations in porous SiC structures are determined.

Keywords: silicon carbide, porous structure, external influences, self-organization

Funding: This study was funded by Russian Science Foundation grant number RSF 22 12-00003.

Citation: Mynbaeva M.G., Lebedev S.P., Self-organization of the structure of porous silicon carbide under external influences, St. Petersburg State Polytechnical University Journal. Physics and Mathematics. 16 (1.1) (2023) 79–83. DOI: <https://doi.org/10.18721/JPM.161.113>

This is an open access article under the CC BY-NC 4.0 license (<https://creativecommons.org/licenses/by-nc/4.0/>)

Материалы конференции

УДК 538.911

DOI: <https://doi.org/10.18721/JPM.161.113>

Самоорганизация структуры пористого карбида кремния под внешними воздействиями

М.Г. Мынбаева ¹✉, С.П. Лебедев ¹

¹Физико-технический институт им. А.Ф. Иоффе РАН, Санкт-Петербург, Россия

✉ mgm@mail.ioffe.ru

Аннотация. В данной работе представлены результаты исследования влияния внешних воздействий на структуру и фазовый состав пористого карбида кремния. Показано, как проведение стандартных технологических операций позволяет значительно расширить разнообразие морфологических форм пористых структур на основе SiC.

Ключевые слова: карбид кремния, пористая структура, внешние воздействия, самоорганизация

Финансирование: Работа выполнена в рамках гранта Российского научного фонда номер «РНФ-22-12-00003».

Ссылка при цитировании: Мынбаева М.Г., Лебедев С.П., Самоорганизация структуры пористого карбида кремния под внешними воздействиями // Научно-технические ведомости СПбГПУ. Физико-математические науки. 2023. Т. 16. № 1.1. С. 79–83. DOI: <https://doi.org/10.18721/JPM.161.113>

Статья открытого доступа, распространяемая по лицензии CC BY-NC 4.0 (<https://creativecommons.org/licenses/by-nc/4.0/>)

Introduction

The study of the mechanisms of structural self-organization in solids has undoubted prospects for developing foundations for new technologies of multifunctional materials [1]. Self organization should be understood as a change in the spatial ordering of substructures in multiphase systems under internal factors or external influences and is manifested in large variety of secondary ordered structures. Porous materials obtained as a result of electrochemical processing (anodization) of semiconductors, are a special class of two-phase systems; their functional properties are determined by dimensional and geometric characteristics as the volume of the pore space and pore geometry, as well as by the properties of the crystalline matrix. A high specific surface area and a high proportion of atoms bound to the free surface are important characteristics of porous structures that determine an increase in the probability of the formation of surface nano-sized phases under the action of chemical potential gradients and diffusion mass transfer. This makes it possible to develop new approaches for obtaining materials with functional properties that are unattainable within the framework of traditional technologies. At present, porous silicon, which is used in modern sensor and membrane devices, nanoelectronics, photonics, and bioengineering, remains the most studied porous semiconductor. Porous materials based on binary semiconductor compounds, have not yet found such a wide practical application. This is partly due to insufficient knowledge of the mechanisms of formation and evolution of their structure under external action and the lack of predictive estimates of the stability of their properties in specific applications. At the same time, an urgent task is to obtain materials with a given set of low-dimensional substructures based on wide-gap semiconductors for solving various practical problems. In particular, the unique combination of high corrosion, chemical, radiation, and thermal resistance of the crystalline framework, which is characteristic of porous structures based on silicon carbide, determines the prospects for their use in mobile hydrogen storage systems, where one of the key ways to increase the storage capacity is to create storage elements based on three-dimensional solid-state frameworks with an increased specific surface area [1]. In addition to being used in technical fields and taking into account the fact that SiC does not have a toxic effect on a living organism as well as its ability to maintain its physical properties in a biologically active environment, porous SiC (PSC) can be used as a basis for obtaining structures with a complex architecture for new biomedical technologies [2]. The foregoing determines the relevance of the research topic, some of the results of which are presented in this paper.

Materials and Methods

In this section it is shown how by using standard procedures, such as annealing and ion plasma treatment, one can control the properties of porous structures obtained by anodization of single-crystal 6H-SiC. In (Figures 1, *a*, *b*) shown is an example of significant structural changes, that occurred in the volume of the microporous SiC layer under annealing in vacuum at 1700 °C. As can be seen, the channel microstructure of PSC has been transformed into a structure, formed by isolated faceted pores. The explanation of the observed structural changes can be given based

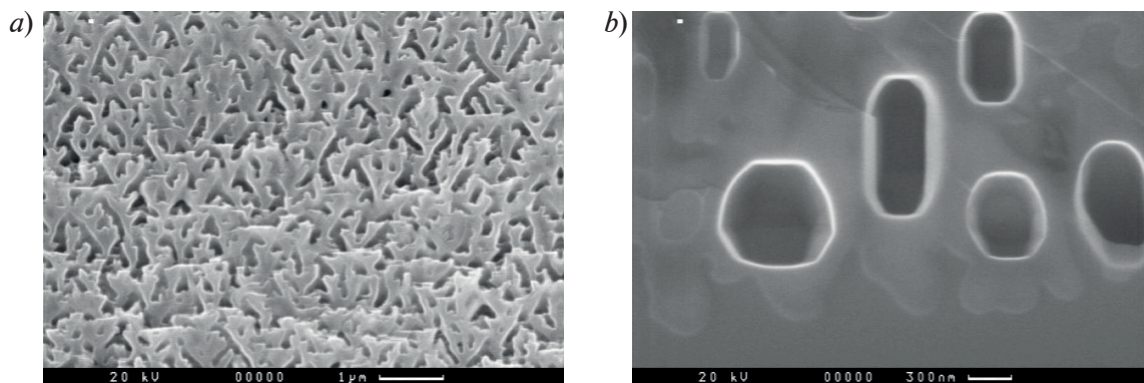


Fig.1. Scanning electron microscopy (SEM) images of transverse cleavages of initial microporous structure (*a*) and the same structure after annealing in vacuum at a temperature of 1700 °C (*b*)



on the known mechanisms of self-diffusion, used in the classical theory of sintering. With regard to two-phase (porous) solids, the term “sintering” refers to the processes of merging of pores (coalescence), leading to enlargement and change in the shape and size of pores under external influences. The driving force behind coalescence processes is the tendency of the two phase system to reduce the free energy, which is realized through a decrease in the proportion of the internal free surface, associated with the presence of pores in the crystalline matrix [3].

Results and Discussion

In the framework of the experiments, the problem of determining the effect of annealing conditions on the change in the chemical composition of porous SiC samples was studied. Annealing was carried out in high vacuum and in an argon (Ar) atmosphere at temperatures 900–1700 °C. Table 1 summarizes the Auger electron spectroscopy (AES) depth profiling data for PSC samples with a microporous structure obtained based on 6H-SiC wafers. Depending on the annealing conditions, a change in the composition was observed towards an increase in the carbon content up to a depth of 400 nm. This was indicative of a significant difference in the behavior of PSC samples and ordinary silicon carbide material annealed under similar conditions; in the latter case, the thickness of carbon-enriched layers was determined to be in order of single units of nanometers. As follows from Table 1, from the point of view of stoichiometry, PSC samples demonstrated thermal stability up to a temperature of 1500 °C, when annealing was carried out in an argon atmosphere. Heating of the samples in vacuum lead to PSC graphitization already at 1200 °C, when taking into account the results of the experiments on annealing 3D-SiC/2D-C hierarchical structures, that were fabricated on the basis of microporous SiC. Such self-organized structures represented a three-dimensional SiC matrix with a two dimensional carbon coating on its free surfaces [4, 5]. Given the proven compatibility of SiC and nanocarbon-based materials with human tissues, the obtained 3D-SiC/2D-C structures have great potential for developing tissue-inducing matrices and for other similar applications.

Plasma treatment can also lead to similar significant changes in the porous structure. Figure 2 shows images of a cleavage of a sample with a microporous structure before and after exposure to radio frequency (RF, 15 MHz, 175 W) Ar⁺ ion plasma.

Table 1

AES profiling data for 6H-PSC samples with a micro-porous structure

Depth of AES analysis	<i>T</i> (°C)	C/Si ratio (%)	
0 nm	900 (Ar)	67.15	32.85
15 nm		48.19	51.81
400 nm		45.1	54.9
0 nm	1200 (Ar)	68.45	31.55
15 nm		48.87	51.13
400 nm		44.25	55.73
0 nm	1500 (Ar)	64.24	35.76
15 nm		50.03	49.97
400 nm		45.22	54.78
0 nm	1700 (Ar)	90.08	9.92
15 nm		58.64	41.36
400 nm		50.82	49.18
0 nm	1200 (vac.)	89.87	10.13
15 nm		50.56	49.44
400 nm		48.48	51.52
0 nm	1500 (vac.)	100.0	0
15 nm		92.50	7.50
400 nm		54.00	46.0
0 nm	1700 (vac.)	100	0
15 nm		95.65	4.35
400 nm		69.03	0.97

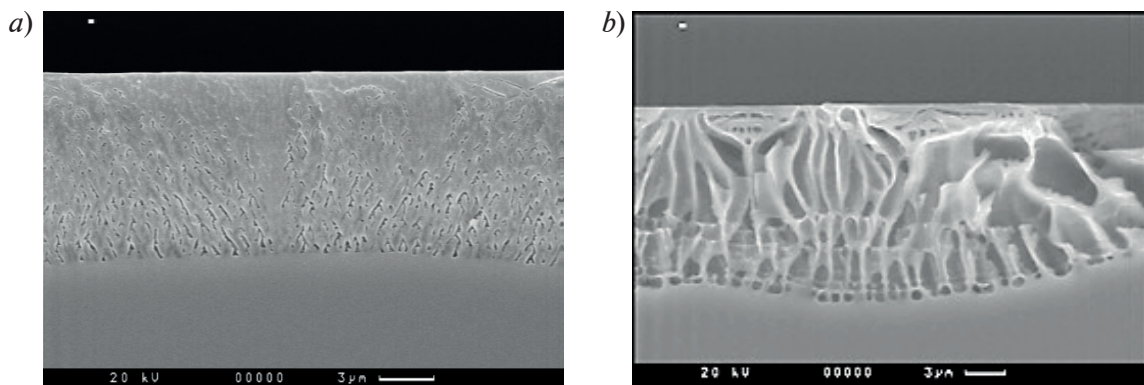


Fig. 2. SEM images of transverse cleavages of the original sample with a layer of microporous SiC, formed on the basis of a 6H-SiC wafer (*a*) and the microporous SiC layer exposed to RF Ar-ion plasma (*b*)

In contrast to thermally stimulated pore growth through coalescence proceeding according to a purely vacancy mechanism, i.e., due to the diffusion “pumping” of vacancies from smaller pores to large ones through the crystalline matrix of the porous structure, radiation-stimulated growth occurs due to the fact that small pores intensively absorb interstitial atoms that are generated under such exposure, and, as a result, disappear, while the remaining pores become larger due to the influx of excess vacancies formed in this case [6]. As follows from the results obtained in this study, changes occur not only in the pore volume, but also in the crystalline matrix of porous structures. The latter include polytype transformations in SiC. Earlier we have shown that low-temperature (2 K) photoluminescence (PL) spectra of the initial 6H-SiC and PSC samples after plasma treatment could be significantly different [7]. Namely, PL spectra of the original sample represented a set of lines in the infrared range with maxima in 1.20–1.50 eV energy range. This luminescence is associated with defects in SiC. On the contrary, the treated porous material was dominated by luminescence in the visible range with photon energy 2.40–3.30 eV. The observed lines were attributed to exciton recombination in the corresponding SiC polytypes: 3.30 eV (6H), 3.28 eV (4H), and 2.86 eV (24R) [8]. Along with that, it was proved that the anodization modes used to obtain porous SiC did not lead to a change in the polytype of the initial material. The observation of excitonic luminescence in the plasma treated material, which is characteristic of nanostructured semiconductors, indicates the appearance of crystallites with a lateral size of a few nanometers. At the same time, it is known that free surfaces in nanostructured materials contribute to a decrease in the activation energy of solid-state processes much more significantly than in the case of their bulk counterparts [9]. Thus, the formation of a multi-polytype substructure in PSC may be an evidence of the occurrence of solid-state transformations in the crystalline matrix of porous SiC.

Conclusion

We discussed selected results of the comprehensive study of effect of external influences on the structure and phase transformations in porous SiC. The proposed approaches open up new possibilities for the formation of complex hierarchical and hybrid structures formed from the atoms of a three-dimensional crystalline matrix of the porous material. Such structures are promising for a wide range of possible applications that go beyond the traditional application of orthodox semiconductors to the modern interdisciplinary scientific areas.

REFERENCES

1. Jastrzebski K., Kula P., Emerging technology for a green sustainable energy promising materials for hydrogen storage, from nanotubes to grapheme, Review, Materials. 14 (2499) (2021) 1–24.
2. Sadow S.E., Silicon carbide biotechnology, Biocompatible Semiconductor for Advanced Biomedical Devices and Applications, second ed. Elsevier, Amsterdam (2016).
3. Geguzin Ya.E., Fizika spekaniya, Nauka, Moskva (1984) (Гегузин Я.Е., Физика спекания, Наука, Москва. 1984).



4. Mynbaeva M.G., Sitnikova A.A., Lebedev S.P., Petrov V.N., Kirilenko D.A., Kotousova I.S., Smirnov A.N., Lavrent'ev A.A., Graphene-on-porous-silicon carbide structures, *Materials Science Forum*. 740–742 (2013) 133–136.
5. Mynbaeva M.G., Sitnikova A.A., Kirilenko D.A., Kotousova I.S., Graphene/silicon carbide-based scaffolds, *Journal of Physics D: Applied Physics*. 45(335303) (2012) 1–7.
6. Dubinko V.I., Ostapchuk P.N., Slezov V.V., Theory of radiation-induced and thermal coarsening of the void ensemble in metals under irradiation, *Journal of Nuclear Materials*. 161 (1989) 239–260.
7. Torchynska T.V., Cano A.D., Dubic M., Ostapenko S., Mynbaeva M.G., Stimulation of excitonic and defect-related luminescence in porous SiC, *Physica B: Condensed Matter*. 376 (2006) 367–369.
8. Devaty R.P., Choyke J.W., Optical characterization of silicon carbide polytypes, *Physica Status Solidi A*. 162 (1997) 5–38.
9. Righi M.C., Pignedoli C.A., Borghi G., Felice R.Di., Bertoni C.M., Catellani A., Surface-induced stacking transition at SiC(0001), *Physical Review B*. 66 (2020) 045320 1–7.

THE AUTHORS

MYNBAEVA Marina I.
mgm@mail.ioffe.ru
ORCID: 0000-0002-6321-1724

LEBEDEV Sergey P.
lebedev.sergey@mail.ioffe.ru
ORCID: 0000-0002-5078-1322

Received 19.10.2022. Approved after reviewing 08.11.2022. Accepted 10.11.2022.

Conference materials

UDC 538.913

DOI: <https://doi.org/10.18721/JPM.161.114>

Conformational disorder and its effect on structural phase transitions in tricosane $C_{23}H_{48}$

S.A. Gureva ¹✉, V.A. Marikhin ¹, E.N. Vlasova ²

¹Ioffe Institute, St. Petersburg, Russia;

²Institute of Macromolecular Compounds, St. Petersburg, Russia

✉ swet.gurjewa@gmail.com

Abstract. The kinetics of the first-order solid-solid structural phase transition in monodisperse n-alkane samples of odd tricosane $C_{23}H_{48}$ was studied by FTIR spectroscopy. The detailed study of the structure rearrangements of long-chain molecular crystals of n-alkanes during solid-state transitions has been carried out and the existence of many irregular conformers in solid phases of tricosane, the concentration of which reaches a maximum when approaching the melting point, has been demonstrated. The presence of these conformational defects has been found to promote the development of a new phase in the bulk of the initial one and to facilitate the transitions between different intermediate rotator phases in the solid state. Thus, the significant role has been demonstrated for the appearance of various intramolecular conformational defects during heating of n-alkanes, which promote interfacial transitions from the solid to the liquid state, weakening the intermolecular interaction and increasing the freedom degree of molecules.

Keywords: n-alkane, phase transition, IR spectroscopy

Citation: Gureva S.A., Marikhin V.A., Vlasova E.N., Conformational disorder and its effect on structural phase transitions in tricosane $C_{23}H_{48}$, St. Petersburg State Polytechnical University Journal. Physics and Mathematics. 16 (1.1) (2023) 84–89. DOI: <https://doi.org/10.18721/JPM.161.114>

This is an open access article under the CC BY-NC 4.0 license (<https://creativecommons.org/licenses/by-nc/4.0/>)

Материалы конференции

УДК 538.913

DOI: <https://doi.org/10.18721/JPM.161.114>

Конформационный беспорядок и его влияние на структурные фазовые переходы в трикозанае $C_{23}H_{48}$

С.А. Гурьева ¹✉, В.А. Марихин ¹, Е.Н. Власова ²

¹Физико-технический институт им. А.Ф. Иоффе РАН, Санкт-Петербург, Россия;

²Институт высокомолекулярных соединений РАН, Санкт-Петербург, Россия

✉ swet.gurjewa@gmail.com

Аннотация. Методом ИК-Фурье спектроскопии исследована кинетика твердофазного структурного перехода первого рода в монодисперсных n-алканах на примере нечетного трикозана $C_{23}H_{48}$. Проведено детальное изучение перестроений структуры длинноцепочечных молекулярных кристаллов n-алканов при твердофазных переходах и показано существование множества нерегулярных конформеров в твердых фазах трикозана, концентрация которых достигает максимума при приближении к температуре плавления. Обнаружено, что возникновение конформационных дефектов способствует развитию новой фазы в объеме старой и облегчает переходы между различными промежуточными ротационными фазами в твердом состоянии. Таким образом, продемонстрирована существенная роль возникновения различных внутримолекулярных конформационных дефектов при нагревании n-алканов, которые способствуют

межфазным переходам из твердого состояния в жидкое, ослабляя межмолекулярное взаимодействие и увеличивая степень свободы молекул.

Ключевые слова: n-алкан, фазовый переход, ИК-спектроскопия

Ссылка при цитировании: Гурьева С.А., Марихин В.А., Власова Е.Н., Конформационный беспорядок и его влияние на структурные фазовые переходы в трикозане $C_{23}H_{48}$ // Научно-технические ведомости СПбГПУ. Физико-математические науки. 2023. Т. 16. № 1.1. С. 84–89. DOI: <https://doi.org/10.18721/JPM.161.114>

Статья открытого доступа, распространяемая по лицензии CC BY-NC 4.0 (<https://creativecommons.org/licenses/by-nc/4.0/>)

Introduction

Monodisperse long-chain molecular crystals (LCMCs) of normal alkanes (n-alkanes) with the general formula C_nH_{2n+2} and variable chain length are convenient model objects for polymers, which makes it possible to study the development of phase transitions (PTs) at a quantitative level.

It was shown by DSC [1–3] that when various LCMCs (i.e., n-alkanes, n-alcohols, mono- and dicarboxylic acids) are heated, these compounds initially undergo a first order solid-solid (structural) phase transition (PT-1) at temperatures $T_{PT-1} < T_m$, followed by an order-disorder phase transition (PT-2) accompanied by melting of structures at T_m .

The object of present research was one of the representatives of n-alkanes, namely, tricosane $C_{23}H_{48}$ produced by Sigma-Aldrich Company. The samples possess a very high degree of purification (about 99.9%). Moreover, the samples are characterized by monodispersity with an accuracy of one carbon-carbon bond along the chain length. Since odd n-alkanes are characterized by sub-cells with molecules perpendicular to the basal planes of the lamellae (in the particular case, sub-cells of orthorhombic symmetry [4]), the chain length and each lamella thickness of the studied samples are the same and are about 3 nm.

The highlight of our study series on these samples is that we can use FTIR spectroscopy to detect the slightest step-by-step changes of the molecular packing in crystalline sub-cells inside the lamella based on specific shifts in the vibrational spectra of molecules with increasing temperature.

In our previous works [5, 6] we have already studied the kinetics of the PT-1 development in monodisperse n-alkanes with odd chain lengths, using tricosane $C_{23}H_{48}$ as an example. Soundly based on the results obtained on the temperature changes in the vibrational modes of the methylene CH_2 trans-sequences in the crystalline lamella cores, it was found that the PT-1 develops according to a heterogeneous mechanism with the formation of a new phase nanonuclei in the volume of the old one in the temperature range $\Delta T = 1–2$ °C in agreement with the theory of diffuse first order phase transitions [7]. The revealed frequency shifts of the bands in the IR spectra indicate a gradual weakening of intermolecular interactions due to the transformation of the initial orthorhombic sub-cells into hexagonal ones. In addition, a new manifestation of the parity effect of n-alkanes was discovered, which consists in the fact that during the structural transition the initial nuclei of the hexagonal phase are formed in the interlamellar space containing the terminal CH_3 and closest to them CH_2 groups, and only then the transition affects the lamella cores (for even alkanes, an inverse relationship is observed [6]).

The present work is devoted to an even more detailed study of the structure rearrangements of long-chain molecular crystals of n-alkanes during solid-solid phase transitions. For this purpose, special attention is paid to the study of the nucleation and development of conformational defects, i.e., various combinations of trans- and gauche-conformers in the chains.

Experimental section

The sample preparation procedure was as follows: monodisperse tricosane in the original form of synthesized flakes was placed on NaCl plates of FTIR spectrometer, and then flakes were melted and slowly cooled to obtain an equilibrium crystal structure. The sample thickness was 10–20 μm . The absorption spectra of tricosane samples were recorded by the Bruker IFS-88 FTIR spectrometer in the temperature range from 21 to 48 °C with a step $\Delta T = 2$ °C overall and

a finer step $\Delta T = 0.1 \text{ }^\circ\text{C}$ in the PT-1 region. The samples were kept for 10 min at each step of temperature increase to achieve the appropriate equilibrium state.

To reveal changes in the concentrations of conformational defects in chains during heating, the spectral region of $\nu = 1200\text{--}1400 \text{ cm}^{-1}$ was studied (Fig. 1), which contains information about a large number of defects [8]. A complication in the selection of bands associated with conformers is caused by the presence of a weak progression of methylene wagging vibrations in the spectrum. Thus, the separation of overlapping bands into individual components and their subsequent processing were performed using the Fityk 1.3.1 program (Fig. 1) [9].

It is well known that a number of wagging progression bands are expected in the IR spectra of short trans-chains, since their presence indicates a high regularity in the crystalline cores of the lamellae (Fig. 1). It should be noted that the bands are arranged in a progression at approximately equal distances from each other, and for odd molecules there are twice as many allowed absorption bands as was observed for even ones in [10].

For tricosane irregular conformers of the following types were found in the studied region of the spectrum at room temperature: 1) kinks gtg^* ($\nu = 1312 \text{ cm}^{-1}$) and gtg ($\nu = 1371 \text{ cm}^{-1}$), 2) double gauche-conformers gg^* ($\nu = 1353 \text{ cm}^{-1}$), 3) end gauche-conformers gt_m ($\nu = 1339 \text{ cm}^{-1}$) [11–13], where t and g denote the regular trans and irregular gauche portions of the chain, respectively. All of the above types of defects are present in the spectrum of Fig. 1. The change in the intensity of the corresponding IR bands upon heating of n-alkane indicates an increase in the concentration of conformers, which leads to a violation of the crystallographic order of the molecular packing in the lamellae.

In addition, a clearly pronounced band of the symmetric scissoring $B_{\text{CH}_3}^S$ vibrations of terminal CH_3 groups are observed in the studied frequency range (in an even alkane, the corresponding band overlaps the kink gtg [10]).

Heating LCMCs of n-alkanes leads, firstly, to a thermal expansion of crystals, and secondly, to an accompanying process — the thermal activation of various conformational defects. Thus, there is an increase in the freedom of a molecule movement, and the probability of the violation of the chain regularity also increases. The strongest increase in the intensity of the corresponding absorption bands is observed at a temperature close to the melting point of the sample $T_m = 47.4 \text{ }^\circ\text{C}$ [14] (Fig. 2).

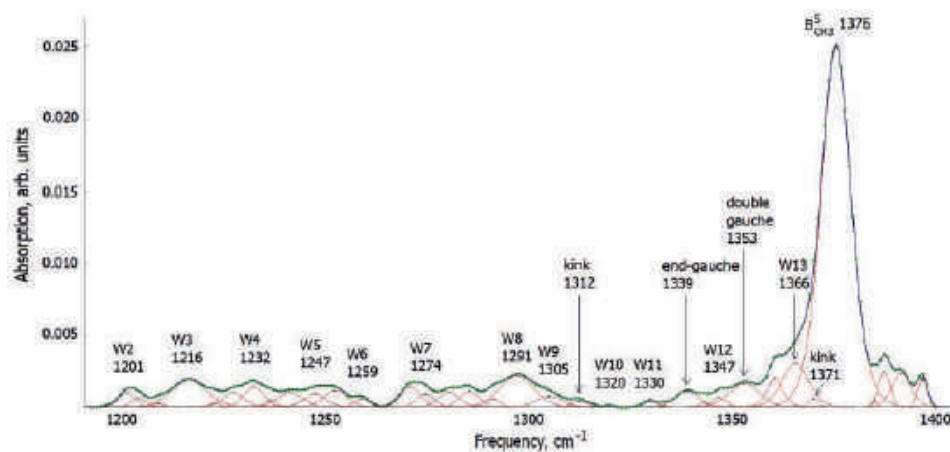


Fig. 1. The IR spectrum of tricosane $\text{C}_{23}\text{H}_{48}$ in the region of wagging vibrations at $21.0 \text{ }^\circ\text{C}$

In turn, the increase in the concentration of the conformational defects leads to a decrease in the regularity of the molecule structure in the lamella cores, and, consequently, a reduction in the number of bands in the wagging vibration progression. Fig. 2 shows the essential reduction in the band number in the wagging vibration progression of methylene at the sufficiently high temperature, which indicates a violation of the regular arrangement of oscillators (methylene CH_2 groups) along the chain. However, the fact that the band progression is retained even in the near-melt state indicates the presence of short trans-sequences in the crystalline cores of the lamellae near T_m .

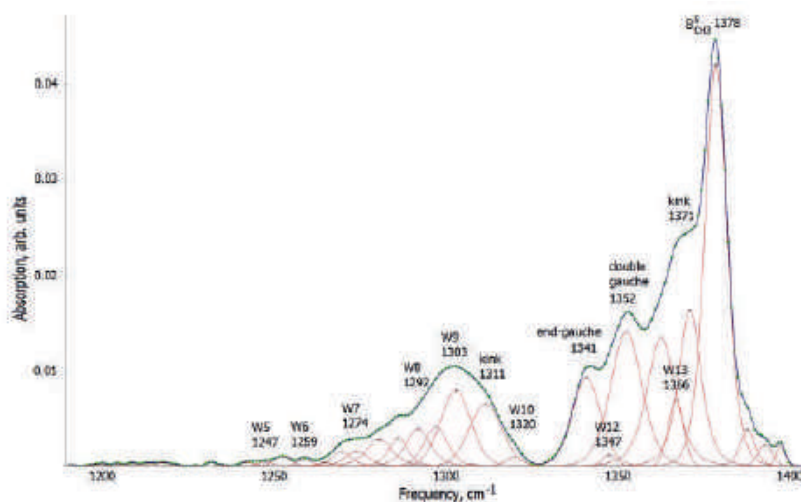


Fig. 2. The IR spectrum of tricosane $C_{23}H_{48}$ in the region of wagging vibrations at 47.8 °C

Results and Discussions

It is known that n-alkanes are characterized by the formation of a number of intermediate rotator phases during transitions between fully ordered crystalline and isotropic liquid states. According to [14, 15], when tricosane is heated, the following sequence of phases is expected to occur: the orthorhombic crystal, the R_V phase (tilted R_I), the R_I phase (distorted hexagonal structure), true hexagonal R_{II} phase, the liquid. Our earlier study [6] confirmed the possibility of the formation of rotator phases upon heating of tricosane based on changes in the spectral range of the C-H bond stretching vibrations. It has been suggested that the detected changes in the contact between the terminal groups of molecules in adjacent lamellae at 40.6–40.8 °C may be associated with the R_I - R_{II} transition, during which the type of molecular stacking in lamellae changes from two-layer ABAB to three-layer ABC. It can be assumed that the thermal activation of conformational defects facilitates the transitions between rotator phases, and, consequently, sharp changes in the concentrations of conformers should occur at appropriate temperatures.

Indeed, the analysis of the temperature dependences of the intensities of the absorption bands corresponding to different types of defects demonstrates sharp changes in the PT-1 region for tricosane $C_{23}H_{48}$ (Fig. 3 and 4).

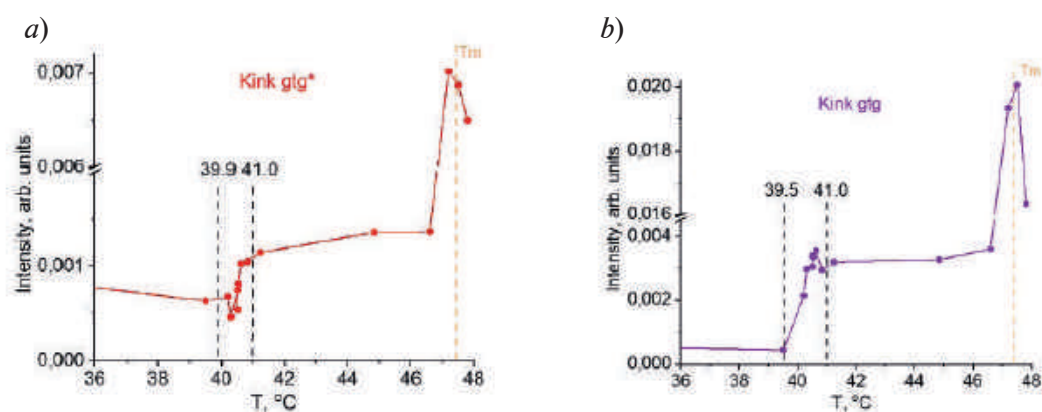


Fig. 3. Temperature dependences of the intensities of the absorption bands associated with nonplanar conformers: (a) kinks gfg^* ($\nu = 1312 \text{ cm}^{-1}$), and (b) kinks gfg ($\nu = 1371 \text{ cm}^{-1}$), in tricosane $C_{23}H_{48}$

Based on Figures 3 and 4, it can be concluded that the content of a small number of irregular conformers is still in the initial orthorhombic phase, then their concentration gradually increases when the sample is heated. It can be seen that the jumps in the intensity of two types of kinks observed at a temperature of about 40.6 °C (Fig. 3, a, b) indeed confirms the existence of some additional structural transition (the R_I - R_{II} transition). It can be argued that the increase in the

number of defects for the odd n-alkane occurs at a later stage of the structural transition than was found for the even n-alkane [10], for which the preliminary R_V - R_I transition was clearly observed.

Upon further transition to the fully hexagonal phase R_{II} at $T \geq 41.0$ °C, the kink concentrations increase by factors of 1.8 and 6.9 for gtg^* and gtg , respectively (Fig. 3, *a*, *b*) as compared to the corresponding values in the initial phase. The increase in the number of kinks is consistent with a higher freedom degree of molecules in hexagonal packing. On the contrary, the number of double gauche conformers becomes 2.2 times less (Fig. 4, *b*), which was also obtained for even tetracosane [10]. The concentration of end defects gradually increases upon heating, experiencing almost no significant changes throughout the entire structural transition (Fig. 4, *a*).

As expected, the most considerable growth in the number of conformers is characteristic of the transition of the hexagonal phase R_{II} to the melt (Fig. 3 and 4).

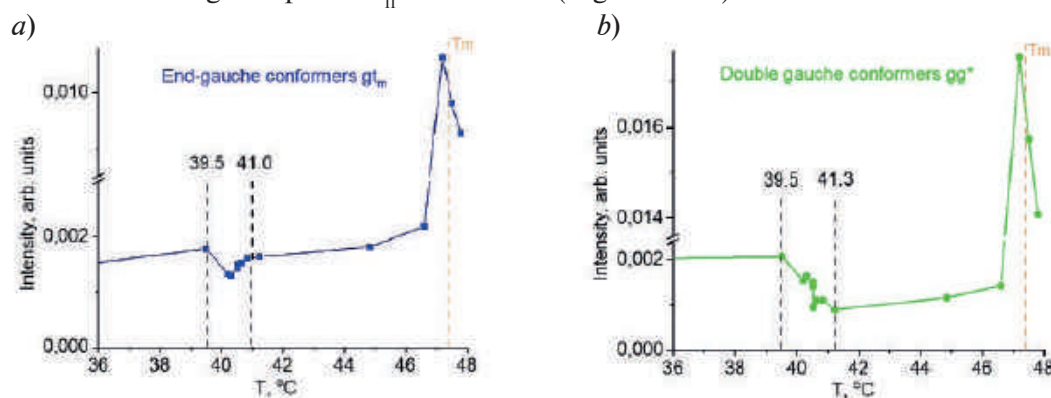


Fig. 4. Temperature dependences of the intensities of the absorption bands associated with nonplanar conformers: (a) end-gauche conformers gt_m ($\nu = 1339$ cm^{-1}), and (b) double gauche conformers gg^* ($\nu = 1353$ cm^{-1}), in tricosane $\text{C}_{23}\text{H}_{48}$

It can be noted that changes in the concentrations of all considered types of defects (both terminal and intrachain) occur in the same temperature range. Therefore, it is most likely that gtg^* and gtg kinks are predominantly generated in the near-surface layers of lamellae.

Moreover, it can be concluded that the thermal activation of conformational defects contributes to the structural transformations of tricosane in the temperature range $\Delta T = 39.5$ – 41.3 °C, which corresponds to the interval of the PT-1 development in the interlamellar space (containing the terminal CH_3 and closest to them CH_2 groups) previously determined in [6]. Thus, it can be argued that in odd n-alkanes the conformers that appear at the chain ends are directly involved in the mechanism of the formation of the nanonuclei of the new hexagonal phase.

Conclusion

The kinetics of the first-order solid-solid structural phase transition in monodisperse n-alkane samples of odd tricosane $\text{C}_{23}\text{H}_{48}$ was studied by FTIR spectroscopy. In order to elucidate the mechanism of the formation of the new phase nanonuclei in tricosane, the absorption bands associated with conformational defects were considered in detail. Analysis of the intensity temperature dependence of irregular conformer absorption bands showed the sharp jump in their concentration at the R_I - R_{II} transition, i.e., at the transition to completely hexagonal packing of molecules.

It has been determined that upon transition to the hexagonal phase the number of low energy defects, such as gtg^* and gtg kinks, is the most probably to increase by a factor of 2–7 at the chain ends. This can be explained by the fact that during the thermal expansion of crystals the formation of kinks in some molecules in the near-surface layers of the lamellae is energetically favorable; accordingly, the distance between neighboring chains increases. As a consequence, the ends of 3 to 4 carbon atoms slip out more easily from the lamellae cores. Furthermore, it is advantageous for these chains segments to rotate and become parallel to the lamella base planes in the interlamellar space. In addition, during the transition to the hexagonal phase the interlamellar space increases too, which also contributes to the formation of conformational defects. The results obtained demonstrate the high sensitivity of FTIR spectroscopy to initial changes in the molecular structure and the nature of their stacking in lamellae.



Therefore, the significant role has been demonstrated for the appearance of various intramolecular conformational defects during heating of n-alkanes, which consists in the fact that the defects contribute to the interfacial transitions from the solid to the liquid state, weakening the intermolecular interaction and increasing the freedom degree of molecules.

REFERENCES

1. Egorov V.M., Marikhin V.A., Myasnikova L.P., Phase transitions in molecular crystals of dicarboxylic acids, *Physics of the Solid State*. 55 (5) (2013) 1057–1062.
2. Egorov V.M., Marikhin V.A., Phase transitions in molecular crystals of the paraffin series: heneicosane and docosane, *Physics of the Solid State*. 58 (12) (2016) 2574–2579.
3. Borisov A.K., Egorov V.M., Marikhin V.A., An investigation of the thermodynamic properties of long-chain molecular crystals and the possibility of their application as phase change materials, *Journal of Physics: Conference Series*. 1400 (5) (2019) 055020.
4. Smith A.E., The crystal structure of the normal paraffin hydrocarbons, *The Journal of Chemical Physics*. 21(12) (1953) 2229–2231.
5. Gureva S.A., Marikhin V.A., Myasnikova L.P., Volchek B.Z., Medvedeva D.A., Crystal structure transformations during phase transitions in homologues of n-alkanes: $C_{23}H_{48}$, $C_{24}H_{50}$, $C_{25}H_{52}$, as revealed by FT-IR spectroscopy, *Journal of Physics: Conference Series*. 1400 (5) (2019) 055040.
6. Gureva S.A., Marikhin V.A., Myasnikova L.P., Volchek B.Z., Medvedeva D.A., The effect of the n-alkane evenness on structural phase transitions, *Journal of Physics: Conference Series*. 1697 (2020) 012093.
7. Malygin G.A., Diffuse martensitic transitions and the plasticity of crystals with a shape memory effect, *Physics-Uspexhi*. 171(2) (2001) 173–197.
8. Snyder R.G., Vibrational spectra of crystalline n-paraffins. Part I: Methylene rocking and wagging modes, *Journal of Molecular Spectroscopy*. 4 (1960) 411–434.
9. Wojdyr M., Fityk: A general-purpose peak fitting program, *Journal of Applied Crystallography*. 43 (5) (2010) 1126–1128.
10. Gureva S.A., Marikhin V.A., Myasnikova L.P., Volchek B.Z., Medvedeva D.A., The influence of conformational defects on the development of structural phase transition in tetracosane $C_{24}H_{50}$, *Journal of Physics: Conference Series*. 2103 (2021) 012091.
11. Snyder R.G., Maroncelli M., Qi S.P., Strauss H.L., Phase transitions and nonplanar conformers in crystalline n-alkanes, *Science*. 214 (4517) (1981) 188–190.
12. Zerbi G., Magni R., Gussoni M., Moritz K.H., Bigotto A., Dirlikov S., Molecular mechanics for phase transition and melting of n-alkanes: A spectroscopic study of molecular mobility of solid n-nonadecane, *The Journal of Chemical Physics*. 75 (7) (1981) 3175–3194.
13. Maroncelli M., Qi S.P., Strauss H.L., Snyder R.G., Nonplanar conformers and the phase behavior of solid n-alkanes, *Journal of the American Chemical Society*. 104 (23) (1982) 6237–6247.
14. Sirota E.B., King H.E., Singer D.M., Shao H.H., Rotator phases of the normal alkanes: An X-ray scattering study, *The Journal of Chemical Physics*. 98 (7) (1993) 5809–5824.
15. Sirota E.B., Singer D.M., Phase transitions among the rotator phases of the normal alkanes, *The Journal of Chemical Physics*. 101 (12) (1994) 10873–10882.

THE AUTHORS

GUREVA Svetlana A.
swet.gurjewa@gmail.com
ORCID: 0000-0001-7426-7304

VLASOVA Elena N.
spectra@imc.macro.ru
ORCID: 0000-0002-4644-0445

MARIKHIN Vyacheslav A.
v.marikhin@mail.ioffe.ru
ORCID: 0000-0001-7088-5914

Received 19.10.2022. Approved after reviewing 09.11.2022. Accepted 09.11.2022.

Conference materials

UDC 538.911

DOI: <https://doi.org/10.18721/JPM.161.115>

Dimensional effect of nanocrystalline elements of the polyethylene structure

A.K. Borisov ¹✉, V.M. Egorov ¹, V.A. Marikhin ¹, L.P. Myasnikova ¹

¹Ioffe Institute, St. Petersburg, Russia

✉ borisov.ak@mail.ioffe.ru

Abstract. The method for calculating the size distribution of nanocrystalline elements in lamellar and fibrillar polymer morphologies was proposed. The distribution of the longitudinal size of these elements in lamellas and microfibrils of ultrahigh molecular weight polyethylene was calculated using differential scanning calorimetry data. The calculation results are consistent with the data obtained by the X-ray method.

Keywords: ultrahigh molecular weight polyethylene, lamella, fibril, differential scanning calorimetry, phase transition

Citation: Borisov A.K., Egorov V.M., Marikhin V.A., Myasnikova L.P., Dimensional effect of nanocrystalline elements of the polyethylene structure, St. Petersburg State Polytechnical University Journal. Physics and Mathematics. 16 (1.1) (2023) 90–96. DOI: <https://doi.org/10.18721/JPM.161.115>

This is an open access article under the CC BY-NC 4.0 license (<https://creativecommons.org/licenses/by-nc/4.0/>)

Материалы конференции

УДК 538.911

DOI: <https://doi.org/10.18721/JPM.161.115>

Размерный эффект нанокристаллических элементов структуры полиэтилена

А.К. Борисов ¹✉, В.М. Егоров ¹, В.А. Марихин ¹, Л.П. Мясникова ¹

¹Физико-технический институт им. А.Ф. Иоффе РАН, Санкт-Петербург, Россия

✉ borisov.ak@mail.ioffe.ru

Аннотация. Предложен метод расчета распределения по размерам нанокристаллических элементов ламеллярной и фибриллярной надмолекулярных структур полимера. Расчет распределения продольного размера этих элементов в ламелях и микрофибриллах сверхвысокомолекулярного полиэтилена выполнен с использованием данных дифференциальной сканирующей калориметрии. Результаты расчетов согласуются с данными, полученными рентгеновским методом.

Ключевые слова: сверхвысокомолекулярный полиэтилен, ламель, фибрилла, дифференциальная сканирующая калориметрия, фазовый переход

Ссылка при цитировании: Борисов А.К., Егоров В.М., Марихин В.А., Мясникова Л.П., Размерный эффект нанокристаллических элементов структуры полиэтилена // Научно-технические ведомости СПбГПУ. Физико-математические науки. 2023. Т. 16. № 1.1. С. 90–96. DOI: <https://doi.org/10.18721/JPM.161.115>

Статья открытого доступа, распространяемая по лицензии CC BY-NC 4.0 (<https://creativecommons.org/licenses/by-nc/4.0/>)

Introduction

In the last decade, significant progress has been made in the creation of structural materials used in products that require high mechanical characteristics and special reliability. These materials include highly oriented fibers and threads obtained by gel technology from ultra-high molecular weight polyethylene (UHMWPE). They demonstrate high values of strength and elastic modulus [1, 2], but also have significant potential for their further increase, since the values currently obtained are significantly lower than theoretical estimates [3].

Since there is a relationship between the mechanical properties of polymeric materials and morphology, it is necessary to find out how the morphology is formed at each stage of fiber production. In this work, we propose a method based on the analysis of the shape of differential scanning calorimetry (DSC) melting curves, which makes it possible to obtain the size distribution of nanocrystalline elements in a polymer with various morphologies, including lamellar and fibrillar structures.

Samples and experiment

The thermophysical characteristics of the following samples were studied: the initial xerogel film obtained from a 1% solution in mineral oil of UHMWPE nascent powder with an average viscosity molecular weight $M_w = 3 \cdot 10^6$, and threads with different degrees of drawing obtained by multistage zone orientational hardening of the initial film on local heaters [4]. The samples listed above were studied using a DSC PerkinElmer calorimeter.

Figure 1 shows DSC curves that demonstrate the change in the melting peak of UHMWPE threads with increasing draw ratio (λ). It can be seen that the temperature of the maximum of the endothermic melting peak T_{\max} shifts to high temperatures with increasing λ .

The shape of the peak also changes significantly: the amplitude increases, and at the first stage ($\lambda < 50$) a low-temperature shoulder is observed. At higher degrees of draw ratio the shoulder disappears, and the melting enthalpy ΔH and, accordingly, the degree of crystallinity increase by 10–30%. It is clear that the changes in the quantitative characteristics of the melting peak reflect the radical rearrangement of morphology that occurs in the polymer upon orientation. First, this affects crystalline formations, the melting point of which is different within a wide melting temperature range. Apparently, these crystalline formations differ from each other in size, since the same methylene groups $-\text{CH}_2-$ form them and, therefore, from the point of view of the internal structure, they are identical. In this case, the temperature interval and the shape of the endothermic melting peak are related to the size distribution of crystalline formations.

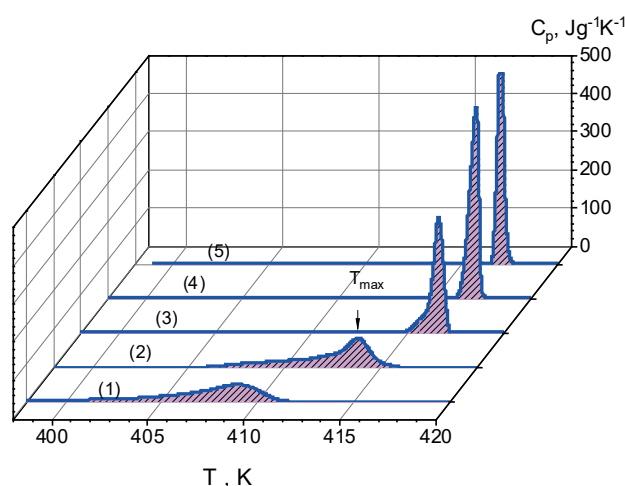


Fig. 1. DSC curves obtained by heating UHMWPE samples ($V = 5$ K/min). Initial film (1), oriented UHMWPE filaments with draw ratio $\lambda = 9$ (2), $\lambda = 43$ (3), $\lambda = 95$ (4), $\lambda = 170$ (5)

Theoretical calculations

Before calculating the distribution according to the experimental DSC curves shown in Figure 1, it is necessary to take into account the methodological error. In [5] we presented a method for determining the methodological error ΔT , according to which, under the same experimental conditions, the value of ΔT can be determined for one of the samples and used for the entire sample. In accordance with [6], extrapolation of the experimental linear dependence $T_{\max} = f(V^{1/2})$ to $V = 0$ makes it possible to determine ΔT , which in our case was $\Delta T = 1.6$ K.

In [7] we proposed a method that makes it possible to obtain the size distribution of crystalline formations in a polymer by analyzing the shape of DSC curves. The method is based on the fact that during melting the heat flux is directly proportional to the mass fraction of crystallites that melt at temperature depending on their size. Therefore, the heat flux depending on the temperature can be converted into a heat flux distribution depending on the longitudinal size of the crystallite according to the following relation:

$$dH / dl_1 = (dT / dl_1)(dH / dT), \quad (1)$$

where dH/dT is the experimental dependence of the heat flux on temperature, determined from the DSC curve, taking into account the scanning speed; l_1 is the longitudinal size of the crystallite, equal to $l_1 = h \times n$, where n is the number of C-C bonds in the main chain, h is the length of the bond projection onto the axis of the macromolecule (for polyethylene, $h = 0.124$ nm). The dependence dT/dl_1 is obtained from the generalized Gibbs Thomson equation based on the balance of surface and volume energies [8, 9]:

$$T(l_1) = T_0[1 - 2 / \Delta H_0(\sigma / l_2 + \sigma / l_3 + \sigma_e / l_1)], \quad (2)$$

where l_2 and l_3 are the dimensions of the crystallite in the plane perpendicular to the longitudinal axis of the macromolecule; σ is the surface energy of the side surfaces of the crystallite; σ_e is the surface energy of the end surface; $\Delta H_0 = 293$ J/cm³ and $T_0 = 415$ K are the enthalpy of phase transition and the melting point of an ideal polyethylene crystal [6], respectively.

In the initial xerogel film the UHMWPE morphology consists of stacks of lamellae; l_2 and $l_3 \gg l_1$. Therefore, in expression (2) the terms σ/l_2 and σ/l_3 can be neglected:

$$T(l_1) = T_0[1 - 2 \sigma_e / \Delta H_0 l_1] \quad (3)$$

However, the distribution dH/dl_1 calculated from relations (1) and (3) is not a distribution of the number of lamellas versus thickness, since thicker lamellas absorb more heat. This distribution cannot be compared with distributions obtained by other methods that determine the number of lamellae of a certain thickness. Therefore, for a correct comparison, it is necessary to normalize to l_1 . Figure 2 (curve 1) shows the calculation of $l_1^{-1} \cdot dH/dl_1$ as a percentage for the initial non-oriented sample. The calculations used the value of the surface energy $\sigma_e = 9 \cdot 10^{-6}$ J/cm² [8]. It can be seen from the figure that the maximum number of lamellae is in the range of 6–8 nm (18%), and the bulk of lamellae (~ 80%) have thicknesses from 4 to 14 nm.

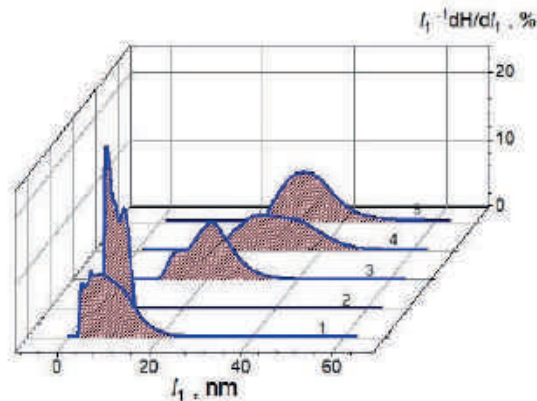


Fig. 2. The dependence of the number of crystalline formations on their longitudinal size, expressed as a percentage. Initial film (1), oriented UHMWPE with draw ratio $\lambda = 9$ (2), $\lambda = 43$ (3), $\lambda = 95$ (4), $\lambda = 170$ (5)

The lamellar morphology of the initial xerogel film undergoes strong changes during orientational drawing: the lamellar structure is rearranged into a fibrillar one [1]. It is known [3] that the morphology of a fibril consists of a successive alternation of crystalline and disordered regions, in which a large number of macromolecules emerging from the previous crystallite pass into the next one. The parameters l_2 and l_3 of the crystalline regions of fibrils are comparable with l_1 . In the first approximation, the surface energy can be considered the same for all side surfaces and, therefore, only the end σ_e and lateral σ surface energies can be used. Thus, the dimensions of the cross section of crystallites will be equal: $l_2 = l_3 = l$. Expression (2) takes the following form:

$$T(l_1) = T_0 [1 - 2 / \Delta H_0 (2\sigma / l + \sigma_e / l_1)] \quad (4)$$

To determine the surface energy σ , i.e., energy of intermolecular interaction per unit area $\sim 0.2 \text{ nm}^2$ of the methylene group $-\text{CH}_2-$, it is necessary to determine the part of the cohesive energy $E_c = 3.6 \text{ kJ/mol}$ [10], which is related to the van der Waals interaction in the disordered phase. It is known [10] that this part is $(0.35 \pm 0.05) E_c$. An estimate based on the above parameters gives the value of the lateral surface energy equal to $\sigma \approx 9 \text{ erg/cm}^2$.

The value of the end surface energy σ_e associated with intrafibrillar disordered regions is much more difficult to determine. It is worth noting here that it is the structure of these regions that controls the orientational strength of the oriented polymer. There are several models [11] that describe the structural elements of intrafibrillar disordered regions. Figure 3 schematically shows the most significant of them. To obtain a complete understanding of the formation of the end surface of crystallites, a detailed analysis of these elements is required.

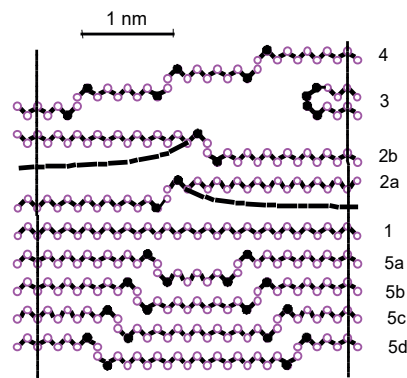


Fig. 3. Structural elements of the intrafibrillar region of the microfibril. Dashed lines are the boundaries of crystalline formations. Filled circles are gauche isomers

Let us consider the possibility of occurrence of the elements shown in Figure 3:

1 – crystalline bridges or completely straightened molecules in the trans-conformation between adjacent microfibril crystallites (see Fig. 3, position 1). The presence of such structures is confirmed by X-ray studies [12], which found that the effective average crystallite size exceeds a large period, which can be explained by a significant number of straightened molecules in the disordered regions of microfibrils;

2 – conformational defects in straightened segments of macromolecules formed by a *kink* isomer, consisting of a combination of the simplest isomers with *trans* and *gauche* conformations. Low energy *trans* conformations are denoted by *t* and higher energy conformations by *g*. Thus, the simplest *kink* conformer with *ttt-g-t-g-ttt* alternation is denoted by *2g1*. According to the so-called crankshaft model [8], kink isomers are represented as differently directed steps on a macromolecule (see Figure 3, positions 2, *a*, *b*). The *2g1* conformers are equilibrium defects. According to an alternative model [12], a conformational defect in a straightened segment of a macromolecule is a step with a small segment of the chain adjusting as it moves away from the turning point of the chain (see Fig. 3, positions 2, *a*, *b*, dash-dotted lines);

3 – irregular and regular loops formed by returning some of the molecules to the same crystallite from which they left. Four *gauche* conformers form regular loops or folds that form the surface of the crystals in the lamellae (see Fig. 3, position 3). More *gauche* conformers form irregular loops;

4 – curved tie molecules connecting the crystallites to each other (see Fig. 3, position 4). Curvature due to the presence of one *gauche* isomer on each side of neighboring crystallites. The degree of curvature is determined by the number of *gauche* isomers that can lie in between these “surface” *gauche* isomers;

5 – the “crankshaft” structure formed by multidirectional steps or *kink* isomers [14] (see Fig. 3, position 5, *a*). The possibility of the existence of a combination of such structures is assumed (see Fig. 4, positions 5, *b, c, d*). It is based on the fact that if the excess volume of one step is $3/4v_0$, where v_0 is the volume of the CH_2 group, then the excess volume of each of the contributing steps is only $1/4v_0$ [15], i.e., in this case, a cooperative effect is observed.

The orientational drawing of the polymer occurs at elevated temperatures and is accompanied by an increase in the degree of crystallinity. It is carried out by reducing the defectiveness of the disordered interlayer. The molecular mechanism of this process is associated with multidirectional diffusion of *kinks* or *double kinks* along the polymer chain, followed by annihilation at the ends of macromolecules or the formation of a crankshaft type defect and their combinations.

Each of the above combinations of isomers in the intrafibrillar region makes a different contribution to the end surface energy. For *kink* defects (see Fig. 3, positions 2 and 2*a*) containing two *gauche* isomers, the surface energy is determined by one *gauche* isomer, since the step forms the elementary surface of two adjacent crystals. In the case of the “crankshaft” (see Fig. 3, positions 5*a, b, c, d*), the surface energy is produced by two *gauche* isomers, and finally in the case of a regular fold (see Fig. 3, position 3), by four. Curved tie molecules that connect the crystallites to each other (see Fig. 3, position 4) are straightened due to the diffusion of *kinks* during orientational drawing at elevated temperatures and then turn into steps (see Fig. 3, positions 2 and 2, *a*).

To determine the end surface energy σ_e created by one *gauche* isomer, it is necessary to find the fraction of the formation energy of this defect $\Delta E = 2.5$ kJ/mol per unit area $\Delta S \approx 0.18$ nm² of the chain end surface. An estimate of the ratio $\Delta E/\Delta S$ gives the value of the end surface energy equal to $\sigma_{e1} \approx 11$ erg/cm². In the case of the “crankshaft”, the surface energy already formed by two *gauche* isomers will be twice as high ($\sigma_{e2} \approx 22$ erg/cm²).

To calculate dH/dL using relations (1) and (4) for a fibrillar structure, in addition to the values of the end and side surface energies, it is necessary to determine the parameter l , the size of the microfibril in cross section. Figure 2 (curves 2–5) shows the calculation of the dH/dL distribution for oriented PE samples with fibrillar morphology. In calculations $l = 40$ nm and $\sigma_{e1} \approx 11$ erg/cm² were used.

Figure 2 shows the complex nature of the change in the size distribution of crystallites with orientation. At the first stage of orientation (curve 2) a sharp decrease in the width of the distribution and a shift to low dimensions are observed. This is due to the transition from the lamellar morphology of the original sample to the fibrillar one with a large proportion of the disordered part. Further orientation is accompanied by an increase in the size of crystalline regions, an increase in the spreading of distributions, and a decrease in the proportion of the disordered part (see Fig. 2, curves 3–5).

To compare the obtained distributions with the X-ray data published in [12], it was necessary to determine the weighted average lm in the dH/dl_1 distribution. The value of l_m was determined by the relation $l_m = \Sigma l_i(dH/dl_1)_i / \Sigma (dH/dl_1)_i$, where l_i is the current value of l_1 in the distribution; $(dH/dl_1)_i$ is the current value of dH/dl_1 at $l_1 = l_i$.

Figure 4 shows the dependences of the weighted average values of the longitudinal sizes of crystallites l_m on the degree of orientation of the initial xerogel film, obtained from X-ray data (1) and calculated values of l_m (2, 3). It can be seen from the figure that the distributions of the longitudinal sizes of crystallites obtained on the basis of X-ray (1) and DSC data (2) fit into one dependence. In this case, the value of the end surface energy σ_{e1} created by one *gauche* isomer was used in the calculations.

It can be seen from the figure that the dependence sharply increases at the initial stage, and then, in the range $\lambda \approx 50-150$, it reaches saturation. This process is associated with the diffusion of *kinks* or *double kinks* that form the surface energy σ_{e1} , since they either annihilate upon reaching the end of the chain or meet with a double *kink* in the opposite direction and form a “crankshaft” structure. With a large number of these elements in the limited space of the intrafibrillar region, they can cooperate into a structure similar to that shown in Figure 3 (positions 5*a, b, c* and *d*).

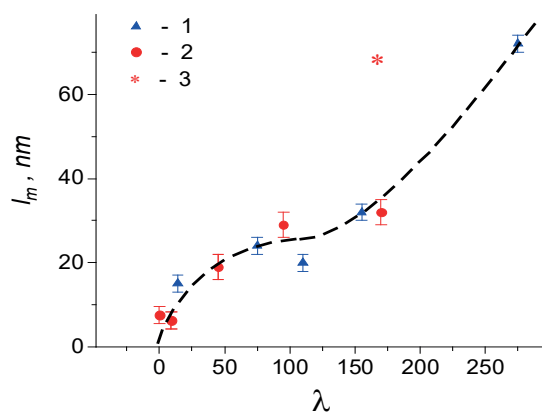


Fig. 4. Dependences of the weighted average values of the longitudinal sizes of crystallites on the degree of orientation according to X-ray data (1) and calculated at σ_{e1} (2) and σ_{e2} (3).

In such a structure, the cooperative excess volume will be less than the sum of the excess volumes of the independent elements of this structure.

For ultra-high orientation draw ratio ($\lambda \approx 270$) there is a sharp increase in $l_m(\lambda)$ (see Fig. 4). According to relation (4), such a rise can be caused by two reasons. First, the inclusion of crystalline formations with increased end surface energy into the process of orientational ordering. The calculation using the value of the end surface energy σ_{e2} , formed by the elements of the crankshaft type structure, indeed shows (see Fig. 4, position 3) a significant increase in l_m . An increase in the drawing temperature, which can exceed the melting temperature of an equilibrium PE crystal [16], leads to an acceleration of diffusion and annihilation of complex combinations of defects on the surface of crystalline formations, which leads to a high surface end energy.

The second reason for the sharp rise may be the dependence of l_m on the transverse size of the crystallite, i.e., on the parameter l in relation (4). Such a process should occur as the density of defects in the disordered interlayer decreases and the number of crystalline bridges in the *trans* conformation between neighboring crystallites in the microfibril increases. In the limiting case (at $l_m \rightarrow \infty$), relation (4) implies that the parameter l tends to 0.1–0.2 nm, i.e., the transverse size of the crystallite becomes comparable to the transverse size of a single polyethylene chain.

Conclusion

Thus, the method proposed in this work for calculating the size distribution of nanocrystalline elements of lamellar and fibrillar polymer morphologies made it possible to reveal a number of features of the process of orientational drawing of ultrahigh molecular weight polyethylene. Based on the analysis of these features, a model is proposed that describes the evolution of the disordered part of the polymer morphology. The results of calculations based on the weighted averages in the distribution obtained from calorimetric data are consistent with the data obtained by the X-ray method.

REFERENCES

1. Marikhin V., Myasnikova L., Boiko Yu., Ivan'kova E., Radovanova E., Yakushev P., Reactor Powder Morphology, Ch. 10, Nova Publishers. New York (2011).
2. Boiko Y.M., Marikhin V.A., Moskalyuk O.A., Myasnikova L.P., On the determination of the elastic modulus of ultraoriented high-strength film threads obtained by drawing of ultra-high-molecular-weight polyethylene xerogels, Physics of the Solid State. 61 (44) (2019) 44–47.
3. Marikhin V.A., Myasnikova L.P., Structural basis of high-strength high-modulus polymers, Oriented Polymer Materials. (1996) 38–98.
4. Marikhin V.A., Myasnikova L.P., Heterogeneity of structure and mechanical properties of polymers, Makromol. Chemie. Macromol. Symp. B. 41 (1991) 209–227.
5. Egorov V.M., Borisov A.K., Marikhin V.A., Formation of nanonuclei during a structural phase transition in molecular crystals of normal alkanes, Physics of the Solid State. 63 (3) (2021) 498–504.

6. **Illers K.-H.**, Die ermittlung des schmelzpunktes von kristallinen polymeren mittels wärmeflusskalorimetrie (DSC), *European Polymer Journal*. 10 (10) (1974) 911–916.
7. **Egorov V.M., Borisov A.K., Marikhin V.A.**, Thermal conductivity of a composite based on n-alkane and nanosized additives, *Technical Physics Letters*. 48 (1) (2022) 49–52.
8. **Wunderlich B.**, *Macromolecular physics*, Vol. 3. Academic Press. London (1980).
9. **Hoffman J.D.**, *Treatise on solid state chemistry*, Vol. 3. Plenum Press. New York (1976).
10. **Van Krevelen D.W.**, *Properties of polymers correlations with chemical structure*. New York (1972).
11. **Marikhin V.A., Myasnikova L.P.**, *Nadmolekulyarnaya struktura polimerov*, Chemistry. Leningrad (1977).
12. **Marikhin V.A., Myasnikova L.P., Uspensky M.D.**, Features of orientation drawing of gel-crystallized polyethylene, *Polymer Science Series A*. 35 (6) (1993) 686–692.
13. **Gotlib Y.A., Darinskiy A.A., Svetlov Y.E.**, *Fizicheskaya kinetika makromolekul*, Chemistry. Leningrad (1986).
14. **Marikhin V.A.**, The structure of amorphous sections of microfibrils of oriented polymers, *Physics of the Solid State*. 19 (4) (1977) 1036–1039.
15. **Kausch H.**, *Polymer fracture*, Plenum Press. Springer-Verlag, Berlin (1978).
16. **Bershtein V.A., Savitsky A.V., Egorov V.M.**, Melting of polyethylene with strength close to theoretical, *Polymer Science Series A*. 27 (2) (1985) 113–116.

THE AUTHORS

BORISOV Artem K.
borisov.ak@mail.ioffe.ru
ORCID: 0000-0001-8010-5467

MARIKHIN Vyacheslav A.
v.marikhin@mail.ioffe.ru
ORCID: 0000-0001-7088-5914

EGOROV Victor M.
victor_egorov1@inbox.ru
ORCID: 0000-0002-8742-2710

MYASNIKOVA Lyubov P.
liu2000@mail.ru
ORCID: 0000-0003-0648-5056

Received 19.10.2022. Approved after reviewing 14.11.2022. Accepted 15.11.2022.

Conference materials
UDC 549.08; 538.975
DOI: <https://doi.org/10.18721/JPM.161.116>

Frequency and concentration dependences of the electrical properties of natural disordered carbon in the high-frequency region

Ye.A. Golubev ¹✉, I.V. Antonets ², R.I. Korolev ²

¹Institute of Geology of Komi SC UB RAS, Syktyvkar, Russia;

²Syktyvkar state University the name of Pitirim Sorokin, Syktyvkar, Russia

✉ yevgenyGolubev74@mail.ru

Abstract. Disordered sp^2 carbon of geological origin (shungite rocks of Karelia) with a set of various nanostructures (fullerene-like, graphene, ribbons) has promising technological properties. In this work, we studied the effect of nanosized carbon structures on the electrical properties. The impedance, active and reactance resistance, inductance of carbon-containing materials were measured in the frequency range from 50 kHz to 15 MHz. The inductive nature of the conductivity of shungite carbon was found. With increasing frequency, the resistance of shungite carbon increases. This nature of conductivity can be associated with the predominant effect on the electrical properties in shungites of nanosized ribbon structures.

Keywords: disordered sp^2 carbon, nanostructure, electrophysical characteristics

Funding: This study was funded by RSF according to the research project No. 21 47 00019.

Citation: Golubev Ye.A., Antonets I.V., Korolev R.I. Frequency and concentration dependences of the electrical properties of natural disordered carbon in the high-frequency region, St. Petersburg State Polytechnical University Journal. St. Petersburg State Polytechnical University Journal. Physics and Mathematics. 16 (1.1) (2023) 97–101. DOI: <https://doi.org/10.18721/JPM.161.116>

This is an open access article under the CC BY-NC 4.0 license (<https://creativecommons.org/licenses/by-nc/4.0/>)

Материалы конференции
УДК 549.08; 538.975
DOI: <https://doi.org/10.18721/JPM.161.116>

Частотные и концентрационные зависимости электрических свойств природного неупорядоченного углерода в высокочастотной области

Е.А. Голубев ¹✉, И.В. Антонетц ², Р.И. Королев ²

¹Институт геологии ФИЦ Коми НЦ УрО РАН, г. Сыктывкар, Россия;

²Сыктывкарский государственный университет имени Питирима Сорокина, г. Сыктывкар, Россия

✉ yevgenyGolubev74@mail.ru

Аннотация. Перспективными технологическими свойствами обладает разупорядоченный sp^2 -углерод геологического происхождения (шунгитовые породы Карелии) с набором различных наноструктур (фуллереноподобная, графеновая, ленточная). В данной работе мы исследовали влияние наноразмерных углеродных структур на электрические свойства. Измерялись импеданс, активное и реактивное сопротивление, индуктивность углеродсодержащих в диапазоне частот от 50 кГц до 15 МГц. Обнаружен индуктивный характер электропроводности шунгитового углерода. С увеличением частоты сопротивление шунгитового углерода увеличивается. Такой характер проводимости может быть связан с преимущественным влиянием на электрические свойства в шунгитах наноразмерных ленточных структур.

Ключевые слова: разупорядоченный sp^2 -углерод, наноструктура, электрофизические характеристики

Финансирование: грант РФФ 21-47-00019, «Interphase interactions and formation mechanisms of nanophases of natural amorphous carbons and aluminosilicate minerals and their inspirations on the construction of nature-like nanocomposites».

Ссылка при цитировании: Голубев Е.А., Антонец И.В., Королев Р.И. Частотные и концентрационные зависимости электрических свойств природного неупорядоченного углерода в высокочастотной области // Научно-технические ведомости СПбГПУ. Физико-математические науки. 2023. Т. 16. № 1.1. С. 97–101. DOI: <https://doi.org/10.18721/JPM.161.116>

Статья открытого доступа, распространяемая по лицензии CC BY-NC 4.0 (<https://creativecommons.org/licenses/by-nc/4.0/>)

Introduction

In the shungite rocks of Karelia, disordered sp^2 carbon with a set of various nanostructures (fullerene-like, graphene, ribbon) was formed under geological conditions [1]. Promising technological properties of shungites (high electrical conductivity, reflection and absorption of microwave radiation, chemical stability and heat resistance) are associated with these nanostructures and porosity [2–9]. The carbon content in shungites varies from 2 to 97 at. %, and inclusions of minerals (mainly quartz) control some of their physical properties. In general, shungite is a natural carbon-mineral composite with alternating conductive (carbon) and non conductive (quartz) areas. Electrically conductive properties serve as the key both to the knowledge of the structural features of shungite carbon and to the expansion of promising technological applications. Previous studies of the frequency dependence of electrical properties on carbon content in the frequency range 100 Hz–200 kHz showed [10] that significant changes in electrical properties with increasing frequency start at frequencies of the first hundreds of kHz. In this regard, it is of interest to study the electrophysical characteristics of shungites and disordered carbon in a wider frequency range, primarily megahertz.

In this paper we present an analysis of the effect of nanosized carbon structures on the electrical properties based on modern structural studies of shungites and the frequency dependences of the total impedance, active and reactive resistances, phase angle, dielectric loss tangent, and specific conductivity of shungite samples.

Experimental

The measurement of the frequency dependence of complex resistance (impedance) is widely used to study the electrophysical properties of porous carbon materials. This paper presents the averaged results of measurements of the impedance and the phase angle, as well as the results of calculations of active and reactive resistances, the tangent of the dielectric loss angle, inductance and conductivity of shungite samples depending on the frequency and carbon content.

To study the conductive properties shungite samples with a carbon content of 5 to 97 at. % were used. The shungites can be conditionally divided into samples with high, medium and low carbon content. An E7-29 immittance meter (Minsk Scientific and Research Instrument-Making Institute, Belarus) was used to measure the impedance and phase angle in the frequency range from 50 kHz to 15 MHz.

The samples had the shape of a square tablet with side sizes from 7 to 10 mm and with thickness 1.5 mm. Measurements of inductance, impedance and phase angle were carried out in six separate areas for shungite with a carbon concentration below 50 at. %, and in 3–5 areas for shungites with a carbon concentration above 50 at. %. All measurements were carried out at room temperature.

Results

Figure 1 shows the dependence of the impedance modulus of shungite on the carbon content. The shungite impedance decreases with a carbon content increasing. The effect of the carbon content on the impedance Z is especially strong in the range of 5–35 at. %. At carbon content above 35 at. %, the decrease in the impedance value is much weaker.

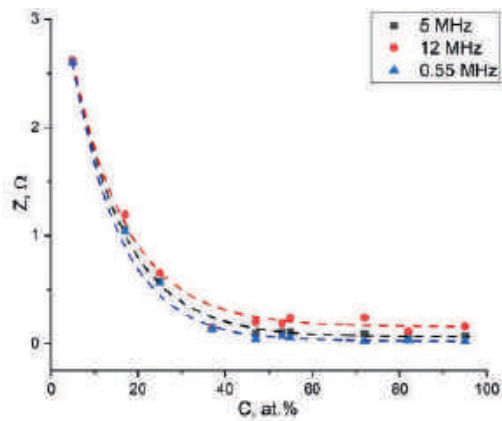


Fig. 1. Dependence of impedance on carbon content in shungites

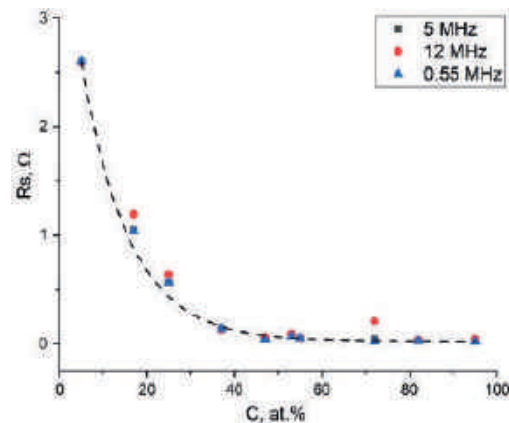


Fig. 2. Dependences of active resistance on carbon content

Phase angle θ and impedance Z are related to active R and reactance X by the following expressions:

$$R = \frac{|Z|}{\sqrt{\tan^2\theta + 1}} = |Z| \cos\theta, \quad (1)$$

$$X = \frac{|Z| \tan\theta}{\sqrt{\tan^2\theta + 1}} = |Z| \sin\theta. \quad (2)$$

Using these expressions, we calculated active (Fig. 2) and reactance resistances and conductivity (Fig. 3).

The largest contribution of inductance to reactance occurs in the range of 50 kHz–15 MHz. We estimated the value of inductance for shungite samples in the indicated range (Fig. 4). For all samples of shungite the inductance is approximately at the same level (2 ± 1) nH. Only for the sample with the lowest carbon content, the value of the inductance is much larger.

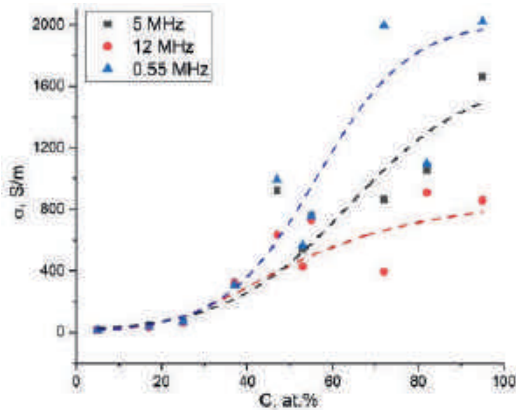


Fig. 3. Conductivity vs carbon content

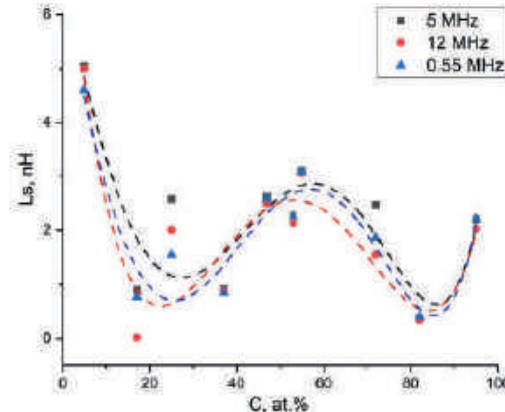


Fig. 4. Inductance vs carbon content

Discussion

For shungites the dependence of conductivity on frequency increases with increasing carbon content, and this dependence becomes significant at a carbon content of about 35%. The complex resistance (impedance Z) practically does not depend on the frequency. This is because active resistance dominates in shungites with a carbon content of up to 35%. The reactive part of the resistance is present, but its absolute values are small (0.1–0.4 Ω), even for samples with a low carbon content, where the reactance is greatest. At high values of active resistance for low-carbon samples (up to $C = 35\%$), the contribution of reactance is very small, and there is no effect of reactance on the total conductivity. Starting from $C = 35\%$, the value of active resistance drops sharply, and reactance begins to play a more significant role.

The increase in reactive resistance with frequency (Fig. 4) indicates the predominance of inductive resistance in shungites. The largest absolute value of the inductance is in samples with the lowest carbon content.

The inductive nature of conductivity at frequencies of 50 kHz–15 MHz can be associated with multilayer ribbon and fullerene-like structures of shungite carbon (Fig. 5), as well as with non-conductive inclusions up to several micrometers in size, which are covered with a thin film of ordered graphite carbon. Such structures can act as inductors or solenoids. The geometric parameters (the length and thickness of graphene-layer ribbons, the diameter of the turns) provide the predominant contribution of such structures to the inductive electrophysical properties in the measured frequency range.

The decrease in conductivity with increasing current frequency may be due to the routine mechanism of the increase in active resistance in the AC circuit. This mechanism consists in the uneven distribution of alternating current over the cross section of the conductor under the action of electromotive force (EMF) of self-induction. EMF is induced in the conductor by a magnetic field, which is created by the current passing through the conductor, and displaces the current to the surface of the conductor, reducing its useful cross section. If ribbon carbon structures with a thickness of 2–5 nm (Fig. 5), consisting of 5–15 graphene layers, are considered as key conductors in shungites, then such tapes correspond to the key paths of current propagation in shungites.

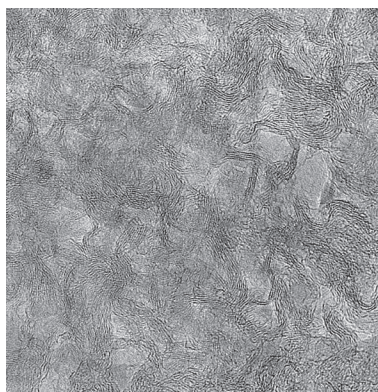


Fig. 5. Typical ribbon-graphene structure of shungite carbon

Conclusion

In the presented work, the electrophysical properties (impedance, active and reactive resistance, inductance) of carbon-containing natural composites (shungites) were measured at frequencies 50 kHz–15 MHz and calculated. Shungite samples with carbon content of 5–97 at. % were studied. These electrophysical properties were analyzed as frequency and concentration dependences.

A successively increasing dependence of the conductivity on the current frequency with an increase in the carbon content is found. The conductivity decreases with increasing current frequency. The complex resistance is practically independent of frequency due to the predominance of the active component.

The electrophysical properties can first be associated with ribbon carbon nanostructures in shungites, which create an inductive reactance and increase the active resistance in alternating current.

REFERENCES

1. Golubev Ye.A., Rozhkova N.N., Kabachkov Ye.N., Shul'ga Yu.M., Natkaniec-Holderne K., Natkaniec I., Antonets I.V., Makeev B.A., Popova N.A., Popova V.A., Sheka E.F., Sp² amorphous carbons in view of multianalytical consideration: Normal, expected and new, *Journal of Non-Crystalline Solids*. 524 (2019) 119608.
2. Vieira L.S., A review on the use of glassy carbon in advanced technological applications, *Carbon*. 186 (2022) 282–302.
3. Kovalevski V.V., Buseck P.R., Cowley J.M., Comparison of carbon in shungite rocks to other natural carbons: an X-ray and TEM study, *Carbon*. 39 (2001) 243–256.



4. **Lynkov L.M., Borbotko T.V., Krishtopova Ye.A.**, Radiopogloshchayushchiye svoystva nikelsoderzhashchego poroshkoobraznogo shungita, Pisma v zhurnal tekhnicheskoy fiziki. 35 (9) (2009) 44–48.
5. **Moshnikov I.A., Kovalevski V.V.**, Electrophysical properties of shungites at low temperatures, Nanosystems: Physics, Chemistry, Mathematics. 1 (2016) 214–219.
6. **Augustyniak-Jablokow M.A., Yablokov Y.V., Andrzejewski B., Kempinski W., Losr S., Tadyszak K., Yablokov M.Y., Zhikharev V.A.**, EPR and magnetism of the nanostructured natural carbonaceous material shungite, Physics and Chemistry of Minerals. 37 (2010) 237–247.
7. **Chmutin I.A., Ryvkina N.G., Solovieva A.B., Kedrina N.F., Timofeeva V., Rozhkova N.N., McQueen D.H.**, Electric properties of composites with a shungite filler, Polymer Science Series A. 46 (6) (2004) 664–671.
8. **Golubev Ye.A., Antonets I.V., Shcheglov V.I.**, Static and dynamic conductivity of nanostructured carbonaceous shungite geomaterials, Materials Chemistry and Physics. 226 (2019) 195–203.
9. **Chou N.H., Pierce N., Lei Y., Perea-Lopez N., Fujisawa K., Subramanian S., Robinson J.A., Chen G., Omichi K., Rozhkov S.S., Rozhkova N.N., Terrones M., Harutyunyan A.R.**, Carbon-rich shungite as a natural resource for efficient Li-ion battery electrodes, Carbon. 130 (2018) 105–111.
10. **Antonets I.V., Golubev Ye.A., Korolev R.I.**, Electrophysical Parameters of Shungite, AIP Conference Proceedings. Proceedings of the II International Conference on Advances in Materials, Systems and Technologies. 2467 (2022) 020026.

THE AUTHORS

GOLUBEV Yevgeny A.
yevgenyGolubev74@mail.ru
ORCID: 0000-0001-5354-937X

KOROLEV Roman I.
korolev36a@gmail.com

ANTONETS Igor V.
aiv@mail.ru
ORCID: 0000-0003-1103-4313

Received 25.10.2022. Approved after reviewing 06.12.2022. Accepted 06.12.2022.

Conference materials
UDC 538.9, 535.3
DOI: <https://doi.org/10.18721/JPM.161.117>

Influence of the refractive index gradient on the transmission coefficient in the 1.5-micron range in an electro-optical converter based on lithium niobate

S.A. Shmargilov¹, V.V. Galutskiy¹✉, K.V. Puzanovskiy¹, E.V. Stroganova¹

¹Kuban State University, Krasnodar, Russia

✉ galutskiy17v@mail.ru

Abstract. The paper presents the results of a study of the effect of the composition gradient and refractive index on the attenuation of an optical signal at a wavelength of 1.55 microns. The attenuation measurements were carried out by the breakage method and the comparison method, the attenuation by both methods was 0.9 dB/cm when waveguides were formed along the change in the lithium composition in the crystal plate of the composition $\text{Li}_{0.94\dots 0.98}\text{Nb}_{1.06\dots 1.02}\text{O}_{3.12\dots 3.04}$

Keywords: optical waveguide, optical losses, lithium niobate

Funding: The research leading to these results has received funding by the Ministry of Science and Higher Education of the Russian Federation (FZEN-2020-0022), RFBR No. 20 02 00529-a and the Kuban Science Foundation project No. MFI-20.1/129.

Citation: Shmargilov S.A., Galutskiy V.V., Puzanovskiy K.V., Stroganova E.V., Influence of the refractive index gradient on the transmission coefficient in the 1.5-micron range in an electro-optical converter based on lithium niobate, St. Petersburg State Polytechnical University Journal. Physics and Mathematics. 16 (1.1) (2023) 102–108. DOI: <https://doi.org/10.18721/JPM.161.117>

This is an open access article under the CC BY-NC 4.0 license (<https://creativecommons.org/licenses/by-nc/4.0/>)

Материалы конференции
УДК 538.9, 535.3
DOI: <https://doi.org/10.18721/JPM.161.117>

Исследование особенностей влияния градиента показателя преломления на коэффициент пропускания в 1,5 мкм диапазоне в электрооптическом преобразователе на основе ниобата лития

С.А. Шмаргилов¹, В.В. Галуцкий¹✉, К.В. Пузановский¹, Е.В. Строганова¹

¹Кубанский государственный университет, г. Краснодар, Россия

✉ galutskiy17v@mail.ru

Аннотация. В статье представлены результаты исследования влияния градиента состава и показателя преломления на затухание оптического сигнала на длине волны 1,55 мкм. Измерения затухания проводились методом обрыва и методом сравнения, затухание по данным обоих методов составило 0,9 дБ/см, когда вдоль изменения содержания лития в кристаллической пластине формировались волноводы состава $\text{Li}_{0.94\dots 0.98}\text{Nb}_{1.06\dots 1.02}\text{O}_{3.12\dots 3.04}$

Ключевые слова: оптический волновод, оптические потери, ниобат лития

Финансирование: Работа выполнена в рамках проекта FZEN-2020-0022, РФФИ № 20-02-00529-а и КНФ проект № MFI-20.1/129.

Ссылка при цитировании: Шмаргилов С.А., Галуцкий В.В., Пузановский К.В., Строганова Е.В. Исследование особенностей влияния градиента показателя преломления на коэффициент пропускания в 1,5 мкм диапазоне в электрооптическом преобразователе на основе ниобата лития // Научно-технические ведомости СПбГПУ.



Физико-математические науки. 2023. Т. 16. № 1.1. С. 102–108. DOI: <https://doi.org/10.18721/JPM.161.117>

Статья открытого доступа, распространяемая по лицензии CC BY-NC 4.0 (<https://creativecommons.org/licenses/by-nc/4.0/>)

Introduction

Lithium niobate modulators are one of many optoelectronic modulators developed in recent years. This was facilitated by the needs of the market of fiber-optic telecommunication systems [1]. To date the use of electro-optical modulators is not limited only to telecommunication systems. The advantages of a lithium niobate-based modulator are high modulation frequency, and the ability to work at different wavelengths. One of the disadvantages of electro-optical modulators is their susceptibility to various drift phenomena in the crystal matrix [1].

Important elements of the modulator based on the Mach-Zehnder interferometer are waveguides, the parameters of which affect its characteristics. Reducing optical signal losses in waveguides, increasing stability relative to drift phenomena are important areas for improving the characteristics of the device.

Earlier [2], to increase the temperature stability of optical radiation converters, it was proposed to use the gradient of the composition of the lithium niobate crystal plate. Therefore, the aim of the research was to estimate losses in waveguides in lithium niobate crystals with a gradient of composition.

Materials and Methods

An important part of solving the problem of determining the characteristic features of the formation of periodically polarized structures in the obtained samples of gradient ferroelectrics is the data on the magnitude of the coercive field of the grown gradient crystals. To determine the values characterizing the magnitude of the field required for local reorientation of ferroelectric domains, a processed plate cut from a gradient single crystal of lithium niobate (z -slice) was fixed in a high-voltage cell with liquid electrodes. LiCl solution was used as electrodes. A linearly increasing voltage was generated at the output of the digital functional signal generator, which was amplified by a high-voltage controlled power supply. The voltage through the electrolyte falls on the surface of the plate. We recorded current and voltage at the independent oscilloscope inputs CH1 and CH2 simultaneously. The voltage that corresponds to the site of a steep increase in current (with a simultaneous decrease in voltage drop), taking into account the thickness of the crystal, gives the strength of the coercive field.

By measuring the time local dependences of the current and the applied voltage associated with a specific point on the surface of a crystal plate with a thickness of 1.3 mm, the voltage values at which the domains are reoriented at this point of the plate were determined. Then the local value of the coercive field was compared to the lithium crystal composition [3] (Fig. 1).

To estimate losses in waveguide channels in the presence of a gradient distribution of optical properties, a crystal plate cut from gradient lithium niobate was prepared. A lithium niobate crystal with a gradient distribution of the main components was grown by the Czochralski method with liquid recharge [4]. The embedded distribution of the composition gradient was $\text{Li}_{0.94...0.98}\text{Nb}_{1.06...1.02}\text{O}_{3.12...3.04}$, after growing from the crystal along the direction of stretching, a plate with a thickness of 3 mm was cut out and its orientation relative to the C axis was performed.

The formation of submerged waveguide layers in a crystal plate with a gradient of composition was carried out in several stages: thermal vacuum deposition of a metal film (masking), photolithography (application and etching of photoresist and film), creation of waveguide layers on the crystal surface (proton-ion exchange), sinking of waveguides into the crystal (post-exchange annealing) [5].

At the first stage of creating waveguides in lithium niobate a thin metal film was applied to the polished crystal under study. The application of a thin metal film took place in a vacuum installation VUP-5 by thermal evaporation. Metal aluminum was used for spraying, which was placed in the evaporator. During spraying the substrate was heated with a heater, which

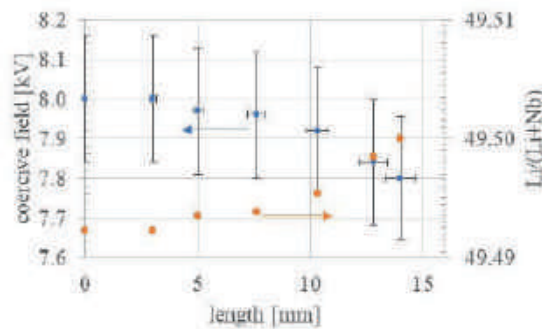


Fig. 1. Radial distribution of the magnitude of the coercive field for a plate cut out in the initial part of the crystal (during the transition from the expansion cone to the cylindrical part)

contributed to the impurities desorption from its surface before spraying, and during deposition created conditions for improving the structure of the growing film. The spraying process took place in three stages: evaporation of the substance, vapor propagation of the evaporated substance, condensation of vapors of the evaporated substance on the substrate and the formation of a film structure.

The next stage of the work was the photolithography process. To estimate optical losses in waveguides in gradient lithium niobate, a photomask was developed in the Autodesk AutoCAD program, shown in Figure 2. The width of the lines is 3–10 microns. The photomask format represented a geometric variety aimed at investigating the possibility of forming waveguide structures of a given geometry in gradient lithium niobate, and included rounding and branching at right angles. The photolithography process used took place in the sequence: the formation of a photoresistive layer, the application of a photoresist and its drying, the formation of a protective relief in the photoresist layer, exposure and manifestation, the creation of a relief image on the substrate, etching of the technological layer of metal and the removal of the photoresist layer.

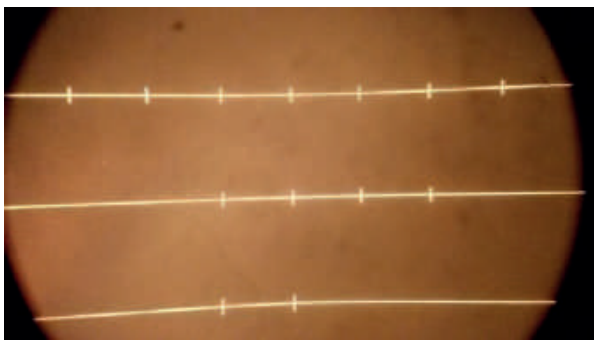


Fig. 2. View of the photomask

One of the ways to estimate losses in the waveguides formed was to provide an additional controllable loss value. Such a controlled quantity was the crosshairs (intersections) in the waveguide channel, and in neighboring waveguide channels, the number of intersections monotonically increases (Fig. 2). When passing a waveguide, the signal must experience attenuation due to scattering in the waveguide channel and due to scattering at intersections. With continuous scanning from a waveguide with fewer intersections to a waveguide with more intersections, a monotonous decrease in

signal power at the waveguide output was expected. When estimating the scattering caused by signal attenuation in the waveguide, a large-scale loss estimation coefficient appears associated with losses at the intersection points. With such an estimation of losses in the waveguide channel, there is no need to trim the waveguide channel to estimate attenuation per unit length.

Then, using the [6] proton exchange method, waveguides were formed in a benzoic acid melt in an alundum ceramic crucible in a crystal plate made of gradient lithium niobate. The substrate made of gradient lithium niobate was exposed to temperature in three stages: heating from 24 to 225 °C for 30 minutes, exposure at a temperature of 225 °C for 6 hours, cooling of the crystalline substrate to room temperature. Temperature control was carried out using a K type thermocouple, the signal from which served as a feedback signal for a control system based on a programmable thermostat and a heating element [7]. During the proton-ion exchange the temperature inside the crucible with the melt was in the corridor 2–3 K from the pre-set temperature.

As a result of the application of the described techniques, waveguide layers were obtained on the surface of a lithium niobate crystal with a gradient of composition. After the polishing stage of the ends, the resulting sample was checked with an optical microscope for the presence of optical waveguides.



Fig. 3. Surface optical waveguide

The type of waveguides obtained is shown in Figure 3.

After obtaining the surface waveguide shown in Figure 2, it was sunk into a lithium niobate crystal [8].

For this purpose, post-exchange annealing was used under the following conditions: heating from 25 to 300 °C in 45 minutes, exposure at 300 °C for 3 hours, cooling of the crystal to room temperature. During post-exchange annealing, the surface layer changed the refractive index due to diffusion of lithium ions, which corresponded to the movement of the waveguide deep into the crystalline substrate of lithium niobate. Also during the formation of the buried waveguides, the waveguide took a rounded shape.

Results and Discussion

To measure the optical losses in the resulting submerged waveguides in a substrate of gradient lithium niobate, an optical circuit was created, shown in Figure 4.

In this scheme, a semiconductor laser with a fiber output operating at 1550 and 630 nm wavelengths was used as a source of coherent optical radiation, a red laser was used to adjust the optical circuit, and lasers with a wavelength of 1550 nm radiation were used directly for measurements. Holders for the fiber laser output patch cord and a collecting lens with a focal length of 30 mm were also used in a pair to focus the input radiation on the end of the plate under study, where the received waveguides are located [9].

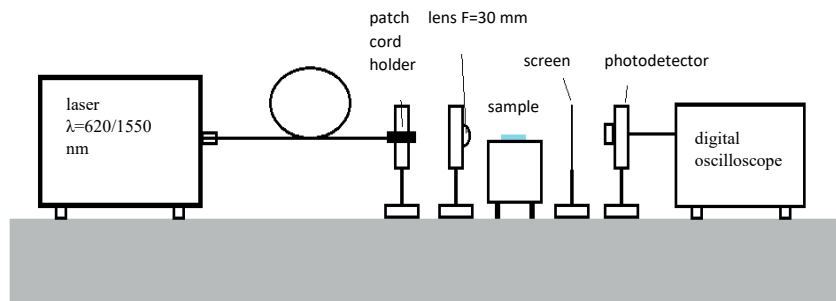


Fig. 4. Optical loss measurement scheme in waveguides

To position the manufactured waveguides relative to the axis of the input radiation a three axis microposition platform was used, the adjustments of which were used to achieve the input of focused optical radiation into the end of the waveguide. A collecting lens with such a focal length was selected so that the focused beam corresponded to the intended aperture of the resulting waveguide.

After the optical radiation passed through the waveguides in the substrate, an opaque screen with a horizontal slot of about 2 mm was installed on the path of the optical axis. This was done to cut off reflections and reflexes from the surface of the plate, which is located on the microposition table. Thus, the photodetector located last in this optical measuring circuit receives only radiation that has passed only through the end of the plate and the main part of this radiation passes through waveguides running along the propagation path of the reference radiation.

After setting up the optical circuit, the plate was moved only in the horizontal plane of the table, thereby the radiation fell into the end of the waveguide or simply into the end of the plate without a waveguide structure.

To measure losses in waveguides, the classical breakage method was chosen as a reference, when losses in a full-length waveguide are measured, then the waveguide is shortened by 2 times and the measurements are repeated. This technique makes it possible to eliminate losses and scattering at the input and output from the waveguide and to obtain relative values of losses in the resulting waveguides. This technique was applied to waveguides without formed intersections (Fig. 3).

By feeding optical radiation through the fiber output to the end of the crystal and adjusting the position of the positional table in 3 directions, we ensure that the optical radiation is introduced into the waveguide. The optical fiber from the output of the laser emitter is fed through a patch cord to the sample under study. Immediately before insertion into the end of the crystal, the fiber is cleaved on a fiber cleaver so that the edge of the fiber is flat and even. This makes it possible to concentrate optical radiation in a beam with a diameter of about 10–15 mm, which is comparable to the size of the waveguide on the crystal surface. The optical fiber is brought as close as possible to the end (Fig. 6), but not in contact with it, being a continuation of the waveguide, which is located in the figure in the horizontal plane.

To measure the relative optical losses, a 25 mm long waveguide and its half (after the segment), 12.5 mm, were used. Based on the measurements, the optical losses in the waveguide at a wavelength of 1.55 microns amounted to 0.9 dB/cm.

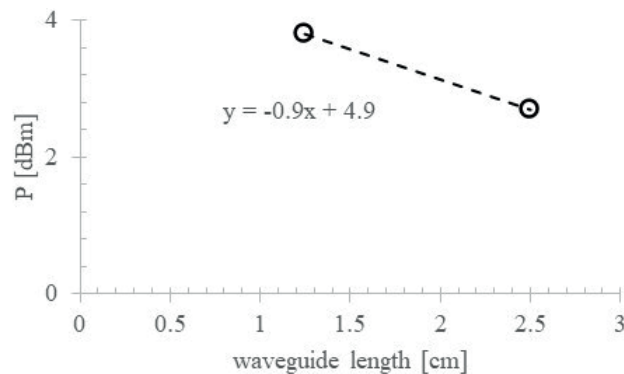


Fig. 5. Dependence of the output signal at a wavelength of 1.55 microns on the length of the waveguide

The scheme of another technique (similar to the insertion loss technique) used to estimate optical losses in a waveguide in gradient lithium niobate is shown in Figure 6. The technique includes measurement of losses in full-length waveguides. The waveguide loss component will remain constant, and the component from the intersections will be added depending on their number. With the same total length of the waveguide L , the same length of the waveguide between the intersections x_0 and a different number of intersections n in the waveguides (Fig. 2), the recorded signal will decrease with increasing losses at each intersection. Taking into account some constant component of losses at each intersection of the waveguide, the total number of losses due to intersections is $n \cdot \alpha_1$, where α_1 is the loss in Db at one intersection. Then, the signal recorded by the photodetector when scanning along waveguides with different numbers of intersections will have a constant component associated with attenuation in the waveguide and a component of attenuation at intersections:

$$\lg(P) = \lg(P_0) + 0.1 \cdot \alpha \cdot L + 0.1 \cdot n \cdot \alpha_1, \quad (1)$$

where α is the loss in the waveguide.

Putting $\lg(P)$ values on the chart (Fig. 7) on the ordinate axis, and n values on the abscissa axis, we obtain a series of points by approximating them with a straight line of the form

$$\lg(P) = A - n \cdot \alpha_1, \quad (2)$$

so, we determine the attenuation value at one intersection. Then, knowing the fixed distance between the intersections x_0 , we represent the recorded power by the photodetector as:

$$\lg(P) = \lg(P_0) + 0.1 \cdot \alpha \cdot (x_1 + x_2) + 0.1 \cdot (n - 1) \cdot \alpha \cdot x_0 + 0.1 \cdot n \cdot \alpha_1, \quad (3)$$

where x_1, x_2 are the edge sections of the waveguide from the ends of the plate to the first and last intersection.



Approximating the $\lg(P)$ values by the expression:

$$\lg(P) = B + 0.1 \cdot (n-1) \cdot \alpha \cdot x_0 + 0.1 \cdot n \cdot \alpha_1, \quad (4)$$

we find the parameters B and α .



Fig. 6. General view of the measurement scheme

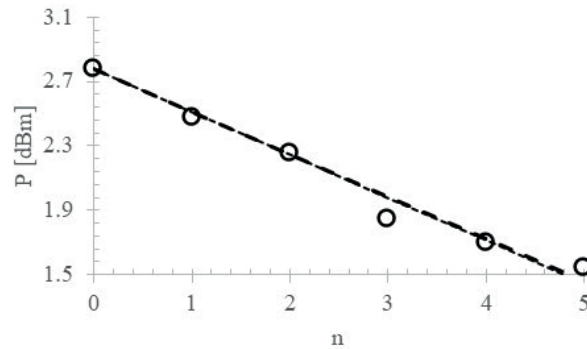


Fig. 7. Dependence of the output radiation power on the number of intersections and its approximation

Based on the data obtained, the losses at intersections amounted to 2.6 dB, the losses in the waveguide determined by this method amounted to 0.9 dB/cm, which correlates with the measurement data given in [6], where losses in non-annealed lithium niobate waveguides from 0.5 to 1 dB/cm are estimated.

Conclusion

Thus, the formation of waveguides in gradient lithium niobate with a composition $\text{Li}_{0.94...0.98}\text{Nb}_{1.06...1.02}\text{O}_{3.12...3.04}$ was carried out when heated to a temperature of 300 °C for 45 minutes and held at a temperature of 300 °C for 3 hours. To measure attenuation in the formed gradient waveguides, the breakage methods and the insertion method were used, by forming regular additional losses at the intersections of waveguides. The results of the attenuation measurement in the formed gradient waveguides obtained by both methods were 0.9 dB/cm.

REFERENCES

1. Sidorkin A.S., Nesterenko L.P., Gagou Y., Saint-Gregoire P., Pakhomov A.Y., Popravko N.G., Switching properties of ferroelectric perovskite superlattices, *Ferroelectrics*. 544 (1) (2019) 43–48.
2. Galutskiy V.V., Stroganova E.V., Shmargilov S.A., Yakovenko N.A., Frequency conversion in compositionally graded PPLN crystals, *Quantum Electronics*. 44 (1) (2014) 30–33.
3. Sidorov N.V., Volk T.R., Mavrin B.N., Kalinnikov V.T., Lithium niobate: defects, photorefraction, the vibrational Spectrum, the polaritons, Nauka, Moscow. 2003.
4. Galutskiy V.V., Vatlina M.I., Stroganova E.V., Growth of single crystal with a gradient of concentration of impurities by the Czochralski method using additional liquid charging, *Journal of Crystal Growth*. 311 (4) (2009) 1190–1194.
5. Bezpaly A.D., Verhoturov A.O., Shandarov V.M., Optical formation of channel waveguides and planar diffraction gratings in a photorefractive near-surface layer of lithium niobate, *Scientific Notes of the Faculty of Physics of Moscow University*. 5 (2016) 165308.
6. Kostritskiy S.M., Korkishko Y.N., Fedorov V.A., Frolova M.V., Korepanov N.S., Moretti P., Structure and properties of optical waveguides in stoichiometric LiNbO₃ crystals, *Izvestia of Higher Educational Institutions. Electronics*. 2 (22) (2009) 22–30.
7. Borodin Y.V., Low-temperature nanodoping of protonated LiNbO₃ crystals by univalent ions, *Technical Physics*. 60 (1) (2015) 107–111.
8. Muller H.G., Stapleton A.D., Foran B.J., Radhakrishnan G., Kim H.I., Adams P.M., Lipeles R.A., Herman P., Reduction of lattice defects in proton-exchanged lithium niobate waveguides, *Journal of Applied Physics*. 110 (2011) 033539.

9. **Bessonova S.V., Buritskiy K.S., Chernih V.A., Sherbakov E.A.**, Measurement of losses in optical waveguides made of lithium niobate using a single-frequency semiconductor laser, *Quantum Electron.* 19 (4) (1989), 559–560.

THE AUTHORS

SHMARGILOV Sergey A.
ftf122@mail.ru

PUZANOVSKIY Kirill V.
puzanovsky.kv@yandex.ru
ORCID: 0000-0003-0840-8089

GALUTSKIY Valeriy V.
galutskiy17v@mail.ru
ORCID: 0000-0002-8837-1011

STROGANOVA Elena V.
stroganova@kubsu.ru
ORCID: 0000-0002-3625-3515

Received 26.10.2022. Approved after reviewing 09.11.2022. Accepted 09.11.2022.

Conference materials
UDC 534.13; 539.3; 538.9
DOI: <https://doi.org/10.18721/JPM.161.118>

Study of mechanical resonance frequencies in tapered nanowires

M.S. Dunaevskiy¹✉

¹Ioffe Institute, St. Petersburg, Russia

✉ Mike.Dunaeffsky@mail.ioffe.ru

Abstract. In this paper, the transcendental equation was obtained in the framework of the Euler–Bernoulli beam theory, which allows obtaining the values of resonant frequencies for any tapered nanowire. Calculations of the frequencies of the first few resonances of mechanical oscillations for nanowires with various conicity (the average radius and length of the nanowire remained constant) were performed. It was established that the frequencies of the first three modes increase with an increase in the conicity angle, while the frequency of the fourth mode ($n = 4$) is nearly constant and independent of the conicity angle. It was also established that the frequencies of the higher order ($n > 4$) modes decrease with an increase in the conicity angle. The ratios of the resonance values of the first few modes can be used to clarify the conicity value, which is necessary when determining the Young's modulus of tapered nanowires.

Keywords: nanowires, tapered nanowires, mechanical resonances frequencies, Young's modulus

Citation: Dunaevskiy M.S., Study of mechanical resonance frequencies in tapered nanowires, St. Petersburg State Polytechnical University Journal. St. Petersburg State Polytechnical University Journal. Physics and Mathematics. 16 (1.1) (2023) 109–112. DOI: <https://doi.org/10.18721/JPM.161.118>

This is an open access article under the CC BY-NC 4.0 license (<https://creativecommons.org/licenses/by-nc/4.0/>)

Материалы конференции
УДК 534.13; 539.3; 538.9
DOI: <https://doi.org/10.18721/JPM.161.118>

Механические резонансы в конических нитевидных нанокристаллах

М.С. Дунаевский¹✉

¹Физико-технический институт им. А.Ф. Иоффе РАН, Санкт-Петербург, Россия

✉ Mike.Dunaeffsky@mail.ioffe.ru

Аннотация. В данной работе в рамках теории Эйлера–Бернулли получено трансцендентное уравнение, позволяющее получить значения резонансных частот для любых конических нитевидных нанокристаллов. Проведены расчеты частот первых нескольких резонансов механических колебаний для нитевидных нанокристаллов различной конусности (средний радиус и длина нитевидных нанокристаллов при этом оставались постоянными). Установлено, что частоты первых трех мод увеличиваются с увеличением угла конусности, а частота четвертой моды ($n = 4$) практически постоянна и не зависит от угла конусности. Установлено также, что частоты мод высших порядков ($n > 4$) уменьшаются с увеличением угла конусности. Соотношения резонансных значений первых нескольких мод могут быть использованы для уточнения значения конусности, которое необходимо при определении модуля Юнга конических нитевидных нанокристаллов.

Ключевые слова: нитевидные нанокристаллы, конические нитевидные нанокристаллы, частоты механических резонансов, модуль Юнга

Ссылка при цитировании: Дунаевский М.С. Механические резонансы в конических нитевидных нанокристаллах // Научно-технические ведомости СПбГПУ.

Физико-математические науки. 2023. Т. 16. № 1.1. С. 109–112. DOI: <https://doi.org/10.18721/JPM.161.118>

Статья открытого доступа, распространяемая по лицензии CC BY-NC 4.0 (<https://creativecommons.org/licenses/by-nc/4.0/>)

Introduction

Studies of transport, optical and mechanical properties of semiconductor nanowires (NW) have been of interest recently. A feature of thin nanowires is their ability to withstand without breaking quite large mechanical stresses and deformations (up to 10%) [1]. Semiconductor nanowires can be used in sensor devices [2], triboelectric nanogenerators [3] and flexible microelectronics devices. Thus, the study of the mechanical properties of nanowires, the measurement of their elastic modules [4], as well as their resonant frequencies of mechanical oscillations, is an actual task today.

In this work, the calculation (based on the Euler–Bernoulli beam theory) of resonant frequencies values for tapered nanowires will be performed. The dependence of the resonant frequencies values on the conicity parameter of the nanowire will be investigated, while the average radius and the length of the nanowire will be fixed. Calculations of resonant frequencies for some typical tapered shaped III-V nanowires will be performed. Based on the measurement of several resonant frequencies, the approach will be proposed to clarify the value of the conicity parameter, which is necessary for measuring the Young’s modulus of tapered nanowires.

Results and Discussion

Figure 1, a shows a scheme of tapered nanowire oscillation. The figure shows the main geometric parameters describing the conical nanowire (R_b is radius at the base of NW, R_t is radius at the top of NW, R is average radius of NW, L is length of the nanowire, α is angle of conicity). Figure 1, b shows a schematic image of the oscillating nanowire (mode $n = 2$). It should be noted here, that the tapered nanowire, as well as a cylindrical one, has an endless set of oscillation modes and resonant frequencies. In this work, we will consider the case of the oscillations of nanowire, when the base of the nanowire is fixed, and the top end of NW is free. This corresponds to common situation when the nanowire was grown epitaxially on the substrate.

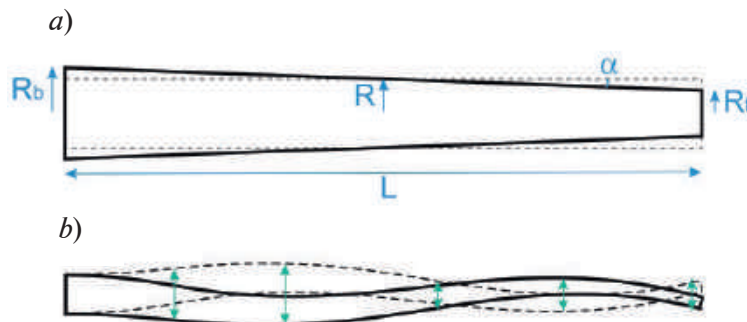


Fig. 1. Scheme of tapered nanowire (R_b is radius at the base of NW, R_t is radius at the top of NW, R is average radius of NW, L is length of the nanowire, α is angle of conicity) (a); schematic image of the oscillating nanowire (mode $n = 2$) (b)

Below is the time-dependent Euler- Bernoulli equation of the oscillating nanowire together with the boundary conditions for nanowire with the fixed base and the free upper end.

$$\frac{\partial^2}{\partial x^2} (EI(x) \frac{\partial^2 u(x,t)}{\partial x^2}) = -\mu(x) \frac{\partial^2 u(x,t)}{\partial t^2}, \quad (1)$$

$$u(x = 0, t) = 0, \quad (1.a)$$

$$\frac{\partial u}{\partial x} (x = 0, t) = 0, \quad (1.b)$$



$$\frac{\partial^2 u}{\partial x^2}(x=L, t) = 0, \quad (1.c)$$

$$\frac{\partial}{\partial x} \left(x^4 \frac{\partial^2 u}{\partial x^2} \right) (x=L, t) = 0, \quad (1.d)$$

where E is the nanowire Young's modulus, $I(x) = \pi R^4(x)/4$ is the second area moment of inertia of the tapered nanowire, L is the length of NW, $\mu(x)$ is the mass per unit length $\mu(x) = \rho \pi R^2(x)$, $R(x)$ is the local radius of the nanowire $R(x) = \alpha x$, α is the conicity angle of NW. Dependence on time is taken into account as follows: $u \sim \exp[i\omega t]$, which allows one to obtain the next equation

$$\frac{\partial^2}{\partial x^2} \left(x^4 \frac{\partial^2 u(x)}{\partial x^2} \right) = \frac{4\rho}{E\alpha^2} x^2 \omega^2 u(x). \quad (2)$$

The general solution of this equation can be expressed through the Bessel functions (J_2 , Y_2 , I_2 , K_2) in the following form.

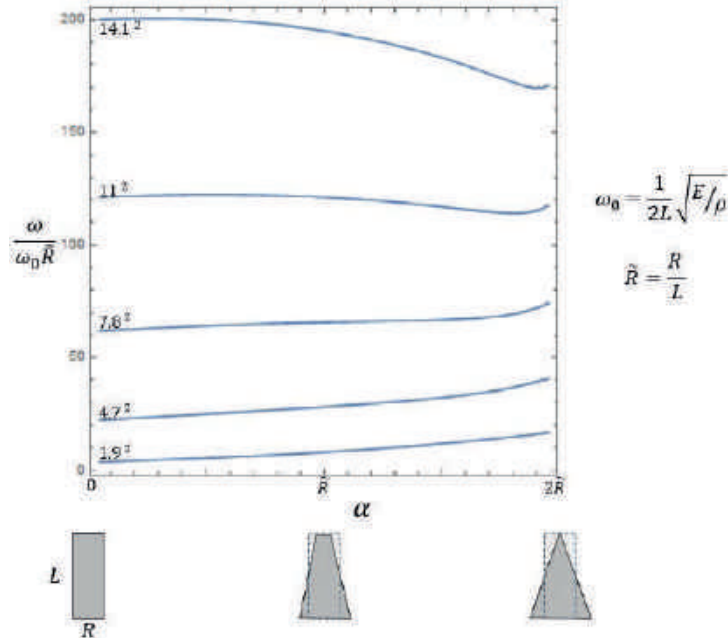


Fig.2 Calculated values of resonant frequencies for the first five oscillation modes depending on the conicity coefficient α for nanowire with $R/L=0.1$

$$u(\xi) = A\xi^{-1}J_2(2\sqrt{\xi}) + B\xi^{-1}Y_2(2\sqrt{\xi}) + C\xi^{-1}I_2(2\sqrt{\xi}) + D\xi^{-1}K_2(2\sqrt{\xi}). \quad (3)$$

Here ξ is the dimensionless position at the nanowire $\xi = 2x\omega(\rho/E)^{1/2}/\alpha$.

By using the expression (3) in the boundary conditions, one gets a system of the following four linear equations:

$$AJ_2(2\sqrt{b}) + BY_2(2\sqrt{b}) + CI_2(2\sqrt{b}) + DK_2(2\sqrt{b}) = 0, \quad (4.1)$$

$$AJ_3(2\sqrt{b}) + BY_3(2\sqrt{b}) - CI_3(2\sqrt{b}) + DK_3(2\sqrt{b}) = 0, \quad (4.2)$$

$$AJ_3(2\sqrt{t}) + BY_3(2\sqrt{t}) + CI_3(2\sqrt{t}) - DK_3(2\sqrt{t}) = 0, \quad (4.3)$$

$$AJ_4(2\sqrt{t}) + BY_4(2\sqrt{t}) + CI_4(2\sqrt{t}) + DK_4(2\sqrt{t}) = 0. \quad (4.4)$$

Here $b = (\omega/\omega_0)(R/L - \alpha/2)/\alpha^2$ is the dimensionless position of bottom (fixed) end of the nanowire and $t = (\omega/\omega_0)(R/L + \alpha/2)/\alpha^2$ is the position of top (free) end of the NW. This system of equations (4.1-4.4) has non-trivial solutions when the determinant of the corresponding matrix

is equal to zero. Thus, by setting the determinant of the matrix to zero, one can get an equation whose most compact form is given below:

$$\{J_2 I_3\}(t)\{Y_3 K_4\}(b) + [J_2 K_3](t)[Y_3 I_4](b) - \{Y_2 I_3\}(t)\{J_3 K_4\}(b) - [Y_2 K_3](t)[J_3 I_4](b) = 1 / \pi \sqrt{bt}. \quad (5)$$

“Commutator-like” and “anticommutator-like” brackets are introduced here:

$$\begin{aligned} \{F_n G_m\}(x) &= F_n(x)G_m(x) + F_m(x)G_n(x), \\ [F_n G_m](x) &= F_n(x)G_m(x) - F_m(x)G_n(x). \end{aligned} \quad (6)$$

Using equation (5), one can numerically obtain the resonant frequencies for various conicity angles of NW. Figure 2 shows the results of the calculation of resonant frequencies for the first five oscillation modes depending on the conicity coefficient. It should be noted that the calculated values of the resonant frequencies on the left side of the graph ($\alpha = 0$) exactly correspond to the resonant frequencies for a non-tapered cylindrical nanowire. It can be seen that the frequencies of the first three modes increase with an increase in the conicity angle, while the frequency of the fourth mode ($n = 4$) is nearly constant and non-depended on the conicity angle. The frequencies of the higher order ($n > 4$) modes also decrease with an increase in the conicity angle.

Conclusion

Since the values of resonant frequencies can be experimentally determined with a high degree of accuracy, it becomes possible to refine the value of the conicity angle α from the ratios of the frequencies of the first several resonances (ω_2/ω_1 and ω_3/ω_1). This is actual for the accurate determination of the Young's modulus in sufficiently thin conical NWs.

REFERENCES

1. Wang Y., Wang L., Joyce H., Gao Q., Liao X., Mai Y., Tan H., Zou J., Ringer S., Gao H., Jagadish C., Super deformability and Young's modulus of GaAs nanowires, *Adv. Mater.* 23 (2011) 1356–1360.
2. Alekseev P., Sharov V., Dunaevskiy M., Kirilenko D., Ilkiv I., Reznik R., Cirlin G., Berkovits V., Control of conductivity of $\text{In}_x\text{Ga}_{1-x}\text{As}$ nanowires by applied tension and surface states, *Nano Letters.* 19 (2019) 4463–4469.
3. Alekseev P., Sharov V., Geydt P., Dunaevskiy M., Lysak V., Cirlin G., Reznik R., Khrebtov A., Soshnikov I., Lähderanta E., Piezoelectric current generation in wurtzite GaAs nanowires, *Phys. Stat. Sol. RRL.* 12 (2018) 1700358.
4. Dunaevskiy M., Geydt P., Lähderanta E., Alekseev P., Haggrén T., Kakko J., Jiang H., Lipsanen H., Young's modulus of wurtzite and zinc blende InP nanowires, *Nano Letters.* 17 (2017) 3441–3446.

THE AUTHORS

DUNAEVSKIY Mikhail S.
Mike.Dunaeffsky@mail.ioffe.ru
ORCID: 0000-0001-6038-223X

Received 28.10.2022. Approved after reviewing 08.11.2022. Accepted 21.11.2022.

Conference materials

UDC 546.281

DOI: <https://doi.org/10.18721/JPM.161.119>

Evolution of the crystal microstructure of hybrid SiC/Si substrates grown by the method of atomic substitution

I.A. Ereemeev¹✉, M.G. Vorobev¹, A.S. Grashchenko¹, E.V. Pirogov²,
V.D. Andreeva³, A.V. Osipov¹, S.A. Kukushkin¹

¹Institute for Problems of Mechanical Engineering RAS, St. Petersburg, Russia;

²Alferov University, St. Petersburg, Russia;

³Peter the Great St. Petersburg Polytechnic University, St. Petersburg, Russia

✉ iuriyereemeev528@gmail.com

Abstract. 3C-SiC/Si (111) hybrid structures are grown by the method of coordinated atomic substitution on the boron- and phosphorus-doped Si(111) substrates. The evolution of the microstructure is analyzed in the time range of 1–40 minutes. The results show the reconstruction of the 3C-SiC (111) film at 3–5 minutes of the growth. The difference between strain in the SiC film obtained on *p*-Si and *n*-Si is shown using XRD and Raman techniques.

Keywords: silicon carbide, elastic strain, coordinated atomic substitution, microstructure

Funding: This study was carried out within the framework of the Russian Science Foundation, project no. 20-12-00193.

Citation: Ereemeev I.A., Vorobev M.G., Grashchenko A.S., Pirogov E.V., Andreeva V.D., Osipov A.V., Kukushkin S.A., Evolution of the crystal microstructure of hybrid SiC/Si substrates grown by the method of atomic substitution. St. Petersburg State Polytechnical University Journal. Physics and Mathematics. 16 (1.1) (2023) 113–118. DOI: <https://doi.org/10.18721/JPM.161.119>

This is an open access article under the CC BY-NC 4.0 license (<https://creativecommons.org/licenses/by-nc/4.0/>)

Материалы конференции

УДК 546.281

DOI: <https://doi.org/10.18721/JPM.161.119>

Эволюция кристаллической микроструктуры гибридных подложек SiC/Si во время роста методом замещения атомов

Ю.А. Еремеев¹✉, М.Г. Воробьев¹, А.С. Гращенко¹, Е.В. Пирогов²,
В.Д. Андреева³, А.В. Осипов¹, С.А. Кукушкин¹

¹Институт проблем машиноведения РАН, Санкт-Петербург, Россия;

²Академический университет имени Ж.И. Алфёрова, Санкт-Петербург, Россия;

³Санкт-Петербургский политехнический университет Петра Великого, Санкт-Петербург, Россия

✉ iuriyereemeev528@gmail.com

Аннотация. Гибридные структуры 3C-SiC/Si выращены методом согласованного замещения атомов на подложках Si(111), легированных фосфором или бором. Эволюция микроструктуры в процессе роста анализировалась для интервала времени 1–40 минут. Результаты показывают реконструкцию пленок 3C-SiC(111) на 3–5 минуте роста. Обнаружено отличие в деформации пленки SiC на подложках Si *p*- и *n*-типов проводимости.

Ключевые слова: карбид кремния, упругие деформации, согласованное замещение атомов, микроструктура

Финансирование: Исследование выполнено в рамках проекта Российского научного фонда № 20-12-00193.

Ссылка при цитировании: Еремеев Ю.А., Воробьев М.Г., Гращенко А.С., Пирогов Е.В., Андреева В.Д., Осипов А.В., Кукушкин С.А. Эволюция кристаллической микроструктуры гибридных подложек SiC/Si во время роста методом замещения атомов // Научно-технические ведомости СПбГПУ. Физико-математические науки. 2023. Т. 16. № 1.1. С. 113–118. DOI: <https://doi.org/10.18721/JPM.161.119>

Статья открытого доступа, распространяемая по лицензии CC BY-NC 4.0 (<https://creativecommons.org/licenses/by-nc/4.0/>)

Introduction

A series of reviews have been published describing the method of atomic substitution [1, 2]. The method enables the growth of the epitaxial SiC films on Si interface notwithstanding the high lattice mismatch (19%). The classic methods of chemical vapour deposition (CVD) do not allow for the growth of the SiC layers with the analogous crystalline quality [3]. In accord with [1, 2], the typical hybrid SiC/Si structure grown by the method of atomic substitution consists of 100 nm of the SiC film, 1–5 μm of the macroporous silicon and the Si substrate.

The evolution of the Si microstructure during the substitution of the Si atoms has been studied by different methods [1–3]. In situ measurements of the reflection of 650nm laser beam show the rapid formation of the rough interface layer at the beginning of the process. This happens due to the simultaneous formation of the SiC film with the contraction pore after 14–320 seconds of the growth [1]. Then the reflectivity gradually increases with time and the SiC film becomes smoother. The interim stages of the synthesis of the hybrid SiC/Si structures are analysed by the x-ray diffraction (XRD) and total reflection methods [3]. It is shown that the evolution of the structure is influenced by the temperature, pressure in the reactor and a substrate orientation. The great change of the strain occurs in the SiC film during growth. Namely, the tensile to compressive strain replacement happens at 10–12 minutes of the process. However, the hybrid SiC/Si structures in [3] are obtained without SiH_4 in the reaction zone. It is shown in [1] that SiH_4 'heals' the contraction pores, which modify the evolution of the microstructure in the growth process. Despite that, the SiC film morphology and elastic stresses are influenced by the conductivity of the Si substrate [4].

The aim of this work is to trace the evolution of the elastic strain occurring in 3C-SiC(111) film during growth by the method of atomic substitution. The hybrid 3C-SiC(111)/Si(111) structures are grown in the mixture of CO and SiH_4 gases. The Si(111) substrates with different types of conductivity are used. The structures are analyzed by XRD and Raman techniques. The optimum growth time for the formation of the 3C-SiC films on Si(111) substrate is suggested.

Materials and Methods

The growth of the SiC layer is carried out on the *p*- and *n*-type 1.5" Si(111) substrates with the resistance 50 $\Omega\cdot\text{cm}$ and $>10 \Omega\cdot\text{cm}$ respectively. The wafers are terminated by hydrogen in alkaline solutions with the purpose of the pre-growth passivation of the surface [5]. The synthesis of SiC is provided at a temperature of 1270 $^\circ\text{C}$ and a pressure of 360 Pa. The gas mixture CO/ SiH_4 is used with a flow ratio of 20/1. The growth is carried out during 1, 3, 5 and 40 minutes. The samples are studied by XRD and Raman techniques. The XRD results show the presence of compressive deformations in the SiC film, which depends on the growth time.

XRD analysis

XRD spectra of the hybrid SiC/Si structures are measured using Bruker advance d8 (Fig. 1, a). The spectra show the following peaks Si(111) at $2\theta = 28.5^\circ$, SiC(111) at $2\theta = 35.6^\circ$, Si(222) at $2\theta = 59^\circ$. The splitting of the Si(222) peak can be explained by the diffraction of $\text{CuK}\alpha_1$ and $\text{CuK}\alpha_2$ lines.

The SiC(220) peak is clearly seen only for 40 minutes of the growth, which confirms that the SiC film consists only of the SiC(111) layers of perfect crystalline quality (Fig. 1, b).

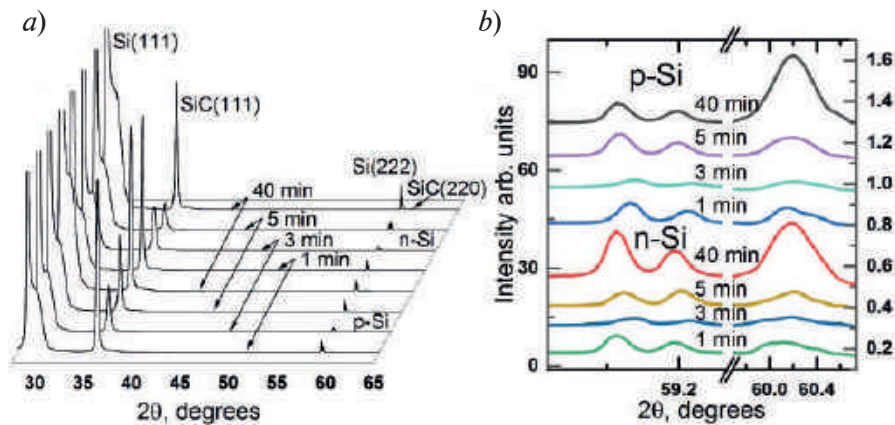


Fig. 1. XRD spectra of the 3C-SiC(111)/Si(111) substrates grown by the method of atomic substitution on *p*- and *n*-Si(111) substrates measured by Bruker advance d8 (a); the Si(222) and SiC(220) peaks from the spectra (b)

The amplitude of the SiC(220) peak is about two hundreds of times smaller than SiC(111). The elastic deformations are calculated from the positions of the 3C-SiC(111) peaks on the rocking curve $\omega - 2\theta$. The spectra are shown in the figure 2. The peaks parameters are written in the table 1. FWHM of the peaks is small for 1 and 40 minutes of the growth, which does not depend on substrate conductivity. The difference between FWHM for the interim growth time is seen, which relates to the quality of the layer. The elastic strain is less compressive for the *n*-Si substrates.

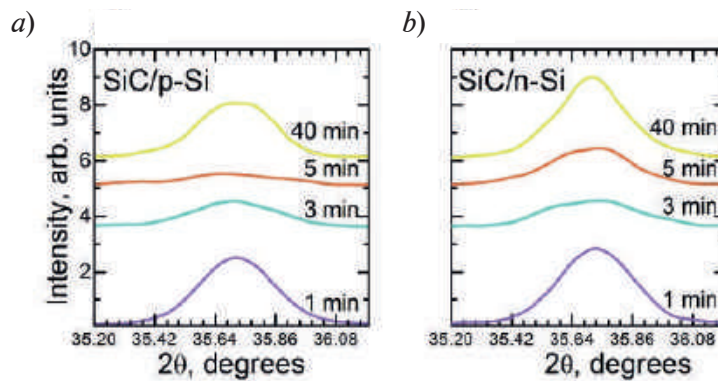


Fig. 2. XRD $\omega - 2\theta$ spectra of the hybrid 3C-SiC(111)/Si(111) substrates at 3C-SiC(111) peak for the different growth times on (a) boron- and (b) phosphorus-doped silicon substrates obtained by DRON-8

Table 1

The parameters of the 3C-SiC (111) XRD peaks and related strain and stress

Time, min	2θ , degrees	FWHM, arcmin	ϵ
<i>p</i> -Si substrate			
1	35.726	16.250	-2.3×10^{-3}
3	35.721	23.491	-2.2×10^{-3}
5	35.707	18.464	-1.8×10^{-3}
40	35.710	15.156	-1.9×10^{-3}
<i>n</i> -Si substrate			
1	35.722	16.252	-2.2×10^{-3}
3	35.701	19.926	-1.6×10^{-3}
5	35.685	38.909	-1.2×10^{-3}
40	35.708	16.971	-1.8×10^{-3}

The theory of the method of atomic substitution declares that the SiC films are compressed at the time, when SiC and the contraction pore nucleate. This happens due to the conjugation of 5 elementary cells of 3C-SiC(111) and 4 cells of Si(111) via the formation of the intermediate structures. It was suggested that the intermediate structures emerging during the growth possess the donor-like properties [4]. Consequently, the emerging becomes harder on the *n*-type Si substrates than on *p*-Si. However, the transformation of the intermediate structures into SiC is faster for *n*-Si and the resulting film becomes less stressed. It should be noted that if SiH₄ is not used in the reaction zone, then the tense SiC film forms in the first 10 minutes of the growth [4].

In the end, the 3C-SiC(111) films obtained after 1 minute of the growth have a big intensity of the SiC(111) peaks and small FWHM for the both substrate types. Stress values in the SiC films obtained after 1 minute of growth correspond to those obtained after 40 minutes.

Raman analysis

The Raman spectra of the hybrid SiC/Si (111) structures grown by the method of atomic substitution on the Si(111) substrates are analysed. The following results are obtained. First, the SiC film consists of only cubic polytype as expected from XRD. Second, the spectra are different for the SiC film “hanging” on the contraction pore and at the SiC/Si contact (figures 3, *a* and *b*). At the pore area, the intensity of Si lines decreases (520cm⁻¹) and the intensity of the SiC line increases (figure 3, *c* and *d*). These results are explained by the multiple internal reflections of the wave inside the pore [6].

The next model is used to calculate effective strain from the positions of the TO peaks [7].

$$\varepsilon_e = \frac{\Delta a}{a} = \frac{(796.5 - E_c)}{3734}, \quad (1)$$

where $\Delta a/a$ is the elastic strain, E_c is the peak position for the SiC film.

The peak positions at the centre and the edge of the pore differ by 1 cm⁻¹. Despite that, the effective strain is smaller for the *n*-Si substrates than for *p*-Si (table 2), which is consistent with the results from the XRD measurements. The results show the change in the strain during SiC formation at the third minute of the growth.

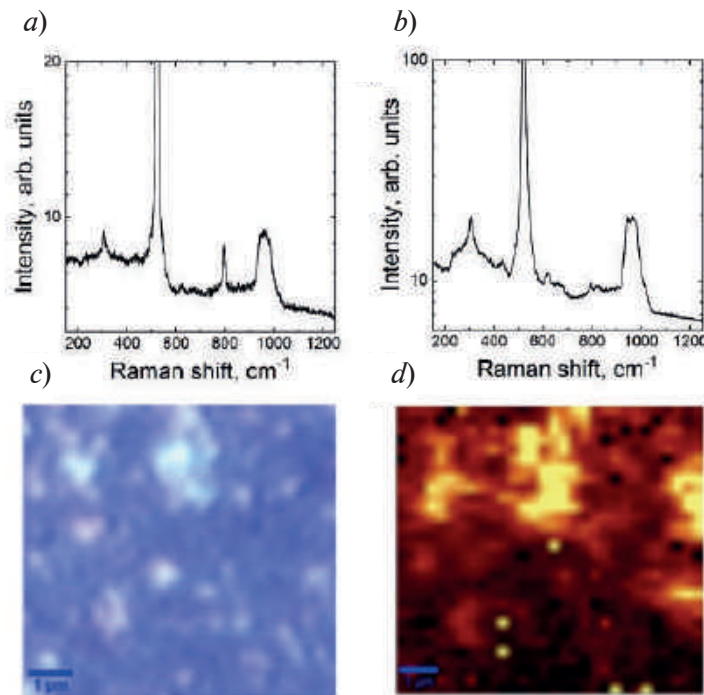


Fig. 3. The Raman spectra measured at the centre of the contraction pore area (*a*) and at the edge of the pore (*b*), micrograph of the hybrid SiC/Si (111) substrate (*c*), map of the intensity of the SiC TO-mode measured at the micrographs area (*d*); light places correspond to the high intensity of the line

Table 2

The positions of the SiC TO Raman peaks and related strain calculated in the frame of the model [7]

Time, min	Peak position, cm ⁻¹	ε_e
	<i>p</i> -Si substrate	
1	793.1	9.2×10^{-4}
3	790.9	1.5×10^{-3}
5	793.2	8.9×10^{-4}
40	793.2	8.9×10^{-4}
	<i>n</i> -Si substrate	
1	794.1	6.3×10^{-4}
3	794.7	4.9×10^{-4}
5	794.2	6.1×10^{-4}
40	793.4	8.2×10^{-4}

Conclusion

The 3C-SiC/Si(111) hybrid substrates are grown by the method of atomic substitution and analysed using XRD and Raman techniques. XRD shows that the strain in the SiC films are different for 1, 3, 5 and 40 minutes of the growth. The strain is compressive, which is the consequence of the presence of SiH₄ in the reaction zone. Raman spectra show that the strain in the SiC film is not uniformly distributed across the pore area. SiC film stretches at the region of the contact with the Si surface. The difference between the effective strain in the SiC film obtained on *n*-Si and *p*-Si substrates is demonstrated.

REFERENCES

1. Kukushkin S.A., Osipov A.V., Theory and practice of SiC growth on Si and its applications to wide-gap semiconductor films, *Journal of Physics D: Applied Physics*, (47) (2014) 313001.
2. Kukushkin S.A., Osipov A.V., Nanoscale Single-Crystal Silicon Carbide on Silicon and Unique Properties of This Material, *Inorganic Materials*, (57) (2021) 1319–1339.
3. Kukushkin S.A., Osipov A.V., Osipova E.V., Stozharov V.M., Study of silicon-to-silicon carbide transformation stages in the process of atomic substitution by the methods of total external X-ray reflection and X-ray diffractometry, *3* (64) (2022), 315–325.
4. Kukushkin S.A., Osipov A.V., Soshnikov I.P., Growth of epitaxial SiC layer on Si(100) surface of *n*- and *p*- type of conductivity by the atoms substitution method, *52* (2017) 29–42.
5. Kalinkin I.P., Kukushkin S.A., Osipov A.V., Effect of Chemical Treatment of a Silicon Surface on the Quality and Structure of Silicon-Carbide Epitaxial Films Synthesized by Atom Substitution, *Semiconductors*, 6 (52) (2018) 802–808.
6. Wasyluk J., Perova T.S., Kukushkin S.A., Osipov A.V., Feoktistov N.A. and Grudinkin S.A., Raman investigation of different polytypes in SiC thin films grown by solid-gas phase epitaxy on Si (111) and 6H-SiC substrates, *Materials Science Forum*, (645-648) (2010) 359–362.
7. Olego D., Cardona M., Vogl P., Pressure dependence of the optical phonons and transverse effective charge in 3C-SiC, *Phys. Rev. B* (25) (1982) 3878.

THE AUTHORS

EREMEEV Iurii A.
iuriyeremeev528@gmail.com
ORCID: 0000-0002-4449-5784

VOROBEEV Maxim G.
vmaximg@bk.ru
ORCID: 0000-0002-9955-4403

GRASHCHENKO Alexander S.
asgrashchenko@bk.ru
ORCID: 0000-0002-4746-4238

OSIPOV Andrey V.
andrey.v.osipov@gmail.com
ORCID: 0000-0002-2911-7806

PIROGOV Evgeny V.
zzzavr@gmail.com
ORCID: 0000-0001-7186-3768

KUKUSHKIN Sergey A.
sergey.a.kukushkin@gmail.com
ORCID: 0000-0002-2973-8645

ANDREEVA Valentina D.
avd2007@bk.ru
ORCID: 0000-0001-6085-4153

Received 24.10.2022. Approved after reviewing 09.11.2022. Accepted 09.11.2022.

Conference materials

UDC 538.9

DOI: <https://doi.org/10.18721/JPM.161.120>

Temperature distribution in InAsSbP/InAsSb/InAs double heterostructure on-chip sensors

T.S. Likhmyrina ¹✉, A.A. Klimov ¹, R.E. Kunkov ¹, N.M. Lebedeva ¹,
B.A. Matveev ¹, A.E. Chernyakov ²

¹ Ioffe Institute, St. Petersburg, Russia;

² Submicron Heterostructures for Microelectronics, Research & Engineering Center, St. Petersburg, Russia
✉ t.likhmyrina@mail.ioffe.ru

Abstract. The paper presents temperature distribution analysis in activated on-chip chemical sensor based on p-InAsSbP/n-InAsSb/n-InAs 1×3 diode array. Temperature distributions were obtained both experimentally with the use of infrared microscopy, by I-V characteristic analysis and by finite element modelling. The simulated temperature values are in reasonable agreement with experimental data, allowing one to establish a relationship between the temperature of active elements of the sensor. The relationship is important for the improvement of chemical analysis accuracy.

Keywords: Temperature distribution, 1×3 diode array, on-chip chemical sensor, mid-IR photodiodes, mid-IR LEDs, modelling, IR microscopy

Funding: Part of the work performed at Ioffe Institute was funded by RF Ministry of Science and High Education grant number 075-15-2021-936 (int. No. 13.2251.21.0001) relating to the project “Embedded electronic solutions for polymer innovative scanning methods using light emitting devices for diagnostic routines”.

Citation: Likhmyrina T.S., Klimov A.A., Kunkov R.E., Lebedeva N.M., Matveev B.A., Chernyakov A.E., Temperature distribution in InAsSbP/InAsSb/InAs double heterostructure on-chip sensors, St. Petersburg State Polytechnical University Journal. Physics and Mathematics. 16 (1.1) (2023) 119–125. DOI: <https://doi.org/10.18721/JPM.161.120>

This is an open access article under the CC BY-NC 4.0 license (<https://creativecommons.org/licenses/by-nc/4.0/>)

Материалы конференции

УДК 538.9

DOI: <https://doi.org/10.18721/JPM.161.120>

Распределение температуры в микрооптопарах на основе двойной гетероструктуры InAsSbP/InAsSb/InAs

Т.С. Лухмырина ¹✉, А.А. Климов ¹, Р.Е. Кунков ¹, Н.М. Лебедева ¹,
Б.А. Матвеев ¹, А.Е. Черняков ²

¹ Физико-технический институт им. А.Ф. Иоффе РАН, Санкт-Петербург, Россия;

² НТЦ микроэлектроники РАН, Санкт-Петербург, Россия

✉ t.likhmyrina@mail.ioffe.ru

Аннотация. В работе проведен анализ распределения температуры в активированной микрооптопаре, представляющей собой чип из монолитной двойной гетероструктуры p-InAsSbP/n-InAsSb/n-InAs 1×3. Распределения были получены как экспериментально с помощью инфракрасной микроскопии и анализа ВАХ, так и с помощью моделирования методом конечных элементов. Смоделированные значения температуры удовлетворительно согласуются с экспериментальными данными, что позволяет установить зависимость между температурой активных элементов датчика и важно для повышения точности химического анализа.

Ключевые слова: распределение температуры, микрооптопара, фотодиоды среднего ИК-диапазона, светодиоды среднего ИК-диапазона, моделирование, ИК-микроскопия

Финансирование: Часть работы, выполненная в ФТИ им. А.Ф. Иоффе, выполнена при поддержке Министерства науки и высшего образования РФ в рамках проекта «Встроенные Электронные Решения для Инновационных Сканирующих Устройств Диагностики Полимеров на Основе Источников Излучения» (№ 13.2251.21.0001, соглашение № 075-15-2021-936).

Ссылка при цитировании: Лухмырина Т.С., Климов А.А., Кунков Р.Э., Лебедева Н.М., Матвеев Б.А., Черняков А.Е. Распределение температуры в микрооптопарах на основе двойной гетероструктуры InAsSbP/InAsSb/InAs // Научно-технические ведомости СПбГПУ. Физико-математические науки. 2023. Т. 16. № 1.1. С. 119–125. DOI: <https://doi.org/10.18721/JPM.161.120>

Статья открытого доступа, распространяемая по лицензии CC BY-NC 4.0 (<https://creativecommons.org/licenses/by-nc/4.0/>)

Introduction

Optical chemical sensors are widely used in medicine and industry due to their high reliability and accuracy [1–3]. The expansion of their application areas is facilitated by the use of semiconductor technology, resulting in miniaturized on-chip sensors consisting of an optically coupled diode source and a radiation receiver integrated on a single semiconductor substrate [4–7]. Their operation principle is based on the phenomenon of attenuated total reflection resulting in evanescent wave formation when reflecting light at the interface between the substrate and the analyte. Reflected light intensity recorded by photodiode (PD) is weakening both by analyte absorption and by the angle of total internal reflection increase.

As active part of the sensor (LED) is not solely a source of electroluminescence (EL), but also a source of heat, LED and PD temperature measurements are required to be made especially in miniature or/and monolithic sensors [4, 5]. To improve measurement accuracy in such sensors, it is necessary to know a relationship between the PD and LED temperature. To address this issue, in this work we propose an approach for the above improvement based on a combination of experimental PD temperature values obtained from the analysis of its current-voltage characteristic (I - V), infrared (IR) microscope data and results of numerical simulation.

Results and Discussion

We used liquid phase epitaxy grown InAsSbP/InAsSb/InAs heterostructure consisting of n-type InAs (100) substrate with $n = 2 \cdot 10^{16} \text{ cm}^{-3}$, $\sim 10 \text{ }\mu\text{m}$ thick undoped n-InAs_{1-x}Sb_x active (absorbing) layer and p-InAs_{1-x-y}Sb_xP_y (Zn) cladding (contact layer) (see Fig. 1, *b*). The band schematic of this heterostructure and the ability to operate both as PD and LED have been previously described in ref. [8]. The use of the term “double heterostructure” (DH) is not quite fair in relation to the above heterostructure, but here we use it like in ref. [8].

Diodes were processed onto a 160 μm thick wafer with 26 μm high circular mesas ($\varnothing_m = 190 \text{ }\mu\text{m}$) by standard photolithography and wet chemical etching. Circular Au-based anode ($\varnothing_a = 170 \text{ }\mu\text{m}$) and cathode contacts were formed on the same chip side by sputtering and thermal evaporation in vacuum followed by thick (3 μm) gold plating deposition as shown in Fig. 1, *a*. Chip contained three diodes (the “1×3 linear array”), each diode lateral size was 580×400 μm (see Fig. 1, *a*). Flip-chip bonding/packaging procedure has been implemented using the 2×2 mm submount made from insulating AlN with Cu-Ni-Au metallization at bonding pads, as shown in Fig. 1, *b*. The diodes were connected via a pair of anode (A) – cathode (C) with a number corresponding to the number of the diode (#D1, #D2 and #D3).

To get the temperature distribution on the chip surface (IR map), the IR thermal radiation was mapped using the UTK1 IR microscope developed at the Institute of Semiconductor Physics, Siberian Branch of Russian Academy of Sciences [10]. Temperature distribution from the IR maps was obtained via preliminary calibration that was made in the range of 290–360 K at zero LED current.

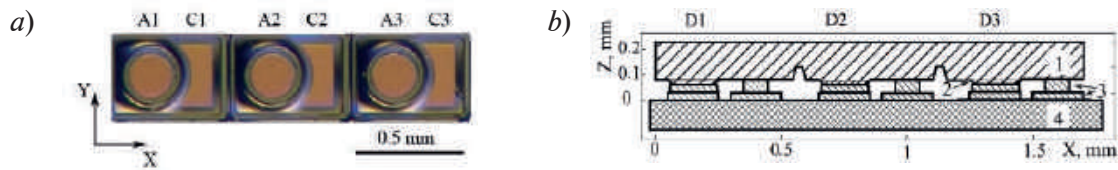


Fig. 1. Top view of the monolithic 1×3 chip (100) surface with three mesas. A1, A2, A3, C1, C2, C3 anodes and cathodes of diodes D1, D2, D3 accordingly (a). Schematic diagram of the cross section of the sensor onto submount: 1) InAs substrate, 2) chip active layer and contact layer, 3) solder and submount metallization, 4) AlN based submount (b)

Fig. 2 shows IR microscope sensitivity spectrum as well as the EL spectrum of the diodes under study. These spectra do not overlap, and one can expect the absence of the luminescence contribution to the IR maps.

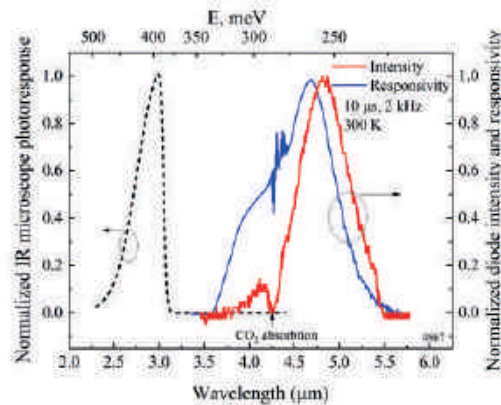


Fig. 2. IR microscope sensor sensitivity (dashed curve) and electroluminescence LED spectrum (solid curve)

The above overlapping absence is confirmed by the measurements of the effective temperature distribution on the chip surface at various ambient temperatures, with forward and reverse D2 bias shown in Fig. 3. The experimental values presented by curves in Fig. 3 are close, which indicates the absence of the EL (at forward bias) and negative luminescence (reverse bias) contribution. The intensity values at 298 K in Fig. 3 are quite “noisy” due to low thermal radiation power; at 323 K this “noise” is not so pronounced because of thermal radiation power enhancement.

The I - V characteristics were measured in continuous wave (CW) mode using a SourceMeter Keithley 6430 simultaneously with intensity distribution measurements (intensity maps). During the first part of an experiment the diode D2 was activated, while the I - V characteristics were

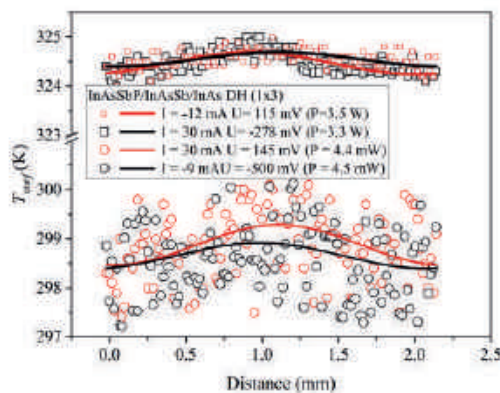


Fig. 3. Temperature distribution along the sensor substrate surface at diode D2 activation (see dots) and curves averaging temperature values obtained from IR maps. The square dot group (\square , \square) was obtained at a temperature of 323 K, and the round one (\circ , \circ) at 298 K. Red dot/curve data were obtained at forward bias, and black dot/curve data at reverse bias, while the electric power for both modes of operation was the same.

measured in both D1 and D3 diodes, in the second part the diode D1 was activated, and the $I-V$ characteristics were measured in the D2 and D3 diodes.

Fig. 4, *a* shows the $I-V$ characteristics of the diode D1 at various AlN submount temperatures, depicting increase of the current with temperature growth. The temperature dependence of the zero bias resistance R_0 shown in Fig. 4, *b* is described by the standard expression for the diffusion-limited current:

$$R_0 \sim \exp(E_a / (\beta k T)), \quad (1)$$

here k is Boltzmann's constant, T is temperature, $\beta \approx 1$, $E_a = 0.26$ eV. The R_0 values obtained from data in Fig. 4, *b* were used to determine the PD temperature.

The thermal conductivities of the sensor layers (Fig. 1, *b*) and their thermal resistances were determined using the “Thermaltester T3Ster” tool (see Fig. 5). Left part of Fig. 5 relates to the diode active and contact layers (item 2 in Fig. 1, *b*), which have a total thermal resistance $R_{th} = 33$ K/W (thermal conductivity $K \approx 24$ W/(K*m)). Middle part corresponds to the composite layer consisting of solder, submount metallization and transition sublayer plating-submount (item 3 in Fig. 1, *b*) with a total $R_{th} = 33$ K/W ($K \approx 31$ W/(K*m)), and right sector is responsible for the thermal resistance of the AlN submount (item 4 in Fig. 1, *b*) with $R_{th} = 18$ K/W ($K \approx 246$ W/(K*m)). The thermal conductivities of the active and contact layers and of the submount are close to the values in [11].

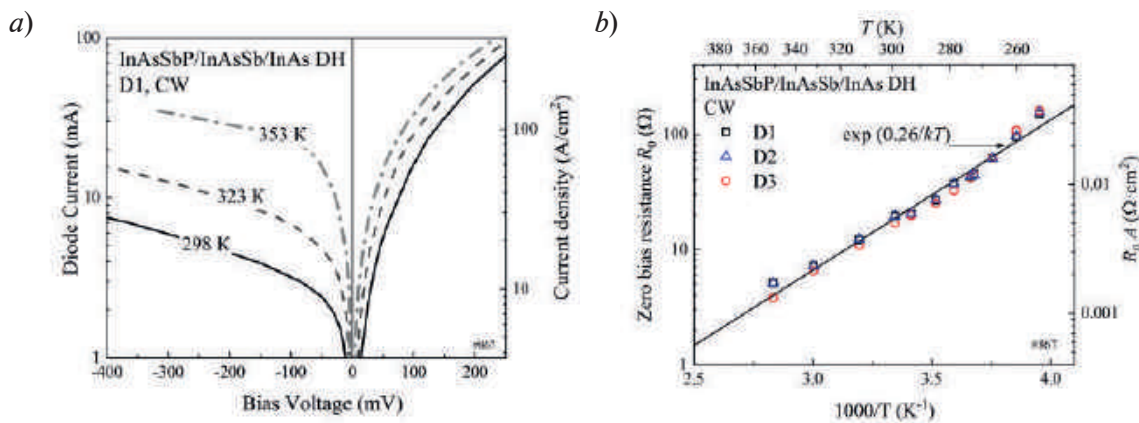


Fig. 4. $I-V$ characteristics of D1 diode at various temperatures (*a*). Temperature dependence of zero-bias resistance of the monolithic sensor diodes in the 260–360 K range (*b*)

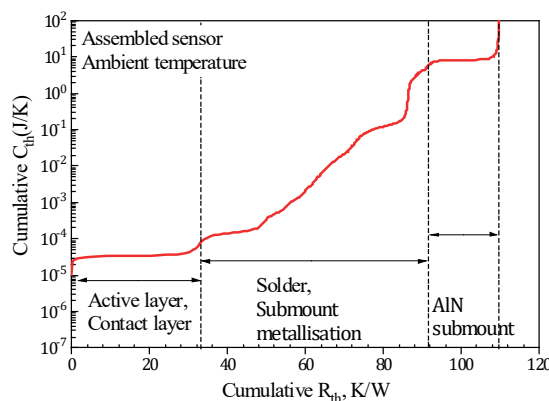


Fig. 5. Cumulative structure functions of assembled sensor including DH layers and submount

In Fig. 6, *a* and Fig. 7, *a* solid lines show the temperature distribution of T_{surf} along the chip surface. The horizontal segments show the average temperature of the active region (item 2 in Fig. 1, *b*) of non-activated diodes (T_{Di}): diode D1 and D3 (Fig. 6, *a*) or diode D2 and D3 (Fig. 7, *a*), obtained from the $R_0(T)$ data. Curves shown in Fig. 6, *a* are asymmetric due to the asymmetry of the on-chip sensor design: the active region of diode D2 is shifted to the right relative to the center of the chip. This “asymmetry” also explains the fact that $T_{D1} > T_{D3}$.

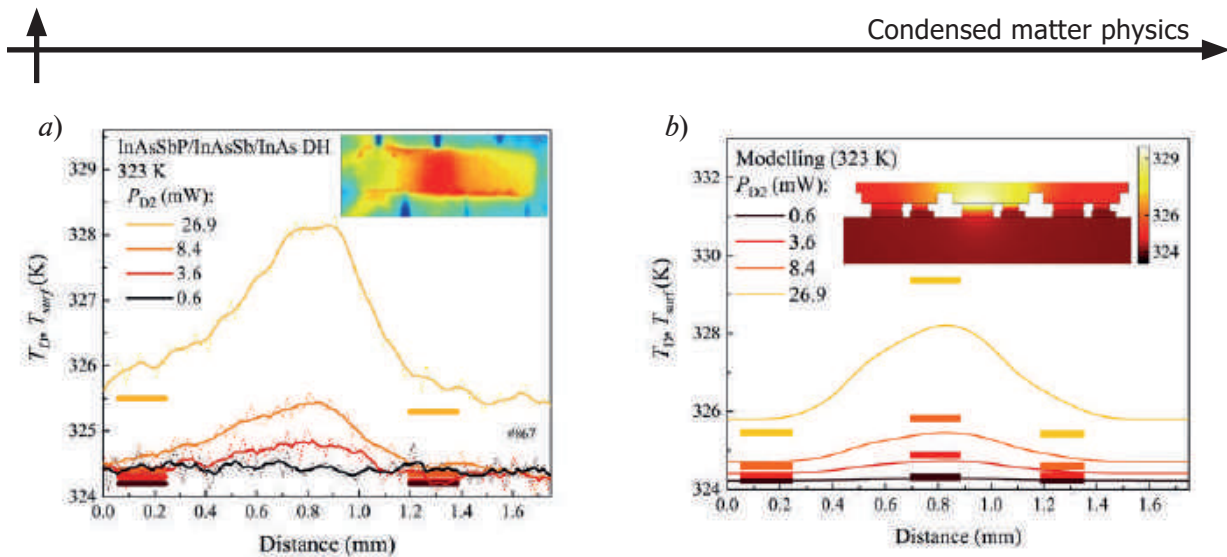


Fig. 6. Temperature distribution on the sensor surface in the center along the X-axis obtained by IR microscope at various electric power applied to diode D2 (solid lines). The temperature of the active region diode D1 and D3 (the segments), from the measurement of R_0 . Inset shows an IR map at $P = 26.9$ mW (a). The modeled distribution temperature along the chip surface center at various currents in diode D2 (solid lines). The segments are the calculated average temperature of the active regions of diodes. Inset shows the modeled temperature distribution gradients of the sensor cross section (b)

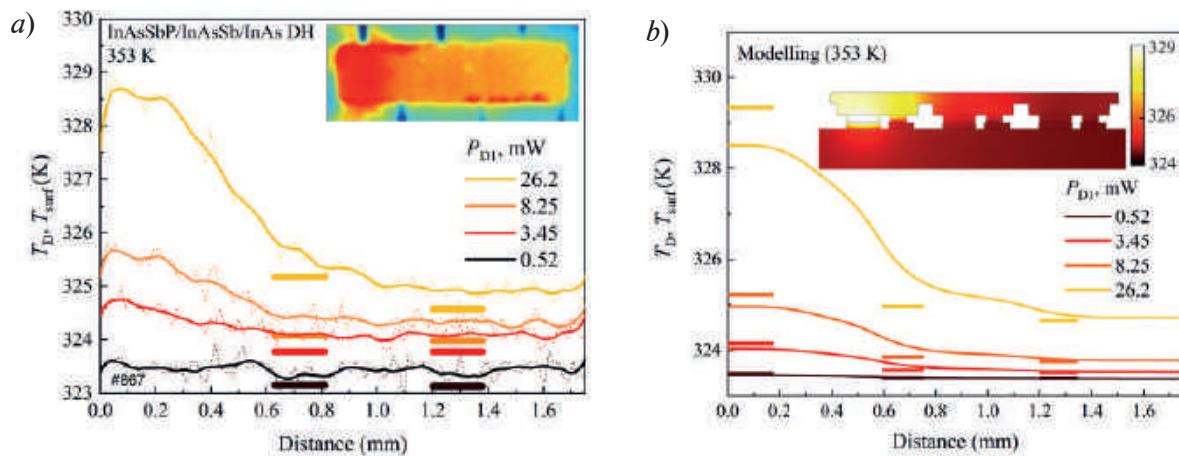


Fig. 7. Temperature distribution on the sensor surface in the center along the X axis obtained by IR microscope at various electric power applied to diode D1 (solid lines). The temperature of the active region diode D2 and D3 (the segments), from the measurement of R_0 . Inset shows an IR map at $P = 26.2$ mW (a). The modeled distribution temperature along the chip surface center at various currents in diode D1 (solid lines). The segments are the calculated average temperature of active regions of diodes. Inset shows the modeled temperature distribution gradients of the sensor cross section (b)

Temperature spatial 3D distribution modeling were performed by the finite element method in the Comsol Multiphysics software by solving the stationary heat equation. The geometry of the 3D model repeated the structure shown in Fig. 1, b. The thermal conductivities of the active and contact, metallization, and AlN submount were taken from the above measurements (Fig. 5). It was assumed that the electrical power ($P = I \cdot U$) applied to the LED is totally transferred to heat, since LED internal quantum efficiency is less than 10% and most of EL radiation is reflected back at InAs/air interface [9]. Modelling results are shown in Fig. 6, b and Fig. 7, b, curves and horizontal segments were calculated for the same chip parts as in Fig. 6, a and Fig. 7, a. The relative mismatch of simulated and experimental values is less than 5%. The ratio between T_D and T_{surf} and the dependence of T_D и T_{surf} on the LED power are nearly the same. The modeled temperature of the cross section given in the inset in Fig. 6, b illustrating the temperature distribution along the Z axis in diodes D1 and D3 shows that the temperature at a surface is higher than in active layers, the same is shown in the inset in Fig. 7, b for the diodes D2 and D3.

The calculated dependence of $(T_D^{\text{LED}} - T_D^{\text{PD}})$ on power appeared to be close to linear, which agrees with the results in ref. [12] and thus it is possible to elaborate simple empiric relationship between the temperature of the LED and PD in the monolithic sensor chip. This relationship will be very useful for future on-chip sensor [4, 5] data corrections.

Conclusion

In on-chip chemical sensor consisting of p InAsSbP/n-InAsSb/n-InAs DH (mesa diameter $190 \mu\text{m}$, $\lambda = 4.7 \mu\text{m}$) 1×3 diode array (one LED and two PDs) with overall lateral size $400 \times 1700 \mu\text{m}$ flip-chip bonded on AlN submount thermal resistances/conductivities of the active and contact layer resistances constitute $R_{\text{th}} = 33 \text{ K/W}$ (thermal conductivity $K \approx 24 \text{ W/(K} \cdot \text{m)}$), for layer consisting of solder, submount metallization and transition sublayer plating-submount, $R_{\text{th}} = 33 \text{ K/W}$ ($K \approx 31 \text{ W/(K} \cdot \text{m)}$), for AlN submount, $R_{\text{th}} = 18 \text{ K/W}$ ($K \approx 246 \text{ W/(K} \cdot \text{m)}$).

Finite element modeled temperature was 328.1 K when the middle (central) diode is activated with electrical power of 26.2 mW and 328.5 K when the edge one is activated (electrical power is 26.9 mW) at submount temperature 323 K . It was shown that PD surface temperature is higher by about 0.5 K than in PD active layer at LED power of 26.2 mW . Dependence of the LED temperature and dependence of difference between LED and PD temperatures on the applied power can be approximated by a linear function. The simulated values were close to those obtained from optical measurements with IR microscope.

We believe that the obtained results will be valid for diode arrays of similar geometry and thus will be useful in evanescent wave chemical on-chip sensor calibration algorithm significantly improving the analysis accuracy.

Acknowledgments

Part of the work was carried out with the support of the Center of Multi-User Facilities “Element Base of Microwave Photonics and Nanoelectronics: Technology, Diagnostics, and Metrology” and support of the IoffeLED, Ltd.

REFERENCES

1. Seichter F., Vogt J., Tütüncü E., Hagemann L. T., Wachter U., Gröger M., Kress S., Radermacher P., Mizaikoff B., Metabolic monitoring via on-line analysis of ^{13}C -enriched carbon dioxide in exhaled mouse breath using substrate-integrated hollow waveguide infrared spectroscopy and luminescence sensing combined with Bayesian sampling, *Journal of breath research*. 15 (2) (2021) 026013.
2. Huertas C.S., Calvo-Lozano O., Mitchell A., Lechuga L.M., Advanced evanescent-wave optical biosensors for the detection of nucleic acids: An analytic perspective, *Frontiers in chemistry*. 7 (2019) 724.
3. Wolfbeis O.S., Chemical sensors—survey and trends, *Fresenius' Journal of Analytical Chemistry*. 337 (5) (1990) 522–527.
4. Karandashev S.A., Lukhmyrina T.S., Matveev B.A., Remennyi M.A., Usikova A.A., On the Use of Indium Arsenide as the Waveguide Material in the Measurements by Attenuated Total Reflectance, *Optics and Spectroscopy*. 129 (11) (2021) 1231–1235.
5. Karandashev S.A., Lukhmyrina T.S., Matveev B.A., Remennyi M.A., Usikova A.A., p-InAsSbP/n-InAs Double Heterostructure as an On-Chip Midinfrared Evanescent Wave Sensor of Liquids. *physica status solidi (a)*. 219 (2) (2022) 2100456.
6. Chen L., An X., Jing J., Jin H., Chu Z., Li K.H., Ultracompact chip-scale refractometer based on an InGaN-based monolithic photonic chip, *ACS Applied Materials & Interfaces*. 12 (44) (2020) 49748–49754.
7. Yin J., Chen L., Luo Y., Wang Q., Yu H., Li K.H., Performance of InGaN green light-emitting diodes with on-chip photodetectors based on wire-bonding and flip-chip configurations, *Applied Optics*. 60 (9) (2021) 2599–2603.
8. Brunkov P.N., Il'inskaya N.D., Karandashev S.A., Lavrov A.A., Matveev B.A., Remennyi M.A., Usikova A.A., InAsSbP/InAs $_{0.9}\text{Sb}_{0.1}$ /InAs DH photodiodes ($\lambda_{0.1} = 5.2 \mu\text{m}$, 300 K) operating in the $77\text{--}353 \text{ K}$ temperature range, *Infrared Physics & Technology*. 73 (2015) 232–237.
9. Karandashev S.A., Matveev B.A., Remennyi M.A., Indium arsenide-based spontaneous emission sources (review: a decade later), *Semiconductors*. 53 (2) (2019) 139–149.



10. **Bazovkin V. M., Mzhel'skii I. V., Kuryshev G. L., Polovinkin V. G.**, Infrared scanning microscope with high spatial resolution, *Optoelectronics, Instrumentation and Data Processing*. 47 (5) (2011) 498–502.
11. **Li W., Mingo N.**, Thermal conductivity of bulk and nanowire InAs, AlN, and BeO polymorphs from first principles, *Journal of Applied Physics*. 114 (18) (2013) 183505.
12. **Lawler J. V., Currano J.**, Thermal simulations of packaged IR LED arrays, *Technologies for Synthetic Environments: Hardware-in-the-Loop Testing XIII*. 6942 (2008) 112–124.

THE AUTHORS

LUKHYMYRINA Tatiana S.

lukhmyrina@ioffe.mail.ru

ORCID: 0000-0002-3989-6487

KLIMOV Aleksandr A.

a.klimov@mail.ioffe.ru

ORCID: 0000-0001-5642-0483

KUNKOV Roman E.

romunkov@yandex.ru

ORCID: 0000-0002-2377-2287

LEBEDEVA Natalia M.

natali_lebedeva@mail.ioffe.ru

ORCID: 0000-0002-6980-8214

MATVEEV Boris A.

bmat@iropt3.ioffe.ru

ORCID: 0000-0002-7059-5690

CHERNYAKOV Anton E.

chernyakov.anton@yandex.ru

ORCID: 0000-0002-8153-9512

Received 24.10.2022. Approved after reviewing 08.11.2022. Accepted 08.11.2022.

Conference materials
UDC 539.216:535.346
DOI: <https://doi.org/10.18721/JPM.161.121>

Propagation of surface plasmon-polaritons in metal-dielectric structures based on opals

N.I. Puchkov ¹✉, V.G. Solovyev ^{1,2}, A.V. Cvetkov ¹, M.V. Yanikov ¹

¹ Pskov State University, Pskov, Russia;

² S. M. Budienny Military Telecommunications Academy, St. Petersburg, Russia

✉ muxanin@mail.ru

Abstract. Calculations based on the analysis of experimental data allow us to estimate a period of a two-dimensional diffraction grating made of opal globules and to make assumptions about possible directions of surface plasmon-polaritons propagation in metal-dielectric hybrid plasmon-photonics crystals.

Keywords: surface plasmon-polaritons, opal globules, metal-dielectric structure, hybrid plasmon-photonics crystal

Funding: This work was partially supported by the German Academic Exchange Service (DAAD) and by the Russian Foundation for Basic Research (RFBR), project no. 20-32-90003.

Citation: Puchkov N.I., Solovyev V.G., Cvetkov A.V., Yanikov M.V., Propagation of surface plasmon-polaritons in metal-dielectric structures based on opals, St. Petersburg State Polytechnical University Journal. Physics and Mathematics. 16 (1.1) (2023) 126–130. DOI: <https://doi.org/10.18721/JPM.161.121>

This is an open access article under the CC BY-NC 4.0 license (<https://creativecommons.org/licenses/by-nc/4.0/>)

Материалы конференции
УДК 539.216:535.346
DOI: <https://doi.org/10.18721/JPM.161.121>

Распространение поверхностных плазмон-поляритонов в металлодиэлектрических структурах на основе опалов

Н.И. Пучков ¹✉, В.Г. Соловьев ^{1,2}, А.В. Цветков ¹, М.В. Яников ¹

¹ Псковский государственный университет, г. Псков, Россия;

² Военная академия связи имени Маршала Советского Союза С.М. Буденного, Санкт Петербург, Россия

✉ muxanin@mail.ru

Аннотация. Расчеты, проведенные на основе анализа экспериментальных данных, позволяют оценить период двумерной дифракционной решетки из опаловых глобул и высказать предположения о возможных направлениях распространения поверхностных плазмон-поляритонов в металлодиэлектрических плазмонно-фотонных гетерокристаллах.

Ключевые слова: поверхностные плазмон-поляритоны, опаловые глобулы, металлодиэлектрические структуры, плазмонно-фотонные гетерокристаллы.

Финансирование: Работа выполнена при частичной финансовой поддержке Германской службы академических обменов (DAAD) и РФФИ в рамках научного проекта № 20 32 90003.

Ссылка при цитировании: Пучков Н. И., Соловьев В. Г., Цветков А. В., Яников М. В. Распространение поверхностных плазмон-поляритонов в металлодиэлектрических структурах на основе опалов // Научно-технические ведомости



СПбГПУ. Физико-математические науки. 2023. Т. 16. № 1.1. С. 126–130. DOI: <https://doi.org/10.18721/JPM.161.121>

Статья открытого доступа, распространяемая по лицензии CC BY-NC 4.0 (<https://creativecommons.org/licenses/by-nc/4.0/>)

Introduction

Surface plasmon-polaritons are electromagnetic (EM) waves propagating along the metal-dielectric interface [1]. In the last decades, surface plasmon-polaritons (SPPs) were successfully used in photonic crystal devices [2–4] significantly expanding their functionality in EM radiation flow control [5–8]. In this paper, the peculiarities of SPP propagation in hybrid plasmon-photonic crystals obtained by successive deposition of metal (Ag) and dielectric (SiO₂) films on a monolayer of opal globules [9] are analyzed.

The law of SPP dispersion and the condition of phase synchronism when the SPP is excited by light with a wavelength λ incident on an opal lattice with a period a (Fig. 1) have the form [1]:

$$\beta = \frac{\omega}{c} \left(\frac{\varepsilon_1 \varepsilon_2}{\varepsilon_1 + \varepsilon_2} \right)^{1/2} = k_x + 2\pi \frac{l}{a}, \quad (1)$$

where β and $k_x = k \sin \theta = (\omega/c) \sin \theta$ are tangential projections of wave vectors of SPP and photon of visible light with a frequency ω , respectively, θ is the angle of light incidence, $\varepsilon_1 = 1 - (\omega/\omega_p)^2$ and ε_2 are the dielectric permittivities of metal and dielectric, respectively, a is the period of grating, l being an integer. Note that silver plasma frequency $\omega_p \gg \omega$ ($\lambda_p = 2\pi(c/\omega_p) \approx 136$ nm). Thus, equation (1) makes it possible to estimate period of opal grating and consequently — possible directions of SPP propagation.

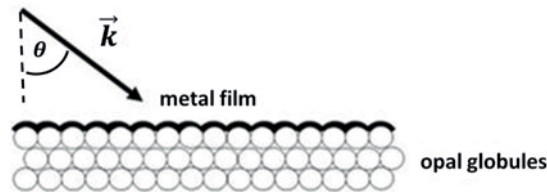


Fig. 1. Phase-matching of light to SPPs using the metal-dielectric opal based grating

Results and Discussion

Formerly [6–8], we attributed some transmission maxima in optical spectra of hybrid plasmon-photonic crystals Ag/SiO₂/Ag/ML/Ag (Fig. 2 [8]) to an extraordinary transmission (EOT) and minima correlating with resonator Ag/SiO₂/Ag peak positions — to an extraordinary absorption (EOA) associated with the excitation of ‘bright’ and ‘dark’ surface plasmon-polaritons, respectively.

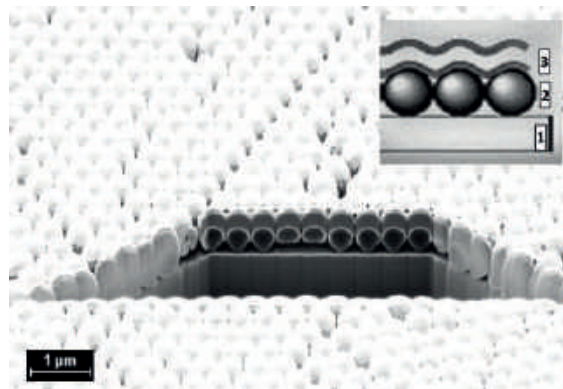


Fig. 2. SEM image of a sample of a hybrid plasmon-photonic crystal Ag/SiO₂/Ag/ML/Ag. Insert: 1 – glass substrate, 2 – monolayer (ML) of opal globules, 3 – resonator Ag/SiO₂/Ag [8].

Fig. 3 demonstrates angular dependence of transmission coefficients of a resonator Ag/SiO₂/Ag (with its maxima correlating with EOA peak positions) for different wavelengths.

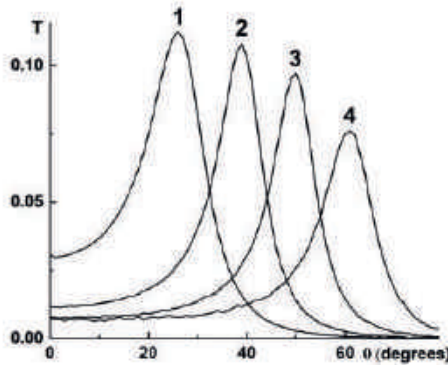


Fig. 3. Angular dependences of transmission coefficients of a resonator Ag/SiO₂/Ag (with maxima correlating with EOA peak positions) for wavelengths of 525 nm (1), 500 nm (2), 475 nm (3), and 450 nm (4)

We can use these experimental data to confirm that in our case equation (1) holds. Assuming $l = 1$ this equation could be rearranged as follows:

$$\left[\varepsilon_2 \frac{(\lambda/\lambda_p)^2 - 1}{(\lambda/\lambda_p)^2 - (1 + \varepsilon_2)} \right]^{1/2} - \frac{\lambda}{a} = \sin \theta.$$

Thus, the theory predicts a direct proportionality between two values: $X = \sin\theta$ and

$$Y = \left[\varepsilon_2 \frac{(\lambda / \lambda_p)^2 - 1}{(\lambda / \lambda_p)^2 - (1 + \varepsilon_2)} \right]^{1/2} - \frac{\lambda}{a}.$$

Experimental results (Fig. 4) confirms this prediction (and, consequently, the excitation of SPPs in this hybrid plasmon-photonic crystals in the conditions under consideration) for small angle of incidence, the best fit parameter a being $a = 363$ nm.

On the other hand, it should be mentioned that the inclination angles of the straight lines in Fig. 4 are too small. The explanation of this fact requires the use of a more complex model that takes into account the peculiarities of the hybrid plasmon-photonic structures under study.

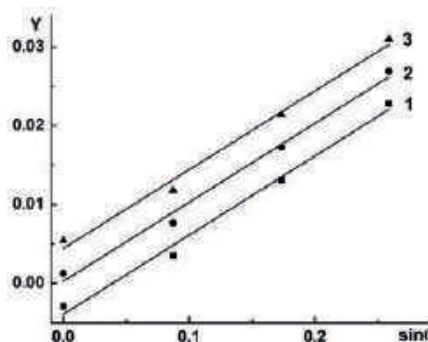


Fig. 4. Angular dependence of the Y value (see text) for different period a values: 362 nm (1), 363 nm (2), and 364 nm (3). Pearson correlation coefficient: $r = 0.995$

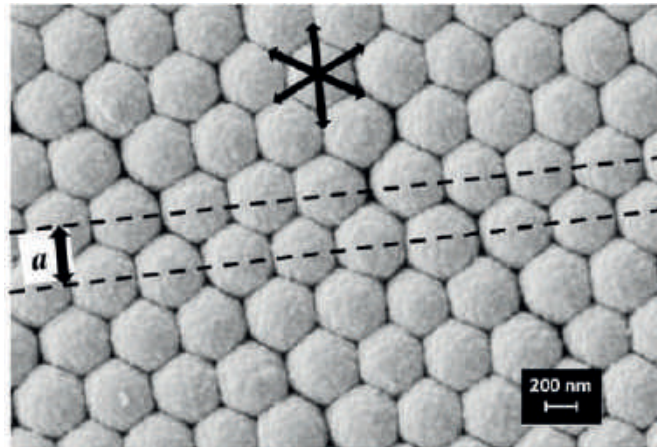


Fig. 5. SEM image of opal globules monolayer. Arrows indicate the corresponding lattice period and probable directions of SPP propagation

Our estimation of the grating period ($a = 363$ nm) is in reasonable agreement with one of the parameters of a two-dimensional diffraction grating $a = D \sqrt{3}/2 \approx 358$ nm [10], where, in accordance with data of electron microscopy, the diameter of opal globules is $D \approx 413$ nm. This result within the limits of experimental errors is also consistent with the value $a \approx 385$ nm obtained earlier [7] by another method. Fig. 5 illustrates corresponding lattice period and probable directions of SPP propagation.

Acknowledgments

The authors are grateful to [S.G. Romanov](#), A.I. Vanin, Yu.A. Kumzerov, S.D. Khanin, U. Peschel and D. Ploss for help, useful discussions, providing samples for research, and assistance in conducting experiments.

REFERENCES

1. **Maier S.A.**, Plasmonics: Fundamentals and applications, Springer, New York, 2007.
2. **Joannopoulos J.D., Johnson S.G., Winn J.N., Meade R.D.**, Photonic crystals: Molding the flow of light, Princeton University Press, Princeton, 2008.
3. Photonic crystals: Advances in design, fabrication, and characterization, Editors K. Busch, S. Lölkes, R.B. Wehrspohn, H. Föll, Wiley-VCH, Berlin, 2004.
4. Optical properties of photonic structures: Interplay of order and disorder, Editors M.F. Limonov, R.V. De La Rue, CRC Press, London, 2012.
5. **Romanov S.G., Korovin A.V., Regensburger A., Peschel U.**, Hybrid colloidal plasmonic-photonic crystals, *Advanced Materials*. 23 (2011) 2515–2533.
6. **Vanin A.I., Lukin A E., Romanov S.G., Solovyev V.G., Khanin S.D., Yanikov M.V.**, Optical properties of metal-dielectric structures based on photon-crystal opal matrices, *Physics of the Solid State*. 60 (2018) 774–777.
7. **Vanin A.I., Kumzerov Yu.A., Romanov S.G., Solovyev V.G., Khanin S.D., Cvetkov A.V., Yanikov M.V.**, Transmission and conversion of electromagnetic radiation by photonic crystal metal-dielectric systems based on opals, *Optics and Spectroscopy*. 128 (2020) 2022–2027.
8. **Khanin S.D., Vanin A.I., Kumzerov Yu.A., Solovyev V.G., Cvetkov A.V., Yanikov M.V.**, Peculiar properties of electromagnetic radiation propagation in photonic crystalline metal-dielectric systems based on opals, *Radio communication technology*. 4 (2021) 89–99.
9. **Balakirev V.G., Bogomolov V.N., Zhuravlev V.V., Kumzerov Yu.A., Petranovskii V.P., Romanov S.G., Samoilovich L.A.**, Three-dimensional superlattices in opal matrices, *Crystallography Reports*. 38 (1993) 348–353.
10. **Romanov S.G.**, Light diffraction features in an ordered monolayer of spheres, *Physics of the Solid State*. 59 (2017) 1356–1367.

THE AUTHORS

PUCHKOV Nikolai I.

muxanin@mail.ru

ORCID: 0000-0002-0494-3132

CVETKOV Alexander V.

aleksandr23031994@gmail.com

ORCID: 0000-0001-8340-9896

SOLOVYEV Vladimir G.

solovyev_v55@mail.ru

ORCID: 0000-0002-8452-6928

YANIKOV Mikhail V.

losthighway@mail.ru

ORCID: 0000-0002-0116-2787

Received 26.10.2022. Approved after reviewing 08.11.2022. Accepted 08.11.2022.

Conference materials

UDC 535.341

DOI: <https://doi.org/10.18721/JPM.161.122>

Alkali ion effect on phase transition temperatures of CuCl nanocrystals in potassium-alumina-borate glass

A.N. Babkina ¹✉, K.S. Zyryanova ¹, E.V. Kulpina ¹, R.R. Gavrilov ¹

¹ ITMO University, St. Petersburg, Russia

✉ babkina.anastasya@bk.ru

Abstract. The effect of the Na/K ratio on the phase transition temperatures of CuCl nanocrystals in potassium-alumina-borate glass is studied. The size effect in the location of the exciton absorption is confirmed. By increasing the content of sodium ions in glass, it is possible to increase the melting point of CuCl crystals with a mean size of 3.1 nm from 152 to 168 °C. It is assumed that in the matrix of potassium alumina-borate glass, instead of pure CuCl crystals, a CuCl-RCl (R = Na, K) solid solution crystallizes during the heat treatment.

Keywords: copper halides, melting temperature, crystallization temperature, solid solution

Funding: This research was supported by Russian Science Foundation (Agreement No. 19-72-10036).

Citation: Babkina A.N., Zyryanova K.S., Kulpina E.V., Gavrilov R.R., Alkali ion effect on phase transition temperatures of CuCl nanocrystals in potassium-alumina-borate glass, St. Petersburg State Polytechnical University Journal. Physics and Mathematics. 16 (1.1) (2023) 131–136. DOI: <https://doi.org/10.18721/JPM.161.122>

This is an open access article under the CC BY-NC 4.0 license (<https://creativecommons.org/licenses/by-nc/4.0/>)

Материалы конференции

УДК 535.341

DOI: <https://doi.org/10.18721/JPM.161.122>

Влияние вида щелочного иона на температуры фазовых переходов нанокристаллов CuCl в калиево-алюмооборатном стекле

А.Н. Бабкина ¹ ✉, К.С. Зырянова ¹, Е.В. Кульпина ¹, Р.Р. Гаврилов ¹

¹ Университет ИТМО, Санкт-Петербург, Россия

✉ babkina.anastasya@bk.ru

Аннотация. В работе показаны результаты исследования влияния соотношения Na/K на температуры фазовых переходов нанокристаллов CuCl в калиево-алюмооборатном стекле. Подтвержден размерный эффект в месте поглощения экситона. С увеличением содержания ионов натрия в стекле температура плавления нанокристаллов CuCl среднего размера 3,1 нм увеличивается с 152 до 168 °C. Предполагается, что в матрице калиево-алюмооборатного стекла вместо чистых кристаллов CuCl при термообработке кристаллизуется твердый раствор CuCl-RCl (R = Na, K).

Ключевые слова: галогениды меди, температура плавления, температура кристаллизации, твердый раствор

Финансирование: This research was supported by Russian Science Foundation (Agreement № 19-72-10036).

Ссылка при цитировании: Бабкина А.Н., Зырянова К.С., Кульпина Е.В., Гаврилов Р.Р. Влияние вида щелочного иона на температуры фазовых переходов нанокристаллов CuCl в калиево-алюмооборатном стекле // Научно-технические ведомости СПбГПУ.

Физико-математические науки. 2023. Т. 16. № 1.1. С. 131–136. DOI: <https://doi.org/10.18721/JPM.161.122>

Статья открытого доступа, распространяемая по лицензии CC BY-NC 4.0 (<https://creativecommons.org/licenses/by-nc/4.0/>)

Introduction

Tsekhomsky and Golubkov [1, 2] showed that temperature measurements of X-ray scattering at small angles can show phase transformations of copper halide crystals in photochromic glass. In addition, it was found that not pure CuCl microcrystals, but a CuCl-NaCl solid solution [2] are precipitated in the borosilicate glass matrix, which was confirmed by the dependence of phase transformation temperatures and photochemical response on the content of sodium chloride in the glass composition. It was shown in the work that at a constant concentration of chloride ions and successive equimolecular replacement of sodium by potassium, the temperatures of phase transformations of copper halides decrease [3]. This once again confirms the theory of the presence of a CuCl-RCl (R = Na, K) solid solution in the glass matrix. However, unlike borosilicate glass, borate glass with copper halide nanocrystals does not exhibit photochromism [4] and, probably, the composition of the crystalline phase in it may differ.

Therefore, in this work, we studied the phase transition temperatures of CuCl nanocrystals in potassium-aluminum-borate glass depending on the alkali ions content in the composition.

Experimental methods

In this work, nanosized copper (I) halide crystals were nucleated in potassium-aluminum-borate glass matrix with different ratios of alkali ions dopants: 4K-1Na (# 1), 3K-2Na (# 2), 2K-3Na (# 3), 1K-4Na (# 4). Synthesis was carried out in a laboratory electric furnace (Gero, Germany) at a temperature of 1350 °C in a corundum crucible with stirring of the melt with a platinum stirrer for 1 hour. After synthesis, the initial glasses were thermally treated at temperatures of 410, 430, and 450 °C for nucleation of copper (I) chloride crystals in the glass matrix.

The absorption spectra of glass samples in the temperature range from -196 to 20 °C were recorded on a Lambda 650 spectrophotometer in the range of 200–900 nm. Sample was cooled down using a Specac two-chamber cryostat (Great Britain), a West 6100+ temperature control unit, a vacuum pump (KNF Laboport, Germany), and liquid nitrogen. In the temperature range from 18 to 200 °C, the optical density spectra of glass samples were recorded on an optothermal setup consisting of a broad-spectrum lamp as a radiation source, an Avaspec 2048 fiber spectrometer (Avantes) as a radiation detector, a temperature cell with quartz windows, a sample holder inside it and a platinum thermocouple for monitoring the sample's temperature during measurements. The change in the sample's temperature had the form of a continuous cycle of heating and subsequent cooling with temperature change at a rate of 2.5 °C/min.

Experimental results

The absorption spectra of glasses after the heat treatment (HT) acquired an intense absorption band in the near UV region (Fig. 1), which corresponds to the absorption of CuCl nanocrystals [5, 6]. The crystallization of CuCl nanophase in amorphous environment is described by the diffusion-induced phase separation process [7]. During their growth the nanocrystals can be represented as a semiconductor ball with a size corresponding to the width of a potential quantum well, inside of which the motion of the confined exciton can be calculated. The basis of this method was first proposed in [8] and then confirmed by optical spectroscopy data of CuCl nanocrystals in borosilicate glass [9]. Since this method was tested specifically on CuCl crystals, we also use during calculations.

Since CuCl crystals for most cases were bigger than the Bohr exciton size [5], the case of weak confinement was used. The calculation was carried out using $E_g(\text{CuCl}) = 3.2949 \text{ eV}$, – bandgap of the bulk crystal at 77 K, $E_b = 0.190 \text{ eV}$ – exciton binding energy, $M(\text{CuCl}) = 1.9 \cdot m_0$ [10, 11] – effective exciton mass (m_0 – electron rest mass) via equation used in [12].

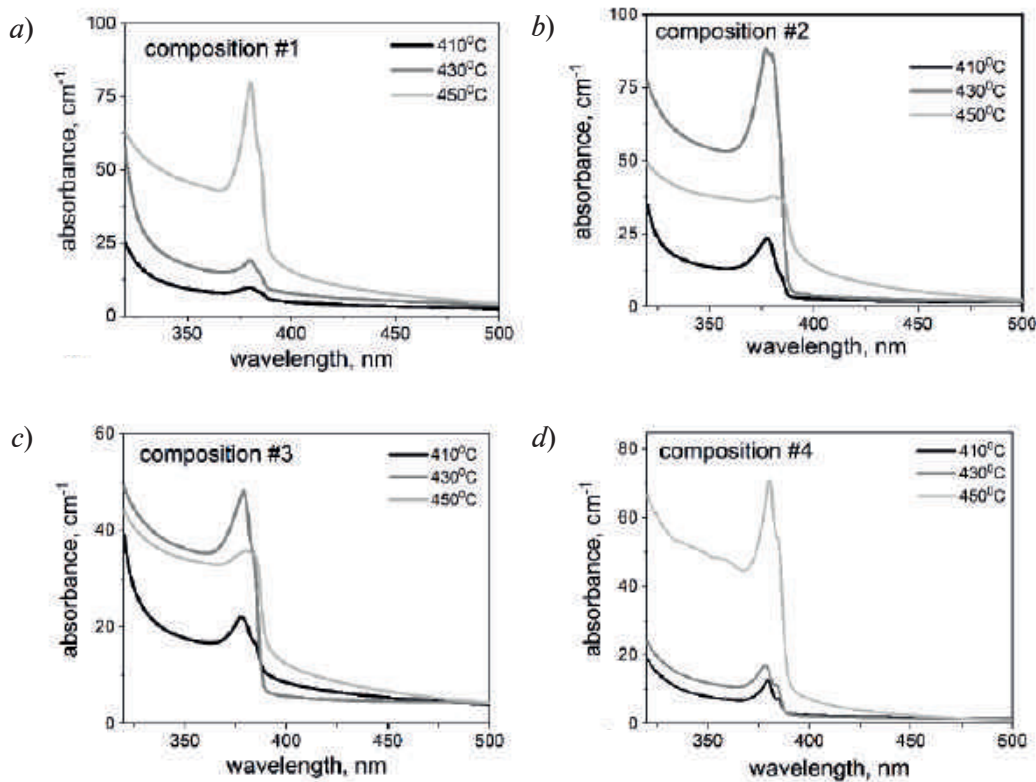


Fig. 1. Absorption spectra of compositions #1(a), #2 (b), #3 (c), #4 (d) after different HT temperatures (registration temperature = -196°C)

According to calculations, the mean size of CuCl nanocrystals in all compositions was 2.3 ± 0.5 nm after 410°C HT, 2.7 ± 0.5 nm after 430°C HT, 3.1 ± 0.5 nm after 450°C HT.

Due to relatively small size of nanocrystals, it is difficult to use X-ray methods to determine the mean size and phase transformation temperatures. Therefore, to study phase transitions, an opto-thermal method was chosen, which consisted in recording the absorption spectra of CuCl nanocrystals during heating and subsequent cooling of glass samples. Since exciton absorption is directly inherent only in CuCl nanocrystals, a decrease in its intensity can be associated with thermal recombination of excitons; however, its complete disappearance indicates the absence of crystals in the glass matrix. Similarly, the appearance of exciton absorption indicates the appearance of crystals in the glass matrix. This method was successfully tested on copper halide crystals [13, 14], where it was shown that the phase transformation temperatures obtained by X-ray and optical methods coincided.

During heating of glass samples with CuCl nanocrystals, the maximum of the absorption band shifted to the short-wavelength region, and the absorption intensity decreased until it disappeared completely. The temperature, at which the exciton absorption completely disappeared, was determined as the melting temperature of nanocrystals. Upon subsequent cooling of the sample from temperatures below T_g , an overcooling region was observed, in which the intensity of exciton absorption remained equal minimal. The temperature at which the increase in the intensity of exciton absorption began was determined as the temperature of crystallization onset (Fig. 2). When the composition of the glass matrix is constant, the revealed temperatures of phase transitions depend only on the mean size of crystals ensemble [14].

Discussion

Fig. 2 shows that, within the same composition, with an increase in the HT temperature the heating-cooling curves shift to higher temperatures. This is a manifestation of the size effect. It is interesting to note that for crystals with the smallest size, the intensity of exciton absorption did not reach the initial values during cooling to room temperature. Thus, at room temperature some of the crystals were still in the state of a supercooled liquid.

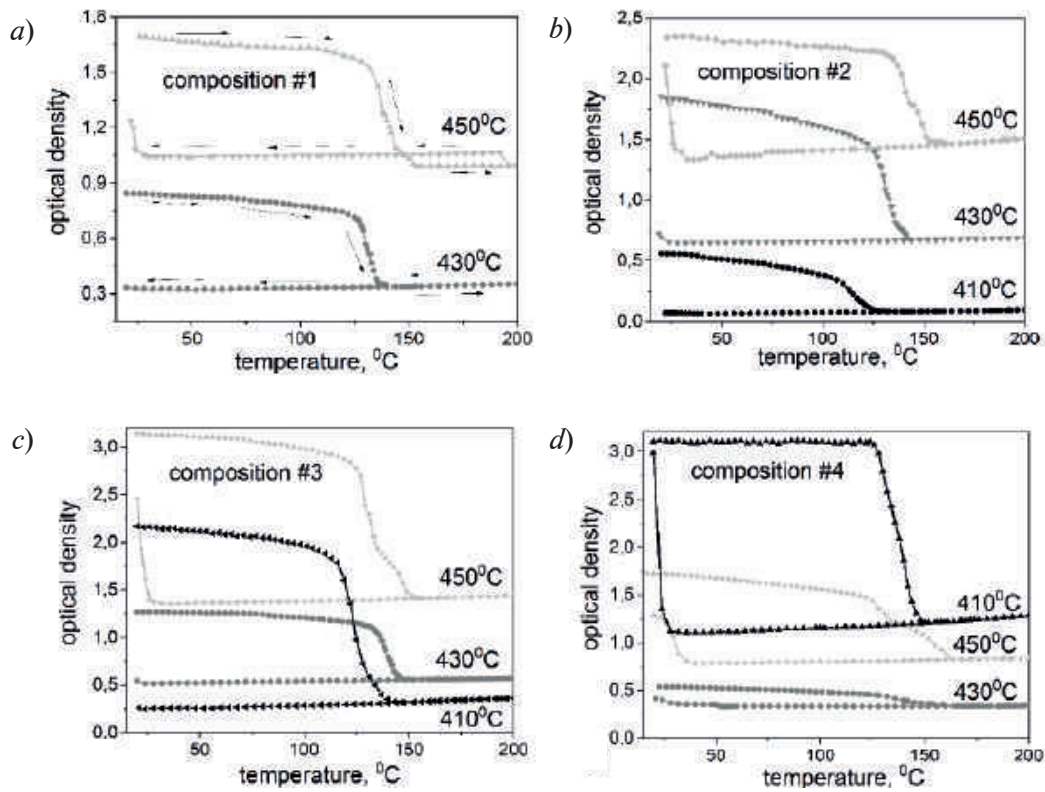


Fig. 2. Temperature dependence of optical density in the exciton absorption maximum of CuCl during heating and cooling of samples #1 (a), #2 (b), #3 (c), #4 (d) after heat treatment at 410, 430, 450 °C

The phase transition temperatures determined are shown in Fig. 3. With an increase in the sodium content in the additives, the melting and crystallization temperatures of nanocrystals increase, which was shown in [3]. The presence of potassium and sodium halides did not reveal itself either in the spectral data or in the diffraction patterns. Since the process of crystal formation in the glass matrix is of a diffusion nature, there is a high probability that a transition layer exists around the crystalline phase, the chemical composition of which differs both from the composition of the crystals and the glass matrix. Sodium and potassium chlorides were introduced into the composition in the form of ready-made reagents and were used as a source of chloride ions. Therefore, it can be assumed that the transition layer, in addition to chlorine and copper ions, is also saturated with alkali metal ions. The melting temperature of the eutectic composition CuCl-NaCl is 326 °C [15], CuCl-KCl is 146 °C [16]. Considering the influence of the size effect and the simultaneous presence of two alkali ions in the glass composition, it can be assumed that the recorded melting temperatures will have intermediate values between these two,

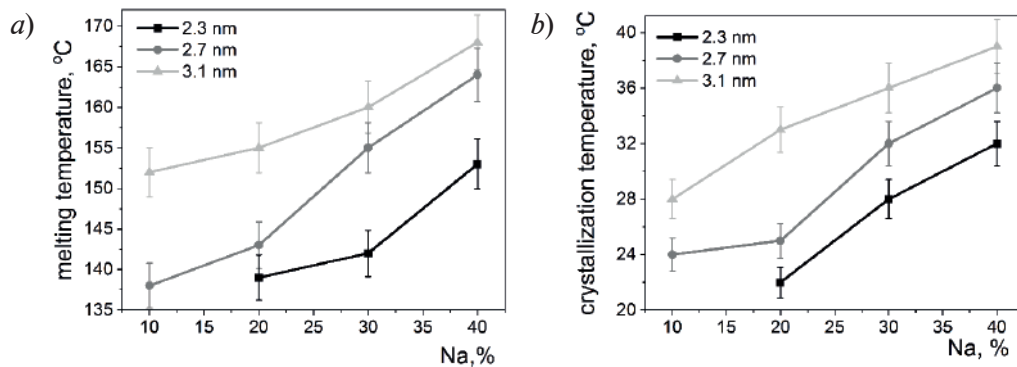


Fig. 3. Dependence of the melting (a) and crystallization (b) temperature of CuCl nanocrystals on Na/K ratio for crystals with different sizes



which we see in the experimental results. Based on these considerations, it can be concluded that in the borate glass matrix, just as in borosilicate glass, not pure copper chloride crystals are nucleated during the heat treatment, but a solid solution of copper chloride and alkali metal chloride.

Conclusion

The paper showed the influence of the size effect on the exciton absorption spectra of CuCl nanocrystals. The mean size of an ensemble of crystals precipitated during heat treatment in glass matrix was calculated depending on the heat treatment temperature. The influence of the size effect on the phase transition temperatures of CuCl was shown. When the Na/K ratio in the glass composition varied, the temperatures of phase transitions of CuCl nanocrystals of the same size changed. It has been found that the melting and crystallization temperatures of the crystalline phase increased with the content of sodium ions. Arguments were presented showing the possibility of crystallization during heat treatment in the potassium-alumina-borate glass not of pure CuCl nanocrystals but of CuCl-RCl (R = Na, K) solid solution.

REFERENCES

1. Golubkov V.V., Tsekhomskii V.A., Phase changes in Copper Halide photochromic glasses, *Sov. J. Glas. Phys. Chem.* 8 (4) (1982) 416–422.
2. Golubkov V.V., Tsekhomskii V.A., Role of Sodium Chloride in the formation of a light-sensitive phase in Copper Halide photochromic glass, *Sov. J. Glas. Phys. Chem.* 12 (2) (1986) 206–215.
3. Golubkov V.V., Tsekhomskii V.A., Composition and structure of copper halide phase in sodium and potassium aluminoborosilicate glasses., *Glas. Phys. Chem.* 24 (1) (1998) 41–46.
4. Babkina A.N., Shirshnev P.S., Nikonorov N.V., Efimov A.M., Features of copper chloride nanocrystals formation in potassium aluminoborate glass, *J. Non. Cryst. Solids.* 471 (2017) 362–367.
5. Kadono K., Suetsugu T., Ohtani T., Einishi T., Tarumi T., Yazawa T., Distributions of copper and CuBr in CuBr nanocrystallite-dispersed glasses prepared by copper staining, *J. Non. Cryst. Solids.* 353 (1) (2007) 6–11.
6. Valov P.M., Leiman V.I., Maksimov V.M., Derkacheva O.Y., Nucleation kinetics in a CuCl solid solution in glass: Calculation and comparison with experiment, *Phys. Solid State.* 53 (3) (2011) 476–481.
7. Ekimov A., Growth and optical properties of semiconductor nanocrystals in a glass matrix, *J. Lumin.* 70 (1–6) (1996) 1–20.
8. Efros A.L., Efros, A.L., Interband absorption of light in a semiconductor sphere, *Sov. Physics. Semicond.* 16(7) (1982) 772–775.
9. Onushchenko A.A., Ekimov A.I., Quantum size effect in three-dimensional microscopic semiconductor crystals, *Jetp Lett.* 34 (6) (1981) 363–366.
10. Ekimov A.I., Onushchenko A.A., Plyukhin A.G., Efros A.L., Size quantization of excitons and determination of the parameters of their energy spectrum in CuCl, *Sov. Phys. JETP.* 61 (4) (1985) 891–897.
11. Valov P.M., Leiman V.I., Formation and growth of CuCl phase nuclei in glass, *Phys. Solid State.* 47(11) (2005) 2148–2153.
12. Babkina A.N., Zyryanova K.S., Egorova Y.B., Kulagina A.S., Gavrilov R.R., Monogarova A.A., Investigation of spectral properties of potassium-aluminum-borate glass with CuCl - CuBr nanocrystals, *J. Phys. Conf. Ser.* 2103 (2021) 012172.
13. Golubkov V.V., Kim A.A., Nikonorov N.V., Tsekhomskii V.A., Shirshnev P.S., Precipitation of nanosized crystals CuBr and CuCl in potassium aluminoborate glasses, *Glas. Phys. Chem.* 38 (3) (2012) 259–268.
14. Babkina A.N., Nikonorov N.V., Tsekhomskii V.A., Shirshnev P.S., The effect of temperature on the exciton absorption of copper chloride and copper bromide nanocrystals in potassium-aluminum-borate glass, *Glas. Phys. Chem.* 41(1) (2015) 81–88.
15. Haselhoff M., Weber H.J., Preparation of CuCl nanocrystals in NaCl, *Mater. Res. Bull.* 30 (5) (1995) 607–612.

16. **Niazi S., Bonk A., Hanke A., Baben M., Reis B., Olsen E., Nygerd, H.S.**, Thermal stability, hydrolysis and thermodynamic properties of molten KCl-CuCl, *Materialia*. 21(December) (2022) 101296.

THE AUTHORS

BABKINA Anastasiia N.

babkina.anastasya@bk.ru

ZYRYANOVA Ksenia S.

ms.z.k.s@mail.ru

ORCID: 0000-0001-6733-1443

KULPINA Ekaterina V.

katrinakulpina@yandex.ru

ORCID: 0000-0003-2896-2896

GAVRILOV Ruslan R.

babkinauha@yandex.ru

ORCID: 0000-0003-0757-9927

Received 26.10.2022. Approved after reviewing 09.11.2022. Accepted 09.11.2022.

Conference materials
UDC 621.315.592
DOI: <https://doi.org/10.18721/JPM.161.123>

Two-dimensional plasmon excitations in a random array of quantum antidots

Yu.B. Vasilyev ✉

Ioffe Institute, St.Peterssburg, Russia

✉ yu.vasilyev@mail.ioffe.ru

Abstract. Terahertz absorption in two-dimensional electron systems in an AlGaAs/GaAs heterojunction containing a layer of self-organizing antidots is experimentally studied. A magnetoplasmon mode is observed in a magnetic field. When the electron density at the heterojunction is less than the density of the disorder potential minima induced by the antidots we found the drastic narrowing of the absorption line with magnetic field. We interpret this effect by magnetic field induced localization. The localized plasmon resonances are coupled by the Coulomb electron-electron interactions leading to collective magnetoplasmon excitations.

Keywords: heterojunction, magnetoplasmon, antidots, terahertz absorption

Citation: Vasilyev Yu.B., Two-dimensional plasmon excitations in a random array of quantum antidots, St. Petersburg State Polytechnical University Journal. Physics and Mathematics. 16 (1.1) (2023) 137–141. DOI: <https://doi.org/10.18721/JPM.161.123>

This is an open access article under the CC BY-NC 4.0 license (<https://creativecommons.org/licenses/by-nc/4.0/>)

Материалы конференции
УДК 621.315.592
DOI: <https://doi.org/10.18721/JPM.161.123>

Двумерные плазменные возбуждения в неупорядоченном массиве квантовых антиточек

Ю.Б. Васильев ✉

Физико-технический институт им. А.Ф. Иоффе РАН, Санкт-Петербург, Россия

✉ yu.vasilyev@mail.ioffe.ru

Аннотация. Экспериментально изучаются плазменные возбуждения в двумерных электронных системах в гетеропереходе AlGaAs/GaAs, содержащем слой самоорганизующихся антиточек. В магнитном поле в спектрах терагерцового поглощения, наблюдается плазменная линия, ширина которой сильно уменьшается с ростом магнитного поля, что можно объяснить локализацией плазмонов магнитным полем и возникновением коллективной магнитоплазменной моды.

Ключевые слова: гетеропереход, магнитоплазмон, антиточки, терагерцовое поглощение

Ссылка при цитировании: Васильев Ю.Б. Двумерные плазменные возбуждения в неупорядоченном массиве квантовых антиточек // Научно-технические ведомости СПбГПУ. Физико-математические науки. 2023. Т. 16. № 1.1. С. 137–141. DOI: <https://doi.org/10.18721/JPM.161.123>

Статья открытого доступа, распространяемая по лицензии CC BY-NC 4.0 (<https://creativecommons.org/licenses/by-nc/4.0/>)

Introduction

Plasma oscillations in two-dimensional electron gas (2DEG) have been studied for a long time [1]. To excite plasmons with a frequency ω_p , the condition $\omega_p \tau \gg 1$ is required, where τ is the electron relaxation time. Therefore, experiments with plasmons, as a rule, are carried out

at cryogenic temperatures in the terahertz frequency range. In addition, the complexity of such studies is due to the fact that plasma waves do not interact with light in free space due to the large mismatch of their wave vectors. There are various approaches to overcome these limitations based on light diffraction. For example, low-dimensional structures (stripes and disks) [2, 3], light scattering on diffraction gratings and on various types of inhomogeneities are used [4]. Alternatively, efficient coupling of light to plasma oscillations can be achieved in periodically modulated structures such as an array of antidots [5].

In this paper, we study the excitation of two-dimensional plasmons in a random array of quantum antidots. Due to the absence of periodicity, broad plasma modes are excited in such a grating. Remarkably, the application of a strong enough magnetic field leads to the formation of a very narrow magnetoplasmon mode, which can be explained by the localization of plasmons by the magnetic field and the excitation of the collective plasma mode. It is generally accepted that strongly correlated states both in the liquid and in the solid phases form only in pure systems without disorder. Here we present results on terahertz transmission demonstrating the appearance of a strongly correlated phase in a disordered 2DEG. We study a system where the disorder potential is induced by a random array of self-organized islands embedded at the plane of 2DEG. An in-plane electron-density modulation provides coupling to the wave vectors, $q \sim 1/l_0$, (l_0 is the magnetic length) that allows excitation of the 2DEG. When the electron density is less than the density of the disorder minima we observed that the Coulomb electron-electron interactions are dominant and govern the in-plane distribution of electrons. This observation allows us to suppose a formation of a strongly correlated state in a disordered 2DEG that couples the localized plasmon resonances together.

Materials and Methods

Plasma excitations in a 2DEG of a heterojunction were studied by the terahertz transmission method at a temperature $T = 2$ K using a Fourier spectrometer in magnetic fields up to 12 T applied perpendicular to the sample. All spectra were normalized to the spectrum in the absence of a magnetic field in order to exclude the influence of the background on the measurements.

The samples used in the experiment (Fig. 1, left) consist of an inverted single AlGaAs/GaAs heterojunction with an array of self-organized AlInAs quantum islands formed in the heterojunction interface. The data obtained by scanning tunneling and atomic force microscopy show that the islands are round in shape with a diameter of 6 to 12 nm and a “height” in the growth direction of ~ 1 nm. Their concentration is about 10^{11} cm^{-2} , so the average distance between them is ~ 10 nm [6]. Due to the higher conduction band minimum energy and band gap of AlInAs compared to GaAs, AlInAs islands are electron-free regions and therefore have antidot characteristics, providing a short-range repulsive potential for electrons in GaAs. Below we present the results for a sample with an electron concentration of $n_s = 5.2 \times 10^{10} \text{ cm}^{-2}$, in which the change in the electron concentration was carried out using a metal gate.

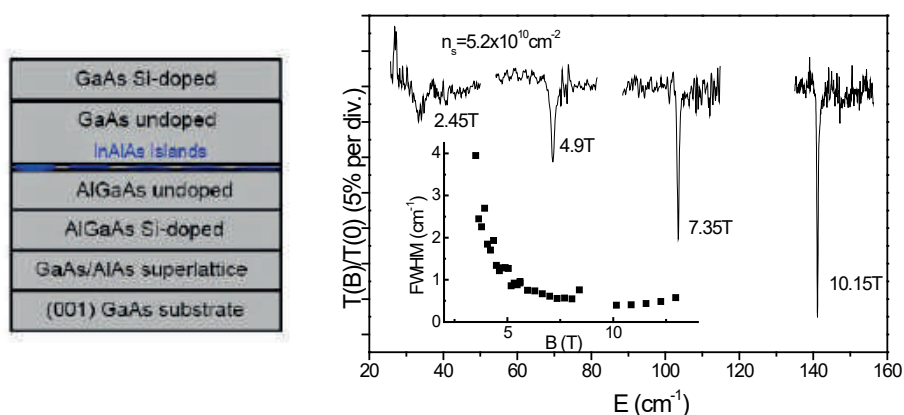


Fig. 1. A scheme of the structure with self-organized islands (left) and CR absorption spectra at fixed magnetic fields and the CR linewidth as a function of magnetic field (inset) at $n_s = 5.2 \times 10^{10} \text{ cm}^{-2}$

Results and Discussion

A representative set of cyclotron resonance (CR) traces is shown in Fig. 1 (right) for a sample with a carrier density, n_s of $5.2 \times 10^{10} \text{ cm}^{-2}$. The CR spectra were obtained at fixed magnetic fields. It is evident that the linewidth changes with magnetic field and becomes very narrow at high magnetic fields. The measured spectra were analyzed by evaluating the full width at half maximum (FWHM) which is plotted as a function of the magnetic field in the inset of Fig. 1. It is clearly seen that the CR line width considerably decreases with increasing magnetic field. The FWHM becomes as small as 1 cm^{-1} at magnetic fields around 4 T and further smoothly decreases down to 0.4 cm^{-1} for higher fields. Such a small linewidth is comparable to that reported for the highest-quality GaAs/AlGaAs heterostructures [7] and is surprising for such a disordered system. The very narrow CR line suggests that electron scattering is dramatically reduced by an increasing magnetic field. At low magnetic fields, the transport mobility has been determined from Shubnikov-de Haas (SdH) measurements (not shown) as $\mu_T = 9.3 \times 10^4 \text{ cm}^2/\text{Vs}$, for a sample with $n_s = 8.5 \times 10^{10} \text{ cm}^{-2}$. The low transport mobility is expected because of the scattering by the inserted InAlAs islands. The absence of the spin splitting of the SdH oscillations [6] also indicates the presence of strong Landau level broadening due to disorder at low magnetic fields [8].

The absorption peak displays a shift towards higher energies when the electron density is increased as shown in Fig. 2, *a*. There we plotted the dependence of the peak position as a function of the electron density at $B = 12.6 \text{ T}$. The position of the mode E is described by the expression

$$E = \omega_c / 2 + (\omega_c^2 / 4 + \omega_0^2)^{1/2} \quad (1)$$

where ω_c is the cyclotron frequency and ω_0 is the characteristic frequency of the confining random potential approximated by a parabola. The clear correlation between the confinement potential and the electron density (Fig. 2, *b*) supports the proposal that the cyclotron resonance in disordered systems is not only influenced by the confining potential of the disorder (in our case antidots) but also by electron-electron interaction. A possible explanation of the observed cyclotron resonance features is based on the picture in which resonant frequencies of electrons occupying different minima of the random potential are coupled via Coulomb interaction into a single collective mode. The coupling leads to the suppression of inhomogeneous broadening of the cyclotron line. The increase of the coupling frequency ω_0 with the electron density originates mainly from the electron-electron interaction.

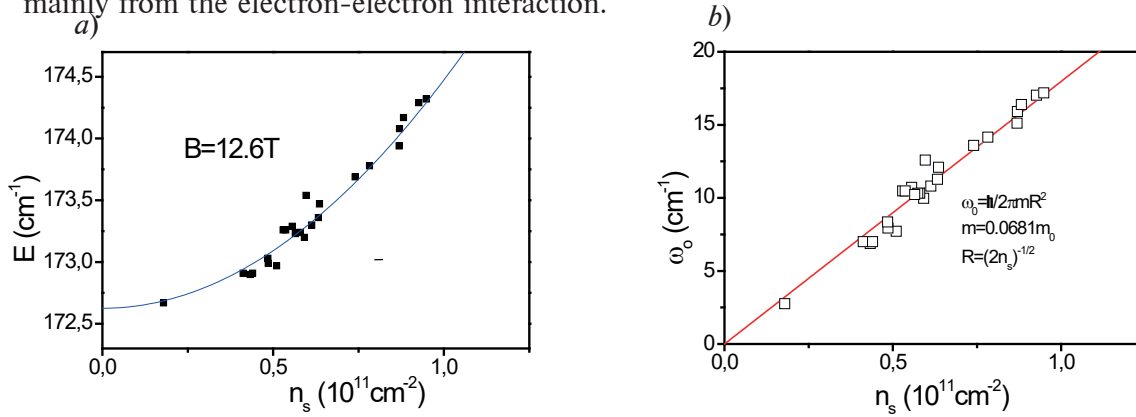


Fig. 2. Dependences of the peak position E (a) and the frequency of the confining random potential ω_0 (b) vs the electron density at $B = 12.6 \text{ T}$

The presence of the antidots results in variation of the electron ground states due to the fluctuation of the effective width of the confining potential well. The amplitude of the bare random potential, created by the antidots, can be (very roughly) estimated as 1.5 meV , which is still far more than $kT = 0.0172 \text{ meV}$ (2 K). However, a 2D potential minimum of such an energy and lateral size of the order of 10 nm cannot effectively hold an electron. So, without a magnetic field the antidots act as an additional interface roughness. The situation changes drastically, when we apply a strong magnetic field and the magnetic length becomes comparable to the effective distance between the antidots. In this case each electron is confined in lateral directions by the

magnetic field and the energy of the electron depends on the lateral position of the wave function center with respect to lateral positions of antidots. At these conditions it becomes “profitable” for the electrons to occupy the potential minima between the antidots. Electrons are shrunk into a size of $l_0 = (\hbar c/eH)^{1/2}$. Because the islands are neutral, the system can be considered as an insulator plate containing random neutral traps separated by a mean distance $N^{-1/2}$. N is the total number of the traps. The traps have different ionization energies. Also the distances between the traps are unequal. The electron density n_s is less than N and only some of the traps are occupied by electrons. The electrons occupy the traps such in a way as to minimize the energy of their mutual repulsion and to maximize their separation. The mean distance between occupied traps is $R \sim n_s^{-1/2}$. Since the traps are randomly distributed, the lattice created by the electrons is quasi-periodic. The lattice period R fluctuates with a characteristic scale of $N^{-1/2}$.

It is important to stress that the excitation correlated with the electron density could be observed in CR only for a lateral electron system with non-parabolic or random lateral potential. Indeed, in a periodic lateral array of parabolic quantum dots with interacting electrons, the collective excitation frequencies at zero in-plane wave vector are independent of the Coulomb interaction and the electron number according to the generalized Kohn's theorem [9–11]. In a random array of antidots, the electrons can be confined in randomly distributed lateral potential wells. In this case the frequencies may depend on the Coulomb interaction and the electron number because the center-of-motion coordinates are no longer separated from the internal motion coordinates. We also note that to study collective excitations of 2DEG in the quantum Hall states requires overcoming experimental difficulties. To excite collective states by a light wave, it is necessary to introduce a certain period modulation into the system to provide excitation of the wave vector q . Electron-electron interactions in the quantum Hall states require a transfer of large wave vectors, $q \sim 1/l_0$, where l_0 is the magnetic length. Conventional grating diffraction does not provide such q . We overcome these restrictions and successfully excite the required wave vectors in 2DES with density modulation induced by the random potential of antidots with average distance between them close to the magnetic length (~ 10 nm).

Conclusion

In conclusion, CR experiments were performed on GaAs/AlGaAs heterostructures containing self-organized antidots. An extremely sharp resonance line is observed in strong magnetic field with an energy position shifted to higher energies with electron density. Our results indicate the existence of a strongly correlated magnetoplasmon excitation present in disordered two-dimensional systems in the extreme quantum limit when the electron density is less than the density of the antidots and the magnetic length is less than the mean distance between the antidots. The effect of electron-electron interactions becomes visible in CR measurements due to the non-applicability of Kohn's theorem in the presence of an artificial scattering potential. The strongly correlated state in a random array of self-organized quantum antidots in the presence of an applied magnetic field may be one of the routes to experimental realization of magnetoplasmon qubits.

Acknowledgments

I am grateful to M. Zundel for growing the samples and to A. Govorov for discussions. The experiments were carried out at MPI, Stuttgart.

REFERENCES

1. **Muravev V.M., Kukushkin I.V.**, Collective plasma excitations in two-dimensional electron systems, *Physics-Uspekhi*. 63 (10) (2021) 975–993.
2. **Muravev V.M., Fortunatov A.A., Dremin A.A., Kukushkin I.V.**, Experimental investigation of plasma excitations in asymmetric stripes of two-dimensional electrons. *JETP Letters* 92 (7) (2010) 466–469.
3. **Muravev V.M., Zarezin A.M., Gusikhin P.A., Kukushkin I.V., Shupletsov A.V.**, Proximity plasma excitations in disk and ring geometries, *Phys. Rev. B* 100 (20) (2019) 205405–205405.
4. **Lusakowski J.**, Plasmon-terahertz photon interaction in high-electron-mobility heterostructures, *Semicond. Sci. Technol.* 32 (1) (2017) 013004–013004.



5. Kern K., Heitmann D., Grambow P., Zhang Y.H., Ploog K., Collective excitations in antidots, Physical Review Letters 66 (12) (1991) 1618–1621.
6. Vasilyev Y., Suchalkin S., Zundel M., Heisenberg D., Eberl K., Klitzing K.V., Properties of two-dimensional electron gas containing self-organized quantum antidots, Applied Physics Letters 75 (19) (1999) 2942–2944.
7. Nicholas R.J., Hopkins M.A., Barnes D.J., Brummell M.A., Sigg H., Heitmann D., Ensslin K., Harris J.J., Foxon C.T., Weimann G., Anomalies in the cyclotron resonance in high-mobility GaAs-Ga_{1-x}Al_xAs heterojunctions, Phys. Rev. B 39 (15) (1989) 10955–10962.
8. Fogler M.M., and Shklovskii B.I., Collapse of spin splitting in the quantum Hall effect, Phys. Rev. B 52 (24) (1995) 17366–1737852.
9. Dempsey J., Johnson N.F., Brey L., Halperin B.I., Collective modes in quantum-dot arrays in magnetic fields, Phys. Rev. B 42 (18) (1990) 11708–11713.
10. Govorov A.O. and Chaplik A.V., Optical properties of quantum dots in a magnetic field, Sov. Phys. JETP 72 (6) (1991) 1037–1046.
11. Chaplik A.V. and Govorov A.O., Quantum fluctuations in a quantum dot array in the regime of ferroelectric phase transitions, Journal of Physics: Condensed Matter 8(22) (1996). 4071–4077.

THE AUTHORS

VASILYEV Yuri B.

yu.vasilyev@mail.ioffe.ru

ORCID: 0000-0001-6547-2744

Received 25.10.2022. Approved after reviewing 08.11.2022. Accepted 08.11.2022.

Conference materials

UDC 538.945.9

DOI: <https://doi.org/10.18721/JPM.161.124>

Study of the anisotropy of critical currents in 2G-HTSC tapes by a non-contact method

D.S. Chikurov ¹✉, M.P. Volkov ¹

¹ Ioffe Institute, Saint-Petersburg, Russia

✉ d.chikurov@yandex.ru

Abstract. A simple and reliable method for determining the critical current of a HTSC tape is a non-contact method based on capturing the magnetic flux by a closed superconducting ring made of this tape and measuring the magnetic field in the center of the ring with a field sensor. This method also makes it possible to obtain the dependence of the critical current on the magnetic field by applying a magnetic field locally on a small section of the tape. A local magnetic field can be created using strong permanent magnets, which also makes it possible to apply the field at different angles relative to the plane of the tape and to determine the anisotropy of critical currents. Using this method, experiments were carried out on rings made of a SuperOx HTSC tape at $T = 77$ K and in a magnetic field up to 4 kOe. The values obtained for the anisotropy of critical currents are in good agreement with the data given by the manufacturer.

Keywords: superconductivity, HTSC, critical current, anisotropy, magnetic flux capture

Citation: Chikurov D.S., Volkov M.P., Study of the anisotropy of critical currents in 2G-HTSC tapes by a non-contact method, St. Petersburg State Polytechnical University Journal. Physics and Mathematics. 16 (1.1) (2023) 142–145. DOI: <https://doi.org/10.18721/JPM.161.124>

This is an open access article under the CC BY-NC 4.0 license (<https://creativecommons.org/licenses/by-nc/4.0/>)

Материалы конференции

УДК 538.945.9

DOI: <https://doi.org/10.18721/JPM.161.124>

Исследование анизотропии критических токов в лентах ВТСП 2 поколения бесконтактным методом

Д.С. Чикуров ¹✉, М.П. Волков ¹

¹ Физико-технический институт им. А.Ф. Иоффе РАН, Санкт-Петербург, Россия

✉ d.chikurov@yandex.ru

Аннотация. Простым и надежным методом определения критического тока ВТСП-ленты является бесконтактный метод, основанный на захвате магнитного потока замкнутым сверхпроводящим кольцом из этой ленты и измерении магнитного поля в центре кольца датчиком поля. Этот метод также позволяет получить зависимость критического тока от магнитного поля путем локального приложения магнитного поля к небольшому участку ленты. Локальное магнитное поле можно создать с помощью сильных постоянных магнитов, что также позволяет прикладывать поле под разными углами относительно плоскости ленты и определять анизотропию критических токов. С использованием этого метода были проведены эксперименты на кольцах из ВТСП-ленты SuperOx при $T = 77$ К и в магнитном поле до 4 кЭ. Полученные значения анизотропии критических токов хорошо согласуются с данными производителя.

Ключевые слова: сверхпроводимость, ВТСП, критический ток, анизотропия, захват магнитного потока

Ссылка при цитировании: Чикуров Д.С., Волков М.П. Исследование анизотропии критических токов в лентах ВТСП 2 поколения бесконтактным методом // Научно-



технические ведомости СПбГПУ. Физико-математические науки. 2023. Т. 16. № 1.1. С. 142–145. DOI: <https://doi.org/10.18721/JPM.161.124>

Статья открытого доступа, распространяемая по лицензии CC BY-NC 4.0 (<https://creativecommons.org/licenses/by-nc/4.0/>)

Introduction

Progress in the creation of second-generation HTSC tapes has led to the industrial production of tapes with high critical currents at nitrogen temperature [1]. The tape manufacturers typically determine critical currents by measuring the magnetic field created by the current over the tape. This method makes it possible to obtain data on the homogeneity of the critical current along the length of the tape; however, the absolute values of the critical currents with this approach are not determined accurately enough due to the strong inhomogeneity of the current field near the tape. To calibrate the measuring system, it is necessary to measure periodically the critical current by the direct 4-probe method [2]. Additional difficulties arise when measuring critical currents in tapes in a large magnetic field, when a small current field is measured against the background of a large external magnetic field [3].

A convenient method for estimating critical currents and their anisotropy in HTSC tapes is a non-contact method based on the measurement of the magnetic field captured in a ring made of a tape [4]. When a magnetic flux of sufficient magnitude is created inside the ring using permanent magnets or an electromagnet and then this flux is reduced to zero, the magnetic flux created by the critical current is captured in the ring. The field of this current is measured in the center of the ring by a Hall sensor. This method makes it possible to obtain accurate values of the critical current, since the current field in the center of the ring is sufficiently homogeneous. At the same time, the anisotropy of critical currents in small fields can be measured using a system of permanent magnets. Since the critical current decreases with increasing magnetic field, it is enough to apply the field on a small section of the tape and then the critical current of the ring will be determined by the critical current of this section. For a number of technical applications, such as power lines or current limiters, it is essential to know the dependence of critical currents on a magnetic field of small magnitude (about 200 mT) when the magnetic field is oriented along and across the tape plane. The anisotropy of critical currents in HTSC tapes is connected with the significant anisotropy of the ReBCO compound itself and with the shape anisotropy, when the role of the surface is significant in the parallel orientation [5]. The relative influence of these two effects may vary from manufacturer to manufacturer, so it is important to have a simple and reliable method for estimating the magnitude and anisotropy of the critical currents of a particular HTS tape.

To avoid problems with creating a ring by soldering, one can create a ring using the following method: make a slit lengthwise of the HTSC tape, not reaching the edges of the tape, push the resulting half-width strips apart and fix the resulting ring on a light and rigid dielectric ring. Such a ring will not have weak points, as in the case of soldering or other connections, this ring will have a continuous HTS layer. By increasing the magnetic field through the superconducting ring, a current arises, which creates a flux opposite to the applied one. The magnitude of the counter magnetic flux is limited by the magnitude of ring critical current. By measuring the field at the center of the ring associated with the maximum trapped flux, we can determine critical currents with high accuracy. This method was used both to determine the critical currents and the relaxation of the critical current with time [6]. This method makes it possible also to determine the dependence of the critical current on the field applied normally or parallel to the plane of the strip. Since the critical current decreases with magnetic field increasing, it is sufficient to apply a magnetic field only on a local section of the tape, and then the total critical current will be determined by the critical current of this section. To create a local magnetic field, it is sufficient to use permanent magnets, which can be placed along or across the plane of the tape.

Materials and Methods

Experiments were carried out on rings made from SuperOx HTS tape, 4 mm wide, with the critical current value at $T = 77$ K declared by the manufacturer 170 A.

To estimate the critical current of the tape, preliminary experiments were carried out to measure the magnetization M of a square piece of tape (4×4 mm) by VSM magnetometer in a transverse field at $T = 77$ K. In the Bean model, there is a simple relation between the critical current and the width ΔM of the major magnetization loop [7]:

$$J_c = (3d/a) \cdot \Delta M,$$

where d is thickness, a is the side of the square, ΔM is magnetization hysteresis width. The critical current calculated from the hysteresis of the magnetization curve at $H = 0$ was 71 A. This value of the critical current is slightly less than the expected value $170/2=85$ A. Considering that the used formula underestimates the J_c values by about 15 percent in the region of small fields [7], we obtain good agreement between the calculated and declared J_c values.

Results and Discussion

For the ring experiments in a piece of HTS tape 10 cm long, a cut was made with a diamond disk 7 cm long, not reaching the edges of the tape (Fig. 1, *b*). The magnetic flux inside the ring was introduced using a solenoid located in the center of the ring. The local magnetic field was created by two permanent NdFeB alloy magnets located opposite each other closer to the cut edge (Fig. 1, *a*). The distance between the magnets (i.e. the magnitude of the magnetic field in the gap) and the orientation of the magnetic field relative to the plane of the tape could be controlled by a mechanical device from outside the liquid nitrogen container. The measurements were carried out at liquid nitrogen temperature ($T = 77$ K), i.e., below the critical temperature of the HTSC ($T_c = 90$ K). To measure the field, a Hall sensor installed at the center of the solenoid was used.

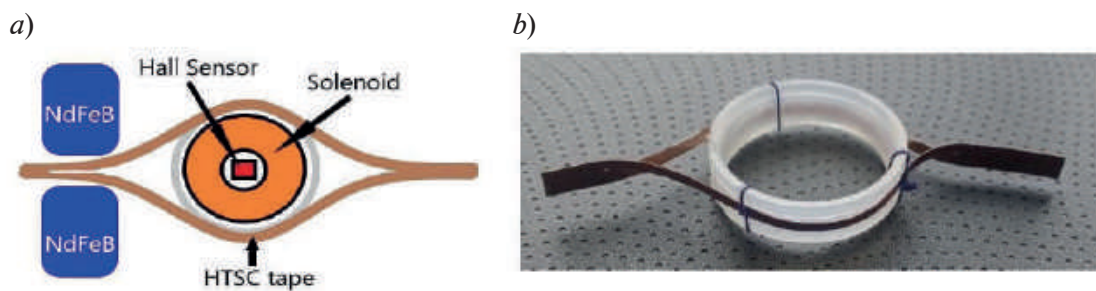


Fig. 1. Schematic representation of the design for measuring the critical current of the HTSC ring (*a*), photo of the HTSC ring (*b*)

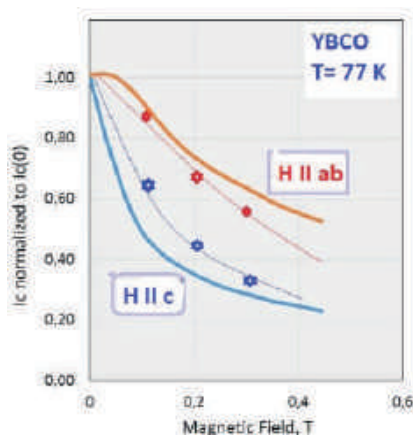


Fig. 2. Magnetic field dependence of critical current for SuperOx YBCO tape at $T = 77$ K. Magnetic field direction is along tape ($H \parallel ab$) and normal to tape ($H \parallel c$). Bold lines – data from [8], asterisks – our data obtained by non-contact method

First, the ring critical current was measured at $H = 0$ (without permanent magnets). It was found that, starting from a certain value of the external flux, the captured magnetic field (after the removal of the external flux) remained constant and equals to 4 mT. For the used ring with a diameter of 3 cm, this field corresponds to a current in the ring of about 100 A, that is higher than the expected value 85 A. Considering that the declared by the manufacturer J_c value is the smallest local value of the critical current of a long tape, it can be expected that in individual small pieces of the tape, the J_c values can be higher.

Using the permanent magnets the J_c values were measured at magnetic field direction along tape ($H \parallel ab$) and normal to tape ($H \parallel c$) (Fig. 2, asterisks) at a few magnetic fields and $T = 77$ K. The bold lines on Fig. 2 represent data for another SuperOx tape provided by the



tape manufacturer [8]. One can see good qualitative agreement between the two datasets. Thus, the trapped magnetic flux method is an express method for measuring the dependence of the tape critical currents on the value and direction of the external magnetic field.

Conclusion

In the course of this work, the critical currents of the SuperOx HTS tape were measured by non-contact methods. The first method consisted in measuring the magnetization curve with a vibrating magnetometer and then converting the magnetization into a critical current using the equations. This method gives a discrepancy with the actual values by 15 %.

Another method of non-contact measurement of the critical current is to measure the trapped flux of a ring made from HTSC tape. The declared by the manufacturer J_c value is the smallest local value of the critical current of a long tape, it can be expected that in individual small pieces of the tape, the J_c values can be higher.

In addition, this method makes it possible to measure the anisotropy of the critical current if a magnetic field is applied locally to the section of the ring. The values obtained for the anisotropy of critical current are in good agreement with the values obtained by the manufacturer.

Acknowledgments

We thank SuperOx for providing samples of the HTSC tapes.

REFERENCES

1. **Uglietti D.**, A review of commercial high temperature superconducting materials for large magnets: From wires and tapes to cables and conductors, 2019 Supercond. Sci. Technol. 32 (5) (2019).
2. **Markelova A., Valikov A., Chepikov V., Petrzhik A., Massalimov B., Degtyarenko P., Uzkiha R., Soldatenko A., Molodyk A., Kideok Sim, Soon Hwang**, 2G HTS wire with enhanced engineering current density attained through the deposition of HTS layer with increased thickness, Progress in Superconductivity and Cryogenics 21 (4) (2019) 29–33.
3. **Li Y., Chen S., Paidpilli M., Jain R., Goel C., Selvamanickam V.**, A Reel-to-Reel Scanning Hall Probe Microscope for Characterizing Long REBCO Conductor in Magnetic Fields Up to 5 Tesla, IEEE Transactions on Applied Superconductivity 32 (4) (2022).
4. **Lee S., Kim W., Kim Y., Park S., Lee J., Hahn J., Hong G., Park I., Park C., Choi K.**, Characteristics of an HTS Pancake Coil in Persistent Current Mode Using Wind-and-Flip Winding Method, IEEE Transactions on applied superconductivity 23 (3) (2013).
5. **Zhang X., Zhong Z., Geng J., Shen B., Ma J., Li C., Zhang H., Dong Q., Coombs T.**, Study of Critical Current and n-Values of 2G HTS Tapes: Their Magnetic Field-Angular Dependence, J Supercond. Nov. Magn. 31 (2018) 3847–3854.
6. **Charles C., Paul N., George A., Jason D., Daniel J., Brian K.**, Investigation of the Relaxation of Persistent Current in Superconducting Closed Loops Made Out of YBCO Coated Conductors, IEEE Transactions on Applied Superconductivity 25 (3) (2015) 8200805.
7. **Shantsev D., Galperin Y., Johansen T.**, Thin superconducting disk with field-dependent critical current, Phys. Rev. B 61 (14) (2000) 9699–9706.
8. **Samoilenkov S.**, “Innovative coated conductors from SuperOx for power applications”, EUCAS 2021, Sept 5-9, Moscow.

THE AUTHORS

CHIKUROV Daniil S.
d.chikurov@yandex.ru
ORCHID: 0000-0003-4879-0518

VOLKOV Mihail P.
m.volkov@mail.ioffe.ru

Received 26.10.2022. Approved after reviewing 14.11.2022. Accepted 15.11.2022.

Conference materials

UDC 548.73

DOI: <https://doi.org/10.18721/JPM.161.125>

Study of defects in shaped sapphire crystals by synchrotron X-ray phase contrast imaging

T.S. Argunova ¹✉, V.G. Kohn ², V.M. Krymov ¹

¹Ioffe Institute, St. Petersburg, Russia;

²National Research Centre "Kurchatov Institute", Moscow, Russia

✉ argunova@mail.ioffe.ru

Abstract. Single crystalline sapphire ribbons grown by the Stepanov method exhibit relatively high dislocation densities and often contain slightly misoriented grains. In order to understand the formation of dislocation structures during growth, we studied neck portions cut off perpendicular to the growth axis $[\bar{1}010]$ of basal-plane-faceted ribbons. The samples have been characterized using phase-contrast and Bragg-diffraction imaging (topography) with synchrotron radiation. It has been found that in the growth direction from the neck towards the main body of the ribbon the dislocation density increases due to multiplication of dislocations. Combining the both imaging techniques, the dislocations were shown to be located around gas voids in sapphire crystals. Computer simulations of the phase-contrast images were carried out to obtain the correct size of the voids.

Keywords: synchrotron phase contrast imaging, computer simulations, shaped sapphire

Funding: This study was funded by Russian Foundation for Basic Research (RFBR), grant numbers 19-29-12041 mk and 19-29-12043 mk.

Citation: Argunova T.S., Kohn V.G., Krymov V.M., Study of defects in shaped sapphire crystals by synchrotron X-ray phase contrast imaging, St. Petersburg State Polytechnical University Journal. Physics and Mathematics. 16 (1.1) (2023) 146–152. DOI: <https://doi.org/10.18721/JPM.161.125>

This is an open access article under the CC BY-NC 4.0 license (<https://creativecommons.org/licenses/by-nc/4.0/>)

Материалы конференции

УДК 548.73

DOI: <https://doi.org/10.18721/JPM.161.125>

Исследование дефектов в профилированных кристаллах сапфира методом фазово-контрастного изображения в синхротронном излучении

Т.С. Аргунова ¹✉, В.Г. Кон ², В.М. Крымов ¹

¹Физико-технический институт им. А.Ф. Иоффе РАН, Санкт-Петербург, Россия;

²Национальный исследовательский центр "Курчатовский институт", г. Москва, Россия

✉ argunova@mail.ioffe.ru

Аннотация. Способом Степанова выращивают изделия из сапфира ($\alpha\text{-Al}_2\text{O}_3$) контролируемых размеров и формы. Исследование дефектов в профилированном сапфире проводилось путем совместного использования методов фазово-контрастного изображения и топографии в синхротронном излучении. Взаимодополняющий характер методов, состоящий в том, что метод фазового контраста выявляет размер газового включения, а топограмма показывает дислокации решетки, позволил охарактеризовать концентраторы напряжений и провести анализ типов дислокаций. Таким образом, нами решена задача определения размеров газовых микровключений и выявлена их роль в формировании дислокационных ансамблей.



Ключевые слова: синхротронное излучение, фазово-контрастное изображение, компьютерное моделирование, профилированный сапфир

Финансирование: Работа выполнена при поддержке Российского Фонда Фундаментальных Исследований (РФФИ), гранты № 19-29-12041 мк и № 19-29-12043 мк.

Ссылка при цитировании: Аргунова Т.С., Кон В.Г., Крымов В.М., Исследование дефектов в профилированных кристаллах сапфира методом фазово-контрастного изображения в синхротронном излучении // Научно-технические ведомости СПбГПУ. Физико-математические науки. 2023. Т. 16. № 1.1. С. 146–152. DOI: <https://doi.org/10.18721/JPM.161.125>

Статья открытого доступа, распространяемая по лицензии CC BY-NC 4.0 (<https://creativecommons.org/licenses/by-nc/4.0/>)

Introduction

Shaped sapphire crystals are produced by melt crystallization. Originally developed by Stepanov and named after him, the shaped crystal growth method was extended by LaBelle, Chalmers, et al. The crystallization was described as edge-defined, film-fed growth (EFG) process. A variety of instruments based on many sizes and shapes of sapphire, including tubes, rods, needles, and filaments are profitably used in optical, medical, and electrical devices (see, e.g., review [1]). In addition, EFG single-crystal plates of large diameter were produced to meet the objectives of Light Emitting Diodes (LEDs) market [2]. Nevertheless, sapphire ribbons with large {0001} basal faces are not suitable for mass production of LED substrates due to structural defects [3]. Conventionally grown sapphire windows have the wide front side surface of the prismatic orientation {11 $\bar{2}$ 0}.

Crystals grown from a gas-saturated melt usually contain gas inclusions, or voids. The gas voids are formed due to the entrapment of gas bubbles that originate in the vicinity of the melt-solid interface. The distribution of the voids was found to depend on a number of parameters. By controlling the pulling rate, a stability of the melt meniscus, a design of the shaper, *etc.*, a reduction in the number of the voids is achieved [4]. In practice, the complete removal of voids hardly ever occurs in shaped sapphire growth processes.

Gas voids in sapphire ribbons seriously deteriorate the crystal quality and hence the application of these products. X-ray Bragg diffraction topography was used to visualize structural defects and voids in basal-plane-faceted ribbons [5]. As a result, an increase in the dislocation density near the voids indicated that the voids initiated dislocations. However, the dislocation density was too high to allow an analysis of the types and a quantification of the number of dislocations in the bulk of the crystal. The proposed model explained the formation of a block structure [5], but knowledge regarding stress concentrators was very limited.

The purpose of this paper was to partially fill these gaps. In a strongly deformed region around the generation source of dislocations, the x-ray topographic images of the source and individual dislocations superimpose and are no longer distinguishable. Therefore we decided to take advantage of the properties of a third-generation synchrotron radiation (SR) beam and use the in-line phase-contrast imaging (PCI) method [6]. The transverse coherence length of SR beams typically equals 30–50 μm , while it is less than 1 μm for usual laboratory sources. A partially coherent SR beam makes it possible to visualize μm -sized inhomogeneities by the total phase shift along the beam path. In the case of sapphire, negligible absorption when working in the 16–22 keV range produces no absorption contrast from a microvoid. However, phase contrast appears if the detector is moved away from the sample. The objectives of the article were to detect the microvoids and study the extent to which their size and shape are described by the PCI.

Materials and Methods

Phase-contrast imaging

A basal-plane-faceted ribbon $31 \times 1.3 \times 265$ ($W \times H \times L$) mm^3 was grown by the Stepanov/EFG method. The growth process took place in a specially designed thermal zone where heat shields were used. The growth rate was $1 \text{ mm} \times \text{min}^{-1}$. The wide as-grown surfaces of the ribbon were

smooth and mirror-like. Laser adjustment of the seed relative to the pulling device and shaper allowed us to achieve high orientation accuracy. The misorientation of the surface relative to the basal face was several arc minutes. A 1 mm thick sample with a neck was cut out along the $[\bar{1}2\bar{1}0]$ direction from the neck portion of the ribbon. Preliminary characterization of the ribbon surfaces using optical microscopy showed that the sample did not contain blocks. The formation of blocks began at a distance of about 200 mm from the seed. The scheme of the ribbon orientation and the sample is shown in Fig. 1.

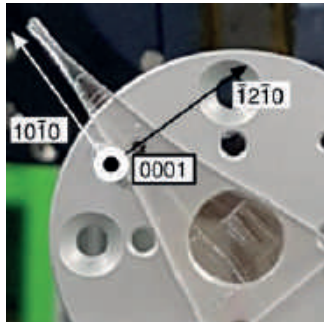


Fig. 1. Neck portion of sapphire ribbon



Fig. 2. Schematic display of the experimental setup for phase-contrast imaging. Object thickness $t \ll Z_1 \ll Z_0$

Fig. 2 schematically represents the principle of in-line phase-contrast imaging. The sample is illuminated by a synchrotron x-ray beam monochromated to a wavelength λ . Due to the large source-to-sample distance Z_0 and the small size σ of the source, a highly spatial coherent beam is produced. In such a condition, the transverse coherence length, given by the relation $d = \lambda Z_0 / 2\sigma$, results to be at least several tens of micrometers. A CCD detector is placed at distance Z_1 from the sample, typically in the range from a few centimeters to about a meter. It is known that in the near-field region of object-to-detector distances, the transverse dimension of, say, a pore can be determined from image pixels (measured directly on images), provided that the detector resolution is satisfactory. The near-field condition is fulfilled for $2r_1 \ll D$, where $r_1 = (\lambda Z_1)^{1/2}$ is the radius of the first Fresnel zone at a distance Z_1 from a void of size D . Note that if D were a few microns, then the correct estimate for the distance Z_1 , where the actual size correlates with the image size, would be about 10 times smaller than Z_c , where Z_c corresponds to $r_1 = D/2$. For a micropipe as an example, $Z_1 = 0.1$ cm with a micropipe diameter $D = 2 \mu\text{m}$ and $\lambda = 0.775 \text{ \AA}$ [7]. This means that the image must be recorded very close to the sample, when Z_1 is in the millimeter range. Moving further from the sample towards the far-field region, where $2r_1 \gg D$, the image size is increased and many Fresnel zones are formed. One can find the real size from the phase shift of x-rays transmitting through an object by recording images at multiple distances and solving the inverse problem.

Experiments were performed at the Pohang Light Source (PLS), Pohang, South Korea, at a beamline devoted to imaging. PLS operates at 3 GeV with an emittance of $12 \mu\text{m} \times \text{rad}$. 6C imaging beamline is characterized by a small vertical size of the source σ : $495(H) \times 29(V) \mu\text{m}^2$ and a large source-to-sample distance L (36 m). The broad spectrum of wavelengths provided by the multi-pole wiggler was monochromated by two parallel silicon crystals with reflection 111. The energy resolution was $\Delta E/E \approx 10^{-4}$. The actual photon energy was $E = 25$ keV. The Zyla CCD camera (Andor, Oxford Instruments, UK) had 2560×2160 pixel resolution and $6.5 \times 6.5 \mu\text{m}^2$ pixel size. Therefore the maximal sample area (the field of view, FOV) that a camera could image was $16.6 \times 14.0 \text{ mm}^2$. Image recording was preceded by a conversion step in which the LuAG:Ce scintillator converted radiation into light. An optical lens served as the coupling element between the scintillator and the CCD. The lens affected the FOV size and image resolution.

Note that the PCI technique differs from X-ray microscopy in that PCI does not use focusing optics. Hence, a wide partially coherent SR beam makes it possible to image microvoids in the entire volume of large and rather thick samples. At the same time, a magnifying lens allows high-resolution imaging with medium-resolution detectors. When a visible light image is magnified by $20 \times$, the pixel-to-object size ratio decreases. Formally speaking, the effective pixel size is reduced from 6.5 to $0.32 \mu\text{m}$.

X-ray topography

Crystal defects such as dislocations were visualized using Bragg-diffraction imaging (X-ray topography, XRT). A multilayer mirror with an energy resolution of $\Delta E/E \approx 2\%$ at 15 keV provided a monochromatic beam by using vertical projection of the source. Typical exposure times were short due to high intensity available at the PLS 6C wiggler beamline. They ranged from several tens of seconds (on the fine-grain film Kodak M100) to several seconds (on the detector). High-speed images were recorded on a large view field ($64 \times 42 \text{ mm}^2$) detector (VHR CCD, Photonic Science, UK) with a pixel pitch of $16 \mu\text{m}$.

Comparison of PC and XRT images could not be performed within the same experimental session due to differences in setups and viewing angles. Nevertheless, PC images were recorded when the sample was set in the azimuth position for Laue diffraction.

Results

Figure 3 shows X-ray topographs taken on film (*a*) and CCD (*b*). The topographs were acquired from the region located near the beginning of the sapphire ribbon. The high-speed CCD image visualizes structural features distributed over a large sample area. At a distance of approximately 15 mm from the crystal neck generation sources of dislocations can be observed. The sources and nearby dislocations form rows in mutually orthogonal directions: along and across the ribbon growth. The numbers 1–4 indicate the longitudinal rows. Among the transverse ones, rows 5 and 6 are closest to the neck.

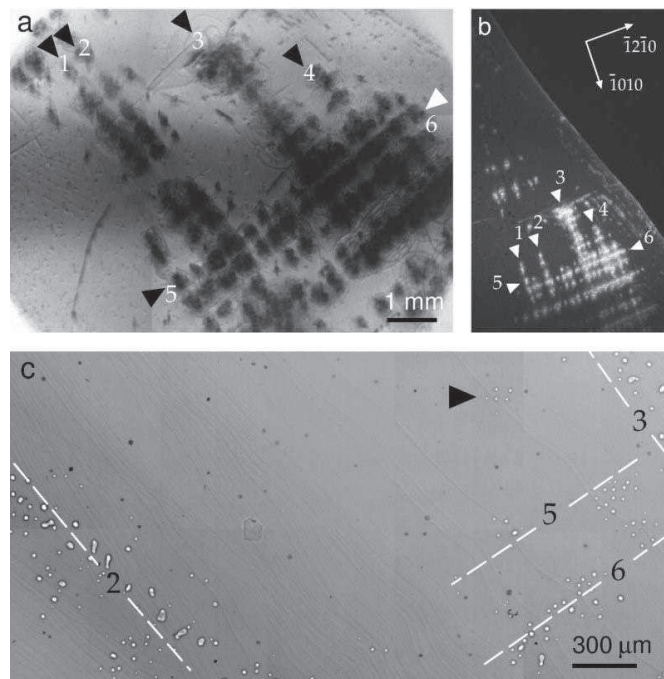


Fig. 3. Synchrotron X-ray topographs of dislocations in sapphire in reflections 1120 (*a*) and 000.18 (*b*). $E = 15 \text{ keV}$. The diffraction vector is directed from bottom to top (*c*). Phase-contrast images combined together to map the area shown in (*a*)

Note that X-ray topography is well suited for observing defects like dislocations and inclusions in high-quality sapphire crystals. But in the case of very high local concentration of dislocations, the images of individual defects are superimposed. This is the case of the ribbon shown in Fig. 3. Therefore, in order to observe the generation sources separately from dislocations, we decided to take advantage of the PCI method.

The sources of dislocations are unevenly distributed over the area of the sample. The voids in the phase-contrast image are arranged in a similar way. Their dense distribution in the longitudinal (2, 3) and transverse (5, 6) directions is shown by dashed lines in Fig. 3, *c*. A direct comparison of the topographs and the phase-contrast image reveals the relationship between dislocations nucleated in the ribbon and gas voids.

Several features are apparent in Fig. 3. Firstly, the dislocation density changes on the topographs and depends on the direction of the diffraction vector. Secondly, unidentified point-like objects are visible among the gas voids. Finally, dislocations are associated not only with voids but also with groups of voids located in a certain configuration. The fact that the dominant slip system of dislocations is basal slip explains the change in their density on the topographs. Point-like contrasts can most probably be interpreted as molybdenum inclusions arising from the crucible and shaper.

The emission of dislocations from a void or group of voids in sapphire has not yet been quantified. So far, there is no quantitative explanation that takes into account the sizes of the voids. In the local region between rows 2 and 3 bounded by transverse row 5, groups of voids are visible that are not associated with dislocations. One of these groups is marked with an arrow (Fig. 3, c). As an example, we chose this group to calculate the size of voids.

Optical microscopy is commonly used for void sizing in sapphire crystals. However, when performing high magnification (about 100 times) optical microscopy, the reduced focus length is required to detect μm -sized gas inclusions, which limits the possibilities of visible light imaging to thin samples. The large thickness of the ribbon (about 1 mm) does not permit an accurate determination of the microvoid diameter. The PCI technique, which can be applied to both thin and thick specimens, enables a more complete description of sizes and shapes by solving the inverse problem. Therefore, in the present work, we used computer simulations to obtain the correct information from the images of voids.

Computer simulation

Phase-contrast images were recorded on a CCD and saved in Tag Image File Format (TIFF) 16 bit with a range of tag values from 0 to 65536. Analysis of the experimental image (2560×2160 pixels) taken at a distance of $Z_1 = 14$ cm showed that the tag values are in the range from 26616 to 43888. The group of selected voids was located on a fragment of 490×490 pixels. Within the fragment, the range of the tag values was even smaller: from 35738 to 41615.

The image contrast equals the difference between the maximal and minimal intensities of the image divided by the sum of these values. Therefore, the contrast was quite small: $V = 0.076$. At another distance $Z_1 = 25$ cm we got $V = 0.114$. That is, when the distance doubled, the contrast also doubled. In addition, as the distance increased the structure of the image changed slightly, namely, the areas of white (maximum) and black (minimum) colors.

Images of spherical voids have a simple structure consisting of a black ring around the edge and a light color in the middle of void. Outer diameter, black ring width, and void contrast increase with distance. For $Z_1 = 25$ cm, the diameter is 50 pixels. Given that the pixel size is $0.32 \mu\text{m}$, we get $16 \mu\text{m}$. Based on the model of a spherical pore with a diameter of $16 \mu\text{m}$, we calculated images of the pore at a given distance Z_1 . The calculation was performed using the XRWP2 (X-ray Wave Propagation 2D) program in the framework of the phase-contrast theory of three-dimensional objects. The program was written by V.G. Kohn using own ACL programming language [8], which is executed by the vkACL.jar interpreter elaborated with Java.

Wave propagation through an object is described by the transmission function, while propagation in free space is calculated according to the Huygens–Fresnel principle as the convolution of the wave function with the Fresnel propagator. The convolution is computed through the Fourier transform method. The fast Fourier transformation (FFT) method was applied.

The simulations were carried out for fully coherent monochromatic radiation from a point source. The source size, non-monochromaticity and detector resolution were counted on the intensity level. It is often sufficient to compute the convolution of the two-dimensional intensity distribution on the detector with a Gaussian of a given width. The FWHM (full width at half maximum) of the Gaussian in both directions were equal to each other, but the values were fitted. Fig. 4 shows the result obtained under the following conditions: void diameter is $16 \mu\text{m}$; distance $Z_1 = 14$ cm and 25 cm; photon energy 25 keV, FWHM $5 \mu\text{m}$. The contrast values of the simulated images were 0.133 и 0.241. These contrasts are higher than the experimental ones but they show the same trends.

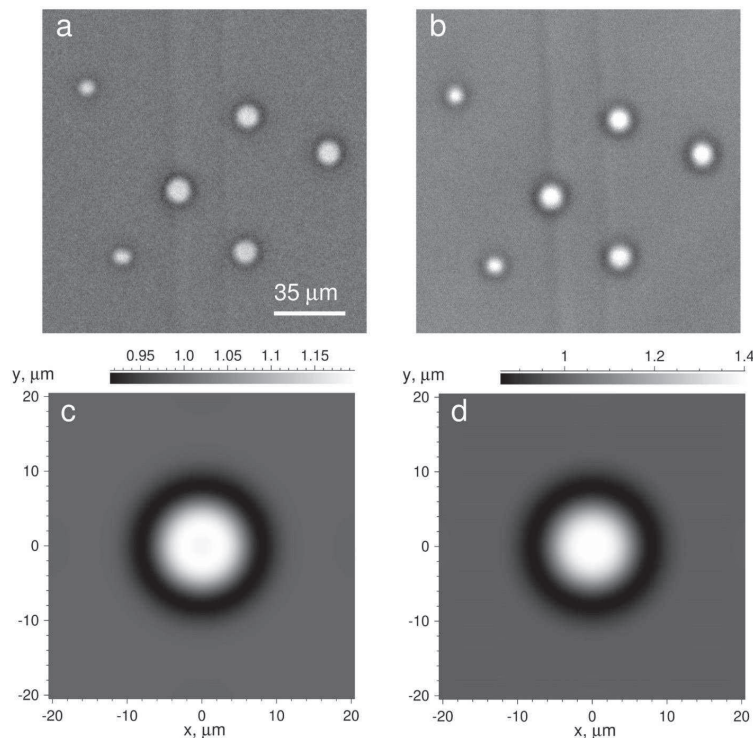


Fig. 4. Phase-contrast images of voids recorded at $Z_1 = 14$ cm (a) and $Z_1 = 25$ cm (b). Computed images of a void with a diameter of $16 \mu\text{m}$ at a distance of 14 cm (c) and 25 cm (d). The computation was made for the rightmost void in the experimental images

Summary

The combination of synchrotron radiation phase-contrast and Bragg-diffraction imaging makes it possible to visualize and characterize defects in profiled sapphire products, particularly in ribbons. Direct comparison of topographs and phase-contrast images reveals the relationships between gas voids and dislocations. The latter are present around the void, since the concentration of stresses at the edges of the void can promote dislocation emission. Computer simulations of phase-contrast images, performed using the author's computer program, solved the problem of determining the void size. Quantitative data (void size, void density, close distances between voids) will be used to build elastic models aimed at describing defect formation in basal-faceted sapphire ribbons.

REFERENCES

1. **Katyba G., Zaytsev K., Dolganova I., Shikunova I., Chernomyrdin N., Yurchenko S., Komandin G., Reshetov I., Nesvizhevsky V., Kurlov V.**, Sapphire shaped crystals for waveguiding, sensing and exposure applications, *Prog. Cryst. Growth*. Ch. 64 (2018) 133–151.
2. **Bruni F.**, Crystal growth of sapphire for substrates for high-brightness, light emitting diodes, *Cryst. Res. Technol.* 50 (1) (2015) 133–142.
3. **Denisov A., Molchanov A., Punin Yu., Krymov V., Müller G., Friedrich J.**, Analysis of the growth conditions of long single crystalline basal-plane-faceted sapphire ribbons by the Stepanov/EFG technique, *J. Cryst. Growth*. 344 (1) (2012) 38–44.
4. **Bunoiu O., Duffar Th., Nicoara I.**, Gas bubbles in shaped sapphire, *Prog. Cryst. Growth*. Ch. 56 (2010) 123–145.
5. **Kuandykov L., Bakholdin S., Shulpina I., Antonov P.**, Model of a block structure generation in basal-faceted sapphire ribbons, *J. Cryst. Growth*. 275 (1-2) (2005) e625–e631.
6. **Snigirev A., Snigireva I., Kohn V., Kuznetsov S., Schelokov I.**, On the possibilities of x-ray phase contrast microimaging by coherent high-energy synchrotron radiation, *Rev. Sci. Instrum.* 66 (12) (1995) 5486–5492.

7. **Argunova T., Kohn V.**, Problems with evaluation of micro-pore size in silicon carbide using synchrotron x-ray phase contrast imaging, *Materials*. 15 (2022) 856(1–7).

8. **Kohn V.**, 2006. URL: <http://kohnvict.ucoz.ru/acl/acl.htm> Accessed Oct. 19, 2022.

THE AUTHORS

ARGUNOVA Tatiana S.

argunova@mail.ioffe.ru

ORCID: 0000-0003-2085-6183

KRYMOV Vladimir M.

v.krymov@mail.ioffe.ru

KOHN Victor G.

kohnvict@yandex.ru

ORCID: 0000-0003-4332-9896

Received 26.10.2022. Approved after reviewing 08.11.2022. Accepted 07.12.2022.

Conference materials

UDC 538.975

DOI: <https://doi.org/10.18721/JPM.161.126>

Features of MBE growth of AlGaAs nanowires with InAs quantum dots on the silicon surface

R.R. Reznik^{1,2,3✉}, V.O. Gridchin^{1,2,3}, K.P. Kotlyar¹,
A.S. Dragunova^{2,4}, N.V. Kryzhanovskaya⁴, Yu.B. Samsonenko^{2,3},
I.P. Soshnikov², A.I. Khrebtov¹, G.E. Cirlin^{1,2,3}

¹ Saint-Petersburg State University, St. Petersburg, Russia;

² Alferov University, St. Petersburg, Russia;

³ IAI RAS, St Petersburg, Russia;

⁴ HSE University, St. Petersburg, Russia

✉ r.reznik@spbu.ru

Abstract. AlGaAs nanowires with InAs quantum dots on the silicon surface were synthesized by molecular-beam epitaxy. Morphological and optical properties of grown nanostructures were studied. It is important to note, that emission from quantum dots is observed in the wavelength range from 780 to 970 nm. Assumptions about the nature of short-wave radiation from quantum dots were formulated. In particular, one of the reasons may be the significant desorption of indium atoms and the presence of gallium atoms in the catalyst droplets during growth at the substrate temperature of 510 °C. Our work, therefore, opens new prospects for integration of direct bandgap semiconductors with silicon platform.

Keywords: III-V semiconductors, nanowires, quantum dots, molecular-beam epitaxy, silicon

Funding: The samples were grown under financial support of St. Petersburg State University research grant 93020138. Morphological properties measurements were done under support of Ministry of Science and Higher Education of the Russian Federation (state task No. 0791-2020-0003). Optical studies of grown samples were done under financial support of the Russian Science Foundation Grant No. 21-72-00099.

Citation: Reznik R.R., Gridchin V.O., Kotlyar K.P., Dragunova A.S., Kryzhanovskaya N.V., Samsonenko Yu.B., Soshnikov I.P., Khrebtov A.I., Cirlin G.E., Features of MBE growth of AlGaAs nanowires with InAs quantum dots on the silicon surface, St. Petersburg State Polytechnical University Journal. Physics and Mathematics. 16 (1.1) (2023) 153–157. DOI: <https://doi.org/10.18721/JPM.161.126>

This is an open access article under the CC BY-NC 4.0 license (<https://creativecommons.org/licenses/by-nc/4.0/>)

Материалы конференции

УДК 538.975

DOI: <https://doi.org/10.18721/JPM.161.126>

Особенности роста нитевидных нанокристаллов AlGaAs с квантовыми точками InAs на поверхности кремния методом роста МПЭ

Р.Р. Резник^{1,2,3✉}, В.О. Гридчин^{1,2,3}, К.П. Котляр¹,
А.С. Драгунова^{2,4}, Н.В. Крыжановская⁴, Ю.Б. Самсоненко^{2,3},
И.П. Сошников², А.И. Хребтов¹, Г.Э. Цырлин^{1,2,3}

¹ Санкт-Петербургский государственный университет, Санкт-Петербург, Россия;

² Академический университет им. Ж.И. Алферова РАН, Санкт-Петербург, Россия;

³ Институт аналитического приборостроения РАН, Санкт-Петербург, Россия;

⁴ Национальный исследовательский университет «Высшая школа экономики», Санкт-Петербург, Россия

✉ r.reznik@spbu.ru

Аннотация. Методом молекулярно-пучковой эпитаксии были синтезированы AlGaAs нитевидные нанокристаллы с InAs квантовыми точками на поверхности кремния. Были исследованы морфологические и оптические свойства выращенных наноструктур. Важно отметить, что излучение из квантовых точек наблюдается в диапазоне длин волн от 780 до 970 нм. Сформулированы предположения о природе коротковолнового излучения квантовых точек. В частности, одной из причин может являться высокий уровень десорбции атомов индия и присутствие атомов галлия в каплях катализатора в процессе роста при температуре подложки 510 °С. Таким образом, наша работа открывает новые перспективы для интеграции прямозонных полупроводников с кремниевой пластиной.

Ключевые слова: III-V полупроводники, нитевидные нанокристаллы, квантовые точки, молекулярно-пучковая эпитаксия, кремний

Финансирование: Экспериментальные образцы были выращены при финансовой поддержке Санкт-Петербургского государственного университета в рамках исследовательского гранта № 93020138. Исследования морфологических свойств выращенных образцов были выполнены при поддержке Министерства науки и высшего образования Российской Федерации (госзадание № 0791-2020-0003). Исследования оптических свойств выращенных образцов были выполнены при финансовой поддержке гранта РФФИ № 21-72-00099.

Ссылка при цитировании: Резник Р.Р., Гридчин В.О., Котляр К.П., Драгунова А.С., Крыжановская Н.В., Самсоненко Ю.Б., Сошников И.П., Хребтов А.И., Цырлин Г.Э. Особенности роста нитевидных нанокристаллов AlGaAs с квантовыми точками InAs на поверхности кремния методом роста МПЭ // Научно-технические ведомости СПбГПУ. Физико-математические науки. 2023. Т. 16. № 1.1. С. 153–157. DOI: <https://doi.org/10.18721/JPM.161.126>

Статья открытого доступа, распространяемая по лицензии CC BY-NC 4.0 (<https://creativecommons.org/licenses/by-nc/4.0/>)

Introduction

Nowadays semiconductor materials based on III-V compounds attract increased attention for optoelectronic applications due to their direct band gap nature [1]. With a decrease in the size of such materials below the de Broglie wavelength, they begin to exhibit quantum properties, which allow the creation of new generation devices [2]. Of particular interest are combinations of objects with different dimensionalities. For example, modern methods of creating nanostructures make it possible to form in the body of nanowires (NWs) narrow-gap nanoobjects – quantum dots (QDs) [3]. The size and density of such QDs can be strictly determined by the growth parameters and the NW itself can act as a waveguide for directional emission from the QDs [4]. It is important to note that, due to the unique morphology of the NWs, such structures can be synthesized on mismatched surfaces [5–7], which makes it possible to advance in solving the problem of integrating III-V direct-gap nanostructures with silicon technology [5, 6]. Our previous successes in the formation of such structures were associated with synthesis InAsP QDs in InP NWs [8, 9] and GaAs QDs in AlGaAs NWs [10–13] on the surfaces of a silicon wafers by molecular-beam epitaxy (MBE) technique. In particular, it was shown that nanostructures based on GaAs QDs in AlGaAs NW are efficient and directed sources of single photons in the wavelength range of 750–800 nm [14, 15], which indicates the promise of their application for quantum informatics. However, in this case, the change in the emission wavelength occurs due to the change in the size of the QDs and is strictly limited. Therefore, to increase the number of applications based on QDs in NWs, it is necessary to expand the range of QDs materials.

In this work, in order to shift quantum light sources emission to longer wavelengths, AlGaAs NWs with InAs QDs were synthesized by MBE.

© Резник Р.Р., Гридчин В.О., Котляр К.П., Драгунова А.С., Крыжановская Н.В., Самсоненко Ю.Б., Сошников И.П., Хребтов А.И., Цырлин Г.Э., 2023. Издатель: Санкт-Петербургский политехнический университет Петра Великого.

Materials and Methods

Experimental samples were synthesized using Riber Compact 21 MBE setup equipped with Gallium (Ga), Indium (In), Arsenic (As) effusion sources and additional chamber for metallization. On the preliminary stage Si(111) wafers were cleaned in 10:1 aqueous solution of HF. Then silicon substrates were immediately loaded into the metallization chamber and were heated up to the 850 °C for 20 minutes. After thermal cleaning of the substrates their temperature was decreased to 550 °C. After stabilization of the substrates temperature a thin layer of Au was deposited on the wafers surface for following Au-droplets formation during 50 seconds. After that temperature of the wafer was cooled down to room temperature and substrates were transferred into the growth chamber without the violation of ultrahigh-vacuum conditions where they were heated to 510 °C. The growth of nanostructures was carried out in several stages. Firstly, Ga, Al and As sources were opened for AlGaAs NWs growth for 13 minutes. Then the Al and Ga sources were closed and the In source was opened at the same time for InAs QDs formation during 5 seconds. Finally, the In source was closed and Al and Ga sources were opened for following growth of AlGaAs NWs during 14 minutes. During the entire growth, the fluxes from the sources were constant and corresponded to the growth rates of the planar layers 0.7 monolayers per second (ML/s) for Ga, 0.3 ML/s for Al and 0.4 ML/s according previous calibrations in GaAs(100) surface. Reflection high-energy electron diffraction (RHEED) patterns dynamics observation showed wurzite crystallographic structure formed already after 1 minute of growth.

The morphological properties of grown experimental samples were studied by scanning electron microscopy (SEM) using Supra 25 Zeiss microscope. Optical properties of samples were studied with the use of the macro-photoluminescence (PL) technique at 77 K.

Results and Discussion

Figure 1 shows the typical SEM image of nanostructures grown on Si(111) substrate. It can be seen from the figure that the average AlGaAs NWs height is 1.6 μm . At the same time, the diameter of NWs is not inhomogeneous in height, since NWs have a pencil shape. The NWs diameter is 140 nm at the base and 15 nm at the top. It is important to note, that most of the AlGaAs NWs formed in the $\langle 111 \rangle$ direction. This fact indicates the epitaxial nature of NW growth on the silicon surface.

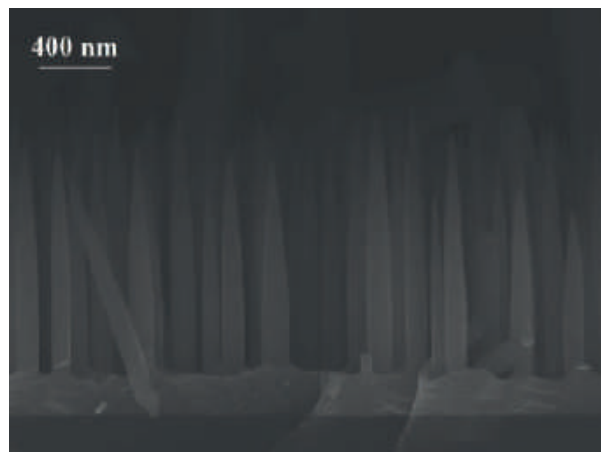


Fig.1. Typical SEM image of AlGaAs NWs with InAs QDs grown on Si(111) substrate

Typical PL spectrum corresponding to emission from InAs QDs is shown in Fig. 2. As can be seen from the figure, emission from QDs is observed in the wavelength range from 780 to 970 nm. However, it is well-known that bulk InAs emits in the longer wavelength range. One of the explanations for the shorter wavelength emission from the grown nanostructures can be a significant desorption of In atoms from the catalyst droplets at 510 °C and the presence of Ga atoms in this droplet. Thus, the chemical composition of QDs can correspond to InGaAs solid solution. Moreover, the presence of size quantization and mechanical stresses due to the mismatch of lattice parameters can also lead to a shift in the wavelengths of emission to the short-wavelength region. Detailed studies of this phenomenon nature will be carried out in subsequent works.

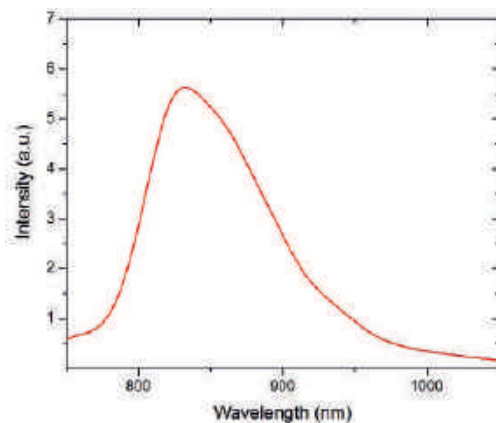


Fig. 2. Typical PL spectrum at room temperature corresponding to emission from InAs QDs

Conclusion

In conclusion, AlGaAs NWs with InAs QDs on the silicon surface were synthesized by MBE. Morphological and optical properties of grown nanostructures were studied. It is important to note, that emission from QDs is observed in the wavelength range from 780 to 970 nm. Assumptions about the nature of short-wave radiation from QDs were formulated. In particular, one of the reasons may be the significant desorption of indium atoms and the presence of gallium atoms in the catalyst droplets during growth at the substrate temperature of 510 °C. Our work, therefore, opens new prospects for integration of direct bandgap semiconductors with silicon platform.

Acknowledgments

The samples were grown under financial support of St. Petersburg State University research grant 93020138. Morphological properties measurements were done under support of Ministry of Science and Higher Education of the Russian Federation (state task no. 0791-2020-0003). Optical studies of grown samples were done under financial support of the Russian Science Foundation Grant no. 21-72-00099.

REFERENCES

1. Dubrovskii V.G., Cirlin G.E., Ustinov V.M., Semiconductor nanowhiskers: synthesis, properties, and applications, *Semiconductors*. 43 (12) (2009) 1539–1584.
2. Wallquist M., Hammerer K., Rabl P., Lukin M., Zoller P., Hybrid quantum devices and quantum engineering, *Physica Scripta*, 2009 (T137) (2009) 014001.
3. Heiss M., Fontana Y., Gustafsson A., Wüst G., Magen C., O’regan D. D., Luo J. W., Ketterer B., Conesa-Boj S., Kuhlmann A.V., Houel J., Russo-Averchi E., Morante J.R., Cantoni M., Marzari N., Arbiol J., Zunger A., Warburton R.J., Fontcuberta i Morral A., Self-assembled quantum dots in a nanowire system for quantum photonics, *Nature materials*. 12 (5) (2013) 439–444.
4. Reznik R.R., Morozov K.M., Krestnikov I.L., Kotlyar K.P., Soshnikov I.P., Leandro L., Akopian N., Cirlin G.E., Directional Radiation from GaAs quantum dots in AlGaAs nanowires, *Technical Physics Letters*. 47 (5) (2021) 405–408.
5. Glas F., Critical dimensions for the plastic relaxation of strained axial heterostructures in free-standing nanowires, *Physical Review B*. 74 (12) (2006) 121302.
6. Chuang L.C., Moewe M., Chase C., Kobayashi N.P., Chang-Hasnain C., Crankshaw S., Critical diameter for III-V nanowires grown on lattice-mismatched substrates, *Applied physics letters*. 90 (4) (2007) 043115.
7. Moewe M., Chuang L.C., Dubrovskii V.G., Chang-Hasnain C., Growth mechanisms and crystallographic structure of InP nanowires on lattice-mismatched substrates, *Journal of Applied Physics*. 104 (4) (2008) 044313.
8. Reznik R.R., Cirlin G.E., Shtrom I.V., Khrebtov A.I., Soshnikov I.P., Kryzhanovskaya N.V., Moiseev E.I., Zhukov A.E., Coherent growth of InP/InAsP/InP nanowires on a Si (111) surface by molecular-beam epitaxy, *Technical Physics Letters*. 44 (2) (2018) 112–114.

9. Cirlin G.E., Reznik R.R., Samsonenko Y.B., Khrebtov A.I., Kotlyar K.P., Ilkiv I.V., Soshnikov I.P., Kirilenko D.A., Kryzhanovskaya N.V., Phosphorus-Based Nanowires Grown by Molecular-Beam Epitaxy on Silicon, *Semiconductors*. 52 (11) (2018) 1416–1419.
10. Leandro L., Reznik R., Clement J.D., Repun J., Reynolds M., Ubyivovk E.V., Shtrom I.V., Cirlin G., Akopian N., Wurtzite AlGaAs Nanowires, *Scientific reports*. 10 (1) (2020) 1–6.
11. Cirlin G.E., Reznik R.R., Shtrom I.V., Khrebtov A.I., Samsonenko Y.B., Kukushkin S.A., Kasama T., Akopian N., Leonardo L., Hybrid GaAs/AlGaAs nanowire—quantum dot system for single photon sources, *Semiconductors*. 52 (4) (2018) 462–464.
12. Cirlin G.E., Shtrom I.V., Reznik R.R., Samsonenko Y.B., Khrebtov A.I., Bouravleuv A.D., Soshnikov I.P., Hybrid AlGaAs/GaAs/AlGaAs nanowires with a quantum dot grown by molecular beam epitaxy on silicon, *Semiconductors*. 50 (11) (2016) 1421–1424.
13. Leandro L., Hastrup J., Reznik R., Cirlin G., Akopian N., Resonant excitation of nanowire quantum dots, *npj Quantum Information*. 6 (1) (2020) 1–5.
14. Leandro L., Gunnarsson C.P., Reznik R., Juns K.D., Shtrom I., Khrebtov A., Kasama T., Zwiller V., Cirlin G., Akopian N., Nanowire quantum dots tuned to atomic resonances, *Nano letters*. 18 (11) (2018) 7217–7221.
15. Cirlin G.E., Reznik R.R., Shtrom I.V., Khrebtov A.I., Soshnikov I.P., Kukushkin S.A., Leandro L., Kasama T., Akopian N., AlGaAs and AlGaAs/GaAs/AlGaAs nanowires grown by molecular beam epitaxy on silicon substrates, *Journal of Physics D: Applied Physics*. 50 (48) (2017) 484003.

THE AUTHORS

REZNIK Rodion R.

moment92@mail.ru

ORCID: 0000-0003-1420-7515

GRIDCHIN Vladislav O.

gridchinvo@yandex.ru

ORCID: 0000-0002-6522-3673

KOTLYAR Konstantin P.

konstantin21kt@gmail.com

ORCID: 0000-0002-0305-0156

DRAGUNOVA Anna S.

anndra@list.ru

ORCID: 0000-0002-0181-0262

KRYZHANOVSKAYA Natalia V.

nataliakryzh@gmail.com

ORCID: 0000-0002-4945-9803

SAMSONENKO Yurii B.

yu_samsonenko@mail.ru

ORCID: 0000-0002-7119-3925

SOSHNIKOV Ilya P.

ipsosh@beam.ioffe.ru

ORCID: 0000-0002-9001-7599

KHREBTOV Artem I.

khrebtovart@mail.ru

ORCID: 0000-0001-5515-323X

CIRLIN George E.

george.cirlin@mail.ru

ORCID: 0000-0003-0476-3630

Received 27.10.2022. Approved after reviewing 21.11.2022. Accepted 21.11.2022.

Conference materials

UDC 538.911

DOI: <https://doi.org/10.18721/JPM.161.127>

Formation of a dielectric sublayer heterostructure of lead-tin telluride

A.K. Kaveev ¹✉

¹Ioffe Institute, Saint-Petersburg, Russia

✉ kaveev@mail.ioffe.ru

Abstract. We have optimized the growth parameters of the buffer layer for further $\text{Pb}_{1-x}\text{Sn}_x\text{Te}$ ($x \geq 0.4$) deposition from the point of view of smoothness and crystalline quality. The latter has the properties of a crystalline topological insulator. A three-component heterostructure consisting of fluorite CaF_2 , BaF_2 , and cubic $\text{Pb}_{0.7}\text{Sn}_{0.3}\text{Te}:\text{In}$ layers was formed on the Si(111). The surface morphology of this hybrid heterostructure was studied depending on the growth temperature and the thickness.

Keywords: Molecular beam epitaxy, $\text{Pb}_{0.7}\text{Sn}_{0.3}\text{Te}$, topological insulators

Citation: Kaveev A.K., Formation of a dielectric sublayer heterostructure of lead-tin telluride, St. Petersburg State Polytechnical University Journal. Physics and Mathematics. 16 (1.1) (2023) 158–161. DOI: <https://doi.org/10.18721/JPM.161.127>

This is an open access article under the CC BY-NC 4.0 license (<https://creativecommons.org/licenses/by-nc/4.0/>)

Материалы конференции

УДК 538.911

DOI: <https://doi.org/10.18721/JPM.161.127>

Формирование диэлектрической гетероструктуры-подслоя для получения пленок теллурида свинца-олова

A.K. Кавеев ¹✉

¹Физико-технический институт им. А.Ф. Иоффе РАН, Санкт-Петербург, Россия

✉ kaveev@mail.ioffe.ru

Аннотация. Оптимизированы ростовые параметры буферного подслоя для дальнейшего нанесения пленок $\text{Pb}_{1-x}\text{Sn}_x\text{Te}$ ($x \geq 0.4$) с точки зрения планарности и кристаллического качества. Трехкомпонентная гетероструктура, состоящая из слоев CaF_2 , BaF_2 , и $\text{Pb}_{0.7}\text{Sn}_{0.3}\text{Te}:\text{In}$ сформирована на поверхности Si(111). Изучено влияние температуры роста и толщины на морфологию поверхности гетероструктуры.

Ключевые слова: молекулярно-лучевая эпитаксия, $\text{Pb}_{0.7}\text{Sn}_{0.3}\text{Te}$, топологические изоляторы

Ссылка при цитировании: Кавеев А.К. Формирование диэлектрической структуры-подслоя для теллурида свинца-олова // Научно-технические ведомости СПбГПУ. Физико-математические науки. 2023. Т. 16. № 1.1. С. 158–161. DOI: <https://doi.org/10.18721/JPM.161.127>

Статья открытого доступа, распространяемая по лицензии CC BY-NC 4.0 (<https://creativecommons.org/licenses/by-nc/4.0/>)

Introduction

Crystalline topological insulators (TIs) based on the $\text{Pb}_{1-x}\text{Sn}_x\text{Te}$ compound are promising from the point of view of practical applications [1], due to the possibility of creating TIs with a volume less shunting the conductivity of topological states due to the possibility of controlling the composition (x value), in contrast to the already classical TIs based on V_2VI_3 compounds. In addition to controlling the composition, it is equally important to obtain low-defect $\text{Pb}_{1-x}\text{Sn}_x\text{Te}$ films,



also from the point of view of reducing the shunting effect of the volume. This task is non-trivial due to the problems that arise during the epitaxial growth of $\text{Pb}_{1-x}\text{Sn}_x\text{Te}$. To ensure the presence of conducting topological states, it is necessary to obtain a planar layer with a high crystalline quality.

Materials and Methods

CaF_2 , BaF_2 and $\text{Pb}_{1-x}\text{Sn}_x\text{Te}$ films were deposited on Si(111) surface with use of conventional molecular beam epitaxy method, using a single crucible. Si mono-crystalline substrates were cleaned by Shiraki method [2] which represents sequential growth and etching of an oxide layer on the substrate. The final oxide layer was thermally eliminated in the growth chamber with formation of Si (111) 7×7 surface reconstruction. The crystallinity and epitaxial relations of the grown layers were controlled by in-situ reflection high energy electron diffraction (RHEED). The surface morphology was studied using atomic force microscopy technique in semi-contact mode.

Results and Discussion

In this work, optimization of the buffer layer for further deposition of $\text{Pb}_{1-x}\text{Sn}_x\text{Te}$ ($x \geq 0.4$), which has topological properties, was carried out. For this purpose, a multilayer structure consisting of CaF_2 , BaF_2 , and $\text{Pb}_{0.7}\text{Sn}_{0.3}\text{Te}:\text{In}$ layers was deposited on the Si(111) surface. It is known that $\text{BaF}_2/\text{CaF}_2/\text{Si}(111)$ binary buffer layers were used for the epitaxial growth of $\text{Pb}_{1-x}\text{Sn}_x\text{Te}$ films on silicon [3]. At the same time, the height of the surface relief of the resulting buffer layers was too high due to insufficient optimization of the growth parameters and imperfection of these layers. It is known [4] that calcium fluoride, when applied to the (111) silicon surface by molecular beam epitaxy, forms layers of high crystalline quality, but different surface morphology, depending on the deposition temperature. The formation of islands of various heights and lateral sizes is possible. In this work, it was necessary to provide the smoothest possible surface. For this, the temperature regimes and the thickness of the calcium fluoride layer were varied. Next, a layer of barium fluoride was deposited on the surface of calcium fluoride, providing a smoother transition in the lattice constant from CaF_2 to $\text{Pb}_{1-x}\text{Sn}_x\text{Te}$. Figure 1, *a–g* shows a number of atomic force microscopy images of a $\text{BaF}_2/\text{CaF}_2/\text{Si}(111)$ heterostructure of various configurations. A number of parameters were determined that provide a combination of thin fluorite sublayers (which ensures their low imperfection) with their high smoothness. It has been shown that a decrease in the growth temperature of calcium fluoride and barium fluoride leads to a decrease in the lateral dimensions of the islands. The smoothest surface relief is achieved at low growth temperatures (250°C). This correlates with the results of [5], where the high planarity of calcium fluoride films with a thickness of a unit of nanometers deposited at a given temperature was demonstrated. Attempts to increase the growth temperature of one of the two sublayers in order to improve the crystalline quality lead to an enlargement of the islands and coarsening of the relief, which is undesirable for the task of obtaining the smoothest layers posed in this work. It is also sometimes possible to form cracks in the film due to the difference in temperature expansion coefficients. At the same time, a fairly smooth relief is also obtained using two-stage (low and high temperatures) growth of calcium fluoride, followed by a low-temperature deposition of a layer of barium fluoride (Fig. 1, *e*). At the same time, direct deposition of a thin layer of $\text{Pb}_{1-x}\text{Sn}_x\text{Te}$ on a fluorite bilayer does not provide sufficient smoothness and sufficient crystalline quality for the formation of topological states. Good quality can be achieved only with the help of homoepitaxial growth of this material on a sufficiently thick sublayer. In this case, it is also necessary to achieve a low conductivity of this sublayer by doping it, which ensures the regulation of the position of the Fermi level. The experiments performed with fluorite bilayers made it possible to proceed to experiments with the deposition of the third buffer sublayer, the dielectric $\text{Pb}_{0.7}\text{Sn}_{0.3}\text{Te}:\text{In}$. This sublayer was grown at various temperatures from 250 to 450°C (Fig. 1, *h*, and Fig. 2). The experiments also showed the importance of applying large (more than 500 nm) thicknesses of this sublayer to ensure its continuity, the absence of holes in the film, and to achieve a high surface planarity.

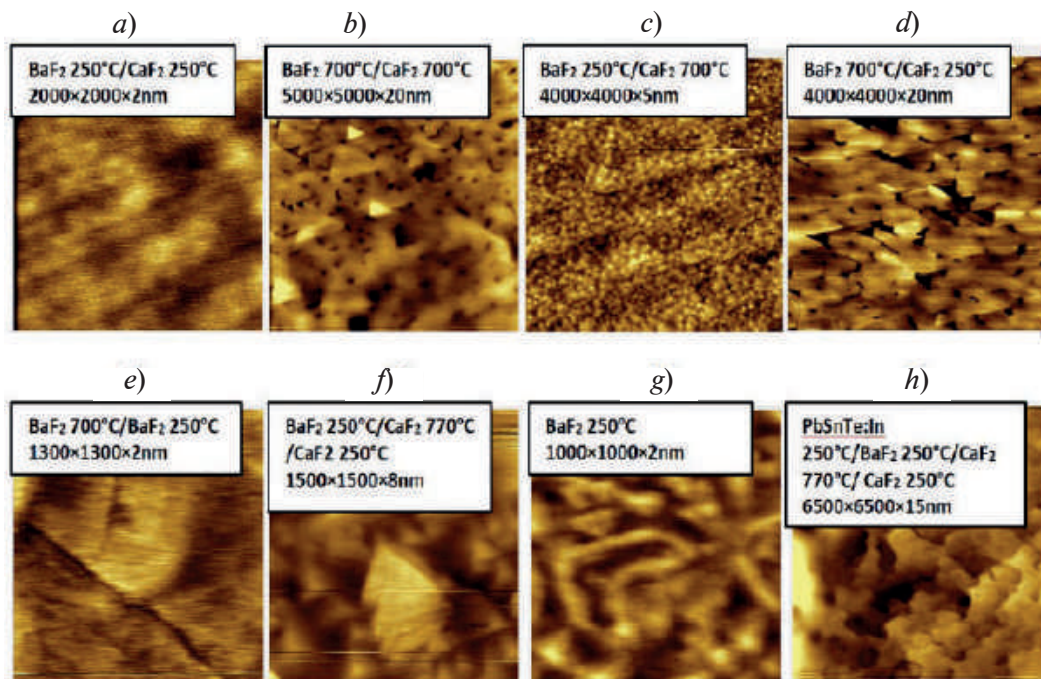


Fig. 1. Surface morphology of the BaF₂/CaF₂ buffer layer (a–g), grown under different conditions, and the optimized Pb_{0.7}Sn_{0.3}Te:In/BaF₂/CaF₂/Si(111) buffer layer (h). (a–d) BaF₂ and CaF₂ thickness is 20 and 10 nm, respectively. Layer thicknesses are 10 and 3 nm (e), 15, 7, and 3 nm (f), 20 nm (g), 300, 15, 7, and 3 nm (h)

Figure 2 shows examples of the surface morphology of the third buffer sublayer obtained under various conditions. The dielectric properties of this sublayer will be measured at the next stage of work by conducting electro-physical measurements. In the future, thin (10–20 nm) layers of stoichiometry close to Pb_{0.6}Sn_{0.4}Te with an excess of Sn will be deposited on this sublayer, providing the presence of conducting topological states. The evolution of the surface during the formation of a three-layer buffer layer was studied in situ using RHEED technique.

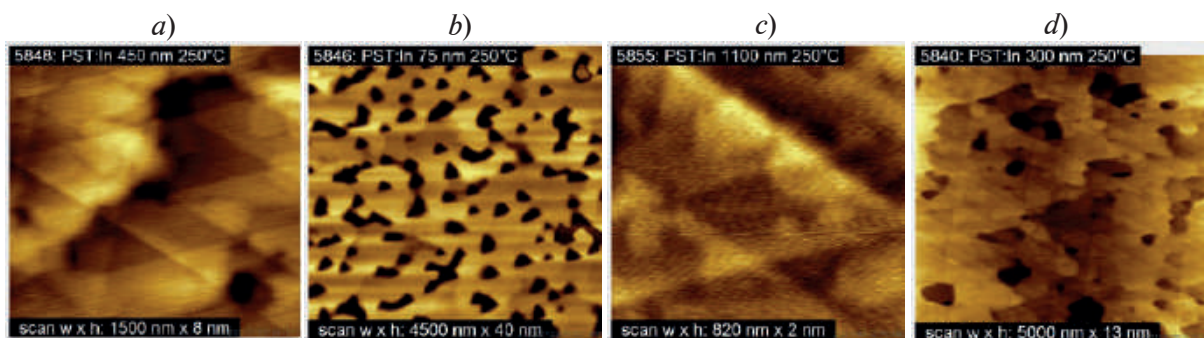


Fig. 2. Morphology of the surface of the third buffer sublayer Pb_{0.7}Sn_{0.3}Te:In depending on the growth conditions. (a) – deposition of BaF₂ and CaF₂ on the bilayer with parameters corresponding to Fig. 1, f; (b) – the same but thinner Pb_{0.7}Sn_{0.3}Te:In layer; (c) – deposition of BaF₂ and CaF₂ on the bilayer with parameters corresponding to Fig. 1, a; (d) – the same parameters, but a thinner Pb_{0.7}Sn_{0.3}Te:In layer grown a lower temperature

Figure 3 shows the change in RHEED patterns upon successive deposition of 10 nm calcium fluoride (a), 15 nm barium fluoride (b), and 1000 nm Pb_{0.7}Sn_{0.3}Te:In at the initial (c) and final (d) moment of growth at a temperature of 250 °C. It can be seen that calcium and barium fluorides grow in a planar manner, as evidenced by the streaks in the RHEED patterns. Further, at the initial stage of growth, the three-dimensional (island) growth of Pb_{0.7}Sn_{0.3}Te:In occurs.



Twinning of the reflections indicates a two-domain character of growth, which is characteristic of a cubic crystal lattice with a (111) growth surface. In our earlier work [6], trial experiments were carried out on the deposition of thin $\text{Pb}_{0.7}\text{Sn}_{0.3}\text{Te}$ films on Si(111) using a calcium fluoride buffer sublayer. Epitaxial relations with respect to silicon were established: (111) $\text{Pb}_{0.7}\text{Sn}_{0.3}\text{Te} \parallel (111)$ Si, $[\bar{1}\bar{2}1]$ $\text{Pb}_{0.7}\text{Sn}_{0.3}\text{Te} \parallel [2\bar{1}\bar{1}]$ Si. In the present case, these relations are obviously preserved. With an increase in the thickness of the deposited material, point reflections are replaced by streaks, which indicate the fusion of islands (the Stranski-Krastanov growth regime) and the formation of a smooth surface. This RHEED pattern (Fig. 3, *d*) is in accordance with Fig. 2, *d*, which indeed demonstrates a smooth surface with characteristic dislocation glide plane exits at an angle of 60° , also characteristic of the growth surface (111) of the cubic crystal lattice.

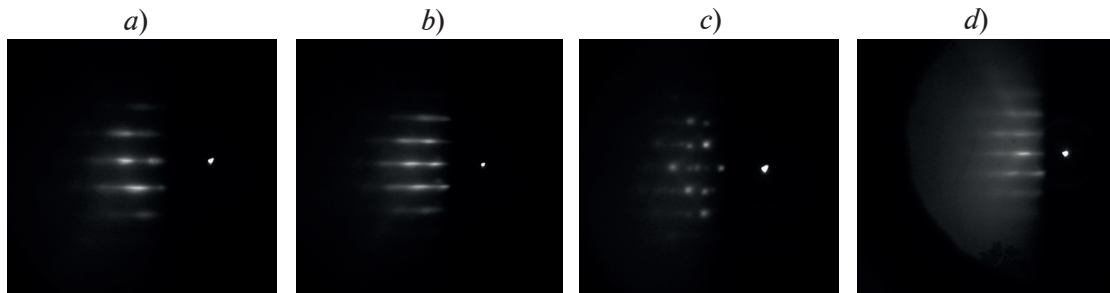


Fig. 3. Changes in RHEED patterns upon deposition of 10 nm calcium fluoride (*a*), 15 nm barium fluoride (*b*), and 1000 nm $\text{Pb}_{0.7}\text{Sn}_{0.3}\text{Te}:\text{In}$ at initial (*c*) and final (*d*) moment of growth at a temperature of 250°C

Conclusion

As a result of this work, a number of growth regimes were sorted out and growth parameters were optimized for the three-layer epitaxial heterostructure $\text{Pb}_{0.7}\text{Sn}_{0.3}\text{Te}:\text{In}/\text{BaF}_2/\text{CaF}_2/\text{Si}(111)$. The possibility of planar low-defect growth of the third sublayer – $\text{Pb}_{0.7}\text{Sn}_{0.3}\text{Te}:\text{In}$, is shown, which is necessary for further homoepitaxial growth of $\text{Pb}_{1-x}\text{Sn}_x\text{Te}$ with an increased value of the parameter $x \geq 0.4$ in order to obtain topological surface states.

REFERENCES

1. Hsieh T.H., Lin H., Liu J., Duan W., Bansil A. and Fu L., Topological crystalline insulators in the SnTe material class, *Nature communications*. 3 (982) (2012) 1–7.
2. Ishizaka A. and Shiraki Y., Low Temperature Surface Cleaning of Silicon and Its Application to Silicon MBE, *Journal of Electrochemical Society*. 133 (1986) 666–671.
3. Akimov A., Belenchuk A., Klimov A., Kachanova M., Neizvestny I., Suprun S., Shapoval O., Sherstyakova V. and Shumsky V., Thin-film $\text{PbSnTe}:\text{In}/\text{BaF}_2/\text{CaF}_2/\text{Si}$ structures for monolithic matrix photodetectors operating in the far infrared range, *Technical Physics Letters*. 35 (2009) 524–527.
4. Lucas C., Loretto D. and Wong G., Epitaxial growth mechanisms and structure of $\text{CaF}_2/\text{Si}(111)$, *Physical Review B* 50 (1994) 14340–14353.
5. Illarionov Y., Bانشchikov A., Polyushkin D., Watcher S., Knobloch T., Thesberg M., Mennel L., Paur M., Stoger-Pollach M., Steiger-Thirsfeld A., Vexler M., Waltl M., Sokolov N., Mueller T. and Grasser T., Ultrathin calcium fluoride insulators for two-dimensional field-effect transistors, *Nature Electronics*. 2 (2019) 230–235.
6. Kaveev A., Bondarenko D., Tereshchenko O., Structural Characterization of $\text{Pb}_{0.7}\text{Sn}_{0.3}\text{Te}$ Crystalline Topological Insulator Thin Films Grown on Si(111), *Semiconductors*. 55 (8) (2021) 625–628.

THE AUTHORS

KAVEEV Andrey K.

kaveev@mail.ioffe.ru

Received 28.10.2022. Approved after reviewing 14.11.2022. Accepted 14.11.2022.

Conference materials

UDC 537.9

DOI: <https://doi.org/10.18721/JPM.161.128>

Dislocation-related photoluminescence in self-implanted silicon with different surface orientation

D.S. Korolev ¹✉, A.N. Tereshchenko ², A.A. Nikolskaya ¹,
A.N. Mikhaylov ¹, A.I. Belov ¹, D.I. Tetelbaum ¹

¹Lobachevsky University, Nizhny Novgorod, Russia;

²Institute of Solid State Physics RAS, Chernogolovka, Russia

✉ dmkorolev@phys.unn.ru

Abstract. The regularities of the influence of initial substrate orientation and annealing conditions on the intensity and temperature dependence of the D1 luminescence line for the *p*-type silicon samples implanted with silicon ions followed by subsequent annealing are studied. It is shown that the luminescent properties of the samples depend both on surface orientation and on annealing temperature. For a silicon sample with (111) surface orientation, under certain heat treatment conditions, an anomalous temperature dependence of the D1 line intensity is demonstrated with the appearance of a second maximum in this dependence at temperatures of about 80 K.

Keywords: silicon, ion implantation, annealing, photoluminescence

Funding: The work was supported by the Grant of the President of Russian Federation (МК-4092.2021.1.2) and partially within the framework of the state task of the Institute of Solid State Physics RAS.

Citation: Korolev D.S., Tereshchenko A.N., Nikolskaya A.A., Mikhaylov A.N., Belov A.I., Tetelbaum D.I., Dislocation-related photoluminescence in self-implanted silicon with different surface orientation. St. Petersburg State Polytechnical University Journal. Physics and Mathematics. 16 (1.1) (2023) 162–166. DOI: <https://doi.org/10.18721/JPM.161.128>

This is an open access article under the CC BY-NC 4.0 license (<https://creativecommons.org/licenses/by-nc/4.0/>)

Материалы конференции

УДК 537.9

DOI: <https://doi.org/10.18721/JPM.161.128>

Дислокационная фотолюминесценция в самоимплантированном кремнии с различными ориентациями поверхности

Д.С. Королев ¹✉, А.Н. Терещенко ², А.А. Никольская ¹,
А.Н. Михайлов ¹, А.И. Белов ¹, Д.И. Тетельбаум ¹

¹Нижегородский государственный университет им. Н.И. Лобачевского, г. Нижний Новгород, Россия;

²Институт физики твердого тела РАН, г. Черноголовка, Россия

✉ dmkorolev@phys.unn.ru

Аннотация. Исследованы закономерности влияния ориентации исходной подложки и условий постимплантационного отжига на интенсивность и температурную зависимость интенсивности линии D1 для образцов кремния *p*-типа, имплантированного ионами кремния, с последующим отжигом. Показано, что люминесцентные свойства образцов зависят как от ориентации поверхности, так и от температуры отжига. Для образца Si (111) при определенных условиях термообработки продемонстрировано anomalous поведение температурной зависимости интенсивности линии D1 с появлением второго максимума на этой зависимости при температурах порядка 80 K.

Ключевые слова: кремний, ионная имплантация, отжиг, фотолюминесценция



Финансирование: Работа поддержана грантом Президента РФ (МК-4092.2021.1.2) и частично выполнена при поддержке в рамках государственного задания Института физики твердого тела РАН.

Ссылка при цитировании: Королев Д.С., Терещенко А.Н., Никольская А.А., Михайлов А.Н., Белов А.И., Тетельбаум Д.И. Дислокационная фотолуминесценция в самоимплантированном кремнии с различными ориентациями поверхности // Научно-технические ведомости СПбГПУ. Физико-математические науки. 2023. Т. 16. № 1.1. С. 162–166. DOI: <https://doi.org/10.18721/JPM.161.128>

Статья открытого доступа, распространяемая по лицензии CC BY-NC 4.0 (<https://creativecommons.org/licenses/by-nc/4.0/>)

Introduction

The task of creating an efficient silicon-based light emitting source remains one of the most important problems of modern optoelectronics. The indirect bandgap of this semiconductor leads to a low probability of radiative interband transitions. To date, there are several approaches to solving this problem. The most thoroughly studied among them are the formation of silicon nanocrystals in dielectric matrices, the formation of A_3B_5/Si hybrid structures, the introduction of erbium into silicon structures [1, 2] as well as synthesis of light-emitting precipitates of iron disilicide $\beta\text{-FeSi}_2$ [3] and implantation of rare-earth ions into silicon [4, 5]. However, using the abovementioned approaches, it was not possible to achieve the emission intensity sufficient for the use in optoelectronic integrated circuits. One of the methods for creating light-emitting structures based on silicon can be the synthesis of dislocation-related luminescence (DL) centers, the main D1 line of which is at the “communication” wavelength of $\sim 1.5 \mu\text{m}$. The promise of this method was previously demonstrated for LED structures in which the DL centers were obtained by plastic deformation [6]. However, this method is incompatible with silicon technology. There are some other methods, such as laser melting [7, 8], mechanical polishing and annealing [9], growth of heterostructures such as SiGe/Si [10].

Previously, we demonstrated the possibility of formation of DL centers by self-implantation of silicon (implantation of Si^+ ions into silicon) and possibility of controlling the light-emitting properties of such structures by additional ion-beam and thermal treatment [11–13]. In particular, it was found that, in the samples additionally doped with boron, an anomalous behavior of the temperature dependence of the D1 line photoluminescence intensity is observed, which consists in the appearance of an additional peak in the temperature region of 60–100 K, which was not previously observed [13, 14]. However, for the silicon samples in which the dislocation structure was obtained by plastic deformation, different luminescence behavior was shown for the samples with different surface orientations [6].

In this work, the features of the luminescence properties of the $p\text{-Si}$ samples with different surface orientations, in which DL centers are formed by implantation of Si^+ ions followed by annealing in different atmospheres, are studied.

Materials and Methods

$P\text{-Cz-Si}$ with the (111) and (100) surface orientations and resistivity of 10 and 12 $\Omega\cdot\text{cm}$, respectively, were used as the initial samples. The formation of a dislocation structure was carried out by implantation of Si^+ ions with an energy of 100 keV and a dose of $1\cdot 10^{15} \text{ cm}^{-2}$ with subsequent thermal annealing at temperatures of 900 and 1100 $^\circ\text{C}$ in nitrogen and oxygen atmospheres (1 h). Previously, we have found that varying the annealing conditions (annealing temperature and atmosphere) leads to a significant change in the DL parameters [12], but the features of this process were not studied and silicon wafers with different types of conductivity were used as the initial samples. The photoluminescence (PL) was measured in the temperature range of 4.2–300 K by using a standard phase-sensitive technique with a cooled germanium photoresistance as a detector. PL was excited by photons with a wavelength of 920 nm at an optical excitation level of 10 mW/mm², corresponding to the linear part of the dependence of the PL intensity on the pump power.

Results and Discussion

Figure 1 shows the PL spectra (70 K) for the *p*-Si samples with different surface orientations irradiated with Si⁺ ions followed by annealing at 900 and 1100 °C in oxygen and nitrogen atmospheres. After implantation and annealing, a PL band appears in the spectra at a wavelength of ~ 1.5 μm, corresponding to the position of the D1 line of the DL, associated with the formation of a dislocation structure.

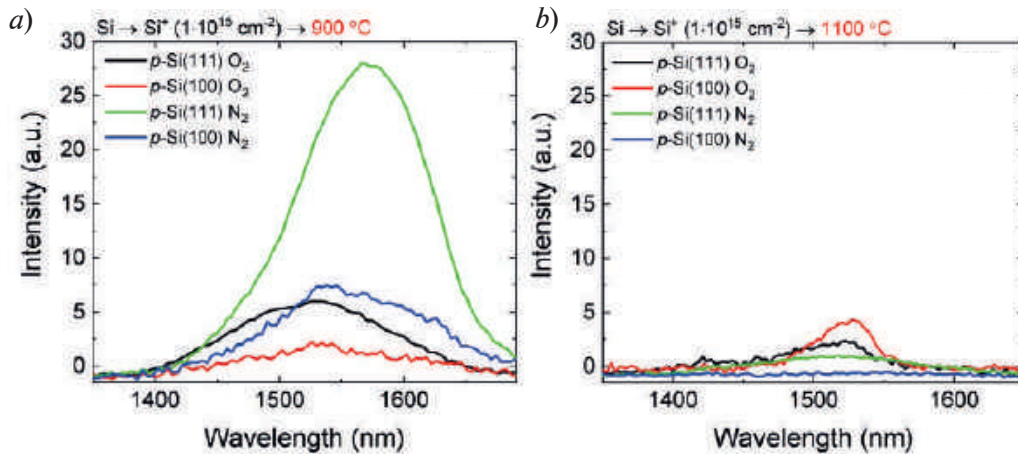


Fig. 1. PL spectra of the *p*-Si samples with different surface orientations irradiated with silicon ions after annealing at 900 (a) and 1100 °C (b) in nitrogen and oxygen atmospheres for 1 h

Annealing at a temperature of 900 °C leads to the appearance of the D1 DL line for all studied samples. Luminescence intensity of the samples after annealing in a nitrogen atmosphere is higher than that after annealing in an oxidizing atmosphere. A long-wavelength shift of the spectra is also observed for the samples after annealing in a nitrogen atmosphere. A comparison of the DL intensity for the samples annealed under the same conditions shows that, for the *p*-Si (111) samples, the intensity is much higher than that for the samples with (100) surface orientation. Increasing the annealing temperature to 1100 °C leads to a significant change in the PL spectra. Thus, for the case of annealing in an N₂ atmosphere, luminescence is practically not observed. In the case of annealing in an oxidizing atmosphere, the situation is opposite to that observed at a lower used annealing temperature: the luminescence intensity for the sample with the (100) surface orientation is higher than that for the sample with the (111) surface orientation. A noticeable shift in the position of the D1 line during annealing at a temperature of 1100 °C is not observed.

Let us consider the temperature dependence of the D1 DL line intensity. Figure 2 shows the temperature dependence of the intensity of the D1 line at the maximum for the *p*-Si samples with different surface orientations, irradiated with Si⁺ ions, followed by annealing in different atmospheres. A typical shape of the temperature dependence of the D1 line is a curve with a maximum at a temperature of ~ 20 K followed by rapid temperature quenching of the intensity to temperatures of 30–40 K [15]. At low temperatures (6–30 K), the Si (100) sample exhibits the highest DL intensity after annealing in an oxidizing atmosphere at 1100 °C. In this case, all the samples annealed at a temperature of 1100 °C demonstrate rapid thermal quenching of luminescence. The situation is somewhat different for the samples after annealing at a temperature of 900 °C. Thus, for the samples after annealing in a nitrogen atmosphere, the temperature quenching is less pronounced than for the samples annealed in oxygen. The most interesting result was obtained for the *p*-Si sample with (111) surface orientation after annealing in a nitrogen atmosphere: the luminescence intensity does not only decrease at temperatures above 30 K, but also increases up to 70 K. Significant quenching of the D1 line occurs only at temperatures above 150 K.

Let us now consider what the observed effect can be associated with. It was previously shown that the presence of additionally implanted boron atoms under certain implantation regimes leads to a similar behavior of the temperature dependence of the D1 line intensity – the presence of an additional high-temperature maximum on the temperature dependence, which may be due to the

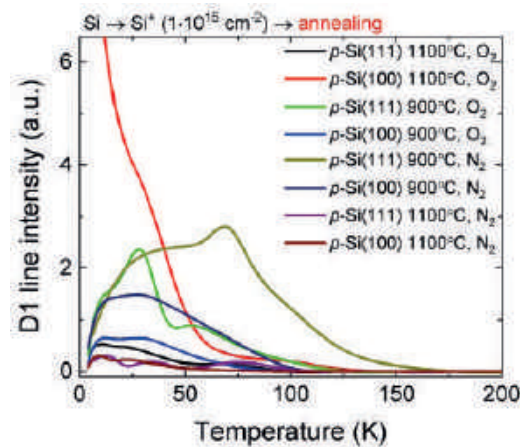


Fig. 2. Temperature dependence of the D1 line intensity for the *p*-Si samples with different surface orientations irradiated with Si⁺ ions with the dose of $1 \cdot 10^{15} \text{ cm}^{-2}$ after annealing in oxygen and nitrogen atmospheres at 900 and 1100 °C (1 h)

formation of boron-containing complexes that introduce additional energy levels into the band gap of silicon [15]. These levels can additionally “pump” charge carriers to light-emitting levels leading to an increase in the luminescence intensity at certain temperatures. Apparently, the formation of such complexes can also be expected in our case upon ion irradiation of the samples initially containing boron atoms. The nature of these complexes has not been fully established, however, apparently, their formation is dominated by intrinsic interstitial atoms formed during implantation process. The formation of interstitials does not significantly depend on the orientation of silicon crystal surface, but the diffusion of Frenkel pair components differs significantly for the crystals with different surface orientations [16]. Therefore, it should be expected that the formation of complexes of interstitials with boron atoms for the samples with (111) orientation occurs more efficiently than for the Si (100) samples. The presence of a high-temperature maximum in the temperature dependence for the samples after annealing at 900 °C indicates that these complexes persist at least up to this temperature. Increasing the annealing temperature to 1100 °C leads to the disappearance of this maximum probably due to the decomposition of such defect-impurity complexes.

Conclusion

The effect of surface orientation and post-implantation annealing conditions on the parameters of the D1 line of dislocation-related luminescence in self-implanted silicon has been studied. It is shown that annealing at a temperature of 900 °C leads to the appearance of more intense luminescence compared to the samples annealed at 1100 °C. The luminescence intensity in the Si (111) samples turns out to be noticeably higher than that for the Si (100) samples annealed under the same conditions. The most interesting fact is that, for the Si (111) sample, under certain heat treatment conditions, an anomalous temperature dependence of the intensity of the D1 line of dislocation-related photoluminescence is observed, and luminescence is retained up to the temperatures close to room temperature. This opens up prospects for the possible practical application of silicon light-emitting structures with dislocation-related luminescence in new-generation optoelectronic devices.

Acknowledgments

The work was supported by the Grant of the President of Russian Federation (MK-4092.2021.1.2) and partially within the framework of the state task of the Institute of Solid State Physics RAS.

REFERENCES

1. Pavesi L., Thirty Years in Silicon Photonics: A Personal View, *Front. Phys.* 9 (2021) 786028.
2. Saar A., Photoluminescence from silicon nanostructures: The mutual role of quantum confinement and surface chemistry, *J. Nanophoton.* 3 (2009) 032501.

3. Shevlyagin A.V., Goroshko D.L., Chusovitin E.A., Balagan S.A., Dotsenko S.A., Galkin K.N., Galkin N.G., Shamirzaev T.S., Gutakovskii A.K., Latyshev A.V., Iinuma M., Terai Y., A room-temperature-operated Si LED with β -FeSi₂ nanocrystals in the active layer: μ W emission power at 1.5 μ m, J. Appl. Phys. 121 (2017) 113101.
4. Zhou S., Milosavljevic M., Xia X., Gao Y., Lourenco M., Homewood K., Room-temperature 2 μ m luminescence from Tm doped silicon light emitting diodes and SOI substrates, Curr. Appl. Phys. 31 (2021) 38–45.
5. Sobolev N.A., Emel'yanov A.M., Filin Y.N., Melekh B.T., Nikolaev Y.A., Yakimenko A.N., Infrared photoluminescence from holmium ions in single-crystal silicon and holmium oxide, Semicond. Sci. Technol. 15 (2000) 511.
6. Kveder V.V., Steinman E.A., Shevchenko S.A., Grimmeiss H.G., Dislocation-related electroluminescence at room temperature in plastically deformed silicon, Physical Review B 51 (1995) 10520–10526.
7. Sveinbjornsson E.O., Weber J., Room temperature electroluminescence from dislocation-rich silicon, Appl. Phys. Lett. 69 (1996) 2686.
8. Menold T., Hadjixenophontos E., Lawitzki R., Schmitz G., Ametowobla M., Crystal defects in monocrystalline silicon induced by spot laser melting, J. Appl. Phys. 127 (2020) 093102.
9. Batalov R.I., Bayazitov R.M., Khusnullin N.M., Terukov E.I., Kudoyarova V.K., Mosina G.N., Andreev B.A., Kryzhkov D.I., Structure, Impurity Composition, and Photoluminescence of Mechanically Polished Layers of Single-Crystal Silicon, Phys. Solid State 47 (2005) 1–4.
10. Paul D.J., Si/SiGe heterostructures: from material and physics to devices and circuits, Semicond. Sci. Technol. 19 (2004) R75–R108.
11. Mikhaylov A.N., Belov A.I., Korolev D.S., Timofeeva A.O., Vasiliev V.K., Shushunov A.N., Bobrov A.I., Pavlov D.A., Tetelbaum D.I., Shek E.I., Effect of ion doping on the dislocation-related photoluminescence in Si⁺-implanted silicon, Semiconductors 48 (2014) 199–203.
12. Tetelbaum D.I., Mikhaylov A.N., Belov A.I., Korolev D.S., Shushunov A.N., Bobrov A.I., Pavlov D.A., Shek E.I., Sobolev N.A., Localization of dislocation-related luminescence centers in self-ion implanted silicon and effect of additional boron ion doping, Physica status solidi (c) 12 (2015) 84–88.
13. Tereshchenko A.N., Korolev D.S., Mikhaylov A.N., Belov A.I., Nikolskaya A.A., Pavlov D.A., Tetelbaum D.I., Steinman E.A., Effect of Boron Impurity on the Light-Emitting Properties of Dislocation Structures Formed in Silicon by Si⁺ Ion Implantation, Semiconductors 52 (2018) 843.
14. Nikolskaya A.A., Korolev D.S., Tereshchenko A.N., Pavlenkov V.I., Nagornyy S.N., Belov A.I., Vasiliev V.K., Mikhaylov A.N., Tetelbaum D.I., Temperature dependence of dislocation-related photoluminescence (D1) of self-implanted silicon subjected to additional boron implantation, NIMB 472 (2020) 32–35.
15. Sauer R., Weber J., Stolz J., Weber E.R., Küsters K., Alexander H., Dislocation-Related Photoluminescence in Silicon, Appl. Phys. A 36 (1985) 1–13.
16. Pichler P., Intrinsic Point Defects, Impurities, and Their Diffusion in Silicon, Springer-Verlag Wien, New York, 2004.

THE AUTHORS

KOROLEV Dmitry S.
dmkorolev@phys.unn.ru
ORCID: 0000-0003-1440-2994

MIKHAYLOV Alexey N.
mian@nifti.unn.ru
ORCID: 0000-0001-5505-7352

TERESHCHENKO Alexey N.
tan@issp.ac.ru
ORCID: 0000-0002-1018-1111

BELOV Alexey I.
belov@nifti.unn.ru
ORCID: 0000-0002-1222-7769

NIKOLSKAYA Alena A.
nikolskaya@nifti.unn.ru
ORCID: 0000-0001-6059-6684

TETELBAUM David I.
tetelbaum@phys.unn.ru
ORCID: 0000-0003-0396-7703

Received 28.10.2022. Approved after reviewing 14.11.2022. Accepted 23.11.2022.

Conference materials

UDC 621.382.2

DOI: <https://doi.org/10.18721/JPM.161.129>

Comprehensive study of the power capabilities of UV-C LEDs in pulsed and continuous modes

A.E. Ivanov^{1,2✉}, A.E. Chernyakov¹, A.L. Zakgeim¹

¹SHM R&E Center, RAS, St. Petersburg, Russia;

²St.-Petersburg State Electrotechnical University «LETI», St. Petersburg, Russia

✉ a-e-ivano-v@yandex.ru

Abstract. Data is reported on study of light-current characteristics and thermal properties of flip-chip AlGaIn UV-C LED over a wide range of excitation levels: up to 2 kA/cm² in pulse mode. The tailor-made microscope based on InAs matrix with photosensitivity in 2.5–3.1 μm range was employed for getting IR-intensity maps and revealing of temperature distribution across the emitting chips. The work is aimed at detailed study the factors limiting the energy capabilities of UV-C LEDs.

Keywords: power UV-C LED, thermal resistance, temperature mapping

Citation: Ivanov A.E., Chernyakov A.E., Zakgeim A.L., Comprehensive Study of the Power Capabilities of UV-C LEDs in Pulsed and Continuous Modes. St. Petersburg State Polytechnical University Journal. Physics and Mathematics. 16 (1.1) (2023) 167–171. DOI: <https://doi.org/10.18721/JPM.161.129>

This is an open access article under the CC BY-NC 4.0 license (<https://creativecommons.org/licenses/by-nc/4.0/>)

Материалы конференции

УДК 621.382.2

DOI: <https://doi.org/10.18721/JPM.161.129>

Комплексное исследование энергетических возможностей светодиодов UV-C в импульсном и непрерывном режимах

А.Е. Иванов^{1,2✉}, А.Е. Черняков¹, А.Л. Закгейм¹

¹НТЦ микроэлектроники РАН, Санкт-Петербург, Россия;

²СПбГЭТУ «ЛЭТИ», Санкт-Петербург, Россия

✉ a-e-ivano-v@yandex.ru

Аннотация. Представлены данные по исследованию электрооптических характеристик и тепловых свойств «флип-чип» AlGaIn светодиодов UV-C в широком диапазоне токов: до 2 кА/см² в импульсном режиме. С помощью ИК-микроскопа получены карты распределения температуры по СД чипу. Работа направлена на детальное изучение факторов, ограничивающих энергетические возможности светодиодов UV-C.

Ключевые слова: мощные UV-C светодиоды, тепловое сопротивление, температурный мэппинг

Ссылка при цитировании: Иванов А.Е., Черняков А.Е., Закгейм А.Л. Комплексное исследование энергетических возможностей светодиодов UV-C в импульсном и непрерывном режимах // Научно-технические ведомости СПбГПУ. Физико-математические науки. 2023. Т. 16. № 1.1. С. 167–171. DOI: <https://doi.org/10.18721/JPM.161.129>

Статья открытого доступа, распространяемая по лицензии CC BY-NC 4.0 (<https://creativecommons.org/licenses/by-nc/4.0/>)

Introduction

UV-C light emitting diodes (LEDs) are environmentally friendly, mercury free, and nonpolluting sources of UV radiation in contrast to traditional mercury sources. The sterilization wavelength is concentrated between 260 and 280 nm. Studies have documented the wide use of UV-C LEDs in medical phototherapy and in the disinfection and sterilization of water, food, and medicine for safe consumption [1–3]. Traditional mercury UV lamps are disadvantaged by their long warm-up times, short lifetime, risk of exploding and environmental pollution; UV-C LEDs are superior in all aforementioned aspects [4].

The driving current, chip area of UV-C LEDs and the level of integration of LED matrixes are continuously increased to provide ever higher output light flux. The new developments require pay more attention to achieving the maximum possible radiation power while maintaining an acceptable efficiency. In other words, elucidation of the main factors of an electronic or thermal nature that limit the power of devices [5, 6].

Experimental Setup

1. Test sample

The investigated LED chips produced by Bolb Inc. had a peak emission wavelength $\lambda_{\text{peak}} = 280$ nm. The flip-chip LED (Fig. 1, a) had the emission area of $1280 \times 1160 \mu\text{m}^2$ and simple multi-strip interdigital contact pad topology (Fig. 1, b). For high current operation the chip was soldered on AlN plate, which was then mounted on bulky heat sinks.

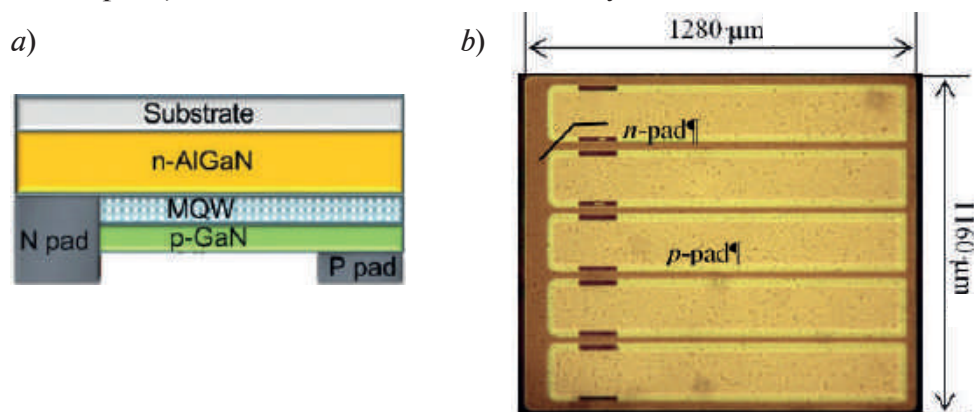


Fig. 1. Structure scheme of the flip-chip LED (a) and image of the test sample (b)

2. Current-voltage and light-current characteristics of LEDs

The studies were carried out up to $I = 350$ mA in continuous mode and up to $I = 20$ A in pulsed mode ($\tau \sim 100$ ns). In Fig. 2 the current dependences of radiation power P_{opt} and external quantum efficiency η_{EQE} are presented, while Fig. 3 shows the temperature dependences of spectrum. The entire range of current changes during measurements covered five orders of magnitude from fractions of a milliamp to 20 A. The pulse mode during measurements ($\tau = 100$ ns, $f = 100$ Hz) was provided by an Agilent 8114A generator with a PicoLAS LDPV 80-100 V3.3 amplifier. Optical power and emission spectra were recorded using the OL 770-LED Highspeed LED Test and Measurement System [7].

3. IR thermal imaging

The determining the surface temperature distribution is based on the application of thermal imaging equipment. It allows one to measure the temperature directly and thus to obtain more detailed information on the temperature distribution. To obtain the temperature distribution over the chip, the IR thermal radiation in the spectral range of $2.5\text{--}3.1 \mu\text{m}$ was mapped by a specially designed IR microscope. We would like to emphasize that using a relatively short wavelength IR radiation (compared to an $5\text{--}12 \mu\text{m}$ range utilized in conventional thermal-imaging systems) allowed us to reduce diffraction blurring and thus to improve the spatial resolution of the IR mapping down to $3 \mu\text{m}$.

The main methodological problems of thermal imaging of AlGaIn structures are: (i) the transparency of the sapphire substrate and epitaxial layers for IR radiation and (ii) a large difference in the emissivity of the materials utilized in the LED, i.e., semiconductor layers, metallic electrodes, reflective coatings, mounting elements, etc. [8]. So, extraction of correct temperature distributions from the IR images requires preliminary calibration of data for every particular object. Such a calibration was made with the temperature control by external heater in the range of 20–100 °C and recording the IR radiation from the LED chip at zero current. The calibrated relationship between the IR radiation intensity and temperature was then used to determine the absolute temperature under operation current ($I = 350$ mA).

4. Thermal resistances

The total thermal resistance R_{th} and thermal resistance R_i of internal elements of the LED an equivalent thermal circuit were determined via operating voltage relaxation method [9], using the Thermal Transient Tester T3Ster by MicRed, Ltd. For this purpose, a relationship between the voltage and temperature was determined from preliminary calibration of every LED.

The 1D heat transfer through the active region and AlN substrate was considered similarly to the current flow in an equivalent electrical circuit. Generally, there are two conventional models for building up the equivalent circuit; we used Cauer's one combines all the capacitances to a common bus.

Results and Discussion

The current dependences of the emitted power and spectral characteristics of investigated AlGaIn LEDs, including their distribution (mapping) over the radiating surface, were studied in a wide range of operating currents from milliamp currents up to 350 mA in continuous mode and 20 A in pulsed mode.

In Fig. 2, the current dependences of radiation power P_{opt} and external quantum efficiency η_{EQE} are presented. As can be seen from Fig. 2, the sharp changes of EQE (approximately up to 4–5 A) and then the tendency to saturation take place. That dependence is in good correlation with the conventional ABC-model. The value of η_{EQE} is only 3 % in maximum and decreases to 1 % at current 20 A. The low value of efficiency can be explained by low extraction radiation coefficient due to the large area of non-reflective contacts. Despite this fact, the output optical power density reaches level of ~ 1 W/mm².

The spectral analysis of emission (Fig. 3) showed low dependence on temperature. The peak wavelength at operating current 350 mA is $\lambda_{peak} = 279.5$ nm without heating and $\lambda_{peak} = 280$ nm at the external heating up to 90 °C. Thus, the temperature coefficient of the peak wavelength is only $TK\lambda_{peak} = 0.08$ Å/K.

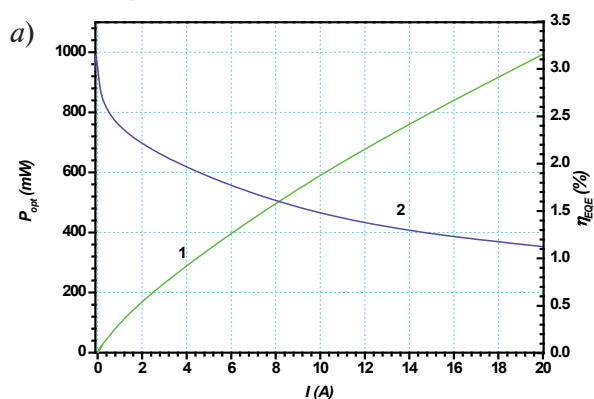


Fig. 2. Optical output power P_{opt} (1) and external quantum efficiency η_{EQE} (2) of the LED dependences on current

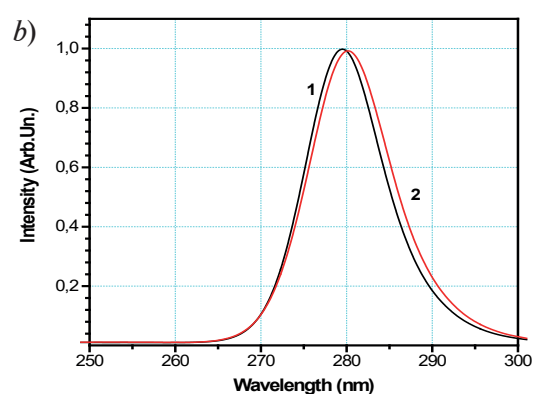


Fig. 3. Peak wavelength λ_{peak} dependences on wavelength at operating current $I = 350$ mA and temperature of 25 °C (1), 90 °C (2)

Figure 4 shows a map of temperature distributions over the area of LED chip at the continuous operating current 350 mA. At the current of 350 mA, the temperature distributions remain to be nearly uniform, indicating good lateral heat spreading inside the LED chip. And the temperature of surface is 60 °C with temperature of ambient 25 °C, consequently the overheating is 35 °C.

The latter conclusion is also supported by the cumulative structure functions (CSFs) measured by the T3Ster tester (see Fig. 5). The sum of the thermal resistances $R_{th} = 25$ K/W is associated the overheating of chip relatively ambient. It can be noted much more thermal resistances of the UV LED in comparison with similar blue LEDs (~ 5 K/W) which requires additional consideration.

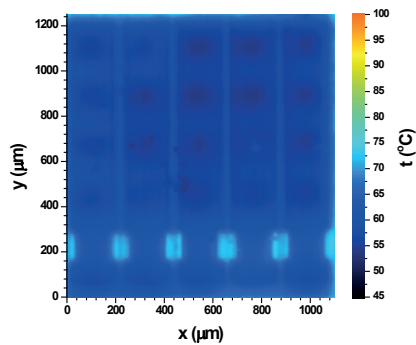


Fig. 4. The IR thermal image of chip at the current 350 mA

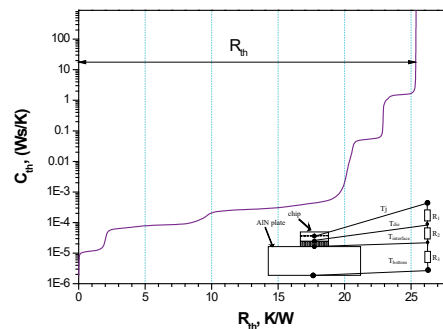


Fig. 5. The cumulative structure functions of the LED at the current 350 mA

Conclusion

Optical, electrical and thermal characteristics of high-power AlGaIn UV-C LEDs of “flip-chip” design have been studied over a wide range of excitation levels in continuous and pulsed modes. The temperature and current dependences of conversion efficiency and output power, as well as the drift of spectral parameters λ_{peak} and FWHM have been determined. The operation capacity of LEDs in pulse mode up to current ~ 20 A with an output power ~ 1 W has been established.

The thermal properties of UV-C LEDs were investigated both by infrared microscopy techniques (temperature mapping) and by analysis of the equivalent thermal circuit by voltage relaxation method, using the Thermal Transient Tester T3Ster. The uniformity of the temperature distribution over the entire area of the chip was established for all operating currents, that is, the absence of the effects of current crowding and the occurrence of temperature gradients. The quantum efficiency droop with increasing current is determined by recombination processes, apparently the growth of nonradiative Auger recombination.

Acknowledgements

This work was carried out at the Center of Multi-User Facilities “Element Base of Microwave Photonics and Nanoelectronics: Technology, Diagnostics, and Metrology”.

REFERENCES

1. Pousty D., Hofmann R., Gerchman Y., Mamane H., Wavelength-dependent time-dose reciprocity and stress mechanism for UV-LED disinfection of escherichia coli, *Journal of Photochemistry. and Photobiology B: Biology.* 217 (2021) 129–136.
2. Gerchman Y., Mamane H., Friedman N., Mandelboim M., UV-LED disinfection of Coronavirus: Wavelength effect, *Journal of Photochemistry and Photobiology B: Biology.* 212 (2020) 44–49.
3. Szolga L.A., Cilean T.R., Water Sterilization Using Power UV LEDs In: 8th International Conference on Electrical and Electronics Engineering, Antalya, Turkey. 1 (2021) 49–53
4. Meneghini M., Piva F., De Santi C., Trivellin N., Buffolo M., Roccato N., Zanoni E., *SPIE GaN Materials&Devices XVII.* 12001 (2022) 73–83.
5. Lin S.-H., Tseng M.-C., Horng R.-H., Lai S., Peng K.-W., Shen M.-Ch., Wu D.-S., Lien Sh.-Y., Kuo H.-Ch., Chen Z., Wu T., Thermal behavior of AlGaIn-based deep-UV LEDs *Journal Optical Express.* 30 (10) (2021) 16827–16836.
6. Wu S., Guttman M., Lobo-Ploch N., Gindele F., Susilo N., Knauer A., Kolbe T., Raß J., Hagedorn S., Kyong Cho S., Hilbrich K., Feneberg M., Goldhahn R., Einfeldt S., Wernicke T.,



Weyers M., Kneissl M., Enhanced light extraction efficiency of UV LEDs by encapsulation with UV-transparent silicone resin, *Journal Semiconductor Science and Technology*. 37 (6) (2022) 1361–1366.

7. **Zakgeim A.L., Chernyakov A.E.**, A Measuring System for Obtaining Spectroradiometric Photocolorimetric and Thermal Characteristics of Semiconductor Radiators, *Journal LIGHT & ENGINEERING*. 21 (4) (2013) 64–70.

8. **Bazovkin V.M., Mzhel'skii I.V., Kurishev G.L., Polovinkin V.G.**, Infrared scanning microscope with high spatial resolution, *Journal Optoelectronics, Instrumentation and Data Processing*. 47 (2011) 498–502.

9. **Szabo P., Poppe A., Farkas G., Szekely V., Courtois B., Rencz M.**, Thermal characterization and compact modeling of stacked die packages, *Thermal and Thermomechanical Phenomena in Electronics Systems 2006. The Tenth Intersociety Conference (2006)* 251–257.

THE AUTHORS

IVANOV Anton E.

a-e-ivanov@yandex.ru

ORCID: 0000-0003-2819-1534

ZAKGEIM Alexander L.

zakgeim@mail.ioffe.ru

ORCID: 0000-0002-1887-2064

CHERNYAKOV Anton E.

chernyakov.anton@yandex.ru

ORCID: 0000-0002-8153-9512

Received 31.10.2022. Approved after reviewing 10.11.2022. Accepted 10.11.2022.

Conference materials

UDC 538.945

DOI: <https://doi.org/10.18721/JPM.161.130>

Magnetization of different types of reduced graphene oxide in composites based on polystyrene

A.N. Ionov¹, M.P. Volkov¹, M.N. Nikolaeva², R.Y. Smyslov^{2,3}, A.N. Bugrov^{2,4}✉

¹Ioffe Physical-Technical Institute, RAS, St. Petersburg, Russia;

²Institute of Macromolecular Compounds, RAS, St. Petersburg, Russia;

³Institute of Biomedical Systems and Biotechnology, Graduate School of Biomedical Systems and Technology, Peter the Great St. Petersburg Polytechnic University, St. Petersburg, Russia;

⁴Department of Physical Chemistry, Saint-Petersburg Electrotechnical University, St. Petersburg, Russia

✉ anbugrov@etu.ru

Abstract. The transition from 'the initial graphite material, consisting of multilayer graphene of macroscopic size, to its oxidized form occurring as films, followed by their thermal reduction in an atmosphere of hydrogen, allows for obtaining submicron galleries of reduced graphene oxide with oxygen-containing groups on the surface. Such hydroxyl and carboxyl groups were used to functionalize the surface of graphene nanosheets with methacrylate groups to twist graphene layers relative to each other during in-situ copolymerization with styrene. In such a composite, mechanical stresses and defects are potential in the graphene nanosheets, which may be the reason for local superconductivity at room temperature. A similar effect was also recorded for photoreduced graphene oxide with a perforated surface as a component of a polystyrene-based composite.

Keywords: UV irradiation, reduced graphene oxide, polymeric matrix, percolation, carbon electronics

Funding: The work was supported by the RFBR grant No. 20-02-00918 A.

Citation: Ionov A.N., Volkov M.P., Nikolaeva M.N., Smyslov R.Y., Bugrov A.N., Magnetization of different types of reduced graphene oxide in composites based on polystyrene, St. Petersburg State Polytechnical University Journal. Physics and Mathematics. 16 (1.1) (2023) 172–177. DOI: <https://doi.org/10.18721/JPM.161.130>

This is an open access article under the CC BY-NC 4.0 license (<https://creativecommons.org/licenses/by-nc/4.0/>)

Материалы конференции

УДК 538.945

DOI: <https://doi.org/10.18721/JPM.161.130>

Магнитичность различных типов восстановленного оксида графена в композитах на основе полистирола

А.Н. Ионов¹, М.П. Волков¹, М.Н. Николаева², Р.Ю. Смыслов^{2,3}, А.Н. Бугров^{2,4}✉

¹Физико-технический институт им. А.Ф. Иоффе РАН, Санкт-Петербург, Россия;

²Институт высокомолекулярных соединений РАН, Санкт-Петербург, Россия;

³Институт биомедицинских систем и биотехнологий, Высшая школа биомедицинских систем и технологий, Санкт-Петербургский политехнический университет Петра Великого, Санкт-Петербург, Россия;

⁴Санкт-Петербургский государственный электротехнический университет, Санкт-Петербург, Россия

✉ anbugrov@etu.ru

Аннотация. Переход от графита, состоящего из многослойного графена макроскопических размеров, к его окисленной форме в виде пленок, с последующим их термическим восстановлением в атмосфере водорода, позволяет получить субмикронные галереи восстановленного оксида графена с кислородсодержащими группами на



поверхности. Такие гидроксильные и карбоксильные группы были использованы для функционализации поверхности графеновых наноллистов метакрилатными группами для скручивания графеновых слоев относительно друг друга при *in-situ* сополимеризации со стиролом. В таком композите возможны механические напряжения и дефекты в графеновых наноллистах, что может быть причиной локальной сверхпроводимости при комнатной температуре. Аналогичный эффект был также зарегистрирован для фотовосстановленного оксида графена с перфорированной поверхностью в качестве компонента композита на основе полистирола.

Ключевые слова: УФ-облучение, восстановленный оксид графена, полимерная матрица, перколяция, углеродная электроника

Финансирование: Работа выполнена при поддержке гранта РФФИ № 20-02-00918 А.

Ссылка при цитировании: Ионов А.Н., Волков М.П., Николаева М.Н., Смыслов Р.Ю., Бугров А.Н. Намагниченность различных типов восстановленного оксида графена в композитах на основе полистирола // Научно-технические ведомости СПбГПУ. Физико-математические науки. 2023. Т. 16. № 1.1. С. 172–177. DOI: <https://doi.org/10.18721/JPM.161.130>

Статья открытого доступа, распространяемая по лицензии CC BY-NC 4.0 (<https://creativecommons.org/licenses/by-nc/4.0/>)

Introduction

Since discovering the superconductivity effect, researchers worldwide have simultaneously focused on creating the theoretical models predicting a high critical temperature (T_c) and synthesizing new superconducting materials with high T_c . Many theoretical studies indicate high-temperature superconductivity up to room temperature in a graphene material due to deformation stresses [1, 2]. According to theoretical models, deformation stresses can radically change the density of electronic states in regions with mesoscopic dimensions and exponentially increase the value of T_c . The assumption of the role of deformation in the appearance of superconductivity is consistent with the experimental results obtained in the composite based on polystyrene (PS) with incorporated mesoscopic size graphene where stresses were created in graphene nanosheets (GNSs) due to covalent bonds between dielectric polymer matrix and conductive carbon filler. Such composite exhibited Josephson $I-V$ characteristics, which can undoubtedly be interpreted as the manifestation of the superconductivity effect [3, 4]. No superconductivity effects were observed in experiments in which graphene was used as a filler in polymer, i.e., without the formation of covalent bonds.

Spintronics can also become an additional stimulus for studying the effect of superconductivity in the composite based on PS with covalent bonded graphene, even on a mesoscopic scale. Indeed, as well known, spintronics uses two essential properties of the electron: charge and spin. Such a superconducting composite could be ideal for spintronics in charge transfer efficiency at room temperature. In addition, it will be possible to realize the ferromagnetic order in the nanoscale filler by the rearrangement of the supramolecular structure of the material during synthesis: The order is realized in the GNSs during *in-situ* copolymerization with the polymer matrix. Optimism in solving this problem is because the ferromagnetic state can occur in carbon nanomaterials, such as graphene nanoribbons and nanoplates [5], and a composite with graphene needles [6].

Reduced graphene oxide (rGO) is the prospect of fabricating organic-inorganic composites with unique electrical and magnetic properties. Our work aimed to synthesize PS/rGO composites in which the two components are covalently bound together. We show that composite magnetization plots can demonstrate type-II superconductivity without subtracting any diamagnetic and paramagnetic contributions. In addition, we noted that the effect of superconductivity depends on the oxygen-containing residues detected through a paramagnetic signal when measuring static magnetization at low temperature and on covalently binding rGO flakes with the macromolecules of PS.

Materials and Methods

Colloidal suspensions of multilayer graphene oxide (GO) were obtained from natural crystalline graphite using a modified Hummers method [7]. GO films, extracted at suspension evaporation, were reduced thermally or under the action of ultraviolet (UV) radiation in an inert atmosphere. The rGO differed from that obtained from graphite by mechanical scotch splitting [8]. In particular, after the reduction, the oxygen content in rGO decreases significantly but does not disappear completely [9]. It was found that during thermal reduction of GO in an argon atmosphere, the content of oxygen-containing groups is lower than in a hydrogen environment. In the case of UV photo-reduction of GO films and the removal of hydroxyl and carboxyl groups, the surface of graphene sheets is perforated with the formation of micron-sized holes [10]. The rGO surface was functionalized with methacrylate groups by alkaline hydrolysis of methoxyl groups of 3-(trimethoxysilyl)propyl methacrylate (TMSPM, CAS Number: 2530-85-0, Aldrich) and the subsequent condensation between them and the surface hydroxyls of graphene sheets [11, 12].

The composite systems contained 1–3 wt.% rGO assemblies with several microns long/wide and up to 200 nm thick, according to scanning electron microscopy (Zeiss EVO 50 instrument) [11]. Magnetic measurements of the samples were performed on the vibration magnetometer of the PPMS9 (Quantum Design) complex in the temperature range of 2–400 K and magnetic fields from 0 to 8000 A·m⁻¹

Results and Discussion

The temperature (Fig. 1, curve 1) and field dependences (Fig. 2, a) of static magnetization measured on a vibration magnetometer for a composite based on GO reduced in an argon atmosphere, modified with TMSPM, and in-situ copolymerized with the macromolecules of PS (System 1) exhibit only the magnetization of the diamagnetic type, which as well-known does not depend on temperature. In comparison, PS containing thermally-reduced in a hydrogen atmosphere and covalently-bound rGO flakes (System 2) gives a gradually increasing paramagnetic response at low temperature, suppressing the diamagnetic behavior (Fig. 1, curve 2).

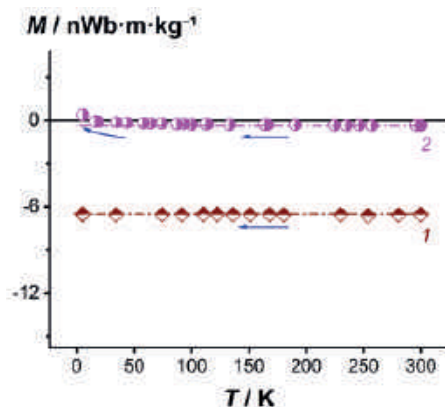


Fig. 1. Temperature dependence of the static magnetization for Systems 1 (1) and 2 (2) in cooling at $H = 40 \text{ kA}\cdot\text{m}^{-1}$

According to elemental analysis and X-ray photoelectron spectroscopy, a significant paramagnetic contribution is associated with the large content of oxygen-containing groups, which depends on the reduction conditions of rGO.

Fig. 2, b shows the field dependence of static magnetization for System 2. This type of hysteresis is not observed in ferromagnets but is characteristic of granular type-II superconductors [13]. As the magnetic field increases, the anomalously high magnetization component is suppressed, as observed in superconductors [14]. Only diamagnetism manifests in the composite in strong magnetic fields due to PS and the rGO (300 K). It should be noted that in weak magnetic fields, an abnormally high increase in magnetization with a small hysteresis turned counterclockwise is observed [15].

To prove our hypothesis, we have the film of GO reduced by UV irradiation (UV-rGO) according [16, 17]. In an argon atmosphere, the UV irradiation procedure is also accompanied

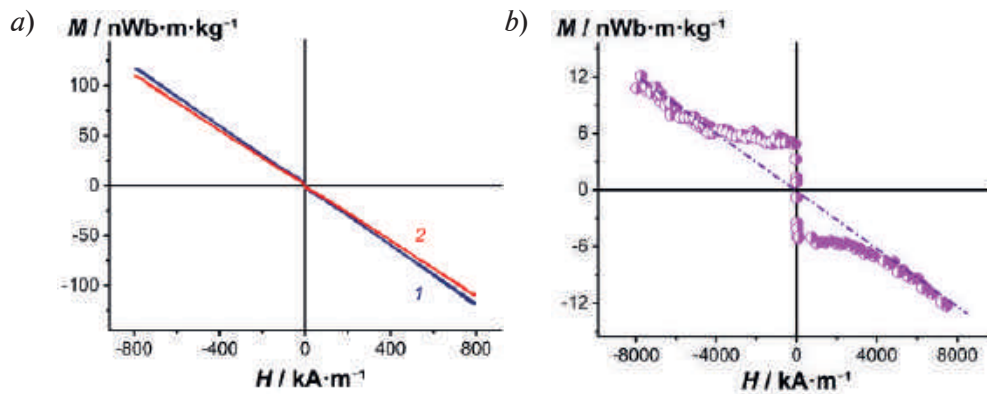


Fig. 2. The field dependence of the static magnetization for System 1 (a) at $T = 50$ (1) and 300 K (2), and System 2 (b) at $T = 300$ K

by many submicron holes in graphene flakes, just as after proton irradiation [8]. We tested this hypothesis by purposefully synthesizing and investigating a PS-based composite (System 3). For that, TMSPM was covalently bonded to the surface of UV-rGO flakes having typical dimensions of several microns in width and up to 200 nm in thickness, and then was cross-linked with PS chains in the process of in-situ radical polymerization of styrene. Two types of styrene were used: giving or not ferromagnetic ordering. As a result, polystyrene was obtained with magnetic impurities (PS_{Ferro}) and without them (PS) [10].

As a specified outcome, the photoreduction has many submicron holes distributed within the UV-rGO flakes, containing defective edge structures comprising carboxyl and hydroxyl groups. The impact of UV irradiation on GNSs is like irradiation with high-energy protons. Under the model [18], it should cause a defect-induced magnetic order (ferromagnetic-like loop) in UV-rGO flakes on the mesoscopic scale (Fig 3, curve 1). The PS_{Ferro} /UV-rGO composite (System 3 in Fig 3, curve 3) has a hysteresis loop of the same size as PS_{Ferro} (curve 2), and it is much smaller than the one for UV-rGO (curve 1). Consequently, introducing a magnetic component to the PS-based composite suppresses the hysteresis magnetization loop for UV-rGO as a part of the composite because of the internal magnetic field emerging in a system. This result is exclusively characteristic in type-II superconductors [19].

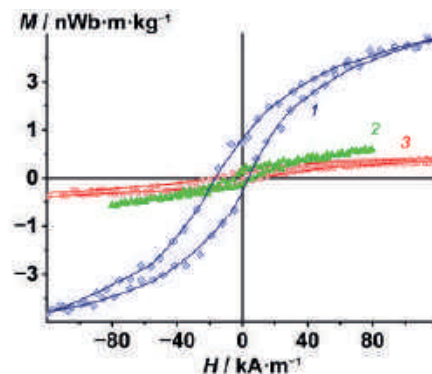


Fig. 3. Magnetic field dependence of the specific magnetic moment for UV-rGO flakes (1), PS_{Ferro} (2), and System 3 (3) at $T = 200$ K

Conclusion

In this paper, summarizing our earlier studies, we can conclude that the registered magnetization graphs for composites based on PS with covalently attached rGO flakes have a form characteristic of type II superconductors. The anomalously low resistivity of sheets twisted in the process of copolymerization with styrene is due to the concentration of oxygen-containing residues on their surface. These groups allow the creation of defects and additional mechanical stresses in the GNSs and provide displacement of the sheets relative to each other when they are included in the polymer chain, which leads to the formation of magnetic order in this kind of composites.

By the example of the composite with UV-rGO, it is demonstrated that the magnetization of the carbon filler flakes has a ferromagnetic hysteresis type. However, the experiment with the inclusion of a ferromagnetic impurity in System 3 did not increase the ferromagnetic magnetization according to the additivity principle, and the hysteresis loop was more pronounced for PS-based composites without ferromagnetism than for UV-rGO flakes. This observation questions the long-range magnetic order model caused by point defects in mesoscopic graphite samples with ferromagnetic loop behavior. Guided by the above, we can conclude that the hysteresis observed in the UV-rGO flakes at high temperatures may be due solely to type II superconductivity rather than ferromagnetic ordering.

REFERENCES

1. **Uchoa B., Barlas Y.**, Superconducting states in pseudo-Landau-levels of strained graphene, *Phys. Rev. Lett.* 111 (4) (2013) 046604–046609.
2. **Volovik G.E.**, Graphite, graphene and the flat band superconductivity, *JETP Lett.* 107 (8) (2018) 516–517.
3. **Ionov A.N.**, Josephson current-voltage characteristic of a composite based on polystyrene and graphene oxide, *Technical Physics Letter.* 41 (7) (2015) 651–653.
4. **Ionov A.N.**, Josephson-like behaviour of the current-voltage characteristics of multi-graphene flakes embedded in polystyrene, *J. Low. Temp. Phys.* 185 (5–6) (2016) 515–521.
5. **Yazyev O.V.**, Emergence of magnetism in graphene materials and nanostructures, *Rep. Prog. Phys.* 73 (5) (2010) 056501–0565019.
6. **Alimohammadian M., Sohrabi B.**, Manipulating electronic structure of graphene for producing ferromagnetic graphene particles by Leidenfrost effect-based method, *Scientific Reports.* 10 (1) (2020) 6874–6883.
7. **Aleksenskii A.E., Brunkov P.N., Dideikin A.T., Kirilenko D.A., Kudashova Y.V., Sakseev D.A., Sevryuk V.A., Shestakov M.S.**, Single-layer graphene oxide films on a silicon surface, *Tech. Phys.* 58 (11) (2013) 1614–1618.
8. **Geim A.K., Novoselov K.S.**, The rise of graphene, *Nat. Mater.* 6 (3) (2007) 183–191.
9. **Papageorgiou D.G., Kinloch I.A., Young R.J.**, Mechanical properties of graphene and graphene-based nanocomposites, *Progress in Materials Science.* 90 (2017) 75–127.
10. **Ionov A.N., Volkov M.P., Nikolaeva M.N., Smyslov R.Y., Bugrov A.N.**, Magnetization of ultraviolet-reduced graphene oxide flakes in composites based on polystyrene, *Materials.* 14 (10) (2021) 2519–2532.
11. **Nikolaeva M.N., Bugrov A.N., Anan'eva T.D., Dideikin A.T.**, Conductive properties of the composite films of graphene oxide based on polystyrene in a metal-polymer-metal structure, *Russ. J. Appl. Chem.* 87 (8) (2014) 1151–1155.
12. **Nikolaeva M.N., Anan'eva T.D., Bugrov A.N., Dideikin A.T., Ivankova E.M.**, Correlation between structure and resistance of composites based on polystyrene and multilayered graphene oxide, *Nanosystems: physics, chemistry, mathematics.* 8 (2) (2017) 266–271.
13. **Yakinci Z.D., Gokhfeld D.M., Altin E., Kurt F., Altin S., Demirel S., Aksan M.A., Yakinci M.E.**, Jc enhancement and flux pinning of Se substituted YBCO compound, *J. Matte. Sci. Matter. Electron.* 24 (12) (2013) 4790–4797.
14. **De Gennes P.G.**, Superconductivity of metals and alloy (Advanced Books Classics), CRC Press: Boca Raton, FL, USA, 2018.
15. **Ionov A.N., Volkov M.P., Nikolaeva M.N., Smyslov R.Y., Bugrov A.N.**, The magnetization of a composite based on reduced graphene oxide and polystyrene. *Nanomaterials.* 11 (2) (2021) 403–420.
16. **Zhang Y.-L., Guo L., Xia H., Chen Q.-D., Feng J., Sun H.-B.**, Photoreduction of graphene oxides: Methods, properties, and applications, *Adv. Opt. Mater.* 2 (1) (2014) 10–28.
17. **Rabchinskii M.K., Shnitov V.V., Stolyarova D.Y., Ryzhkov S.A., Baidakova M.V., Lobanova E.Y., Shvidchenko A.V., Besedina N.A., Smirnov D.A.**, Graphene oxide conversion into controllably carboxylated graphene layers via photoreduction process in the inert atmosphere, In: Proceedings of the 14th International conference “Advanced Carbon Nanostructures” (ACNS'2019), *Fuller. Nanotub. Carbon Nanostruct.* 28 (3) (2019) 221–225.



18. Esquinazi P., Hergert W., Spemann D., Setzer A., Ernst A., Defect-induced magnetism in solids, IEEE Trans. Magn. 49 (8) (2013) 4668–4676.

19. Abrikosov A.A., Gor'kov L.P., Contribution to the theory of superconducting alloys with paramagnetic impurities, Sov. Phys. JETP. 12 (6) (1961) 1243–1253.

THE AUTHORS

IONOV Alexander N.

ionov@tuch.ioffe.ru

ORCID: 0000-0002-5207-2642

SMYSLOV Ruslan Y.

urs@macro.ru

ORCID: 0000-0003-3633-4347

VOLKOV Michael P.

m.volkov@mail.ioffe.ru

ORCID: 0000-0003-4007-5640

BUGROV Alexander N.

anbugrov@etu.ru

ORCID: 0000-0003-1052-4919

NIKOLAEVA Marianna N.

marianna_n@mail.ru

ORCID: 0000-0002-5034-7665

Received 28.10.2022. Approved after reviewing 08.11.2022. Accepted 14.11.2022.

Conference materials

UDC 539.21

DOI: <https://doi.org/10.18721/JPM.161.131>

Quasi-local vibrations of amorphous solids in correlated random matrix theory

D.A. Conyuh ¹✉, Ya.M. Beltukov ¹

¹Ioffe Institute, Saint-Petersburg, Russia

✉ Conyuh.Dmitry@mail.ioffe.ru

Abstract. We apply the random matrix theory to the study of quasi-localized modes in amorphous solids having correlated disorder due to the stability criterion. We demonstrate that the number and properties of quasi-local vibrations depend significantly on how much the statistics of the dynamical matrix elements differs from the Gaussian one. The quasi-localized regime of the vibrational density of states can be understood in the framework of a perturbation theory, which managed to identify the low-frequency asymptotic.

Keywords: amorphous solids, quasi-localized modes, random matrices

Funding: This study was funded by the Council of the President of the Russian Federation for State Support of Young Scientists and Leading Scientific Schools (project no. МК-1893.2022.1.2).

Citation: Conyuh D.A., Beltukov Ya.M., Quasi-local vibrations of amorphous solids in correlated random matrix theory. St. Petersburg State Polytechnical University Journal. Physics and Mathematics. 16 (1.1) (2023) 178–184. DOI: <https://doi.org/10.18721/JPM.161.131>

This is an open access article under the CC BY-NC 4.0 license (<https://creativecommons.org/licenses/by-nc/4.0/>)

Материалы конференции

УДК 539.21

DOI: <https://doi.org/10.18721/JPM.161.131>

Квазилокальные колебания в аморфных твердых телах в рамках теории коррелированных случайных матриц

Д.А. Конюх ¹✉, Я.М. Бельтюков ²

¹Физико-технический институт им. А.Ф. Иоффе РАН, Санкт-Петербург, Россия

✉ Conyuh.Dmitry@mail.ioffe.ru

Аннотация. Нами применена теория случайных коррелированных матриц для исследования квазилокальных мод в аморфных твердых телах, имеющих коррелированный беспорядок за счет критерия устойчивости. Мы показали, что количество и свойства квазилокальных колебаний существенно зависят от того, насколько статистика элементов динамической матрицы отличается от гауссовой. Вклад квазилокальных колебаний в плотность колебательных состояний может быть изучен в рамках теории возмущений, которая позволяет найти низкочастотную асимптотику плотности состояний.

Ключевые слова: аморфные тела, квазилокальные колебания, случайные матрицы

Финансирование: Работа выполнена при поддержке Совета по грантам Президента Российской Федерации (проект номер МК-1893.2022.1.2).

Ссылка при цитировании: Конюх Д.А., Бельтюков Я.М. Квазилокальные колебания в аморфных твердых телах в рамках теории коррелированных случайных матриц // Научно-технические ведомости СПбГПУ. Физико-математические науки. 2023. Т. 16. № 1.1. С. 178–184. DOI: <https://doi.org/10.18721/JPM.161.131>

Статья открытого доступа, распространяемая по лицензии CC BY-NC 4.0 (<https://creativecommons.org/licenses/by-nc/4.0/>)



Introduction

Revealing the microscopic nature of the vibrations of strongly disordered mechanical systems is the main goal of past and current research. Examples of such systems are amorphous dielectrics, or glasses. It is well-known that there are two fundamentally different types of delocalized vibrations propagating in glasses: low-frequency plane waves, or phonons, with a certain mean free path and diffusons, which propagate through the system by diffusion energy transfer [1]. The universal properties of amorphous systems critically depend on the transport properties of phonons and diffusons and are evident in many important experimental research methods and practical problems [2, 3].

In addition to phonons and diffusons, the so-called quasi-local vibrations (QLVs) are responsible for the low-frequency properties of amorphous solids at frequencies around 1 THz [4]. These excitations are long-lived vibrations of small groups of atoms, weakly connected with their surroundings [3]. The study of QLVs properties is complicated by the fact that they are difficult to distinguish from the usual Rayleigh scattering of phonons on disorder [5, 6].

As recent studies show, a population of quasi-localized modes is affected by glass cooling processes and its preparation protocol [7–9]. Anomalously soft regions near the loss of stability are inherent in such systems and lead to force constants correlation due to microscopic disorder of glass and mechanical frustration [10, 11]. However, the main features of QLVs are independent of spatial dimension [5, 12], cooling rate [7], microscopic details [5, 13, 14], and even persist in the most deeply supercooled computer glasses [8]. One can assume that there is a universal relation between QLVs and structural correlated disorder in amorphous solids formed during the cooling processes.

There are various theoretical works aimed at investigating QLVs, in particular, the soft-potential model [15–17]. In these works, it was shown that QLVs determine the main contribution to the scattering of acoustic phonons. However, the question about the influence of structural correlated disorder in amorphous solids on QLVs remains open. Since glass-forming systems settle into disordered configurations, their dynamical matrices are naturally characterized by a specific distribution of elements, which so far has received very little attention. In the present paper we shed light on this aspect in the framework of the random matrix theory.

Materials and Methods

In our earlier investigation we applied the random matrix theory approach to detailed study of the low-frequency excitations of strongly disordered systems [18, 19]. In this model the main glasses properties like the boson peak and the Ioffe–Regel crossover between phonons and diffusons are manifested. Now we study how the random matrix theory reproduces the soft regions and how the statistic of matrix element affects the statistic of QLVs.

The vibrations of solids are characterized by the eigenvectors and eigenvalues of the dynamical matrix M , which has a relation with the force constant matrix $M_{ij} = (m_i m_j)^{-1/2} \Phi_{ij}$ [20]. The elements of M have a specific nature depending on the medium in hand. However, the dynamical matrix M has a common structure caused by the symmetrical mechanical properties. One of them is the mechanical stability of the system near its equilibrium position. It leads to the positive definite symmetric M with non-negative eigenvalues which are eigenfrequencies squared ω^2 . Second, the potential energy is invariant under the continuous translation of the system which leads to the sum rule $\sum_i M_{ij} = \sum_j M_{ij} = 0$.

Taking into account the above properties, the dynamical matrix M can be written in the form $M = AA^T$. The matrix A plays the role of an incident matrix, whose rows indicate the degrees of freedom and columns indicate the bonds of a system. In general, the matrix A is a rectangular $N \times K$ matrix A . We consider a scalar model in which the displacements of the atoms are collinear and are described by scalar quantities. In this model, the number of atoms is equal to the number of degrees of freedom N . The parameter $\kappa = (K - N)/N$ defines the relative excess of the total number of bonds K in comparison to the total number of degrees of freedom N . According to the Maxwell counting rule [21], in a stable system with a finite rigidity the number of bonds should be larger than the number of degrees of freedom. Therefore, the parameter κ varies in a wide range $0 \leq \kappa < \infty$ and controls the relationship between stiffness and disorder in the system. For $\kappa \ll 1$

we obtain a strongly disordered amorphous solid, which is the most important case for the current study. It must be stressed that elements of A correlated by the sum rule $\sum_i A_{ik} = 0$ to satisfy the condition of the translational invariance.

In amorphous solids under consideration, the elements of A have a random nature due to the presence of disorder in such systems. Also, in real amorphous solids short-range interaction between atoms dominates over the far-range interaction, which leads to highly sparse matrix A . In this light, we consider a model of disordered system based on the following rules. For $\kappa = 0$ the matrix A is the square matrix, build on the simple cubic lattice with the lattice constants $a_0 = 1$ and atomic masses $m_i = 1$. Each atom is placed in a site of lattice, but the interaction between atoms is random, therefore, the elements of A are random numbers. We consider the case of the short-range interaction in which A_{ij} is a nonzero random number only if atoms with indices i and j are nearest neighbors in this lattice. For the simple cubic lattice, the coordination number $n = 6$, therefore, the matrix A has only 6 non-zero non-diagonal elements in every column. The diagonal element $A_{ii} = -\sum_{j \neq i} A_{ji}$.

For $\kappa \neq 0$ the matrix A is the rectangular matrix. To accurately account the sum rule, we do the following procedure. We take two independent realizations of the square random matrix A constructed in accordance with the above rules, and we add randomly chosen κN columns of one matrix to the right of the other matrix. This random addition of the new columns corresponds to a random addition of new bonds to the vibrational system. As a result of this addition of bonds, we get a rectangular matrix A with $\kappa \geq 0$ satisfying the sum rule.

There is a probability that all elements A_{ik} in the i th row of the matrix A have small values. It leads to a soft area, i -atom of which is weakly connected with its surroundings. Such a soft region leads to the formation of the QLV characterized by a small eigenfrequency ω_{qlv} . The density of QLVs is defined by the distribution of ω_{qlv} . We assume that the matrix elements A_{ik} for $k > N$ are zero which has the probability $(1 - \kappa)^{n+1}$ in the model under consideration.

For small values of matrix elements in the i th row of the matrix A , one can present the matrix A as

$$A = A_0 + V, \quad (1)$$

where the matrix A_0 has all zero elements in the i th row, and the perturbation matrix V has n non-zero elements v_1, \dots, v_n which correspond to interaction with the nearest neighbor and one element obeying the sum rule $V_{ii} = -\sum_{j \neq i} V_{ji}$. It must be stressed that matrices save the simple cubic lattice structure for atomic arrangement, and the sum rule is still imposed on them. Taking into account the random matrix model $M = AA^T$, the dynamical matrix takes the next form:

$$M = A_0 A_0^T + A_0 V^T + V A_0^T + V V^T. \quad (2)$$

In the framework of the downfolding method [22], the frequency of QLV ω_{qlv} can be found from (2) to the second-order perturbation theory on the perturbation V :

$$\omega_{\text{qlv}}^2 = \{V H V^T\}_{ii}, \quad (3)$$

where

$$H = I - A_0^T (A_0 A_0^T)^{-1} A_0, \quad (4)$$

and I is $K \times K$ identity matrix. From equation (3) it follows that the frequency of QLV can be written from the sum of quadratic form:

$$\omega_{\text{qlv}}^2 = \sum_{k'l'=1}^{n+1} C_{k'l'} v_k v_{l'}, \quad (5)$$

where v_k for $k' = 1, \dots, n+1$ are non-zero elements V_{ik} for $k = 1, \dots, K$, and the matrix C is the truncation of the matrix H to the set of non-zero elements in the i th row of the matrix V .

The sum rule $V_{ii} = -\sum_{j \neq i} V_{ji}$ corresponds to the rule $v_i = -\sum_{j \neq i} \tilde{v}_j$, where the element v_i is the V_{ii} , and elements \tilde{v}_j are non-zero elements V_{ji} of the i th column of the matrix V . Therefore, equation (5) takes the form:

$$\omega_{\text{qlv}}^2 = \sum_{k'l'=1}^{n+1} (C_{k'l'} v_k v_{l'} - 2C_{k'l'} v_k \tilde{v}_{l'} + C_{l'i'} \tilde{v}_k \tilde{v}_{l'}), \quad (6)$$

As a result, we obtain the following low-frequency density of QLVs (QLVDOS):

$$\rho_{\text{qlv}}(\omega) = \left\langle \det C^{-1/2} \right\rangle (1 - \kappa)^{n+1} \frac{2\pi^{(n+1)/2} \omega^n}{\Gamma\left(\frac{n+1}{2}\right)} \prod_{k'=1}^{n+1} \rho_{k'}(0), \quad (7)$$

where angle brackets denote the averaging over different realizations of the matrix A_0 , Γ is the Gamma-function, $\rho_k(v)$ is the probability density function of v_k .

Results and Discussion

The theoretical result (7) compared with the vibrational density of states (VDOS) obtained by the full diagonalization of matrices M . We consider the small systems in which the smallest frequency of phonons is limited by the system size. In such systems, the quasi-localized modes are well distinguishable from phonons due to their low number, and the QLVDOS is a low-frequency region $\omega \ll 1$ of VDOS. Also, for additional identification of QLVs, we consider two different cases of statistics of matrix elements A_{ik} : Gaussian and strongly non-Gaussian statistics. This consideration is due to the significant dependence of the number of soft regions formed by small values of matrix elements A_{ik} on its statistics. How it was demonstrated in our early work, for strongly non-Gaussian statistics the number of quasi-localized modes increases in comparison with the Gaussian statistics [19].

Figure 1 shows the numerical calculation of VDOS in the case of Gaussian statistics. We consider the simple case of independent Gaussian random numbers A_{ik} with zero mean and unit variance. In this case, the probability density function of v_i , is $\rho_i(0) = 1/\sqrt{2\pi n}$, and $\rho_k(0) = 1/\sqrt{2\pi}$ for $k \neq i$. Then, the QLVDOS (7) takes the form

$$\rho_{\text{qlv}}(\omega) = \left\langle \det C^{-1/2} \right\rangle (1 - \kappa)^{n+1} \frac{2^{(1-n)/2} \omega^n}{\Gamma\left(\frac{n+1}{2}\right) \sqrt{n}}. \quad (8)$$

In Fig. 1, this QLVs contribution $\rho(\omega) \propto \omega^n$ is marked with a solid line. To obtain the coefficient of equation (8) the averaging in $\langle \det C^{-1/2} \rangle$ may be performed numerically. For large enough system size one can show that

$$\left\langle \det C^{-1/2} \right\rangle \propto \kappa^{-(n+1)/2}, \quad (9)$$

since the typical value of the elements of matrix C is proportional to κ if no finite-size effects are present.

In order to set the non-Gaussian statistics of matrix elements and simulate a wide range of different magnitudes of non-zero matrix elements, we multiply the standard Gaussian random number by log-uniform random variable. In this case the random variable has a form

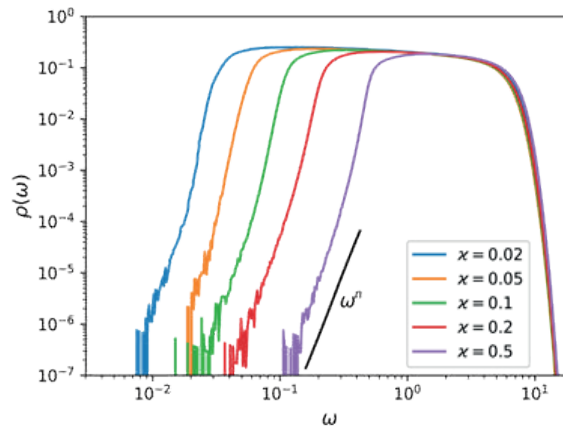


Fig. 1. Vibrational density of states in the case of Gaussian statistics for different parameters κ . The solid line marks the QLVs contribution $\rho(\omega) \propto \omega^n$. The matrix A is built on the simple cubic lattice with $10 \times 10 \times 10$ atoms

$$v_{k'} = c\eta_{k'} \exp \zeta_{k'}, \quad (10)$$

where $\eta_{k'}$ is the Gaussian random number with zero mean and unit variance and $\zeta_{k'}$ is an independent random number uniformly distributed in the interval $(-b/2, b/2)$. The normalization constant $c = \sqrt{(b/\sinh(b))}$ is chosen to provide the unit variance of $v_{k'}$. The resulting probability density function of the random variable $v_{k'}$ has a form

$$p(v_{k'}) = \frac{1}{2bv_{k'}} \left(\operatorname{erf} \left(\frac{v_{k'} e^{b/2}}{\sqrt{2c}} \right) - \operatorname{erf} \left(\frac{v_{k'} e^{-b/2}}{\sqrt{2c}} \right) \right). \quad (11)$$

For $b \gg 1$ it is close to the Gaussian distribution. However, with the increasing of b , the distribution of $v_{k'}$ becomes closer to the reciprocal distribution $\sim 1/|v_{k'}|$, therefore, the parameter b is treated as a non-Gaussianness parameter.

Figure 2 shows an increase in the number of quasi-localized modes with an increase in the non-Gaussian parameter b . As in the case of Gaussian statistics, there is the low-frequency QLVs contribution $\rho(\omega) \propto \omega^n$. The distribution of $v_{k'}$ can be viewed as a mixed distribution of Gaussian random numbers in which the standard deviation is random. Then, the QLV DOS (7) takes the form

$$\rho_{\text{qlv}}(\omega) = \langle \det C^{-1/2} \rangle (1-\kappa)^{n+1} \frac{2^{(1-n)/2} \omega^n}{\Gamma\left(\frac{n+1}{2}\right)} \left(\frac{2}{b} \sinh \frac{b}{2} \right)^n \left\langle \left(\sum_{k'=1}^n e^{2b\zeta_{k'}} \right)^{1/2} \right\rangle, \quad (12)$$

which gives the low-frequency QLVs contribution $\rho(\omega) \propto \omega^n$. Here we use the averaging over different realizations of $\zeta_{k'}$ distributed uniformly in the interval $(-b/2, b/2)$.

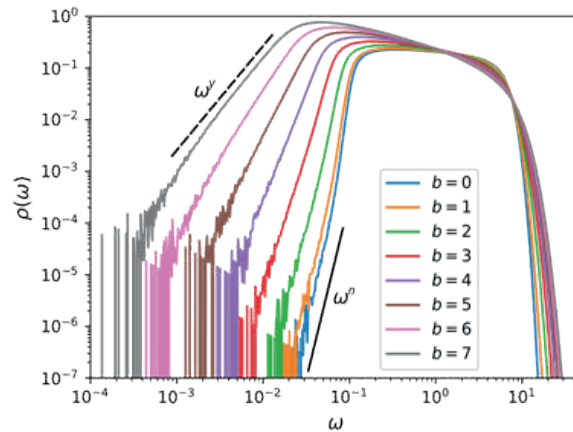


Fig. 2. Vibrational density of states in the case of non-Gaussian statistics with parameter $\kappa = 0.1$ for different parameters b . The solid line marks the QLVs contribution $\rho(\omega) \propto \omega^n$. The dashed line marks the result $\rho(\omega) \propto \omega^\gamma$ for intermediate range of frequencies. The matrix A is built on the simple cubic lattice with $10 \times 10 \times 10$ atoms

However, in contrast to Gaussian statistics, in the case of strongly non-Gaussian statistics the intermediate range of frequencies has additional contribution $\rho(\omega) \propto \omega^\gamma$ with $\gamma < n$. For $b \gg 1$ the random variables v and \hat{v} are distributed over an exponentially large range of values, thus $\omega \approx \max_{k'}(vk')$ is determined by the maximum value of v , and one can find the next relation for the γ :

$$\gamma = \frac{4n-2}{b} - 1. \quad (13)$$

This expression allows us to describe intermediate degrees of $\rho(\omega)$ for the case of strongly non-Gaussian statistics $b \gg 1$, which corresponds to different slopes in Fig. 2. From the point of view of statistical properties of the matrix A , one can consider the γ as an effective number of neighbors.

Conclusion

Summarizing, we apply the random matrix model to analyze the quasi-local vibrations, which exist in strongly disordered systems like amorphous solids. In this model, the dynamical matrix



is expressed as $M = AA^T$, and numbers and properties of quasi-local vibrations are essentially dependent on the statistic of matrix element A_{ik} . We have shown that as the degree of non-Gaussianness b of the dynamic matrix elements increases, the number of quasi-local vibrations increases too, which manifests itself in their vibrational density of states $\rho_{\text{qlv}}(\omega)$. For accurate analysis of quasi-local vibrations, we consider a small system with a low number of phonons, atoms of which are placed in sites of a regular lattice. In a perturbation theory framework we analyzed the low-frequency asymptotic of $\rho(\omega)$ and found that $\rho_{\text{qlv}}(\omega) \simeq \omega^n$ for small frequencies with coordination number n , and $\rho_{\text{qlv}}(\omega) \simeq \omega^\gamma$ with $\gamma < n$ in the intermediate range of frequencies for strongly non-Gaussian distribution.

REFERENCES

1. Allen P.B., Feldman J.L., Thermal conductivity of disordered harmonic solids, *Physical Review B*, 48 (17) (1993) 12581.
2. Phillips W.A., Anderson A.C., *Amorphous solids: low-temperature properties*, Vol. 24, Springer-Verlag, Berlin, 1981.
3. Parshin D.A., Soft-potential model and universal properties of glasses, *Physics of the Solid State*, 36 (7) (1994) 991–1024.
4. Laird B.B., Schober H., Localized low-frequency vibrational modes in a simple model glass, *Physical review letters*, 66 (5) (1991) 636.
5. Kapteijns G., Bouchbinder E., Lerner E., Universal nonphononic density of states in 2D, 3D, and 4D glasses, *Physical review letters*, 121 (5) (2018) 055501.
6. Shimada M., Mizuno H., Ikeda A., Vibrational spectrum derived from local mechanical response in disordered solids, *Soft Matter*, 16 (31) (2020) 7279–7288.
7. Lerner E., Bouchbinder E., Effect of instantaneous and continuous quenches on the density of vibrational modes in model glasses, *Physical Review E*, 96 (2) (2017) 020104.
8. Wang L., Ninarello A., Guan P., Berthier L., Szamel G., Flenner E., Low-frequency vibrational modes of stable glasses, *Nature communications*, 10 (1) (2019) 1–7.
9. Rainone C., Bouchbinder E., Lerner E., Pinching a glass reveals key properties of its soft spots, *Proceedings of the National Academy of Sciences*, 117 (10) (2020) 5228–5234.
10. Alexander S., *Amorphous solids: their structure, lattice dynamics and elasticity*, *Physics reports*, 296 (2-4) (1998) 65–236.
11. Lerner E., Bouchbinder E., Frustration-induced internal stresses are responsible for quasilocalized modes in structural glasses, *Physical Review E*, 97 (3) (2018) 032140.
12. Charbonneau P., Corwin E.I., Parisi G., Poncet A., Zamponi F., Universal non-Debye scaling in the density of states of amorphous solids, *Physical review letters*, 117 (4) (2016) 045503.
13. Lerner E., Dyring G., Bouchbinder E., Statistics and properties of low-frequency vibrational modes in structural glasses, *Physical review letters*, 117 (3) (2016) 035501.
14. Mizuno H., Shiba H., Ikeda A., Continuum limit of the vibrational properties of amorphous solids, *Proceedings of the National Academy of Sciences*, 114 (46) (2017) E9767–E9774.
15. Buchenau U., Galperin Y.M., Gurevich V.L., Schober H.R., Anharmonic potentials and vibrational localization in glasses, *Physical Review B*, 43 (6) (1991) 5039.
16. Parshin D. A., Interactions of soft atomic potentials and universality of low-temperature properties of glasses, *Physical Review B*, 49 (14) (1994) 9400.
17. Ji W., Popović M., de Geus T.W.J., Lerner E., Wyart M., Theory for the density of interacting quasilocalized modes in amorphous solids, *Physical Review E*, 99 (2) (2019) 023003.
18. Beltukov Y.M., Kozub V.I., Parshin D.A., Ioffe-Regel criterion and diffusion of vibrations in random lattices, *Physical Review B*, 87 (13) (2013) 134203.
19. Conyuh D.A., Beltukov Y.M., Random matrix approach to the boson peak and Ioffe-Regel criterion in amorphous solids, *Physical Review B*, 103 (10) (2021) 104204.
20. Maradudin A.A., Montroll E.W., Weiss G.H., Ipatova I.P., *Theory of lattice dynamics in the harmonic approximation*, Vol. 3, New York: Academic press, 1963.
21. Maxwell J.C., L. on the calculation of the equilibrium and stiffness of frames, *The London, Edinburgh, and Dublin Philosophical Magazine and Journal of Science*, 27 (182) (1864) 294–299.
22. Zurek E., Jepsen O., Andersen O.K., Muffin-Tin Orbital Wannier-Like Functions for Insulators and Metals, *ChemPhysChem*, 6 (9) (2005) 1934–1942.

THE AUTHORS

CONYUH Dmitry A.

Conyuh.Dmitry@mail.ioffe.ru

ORCID: 0000-0003-3729-4156

BELTUKOV Yaroslav M.

ybeltukov@gmail.com

ORCID: 0000-0002-3648-0312

Received 30.10.2022. Approved after reviewing 08.11.2022. Accepted 08.11.2022.

Conference materials

UDC 537.9

DOI: <https://doi.org/10.18721/JPM.161.132>

Interconnect elements of magnonic networks based on controlled meander 3D magnonic structures

A.A. Martyshkin¹, Y.A. Gubanova¹✉, E.N. Beginin¹, A.V. Sadovnikov¹

¹ Saratov State University, Saratov, Russia

✉ yulya29022095@gmail.com

Abstract. Here we propose the different simple building block of the three-dimensional (3D) magnonic network in the form of the joined orthogonal sections of magnonic waveguides. It was shown, that the proposed 3D structures allows the transmission of spin-wave signals in the regime of surface magnetostatic wave propagation without the significant losses due to the junction region. Micromagnetic simulation was used to reveal the mechanism of spin-wave propagation across 3D junction. An electrodynamic problem is considered by the finite element method and the dispersion characteristics of spin waves (SW) are constructed with a change in the geometric parameters of the meander. The nature of the change in the frequency ranges of the Bragg band gaps depending on the meander profile has been studied in detail. It was demonstrated that spin-wave waveguiding 3D structure with broken translational symmetry exploiting the vertical spin-wave transport provides the transmission of the information signal in three-dimensional configuration of magnonic networks.

Keywords: Spin wave, micromagnetic calculation, 3D structure, Brillouin-spectroscopy

Funding: Ministry of Education and Science of the Russian Federation as part of the state assignment (project No. FSRR-2023-0008).

Citation: Martyshkin A.A., Gubanova Y.A., Beginin E.N., Sadovnikov A.V., Interconnect elements of magnonic networks based on controlled meander 3D magnonic structures. St. Petersburg State Polytechnical University Journal. Physics and Mathematics. 16 (1.1) (2023) 185–190. DOI: <https://doi.org/10.18721/JPM.161.132>

This is an open access article under the CC BY-NC 4.0 license (<https://creativecommons.org/licenses/by-nc/4.0/>)

Материалы конференции

УДК 537.9

DOI: <https://doi.org/10.18721/JPM.161.132>

Элементы межсоединений магнонных сетей на основе управляемых меандровых 3D-магнонных структур

A.A. Мартышкин¹, Ю.А. Губанова¹✉, Е.Н. Бегинин¹, А.В. Садовников¹

¹ Саратовский национальный исследовательский государственный университет имени Н.Г. Чернышевского, г. Саратов, Россия

✉ yulya29022095@gmail.com

Аннотация. В работе исследованы различные элементы трехмерной (3D) магнонной сети в виде соединенных ортогональных секций магнонных волноводов. Было показано, что предложенные 3D структуры позволяют передавать спин-волновые сигналы в режиме распространения поверхностных магнитостатических волн без потерь в нерегулярной области структуры. Для выявления механизма распространения спиновых волн через 3D-переход использовалось микромагнитное моделирование. Методом конечных элементов рассмотрена электродинамическая задача и построены дисперсионные характеристики спиновых волн (СВ) при изменении геометрических параметров меандра. Подробно изучен характер изменения частотных диапазонов брэгговских запрещенных зон в зависимости от профиля меандра. Продемонстрировано, что спин-волновая 3D-структура с нарушением трансляционной симметрией, использующей

вертикальный спин-волновой транспорт, обеспечивает передачу информационного сигнала в трехмерной конфигурации магнонных сетей.

Ключевые слова: Спиновые волны, микромагнитное моделирование, трехмерные структуры, Манделштам-бриллюэновская спектроскопия

Финансирование: Минобрнауки России в рамках выполнения государственного задания (проект № FSRR-2023-0008).

Ссылка при цитировании: Мартышкин А.А., Губанова Ю.А., Бегинин Е.Н., Садовников А.В. Элементы межсоединений магнонных сетей на основе управляемых меандровых 3D-магнонных структур // Научно-технические ведомости СПбГПУ. Физико-математические науки. 2023. Т. 16. № 1.1. С. 185–190. DOI: <https://doi.org/10.18721/JPM.161.132>

Статья открытого доступа, распространяемая по лицензии CC BY-NC 4.0 (<https://creativecommons.org/licenses/by-nc/4.0/>)

Introduction

The transition from a two-dimensional architecture of magnon networks to a three-dimensional one is currently of great interest due to the development of data processing and storage concepts based on magnonic principles [1]. In electronics, 3D circuits require efficient removal of Joule heat from computational elements, which is a technological challenge. Magnonics allows you to transmit an information signal encoded in the amplitude and phase of spin waves (SW), while the transport properties of spin-polarized electrons are not used, and information is transferred by signal transmission using spin wave [2]. With this approach, it is possible to implement a number of signal processing functional blocks with low power consumption compatible with semiconductor electronic circuits and the possibility of miniaturization to nanometer sizes of structures [3].

One of the options for creating interconnect elements based on magnetic quasi-two-dimensional and three-dimensional (3D) structures in lateral and vertical topologies with micro- and nanometer-sized waveguide elements is a base element made in the form of ferrite microwave guides located on the same substrate and connected through the side wall [4]. In this case, the interconnections will perform not only the transmission of the information signal, but also functional processing, implementing the modes of parallel and multi-stream (de)multiplexing of the spin-wave signal in the frequency, time and space domains. Most circuits based on magnon logic are magnetized in a plane, which imposes restrictions on signal routing, since magnon networks limited to one functional level have a critical signal propagation length and a large device area [5]. Structures with the possibility of vertical transport of a spin-wave signal [6] make it possible to create three-dimensional magnon networks (MS) with a large number of functional blocks in a smaller volume.

Meander-type ferromagnetic films grown on the surface of periodically structured substrates can be considered as a three-dimensional magnonic crystal structure. Composite magnon crystals are in fact magnonic metamaterials with periodically varying parameters that exhibit SW delay control, and analysis of the dispersion response of such structures indicates that the SW spectrum can be divided into periodically alternating frequency bands in which SW propagation is observed (passbands), and frequency bands in which no SW propagation occurs due to additional attenuation arising from Bragg interference of incident and reflected waves. The formation of such band gaps in the magnon spectrum makes it possible to use MCs as filters for the SW signal. The study of MC with different periodicity in one and two dimensions [7] led to the development of the field of magnonics [8].

The 3D structures considered in this paper can be used as interconnection elements for multilayer topologies of magnon networks that perform the functions of information signal processing [9].

Vertical interconnection elements of 3D magnonic networks

We investigate vertical transport of spin waves in two structures shown in Fig. 1, *a*, *b*. The structure in the form of an orthogonal connection of two magnetic thin-film sections S_1 and



S_2 is shown in Fig. 1, *a*. A stepped structure consisting of the connection of three separate sections S_3 , S_4 and S_5 is shown in Fig. 1, *b*. Thin film yttrium iron garnet (YIG) [$\text{Y}_3\text{Fe}_5\text{O}_{12}$ (111)] $1\ \mu\text{m}$ thick and saturation magnetization $M_0 = 1.39 \times 10^5\ \text{A/m}$ on a gallium-gadolinium garnet substrate $500\ \mu\text{m}$ thick (GGG) [$\text{Gd}_3\text{Ga}_5\text{O}_{12}$ (111)]. YIG film exchange constant was taken equal to $A_{ex} = 3.614 \times 10^{-12}\ \text{J/m}$. Waveguide width in the numerical calculation $w = 100\ \mu\text{m}$ was changed to the case of a transversely limitless YIG film. The length of the waveguides S_1 , S_2 was $L_1 = L_2 = 1000\ \mu\text{m}$. The structures were placed in an external magnetic field $H_0 = 1200\ \text{Oe}$ directed along the y -axis to effectively excite a magnetostatic surface spin wave (MSSW) in the S_1 region [10]. The stepped structure shown in Fig. 1, *b* is formed by sections $S_3 = S_4 = S_5$ with length $L_3 = L_4 = L_5 = 1000\ \mu\text{m}$.

To investigate the properties of propagation of a spin-wave signal in the investigated structures with broken translational symmetry, we used the method of numerical micromagnetic simulations based on a numerical solution of the Landau–Lifshitz–Gilbert equation [11, 12]:

$$\frac{\partial \vec{M}}{\partial t} = \gamma [\vec{H}_{eff} \times \vec{M}] + \frac{\alpha}{M_0} \left[\vec{M} \times \frac{\partial \vec{M}}{\partial t} \right],$$

where \vec{M} is the magnetization vector, $\alpha = 10^{-5}$ is the damping parameter, $\vec{H}_{eff} = -\frac{\delta E}{\delta \vec{M}}$ is the effective magnetic field, E is the free energy of the magnet. The contribution of magnetocrystalline anisotropy in the plane of the film in view of its smallness can be neglected. To reduce the signal reflections from the boundaries of the computational domain in numerical simulation, two regions at the beginning and end of the waveguide with a low damping parameter α decreasing in geometrical progression from $\alpha = 10^{-5}$ to $\alpha = 10^{-1}$.

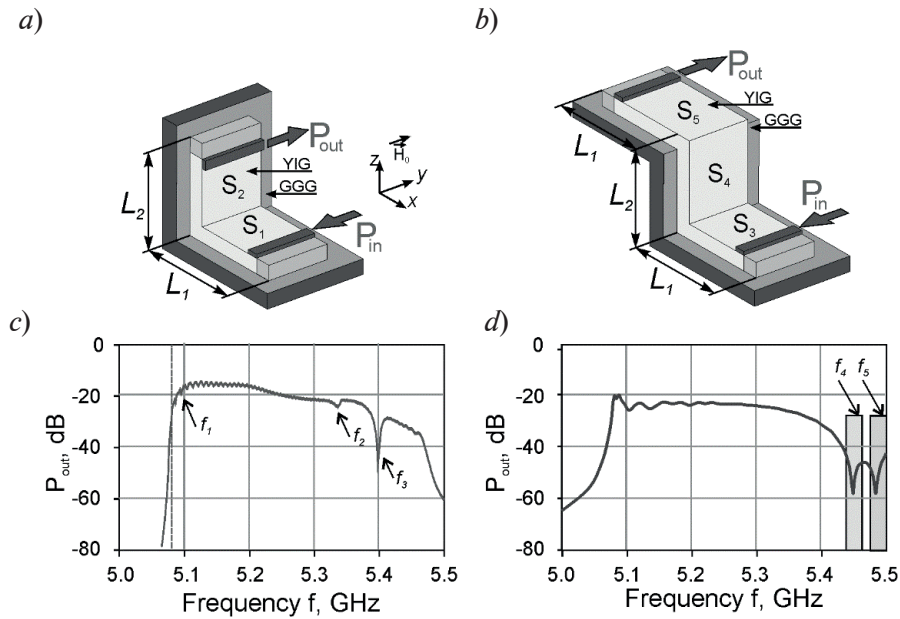


Fig. 1. Schematic view of interconnect element in the form of an L-shaped (*a*) and step-shaped (*b*) junction of magnetic films; the transmission spectrum of the output signal for the L-shaped (*c*) and for step-shaped (*d*) structure

To calculate the output signal spectrum, the problem of excitation of a SW was solved for the L-shaped structure using the excitation method in the region of the microwave S_1 and receiving the SW in the waveguide S_2 . The SW excitation in the numerical counting was carried out by setting the value of the alternating magnetic field in the form $B_x(t) = b_0 \text{sinc}(2\pi f_0(t-t_0))$, where $b_0 = 10^{-3}\ \text{T}$, $f_0 = 4\ \text{GHz}$, $t_0 = 0.1\ \text{ns}$.

The frequency spectrum of such a function has a rectangular shape with a cut-off frequency f_0 . The source was localized in the signal source region inside the waveguide, the size of which was $5\ \mu\text{m}$ in the direction of the x -axis. This method of excitation is close to the standard excitation of microwave oscillations of magnetization using a microstrip antenna with a thickness

of 2 μm and a width of 5 μm located on the surface of the YIG film [13]. After the excitation of the pulse, the magnetization behavior of time was fixed for $T_m = 300$ ns. Then the array of obtained data was subjected to Fourier transform and as a result, the output signal spectrum was obtained for the reference structure and the L -shaped microwave guide under study. Fig. 1, c shows the results of calculating the spectrum of the spin-wave signal in the output section of microwave S_2 of an investigated irregular structure with broken translational symmetry. The beginning of the frequency bandwidth of the structures under study corresponds to the frequency $f_0 = \sqrt{f_H(f_H + f_M)} = 5.096$ GHz, where $f_H = \gamma H_0$, $f_M = \gamma \mu M_0$, γ is the gyromagnetic ratio for YIG.

At the frequencies f_2 and f_3 , the irregularity region is the source of short dipole-exchange waves [14] due to the presence of a gradient of the internal magnetic field in the region of the bending of the L -shaped microstructure. This mechanism for generating short SWs in this case can explain the characteristic dips in the output power spectrum (Fig. 1, d) at frequencies f_2 and f_3 . As shown in [15], MSSWs propagating along the x -axis are weakly reflected from the joints of the vertical and horizontal segments.

The origin of multiple dips in the shaded region in Fig. 1, d denoted with f_4 and f_5 can be originated from inhomogeneous magnetic field in the double junction region in the case of step-shaped junction (Fig. 1, b) in comparison with L -shaped structure (Fig. 1, a). The conditions for short spin wave generation in the former case are originated from the non-uniform distribution of the internal magnetic field in the two regions: junction of section S_5 and S_4 ; junction of section S_4 and S_3 . The detailed mechanism of this dips formation are beyond the current manuscript.

Control of band gaps in three-dimensional meander structures

Combining L -shaped interconnect elements into a meander array makes it possible to avoid the limitations associated with attempts to control SW [16], which are difficult to implement using plane magnetized films due to the anisotropic dispersion of SW, which depends on the relative orientation of the magnetization and the wave vector.

Figure 2, a shows a segment of a periodic 3D magnon YIG structure in cross section used to simulate a meander structure with the following parameters: modulation period $L = 740$ nm, height of the lower horizontal sections $m_1 = 50$ nm, height of the upper horizontal sections $m_2 = 50$ nm, thickness of the vertical sections $m_3 = 50$ nm, drop height $p = 120$ nm. The direction of the external magnetic field was directed along the z -axis.

Numerical simulation was carried out by solving the system of Maxwell equations by the finite element method in the COMSOL Multiphysics software product. The calculation of the dispersion characteristics was carried out considering the fact that the components of the electromagnetic field depended on the frequency according to the harmonic law. The equation for the electric field strength vector \mathbf{E} had the following form:

$$\nabla \times (\hat{\mu}^{-1} \nabla \times \mathbf{E}) - k^2 \varepsilon \mathbf{E} = 0$$

where $k = \omega/c$ is the wave number in vacuum, $\omega = 2\pi/f$ is the circular frequency, f is the frequency of the electromagnetic wave, and ε is the effective value of the permittivity. In this case, the magnetic permeability tensor for tangential magnetization has the form:

$$\hat{\mu} = \begin{vmatrix} \mu(f) & -i\mu_a(f) & 0 \\ i\mu_a(f) & \mu(f) & 0 \\ 0 & 0 & 1 \end{vmatrix},$$

$$\mu(f) = \frac{-f_B(f_B + f_M) - f^2}{f_B^2 - f^2},$$

$$\mu_a(f) = \frac{f_M f}{f_B^2 - f^2}.$$

It should be noted that this method makes it possible to make calculations considering the non-single-year distribution of the internal magnetic field.

As a result of numerical simulation, dispersion characteristics were obtained for direct and

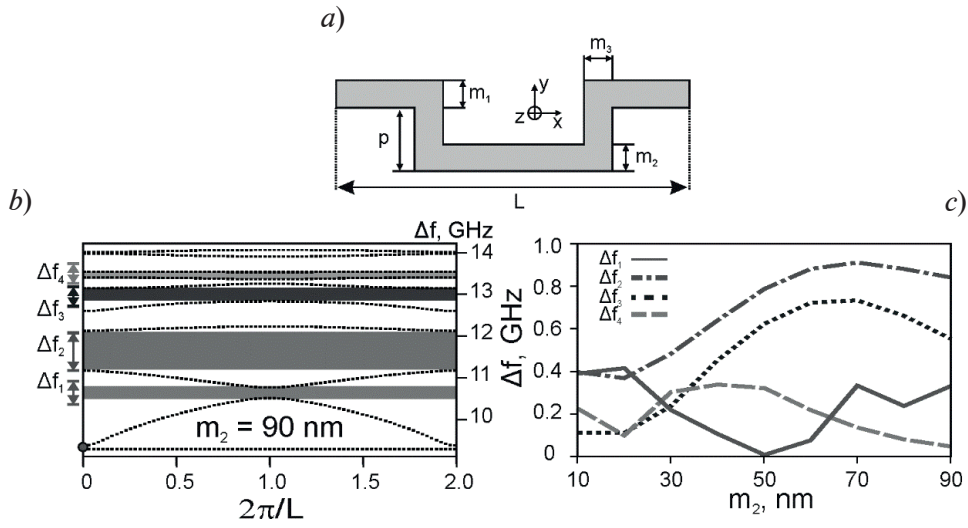


Fig. 2. Schematic view of the meander structure (a), dispersion characteristic at $m_2 = 90$ nm (b), dependence of the frequency ranges of the Bragg band gaps on the change in the drop height p (c)

counterpropagating waves with a section width $m_2 = 90$ nm (Fig. 2, b). On the dispersion characteristics, one can see the frequency ranges of the Bragg band gaps in which the propagation of spin waves is impossible. It can be seen that at $m_2 = 90$ nm in the frequency range Δf_1 in the SW spectrum, the first band gap is formed (near the wave number $k \sim k_B = 2\pi/L$). The color on the dispersion characteristics indicates the frequency ranges of the Bragg band gaps. In this case, the frequency band gap has the greatest value for the low-frequency mode in the region Δf_2 for waves with a wave number near $k \sim 2k_B$. The next band gap is formed for SW with a wave number near $k \sim 2k_B$, its width is denoted by Δf_3 . For the blocking zone for SW with a wave number near $k \sim 4k_B$, the designation Δf_4 is introduced.

To analyze the effect of a change in the thickness of the vertical sections m_2 on the nature of the dispersion characteristic, the value of m_2 took a value from 10 to 90 nm. As a result, it was found that at $k = 1$ it is possible to control the widths of the Bragg band gaps.

Fig. 2, c shows the dependence of frequency ranges of SW non-transmission on the parameter m_2 for four bands Δf_1 , Δf_2 and Δf_3 , Δf_4 (solid, dashed-dotted, dashed and dotted respectively). The horizontal segment thickness parameter m_2 was varied in the range from 10 nm to 90 nm. The thickness of the ferromagnetic layer in the vertical section was $m_3 = 25$ nm, and the difference $p = 100$ nm. At the value of the parameter $m_2 = 50$ nm, the value of the frequency range of the first band gap, for waves with a wave number near $k \sim k_B$, is maximum and is 0.42 GHz. However, for SW with a wave number near $k \sim 2k_B$ and $k \sim 4k_B$, the maximum value of the frequency band gap width is observed at approximately $m \sim 70$ nm. For SW with a wave number near $k \sim 6k_B$ at parameter values $m_2 \sim 90$ nm, the value of the frequency band gap is minimal. Near these values of the parameter $m_2 \sim 50$ nm, the band gap Δf_1 is closed.

This means that in the vicinity of these values p of the parameter m_2 one can observe the closure of the band gap Δf_1 . By varying the meander modulation depth, it is possible to control the width of the non-transmission frequency band in the spectrum of spin waves propagating in a meander structure, which can be used in the design and manufacture of microwave filters based on nanoscale magnon-crystalline structures made in the form of meander ferromagnetic films.

REFERENCES

1. Nikitov S.A., Safin A.R., Kalyabin D.V. et al., Dielectric magnonics: from gigahertz to terahertz, *Physics—Uspekhi*. 10 (63) (2020) 945–974.
2. Allwood D.A., Xiong G., Faulkner C.C., Atkinson D., Petit D, Cowburn R.P., Magnetic domain-wall logic. *Science*. 309 (5741) (2005) 1688-1692.
3. Barman A., Gubbiotti G., Ladak S., Adeyeye A.O., Krawczyk M., Gräfe J., Winklhofer M., The 2021 magnonics roadmap. *Journal of Physics: Condensed Matter*, 33 (41) (2021) 413001.

4. **Sadovnikov A.V., Beginin E.N., Sheshukova S.E., Romanenko D.V., Sharaevskii Yu.P., Nikitov S.A.**, Directional multimode coupler for planar magnonics: Side-coupled magnetic stripes. *Applied Physics Letters*, 107 (20) (2015) 202405.
5. **Niemier M.T., Bernstein G.H., Csaba G., Dingler A., Hu X.S., Kurtz S., Liu S., Nahas J., Porod W., Siddiq M., Varga E.**, Nanomagnet logic: progress toward system-level integration. *Journal of Physics: Condensed Matter*, 23 (49) (2011) 493202.
6. **Martyshkin A.A., Beginin E.N., Stognij A.I., Nikitov S.A., Sadovnikov A.V.**, Vertical spin-wave transport in magnonic waveguides with broken translation symmetry. *IEEE Magnetics Letters*, 10 (2019) 1–5.
7. **Nikitov S.A., Tailhades Ph., Tsai C.S.**, Spin waves in periodic magnetic structures—magnonic crystals. *Journal of Magnetism and Magnetic Materials*, 236 (3) (2001) 320–330 2001.
8. **Chumak A.V., Serga A.A., Hillebrands B.**, Magnonic crystals for data processing. *Journal of Physics D: Applied Physics*, 50(24) (2017) 244001.
9. **Beginin E.N. et. al.**, *Three-Dimensional Magnonics* CRC Press.
10. **Damon W., Eshbach J.R. Damon, R.W. & Eshbach J.R.**, Magnetostatic modes of a ferromagnet slab. *Journal of Physics and Chemistry of Solids*, 19 (3-4) (1961) 308-320.
11. **Landau L.D., Lifschitz E.M.**, *Phys. Z. Sowjet*, 8 (153) (1935).
12. **Vansteenkiste A., Leliaert J., Dvornik M., Helsen M., Garcia-Sanchez F., Waeyenberge B., Garcia-Sanchez F., & Van Waeyenberge B.**, The design and verification of MuMax3. *AIP advances*, 4 (10) (2014) 107133.
13. **Sadovnikov A.V., Grachev A.A., Sheshukova S.E., Sharaevskii Yu.P., Serdobintsev A.A., Mitin D.M., Nikitov S.A.**, Magnon straintronics: Reconfigurable spin-wave routing in strain-controlled bilateral magnetic stripes. *Physical review letters*, 120 (25) (2018) 257203.
14. **Davies C.S., Francis A., Sadovnikov A.V., Chertopalov S.V., Bryan M.T., Grishin S.V., Allwood D.A., Sharaevskii Y.P., Nikitov S.A., Kruglyak V.V.**, Towards graded-index magnonics: Steering spin waves in magnonic networks. *Physical Review B*, 92 (2) (2015) 020408.
15. **Beginin E.N., Sadovnikov A.V., Sharaevskaya A.Y., Stognij A.I., Nikitov S.A.**, Spin wave steering in three-dimensional magnonic networks. *Applied Physics Letters*, 112(12) (2018) 122404.
16. **Vogt K., Fradin F.Y., Pearson J.E., Sebastian T., Bader S.D., Hillebrands B., Hoffmann A., Schultheiss H.**, Realization of a spin-wave multiplexer. *Nature communications*, 5 (1) (2014) 1–5.

THE AUTHORS

MARTYSHKIN Alexandr A.
aamartyshkin@gmail.com

BEGININ Eugeny N.
egbegin@gmail.com

GUBANOVA Yulya A.
yulya29022095@gmail.com

SADOVNIKOV Alexandr V.
sadovnikovav@gmail.com

Received 30.10.2022. Approved after reviewing 24.03.2023. Accepted 24.03.2023.

Conference materials

UDC 538.913

DOI: <https://doi.org/10.18721/JPM.161.133>

Effect of surface curvature of an FCC crystal on the characteristics of localized vibrations of atoms

A.I. Cherednichenko ¹✉, P.V. Zakharov ², A.M. Eremin ³, M.D. Starostenkov ⁴,
E.A. Korznikova ⁵, S.V. Dmitriev ⁶

¹ Shukshin Altai State University for Humanities and Pedagogy, Biysk, Russia;

² Peter the Great St. Petersburg Polytechnic University, St. Petersburg, Russia;

³ Biysk Technological Institute (branch) of the Altai State Technical University, Biysk, Russia;

⁴ Polzunov Altai State Technical University, Barnaul, Russia;

⁵ Ufa State Aviation Technical University, Ufa, Russia;

⁶ Institute of Molecule and Crystal Physics, Ufa Federal Research Center of RAS, Ufa, Russia

✉ anton.chered@mail.ru

Abstract. Localized states of discrete structures play an important role in energy transfer and reduction of potential barriers for local structure transformation. In this paper, we consider the influence of the surface curvature of the crystal with cylindrical symmetry on the possibility of excitation of surface localized modes. The study is performed by means of molecular dynamics method. A face-centered cubic crystal of composition A_3B with an $L1_2$ superstructure, where component A is Pt, B is Al is considered. The interaction of particles was described by the interatomic potential obtained by the embedded atom method. We demonstrate the fundamental possibility of the existence of localized modes on the surface under consideration. External oscillations, in turn, can imitate the boundary conditions corresponding to the dynamics of the crystal volume, thereby leading to the consideration of modes located far from the surface. The energy and dynamic characteristics of localized excitations are calculated as functions of the curvature and location of the atom on the crystal surface.

Keywords: localized states, surface, molecular dynamics

Funding: The work was carried out within the framework of the project of the Russian Science Foundation No. 21-12-00275.

Citation: Cherednichenko A.I., Zakharov P.V., Eremin A.M., Starostenkov M.D., Korznikova E.A., Dmitriev S.V., Effect of surface curvature of an FCC crystal on the characteristics of localized vibrations of atoms, St. Petersburg State Polytechnical University Journal. Physics and Mathematics. 16 (1.1) (2023) 191–196. DOI: <https://doi.org/10.18721/JPM.161.133>

This is an open access article under the CC BY-NC 4.0 license (<https://creativecommons.org/licenses/by-nc/4.0/>)

Материалы конференции

УДК 538.913

DOI: <https://doi.org/10.18721/JPM.161.133>

Влияние кривизны поверхности ГЦК кристалла на характеристики локализованных колебаний атомов

А.И. Чередниченко ¹✉, П.В. Захаров ², А.М. Ерёмин ³, М.Д. Старостенков ⁴,
Е.А. Корзникова ⁵, С.В. Дмитриев ⁶

¹ Алтайский государственный гуманитарно-педагогический университет им. В.М. Шукшина, г. Бийск, Россия;

² Санкт-Петербургский политехнический университет Петра Великого, Санкт-Петербург, Россия;

³ Бийский технологический институт (филиал) Алтайского государственного технического университета им. И.И. Ползунова, г. Бийск, Россия;

⁴ Алтайский государственный технический университет им. И.И. Ползунова, г. Барнаул, Россия;

⁵ Уфимский государственный авиационный технический университет, г. Уфа, Россия;

⁶ Институт физики молекул и кристаллов Уфимского федерального исследовательского центра Российской академии наук, г. Уфа, Россия

✉ anton.chered@mail.ru

Аннотация. Исследование проводится методом молекулярной динамики. Рассмотрен гранецентрированный кубический кристалл состава A_3B со сверхструктурой $L1_2$, где компонент A – Pt, B – Al. Взаимодействие частиц описывалось межатомным потенциалом, полученным методом внедренного атома. Показана принципиальная возможность существования локализованных мод на рассматриваемой поверхности. Рассчитаны энергетические и динамические характеристики локализованных возбуждений в зависимости от кривизны и положения атома на поверхности кристалла.

Ключевые слова: локализованные состояния, поверхность, молекулярная динамика

Финансирование: Работа выполнена в рамках проекта РНФ № 21-12-00275.

Ссылка при цитировании: Чердниченко А.И., Захаров П.В., Ерёмин А.М., Старостенков М.Д., Корзникова Е.А., Дмитриев С.В. Влияние кривизны поверхности ГЦК кристалла на характеристики локализованных колебаний атомов // Научно-технические ведомости СПбГПУ. Физико-математические науки. 2023. Т. 16. № 1.1. С. 191–196. DOI: <https://doi.org/10.18721/JPM.161.133>

Статья открытого доступа, распространяемая по лицензии CC BY-NC 4.0 (<https://creativecommons.org/licenses/by-nc/4.0/>)

Introduction

Dynamic discrete structures play an important role in a large number of processes in nature and technology. The possibility of supporting localized excitations by such structures expands the prospects for their application [1–5]. Localized states in a discrete system are possible with the manifestation of nonlinearity of connections. In the general case, this leads to the formation of various types of localized modes and states of the structure.

Local excitations of the atomic structure near the surface of crystals can lead to various nonlinear effects that affect the structural and energy transformations of the material at a significant distance from the surface [6–8]. In this case, the properties of localized excitations change depending on the energy relief of the surface. For simple cases, in [9], we considered oscillatory modes near the surface and their characteristics from the standpoint of the concept of discrete breathers [10]. In this case, it should be noted that we are talking about localized modes near inhomogeneities, because a nonlinear localized mode can be called a discrete breather if it exists in a medium with translational symmetry without distortion. The presence of any defects and inhomogeneities does not provide this condition. However, the possibility of energy transfer from the surface into the interior of such a system, shown by us in [9], indicates a direct relationship between these types of oscillations. Due to the high degree of DB localization in this type of crystal, one can speak of discrete breathers already at several interatomic distances from the surface. In addition, in the case of external influences on the crystal, which lead to the excitation of modes, it is possible to create conditions under which these oscillations will correspond to discrete breathers inside the crystal.

External periodic influences can lead to the manifestation of the effect of supratransmission. Which consists in the transfer of energy at frequencies outside the spectrum of the system [11, 12]. We have shown the possibility of manifestation of this effect in this crystal [13]. Noteworthy is the role of discrete breathers in the formation of conditions for energy transport through the crystal. They are a kind of accumulators that accumulate vibrational energy and ensure its further transmission.

In this work, high-amplitude vibrations of atoms on the surface of a crystal of cylindrical symmetry of various curvatures are studied by the method of atomistic simulation.

Materials and Methods

The model was an A_3B lattice with an $L1_2$ superstructure in the form of a cylinder of various diameters. Depending on the plane and diameter of the cylinder, the configuration of the crystal surface, including the energy relief, changed, which affected the conditions for the formation of the considered vibrational modes.

Cylinder-shaped models of Pt_3Al crystals have been created. The crystal lattice parameter $a = 3.876 \text{ \AA}$ was taken as the unit for measuring the dimensions of the models. So the height of the cylinders is $15a$, the radii vary from $1a$ to $10a$ in increments of $0.5a$. The number of atoms in the models varies from 195 to 18825. It is easy to see that the surface structure is repeated for cylinders with radii of 1, 3, 4, 5, 6, 7, 8, 9, 10. The axes correspond to the following crystallographic directions: X – $\langle 100 \rangle$, Y – $\langle 010 \rangle$, Z – $\langle 001 \rangle$. To simulate the interatomic interaction, the potential obtained by the embedded atom method (EAM) was used. Let us consider in more detail the process of constructing the EAM potential by the method proposed in [14]. The total energy E of the crystal can be expressed as

$$E = \frac{1}{2} \sum_{i,j,i \neq j} \varphi_{ij}(r_{ij}) + \sum_i F_i(\rho_i), \quad (1)$$

where φ_{ij} represents the pair energy between atoms i and j separated from each other by a distance r_{ij} , and F_i is the nesting energy associated with nested atom i at a local location with electron density ρ_i . For an alloy, the EAM potential contains not only the three functions φ , ρ , and F for each of the constituent elements, but also the pair energy φ_{ab} between different elements a and b ($a \neq b$). As a result, the functions φ , ρ , and F adapted for elemental metals cannot be directly applied to alloy or multilayer systems. However, by normalizing the EAM potentials and introducing an alloy model, a procedure for generalizing the EAM potentials and their cutoff distances was proposed by Zhou [15].

The technique for studying vibrations of surface atoms consisted in the initial analysis of possible configurations of atoms on the surface. Next, the atoms of the light sublattice, Al, were chosen, because namely, they can be carriers of localized modes in the bulk of the crystal. After that, such atoms were removed from the equilibrium position and their dynamic parameters were calculated as a function of time. The cylinder model was previously minimized in energy at zero Kelvin. The entire modeling process was carried out in the LAMMPS environment [16]. Visualization was performed using OVITO [17].

Results and Discussion

Initially, the state of the model as a whole was analyzed. This is how the potential energy per atom was calculated for models with different radii. The corresponding dependence is shown in graph in Fig. 1, *a* for both components of the alloy, and the distribution of potential energy in the cylinder section is also shown. This makes it possible to estimate the contribution of the free surface to the specific binding energy for each type of crystal atoms and to take this into account in the presence of differences in vibrations for different vibrational modes.

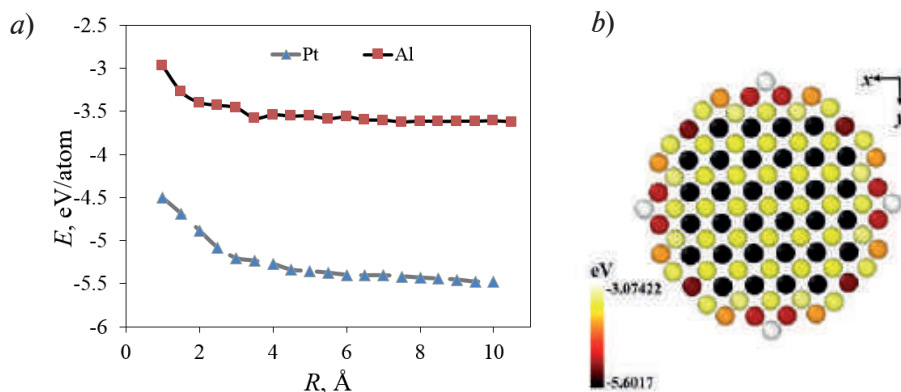


Fig. 1. Energy parameters of the model: potential energy per atom vs the radius of the cylinder model (*a*), visualization of the potential energy distribution on the example of a model with a radius of 4 lattice constants (*b*)

Next, we consider the dependence of the energy of the most loosely bound Al atom on the distance from the crystal surface (Fig. 2). The atom (indicated by the number I in Fig. 3) was removed at a distance S from the perpendicular surface, and the binding energy was calculated. The figure shows two results for the minimum cylinder size and for a cylinder with a radius of $5a$. The difference is not significant, which may indicate that the curvature of the surface does not play a significant role when considering single atoms. However, the shape of the curve indicates possible features of oscillations for different initial amplitudes.

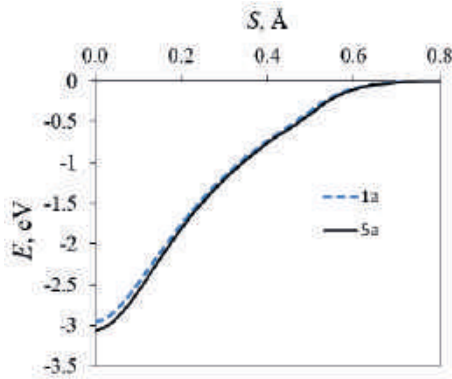


Fig. 2. Dependence of the binding energy of the Al atom on the distance S as it moves away from the surface of the cylinder for two cases: radius $1a$ and $5a$

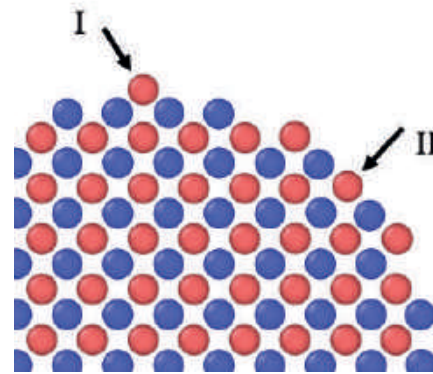


Fig. 3. Atoms whose modes were studied in the work

Two Al atoms were considered, shown on the cut of the cylinder in Fig. 3. In Fig. 3 shows the characteristic position of such atoms, however, all variants of the cylinder diameter indicated in the model description section were considered. For models with a small radius, i.e. the first two points on the graph in Fig. 1, a for the Al atom, there were no stable oscillations. A significant gradient in energy led to the fact that the oscillatory system was not stable, and the slightest imbalance in the system led to the destruction of the oscillations. With an increase in the size of the model, the oscillations showed greater stability and the radius of curvature did not have a significant effect on the duration of the oscillations. In the case of consideration of vibrations of atom I, they remained stable in the range of amplitudes 0.2 – 0.55 Å. The upper limit corresponds to the inflection of the function on the graph of Fig. 2. In this case, the oscillations are harmonic in nature, and their modulation was also observed, depending on the initial amplitude of the deviation of the atoms (Fig. 4). In fact, modulation indicates a displacement of the center of oscillation relative to the surface and does not affect the amplitude or frequencies. In this case, it makes sense to talk about complex oscillations of the system.

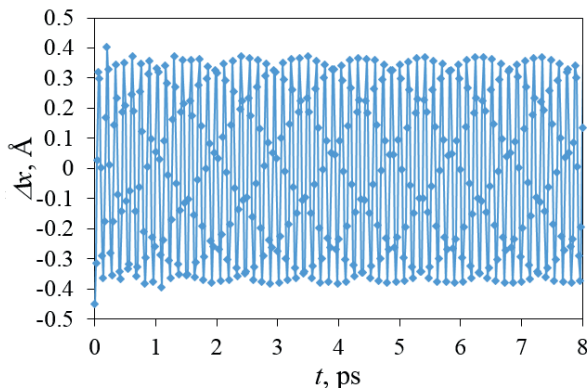


Fig. 4. Time dependence of the atomic coordinate, with an initial deviation of 0.45 Å, for a cylindrical surface with a radius of $6a$

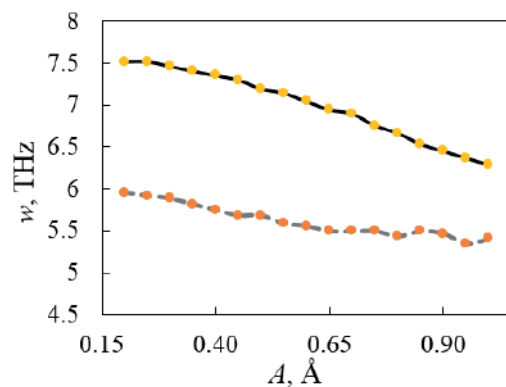


Fig. 5. The dependence of the frequency on the amplitude for the considered configurations of atoms on the surface



One of the main characteristics of discrete breathers is the type of amplitude-frequency dependence. In the bulk part of the crystal, we observe a soft type of nonlinearity, i.e. with decreasing frequency with increasing amplitude.

Similar behavior is observed in Fig. 5 for both variants of atomic position on the surface. Surface effects, in turn, have an influence, and the frequency in this case lies in the range characteristic of the acoustic branch of the phonon spectrum of the crystal.

The obtained results qualitatively correlate with [9] where it was shown that differences of the lattice in the bulk part and on the edge of the crystal result in considerable shift of amplitude-frequency characteristics of discrete breathers. A stronger decrease of the $A(\omega)$ dependence in Fig. 5 can be attributed to the higher curvature in the vicinity of the atom location where the bond length can be higher. This fact of the dependence of nonlinear localization properties on its location with respect to the crystal surface is an important issue, since in most real crystals there are a large number of surface defects, such as grain boundaries [18], where the characteristics of discrete breathers are also likely to be different from those in an ideal lattice. It can also be noted that in such cases the implementation of highly symmetrical breathers can be difficult due to the variable lattice parameter [19] and can reveal some properties of breathers in 2D structures [19–21]. In the future, it is planned to study the dynamics of the modulation instability of delocalized modes [22–25] in such crystals in order to understand the effect of the presence of a surface on the formation of discrete breathers because of the decay of delocalized nonlinear modes.

Conclusion

Various surface configurations and directions of displacement of atoms from the equilibrium position are considered by means of computer experiments. The influence of the potential relief on the possibility of stable localized excitations is analyzed. It is shown that for small radii of the considered cylindrical surfaces, stable excitations do not occur: localized oscillations are rapidly destroyed. The obtained numerical results within the framework of the considered model of interatomic interaction show the possibility of sufficiently long oscillations on the surface of the model, the curvature of which has more than four lattice parameters. The study contributes to fundamental understanding of the behavior of discrete breathers in the vicinity of the surface crystal, having a potential effect on the macroscopic characteristics of the considered material [26].

Acknowledgments

The work was carried out within the framework of the project of the Russian Science Foundation No. 21-12-00275. The part of results of the work were obtained using computational resources of Peter the Great Saint-Petersburg Polytechnic University Supercomputing Center (www.spbstu.ru).

REFERENCES

1. **Chong C., Porter M., Kevrekidis P., Daraio Ch.**, Nonlinear Coherent Structures in Granular Crystals, *Journal of physics Condensed matter*. 29 (2016).
2. **Christodoulides D.N., Efremidis N.K.**, Discrete temporal solitons along a chain of nonlinear coupled microcavities embedded in photonic crystals, *Optics Letters*. 27 (2002) 568–70.
3. **Landa H., Reznik B., Brox J., Mielenz M., Schaetz T.**, Structure, dynamics and bifurcations of discrete solitons in trapped ion crystals, *New Journal of Physics*. 15 (2013).
4. **Landa H., Retzker A., Schaetz T., Reznik B.**, Entanglement generation using discrete solitons in Coulomb crystals, *Physical Review Letters*. 113 (5) (2014) 053001.
5. **Sato M., Sievers A.**, Direct observation of the discrete character of intrinsic localized modes in an antiferromagnet, *Nature*. 432 (2004) 486–8.
6. **Flach S., Gorbach A.**, Discrete breathers – Advances in theory and applications, *Phys. Rep.* 467 (1) (2008) 1–116.
7. **Kondratyev V.N., Di Toro M.**, Higher order long range correlations in nuclear structure and dynamics, *Phys. Rev. C*. 53 (5) (1996) 2176–80.
8. **Berini P.**, Long-range surface plasmon polaritons, *Advances in Optics and Photonics*. 1 (3) (2009) 484–588.
9. **Zakharov P.V., Korznikova E.A., Dmitriev S.V., Ekomasov E.G., Zhou K.**, Surface discrete breathers in Pt₃Al intermetallic alloy, *Surface Science*. 679 (2019) 1–5.

10. **Flach S., Willis C.R.**, Discrete Breathers, *Phys. Rep.* 295 (1998) 181–264.
11. **Geniet F., Leon J.**, Energy transmission in the forbidden band gap of a nonlinear chain, *Physical Review Letters*. 89 (13) (2002) 1341021–24.
12. **Machas-Dhaz J.E., Puri A.**, On the transmission of binary bits in discrete Josephson-junction arrays, *Physics Letters, Section A: General, Atomic and Solid State Physics*. 372 (30) (2008) 5004–10.
13. **Cherednichenko A.I., Zakharov P.V., Starostenkov M.D., Sysoeva M.O., Eremin A.M.**, Nonlinear supratransmission in a Pt₃Al crystal at intense external influence, *Computer Research and Modeling*. 11 (2019) 109–17.
14. **Lutsenko I.S., Zakharov P.V., Starostenkov M.D., Dmitriev S.V., Korznikova E.A.**, Stability of supratransmission waves in a crystal of A₃B stoichiometry upon interaction with single dislocations, *Journal of Physics: Conference Series*. 2103 (1) (2021) 012079.
15. **Zhou X.W., Johnson R.A., Wadley H.N.G.**, Misfit-energy-increasing dislocations in vapor-deposited CoFe/NiFe multilayers, *Phys. Rev. B*. 69 (2004) 144113.
16. LAMMPS Molecular Dynamics Simulator. URL: <https://www.lammps.org>. Accessed May 11, 2022.
17. OVITO Open Visualization Tool. URL: <https://www.ovito.org>. Accessed May 11, 2022.
18. **Korznikova G., Czepe T., Khalikova G., Gunderov D., Korznikova E., Litynska-Dobrzynska L., Szezynger M.**, Microstructure and mechanical properties of Cu-graphene composites produced by two high pressure torsion procedures, *Materials Characterization*. 161 (2020) 110122.
19. **Korznikova E.A., Fomin S.Y., Soboleva E.G., Dmitriev S.V.**, Highly symmetric discrete breather in a two-dimensional Morse crystal, *JETP Letters*. 103 (2016) 277–281.
20. **Baimova J.A., Dmitriev S.V., Zhou K.**, Discrete breather clusters in strained graphene, *EPL (Europhysics Letters)*. 100 (2012) 36005.
21. **Barani E., Korznikova E., Chetverikov A., Zhou K., Dmitriev S.**, Gap discrete breathers in strained boron nitride, *PHYSICS LETTERS A*. 381 (2017) 3553–3557.
22. **Abdullina D.U., Semenova M.N., Semenov A.S., Korznikova E.A., Dmitriev S.V.**, Stability of delocalized nonlinear vibrational modes in graphene lattice, *The European Physical Journal B*. 92 (2019) 249.
23. **Korznikova E.A., Bachurin D.V., Fomin S.Y., Chetverikov A.P., Dmitriev S.V.**, Instability of vibrational modes in hexagonal lattice, *The European Physical Journal B*. 90 (2017).
24. **Korznikova E.A., Shcherbinin S.A., Ryabov D.S., Chechin G.M., Ekomasov E.G., Barani E., Zhou K., Dmitriev S.V.**, Delocalized Nonlinear Vibrational Modes in Graphene: Second Harmonic Generation and Negative Pressure, *Physica Status Solidi (B) Basic Research*. 256 (2019).
25. **Shcherbinin S.A., Semenova M.N., Semenov A.S., Korznikova E.A., Chechin G.M., Dmitriev S.V.**, Dynamics of a Three-Component Delocalized Nonlinear Vibrational Mode in Graphene, *Physics of the Solid State*. 61 (2019) 2139–44.
26. **Korznikova E., Morkina A., Singh M., Krivtsov A., Kuzkin V., Gani V., Bebikhov Y., Dmitriev S.**, Effect of discrete breathers on macroscopic properties of the Fermi-Pasta-Ulam chain, *European physical journal B*. 93 (2020).

THE AUTHORS

CHEREDNICHENKO Anton I.
anton.chered@mail.ru
ORCID: 0000-0001-8974-7538

STAROSTENKOV Mikhail D.
genphys@mail.ru
ORCID: 0000-0002-6326-7613

ZAKHAROV Pavel V.
zakharovpvl@rambler.ru
ORCID: 0000-0002-6410-1594

KORZNIKOVA Elena A.
elena.a.korznikova@gmail.com
ORCID: 0000-0002-5975-4849

EREMIN Alexander M.
eam77@yandex.ru
ORCID: 0000-0002-3453-2860

DMITRIEV Sergey V.
dmitriev.sergey.v@gmail.com
ORCID: 0000-0002-6744-4445

Received 02.11.2022. Approved after reviewing 10.11.2022. Accepted 10.11.2022.

Conference materials

UDC 538.9

DOI: <https://doi.org/10.18721/JPM.161.134>

Calculation of correlation lengths in 2D Lennard-Jones fluids

I.V. Simkin ¹✉, E.V. Yakovlev ¹, N.P. Kryuchkov ¹, S.A. Korsakova ¹, S.O. Yurchenko ¹

¹ Bauman Moscow State Technical University, Moscow, Russia

✉ vanyasimkin@gmail.com

Abstract. The process of spinodal decomposition in two-dimensional system that was obtained by molecular dynamics simulation has been analysed using the correlation of reciprocal areas of the Voronoi cells. Correlation lengths dependence on the temperature and the critical exponent of the LJ12-6 system in the fluctuation region by the general renormalization group (RG) framework were calculated. We showed the agreement of the calculated critical exponent ν with both experiments and theory. The proposed methodology for correlations of the reciprocal areas of the Voronoi cells is well applicable in the experiments with 2D colloidal systems.

Keywords: soft matter, colloidal particles, tuned self-assembly, phase transitions, molecular dynamics

Funding: I.V.S., E.V.Y., N.P.K., S.A.K and S.O.Y. acknowledge BMSTU State Assignment for infrastructural support. Studies are supported by the Russian Science Foundation, Grant No. 20-12-00356.

Citation: Simkin I.V., Yakovlev E.V., Kryuchkov N.P., Korsakova S.A., Yurchenko S.O., Calculation of correlation lengths in 2D Lennard-Jones fluids, St. Petersburg State Polytechnical University Journal. Physics and Mathematics. 16 (1.1) (2023) 197–204. DOI: <https://doi.org/10.18721/JPM.161.134>

This is an open access article under the CC BY-NC 4.0 license (<https://creativecommons.org/licenses/by-nc/4.0/>)

Материалы конференции

УДК 538.9

DOI: <https://doi.org/10.18721/JPM.161.134>

Вычисление корреляционных длин в двумерных жидкостях с потенциалом Леннарда-Джонса

И.В. Симкин ¹✉, Е.В. Яковлев ¹, Н.П. Крючков ¹, С.А. Корсакова ¹, С.О. Юрченко ¹

¹ Московский государственный технический университет им. Н.Э. Баумана, г. Москва, Россия

✉ vanyasimkin@gmail.com

Аннотация. Проанализирован процесс спинопального распада в двумерной системе, полученный методом молекулярной динамики с помощью корреляции обратных площадей ячеек Вороного. Рассчитана зависимость корреляционных длин от эффективной температуры системы с потенциалом взаимодействия LJ12-6 в области спинопального распада. Показано соответствие вычисленного критического индекса ν как экспериментальным исследованиям фазовых переходов в двумерных ферромагнетиках, так и теоретическим исследованиям систем Изинга. Предложенный метод корреляций обратных площадей ячеек Вороного может быть применим в экспериментах с двумерными коллоидными системами.

Ключевые слова: мягкая материя, коллоидные частицы, управляемая самосборка, фазовые переходы, метод молекулярной динамики

Финансирование: Работа выполнена при поддержке Гранта РФФИ № 20-12-00356 по теме: “Коллективная динамика, упругие и транспортные свойства классических жидкостей в различных режимах межчастичного взаимодействия” на базе МГТУ им. Н.Э. Баумана

Ссылка при цитировании: Симкин И.В., Яковлев Е.В., Крючков Н.П., Корсакова С.А., Юрченко С.О. Вычисление корреляционных длин в двумерных жидкостях с потенциалом Леннарда-Джонса // Научно-технические ведомости СПбГПУ. Физико-математические науки. 2023. Т. 16. № 1.1. С. 197–204. DOI: <https://doi.org/10.18721/JPM.161.134>

Статья открытого доступа, распространяемая по лицензии CC BY-NC 4.0 (<https://creativecommons.org/licenses/by-nc/4.0/>)

Introduction

Method for the characterization various phases of matter is one of the central tasks of condensed matter physics and materials science. In particular, the study of the phase transitions in 2D systems has played a crucial role for understanding of the phase transitions and it can be extended to other complex systems. Understanding the process of the phase transitions in 2D systems plays important role in a number of areas, from photonics and electronics [1–8], to novel materials [9, 10], and biophysics [11], since knowledge of the phase behavior opens way to designing systems with the necessary properties.

A great number of phase transitions phenomena studies are carried out by methods of the molecular dynamics (MD) and Monte Carlo (MC) simulation. One of the simplest model which is capable of reproducing gas, liquid, and solid phases behaviour is the Lennard-Jones (LJ) system. Such systems make it possible to study melting and crystallization [12–14], condensation and evaporation [15], spinodal decomposition [16–18].

One of the platforms mimicing molecular behavior are colloidal systems [19–23]. The studies in such systems include crystallization and melting [24–31], reentrant and solid-solid phase transitions [32–34], condensation and critical phenomena [35–37], molecular-like interactions [38, 39], sublimation [40], gelation, slow dynamics in glasses [41–44], the role of three-body interactions of phase transitions [45].

Tunable interactions between colloidal particles can be provided using different physical mechanisms [46]: electrostatic interactions in solvents, [47, 48], tunable interactions induced by external magnetic fields [27, 49], alternating anisotropic and rotating electric fields [50, 51]. Rotating electric fields make it possible to induce and to control interparticle interactions in colloidal systems, and collective dynamics of colloidal particles can be visualized in real time with the spatial resolution of individual particles. In rotating electric fields, interparticle interactions in a colloidal system monolayer are tuned by the following mechanism [51–54]: an external electric field polarizes colloidal particles, that leads to anisotropic interactions; a fast (compared to the particle diffusion time) rotation of the field in the plane of the system makes it possible to achieve isotropic tuned dipole attraction at large distances [51, 54]. The colloidal system in the rotating electric field provides a rich variety of different interactions, including repulsion, attraction, combination of short-range repulsion with long-range attraction, barrier-type interactions with short-range attraction and long-range repulsion, and double-scale repulsive (core-shell) interparticle interactions [55]. This makes it possible to use such system for particle-resolved study of phase transitions [17].

It is required a methodology to study critical phenomena in colloids. The divergence of the correlation length for a mixed phase transition in a 2D colloid model system with nearest neighbor interaction has been shown in Paper [56]. The authors in [57] attempted to calculate the correlation length using the effective interfacial thickness in 2D LJ fluids. In our work, we suggest using the correlation function of reciprocal areas of the Voronoi cells critical temperature vicinity. It allows us to calculate the dependence of the correlation length on the temperature and to determine critical exponent ν in 2D systems.

Materials and Methods

To study the efficiency of density-density correlation method (correlation of reciprocal areas of the Voronoi cells), we performed MD simulations of the system undergoing spinodal decomposition.

We considered system of particles interacting via the potential:

$$\phi_{12-6}(r) = 4 \epsilon \left[\left(\frac{\lambda}{r} \right)^{12} - \left(\frac{\lambda}{r} \right)^6 \right]. \quad (1)$$

Where $\phi_{12-6}(r)$ is the usual Lennard–Jones potential (LJ12-6 potential), ϵ and λ are the strength and range of the interaction, respectively. We use the dimensionless temperature $T/\epsilon \rightarrow T$, distance $r/\lambda \rightarrow r$, surface number density $n\lambda^2/m \rightarrow n$, and time

$$t \sqrt{\frac{\epsilon}{m}} \lambda^2 \rightarrow t$$

(here, m is the mass of the particle).

To obtain correlation length dependence on the temperature the MD simulations of a system containing $N = 10^4$ particles were performed in an NVT ensemble for different temperatures above the critical. Initially particles were distributed uniformly over the simulation region with periodic boundary conditions. Then at every temperature, it was integrated for 10^6 steps until the equilibrium state was reached. The time step of $\Delta t = 5 \times 10^{-3}$ was used. The last 10 snapshots of the system were used for correlation lengths calculations with a sampling rate of 5×10^{-3} steps. The cutoff radius was set to $r_c = 5$.

During spinodal decomposition a new state of reduced symmetry emerges continuously from the disordered or symmetric phase as the temperature is reduced. To analyze the fluctuations in the system, it is proposed to use correlation of reciprocal areas of the Voronoi cells $C(r, r')$.

Let us define the correlation function $C(r, r')$:

$$C(r, r') = \langle \phi(r) \phi(r') \rangle. \quad (2)$$

The correlator of the system was calculated as reciprocal areas product of the Voronoi cells of particles at the radius-vector $r - r'$, averaged over each particle $r - r'$. Figure 1 shows the mechanism for calculating the correlator $C(r, r')$. The area of the Voronoi cell $\phi(r)$ corresponding to the particle at the r' multiplied by the reciprocal area $\phi(r)$ corresponding to the particle at the $r - r'$.

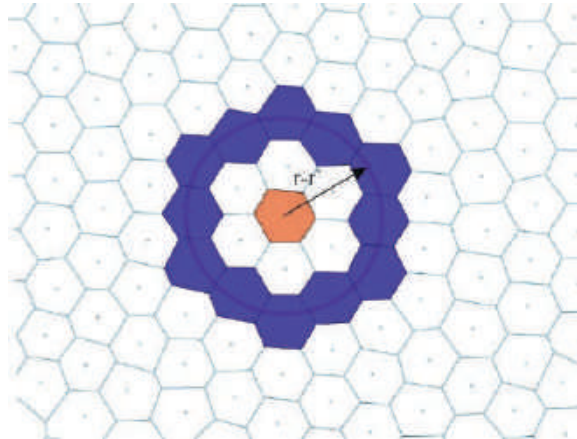


Fig. 1. The field of Voronoi cells for calculating correlator of the system. Voronoi cell corresponding to the particle at the radius vector r is colored orange; Voronoi cells corresponding to the particles at the radius vector $r-r'$ over which averaging is carried out are colored blue

The correlator $C(r, r')$ of the system decreases rapidly with distance above the critical point T_c and nonzero at and below T_c .

In the self-consistent field theory, from the Ginzburg-Landau free energy equation, the correlator $C(r, r')$ of the system is given as follows [58]:

$$C(r) = r^{1-\frac{d}{2}} K_{\frac{d}{2}-1} \left(\frac{r}{\xi} \right), \quad (3)$$

where due to symmetry we can write $C(r)$ instead of $C(r, r')$, ξ is the correlation length, d is the dimension of the system and K_n is the Macdonald function of the n -th order.

Results and Discussion

The correlator (eq. 2) was calculated for the MD system in the vicinity of critical point temperature range. The correlator dependence on the distance and its fit by (eq. 3) are shown in Figure 2.

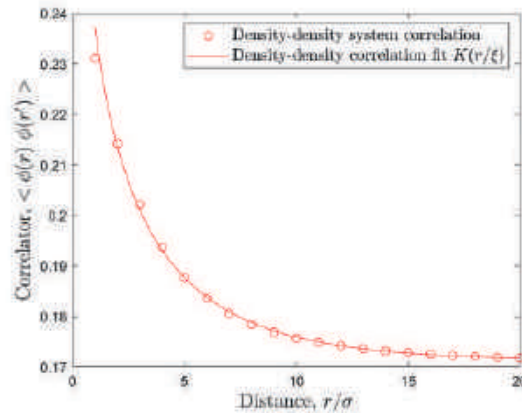


Fig. 2. The correlator dependence on distance of the 2D LJ12-6 system. Red symbols \circ correspond to calculated correlation, σ is the particle radius. Red solid line is the fit of the calculated correlator (eq. 2) by the equation (3)

From the approximation of the correlator $C(r)$ by the Macdonald function (eq. 3) the correlation length ξ for different temperatures were calculated. Several MD simulation timesteps were considered and Figure 3 shows the average correlation length dependence on reduced temperature $\tau = \frac{T - T_{cp}}{T_{cp}}$, where T_{cp} is the critical temperature.

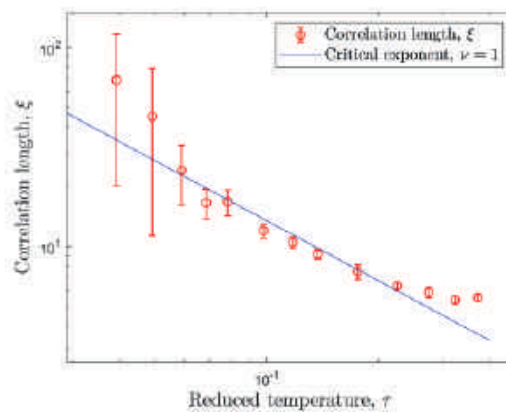


Fig. 3 The correlation length dependence on reduced temperature τ . Red symbols \circ correspond to correlation length; vertical bars correspond to confidence interval of the averaged correlation lengths at several timesteps (confidence level 0.95). Blue solid line is the fit of the correlation length critical behavior (eq. 4)

Critical exponents phenomenologically describe the behavior of many-body systems close to criticality. The behavior of the correlation length on reduced temperature in the fluctuation region is described by the critical exponent ν :

$$\xi = \tau^{-\nu}. \quad (4)$$



Using equation (4) the critical exponent for the 2D LJ system was determined to be $\nu = 1.00 \pm 0.07$. For comparison, Table 1 shows some estimations for the critical exponent ν of two-dimensional systems. One can see agreement with the proposed method.

Table 1

Experimentally measured critical exponents of some two-dimensional systems

System	ν	Class	Ref.
Rb ₂ CoF ₄	0.99(4)	Ising	[59], [60]
K ₂ CoF ₄	0.97(4)	Ising	[61], [60]
Fe/W(110)	0.93(14)	Ising	[62]
LJ12-6	1.00(7)	Ising	Current work

The LJ12-6 interaction demonstrates a 2D Ising-like critical behavior [63]. For two-dimensional Ising systems it is shown that the critical exponent $\nu = 1$ [64].

Conclusion

Thus, methodology for calculating the correlator of reciprocal areas of the Voronoi cells was tested on the LJ12-6 two-dimensional system. Correlation lengths in the area above the critical transition was estimated. The critical exponent ν describing the behavior of the correlation lengths in the fluctuation region was determined. Results were compared with both experimental and theoretical data. This methodology of critical exponent estimation is well applicable for two-dimensional systems and can be applied to experimental systems of colloidal particles in the external electric rotating fields.

REFERENCES

1. **Ricard Alert, Pietro Tierno and Jaume Casademunt**, Mixed-order phase transition in a colloidal crystal, Proceedings of the National Academy of Sciences, 114.49 (2017) 12906–12909.
2. **Ahmed M. Alsayed, Mohammad F. Islam, Jian Zhang, Peter J. Collings and Arjun G. Yodh**, Premelting at defects within bulk colloidal crystals, Science, 309.5738 (2005) 1207–1210.
3. **Andrew I. Campbell, Valerie J. Anderson, Jeroen S. van Duijneveldt and Paul Bartlett**, Dynamical arrest in attractive colloids, The effect of long-range repulsion, Physical review letters, 94.20 (2005) 208301.
4. **Bing-Yang Cao, Jian-Fei Xie and Sergei S. Sazhin**, Molecular dynamics study on evaporation and condensation of n-dodecane at liquid–vapor phase equilibria, The Journal of chemical physics, 134.16 (2011) 164309.
5. **Yuan Cao, Valla Fatemi, Shiang Fang, Kenji Watanabe, Takashi Taniguchi, Efthimios Kaxiras and Pablo Jarillo-Herrero**, Unconventional superconductivity in magic-angle graphene superlattices, Nature, 556.7699 (2018) 43–50.
6. **Malcolm F. Collins**, Magnetic critical scattering. volume 4. Oxford university press, 1989.
7. **Jure Dobnikar, Alexey Snezhko and Anand Yethiraj**, Emergent colloidal dynamics in electromagnetic fields, Soft Matter, 9.14 (2013) 3693–3704.
8. **H.J. Elmers, J. Hauschild, H. Huche, U. Gradmann, H. Bethge, D. Heuer and U. Kuhler**, Submonolayer magnetism of Fe (110) on W (110), Finite width scaling of stripes and percolation between islands, Physical review letters, 73.6 (1994) 898.
9. **Nils Elsner, C. Patrick Royall, Brian Vincent and David R.E. Snoswell**, Simple models for two-dimensional tunable colloidal crystals in rotating ac electric fields The Journal of chemical physics, 130.15 (2009) 154901.
10. **W Neil Everett, Hung-Jen Wu, Samartha G. Anekal, Hung-Jue Sue and Michael A. Bevan**, Diffusing colloidal probes of protein and synthetic macromolecule interactions Biophysical journal, 92.3 (2007) 1005–1013.
11. **Alberto Fernandez-Nieves and Antonio Manuel Puertas**, Fluids, colloids and soft materials, an introduction to soft matter physics. John Wiley & Sons, 2016.

12. **Seth Fraden, Alan J. Hurd and Robert B. Meyer**, Electric-field-induced association of colloidal particles, *Physical review letters*, 63.21 (1989) 2373.
13. **Hironobu Ikeda and Kinshiro Hirakawa**, Neutron scattering study of two-dimensional Ising nature of K_2CoF_4 , *Solid State Communications*, 14.7 (1974) 529–532.
14. **Hironobu Ikeda, Masatsugu Suzuki and Michael T. Hutchings**, Neutron Scattering Investigation of Static Critical Phenomena in the Two-Dimensional Antiferromagnets: $Rb_2Co_{1-c}Mg_cF_4$, *Journal of the Physical Society of Japan*, 46.4 (1979) 1153–1160.
15. **Alexei Ivlev, Gregor Morfill, Hartmut Lowen and C Patrick Royall**, Complex plasmas and colloidal dispersions: particle-resolved studies of classical liquids and solids. volume 5. World Scientific Publishing Company, 2012.
16. **Jaime J. Juárez, Sarah E. Feicht and Michael A. Bevan**, Electric field mediated assembly of three dimensional equilibrium colloidal crystals, *Soft Matter*, 8.1 (2012) 94–103.
17. **L.P. Kadanoff**, *Physics 2* (1966) 263; *ME Fisher, Rep. Prog. Phys.*, 30 (1967) 615.
18. **Charles L. Kane and Eugene J. Mele**, Quantum spin Hall effect in graphene in *Physical review letters*, 95.22 (2005) 226801.
19. **Kirill A. Komarov, Nikita P. Kryuchkov and Stanislav O. Yurchenko**, Tunable interactions between particles in conically rotating electric fields, *Soft Matter.*, 14.47 (2018) 9657–9674.
20. **Markus König, Steffen Wiedmann, Christoph Brune, Andreas Roth, Hartmut Buhmann, Laurens W Molenkamp, Xiao-Liang Qi and Shou-Cheng Zhang**, Quantum spin Hall insulator state in HgTe quantum wells, *Science*, 318.5851 (2007) 766–770.
21. **Nikita P. Kryuchkov, Nikita A. Dmitryuk, Wei Li, Pavel V. Ovcharov, Yilong Han, Andrei V. Sapelkin and Stanislav O. Yurchenko**, Mean-field model of melting in superheated crystals based on a single experimentally measurable order parameter, *Scientific reports*, 11.1 (2021) 1–15.
22. **Nikita P. Kryuchkov, Sergey A. Khrapak and Stanislav O. Yurchenko**, Thermodynamics of two-dimensional Yukawa systems across coupling regimes, *The Journal of Chemical Physics*, 146.13 (2017) 134702.
23. **Nikita P. Kryuchkov, Frank Smallenburg, Alexei V. Ivlev, Stanislav O. Yurchenko and Hartmut Löwen**, Phase diagram of two-dimensional colloids with Yukawa repulsion and dipolar attraction, *The Journal of chemical physics*, 150.10 (2019) 104903.
24. **Volodymyr L. Kulinskii and A. Maslechno**, Surface Tension of the Liquid–Vapor Interface of the Lennard–Jones Fluids from the Ising Model, *The Journal of Physical Chemistry C*, 120.16 (2016) 8790–8803.
25. **Lev Davidovich Landau and Evgenii M. Lifshitz**, *Statistical Physics, Volume 5.* volume 5. Elsevier, 2013.
26. **Pierre-François Lenne and Vikas Trivedi**, Sculpting tissues by phase transitions, *Nature Communications*, 13.1 (2022) 1–14.
27. **Bo Li, Xiuming Xiao, Shuxia Wang, Weijia Wen and Ziren Wang**, Real-space mapping of the two-dimensional phase diagrams in attractive colloidal systems, *Physical Review X*, 9.3 (2019) 031032.
28. **Bo Li, Di Zhou and Yilong Han**, Assembly and phase transitions of colloidal crystals, *Nature Reviews Materials*, 1.2 (2016) 1–13.
29. **Hartmut Löwen**, Melting, freezing and colloidal suspensions, *Physics Reports*, 237.5 (1994) 249–324.
30. **Erik Luijten and Henk W.J. Blöte**, Boundary between long-range and short-range critical behavior in systems with algebraic interactions, *Physical review letters*, 89.2 (2002) 025703.
31. **F Martínez-Pedrero, J. Benet, J.E.F. Rubio, E. Sanz, R.G. Rubio and F. Ortega**, Field-induced sublimation in perfect two-dimensional colloidal crystals, *Physical Review E*, 89.1 (2014) 012306.
32. **Michael R. Mruzik, Farid F. Abraham and G.M. Pound**, Phase separation in fluid systems by spinodal decomposition. II. A molecular dynamics computer simulation, *The Journal of Chemical Physics*, 69.8 (1978) 3462–3467.
33. **Kostya S. Novoselov, D. Jiang, F. Schedin, T.J. Booth, V.V. Khotkevich, S.V. Morozov and Andre K. Geim**, Two-dimensional atomic crystals, *Proceedings of the National Academy of Sciences*, 102.30 (2005) 10451–10453.
34. **Pavel V. Ovcharov, Nikita P. Kryuchkov, Kirill I. Zaytsev and Stanislav O. Yurchenko**, Particle-resolved phase identification in two-dimensional condensable systems, *The Journal of Physical Chemistry C*, 121.48 (2017) 26860–26868.
35. **Divya Paloli, Priti S. Mohanty, Jerome J. Crassous, Emanuela Zaccarelli and Peter Schurtenberger**, Fluid–solid transitions in soft-repulsive colloids, *Soft Matter.*, 9.11 (2013) 3000–3004.



36. **C. Patrick Royall, Dirk GAL Aarts and Hajime Tanaka**, Bridging length scales in colloidal liquids and interfaces from near-critical divergence to single particles, *Nature Physics*, 3.9 (2007) 636–640.
37. **Yi Peng, Feng Wang, Ziren Wang, Ahmed M. Alsayed, Zexin Zhang, Arjun G. Yodh and Yilong Han**, Two-step nucleation mechanism in solid–solid phase transitions, *Nature materials*, 14.1 (2015) 101–108.
38. **An T. Pham, Yuan Zhuang, Paige Detwiler, Joshua E.S. Socolar**, Patrick Charbonneau and Benjamin B Yellen. Phase diagram and aggregation dynamics of a monolayer of paramagnetic colloids, *Physical Review E*, 95.5 (2017) 052607.
39. **Peter N. Pusey**, Complex Plasmas and Colloidal Dispersions: Particle-Resolved Studies of Classical Liquids and Solids, *Physics Today*, 66.2 (2013) 48.
40. **Xiaofeng Qian, Junwei Liu, Liang Fu and Ju Li**, Quantum spin Hall effect in two-dimensional transition metal dichalcogenides, *Science*, 346.6215 (2014) 1344–1347.
41. **C. Patrick Royall, Mirjam E. Leunissen, Antti-Pekka Hynninen, Marjolein Dijkstra and Alfons van Blaaderen**. Re-entrant melting and freezing in a model system of charged colloids, *The Journal of chemical physics*, 124.24 (2006) 244706.
42. **C. Patrick Royall and Stephen R. Williams**, The role of local structure in dynamical arrest, *Physics Reports*, 560 (2015) 1–75.
43. **Valentin N. Ryzhov, E.E. Tareyeva, Yu.D. Fomin and Elena N. Tsiok**, Berezinskii–Kosterlitz–Thouless transition and two-dimensional melting, *Physics-Uspekhi*, 60.9 (2017) 857.
44. **Valentin N. Ryzhov, E.E. Tareyeva, Yu.D. Fomin and Elena N. Tsiok**, Complex phase diagrams of systems with isotropic potentials, results of computer simulations, *Physics-Uspekhi*, 63.5 (2020) 417.
45. **Yu Saito, Tsutomu Nojima and Yoshihiro Iwasa**, Highly crystalline 2D superconductors, *Nature Reviews Materials*, 2.1 (2016) 1–18.
46. **D.R.E. Snoswell, C.L. Bower, P. Ivanov, M.J. Cryan, J.G. Rarity and B. Vincent**, Dynamic control of lattice spacing within colloidal crystals, *New Journal of Physics*, 8.11 (2006) 267.
47. **Joris Sprakel, Alessio Zaccone, Frans Spaepen, Peter Schall and David A Weitz**, Direct observation of entropic stabilization of bcc crystals near melting, *Physical Review Letters*, 118.8 (2017) 088003.
48. **Anna Stradner and Peter Schurtenberger**, Potential and limits of a colloid approach to protein solutions, *Soft Matter.*, 16.2 (2020) 307–323.
49. **Jade Taffs, Stephen R. Williams, Hajime Tanaka and C. Patrick Royall**, Structure and kinetics in the freezing of nearly hard spheres, *Soft Matter.*, 9.1 (2013) 297–305.
50. **Shujie Tang, Chaofan Zhang, Dillon Wong, Zahra Pedramrazi, Hsin-Zon Tsai, Chunjing Jia, Brian Moritz, Martin Claassen, Hyejin Ryu, Salman Kahn and others**, Quantum spin Hall state in monolayer 1T'-WTe₂, *Nature Physics*, 13.7 (2017) 683–687.
51. **Elena N. Tsiok, Yuri D. Fomin, Eugene A. Gaiduk, Elena E. Tareyeva, Valentin N. Ryzhov, Pavel A. Libet, Nikita A. Dmitryuk, Nikita P. Kryuchkov and Stanislav O. Yurchenko**, The role of attraction in the phase diagrams and melting scenarios of generalized 2D Lennard-Jones systems, *The Journal of Chemical Physics*, 156.11 (2022) 114703.
52. **Ziren Wang, Feng Wang, Yi Peng, Zhongyu Zheng and Yilong Han**, Imaging the homogeneous nucleation during the melting of superheated colloidal crystals, *Science*, 338.6103 (2012) 87–90.
53. **Eric R. Weeks, John C. Crocker, Andrew C. Levitt, Andrew Schofield and David A. Weitz**, Three-dimensional direct imaging of structural relaxation near the colloidal glass transition, *Science*, 287.5453 (2000) 627–631.
54. **Sanfeng Wu, Valla Fatemi, Quinn D. Gibson, Kenji Watanabe, Takashi Taniguchi, Robert J. Cava and Pablo Jarillo-Herrero**, Observation of the quantum spin Hall effect up to 100 kelvin in a monolayer crystal, *Science*, 359.6371 (2018) 76–79.
55. **Xiaoxiang Xi, Zefang Wang, Weiwei Zhao, Ju-Hyun Park, Kam Tuen Law, Helmuth Berger, Laszlo Forro, Jie Shan and Kin Fai Mak**, Ising pairing in superconducting NbSe₂ atomic layers, *Nature Physics*, 12.2 (2016) 139–143.
56. **Egor V. Yakovlev, Kirill A. Komarov, Kirill I. Zaytsev, Nikita P. Kryuchkov, Kirill I. Koshelev, Arsen K. Zotov, Dmitry A. Shelestov, Victor L. Tolstoguzov, Vladimir N. Kurlov, Alexei V. Ivlev and others**, Tunable two-dimensional assembly of colloidal particles in rotating electric fields, *Scientific reports*, 7.1 (2017) 1–10.
57. **Egor V. Yakovlev, Nikita P. Kryuchkov, Sofia A. Korsakova, Nikita A. Dmitryuk, Pavel V. Ovcharov, Mihail M. Andronic, Ilya A. Rodionov, Andrei V. Sapelkin and Stanislav O. Yurchenko**, 2D

colloids in rotating electric fields: A laboratory of strong tunable three- body interactions, Journal of Colloid and Interface Science, 608 (2022) 564–574.

58. **Heejun Yang, Sung Wng Kim, Manish Chhowalla and Young Hee Lee**, Structural and quantum-state phase transitions in van der Waals layered materials, Nature Physics, 13.10 (2017) 931–937.

59. **Anand Yethiraj and Alfons van Blaaderen**, A colloidal model system with an interaction tunable from hard sphere to soft and dipolar, nature, 421.6922 (2003) 513–517.

60. **Alessio Zaccone, Jerome J. Crassous and Matthias Ballauff**, Colloidal gelation with variable attraction energy, The Journal of chemical physics, 138.10 (2013) 104908.

61. **Klaus Zahn, R. Lenke and Georg Maret**, Two-stage melting of paramagnetic colloidal crystals in two dimensions, Physical review letters, 82.13 (1999) 2721.

62. **Klaus Zahn and Georg Maret**, Dynamic criteria for melting in two dimensions, Physical Review Letters, 85.17 (2000) 3656.

63. **Isla Zhang, C. Patrick Royall, Malcolm A. Faers and Paul Bartlett**, Phase separation dynamics in colloid–polymer mixtures, the effect of interaction range, Soft Matter , 9.6 (2013) 2076–2084.

64. **Chao Zhu, Suxia Liang, Erhong Song, Yuanjun Zhou, Wen Wang, Feng Shan, Yantao Shi, Ce Hao, Kuibo Yin, Tong Zhang and others**, In-situ liquid cell transmission electron microscopy investigation on oriented attachment of gold nanoparticles, in Nature communications, 9.1 (2018) 1–7.

THE AUTHORS

SIMKIN Ivan V.

vanyasimkin@gmail.com

ORCID: 0000-0003-1650-4177

YAKOVLEV Egor V.

yakov.egor@gmail.com

ORCID: 0000-0001-5093-2349

KRYUCHKOV Nikita P.

kruchkov_nkt@mail.ru

ORCID: 0000-0002-9085-1284

KORSAKOVA Sofia A.

sofia.korsakova@gmail.com

YURCHENKO Stanislav O.

st.yurchenko@mail.ru

ORCID: 0000-0001-6821-904X

Received 23.11.2022. Approved after reviewing 06.12.2022. Accepted 12.12.2022.

Conference materials

UDC 538.9

DOI: <https://doi.org/10.18721/JPM.161.135>

Application of conical magnetic rotating fields for controlled colloidal self-assembly

P.A. Libet ¹✉, A.A. Shirokova ¹, I.V. Simkin ¹, E.V. Yakovlev ¹, S.O. Yurchenko ¹

¹ Bauman Moscow State Technical University, Moscow, Russia

✉ libetpa@gmail.com

Abstract. Tunable interactions under the influence of external electric and magnetic fields open the way to controlled transport and self-organization in model and living systems. In this paper, we establish new experimental system parameters for tuning interparticle interactions in colloidal systems using a three-dimensional precessing conical magnetic field. The paper presents a digital twin of the experimental setup, simulation of electromagnetic fields in order to find the optimal self-assembly parameters. The results of pilot experiments with magnetic particles of silicon dioxide 2.47 μm in size in deionized water are demonstrated, the phenomenon of controlled self-assembly is shown.

Keywords: soft matter, self-assembly, magnetic fields, colloids

Funding: Libet P.A., Shirokova A.A., Simkin I.V., Yakovlev E.V., Yurchenko S.O. acknowledge BMSTU State Assignment for infrastructural support in digital twin creation and multi-axial magnetic field numerical simulations. The Russian Science Foundation, Grant No. 19-12-00092, supports pilot experiments and experimental setup assembly.

Citation: Libet P.A., Shirokova A.A., Simkin I.V., Yakovlev E.V., Yurchenko S.O., Application of conical magnetic rotating fields for controlled colloidal self-assembly, St. Petersburg State Polytechnical University Journal. Physics and Mathematics. 16 (1.1) (2023) 205–210. DOI: <https://doi.org/10.18721/JPM.161.135>

This is an open access article under the CC BY-NC 4.0 license (<https://creativecommons.org/licenses/by-nc/4.0/>)

Материалы конференции

УДК 538.9

DOI: <https://doi.org/10.18721/JPM.161.135>

Применение конических магнитных вращающихся полей для управляемой коллоидной самосборки

П.А. Либет ¹✉, А.А. Широкова ¹, И.В. Симкин ¹, Е.В. Яковлев ¹, С.О. Юрченко ¹

¹ Московский государственный технический университет им. Н.Э. Баумана, г. Москва, Россия

✉ libetpa@gmail.com

Аннотация. Управляемые взаимодействия под действием внешних электрических и магнитных полей открывают путь к управляемому транспорту и самоорганизации в модельных и живых системах. В этой статье мы устанавливаем параметры новой экспериментальной системы для управления межчастичным взаимодействием в коллоидных системах с использованием трехмерного вращающегося конического магнитного поля. В работе представлен цифровой двойник экспериментальной установки, симуляция электромагнитных полей с целью поиска оптимальных параметров самосборки. Приведены результаты пилотных экспериментов с магнитными частицами диоксида кремния размером 2,47 мкм в деионизированной воде, показано явление управляемой самосборки.

Ключевые слова: мягкая материя, самосборка, магнитные поля, коллоиды

Финансирование: Авторы благодарят МГТУ им. Н.Э. Баумана за инфраструктурную

поддержку создания цифрового двойника и численного моделирования многоосного магнитного поля. Пилотные эксперименты и сборка экспериментальной установки поддержаны грантом No. 19-12-00092 Российского научного фонда.

Ссылка при цитировании: Либет П.А., Широкова А.А., Симкин И.В., Яковлев Е.В., Юрченко С.О. Применение конических магнитных вращающихся полей для управляемой коллоидной самосборки // Научно-технические ведомости СПбГПУ. Физико-математические науки. 2023. Т. 16. № 1.1. С. 205–210. DOI: <https://doi.org/10.18721/JPM.161.135>

Статья открытого доступа, распространяемая по лицензии CC BY-NC 4.0 (<https://creativecommons.org/licenses/by-nc/4.0/>)

Introduction

Systems with tunable interactions [1] represent a promising class of model systems that are important for fundamental and applied research. Tunable interactions directed by external electric [2–7] or magnetic field [8–15] play a major role in many fields of colloidal matter, such as phase transitions [10, 16–19], collective dynamics [20, 21], guided transport in colloidal [22–24] and living [25–27] systems and pattern formation [28, 29].

Of particular interest is the formation of condensed phases from colloidal suspensions in a precessing multi-axial magnetic field [11]. By varying the precessing angle of the 3D conical fields, we get different colloidal patterns. It is known that at magic angle 54.7° [30, 31], interactions become spatially isotropic being attractive or repulsive depending on particle and solvent permittivity. In fact, such an interaction should lead to the appearance of equilibrium micro-phases; however, to date the issue of tunable interactions across magic spatial hodographs in colloids has not been well studied.

Moreover, multi-axial rotating magnetic field is a promising tool for additive manufacturing, especially 3D printing, and for obtaining new materials. To address these issues, we have performed numerical simulations of multi-axial rotating magnetic field and developed three-dimensional magnetic setup to examine dynamics of colloidal and living systems at different precessing angles of external rotating magnetic field.

Materials and Methods

At the stage of setup creation, an extremely important step is design and optimization of experimental setup parameters and geometric features using an experimental setup digital twin.

In fact, the goal was to achieve a magnetic field with strength of the order of $H \approx 100$ Oe and homogeneity 99% at the center with a square of 2.5 mm. In addition, due to the fact that the objective of the microscope must fit close enough to the sample under study, we designed a coil frame through the center of which the microscope passes.

The digital twin shown in Fig. 1 consists of four multilayer coils on a magnetic core in a horizontal plane and two vertical coils on a frame. A sinusoidal current is applied to the winding, which gives rise to the appearance of a rotating magnetic field. The test sample, placed on a glass substrate, is illuminated by an external light source. The image is digitized using a microscope objective, an infinity-corrected objective and a CCD camera.

Using the Finite Element Method (FEM), a numerical model of the experimental setup was created. Breaking our three-dimensional model into a finite number of subdomains, we solve the equations of electromagnetism:

$$\nabla \times H = J \quad (1)$$

$$\nabla \times A = B \quad (2)$$

$$J = \sigma E + J_e \quad (3)$$

with boundary condition $n \times A = 0$.

In fact, the use of a high permeability core greatly influences the B – H curve and the intensity of the magnetic field. The relationship between magnetic induction and magnetic field strength

through magnetic permeability is introduced as:

$$B = \mu H \quad (4)$$

It is more convenient to use the dimensionless relative magnetic permeability $\mu_r = \mu/\mu_0$. It is known that the relative magnetic permeability is related to the susceptibility through the relationship $\mu_r = 1 + 4\pi\chi$. The magnetic permeability depends on the properties of the substance and, as in our case, for anisotropic substances, on the magnitude and direction of the magnetic field.

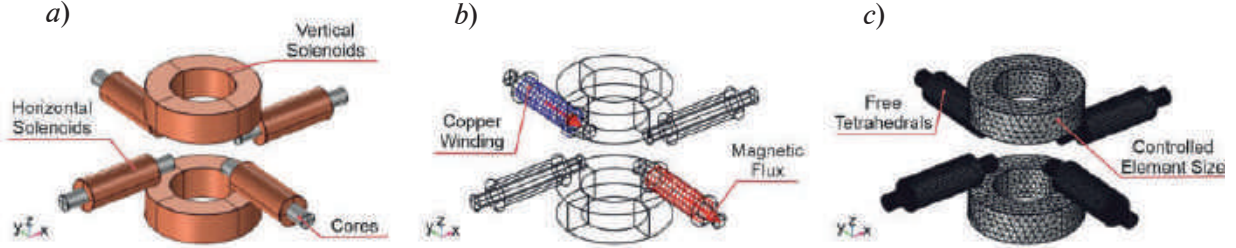


Fig. 1. Experimental setup digital twin: an external view of the installation, horizontal core solenoids and vertical solenoids (a), a consideration of copper winding for the direction of the magnetic induction vector (b), a decomposition of the 3D model into finite elements (c)

We considered a few variants of cores and the most convenient one turned out to be a ferrite core with a relative magnetic permeability $\mu_r = 400$.

To create a more intense magnetic field, it is much more rational to use multilayer coils. It is known that the inductance of a multilayer coil on a core is calculated by the equation,

$$L = \frac{\mu_0 \mu_r \cdot S_c \cdot N^2}{l_{avg}} \quad (5)$$

where $\mu_0 = 4\pi \cdot 10^{-7}$ H/m, μ_r is the relative permeability, S_c is the cross-sectional area of the magnetic circuit, N is the number of turns, l_{avg} is the average length of the magnetic field line.

From the Eq. 5 it can be seen that the inductance depends quadratically on the number of turns and linearly on the magnetic permeability.

Using a copper wire with $d = 0.5$ mm and a frame with a long winding $l = 19$ mm, taking into account the insulation, we got $N \approx 1200$ turns, consisting of 36 layers. The inductance of such a coil is $L \approx 67.8$ mH.

The homogenized multi-layer circular coils used numerically, shown in Fig. 1, make it possible to vary the current strength, the number of turns and the distance between the coils to achieve a uniform magnetic field profile of the desired strength.

In fact, differences in the inductances of the coils are compensated by changing the distance between them, which makes it possible to create unique conic fields.

The vertical coils in the final winding consist of 40 turns and 30 layers ($N = 1200$), and the horizontal coils of 100 turns and 10 layers ($N = 1000$). Both coils are wound with copper wire with a diameter of $d_w = 0.5$ mm and a conductivity of $\sigma = 10^6$ S/m. The winding is supplied with an alternating current with a power of $I = 1$ A with a frequency of $\nu_0 = 1-20$ Hz.

As a pilot experiment we examined a system of magnetic particles of silicon dioxide $2.47 \mu\text{m}$ in size in deionized water.

Results and discussion

As a numerical solution result of Eq. 1–3, we obtained the field distributions in three different operating modes shown in Fig. 2. The setup allows one to work with both two-dimensional and three-dimensional rotating magnetic fields. The intensity of the magnetic field in the center is controlled by the strength of the current supplied to the coil windings and varies from 0 to 170 Oe. The independence of the vertical and horizontal coils makes it possible to control the precession angle of the conical field by adjusting the current strength on the planar and vertical coils.

The results of pilot experiments are demonstrated in Fig. 3. In multi-axial regime there is a colloidal system exhibiting precessing in a magnetic field with spatial hodograph at a conical angle θ .

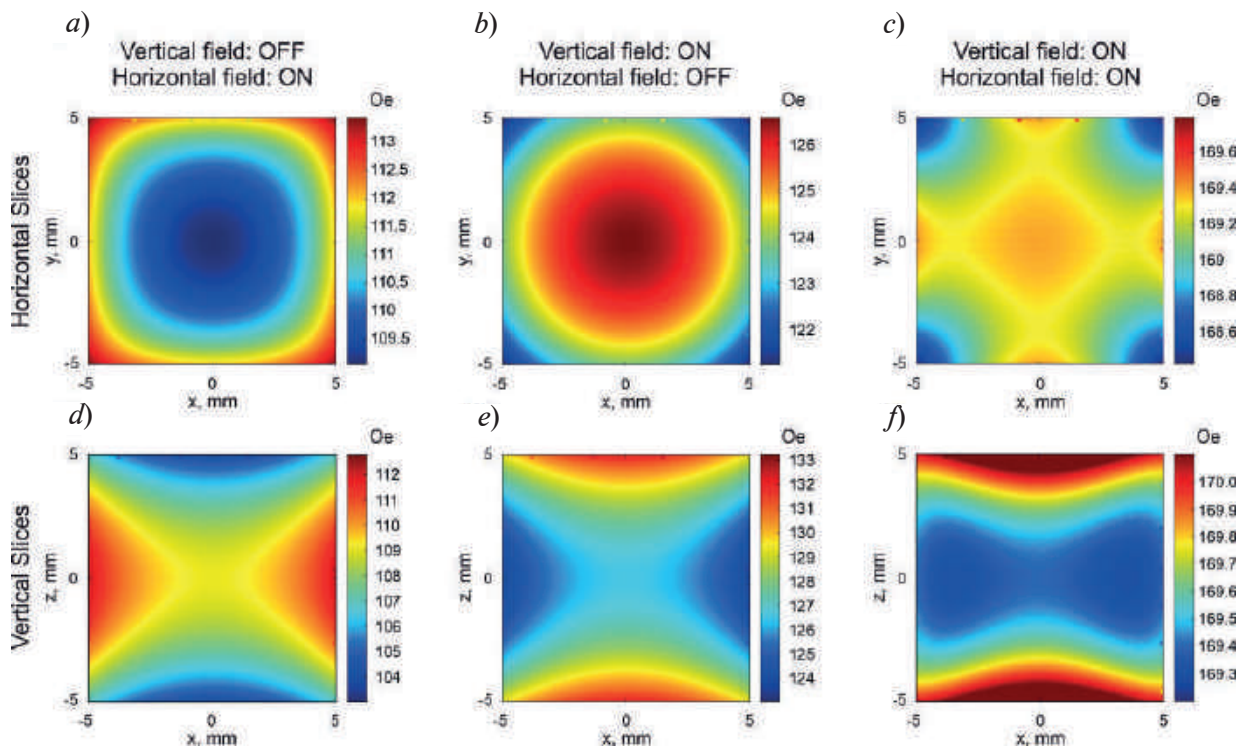


Fig. 2. Numerical simulation of magnetic fields in three operating modes (averaged period): electric field strength slices in horizontal plane (*a*, *b*, *c*); electric field strength slices in vertical plane (*d*, *e*, *f*)

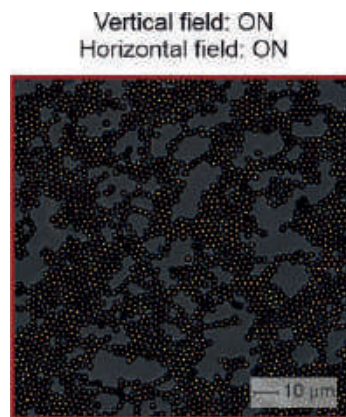


Fig. 3. Experimental snapshot of colloidal system: pilot experiments in horizontal and vertical fields simultaneously

Conclusion

As we mentioned before, we are able to control the conical angle and systems precessing at different conical and magical angles which is also a good testbed for prospective studies.

As a result, by creating a digital twin of the experimental setup, we were able to design the optimal geometry and select the appropriate parameters for vertical and planar coils. This step is important in terms of creating new equipment for observing various phenomena in the field of soft matter physics and general condensed matter phenomena. By carrying out pilot experiments, we proved the possibility of self-assembly of colloidal structures into aggregates.

In addition, this setup can be used to carry out promising studies in the field of targeted drug delivery, 3D printing and other applications in the field of colloidal and living matter.



REFERENCES

1. **Cai Z., et al.**, From colloidal particles to photonic crystals: advances in self-assembly and their emerging applications, *Chemical Society Reviews*. 50 (10) (2021) 5898–5951.
2. **Yakovlev E.V., et al.**, 2D colloids in rotating electric fields: A laboratory of strong tunable three-body interactions, *Journal of Colloid and Interface Science*. 608 (2022) 564–574.
3. **Yakovlev E.V., Ovcharov P.V., Yurchenko S.O.**, “Tunable colloids”: Experimental complex for studying generic phenomena in classical condensed matter, *Journal of Physics: Conference Series*. IOP Publishing, 1135 (1) (2018) 012039.
4. **Zhang B., Snezhko A., Sokolov A.**, Guiding self-assembly of active colloids by temporal modulation of activity, *Physical Review Letters*. 128 (1) (2022) 018004.
5. **Komarov K.A., Kryuchkov N.P., Yurchenko S.O.**, Tunable interactions between particles in conically rotating electric fields, *Soft Matter*. 14 (47) (2018) 9657–9674.
6. **Azari A., et al.**, Directed self-assembly of polarizable ellipsoids in an external electric field, *Langmuir*. 33 (48) (2017) 13834–13840.
7. **Yakovlev E.V., et al.**, Tunable two-dimensional assembly of colloidal particles in rotating electric fields, *Scientific reports*. 7 (1) (2017) 1–10.
8. **Pal A., et al.**, Shape Matters in Magnetic-Field-Assisted Assembly of Prolate Colloids, *ACS nano*. 16 (2) (2022) 2558–2568.
9. **Coughlan A.C.H., Bevan M.A.**, Effective colloidal interactions in rotating magnetic fields, *The Journal of chemical physics*. 147 (7) (2017) 074903.
10. **Du D., et al.**, Generating an in situ tunable interaction potential for probing 2-D colloidal phase behavior, *Soft Matter*. 9 (29) (2013) 6867–6875.
11. **Solis K.J., Martin J.E.**, Chevrons, filaments, spinning clusters and phase coexistence: emergent dynamics of 2- and 3-d particle suspensions driven by multiaxial magnetic fields, *Soft matter*. 13 (34) (2017) 5676–5683.
12. **Mohapatra J., et al.**, Magnetic-field-induced self-assembly of FeCo/CoFe₂O₄ core/shell nanoparticles with tunable collective magnetic properties, *Nanoscale*. 13 (8) (2021) 4519–4529.
13. **Byrom J., Biswal S.L.**, Magnetic field directed assembly of two-dimensional fractal colloidal aggregates, *Soft Matter*. 9 (2013) 9167–9173.
14. **Tierno P., Muruganathan R., Fischer T.M.**, Viscoelasticity of dynamically self-assembled paramagnetic colloidal clusters, *Physical review letters*. 98 (2) (2007) 028301.
15. **Elismaili M., et al.**, Rotation dynamics and internal structure of self-assembled binary paramagnetic colloidal clusters, *The Journal of Chemical Physics*. 155 (15) (2021) 154902.
16. **Lyu J., et al.**, Electric Field-Induced Phase Transition of Nanowires on Germanium (001) Surfaces, *The Journal of Physical Chemistry Letters*. 13 (4) (2022) 1063–1068.
17. **Kryuchkov N.P., et al.**, Phase diagram of two-dimensional colloids with Yukawa repulsion and dipolar attraction, *The Journal of chemical physics*. 150 (10) (2019) 104903.
18. **Ovcharov P.V., et al.**, Particle-resolved phase identification in two-dimensional condensable systems, *The Journal of Physical Chemistry C*. 121 (48) (2017) 26860–26868.
19. **Monovoukas Y., Gast A.P.**, The experimental phase diagram of charged colloidal suspensions, *Journal of colloid and interface science*. 128 (2) (1989) 533–548.
20. **Klapp S.H.L.**, Collective dynamics of dipolar and multipolar colloids: From passive to active systems, *Current opinion in colloid & interface science*. 21 (2016) 76–85.
21. **Weddemann A., et al.**, Magnetic field induced assembly of highly ordered two-dimensional particle arrays, *Langmuir*. 26 (24) (2010) 19225–19229.
22. **Demirurs A.F., et al.**, Active cargo transport with Janus colloidal shuttles using electric and magnetic fields, *Soft Matter*. 14 (23) (2018) 4741–4749.
23. **Spatafora-Salazar A., et al.**, Hierarchical assemblies of superparamagnetic colloids in time-varying magnetic fields, *Soft Matter*. 17 (5) (2021) 1120–1155.
24. **Durán J.D. G., et al.**, Magnetic colloids as drug vehicles, *Journal of Pharmaceutical Sciences*. 97 (8) (2008) 2948–2983.
25. **Mohajer J. K., et al.**, Biological effects of static magnetic field exposure in the context of MR-guided radiotherapy, *The British Journal of Radiology*. 92 (1094) (2019) 20180484.
26. **Mamuti M., et al.**, In vivo self-assembled nanomedicine, *Nano Today*. 36 (2021) 101036.
27. **Xu L., et al.**, Facile anchoring mussel adhesive mimic tentacles on biodegradable polymer cargo

carriers via self-assembly for microplastic-free cosmetics, *Journal of Colloid and Interface Science*. 612 (2022) 13–22.

28. **Hegde O., et al.**, Multiscale vapor-mediated dendritic pattern formation and bacterial aggregation in complex respiratory biofluid droplets, *Journal of Colloid and Interface Science*. 606 (2022) 2011–2023.

29. **Itatani M., et al.**, Phase separation mechanism for a unified understanding of dissipative pattern formation in a Liesegang system, *Physical Chemistry Chemical Physics*. 24 (4) (2022) 2088–2094.

30. **Komarov K.A., Yurchenko S.O.**, Colloids in rotating electric and magnetic fields: Designing tunable interactions with spatial field hodographs, *Soft Matter*. 16 (35) (2020) 8155–8168.

31. **Chen P. et al.** Magic angle spinning spheres, *Science advances*. 4 (9) (2018) 1540.

THE AUTHORS

LIBET Pavel A.

libetpa@gmail.com

ORCID: 0000-0001-7274-4605

SHIROKOVA Anastasia A.

shirokova2001@yandex.ru

SIMKIN Ivan V.

vanyasimkin@gmail.com

ORCID: 0000-0003-1650-4177

YAKOVLEV Egor V.

yakov.egor@gmail.com

ORCID: 0000-0001-5093-2349

YURCHENKO Stanislav O.

st.yurchenko@mail.ru

ORCID: 0000-0001-6821-904X

Received 24.11.2022. Approved after reviewing 09.12.2022. Accepted 09.12.2022.

Conference materials

UDC 544.2

DOI: <https://doi.org/10.18721/JPM.161.136>

Features of electrochemical behavior of an amorphous iron-based alloy in acidic solutions containing potassium rhodanide

V.A. Fedorov ¹✉, D.V. Balybin ¹, T.N. Pluzhnikova ¹, M.V. Boitsova ¹,
D.Yu. Fedotov ¹, A.D. Berezner ¹, A.V. Yakovlev ¹

¹Derzhavin Tambov State University, Tambov, Russia

✉ fedorov-tsu.tmb@inbox.ru

Abstract. Impact of acidic solution with potassium rhodanide on partial electrode reactions was studied in AMAG-200 metallic glass (MG). Increase of acidity leads to growth of electrochemical reactions. With (mol/l) growth of potassium rhodanide in hydrochloric solution, radius of a circular Nyquist diagram increases that testifies to better corrosion resistance of AMAG-200 MG in mentioned environment. Surface coverage ratio of rhodanide-ions increases up to the 0.9–0.99 maximum with adding of potassium rhodanide. Because of the physic-mechanical features of the solution, surface co-adsorption of rhodanide-ions, Cl⁻, H₃O⁺ ions, and HSCN, H₂O molecules is possible that can lead to competitive adsorption, noticing in diagrams.

Keywords: potassium rhodanide, electrochemistry, acidic solutions

Funding: This study was funded by the Russian Science Foundation (grant No. 22-22-00226).

Citation: Fedorov V.A., Balybin D.V., Pluzhnikova T.N., Boitsova M.V., Fedotov D.Yu., Berezner A.D., Yakovlev A.V., Features of electrochemical behavior of an amorphous iron-based alloy in acidic solutions containing potassium rhodanide, St. Petersburg State Polytechnical University Journal. Physics and Mathematics. 16 (1.1) (2023) 211–217. DOI: <https://doi.org/10.18721/JPM.161.136>

This is an open access article under the CC BY-NC 4.0 license (<https://creativecommons.org/licenses/by-nc/4.0/>)

Материалы конференции

УДК 544.2

DOI: <https://doi.org/10.18721/JPM.161.136>

Особенности электрохимического поведения аморфного сплава на основе железа в кислых растворах, содержащих роданид калия

В.А. Федоров ¹✉, Д.В. Балыбин ¹, Т.Н. Плужникова ¹, М.В. Бойцова ¹,
Д.Ю. Федотов ¹, А.Д. Березнер ¹, А.В. Яковлев ¹

¹Тамбовский государственный университет имени Г.Р. Державина, г. Тамбов, Россия

✉ fedorov-tsu.tmb@inbox.ru

Аннотация. Изучено влияние кислотности среды и добавок роданида калия на скорость парциальных электродных реакций на аморфном сплаве АМАГ-200. Рост кислотности среды приводит к увеличению скоростей электродных реакций. При увеличении содержания роданида калия в солянокислых растворах радиус полуокружностей годографов возрастает, что указывает на повышение коррозионной стойкости АМАГ-200 в изученных средах. Степень заполнения поверхности роданид ионами увеличивается с ростом концентрации добавки и достигает значения 0,9–0,99 при максимальной концентрации роданида калия. Исходя из физико-химических особенностей состава раствора следует вероятная соадсорбция поверхностно-активных роданид – ионов и молекул HSCN, H₂O, а также ионов Cl⁻, H₃O⁺, что приводит к конкурентным процессам адсорбции и может в определенной степени объяснять наблюдаемые зависимости.

Ключевые слова: роданид калия, электрохимия, кислые растворы

Финансирование: Работа поддержана Российским научным фондом (грант № 22-22-00226).

Ссылка при цитировании: Федоров В.А., Балыбин Д.В., Плужникова Т.Н., Бойцова М.В., Федотов Д.Ю., Березнер А.Д., Яковлев А.В. Особенности электрохимического поведения аморфного сплава на основе железа в кислых растворах, содержащих роданид калия // Научно-технические ведомости СПбГПУ. Физико-математические науки. 2023. Т. 16. № 1.1. С. 211–217. DOI: <https://doi.org/10.18721/JPM.161.136>

Статья открытого доступа, распространяемая по лицензии CC BY-NC 4.0 (<https://creativecommons.org/licenses/by-nc/4.0/>)

Introduction

Broader usage of amorphous metallic alloys (AMAs) or metallic glasses (MGs) stimulates practical study their corrosion resistance. Iron based AMAs resist stronger to corrosion compare with their crystalline analogs [1] that is caused by absence of typical crystalline defects in a disordered structure [2]. Corrosion resistance can be increased with structural relaxation that caused by less residual stress, probable growth of activation energy and surface atomic restructure [3] with less potential of corrosion zones [4]. By study of reaction between Ringer's solution and Fe-based ribbon MGs, substantially better corrosion resistance was shown at higher concentration of niobium [5]. In Mo-doped alloy, partial replacement by niobium also improves corrosion resistance [6]. Moreover, the dope elements such as tungsten, yttrium, manganese and nitrogen [7] are used in Fe-based alloys with molybdenum phase, and it provides more corrosion resistance because of additional oxides and nitrogen bonding in the passivation layer. Impact of molybdenum doping on corrosion parameters in Fe-based MGs also depends on the ambient acidity [8, 9]. Amorphising dopants also affect corrosion resistance. For example, phosphorus is more effective than boron as anticorrosive agent. The presence of carbon in bulk MGs accelerates their dissolution [10], but silicon improves corrosion resistivity [11, 12]. Thus, corrosion behaviour of Fe-based AMAs is not fully studied because of multicomponent chemical reactions.

The main goal is studying the impact of ambient acidity and potassium rhodanide (KSCN) on electrochemical and adsorption processes in Fe-based metallic glasses.

Materials and Methods

For estimation of the rates in partial electromechanical reactions, we used polarization methods. The measurements were carried out with Solartron 1287 potentiostat, static electrode and harmonic analyser. Acidic solutions of x M HCl + y mM KSCN with $x = 0.05; 0.1; 0.5; y = 0.5; 1.0; 5.0, 10.0$ were used in the estimation of corrosion resistance and electrochemical behaviour of Fe-based metallic glasses. KSCN was injected for the study of surface active rhodanide-ion adsorption in amorphous structure. The working electrochemical electrode of 0.5 cm^2 active surface area was preliminary degreased with acetone and then preset in insulating epoxy base. For electrochemical etching, a three-electrode "Pyrex" glass cell with the separated anode and cathode terminals was used. A silver chloride electrode was used for control and auxiliary one was made of Pt. Measured potentials were converted by the standard hydrogen scale. The experiments were carried from cathode to anode space by the potentiodynamic polarization with 0.66 mV/s scan rate.

Impedance measurements were also conducted in the same three-electrode cell with a specimen of AMAG-200 MG as a planar electrode. Frequency was varied from 0.05 to 10 kHz with voltage amplitude 10 mV. The electrode was etched in solution at 900 seconds for the exception of transient response.

Measured hodographs were processed with a ZView 3.0a software, which offers many equivalent electric schemes (and their voltage-current values) up to 20 circuit elements after coefficient selection by a simplex method. Values in similar schemes were averaged for several

typical experiments. Only data with the less 5% calculated error were used.

Surface coverage ratio Θ was measured by the equation [13]:

$$\Theta = \frac{C_0 - C_j}{C_0 - C_\infty} \quad (1)$$

where C_0 , C_j are electrode capacity of clear and doped solvent, C_∞ is constant capacity at higher solvent concentration.

Results and Discussion

A. Impedance measurements with AMAG-200 in acidic aqueous solutions doped by KSCN.

Impedance hodographs with non-zero corrosion potential in the aqueous solutions have a circle form deformed in the low-frequency spectrum both with KSCN doping and without it. Equivalent electric scheme [14] with AMAG-200 electrode consists of R_s (electrolyte) and R_l (anodic current) resistivity with adsorption C_a (capacity) and R_a (resistance) of transition bonds in anode reaction. To the cathode restorative process of proton donors and dissolved oxygen, the series coupling of R_2 (cathode current) and Z_D (diffusion impedance) is corresponded. As seen from experimental and model curves (Fig. 1), the proposed schemes describe well boundary processes between the electrode and solution.

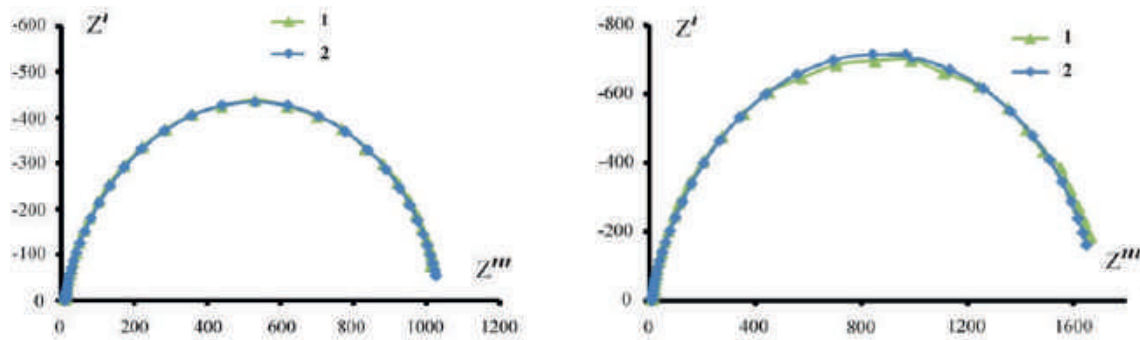


Fig. 1. Nyquist diagram for AMAG-200: (a) 0.05M HCl (base); (b) base solution with 0.5 mM of KSCN. Z' and Z'' are calculated in $\text{Ohm}\cdot\text{cm}^2$; the 1st curve corresponds to experiment and the 2nd one corresponds to calculation

Table 1

Parameters of equivalent scheme with AMAG-200 electrode in 0.05M of HCl and different concentration of KCNS. Listed values have quite other SI units despite their symbols and titles in the text, but they better describe the surface dynamics and are common in electrochemistry by these names

Solution Element	0.05M HCl (base)	0.05M HCl + 0.5 mmol/l KSCN	0.05M HCl + 1 mmol/l KSCN	0.05M HCl + 5 mmol/l KSCN	0.05M HCl + 10 mmol/l KSCN
$R_s, \text{Ohm}\cdot\text{cm}^2$	10	10.65	15.5	10.6	9.7
$R_2, \text{Ohm}\cdot\text{cm}^2$	$2.8952 \cdot 10^{-5}$	$7.8159 \cdot 10^{-8}$	12.37	83.5	21.04
$Z_D(R), \text{Ohm}\cdot\text{cm}^2$	1033	1705	42146	102730	91815
$Z_D(T), \text{Ohm}\cdot\text{cm}^2$	0.18804	0.40875	19.99	40.99	27.17
$Z_D(P), \text{Ohm}\cdot\text{cm}^2$	0.40438	0.41997	0.71315	0.785	0.722
$R_l, \text{Ohm}\cdot\text{cm}^2$	426290	112780	2434	8390	3755
$C_a \times 10^{-5}, \text{F}/\text{cm}^2$	3.6605	5.2542	2.4835	1.9671	2.7802
$R_a, \text{Ohm}\cdot\text{cm}^2$	9.714	5.575	840.9	12.17	1305
$C_{dl} \times 10^{-5}, \text{F}/\text{cm}^2$	3.2151	2.9774	1.3313	1.5052	0.78702

With increasing of KSCN concentration, radius of the semi-circle increases. The similar curves are received to HCl solutions with 1.0; 5.0 and 10.0 mM of KCNS doping, where radius increases at higher dopant concentration.

According to electrochemical data (in Table 1), R_2 increases at higher concentration of KSCN, but 5 mM of KSCN solution does not correlate with this tendency.

It can be caused by the involvement of SCN^- , Cl^- and H_3O^+ surface ions in competitive adsorption on active surface centres. Moreover, adsorption of water and HSCN molecules, which forms in hydrochloric environment, must be noted. Similar effect was observed earlier [23, 24].

Deviation of the parameters from 0.05M of HCl solution with 5 mM of KSCN dopant can be explained as follow processes. One side, reaction rate can change non-linear depends on either single ion or co-adsorption with Cl^- , H_3O^+ ions and H_2O , HSCN molecules. Other side, coverage of active centres by SCN particles is possible, so that forming of the second monolayer occurs despite the finally unformed first one [15].

As seen from the Table 2, monotonous decrease of C_{dl} with a higher KSCN concentration happens on the “metal-solution” boundary.

Table 2

Coverage ratio Θ and double layer capacity C_{dl} at KSCN concentration in 0.05M of HCl

C_{KSCN} , mM	base value	0.5	1	5	10
C_{dl} , μF	32.151	29.774	13.313	15.052	7.8702
Θ	–	0.097	0.764	0.693	0.985

This fact testifies to adsorption of doped particles on the amorphous surface. According to Damaskin’s and Podlovchenko’s calculations of Θ [13], its increase for rhodanide-ions on amorphous surface centres occurs at higher ionic concentrations in solution. Note that described surface significantly differs from typical metal one, and it manifests itself first of all in atomic order. Thus, the amorphous surface also contains the active centres, which impact the electrode processes so, in relation between Θ and concentration of SCN^- , coverage only the active centres instead whole surface must be noted.

According to Table 2, coverage ratio is about 0.1 at surface anion adsorption 0.5 mM of KSCN yet, and further doping to 1 and 5 mM of KSCN gives the bend in $\Theta(C_{\text{KCNS}})$ curve that can be caused by secondary processes (chloride ion co-adsorption, for example). Note that solution 0.05M of HCl with doping 5 mM of KSCN does not fit into tendency by R_2 (see Table 1), and curve bending is observed at the same point (in Fig. 2).

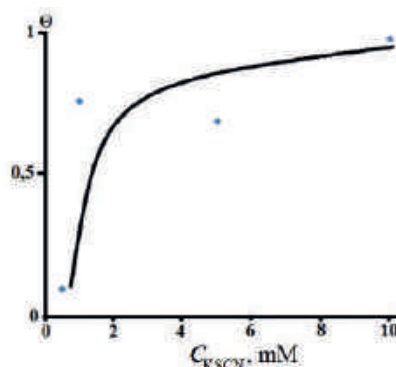


Fig. 2. Adsorption isotherm of SCN^- ions from solution 0.05M of HCl with different doping of potassium rhodanide in AMAG-200 metallic glass. The curve was plotted in error corridor with respect to one of Langmuir adsorption isotherms

Totally, at a maximal concentration of dopant, coverage of almost all active surface centres happens in MG that is confirmed by $\Theta = 0.985$ at $C_{\text{KSCN}} = 10$ mM.

For solutions with acidity 0.1 and 0.5M of HCl at doping of potassium rhodanide, the similar dynamics of Nyquist diagram and $\Theta(C_{\text{KCNS}})$ preserve. By value of Θ , we can conclude about insignificant difference of adsorption isotherms, plotted for SCN^- ions at 0.05, 0.1 and 0.5 M of HCl in MG. Personal parameters of the isotherms are listed in Table 3.

Relation data for coverage ratio Θ and double layer capacity C_{dl} at KSCN concentrations in 0.1 and 0.5M of HCl

0.1M HCl					
C_{KSCN} , mM	base value	0.5	1	5	10
C_{dl} , μ F	47.309	41.587	18.555	18.024	5.987
Θ	–	0.135	0.681	0.692	0.985
0.5M HCl					
C_{KSCN} , mM	base value	0.5	1	5	10
C_{dl} , μ F	35.976	28.869	44.816	8.1645	7.7336
Θ	–	0.229	0.284	0.871	0.908

Table 4

Ratio between HSCN molecules and SCN-ions with respect to acidity of solution

$[HSCN] / [SCN]$	0.36	0.71	3.57
$[H^+]$	0.05	0.1	0.5

Dynamics of adsorption isotherm does not change qualitatively but coverage ratio is about 0.9–0.99 at a maximal concentration of potassium rhodanide. Increased acidity intensifies hydrolysis of KSCN salt and rhodanide-ions become partially into HSCN form with less adsorption activity on the amorphous surface, so it can cause lesser Θ_{max} (i.e., $KSCN + HCl = HSCN + KCl$).

In this case, a share ratio between molecular HSCN forms and SCN- ions can be calculated with respect to acidity (Table 4).

Thus, adsorption of HSCN molecules can occur with less heat in compare with SCN⁻ rhodanide ions, and it gives less coverage ratio at maximal studied concentrations of potassium rhodanide. Moreover, HSCN and SCN⁻ components can impact differently not only in electrode process but also in the solid-phase hydrogen diffusion through amorphous alloy.

From obtained impedance data, we can conclude the change of anode and cathode reactions rates while using rhodanide-ions in Fe-based MG, but it is not always linear and simple process. In all investigated solutions, double-layer capacity decreases with higher concentration of KSCN that testifies about surface adsorption of dopant in amorphous alloy. Adsorption isotherms, plotted by collecting results, have the same form qualitatively. However, for solutions 0.05 and 0.1 M of HCl, data coincide practically at considered content of KSCN, but for 0.5 M of HCl, the maximal coverage ratio is about 0.91 at the most doping of KSCN, and it is 10% less than for solutions 0.05 and 0.1 M of HCl.

B. Electrochemical measurements with AMAG-200 in acidic aqueous solutions doped by KSCN

Polarizing curves of AMAG-200 have a typical form for clean iron and Fe-based alloys. In cathode part, a segment of controlled diffusion absents and passivation is not observed in anode one. Cathode polarizing curves in base solutions 0.1 M of HCl are approximated by linear parts with bc Tafel angle, which is about 0.12 V, and anode plots have a typical view with b_a one about 0.06 V (Fig. 3 and 4).

Using of minimal doping does not significantly change the polarizing dynamic if only corrosion potential shifts to the anode area. However, there is change both of $b_c = 0.15$ V and curve in anode area with growth of KSCN concentration up to 1 mM despite the curve slope does not strongly change in compare with solution of 0.5 mM doping. Note that rate of both anode and cathode processes retards at doping 1 mM of KSCN.

Increase of KSCN dopant concentration up to 5 and 10 mM also does not significantly change the dynamics and Tafel angles, but quite balanced the potential and stopped corrosion generally. Compared with [16], polarizing curves have the same form for industrial (polycrystalline) steel.

Mentioned doping is a corrosion stimulus for iron and its alloys, but, in some observed cases, dopant can be inhibitor that is seen from the polarizing curves. Correlation between electrochemical and impedance data can be explained by growth of the surface coverage ratio at higher concentration of KSCN.

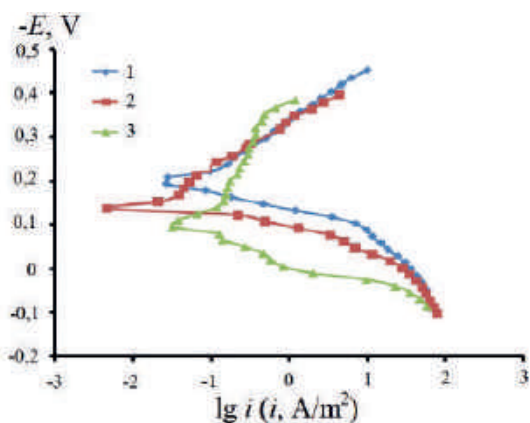


Fig. 3. Polarizing curves of AMAG-200 MG in solution 0.1 M of HCl (1); doped by 0.5 mM of KSCN (2); with 1 mM of KSCN (3)

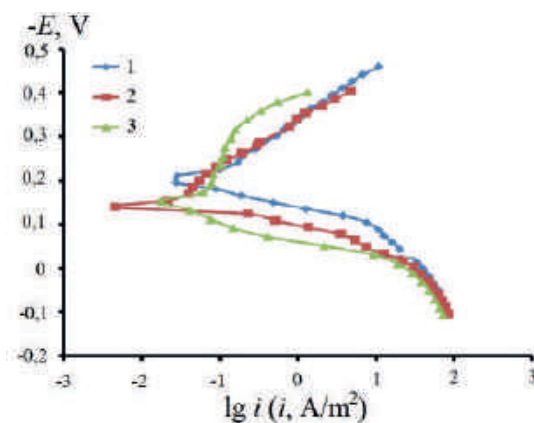


Fig. 4. Polarizing curves of AMAG-200 MG in solution 0.1 M of HCl (1); doped by 5 mM of KSCN (2); with 10 mM of KSCN (3)

Conclusion

Potassium rhodanide does not obviously change the rates of partial electrode reactions in AMAG-200 amorphous alloy. Analogous relationships were observed in iron (polycrystalline steel) earlier.

For all investigated solutions, surface coverage ratio Θ is more than 90% at filling by SCN^- ions with respect to impedance measurements.

Ionic adsorption of SCN^- can be retarded by competitive co-adsorption of H_3O^+ , Cl^- and HSCN components that can affect the rate of electrode reactions.

REFERENCES

1. Souza C.A.C., Ribeiro D.V., Kiminami C.S., Corrosion resistance of Fe-Cr-based amorphous alloys: An overview, North-Holland Journal of Non-Crystalline Solids. 442 (2016) 56–66.
2. Belkhaoudaa M., Bazzia L., Benhachemib A., Salghic R., Hammoutid B., Kertite S., Effect of the heat treatment on the corrosion behaviour of amorphous Fe-Cr-P-C-Si alloy in 0.5 M H_2SO_4 , J. Appl. Surf. Sci. 252 (2006) 7921–7925.
3. Chattoraj I., Baunack S., Stoica M., Gebert A., Electrochemical response of $\text{Fe}_{65.5}\text{Cr}_4\text{Mo}_4\text{Ga}_4\text{P}_{12}\text{C}_5\text{B}_{5.5}$ bulk amorphous alloy in different aqueous media, Materials and Corrosion. 55 (1) (2004) 36–42.
4. Vyugov P.N., Dmitrenko A.E., Metallic glasses, Questions of atomic science and technology. Series: Vacuum, pure materials, superconductors. 6 (2004) 185–191.
5. Zohdi H., Shahverdi H.R., Hadavi S.M.M., Effect of Nb addition on corrosion behavior of Fe-based metallic glasses in Ringer's solution for biomedical applications, Electrochem. Commun. 13 (2011) 840–843.
6. Pang S.J., Zhang T., Asami K., Inoue A., New Fe-Cr-Mo-(Nb,Ta)C-B glassy alloys with high glass-forming ability and good corrosion resistance, Mater. Trans. JIM. 42 (2001) 376–379.
7. Gostin P.F., Gebert A., Schultz L., Comparison of the corrosion of bulk amorphous steel with conventional steel, Corros. Sci. 52 (2010) 273–281.
8. Liqun M., Inoue A., On glass-forming ability of Fe-based amorphous alloys, Mater. Lett. 38 (1999) 58–61.
9. Inoue A., Takeuchi A., Mixing enthalpy of liquid phase calculated by miedema's scheme and approximated with sub-regular solution model for assessing forming ability of amorphous and glassy alloys, Intermetallics. 18 (2010) 1779–1789.
10. Gostin P.F., Oswald S., Schultz L., Geber A., Acid corrosion process of Fe-based bulk metallic glass, Corros. Sci. 62 (2012) 112–121.
11. Guo R.Q., Zhang C., Yang Y., Peng Y., Liu L., Corrosion and wear resistance of a Fe based amorphous coating in underground environment, Intermetallic. 30 (2012) 94–99.
12. Lopez M.F., Escudero M.L., Vida E., The corrosion resistance can be improved by an addition of Si element in the Fe-Cr-Ni alloy, Electroquim. Acta. 42 (1997) 659–665.



13. **Damaskin B.B., Petriy O.A., Batrakov V.V.**, Adsorption of Organic Compounds on Electrodes, Nauka, Moscow, 1968.
14. **Kichigin V.I., Polyakova M.V., Syur G.A., Bezmaternykh N.V., Koshcheev O.P., Rabinovich A.I.**, Protection of metals 38 (2002) 632–639.
15. **Balybin D.V.**, Abstract of the dissertation of the candidate of chemical sciences, Tambov, PhD thesis, 2011.
16. **Protasov A.S.**, Abstract of the dissertation of the candidate of chemical sciences, Tambov, PhD thesis, 2009.

THE AUTHORS

FEDOROV Victor A.
fedorov-tsu.tmb@inbox.ru
ORCID: 0000-0002-3191-3748

BALYBIN Dmitry V.
balybindv@gmail.com

PLUZHNIKOVA Tatiana N.
plushnik@mail.ru
ORCID: 0000-0003-4319-1786

BOYTSOVA Margarita V.
mvboitsova@mail.ru

FEDOTOV Dmitry Yu.
dmitry_989@mail.ru

BEREZNER Arseniy D.
qwert1009@mail.ru
ORCID: 0000-0001-5957-4525

YAKOVLEV Alexey V.
dak-83@mail.ru

Received 05.12.2022. Approved after reviewing 21.12.2022. Accepted 23.12.2022.

SIMULATION OF PHYSICAL PROCESSES

Conference materials

UDC 532.517.3

DOI: <https://doi.org/10.18721/JPM.161.137>

Application of global stability analysis to predicting characteristics of Tollmien-Schlichting waves

K.V. Belyaev¹, A. Garbaruk¹, V.D. Golubkov¹✉, M.Kh. Strelets¹

¹Peter the Great St. Petersburg Polytechnic University, St. Petersburg, Russia

✉ golubkovvd@gmail.com

Abstract. A numerical procedure is presented for computing characteristics of Tollmien–Schlichting (T-S) waves in the course of their downstream evolution. It is based on the Global Stability Analysis of steady solutions of the full compressible Navier-Stokes equations and, therefore, does not have the restrictions associated with the parallel or quasi-parallel flow assumptions used in the classical methods of the linear stability analysis based on the boundary layer approximation. Hence, the methodology may be applied not only to simple boundary layers on smooth surfaces but also to non-parallel flows, e.g. those over surfaces with irregularities (steps, gaps, etc.). The developed procedure is validated by the comparison of the computed distribution of the T-S amplification factor (N-factor) in the zero pressure gradient boundary layer with the similar distribution computed based on the solution of the Orr-Sommerfeld equation and is shown to be accurate and robust.

Keywords: Global stability analysis, Tollmien-Schlichting waves, Boundary layer

Funding: The study is conducted with financial support of Russian Scientific Foundation, Grant No. 22-11-00041.

Citation: Belyaev K.V., Garbaruk A., Golubkov V.D., Strelets M.Kh., Application of global stability analysis to predicting characteristics of Tollmien-Schlichting waves, St. Petersburg State Polytechnical University Journal. Physics and Mathematics. 16 (1.1) (2023) 218–224. DOI: <https://doi.org/10.18721/JPM.161.137>

This is an open access article under the CC BY-NC 4.0 license (<https://creativecommons.org/licenses/by-nc/4.0/>)

Материалы конференции

УДК 532.517.3

DOI: <https://doi.org/10.18721/JPM.161.137>

Применение глобального анализа устойчивости для расчета характеристик волн Толлмина-Шлихтинга в пограничном слое на плоской пластине

К.В. Беляев¹, А.В. Гарбарук¹, В.Д. Голубков¹✉, М.Х. Стрелец¹

¹Санкт-Петербургский политехнический университет Петра Великого, Санкт-Петербург, Россия

✉ golubkovvd@gmail.com

Аннотация. Представлена методика численного расчета характеристик волн Толлмина-Шлихтинга, распространяющихся вдоль пограничного слоя. Она основана на глобальном анализе устойчивости стационарных решений полных сжимаемых уравнений Навье-Стокса и потому не имеет ограничений, связанных с параллельностью или квазитрехмерностью потока, используемых в классических методах линейного анализа устойчивости уравнений пограничного слоя. Представленная методика может быть применена не только к простым пограничным слоям на гладких поверхностях, но и к непараллельным течениям, например, на поверхностях с уступами, кавернами и т.д. Точность и численная устойчивость разработанной процедуры верифицирована при помощи сравнения распределений N-факторов для волн Толлмина-Шлихтинга



в пограничном слое без градиента давления с распределениями, посчитанными по решениям уравнения Орра-Зоммерфельда.

Ключевые слова: глобальный анализ устойчивости, волны Толлмина-Шлихтинга, пограничный слой

Финансирование: Работа выполнена при финансовой поддержке РФФ, грант № 22-11-00041.

Ссылка при цитировании: Беляев К.В., Гарбарук А.В., Голубков В.Д., Стрелец М.Х. Применение глобального анализа устойчивости для расчета характеристик волн Толлмина-Шлихтинга в пограничном слое на плоской пластине // Научно-технические ведомости СПбГПУ. Физико-математические науки. 2023. Т. 16. № 1.1. С. 218–224. DOI: <https://doi.org/10.18721/JPM.161.137>

Статья открытого доступа, распространяемая по лицензии CC BY-NC 4.0 (<https://creativecommons.org/licenses/by-nc/4.0/>)

Introduction

Development of T-S waves is a key mechanism of convective instability of wall-bounded laminar flows, which plays a crucial role in the natural laminar-turbulence transition. This has stimulated numerous experimental, theoretical, and numerical studies of the T-S waves (see, e.g. monographs [1, 2] and a review paper [3]). In this paper we present first results of the project funded by the Russian Scientific Foundation and devoted to the development of a general methodology for predicting of the T-S waves evolution based on the Global Stability Analysis (GSA) of steady solutions of the full compressible Navier-Stokes (N-S) equations. Unlike the existing methods, the proposed methodology is applicable not only to simple boundary layers forming on smooth surfaces (parallel and quasi-parallel flows), but also to essentially non-parallel flows. It presents a three-stage numerical procedure. In the first stage, numerical solution of the steady N-S equations is obtained for the flow which stability is analyzed, i.e., the “baseflow” is defined. In the second stage, GSA of the baseflow is conducted which outcome is a set of complex eigenvalues and corresponding eigenvectors. Imaginary parts of the eigenvalues present the frequencies and the real part – the growth or decay (depending on the sign) rates of the small disturbances, while the real parts of the corresponding eigenvectors define the spatial shape of the disturbances. Finally, the third stage of the procedure consists in post-processing of the results of GSA, which allows defining streamwise distribution of the T-S waves amplification factor (N-factor), characterizing the growth rate of their amplitude in the course of downstream propagations.

The paper is organized as follows. Section 2 presents a brief overview of the methodology. Section 3 contains an example of its application to the predicting the T-S waves evolution in the zero pressure gradient boundary layer (ZPG BL), namely, the corresponding problem statement, some numerical details, results of the computations and their comparison with those of the classic 1D linear stability analysis. Finally, Section 4 summarizes major results of the study and presents its outlook.

Overview of the methodology

For the numerical integration of the compressible N-S equations performed in the first stage of the proposed procedure, an in-house CFD solver is used. It employs an implicit finite-volume formulation on structured multi-block overlapping grids. For approximation of the inviscid fluxes in the compressible N-S equations, the third-order upwind-biased scheme of Roe [4] is used, while the viscous fluxes are approximated with the second-order central scheme. The solver uses local time-stepping, which provides an iterative procedure for obtaining a steady solution, if it exists. In order to damp unsteadiness, the time integration is carried out with the use of a large time step (large Courant–Friedrichs–Lewy number), which is enabled by the use of an implicit scheme.

In the second stage, the GSA is conducted of the deeply converged (the maximum non-

dimensional residual is less than 10^{-7}) steady N-S solution obtained in the first stage. This is done with the use of the software earlier developed for GSA in the works [5, 6]. It is based on solution of the linear equations for the small perturbations, which are derived from the unsteady N-S equations. Unlike the original Roe scheme, the numerical scheme used for these linear equations employs the simple upwind finite-difference approximations based on the sign of the cell-face normal component of the baseflow velocity.

Finally, a post-processing of the GSA results is performed, which includes the following steps.

First, the complex eigenvectors are filtered with the use of the Kolmogorov-Zurbenko filter [7]. Then, streamwise distributions of the T-S waves amplitude, $A(x)$, is computed. It is defined as a local (at a given x) maximum amplitude of the filtered eigenvectors: $A(x) = \max_y \{A(x, y)\}$. Then, extracting is carried out of the streamwise distribution of the wavelength of the T-S waves, $\lambda(x)$, which is defined as the difference of the streamwise coordinates of the neighbouring maximums, $x_{\max}^{k+1} - x_{\max}^k$, in the real part of the eigenvector. After that, the group velocity of the T-S waves is calculated with the use of the relation $U_g = d\omega_i / d\alpha$, where ω_i is the frequency of the disturbances from the GSA and $\alpha = 2\pi / \lambda$. Finally, the last step of the post-processing consists in computing the streamwise variation of the amplitude of the running T-S wave, $B(x)$, and of its amplification factor $N(x)$. These parameters are computed based on the following consideration.

Let $\Delta x = x - x_0$ be the distance run by T-S waves for the time interval Δt . Then, the spatial decay-rate of these waves amplitude during this interval constitutes $D = \exp(\omega_i \Delta t)$. Assuming that the group velocity does not depend on x , the normalized distribution of $B(x)/B(x_0)$ accounting for this decay may be computed as: $B(x)/B(x_0) = A(x)/A(x_0) \cdot \exp(\omega_i \Delta x / U_g)$. This, in turn, allows a direct computation of the N-factor defined as $N = \ln[B(x)/B_{\min}]$, where B_{\min} is the minimum value of $B(x)$ within the considered interval.

Application to ZPG BL

In order to assess robustness and accuracy of the methodology briefly outlined above it has been applied to the flow over a flat plate (zero pressure gradient boundary layer – ZPG BL).

Problem statement and results of the baseflow computations

We consider a ZPG BL at the Mach number $M_\infty = 0.05$ and the Reynolds number $Re_0 = L_0 U_\infty / \nu = 3 \cdot 10^6$, where L_0 is the distance from the plate leading edge to the end of the T-S instability region at non-dimensional frequency normalized by the viscous time $F = 10^6 \omega_i / U_\infty^2 \nu$ equal to 30 according to the 1D linear stability theory. Corresponding frequency normalized by the convective time used in the GSA $\bar{\omega}_i = \omega_i (U_\infty / L_0) \equiv F \cdot Re_0 / 10^6 = 3F = 90$ (hereafter, the bar over ω_i is dropped).

The computations were carried out for the plate of the length $2L_0$. In order to mitigate the effect of the inflow boundary conditions on the baseflow solution which stability is analyzed by the GSA, the computational domain is extended by adding the inviscid region with the length of $0.2L_0$ upstream of the plate leading edge (see Fig. 1). This results in the total length of the domain equal to $2.2L_0$. The size of the domain in the plate-normal direction is set equal to $0.2L_0$, which corresponds to about 40 boundary layer thicknesses at the outflow of the domain.

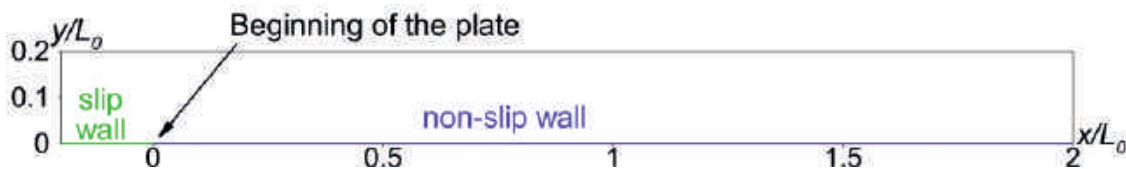


Fig. 1. Computational domain used for N-S computation of ZPG BL

The boundary conditions for the baseflow computations are imposed as follows.

At $y = 0$ and $x < 0$ the free slip (symmetry) conditions are specified, whereas at $y = 0$ and $x > 0$, the no-slip and non-permeability conditions for the velocity and the adiabatic conditions for the temperature are used.



At the free boundaries (inflow, outflow and upper ones) the characteristic boundary conditions are employed with the Riemann invariants defined by the free-flow parameters.

A size of the computational (x, y) -grid used in the computation is 10500×196 (2.058×10^6 cells total). The grid is gradually refined in y -direction near the plate surface ($y = 0$) and in the x -direction near the leading edge of the plate ($x = 0$). Outside the regions with the refined grid, its streamwise step $\Delta x/L_0 = 2 \cdot 10^{-4}$ (e. g., at $F = 30$, this corresponds to about 100 points per wavelength) and the wall-normal one $\Delta y/L_0 = 5 \cdot 10^{-4}$. Note that this grid is actually designed for the GSA and is definitely excessive for the baseflow computation. However, this allows getting 100% grid-independent solution, on the one hand, and, on the other hand, permits avoiding interpolation of the baseflow solution on a finer GSA grid, which would be needed otherwise, with an insignificant penalty in terms of the additional CPU time because of the relatively low cost of the baseflow computation.

Figure 2 shows the baseflow velocity profile at $x/L_0 = 0.5$. One can see that it virtually coincides with the self-similar Blasius profile for the incompressible ZPG BL, which is not surprising for the considered low Mach number flow.

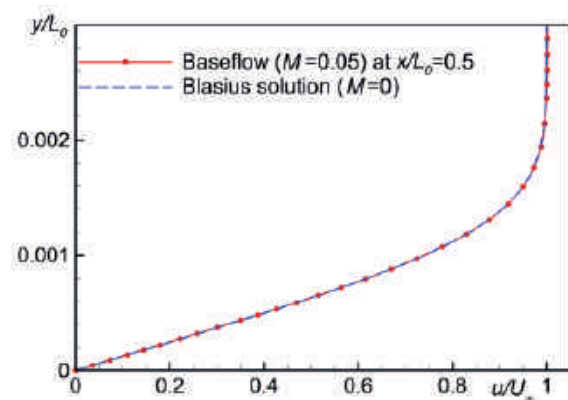


Fig. 2. Comparison of computed baseflow streamwise velocity profile at $x/L_0 = 0.5$ with self-similar Blasius solution

GSA problem setup and results

The problem setup has been defined based on results of a series of preliminary GSA computations with different sizes of the computational domain and two types of the boundary conditions (BCs) for the disturbances at its free boundaries, namely, Robin's conditions [8] and zero Dirichlet ones. These computations were aimed at finding a combination of the domain size and the BCs ensuring a minimum damage of results of the GSA caused by the approximate BCs. Their results (not shown) suggest that in this sense an optimal combination is the Dirichlet conditions imposed at the boundaries of the domain shown by red lines in Fig. 3. Its inlet and outlet are located at $x_1/L_0 = 0.15$ and $x_2/L_0 = 1.8$ respectively. According to the 1D linear stability theory, at the considered Reynolds number Re_0 , this domain covers the entire range of the T-S instability for the frequencies within the range $40 \geq F \geq 20$ or $120 \geq \omega_i \geq 60$. The upper boundary of the domain is located at $y/L_0 = 0.12$.

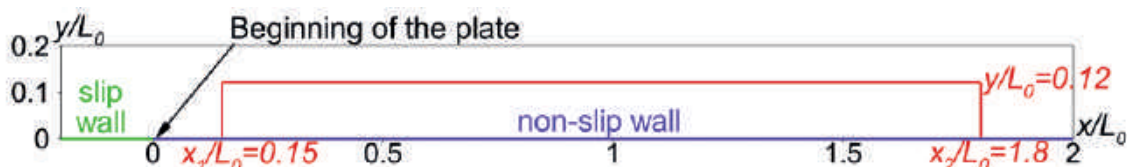


Fig. 3. Computational domain used in GSA of ZPG BL

Major results of the second stage of the proposed methodology, i.e., “raw” results of the GSA of the baseflow presented above are shown in Fig. 4 in the form of the growth rate – frequency map and of an example of the real part of the v -component of the eigenvector at $\omega_i = 90$ ($F = 30$).

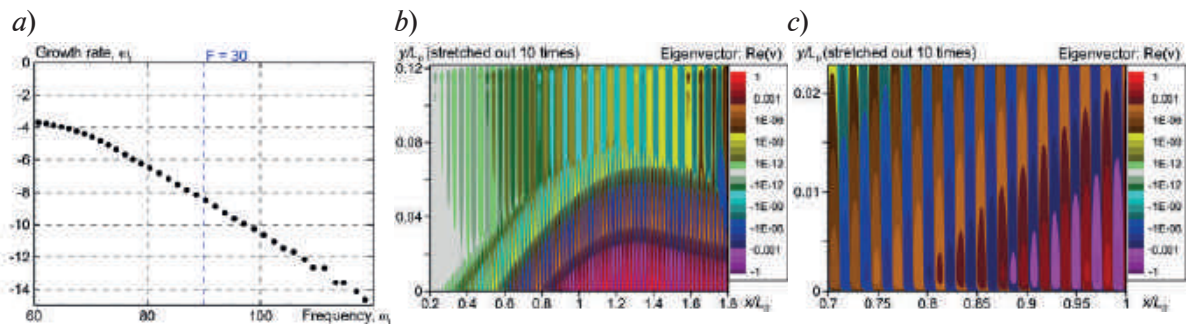


Fig. 4. Growth rate – frequency map (a), contours of real part of v -component of eigenvector corresponding to $\omega_i = 90$ (b), and its zoomed in fragment (c)

These results look quite reasonable and qualitatively similar to those available in the literature (see, e.g. [9, 10]).

We now move to the results of the last stage of the proposed procedure (GSA post-processing), which are presented in Fig. 5–7.

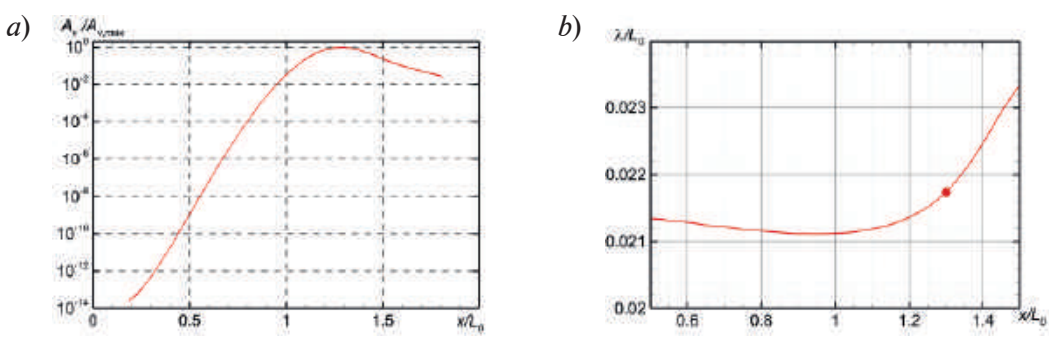


Fig. 5. Streamwise distributions of normalized amplitude of v -component of disturbances (a) and of T-S wavelength (b) at $\omega_i = 90$ ($F = 30$)

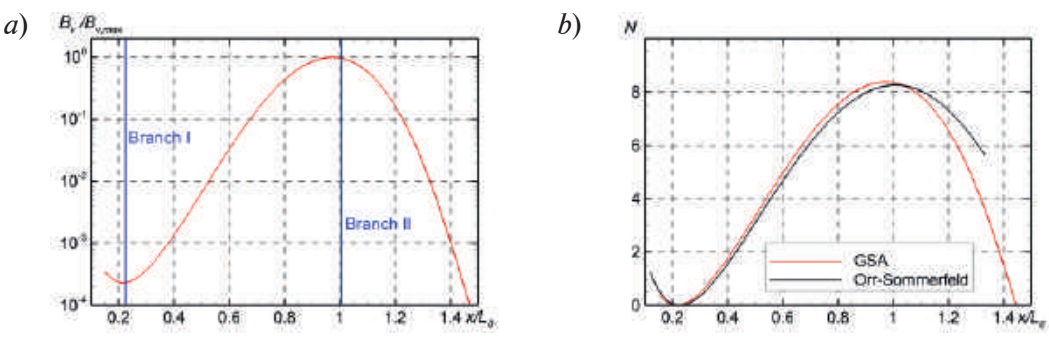


Fig. 6. Streamwise distribution of amplitude of running T-S wave with account of its decay (a) and its N -factor (b) at $F = 30$ ($\omega_i = 90$). Blue vertical lines show the instability boundaries on the first and second branches of T-S neutral curve according to Orr-Sommerfeld theory

In particular, the left frame of Fig. 5 shows the streamwise distributions of the normalized T-S waves amplitude $A_v(x) = A_{v,max}$, where $A_{v,max}$ is the maximum value of $A_v(x)$ reached at $x/L = 1.3$. The right frame of the figure depicts the plot of the streamwise distribution of the T-S wavelength $\lambda(x)$. One can see that the variation of the latter is marginal (about 7%). Considering this, for the further post-processing we use the value of $\lambda(x)$ at $x/L = 1.3$ where $A_v(x)$ reaches its maximum. This value is shown by the circle in the figure.

Given the wavelength dependence on the frequency is known, the group velocity of the T-S waves may be calculated as $U_g = d\omega_i/d\alpha$ (see Section 2). At $F = 30$, this gives $U_g = 0.36U_\infty$ which is close to the value of $U_g = 0.38U_\infty$ predicted by the 1D stability theory. This, in turn, allows computing the streamwise distribution of the amplitude of the running T-S wave with account of



its decay (see Section 2). An example of such distribution at $F = 30$ ($\omega_i = 90$) is shown in the left frame of Fig. 6, while the corresponding distribution of the T-S N -factor $N(x) = \ln[B_v(x)/B_{v,\min}]$ is presented in its right frame.

The figure also compares results of the present study with the similar Orr-Sommerfeld results for the incompressible flow. The comparison suggests very close agreement of the both approaches. This observation is supported by Fig. 7, which depicts a plot of N as the function of frequency. Thus, the results obtained are in good agreement with the theory, which indicates the reliability of the GSA itself and the developed technique as a whole.

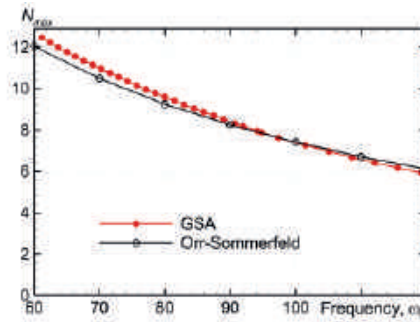


Fig. 7. Comparison of N -factor of T-S waves as function of frequency computed in the present study with Orr-Sommerfeld solution

Conclusion and outlook

The paper presents an outline of a general numerical methodology for predicting characteristics of the Tollmien–Schlichting waves based on the Global Stability Analysis of steady solutions of the full compressible Navier-Stokes equations. Unlike existing methods, this methodology does not rely upon the assumptions of parallel or quasi-parallel flow character, which opens a way to analyses of essentially non-parallel wall-bounded flows. It presents a three-stage procedure including 1) numerical solution of the steady Navier-Stokes equations for the flow in question, 2) Global Stability Analysis of this solution, and 3) post-processing of the results of this analysis aimed at extracting major characteristics of the Tollmien–Schlichting waves. Robustness and high accuracy of the proposed approach are demonstrated by its application to the canonic flat plate boundary layer, as an example: obtained results are in a good agreement with similar results of the classic linear stability analysis based on the Orr-Sommerfeld equation. This justifies applying the approach to studying the Tollmien–Schlichting waves in complex flows, particularly in the boundary layers on curved smooth surfaces and those with geometric irregularities (gaps, steps, etc.), which will be performed in the further work.

Acknowledgments

The computations were performed on the HP computing facilities of Peter the Great Saint-Petersburg Polytechnic University (<http://www.spbstu.ru>).

REFERENCES

1. Zhigulev V.N., Tumin A.M., Emergency of Turbulence, Nauka, Novosibirsk, 1987.
2. Boiko A.V., Grek G.R., Dovgal A.V., Kozlov V.V., Physical Mechanisms of Transition to Turbulence in Open Flows, URSS Publishing Group, 2006.
3. Theofilis V., Global linear instability. Annual Review Fluid Mech. (43) (2011) 319–352.
4. Roe P.L., Approximate Riemann solvers, parameter vectors, and difference schemes. Journal of Comput. Phys. 2 (43) (1981) 357–372.
5. Crouch J.D., Garbaruk A.V., Magidov D., Predicting the onset of flow unsteadiness based on global instability. Journal of Computational Physics. 2 (224) (2007) 924–940.
6. Crouch J.D., Garbaruk A., Strelets. M., Global instability in the onset of transonic-wing buffet. Journal of Fluid Mechanics. (881) (2019) 3–22.
7. Yang W., Zurbenko I., Kolmogorov–Zurbenko filters. WIREs Comp Stat. 2 (2010) 340–351.

8. **Gustafson K.**, Domain Decomposition, Operator Trigonometry, Robin Condition. Contemporary Mathematics. (218) (1998) 432–437.

9. **Ehrenstein U., Gallaire F.**, On two-dimensional temporal modes in spatially evolving open flows: the flat-plate boundary layer. Journal of Fluid Mechanics. (536) (2005) 209–218.

10. **Henningson D.S., Akervik E.**, The use of global modes to understand transition and perform flow control. Physics of Fluids. (20) (2008) 031302.

THE AUTHORS

BELYAEV Kirill V.

kira@cfд.spbstu.ru

ORCID: 0000-0001-7272-2342

GOLUBKOV Valentin D.

golubkovvd@gmail.com

ORCID: 0000-0001-9473-7430

GARBARUK Andrey

agarbaruk@cfд.spbstu.ru

ORCID: 0000-0002-2775-9864

STRELETS Mikhail Kh.

strelets@cfд.spb.ru

ORCID: 0000-0002-4608-388X

Received 05.10.2022. Approved after reviewing 14.11.2022. Accepted 15.11.2022.

Conference materials
UDC 539.21: 536.911+536.912
DOI: <https://doi.org/10.18721/JPM.161.138>

Adaptation of the Monte-Carlo method for modeling layer-by-layer growth of clusters and nanoalloys

V.S. Myasnichenko ¹✉, D.N. Sokolov ¹, N.Yu. Sdobnyakov ¹, P.M. Ershov ¹,
N.I. Nepsha ¹, A.D. Veselov ¹, S.A. Veresov ¹, R. Mikhov ², L. Kirilov ²

¹Tver State University, Tver, Russia;

²Institute of Information and Communication Technologies, Bulgarian Academy of Sciences, Sofia, Bulgaria
✉ viplabs@ya.ru

Abstract. In this paper, we study the layer-by-layer growth process of a bimetallic nanoparticle Au-Ag having face-centered cubic and decahedron structure. The Monte Carlo method was chosen to implement this problem combined with an approach from molecular dynamics. The Monte Carlo method allows solving of problems with periodic boundary conditions. Computer implementations of the method have been developed in two different software products Metropolis (Tver State University) and Tsuyoyama (Institute of Information and Communication Technologies). Interaction between atoms is calculated using multi-body tight-binding model. It is established that the order of addition of atoms (simultaneous or layered) affects the chemical ordering in the studied gold-silver equiatomic nanoalloys. In addition, the difference between the values of specific energy corresponding to Metropolis and Tsuyoyama software becomes quite small, supporting the inference that the numerical procedure for the layer-by-layer growth is adequate.

Keywords: computer simulation, Monte-Carlo method, molecular dynamics method, layer-by-layer growth, nanoalloy

Funding: The research was carried out with the support of the Ministry of Education and Science of the Russian Federation as part of the state task in the field of scientific activity (projects no. 0817-2020-0007 and no. 0817-2023-0006) and Bulgarian National Science Fund under the grants KP-06-N52/7 and KP-06-N52/5.

Citation: Myasnichenko V.S., Sokolov D.N., Sdobnyakov N.Yu., Ershov P.M., Nepsha N.I., Veselov A.D., Veresov S.A., Mikhov R., Kirilov L., Adaptation of the Monte-Carlo method for modeling layer-by-layer growth of clusters and nanoalloys, St. Petersburg State Polytechnical University Journal. Physics and Mathematics. 16 (1.1) (2023) 225–230. DOI: <https://doi.org/10.18721/JPM.161.138>

This is an open access article under the CC BY-NC 4.0 license (<https://creativecommons.org/licenses/by-nc/4.0/>)

Материалы конференции
УДК 539.21: 536.911+536.912
DOI: <https://doi.org/10.18721/JPM.161.138>

Адаптация метода Монте-Карло для моделирования послойного роста кластеров и наносплавов

В.С. Мясниченко ¹✉, Д.Н. Соколов ¹, Н.Ю. Сдобняков ¹, П.М. Ершов ¹,
Н.И. Непша ¹, А.Д. Веселов ¹, С.А. Вересов ¹, Р. Михов ², Л. Кирилов ²

¹Тверской государственный университет, г. Тверь, Россия;

²Институт информационных и коммуникационных технологий
Болгарской академии наук, г. София, Болгария

✉ viplabs@ya.ru

Аннотация. В данной работе исследуется процесс послойного роста биметаллической наночастицы Au-Ag, имеющей гранецентрированную кубическую и декаэдрическую

структуру. Для решения этой задачи был выбран метод Монте-Карло в сочетании с методом молекулярной динамики. Метод Монте-Карло позволяет решать задачи с периодическими краевыми условиями. Реализация метода производилась в двух разных программных продуктах Metropolis (Тверской государственной университет) и Tsuyouama (Институт информационных и коммуникационных технологий). Взаимодействие между атомами описывается с использованием многочастичного потенциала сильной связи. Установлено, что порядок присоединения атомов (одновременный или послойный) влияет на химическую упорядоченность в исследованных эквиатомных наносплавах золото-серебро. Кроме того, разница между значениями удельной энергии, соответствующей использованию программ Metropolis и Tsuyouama, становится достаточно малой, что подтверждает вывод об адекватности численной процедуры послойного роста.

Ключевые слова: компьютерное моделирование, метод Монте-Карло, метод молекулярной динамики, послойный рост, наносплав

Финансирование: Исследования выполнены при поддержке Министерства образования и науки Российской Федерации в рамках выполнения государственного задания в сфере научной деятельности (проект № 0817-2020-0007 и № 0817-2023-0006) и Болгарского национального научного фонда гранты КР-06-N52/7 и КР-06-N52/5.

Ссылка при цитировании: Мясниченко В.С., Соколов Д.Н., Сдобняков Н., Ершов П.М., Непша Н.И., Веселов А.Д., Вересов С.А., Михов Р., Кирилов Л. Адаптация метода Монте-Карло для моделирования послойного роста кластеров и наносплавов // Научно-технические ведомости СПбГПУ. Физико-математические науки. 2023. Т. 16. № 1.1. С. 225–230. DOI: <https://doi.org/10.18721/JPM.161.138>

Статья открытого доступа, распространяемая по лицензии CC BY-NC 4.0 (<https://creativecommons.org/licenses/by-nc/4.0/>)

Introduction

To date, researchers around the world actively use the molecular dynamics method as a tool for conducting atomistic modeling of nanosystems. While the Monte Carlo method [1] is rarely used by researchers to study the properties of mono- and bimetallic nanosystems [2–4]. Most theoretical studies of the properties of metal clusters use the procedure of simple cutting of particles from a bulk crystal structure. Thus, in [5], we presented a method for obtaining a stable structure of one-dimensional bimetallic nanoobjects. The approach is based on applying the Metropolis algorithm [6] to a periodic lattice of nodes in combination with subsequent relaxation according to the molecular dynamics method. Here, the interaction between atoms is described in terms of the tight binding potential [7]. The main advantage of the many-body interaction potential, as compared to the simple pair potential, consists in its better reproduction of some of the main features of metallic systems.

The stochastic Monte Carlo method [8] is used to study model systems up to a million atoms in size at relatively high cooling rates [9, 10]. In particular, Monte Carlo simulation was performed in [11, 12] to study ordering in bimetallic nanoalloys of a wide range of sizes in combination with semiempirical potentials. Since the successful application of simulated annealing is critically dependent on proper temperature control, one of its most important parameters is the initial temperature, which must be sufficiently high to allow the system to explore different global configurations without hitting a local minimum too early. However, a lower initial temperature allows a solution to be obtained with fewer iterations of the Metropolis algorithm.

The problem of layer-by-layer growth of crystals was previously addressed by researchers. For example, in [13], a metric model of layer-by-layer self-similar crystal growth is studied for solving practical problems of single and mass crystallization. The problem of modeling layer-by-layer growth at the nanolevel has a number of fundamental features associated with both size effects and manifestations of symmetry types that are not typical for bulk crystals [14]. Au-Ag nanoparticles [15] are promising cocatalysts for photocatalytic hydrogen reduction. However, the effect of chemical ordering on the electronic properties of nanoparticles is not well



understood other than in terms of quantum effects due to small sizes. Thus, in [16], the structural properties of 147-atomic cuboctahedral Au-Ag clusters are studied, using empirical potentials in combination with the ‘atomic-swap basin-hopping’ metaheuristic optimization method and comparing with the minima obtained by the density functional theory. Calculations show that Au atoms predominantly occupy near- surface positions in bimetallic structures, which leads to the formation of a pseudo-onion structure for compositions enriched in Ag.

The aim of this work is to adapt the Monte Carlo method implemented in two different software products (Metropolis and Tsuyoyama) to simulate the layer-by-layer growth process using Au-Ag bimetallic nanoclusters with different structure (face-centered cubic – fcc and decahedron – dec).

Computer simulation results and discussion

The layer-by-layer growth scheme is implemented in the Metropolis software [1] as follows. At the first stage, the core energy of the nanoparticle in the initial configuration is minimized, after which the freezing process is initiated. At the second stage, the first layer is added and the process of minimizing its energy is commenced, followed by freezing of the first layer. This procedure is additionally repeated with subsequent layers.

The cyclical energy minimization procedure starting at 0 K takes place as follows. At the first step, a full cycle of Monte Carlo steps is processed, after which the energy value of the system is stored. At the second step, we again work out the entire cycle of Monte Carlo steps, after which the convergence condition is checked according to the equation

$$|E_{\min}(i) - E_{\min}(i-1)| < \varepsilon, \quad (1)$$

where $E_{\min}(i)$ is the energy at the current iteration, $E_{\min}(i-1)$ is the energy at the previous iteration, while the parameter ε is initially set manually. If it is necessary to minimize the energy at an arbitrary temperature, for example, at $T = 300$ K (this value was used in calculation), then the `run_temperature(300)` and `config_minimize_energy(params)` functions are used. Thus, before minimization (which is carried out at 0 K), the given configuration is maintained at $T = 300$ K, then the above-described algorithm is repeated when adding layers in a cycle.

The algorithm implemented in Tsuyoyama is described in [17]. For each layer, the growth atoms are first placed into random empty nodes, then a number of iterations are performed on the particle. At each iteration, one atom may jump into an empty node (both are chosen at random). If the jump would decrease the potential energy, it is performed unconditionally. Otherwise, it may or may not be performed, with the jump probability given as:

$$P = \exp(-\Delta E / kT), \quad (2)$$

where ΔE is the energy difference of the configurations and T is the current temperature of the system. The temperature, which is initially set at 2000 K, is then gradually decreased as the algorithm proceeds. We used a linear formula for the cooling, subtracting a small amount once every 10000 iterations. The algorithm ends after 500 million iterations, when the temperature reaches 100 K. After repeating each run of the algorithm 30 times, the two best results are chosen.

At the stage of approbation of the software product Metropolis [1], we simulated the layer-by-layer growth of a bimetallic nanoparticle having an initial size of 146 atoms (1.5 nm). Figures 1 and 2 show as example the sequence of growth of decahedral nanoparticles using alternative software products Metropolis [1] and Tsuyoyama [17]. As can be seen overall surface is

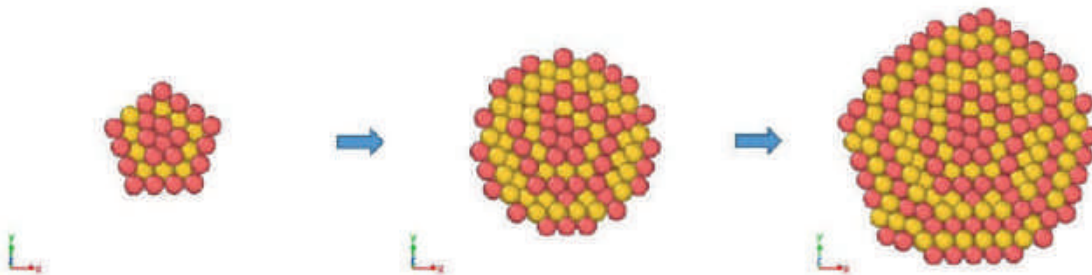


Fig. 1. Layer-by-layer growth of Au-Ag (dec) nanoparticles, in the (001) plane cross section. Metropolis software. Here and further, yellow atoms represent gold, while red atoms are silver

predominantly filled with Ag atoms (see Figure 1 and left picture in Figure 3), while the Au atoms present in sufficient quantity (see right picture in Figure 3) on the {111} faces of the resulting 3.5 nm nanoparticle. The “alternate” segregation of two metals on the near-surface layers of the nanoalloy was also revealed. Tables 1 and 2 present the calculations of specific energies per atom of Au-Ag nanoparticles, which were obtained by layer-by-layer growth procedure around the core. For the aforementioned software, two independent series of experiments are presented.

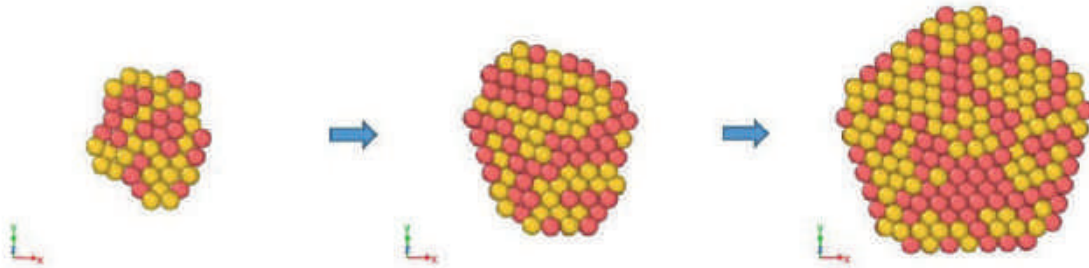


Fig. 2. Layer-by-layer growth of Au-Ag (dec) nanoparticles, in the (001) plane cross section. Tsuyoyama software

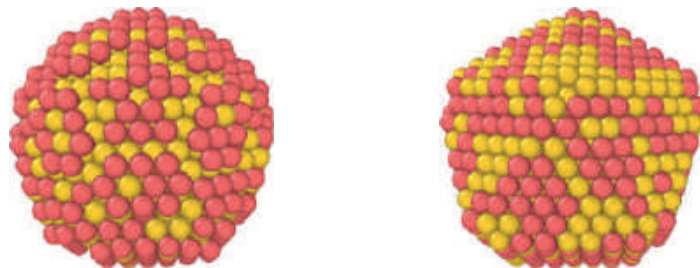


Fig. 3. Surface of the final grown decahedral Au-Ag nanoparticle: results of the Metropolis software on the left and Tsuyoyama software on the right, respectively

Table 1

Specific energy (eV/atom) of Au-Ag nanoparticles based on the FCC lattice

Layer number	Metropolis		Tsuyoyama		N, atoms	Total atoms
	Series 1	Series 2	Series 1	Series 2		
Core	-3.1141	-3.1144	-3.1512	-3.1531	146	146
+Layer 1	-3.2393	-3.2407	-3.2434	-3.2443	448	594
+Layer 2	-3.2825	-3.2829	-3.2820	-3.2831	906	1500

Table 2

Specific energy (eV/atom) of Au-Ag nanoparticles based on the dec lattice

Layer number	Metropolis		Tsuyoyama		N, atoms	Total atoms
	Series 1	Series 2	Series 1	Series 2		
Core	-3.1241	-3.1244	-3.1564	-3.1567	146	146
+Layer 1	-3.2375	-3.2410	-3.2395	-3.2417	448	594
+Layer 2	-3.2835	-3.2836	-3.2829	-3.2827	906	1500

Conclusion

An analysis of the data presented in Tables 1 and 2 suggests that both programs used predict a monotonic decrease of the specific energy of Au-Ag nanoparticles. In the size range under investigation, it is still impossible to unequivocally state which of the two structures (fcc or dec) will be more stable. With an increase in the number of atoms in Au-Ag nanoparticles, the difference between the values of specific energy corresponding to Metropolis [18] and Tsuyoyama software



becomes quite small, supporting the inference that the numerical procedure for the layer-by-layer growth is adequate. Thus, the study allows us to conclude that the order of atoms addition (simultaneous or layer-by-layer) affects the chemical ordering in equiatomic Au-Ag nanoalloys with a diameter of about 4 nm. Therefore, the growth parameters of bimetallic nanoalloys can affect their physical and chemical properties, as well as influencing the size effect [1].

REFERENCES

1. **Samsonov V.M., Sdobnyakov N.Yu., Myasnichenko V.S., Talyzin I.V., Kulagin V.V., Vasilyev S.A., Bembel A.G., Kartoshkin A.Yu., Sokolov D.N.**, Comparative analysis of the size dependence of the melting and crystallization temperatures in silver nanoparticles via the molecular dynamics and Monte-Carlo methods, *Journal of Surface Investigation: X-ray, Synchrotron and Neutron Techniques*. 12 (6) (2018) 1206–1209.
2. **Myasnichenko V., Fidanova S., Mikhov R., Kirilov L., Sdobnyakov N.**, Representation of initial temperature as a function in simulated annealing approach for metal nanoparticle structures modeling, *Advances in High Performance Computing, Studies in Computational Intelligence*. 902 (2021) 61–72.
3. **Myasnichenko V., Mikhov R., Kirilov L., Sdobnyakov N., Sokolov D., Fidanova S.**, Simulation of diffusion processes in bimetallic nanofilms, *Recent Advances in Computational Optimization, Studies in Computational Intelligence*. 986 (2022) 221–233.
4. **Mikhov R., Myasnichenko V., Kirilov L., Sdobnyakov N., Matrenin P., Sokolov D., Fidanova S.**, On the problem of bimetallic nanostructures optimization: an extended two-stage Monte Carlo approach, *Recent Advances in Computational Optimization, Studies in Computational Intelligence*. 986 (2022) 235–250.
5. **Myasnichenko V., Sdobnyakov N., Kirilov L., Mikhov R., Fidanova S.**, Monte Carlo approach for modeling and optimization of one-dimensional bimetallic nanostructures, *Lecture Notes in Computer Science. Conference paper: International Conference on Numerical Methods and Applications*. 11189 (2019) 133–141.
6. **Metropolis N., Rosenbluth A.W., Rosenbluth M.N., Teller A.H., Teller E.**, Equation of state calculations by fast computing machines, *The Journal of Chemical Physics*. 21 (6) (1953) 1087–1092.
7. **Cleri F., Rosato V.**, Tight-binding potentials for transition metals and alloys, *Physical Review B*. 48 (1) (1993) 22–33.
8. **Metropolis N., Ulam S.**, The Monte Carlo Method, *Journal of the American Statistical Association*. 44 (247) (1949) 335–341.
9. **Flenner E., Janosi L., Barz B., et al.**, Kinetic Monte Carlo and cellular particle dynamics simulations of multicellular systems, *Physical Review E*. 85 (3) (2012) 031907.
10. **Yun K., Cho Y.-H., Cha P.-R., Lee J., Nam H.-S., Oh J.S., Choi J.-H., Lee S.-C.**, Monte Carlo simulations of the structure of Pt-based bimetallic nanoparticles, *Acta Materialia*. 60 (12) (2012) 4908–4916.
11. **Tang J., Deng L., Xiao S., Deng H., Zhang X., Hu W.**, Chemical ordering and surface segregation in Cu–Pt nanoalloys: the synergetic roles in the formation of multishell structures, *The Journal of Chemical Physics C*. 119 (37) (2015) 21515–21527.
12. **Berthier F., Maras E., Legrand B.**, Phase diagrams of nanoalloys: influence of size and morphology, *Physical Chemistry Chemical Physics*. 17 (42) (2015) 28347–28353.
13. **Bezrodnyy D.A., Filimonov S.N.**, Computer simulations of the layer-by-layer growth of 3D-island facets, *Russian Physics Journal*. 56 (8/3) 2013 156–158. (In Russian).
14. **Madison A.E.**, Symmetry of quasicrystals, *Physics of the Solid State*. 55 (2013) 855–867.
15. **Shore M.S., Wang J., Johnston-Peck A.C., Oldenburg A.L., Tracy J.B.**, Synthesis of Au(Core)/Ag(Shell) nanoparticles and their conversion to AuAg alloy nanoparticles, *Small*. 7 (2) (2011) 230–234.
16. **Gould A.L., Heard C.J., Logsdail A.J., Catlow C.R.A.**, Segregation effects on the properties of (AuAg)₁₄₇, *Physical Chemistry Chemical Physics*. 16 (39) (2014) 21049–21061.
17. **Myasnichenko V., Sdobnyakov N., Kirilov L., Mikhov R., Fidanova S.**, Structural instability of gold and bimetallic nanowires using Monte Carlo simulation, *Recent Advances in Computational Optimization: Results of the Workshop on Computational Optimization and Numerical Search and Optimization 2018, Studies in Computational Intelligence*. 838 (2020) 133–145.

18. **Sokolov D.N., Sdobnyakov N.Yu., Savina K.G., Kolosov A.Yu., Myasnichenko V.S.**, New opportunities for high-performance simulations of nanosystem using Metropolis software, Physical and chemical aspects of the study of clusters, nanostructures and nanomaterials. 13 (2021) 624-638.

THE AUTHORS

MYASNICHENKO Vladimir S.
viplabs@ya.ru
ORCID: 0000-0003-4355-7055

SOKOLOV Denis N.
ORCID: 0000-0003-2411-0143
dnsokolov@mail.ru

SDOBNYAKOV Nickolay Yu.
nsdobnyakov@mail.ru
ORCID: 0000-0003-1749-0336

ERSHOV Pavel M.
ershovpaul@gmail.com
ORCID: 0000-0002-7083-214X

NEPSHA Nikita I.
nepsha.nikita@yandex.ru

VESELOV Alexey D.
armagidon69@mail.ru

VERESOV Sergey A.
veresovsergei@mail.ru

MIKHOV Rossen
rmikhov@abv.bg
ORCID: 0000-0001-7186-0110

KIRILOV Leoneed
l_kirilov_8@abv.bg
ORCID: 0000-0001-8424-9070

Received 10.10.2022. Approved after reviewing 08.11.2022. Accepted 08.11.2022.

Conference materials

UDC 538.951

DOI: <https://doi.org/10.18721/JPM.161.139>

Fracture modeling with the discrete elements method

V.L. Hilarov ¹✉, E.E. Damaskinskaya ¹

¹ Ioffe Institute, St. Petersburg, Russia

✉ Vladimir.Hilarov@mail.ioffe.ru

Abstract. The discrete element method (DEM) is used to reveal the main features of fracture in materials with different degree of heterogeneity. It is shown that this method adequately describes the main properties of materials in the fracture process such as brittle and ductile behavior, two-staged nature of fracture in heterogeneous materials, heterogeneity of the spatial distribution of local internal stresses depending on the degree of material heterogeneity.

Keywords: materials fracture, Discrete Elements Method, heterogeneity

Funding: The work has been carried out within the State task of the Ioffe Institute “Problems of strength physics: the processes of solids fracture, principles of strengthening materials and increasing the dynamic strength of materials, the creation of crack-resistant, wear-resistant materials, the development of technologies for light transparent armor” (subject code [0040-2014-0008]).

Citation: Hilarov V.L., Damaskinskaya E.E., Fracture modeling with the discrete elements method, St. Petersburg State Polytechnical University Journal. Physics and Mathematics. 16 (1.1) (2023) 231–235. DOI: <https://doi.org/10.18721/JPM.161.139>

This is an open access article under the CC BY-NC 4.0 license (<https://creativecommons.org/licenses/by-nc/4.0/>)

Материалы конференции

УДК 538.951

DOI: <https://doi.org/10.18721/JPM.161.139>

Применение метода дискретных элементов для моделирования разрушения поликристаллических материалов

В.Л. Гиляров ¹✉, Е.Е. Дамаскинская ¹

¹ Физико-технический институт им. А.Ф. Иоффе РАН, Санкт-Петербург, Россия

✉ Vladimir.Hilarov@mail.ioffe.ru

Аннотация. Метод дискретных элементов применен для выявления закономерностей разрушения гетерогенных материалов. Показано, что модель адекватно описывает разрушение хрупких и пластичных материалов, двухстадийный характер разрушения гетерогенных материалов, а также неоднородность пространственного распределения внутренних локальных напряжений в зависимости от гетерогенности материала.

Ключевые слова: прочность и разрушение материалов, метод дискретных элементов

Финансирование: Работа выполнена в рамках Государственного задания ФТИ им. А.Ф. Иоффе «Проблемы физики прочности: процессы разрушения твердых тел, принципы упрочнения материалов и повышения динамической прочности материалов, создание трещиностойких, износостойких материалов, разработка технологий легкой прозрачной брони» (код темы [0040-2014-0008]).

Ссылка при цитировании: Гиляров В.Л., Дамаскинская Е.Е. Применение метода дискретных элементов для моделирования разрушения поликристаллических материалов // Научно-технические ведомости СПбГПУ. Физико-математические науки. 2023. Т. 16. № 1.1. С. 231–235. DOI: <https://doi.org/10.18721/JPM.161.139>

Статья открытого доступа, распространяемая по лицензии CC BY-NC 4.0 (<https://creativecommons.org/licenses/by-nc/4.0/>)

Introduction

Fracture of materials remains to be the actual problem in connection with ongoing natural and technogenic catastrophes. At the same time, it is important to understand that fracture is not some kind of critical event that can be prevented by using materials with a safety margin or geometric dimensions with the ability to withstand the specified mechanical loads. On the contrary, fracture is a process evolving in space and time [1], and the parameters of materials, such as elastic moduli, local mechanical stresses and strains, structural rearrangements, and discontinuities, can undergo significant changes in this process. This process can be accompanied by various types of radiation (acoustic and electronic emission, mechanoluminescence), the parameters of which can serve as indicators or precursors of various kinds of events in the fracture process.

In contrast to the continual mechanics methods, the discrete element method (DEM) used in this work allows one to take into account explicitly the appearance of the local discontinuities during fracture process. We used the model of spherical particles (simulating polycrystalline grains) connected by bonds (simulating grain boundaries) located at the particle contacts. This bonded particle model (BPM) is described in detail in [2], and its various modifications are widely used to study the behavior of materials under mechanical load (for example, [3–8]). In the BPM model, the formation of cracks is determined by the breaking of bonds between particles, and their propagation is provided by the coalescence of many broken bonds [9].

The goal of this work was to study how the degree of materials heterogeneity influence the character of destruction and acoustic emission (AE) accompanying the fracture process. The breaking of a single bond was considered an elementary act of AE. Calculations were carried out in the freely distributed software package MUSEN [10]

Computer simulation

Cylindrical samples with a diameter of 10 mm and a height of 20 mm were modeled. The dimensions were selected in such a way that it was possible to compare the results obtained by computer modeling with the results of laboratory experiments obtained earlier on samples of the same dimensions. The cylinders were filled with spherical particles of the same or different radii and packed by the MUSEM packing generator until a porosity of 0.35–0.37 was reached. In this case, the overlap of the contacting spheres did not exceed 0.0001 mm.

Mechanical parameters of materials such as Young modules, Poisson ratios, normal and tangential strengths were set characteristic of rocks (quartz, orthoclase, oligoclase). We did not have a goal to compare values of the calculated strength of materials with their experimental strength, so the calibration of these parameters was not carried out. Two types of samples with different degrees of heterogeneity were used:

1. Homogeneous sample: grains (particles) and bonds with the properties of granite. The particle size was 0.4 mm, their number – 28125.

2. Grains (particles) with diameters obtained by a random number generator with a normal distribution (mean value of 0.3 mm and a standard deviation of 0.1 mm). Three types of particles (quartz, orthoclase, oligoclase) were generated with a percentage composition characteristic for granite; their number is 48695.

Bonds were formed at the places of particle contacts. Particles of the same material were connected by a bond from the matching material, and particles of different materials were connected either by low-strength brittle glass bonds (hereinafter referred to as the set of bonds type 1) or by low-modulus bonds [11] (hereinafter referred to as the set of bonds type 2). The bond diameter (d) was automatically chosen by the bond generator to be equal to the smaller diameter of the pair of connected particles 1 and 2: $d = \min \{d_1, d_2\}$ [10]. The maximum bond length (L_{max}) was chosen in such a way that one more particle could not fit between a pair of connected particles. The minimum length L_{min} was usually set to zero. It should be noted that with such a choice of L_{min} , the system can spontaneously explode, since



Fig 1. The sample and the simulation scheme



the overlap of particles mentioned above was allowed. If this happened, then the minimum bond length was taken equal to the maximum particle overlap (0.0001 mm) with the opposite sign.

The sample was placed in a virtual press, in which the lower plate was fixed, while the upper one descended at a speed of $v = 0.02$ m/s until the sample was destroyed (Fig. 1). Various mechanical parameters were recorded during the fracture process.

Results and Discussion

Figure 2 shows loading diagrams for samples of different heterogeneity and a homogeneous sample. The deformation was calculated using the formula $\varepsilon = v \cdot t$. Stress calculations were based on forces acting on the loading plates. Since in the numerical experiment it is generally impossible to maintain the equality of forces acting on the plates [12], the stress was calculated with the help of the formula $\sigma = 0.5 (F_t + F_b)/S$, S is the initial cross section, indices t and b correspond to top and bottom.

One can see that more homogeneous samples (1 and 2 in Fig. 2, *a* and Fig. 2, *b*) are characterized by brittle behavior (linear increase in stress versus deformation) and a sharp decrease after reaching the maximum value. For more heterogeneous samples (curves 3–5 in Fig. 2, *a*), the presence of a nonlinear (plastic) stage in the loading diagram is observed. This is because weaker bonds break first, and only after that the strong ones.

The spatial inhomogeneity of bonds breakage is shown in Fig. 3. The sample was divided into 10 layers perpendicular to its height, and the fracture characteristics were calculated in each layer for each saved time point. Fig. 3, *a* shows the time dependence of the number of intact bonds averaged over layers (N) for the three samples under consideration: homogenous sample with the stress-strain curve on the Fig. 2, *b*, the sample with stress-strain curve 1 on the Fig. 2, *a* and the sample with the bonds of type 1 described above. Diameter of bonds in all these cases was 0.1 mm. Coefficient of variation (the ratio of N to its standard deviation) was chosen as a measure of spatial heterogeneity and is shown in Fig. 3, *b*.

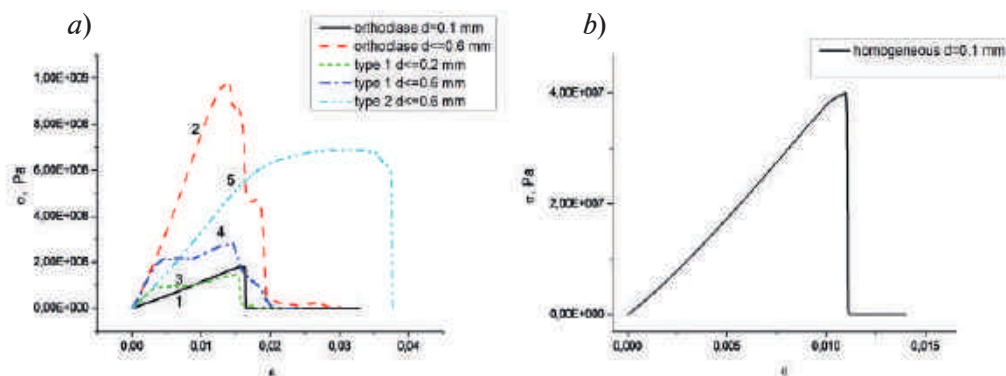


Fig. 2. Loading diagrams for samples with different types of bonds (*a*) and a homogeneous sample (*b*)

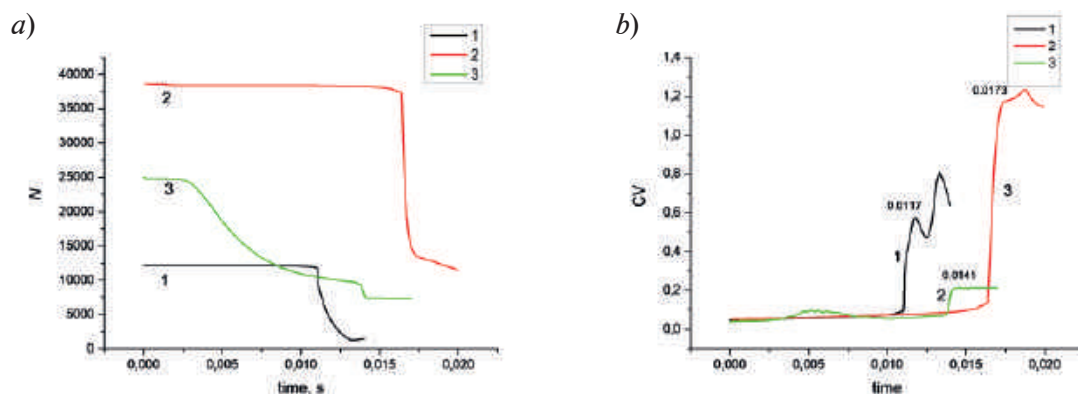


Fig. 3. Time dependence of the number of intact bonds averaged over the layers (N) (*a*) and the coefficient of variation (CV): 1 — homogeneous sample, 2 — sample with orthoclase bonds, 3 — sample with type 1 bonds (see text)

Brittle fracture is observed for samples 1 and 2: a negligible decrease in the number of intact bonds with a low coefficient of variation (spatial homogeneity) for quite a long simulation time and an after that, the rapid increase in CV close to the moment of destruction (localization of fracture and crack propagation). For heterogeneous sample 3, damage accumulates at much shorter times. However, the coefficient of variation at this stage is also small, which indicates that the damage accumulates more or less uniformly throughout the sample volume. This confirms the validity of the two-staged destruction model of heterogeneous materials proposed in [13, 14]. The rapid increase in the coefficient of variation is not very large too. This corresponds to the homogeneous nature of fracture in heterogeneous samples previously discovered in laboratory experiments [15], and a similar result obtained in the cellular automaton model [16].

For each layer, maximum tensile stresses acting on bonds σ_{max} were calculated. The reasons for the appearance of local tensile stresses under the action of an external compressive stress are well known (see, for example, [2]) and are not discussed here. Fig. 4, *a* shows the time dependences of the layer-averaged $\langle \sigma_{max} \rangle$ values. Fig. 4, *b* shows the time dependences of the coefficient of variation over the layers of the σ_{max} values.

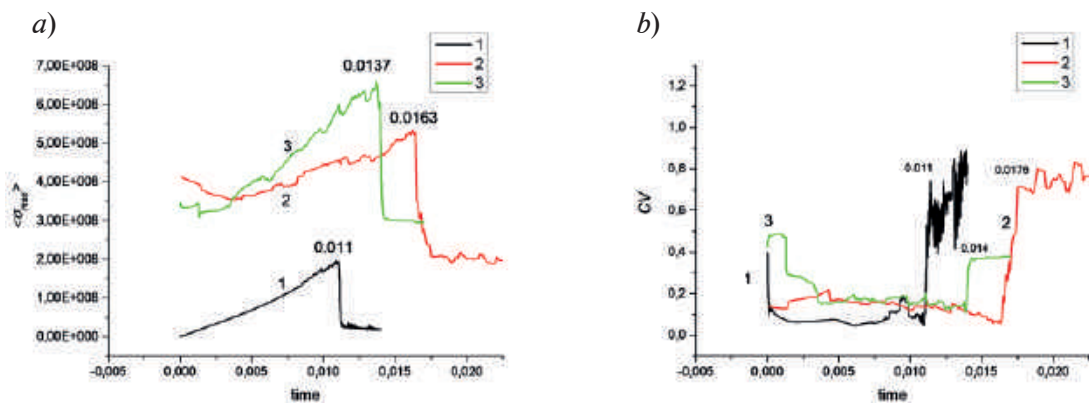


Fig. 4. Maximum tensile stresses averaged over layers (*a*) and their coefficients of variation (*b*): 1 – homogeneous sample, 2 – sample with orthoclase bonds, 3 – sample with type 1 bonds. The numbers on the graphs represent timestamps

In order to understand the time behavior of tensile stresses, one must keep in mind that the structure of grains and their boundaries (particles and bonds) created at the stage of material formation is not an equilibrium one and contains significant internal local stresses. At the initial stage of mechanical loading, these stresses relax. This relaxation time is so short compared to the characteristic loading time that it does not affect significantly the results obtained. This results in the nonmonotonicity of their time dependence at this stage (Fig. 4, *a*) and a significant coefficient of variation in Fig. 4, *b*. As stresses relax, they become more homogenous in the volume of the sample (Fig. 4, *b*) and increase in time (Fig. 4, *a*) until the conditions for the creation of a fracture center are formed. After this center is formed, local stresses again become significantly inhomogeneous in volume (Fig. 4, *b*). In a heterogeneous sample, the rate of this inhomogeneity is less than in samples that are more homogeneous.

Conclusion

The considered model of polycrystalline materials realistically describes some features of their destruction in cases where the main processes occur along grain boundaries. These features include the brittle nature of the destruction of homogeneous materials and the presence of nonlinear elasticity (plasticity) for more heterogeneous materials, revealed via the sigma-epsilon loading diagram (equation of state). For heterogeneous materials, the model predicts a two-stage nature of their fracture process, when at the first stage, the accumulation of defects occurs uniformly over the sample and at the second stage the formation and growth of the fracture center takes place.

The calculation of the maximum local stresses showed that the homogeneity of the material leads to greater spatial heterogeneity of local stresses and vice versa. The same behavior of local internal stresses calculated based on the kinetic concept of S.N. Zhurkov, was noted in laboratory experiments in [16].

**REFERENCES**

1. **Zhurkov S.N.**, Kinetic concept of the strength of solids, *Int. J. Fracture Mechanics*.1 (1965) 311–23.
2. **Potyondy D.O., Cundall P.A.**, A bonded-particle model for rock, *Int. J. Rock Mech. Min. Sci.* 41 (2004) 1329–64.
3. **Hazzard J.F., Young R.P.**, Simulating acoustic emissions in bonded-particle models of rock, *Int. J. Rock Mech. Min. Sci.* 37 (2000) 867–872.
4. **Hofmann H., Babadagli T., Zimmermann G.**, A grain based modeling study of fracture branching during compression tests in granites, *Int. J. Rock Mech. Min. Sci.* 77 (2015) 152–162.
5. **Vora, H.B., Morgan J.K.J.**, Microscale characterization of fracture growth and associated energy in granite and sandstone analogs: insights using the discrete element method, *Geophys. Research: Solid Earth.* 124 (2019) 7993–8012.
6. **Cho N., Martin C.D., Segol D.C.**, A clumped particle model for rock, *Int. J. Rock Mech. Min. Sci.* 44 (2007) 997–1010.
7. **Hazzard J.F., Young R.P.**, Moment tensors and micromechanical model, *Tectonophysics.* 356 (2002) 181–197.
8. **Zhang X.P., Wong L.N.Y.**, Cracking Processes in Rock-Like Material Containing a Single Flaw Under Uniaxial Compression: A Numerical Study Based on Parallel Bonded-Particle Model Approach, *Rock Mech. and Rock Engineering.* 45 (2012) 711–37.
9. **Lisjak A., Grasselli G.**, A review of discrete modeling techniques for fracturing processes in discontinuous rock masses, *J. of Rock Mech. and Geotechnical Engineering.* 6 (2014) 301–314.
10. **Dosta M., Skorych V.**, MUSEN: An open-source framework for GPU-accelerated DEM simulations, *SoftwareX.* 12 (2020) 100618.
11. **Li X.F., Zhang Q.B., Li H.B., Zhao J.**, Grain-Based Discrete Element Method (GB-DEM) Modelling of Multi-scale Fracturing in Rocks Under Dynamic Loading Rock, *Mech. and Rock Engineering.* 51 (2018) 3785–3817.
12. **Brown N.J.**, Discrete Element Modelling of Cementitious Materials. Ph.D. Thesis (Edinburgh: The University of Edinburgh), 2013, p. 247.
13. **Zhurkov S.N., Kuksenko V.S.**, Micromechanics of fracture of polymers, *Polymer Mechanics (rus).* 10 (1974) 792.
14. **Kuksenko V., Tomilin N., Damaskinskaya E., Lockner D.**, A two-stage model of fracture of rocks, *Pure and Applied Geophysics.* 146 (1996) 253–263.
15. **Hilarov V.L., Damaskinskaya E.E.**, On the Local Stress Fields in Inhomogeneous Media Determined by the Acoustic Emission Method, *Physics of the Solid State.* 63 (2021) 839–843.
16. **Hilarov V.L.** Simulation of crack growth during fracture of heterogeneous materials, *Physics of the Solid State.* 53 (2011) 758–762.

THE AUTHORS

HILAROV Vladimir L.
Vladimir.Hilarov@mail.ioffe.ru
ORCID: 0000-0002-9211-6144

DAMASKINSKAYA Ekaterina E.
kat.dama@mail.ioffe.ru
ORCID: 0000-0001-6328-0917

Received 12.10.2022. Approved after reviewing 08.11.2022. Accepted 08.11.2022.

Conference materials

UDC 532.517.4

DOI: <https://doi.org/10.18721/JPM.161.140>

Application of machine learning approach for turbulence model improvement for flow around airfoil near stall conditions

A.A. Matyushenko ¹✉, V.D. Golubkov ¹, A.V. Garbaruk ¹, M.Kh. Strelets ¹

¹ Peter the Great St. Petersburg Polytechnic University, Saint-Petersburg, Russia

✉ alexey.matyushenko@mail.com

Abstract. The work is devoted to the improvement of the $k-\omega$ BSL turbulence model for the closure of Reynolds averaged Navier-Stokes (RANS) equations with the use of machine learning (ML) methods. The correction developed for this model enhances its accuracy in calculating airfoil flows at stall angles of attack. Testing of the modified model on the flows around different airfoils reveals its superiority for this type of flows. The results demonstrate efficiency of the ML methods for turbulence model improvement.

Keywords: machine learning, RANS-modeling, stall conditions

Citation: Matyushenko A.A., Golubkov V.D., Garbaruk A.V., Strelets M.Kh., Application of machine learning approach for turbulence model improvement for flow around airfoil near stall conditions. St. Petersburg State Polytechnical University Journal. Physics and Mathematics. 16 (1.1) (2023) 236–242. DOI: <https://doi.org/10.18721/JPM.161.140>

This is an open access article under the CC BY-NC 4.0 license (<https://creativecommons.org/licenses/by-nc/4.0/>)

Материалы конференции

УДК 532.517.4

DOI: <https://doi.org/10.18721/JPM.161.140>

Использование машинного обучения для улучшения модели турбулентности при обтекании крылового профиля в условиях срыва потока

А.А. Матюшенко ¹✉, В.Д. Голубков ¹, А.В. Гарбарук ¹, М.Х. Стрелец ¹

¹ Санкт-Петербургский политехнический университет Петра Великого, Санкт-Петербург, Россия

✉ alexey.matyushenko@mail.com

Аннотация. Данная работа посвящена улучшению модели турбулентности $k-\omega$ BSL, используемой для замыкания осредненных по Рейнольдсу уравнений Навье-Стокса, при помощи методов машинного обучения. Коррекция, разработанная для этой модели, повышает ее точность при расчете обтеканий крыловых профилей при углах атаки срыва потока. Тестирование модифицированной модели для различных крыловых профилей доказывает приоритетность ее использования для данного типа течений. Результаты демонстрируют эффективность методов машинного обучения для улучшения моделей турбулентности.

Ключевые слова: машинное обучение, RANS-моделирование, срыв потока

Ссылка при цитировании: Матюшенко А.А., Голубков В.Д., Гарбарук А.В., Стрелец М.Х. Использование машинного обучения для улучшения модели турбулентности при обтекании крылового профиля в условиях срыва потока // Научно-технические ведомости СПбГПУ. Физико-математические науки. 2023. Т. 16. № 1.1. С. 236–242. DOI: <https://doi.org/10.18721/JPM.161.140>

Статья открытого доступа, распространяемая по лицензии CC BY-NC 4.0 (<https://creativecommons.org/licenses/by-nc/4.0/>)



Introduction

Models for closure the Reynolds Averaged Navier-Stokes (RANS) equations have been developed for almost 100 years and up to the present time they occupy a dominant position in solving applied problems of calculating turbulent flows. The main advantages of these models are the simplicity of their implementation and efficiency, as well as the availability of well-established computing technologies for performing calculations using them. This opens up the possibility of carrying out serial calculations necessary for the creation and optimization of new designs. However, even the best RANS models are not universal; provide a reliable prediction of averaged characteristics only for a limited range of relatively simple flows, which serves as a stimulus for numerous studies devoted to the construction of new and improving the accuracy of existing models.

Until recently, the model improvement study was carried out “by hand” and largely relied on physical intuition, and its success largely depended on the experience of researchers, which led to a certain “stagnation” in this area. On the other hand, advances in the development of measurement methods and computing systems have led to the fact that in recent years the knowledge base on the results of physical and numerical experiments with a high accuracy (“reference” data) has significantly expanded and effective tools have appeared that allow analysing large volumes of such data. In this regard, the possibility of improving existing turbulence models based on information obtained from the analysis of “reference” data has opened up. One of the most effective methods for solving this problem are Machine Learning (ML) methods, which allow to analyse and generalize huge arrays of reference data and connect many objects of the training sample with many answers using a special function called the Neural Networks (NN). This function, which is a correction to the model under consideration, can later be used to solve problems that were not included in the training set.

The first works aimed at improving RANS models using “reference” data and machine learning methods were devoted to eliminating the so-called parametric uncertainties caused by inaccuracies in determining the empirical constants of RANS models [1-3]. However, as shown in [4], a much more significant contribution to the discrepancy between the simulation result and “reference” data is made by the so-called structural uncertainties due to the imperfect formulation of the models. This gave impetus to the development of methods aimed at eliminating structural uncertainties by introducing appropriate functional corrections into the model equations [5-7]. However, when using ML methods that use “reference” data to eliminate structural uncertainties, the difficult task of matching between the learning environment (for example, DNS data) and the learning object (RANS model) arises. Thus, according to [8,9], if even very accurate DNS data are used as input data for ML, then the results of RANS modeling supplemented with such ML, contrary to expectations, may turn out to be unsatisfactory.

To eliminate this shortcoming, Duraisamy et al. [10] proposed a two-stage technique for supplementing RANS models with “reference” FIML (Field Inversion and Machine Learning) data. Within the framework of this technique, the result of solving the inverse problem is used as input data for ML, which is the spatial distribution of the correction introduced into the model to eliminate structural uncertainties. Later, this approach was developed and tested by the Duraisamy group on various problems, including the flow around airfoils at high angles of attack [11, 12].

One of the task where computation accuracy can be significantly improved by modification of the turbulence model is flow around airfoils at stall angle of attack where the flow is separated and maximal lift coefficient is achieved. This task is very important for aviation and wind power, as well as for turbomachinery flows. Even the best turbulence models systematically overpredict the maximum lift coefficient and corresponding angle of attack [13].

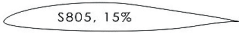
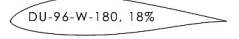
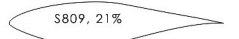
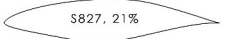
Recently FIML method was implemented into ANSYS Fluent code. In the current work it is used for improvement of the $k-\omega$ BSL [14] turbulence model for the flows around airfoils with the double precision version of ANSYS Fluent 2022R1. The pressure-based coupled solver was employed with the Second Order Upwind discretization scheme for the convective terms in all transport equations. All the presented results are grid and iterative converged.

Considered testcases

Four aerodynamic airfoils were considered for development of the model modification and its verification. S805 airfoil at $\alpha = 11^\circ$ was chosen for the model development, whereas prediction of flow around S805, S809, S827, DU-96-W-180 airfoils in wide range of angles of attack was used during its verification study. Experimental investigations of the considered airfoils [15–18] were carried out in low turbulence wind tunnels ($I < 1\%$). at relatively high Reynolds number ($Re > 10^6$) based on airfoils chord and freestream velocity. Since the experimental Mach number did not exceed 0.15, incompressible flow is considered. For all cases, the computational domain shown a rectangular shape representing a 2D slice of a wind tunnel test section with the height H corresponding to experimental one. The angle of attack corresponds to the geometrical rotation airfoil in the tunnel. The size of the computational domain and flow parameters are presented in Table 1.

Table 1

Setup parameters for the flow around considered airfoils

Airfoil	H/C	Re	Tu, (%)
 S805, 15%	3.6	1×10^6	0.05
 DU-96-W-180, 18%	3.0	2×10^6	0.04
 S809, 21%	5.0	4×10^6	0.06
 S827, 21%	3.0	3×10^6	0.08

Inlet and outlet boundaries are located at a distance of about $10C$ upstream and downstream of the airfoil leading edge. The boundary conditions are set as follows. Non-slip conditions are specified on the airfoil. A constant velocity is specified at the inlet section of the computational domain. Inlet turbulent kinetic energy corresponds to experimental turbulence intensity and the specific dissipation rate is specified as $\omega = 10 \cdot U_\infty / C$ [14]. No-slip conditions are used on the airfoil surface and constant pressure is specified on the outlet. The computational meshes were refined normal to the wall in order to resolve the viscous sublayer ($\Delta y_1^+ < 1$), near the leading edge in the streamwise direction for a proper resolution of thin boundary layer, and near the trailing edge. This results in about 400 points along the airfoil and a total mesh size of about 100,000 cells.

Modification of the model

The modification was developed by adding source term S_ω in ω equation of the original BSL model:

$$\underbrace{\frac{\partial(\rho\omega)}{\partial t} + \frac{\partial(\rho u_j \omega)}{\partial x_j} = \frac{\gamma}{v_t} P_k - \beta \rho \omega^2 + \frac{\partial}{\partial x_j} [(\mu_t + \sigma_\omega \mu_t) \frac{\partial \omega}{\partial x_j}] + 2(1 - F_1) \frac{\rho \sigma_{\omega 2}}{\omega} \frac{\partial k}{\partial x_j} \frac{\partial \omega}{\partial x_j}}_{\omega\text{-equation of the original BSL model [14]} + S_\omega} \quad (1)$$

with

$$S_\omega = C_\omega \rho \omega^2 \quad (2)$$

where C_ω is a function of non-dimensional parameters, obtained using machine learning methods in several stages. At the first stage the optimized field of C_ω was obtained using the adjoint solver in combination with simple iterative optimizer by minimization of the cost function E

$$C_\omega = C_{\omega, adjoint}^i = C_{\omega, adjoint}^{i-1} - \lambda \frac{\partial E}{\partial C_{\omega, adjoint}^{i-1}}. \quad (3)$$

Here λ is the non-dimensional adaptive parameter responsible for the speed of optimization. The definition of E will be given later.

The second stage is an approximation of the adjoint optimized C_ω field from the first stage by neural network as a function of input non-dimensional parameters:

$$C_\omega = C_{\omega,NN} = NN(input_1, \dots, input_n) \quad (4)$$

Finally the C_ω coefficient was applied to the ω equation and verification study of the modified model (BSL-NN) was performed.

Optimisation of C_ω field and NN training

As mentioned above, the model modification was developed based on the prediction of flow around S805 airfoil at near stall angle of attack $\alpha = 11^\circ$. For such flow regime the original BSL model delays separation on the suction side and, as consequence, overpredicts experimental lift coefficient. Therefore the cost function E from Eq. (3) is built based on the difference between the computational C_L and experimental $C_{L,exp} = 1.19623$ value of lift coefficient (first term) and minimization of C_ω (second term), reads as:

$$E = |C_L - C_{L,exp}| + \beta \sum_{cells} (C_{\omega,adjoint})^2 \quad (5)$$

During the adjoint optimization design iterations the computational lift coefficient is adjusted to the experimental value by modification of the C_ω fields shown in Fig. 1 (right). It is well seen that the C_ω is positive on the suction side of the airfoil. Thus S_ω source term provides the additional dissipation and, as consequence, accelerated separation on the suction side. These effect is confirmed by streamwise velocity contours and streamlines which visualize the separation zone on the suction side of the airfoil for the original and the modified models (Fig. 2). The modification strongly shifts the separation point toward leading edge and increases the size of recirculation zone. This improves the agreement of the computed pressure coefficient with the experimental data (Fig. 3).

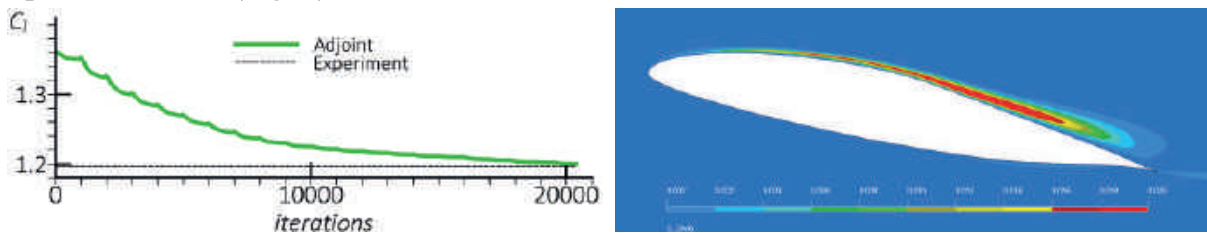


Fig. 1. Convergence history of simple optimizer and optimized C_ω field for S805 airfoil at $\alpha = 11^\circ$

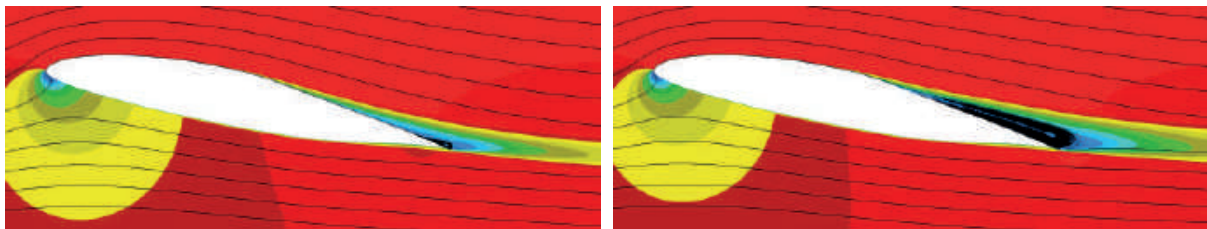


Fig. 2. Contours of streamwise velocity component and streamlines for original (left) and optimized (right) BSL model for S805 airfoil at $\alpha = 11^\circ$

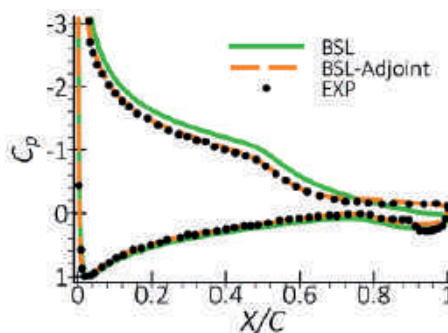


Fig. 3. Distribution of pressure coefficient on the S805 airfoil at $\alpha = 11^\circ$ for the original and adjoint modified BSL model

During NN training of the C_{ω} is considered as a function of three parameters

$$C_{\omega, NN} = NN\left(\frac{S}{0.3\omega}, \frac{\sqrt{k}}{0.09\omega d_w}, \frac{v_t}{v}\right). \quad (6)$$

The training is carried out using three hidden layers (24,16 and 8 nodes) with following activation function:

$$f(x) = \frac{1}{1+|x|}. \quad (7)$$

The comparison of the skin friction and pressure coefficient on the airfoil shown in Fig. 4 demonstrates that the NN results is almost the same as results obtained with the adjoint solver. Taking into account the good agreement of the adjoint results with the experimental data one can see that the modified model also predicts experimental distribution well.

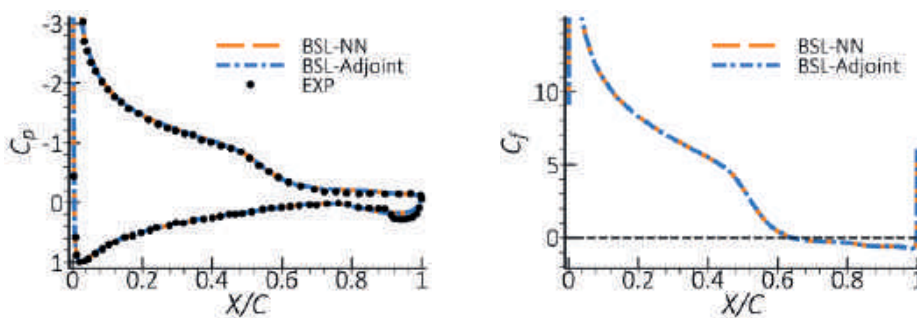


Fig. 4. Distribution of pressure (left) and skin friction (right) coefficient for S805 airfoil at $\alpha = 11^\circ$ predicted with the adjoint and NN modified BSL model

Verification of modified model

Computations using the original and modified versions of the BSL model for the considered airfoils show that both models predict virtually the same lift coefficient for low and angles of attack ($\alpha < 10^\circ$) when the flow is attached (Fig. 5). At higher angles of attack the modified BSL-NN model predicts lower value of the lift coefficient due to the larger size of the recirculation zone. Thus lift coefficient distribution for modified version is in better agreement with the experimental data for all the considered airfoils over a wide range of angles of attack than the original BSL model, which strongly overpredicts lift value. For S827 airfoil BSL-NN model improves prediction of the lift coefficient even at low angles attack due to earlier stall than for other cases. For this airfoil separation on the suction side starts at $\alpha = 1^\circ$. However for some angles of attack in stall regime the BSL-NN results still differ from the experimental data. This phenomenon can be described by the effect of the 3D so-called “mushroom cells” structures in the experiment, which cannot be predicted in 2D setup.

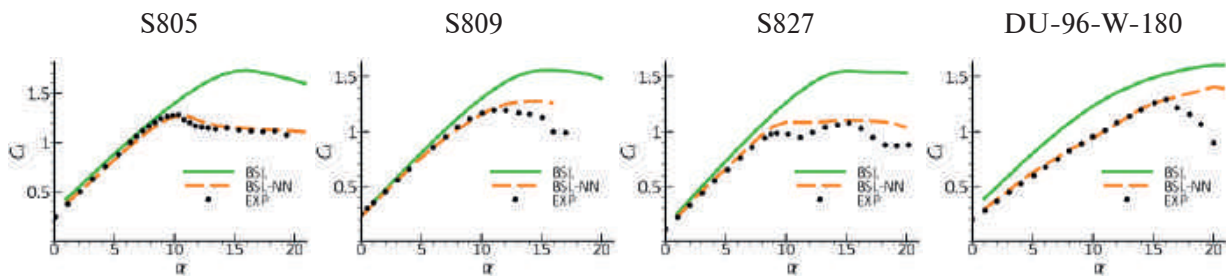


Fig. 5. Comparison of experimental and computational lift coefficient at different angles of attack for original BSL and modified BSL-NN model



Conclusions

Proposed modification of the k - ω BSL turbulence model with machine learning methods significantly improves the accuracy of prediction of aerodynamic characteristics over airfoils in wide range of angles of attack ($\alpha = 0^\circ - 20^\circ$). The results demonstrate the efficiency of the machine learning methods for turbulence model improvement.

Acknowledgements

The results of the work were obtained using computational resources of Peter the Great Saint-Petersburg Polytechnic University Supercomputing Center (<http://www.spbstu.ru>).

The study was carried out within the framework of the scientific program of the National Center for Physics and Mathematics (project “Mathematical modeling on supercomputers with exa- and zettaflops performance”).

REFERENCES

1. **Cheung S.H., Oliver T.A., Prudencio E.E., Prudhomme S. and Moser R.D.**, Bayesian uncertainty analysis with applications to turbulence modeling *Reliab. Eng. Syst. Saf.* 96 (2011) (9) 1137–1149.
2. **Margheri L., Meldi M., Salvetti M. and Sagaut P.**, Epistemic uncertainties in RANS model free coefficients *Comput. Fluids* 102 (2014) 315–335.
3. **Edeling W.N., Schmelzer M., Cinnella P. and Dwight R.P.**, Bayesian predictions of Reynolds-averaged Navier–Stokes uncertainties using maximum a posteriori estimates, *AIAA J.* 5 (6) (2018) 2018–2029.
4. **Papadimitriou D.I. and Papadimitriou C.**, Bayesian uncertainty quantification of turbulence models based on high-order adjoint *Comput. Fluids* 120 (2015) 82–97.
5. **Dow E. and Wang Q.**, Quantification of structural uncertainties in the k - ω turbulence model, 52nd AIAA/ASME/ASCE/AHS/ASC Structures, Structural Dynamics and Materials Conference, Denver Colorado AIAA April Paper (2011) 2011–1762.
6. **Singh A.P. and Duraisamy K.**, Using field inversion to quantify functional errors in turbulence closures *Phys. Fluids* 28 (2016) 045110.
7. **Xiao H., Wu J.L., Wang J.X., Sun R. and Roy C.**, Quantifying and reducing model-form uncertainties in Reynolds-averaged Navier–Stokes simulations: a data-driven, physics-informed Bayesian approach *J. Comput. Phys.* 324 (2016) 115–136.
8. **Poroseva S.V., Colmenares F.J.D., Murman S.M.**, On the accuracy of RANS simulations with DNS data *Phys. Fluids* 28 (2016) (11)
9. **Thompson R.L., Sampaio L.E.B., de Bragança Alves F.A., Thais L. and Mompean G.**, A methodology to evaluate statistical errors in DNS data of plane channel flows *Comput. Fluids* 130(2016) 1–7.
10. **Duraisamy K., Zhang Z.J., Singh A.P.**, New Approaches in Turbulence and Transition Modeling Using Data-driven Tehniques 53rd AIAA Aerospace Sciences Meeting AIAA SciTech AIAA Paper (2015) 2015–1284.
11. **Parish E.J., Duraisamy K.**, A paradigm for data-driven predictive modeling using field inversion and machine learning *J. Comput. Phys.* 305 758–774.
12. **Singh A., Medida S., Duraisamy K.**, Machine-Learning-Augmented Predictive Modeling of Turbulent Separated Flows over Airfoils *AIAA J.* 55 (7) (2017) 2215–2227.
13. **Matyushenko A.A., Kotov E.V. and Garbaruk A.V.**, Calculations of flow around airfoils using two-dimensional RANS: an analysis of the reduction in accuracy *St. Petersburg Polytechnical University Journal: Physics and Mathematics* 3 (1) (2017) 15–21.
14. **Menter F.R.**, Zonal Two Equation k - ω Turbulence Models for Aerodynamic Flows AIAA Paper (1993) 93–2906.
15. **Somers D.M.**, Design and Experimental Results for the S805 Airfoil NREL/SR-(1997) 440–6917.
16. **Somers D.M.**, Design and Experimental Results for the S827 Airfoil Period of Performance (2005) 1998–1999.
17. **Somers D.M.**, Design and Experimental Results for the S809 Airfoil, NRELSR-(1997)440–6918.
18. **Timmer W.A. and R.P.J.O.M. van Rooij**, Summary of the Delft University Wind Turbine Dedicated Airfoils AIAA Paper (2003) 0352.

THE AUTHORS

MATYUSHENKO Aleksey A.
aleksey.matyushenko@gmail.com

GOLUBKOV Valentin D.
golubkovvd@gmail.com
ORCID: 0000-0001-9473-7430

GARBARUK Andrey V.
agarbaruk@mail.ru
ORCID: 0000-0002-2775-9864

STRELETS Michael Kh.
strelets@mail.rcom.ru

Received 17.10.2022. Approved after reviewing 06.12.2022. Accepted 07.12.2022.

Conference materials

UDC 533.697

DOI: <https://doi.org/10.18721/JPM.161.141>

Accuracy of flow simulation in a low-pressure turbine using a laminar-turbulent transition model

O.V. Marakueva¹, A.P. Duben²✉,

¹ LLC "Numerical Calculations Russia", Saint Petersburg, Russia;

² Keldysh Institute of Applied Mathematics of RAS, Moscow, Russia

✉ aduben@keldysh.ru

Abstract. Nowadays, in order to decrease the aircraft engine weight, designers are forced to reduce the number of blades in the low-pressure turbine (LPT) since LPT is one of the heaviest components. The LPT operates in a wide range of Reynolds numbers, which can reach values of less than 10^5 at cruise mode. The correct modeling of the laminar-turbulent transition (LT) in the boundary layer of LPT blades is crucial for predicting the efficiency characteristics. The aim of the study is to evaluate the capabilities of several variants of the LT model for modeling the flow over the LPT blade. The SST $\gamma - \text{Re}_{\theta r}$ model with different closing correlations, which control the transition onset and transition length, is considered. They are implemented in the research code NOISEtte. Validation of the realization is done on the basis of computations of flat plate flows from the ERCOFTAC database (experimental series T3). The flow in the turbine high-loaded cascade T106C is considered. Together with the experimental data, the results of scale-resolving simulation are used as the reference. The influence of the choice of empirical correlations for the $\gamma - \text{Re}_{\theta r}$ model on the aerodynamic characteristics near the surface of the blade and at the outlet is evaluated. The results compared with those obtained using the same model and correlations within commercial code Numeca. The study revealed that the results of the same empirical correlations obtained using different flow solvers differ noticeably from each other.

Keywords: laminar-turbulent transition, transition model, low pressure turbine, EBR

Funding: This work has been funded by the Russian science foundation, project 21-71-10100.

Citation: Marakueva O.V., Duben A.P., Accuracy of flow simulation in a low-pressure turbine using a laminar-turbulent transition model, St. Petersburg State Polytechnical University Journal. Physics and Mathematics. 16 (1.1) (2023) 243–249. DOI: <https://doi.org/10.18721/JPM.161.141>

This is an open access article under the CC BY-NC 4.0 license (<https://creativecommons.org/licenses/by-nc/4.0/>)

Материалы конференции

УДК 533.697

DOI: <https://doi.org/10.18721/JPM.161.141>

О точности моделирования течения в турбине низкого давления с использованием модели ламинарно-турбулентного перехода

О.В. Маракужева¹, А.П. Дубень²✉

¹ ООО «Инженерный Центр Численных Исследований», Санкт-Петербург, Россия;

² ИПМ им. М.В. Келдыша РАН, г. Москва, Россия

✉ aduben@keldysh.ru

Аннотация. Корректное моделирование ламинарно-турбулентного перехода (ЛТ) в пограничном слое лопаток турбины низкого давления (ТНД) имеет существенное значение для прогнозирования параметров эффективности. Целью исследования является оценка возможностей нескольких вариантов ЛТ модели для моделирования обтекания лопатки ТНД. Рассматривается модель SST $\gamma - \text{Re}_{\theta r}$ с различными замыкающими

корреляциями, определяющими начало и продолжительность перехода. Модель реализована в исследовательском коде NOISEtte. Проверка реализации выполнена на базе расчетов плоских течений из базы данных ERCOFTAC (экспериментальная серия T3). Рассмотрено течение в высоконагруженной плоской решетке T106C.

Ключевые слова: ламинарно-турбулентный переход, модель перехода, ТНД, EBR

Финансирование: Работа выполнена при поддержке РФФ, проект 21-71-10100.

Ссылка при цитировании: Маракуева О.В., Дубень А.П. О точности моделирования течения в турбине низкого давления с использованием модели ламинарно-турбулентного перехода // Научно-технические ведомости СПбГПУ. Физико-математические науки. 2023. Т. 16. № 1.1. С. 243–249. DOI: <https://doi.org/10.18721/JPM.161.141>

Статья открытого доступа, распространяемая по лицензии CC BY-NC 4.0 (<https://creativecommons.org/licenses/by-nc/4.0/>)

Introduction

Nowadays, in order to decrease the aircraft engine weight, designers are forced to reduce the number of blades in the low-pressure turbine (LPT) since LPT is one of the heaviest components. At the same time, aerodynamic load on a given stage is maintained the same, which implies an increase of the loading per blade. The LPT typically operates in a wide range of Reynolds numbers reaching 10^5 and even less at cruise mode, so the boundary layer mostly remains laminar. Stronger pressure gradients arising from the higher loading on a blade may cause a separation of the laminar boundary layer and a formation of a separation bubble. So the transition occurs in the shear layer, but depending on the turbulence intensity and scales, the reattachment process may not happen. The separation-induced laminar-turbulent transition (LT) could lead to a significant loss in lift and a drop in efficiency. That is why the accurate numerical simulation of the laminar-turbulent boundary layer transition is crucial for the LPT characteristics prediction while its design.

The aim of the study is to evaluate the capabilities of several variants of the LT model for modeling the flow over the LPT blade.

We consider the widely used SST $\gamma - \widetilde{Re}_{\theta}$ model [1] with different closing correlations [1–4] which control the transition onset and transition length. We use the well-known ERCOFTAC T3 series flat-plate test cases [5] and the Schubauer and Klebanoff flat-plate test case [6] to validate the original $\gamma - \widetilde{Re}_{\theta}$ model [1] realization in the research code NOISEtte. Along with that, we consider the impact of alternative correlations [2–4].

We simulate the flow in the turbine high-loaded cascade T106C [7] to evaluate the capabilities of empirical correlations for the $\gamma - \widetilde{Re}_{\theta}$ model. The flow is characterized by the presence of LT transition caused by the separation of the laminar boundary layer with the formation of a short separation bubble at low Reynolds numbers. We evaluate the results in comparison with the reference data (experimental data [7] and the results of the scale-resolving large-eddy simulation, LES, [8]) and the results obtained using the same model within commercial code Numeca. We analyze the impact of Reynolds number and inflow parameters on the aerodynamic parameters near blade surface and at the outlet.

Mathematical models and numerical schemes

We exploit the numerical algorithm realized in the NOISEtte research code which is based on the Navier-Stokes equations for compressible ideal gas. The Reynolds Averaged Navier-Stokes (RANS) approach with the SST $\gamma - \widetilde{Re}_{\theta}$ [1] turbulence model considering LT transition is used as a closure. Along with the empirical correlations to control the transition onset and transition length from the original paper [1] (hereinafter referred to as Langtry), we consider the ones presented in the papers: [4] (Malan), [3] (Sorensen) and [2] (Kelterer).

The NOISEtte [9] algorithm realizes a vertex-centered numerical scheme on mixed-element unstructured meshes for spatial discretization. It is based on the family of edge-based reconstruction schemes EBR [10] for convective fluxes. It provides higher accuracy (in terms of absolute numerical error) on unstructured meshes and can locally reach order of accuracy up to the 5th.



The convective fluxes for the turbulence transport equations are discretized using the TVD3 [11] numerical scheme. Time integration is carrying out using the 1st order implicit Newton-based scheme BDF1. The system of algebraic equations is solved using the preconditioned BiCGSTAB solver [12].

Validation on T3 plate

We exploit the ERCOFTAC T3 series of flat-plate tests and the Schubauer and Klebanoff (S&K) [5, 6] flat-plate test cases to validate the implemented $LT \gamma - \widetilde{Re}_{0t}$ model. These experiments are widely used to test the capability of turbulence models to predict transitional flow under the freestream turbulence effect at zero and varying pressure gradient conditions. The inlet conditions for the test cases are summarized in Table 1. The air properties, density $\rho_0 = 1.2 \text{ kg/m}^3$ and viscosity $\mu_0 = 1.8 \cdot 10^{-5} \text{ kg/(m}\cdot\text{s)}$, are set for all the considered cases. The Reynolds number per meter is calculated as follows: $Re_1 = \rho_0 \cdot U_{in} \cdot 1 / \mu_0$.

Table 1

The inlet conditions for the test cases

Case	U_{in} , m/s	Tu_{in} , %	μ_t/μ	$Re_1/10^6$	Case	U_{in} , m/s	Tu_{in} , %	μ_t/μ	$Re_1/10^6$
T3A	5.4	3.3	12.0	0.36	T3C5	9.0	3.0	15.0	0.6
T3B	9.4	6.5	100.0	0.627	T3C2	5.29	3.0	8.0	0.353
T3A-	19.8	0.874	8.72	1.32	T3C3	4.0	3.0	5.0	0.267
S&K	50.1	0.3	1.0	3.34	T3C4	1.37	3.0	2.0	0.091

The T3A, T3B and T3A- cases are characterized by zero pressure gradients (ZPG) and varying levels of freestream turbulence intensity (FSTI) for the bypass transition occurrence. The S&K corresponds to the natural transition as it has a low FSTI. The T3C test cases are the flows over a flat plate with a favorable and adverse pressure gradient. For the T3A, T3A- and T3B and S&K cases the computational domain is a rectangle $3 \times 0.5 \text{ m}$ with mesh 230×158 nodes in x and y directions. For the T3C cases the computational domain has a length 2 m and the curved upper boundary, the mesh size is 257×129 . The distance to the first near-wall node provides y^+ values below 1 to ensure no-slip adiabatic wall boundary conditions. The upper wall is specified as a free slip wall, the inlet turbulent quantities are specified in order to match the measured decay of freestream turbulence. All presented results are mesh converged. The data presented in this paper was obtained on meshes close in resolution to those used in [1, 13].

The results of the simulations in comparison with reference data (experimental data [5, 6] and data obtained using the ANSYS CFX solver taken from [13]) are shown in Fig. 1. They are accompanied by those obtained using both the SST model [14] without taking into account the LT transition (marked as Turbulent) and without any turbulence model consideration (Laminar). The “laminar” solutions for the T3C cases are characterized by the absence of convergence so they are not shown in the graphs in Fig. 1 bottom. The distributions of friction coefficient obtained using the $\gamma - \widetilde{Re}_{0t}$ model with the Langtry correlation correspond to the results from the original papers of Langtry and Menter [1] and Menter et al. [13]. Note that the transition for the T3C5 case with favorable pressure gradient is delayed when the LT Langtry model is applied. This is consistent with the ANSYS results taken from [13] and is explained by the fact that the original $\gamma - \widetilde{Re}_{0t}$ model was tuned on higher inlet turbulence intensity for this test case: Tu_{in} was set to 4% in [1] while it is equal to the experimental value (3%) in both [13] and the present simulation.

The alternative (to Langtry) correlations are characterized by a different behavior, consistent with the reference data in various extents, as it is seen from Fig. 1. The usage of the Malan’s one yields similar behavior as the original $\gamma - \widetilde{Re}_{0t}$ model for both ZPG cases and the cases with streamwise pressure gradient. The correlation of Kelterer leads to a better prediction for the T3C cases, compared with the remaining ones. The only case that is well captured by all the correlations is the T3C4 where the transition forced by separation of the laminar boundary layer is observed. Overall, we state that the validation of the $\gamma - \widetilde{Re}_{0t}$ model realization within the NOISEtte code is done.

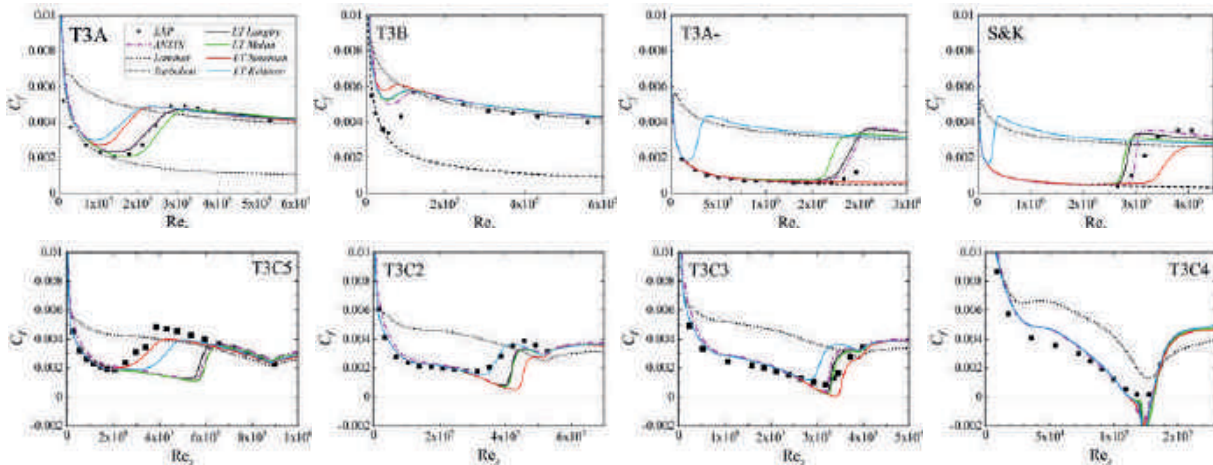


Fig.1. T3 plate results: friction coefficient (C_f) distributions

T106C LPT results

We consider the numerical investigation of the high-lift T106C low pressure turbine blade profile imposed to a uniform incoming flow. It is characterized by the presence of a separation bubble that occurs in the decelerating part of the blade suction side at low Reynolds numbers. The main geometrical parameters of the cascade T106C are presented in Fig. 2. In more detail the description of the experimental set-up is given in [7].

The flow parameters at the inlet and outlet are defined by the theoretical (design) exit Mach number Ma_{2th} and Reynolds number Re_{2th} under the assumption of isentropic flow in the cascade:

$$Ma_{2th} = \sqrt{\frac{2}{\gamma-1} \left[\left(\frac{P_{t1}}{P_k} \right)^{\frac{\gamma-1}{\gamma}} - 1 \right]} \quad (1)$$

$$Re_{2th} = \sqrt{\frac{\gamma}{R} \frac{l}{C_s} \frac{Ma_{2th} \cdot P_k \cdot [T_{t1} / (1 + 0.5 \cdot (\gamma-1) \cdot Ma_{2th}^2) + S]}{[T_{t1} / (1 + 0.5 \cdot (\gamma-1) \cdot Ma_{2th}^2)]^2}} \quad (2)$$

Here P_{t1} is the inlet total pressure, P_k is the outlet static pressure, C_s and S are the constants of the Sutherland's law for dynamic viscosity, R and γ are the universal gas constant and heat capacity ratio, correspondingly. The total temperature at the inlet is equal to $T_{t1} = 303.15$ K.

We present the results of RANS simulations using the $\gamma - \tilde{Re}_{\theta}$ model for zero incidence angle at

$Re_{2th} = 90 \cdot 10^3$, $200 \cdot 10^3$ and $500 \cdot 10^3$. The turbulence intensity Tu of the incoming flow in the experiment [7] is in the range of 2.9–3.1%, the streamwise integral length scale is $\Lambda = 20$ mm. In order to reproduce the experimental flow conditions, we set the parameters at the inlet boundary as follows: total pressure P_{t1} according to the regime (7860.8 Pa, 17468 Pa and 43667.6 Pa for $Re_{2th} = 90 \cdot 10^3$, $200 \cdot 10^3$ and $500 \cdot 10^3$, correspondingly), total temperature $T_{t1} = 303.15$ K, flow direction ($V_x = 0.79$, $V_y = 0.61$), turbulence intensity $Tu = 3\%$ and turbulent length scale $\Lambda = 20$ mm. The static pressure values P_k are fixed at the outlet according to the regime (5900 Pa, 13110 Pa and 32775 Pa). To estimate the total pressure loss (ζ), the measurements are made in the section located at $0.4 l_x$ downstream the blade trailing edge:

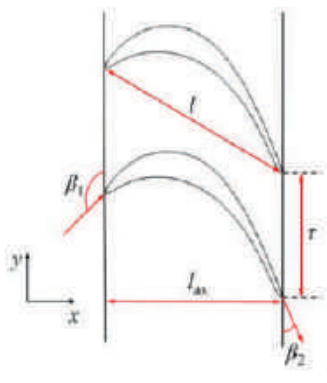


Fig. 2. T106C profile. $l=100$ mm is chord length; $l_{ax}=l_x=85.9$ mm – axial chord length; $\tau=0.95$ – pitch to chord ratio; $\beta_1=127.7^\circ$, $\beta_2=29.4^\circ$ – inlet and outlet flow angles



$$\zeta = \frac{P_{t1} - P_{t2}}{P_{t1} - P_k} \cdot 100\% \quad (3)$$

The computations are performed for the 2D cross section of the blade using an unstructured mesh, which has 128k nodes. It is the twice coarsened 2D section of the mesh used for the LES simulation [8]. It is built so that the key and sensitive areas of the flow field are covered with the mesh of high resolution. Among these areas is the region near the blade surface with the mesh wall-tangential step $\Delta_\tau = 3 \cdot 10^{-3}l$, the wake region downstream the trailing edge with the isotropic mesh step $\Delta = 2 \cdot 10^{-3}l$. The first wall-normal mesh step is chosen in such a way that the value y^+ does not exceed 1 for the maximal Reynolds number $Re_{2th} = 500 \cdot 10^3$. The periodicity boundary conditions are used along the Y axis.

The results of the simulations are presented in Fig. 3–4 (surface and outflow profiles) and 5 (integral total pressure losses). Fig. 3–4 present distributions of isentropic Mach number (left), friction coefficient to static pressure ratio at section where the total pressure losses are measured (right). They are accompanied by the results obtained using the Numeca commercial code. We evaluate the $\gamma - \tilde{Re}_{\theta_i}$ LT model performance by comparing with the reference data, both experimental [7] and results of the LES simulations [8]. Analyzing the figures 3 and 4 it could be stated that the main mechanism of LT transition (separation of laminar boundary layer and its reattachment followed by its turbulization) is predicted by all the considered correlations, albeit with varying extent of accuracy. The following features of the presented results are striking. First of all, a different behavior of the results obtained when using the same correlations but different codes is revealed. Among others, the following is distinct: the correlation from the original model (Langtry) is more consistent with the reference for NOISEtte in contrast to the Numeca. This fact confirms correctness of the realization of the $\gamma - \tilde{Re}_{\theta_i}$ model within NOISEtte.

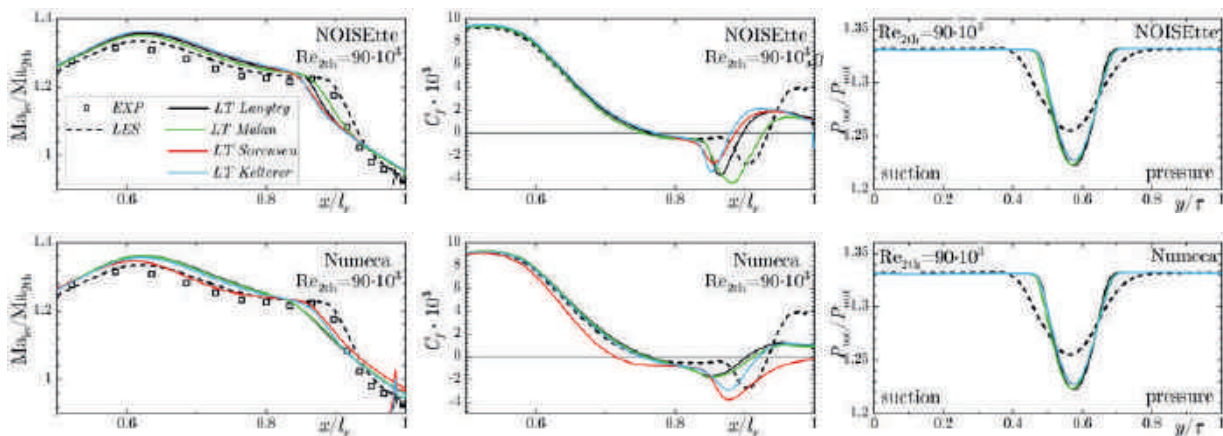


Fig.3. T106C results for $Re_{2th} = 90 \cdot 10^3$

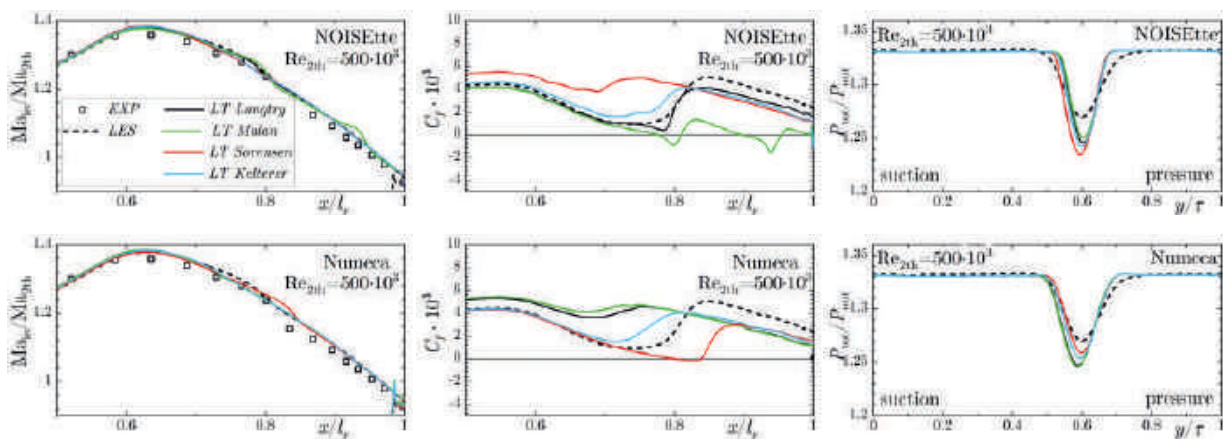


Fig.4. T106C results for $Re_{2th} = 500 \cdot 10^3$

As for alternative correlations, the Malan leads to separation for $Re_{2th} = 500 \cdot 10^3$ using NOISEtte while it does not for Numeca and the Sorensen behavior is noticeably discrepant for the codes too. The difference can be explained by the use of distinguishing numerical algorithms in the considered codes. This effect has been also found in other works (in particular, in [2]). However, we see that the most stable, less “code-dependent” behavior of the solution is achieved using the Kelterer correlation. Analyzing the graphs in Fig. 5, one finds that total pressure loss predictions differ less for lower Reynolds numbers than for higher ones. It yields to a greater scatter of the computational results for relative losses (Fig. 5) that is more pronounced for the Numeca ones.

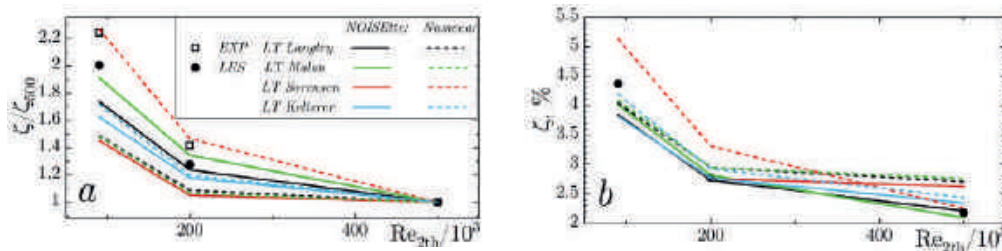


Fig. 5. T106C integral total pressure losses: relative (a) and absolute (b)

Conclusions

The study deals with a laminar-turbulent transition model towards prediction of flows typical for turbomachinery. The SST $\gamma - \widetilde{Re}_{\theta_t}$ model [1] with different closing empirical correlations [1, 2, 3, 4] which control the transition onset and transition length is considered. The results of simulations using their realizations in the research code NOISEtte are evaluated. We have carried out the validation based on the ERCOFTAC T3 series [5] and the Schubauer and Klebanoff [6] flat-plate test cases. The impact of the alternative (to those used in the original SST $\gamma - \widetilde{Re}_{\theta_t}$ model) correlations [2, 3, 4] on the flat plate flows are considered. They are characterized by a different behavior, consistent with the reference data in various extents.

The simulations of the flow in the turbine high-loaded cascade T106C [7] are carried out to evaluate the capabilities of the empirical correlations for the $\gamma - \widetilde{Re}_{\theta_t}$ model. The results are compared with reference data (both experimental and LES simulation results) and data obtained using the same model and correlations implemented in the commercial code Numeca. The study revealed that usage of the same empirical correlations realized in different flow solvers (NOISEtte and Numeca) differ noticeably from each other. At the same time, the correlation of the obtained results is more consistent with the reference for NOISEtte, in contrast to the Numeca results. Among the considered correlations, the most stable, “code-independent” behavior of the solution is achieved using the Kelterer. It can be argued that the implementation of the $\gamma - \widetilde{Re}_{\theta_t}$ model in the NOISEtte numerical algorithm is validated.

Acknowledgments

The research is carried out using the equipment of shared resource center of kiam RAS (<http://ckp.kiam.ru>). the authors thankfully acknowledge these institutions. we thank Andrey Garbaruk from SPBPU for the provided materials and consultations concerning the T3 flat plate test cases.

REFERENCES

1. Langtry R.B., Menter F.R., AIAA J. 47 (2009) 2894–2906.
2. Kelterer M.E. et al., Turbomach., Parts A, B, and C (ASME) (2010) Vol. 7.
3. Sorensen N.N., Wind Energy 12 (2009) 715–733.
4. Malan P., Suluksna K., Juntasaro E., AIAA Paper (2009) 2009–1142.
5. Savill A., Some recent progress in the turbulence modelling of by-pass transition (Elsevier) chap Near-Wall Turbulent Flows, p 829 (1993).
6. Schubauer G., Klebanoff P., Contribution on the mechanics of boundary layer transition Tech. Rep. NACA-TN-3489 NACA (1955).



7. Stotz S., Guendogdu Y., Niehuis R., Journal of Turbomachinery (2017) 139.
8. Duben A., et al., J. Phys. Conf. Ser. 1891 012018 (2021).
9. Gorobets A., Lobachevskii J. Math. 39 (2018) 524–532.
10. Abalakin I., Bakhvalov P., Kozubskaya T., Int. J. Numer. Methods Fluids 81 (2015) 331–356.
11. Bakhvalov P., Kozubskaya T., Comput. Fluids 157 (2017) 312–324.
12. Van der Vorst H.A., SIAM J. Sci. Comput. 13 (1992) 631–644.
13. Menter F.R. et al., Flow Turbul. Combust. 95 (2015) 583–619.
14. Menter F.R., AIAA J. 32 (1994) 1598–1605.

THE AUTHORS

MARAKUEVA Olga V.
o.marakueva@rescent.ru
ORCID: 0000-0002-8015-3669

DUBEN Alexey P.
aduben@keldysh.ru
ORCID: 0000-0002-2280-4400

Received 18.10.2022. Approved after reviewing 13.12.2022. Accepted 13.12.2022.

Conference materials

UDC 534-16

DOI: <https://doi.org/10.18721/JPM.161.142>

Simulation of vibrations in hydrogenated diamond-like nanofilms

G.S. Ivanchenko ¹✉, A.V. Ten ¹

¹ Volgograd State University, Volgograd, Russian Federation

✉ genaivanchenko@volsu.ru

Abstract. The paper calculates the phonon spectrum of diamane [1] in the framework of the Hamilton formalism. The geometric model of diamane is represented as a two-layer graphene, but each C-atom has sp^3 hybridization of external electronic orbitals. The carbon atoms of one of the grapheme sublattices are covalently bound to the atoms of the second graphene layer, and the outer hydrogen atoms are covalently connected to the atoms of the second sublattice. A diamane unit cell contains two carbon atoms from a graphene unit cell and one hydrogen atom. When constructing the model, the curvature of the graphene plane was taken into account as a result of the addition of hydrogen atoms to it and the change in the hybridization of the external electronic orbitals of carbon atoms from sp^2 to sp^3 . The interaction between hydrogen atoms was not taken into account.

Keywords: diamane, phonon spectrum, dispersion equation

Citation: Ivanchenko G.S., Ten A.V., Simulation of vibrations in hydrogenated diamond-like nanofilms. St. Petersburg State Polytechnical University Journal. Physics and Mathematics. 16 (1.1) (2023) 250–254. DOI: <https://doi.org/10.18721/JPM.161.142>

This is an open access article under the CC BY-NC 4.0 license (<https://creativecommons.org/licenses/by-nc/4.0/>)

Материалы конференции

УДК 534-16

DOI: <https://doi.org/10.18721/JPM.161.142>

Моделирование колебаний в гидрированных алмазоподобных нанопленках

Г.С. Иванченко ¹✉, А.В. Тен ¹

¹ Волгоградский государственный университет, г. Волгоград, Россия

✉ genaivanchenko@volsu.ru

Аннотация. Был проведен расчет фононного спектра гидрированного двухслойного графена [1]. При построении модели была учтена деформация графеновой плоскости в результате присоединения к ней атомов водорода и изменение гибридизации внешних электронных орбиталей атомов углерода.

Ключевые слова: алмаз, фононный спектр, дисперсионное уравнение

Ссылка при цитировании: Иванченко Г.С., Тен А.В. Моделирование колебаний в гидрированных алмазоподобных нанопленках// Научно-технические ведомости СПбГПУ. Физико-математические науки. 2023. Т. 16. № 1.1. С. 250–254. DOI: <https://doi.org/10.18721/JPM.161.142>

Статья открытого доступа, распространяемая по лицензии CC BY-NC 4.0 (<https://creativecommons.org/licenses/by-nc/4.0/>)

Introduction

Numerous works have been devoted to the study of carbon-based nanoscale materials [2] and it is due to their unique properties and the possibility of application in various fields of science and technology. Graphene, predicted theoretically more than half a century ago and obtained experimentally in 2005 [3] has high conductivity, thermal conductivity,



hydrophobicity, and so on. Therefore, various modifications based on graphene itself [4], graphane [5], bigraphene with possible impurities [6, 7], diamane [8] also attract the attention of scientists. The relevance of this study is also due to the fact that oscillatory processes in crystal lattices can affect the kinetics of electron transfer [9, 10]. All of the above suggests that the study of the vibrational properties of hydrogenated diamond-like nanofilms is topical.

Investigation of the diamane vibrational properties

The calculation phonon spectrum of the diamane was carried out on the basis of a combination of the classical and quantum approaches. The consideration is based on the Hamiltonian approach, but the parameters of the model Hamiltonian were obtained using quantum chemical calculations [11]. The elementary cell of the diamane (Fig. 1) contains three atoms (two carbon atoms and one hydrogen atom). The letters *A*, *B* denote the carbon atoms of the graphene sublattices, and the letters *C* denote the hydrogen atoms located above and below the graphene layer, respectively (Fig. 2). Here Δ_1 , Δ_2 are the translation vectors of the crystal lattice. The parameters of the geometric model are presented below for the diamane *ABAB* packaging:

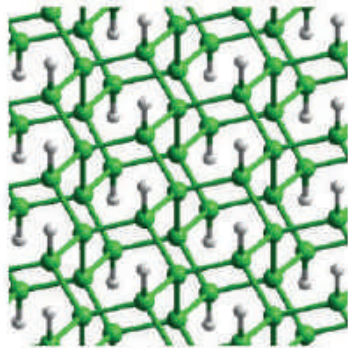


Fig. 1. The diamane structure

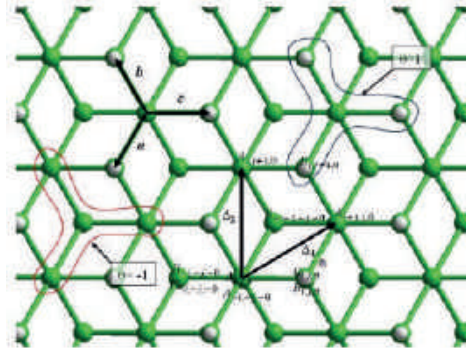


Fig. 2. Geometric model of the diamane

$$\frac{\mathbf{a}}{a_1} = \left(-\frac{1}{2} \sin \delta, -\frac{\sqrt{3}}{2} \sin \delta, \cos \delta \right),$$

$$\frac{\mathbf{b}}{a_1} = \left(-\frac{1}{2} \sin \delta, \frac{\sqrt{3}}{2} \sin \delta, \cos \delta \right),$$

$$\frac{\mathbf{c}}{a_1} = (\sin \delta, 0, \cos \delta),$$

$$\frac{\mathbf{d}_1}{a_2} = (0, 0, 1), \quad \frac{\mathbf{d}_2}{b_0} = (0, 0, 1),$$

$$\frac{\Delta_1}{a_1} = \frac{\mathbf{c} - \mathbf{a}}{a_1} = \left(\frac{3}{2} \sin \delta, \frac{\sqrt{3}}{2} \sin \delta, 0 \right), \quad \frac{\Delta_2}{a_1} = \frac{\mathbf{b} - \mathbf{a}}{a_1} = (0, \sqrt{3} \sin \delta, 0).$$

where δ is the angle formed by the z -axis with each of the vectors \mathbf{a} , \mathbf{b} , \mathbf{c} .

The radius vectors of the sublattices nodes *A*, *B*, *C* in equilibrium can be represented as:

$$\mathbf{r}_{0,0,1}^A = \frac{\mathbf{d}_1}{2}, \quad \mathbf{r}_{0,0,1}^B = \mathbf{r}_{0,0,1}^A + \mathbf{c} = \frac{\mathbf{d}_1}{2} + \mathbf{c},$$

$$\mathbf{r}_{i,j,0}^A = \theta \left(\mathbf{r}_{0,0,1}^A + i\Delta_1 + j\Delta_2 \right), \quad \mathbf{r}_{i,j,0}^B = \theta \left(\mathbf{r}_{0,0,1}^B + i\Delta_1 + j\Delta_2 \right),$$

$$\mathbf{r}_{i,j,0}^C = \mathbf{r}_{i,j,0}^B + \theta \mathbf{d} = \theta \left(\mathbf{r}_{0,0,1}^B + i\Delta_1 + j\Delta_2 + \mathbf{d}_2 \right),$$

where the vectors Δ_s are the basis translation vectors of the layers of the diamane $s = 1, 2$; $\theta = \pm 1$. Detailed description of the parameter θ is shown in Figure 3.

We write the system Hamiltonian in the harmonic approximation, while taking into account the interaction of each of the atoms only with the nearest neighbors:

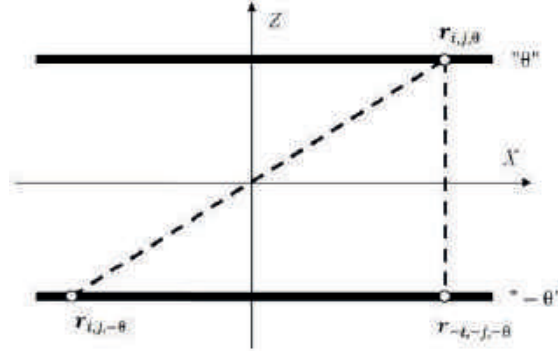


Fig. 3. Indefinite layer symmetry

$$H = \frac{1}{2m_1} \sum_{i,j,\theta} (p_{i,j,\theta}^A)^2 + p_{i,j,\theta}^B)^2 + \frac{1}{2m_2} \sum_{i,j,\theta} p_{i,j,\theta}^C)^2 + \frac{k_1}{4} \sum_{i,j,\theta} \left(2(r_{i,j,\theta}^A - r_{i,j,\theta}^B)^2 + (r_{i,j,\theta}^A - r_{i-1,j,\theta}^B)^2 + (r_{i,j,\theta}^A - r_{i-1,j+1,\theta}^B)^2 + (r_{i+1,j,\theta}^A - r_{i,j,\theta}^B)^2 + (r_{i+1,j-1,\theta}^A - r_{i,j,\theta}^B)^2 \right) + \frac{k_2}{4} \sum_{i,j,\theta} (r_{i,j,\theta}^A - r_{-i,-j,-\theta}^A)^2 + \frac{k_3}{2} \sum_{i,j,\theta} (r_{i,j,\theta}^B - r_{i,j,\theta}^C)^2. \quad (1)$$

Here m_1, m_2 are the masses of carbon and hydrogen atoms, respectively, k_1, k_2, k_3 are coupling constant (see Table 1), $r_{i,j,\theta}$ are the radius vectors of atoms, $p_{i,j,\theta}$ are the atoms moments.

Table 1

Atomic geometry of the diamane

	C_A-C_B	C_A-C_A	C_B-H
$a, \text{\AA}$	1.53	1.52	1.1
$k, N/m$	408	405	453

Obtaining the dispersion equation

Using the Hamiltonian system, we write down the equations of atoms motion. We find the first derivative with respect to the coordinate of each of the elementary cell and substitute it into the

expression $m_1 \ddot{r}_{i,j} = -\frac{\partial H}{\partial r_{i,j}}$. Let us introduce a small displacement from the equilibrium position:

$$r_{i,j,\theta} \rightarrow r_{i,j,\theta} + \tilde{r}_{i,j,\theta}.$$

As a result we get:

$$\begin{cases} m_1 \ddot{\tilde{r}}_{i,j,\theta}^A = -k_1 (3\tilde{r}_{i,j,\theta}^A - \tilde{r}_{i,j,\theta}^B - \tilde{r}_{i-1,j,\theta}^B - \tilde{r}_{i-1,j+1,\theta}^B) - k_2 (\tilde{r}_{i,j,\theta}^A - \tilde{r}_{-i,-j,-\theta}^A), \\ m_1 \ddot{\tilde{r}}_{i,j,\theta}^B = -k_1 (3\tilde{r}_{i,j,\theta}^B - \tilde{r}_{i,j,\theta}^A - \tilde{r}_{i+1,j,\theta}^A - \tilde{r}_{i+1,j-1,\theta}^A) - k_3 (\tilde{r}_{i,j,\theta}^B - \tilde{r}_{i,j,\theta}^C), \\ m_2 \ddot{\tilde{r}}_{i,j,\theta}^C = -k_3 (\tilde{r}_{i,j,\theta}^C - \tilde{r}_{i,j,\theta}^B). \end{cases} \quad (2)$$

Substituting the radius vectors with the functions describing the harmonic waves propagating along the graphane sheet we obtained:

$$\begin{cases} \tilde{\mathbf{r}}_{i,j,0}^A = \mathbf{A} \exp\{-i\omega t + i\mathbf{k}\mathbf{r}_{i,j,0}^A\}, \\ \tilde{\mathbf{r}}_{i,j,0}^B = \mathbf{B} \exp\{-i\omega t + i\mathbf{k}\mathbf{r}_{i,j,0}^B\}, \\ \tilde{\mathbf{r}}_{i,j,0}^C = \mathbf{C} \exp\{-i\omega t + i\mathbf{k}\mathbf{r}_{i,j,0}^C\}, \end{cases} \quad (3)$$

where k is the wave vector, ω is the cyclic frequency of the propagating wave; A , B , C are the vibration amplitudes of the corresponding atoms. We obtain a homogeneous system of linear algebraic equations with respect to the oscillation amplitudes.

We introduce the following notation:

$$\omega_1^2 = \frac{k_1}{m_1}, \quad \omega_2^2 = \frac{k_2}{m_1}, \quad \omega_3^2 = \frac{k_3}{m_1}, \quad \omega_4^2 = \frac{k_3}{m_2},$$

$$\mu = 1 + 8 \cos\left(\frac{\mathbf{k}(\Delta_1 - \Delta_2)}{2}\right) \cos\left(\frac{\mathbf{k}\Delta_1}{2}\right) \cos\left(\frac{\mathbf{k}\Delta_2}{2}\right).$$

This system will have non-trivial solutions if the determinant of the main matrix see (4) of the system is equal to zero. Thus, we obtain a dispersion equation for the phonon spectrum of diamane. This equation is a third-degree equation with respect to the square of the frequency:

$$\begin{vmatrix} \omega^2 - 3\omega_1^2 - \omega_2^2(1 - e^{-i\theta k d_1}) & \omega_1^2(e^{i\theta k c} + e^{i\theta k(c-\Delta_1)} + e^{i\theta k(c-\Delta_1+\Delta_2)}) & 0 \\ \omega_1^2(e^{i\theta k c} + e^{i\theta k(c-\Delta_1)} + e^{i\theta k(c-\Delta_1+\Delta_2)}) & \omega^2 - 3\omega_1^2 - \omega_3^2 & \omega_3^2 e^{i\theta k d_2} \\ 0 & \omega_4^2 e^{-i\theta k d_2} & \omega^2 - \omega_4^2 \end{vmatrix} = 0. \quad (4)$$

Using the technique described in [12], the dispersion equation for the phonon spectrum of the diamane was obtained. It has two independent equations:

$$\begin{aligned} & \omega^6 - \omega^4(6\omega_1^2 + (\omega_2^2 \pm \omega_2^2) + \omega_3^2 + \omega_4^2) + \\ & + \omega^2(3\omega_1^2(3\omega_1^2 + \omega_3^2 + 2\omega_4^2) - (\pm\omega_2^2 - \omega_2^2)(3\omega_1^2 + \omega_3^2 + \omega_4^2) - \omega_1^4\mu) + \\ & \pm 3\omega_1^2\omega_2^2\omega_4^2 + 3\omega_1^2\omega_3^2\omega_4^2 + \omega_2^2\omega_3^2\omega_4^2(1 \pm 2) + \omega_1^4\omega_4^2\mu = 0. \end{aligned} \quad (5)$$

In a simpler form, these equations are:

$$\alpha_1(\omega^2)^3 + \alpha_2(\omega^2)^2 + \alpha_3\omega^2 + \alpha_4 = 0. \quad (6)$$

where the coefficients α_i , $i = 1-4$ are different form depending on the choice of sign in the original equation, ω_1 , ω_2 , ω_3 , ω_4 are parameters defined as the ratio of the bond stiffness between atoms to the mass of one of the atoms (see (5)).

The solution for such equations can be obtained analytically. For the solution, it is necessary to take into account the size of the film, and therefore, boundary conditions will be imposed on the wave number. As a result, the Hamiltonian system was compiled and the equations of motion of the diamane atoms were written.

Conclusion

Thus, we obtain a set of two equations of the third degree with respect to the frequency square. The equations are simple due to the choice of a unit cell of three atoms of one layer and the introduction of a coordinate system that takes into account the odd symmetry of the layers (Fig. 3).

As a result of solving the dispersion equation, a diamane phonon spectrum consisting of acoustic and optical modes will be obtained. By the inclination angle of the acoustic mode, it is possible to calculate the sound speed in this medium. The maximum energy of the optical modes will make it possible to estimate the Debye diamane temperature.

REFERENCES

1. **Chernozatonskii L.A., Sorokin P.B., Kvashnin A.G., Kvashnin D.G.**, Diamond-like C₂H nanolayer, diamane: Simulation of the structure and properties, Journal of Experimental and Theoretical Physics Letters. 90 (2) (2009) 134–138.
2. **Wallace P.R.**, The Band Theory of Graphite, Physical Review. 71 (1947) 622.
3. **Novoselov K.S. et al.**, Two-dimensional gas of massless Dirac fermions in grapheme, Nature, 438 (2005) 197.
4. **Konobeeva N.N.**, Influence of the atomic-molecular structure on tunnel characteristics in carbon nanostructures, Mathematical Physics and Computer Simulation. 20(6) (2017) 63–71.
5. **Ivanchenko G.S. Ten A.V., Kuzmin N.M., Butenko M.A., Khokhlova S.S., Sivolobov S.V., Kolobanov R.V.**, Phonon Properties of Hydrogenated Carbon Nanofilms, Inženernyj vestnik Dona (2021).
6. **Ten (Pak) A.V., Belonenko M.B.**, The evolution of few cycles optical pulses in a double-layer graphene – boron nitride taking into account nonlinearity of a medium, Nanosystems: Physics, Chemistry, Mathematics. 5 (1) (2014) 155–159.
7. **Ten (Pak) A.V., Belonenko M.B.**, Waveguides based on alternating graphene-boron-nitride layers, Technical Physics Letters. 39 (24) (2013) 63–70.
8. **Chernozatonskii L.A., Demin V.A.**, Diamond-like films of several folded graphenes, JETP Letters. 155(3) (2022) 184–189.
9. **Mikhailova V.A., Mikhailova E.A.**, Effect of vibrational transitions on the nonthermal charge transfer probability, Mathematical Physics and Computer Simulation. 22 (3) (2019) 76–85.
10. **Barykov V.Yu., Tkacheva A.V., Ivanov A.I.**, Influence of environment reorganization energy and its dynamic properties on vibrational spectral effect in the kinetics of photo-induced electron transfer, Bulletin of the Volgograd State University. Series 1: Math. Phys. 2 (2016) 70–83.
11. **Shamina E.N., Lebedev N.G.**, Influence of adsorption of atoms and molecules of oxygen on the electronic structure of graphene nanoribbons, Mathematical Physics and Computer Simulation, 20 (4) (2017) 95–102.
12. **Ivanchenko G.S., Lebedev N.G.**, Phonon spectrum of double-wall carbon nanotubes, Solid State Physics, 48 (12) (2006) 2223–2227.

THE AUTHORS

IVANCHENKO Gennadii S.
genaivanchenko@volsu.ru
ORCID: 0000-0001-9276-1381

TEN Anastasia V.
ten.anastasia@volsu.ru
ORCID: 0000-0002-1806-5270

Received 20.10.2022. Approved after reviewing 08.11.2022. Accepted 08.11.2022.

Conference materials

UDC 532.517.4

DOI: <https://doi.org/10.18721/JPM.161.143>

Zonal RANS-IDDES of asymmetric curved wake subjected to adverse pressure gradient

E.K. Guseva¹, M.L. Shur¹, A.S. Stabnikov¹✉, P. Ströer², A.K. Travin¹

¹Peter the Great St. Petersburg Polytechnic University, Saint-Petersburg, Russia;

²DLR (German Aerospace Center), Institute of Aerodynamics and Flow Technology, Göttingen, Germany

✉ an.stabnikov@gmail.com

Abstract. Results are presented of high-fidelity scale-resolving simulations of an asymmetric curved turbulent wake subjected to adverse pressure gradient based on the zonal RANS-IDDES approach to turbulence representation. The work is performed within the framework of a joint German-Russian project “Complex Wake Flows” and presents a continuation of the computational/experimental studies of the straight symmetric wakes carried out by the same team during 2017-2019. The addition of asymmetry and longitudinal curvature to the flow model made it more representative in terms of reproducing the real wakes behind the three-element high-lift wing configurations used during takeoff and landing of an aircraft. The reliability of the obtained results (both the mean flow parameters and the turbulent statistics) is supported by the grid-refinement study, whereas their comparison with the similar results of the RANS computations reveals a considerable discrepancy. This suggests the necessity of the improvement of the RANS models, which is planned for future work.

Keywords: turbulent wakes, adverse pressure gradient, scale-resolving simulations of turbulence, streamline curvature

Funding: The study was funded by RFBR and DFG, project No. 21-58-12002.

Citation: Guseva E.K., Shur M.L., Stabnikov A.S., Ströer P., Travin A.K., Zonal RANS-IDDES of Asymmetric Curved Wake Subjected To Adverse Pressure Gradient, St. Petersburg State Polytechnical University Journal. Physics and Mathematics. 16 (1.1) (2023) 255–261. DOI: <https://doi.org/10.18721/JPM.161.143>

This is an open access article under the CC BY-NC 4.0 license (<https://creativecommons.org/licenses/by-nc/4.0/>)

Материалы конференции

УДК 532.517.4

DOI: <https://doi.org/10.18721/JPM.161.143>

Зонный RANS-IDDES расчет асимметричного криволинейного турбулентного следа, подверженного неблагоприятному градиенту давления

Е.К. Гусева¹, М.Л. Шур¹, А.С. Стабников¹✉, Ф. Штрёер², А.К. Травин¹

¹ Санкт-Петербургский политехнический университет Петра Великого, Санкт-Петербург, Россия;

² DLR (Немецкий Аэрокосмический Центр), Институт аэродинамики и технологии потоков, г. Гёттинген, Германия

✉ an.stabnikov@gmail.com

Аннотация. Представлены результаты расчетов асимметричного криволинейного турбулентного следа, подверженного воздействию неблагоприятного градиента давления, с использованием вихреразрешающего зонного RANS-IDDES подхода к моделированию турбулентности. Работа выполнена в рамках совместного Германско-Российского проекта «Течения в сложных следах». Надежность полученных результатов расчета средних и пульсационных характеристик рассматриваемого следа подтверждается сеточной независимостью полученного решения, в то время как сравнение этих результатов с

результатами расчетов, выполненных в рамках уравнений RANS, свидетельствует о необходимости усовершенствования RANS-моделей турбулентности.

Ключевые слова: турбулентные следы, неблагоприятный градиент давления, вихреразрешающие подходы к моделированию турбулентности, продольная кривизна линий тока

Финансирование: Работа выполнена при финансовой поддержке РФФИ и Немецкого научно-исследовательского сообщества в рамках научного проекта № 21-58-12002.

Ссылка при цитировании: Гусева Е.К., Шур М.Л., Стабников А.С., Штрёер Ф., Травин А.К. Зонный RANS-IDDES расчет асимметричного криволинейного турбулентного следа, подверженного неблагоприятному градиенту давления // Научно-технические ведомости СПбГПУ. Физико-математические науки. 2023. Т. 16. № 1.1. С. 255–261. DOI: <https://doi.org/10.18721/JPM.161.143>

Статья открытого доступа, распространяемая по лицензии CC BY-NC 4.0 (<https://creativecommons.org/licenses/by-nc/4.0/>)

Introduction

Optimization of the high-lift wings employed in the modern commercial airplanes to ensure sufficient lift for low-speed operations (take-off and landing) requires multi-variant computations. Currently they are performed based on the Reynolds-Averaged Navier-Stokes (RANS) equations which have been for many years and still remain the only approach to such computations affordable at the practically meaningful (high) Reynolds numbers. However, in contrast to the wings in cruise flight conditions, the accuracy of the available RANS turbulence models for the high-lift systems at low speed is unsatisfactory, especially near the maximum lift [1]. A major reason is complexity of the corresponding flow-pattern. One of its most challenging feature are turbulent wakes of the upstream wing elements significantly affected by the streamlines curvature and subjected to a strong adverse pressure gradient (APG) induced by the downstream elements. Particularly, the APG causes thickening of the wake, its stagnation or even formation of a reversed flow regions (off-surface separation), which leads to a reduced flow turning and to a loss in lift. Hence, the improvement of the RANS turbulent models is needed, which would ensure the reliable prediction of the complex wake flows. This requires detailed high-fidelity experimental and computational (based on the scale-resolving simulations – SRS) data on the mean characteristics and the turbulence statistics of such flows.

This motivated a joint German-Russian research project “Complex Wake Flows” aimed at the accumulation of such a database and, ultimately, at the development of improved RANS models capable of the accurate prediction of the flows over the high-lift systems. This project presents a direct continuation of the computational/experimental studies of the evolution of the straight symmetric turbulent wakes carried out by the same team during 2017–2019 (see, e.g., [2–4]). The addition of the asymmetry and longitudinal curvature to the flow model implemented in the current project made it more representative in terms of reproducing the real wakes of the three-element high-lift wings.

The preceding paper [5] described the results of the RANS-based aerodynamic design of the experimental flow model of a complex curved turbulent wake with strong curvature and APG effects, which experimental investigation is planned on at the Technical University of Braunschweig (TU BS). In the present paper, we present the first results of the computational part of the project, namely, the results of the high-fidelity SRS of the flow over this model. Sections 2 and 3 below outline, respectively, the wake configuration proposed in [5] and the computational approach used in the simulations. After that, in Section 4, results of the computations are presented and discussed.

Asymmetric curved wake flow model

The design proposed in [5] is based on the currently available at TU BS experimental model of the straight symmetric wake subjected to APG [2] (see left frame in Fig. 1), which allows minimizing



the additional manufacturing efforts. Unlike the straight wake, in the curved wake model (right frame in the figure) the Flat Plate (FP) generating the wake is mounted at non-zero angle of attack relative the direction of the flow at the inlet of the wind tunnel test section. Just as in the straight wake, the APG is created by a pair of symmetrically installed thin airfoils (“liner foils”) placed right downstream of the trailing edge of the FP. However, further downstream, instead of the second pair of the symmetric liner foils, the curved wake model includes an inclined flat plate and a liner foil with deflected flap. The key geometric parameters of the model (the angles of attack of the FP and of the downstream plate and the length and deflection angle of the flap) are adjusted so that, on the one hand, there would be no separation of the flow from either the FP leading edge or from the inner surface of the liner foils and, on the other hand, the APG and the curvature effects in the wake would be strong enough to cause a large stagnation region and to significantly affect the wake turbulence. The latter is confirmed by Fig. 2, which reveals a strong difference of the eddy viscosity fields in the wake predicted by the Spalart-Allmaras (SA) RANS model [6] and its enhanced version (SARC model [7]) known to be capable of realistic prediction of the curvature effect not accounted for in the original model [6]. Note that the curved wake model shown in Fig. 1, which simulations are conducted in the present study, slightly differs from that proposed in [5]. Namely, the angle of deflection of the flap of the second lower liner foil is reduced by $\sim 3^\circ$ with corresponding adjustment of the angle of the upper flat plate to ensure the same “exit” cross-section of the model. This is done in order to prevent the flow separation not only from the inner surfaces of the liner foils but also from the outer surface of the flap, which could cause difficulties both in the experiments and in the simulations.

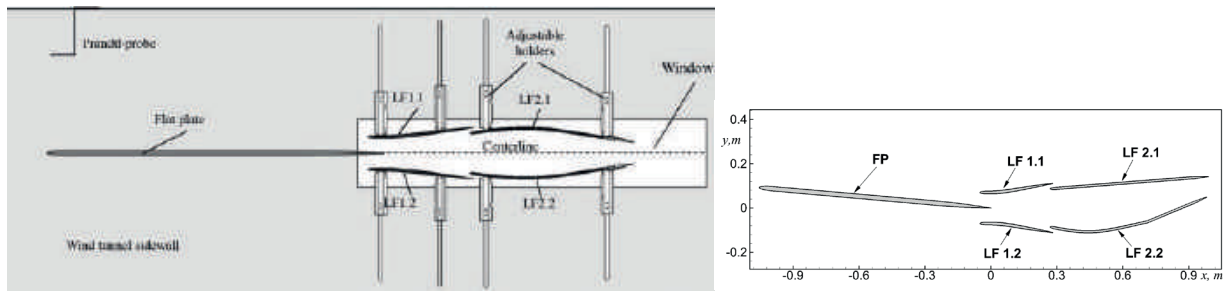


Fig. 1. Sketch of experimental model of straight wake installed in TU BS wind tunnel [2] (left) and asymmetric curved wake model analyzed in the present work (right)

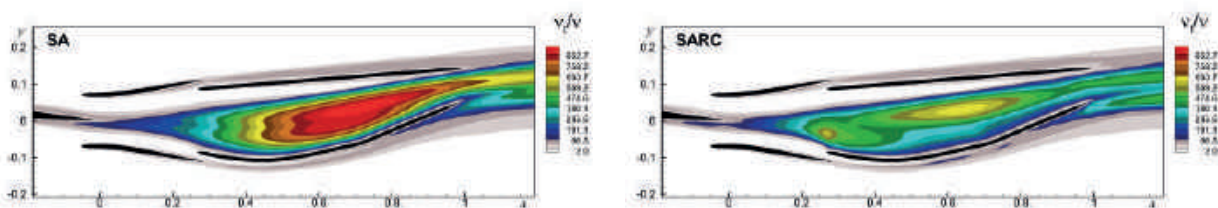


Fig. 2. Fields of normalized eddy viscosity in the curved wake predicted by SA (left) and SARC (right) models

Computational approach and some numerical details

In general, the SRS approach employed in the present work for the computations of the asymmetric curved wake is similar to the approach successfully used in the preceding project [2–4] for the simulation of the straight symmetric wake. It is based on the zonal RANS-LES model with the hybrid IDDES method [8] used for the representation of turbulence in the LES zone. In the presence of resolved turbulence, the IDDES functions as LES with wall modeling (WMLES) in the attached boundary layers and as “pure” LES away from walls. Within the zonal RANS-IDDES, the computational domain is manually subdivided into two RANS and IDDES subdomains (zones) which are shown in Fig. 3 together with the entire computational domain and grid in XY -plane.

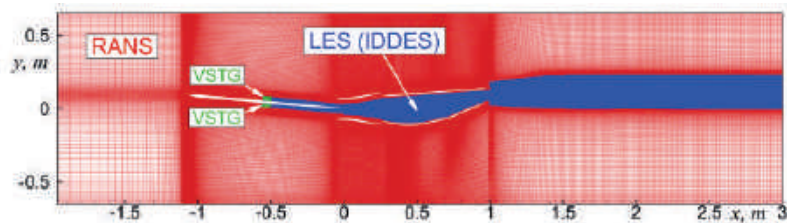


Fig. 3. Computational domain, RANS and IDDES subdomains, and baseline grid in XY -plane

Specifically, the RANS zone (red in Fig. 3) includes the outer (inviscid) part of the computational domain, the initial part of the FP boundary layers, and the boundary layers forming on the liner foils. The IDDES zone (blue in Fig. 3) covers the rest (downstream) part of the FP boundary layers and the FP wake, which is the focus region in this study. To introduce resolved turbulent structures into the IDDES subdomain, which is essential for ensuring a rapid transition from the fully modeled turbulence (RANS sub-domain) to mostly resolved turbulence (IDDES sub-domain) the Volume Synthetic Turbulence Generator (VSTG) [9, 10] is used at the RANS-IDDES interface (in Fig. 3, the area of non-zero VSTG source term is shown in green).

In the RANS zone, the k - ω SST RANS model of Menter [11] is applied, which serves also as the underlying RANS model for the IDDES.

The simulations are performed at the Reynolds number 1.6 million based on the FP length L (1.058 m) and the free stream (inlet) velocity U_0 (25 m/s). Corresponding Mach number is as small as ~ 0.07 , which justifies using the incompressible flow assumption.

The boundary conditions used in the simulations are the same as those employed in the straight wake simulations (see [3] for details). Particularly, in the spanwise direction the periodic boundary conditions are imposed, and in order to check whether the chosen span size of the domain is sufficient to ensure span-size independent mean and statistical flow characteristics, two simulations are carried out in the computational domains with the span size $L_z = 0.1$ m and 0.2 m, respectively.

The computational grids used in the present study are the structured Chimera-type grids with 25 overlapping blocks. The “baseline” grids have around 35 or 70 million cells total, depending on the span size of the domain. In addition, grid-sensitivity of the obtained solution is analyzed by carrying out a simulation at $L_z = 0.1$ m on the “refined” grid which steps in the focus region are reduced compared with the baseline grid by a factor of 1.3 in all the three spatial direction (this grid has ~ 64 million cells total).

The computations are performed with the use of the in-house CFD code “Numerical Turbulence Simulation” (NTS code) [12]. The incompressible branch of the code used in the present study employs the flux-difference splitting method of Rogers and Kwak [13]. In the RANS sub-domain, the inviscid fluxes in the governing equations are approximated with the use of a 3rd-order upwind-biased scheme and in the IDDES sub-domain a 4th-order central scheme is used. The viscous fluxes are approximated with the 2nd-order central scheme. For the time integration, an implicit 2nd-order backward Euler scheme with sub-iterations is applied. The time-step Δt is chosen to ensure less than 1.0 value of Courant number.

Results and Discussion

Sample results of the simulations are shown in Figures 4–7.

In particular, Fig. 4 (left frame) presents a visualization of results of the simulations on the baseline grid in the form of the instantaneous isosurface of the Q -criterion revealing the vortical turbulent structures resolved by the simulation. Both, in the attached boundary layers downstream of the VSTG and in the FP wake the size of the smallest structures is consistent with the grid used, which suggests a correct functionality of both the VSTG and the IDDES in WMLES and pure LES modes. Besides, the figure clearly displays strong asymmetry and curvilinearity of the wake and the presence of a large “hanging” stagnation region caused by the APG.

Convincing additional evidence of the credibility of representation of the wake turbulence in the simulations is the presence of an extended inertial region in the computed spectra of turbulent fluctuations (Fig. 4, right frame) and an increase in the length of this region with grid-refinement due to a decrease of the size of the smallest resolved turbulent structures.

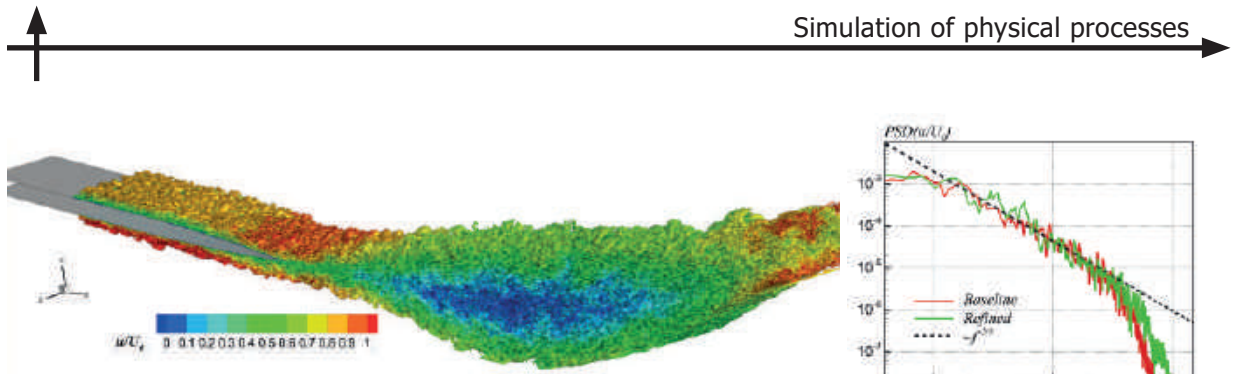


Fig. 4. Isosurface of Q -criterion “colored” by streamwise velocity (baseline grid, $L_z = 0.1\text{m}$) and spectra of streamwise velocity fluctuations obtained on baseline and refined grids ($x = 0.7\text{ m}$, $y = 0$)

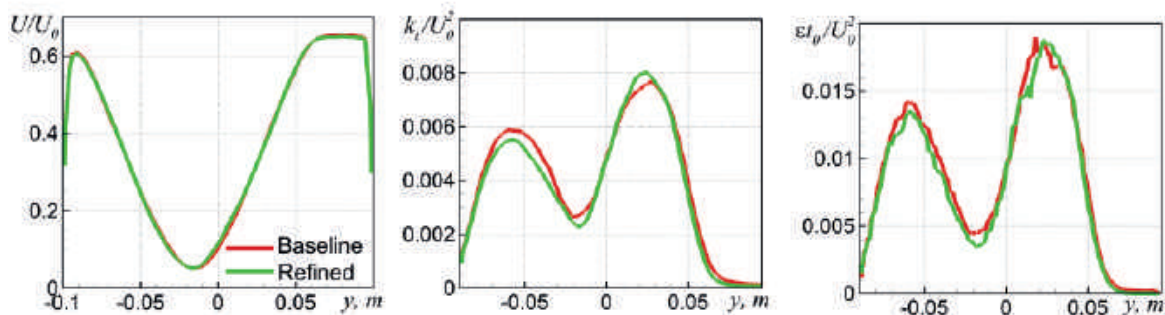


Fig. 5. Profiles of mean velocity, turbulent kinetic energy and its dissipation rate in the mid-wake section ($x = 0.5\text{ m}$) from simulations on baseline and refined grids

Other than that, the Q -isosurface in Fig. 4 does not reveal any large-scale vortical structures with the size of the order of the span-size of the “narrow” computational domain $L_z = 0.1\text{ m}$, which indicates that this L_z -value is sufficient for getting span-size independent solution for the flow under consideration. This is directly confirmed by the comparison (not shown) of the results of the simulations carried out in the narrow and wide ($L_z = 0.2\text{ m}$) domains: both the mean flow parameters and the turbulent statistics obtained in these simulations virtually coincide with each other. As for the grid sensitivity of the predicted flow characteristics, it can be judged by Fig. 5 which compares the profiles of the mean streamwise velocity, the resolved turbulent kinetic energy (TKE), and its dissipation rate extracted from the simulations on the baseline and refined grids. One can see that thanks to the high-order numerics used, the relatively coarse baseline grid ensures accurate (virtually grid-converged) prediction of even the turbulence dissipation rate, which is known to be the most grid-sensitive characteristic of turbulent flows.

In Fig. 6, we compare the mean velocity and the TKE fields obtained by the zonal RANS-IDDES for the straight wake [3] and for the curved wake considered in the present work. The figure shows that the APG-induced stagnation regions in the both wakes are of similar streamwise extent and, roughly, have the same values of the minimum velocity, $U_{\min}/U_0 \approx 0.07$, but the lateral size of this region in the curved wake is significantly narrower than in the straight one. Probably this effect and therefore higher velocity gradients is the cause of the tangibly higher TKE levels in the curved wake predicted by the simulations (see lower row in Fig. 6).

Finally, considering that the ultimate goal of the present project consists in improving the accuracy of RANS turbulence models for the wakes in APG, we have evaluated accuracy of some already existing models by comparing the corresponding 2D RANS predictions of the curved wake characteristics with the predictions of the high-fidelity zonal RANS-IDDES approach.

The steady RANS computations of the wake were performed with the use of three RANS models, which currently are widely used for the computation of aerodynamic flows: the eddy viscosity models SARC [7] and $k-\omega$ SST [11], and the Reynolds-stress transport (RST) LLR-SSG- ω model [14]. Figure 7 presents the comparison of the RANS results obtained with the use of these models with the results of the zonal RANS-IDDES computations. The figure suggests that none of the three RANS models is capable of accurate prediction of the mean velocity field in the wake.

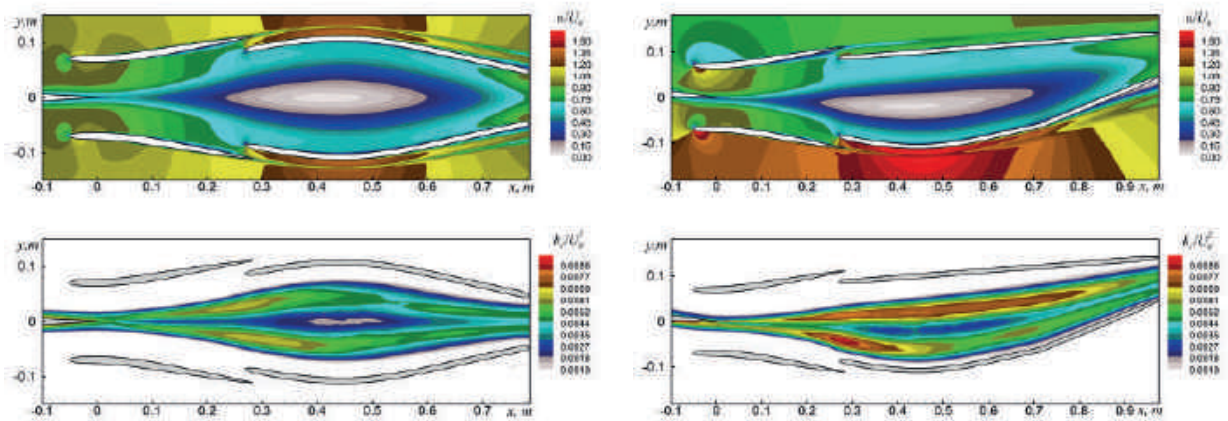


Fig. 6. Zonal RANS-IDDES predictions of mean velocity and TKE fields in the symmetric straight wake [3] (left) and in the asymmetric curved wake considered in the present study (right)

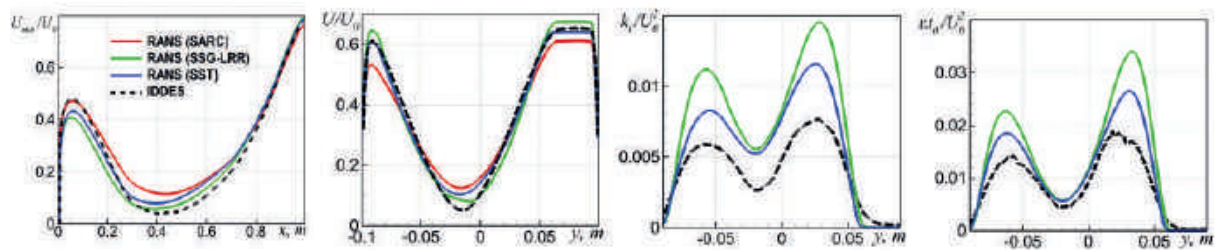


Fig. 7. Comparison of RANS-based and zonal RANS-IDDES predictions of curved wake characteristics: streamwise distributions of the minimum mean velocity in the wake and profiles of mean velocity, TKE and its dissipation rate in the mid-wake section $x = 0.5$ m

Other than that, two of these models, which potentially can claim to the prediction of the TKE and its dissipation rate (the two-equation model [11] and the RST model [14]), strongly overestimate these quantities. This confirms the necessity of the RANS models improvement in order to achieve satisfactory predictions of the characteristics of complex turbulent wakes typical of the low-speed flows over high-lift configurations.

Acknowledgments

Computations were performed with the use of resources of the Supercomputer Center “Polytechnicheskyy” (<http://www.spbstu.ru>).

REFERENCES

1. Rumsey C.L., Ying S. X., Prediction of high lift: review of present CFD capability, Progress in Aerospace Sciences, 38 (2002) 145–80.
2. Breitenstein W., Scholz P., Radespiel R., Burnazzi M., Knopp T., Guseva E., Shur M., Strelets M., A Wind Tunnel Experiment for Symmetric Wakes in Adverse Pressure. AIAA Paper, (2019) 2019–1875.
3. Guseva E., Shur M., Strelets M., Travin A., Breitenstein W., Radespiel R., Scholz P., Burnazzi M., Knopp T., Experimental/Numerical Study of Turbulent Wake in Adverse Pressure Gradient, Notes on Numerical Fluid Mechanics and Multidisciplinary Design, 143 (2020) 401–412.
4. Guseva E.K., Strelets M.Kh., Travin A.K., Burnazzi M., Knopp T., Zonal RANS-IDDES and RANS computations of turbulent wake exposed to adverse pressure gradient, J. Phys.: Conf. Ser. 1135, 012092, 2018.
5. Guseva E., Niculin D., Travin A., Radespiel R., Scholz P., RANS-based design of experimental flow model for investigation of complex curved turbulent wakes subjected to adverse pressure gradient, J. Phys.: Conf. Ser. 2103, 012203, 2021.



6. **Spalart P.R., Allmaras, S.R.**, A one-equation turbulence model for aerodynamic flows, AIAA Paper (1992) 92–043.
7. **Spalart P.R., Shur M.L.**, On the sensitization of simple turbulence models to rotation and curvature. Aerospace Sci. and Technol., 1 (1997) 297–302.
8. **Shur M., Spalart P.R., Strelets M., Travin A.**, A hybrid RANS-LES approach with delayed-DES and wall-modelled LES capabilities, Int. J. Heat and Fluid Flow, 29 (2008) 1638–1649.
9. **Shur M.L., Spalart P.R., Strelets M.Kh., Travin A.K.**, Synthetic Turbulence Generators for RANS-LES Interfaces in Zonal Simulations of Aerodynamic and Aeroacoustic Problems, Flow, Turbulence and Combustion, 93 (2014) 63–92.
10. **Shur M., Strelets M., Travin A.**, Improved embedded approaches: Acoustically adapted versions of STG. Notes Numer. Fluid Mech. and Multidisciplinary Design, 134 (2017) 62–69.
11. **Menter F.R.**, Zonal Two Equation $k-\omega$ Turbulence Models for Aerodynamic Flows, AIAA Paper (1993) 93–2906.
12. **Shur M., Strelets M., Travin A.**, High-order implicit multi-block Navier-Stokes code: Ten-years experience of application to RANS/DES/LES/DNS of turbulent flows, 7th Symposium on Overset Composite Grids and Solution Technology, Invited Lecture, Huntington Beach, CA, Oct. 2004. https://cfdsbstu.ru/agarbaruk/doc/NTS_code.pdf.
13. **Rogers S.E., Kwak D.**, An upwind differencing scheme for the incompressible Navier-Stokes equations, Appl. Numer. Math., 8 (1991) 43–64.
14. **Cecora R., Radespiel R., Eisfeld B., Probst A.**, Differential Reynolds-Stress Modeling for Aeronautics, AIAA Journal, 53 (2014) 937–755.

THE AUTHORS

GUSEVA Ekaterina K.
katia.guseva@inbox.ru
ORCID: 0000-0002-7117-2454

SHUR Mikhail L.
mshur@cfdsbstu.ru
ORCID: 0000-0002-9223-1687

STABNIKOV Andrey S.
An.stabnikov@gmail.com
ORCID: 0000-0001-7011-6197

STRÖER Philip
philip.stroeer@dlr.de

TRAVIN Andrey K.
atravin@cfdsbstu.ru
ORCID: 0000-0003-3995-5085

Received 18.10.2022. Approved after reviewing 08.11.2022. Accepted 25.11.2022.

Conference materials

UDC 53.01

DOI: <https://doi.org/10.18721/JPM.161.144>

Formalized model of cellulose thermopolarization processes in natural wood in a non-uniform temperature field

N.S. Kamalova ¹✉, N.N. Matveev ¹, N.Yu. Evsikova ¹,

V.I. Lisitsyn ¹, S.V. Vnukova ¹, H.T. Nguyen ²

¹Voronezh State University of Forestry and Technologies named after G. F. Morozov, Voronezh, Russia;

²Industrial University of Ho Chi Minh City, Ho Chi Minh City, Vietnam

✉ meetvgltu3@vglta.vrn.ru

Abstract. Temperature fluctuations are the most common and significant factor in the environmental impact on the properties of plastic and biocomposite materials. Therefore, the development of a fundamental concept of the conformation mechanisms of long molecules under conditions of stable temperature gradient is one of the urgent problems of modern technologies in the field of creating materials with given properties. The purpose of the research was substantiation of basic relation for conducting a computational experiment to determine the parameters of the kinetics process for thermally stimulated cellulose polarization within the framework of classical thermodynamics. The objects of the experimental study were microsections of cylindrical birch wood with a thickness of about several hundred microns. During the measurement, the specimens were placed between two massive cylindrical measuring electrodes. Heating was carried out at a constant rate, ensuring the constancy of the temperature gradient along the cut thickness. A potential difference was formed in the wood under experimental conditions due to pyroelectric and piezoelectric effects in cellulose crystallites. The emerging electric field contributes to polarization of the side groups of macromolecules in the amorphous part of the cellulose. In this work, a basic model relation for calculating the potential difference was obtained. The difference occurs in a thin wood specimen. Model efficiency was determined by the method of estimating the dimensionless Nash-Sutcliffe criterion. The proposed model can be applied for data systematization on the thermally stimulated biocomposite polarization (with crystalline and amorphous components). Systematization is made by means of computational experiment to determine the parameters characterizing their unique features.

Keywords: microstructure, crystallites, composites, cellulose macromolecules, synthesized materials

Citation: Kamalova N.S., Matveev N.N., Evsikova N.Yu., Lisitsyn V.I., Vnukova S.V., Nguyen H.T., Formalized model of cellulose thermopolarization processes in natural wood in a non-uniform temperature field, St. Petersburg State Polytechnical University Journal. Physics and Mathematics. 16 (1.1) (2023) 262–268. DOI: <https://doi.org/10.18721/JPM.161.144>

This is an open access article under the CC BY-NC 4.0 license (<https://creativecommons.org/licenses/by-nc/4.0/>)

Материалы конференции

УДК 53.01

DOI: <https://doi.org/10.18721/JPM.161.144>

Формализованная модель процессов термополяризации целлюлозы в натуральной древесине в неоднородном температурном поле

Н.С. Камалова ¹✉, Н.Н. Матвеев ¹, Н.Ю. Евсикова ¹,

В.И. Лисицын ¹, С.В. Внукова ¹, Х.Т. Нгуен ²

¹Воронежский государственный лесотехнический университет имени Г.Ф. Морозова, г. Воронеж, Россия;



² Индустриальный университет Хошимина, г. Хошимин, Вьетнам

✉ meetvgltu3@vglta.vrn.ru

Аннотация. Флуктуации температуры являются наиболее распространенным и существенным фактором воздействия окружающей среды на свойства пластиков и биокompозитов. Поэтому разработка фундаментальной концепции механизмов конформации длинных молекул в условиях устойчивого градиента температуры является одной из актуальных проблем современных технологий в области создания материалов со свойствами, необходимыми для решения определенных задач. Цель работы – обоснование базового соотношения для проведения вычислительного эксперимента по определению параметров процесса кинетики термостимулированной поляризации целлюлозы в природной древесине в рамках классической термодинамики. Объектами экспериментального исследования были микросрезы древесины березы цилиндрической формы толщиной порядка нескольких сотен микрон. В процессе измерения образцы помещались между двумя массивными измерительными электродами цилиндрической формы. Нагревание проводилось с постоянной скоростью, что позволило обеспечить постоянство градиента температуры вдоль толщины среза. В условиях эксперимента в древесине формируется разность потенциалов, обусловленная пироэлектрическим и пьезоэлектрическим эффектами в кристаллитах целлюлозы. Возникающее электрическое поле способствует поляризации боковых групп макромолекул аморфной части составляющих целлюлозы. В работе получено базовое модельное соотношение для расчета разности потенциалов, возникающей в тонком образце древесины. Эффективность модели определялась методом оценки безразмерного критерия Нэша-Сатклиффа. Предлагаемая модель может быть использована для систематизации данных о термостимулированной поляризованности биокompозитов, имеющих кристаллическую и аморфную составляющие, путем вычислительного эксперимента по определению параметров, характеризующих их уникальные особенности.

Ключевые слова: микроструктура, кристаллиты, композиты, макромолекулы целлюлозы, синтезированные материалы

Ссылка при цитировании: Камалова Н.С., Матвеев Н.Н., Евсикова Н.Ю., Лисицын В.И., Внукова С.В., Нгуен Х.Т. Формализованная модель процессов термополяризации целлюлозы в натуральной древесине в неоднородном температурном поле // Научно-технические ведомости СПбГПУ. Физико-математические науки. 2023. Т. 16. № 1.1. С. 262–268. DOI: <https://doi.org/10.18721/JPM.161.144>

Статья открытого доступа, распространяемая по лицензии CC BY-NC 4.0 (<https://creativecommons.org/licenses/by-nc/4.0/>)

Introduction

The optimum of the solutions in the field of designing materials with given properties based on natural composites largely determines understanding of the dynamics of changes in their microstructure under the influence of external factors [1]. Therefore, the characteristics of macromolecules [2–4], physical and chemical properties of cellulose [5–6], and properties of other biocomposite constituents of natural origin [7–8] have been actively studied recently. However, unique supramolecular structure of the polymer composite is mainly destructurized in the process of research [9–11], making it difficult to form ideas about the effect of biocomposite complexity on its properties. Development of methods for non-destructive testing of wood microstructure makes it possible not only to preserve the uniqueness of supramolecular structure during the research, but also to expand existing ideas about thermopolarization mechanisms in complex biocomposites. Temperature influence is the most common environmental factor. Therefore, fundamental concept development of the conformation mechanisms of long molecules under conditions of stable temperature gradient is one of the urgent problems of modern technologies in the field of creating materials with the properties necessary to solve certain tasks.

A formalized model is currently being developed based on long-term studies of polymer polarization processes [12–16]. It would become the basis for a comparative analysis and prediction of the effect of inhomogeneous temperature field on the microstructure of a complex

biocomposite (wood). The purpose of the research was to substantiate the axiomatic relation for conducting a computational experiment. The aim of the experiment is to determine the parameters of the kinetics process of thermally stimulated cellulose polarization in natural wood. The process is based on the analysis of the entropy change in the system under study.

Theoretical part

Temperature gradients induce piezoelectric and pyroelectric effects in wood cellulose crystallites. As a result, a potential difference is formed, contributing to the polarization of macromolecule side groups. It takes place in the amorphous part of cellulose, having natural heterostructure. Thus, the description of a response of a high-molecular-weight biocomposite (wood) to a constant temperature difference is a complex task. Specimen polarization $P_{i\sigma}$ is determined as the sum of four terms comparable in magnitude order [16]:

$$P_{i\sigma} = - \int_{T_0}^{T_0+\Delta T} d_{ijk} c_{kjml} \mu_{ml} \alpha_T dT + \int_{T_0}^{T_0+\Delta T} \gamma_i h dT + \Delta P_{in} + P_{\sigma}, \quad (1)$$

where T_0 is initial temperature, ΔT is temperature change, d_{ijk} is tensor of piezoelectric module, c_{kjml} is modulus of elastic stiffness, μ_{ml} is ratio of Young's modulus of lignin to Young's modulus of cellulose, α_T is coefficient of lignin thermal dilatation, γ_i is cellulose pyroelectric coefficient, h is microsection thickness, ΔP_{in} is change of orientational polarization in the macromolecule side polar groups of the amorphous parts of cellulose and hemicelluloses in the emerging electric field [1, 12–16], P_{σ} is dipole orientational polarization of water molecules in wood pores. With a stationary heat flux in a thin microsection of wood biocomposite, we can assume that d_{ijk} , c_{kjml} , μ_{ml} , α_T and γ_i coefficients practically do not depend on the temperature. Then the equation (1) takes the form:

$$P_{i\sigma} = -d_{ijk} c_{kjml} \mu_{ml} \alpha_T \Delta T + \gamma_i h \Delta T + \Delta P_{in} + P_{\sigma}. \quad (2)$$

The change in the orientation polarization ΔP_{in} at a constant temperature gradient along its thickness is mainly determined by the increase in ΔN number of the ordered side groups (noncrystalline part of cellulose). In the framework of classical electrodynamics, it is determined by the relation $\Delta P_{in} = p_i \Delta N$ (p_i is the average dipole moment of the side group of the cellulose macromolecule, which can be determined from its conformation) [16]. The number of side groups of macromolecules is limited in a microsection by a certain value N^* . The process of orientation of individual side polar groups is a random one. Therefore, we can write the equation for the logarithm of the thermodynamic probability change W in the orientational polarization ΔP_{in} of the side polar groups of a macrosystem of long molecules in the following form:

$$\ln W = \theta \left(\ln \frac{\Delta N}{N^*} - \ln \frac{N^* - \Delta N}{N^*} \right), \quad (3)$$

where θ is all possible orientations of side groups of cellulose macromolecules in a microsection. Transforming the equation (3) for dW/W , we obtain:

$$\frac{dW}{W} = \theta N^* \frac{d(\Delta N)}{(N^* - \Delta N) \Delta N}. \quad (4)$$

The well-known Boltzmann relation determines entropy in the considered system through the logarithm of thermodynamic probability:

$$S = k \ln W, \quad (5)$$

where k is Boltzmann's constant. In the process under study, the decrease in the entropy dS occurs due to the side group orientations. Therefore, it is largely formed by the amount of heat δQ flowing in the microsection under experimental conditions. Then, within the framework of classical thermodynamics we have a relation.

$$k \frac{dW}{W} = dS = \frac{\delta Q}{T} = \lambda \frac{\Delta T}{hT} \sigma dt, \quad (6)$$



where T is ambient temperature. The above-mentioned relation was formed taking into account that, $\delta Q = \lambda(\Delta T/h)\sigma dt$ flows (λ is thermal conductivity of wood) in the approximation of flow stationarity through the microsection area (σ) for an elementary period of time (dt). The following equation can be derived from the relations (4) and (6):

$$\frac{dW}{W} = \theta N^* \frac{d(\Delta N)}{(N^* - \Delta N)\Delta N} = \frac{\lambda\sigma\Delta T}{khT} dt. \quad (7)$$

Let us introduce the notation, meaning the ratio of the stationary heat flux power (through the microsection) to the energy of chaotic motion of all side groups in all possible states in the amorphous part of cellulose. Then (7) is transformed into the following equation:

$$\frac{d(\Delta N)}{(1 - \beta\Delta N)\Delta N} = \alpha dt, \quad (8)$$

where $\beta = 1/N^*$. Taking into account the initial conditions ($t_0 = 0$, $\Delta N = \Delta N_0$), it has an analytical solution. Let us denote $P_0 = p_i\Delta N_0$. Then the equation for the change in the orientational polarization is obtained:

$$\Delta P_{in} = \frac{P_0 \exp(\alpha t)}{1 + \beta P_0 (\exp(\alpha t) - 1)/p_i}. \quad (9)$$

From (2), taking into account (9), an expression follows for determining the potential difference that forms in a dry microsection of wood over time (in the approximation of a flat capacitor):

$$U_s = U_{dpy} + \frac{U_0 \exp(\alpha t)}{1 + \eta(\exp(\alpha t) - 1)}, \quad (10)$$

where U_0 is initial value of potential difference, U_{dpy} is potential difference formed by piezoelectric pyroelectric response of the crystalline cellulose part, $\eta = P_0/(N^*p_i)$ is the proportion of oriented side groups at the initial moment of time.

Relatively recently, the influence of wood moisture on polarization processes in a non-uniform temperature field has been studied. The results showed that potential difference in a specimen with moisture content ϕ can be modeled by the relation [1]:

$$U = U_s \left[1 + \phi\kappa / (\varepsilon_i (1 - \phi)) \right], \quad (11)$$

where κ characterizes polarization properties of bound water in the pores of wood, and ε_i is its dielectric constant. As a result, in the computational experiment, it is expedient to use the following relation:

$$U_s = U_{dps} + \frac{U_{0s} \exp(\alpha t)}{1 + \eta(\exp(\alpha t) - 1)}, \quad (12)$$

where $U_{dps} = U_{dpy} \left[1 + \phi\kappa / (\varepsilon_i (1 - \phi)) \right]$, $U_{0s} = U_0 \left[1 + \phi\kappa / (\varepsilon_i (1 - \phi)) \right]$. Relation (12) is the base for a formalized model of a computational experiment to determine U_{dps} , U_{0s} , α and η parameters. The model is based on the data of the experiment on the formation dynamics of a potential difference in wood microsections in a non-uniform temperature field.

Experimental part

Microsections of birch wood of a cylindrical shape with a thickness of about several hundred microns were studied in this research. During the measurement, the specimens were placed between two massive cylindrical measuring electrodes, the thickness of which significantly exceeded the thickness of the microsection. The upper electrode was equipped with a heat sink, and the side surface of the wood was thermally insulated with a specially made gasket. An inhomogeneous temperature field with a gradient along its thickness was formed in the specimen [16], determined by the following relation:

$$\nabla T = \frac{2\beta_T}{\lambda_0 S} (c_e m_e + c_0 m_0), \quad (13)$$

where c_e is specific heat capacity of the electrode material, m_e is mass of the upper electrode, λ_0 , c_0 , m_0 are thermal conductivity, specific heat capacity, and mass of natural wood microsection, respectively, β_T is bottom electrode heating rate, and S is area of bottom electrode. Thus, in a microsection, the magnitude of the temperature gradient along its thickness was determined by the properties of wood substance and parameters of the measuring cell of flat capacitor. Heating was carried out at a practically constant rate (Fig. 1). Straight line in the figure was constructed using the least squares method, and the relative deviation of the temperature measurement data from it did not exceed 2%. As a result, the temperature gradient under the measurement conditions can be considered a constant according to the relation (13).

In the experiment, biocomposite response to the presence of a constant temperature gradient along the thickness of the microsection was realized in the formation of a potential difference, which was measured with controlled accuracy. Determination of the model parameters in the computational experiment was carried out by the method of soft computations [17]. Optimization was made on the basis of the Nash-Sutcliffe efficiency criterion (ME), which is traditionally used in the problems of checking the adequacy of process models in partially self-organizing systems [18]. According to general ideas, the value of the criterion is calculated by the ratio:

$$ME = 1 - \frac{\sum_k (U_k^{\text{exp}} - U_k^{\text{theory}})^2}{\sum_k (U_k^{\text{exp}} - U_{\text{mean}})^2}, \quad (14)$$

where U_k^{exp} are data of the experiment on measuring the potential difference in the microsection, U_k^{theory} are results of computational experiment (according to the relation (12)), U_{mean} is mean value of U_k^{exp} . The value of the ME criterion cannot be more than a unit. The closer it is to one, the more the model matches the ideal data description.

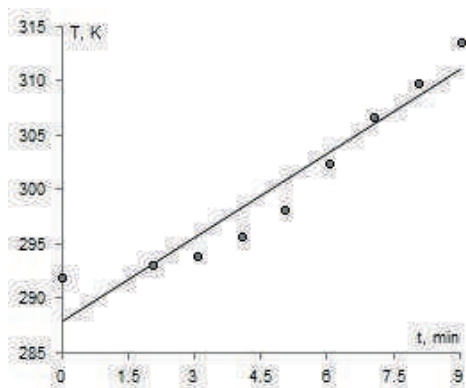


Fig. 1. Dynamics of temperature changes of the heated electrode

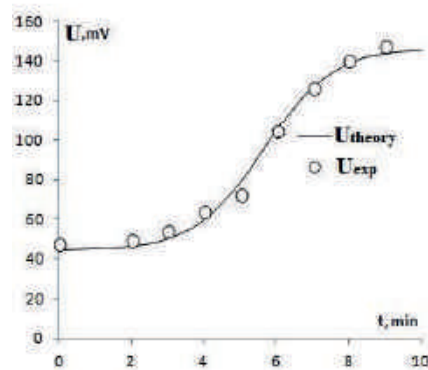


Fig. 2. Dynamics of the potential difference formed in a birch wood specimen with a moisture content of 40% when the lower electrode is heated at $1.43 \text{ K} \cdot \text{min}^{-1}$

Results and Discussion

The analysis of the experimental data showed that the nature of changes in the potential difference magnitude over time is non-linear one (Fig. 2). Potential difference stabilizes from a certain time point, which indirectly indicates the formation of maximum polarization of macromolecule side groups in the microsection.

The results of the computational experiment for birch microsections with a moisture content of 40% showed that the maximum value of the Nash-Sutcliffe criterion was 0.993 with the following model parameters: $U_{0s} = 0.28 \text{ mV}$, $\alpha = 1.04 \text{ min}^{-1}$, $U_{dps} = 44.5 \text{ mV}$ and $\eta = 0.98\%$. At the same time, the average deviation of the experimental data from the data, calculated according to the basic ratio of the proposed model (Fig. 2), did not exceed 4%.

It should be noted that the research demonstrates successful application of computational experiment to the analysis of measurement data on the wood response to the influence of



inhomogeneous temperature field. Thus, it is necessary to combine laboratory tests with the methods of physical and mathematical modeling of the studied processes to identify the kinetic parameters of complex biocomposite microstructure

Conclusion

The conducted studies proved the following:

1) The kinetics of the potential difference formation in inhomogeneous temperature field can be modeled within the framework of classical thermodynamics.

2) The measurement data of the potential difference in inhomogeneous temperature field (in combination with a computational experiment) makes it possible to determine the parameters of kinetic processes in natural heterostructures with sufficiently high accuracy.

3) The parameters of formalized model formed in the framework of thermodynamic approach have clear physical meaning. They can be used in the analysis of the states of supramolecular structure of complex semi crystalline composites.

4) The paper theoretically shows the role of various wood components in the formation of thermally stimulated potential difference in the presence of a constant potential difference in its microsections at room temperature.

5) The proposed method of formalized modeling can become the basis for the methods of comparative evaluation of natural heterostructures, if their microsections can be used in converters of thermal energy into electrical one.

Thus, in this research, a formalized model of the formation processes of potential difference in a non-uniform temperature field was proposed for the first time. Complex wood biocomposite was taken as a material under study. The model was based on the existing representation of the composition and supramolecular composite structure. The main relations were obtained in the framework of classical thermodynamics. In this case, the model can be used to systematize data on thermally stimulated polarization of biocomposites with crystalline and amorphous components.

REFERENCES

1. **Matveev N.N., Kamalova N.S., Evsikova N.Yu., Litvinova Yu.A., Litvinova L.A.**, The mechanism of the appearance of a potential difference in the natural high-molecular heterostructures by natural temperature changes, *Ferroelectrics*. 536 (1) (2018) 187–193.
2. **Gutiérrez T.J., Alvarez V.A.**, Cellulosic materials as natural fillers in starch-containing matrix-based films: a review, *Polymer Bulletin*. 74(6) (2017) 2401–2430.
3. **Bhowmik K.L., Deb K., Bera A., Debnath A., Saha B.**, Interaction of anionic dyes with polyaniline implanted cellulose: Organic π -conjugated macromolecules in environmental applications, *Journal of Molecular Liquids*. 261 (2018) 189–198.
4. **Koide M., Wataoka I., Urakawa H., Kajiwara K., Henniges U., Rosenau T.**, Intrinsic characteristics of cellulose dissolved in an ionic liquid: the shape of a single cellulose molecule in solution, *Cellulose*. 26 (4) (2019) 2233–2242.
5. **Li X., Shao C., Zhuo B., Yang S., Zhu Z., Su C., Yuan Q.**, The use of nanofibrillated cellulose to fabricate a homogeneous and flexible graphene-based electric heating membrane, *International Journal of Biological Macromolecules*. 139 (2019) 1103–1116.
6. **Shestakov S.L., Popova Yu.A., Kozhevnikov A.Yu., Kosyakov D.S., Sypalov S.A.**, The study of water sorption with hydrolysis lignin by solid-state NMR spectroscopy, *Eurasian Chemico-Technological Journal*. 21 (4) (2019) 325–331.
7. **Chan J. C., Paice M., Zhang X.**, Enzymatic oxidation of lignin: challenges and barriers toward practical applications, *ChemCatChem*. 12 (2) (2020) 401–425.
8. **Sixta H., Potthast A., Krottschek A.W.**, *Chemical Pulping Processes Handbook of Pulp*, Vol. 1, ed. H. Sixta, Wiley-VCH Verlag, Weinheim, 2006, 109–391.
9. **Mandelkern L.**, *Crystallization of Polymers*, Vol. 2, Cambridge University Press, Cambridge, 2004.
10. **Nguyen H.T., Sidorkin A.S., Milovidova S.D., Rogazinskaya O.V.**, Investigation of dielectric relaxation in ferroelectric composite nanocrystalline cellulose – triglycine sulfate, *Ferroelectrics*. 498(1) (2016) 27–35.

11. **Vrublevskaya V.I., Matusevich V.O., Kuznetsova V.V.**, Justification of the mechanism of interaction of wood components with moisture, *Forestry Journal*. 3 (357) (2017) 152–163.

12. **Kamalova N.S., Matveev N.N., Evsikova N.Yu., Savrasova N.A.**, Measuring the change in the polarization of an organosilicon flexible polymer upon crystallization in an inhomogeneous temperature field, *Bulletin of the Russian Academy of Sciences: Physics*. 84(9) (2020) 1107–1109.

13. **Matveev N.N., Evsikova N.Yu., Kamalova N.S.**, Formalized modeling of changes in the polarization of a linear pyroelectric in an inhomogeneous temperature field, *Bulletin of the Russian Academy of Sciences: Physics*. 83 (9) (2019) 1114–1115.

14. **Matveev N.N., Evsikova N.Yu., Kamalova N.S., Korotkikh N.I.**, Role of cellulose crystallites in the polarization of a biopolymer composite: Wood in a nonuniform temperature field, *Bulletin of the Russian Academy of Science: Physics*. 77 (8) (2013) 1076–1077.

15. **Matveev N.N., Nguyen H.T., Kamalova N.S., Evsikova N.Yu., Chernykh A.S.**, The wood in the inhomogeneous temperature field: Estimation of cellulose structure parameter fluctuations, *St. Petersburg State Polytechnical University Journal: Physics and Mathematics*. 11 (3) (2018) 9–16.

16. **Matveev N.N., Lisitsyn V.I., Kamalova N.S., Evsikova N.Y.** Formalized model of polarization of a biopolymer composite in an inhomogeneous temperature field, *Plasticheskie massy*. 1 (1–2) (2022) 34–36.

17. **Arnold V.I.**, “Hard” and “Soft” Mathematical Models, MCNMO, Moscow, 2004.

18. **Nash J.E., Sutcliffe J.V.**, River flow forecasting through conceptual models part I – A discussion of principles, *Journal of Hydrology*. 10(3) (1970) 282–290.

THE AUTHORS

KAMALOVA Nina S.

meetvgltu3@vglta.vrn.ru

ORCID: 0000-0001-8293-8593

LISITSYN Viktor I.

idpo@vglta.vrn.ru

ORCID: 0000-0002-2148-1988

MATVEEV Nikolay N.

nmtv@vglta.vrn.ru

ORCID: 0000-0001-9195-9580

VNUKOVA Svetlana V.

vnukovasv@vglta.vrn.ru

ORCID: 0000-0001-6889-9233

EVSIKOVA Natalya Yu.

evsikovany_phlt@vgltu.ru

ORCID: 0000-0001-5288-0140

NGUYEN Hoai Thuong

nguyenthuongfee@iuh.edu.vn

ORCID: 0000-0003-1290-5221

Received 23.10.2022. Approved after reviewing 09.11.2022. Accepted 09.11.2022.

Conference materials
UDC 532.517.2 ,532.133
DOI: <https://doi.org/10.18721/JPM.161.145>

Influence of variable thermophysical properties on the flow of fluids in an annular channel under intensive heat exchange

A.A. Mukhutdinova ¹✉, V.N. Kireev ², S.F. Urmancheev ¹

¹ Mavlyutov Institute of Mechanics, Ufa Federal Research Centre of the RAS, Ufa, Russia

² Bashkir State University, Ufa, Russia

✉ muhutdinova18@gmail.com

Abstract. This paper considers the flow of viscous incompressible fluids in an annular channel, on the inner and outer surfaces of which intensive heat exchange conditions are set, mathematical formulation of which is reduced to boundary conditions of the first kind. Different temperature dependencies of liquid viscosity are considered: monotonic (liquid viscosity decreases monotonously as the temperature rises) and anomalous (liquid viscosity depends on the temperature in a non-monotonic way). Mathematical model comprises continuity, Navier-Stokes and energy conservation equations written in cylindrical coordinate system with axial symmetry considered in dimensionless form. The equations of the mathematical model were solved numerically using the method of control volume. Because of numerical simulation, velocity diagrams in various sections of the annular channel, as well as distributions of temperature and viscosity fields in the flow area, have been plotted. The influence of geometric parameters of the annular channel, heat exchange conditions on its walls and rheological parameters of the fluid on the flow pattern has been determined. It is shown that in a liquid with a non-monotone dependence of viscosity on temperature, the hydrodynamic parameters of the flow significantly depend on the location of the high-viscosity flow region (the “viscous barrier”).

Keywords: annular channel, thermophysical properties, monotonic viscosity temperature dependence, non-monotonic viscosity temperature dependence

Funding: The research was supported by the Russian Science Foundation (Project “Experimental and theoretical investigation of the stability of fluid flow with variable viscosity in flat and annular channels” No. 22-21-00915).

Citation: Mukhutdinova A.A., Kireev V.N., Urmancheev S.F., Influence of variable thermophysical properties on the flow of fluids in an annular channel under intensive heat exchange, St. Petersburg State Polytechnical University Journal. Physics and Mathematics. 16 (1.1) (2023) 269–274. DOI: <https://doi.org/10.18721/JPM.161.145>

This is an open access article under the CC BY-NC 4.0 license (<https://creativecommons.org/licenses/by-nc/4.0/>)

Материалы конференции
УДК 532.517.2 ,532.133
DOI: <https://doi.org/10.18721/JPM.161.145>

Влияние переменных теплофизических свойств на течение жидкостей в кольцевом канале при интенсивном теплообмене

A.A. Мухутдинова ¹✉, В.Н. Киреев ², С.Ф. Урманчиев ¹

¹ Институт механики им. Р.Р. Мавлютова Уфимского федерального исследовательского центра РАН, г. Уфа, Россия;

² Башкирский государственный университет, г. Уфа, Россия

✉ muhutdinova18@gmail.com

Аннотация. В настоящей работе рассматривается течение вязких несжимаемых жидкостей в кольцевом канале, на внутренней и внешней поверхностях которого задаются

условия интенсивного теплообмена. Учитываются различные виды температурных зависимостей вязкости жидкости: монотонная и аномальная. В результате численного моделирования были построены эпюры скоростей в различных сечениях кольцевого канала, а также распределения полей температуры и вязкости в области течения. Показано, что в жидкости с немонотонной зависимостью вязкости от температуры гидродинамические параметры течения существенно зависят от расположения высоковязкой области течения – «вязкого барьера».

Ключевые слова: кольцевой канал, теплофизические свойства, монотонная температурная зависимость вязкости, немонотонная температурная зависимость вязкости

Финансирование: Исследование выполнено при поддержке Российского научного фонда (проект «Экспериментальное и теоретическое исследование устойчивости течения жидкости с переменной вязкостью в плоских и кольцевых каналах» № 22-21-00915).

Ссылка при цитировании: Мухутдинова А.А., Киреев В.Н., Урманчеев С.Ф. Влияние переменных теплофизических свойств на течение жидкостей в кольцевом канале при интенсивном теплообмене // Научно-технические ведомости СПбГПУ. Физико-математические науки. 2023. Т. 16. № 1.1. С. 269–274. DOI: <https://doi.org/10.18721/JPM.161.145>

Статья открытого доступа, распространяемая по лицензии CC BY-NC 4.0 (<https://creativecommons.org/licenses/by-nc/4.0/>)

Introduction

Variations in the thermal properties of fluids can significantly affect the flow pattern and determine the performance of technical systems. In various devices for the heating or cooling of working liquid, shell-and-tube heat exchangers are widely used, in which the coolant flows in an annular channel (gap) formed by two coaxial circular cylinders of different radii. Calculation of thermal and hydraulic parameters of such heat exchangers involves considering the dependence of viscosity, thermal conductivity and heat capacity on temperature. For example, viscosity of formate based coolant Nordway-FORM 60 (Roshal Chemical Plant) in a working temperature range from $-50\text{ }^{\circ}\text{C}$ to $+40\text{ }^{\circ}\text{C}$ decreases 45 times from $108.3\text{ mPa}\cdot\text{s}$ to $2.34\text{ mPa}\cdot\text{s}$ [1–3]. The fuel assemblies of nuclear reactors can serve as an example of such structures. Thus, a theoretical investigation of the hydrodynamic and heat exchange processes at the coolant flow seems to be important.

Statement of the problem

To study features of distribution of hydrodynamic parameters in the flow of thermally incompressible fluid a model problem of the flow of thermally incompressible fluid in an annular channel, formed by two coaxial circular cylinders with the same constant temperatures on internal and external surfaces has been considered. The temperature at which the liquid flows into the channel is denoted by T_w , and the temperature of the channel walls by T_0 , and it is assumed that $T_w > T_0$. The flow of liquid is conditioned by a pressure drop (Fig. 1).

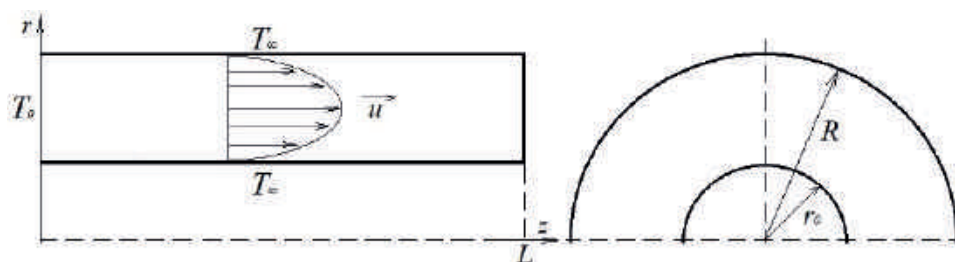


Fig. 1. Channel geometry



Mathematical model of the thermoviscous fluid flow in the annular channel comprises the equations of continuity, Navier-Stokes and energy conservation written in the cylindrical coordinate system with axial symmetry in dimensionless form [4]. Let's denote the dimensionless value of radius by $\tilde{r} = (r - r_0)/(R - r_0)$ and thus $0 \leq \tilde{r} \leq 1$. Further, the value of the dimensionless radius is used without the tilde.

$$\frac{\partial u_r}{\partial r} + \frac{\partial u_z}{\partial z} + \frac{u_r}{r} = 0, \quad (1)$$

$$\frac{\partial u_r}{\partial t} + u_r \frac{\partial u_r}{\partial r} + u_z \frac{\partial u_r}{\partial z} = -\frac{\partial P}{\partial r} + \frac{1}{\text{Re}} \left(\frac{\partial}{\partial r} \left(\mu(T) \frac{\partial u_r}{\partial r} \right) + \frac{\partial}{\partial z} \left(\mu(T) \frac{\partial u_r}{\partial z} \right) + \mu(T) \frac{1}{r} \frac{\partial u_r}{\partial r} \right), \quad (2)$$

$$\frac{\partial u_z}{\partial t} + u_r \frac{\partial u_z}{\partial r} + u_z \frac{\partial u_z}{\partial z} = -\frac{\partial P}{\partial z} + \frac{1}{\text{Re}} \left(\frac{\partial}{\partial r} \left(\mu(T) \frac{\partial u_z}{\partial r} \right) + \frac{\partial}{\partial z} \left(\mu(T) \frac{\partial u_z}{\partial z} \right) + \mu(T) \frac{1}{r} \frac{\partial u_z}{\partial r} \right), \quad (3)$$

$$\frac{\partial T}{\partial t} + u_r \frac{\partial T}{\partial r} + u_z \frac{\partial T}{\partial z} = \frac{1}{\text{Pe}} \left(\frac{\partial^2 T}{\partial r^2} + \frac{\partial^2 T}{\partial z^2} + \frac{1}{r} \frac{\partial T}{\partial r} \right), \quad (4)$$

where u_z , u_r are velocity components; μ is fluid viscosity; P is pressure; T is temperature; Re, Pe are Reynolds and Peclet numbers.

The fluid flow is conditioned by a pressure drop. Two types of temperature dependences of viscosity of liquid are considered: exponential monotonically decreasing dependence [6]

$$\mu = \mu_0 \cdot \exp(-\alpha \cdot (T - T_0)), \quad (5)$$

and anomalous one (viscosity of liquid depends on temperature in a non-monotonous way) [7] (Fig. 2),

$$\mu = \mu_{\min} \left(1 + A \cdot \exp(-B \cdot (T - T_*)^2) \right), \quad (6)$$

where μ_0 is viscosity at temperature T_0 , $\alpha > 0$ is parameter characterizing viscosity change, $A = \mu_{\max}/\mu_{\min} - 1$ and $B > 0$ are parameters characterizing anomalous viscosity dependence on temperature, $T^* = (T_w + T_0)/2$.

Numerical results

The equations of mathematical model are implemented by computer code based on control volume method using SIMPLE (Semi-Implicit Method for Pressure-Linked Equation) algorithm [5] changed to include variable viscosity coefficient and written program in C++ in the cross-platform development environment Qt Creator.

Monotonic viscosity temperature dependence

The longitudinal velocity and viscosity isolines of the thermoviscous liquid flow in the axial section of the annular channel are shown in Fig. 3. Under the problem statement, hot liquid was

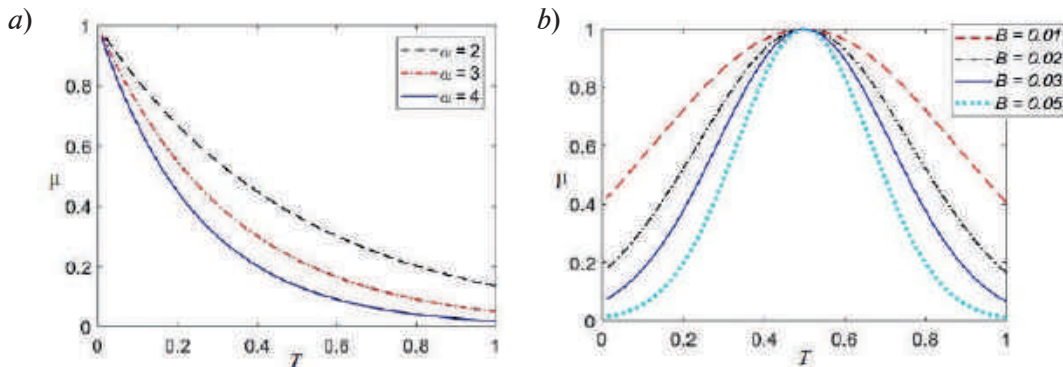


Fig. 2. Monotonic (a) and anomalous (b) viscosity dependence on temperature

supplied to the inlet section and the channel walls were kept cold. A pronounced inhomogeneity of distribution of these parameters seems to be clear. In Fig. 3, *a*, near the inlet section, an area with increased velocity values is detected, which can be interpreted as a zone of flooded jet flow formation associated with viscosity value distribution (Fig. 3, *b*) in the considered flow area.

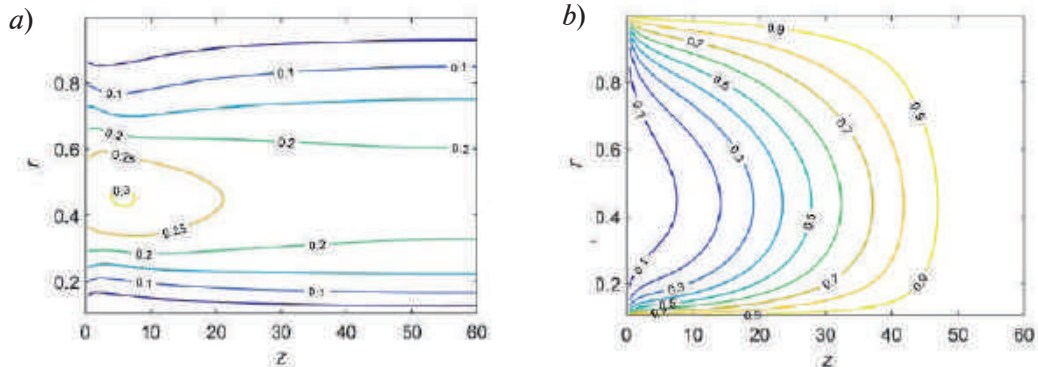


Fig. 3. Steady-state distributions of longitudinal velocity (*a*), viscosity (*b*) in the cooled channel (monotone dependence at $\alpha = 3$)

The effect of the thermal viscosity parameter α on the temperature distribution at $r = 0.5$ is shown in Fig. 4. An increase in this parameter leads to a flatter temperature distribution along the channel axis. Obviously, at $\alpha = 0$, the monotonic decrease in temperature is due to heat transfer at the channel walls.

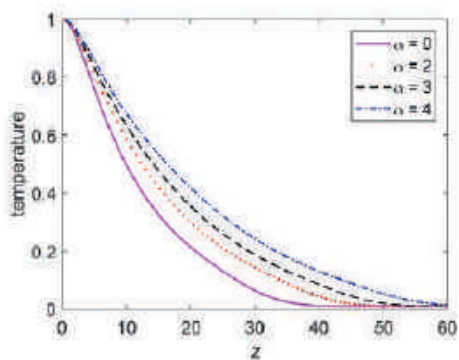


Fig. 4. Steady-state temperature distribution along the channel axis at different thermal viscosity parameters

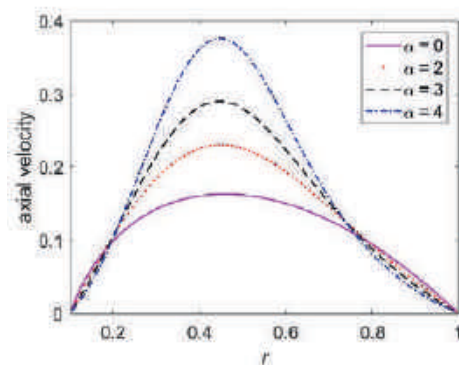


Fig. 5. Longitudinal velocity diagrams of the thermoviscous fluid across the cross section of the annulus at different α thermoviscosity parameters ($z = 10$)

The longitudinal velocity diagrams across the annulus cross section at $z = 10$, depending on the value of parameter α are of considerable interest. The velocity distribution curve at $\alpha = 0$ characterises the Poiseuille flow in the isothermal case. Thus, increasing α leads to increasing maximum value of longitudinal velocity in the flooded jet flow zone.

Non-monotonic viscosity temperature dependence

For the anomalously thermally viscous fluid, the longitudinal velocity and viscosity isolines in the channel axial section are shown in Fig. 6 and Fig. 7 for the values of the anomalous thermal viscosity parameter $B = 0.02$ and $B = 0.05$, respectively. Compared to the monotonic dependence of viscosity change on temperature, in this case, the parameter distributions are more complex. It should be noted only that here, too, the formation of zones of flooded jet flow is observed (Fig. 6, *a* and 7, *a*). At that, for higher value of parameter B in Fig. 7, *a* we have more extended jet with higher value of maximum longitudinal velocity. Peculiarities of flow velocity distribution are directly connected to viscosity field distribution, which in this case leads to formation of a highly viscous region in liquid flow - viscous barrier. At $B = 0.02$, the high-viscosity zone is entirely in considered flow area and its isolines are closed. Whereas at $B = 0.05$ (Fig. 7, *b*) the viscous barrier isolines are open at the same pressure drop value.

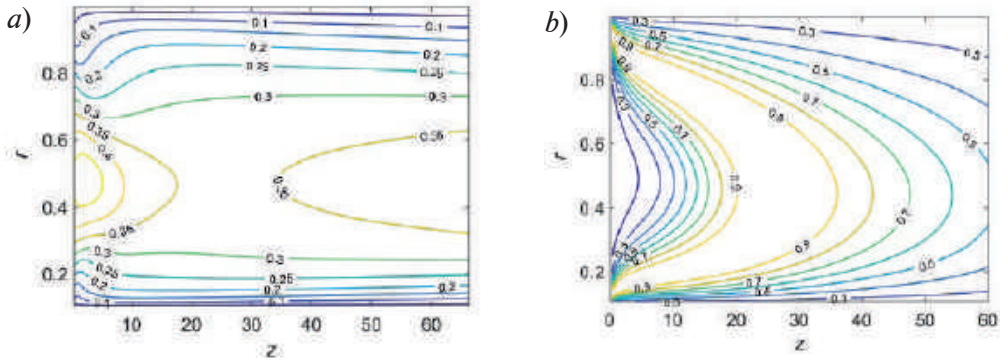


Fig. 6. Steady-state distributions of longitudinal velocity (a), viscosity (b) in the cooled channel (non-monotone dependence at $B = 0.02$)

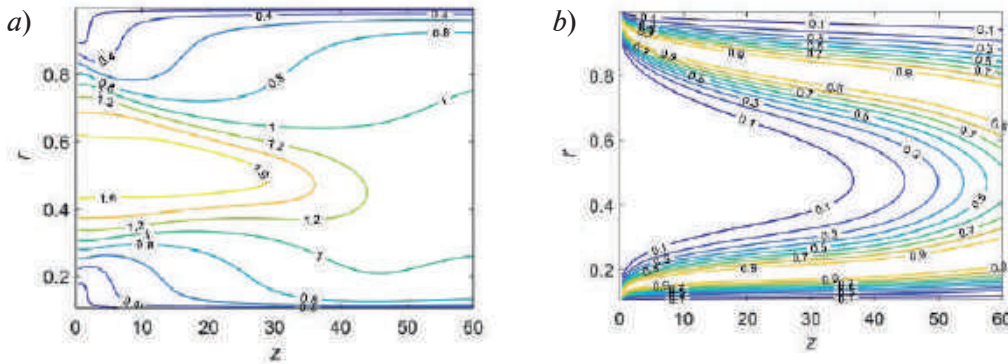


Fig. 7. Steady-state distributions of longitudinal velocity (a), viscosity (b) in the cooled channel (non-monotone dependence at $B = 0.05$)

Fig. 8 and Fig. 9 show plots of temperature change along the channel axis ($r = 0.5$) and longitudinal velocity diagrams ($z = 10$), respectively, for different values of parameter B . At $B = 0$, as in case of monotonic dependence, we deal with fluid having constant viscosity, which does not depend on temperature. At values of $B < 0.05$, the nature of temperature changes qualitatively repeats the dependence for fluids with monotonically decreasing viscosity. However, at $B = 0.05$, the temperature change curve turns from concave to convex, which shows a change in heat transfer along the channel axis. The longitudinal velocity diagrams show an increasing trend in the intensity of the flooded jet stream as the anomalous thermal viscosity parameter increases. At $B = 0.05$, a significant increase not only in maximum velocity value but also in the area covered by the jet flow is noticeable. If we pay attention to Fig. 7, *b*, we can conclude that

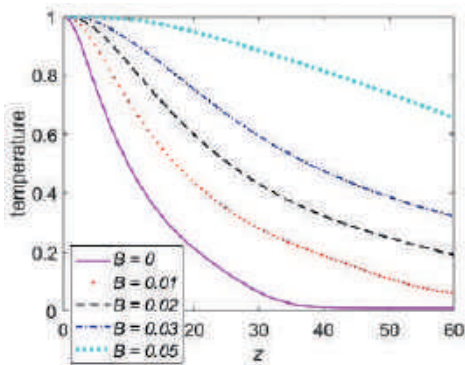


Fig. 8. The steady-state temperature distribution along the channel axis at various anomalous thermal viscosity parameters

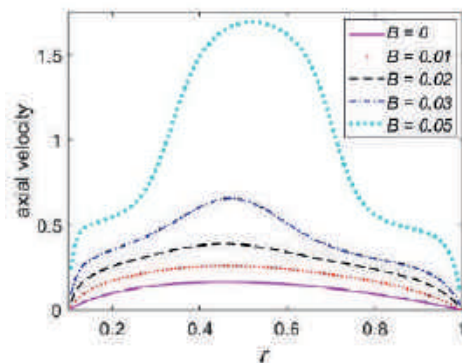


Fig. 9. Longitudinal velocity diagrams of thermoviscous fluid across the cross section of the annulus at different parameters of anomalous thermal B ($z = 10$)

at a ratio of pressure drop, geometrical parameters and heat exchange conditions on the channel walls, the viscous barrier isolines within the channel area appeared to be open, which resulted in an increase of flow velocity and fluid flow rate. Thus, the formation of a viscous barrier in inhomogeneous temperature field leads to a local increase of hydraulic resistance to abnormally thermoviscous liquid flow.

Conclusion

Due to the numerical simulation, the hydrodynamic parameters in the axial and various cross sections of the annular channel have been constructed. The patterns of longitudinal flow velocity, temperature and viscosity field changes depending on the rheological parameters of the fluid characterized by thermoviscous parameters are determined. The essential influence of heat exchange on the hydrodynamic behavior of various thermoviscous liquids has been established.

REFERENCES

1. **Cao H., Li R.**, A liquid plug moving in an annular pipe, Flow analysis Physics of Fluids, 30 (2018).
2. **Bagheri E., Wang B.C.**, Effects of radius ratio on turbulent concentric annular pipe flow and structures, International Journal of Heat and Fluid Flow, 86 (2020).
3. **Lu G., Wang J.**, Experimental investigation on heat transfer characteristics of water flow in a narrow annulus, Applied Thermal Engineering, 28 (2008) 8–13.
4. **Bird R.B., Armstrong R. C., Hassager O.**, Dynamics of Polymeric Fluids, Fluid Mechanics, 1 (1987) 649.
5. **Patankar S.**, Numerical Heat Transfer and Fluid Flow New York, Hemisphere Publishing Corporation, (1980) 200.
6. **Nizamova A.D., Kireev V.N., Urmancheev S.F.**, On stability of thermoviscous liquids laminar flow, Bulletin of Tyumen State University: Ecology and Nature Management, 1 (2) (2015) 104.
7. **Urmancheev S.F., Kireev V.N.**, Steady flow of a liquid with a temperature anomaly of viscosity, Doklady Physics, 49 (5) (2004) 328–333.

THE AUTHORS

MUKHUTDINOVA Aygul A.
muhutdinova18@gmail.com
ORCID: 0000-0002-5009-002X

URMANCHEEV Said F.
said52@mail.ru
ORCID: 0000-0002-1570-5148

KIREEV Victor N.
kireev@anrb.ru
ORCID: 0000-0002-3550-6541

Received 24.10.2022. Approved after reviewing 09.11.2022. Accepted 11.11.2022.

Conference materials

UDC 544

DOI: <https://doi.org/10.18721/JPM.161.146>

Equilibrium shift in chemical reactions

N.A. Charykov^{1,2}, V.V. Kuznetsov¹✉, W. Sadowski³, K.N. Semenov⁴,
V.A. Keskinov², A.A. Blokhin², D.G. Letenko⁵, Z.K. Shamardanov⁶,
B.K. Shaymardanova⁶, N.A. Kulenova⁶, M.A. Sadenova⁶

¹ St. Petersburg Electrotechnical University "LETI", St. Petersburg, Russia;

² St. Petersburg Institute of Technology (Technical University), St. Petersburg, Russia;

³ Gdańsk University of Technology, Gdańsk, Poland;

⁴ Academician I.P. Pavlov First St. Petersburg State Medical University, St. Petersburg, Russia;

⁵ St. Petersburg State University of Architecture and Civil Engineering, St. Petersburg, Russia;

⁶ East Kazakhstan State Technical University, Center "Veritas" Ust-Kamenogorsk, Republic of Kazakhstan

✉ vvkuznetsov@inbox.ru

Abstract. An original approach for describing chemical equilibrium shifts in systems of any physico-chemical nature has been developed. The mathematical expression of the equilibrium principle as formulated by the authors contains, instead of the standard heat and volume changes during a chemical reaction, mixing functions that in some special cases exceed the standard ones. It is shown that in systems with extremely large deviations from ideality (for example, in aqueous solutions of uranyl salts or water-soluble light fullerenes derivatives) the equilibrium shift principle developed by the authors may fundamentally differ from the well-known Le Chatelier-Brown principle).

Keywords: chemical equilibrium, Le Chatelier-Brown principle

Funding: This research has been supported by the Project of Russian Scientific Found (Project № 23-23-00064) and Project of IRN BR10965186 "Development and implementation of geo-information support for "smart" agriculture to improve the management of the agro-industrial complex", funded by the Science Committee of The Ministry of Education and Science of the Republic of Kazakhstan.

Citation: Charykov N.A., Kuznetsov V.V., Sadowski W., Semenov K.N., Keskinov V.A., Blokhin A.A., Letenko D.G., Shamardanov Z.K., Shaymardanova B.K., Kulenova N.A., Sadenova M.A., Equilibrium Shift in Chemical Reactions, St. Petersburg State Polytechnical University Journal. Physics and Mathematics. 16 (1.1) (2023) 275–280. DOI: <https://doi.org/10.18721/JPM.161.146>

This is an open access article under the CC BY-NC 4.0 license (<https://creativecommons.org/licenses/by-nc/4.0/>)

Материалы конференции

УДК 544

DOI: <https://doi.org/10.18721/JPM.161.146>

Смещение равновесия при химической реакции

Н.А. Чарыков^{1,2}, В.В. Кузнецов¹✉, В. Садовски³, К.Н. Семенов⁴,
В.А. Кескинов², А.А. Блохин², Д.Г. Летенко⁵, Ж.К. Шамарданов⁶,
Б.К. Шамарданова⁶, Н.А. Куленова⁶, М.А. Саденова⁶

¹ Санкт-Петербургский государственный электротехнический университет «ЛЭТИ» им. В.И. Ульянова (Ленина), Санкт-Петербург, Россия;

² Санкт-Петербургский государственный технологический институт (технический университет) Санкт-Петербург, Россия;

³ Гданьский политехнический университет, г. Гданьск, Польша;

⁴ Первый Санкт-Петербургский государственный медицинский университет им. академика И.П. Павлова, Санкт-Петербург, Россия;

⁵ Санкт-Петербургский государственный архитектурно-строительный университет, Санкт-Петербург, Россия;

⁶ Восточно-Казахстанский государственный технический университет, Центр «Веритас», г. Усть-Каменогорск, Республика Казахстан

✉ vvkuznetsov@inbox.ru

Аннотация. Разработан оригинальный метод описания сдвигов химического равновесия в системах произвольной физико-химической природы. Математическое выражение принципа в формулировке авторов содержит вместо стандартных теплот и изменений объемов в ходе химической реакции функции смещения, которые в некоторых особых случаях превосходят стандартные. Показано, что в системах с экстремально большими отклонениями от идеальности (например, в водных растворах солей уранила или водорастворимых производных легких фуллеренов) разработанный авторами принцип смещения равновесия может кардинально отличаться от известного принципа Ле Шателье-Брауна.

Ключевые слова: химическое равновесие, принцип Ле-Шателье-Брауна

Финансирование: Исследование выполнено при поддержке Проекта Российского научного фонда (проект № 23-23-00064) и Проекта ИРН BR10965186 «Разработка и внедрение геоинформационного обеспечения «умного» сельского хозяйства для улучшения управления агропромышленным комплексом», финансируемого Комитетом науки Министерства образования и науки Республики Казахстан.

Ссылка при цитировании: Чарыков Н.А., Кузнецов В.В., Садовски В., Семенов К.Н., Кескинов В.А., Блохин А.А., Летенко Д.Г., Шамарданов Ж.К., Шамарданова Б.К., Куленова Н.А., Саденова М.А. Смещение равновесия при химической реакции // Научно-технические ведомости СПбГПУ. Физико-математические науки. 2023. Т. 16. № 1.1. С. 275–280. DOI: <https://doi.org/10.18721/JPM.161.146>

Статья открытого доступа, распространяемая по лицензии CC BY-NC 4.0 (<https://creativecommons.org/licenses/by-nc/4.0/>)

Introduction

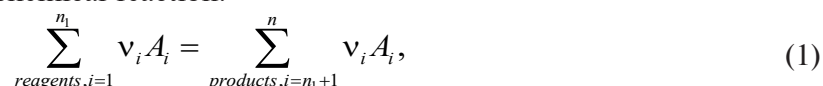
The conditions of chemical equilibrium shifts in the systems with single chemical reaction were elaborated in the classical thermodynamic works and are well known as Le Chatelier-Brown principle or simply Le Chatelier principle. This principle was repeatedly supplemented, justified, and commented in a number of thermodynamic works, e.g., in classical monographs [1–8]. Except of the original author of the principle [9] the fundamental role of J.W. Gibbs should be noted in substantiating this principle [4–6].

The authors consider the presentation in the monograph [10] to be the most successful in terms of simplicity, consistency and generality.

Materials and Methods

Let us consider isolated equilibrium reactions, where reactions have no common reagents or products, or isolated “free” reaction systems. This allows us to consider any reaction separately without taking into account other reactions.

Let us consider equilibrium chemical reaction:



where ν_i is stoichiometric coefficient of molecular A_i in reaction (1), n_1 and n are number of reagents and number of all participants in the reaction (1). Assume that

$$\nu_i < 0 \text{ for reagents } 1 \leq i \leq n_1; \nu_i > 0 \text{ for products } n_1 \leq i \leq n \quad (2)$$

© Чарыков Н.А., Кузнецов В.В., Садовски В., Семенов К.Н., Кескинов В.А., Блохин А.А., Летенко Д.Г., Шамарданов Ж.К., Шамарданова Б.К., Куленова Н.А., Саденова М.А., 2023. Издатель: Санкт-Петербургский политехнический университет Петра Великого.



So, we can simplify eq.(1) to

$$\sum_{i=1}^n \nu_i A_i = 0. \quad (3)$$

Differential equation of chemical equilibrium conservation will be the following:

$$\sum_{i=1}^n \nu_i d\mu_i = 0. \quad (4)$$

Differentiating equation (4) by temperature (T), pressure (P) and molar number of all components (n_i) we get the expression:

$$-\Delta S^{(r)} dT + \Delta V^{(r)} dP - \Delta A f^{(r)} d\xi = 0, \quad (5)$$

where:

$$\Delta S^{(r)} = \sum_{i=1}^n \nu_i S_i, \quad (6)$$

$$\Delta V^{(r)} = \sum_{i=1}^n \nu_i V_i, \quad (7)$$

$$\Delta A f^{(r)} d\xi = \sum_{i=1}^n \nu_i (d\mu_i)_{P,T} = \sum_{i=1}^n \sum_{j=1}^n \nu_i \nu_j G_{ij} d\xi, \quad (8)$$

$$\Delta G^{(r)} = \sum_{i=1}^n \nu_i \mu_i = 0, \quad (9)$$

$$\Delta H^{(r)} = \sum_{i=1}^n \nu_i H_i. \quad (10)$$

In eq.(6–10)

$$S_i = -(d\mu_i / dT)_{P, n_{j \neq i}}, \quad (11)$$

$$V_i = (d\mu_i / dP)_{T, n_{j \neq i}}; H_i = \mu_i + TS_i, \quad (12)$$

are partial molar entropy, partial molar volume and enthalpy of i -th component, respectively; $\Delta A f^{(r)}$ is chemical affinity of reaction (3), ξ is chemical variable, $G_{ij} = (\partial^2 G / \partial n_i \partial n_j)_{T, P, n_{k \neq i, j}}$. According to physical sense, $\Delta S^{(r)}$, $\Delta V^{(r)}$, $\Delta A^{(r)}$, $\Delta G^{(r)}$ are change of entropy, volume, chemical affinity and Gibbs energy, respectively, in the isotherm-isobaric process of the formation of ν_i moles of product $A_i (i = n_1 + 1, n_1 + 2, \dots, n)$ from ν_i moles of reagent $A_i (i = 1, 2, \dots, n_1)$ in the mixed phase (or phases) with infinitely large mass, which contains both reagents and products. According to the sense of ξ :

$$dn_j = \nu_j \xi. \quad (13)$$

According to Sylvester's criterion, bilinear form is then

$$\Delta A f^{(r)} = \sum_{i=1}^n \sum_{j=1}^n \nu_i \nu_j G_{ij} > 0, \quad (14)$$

because the determinant of the matrix of second derivatives is positive:

$$\Delta^{(n)} = \begin{vmatrix} G_{11} & \dots & G_{1n} \\ \vdots & & \vdots \\ G_{n1} & \dots & G_{nn} \end{vmatrix} > 0, \quad (15)$$

where upper index symbolizes determinant dimension. All minors of main diagonal of $\Delta^{(n)}$ are positive also:

$$\Delta^{(n-1)} > 0, \Delta^{(n-2)} > 0, \dots, \Delta^{(1)} > 0, \quad (16)$$

according to the criterion of phase diffusional stability with respect to infinitesimal state changes.

So, one can directly determine the signs of the derivatives:

$$(d\xi/dT)_p = \Delta S^{(r)} / \Delta A f^{(r)} = \Delta H^{(r)} / \Delta A f^{(r)} T > (< or =) 0, \text{ if } \Delta S^{(r)} \text{ or } \Delta H^{(r)} > (< or =) 0, \quad (17)$$

$$(d\xi/dP)_T = -\Delta V^{(r)} / \Delta A f^{(r)} > (< or =) 0, \text{ if } \Delta V^{(r)} > (< or =) 0, \quad (18)$$

$$(dP/dT)_\xi = \Delta S^{(r)} / \Delta V^{(r)} = \Delta H^{(r)} / \Delta V^{(r)} T > (<) 0, \quad (19)$$

if $\Delta V^{(r)}$ and $\Delta S^{(r)}$ have the same (opposite) sign.

Results and Discussion

We compared equations obtained with the classical formulation of the Le Chatelier-Brown principle for chemical equilibrium shift. Standard well-known equations of the Le Chatelier principle for chemical equilibrium shift are the following [8]:

$$(d \ln K_e / dT)_p = d / dT \left[\sum_{i=1}^n \nu_i \ln a_i \right]_p = \Delta H^{(0)} / RT^2, \quad (20)$$

$$(d \ln K_e / dP)_T = d / dP \left[\sum_{i=1}^n \nu_i \ln a_i \right]_T = -\Delta V^{(0)} / RT, \quad (21)$$

where K_e is equilibrium constant of reaction (3); a_i is activity of i -th component; $\Delta H^{(0)}$, $\Delta V^{(0)}$ standard change of enthalpy and standard change of volume in the reaction (3), where the formation of ν_i moles of pure products $A_i (i = n_1+1, n_1+2, \dots, n)$ occurs from ν_i mole of pure reagents $A_i (i = 1, 2, \dots, n_1)$. Moreover, all reagents and products are separated from each other and belong to different pure phases. We immediately get:

$$(d \ln K_e / dT)_p = \left[\sum_{i=1}^n \nu_i^2 (\partial \mu_i / \partial n_i) \right]_{T, P, n_{j \neq i}} (d\xi/dT)_p = Z (d\xi/dT)_p, \quad (22)$$

$$(d \ln K_e / dP)_T = \left[\sum_{i=1}^n \nu_i^2 (\partial \mu_i / \partial n_i) \right]_{T, P, n_{j \neq i}} (d\xi/dP)_T = Z (d\xi/dP)_T, \quad (23)$$

where

$$Z = 1 / RT \left[\sum_{i=1}^n \nu_i^2 (\partial \mu_i / \partial n_i) \right]_{T, P, n_{j \neq i}} > 0, \quad (24)$$

because $(\partial \mu_i / \partial n_i)_{T, P, n_{k \neq j}} > 0$ for all components, according to the criterion of diffusional stability.

So, one can postulate, that, according to the Le Chatelier principle:

$$(d\xi/dT)_p = 1 / Z (\Delta H^{(0)} / RT^2) > (< or =) 0, \text{ if } \Delta H^{(0)} > (< or =) 0, \quad (25)$$

$$(d\xi/dP)_T = -1 / Z (\Delta V^{(0)} / RT) > (< or =) 0, \text{ if } \Delta V^{(0)} < (> or =) 0, \quad (26)$$

And this form is very similar to eq.(17, 18).

Let us assume the difference.

$$\Delta H^{(r)} = \Delta H^{(0)} + \Delta H^{(mix)}; \quad \Delta S^{(r)} = \Delta S^{(0)} + \Delta S^{(mix)}; \quad \Delta V^{(r)} = \Delta V^{(0)} + \Delta V^{(mix)}, \quad (27)$$

where $\Delta F^{(mix)} = \Delta H^{(mix)}$; $\Delta S^{(mix)}$, $\Delta V^{(mix)}$ – are enthalpy, entropy and volume of mixing of reagents-components in the reaction (3) phase, respectively. If products or reagents belong to the different phases with constant composition $\Delta F^{(mix)} = 0$; or, if they form ideal phases-solutions (for example, ideal gaseous solutions), then: $\Delta H^{(mix)} = 0$, $\Delta V^{(mix)} = 0$, and eq.(25, 26) become identical to eq.(17, 18). In the other cases, when products or reagents belong to the same non-ideal phases, as a rule, the following relations between the functions $\Delta F^{(mix)}$ and $\Delta F^{(0)}$ are observed:

$$\Delta F^{(mix)} \ll \Delta F^{(0)} (F = H, S, V). \quad (28)$$

Really, typical values of $\Delta H^{(mix)}$ and $\Delta H^{(0)}$ by absolute values are:

$$\Delta H^{(mix)} = 0 - 10 \text{ kJ / mole}; \quad \Delta H^{(0)} = 0 - 1000 \text{ kJ / mole} \quad (29)$$



and for $\Delta V^{(mix)}$ and $\Delta V^{(0)}$ (gaseous solutions at moderate pressures and temperatures are rare strongly non-ideal):

$$\Delta V^{(mix)} = 0 - 10^{-4} m^3 / \text{mole}; \Delta H^{(0)} = 0 - 10^{-1} m^3 / \text{mole} \quad (30)$$

So, approximate identification of eq. (25, 26) and eq. (17, 18) is also justified.

Two exceptions are the following:

A) The extremely unlikely variant of random coincidences: $\Delta H^{(0)} \approx 0$; $\Delta V^{(0)} \approx 0$ when values of $\Delta H^{(mix)}$; $\Delta V^{(mix)}$ can become decisive.

B) Very high extreme values of positive deviations of excess partial molar functions (activity coefficients γ_i) from the ideality. These cases are realized, in particular, in the systems with the strong hierarchical association, when standard state of dissolved component (normalized on infinitely diluted solution) is far away from its state in real solutions with finite concentrations. The examples of such systems are: $\text{UO}_2\text{Cl}_2\text{-H}_2\text{O}$ at 25 °C, where in the solutions, close to saturation $\gamma_{\text{UO}_2\text{Cl}_2} \approx 1500\text{--}1700$ a.u. [11]; $\text{C}_{60}\text{Sub}_n\text{-H}_2\text{O}$ at 25 °C ($\text{C}_{60}\text{Sub}_n$ is water soluble derivative of fullerene $\text{C}_{60}\text{Sub}_n$ is the substituent: carboxyl, hydroxyl, residues of amino-acid, protein, etc.), where in the comparatively concentrated (but diffusively stable) solutions $\gamma_{\text{C}_{60}\text{Sub}_n} \approx 10\text{--}100$ a.u. [11].

Naturally, use of classical formulations (eq. (25, 26) is very convenient, because data, concerning $\Delta H^{(0)}$ and $\Delta V^{(0)}$ for the reaction are available, and may be simply calculated from tabulated data for all participants of the reaction: standard heats of formation $\Delta H_f^{(0)}$ or standard heats of combustion $\Delta H_c^{(0)}$; isobar heat capacity $C_{p,i}$; standard molar volume $\Delta V_i^{(0)}(T,P)$. But namely for the cases A), B) in practice, eq. (25, 26) are not valid for the description of chemical equilibrium shift in an equilibrium mixture of substances in a natural phase state, and not formally separated for pure components, so eq. (17, 18) look preferable.

Conclusions

Thus, we have developed a method for predicting the shift of chemical equilibrium in highly unideal reaction phases with changes in temperature and pressure, when the classical formulation of the Le Chatelier principle, characterized by the use of standard heats and volume changes, becomes practically inapplicable.

Reaction systems of this type include condensed solutions of nanoclusters, for example, aqueous solutions of water-soluble nanoclusters of fullerene derivatives, such as, for example, $\text{C}_{60}(\text{OH})_{24}\text{-H}_2\text{O}$, which are characterized by extremely high positive deviations from ideality, many times greater than the ideal mixing functions (the natural logarithm of the activity coefficients of nanoclusters with asymmetric normalization of excess functions in such systems can be tens and even hundreds of relative units). The latter circumstance is related to the fact that the state of nanoclusters in real aqueous solutions subject to successive hierarchical association is infinitely far from the standard state corresponding to a hypothetical solution with unit concentration and the properties of an infinitely dilute solution.

REFERENCES

1. Ott B.J., Boerio-Goates J., Chemical Thermodynamics – Principles and Applications. Academic Press, 2000.
2. Servos J.W., Physical Chemistry from Ostwald to Pauling. Princeton University Press, 1990.
3. Bryson, B.A., Short History of Nearly Everything. Broadway Books, (2003) 116–117.
4. Gibbs W.J., Transactions of the Connecticut Academy, III, 108–248, Oct. 1875-May 1876, and 343–524, May 1877-Jul. 1878.
5. Prigogine I., Defay R., Thermodynamique Chimique Conformant aux Methods de Gibbs et De Donder V.I. Paris; Liege;1944 V.II. Paris; Liege, 1946.
6. Donnan F.G., Haas A.A., Commentary on the Scientific Writings of J.W. Gibbs. V.I and II. New Haven, 1936.
7. Guggenheim E.A., Thermodynamics. Amsterdam, 1950. Pp.25.
8. Le Châtelier H.L., Recherches expérimentales et théoriques sur les équilibres chimiques. Annales des mines et des carburants, 1888. 8th ser., N 13, 157–380.
9. Storonkin A.V., Thermodynamics of Heterogeneous Systems. Book I. Part I, II. LGU Leningrad, 1967.

10. **Charykov N.A., Semenov K.N., Keskinov V.V., et al.**, Modeling of systems with aqueous solutions of UO_{22}^{+} salts. An asymmetric model of redundant thermodynamic functions based on the virial decomposition of the Gibbs free energy of the solution-VD-AS. *Radiochemistry*, 59 (2) (2017) 119–126.

11 **Charykov N.A., Semenov K.N., Enriqueta R.L. et al.**, Excess thermodynamic functions in aqueous systems containing soluble fullerene derivatives. *J.of Mol.Liquids*. 256 (2018) 305–311.

THE AUTHORS

CHARYKOV Nikolay A.

ncharykov@yandex.ru

ORCID: 0000-0002-4744-7083

KUZNETSOV Vladimir V.

vvkuznetsov@inbox.ru

ORCID: 0000-0002-9581-9195

SADOWSKI Wojtek

w.sadowski.pg@gmail.com

SEMENOV Konstantin N.

nchary@gmail.com

KESKINOV Victor A.

keski@inbox.ru

BLOKHIN Alexander A.

ncharyk@gmail.com

LETENKO Dmitriy G.

ncari@gmail.com

SHAMARDANOV Zhusulan K.

nchykov@yandex.ru

SHAYMARDANOVA Botogyz K.

char@gmail.com

KULENOVA Natalja A.

arykov@yandex.ru

SADENOVA Marjan A.

cxaz@gmail.com

Received 24.10.2022. Approved after reviewing 14.11.2022. Accepted 14.11.2022.

Conference materials

UDC 532.5, 519.6

DOI: <https://doi.org/10.18721/JPM.161.147>

3D simulation of deformable particle dynamics in channel with hydrodynamic traps

N.B. Fatkullina ¹✉, O.A. Solnyshkina ¹, A.Z. Bulatova ¹, V.A. Andryuschenko ²

¹ Center for Micro and Nanoscale Dynamics of Dispersed Systems, Ufa
University of Science and Technology, Ufa, Russia;

² Kutateladze Institute of Thermal Physics, Novosibirsk, Russia

✉ nazgulbay@mail.ru

Abstract. The importance of adequate simulation of dispersed systems in microchannels with traps is due to the need to solve applied problems arising in the design of microfluidic devices. Depending on the purposes of the devices, the geometry configuration of hydrodynamic traps and their spatial arrangement is chosen. The present work is dedicated to the study of the dynamics of dispersed particles in the viscous fluid flow in a microchannel with hydrodynamic traps. The computational approach is based on the Boundary Element Method, accelerated using the Fast Multipole Method on heterogeneous computing architectures. Simulation results and details of the method are discussed. In addition, the influence of the distance between trap rows and their spatial arrangement on the flow pattern in the microchannel has been investigated.

Keywords: Stokes equations, hydrodynamic traps, microfluidics

Citation: Fatkullina N.B., Solnyshkina O.A., Bulatova A.Z., Andryuschenko V.A., 3D simulation of deformable particle dynamics in channel with hydrodynamic traps, St. Petersburg State Polytechnical University Journal. Physics and Mathematics. 16 (1.1) (2023) 281–287. DOI: <https://doi.org/10.18721/JPM.161.147>

This is an open access article under the CC BY-NC 4.0 license (<https://creativecommons.org/licenses/by-nc/4.0/>)

Материалы конференции

УДК 532.5, 519.6

DOI: <https://doi.org/10.18721/JPM.161.147>

3D моделирование динамики деформируемых частиц в канале с гидродинамическими ловушками

Н.Б. Фаткуллина ¹✉, О.А. Солнышкина ¹, А.З. Булатова ¹, В.А. Андриющенко ²

¹ Центр Микро- и наномасштабной динамики дисперсных систем,
Уфимский университет науки и технологий, г. Уфа, Россия;

² Институт теплофизики СО РАН, г. Новосибирск, Россия

✉ nazgulbay@mail.ru

Аннотация. Важность адекватного моделирования дисперсных систем в микроканалах с ловушками обусловлена необходимостью решения прикладных задач, возникающих при проектировании микрофлюидических устройств. В зависимости от назначения устройств выбирается геометрическая конфигурация гидродинамических ловушек и их пространственное расположение. Настоящая работа посвящена исследованию динамики дисперсных частиц в потоке вязкой жидкости в микроканале с гидродинамическими ловушками. Вычислительный подход основан на методе граничных элементов, ускоренном с помощью метода быстрых мультиполей на гетерогенных вычислительных архитектурах. Результаты моделирования показывают влияние расстояния между рядами ловушек и их пространственного расположения на характер течения в микроканале.

Ключевые слова: уравнения Стокса, гидродинамические ловушки, микрогидродинамика

Ссылка при цитировании: Фаткуллина Н.Б., Солнышкина О.А., Булатова А.З., Андрущенко В.А. 3D моделирование динамики деформируемых частиц в канале с гидродинамическими ловушками // Научно-технические ведомости СПбГПУ. Физико-математические науки. 2023. Т. 16. № 1.1. С. 281–287. DOI: <https://doi.org/10.18721/JPM.161.147>

Статья открытого доступа, распространяемая по лицензии CC BY-NC 4.0 (<https://creativecommons.org/licenses/by-nc/4.0/>)

Introduction

Three-dimensional simulation of viscous fluid flow in microchannels with hydrodynamic traps is important for the design of microfluidic devices (MFDs). Currently, there is a remarkable expansion in the application of different types of MFDs. One of the applications of MFDs is the accurate manipulation of the particles in the flow, e.g. for particle fixation and sorting. At this stage of technological development, many technical approaches to particle and cell capture in microfluidic devices are known. Microfluidic devices are classified according to their functionality into the following categories: sorting or separation of particles, fixation and holding of particles, cultivation of biological objects (cells, bacteria, etc.), sample preparation or sample processing [1]. Depending on the MFD design purposes, various geometry configurations of hydrodynamic traps and their spatial arrangement are chosen. Particle trapping by arrays of microposts is a horizontal trapping method, which can be implemented by simply blocking particles whose size exceeds the distance between neighboring columns. In this approach, the distance between the posts must be adapted to the size of the target particles [2]. One problem with this type of trap, which reduces trapping efficiency, is that particles or droplets can deform and can be pushed through the gaps between the posts. Thus, it is extremely important to select the optimal geometric parameters when designing different types of MFDs.

To solve this problem and reduce the time cost of the experimental research, various numerical approaches for simulation of physical processes at the microscale are actively used. Simulation of emulsion dynamics can be carried out by different numerical approaches, for instance, the Volume of Fluid method [3], the Finite Element Method [4]. However, the high-efficiency computational approaches are required for a more detailed description of the particle deformation in the three-dimensional case in the channels of microfluidic devices. However, such problems have not been solved yet for the flow of deformable droplets in such configurations in 3D case using the Boundary Element Method (BEM). The purpose of this research is to study the efficiency of trap configurations using a numerical approach based on 3D BEM accelerated using a scalable algorithm (FMM – fast multipole method) and a heterogeneous computational architecture (CPUs and GPUs).

Problem statement and mathematical model

This study is devoted to the problem of viscous fluid flow with deformable particles in microchannels with C-shaped hydrodynamic traps under the constant volumetric flow. An array of microposts is a simple and clear method of blocking the particles in the flow. C-traps are represented as cylindrical elements of equal radius, located at equal distances from each other across the flow. Such traps are used in practice to capture of the particles. Two types of traps, symbolized as C4 and C5 (Fig. 1), are considered, as well as two spatial configurations of trap locations: in the form of a triangular array and in chess order. At a certain distance from the trap array, there are several initially spherical droplets.

The processes are considered at small Reynolds numbers under isothermal conditions. The flow of particles (index 2) in incompressible Newtonian fluid (index 1) is described by steady Stokes equations

$$-\nabla p_i + \mu_i \nabla^2 \mathbf{u}_i = 0, \quad \nabla \cdot \mathbf{u}_i = 0, \quad i = 1, 2, \quad (1)$$

where p is a pressure, μ is a dynamic viscosity, \mathbf{u} is a velocity vector.



At the interface, the velocities coincide and the difference of normal stress vectors is set

$$\mathbf{u}_1 = \mathbf{u}_2, \quad \mathbf{f} = \boldsymbol{\sigma}_1 \cdot \mathbf{n} - \boldsymbol{\sigma}_2 \cdot \mathbf{n} = \mathbf{f}_1 - \mathbf{f}_2 = f\mathbf{n}, \quad f = 2\gamma k(\mathbf{x}) + (\rho_1 - \rho_2)(\mathbf{g} \cdot \mathbf{x}), \quad \mathbf{x} \in S_d, \quad (2)$$

where \mathbf{f} is a traction, $\boldsymbol{\sigma}$ is a stress tensor, ρ is the liquid density. On the surface of the non-deformable fixed cylindrical elements forming the trap, the non-slip condition is set

$$\mathbf{u}(\mathbf{x}) = 0, \quad \mathbf{x} \in S_s, \quad \mathbf{x} \in S_s, \quad (3)$$

where S_s is the total rigid elements surface. Droplet motion is characterized by the kinematic condition

$$\frac{d\mathbf{x}}{dt} = \mathbf{u}(\mathbf{x}), \quad \mathbf{x} \in S_d, \quad (4)$$

where $\mathbf{u}(\mathbf{x})$ is the interface velocity, \mathbf{x} is the radius-vector of the point, and S_d is the particle surface.

Three-dimensional simulation of fluid flow and dynamics of non-deformable droplets was performed using software modules based on the accelerated BEM. The basic idea of this method is as follows. The initial differential equations describing the behavior of the function inside and on the domain boundary are reduced to the integral equations that relate only the boundary values. This is one of the main advantages of the BEM, since it eliminates the need to discretize the entire 3D domain. The triangular mesh covers only the surfaces of the considering object. BEM is well suitable for describing three-dimensional particle dynamics with random deformation in domains with complex geometry, as well as in shear flows in an unbounded domain. However, it becomes more difficult to apply the standard non-accelerated BEM for large-scale problems. In this work, the standard BEM is accelerated using both a scalable algorithm (FMM) and a heterogeneous computational architecture. The description of the approach in more detail can be found in [5, 6].

Numerical results and discussion

Viscous fluid flow around the hydrodynamic traps in microchannel. Two hydrodynamic trap configurations are considered in this study (Fig. 1). The C4 trap is presented in the form of four non-deformable cylindrical elements arranged in a semicircle. The cross section of each element has a radius R . The C5 trap consists of five cylinders of the same radius, arranged similarly to the C4 trap. The main difference between the C4 and C5 trap configurations is the number of elements and their spatial arrangement relative to each other. Trap length – L_{trap_x} $6.25 \cdot R$, width – L_{trap_z} $9 \cdot R$, height – L_{trap_y} $10 \cdot R$. Reynolds number was calculated as $Re = 2\rho Q/(\mu(w+h))$, where Q is the liquid volume flow rate, w is the microchannel width, h is the microchannel height. The resulting Re varied from 0.4 to 0.7.

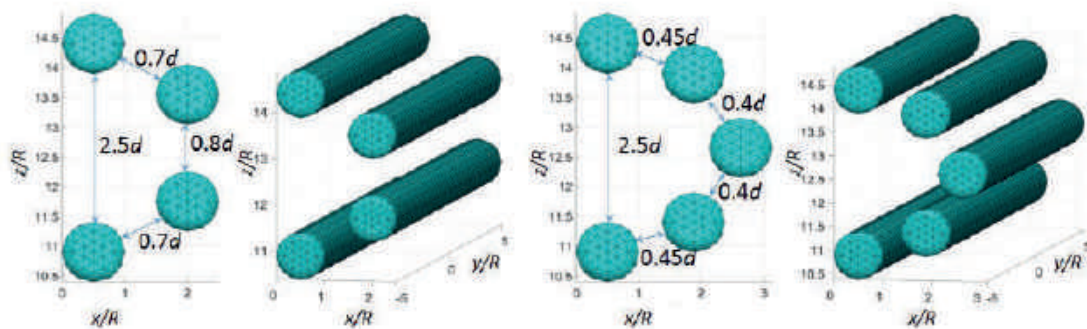


Fig. 1. C4 and C5 hydrodynamic traps configuration

One can see in Fig. 1, there is a narrow channel between the cylindrical elements of the C-trap, which is proportional to the diameter of the cylinder. Such a trap design allows for reducing hydrodynamic resistance in the microfluidic device. Simulation of creeping flows in complex three-dimensional domains consisting of similar traps was carried out in our previous work [7].

To predict the motion of droplets in the fluid flow in a microchannel with complex structure, streamlines for fluid flow without inclusions were initially obtained.

Two cases of the hydrodynamic traps arrays with different spatial configurations of C4 and C5 traps are considered. The total number of traps was 15. The distance between trap rows was $d_x = 2 \cdot L_{trap_x}$, where L_{trap_x} is the width of the trap along the Ox axis. Also, the velocity fields of viscous fluid flow in the microchannel with these spatial arrangements of the traps were calculated (Fig. 2).

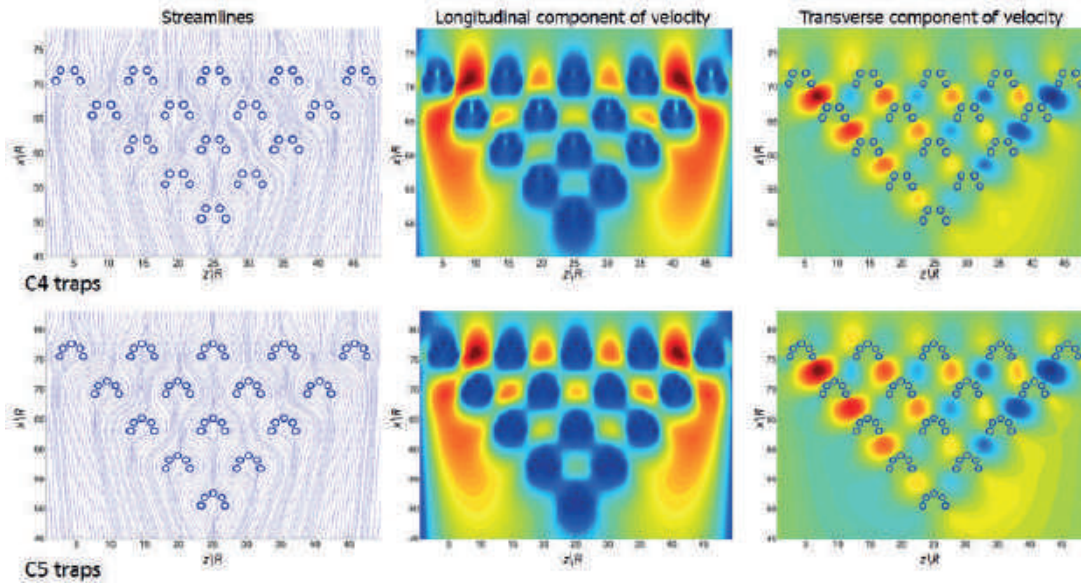


Fig. 2. Streamlines, longitudinal, and transverse components of viscous fluid flow velocity around the triangular array of traps

According to the figures, it can be seen that the greatest velocity of the fluid flow is observed near the walls of the microchannel. The cylindrical element located in the center of the C5 trap creates additional hydrodynamic resistance. This affects the velocity of the fluid flow. That is, the fluid flow velocity is minimal in the center of the C5 trap. This affects the trapping of droplets as they flow in the carrier fluid.

The next configuration consists of 22 hydrodynamic traps located in five rows across the fluid flow in a staggered pattern. The distance between trap rows was also $d_x = 2 \cdot L_{trap_x}$. Fig. 3 shows the streamlines, longitudinal and transverse components of the fluid flow velocity around the trap array, arranged in a chess order.

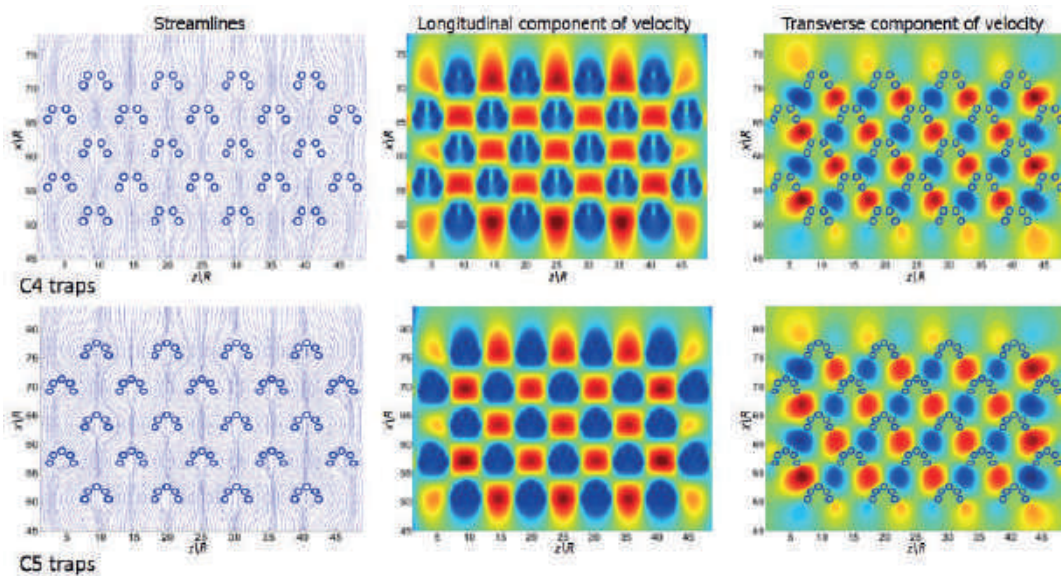


Fig. 3. Streamlines, longitudinal, and transverse components of viscous fluid flow velocity around the chess array of traps



Dispersed particles dynamics in microchannel with hydrodynamic traps. To study droplet dynamics in viscous fluid flow around hydrodynamic traps, droplets of different sizes were considered. The drop diameter ranged from $a = 0.5 \cdot d$ to $a = 1.5 \cdot d$, the distance between the drop centers along the Oz axis was $5 \cdot d$. The ratio of the droplet viscosity to the carrier fluid viscosity was $\lambda = \mu_2/\mu_1 = 10$.

There were $N = 642$ points or $N_{\Delta} = 1280$ triangular elements on each droplet surface. The total computational domain was covered by a triangular mesh consisting of $N_{\Delta} = 367800$ elements for a triangular traps arrangement and $N_{\Delta} = 427440$ for a chess arrangement. Thus, at each time step, the system of linear algebraic equations with more than 10^6 unknowns was solved on a workstation equipped with two Intel Xeon 5660 and one NVIDIA Tesla K20.

Initially, droplets have a spherical shape and are arranged in one row. After some simulation time in the flow, the drops are deformed and fixed in C-shaped hydrodynamic traps, moving according to the flow streamlines, or pass through the gaps between the cylindrical elements due to a change in their shape caused by deformation.

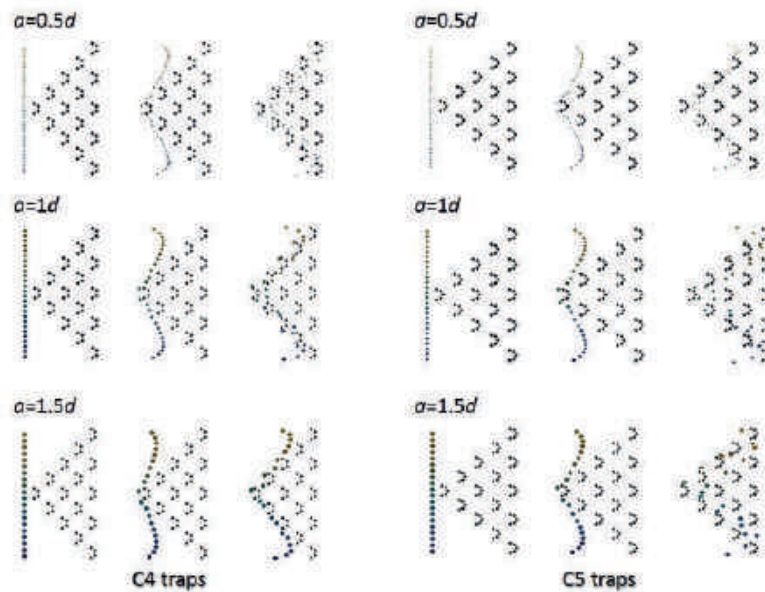


Fig. 4. Trapping of droplets of different radii (triangular array of traps) at non-dimensional time instants $t=0$, $t=15$, $t=30$ (from left to right)

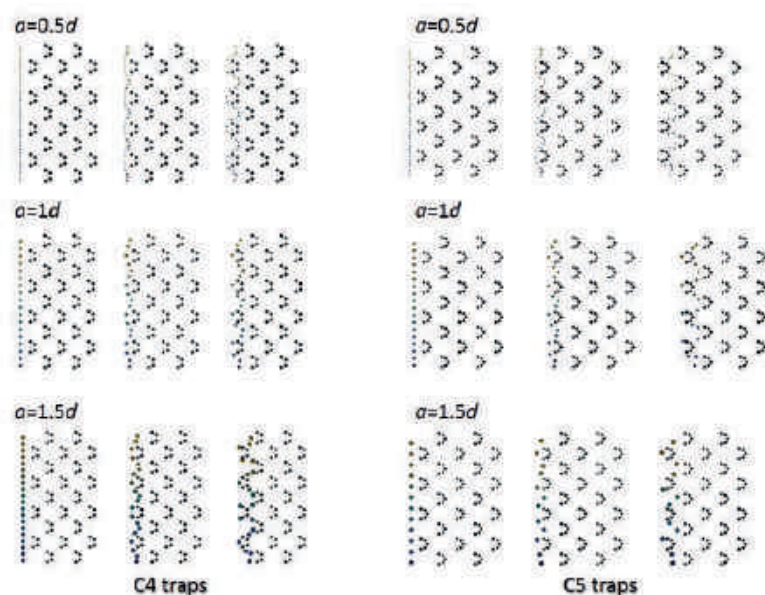


Fig. 5. Trapping of droplets of different radii (chess array of traps) at non-dimensional time instants $t=0$, $t=15$, $t=30$ (from left to right)

Fig. 4 shows the dynamics of droplets in a microchannel with C4 and C5 hydrodynamic traps arranged in the form of a triangle. The spatial arrangement of droplets of different radii relative to hydrodynamic traps at the time moments $t=0$, $t=15$, $t=30$ is shown. Note that these computations are performed for the non-dimensional time $t = t_{non-dim} = \gamma t_{dim} / (\mu_1 a)$. Fig. 5 demonstrates the dynamics of trapping of deformable droplets of different radii by hydrodynamic traps arranged in a chess order at the same moments of time.

Calculation results on Fig. 4 and Fig. 5 show that droplets move faster in the case of a triangular trap arrangement, because the total hydrodynamic resistance of the channel with a trap section in the triangular case is lower than for a chess arrangement of the traps. In addition, due to significant hydrodynamic resistance, the particles tend to flow around the traps in the main liquid flow, rather than flowing into the trap. Thus, the chess arrangement of the traps is preferable because the traps in each successive row are located in the area of maximum flow velocities. The efficiency of droplet capture also depends significantly on the particle size and deformability. Larger droplets are trapped faster compared to smaller ones. The trapping of deformable particles is faster in case of the C4 trap than in case of the C5 trap.

Conclusion

The numerical approach based on the accelerated boundary element method has been applied to study the dynamics of deformable inclusions in microchannels with hydrodynamic traps in three-dimensional case. The streamlines and components of liquid flow velocity in a flat microchannel of rectangular cross section around the traps of two configurations (C4 and C5, arranged in chess order and in the form of a triangle) were obtained. The results of the simulation of the dynamics of deformable droplets of different radii in the microchannel with hydrodynamic traps have been obtained. It is revealed that with each successive row in the trap array, the efficiency of trapping of deformable droplets increases.

The results showed that the velocity components change significantly with increasing distance between the traps, which affects the dynamics of particles in the considered segment of the microchannel. From the obtained flow patterns, it can be concluded that the capture efficiency of particles with a larger distance between the traps will be higher. It is shown that for qualitative fixation of droplets, it is necessary to select the optimal size and geometry of traps, taking into account the deformability of droplets.

Acknowledgments

The investigation was financially supported by IT SB RAS (Project No. 122020200256-6).

REFERENCES

1. Kukhtevich I.V., Evstrapov A.A., Bukatin A.S., Microfluidic devices for cell research (review), *Scientific instrumentation*. 23 (4) (2013) 66–75.
2. Xu X., Li Z., Nehorai A., Finite element simulations of hydrodynamic trapping in microfluidic particle-trap array systems, *Biomicrofluidics*. 7 (2013) 1–17.
3. Kovaleva L.A., Musin A.A., Fatkhullina Yu.I., Microwave Heating of an Emulsion Drop, *High Temperature*. 56 (2) (2018) 234–238.
4. Rezaei B., Zand M.M., Javidi R., Numerical simulation of critical particle size in asymmetrical deterministic lateral displacement, *Journal of Chromatography A*. 1649 (462216) (2021).
5. Solnyshkina O.A., Batyrshin E.S., Pityuk Yu.A., Investigation of Hydrodynamic Flows in Micromodels of Double Porosity Media, *Fluid Dynamics*. 56 (4) (2021) 451–459.
6. Abramova O.A., Pityuk Yu.A., Gumerov N.A., Akhatov I.S., Numerical simulation of the hydrodynamic flow of a viscous fluid around the fixed elements of various cross-section shapes, *Communications in Computer and Information Science*. 965 (2019) 427–438.
7. Solnyshkina O.A., Fatkullina N.B., Viscous fluid flow in a microchannel with hydrodynamic traps, *Journal of Physics: Conference Series*. 1675 (1) (2020) 1–7.



THE AUTHORS

FATKULLINA Nazgul B.
nazgulbay@mail.ru
ORCID: 0000-0002-3944-1976

BULATOVA Aiguzel Z.
bulatova29@yandex.ru
ORCID: 0000-0003-1741-7024

SOLNYSHKINA Olga A.
olgasolnyshkina@gmail.com

ANDRYUSCHENKO Vladimir A.
vladimir.andrushenko@gmail.com

Received 26.10.2022. Approved after reviewing 08.11.2022. Accepted 16.11.2022.

Conference materials

UDC 532.5; 519.6

DOI: <https://doi.org/10.18721/JPM.161.148>

Numerical study of the rheological characteristics of dispersed systems in shear flow using the boundary element method

A.Z. Bulatova ¹✉, O.A. Solnyskina ¹, N.B. Fatkullina ¹

¹Center for Micro and Nanoscale Dynamics of Dispersed Systems,
Ufa University of Science and Technology, Ufa, Russia

✉ bulatova29@yandex.ru

Abstract. Dispersed systems are widely used in chemical, biochemical and pharmaceutical industries. This work is dedicated to the study of the dependence of macroscopic parameters of emulsions, such as effective viscosity, on the microlevel structure and physical properties of emulsion droplets. The numerical approach is based on the accelerated boundary element method in three dimensions. In this paper, we consider the dynamics of two close deformable droplets of equal radius in the volume of a viscous incompressible fluid under the action of a shear flow. Time evolution of minimal distance between droplet surfaces has been considered. A parametric study of the dispersed phase contribution to the stress tensor of a dispersed system as a whole, as well as the first and second differences of normal stresses, is conducted.

Keywords: dispersed systems, shear flow, rheology, boundary element method

Funding: The reported study was funded by the Russian Science Foundation within the research project No. 21-79-10212.

Citation: Bulatova A.Z., Solnyshkina O.A., Fatkullina N.B., Numerical study of the rheological characteristics of dispersed systems in shear flow using the boundary element method, St. Petersburg State Polytechnical University Journal. Physics and Mathematics. 16 (1.1) (2023) 288–294. DOI: <https://doi.org/10.18721/JPM.161.148>

This is an open access article under the CC BY-NC 4.0 license (<https://creativecommons.org/licenses/by-nc/4.0/>)

Материалы конференции

УДК 532.5; 519.6

DOI: <https://doi.org/10.18721/JPM.161.148>

Численное исследование реологических характеристик дисперсных систем в сдвиговом потоке с использованием метода граничных элементов

А.З. Булатова ¹✉, О.А. Солнышкина ¹, Н.Б. Фаткуллина ¹

¹Центр Микро и Наномасштабной динамики дисперсных систем,
Уфимский университет науки и технологий, г. Уфа, Россия

✉ bulatova29@yandex.ru

Аннотация. Дисперсные системы широко используются в химической, биохимической и фармацевтической промышленности. Данная работа посвящена исследованию зависимости макроскопических параметров эмульсий, таких как эффективная вязкость, от микроуровневой структуры и физических свойств капель эмульсии. Численный подход основан на ускоренном методе граничных элементов. В данной работе рассматривается динамика двух близкорасположенных деформируемых капель равных радиусов в объеме вязкой несжимаемой жидкости под действием сдвигового потока. Рассмотрено изменение минимального расстояния между поверхностями капель во времени. Проведено многопараметрическое исследование вклада дисперсной фазы в тензор напряжений дисперсной системы в целом, а также первой и второй разностей нормальных напряжений.



Ключевые слова: дисперсные системы, сдвиговый поток, реология, метод граничных элементов

Финансирование: Исследование выполнено при финансовой поддержке Российского научного фонда в рамках научного проекта № 21-79-10212.

Ссылка при цитировании: Булатова А.З., Солнышкина О.А., Фаткуллина Н.Б. Численное исследование реологических характеристик дисперсных систем в сдвиговом потоке с использованием метода граничных элементов // Научно-технические ведомости СПбГПУ. Физико-математические науки. 2023. Т. 16. № 1.1. С. 288–294. DOI: <https://doi.org/10.18721/JPM.161.148>

Статья открытого доступа, распространяемая по лицензии CC BY-NC 4.0 (<https://creativecommons.org/licenses/by-nc/4.0/>)

Introduction

The studying of the behavior, dynamics and physical properties of the dispersed systems (emulsions, suspensions, and bubbly liquids) is relevance due to their widespread use in industry [1-3]. Emulsions occur at all stages of production, processing and transportation of raw materials in the oil industry and the ability to predict the values of rheological characteristics is of great importance. Studies performed over many decades have shown that not only the volume concentration of the dispersed phase, but also the droplet size has a significant influence on the rheology of the disperse system [2].

There are also a number of theoretical models for calculating the rheological characteristics of such dispersed systems, but most of them are based on the Einstein formula with various modifications for more concentrated systems, as well as for various nonspherical forms of solid dispersed inclusions. A large number of published works refer to the study of the rheology of suspensions. Dispersed systems consisting of liquid droplets suspended into another liquid have received much less attention, despite the fact that the rheological behavior of emulsions is much more complicated. For example, suspensions at low concentrations of spherical solids behave as Newtonian fluids, while emulsions of deformable particles demonstrate pseudoplastic and viscoelastic properties even at low volume concentrations of the dispersed phase [3]. In [4–5] peculiarities of non-Newtonian flow of suspensions are explained by changes in their structure, in particular, by appearance and destruction of aggregates of particles. The difficulty of developing theoretical models for determining the rheological characteristics of emulsions consisting of liquid deformable droplets of arbitrary size and distribution is due to the fact that it is quite difficult to predict in advance the shape of a deformed droplet, since it will change differently under the combined action of viscous forces and surface tension forces. Therefore, the use of modern computational approaches to direct calculation of the stress tensor components is a convenient and effective tool for conducting studies of the influence of emulsion microstructure on their rheology.

Among numerical methods of emulsion dynamics modeling, the most widely used ones are the finite-difference methods, the finite-element method, the volume of fluid [6] and the boundary-element method (BEM). The above-mentioned approaches are distinguished between each other by the way of representation of the computational domain and mathematical basis. The purpose of this work is to apply the developed software based on the 3D boundary element method to calculate the effect of droplet deformation during interaction in a shear flow on the values of stress tensor components.

Problem Statement and Numerical Implementation

Mathematical model.

The dynamics of two closely spaced droplets of one Newtonian liquid (index 2) in an unbounded volume of a viscous incompressible fluid (index 1) in a shear flow is considered. It is assumed that the flow is sufficiently slow, therefore inertial effects can be disregarded. The processes are considered for small Reynolds numbers ($Re \ll 1$), at moderate Strouhal numbers $St \sim 1$, in isothermal conditions ($T = const$), and without taking into account the interaction forces between dispersed inclusions (Van der Waals forces).

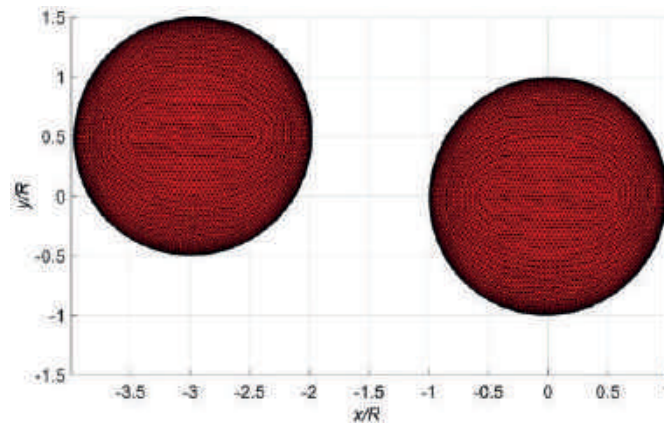


Fig. 1. Discretization of two closely spaced droplets at an initial moment in the xOy plane

The dynamics of the considered system are described by the Stokes equations

$$\nabla \cdot \boldsymbol{\sigma}_i = -\nabla p_i + \mu_i \nabla^2 \mathbf{u}_i = 0, \quad \nabla \cdot \mathbf{u}_i = 0, \quad i = 1, 2, \quad (1)$$

where $\boldsymbol{\sigma}$ is the stress tensor, p is the pressure, μ is the dynamic viscosity, \mathbf{u} is the velocity vector.

The problem is solved under the following boundary conditions. The velocities at the interface are equal and the traction is given

$$\mathbf{u}_1 = \mathbf{u}_2 = \mathbf{u} \quad (2)$$

$$\mathbf{f} = \boldsymbol{\sigma} \cdot \mathbf{n} = \mathbf{f}_1 - \mathbf{f}_2 = f\mathbf{n}, \quad f = \gamma(\nabla \cdot \mathbf{n}) + (\rho_1 - \rho_2)(\mathbf{g} \cdot \mathbf{x}), \quad \mathbf{x} \in S, \quad (3)$$

where \mathbf{n} is the normal to the surface that is directed into the dispersion medium (liquid with index 1), γ is the surface tension coefficient, ρ is the liquid density, \mathbf{g} is the gravity vector, \mathbf{x} is the radius vector of the considered point, S is the drop surface. The constant velocity is specified at the infinity, $\mathbf{u}_1(\mathbf{x}) \rightarrow \mathbf{u}_\infty(\mathbf{x})$.

The dynamics of the fluid-fluid interface can be determined from the kinematic condition

$$\frac{d\mathbf{x}}{dt} = \mathbf{u}(\mathbf{x}), \quad \mathbf{x} \in S. \quad (4)$$

The numerical method for solving the problem is based on the boundary element method. The BEM is well applicable for studying the motion of droplets with arbitrary deformation and for simulation of large volume liquid-liquid systems in infinite domains, because the requirement to completely discretize the three-dimensional domain is eliminated. Only the surfaces of the considered objects are covered by triangular mesh (Fig. 1). The BEM for the flows in the Stokes regime is described in [7] and has been successfully employed to calculate the dynamics and interaction of droplets, bubbles, and solid particles in disperse flows [8–12].

Calculation of the rheological characteristics.

In this paper, we used the approach [13, 14] based on the proposition that the stress tensor of the system Σ is calculated as a stress tensor \mathbf{T} averaged over the isolated volume of the dispersed medium V

$$\Sigma = \frac{1}{V} \int_V \mathbf{T} dV. \quad (5)$$

It was deduced that if the dispersion phase is also a Newtonian fluid and the motion occurs at small Reynolds numbers, then for an emulsion in shear flow $\mathbf{u}_\infty(\mathbf{x}) = (Gy; 0; 0)$ the stress tensor is defined as

$$\sigma_{ij} = -\delta_{ij} p + 2\mu_1 e_{ij} + \alpha \Sigma_{ij}, \quad (6)$$

$$\Sigma_{ij} = \frac{1}{V_2} \int_S [f_i x_i - \mu_1 (1 - \lambda)(u_i n_j + u_j n_i)] dS, \quad i, j = 1, 2, 3, \quad (7)$$



where α is the volume concentration of the dispersed phase, $\lambda = \mu_2/\mu_1$ is the viscosity ratio of the liquid inside droplet volume and outside.

The geometry of the droplets, i.e. their deformation and orientation in space, has a significant influence on the emulsion stress tensor. Based on the calculated velocities and the traction on the surface of each droplet contained in the emulsion volume, one can determine the effective viscosity, first and second differences of normal components of the stress tensor using the following formulae

$$\mu_{eff} = \mu_1 + \alpha \Sigma_{12}^d / G, \quad (8)$$

$$N_1 = \alpha (\Sigma_{11}^d - \Sigma_{22}^d), \quad (9)$$

$$N_2 = \alpha (\Sigma_{22}^d - \Sigma_{33}^d), \quad (10)$$

where μ_{eff} is the effective viscosity of the emulsion, N_1 and N_2 are the first and second normal stress differences correspondingly, the index d denotes the contribution to the stress tensor components from the drops.

To validate the method for determining the rheological characteristics of dispersed systems, the calculated contribution of a single drop to the emulsion stress tensor was compared with the numerical results reported in the literature [15]. The comparison for several values of capillary numbers and for $\lambda = 6.4$ and $\lambda = 1$ were shown a good coincide of the results and were discussed in more details in our previous work [12]. Furthermore, we tested this approach for case of non-spherical rigid particles [10] and for calculation of effective viscosity of suspension with spherical rigid particles and monodispersed and polydispersed emulsions [12].

We consider the dynamics of two closely spaced droplets with high discretization containing $N_\Delta = 20480$ triangular elements on the each droplet surface (Fig. 1). The combination of parameters that describes the deformation of droplets and it's orientation in the shear flow of a viscous incompressible fluid includes the viscosity ratio λ , and the capillary number $Ca = \mu R G / \gamma$, where R is droplet radius, G is shear rate. The calculations have been performed for a range of Ca capillary numbers $Ca = [0.25, 0.5]$ and viscosity ratio $\lambda = 5$. Initially, droplets have a spherical shape and equal size. We consider two values of the distance between coordinates of droplet mass centers along y -axis $dy = 1R$, $dy = 0.7R$, and the distance along x - and z -axes is the same for all cases: $dx = 3R$, $dz = 0$. Under the action of constant shear flow the droplets deform and move and also the distance between droplets' surfaces changes Fig. 2 demonstrates the variation in time of the minimum distance between the droplet surfaces in cases $Ca = 0.3$ (b) and $Ca = 0.25$ (a) ($t = t_{nondim} = \gamma t_{dim} / (\mu_1 R)$ is the dimensionless time, t_{dim} is the dimension time). At the initial moment, the distance between droplet surfaces was $h_{min} = 1.08R$ and $h_{min} = 1.16R$.

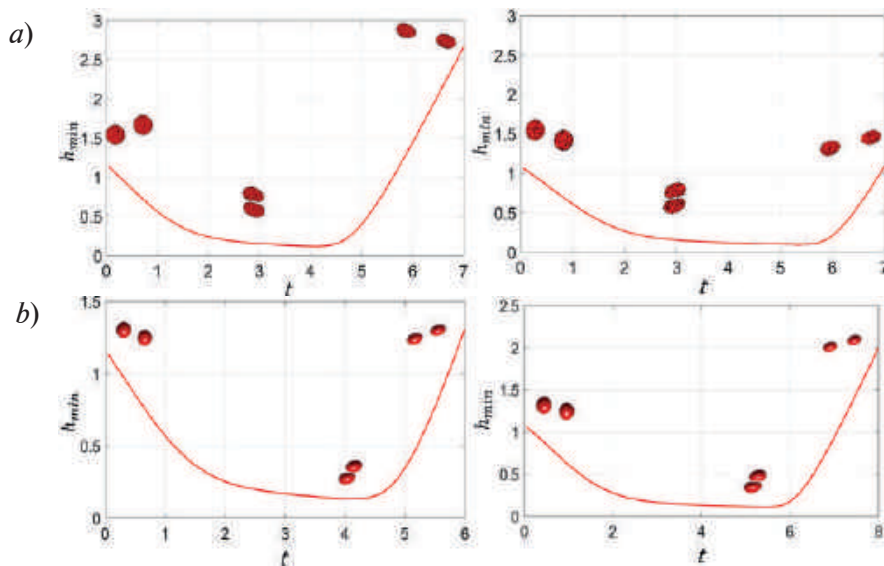


Fig. 2. Time evolution of the minimum distance between the droplets surfaces $Ca = 0.25$ (a), $Ca = 0.3$ (b), $\lambda = 5$, $dy = 1R$ (left column) and $dy = 0.7R$ (right column)

Fig. 2 demonstrates the time evolution of the distance between droplet surfaces. The general behavior of the curves is similar for all considered cases. When the drops move in the flow relative to each other, they approach each other up to some minimum values of the distance between the surfaces. The graph shows a zone of close contact of the drops, when the value h_{min} is minimal and changes insignificantly, and the drops have the maximum effect on the deformation and dynamics each other. The drops coalescence does not occur, and after the end of the close contact zone, the distance between droplets increases. One can see from the Fig. 2 that the smaller the initial distance, the longer the zone of close contact between the drops for both values of the capillary number.

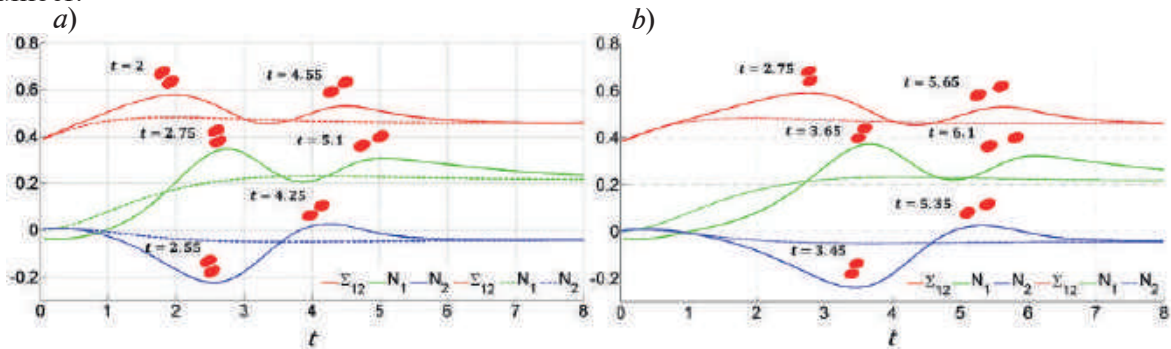


Fig. 3. Time evolution of rheological characteristics of the system in time at $Ca = 0.25$, $\lambda = 5$, $dy = 1R$ (a) and $dy = 0.7R$ (b); solid lines – contribution values of one droplet in case of two close droplets, dashed lines – contribution values of one single droplet in shear flow

The changing of the contribution from two droplets in the rheological functions of the system was investigated. The case when the droplets are a sufficient distance apart, matches the case of dilute emulsion so that the droplets do not influence each other, hence the rheological characteristics of the emulsion do not change in time. However, when considering two close droplets, the influence of the droplets on each other can be observed as in case of more concentrated emulsions, resulting in changes in rheological functions over time. Fig. 3 demonstrates the time evolution of the rheological characteristics (contribution to the effective viscosity of the system Σ_{12} , the first difference of normal stresses N_1 , the second difference of normal stresses N_2) calculated for one of the two interacting droplets (solid lines) and for the single droplet with the same parameters in shear flow (dashed lines). The curves on Fig. 3 demonstrate that the contribution to the components of the stress tensor for interacted droplets differs significantly from the case of well-separated droplets. When the droplets are far enough, their influence on deformation on each other is minimized, and rheological characteristics take constant values. The values of the first and second normal stress difference are indicators of the non-Newtonian behavior of the system and are most different from zero when the droplets are close enough to each other and affect each other, which corresponds to the case of concentrated emulsions.

Furthermore, the effect of droplet deformability on the calculated values of the contributions to the components of the stress tensor was considered. The calculations of Σ_{12} , N_1 , N_2 were conducted for different values of capillary numbers $Ca = [0.25, 0.5]$ in case of two droplets with

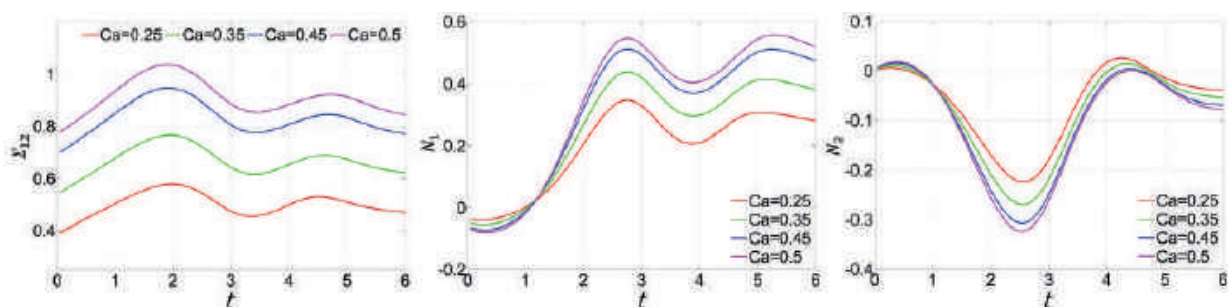


Fig. 4. Time evolution of rheological characteristics of the system in time at different Ca , $\lambda = 5$, $h_{min} = 1.16R$



initial distance between the surfaces $h_{min} = 1.16R$ and for $\lambda = 5$. Fig. 4 demonstrates the time evolution of the rheological characteristics of the system for droplets with different Ca . The graphs show that as Ca and droplet deformability increases, the droplet contribution to the system stress tensor increases.

Conclusion

The possibility of applying the computational approach based on the accelerated three-dimensional boundary element method to the problems of calculating the components of the stress tensor of various types of disperse systems is demonstrated. The dependence of rheological characteristics of the emulsion on its microstructure (relative position and deformability of the droplets) has been investigated. Numerical experiments of the study of the dynamics of two closely spaced droplets in a shear flow have been performed in cases of $Ca = [0.25, 0.5]$, $\lambda = 5$, and different distance between droplets. Reducing this distance increases the contribution to the effective viscosity of the dispersed systems as a whole. The results of calculations of the values of the first and second normal stress differences showed that in the case of more concentrated emulsions, when the droplets actively interact with each other, there will be appear the non-Newtonian effects. It is shown, that the highest values of the stress tensor components correspond to the most deformable drops. The study of changing rheological characteristics at close contact between droplets shows that the properties of the emulsion flow in different areas, for example in microchannels, at dense packing of particles, i.e. when the contact surface between droplets significantly increases, is determined not only by the position and dynamics of droplets in the flow, but also by the nature of interaction between droplets at their close contact. Thus, direct numerical simulation of the emulsion flow consisting of deformable droplets can be utilized for a more complete and reliable description of the rheological features depending on the microstructure.

Acknowledgments

The reported study was funded by the Russian Science Foundation within the research project No. 21-79-10212.

REFERENCES

1. **Edwards D.A., Brenner H., Wasan D.T.**, Interfacial Transport Processes and Rheology, Waltham: Butterworth-Heinemann, Boston, 1991.
2. **Deshpande A.P., Krishnan J.M., Sunil P.B., etc.**, Rheology of Complex Fluids, Springer, New York, 2010.
3. **Malkin A., Isayev A.I.**, Rheology: Concepts, Methods, and Applications, Chem Tec, Toronto, 2012.
4. **Jafari S.M., Assadpoor E., He Y.H., Bhandari B.**, Re-coalescence of emulsion droplets during high-energy emulsification, *Food Hydrocolloids*. 22 (7) (2008) 1191–1202.
5. **Zinchenko A.Z., Davis R.H.**, General rheology of highly concentrated emulsions with insoluble surfactant, *J. Fluid Mech.* 816 (2017) 661–704.
6. **Kovaleva L., Zinnatullin R., Musin A., Gabdrifikov A., Sultanguzhin R., Kireev V.**, Influence of radio-frequency and microwave electromagnetic treatment on water-in-oil emulsion separation, *Colloids and Surfaces A: Phys. and Eng. Aspects*. 614 (2021) 126081.
7. **Pozrikidis C.**, Boundary Integral and Singularity Methods for Linearized Viscous Flow, MA: Cambridge University Press, 1992.
8. **Itkulova Yu.A., Abramova O.A., Gumerov N.A.**, Boundary Element Simulations of Compressible Bubble Dynamics in Stokes Flows, ASME 2013 International Mechanical Engineering Congress and Exposition, Paper No. IMECE2013-63200 (2014).
9. **Abramova O.A., Itkulova Yu.A., Gumerov N.A.**, FMM/GPU Accelerated BEM Simulations of Emulsion Flow in Microchannels, ASME 2013 International Mechanical Engineering Congress and Exposition. Paper No. IMECE2013-63193 (2014).
10. **Abramova O.A., Bulatova A.Z., Fatkullina N.B., Pityuk Yu.A.**, Numerical simulation of the dynamics and calculation of the rheological characteristics of the dispersed systems using BEM, *Journal of Physics: Conference Series (JPCS)*. Ser.1359 (2019) 012025.

11. **Abramova O.A., Pityuk Yu.A., Gumerov N.A., Akhatov I.S.**, High-Performance BEM Simulation of 3D Emulsion Flow, Communications in Computer and Information Science (CCIS). 753 (2017) 317–30.

12. **Pityuk Yu.A., Abramova O.A., Fatkullina N.B., Bulatova A.Z.**, BEM Based Numerical Approach for the Study of the Dispersed Systems Rheological Properties, Recent Research in Control Engineering and Decision Making: Studies in Systems, Decision and Control. 199 (2019) 338–52.

13. **Cunha F.R., Almeida M.H.P., Loewenberg M.**, Direct numerical simulations of emulsion flows, J. Braz. Soc. Mech. Sci. Eng. (2003) 25.

14. **Batchelor G.K.**, The stress in a suspension of force-free particles, J. Fluid Mech. (1970) 545–570.

15. **Kennedy M.R., Pozrikidis C., Skalak R.R.**, Motion and deformation of liquid drops and the rheology of dilute emulsions in simple shear flow, Computers&Fluids. (1994) 251–278.

THE AUTHORS

BULATOVA Aiguzel Z.

bulatova29@yandex.ru

ORCID: 0000-0003-1741-7024

FATKULLINA Nazgul B.

nazgulbay@mail.ru

ORCID: 0000-0002-3944-1976

SOLNYSHKINA Olga A.

olgasolnyshkina@gmail.com

Received 26.10.2022. Approved after reviewing 10.11.2022. Accepted 16.11.2022.

Conference materials

UDC 629.735.33

DOI: <https://doi.org/10.18721/JPM.161.149>

Effect of running propellers on flow and hinge moments of trailing edge mechanization of high aspect ratio

E.A. Pigusov¹, O.V. Pavlenko¹✉, A.V. Kornushenko¹, O.N. Vinogradov¹, M.G. Reslan²

¹Department of aerodynamics, Central Aerohydrodynamic Institute (TsAGI), Zhukovsky, Moscow Region, Russia;

²The Moscow Institute of Physics and Technology (MIPT), Dolgoprudny, Moscow Region, Russia

✉ olga.v.pavlenko@yandex.ru

Abstract. This paper presents the results of a numerical study of the flow of an airplane with a mechanized high aspect ratio wing when the wingtips blown by jets of propellers. The layout of the aircraft with a pulling two-bladed propeller, as well as without installed propellers, is investigated. The effect of propeller slipstream on the airplane aerodynamic characteristics and the hinge moments of the flaps and ailerons is shown. It is shown that the external aileron is exposed to the greatest impact of the propeller slipstream. An increase in the underpressure on the upper surface and a strongly increasing pressure on the lower windward side of the aileron leads to a significant increase in the hinge moment of the external aileron when blown by jets of propeller.

Keywords: pulling airscrew, hinge moment, mechanization of the wing, high aspect ratio wing

Citation: Pigusov E.A., Pavlenko O.V., Kornushenko A.V., Vinogradov O.N., Reslan M.G., Effect of running propellers on flow and hinge moments of trailing edge mechanization of high aspect ratio, St. Petersburg State Polytechnical University Journal. Physics and Mathematics. 16 (1.1) (2023) 295–300. DOI: <https://doi.org/10.18721/JPM.161.149>

This is an open access article under the CC BY-NC 4.0 license (<https://creativecommons.org/licenses/by-nc/4.0/>)

Материалы конференции

УДК 629.735.33

DOI: <https://doi.org/10.18721/JPM.161.149>

Влияние работы воздушных винтов на обтекание и шарнирные моменты механизации задней кромки крыла большого удлинения

E.A. Пигусов¹, О.В. Павленко¹✉, А.В. Корнушенко¹, О.Н. Виноградов¹, М.Г. Реслан²

¹Отделение аэродинамики, Центральный аэрогидродинамический институт (ЦАГИ), Московская область, г. Жуковский, Россия;

²Московский физико-технический институт (МФТИ), г. Долгопрудный, Московская область, Россия

✉ olga.v.pavlenko@yandex.ru

Аннотация. В данной работе представлены результаты численного исследования обтекания самолета с механизированным крылом сверх большого удлинения при обдуве концевых сечений крыла струями воздушных винтов. Исследована компоновка самолета с тянущим двухлопастным воздушным винтом, а также без установленных воздушных винтов. Показано влияние обдува винтом на аэродинамические характеристики самолета и шарнирные моменты закрылков и элеронов.

Ключевые слова: тянущий воздушный винт, шарнирные моменты, механизация крыла, крыло сверхбольшого удлинения

Ссылка при цитировании: Пигусов Е.А., Павленко О.В., Корнушенко А.В., Виноградов О.Н., Реслан М.Г. Влияние работы воздушных винтов на обтекание и шарнирные моменты механизации задней кромки крыла большого удлинения //

Introduction

Currently, the task of studying the interaction of a running propeller of an electric power plant installed in the end section of the wing, including on the high aspect ratio wing used in the layout of solar-powered aircraft, is urgent. To ensure the required take-off and landing characteristics of airplanes with the high aspect ratio wing, effective take-off and landing mechanization is required. In addition, there are increased requirements for the efficiency of control surfaces placed on the wing, including the magnitude of the hinge moments that occur on them during deflection, since these characteristics directly affect the power and dimensions of the servo-compensators [1, 2].

This paper presents the results of a numerical study of the flow around an airplane with the high aspect ratio wing with running propellers and deflected the trailing edge mechanization of the wing.

Materials and Methods

The aerodynamic layout of the airplane has the classical scheme with a high-wing (wing aspect ratio of $\lambda = 23.4$), a fuselage with a circular cross section and a single-fin tail with a stabilizer placed on the fuselage (Fig. 1). At the ends of the rectangular wing, engine nacelles with installing pulling two - bladed propellers with a diameter of 0.22 m are placed. The studies were also carried out without installed propellers. The rotation speed of the propellers $N = 15000$ rpm. The rotation direction of the propellers corresponds to the folding of the vortex shroud from the wingtip.

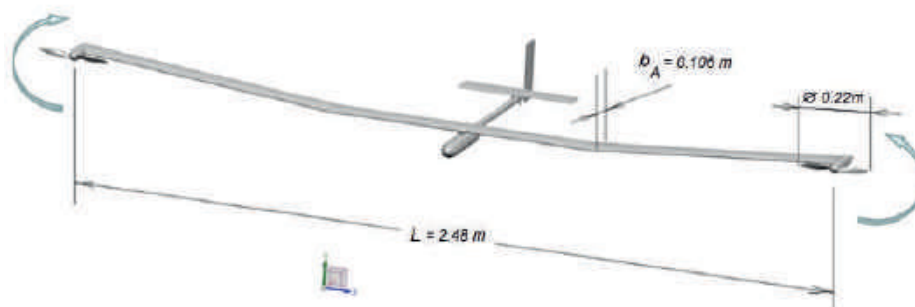


Fig. 1. Airplane main view

The wing is equipped with a plain flap and a two-section aerodynamically-balanced aileron (inner (aileron 1) and outer (aileron 2) sections, Figure 2). The relative chord of the flap and aileron is 15%. The variant of deflection of flaps and ailerons at an angle of $+30^\circ$ is considered. The axis of rotation of the flap and aileron is located at 85% of the wing chord.

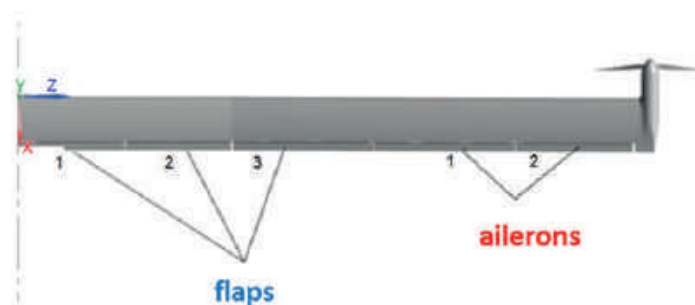


Fig. 2. The layout of flaps and ailerons along the wingspan



Numerical studies on the airplane with and without running propellers was carried out at Mach numbers $M = 0.074$ and Reynolds numbers $Re = 1.78 \cdot 10^6$, which correspond to the take-off mode. The calculations were performed using a program based on solving the Reynolds-averaged Navier-Stokes equations [3–5]. The calculations were performed at a load coefficient value $B = 0.5$. Load coefficient B was determined by the equation (1).

$$B = \frac{P_0}{q_\infty \cdot F}, \quad (1)$$

where P_0 is a propeller thrust, q_∞ is an dynamic pressure in WT, F is a blade swept surface area.

The coefficients of the hinge moments of the ailerons and flaps were determined by the equation (2):

$$C_H = \frac{H}{S \cdot q_\infty \cdot b}, \quad (2)$$

where H is the hinge moment relative to the axis of flap (aileron) rotation, S and b are the area of the flap (aileron) and the chord of the flap (aileron) behind the axis of rotation, respectively, q_∞ is an dynamic pressure.

Results and Discussion

The effect of the propeller mounted at the wingtip on the aerodynamic characteristics of the airplane with the deflected mechanization, depending on the angle of attack, is shown in Fig. 3. The calculation showed that a running propeller mounted at wingtip, with deflected mechanization, leads to a slight increase in the lift coefficient up to an angle of attack of 5° , and at beyond stall angles slightly reduces it. The pitching moment due to propeller slipstream practically does not change. Such a low effect of the propeller slipstream effect on the airplane aerodynamic characteristics is due to the fact that most of the wing mechanization is outside the area of the running propellers. Thus, only the second section of the aileron is mainly located in the slipstream area.

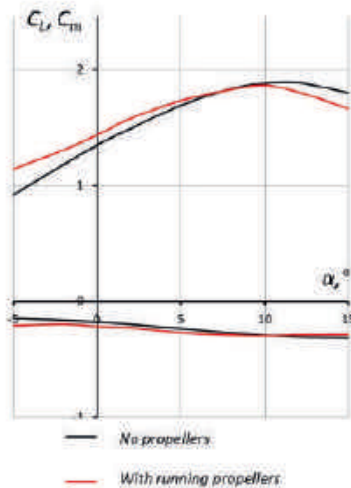


Fig. 3. Lift and pitching moment coefficients versus angle of attack

The values of the hinge moment coefficient of the deflected mechanization by the wingspan at different angles of attack are shown in Fig. 4. The disturbed air flow from the propeller rotating at the wingtips leads to an increase in the hinge moment of the entire deflected wing mechanization (flaps and ailerons) by about 1.5 times, and also increases the derivative of the hinge moment coefficient by the angle of attack. But the aileron 2, located directly behind the propeller, is exposed to the greatest impact of the propeller slipstream. It should be noted that a strong increase in the hinge moment (approximately 3 times) and a sharp increase in the derivative of the hinge moment coefficient of this aileron is observed only in the range of angles of attack from $\alpha = -5^\circ$ to $\alpha = +2^\circ$, which must be taken into account when controlling the aircraft. A similar effect, but to a much lesser extent, the running propeller has an effect on the hinge moment of the aileron 1.

The increase in the magnitude of the hinge moment of mechanization along the wingspan is caused by a change in aerodynamic forces and depends on the pressure distribution at different angles of attack.

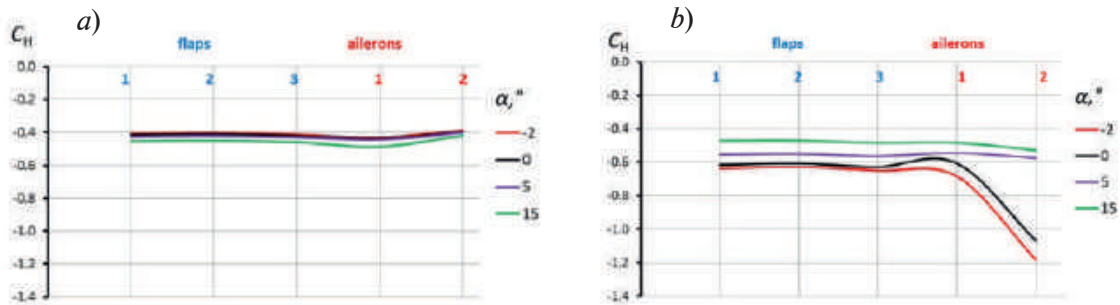


Fig. 4. The magnitude of the hinge moment coefficient of the deflected mechanization along wingspan: no propellers (*a*); with running propellers (*b*)

This is clearly seen in Fig. 5–8, which shows the pressure coefficient distribution over the wing surface, as well as in the section of the aileron 2 at the end of the wing when the propeller is blown at the angles of attack $\alpha = -2^\circ$ and $\alpha = 15^\circ$, which correspond to the maximum and minimum values of the aileron 2 hinge moment coefficient. At the angle of attack $\alpha = -2^\circ$ due to blowing by the propeller, an increase in underpressure is observed on the upper surface of the aileron 2 (Fig. 5, *a* and Fig. 7, *b*), while pressure increases strongly on its lower windward side (Fig. 6, *a* and Fig. 7, *b*). This pressure distribution increases the hinge moment of the deviated aileron by deflecting its back down stream and contributing to its return to its base cruising position. At the lowest value of the hinge moment of the aileron 2, the underpressure its upper surface (Fig. 5, *b* and Fig. 7, *b*) and the pressure on its lower windward side are significantly less (Fig. 6, *b* and Fig. 7, *b*).

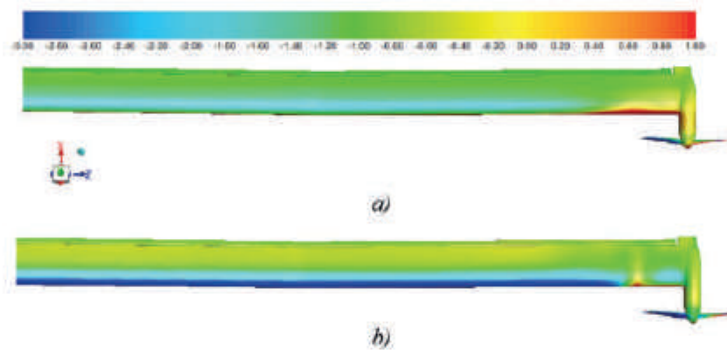


Fig. 5. The propeller slipstream effect on the pressure coefficient distribution of the wing surface with mechanization in the top view: $\alpha = -2^\circ$ (*a*); $\alpha = +15^\circ$ (*b*)

The increment of the pressure coefficient when blown by the propeller slipstream in the middle cross section of the aileron 2 is shown in Fig. 8. Such a change in pressure on the surface of the aileron 2 is associated with a bevel of the flow and a change in the direction of the current lines of the propeller when interacting with the incoming flow V_∞ with a increase in the angle of attack (Fig. 9).

Numerical studies of the aerodynamic characteristics of the wing have shown that with the gap height of $h = 0.02b$ reduces its lift along the entire wingspan and increasing the gap to $h = 0.03b$ gives closer results to the full-scale wing (Fig. 2). The strongest differences are observed in the area of the root section of the slat. Thus, when modelling the stream flowing through the gap between the wing main part and the slat, a simple geometric similarity is not enough. The general view of the flow around the full-scale wing and its separation area is shown in Fig. 3.

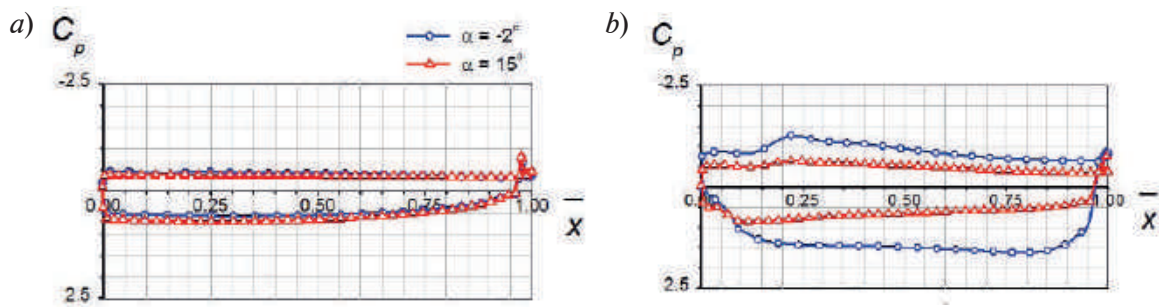


Fig. 7. The pressure coefficient distribution in the middle section of the aileron 2: no propeller (a); with running propeller (b)

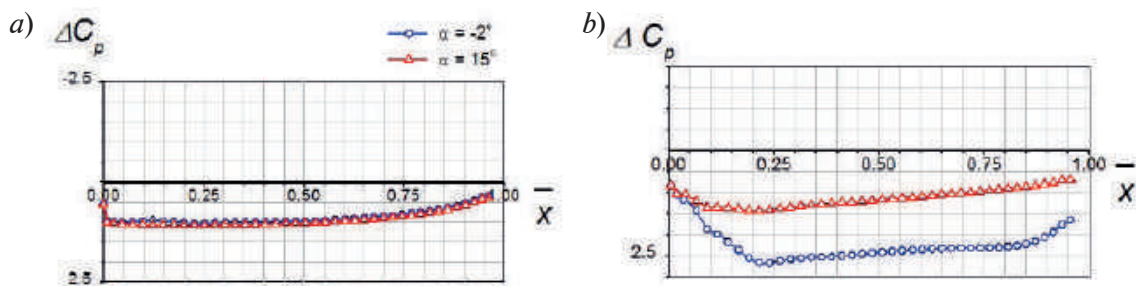


Fig. 8. Increment of the pressure coefficient in the middle section of the aileron 2: no propeller (a); with running propeller (b)

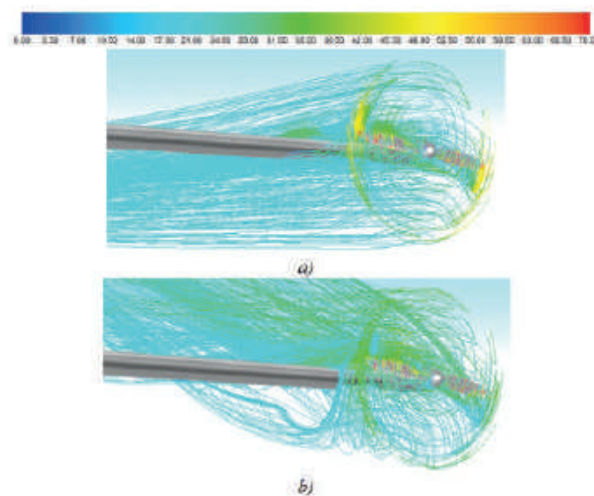


Fig. 9. The current lines behind the propeller: $\alpha = -2^\circ$ (a); $\alpha = +15^\circ$ (b)

Conclusion

The numerical study of the effect of running propellers on the flow and hinge moments of trailing edge mechanization of the high aspect ratio wing showed that the external aileron located directly behind the propeller is exposed to the greatest slipstream effect. A strong increase in the hinge moment and a sharp increase in the derivative of the hinge moment coefficient of the external aileron are observed only in a certain range of angles of attack from -5° to 2° , which must be taken into account when controlling the aircraft. An increase in the underpressure on the upper surface and a strongly increasing pressure on the lower windward side of the aileron leads to a significant increase in the hinge moment of the outer aileron when blown by an air propeller, when the aerodynamic forces that deflect it back along the flow increase.

REFERENCES

1. **Andreev G.T., Ershov A.A., Pavlenko O.V.**, Complex approach to reducing the jointed moments of aircraft control facilities *Avtomatizaciya I sovremennye tehnologii*, 72 (5) (2018) 227–231.
2. **Andreev G.T., Glushenko G.N., Kutukhina N.V., Pavlenko O.V.**, Influence of aerodynamic balance on hinge moments of aircraft control stick *Polyot*, 6 (2013) 18–26.
3. **Alesin V.S., Gubsky V.V., Pavlenko O.V.**, Fuselage and duct interference effect on maximum thrust of the air pushing propeller-duct thruster *Aerospace MAI Journal*, 27 (1) (2020) 7–18. <https://doi.org/10.34759/vst-2020-1-7-18>.
4. **Vinogradov O.N., Kornushenko A.V., Pavlenko O.V., Petrov A.V., Pigusov E.A., Trinh T.N.**, Specifics of propeller and super-high aspect ratio wing interference in non-uniform flow *Aerospace MAI Journal*, 28 (2) (2021) 7–19. <https://doi.org/10.34759/vst-2021-2-7-19>.

THE AUTHORS

PIGUSOV Evgeny A.

pigusoff@gmail.com

ORCID: 0000-0003-4639-0238

VINOGRADOV Oleg N.

oleg.vinogradov@tsagi.ru

ORCID: 0000-0002-4012-621X

PAVLENKO Olga V.

olga.v.pavlenko@yandex.ru

ORCID: 0000-0002-0415-6761

RESLAN Mostafa G.

reslan.mostafa97@gmail.com

ORCID: 0000-0001-9143-6202

KORNUSHENKO Alexander V.

avkornushenko@yandex.ru

ORCID: 0000-0002-6644-606X

Received 28.10.2022. Approved after reviewing 08.11.2022. Accepted 09.11.2022.

Conference materials
UDC УДК 533.95-629.7.036
DOI: <https://doi.org/10.18721/JPM.161.150>

Working process calculation of the control circuit for pulsed operation regime of the MPD accelerator

Yu.N. Tashayev ✉

Moscow State University of Food Production, Moscow, Russia

✉ tashayevyn@mgupp.ru

Abstract. A circuit for controlling the discharge current of an MPD accelerator based on the Morgan circuit is considered. It is shown that theoretically operation regime of the accelerator, depending on the parameters of the circuit, can be stationary, modulation, and pulsed. The necessary condition for the accelerator operation in the periodic mode is established. Calculations of the pulse shape of the discharge current are carried out. The experimentally observed pulse forms are compared with the calculated ones.

Keywords: plasma accelerators, pulsed mode, discrete plasma formations, discharge current, pulse shape, Morgan scheme

Citation: Tashayev Yu.N., Working process calculation of the control circuit for pulsed operation regime of the MPD accelerator, St. Petersburg State Polytechnical University Journal. Physics and Mathematics. 16 (1.1) (2023) 301–308. DOI: <https://doi.org/10.18721/JPM.161.150>

This is an open access article under the CC BY-NC 4.0 license (<https://creativecommons.org/licenses/by-nc/4.0/>)

Материалы конференции
УДК УДК 533.95-629.7.036
DOI: <https://doi.org/10.18721/JPM.161.150>

Расчет рабочего процесса схемы управления импульсным режимом работы МПД ускорителя

Ю.Н. Ташаев ✉

Московский государственный университет пищевых производств, г. Москва, Россия

✉ tashayevyn@mgupp.ru

Аннотация. Рассмотрена схема управления током разряда МПД-ускорителя, основанная на схеме Моргана. Теоретически показано, что режим работы ускорителя в зависимости от параметров схемы может быть стационарным, модуляционным и импульсным. Найдено необходимое условие работы ускорителя в периодическом режиме. Проведены расчеты формы импульса разрядного тока. Найдено условие перехода от модуляционного режима к импульсному. Экспериментально наблюдаемые формы импульсов сравниваются с расчетными.

Ключевые слова: плазменные ускорители, импульсный режим, дискретные плазменные образования, разрядный ток, форма импульса, схема Моргана

Ссылка при цитировании: Ташаев Ю.Н. Расчет рабочего процесса схемы управления импульсным режимом работы МПД ускорителя // Научно-технические ведомости СПбГПУ. Физико-математические науки. 2023. Т. 16. № 1.1. С. 301–308. DOI: <https://doi.org/10.18721/JPM.161.150>

Статья открытого доступа, распространяемая по лицензии CC BY-NC 4.0 (<https://creativecommons.org/licenses/by-nc/4.0/>)

Introduction

The Plasma accelerators were widely used as plasma sources when conducting research on the Earth's magnetosphere with the help of artificial plasma formations [1]. Among the numerous questions posed to the researchers were: studying the structure and dynamics of artificial plasma formations in the ionosphere, studying shock waves, generation of MHD waves, plasma instabilities, studying the interaction of “artificial” plasma formations created by the accelerator with the rocket body and the environment. In particular, when studying low-frequency radiation and magnetic field disturbances in ionospheric plasma, it is necessary to create pulsed plasma formations – plasma clouds or modulated plasma flows. The possibility of using a magnetoplasmodynamic accelerator (MPDA) as a source of discrete plasma formations with a repetition frequency of up to 10 kHz is described in the proposed work.

The implementation of the pulsed and modulation regimes of the accelerator was achieved by including a semiconductor discharge current interrupter based on the Morgan scheme in the pulsed power supply of the accelerator [2]. The proposed circuit of the current interrupter made it possible to obtain not only flows of plasma clouds with a given repetition rate, but also modulated plasma flows with different modulation depths.

Materials and Methods

Fig. 1 shows the Morgan schematic diagram used to control the discharge current of the MPD accelerator. The circuit consists of a semiconductor valve controlled by a rectangular pulse generator assembled on the basis of an asymmetric multivibrator, and connected in parallel with the valve LC chain. The pulse generator was used in the frequency range $f \sim 500\div 1000$ Hz and $f \sim 5\div 10$ kHz. In the pulsed operation mode, (Fig. 2) the accelerator emitted plasma formations with a certain repetition frequency. When generating plasma flows in the modulation mode, the intensity of the plasma jet was a periodic function of time. It was noted in [3] that in a wide range of discharge currents, the volt-ampere characteristic of the MPDA in stationary mode is linear.

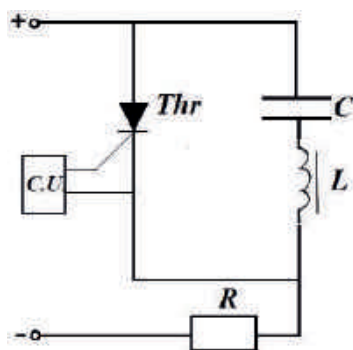


Fig. 1. Schematic diagram of discharge current control

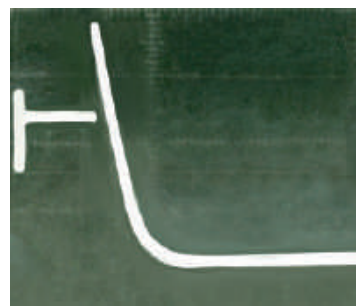


Fig. 2. Pulsed operation regime: discharge current waveform

In the first approximation, the analysis of the operation of the power supply circuit of the accelerator was carried out under the assumption that, in the electrical sense, the discharge chamber of the accelerator is equivalent to the active resistance R , the value of which is fixed and determined by the plasma parameters and the external magnetic field inside the discharge chamber [4]. Preliminary laboratory studies of the stationary operating mode of the accelerator confirm the linearity of the volt-ampere characteristics of the discharge current in a wide range of its values. The resistance of the discharge circuit practically did not depend on the magnitude of the discharge current, but was determined by such parameters as the cathode glow current, the flow rate of the working fluid, the pressure in the vacuum chamber, the shape of the magnetic field created by the solenoid. The analysis of the operation of the scheme will be divided into two stages. The first stage begins when the thyristor is opened by a control signal from the control unit (C.U.) and ends when the current disappears through the thyristor, which leads to its blocking. The second stage begins from the moment the thyristor is turned off and stops at the moment



it is opened by a signal from the C.U. For the periodic repeatability of the processes occurring in the circuit, it is necessary that the values of the current in the circuit and the charge of the capacitor corresponding to the beginning of the first stage coincide with the values of the current and charge at the end of the second stage. Now we will focus in more detail on the work of the scheme. When a voltage pulse is applied from the C.U. on the control electrode of the thyristor, it opens, and the voltage of the power source (ε) is directly applied to the resistance R (i.e., the anode voltage is applied to the plasma accelerator). Through the resistance R almost instantly (neglecting the inductance of the discharge circuit) a current is set to $I_0 = \varepsilon/R$ which means the appearance of a discharge current in the plasma accelerator. At the same time, the capacitance (C) is short-circuited to the inductance (L), and electric current oscillations occur in the circuit, described by the equation

$$I = I_m \cdot \sin(\omega t + \varphi_0),$$

where $\omega = (LC)^{-1/2}$ is the eigen frequency of oscillations. The amplitude I_m and the initial phase φ_0 are related to the initial values of the capacitor charge q_n and the current in the circuit I_n by the relations:

$$\frac{LI_m^2}{2} = \frac{q_n^2}{2C} + \frac{LI_n^2}{2}; \quad \sin \varphi_0 = \frac{I_n}{I_m}. \quad (1)$$

It should be noted that the values of q_n and I_n during the periodic operation of the circuit are set after some relaxation time has passed since the first opening of the thyristor. At the beginning of the circuit operation (at the time of the first opening of the thyristor) there is no current in the circuit, and the charge on the capacitor $Q = C\varepsilon$. At the same time the maximum value of the current in the LC circuit $I_{m0} = \sqrt{(C/L)\cdot\varepsilon} = \omega Q$, so that the thyristor will be locked only when $I_{m0} \geq I_0$, or $\sqrt{(C/L)\cdot\varepsilon} \geq \varepsilon/R$. Entering the parameter $\alpha = 1/R\sqrt{(L/C)}$ we get that the inequality $\alpha \leq 1$ is a necessary condition for the operation of the circuit. Taking into account that the current through the thyristor is the algebraic sum of the discharge current and the current in the LC circuit, then for the thyristor locking time, determined from the condition $I_{tir} = I_0 - I = 0$, we obtain:

$$t_1 = \frac{1}{\omega} (\arcsin \frac{I_0}{I_m} - \varphi_0 + 2\pi). \quad (2)$$

The charge of the capacitor at this time is negative and can be found from the energy conservation law for the LC circuit:

$$Q_0 = -\frac{I_m}{\omega} \sqrt{1 - \frac{I_0^2}{I_m^2}}. \quad (3)$$

Obviously, for the implementation of the periodic operation mode of the accelerator, the following condition must be met:

$$I_m \geq I_0. \quad (4)$$

Time t_1 (2) determines the duration of the stationary value of the discharge current $I = I_0$ and corresponds to the beginning of the second stage of the circuit operation. At the second stage ($t > t_1$), damped electrical oscillations will occur in the RLC circuit. Below are the expressions of the current in the circuit $I(t)$ and the capacitor charge $Q(t)$ satisfying the condition of continuity of functions I and Q , both during the transition to the second stage at time $t = t_1$, and at the time of reopening of the thyristor at $t = T$, where $T = f^{-1}$ is the period of operation of the circuit. During the calculations, the current in the circuit was considered positive if it flowed in the direction of the positive bypass of the circuit (clockwise). It can be shown that at $t = 0$, at the time of thyristor opening, either $I = I_n > 0$, $Q = q_n > 0$, or $I_n = 0$ and $q_n = I_m \omega^{-1}$. In the LC circuit at $t < t_1$, the dependences of the current and charge of the capacitor on time can be written as:

$$I = I_m \cdot \sin(\omega t + \pi - \arcsin \frac{I_n}{I_m}), \quad Q = -\frac{I_m}{\omega} \cdot \cos(\omega t + \pi - \arcsin \frac{I_n}{I_m}). \quad (5)$$

It is taken into account here that in $I = I_m \cdot \sin(\omega t + \varphi_0)$ the initial phase is determined by the expression $\varphi_0 = \pi - \arcsin(I_n/I_m)$, $I_n > 0$, respectively:

$$\left. \frac{dI}{dt} \right|_{t=0} = -I_m \omega \sqrt{1 - \frac{I_n^2}{I_m^2}} < 0, \quad q_n = \frac{I_m}{\omega} \sqrt{1 - \frac{I_n^2}{I_m^2}} > 0.$$

By the time $t_D = \omega^{-1} \cdot \arcsin(I_n/I_m)$ the positive charge of the capacitor reaches its maximum, and by the time $\omega^{-1} \cdot (\pi + \arcsin(I_n/I_m))$ the capacitor is fully recharged. From this moment, the current opposite to the discharge current will begin to increase in the LC circuit, which will lead to the

completion of the first stage by the time t_1 , determined by the expression:

$$t_1 = \omega^{-1} \cdot \left(\pi + \arcsin \frac{I_n}{I_m} + \arcsin \frac{I_0}{I_m} \right). \quad (6)$$

The second stage begins when the thyristor is locked at $t = t_1$ and ends at $t = T$. The dependence of the discharge current on time at $t_1 < t < T$ satisfies the equation of damped oscillations with

initial conditions: $I|_{t=t_1} = I_0$, $dI/dt|_{t=t_1} = \omega \sqrt{I_m^2 - I_0^2} > 0$, and at $0.5 < \alpha \leq 1$ can be represented as:

$$I = I_0 \cdot \frac{e^{-\beta(t-t_1)}}{\sin \theta_0} \cdot \sin(\Omega(t-t_1) + \theta_0), \quad \text{where } 2\beta = \frac{R}{L}, \quad \Omega = \sqrt{|\omega^2 - \beta^2|},$$

$$\theta_0 = \text{arccctg} \left[\Omega^{-1} \cdot \omega \left(\sqrt{\frac{I_m^2}{I_0^2} - 1} + \frac{\beta}{\omega} \right) \right]. \quad (7)$$

The dependence of the capacitor charge on time at the stage of damped oscillations can be represented as:

$$Q = C \cdot \varepsilon + I_0 \omega^{-1} \cdot \frac{e^{-\beta(t-t_1)}}{\sin \theta_0} \cdot \sin[\Omega(t-t_1) + \theta_0 + \theta_1 + \pi], \quad (8)$$

where $\theta_1 = \text{arccctg}(\Omega^{-1} \cdot \beta)$. If the circuit parameters are such that $\alpha < 0.5$, then

$$I = I_0 \cdot \frac{e^{-\beta(t-t_1)}}{\text{sh } \eta_0} \cdot \text{sh}[\Omega(t-t_1) + \eta_0], \quad \eta_0 = \text{arccth} \left[\Omega^{-1} \cdot \omega \left(\sqrt{\frac{I_m^2}{I_0^2} - 1} + \frac{\beta}{\omega} \right) \right],$$

$$Q = C \cdot \varepsilon + I_0 \omega^{-1} \cdot \frac{e^{-\beta(t-t_1)}}{\text{sh } \eta_0} \cdot \text{sh}[\Omega(t-t_1) + \eta_0 + \eta_1 + i \cdot \pi], \quad (9)$$

where $\eta_1 = \text{arccth}(\Omega^{-1} \cdot \beta)$. I_n the special case $\alpha = 0.5$, the expressions for current and charge are obtained by passing to the limit $\Omega \rightarrow 0$:

$$I = I_0 \cdot e^{-\tau} \left[1 + \tau \left(1 + \sqrt{\frac{I_m^2}{I_0^2} - 1} \right) \right], \quad Q = C \cdot \varepsilon \left[1 - e^{-\tau} \left(1 + \frac{1}{2} \sqrt{\frac{I_m^2}{I_0^2} - 1} + \frac{\tau}{2} \cdot \left(1 + \sqrt{\frac{I_m^2}{I_0^2} - 1} \right) \right) \right], \quad (10)$$

where $\tau = \omega \cdot (t - t_1)$. The shape of the discharge current pulse at different $\alpha \leq 1$ is schematically shown in Fig. 3.

At $t < t_1$, the discharge current is constant, and at $t < t_1$, immediately after locking the thyristor, ($I_m > I_0$), there is an increase in current to a certain maximum value $I_{\max} < 2 \cdot I_0$, reached at the time t_{\max} . Later on ($t > t_{\max}$), the current monotonically decreases at $\alpha \leq 0.5$ and at $0.5 \leq \alpha \leq 1$ would oscillate with an exponentially decaying amplitude if the accelerator operation did not depend on the direction of the current in the discharge space. In this case, the reversal of the current to zero at the time

$$t_2 = \omega^{-1} \cdot \left(\pi + \arcsin \frac{I_n}{I_m} + \arcsin \frac{I_0}{I_m} \right) + \Omega^{-1} \cdot (\pi - \theta_0), \quad (11)$$

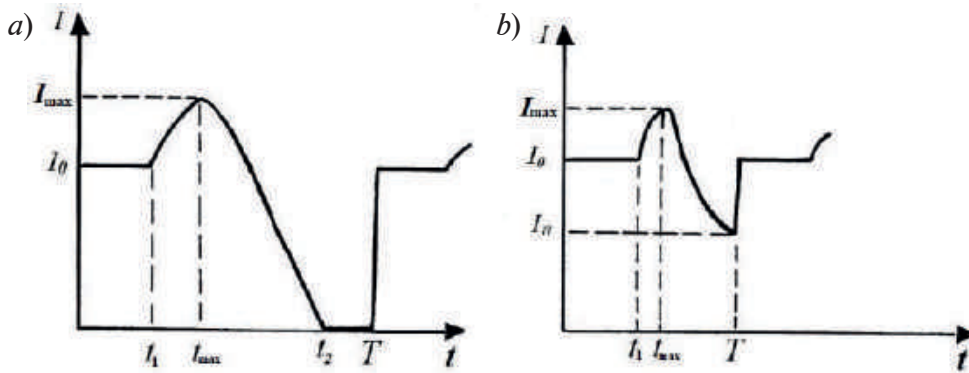


Fig. 3. The shape of the discharge current pulse: pulsed regime (a), modulation regime (b)

will complete the second stage of the accelerator operation. When operating in the modulation mode, the current decreases to the minimum value I_n . The initial discharge current I_n and the initial charge on the capacitor Q_n are determined by the period of operation of the circuit T , set by the rectangular pulse generator, and the dependence of I_n and Q_n (or rather I_m and φ_0) on T is obtained from the solution of a transcendental equation expressing the equality of the initial energy stored in the LC circuit and the energy in it at a time T . By applying external control signals from the C.U, following with a period T , it is possible to achieve a periodic dependence of the discharge current on time. In this case, the choice of the response period of the circuit T will completely determine the initial values of the current and charge of the capacitor, and, consequently, I_m and φ_0 . The characteristic times t_1 , t_{\max} , t_2 and the maximum value of the current I_{\max} will also be uniquely determined. To find the relationship between T and the listed values, it is more effective and convenient to solve the inverse problem: for a fixed I_m ($I_m > I_0$) determine the period T (i.e. the moment when the energy contained in the inductance and capacitance takes the initial value $E = LI_m^2/2$), and then the phase φ_0 . The possibility of solving the inverse problem follows from the following considerations. The change in energy E over time at the second stage ($t > t_1$) is determined by the equation $dE/dT = \varepsilon \cdot I(1 - I/I_0)$ from which it follows that from the moment the thyristor is locked ($I = I_0$), the energy decreases ($dE/dT < 0$, $I > I_0$), reaching a minimum value $E_{\min} < LI_m^2/2$ at the time when the current again takes the value I_0 . Further, the energy monotonically increases, either approaching for a value $E_\infty = C\varepsilon^2/2$ at $\alpha \leq 0.5$, or takes this value at $0.5 \leq \alpha \leq 1$ when the current turns to zero. Note that at $\alpha \leq 0.5$, the initial energy in the circuit cannot exceed the values of E_∞ , and, consequently, the possible values of I_m belong to the interval

$$1 \leq \bar{I}_m \leq \alpha^{-1}. \quad (12)$$

In this case, there will always be a moment in time (T) when the energy in the circuit will take a value corresponding to the first stage of the circuit operation. This will be the period of discharge current oscillations for this value $\bar{I}_m < \alpha^{-1}$. When the circuit is operating on an active load passing current in both directions, the energy in the circuit at the second stage approaches E_∞ with decreasing amplitude when the inequality $0.5 \leq \alpha \leq 1$ is fulfilled. In this case the initial value of the energy E_n may significantly exceed E_∞ . This means that in the process of relaxation of vibrations, energy can be accumulated in the oscillatory circuit. The possibility of periodic operation of the circuit in this case will be determined by the value of the first energy maximum achieved at the time t_2 – the time of the first current vanishing (11)

$$E_{\max} = \frac{LI_0^2}{2} \left(\frac{2\beta}{\omega} + \frac{\Omega}{\omega \cdot \sin \theta_0} \cdot e^{-\frac{\beta}{\Omega}(\pi - \theta_0)} \right)^2. \quad (13)$$

It can be shown that in this case periodic operation of the scheme is possible only when the inequality is fulfilled: $(LI_m^2)/2 \leq E_{\max}(I_m)$, so the possible values of I_m belong to the interval I_m where $1 \leq \bar{I}_m \leq \bar{I}_m^*$ is a solution to the equation:

$$\bar{I}_m = \frac{2\beta}{\omega} + \frac{\Omega}{\omega \sin \theta_0} \cdot e^{-\frac{\beta}{\Omega}(\pi - \theta_0(\bar{I}_m))} \quad \text{or} \quad \bar{I}_m(\alpha) = \alpha^{-1} + \frac{\Omega}{\omega \sin \theta_0} \cdot e^{-\frac{\alpha^{-1}\omega}{2\Omega}(\pi - \theta_0(\bar{I}_m))}. \quad (14)$$

The numerical solution of the equation (14) is shown in Fig. 4, where it is taken into account that for $\alpha \leq 0.5 \Rightarrow \bar{I}_m^* = \alpha^{-1}$. To determine the dependence \bar{I}_m on $\bar{T} = \omega \cdot T$ for various α and possible values \bar{I}_m the following equation was solved numerically by the Newton method:

$$\bar{I}^2(\bar{T}) + \bar{Q}^2(\bar{T}) = \bar{I}_m^2, \quad (15)$$

where $\bar{I} = I/I_0$, $\bar{Q} = Q\omega/I_0$, I and Q are determined by formulas (7)–(10), and $\omega t = \bar{T}$, so that the initial phase φ_0 is determined by the expression

$$\varphi_0 = \pi + \arcsin(\bar{I}(T)/\bar{I}_m). \quad (16)$$

Fig. 5 shows the results of the numerical solution of equation (15) for the values of $\alpha^{-1} = 1.1$; 1.6; 2; 4; 6. Calculations allow for any α for a given period T to determine the corresponding values \bar{I}_m , as well as $\bar{I}(T) = \bar{I}_n$.

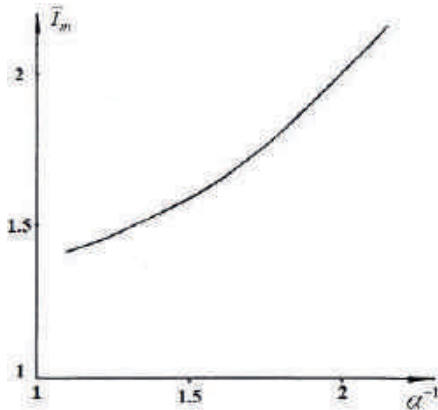


Fig. 4. Function dependence graph of the maximum possible values of the discharge current amplitude I_m from α (pulsed regime)

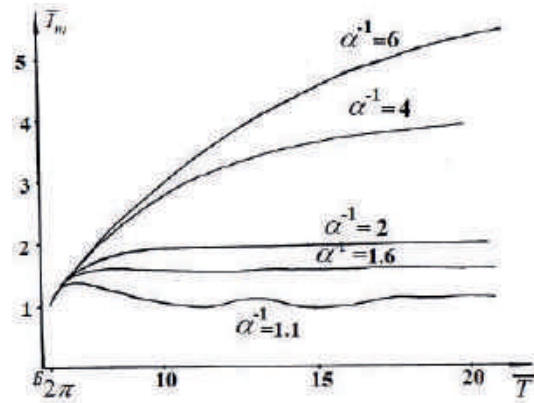


Fig. 5. Function dependence graph of the maximum discharge current amplitude I_m from the circuit operation period T for various α

Results and Discussion

The analysis of the obtained results shows the possibility of the existence of two modes of operation of the circuit: modulation and pulse. In the first case, the current does not have time to turn to 0 by the time T , so that the considered discharge current control scheme only modulates it, and does not lead to a complete rupture. In the pulse mode, the discharge current is different from zero during the time $T_{imp} < T$, and in the remaining time interval $T - T_{imp}$ is zero. With α belonging to the interval: $0.5 < \alpha \leq 1$ it is always possible to specify such a moment in time ($t = t_2$) at which the discharge current turns to zero. Note that when α decreases to a value of 0.5, the value of t_2 increases indefinitely, and when α values are less than 0.5, the current never turns to zero. Therefore, the duration of the current pulse (for all $\alpha < 1$) meant the time during which the current decreases to a certain minimum value, conditionally assumed to be equal to $I_{min} = 0.2 \cdot I_0$. Then, at $I_n > I_{min}$, the circuit will provide a modulation regime of the accelerator operation with a modulation depth of $\gamma = 1 - I_n/I_0$ and at $I_n \leq I_{min}$ – a pulse regime, which can be characterized by a relative pulse duration, defined by the formula $S = T/T_{imp}$. Fig. 6 shows the dependences of $\gamma(T)$ and $S(T)$ at the same values of α . As follows from the results of numerical calculation, the modulation mode is possible only at T , satisfying the inequality $2\pi < \bar{T} \leq \bar{T}^*(\alpha)$. The dependence $\bar{T}^*(\alpha)$ is shown in Fig. 7.

When $\bar{T} > \bar{T}^*(\alpha)$ there is a pulse mode of operation of the circuit. The dependences $\bar{I}_m(\bar{T})$ and $\varphi_0(\bar{T})$ obtained as a result of numerical calculation allow for each fixed value of the parameter α to establish a relationship between the time t_1 , during which the current has a stationary value I_0 , the time t_{max} , at which the current reaches the maximum value, the maximum (I_{max}) and minimum (I_n) possible values of the discharge current with the period of operation of the circuit T . In addition, a dependence of dimensionless time \bar{t}_1 on \bar{T} at the values of α selected above was found.

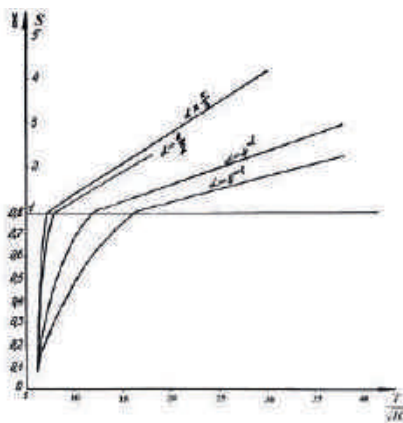


Fig. 6. Function dependence graph of the modulation depth γ and the relative pulse duration S from the circuit operation period T for various values of α

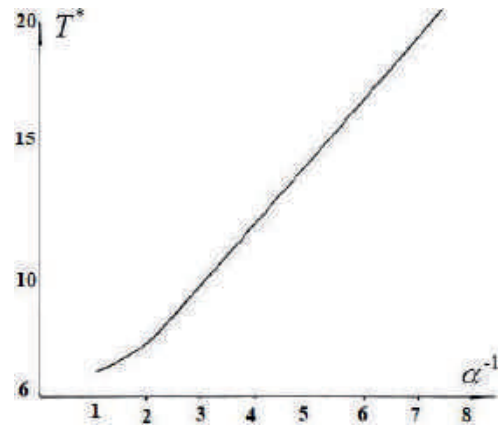


Fig. 7. Function dependence graph of the period T^* of operation of the circuit, corresponding to the transition from the modulation mode to the pulse mode, from α

It shows that at $\alpha < 0.5$, \bar{t}_1 monotonically decreases with an increase \bar{T} from the maximum value equal to 2π (coinciding with \bar{T}_{\min}) to the minimum $t_{1\min}$:

$$\bar{t}_{1\min} = \pi + \arcsin(\alpha). \quad (17)$$

At $0.5 < \alpha < 1$, the dependence is nonmonotonic. The duration of the stationary value of the current decreases rapidly at first, reaching a minimum, and then increases, tending to the value determined by the formula (17). This feature of the dependence $t_1(T)$ at $\alpha > 0.5$ is due to nonmonotonicity $I_m(T)$ at these values of α . Finally the dependences $\tau_{\max} = \omega \cdot (t_{\max} - t_1)$ and the maximum value of the current in the pulse I_{\max} on T at the same α were found.

Conclusion

To create pulsed plasma formations, as well as modulated plasma flows required in active geophysical experiments, the pulse mode of operation of the MPD accelerator was studied. As a result of bench tests, the possibility of operation of the MPD accelerator in pulsed mode with a pulse repetition frequency of up to 10 kHz was experimentally confirmed. The use of a discharge current control scheme based on the Morgan scheme made it possible to provide a pulse mode of operation of the accelerator. The calculations have shown that the operating mode of the accelerator, depending on the parameters of the circuit, can be stationary, modulated and pulsed. The duration of the stationary value of the current, the maximum value of the discharge current, the time when the current reaches the maximum value, the shape of the pulse are determined at a fixed value of the parameter $\alpha = 1/R\sqrt{L/C}$ by the period of the circuit operation. The numerical analysis of the circuit operation makes it possible to predict its operating regime as well as parameters such as the modulation depth (in the modulation mode), the relative pulse duration (in the pulse mode), the duration of the stationary current value, the time at which the current reaches the maximum value. The dependences of the modulation depth (for the modulation mode) and the relative pulse duration (for the pulse mode) on the period of operation of the circuit at different values of α , as well as the dependence on α of the period of operation of the circuit T^* corresponding to the transition from modulation ($T < T^*$) to pulse ($T > T^*$), have been calculated numerically. The minimum possible values of the circuit operation period are found, as well as the maximum possible values of the duration of the first stage, which turned out to be independent of α . The magnitude of the discharge current, being one of the main parameters characterizing the operation of the accelerator, significantly affects plasma parameters such as the concentration of charged particles, electron temperature, directional velocity of ions, etc. Therefore, the shape of the current pulse in the considered discharge circuit control scheme directly determines the parameters of plasma formations generated by the accelerator. The presented discharge current control scheme was used to implement pulse and modulation modes of operation of the MPD accelerator in laboratory conditions. The graphs of the analytically

obtained functional dependence $I(t)$ at different values of the parameter α were compared with the current waveforms obtained during bench experiments. A comparative analysis of the waveforms and graphically presented functional dependencies $I(t)$ showed a fairly good qualitative agreement between them in the frequency range $f \sim 500\text{--}1000$ Hz. In the frequency range $f \sim 10$ kHz, the discharge inertia determined the volt-ampere characteristic of the circuit, so the estimated duration of the stationary stage of plasma formation was markedly different from that found experimentally.

REFERENCES

1. Avdyushin S.I., Podgorny I.M., Popov G.A., Porotnikov A.A., Plasma accelerators using to study physical processes in space, Plasma accelerators and ion injectors, Nauka, Moscow, 1984, 232–250.
2. Gentry F., Gutzwiller F., Gologniak N., von Zastrow E., Controlled semiconductor valves, Mir, Moscow, 1967.
3. Rosinsky S.E., Kubarev Y.V., Pulse mode of MPD accelerator operation, In: Proceedings of the All-Union seminar on the physics of fast plasma processes, Grodno, Grodno University, 1986, 70.
4. Tashayev Y.N., On the creation of a magnetic field of a given geometry in the accelerating channel of the MPD accelerator, In: Proceedings 3rd International Conference on Control Systems, Mathematical Modeling, Automation and Energy Efficiency (SUMMA), IEEE Conference 10.1109 (2021) 1083-1087. DOI: 10.1109/SUMMA53307.2021.9632102

THE AUTHORS

TASHAYEV Yuriy N.
tashayevyn@mgupp.ru
ORCID: 0000-0002-4716-3750

Received 27.10.2022. Approved after reviewing 08.11.2022. Accepted 08.11.2022.

Conference materials

UDC 536.12

DOI: <https://doi.org/10.18721/JPM.161.151>

Numerical simulation of the temperature field distribution in the epitaxial graphene growth setup

S.P. Lebedev ¹✉, S.Iu. Priobrazhenskii ¹, A.V. Plotnikov ¹,
M.G. Mynbaeva ¹, A.A. Lebedev ¹

¹Ioffe Institute, St. Petersburg, Russia

✉ lebedev.sergey@mail.ioffe.ru

Abstract. An approach is presented to optimizing the growth of graphene on silicon carbide (SiC) substrates by using numerical simulation methods. The presented models in axisymmetric approximation show good convergence with experimental results and allow the studies of temperature fields inside closed growth cells. It is concluded that the use of numerical calculation methods is promising for optimizing the design of a technological setup for graphene growth by sublimation of the SiC surface.

Keywords: graphene, silicon carbide, simulation, temperature field distribution, sublimation growth

Funding: S.Iu. Priobrazhenskii acknowledge the support by the Russian Science Foundation grant 22-12-00134; S. P. Lebedev and A. A. Lebedev acknowledge the support by the Ministry of Science and Higher Education of the Russian Federation (agreement № 075-15-2021-1349).

Citation: Lebedev S.P., Priobrazhenskii S.Iu., Plotnikov A.V., Mynbaeva M.G., Lebedev A.A., Numerical simulation of the temperature field distribution in the epitaxial graphene growth setup, St. Petersburg State Polytechnical University Journal. Physics and Mathematics. 16 (1.1) (2023) 309–314. DOI: <https://doi.org/10.18721/JPM.161.151>

This is an open access article under the CC BY-NC 4.0 license (<https://creativecommons.org/licenses/by-nc/4.0/>)

Материалы конференции

УДК 536.12

DOI: <https://doi.org/10.18721/JPM.161.151>

Численное моделирование распределения температурного поля в зоне роста графена, выращиваемого на SiC подложках

С.П. Лебедев ¹✉, С.Ю. Приображенский ¹, А.В. Плотников ¹,
М.Г. Мынбаева ¹, А.А. Лебедев ¹

¹ Физико-технический институт им. А.Ф. Иоффе РАН, Санкт-Петербург, Россия

✉ lebedev.sergey@mail.ioffe.ru

Аннотация. В данной работе представлен подход к оптимизации роста графена на подложках карбида кремния (SiC) с использованием методов численного моделирования. Представленные модели в осесимметричном приближении показывают хорошую сходимость с экспериментальными результатами и позволяют проводить исследование температурных полей внутри закрытых ячеек. Сделан вывод о перспективности применения численных методов расчета для оптимизации конструкции технологической установки роста графена методом сублимации поверхности SiC.

Ключевые слова: графен, карбид кремния, моделирование, распределение температуры, сублимационный рост

Финансирование: С.Ю. Приображенский признателен за поддержку грантом РФФ 22-12-00134, Лебедев С.П. и Лебедев А.А. выражают благодарность Министерству науки и высшего образования Российской Федерации за поддержку (договор № 075-15-2021-1349).

Ссылка при цитировании: Лебедев С.П., Приображенский С.Ю., Плотников А.В., Мынбаева М.Г., Лебедев А.А. Численное моделирование распределения поля температур в установке эпитаксиального выращивания графена // Научно-технические ведомости СПбГПУ. Физико-математические науки. 2023. Т. 16. № 1.1. С. 309–314. DOI: <https://doi.org/10.18721/JPM.161.151>

Статья открытого доступа, распространяемая по лицензии CC BY-NC 4.0 (<https://creativecommons.org/licenses/by-nc/4.0/>)

Introduction

One of the promising ways to obtain two-dimensional graphene films is the method of thermal decomposition (sublimation) of the surface of SiC substrates [1]. This method makes it possible to obtain high-quality graphene/SiC structures suitable for creation of various devices, for example, high-sensitivity sensor elements, whose principle of operation is based on change of resistance of graphene upon adsorption on its surface of low concentrations of bimolecular complexes and gaseous chemical compounds [2–4]. The creation technology of such devices imposes high requirements on the crystal perfection and uniformity of the thus produced graphene.

Growth of graphene layers by SiC surface sublimation flows in high-frequency (HF) induction heating systems at temperatures of 1500–2000 °C [5]. The temperature control in such technological setup is only possible on the surface of the closed growth cell with an optical pyrometer. At the same time, the distribution of the temperature field in the substrate area, which is not available for pyrometric measurements, plays a significant role on the quality and the uniformity of the grown graphene. It is especially important to control the temperature field while making larger the SiC substrates used.

One of the ways to solve this problem is to simulate the processes that take place in a growth setup with the help of specialized mathematical programs. For example, such approach has been successfully used to analyze and correct the growth of bulk crystals in closed systems [6–7]. The data obtained during the simulation describes a number of parameters, including the distribution of the temperature field in the growth area. Thus, this approach can be applied to the study of graphene growth conditions by sublimation of the SiC surface.

The aim of this study was to analyze the possibility of using numerical methods to calculate the thermal fields in the epitaxial graphene growth setup for the further optimization of the existing technology.

Construction of the model

The epitaxial graphene growth setup is a water-cooled quartz chamber with equipment made of graphite elements arranged inside (Fig. 1, *a*). The main element of the internal equipment, which is heated in the electromagnetic field of the inductor, is a heater made of dense grades of graphite. The heater is located inside the porous carbon material insulation. The insulation provides more uniform heating of the growth cell and protection of the external elements of the setup from overheating. The correctness of numerical simulation data depends on the accuracy of setting the parameters of materials and the geometric dimensions of all setup elements.

The COMSOL Multiphysics package was chosen as the working environment for calculating the growth cell heating conditions. A number of simplifications were made at the simulation which do not significantly change the results of calculation. An axisymmetric approximation was used to obtain the 3D structures by rotating the cross-cut of the model configuration [8–9]. Thus, the initial spiral configuration of the HF inductor was converted into a ring set. A number of internal boundaries were excluded for the internal equipment of the growth setup. These simplifications made it possible not only to reduce the dimension of the model by going over to simple 2D domains, but also to include additional physical modules and extend the parameters of solvers. This in turn resulted in an improved accuracy and speed of data acquisition, as well as reduced computing capacity requirements. Fig. 1, *b* shows an example of simulated 3D-image of the graphite equipment heated inside the growth setup.

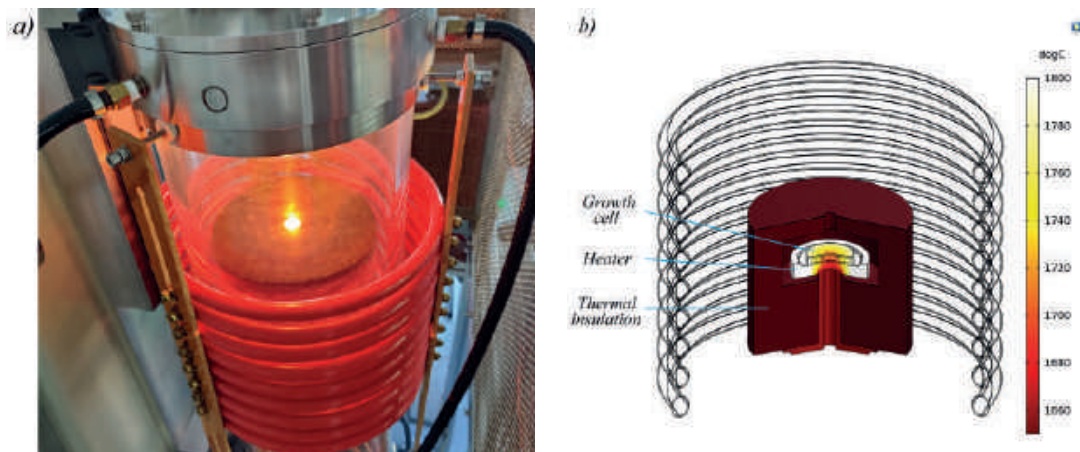


Fig. 1. Image of the epitaxial graphene growth setup (a), simulated 3D-image of the graphite equipment heated inside the growth setup (b)

Two configurations of the internal graphite equipment of the setup, which were applied in experiments to obtain epitaxial graphene, were used for calculations. In the first configuration, the heater is a graphite flat washer on which surface a growth cell with a substrate SiC is placed. In the second configuration, the heater has the shape of a tube, inside which a growth cell with a substrate is situated. Both heaters were made of graphite of the same grade and placed in thermal insulation made of fibrous graphite material.

Simulation results

To study the heating process, the temperature range from 1000 °C to 2000 °C was chosen, since all stages of graphene formation on the SiC surface occur in this temperature interval.

First stage of the study was to compare the simulation data with experimental heating data. The calculated temperatures were taken from the area of the growth cell, which is available for experimental pyrometric measurements. Experimental data was obtained using a Raytek Marathon MR1S infrared optical pyrometer operating in a two-color mode. The temperature measurement error does not exceed $\pm 0.5\%$ over the entire operating range. Fig. 2 shows heating and cooling graphs for two different equipment configurations. The simulation data show a fairly close similarity with the pyrometric data, which indicates that the model and the specification of the main characteristics of the materials used in the installation are correct. Small disarrangements between simulation and experimental data may be due to the imperfection of the design of real thermal insulation, as well as the use of some simplifications in the model, which were discussed above. Nevertheless, the convergence of the experimental and simulation curves and the coincidence of the key points allow further analysis of the thermal fields inside the growth setup.

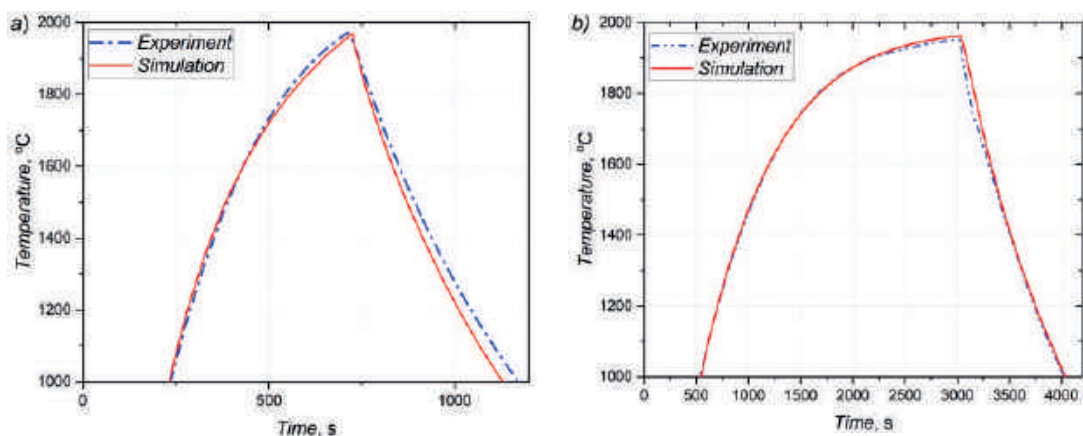


Fig. 2. Comparison of simulation and experimental heating curves for flat heater (a), tube heater (b)

The second stage of the study, the temperature distribution at the location of the SiC substrate in the growth cell for two heaters was compared. The growth cell is a flat graphite cup with a disk cover. The substrate is located in the cell in a special circular recess at the bottom, the diameter of which is 16 mm. The temperature value of 1700 °C in the central region of the substrate location was chosen as a general parameter for comparing the operation of two heaters, since this temperature is characterized by the onset of the formation of a graphene film on the SiC surface. Fig. 3 shows the temperature distribution of the cell cross-section heated by two heater configurations.

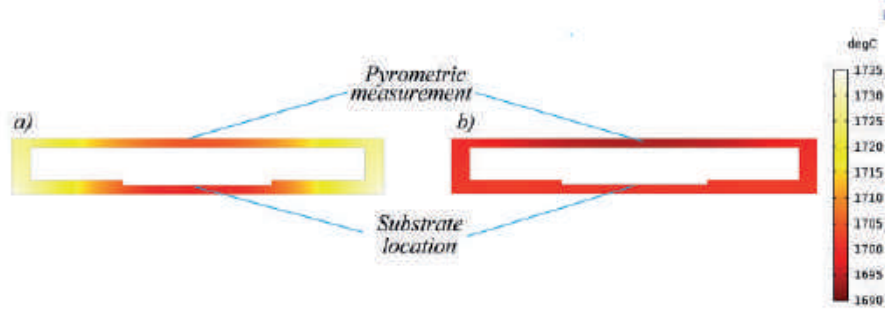


Fig. 3. Temperature distribution in growth cell heated in flat heater (a), tube heater (b)

Fig. 4, a shows images of the temperature distribution at the bottom of the growth cell obtained by simulation heating with different heaters. Fig. 4, b, for greater clarity, shows a graph of the temperature distribution in the substrate area. Based on these images, it can be concluded that the heating of the growth cell in the tube heater is much more uniform. At 1700 °C, the temperature differential in the substrate location for a tube heater is only 2–2.5 °C, and for a flat heater, this value increases to 15–16 °C. Thus, based on simulation data, it is possible to make a clear choice in favour of heating the cell in a tube heater.

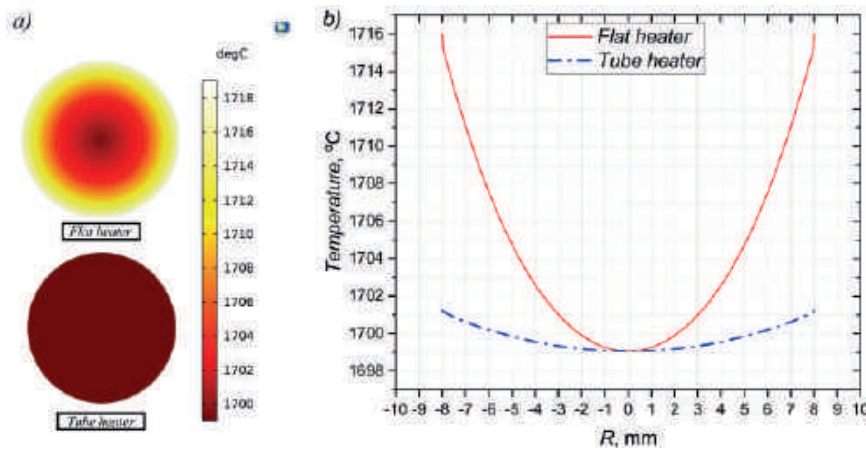


Fig. 4. The temperature distribution at the substrate location in the growth cell heated by flat and tube heaters (a), the temperature distribution graph by the cross-section of the bottom of the cell (b)

Another important heating parameter of the growth cell is the temperature difference between the area where the SiC substrate is situated (bottom of the growth cell) and the area where the temperature is measured with a pyrometer (growth cell cover). A large discrepancy between the temperatures in these regions may give no way of choosing the optimal mode for heating the SiC substrate to the graphene growth temperature, if being guided only by the pyrometer measurements. Simulation data make it possible to estimate the temperature difference and take it into account during the real growth process. Fig. 5 shows the temperature distribution for the substrate location and the growth cell cover. According to this graph, the temperature difference between the cover and the substrate during the growth of graphene should be about 7 °C.

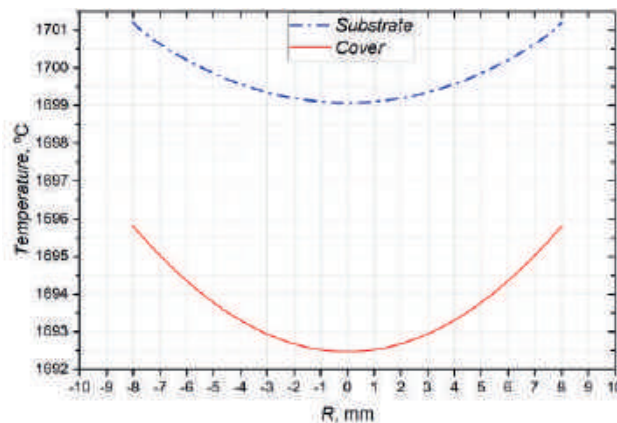


Fig. 5. Temperature distribution in different areas of the growth cell

Conclusion

The possibility of applying numerical methods for calculating thermal fields in the epitaxial graphene growth setup for the subsequent optimization of the existing technology is considered. A good convergence between the calculated and experimental curves of the growth cell surface temperature at the given generator power was demonstrated, which confirms that of the model construction and setting of the basic materials parameters of the setup are correct. Numerical simulation made it possible to compare different configurations of the internal graphene growth equipment, to determine a number of parameters of the thermal field in the growth cell for each case, and to identify the most optimal configuration.

The obtained results demonstrate the promise of using numerical simulation methods not only for determining the parameters of the thermal field in the growth setup, but also for optimizing the design of the setup for graphene growth by the SiC surface sublimation method. Through the use of the COMSOL Multiphysics package, it is possible to study many different options for the setup design and the features of its heating in a relatively short period of time. This factor may play a significant role in the development of this graphene growth technology and its transition from research to industrial production.

Acknowledgments

S. Iu. Priobrazhenskii acknowledge the support by the Russian Science Foundation grant 22-12-00134; S. P. Lebedev and A. A. Lebedev acknowledge the support by the Ministry of Science and Higher Education of the Russian Federation (agreement № 075-15-2021-1349).

REFERENCES

1. Berger C., Song Z., Li T., Li X., Ogbazghi A.Y., Feng R., Dai Z., Marchenkov A.N., Conrad E.H., First P.N. and de Heer W.A., Ultrathin Epitaxial Graphite: 2D Electron Gas Properties and a Route toward Graphene-based Nanoelectronics, *The Journal of Physical Chemistry B*. 108 (52) (2004) 19912–19916.
2. Liu Y., Dong X. and Chen Peng., Biological and chemical sensors based on graphene materials, *Chemical Society Reviews*. 41 (6) (2012) 2283–2307.
3. Hill E.W., Vijayaraghavan A. and Novoselov K., Graphene Sensors, *IEEE Sensors Journal*. 11 (12) (2011) 3161–3170.
4. Lebedev S.P., Usikov A., Novikov S., Shabunina E., Shmidt N.M., Barash I., Roenkov A.D., Lebedev A.A., Makarov Y., Graphene/SiC Functionalization for Blood Type Sensing Applications, *Materials Science Forum*. 924 (2018) 909–912.
5. Lebedev A., Davydov V., Usachov D., Lebedev S., Smirnov A., Eliseyev I., Dunaevskiy M., Gushchina E., Bokai K., Pezold J., High Quality Graphene Grown by Sublimation on 4H-SiC (0001), *Semiconductors*. 52 (14) (2018) 1882–1885.
6. Ramm M., Kulik A., Zhmakin I., Karpov S., Bord O., Demina S., Makarov Yu., Modeling of PVT growth of bulk SiC crystals: general trends and 2" to 4" reactor scaling, *MRS Proceedings*. 616 (2000) 227–233.

7. **Drachev R., Cherednichenko D., Khlebnikov I., Khlebnikov Y. and Sudarshan T.**, Graphitization of the Seeding Surface during the Heating Stage of SiC PVT Bulk Growth, Materials Science Forum. 433-436 (2003) 99–102.

8. **Narita T., Takahashi N., Horii M.**, Investigation of evolution strategy and optimization of induction heating model, IEEE Transactions on Magnetics. 36 (4) (2000) 1085–1088.

9. **Streblau M.**, Mathematical Model of Induction Heating Processes in Axial Symmetric Inductor-Detail Systems, TEM Journal. 3 (2) (2014) 162–166.

THE AUTHORS

LEBEDEV Sergey P.

lebedev.sergey@mail.ioffe.ru

ORCID: 0000-0002-5078-1322

MYNBAEVA Marina G.

mgm@mail.ioffe.ru

ORCID: 0000-0002-6321-1724

PRIOBRAZHENSKII Sergei Iu.

sereyozha@yandex.ru

LEBEDEV Aleksander A.

shura.lebe@mail.ioffe.ru

ORCID: 0000-0003-0829-5053

PLOTNIKOV Andrey V.

xdernx@gmail.com

Received 27.10.2022. Approved after reviewing 10.11.2022. Accepted 25.11.2022.

Conference materials

UDC 629.735.33.05

DOI: <https://doi.org/10.18721/JPM.161.152>

Flow modelling of slotted slat on spin model

E.A. Pigusov ¹✉, M.A. Golovkin ¹, O.V. Pavlenko ¹

¹ Department of aerodynamics, Central Aerohydrodynamic Institute (TsAGI),
Zhukovsky, Moscow Region, Russia

✉ pigusoff@gmail.com

Abstract. The problem of modelling the airflow through the gap between a main wing part and a slat is investigated. Numerical studies of the aerodynamics of a wing with a slat at beyond stall angles characteristic for a spin are carried out. The features of the flow near the slotted slat of the wing model and full-scale wing are revealed. It is shown that with the observance of the geometric similarity on the spin model, the flow and aerodynamic characteristics are somewhat distorted, respectively. It is proposed to simulate the flow around the gap according to the local jet momentum coefficient of the full-scale aircraft and its model.

Keywords: small-size aircraft model, high angles of attack, spin, similarity theory, low Reynolds numbers, jet momentum coefficient

Citation: Pigusov E.A., Golovkin M.A., Pavlenko O.V., Flow modelling of slotted slat on spin model, St. Petersburg State Polytechnical University Journal. Physics and Mathematics. 16 (1.1) (2023) 315–319. DOI: <https://doi.org/10.18721/JPM.161.152>

This is an open access article under the CC BY-NC 4.0 license (<https://creativecommons.org/licenses/by-nc/4.0/>)

Материалы конференции

УДК 629.735.33.05

DOI: <https://doi.org/10.18721/JPM.161.152>

Моделирование обтекания щелевого предкрылка на штопорной модели

Е.А. Пигусов ¹✉, М.А. Головкин ¹, О.В. Павленко ¹

¹ Отделение аэродинамики, Центральный аэрогидродинамический институт (ЦАГИ),
г. Жуковский, Россия

✉ pigusoff@gmail.com

Аннотация. Исследована проблема моделирования течения струи воздуха между основной частью крыла и предкрылком. Проведены численные исследования аэродинамики крыла с предкрылком на закритических углах атаки, характерных для штопора. Предложено проводить моделирование обтекания щели по локальному коэффициенту импульса струи натурного летательного аппарата и его модели.

Ключевые слова: малоразмерная модель самолета, большие углы атаки, штопор, теория подобия, малые числа Рейнольдса, коэффициент импульса струи

Ссылка при цитировании: Пигусов Е.А., Головкин М.А., Павленко О.В. Моделирование обтекания щелевого предкрылка на штопорной модели // Научно-технические ведомости СПбГПУ. Физико-математические науки. 2023. Т. 16. № 1.1. С. 315–319. DOI: <https://doi.org/10.18721/JPM.161.152>

Статья открытого доступа, распространяемая по лицензии CC BY-NC 4.0 (<https://creativecommons.org/licenses/by-nc/4.0/>)

Introduction

Experimental studies of a spin on an airplane wing model in a wind tunnel have shown that the parameters of the gap between the wing main part and the slat significantly affect the characteristics of the spin [1, 2]. A feature of the spin models under study are small overall dimensions, which negatively affects the operation of the wing slotted mechanization at low test speeds and corresponding relatively low values of the Reynolds number. At the same time, the thickness of the boundary layer on the surface of the model in a wind tunnel and on an airplane differs significantly. At the same time, the peculiarities of the flow at the spin and the assessment of measures to exit it impose additional requirements to increase the reliability of the results of wind tunnel tests, including when modeling the flow of slotted mechanization [3–5]. In [2], in order to increase the reliability of test results in the design of small-sized models, it was proposed to provide for the possibility of some increase in the size of the gaps in the wing high-lift devices comply with the similarity in the jet momentum coefficient.

In this paper, the issues of modeling the airflow of the slotted slat on a spin wing model using computational fluid dynamics are considered in more detail.

Materials and Methods

The effect of the gap height between the main wing part and the slat was studied on a spin aerodynamic model made on a scale of 1:11, as well as on a full scale. The scheme of the model wing having a positive "V"-shape of 4° is shown in Fig. 1. In the model formulation, two heights of the gap h between the slat tail and the surface of the wing main part were studied: $h = 0.02b$ (direct scaling of the wing) and $h = 0.03b$ (increased height of the gap), where b is the local chord of the wing. The full-scale wing with only the gap $h = 0.02b$ was studied.

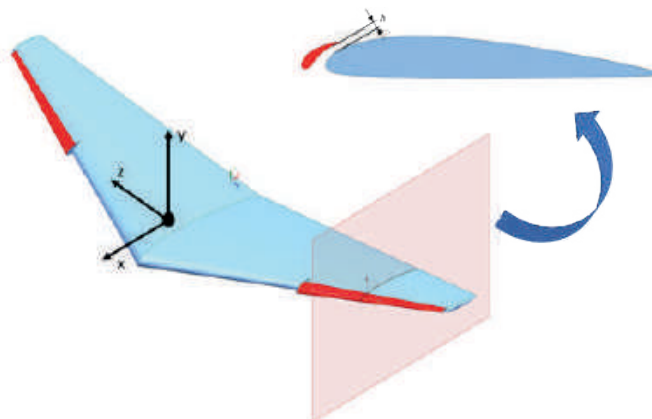


Fig. 1. The scheme of the wing with the slat

Numerical studies of the wing model were carried out on a structured grid (about 20 million cells) according to a program based on solving the Reynolds-averaged Navier-Stokes equations using the k - ε realizable turbulence model, with improved modeling of turbulence parameters near the wall and taking into account the influence of the pressure gradient [6]. Numerical studies were performed at the angle of attack of $\alpha = 60^\circ$ and the flow velocity of $V = 15$ m/s and the Reynolds number $Re = 0.23 \cdot 10^6$ based on the mean aerodynamic chord (MAC) of the wing corresponding to the spin mode of the model of this aircraft. A full-scale wing with a gap height $h = 0.02b$ was calculated in the modes: $\alpha = 60^\circ$, $V = 15$ m/s and 50 m/s at the numbers $Re = 2.48 \cdot 10^6$ and $Re = 8.28 \cdot 10^6$ (based on the MAC), respectively. Thus, at the flow speed of $V = 15$ m/s, the full-scale Reynolds number is almost 10 times higher than the wind tunnel one, and at the speed $V = 50$ m/s it is 36 times higher.

Results and Discussion

Numerical studies of the aerodynamic characteristics of the wing have shown that with the gap height of $h = 0.02b$ reduces its lift along the entire wingspan and increasing the gap to $h = 0.03b$

gives closer results to the full-scale wing (Fig. 2). The strongest differences are observed in the area of the root section of the slat. Thus, when modelling the stream flowing through the gap between the wing main part and the slat, a simple geometric similarity is not enough. The general view of the flow around the full-scale wing and its separation area is shown in Fig. 3.

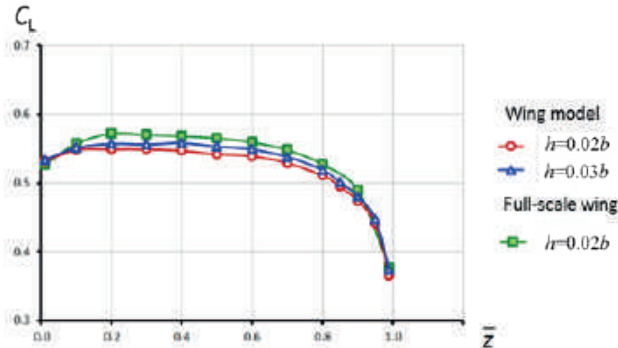


Fig. 2. Distribution of the lift coefficient along the wingspan, $V = 15$ m/s

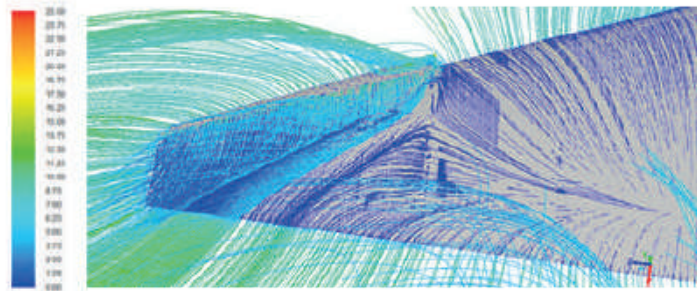


Fig. 3. Distribution of the lift coefficient along the wingspan, $V = 15$ m/s

The velocities distribution in cross sections along the span of the slat (Fig. 4, 5) shows that a slight increase in the gap height leads to an increase in the velocity of air flowing through it and a more correct modelling of the flow on the wing after the air jet comes out of the slot. A comparison of the velocity distribution along the span of the slat in the sections of the wing model with the gap height of $h = 0.03b$ and the full-scale wing with the gap height of $h = 0.02b$ showed their qualitative agreement (Fig. 5). Numerical research showed that in the gap between the main part of the model wing and the slat at $h = 0.02b$, especially in the end sections, where the gap height h is very small and is 1.56 mm, there is a significant deceleration of the air flow (Fig. 4) and, as a consequence, the decrease in the underpressure on the nose of the wing airfoil (Fig. 6).

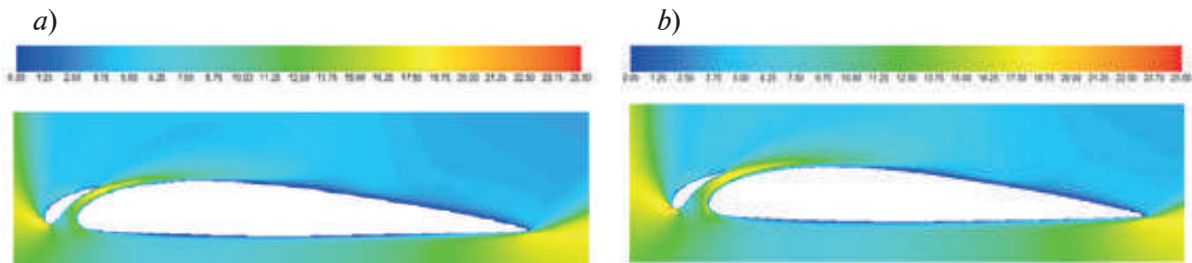


Fig. 4. Velocity distribution in the middle cross-section of the slat on the wing model at the flow velocity $V = 15$ m/s: (a) $h = 0.02b$; (b) $h = 0.03b$

Based on numerical studies of the velocity fields of the flow coming out of the gap between the slat and the wing main part, the distribution of local jet momentum coefficients [2] along the wingspan was determined. The local jet momentum coefficient was defined as the ratio of the amount of movement of the entire impulse flow passing through the gap segment along the span per unit of time to the amount of movement of the undisturbed flow passing through this section of the gap per unit of time.

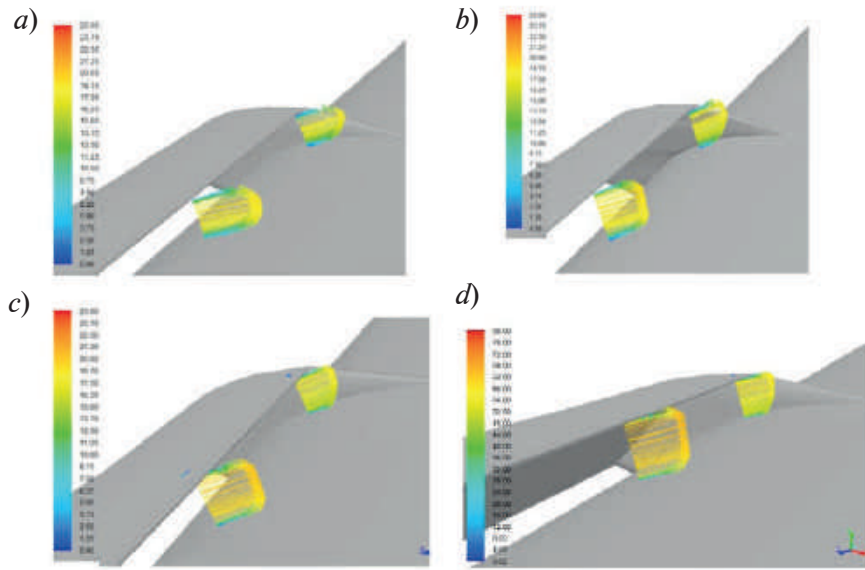


Fig. 5. Velocity distribution (m/s) in the slat slot sections: wing model with $h = 0.02b$ at $V = 15$ m/s (a); wing model with $h = 0.03b$ at $V = 15$ m/s (b); full-scale wing $h = 0.02b$ at $V = 15$ m/s (c); full-scale wing $h = 0.02b$ at $V = 50$ m/s (d)

Fig. 7 shows that the distribution along the slat of the local jet momentum coefficients of C_{μ} for the model with an enlarged gap ($h = 0.03b$) is close to the corresponding distribution for a full-scale aircraft. The presented results of calculations and experimental studies indicate a more adequate modeling of the flow of a full-scale aircraft with an increased size of the gap in the model between the slat and the wing main part.

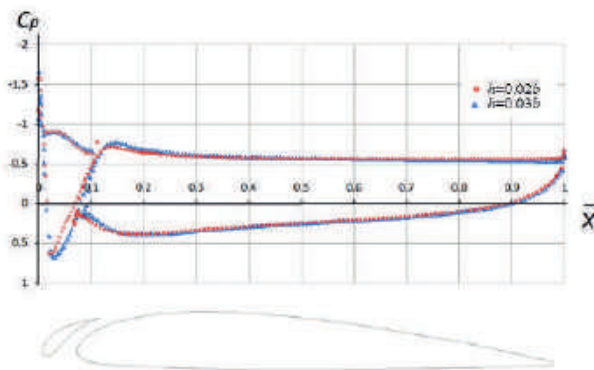


Fig. 6. The distribution of the pressure coefficient in the middle cross section of the slat wing model at $V = 15$ m/s

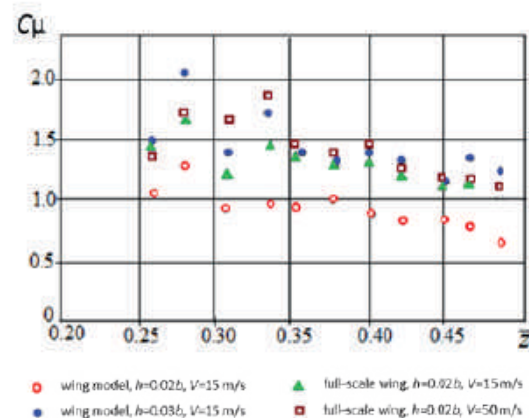


Fig. 7. Distribution of local jet momentum coefficients along the slat span

Conclusion

Numerical studies carried out on the wing with the slat at beyond stall angle of $\alpha = 60^\circ$ have shown that with the observance of the geometric similarity on the spin model including the gap height of the slat, the flow and aerodynamic characteristics are somewhat distorted, respectively. This circumstance leads to the closing of the air flow in the slot of a small experimental model. In this case, the gap, depending on the scale, can be completely immersed in the boundary layer. The solution to this problem, as calculated studies have shown, may be a slight increase in the gap height between the wing main part and the slat, taking into account the similarity in the jet momentum coefficient.



REFERENCES

1. **Bogomazova G.N., Golovkin M.A., Efremov A.A., Pavlenko O.V.**, On Modeling the Operation of Slotted High-Lift Device Elements in a Spin Experiment at Low Reynolds Numbers Russian Aeronautics, 64 (2021) 449–454.
2. **Golovkin V.A., Golovkin M.A., Gorban' V.P., Efremov A.A., Kritsky B.S., Pavlenko O.V., Tsipenko V.G.**, Similarity criteria for modeling the operation of the elements of slotted high-lift devices in a spin experiment TsAGI Science Journal, 53 1 (2022) 3–20.
3. **Bihle W., Barnhart B.**, Spin Prediction Techniques Journal of Aircraft, 20 (2) (1983) 97–101.
4. **Murch A., Foster J.**, Recent NASA Research on Aerodynamic Modeling of Post-Stall and Spin Dynamics of Large Transport Airplanes Proc. 45th AIAA Aerospace Sciences Meeting and Exhibit AIAA Paper, 2007-463 (2007) 1–20.
5. **Farcy D., Khrabrov A.N., Sidoryuk M.E.**, Sensitivity of Spin Parameters to Uncertainties of the Aircraft Aerodynamic Model Journal of Aircraft, 57 5 (2020) 922–937.
6. **Vinogradov O.N., Kornushenko A.V., Pavlenko O.V., Petrov A.V., Pigusov E.A., Trinh Thang Ngoc**, Influence of propeller diameter mounted at wingtip of high aspect ratio wing on aerodynamic performance J. Phys.: Conf. Ser. 1959 (2021) 012051.

THE AUTHORS

GOLOVKIN Mikhail A.

spintest@tsagi.ru

ORCID: 0000-0003-2096-7684

PAVLENKO Olga V.

olga.v.pavlenko@yandex.ru

ORCID: 0000-0002-0415-6761

PIGUSOV Evgeny A.

pigusoff@gmail.com

ORCID: 0000-0003-4639-0238

Received 28.10.2022. Approved after reviewing 10.11.2022. Accepted 10.11.2022.

Conference materials

UDC 519.6

DOI: <https://doi.org/10.18721/JPM.161.153>

Numerical simulation of waveguide couplers using the coupled mode theory for quantum gates implementation

A.A. Lytaev ¹✉, I.Yu. Popov ¹

¹ ITMO University, Saint Petersburg, Russia

✉ 288451@niuitmo.ru

Abstract. The directional coupler formed by a system of two dual-mode optical waveguides is studied with the aim of being used as a switcher for a nonlinear optical CNOT quantum gate. The paper focuses on simulation of behaviour of electromagnetic radiation in regions of juxtaposition and separation, that surround the main coupling region and are composed of several circularly bent waveguides. The modes of bent waveguides are approximated as linear combinations of the guided and leaky modes in the straight waveguide with the same width and refractive indices. An advanced coupled mode theory is applied to describe the coupling between bent parts of the coupler. The system of differential equations for amplitude coefficients is solved with a finite difference method. The influence of signal distortions is analyzed. The results obtained are applied to correct the geometrical parameters of the coupler. The computational error of the whole device due to waveguide bends distortions is estimated to not exceed 5%.

Keywords: waveguides, quantum computing, coupled mode theory, CNOT quantum gate, bent waveguides, leaky modes

Citation: Lytaev A.A., Popov I.Yu., Numerical simulation of waveguide couplers using the coupled mode theory for quantum gates implementation, St. Petersburg State Polytechnical University Journal. Physics and Mathematics. 16 (1.1) (2023) 320–325. DOI: <https://doi.org/10.18721/JPM.161.153>

This is an open access article under the CC BY-NC 4.0 license (<https://creativecommons.org/licenses/by-nc/4.0/>)

Материалы конференции

УДК 519.6

DOI: <https://doi.org/10.18721/JPM.161.153>

Численное моделирование сближения волноводов с помощью теории связанных волноводов для реализации квантовых вентилях

А.А. Лытаев ¹✉, И.Ю. Попов ¹

¹ Университет ИТМО, Санкт-Петербург, Россия

✉ 288451@niuitmo.ru

Аннотация. Данная работа посвящена моделированию взаимодействия системы близко расположенных оптических волноводов с целью ее использования в качестве переключателя для реализации квантового CNOT вентиля. В работе проводится моделирование поведения электромагнитного излучения в областях сближения и удаления волноводов, смежных с прямым участком обмена энергиями, и состоящих из нескольких изогнутых волноводов. Моды изогнутых волноводов приближенно рассматриваются как линейные комбинации направляемых и вытекающих мод прямого волновода с теми же толщиной и коэффициентом преломления. Для описания взаимодействия между изогнутыми частями схемы применяется модифицированная теория связанных мод. Система дифференциальных уравнений решается с помощью метода конечных разностей. Изучается влияние искажений сигнала. Полученные результаты применяются для того, что скорректировать геометрические параметры



системы. В результате моделирования показывается, что вычислительная ошибка вентиля вследствие искажений сигнала на изгибах не превышает 5%.

Ключевые слова: волноводы, квантовые вычисления, теория связанных мод, CNOT квантовый вентиль, изогнутые волноводы, вытекающие моды

Ссылка при цитировании: Лытаев А.А., Попов И.Ю. Численное моделирование сближения волноводов с помощью теории связанных мод для реализации квантовых вентилях // Научно-технические ведомости СПбГПУ. Физико-математические науки. 2023. Т. 16. № 1.1. С. 320–325. DOI: <https://doi.org/10.18721/JPM.161.153>

Статья открытого доступа, распространяемая по лицензии CC BY-NC 4.0 (<https://creativecommons.org/licenses/by-nc/4.0/>)

Introduction

The problem of physical implementation of the prototype of quantum computer is indeed an important question since the idea was proposed by Feynman [1], so it would be possible to solve a series of numerical problems with notable computational acceleration. Quick decoherence is a major obstacle encountered in this way (see, e.g., [2]). The optical model of quantum computations is an essential way to get around this hurdle since photons are known to be characterized with a relatively low interaction efficiency.

There are two main approaches to the optical model, namely linear optical and nonlinear. The former [3] is based on employing various linear optical devices, such as mirrors, beam splitters and phase shifters. In [4] it is shown that this approach allows to create a probabilistic CNOT gate with 1/9 probability of success. Such a low probability makes these gates hardly applicable for a practical computational scheme. The latter approach is described in [5]. It increases the probability of successful gate operation, but at the cost of long optical paths effectively making the gates susceptible to computational errors.

The idea described in [6] is an approach to curtail the optical paths by increasing the intensities of nonlinear interaction. The article introduces the optical scheme to implement the nonlinear CNOT gate that could be used to compute by using both single photon quantum states and classical quantum-like photonic states. In [7] we studied the latter case. Quantum bits are encoded by optical transverse modes of optical waveguides, namely TE_0 mode encodes $|0\rangle$ state and TE_1 encodes $|1\rangle$. The stronger is the TE_1 part of the signal in control waveguide the larger part of it is transferred into the upper arm of the MZI in the target waveguide and the stronger is the phase shift in nonlinear parts with intensity dependent refractive index, while TE_0 mode is pertained in the control waveguide. However, for the scheme to correctly work the coupling length L and the distance between coupled waveguides R are required to be matched in a specific way.

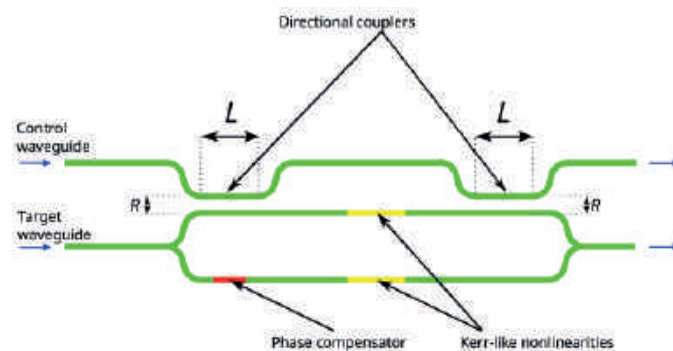


Fig. 1. Optical CNOT quantum gate

In [7] we applied a conventional coupled mode theory [8] to the straight part of the directional coupler and obtained an analytical solution for amplitude coefficients of the modes as trigonometric functions of spatial coordinate, so an explicit condition on the coupling coefficients ratio allowed us to adjust the geometrical parameters in a desired way. However, possible distortions to the state of quantum bit due to coupling and losses in the bent parts of the directional coupler were

not considered. In this paper these parts of the directional coupler are studied. The field in the system is decomposed into a sum of bent waveguide modes and a modified coupled mode theory is applied to access and correct the distortions.

Modes of the bent waveguide

The spectrum of an ideal bent waveguide unlike that of the straight one does not include a discrete set of guided modes; it is fully continuous. However, not unlike the spectrum of straight waveguide radiation modes it can be approximated with a set of modes with complex propagation constants. This decomposition is not unique, in [9] one of the possible ways is discussed. The idea is to represent bent modes as a linear combination of modes of the straight waveguide with the same width and refractive indices. In the plane where the angular distance is zero the field in the bent waveguide can be represented as a linear combination of them of the straight waveguide. The angular distance accumulates the phase and attenuation with a propagation constant

$$\exp[-iv^j d\theta] E_b^j(x)|_{\theta=0} = E_b^j(x)|_{\theta=d\theta} = \sum_{n=1}^N a_n^j E_n(x) \exp[-i\beta_n(R_b+x)dz], \quad (1)$$

where E_b^j is the transverse field distribution of j -th bent mode, E_n is that of n -th straight mode, R_b is a radius of bending and v_j is a propagation constant of the bent mode. It is possible to rewrite the equation (1) into the eigenvalue problem for eigenvalues v_j and eigenvector a^j

$$(R_b B + D^{-1} C B) a^j = v^j a^j, \quad j = 0, 1, 2 \quad (2)$$

where

$$B_{ij} = \beta_i \delta_{ij}, \quad (3)$$

$$C_{ij} = \int_{-\infty}^{+\infty} \overline{E^i(x)} E^j(x) x dx, \quad (4)$$

$$D_{ij} = \int_{-\infty}^{+\infty} \overline{E^i(x)} E^j(x) dx. \quad (5)$$

In [9] the numerical experiment shows that the set of straight waveguide modes composed of all supported guided modes and one leaky mode of the lowest order is sufficient to get a valid approximation of the field in the bent waveguide with sufficiently large radius of curvature.

Snyder [10] shows that leaky mode propagation constants can be found from the same characteristic transcendental equation as that for guided modes, however it should be solved on the complex domain. The root with the real part closest to that of the guided mode of the highest order will represent a lowest order leaky mode. Thus, it could be found with a Newton-Raphson method initialized with the propagation constant of the TE_1 mode. The complex propagation constant describes a leaky mode, that behaves similar to the guided mode in the proximity of the waveguide core, however, is attenuated due to the negative imaginary part. The solution of (2) yields three propagation constants, each of them representing one of the bent modes. v_0 and v_1 are expected to have significantly smaller imaginary parts than that of v_2 since bent TE_2 mode is formed primarily by the straight leaky TE_2 mode. Hence, the model describes two main sources of the signal loss: an attenuation of weakly radiative TE_0 and TE_1 modes and a loss of the signal at straight-to-bent waveguide transitions.

Simulation of coupling in juxtapositions and separations

In this paper regions of juxtaposition and separation that surround the straight part are divided into two bent parts and one straight inclined part (see Fig. 2).

In order to estimate losses in the bent parts and coupling in the whole region a modified coupled mode theory is employed. For simplicity only the coupling between the fields with the same z coordinate is considered, which serves as an approximation of the real field behaviour in the system, however, it is expected to suffice to estimate the distortions due to losses and coupling in the bent parts. Under this assumption it is possible to conduct the same derivation of differential equations for mode amplitude coefficients as it was done for the pair of straight waveguides in [7].

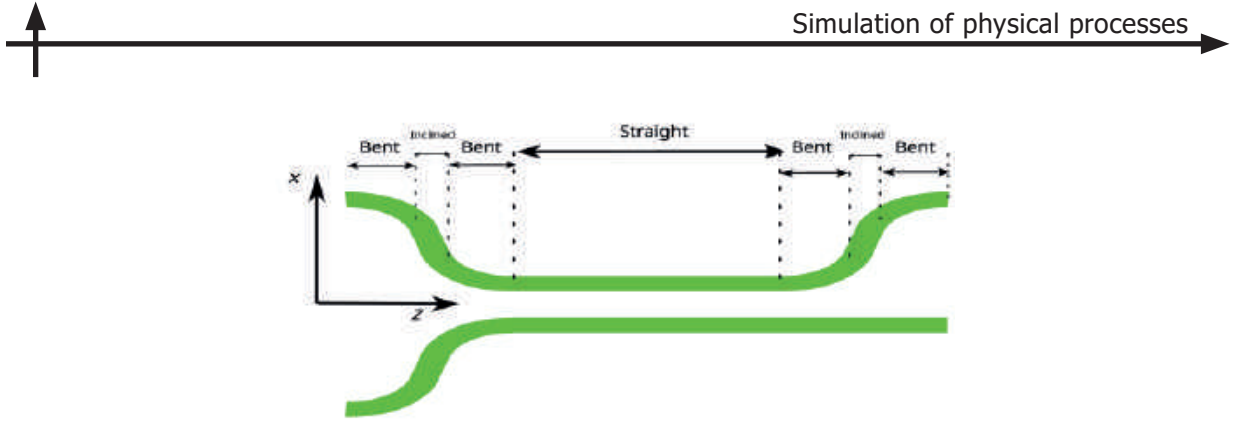


Fig. 2. The scheme of directional coupler

$$\frac{\partial A_{v_1 m_1}}{\partial z} c_{m_1} + \sum_{m_2=0}^1 i A_{((v_1+1) \bmod 2) m_2} \tilde{D}_{m_2}^{m_1} e^{i(\beta_{m_1} - \beta_{m_2})z} = 0. \quad (6)$$

However, it should be noted that coupling coefficients are integrals of bent modes field distributions.

$$\tilde{D}_{m_1}^{m_2} = \int_{-\infty}^{+\infty} (\omega \epsilon_0) (n_{core}^2 - n_{clad}^2) E_{m_1}^b(x) E_{m_2}^b(x) \cos(\alpha) dx, \quad (7)$$

where α is an angle between the direction of the local longitudinal axis of waveguide and the global one. By applying the decomposition (1) it is possible to express bent coupling coefficients in terms of the straight ones as

$$\tilde{D}_{m_1}^{m_2} = \sum_{m_3, m_4=0}^2 a_{m_3}^{m_1} a_{m_4}^{m_2} D_{m_3}^{m_4} \cos(\alpha), \quad m_1, m_2 = 0, 1. \quad (8)$$

The coupled mode theory for inclined straight parts remains the same as for the straight except for multiplication by $\cos(\alpha)$.

In order to account for distortions at straight-to-bent transitions a mode matching procedure is employed, the amplitude coefficients A_{vm} can be expressed from them of bent waveguide modes \tilde{A}_{vm} as

$$A_{vm} = \frac{\int_{-\infty}^{+\infty} (\tilde{A}_{v_0} \overline{E_0(x) E_m^b(x)} + \tilde{A}_{v_1} \overline{E_1(x) E_m^b(x)}) dx}{\int_{-\infty}^{+\infty} \overline{E_m(x) E_m(x)} dx}. \quad (9)$$

The modes of bent waveguides are not orthogonal strictly speaking, however, numerical calculations showed them to be small, thus for simplicity the reverse transition can be described with similar equations

$$\tilde{A}_{vm} = \frac{\int_{-\infty}^{+\infty} (A_{v_0} \overline{E_0^b(x) E_m(x)} + A_{v_1} \overline{E_1^b(x) E_m(x)}) dx}{\int_{-\infty}^{+\infty} \overline{E_m^b(x) E_m^b(x)} dx}. \quad (10)$$

The system of differential equations (6) is solved with the finite difference method.

Numerical results

The technique discussed above was applied to the system with refractive indices of waveguide core and cladding $n_{clad} = 1.57$ and $n_{core} = 1.55$ correspondingly, width of waveguide $d = 1.18 \mu\text{m}$, radiation wavelength $\lambda = 1.064 \mu\text{m}$, radius of bending $R_b = 100 \mu\text{m}$ and the minimal distance between the waveguides outside of the coupling zone $R_f = 100 \mu\text{m}$. The distance between waveguides in the coupling zone is taken from [7] as $R = 2.36 \mu\text{m}$. The resulting propagation constants are given in Table 1. The resulting behaviour of amplitude coefficients of signal modes is given in Figures 3–4.

Amplitude coefficients are normalized at they would be during the measurement at the output since the relation $|A_{v_0}|^2 + |A_{v_1}|^2 = 1$ must be fulfilled despite attenuation and losses at straight-to-bent transitions. It can be concluded that attenuation and straight-to-bent transitions affect both modes in a very similar way and hence do not distort the quantum states notably. However, additional coupling regions do increase the phase of periodic energy exchange between the

Table 1

Propagation constants

Propagation constant	TE ₀	TE ₁	TE ₂
$\beta_{straight}$	9.234	9.156	9.049-0.241i
β_{bent}	9.264-0.005i	9.130-0.005i	9.044-0.236i

Notations: $\beta_{straight}$ and β_{bent} are the propagation constants of given modes in the straight and bent waveguides respectively

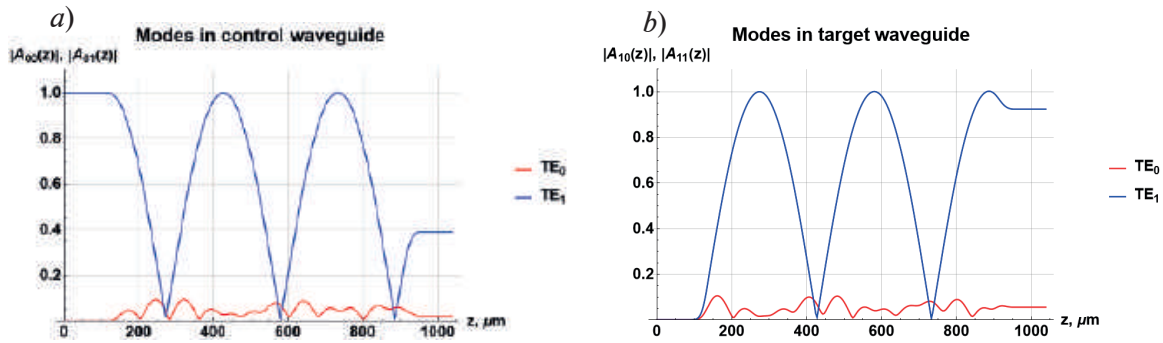


Fig. 3. Amplitude coefficient in (a) control waveguide (b) target waveguide

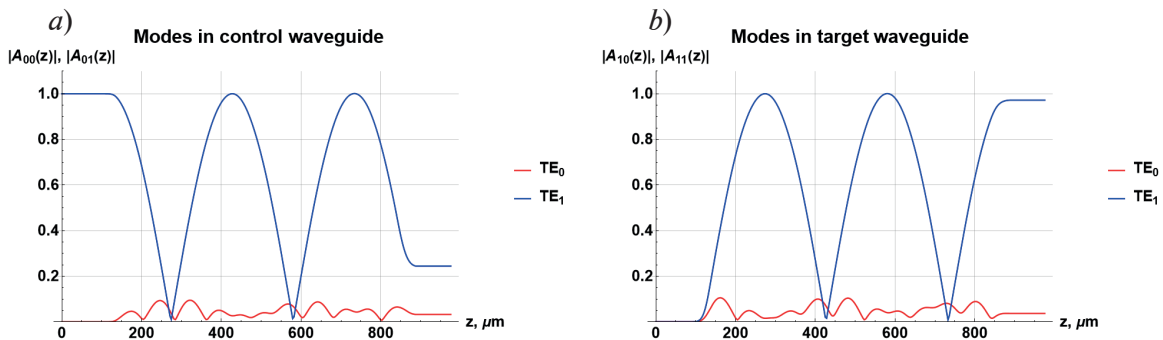


Fig. 4. Amplitude coefficient after corrections to parameter L in (a) control waveguide (b) target waveguide

waveguides, thus the computational error of the device can be reduced by modifying the coupling length L . The results are provided in Fig. 4.

The corrected coupling length L allows the device to transfer the TE_1 mode to the opposite waveguide with the error of 2%, thus the error of the whole CNOT gate can be estimated to be 5%.

Conclusion

The model of directional couplers based on the coupled mode theory discussed provides a tool to perform a computationally fast simulation of the behaviour of electromagnetic radiation within the system. Moreover, it allows to estimate the influence of distortions due to waveguide bending and straight-to-bent transitions. Application of this technique has shown that distortions do not affect the state of waveguide quantum bits notably, while the coupling at juxtapositions and separations do increase the phase of periodic energy exchange between the waveguides, however, it could be negated by decreasing the coupling length L . It was shown that the cumulative computational error due to distortions caused by bent parts and intermodal interaction does not exceed 5%, which could be coped with by application of quantum correction algorithms. However, despite both modes being attenuated similarly, the total attenuation of the signal in the computational scheme was found to be around 25%. That could be a source of potential difficulties for creating the device composed of a large number of CNOT gates applied sequentially.

Acknowledgments

The work was supported by Russian Science Foundation (grant number 22-11-00046).



REFERENCES

1. Feynman R., Quantum mechanical computers, *Foundations of Physics*. 16 (1986) 507–531.
2. Goncharov R.K., Kiselev A.D., Veselkova N.G., Ranim A., Kiselev F.D., Discrimination and decoherence of Schrodinger cat states in lossy quantum channels, *Nanosystems: Physics, Chemistry, Mathematics*. 12 (6) (2021) 697–702.
3. Kok P., Munro W.J., Nemoto K., Ralph T.C., Dowling J.P., Milburn G.J., Linear optical quantum computing with photonic qubits, *Reviews of Modern Physics*. 79 (2007) 135–174.
4. Ralph T.C., Scaling of multiple postselected quantum gates in optics, *Physical Review A*. 70 (2004) 012312.
5. Milburn G.J., Quantum optical Fredkin gate, *Physical Review Letters*, 62 (18) (1989) 2124–2127.
6. Fu J., Tang S., Quantum Computations with Transverse Modes of An Optical Field Propagating in Waveguides, *Chinese Physics Letters*. 20 (9) 1426–1429.
7. Lytaev A.A., Popov I.Yu., Simulation of switchers for CNOT-gates based on optical waveguide interaction with coupled mode theory, *Zhurnal SVMO*. 23 (4) (2021) 433–443.
8. Yariv A., Coupled-mode theory for guided-wave optics, *IEEE Journal of Quantum Electronics*. 9 (9) (1973) 919–933.
9. Melloni A., Carniel F., Costa R., Martinelli M., Determination of bend mode characteristics in dielectric waveguides, *Journal of Lightwave Technology*. 19 (4) (2001) 571–577.
10. Snyder A.W., Love J.D., *Optical Waveguide Theory*, Springer New York, New York, 1983.

THE AUTHORS

LYTAEV Aleksandr A.
288451@niuitmo.ru
ORCID: 0000-0003-1976-3350

POPOV Igor Yu.
popov1955@gmail.com
ORCID: 0000-0002-5251-5327

Received 28.10.2022. Approved after reviewing 09.11.2022. Accepted 09.11.2022.

Conference materials

UDC 532.5

DOI: <https://doi.org/10.18721/JPM.161.154>

Calculation of hydrological connection between the Volga river and the Akhtuba river using numerical hydrodynamic modeling

A.Yu. Klikunova¹✉, A.V. Khoperskov¹

¹ Volgograd State University, Volgograd, Russia

✉ klikunova@volsu.ru

Abstract. The hydrological regime of the Volga river near the Akhtuba river source below the dam of the Volga hydroelectric power station is studied. We use a hydrodynamic model based on the numerical solution of shallow water equations to study the dynamics of discharge water during spring floods. The main result is the determination of the hydrological connection between the water discharge (hydrograph $Q_V(t)$) of the dam of the Volga HPP and the hydrograph of the Akhtuba river source ($Q_A(t)$) depending on the dynamics of the water flow from the Volgograd reservoir to the Volga river. Numerical simulations of the spring flooding process were performed for the northern part of the Volga-Akhtuba floodplain for 2016, 2017 and 2021. The relationship between Q_V and Q_A is non-linear due to the peculiarities of the riverbeds and the interfluvial topography. The results are important for developing solutions aimed at preserving the Volga-Akhtuba floodplain.

Keywords: hydrological regime, hydrodynamic model, spring flooding, hydrograph

Funding: the study was supported by the Ministry of Science and Higher Education of the Russian Federation (government task no. 0633-2020-0003).

Citation: Klikunova A.Yu., Khoperskov A.V., Calculation of hydrological connection between the Volga river and the Akhtuba river using numerical hydrodynamic modeling, St. Petersburg State Polytechnical University Journal. Physics and Mathematics. 16 (1.1) (2023) 326–330. DOI: <https://doi.org/10.18721/JPM.161.154>

This is an open access article under the CC BY-NC 4.0 license (<https://creativecommons.org/licenses/by-nc/4.0/>)

Материалы конференции

УДК 532.5

DOI: <https://doi.org/10.18721/JPM.161.154>

Особенности гидрологической связи между Волгой и Ахтубой по результатам численного гидродинамического моделирования

А.Ю. Кликунова¹✉, А.В. Хоперсков¹

¹ Волгоградский государственный университет, г. Волгоград, Россия

✉ klikunova@volsu.ru

Аннотация. Исследован гидрологический режим в русле реки Волга вблизи истока реки Ахтуба ниже плотины Волжской ГЭС. Мы используем гидродинамическую модель на основе численного решения уравнений мелкой воды для изучения гидрологического режима в периоды весенних паводков. Основным результатом является определение гидрологической связи между гидрографом плотины Волжской ГЭС $Q_V(t)$ и гидрографом истока реки Ахтуба $Q_A(t)$ в зависимости от характера сброса воды из Волгоградского водохранилища в реку Волга. Симуляции процесса весеннего затопления выполнены для условий 2016, 2017 и 2021 годов. Связь между Q_V и Q_A имеет нелинейный характер, обусловленный особенностями речных русел и береговым рельефом. Результаты важны для выработки решений, направленных на сохранение Волго-Ахтубинской поймы.

Ключевые слова: гидрологический режим, гидродинамическая модель, весеннее затопление, гидрограф



Финансирование: работа выполнена в рамках госзадания Министерства науки и высшего образования Российской Федерации (проект 0633-2020-0003).

Ссылка при цитировании: Кликунова А.Ю., Хоперсков А.В. Особенности гидрологической связи между Волгой и Ахтубой по результатам численного гидродинамического моделирования // Научно-технические ведомости СПбГПУ. Физико-математические науки. 2023. Т. 16. № 1.1. С. 326–330. DOI: <https://doi.org/10.18721/JPM.161.154>

Статья открытого доступа, распространяемая по лицензии CC BY-NC 4.0 (<https://creativecommons.org/licenses/by-nc/4.0/>)

Introduction

The hydrological regime of large river systems is essentially nonstationary and is determined by the balance of numerous spatially distributed factors [1–5]. Floodplains are areas that are very sensitive to any noticeable hydrological changes. Anthropogenic factors have a dominant impact on the state of such socio-environmental systems, affecting both the regime of water discharge and the orography [6, 7].

The interfluvium of the Volga and Akhtuba Rivers is a unique natural object experiencing negative trends due to the regulation of the Volga River flow, especially in the spring [3, 6, 8]. The cascade of hydroelectric dams on the Volga River and the Kama River completely controls the spring flood, which is a key factor in floodplain moistening [9]. The landscape of the Volga-Akhtuba floodplain (VAF) is based on the regular spring flooding of the extended flat area between the Volga and Akhtuba rivers from the dam of the Volga hydroelectric power station to the Astrakhan City and beyond, where the floodplain passes into the delta extending into the Caspian Sea (Fig.1). The key point for the VAF is the entrance of the Volga water to Akhtuba branch, which is 6 km below the dam on the left side. The Akhtuba discharge is a few percent of the Volga discharge, but it provides the main flow of spring water to the interfluvium plain.

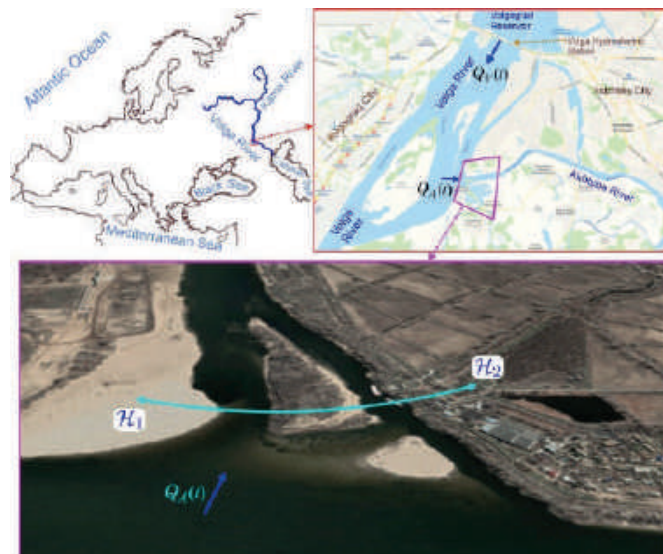


Fig. 1. The Volga River is the largest river in continental Europe, forming single water system with the Kama River (top left). The top right inset shows map of the first 12 km downstream of the Volga from the dam and the Volgograd Reservoir (Yandex). The lower inset is image of the source of the Akhtuba, which branches off from the Volga and forms the left boundary of the Lower Volga valley (Google Earth)

The aim of this work is to determine the hydrological connection between the water discharge in the Volga (hydrograph $Q_V(t)$ [m³/sec] of the HPP dam) and the water discharge in Akhtuba (hydrograph $Q_A(t)$). We use numerical model of the shallow water dynamics with real hydrographs $Q_V(t)$ for recent years.

Results of modeling water dynamics in the Northern part of the Volga-Akhtuba floodplain

An important component of the numerical hydrodynamic model is the Digital Elevation Model (DEM), which determines the topography of both riverbeds and flooded interfluvium (See Fig. 1). We use the DEM built in [3, 10]. The surface water dynamics model is based on the numerical integration of the Saint-Venant equations system [3, 11, 12] using the numerical algorithm CSPH-TVD (Combined Smoothed Particle Hydrodynamics – Total Variation Diminishing) [13]. The numerical model is based on the parallel implementation of the CSPH-TVD method for graphics accelerators (GPUs) using CUDA technology [14].

The computational domain with cell size of 15×15 (m) covers an area of 2500 km^2 . Modeling starts from low-water levels ($5000\text{--}7000 \text{ m}^3/\text{sec}$) and continues until the end of the spring flood lasting 60–90 days for different years, which differ in the behavior of the hydrograph through the Volga dam (Fig. 2, *a*). The volume of water during the low season entering the Akhtuba branch is only 1.5 percent of the total water discharge through the dam. This value can increase up to 10 percent during the flood period, ensuring further flow of water from the Akhtuba River into the network of smaller canals (the so-called eriks) at sufficiently high values of the Q_V hydrograph. We have constructed hydrographs of the source of the Akhtuba River $Q_A(t)$ through the alignment $\mathcal{H}_1 - \mathcal{H}_2$ (See Fig. 1), which are shown in Fig. 2, *b* for the corresponding hydrographs of Volga Hydroelectric Station Dam of $Q_V(t)$.

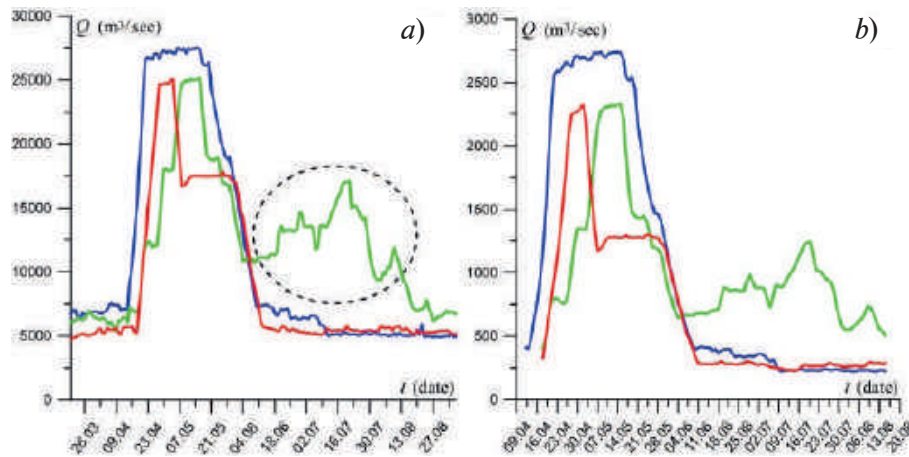


Fig. 2. The hydrographs of the Volga HPP for 2016 (blue line), 2017 (green line) and 2021 (red line) (*a*). The corresponding Akhtuba hydrographs across the river source section according to the results of numerical simulations (See the cross section of the river $\mathcal{H}_1 - \mathcal{H}_2$ in Fig. 1) (*b*)

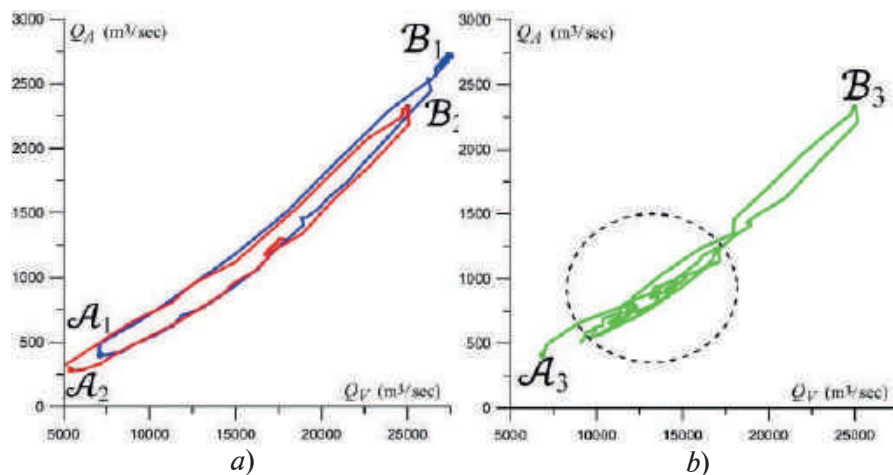


Fig. 3. Dependencies $Q_A(Q_V)$ for spring floods: (*a*) 2016 (blue line), 2021 (red line); (*b*) 2017 (green line). The dotted line indicates the part of the curve as shown in Fig. 2, *a*. The points $\mathcal{A}_{1,2,3}$ show the beginning of the flood. The maximum values of water discharge are indicated by the points $\mathcal{B}_{1,2,3}$



The hydrological connection between these rivers is characterized by the function $Q_A(Q_V)$ (Fig. 3). The hydrograph of 2017 is atypical due to the strong increase in water discharge in summer (Fig. 3, *b*). This significant excess volume of water does not lead to additional wetting of the flat part of the floodplain due to the decrease in Q_V in the period June 4 – June 19. The characteristic nonlinear form of the dependence $Q_A(Q_V)$ is due to the release of water from the main channel (riverbed) of the Volga at the high water stage $Q_V \leq 15\,000\text{ m}^3/\text{sec}$, when the effect of increasing water discharge does not lead to both a proportional increase in Q_A and an increase in the flooded area.

The dependencies of water discharge at the stages of growth and decline are asymmetric, which leads to a hysteresis of the $Q_A(Q_V)$ curve. This effect is associated with a slowdown in the response of the water flow in the Akhtuba channel due to the accumulation of large volume of water in the floodplain. There is another typical feature on the growing branch $Q_A(Q_V)$ in Fig. 3, when the active flooding of the plain begins after the break (See the arrow in the Figure). The Fig. 4 demonstrates such changes in the hydrological state of the floodplain in the numerical model.

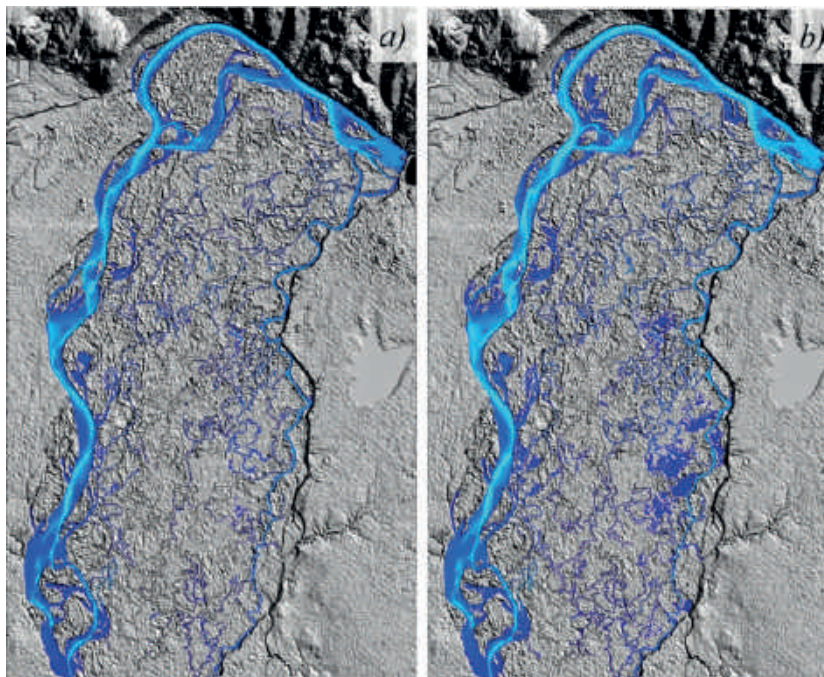


Fig. 4. Examples of flooding in the Northern part of the VAF for two times in 2021: April 22 (*a*), April 26 (*b*)

Our preliminary estimates show that the contribution of the Akhtuba is 70–80 percent to the flooding of the interfluvium, depending on the type of $Q_V(t)$. The direct contribution of the Volga through the left bank does not exceed 30 percent. Therefore, the hydrograph Q_A , and not the traditionally considered hydrograph of the Volga hydroelectric power station, has a decisive role for the Northern part of the VAF.

Conclusion

The series of computational hydrodynamic experiments were performed to simulate the process of spring floods in the Northern part of the Volga-Akhtuba floodplain in order to determine the influence of the Volga HPP hydrograph on the water flow in the Akhtuba River, which is the main channel for moistening the interfluvium.

The hydrological connection between the Volga and Akhtuba rivers is quite complex and significantly depends on the degree of flooding of the plain part during the spring flood. The water volume passing through the Akhtuba is only a few percent of the annual water flow in the Volga. Numerical models give for water volumes: $V_V^{lw} = 136.2\text{ km}^3$ for the low water, $V_A^f = 5.8\text{ km}^3$, $V_V^f = 77.6\text{ km}^3$ for the stage of flooding in 2021.

The entrance to Akhtuba is very sensitive to bottom morphology, so various options are being

considered to enhance the hydrological connection between these rivers. A possible solution is a local increase in the water level in the Volga through new dams [15], which can only be temporary due to the secular lowering of the riverbed in the vicinity of the HPP [9]. A more efficient project is the construction of bypass canal from the Volgograd reservoir to the Akhtuba.

REFERENCES

1. Sun Y., Bricheno L.M., Payo-Payo M., Rahman M.M., Burns N.M., Simulation of freshwater transport network and salt flux in the Bangladesh delta, *Estuarine, Coastal and Shelf Science*. 270 (2022) 107839.
2. Nielsen K., Zakharova E., Tarpanelli A., Andersen O.B. Benveniste J., River levels from multi mission altimetry, a statistical approach, *Remote Sensing of Environment*. 270 (2022) 112876.
3. Isaeva I.I., Voronin A.A., Khoperskov A.V., Kharitonov M.A., Modeling the Territorial Structure Dynamics of the Northern Part of the Volga-Akhtuba Floodplain, *Computation*. 10 (4) (2022) 62.
4. Voronin A., Khoperskov A., Isaeva I., Klikunova A., Control model of the floodplain territories structure, *Advances in Systems Science and Applications*. 20 (3) (2020) 153–165.
5. Sinyukovich V.N., Chernyshov M.S., Water regime of lake Baikal under conditions of climate change and anthropogenic influence, *Quaternary International*. 524 (2019) 93–101.
6. Isaeva I.I., Voronin A.A., Khoperskov A.V., Dubinko K.E., Klikunova A.Y., Decision support system for the socio-economic development of the northern part of the Volga-Akhtuba floodplain (Russia), *Conference on Creativity in Intelligent Technologies and Data Science*. – Springer, Cham. (2019) 63–77.
7. Frolova N.L., Povalishnikova E.S., Kireeva M.B., Classification and zoning of rivers by their water regime: history, methodology, and perspectives, *Water Resources*. 48 (2) (2021) 169–181.
8. Kozlova M.V., Kozlov A.V., Gorelits O.V., Zemlianov I.V., Ecological catastrophe 2015 in Volga-Akhtuba floodplain, implication and background analysis based on remotely sensed and field data, *European Space Agency, (Special Publication) ESA SP*. (2016) SP–740.
9. Golub V.B., Chuvashov A.V., Bondareva V.V., Gerasimova K.A., Nikolaychuk L.F., Maltsev M.V., Results of Long-Term Observations on Stationary Transects in the Volga–Akhtuba Floodplain, *Biology Bulletin*. 47 (10) (2020) 1309–1317.
10. Klikunova A.Yu., Khoperskov A.V., Creation of digital elevation models for river floodplains, *CEUR Workshop Proceedings*. 2391 (2019) 275–284.
11. Khrapov S.S., Khoperskov A.V., Application of Graphics Processing Units for Self-Consistent Modelling of Shallow Water Dynamics and Sediment Transport, *Lobachevskii Journal of Mathematics*. 41 (8) (2020) 1475–1484.
12. Khrapov S.S., Numerical modeling of self-consistent dynamics of shallo and ground waters, *Mathematical Physics and Computer Simulation*. 24 (3) (2021) 45–62.
13. Khrapov S., Pisarev A., Kobelev I., Zhumaliev A., Agafonnikova E., Losev A., Khoperskov A., The Numerical Simulation of Shallow Water: Estimation of the Roughness Coefficient on the Flood Stage, *Advances in Mechanical Engineering*. 2013 (2013) 787016.
14. Dyakonova T., Khoperskov A., Khrapov S., Numerical Model of Shallow Water: The Use of NVIDIA CUDA Graphics Processors, *Communications in Computer and Information Science*. 687 (2016) 132–145.
15. Agafonnikova E.O., Klikunova A.Yu., Khoperskov A.V., A computer simulation of the Volga river hydrological regime: a problem of water-retaining dam optimal location, *Bulletin of the South Ural State University, Series: Mathematical Modelling, Programming and Computer Software*. 10 (3) (2017) 148–155.

THE AUTHORS

KLIKUNOVA Anna Yu.
klikunova@volsu.ru
ORCID: 0000-0002-4055-4601

KHOPERSKOV Alexander V.
khoperskov@volsu.ru
ORCID: 0000-0003-0149-7947

Received 29.10.2022. Approved after reviewing 08.11.2022. Accepted 08.11.2022.

Conference materials

UDC 533.9.01

DOI: <https://doi.org/10.18721/JPM.161.155>

One-dimensional Fokker-Planck equation with relativistic effects for numerical simulations

V.E. Khavin , A.Yu. Popov, N.V. Teplova, G.A. Troshin, E.Z. Gusakov

Ioffe Institute, St. Petersburg, Russia

 havinvasilij@gmail.com

Abstract. This paper presents considerations on the topic of creating one-dimensional Fokker-Planck equation with relativistic effects. The derivation of two-dimensional relativistic equation and an attempt to average to the one-dimensional equation are demonstrated. The results are used for numerical simulations of LHCD.

Keywords: tokamak, current drive, helicon, electron distribution function, relativistic Fokker-Planck equation

Funding: The work is supported by Ioffe state contract 0040-2019-0023.

Citation: Khavin V.E., Popov A.Yu., Teplova N.V., Troshin G.A., Gusakov E.Z., One dimensional Fokker-Planck equation with relativistic effects for numerical simulations of LHCD. St. Petersburg State Polytechnical University Journal. Physics and Mathematics. 16 (1.1) (2023) 331–335. DOI: <https://doi.org/10.18721/JPM.161.155>

This is an open access article under the CC BY-NC 4.0 license (<https://creativecommons.org/licenses/by-nc/4.0/>)

Материалы конференции

УДК 533.9.01

DOI: <https://doi.org/10.18721/JPM.161.155>

Одномерное уравнение Фоккера-Планка с релятивистскими эффектами для численного моделирования

В.Э. Хавин , А.Ю. Попов, Н.В. Теплова, Г.А. Трошин, Е.З. Гусаков

Физико-технический институт им. А.Ф. Иоффе РАН, Санкт-Петербург, Россия

 havinvasilij@gmail.com

Аннотация. В данной работе представлены размышления на тему создания одномерного релятивистского уравнения Фоккера–Планка. Демонстрируется вывод двумерного релятивистского уравнения и попытка усреднения к одномерному уравнению. Результаты работы используются для численного моделирования LHCD.

Ключевые слова: токамак, ток увлечения, геликон, функция распределения электронов, релятивистское уравнение Фоккера–Планка

Финансирование: Работа выполнена в рамках государственного задания ФТИ им. А.Ф. Иоффе 0040-2019-0023.

Ссылка при цитировании: Хавин В.Э., Попов А.Ю., Теплова Н.В., Трошин Г.А., Гусаков Е.З. Одномерное уравнение Фоккера-Планка с релятивистскими эффектами для численного моделирования LHCD. // Научно-технические ведомости СПбГПУ. Физико-математические науки. 2023. Т. 16. № 1.1. С. 331–335. DOI: <https://doi.org/10.18721/JPM.161.155>

Статья открытого доступа, распространяемая по лицензии CC BY-NC 4.0 (<https://creativecommons.org/licenses/by-nc/4.0/>)

Introduction

The neutral beam injection and the injection of the electromagnetic waves are main methods of current generation in a tokamak that have been experimentally verified and validated [1]. At present, the method of generating current using slowed-down high-frequency waves of the lower hybrid (LH) frequency range ($\Delta f \approx (1-10)$ GHz) is widely used in classical tokamaks (with an aspect ratio of $R/a > 2$). It has the highest theoretically and experimentally confirmed efficiency. The method is based on the effect of the transmission of a pulse by a slowed-down RF wave in the lower hybrid frequency range to electrons due to Landau damping. As a result, the electron distribution function (EDF) is deformed, which ensures an increase in the total current in the tokamak plasma.

In the FRTC [2, 3] code, the calculation of the quasilinear diffusion coefficient is performed using the ray tracing method, where the wave equations for LH waves are solved under the geometric optics approximation. The injected wave power is absorbed via the Landau resonance by the electrons with velocities equal to the wave's phase velocity. As a result, the process of quasilinear diffusion on waves forms a plateau in the electron distribution function in the region of resonant velocities (there is a transition of particles from the region of lower to higher velocities with a concomitant increase in the kinetic energy of the particles). During the process there are statistically more fast particles than in an equilibrium state, hence a current arises, the time dynamics of which generate a vortex electric field. In its turn, this field begins to accelerate continuously those electrons in the tail of the distribution function, in which the electric field driving force is stronger than the minimum frictional drag force. Thus, a "tail" of fast particles is formed. The problem with the existing method is that this tail can extend up to speeds of $0.5-0.6 c$ since the code solves the one-dimensional Fokker-Planck equation without relativistic effects. This leads to an increase in the value of the generated current. This can make a negative impact on the planning of further experiments and on the scaling up of this technology to larger machines. Therefore, this paper describes an attempt to develop a one-dimensional relativistic equation, which would be possible to use in conjunction with ray tracing.

Fokker-Planck equation with relativistic effect

Let us consider a wave packet propagating at an angle to the external magnetic field $\mathbf{B}_0 = B_{0ez}$ in a homogeneous plasma. The wave field can be expressed as

$$\vec{E}(\vec{r}) = \int_{-\infty}^{+\infty} dk_z \vec{A}(k_z) \exp(ik_x x + ik_z z - i\omega t) + c.c. \quad (1)$$

Vlasov's kinetic equation with an external magnetic field for magnetized plasma is [4]:

$$\left(\frac{\partial}{\partial t} + v_i \frac{\partial}{\partial x_i} + \frac{\omega_c}{\gamma} \frac{\partial}{\partial \theta} - |e| (E_i + e_{ijk} v_j B_k) \frac{\partial}{\partial p_i} \right) f_e = St(f_e) \quad (2)$$

where θ – azimuth angle of the cylindrical coordinate system in momentum space, $\omega_c = eB_0/mc$,

$p_k = \gamma(v)m_e v_k$, $\gamma = \frac{1}{\sqrt{1 - \frac{v^2}{c^2}}}$ and $St(f_e)$ – collision operator in Landau form.

We will only examine the left-hand side of our equation. We are looking for a solution in the form of $f_e = f_0 + f^{(1)}$, where $f_0(p, t)$ – is an isotropic distribution function and $f^{(1)} = \frac{1}{2\pi} \int_{-\infty}^{\infty} dk_z f^{(1)}(k_z)$

– is the correction associated with the perturbation by waves in the plasma. Let us denote by v_z, k_z the components of the vectors \vec{v}, \vec{k} along \vec{B}_0 field, and by v_\perp, k_\perp the components in the perpendicular \vec{B}_0 plane. Let θ be the angle between \mathbf{v}_\perp and the plane \vec{k}_\perp, \vec{B}_0 (so $[\vec{e}_1 \times \vec{e}_0] = \vec{e}_z$). Substituting all this into equation (1), we can obtain

$$\frac{\partial f}{\partial \vec{p}} [\vec{v} \times \vec{B}_0] = 0 \quad (3)$$

$$(-i\alpha + i\lambda \cos(\theta)) f^{(1)}(k_z) - \frac{|e|\gamma}{2\omega_c} \left(\vec{A} + \frac{\vec{v} \times (\vec{k} \times \vec{A})}{\omega} \right) \frac{\partial f_0}{\partial \vec{p}} = 0 \quad (4)$$

$$\alpha = \frac{(\omega - k_z v_z) \gamma}{\omega_c}, \quad \lambda = \frac{k_x v_\perp \gamma}{\omega_c}, \quad \omega_c = |\omega_{ce}|.$$

From equation (3) it is clear that $\partial f_0 / \partial \theta = 0$, i. e. f_0 can be any function depending only on p_z and p_\perp : $f_0 = f_0(p_\perp, p_\parallel)$. By integrating equation (4), we obtain

$$f^{(1)}(k_z) = \frac{|e|\gamma}{2\omega_c} \exp(i\alpha\theta - i\lambda \sin(\theta)) \int_{-\infty}^0 d\theta' \exp(i\lambda \sin(\theta') - i\alpha\theta') \times$$

$$\left(\begin{aligned} & A_x \left(\left(1 - \frac{k_z v_z}{\omega}\right) \cos(\theta') \frac{\partial}{\partial p_\perp} + \frac{k_z v_\perp}{\omega} \cos(\theta') \frac{\partial}{\partial p_z} \right) + \\ & + A_y \left(\left(1 - \frac{k_z v_z}{\omega}\right) \sin(\theta') \frac{\partial}{\partial p_\perp} + \frac{k_z v_\perp}{\omega} \sin(\theta') \frac{\partial}{\partial p_z} \right) + \\ & + A_z \left(\left(1 - \frac{k_x v_\perp}{\omega} \cos(\theta')\right) \frac{\partial}{\partial p_z} + \frac{k_x v_z}{\omega} \cos(\theta') \frac{\partial}{\partial p_\perp} \right) \end{aligned} \right) f_0(p_\perp, p_z). \quad (5)$$

Using the relation $\exp(i\lambda \sin(\theta)) = \sum_p J_p(\lambda) \exp(ip\theta)$ and holding back only the terms responsible for Landau's resonant interaction with electrons, we find the correction $f^{(1)}(k_z)$:

$$f^{(1)}(k_z) = i \frac{|e|\gamma}{2\omega_c} \frac{\exp(-i\lambda \sin(\theta))}{\alpha} \vec{l}(k_z) \cdot \vec{A}(k_z) \frac{\partial}{\partial p_z} f_0(p_\perp, p_\parallel) \quad (6)$$

$$\text{where } \vec{l}(k_z) = \left[0, iJ_1(\lambda) \frac{k_z v_\perp}{\omega}, J_0(\lambda) \right]_{\omega=k_z v_z}.$$

Substituting this into (2), we obtain an equation to describe the evolution of the function f_0 :

$$\left(\frac{\partial}{\partial t_0} + v_i \frac{\partial}{\partial x_i} + \frac{\omega_c}{\gamma} \frac{\partial}{\partial \theta} \right) f_0 - \frac{|e|}{2} \int_{-\infty}^{+\infty} \frac{dk_z}{2\pi} \left(\frac{\vec{v} \times (\vec{k} \times \vec{A}^*)}{A^* + \frac{\vec{v} \times (\vec{k} \times \vec{A}^*)}{\omega}} \right) \frac{\partial f^{(1)}(k_z)}{\partial \vec{p}} - c.c. = St(f_0)$$

Again, considering only the resonance terms $\omega = k_z v_z$, after averaging over the angle θ , and averaging over the random phase $\langle (\vec{l} \cdot \vec{A}(k_z))^* (\vec{l} \cdot \vec{A}(k_z)) \rangle = 2\pi |\vec{l} \cdot \vec{A}(k_z)|^2$ we get

$$\frac{\partial f_0}{\partial t} - \frac{i|e|^2}{4} \int_{-\infty}^{\infty} dk_z \frac{\partial}{\partial p_z} \frac{|\vec{l}(k_z) \cdot \vec{A}(k_z)|^2}{\omega - k_z v_z} \frac{\partial}{\partial p_z} f_0 - c.c. = St(f_0) \quad (8)$$

Based on the Sokhotski-Plemelj theorem $\int_{-\infty}^{\infty} \frac{f(x)}{x \pm i\epsilon} dx = v.p. \int_{-\infty}^{\infty} \frac{f(x)}{x} dx \pm i\pi f(0)$.

Reducing the corresponding integrals in the sense of the Cauchy principal value, we get:

$$\frac{\partial f_0}{\partial t} - \frac{\pi|e|^2}{2} \int_{-\infty}^{\infty} dk_z \frac{\partial}{\partial p_z} |\vec{l}(k_z) \cdot \vec{A}(k_z)|^2 \delta(\omega - k_z v_z) \frac{\partial}{\partial p_z} f_0 = St(f_0) \quad (9)$$

This is the Fokker-Planck equation, where $\frac{\pi|e|^2}{2} \int_{-\infty}^{\infty} dk_z |(\mathbf{l} \cdot \mathbf{A}(k_z))|^2 \delta(\omega - k_z v_z)$ – is the diffusion coefficient.

To reduce this equation further to a one-dimensional one it is necessary to make some assumptions on the distribution function. In the absence of collisions, the relativistic collision operator from [5] is going to zero and the solution of the equation should be the Maxwell–Jüttner distribution function [5, 6]:

$$f(\vec{p}) = \frac{1}{4\pi m^3 c^3 \beta K_2\left(\frac{1}{\beta}\right)} \exp\left(-\frac{1}{\beta} \sqrt{1 + \left(\frac{p_{\perp}}{mc}\right)^2 + \left(\frac{p_{\parallel}}{mc}\right)^2}\right) \quad (10)$$

where $\beta = T/mc^2$ and K_2 – is the Macdonald function.

Provided that $p_{\perp} \ll p_{\parallel}$

$$f(\vec{p}) \propto \exp\left(-\frac{1}{\beta} \sqrt{1 + \left(\frac{p_{\perp}}{mc}\right)^2 + \left(\frac{p_{\parallel}}{mc}\right)^2}\right) \approx \exp\left(-\frac{1}{\beta} \sqrt{1 + \left(\frac{p_{\parallel}}{mc}\right)^2}\right) \exp\left(-\frac{1}{2\beta} \frac{p_{\perp}^2}{\sqrt{1 + \left(\frac{p_{\parallel}}{mc}\right)^2}}\right) \quad (11)$$

Thus, the attempt to factorize the equilibrium distribution function leads to a nonlinear dependence of the transverse component on the longitudinal momentum. That is, the transverse temperature in such a case is a function of the longitudinal momentum even in the equilibrium case. Accordingly, in the nonequilibrium case, after exposure to the wave field and vortex field, followed by scattering on the cloud of “warm” particles, the transverse component of the distribution function will continue to depend on $\gamma(p_z)$, but only by a law significantly different from the equilibrium one. Hence, it is necessary to average over an arbitrary transverse distribution function. But then we will obtain moments of distribution function that depend on $\gamma(p_z)$. The calculation of the moments would already require further assumptions on the form of the transverse component $f(p)$. Any such assumptions introduce only additional inaccuracy into the calculations, compared with the one-dimensional model without relativism.

Conclusion

As a result, the correct approach from the computational point of view is the subsequent refinement of the two-dimensional model to calculate the distribution function using the ray-tracing module. This approach will allow us to calculate the scattering of particles more correctly and, among other things, to take into account such effect as backward runaway electrons.

Acknowledgments

This work was supported by the state contract of the Ioffe Institute 0034-2021-0002.

REFERENCES

1. Fisch N.J., Mod. Phys. Rev. 59 1987.
2. Esterkin A.R., Piliya A.D., 1996 Nucl. Fusion 36 1501.
3. Saveliev A.N., 2017 EPJ Web of Conferences 157 03045.
4. Alexandrov A.F., Bogdankevich L.S., Rukhadze A.A., 1988 Principles of Plasma Electrodynamics (Moscow: High School).
5. Karney C.F.F., Fisch N.J., 1985 Phys. Fluids 28 116.
6. Jüttner F., 1911 Annalen der Physik, 339 (5) 856.



THE AUTHORS

KHAVIN Vasilij E.
havinvasilij@gmail.com

TROSHIN Grigorii A.
paladinbubble@mail.ru

POPOV Alexei Yu.
a.popov@mail.ioffe.ru

GUSAKOV Evgeniy Z.
evgeniy.gusakov@mail.ioffe.ru

TEPLOVA Natalia V.
natalia.teplova@mail.ioffe.ru

Received 31.10.2022. Approved after reviewing 09.12.2022. Accepted 28.01.2023.

Conference materials
UDC 621.315.592.9+532.5-1/-9
DOI: <https://doi.org/10.18721/JPM.161.156>

Study of the effect of dynamic and temperature inhomogeneities on epitaxial processes in a horizontal CVD reactor

V.A. Ignatenko ¹✉, A.A. Smirnovsky ^{1,2}

¹ Peter the Great St. Petersburg Polytechnic University, St. Petersburg, Russia;

² Ioffe Institute, St. Petersburg, Russia

✉ ignatenko2.v@edu.spbstu.ru

Abstract. In order to investigate the effect of temperature and velocity inhomogeneities at the reactor inlet on the susceptor growth rate distribution, a numerical simulation of the flow in a horizontal CVD reactor was carried out. It was obtained that the velocity inhomogeneity can reach 60%, and this can considerably affect the growth rate distribution on susceptor. To simulate the temperature inhomogeneities, the temperature distribution at the reactor inlet was set separately for the bottom and the main inlet. The temperature inhomogeneity at the bottom inlet affects the growth rate distribution more drastically than at the main inlet. This influence is quite strong and should be taken into account for accurate simulation of the flow and growth processes in similar horizontal CVD reactors.

Keywords: ANSYS Fluent, CFD, numerical simulation, MOVPE, CVD

Citation: Ignatenko V.A., Smirnovsky A.A., Study of the effect of dynamic and temperature inhomogeneities on epitaxial processes in a horizontal CVD reactor, St. Petersburg State Polytechnical University Journal. Physics and Mathematics. 16 (1.1) (2023) 336–340. DOI: <https://doi.org/10.18721/JPM.161.156>

This is an open access article under the CC BY-NC 4.0 license (<https://creativecommons.org/licenses/by-nc/4.0/>)

Материалы конференции
УДК 621.315.592.9+532.5-1/-9
DOI: <https://doi.org/10.18721/JPM.161.156>

Влияние динамических и температурных неоднородностей на эпитаксиальные процессы в горизонтальном CVD-реакторе

В.А. Игнатенко ¹✉, А.А. Смирновский ^{1,2}

¹ Санкт-Петербургский Политехнический Университет Петра Великого, Санкт-Петербург, Россия;

² Физико-технический институт им. Иоффе РАН, Санкт-Петербург, Россия

✉ ignatenko2.v@edu.spbstu.ru

Аннотация. Для исследования влияния температурных и скоростных неоднородностей на входе в реактор на распределение скорости роста на подложкодержателе было проведено численное моделирование потока в горизонтальном CVD-реакторе. Было получено, что неоднородность скорости может достигать 60%, и это может значительно повлиять на распределение скорости роста на подложкодержателе. Для моделирования температурных неоднородностей распределение температуры на входе в реактор задавалось отдельно для нижнего и основного входа. Температурная неоднородность на нижнем входе влияет на распределение скорости роста более сильно, чем на основном входе. Это влияние довольно сильное и должно учитываться для точного моделирования течения и процессов роста в подобных горизонтальных CVD-реакторах.

Ключевые слова: ANSYS Fluent, CFD, компьютерное моделирование, МОСГФЭ, химическая эпитаксия

Ссылка при цитировании: Игнатенко В.А., Смирновский А.А. Влияние динамических и температурных неоднородностей на эпитаксиальные процессы в горизонтальном



CVD-реакторе // Научно-технические ведомости СПбГПУ. Физико-математические науки. 2023. Т. 16. № 1.1. С. 336–340. DOI: <https://doi.org/10.18721/JPM.161.156>

Статья открытого доступа, распространяемая по лицензии CC BY-NC 4.0 (<https://creativecommons.org/licenses/by-nc/4.0/>)

Introduction

Nitride monocrystals have unique physical properties. Such properties as high saturated electron velocity and the ability to form solid solutions make these semiconductor structures indispensable for high-frequency electronic devices. There are several ways to fabricate such structures, and one of the most popular is chemical vapour deposition (CVD) [1]. This method is based on growing a crystal on a susceptor out of gas-phase components as a result of surface chemical reactions. There are several types of such reactors; in this paper we consider a horizontal one. In contrast to vertical ones, horizontal reactors allow multi-parameter optimization over a wide range of parameters. Its relative cheapness is also an advantage. Therefore, the use of horizontal reactors is very prospective.

There are many publications on the physicochemical aspects of the growth of nitride structures in horizontal reactors. In particular, many papers analyze the dependence of epitaxial parameters on pressure [2], susceptor temperature [3], or reagent flow rate [4]. A much smaller number of studies concern hydrodynamic factors. For example, in [5] the influence of precursor supply configuration through different inlets on the epitaxial processes is investigated.

Due to the design features (including the complex reactant supply system) in a horizontal reactor, significant inhomogeneities in velocity and temperature at the reactor inlet can occur. Such effects as, for example, local overheating of the injector caused by irradiation from the susceptor can lead to a flow restructuring and a change in the pattern of the crystal parameters distribution over the susceptor. It is important to consider such effects when designing new reactors and determining its optimal operating conditions. This study was carried out in order to investigate the effect of possible inhomogeneities in a horizontal reactor on epitaxial processes.

Materials and Methods

In this paper the peculiarities of growth processes in the model of the experimental setup “Dragon 125” (125 is the diameter of a susceptor in millimeters), which is currently active in the Science and Technique Center of microelectronics (STC) [6], are analyzed by means of numerical simulation. Numerical simulation replicates in-situ experiments done at the STC. Figure 1 shows the computational domain (only half of the geometry was considered with the symmetry boundary condition). It includes the gas domain (Fig. 1, *a*, *b*) located inside a quartz reactor, which itself is placed inside a nitrogen tank (Fig. 1, *c*). Through the main inlet, aluminum trimethyl and hydrogen are fed. Ammonia is supplied through the bottom inlet. A long slit channel is placed in front of the main inlet, which is set aside in the figure for clarity. The susceptor is heated to a temperature of 1100 °C. External heat transfer boundary condition is set on the rest of the bottom wall. The walls of the nitrogen tank are water-cooled and the temperature on them is assumed to be 150 °C. A crystal is assumed to grow on all the inner walls. In the simulation, this is accounted for by a chemical surface reaction model [7]. The susceptor rotates slowly; its rotation has low effect on the growth processes and is taken into account in the postprocessing of the calculation results by averaging the crystal growth rate in the azimuthal direction.

In front of the bottom inlet the bottom injector is located. It is a mixing chamber from which the gas flows into the slotted channel. In this paper two cases are considered: with and without bottom injector (in the second case a uniform velocity profile on the bottom inlet was set). The flow inside the channels and the chamber is laminar; typical Reynolds number does not exceed 1.

In order to reproduce possible temperature inhomogeneities, temperatures at lines T_1^m , T_2^m , T_1^b , T_2^b and T_3 were varied in the simulation (Fig. 2). A quadratic distribution is set between T_1^m and T_2^m , as well as between T_1^b and T_2^b . A linear distribution is set between T_1^m and T_3 .

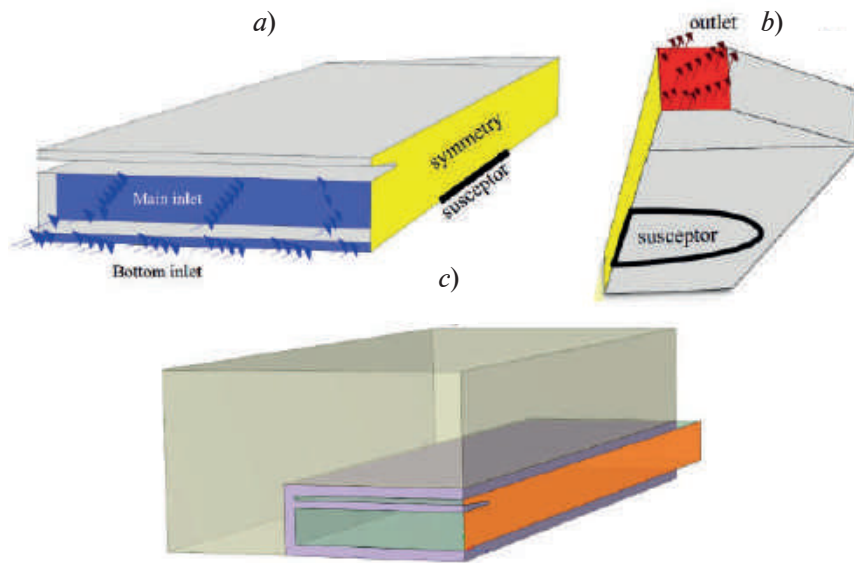


Fig. 1. Computational domain. Gas block (a, b) and the whole geometry (c)

Numerical simulation was performed using ANSYS Fluent. Second Order Upwind numerical scheme was used for spatial approximation. Green-Gauss Cell Based method was used for gradient discretization. SIMPLEC pressure-velocity coupling scheme was used to solve the equations of low-speed flow of a multi-component mixture.

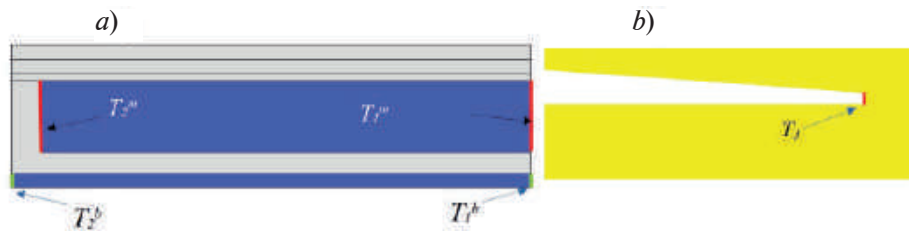


Fig. 2. Schematic diagram of setting temperature boundary conditions. Front view on inlets (a) and view on symmetry plane (b)

Results and Discussion

In the experiment at high flow rates, the velocity inhomogeneity at the bottom inlet with a local maximum on the symmetry plane ($z = 0$) can occur. The characteristic velocity distribution in the outlet section for this case is shown in Fig. 3. The maximum velocity can exceed the average value by 60%, so the assumption of the uniform velocity profile here is not correct.

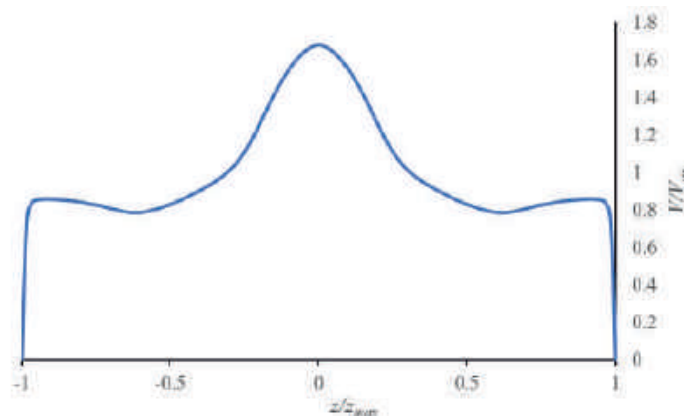


Fig. 3. Velocity distribution at the outlet of the bottom injector

By setting given velocity profile at the bottom inlet, the flow structure in the reactor changes considerably. Fig. 4 shows the field of the vertical velocity component at a distance of 1 calibre from the reactor inlet (1 calibre is bottom inlet height). It can be seen that in the case of a non-uniform profile, there is additional convective flow directed from the main inlet to the susceptor.

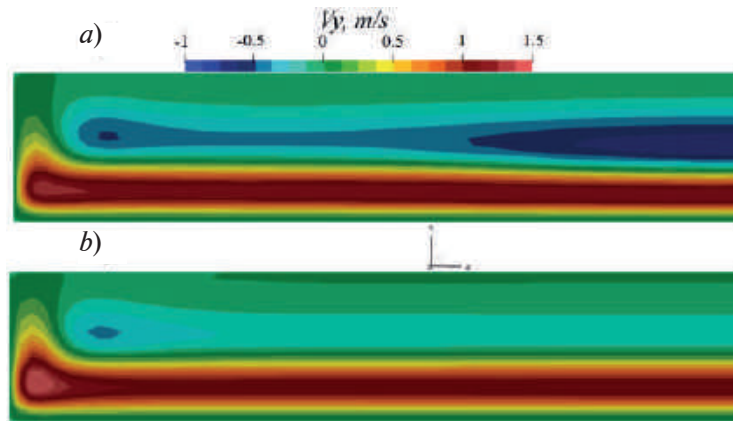


Fig. 4. Vertical velocity component at 1 calibre distance from the reactor inlet with non-uniform (a) and uniform (b) velocity profile at the bottom inlet

In case of non-uniform velocity profile, the growth rate distribution across the susceptor also changes significantly, as can be seen in Fig. 5, where the dependence of the angle-averaged growth rate on the distance from the center of the susceptor is shown. The growth rate at the center of the susceptor increases drastically and decreases at the periphery. Thus, results shown below are obtained with a non-uniform velocity profile at the bottom inlet.

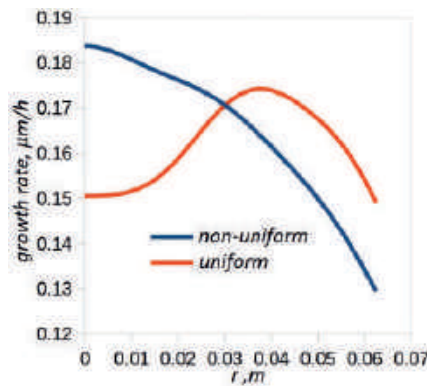


Fig. 5. Averaged growth rate profile obtained with uniform and non-uniform velocity profile at the bottom inlet

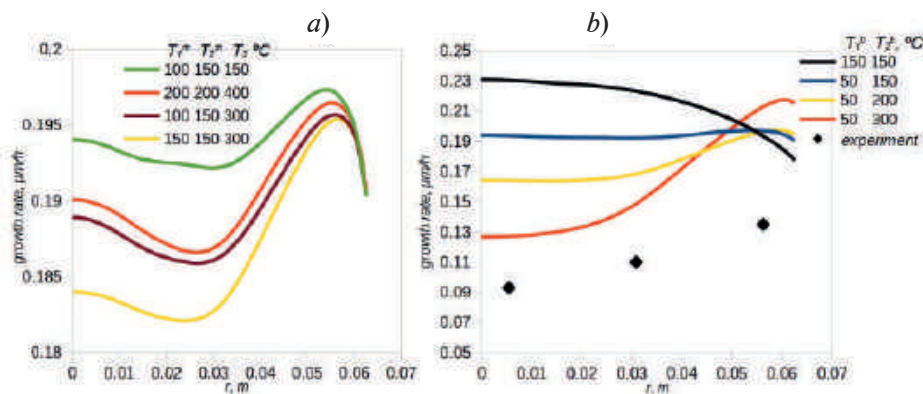


Fig. 6. Growth rate plots for temperature inhomogeneities at the main (a) and bottom (b) inlets

The effect of temperature inhomogeneity at the main inlet is shown in Fig. 6, *a*, where the plots of the averaged growth rate profile are shown. The growth rate decreases with increasing T_1^m , it also decreases with increasing T_3 . It can be seen that these parameters have a stronger influence on the growth rate in the center than in the periphery. Increasing T_2^m only slightly increases the growth rate.

The growth rate profiles for varying temperatures T_1^b and T_2^b are shown in Fig. 6, *b*. It can be seen that the growth rate at the periphery increases with increasing temperature at the wall. The growth rate also increases when the temperature at the middle of the inlet decreases. Note that there is a qualitative agreement with the experimental trend (yellow and red curves).

Conclusion

Numerical simulations were carried out to establish the effect of inhomogeneities in reactor inlet velocity and temperature on the epitaxial processes. The results obtained are important for detailed modelling of the reactor. It is shown that due to the structure of the injector, significant velocity inhomogeneities are formed at the reactor inlet. These inhomogeneities have a significant impact not only on the growth rate level but also on the growth rate distribution over the susceptor. Temperature inhomogeneities at the inlet also affect the growth rate distribution over the susceptor. At the bottom inlet, a temperature lowering at the center (T1b) reduces the growth rate at the center and increases it at the periphery. In contrast, a temperature reduction at the wall (T2b) increases the growth rate at the center and decreases it at the periphery. Temperature inhomogeneities at the main inlet affect the distribution of the growth rate in the opposite way. It should be noted that this effect is weaker than the effect of inhomogeneities at the bottom inlet.

REFERENCES

1. Daulsberg M., Talalaev R.A., Progress in Modeling of III-Nitride MOVPE, Progress in Crystal Growth and Characterization of Materials. 66 (2020) 100486.
2. Lundin W.V., Zavarin E.E., Sizov D.S., Sinitsin M.A., Tsatsul'nikov A.F., Kondratyev A.V., Yakovlev E.V., Talalaev R.A., Effects of reactor pressure and residence time on GaN MOVPE growth efficiency, J. of Crystal Growth. 287 (2006) 605–609.
3. Talalaev R.A., Yakovlev E.V., Karpov S.Yu., Makarov Yu.N., On low temperature kinetic effects in metal–organic vapor phase epitaxy of III–V compounds, J. of Crystal Growth 230 (2001) 232–238.
4. Yakovlev E.V., Talalaev R.A., Makarov Yu.N., Yavich B.S., Wang W.N., Deposition behavior of GaN in AIX 200/4RF-S horizontal reactor, J. of Crystal Growth 261 (2004) 182–189.
5. Yakovlev E.V., Talalaev R.A., Kaluza N., Hardtdegen H., Bay H.L., Influence of the reactor inlet configuration on the AlGaN growth efficiency, J. of Crystal Growth 298 (2007) 413–417.
6. Zavarin E.E., Sakharov A.V., Tsatsul'nikov A.F., Ustinov V.M., Reactors for gallium nitride CVD epitaxy: present and future, Scientific instrumentation engineering, (in Russian) 27 (1) (2017) 5–9.
7. Lobanova A.V., Mazaev K.M., Talalaev R.A., Leys M., Boeykens S., Cheng K., Degroote S., Effect of V/III ratio in AlN and AlGaN MOVPE J. of Crystal Growth 287 (2006) 601–604.

THE AUTHORS

IGNATENKO Viktor A.
ignatenko2.v@edu.spbstu.ru

SMIRNOVSKY Aleksander A.
smirta@mail.ru

Received 27.12.2022. Approved after reviewing 27.12.2022. Accepted 16.01.2023.

ATOM PHYSICS AND PHYSICS OF CLUSTERS AND NANOSTRUCTURES

Conference materials

UDC 538.975

DOI: <https://doi.org/10.18721/JPM.161.157>

Formation of Ge quantum dots on GaN nanowires by molecular beam epitaxy

I.V. Ilkiv^{1,2}✉, K.P. Kotlyar², D.A. Kirilenko³, V.A. Sharov¹,
R.R. Reznik^{1,2}, G.E. Cirlin^{1,4}

¹ Alferov University, St. Petersburg, Russia;

² St. Petersburg State University, St. Petersburg, Russia;

³ Ioffe Institute, St. Petersburg, Russia;

⁴ Institute for Analytical Instrumentation of the RAS, St. Petersburg, Russia

✉ fiskerr@ymail.com

Abstract. Germanium nanocrystals were grown on GaN nanowire sidewalls by molecular beam epitaxy. The transmission electron microscopy measurements revealed the formation of 6–10 nm in size Ge quantum dots, which exhibited diamond cubic crystal structure. Raman spectroscopy indicate that uncapped Ge QDs are stress relaxed compared to ones additionally capped with GaN.

Keywords: nanowire, molecular beam epitaxy, germanium, semiconductors

Funding: The samples were grown under the support of IAI RAS grant FFZM-2022-0008. Optical and structural studies were done under financial support of St. Petersburg State University under research grant no. 93020138.

Citation: Ilkiv I.V., Kotlyar K.P., Kirilenko D.A., Sharov V.A., Reznik R.R., Cirlin G.E. Formation of Ge quantum dots on GaN nanowires by molecular beam epitaxy, St. Petersburg State Polytechnical University Journal. Physics and Mathematics. 16 (1.1) (2023) 341–345. DOI: <https://doi.org/10.18721/JPM.161.157>

This is an open access article under the CC BY-NC 4.0 license (<https://creativecommons.org/licenses/by-nc/4.0/>)

Материалы конференции

УДК 538.975

DOI: <https://doi.org/10.18721/JPM.161.157>

Формирование германиевых квантовых точек на поверхности нитевидных нанокристаллов GaN методом молекулярно-пучковой эпитаксии

И.В. Илькив^{1,2}✉, К.П. Котляр², Д.А. Кириленко³, В.А. Шаров¹,
Р.Р. Резник^{1,2}, Г.Э. Цырлин^{1,4}

¹ Академический университет им. Ж.И. Алфёрова, Санкт-Петербург, Россия;

² Санкт-Петербургский государственный университет, Санкт-Петербург, Россия;

³ Физико-технический институт им. А.Ф.Иоффе РАН, Санкт-Петербург, Россия;

⁴ Институт аналитического приборостроения РАН, Санкт-Петербург, Россия

✉ fiskerr@ymail.com

Аннотация. В настоящей работе исследованы процессы формирования германия на поверхности GaN нитевидных нанокристаллов при молекулярно-пучковой эпитаксии. Продемонстрирована возможность формирования Ge островков размером 6–10 нм на боковых гранях GaN нитевидных нанокристаллов и создания гетероструктур на

их основе. С помощью спектроскопии комбинационного рассеивания показано, что формирование GaN покровного слоя приводит к формированию упругих напряжений в Ge квантовых точках.

Ключевые слова: нитевидные нанокристаллы, молекулярно-пучковая эпитаксия, германий, полупроводники

Финансирование: Синтез образцов был выполнен при финансовой поддержке ИАП по государственному заданию FFZM-2022-0008. Измерения структурных и оптических свойств выполнены в рамках гранта СПбГУ 93020138.

Ссылка при цитировании: Илькив И.В., Котляр К.П., Кириленко Д.А., Шаров В.А., Резник Р.Р., Цырлин Г.Э., Формирование германиевых квантовых точек на поверхности GaN нитевидных нанокристаллов методом молекулярно-пучковой эпитаксии // Научно-технические ведомости СПбГПУ. Физико-математические науки. 2023. Т. 16. № 1.1. С. 341–345. DOI: <https://doi.org/10.18721/JPM.161.157>

Статья открытого доступа, распространяемая по лицензии CC BY-NC 4.0 (<https://creativecommons.org/licenses/by-nc/4.0/>)

Introduction

Germanium based nanomaterials gained large interest because of their interesting optical and electronic properties [1]. Although bulk Ge is an indirect bandgap material, the applying of tensile strain could convert Ge into a direct bandgap semiconductor [2]. It is well known that planar Ge thin films suffer from structural defects. In turn, nanoparticles and quantum dots (QDs) are considerably less sensitive to defects and could hold large strain without plastic relaxation. Such evidences make them very promising for a new class of efficient and tunable optoelectronic devices [3–5]. One of the promising way to obtain tensile-strained Ge QDs is based on the monolithic epitaxial growth on lattices-mismatched substrates. The growth of strained Ge QDs and fabrication of nanocomposite demonstrating efficient photoluminescence have been obtained on Si, GaSb, InAlAs surfaces [6–8].

To obtain more functions and superior properties, recent efforts have focused on using nanowires (NWs) as substrates to produce attractive core/shell structures that combine QDs with NWs. Heterostructured NWs can be realized based on pioneering material combinations, otherwise highly defective in their planar form. Looking at the literature on the QDs growth on NW side-facets, a common works have focused mainly on varying NW dimensions for fixed lattice mismatched systems, such as GaAs/InAs [9], Si/Ge [10–12] or GaAs/Ge [13]. At the same time, exploring other templates could reveal many new and important possibilities for further engineering of III-V/IV NWs.

In this work we looked into the feasibility of using GaN NWs as a substrates for Ge QDs growth. The initial results on Ge QDs formation by molecular beam epitaxy and structural analyses are discussed.

Materials and Methods

Growth experiments were performed using the solid state 21EB200 Riber MBE system additionally equipped with N-plasma source and e-beam evaporator for Ge deposition. The growth of samples was carried out on Si(111) substrates. Prior to growth, wet chemical processing followed with degassing and annealing step at 950 °C were performed to achieve atomically-clean Si(111) 7×7 surface. Afterwards, the temperature was decreased to 840 °C and self-assembled plasma-assisted growth of GaN NWs was carried out. The radio frequency N plasma-source was operated at 400W using a N₂ flow of 1 sccm, Ga flow rate was set to 1.7 Å/s. The total NW growth time was equal to 16 hours. The reflection high-energy electron diffraction (RHEED) method was used to control in situ the processes occurring on the substrate surface. According to the RHEED patterns GaN NWs had pure hexagonal crystal structure. After the formation of GaN NWs, the substrate temperature was decreased to 320 °C and the deposition of Ge was performed. The growth rate of Ge was corresponded to 0.2 Å/s. During the Ge deposition RHEED revealed the formation of mixed hexagonal/cubic phases.

The morphological properties of the samples have been studied using scanning electron microscopy (SEM) Zeiss SUPRA 25. The crystal structure of GaN/Ge NWs was investigated in a JEM-2100F TEM (Jeol) equipped with an EDX spectroscope QUANTAX XFlash 6/60 system, Bruker as well as Raman micro-spectroscopy (Horiba LabRam HR-800 with 532 nm excitation laser and $\times 100$ lens with 0.9 numerical aperture). For TEM and Raman analysis, the NWs were transferred onto Cu grids coated with carbon film by gently rubbing the grid against the substrate to break the NWs at the base.

Results and Discussion

Typical array of GaN NWs grown by plasma-assisted MBE growth is presented in Fig. 1. Vertical NWs with $2.2\ \mu\text{m}$ in length were straight, smooth and exhibited sixfold symmetric facets (see Fig. 1, *a*). The diameters of NWs were about 160 nm, while side-facets width corresponded to 80 nm.

Primary, to investigate the Ge growth, 160 nm layer was deposited on the GaN NWs after their formation. As it can be seen in Fig. 1, *b*, it resulted in the formation of rough polycrystalline shells on NWs and bulbs on NW tips. In turn, nanosized Ge QDs decorated the NW sidewalls were found on the samples with lower germanium coverage (about 60 nm). The density of Ge QDs decreased from NW tips to base, which was apparently related to the high density of GaN NWs.

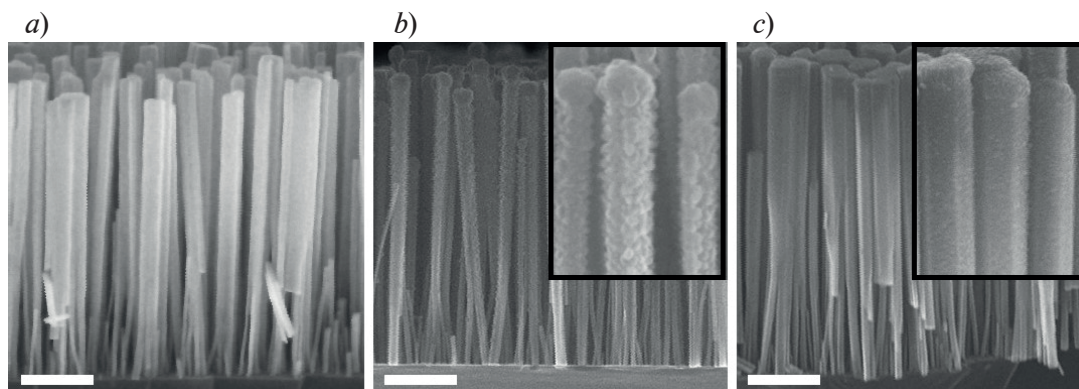


Fig. 1. SEM images of GaN NWs grown on the Si(111) substrates (*a*), GaN/Ge NWs with 1 nm (*b*) and 40 nm (*c*) deposited Ge. The images in the insets illustrate close-up views of NWs. Scale bars correspond to 400 nm

Characterization of GaN-Ge NWs by scanning TEM (STEM) was conducted in high angular annular bright field mode. A low magnification STEM image in the $[1\bar{1}00]$ zone axis confirmed the formation of Ge QDs on GaN NW side sidewalls with no overlap between neighbouring dots, as shown in Fig. 2, *a*. Ge QDs exhibited hemispherical shapes with diameter at the base of about 6–10 nm. The high-resolution TEM image shown in the insertion of Fig. 2, *a* indicates that individual Ge dot has a diamond cubic structure unlike the formation of Ge on AlGaAs or GaAs NWs [14]. This finding was verified also by selected area diffraction patterns taken from GaN NW and Ge QD.

Fig. 3 demonstrates Raman spectra of the sample investigated by HRTEM. Raman spectrum contains two peaks with the maximum at $522\ \text{cm}^{-1}$ and $302\ \text{cm}^{-1}$. The peak at $522\ \text{cm}^{-1}$ is attributed to the well-known A1 (TO) phonon mode of wurtzite GaN [15]. The $302\ \text{cm}^{-1}$ peak is assigned to the Ge–Ge mode and it is closely related to relaxed Ge nanocrystals. Thus, it suggests that the Ge QDs are pure. In addition, the line shape of the Ge QDs was observed to be asymmetric. Similar asymmetric line shape has been reported for InAs QDs and other arsenide material systems [16]. A similar asymmetric phonon line shape of Ge QDs is characteristic of Raman spectra of nanocrystalline structures, which can be described by a model of phonon confinement in nanoclusters of inhomogeneous size [17]. Additionally, it was suggested that the stress Ge QDs can be obtained by embedding into the matrix. For this purpose, capping of the samples with Ge QDs by GaN was carried out. Preliminary studying of the samples obtained revealed the downshifting of Ge QDs peak to $297\ \text{cm}^{-1}$.

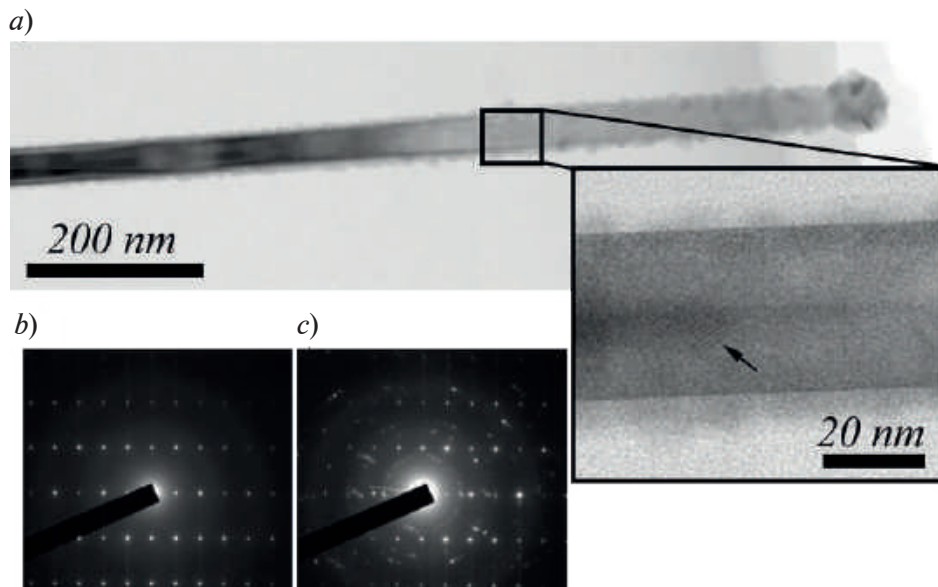


Fig. 2. Low magnification scanning TEM images of GaN/Ge NW and HR TEM image GaN/Ge NW acquired in the $[112\bar{0}]$ zone axis in the insertion. Diffraction pattern of pure hexagonal GaN NWs (b) and of Ge QD from the area pointed by arrow (c)

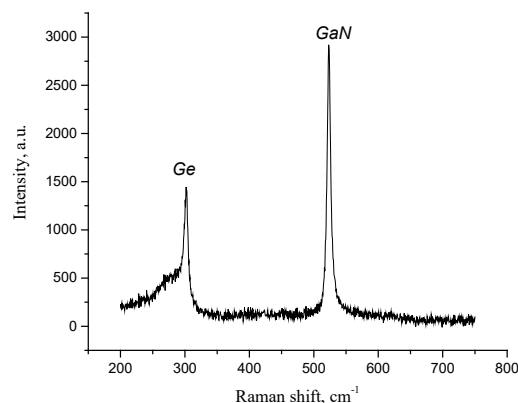


Fig. 3. Survey Raman spectra of GaN/Ge NW heterostructure

Conclusion

In summary, this study demonstrated the growth of 3D epitaxial Ge QDs around GaN nanowires. Cross-sectional TEM verified the surface faceting of the GaN core nanowires as well as the Ge quantum dots. Raman spectroscopy revealed the asymmetric line shape of Ge QDs, which could be caused by the inhomogeneous sizes of the QDs as well as the phonon confinement. The Raman results also indicate strain relaxation in uncapped Ge QDs, as well as strain shifting in Ge QDs additionally capped with GaN.

Acknowledgments

The samples were grown under the support of IAI RAS grant FFZM-2022-0008. Optical and structural studies were done under financial support of St. Petersburg state university under research grant No. 93020138.

REFERENCES

1. Vaughn II D.D., Schaak R.E., Synthesis, properties and applications of colloidal germanium and germanium-based nanomaterials, *Chemical Society Reviews*, 42 (7) (2013) 2861–2879.
2. Fischetti M.V., Laux S.E., Band structure, deformation potentials, and carrier mobility in strained Si, Ge, and SiGe alloys, *Journal of Applied Physics*, 80 (4) (1996) 2234–2252.

3. Xiao X., Li X., Zheng S., Shao J., Xue H., Pang H., Nanostructured germanium anode materials for advanced rechargeable batteries, *Advanced Materials Interfaces*, 4 (6) (2017) 1600798.
4. Shi S., Zaslavsky A., Pacifici D., High-performance germanium quantum dot photodetectors: Response to continuous wave and pulsed excitation, *Applied Physics Letters*, 117 (25) (2020) 251105.
5. Cosentino S., Torrisi G., Raciti R., Zimbone M., Crupi I., Mirabella S., Terrasi A., Growth kinetics of colloidal Ge nanocrystals for light harvesters, *RSC advances*, 6 (44) (2016) 38454–38462.
6. Chen Q., Zhang L., Song Y., Chen X., Koelling S., Zhang Z., Li Y., Koenraad P.M., Sgai J., Tan S.C., Wang S., Gong Q., Highly tensile-strained self-assembled Ge quantum dots on InP substrates for integrated light sources, *ACS Applied Nano Materials*, 4 (1) (2021) 897–906.
7. Zhang Z., Song Y., Chen Q., Gong Q., Wang S., Highly tensile-strained Ge quantum dots on GaSb by MBE for light sources on Si, *IEEE Photonics Society Summer Topical Meeting Series* (2016) 82–83.
8. Valakh M.Y., Lytvyn P.M., Nikolenko A.S., Strelchuk V.V., Krasilnik Z.F., Lobanov D.N., Novikov A.V., Gigantic uphill diffusion during self-assembled growth of Ge quantum dots on strained SiGe sublayers, *Applied Physics Letters*, 96 (14) (2010) 141909.
9. Uccelli E., Arbiol J., Morante J.R., Fontcuberta i Morral A., InAs quantum dot arrays decorating the facets of GaAs nanowires, *ACS nano*, 4 (10) (2010) 5985–5993.
10. Pan Y., Hong G., Raja S.N., Zimmermann S., Tiwari M.K., Poulikakos D., Significant thermal conductivity reduction of silicon nanowire forests through discrete surface doping of germanium, *Applied Physics Letters*, 106 (9) (2015) 093102.
11. Kwon S., Chen Z. C., Kim J. H., Xiang J., Misfit-guided self-organization of anticorrelated Ge quantum dot arrays on Si nanowires, *Nano letters*, 12 (9) (2012) 4757–4762.
12. Weng X., Yang J., Li D., Wang R., Qiu F., Wang C., Yang Y., Review of the preparation and structures of Si nanowires, Ge quantum dots and their composites, *Nano*, 14 (04) (2019) 1930004.
13. Zhang Y., Fonseka H.A., Yang H., Yu X., Jurczak P., Huo S., Liu H., Thermally-driven formation of Ge quantum dots on self-catalysed thin GaAs nanowires, *arXiv preprint arXiv:2103.16915* (2021).
14. Ilkiv I.V., Kotlyar K.P., Kirilenko D.A., Osipov A.V., Soshnikov I.P., Mikushev S.V., Cirilin G.E., Formation of Hexagonal Ge Stripes on the Side Facets of AlGaAs Nanowires: Implications for Near-Infrared Detectors, *ACS Applied Nano Materials*, 4 (7) (2021) 7289–7294.
15. Wang J., Demangeot F., Péchou R., Bayon C., Mlayah A., Daudin B., Size and shape effects in the Raman scattering by single GaN nanowires, *Journal of Applied Physics*, 114 (22) (2013) 223506.
16. Tenne D.A., Bakarov A.K., Toropov A.I., Zahn D.R.T., Raman study of self-assembled InAs quantum dots embedded in AlAs: influence of growth temperature, *Physica E: Low-dimensional Systems and Nanostructures*, 13 (2-4) (2002) 199–202.
17. Campbell I.H., Fauchet P.M., The effects of microcrystal size and shape on the one phonon Raman spectra of crystalline semiconductors, *Solid State Communications*, 58 (10) (1986) 739–741.

THE AUTHORS

ILKIV Igor V.

fiskerr@ymail.com

ORCID: 0000-0001-8968-3626

SHAROV Vladislav A.

vl_sharov@mail.ru

ORCID: 0000-0001-9693-5748

KOTLYAR Konstantin P.

konstantin21kt@gmail.com

ORCID: 0000-0002-0305-0156

REZNIK Rodion R.

moment92@mail.ru

ORCID: 0000-0003-1420-7515

KIRILENKO Demid A.

zumsisai@gmail.com

ORCID: 0000-0002-1571-209X

CIRLIN George E.

george.cirlin@mail.ru

ORCID: 0000-0003-0476-3630

Received 20.10.2022. Approved after reviewing 09.11.2022. Accepted 25.11.2022.

Conference materials

UDC 539.18

DOI: <https://doi.org/10.18721/JPM.161.158>

Conductivity in nanostructured films of paramagnetic manganese phthalocyanine

Yu.I. Sachkov¹✉, P.A. Yunin¹, V.V. Travkin¹

¹Institute for Physics of Microstructures RAS, Afonino, Nizhny Novgorod region, Russia

✉ Sachkov@ipmras.ru

Abstract. Manganese (II) phthalocyanine MnPc is known for its interesting magnetic properties and diverse coordination chemistry, but little is known about its conductivity. In our previous work, we observed how introduction of a permanent magnetic field during deposition modifies the microcrystalline structure of the growing MnPc films. In this paper, we have shown that the magnetic field, together with the substrate temperature, is responsible for the lateral current in the two-terminal MnPc-based cells with interdigital contacts to change, while the influence of atmospheric environment and illumination is much less noticeable.

Keywords: conductivity, vacuum evaporation, film, manganese phthalocyanine

Funding: RNF Grant No. 20-72-00118 “Magnetically induced effects in Mn(II)Pc crystalline films”.

Citation: Sachkov Yu.I., Yunin P.A., Travkin V.V., Conductivity in nanostructured films of paramagnetic manganese phthalocyanine, St. Petersburg State Polytechnical University Journal. Physics and Mathematics. 16 (1.1) (2023) 346–350. DOI: <https://doi.org/10.18721/JPM.161.158>

This is an open access article under the CC BY-NC 4.0 license (<https://creativecommons.org/licenses/by-nc/4.0/>)

Материалы конференции

УДК 539.18

DOI: <https://doi.org/10.18721/JPM.161.158>

Проводимость наноструктурированных пленок фталоцианина марганца

Ю.И. Сачков¹✉, П.А. Юнин¹, В.В. Травкин¹

¹Институт Физики Микроструктур РАН, д. Афонино, Нижегородская обл., Россия

✉ Sachkov@ipmras.ru

Аннотация. Фталоцианин марганца известен своими интересными магнитными свойствами и разнообразием координационных взаимодействий, но о его проводимости в твердой фазе известно немного. В предыдущей работе мы наблюдали, как приложение постоянного магнитного поля во время роста меняет кристаллическую структуру пленок фталоцианина марганца. В данной работе мы показали, что магнитное поле, совместно с температурой подложки, ответственно за изменение токов в двухконтактных устройствах на основе фталоцианина марганца и встречно-штыревых контактов, в то время как влияние окружающей атмосферы и освещения гораздо менее заметны.

Ключевые слова: проводимость, вакуумный рост, пленка, фталоцианин марганца

Финансирование: Грант РНФ № 20-72-00118 «Магнитоиндуцируемые эффекты в кристаллических пленках Mn(II)Pc».

Ссылка при цитировании: Сачков Ю.И., Юнин П.А., Травкин В.В. Проводимость наноструктурированных пленок фталоцианина марганца // Научно-технические

ведомости СПбГПУ. Физико-математические науки. 2023. Т. 16. № 1.1. С. 346–350.
DOI: <https://doi.org/10.18721/JPM.161.158>

Статья открытого доступа, распространяемая по лицензии CC BY-NC 4.0 (<https://creativecommons.org/licenses/by-nc/4.0/>)

Introduction

Bright prospects of quantum computing and magnetic memory [1] have stimulated great interest in the physics of organometallic complexes, such as metal phthalocyanines. However, unlike inorganic (semi)conductors, these molecular materials have a more complex, two-level organization of a solid: the internal atomic structure of molecular skeleton and the arrangement of molecules in a bulk sample, each of which related to its macroscopic electro-physical and magnetic properties.

Phthalocyanines are impurity semiconductors [2, 3] whose conductivity value and even the sign depend on the sample history and the environment. In addition, the understanding of charge transport processes suffers from an uneven microcrystalline morphology of films that have several temperature-dependent polymorphs [2, 3]. It is hence desirable to find a method or experimental setup that would allow reproducibly obtaining phthalocyanine films of a certain structural quality. One of such parameters can be permanent magnetic field introduced into the growth zone during the vacuum deposition process.

Manganese phthalocyanine (MnPc) is a spin 3/2 paramagnetic complex whose molecules form crystalline phases with a herringbone motif, which is characteristic of other planar phthalocyanines. However, MnPc molecules interact more strongly with each other, which leads to an interplanar spacing of 3.2 nm [4] and ferromagnetic behavior of crystals at low temperatures. Although these facts have been known for many years [6], the microscopic transport properties of bulk samples remain practically unclear. For instance, a metastable α -phase of MnPc often mentioned in literature [5] has never been confirmed by X-ray diffraction analysis. Conclusions about its existence and properties are made based on the similarity of the intramolecular architecture of MnPc complex with copper phthalocyanine without taking into account the intermolecular (exchange) interactions [6]. This is probably why the calculations based on simple exchange models cannot predict observed effects [7]. Remarkably, that the conductivity values reported for MnPc are orders of magnitude greater than for its metal-phthalocyanine congeners [8].

The transport properties of conventional phthalocyanines have been actively studied in recent decades. The most troubling issue here is the high content of electrically active impurities reaching 10% in the commercially available materials, which is incomparable with $10^{-7}\%$ in classical semiconductor materials like single-crystal silicon. Gas molecules, oxygen in particular, can penetrate freely into loosely packed molecular samples (films, polycrystals) and act as an electron acceptor thereby increasing the concentration of majority charge carriers, in this case, holes.

The studies on the electro-physical properties of thin MnPc films are seldom, due to widely announced instability of a molecule in air, this issue has been addressed in Ref. [9] in more detail. Here, we report some results of photoelectrical measurements on the MnPc films grown in a magnetic field applied in two different directions relative to the deposition surface.

Preparation of samples and experimental setup

The MnPc powder was recrystallized in a vacuum chamber (VUP 5M) in a crucible at 500 °C and a residual pressure less than 10^{-6} Torr before use. The handling of MnPc in laboratory conditions has been described in [9].

Glass/ITO (Merch, 25 Ohm cm) and ceramic plates equipped with photolithographically deposited interdigitated nickel electrodes (IDE) with a gap of 30 μm and a metallization height of 80 nm were used as substrates. Before being placed in the evaporation chamber, the substrates were cleaned in an ultrasonic bath with acetone and isopropyl alcohol, followed by drying in an argon flow. The deposition rate did not exceed 0.1 Å/s (according to quartz microbalancing) at a vacuum of $5 \cdot 10^{-7}$ Torr. The thickness was 100 nm for the MnPc films deposited on substrates with IDE and 100–300 nm for films on glass/ITO substrates. As a source of the magnetic field in

the growth zone, the H38 class neodymium magnets with dimensions of 55×55×35 mm providing a magnetic field strength of up to 0.6 T were used. The direction of the field lines was always parallel to the deposition surface. During the deposition on substrates with IDE, the magnetic field was oriented both parallel and perpendicular to the electrode fingers – Fig. 2, *b*.

Electrical measurements were carried out using a Keithley 4200 semiconductor characterization system in a sealed cuvette filled with argon or a synthetic air (zero gas) called “air” hereinafter. Readings were taken in a voltage sweep mode (maximum electric field was 30 kV/m, sweep time 2 minutes) or in a constant field mode at 30 kV/m. The measurement cycle was carried out as follows. The measurement started after the cuvette was purged with Ar for 10 min in the dark, 5–10 seconds after applying the bias the light was turned on for 10 min, then turned off and the measurement continued for another 10 min. Surface morphology was studied using a scanning electron microscope Carl Zeiss SUPRA 50 VP. More data on the morphology of MnPc films growth with and without a magnetic field can be found in Ref. [10].

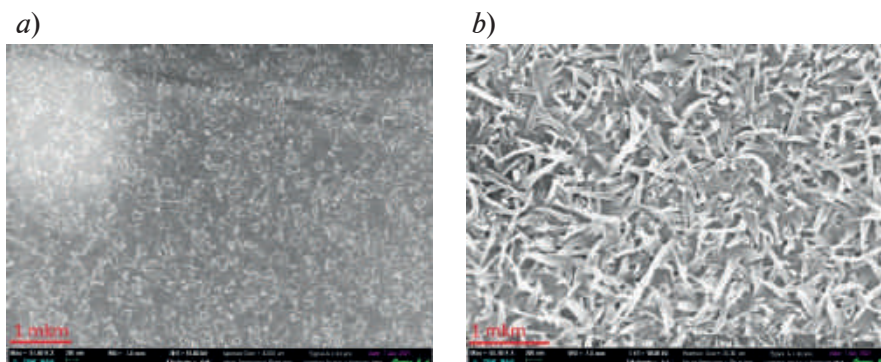


Fig. 1. SEM images of 300 nm thick MnPc film deposited onto ITO/glass substrate at zero field at 25 °C (*a*) and 200 °C (*b*)

Results and discussion

SEM images in Fig. 1, *a* show that the MnPc film grown on cold glass/ITO substrate is continuous, with irregularly shaped surface objects with typical size of 200 nm. The hot-grown MnPc consists of whisker crystals with an aspect ratio of up to 10:1 (crystal length up to 1.5 μm, width up to 150 nm), which likely do not form continuous layer on the substrate – Fig. 1, *b*. Thus, measurements of vertical conductivity give unreliable results due to leakage of the top evaporated metallic electrode and/or “burning out” of single whiskers during current flow. The in-plane (planar, lateral) conductivity measurements are discussed below.

The specific conductivity of MnPc films lies in the range $10^{-10} \div 10^{-7} \text{ Ohm}^{-1}\text{cm}^{-1}$ depending on the type of sample in Table 1, which significantly exceeds the value of $10^{-12} \text{ Ohm}^{-1}\text{cm}^{-1}$ indicated in [11] for copper phthalocyanine. The dark conductivity of the films grown on cold substrate (consist presumably of α -MnPc) is sensitive to the atmosphere – Table 1. It is reduced by a factor of 10 when the sample is exposed to synthetic air for 10 minutes after purging with argon, possibly due to desorption of admixtures. However, magnetic field does not remarkably affect the conductivity of cold-grown samples, so Table 1 focusses on the hot-grown samples. Their dark conductivity is low when the films are grown at zero field but largely increases when a magnetic field is applied, regardless of its direction. All hot-grown films are insensitive to the atmosphere. It should be mentioned that the synthetic air was used, which excludes the ingress of atmospheric gases other than oxygen and nitrogen (water or carbon monoxide for example). The maximum specific conductivity was measured for MnPc films deposited on a hot substrate in the presence of a 0.5T field directed parallel to the electrode fingers – Table 1.

Obviously, the reason of increase in conductivity of films grown with a field by more than two orders of magnitude is their intricate morphology with even more elongated whisker crystals than shown in Fig. 1 (not shown here). This facilitates the transport of charge carriers across the film thanks to the narrower intergrain gap. Direction of the magnetic field lines with respect the electrode fingers during the film grow does not have a clear effect on both the in-plane conductivity and the transition time, because of the large scatter of the derived values (Table 1).

The light-induced current as a constant bias (photoconductivity) is very low, as illustrated in Fig. 2.

Table 1

Dark lateral conductivity and light-induced transients for 100 nm thick MnPc films

Substrate temperature, °C	Magnetic field strength (parallel or perpendicular to the electrode fingers), T	Specific conductivity at $E = 30 \text{ kV/m}$, $\text{Ohm}^{-1}\text{cm}^{-1}$		Transient time of current change, s		
		Atmosphere		Light	Atmosphere	
		Ar	Air		Ar	Air
25	0	2.5×10^{-9}	3.0×10^{-10}	On	526	588
				Off	250	116
200	0	1.0×10^{-10}	1.0×10^{-10}	On	263	161
				Off	141	161
	0.3, perpendicular	6.2×10^{-8}	6.0×10^{-8}	On	455	588
				Off	52	122
	0.3, parallel	2.4×10^{-8}	2.3×10^{-8}	On	250	182
				Off	84	93
	0.5, perpendicular	2.0×10^{-8}	3.0×10^{-8}	On	312	312
				Off	68	91
	0.5, parallel	9.4×10^{-8}	9.6×10^{-8}	On	213	133
				Off	80	82

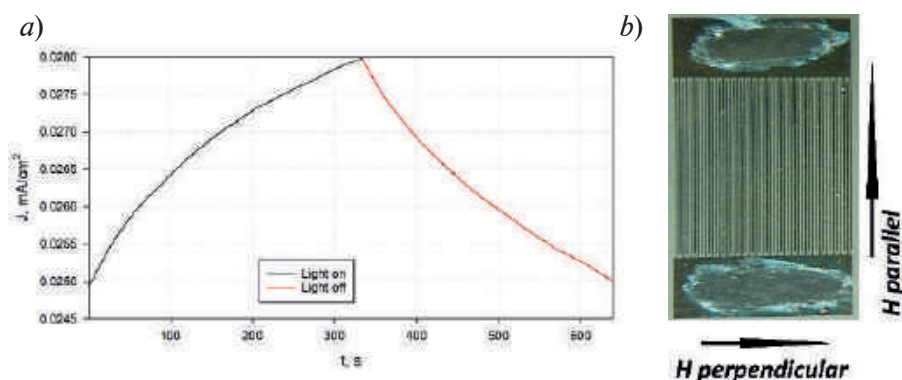


Fig. 2. Time evolution of the current density for a 100 nm MnPc film deposited at 25 °C without magnetic field (measured in Ar) (a); photograph of MnPc film with IDE (b). Parallel and perpendicular orientations of magnetic field are shown relative to contact grid

The relative rise of the signal upon illumination lies with 5%. Nonetheless, after turning the light on, a slow increase of current density is observed with characteristic exponential time from several minutes to hours (Table 1). This time scale is comparable with the processes of desorption of gaseous impurities from the samples due to evacuation or heating [11]. There are large fluctuations in the transient times with no apparent trends among samples (Table 1). However, the time during which the current decays to its initial value after light impact is shorter for all films grown in a magnetic field.

Conclusions

The magnetic field applied during the deposition of paramagnetic MnPc molecules on cold substrates has practically no effect on their dark and photoconductivity. However, the effect manifests itself with an increase in the deposition temperature up to 200 °C. As shown earlier [10], the microstructure of hot-grown films depends on the magnetic field strength but not on the direction: the stronger the superimposed field, the denser the MnPc whiskers. The samples grown in a magnetic field demonstrate faster decay of photocurrent and about two-orders of magnitude higher conductivity. Therefore, the increase in the dark conductivity of the films is associated with

field-induced morphological changes. Different in-plane orientation of the magnetic field does not lead to anisotropy of conductivity, which is consistent with the absence of in-plane anisotropy in morphology.

Acknowledgments

This work was supported by RSF grant № 20-72-00118. Authors used the equipment of the “Physics and Technology of Micro- and Nanostructures” Center at IPM RAS.

REFERENCES

1. **Coronado E.**, Molecular magnetism: from chemical design to spin control in molecules, materials and devices, *Nature Reviews Materials*, 2(5) (2020), 87–104.
2. **Schlettwein D., Meyer J.P., Jaeger N.I.**, Influence of Mn as a redox-active central metal on the electrical conduction behaviour of phthalocyanine thin films, *Journal of Porphyrins and Phthalocyanines*, 1 (4) (2000) 23–30.
3. **Simon J., Andre J.-J.**, *Molecular Semiconductors. Photoelectrical Properties and Solar Cells*. Berlin, Heidelberg, New York, Tokyo., Springer-Verlag, 1985.
4. **Barraclough, C.G., Martin, R.L., Mitra S.**, Paramagnetic anisotropy, electronic structure, and ferromagnetism in spin $S = 3/2$ manganese(II) phthalocyanine, *The Journal of Chemical Physics*, 5 (53) (1970) 1638–1642.
5. **Bartolomé J., Monton C., Schuller I.K.**, Chapter 9. Magnetism of Metal Phthalocyanines in *Molecular Magnets* Berlin: Springer-Verlag, 2014, p. 221–245.
6. **Brena B., Sanyal B., Herper H.C.**, Chemical Switching of the Magnetic Coupling in a MnPc Dimer by Means of Chemisorption and Axial Ligands, *Journal of Physical Chemistry C*, 49 (124) (2020) 27185–27193.
7. **Wu W., Kerridge A., Harker A.H., Fisher A.J.**, Structure-dependent exchange in the organic magnets Cu(II)Pc and Mn(II)Pc, *Physical Review B*, 18 (77) (2008) 184403.
8. **Rajesh K.R., Menon C.S.**, Electrical and optical properties of vacuum deposited MnPc thin films, *European Physical Journal B* 2005, 2(47) (2005) 171–176.
9. **Yunin P.A., Sachkov Yu.I., Travkin V.V., Pakhomov G.L.**, Stability of manganese (II) phthalocyanine films in ambient air, *Macroheterocycles*, 2 (15) (2022).
10. **Yunin P.A., Sachkov Yu.I., Travkin V.V., Skorokhodov E.V., Pakhomov G.L.**, Nanostructuring of Mn(II)Pc thin films by vacuum deposition in a weak magnetic field, *Vacuum*, (194) (2021) 110584
11. **Wright J.**, Gas adsorption on phthalocyanines and its effects on electrical properties, *Progress in Surface Science*, 1-2 (31) (1989) 1–60.

THE AUTHORS

SACHKOV Yuri I.
Sachkov@ipmras.ru
ORCID: 0000-0001-5701-783X

TRAVKIN Vladislav V.
trav@ipmras.ru
ORCID: 0000-0001-7511-1942

YUNIN Pavel A.
yunin@ipmras.ru
ORCID: 0000-0001-7081-2934

Received 13.10.2022. Approved after reviewing 29.03.2023. Accepted 30.03.2023.

Conference materials

UDC 53.043

DOI: <https://doi.org/10.18721/JPM.161.159>

Determination of subcell parameters for multijunction solar cells at radiation exposure

S.A. Levina ¹✉, V.M. Emelyanov ¹, E.D. Filimonov ¹, M.Z. Shvarts ¹

¹Ioffe Institute, St. Petersburg, Russia

✉ levina@mail.ioffe.ru

Abstract. Based on the electroluminescent method and the two-diode equivalent circuit model of a solar cell, the current-voltage characteristics of wide-bandgap subcells in the structure with the corresponding parameters of saturation dark currents are obtained. In addition, the approach has been tested on samples exposed to various radiation doses, which made it possible to determine the degradation rate of the photovoltaic characteristics of solar cells.

Keywords: multijunction solar cell, current-voltage characteristics, saturation dark currents, radiation exposure, degradation

Citation: Levina S.A., Emelyanov V.M., Filimonov E.D., Shvarts M.Z., Determination of subcell parameters for multijunction solar cells at radiation exposure, St. Petersburg State Polytechnical University Journal. Physics and Mathematics. 16 (1.1) (2023) 351–355. DOI: <https://doi.org/10.18721/JPM.161.159>

This is an open access article under the CC BY-NC 4.0 license (<https://creativecommons.org/licenses/by-nc/4.0/>)

Материалы конференции

УДК 53.043

DOI: <https://doi.org/10.18721/JPM.161.159>

Определение параметров многопереходных солнечных элементов, подвергнутых радиационному облучению

С.А. Левина ¹✉, Е.Д. Филимонов ¹, В.М. Емельянов ¹, М.З. Шварц ¹

¹Физико-технический институт им. А.Ф. Иоффе РАН, Санкт-Петербург, Россия

✉ levina@mail.ioffe.ru

Аннотация. В работе исследуются фотоэлектрические характеристики трехпереходных фотопреобразователей. На основе электролюминесцентного метода и двух-диодной эквивалентной модели солнечного элемента получены вольтамперные характеристики широкозонных субэлементов в структуре с соответствующими параметрами темновых токов насыщения. Дополнительно метод опробован на образцах, подверженных различным дозам облучения, что позволило определить темпы деградации параметров фотоэлектрических характеристик солнечных элементов.

Ключевые слова: многопереходный солнечный элемент, вольтамперные характеристики, темновой ток, радиационное облучение, деградация

Ссылка при цитировании: Левина С.А., Емельянов В.М., Филимонов Е.Д., Шварц М.З. Определение параметров субэлементов многопереходных солнечных фотопреобразователей при радиационных испытаниях // Научно-технические ведомости СПбГПУ. Физико-математические науки. 2023. Т. 16. № 1.1. С. 351–355. DOI: <https://doi.org/10.18721/JPM.161.159>

Статья открытого доступа, распространяемая по лицензии CC BY-NC 4.0 (<https://creativecommons.org/licenses/by-nc/4.0/>)

Introduction

In state-of-the-art photovoltaics, III–V monolithic multijunction solar cells (MJ SCs) provide the record-breaking efficiency among all other semiconductor-based photoconverters [1]. The targeted area of such devices application is related to the power supply of various spacecraft (space stations, satellites, moon/mars rovers). One of the main parameters for the successful use of MJ SC in space, in addition to the high sunlight photoconversion efficiency, is tolerance to radiation expose. Therefore, it is essential to take into account the possible degradation of individual subcells in a MJ structure, since each of them can demonstrate a diverse rate of PV parameters diminishing with exposure dose due to differences in the composition, thickness, and doping levels of the semiconductor layers. The spectral dependence of the external quantum efficiency (EQE) and the current-voltage characteristic (I–V curve) make it possible to trace the effect of irradiation on such PV parameters as the efficiency of charge carrier collection in p- and n-regions, series and shunt resistances, diffusion and recombination saturation currents. Moreover, if the registration of the EQE of each p-n junctions is a well-developed practice with an approved research protocol, then the extraction of I–V curves of individual subcells being a part of monolithic MJ SC structure is a non-trivial experimental problem.

Theoretical part

The general equation describing the physical processes in individual subcells of MJ SC is based on an equivalent two-diode circuit model with distributed parameters:

$$J_{dark} = (V + JRs) / Rsh - Jod [\exp(qV/kT) - 1] - Jor [\exp(qV/2kT) - 1], \quad (1)$$

where J_{dark} is current density without external light source [mA/cm²]; J is photocurrent density [mA/cm²]; V is operating voltage (load voltage) [V]; Rs is series resistance [Ohm]; Rsh is shunt resistance [Ohm]; Jod and Jor are the densities of saturation reverse currents for various recombination processes (d corresponds to the diffusion component of the current and characterizes recombination in the quasi-neutral regions of the transition, r is responsible for carrier recombination in the space charge region, as well as for recombination under concentrated exposure) [mA/cm²]; q is the electron charge [C]; k is the Boltzmann constant [J/K]; T is temperature [K].

Semiconductor layers that form photovoltaic subcells are combined in MJ SC structure in a series circuit via tunnel diodes, and direct I–V curves tracing of each of p-n junctions is often impossible. The exception is MJ SC with additional busbars [2], which allow the direct electrical contacting to the subcell of interest. However, such architecture requires complex post-growth processing. Therefore, structures with the third (or fourth) terminals are used only in certain laboratory studies. In all other cases, to extract I–V curves of individual subcells indirect measurement methods are used. In addition, the target task is to determine the voltage of each p-n junctions. Such a problem can be solved by the method [3] based on reciprocity relation between EQE and electroluminescent emission (φ_{EL}) of SC [4]:

$$\varphi_{EL} = EQE(\lambda) \cdot \varphi_{BB} \cdot [\exp(qV(\lambda)/kT) - 1], \quad (2)$$

where J is the density of the photocurrent flowing through the MJ SC, $\varphi_{BB} = 2\pi hc^2/\lambda^5 \exp(-hc/\lambda kT)$ is the black body power density [W/m²/nm] at a given temperature T , λ is wavelength [nm], V is the voltage drop across the subcell.

By transforming equation 2 with respect to the variable V and neglecting the “–1” term after the exponent, it is possible to form the I–V curve of each subcell:

$$V(J) = kT/q [\ln \varphi_{EL}(J) - \ln EQE(\lambda) - \ln \varphi_{BB}(\lambda) - \ln C], \quad (3)$$

where the term $kT/q \cdot \ln C = \delta V = \text{const}$ is introduced to compensate the difference between the relative value of the registered luminescent flux φ_{EL} and its absolute magnitude, and is the throughput function of the optical system used in the experiment. The constant δV for each subcell of a given MJ SC is the same and does not depend on E and J .

Thus, for a solar cell with three ($i = 3$) p-n junctions, the total voltage V_{mjsc} can be found as:

$$V_{mjsc} = \sum_i V_i - 3\delta V. \quad (4)$$

Experimental part

For each MJ SCs, the spectral dependences of EQE were obtained using the lock-in technique (Fig. 1, *a*) and a set of light I–V curves under pulsed illumination (solar simulator AM0 spectrum 1366 W/cm^2) was recorded [5, 6]. The latter allowed to determine dark characteristics without the effects of series resistance (Fig. 1, *b*) using the Isc-Voc method [7].

The electroluminescence flux ϕ_{EL} was recorded by fiber-guided spectrometers (spectral ranges 300–1100 nm and 1000–2500 nm) while current (range $10\text{--}500 \text{ mA/cm}^2$) was passed through MJ SC. To improve the electroluminescence light collection and to enhance the recorded signal the input end of the fiber was equipped with collimator. The measurements were carried out for two direct band gap GaInP and GaAs subcells. Radiative recombination flux of the lower Ge junction with indirect band gap (luminescence peak at energies around 0.68 eV) is very weak and was observed only at high photocurrent densities (more than 1 A/cm^2), which exceeds the allowable operating limits of MJ SCs used in this study.

The calculation of equation 3 was carried out at wavelength at which $V(J)$ does not depend on λ (the methodology of this approach is described in [3]): for GaInP subcell it is approximately 650 nm, for middle GaAs junction it is 870 nm.

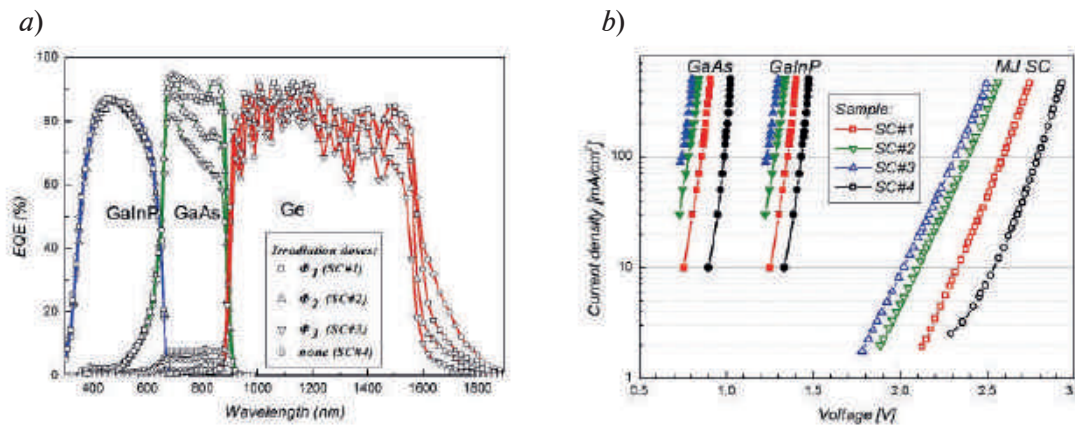


Fig. 1. EQE spectral dependences of MJ SC irradiated by 1 MeV neutrons with fluencies of $\Phi_1=1.5 \cdot 10^{13} \text{ n/cm}^2$ (SC#1), $\Phi_2=1.5 \cdot 10^{14} \text{ n/cm}^2$ (SC#2), $\Phi_3=5 \cdot 10^{14} \text{ n/cm}^2$ (SC#3) (*a*); I-V curves (filled symbols) of GaAs and GaInP subcells obtained from EL measurements (Eq. 2), and I-V curves (open symbols) of MJ SCs obtained by direct Isc-Voc measurements using a four-probe system (*b*)

Results

Based on the obtained data (Fig. 1, *b*) and the two-diode circuit model (eq. 1), in the studied samples the values of dark saturation currents J_{od} (and J_{or}) of wide band gap subcells at different irradiation fluencies were calculated (Fig. 2). It can be seen that the irradiation exposure of MJ SC leads to a degradation of the J_{od} and J_{or} parameters for both subcells by about three orders of magnitude. To determine which of the regions of the subcell (quasi-neutral n- and p-regions or the space charge region) demonstrates the maximum degradation rate at irradiation and has a dominant impact on the photovoltaic characteristics, the derivatives of the $J_{od}(\Phi)$ and $J_{or}(\Phi)$ dependences were estimated. The results of calculation are shown in Table 1. Each linear section of the $J_{od}(\Phi)$ and $J_{or}(\Phi)$ corresponds to different ranges (Fig. 2) of irradiation power increase: range 1 from BOL to $1.5 \cdot 10^{13} \text{ n/cm}^2$; range 2 from $1.5 \cdot 10^{13}$ to $1.5 \cdot 10^{14} \text{ n/cm}^2$; range 3 from $1.5 \cdot 10^{14}$ to $5 \cdot 10^{14} \text{ n/cm}^2$.

Calculations have shown that in subcells the quality of the space charge region decreases most rapidly. Since the narrow band gap Ge junction, in contrast to the wide band gap GaInP and

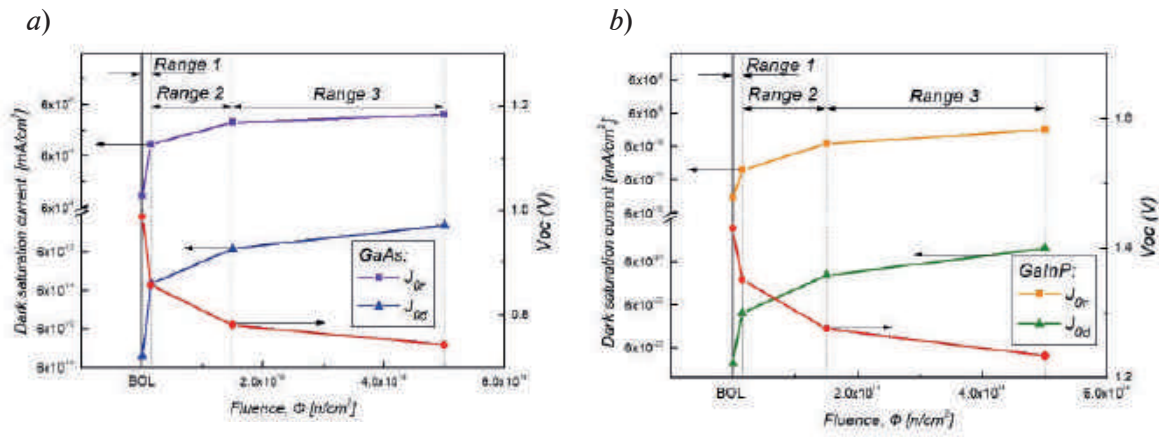


Fig. 2. Dependencies of the recombination (J_{or}) and diffusion (J_{od}) components of the dark saturation current of GaAs (a) and GaInP (b) subcells at different fluencies, and voltage degradation (red lines) at a selected current value of 100 mA/cm². The origin of coordinates along the x-axis corresponds to Beginning-Of-Life (BOL) condition for SC

GaAs, is less sensitive to the particle exposure, it can be concluded that the main contribution to the deterioration of MJ SC output parameters is originated from the middle GaAs p-n junction, which demonstrates the maximum of the $dJ_{or}/d\Phi \approx 10^{-19}$ mA/n.

Table 1

$dJ_0/d\Phi$ [mA/n] for wide-bandgap p-n junctions

Fluence range	Derivative	GaAs subcell	GaInP subcell
Range 1	$dJ_{or}/d\Phi$	$2 \cdot 10^{-19}$	$1 \cdot 10^{-23}$
	$dJ_{od}/d\Phi$	$9 \cdot 10^{-27}$	$4 \cdot 10^{-35}$
Range 2	$dJ_{or}/d\Phi$	$1 \cdot 10^{-19}$	$8 \cdot 10^{-23}$
	$dJ_{od}/d\Phi$	$8 \cdot 10^{-27}$	$3 \cdot 10^{-35}$
Range 3	$dJ_{or}/d\Phi$	$6 \cdot 10^{-20}$	$6 \cdot 10^{-24}$
	$dJ_{od}/d\Phi$	$1 \cdot 10^{-28}$	$5 \cdot 10^{-35}$

Conclusion

The work is devoted to the study of the photovoltaic characteristics of MJ SC before and after particle irradiation exposure. As a result, I-V curves of individual subcells were calculated for several fluencies. Based on the obtained data and the two-diode three-dimensional distributed circuit model of solar cell, the corresponding dark saturation currents characterize various recombination mechanisms were determined. The rates of degradation of saturation currents with increasing dose of irradiation made it possible to trace which of the regions of the subcell plays a dominant role in the deterioration of the photovoltaic characteristics of the p-n junction.

REFERENCES

- Green M., Dunlop E., Hohl-Ebinger J., Yoshita M., Kopidakis N., Hao X., Solar cell efficiency tables (version 59). Prog Photovolt Res Appl. 2022. 30 (1) 3–12.
- Tayagaki T., Makita K., Oshima R., Mizuno H., Sugaya T., Analysis of luminescence coupling effect in three-terminal tandem solar cells, J. Photon. Energy. 8 (4) (2018) 045503.
- Kirchartz T., Rau U., Hermle M., Bett A.W., Helbig A., Werner J.H., Internal voltages in GaInP/GaInAs/Ge multijunction solar cells determined by electroluminescence measurements, Appl. Phys. Lett. 92 (2008) 123502.
- Rau U., Reciprocity relation between photovoltaic quantum efficiency and electroluminescent emission of solar cells, Phys.Rev.B. 76 (2007) 085303.

5. **Levina S.A., Emelyanov V.M., Filimonov E.D., Mintairov M.A., Shvarts M.Z., Andreev V.M.**, Cascade optical coupling and quantum efficiency measurements of MJ SCs, *Solar Energy Materials and Solar Cells*. 213 (2020) 110560.

6. **Shvarts M.Z., Filimonov E.D., Kozhukhovskaia S.A., Mintairov M.A., Timoshina N.Kh., Andreev V.M.**, Current mismatch violation in concentrator multijunction solar cells, *AIP Conference Proceedings*. 1881 (2017) 040006.

7. **Wolf M., Rauschenbach H.**, Series resistance effects on solar cell measurements, *Advanced Energy Conversion*. 3 (1963) 455–479.

THE AUTHORS

LEVINA Svetlana A.
levina@mail.ioffe.ru
ORCID: 0000-0003-4554-3300

EMELYANOV Viktor M.
vm.emelyanov@mail.ioffe.ru
ORCID: 0000-0001-6167-3207

FILIMONOV Eugeny D.
efilimonov@mail.ioffe.ru
ORCID: 0000-0002-7711-2188

SHVARTS Maxim Z.
shvarts@scell.ioffe.ru
ORCID: 0000-0002-2230-7770

Received 19.10.2022. Approved after reviewing 21.11.2022. Accepted 22.11.2022.

Conference materials

UDC 538.915

DOI: <https://doi.org/10.18721/JPM.161.160>

Thermally induced depolarization of fluorescence of matrix-isolated MoS₂ nanodots

D.K. Nelson ¹✉, A.N. Starukhin ¹, D.A. Kurdyukov ¹, E.Yu. Stovpyaga ¹

¹Ioffe Institute, St Petersburg, Russia

✉ d.nelson@mail.ioffe.ru

Abstract. The temperature and viscosity dependences of polarized luminescence of colloidal solutions of MoS₂ nanodots in organic solvents have been studied. It is shown that under conditions of linearly polarized excitation, an ensemble of MoS₂ nanodots behaves as a system of linear oscillators, the initial orientation of which is violated due to the Brownian rotation of the nanodots. Within the framework of the Levshin-Perrin model, the sizes of luminescent nanodots, which vary with the radiation wavelength, are estimated. The data obtained are in agreement with the estimates of the nanodot sizes based on the quantum size effect. It is shown that the polarization features of radiative transitions in MoS₂ nanodots differ from the properties of radiative transitions in MoS₂ monolayers.

Keywords: nanodots, polarized luminescence, quantum size effect

Funding: The work was supported by the RFBR (project No. 20-03-00656).

Citation: Nelson D.K., Starukhin A.N., Kurdyukov D.A., Stovpyaga E.Yu., Thermally induced depolarization of fluorescence of matrix-isolated MoS₂ nanodots, St. Petersburg State Polytechnical University Journal. Physics and Mathematics. 16 (1.1) (2023) 356–362. DOI: <https://doi.org/10.18721/JPM.161.160>

This is an open access article under the CC BY-NC 4.0 license (<https://creativecommons.org/licenses/by-nc/4.0/>)

Материалы конференции

УДК 538.915

DOI: <https://doi.org/10.18721/JPM.161.160>

Термостимулированная деполяризация флюоресценции матрично-изолированных наноточек MoS₂

Д.К. Нельсон ¹✉, А.Н. Старухин ¹, Д.А. Курдюков ¹, Е.Ю. Стовпяга ¹

¹Физико-технический институт им. А.Ф. Иоффе РАН, Санкт-Петербург, Россия

✉ d.nelson@mail.ioffe.ru

Аннотация. Исследована зависимость поляризованной люминесценции коллоидных растворов наноточек MoS₂ в органических растворителях от температуры и вязкости. Показано, что в условиях линейно поляризованного возбуждения ансамбль наноточек MoS₂ ведет себя как система линейных осцилляторов, первоначальная ориентация которых нарушается из-за броуновского вращения наноточек. В рамках модели Левшина-Перрена оценены размеры наноточек, полученные данные согласуются с оценками размеров наноточек, основанными на квантово-размерном эффекте. Показано, что поляризационные особенности излучательных переходов в наноточках MoS₂ отличаются от таковых в монослоях MoS₂.

Ключевые слова: наноточки, поляризованная люминесценция, квантово-размерный эффект

Финансирование: Работа выполнена при финансовой поддержке РФФИ (проект № 20-03-00656).

Ссылка при цитировании: Нельсон Д.К., Старухин А.Н., Курдюков Д.А., Стовпяга Е.Ю. Термостимулированная деполяризация флуоресценции матрично-изолированных наноточек MoS₂ // Научно-технические ведомости СПбГПУ. Физико-математические науки. 2023. Т. 16. № 1.1. С. 356–362. DOI: <https://doi.org/10.18721/JPM.161.160>

Статья открытого доступа, распространяемая по лицензии CC BY-NC 4.0 (<https://creativecommons.org/licenses/by-nc/4.0/>)

Introduction

Molybdenum disulfide belongs to a group of layered crystals characterized by pronounced anisotropy of mechanical and crystallographic properties. Layered crystals are easily split along planes parallel to the crystal layers. This feature of crystals demonstrates that the chemical bonds of atoms inside each layer are much stronger than the bonds between layers, and thus some physical properties of layered crystals (not necessarily all) have a two-dimensional character.

The discovery of the unique properties of monolayer graphite – graphene [1] gave impetus to the study of the properties of thin films and monolayers of other layered crystals, including molybdenum disulfide. The transition from a bulk MoS₂ crystal to a monolayer is accompanied by changes in the band structure of the crystal. In particular, unlike a bulk crystal, a MoS₂ monolayer is a direct band gap semiconductor, which is essential for its application in photonics and optoelectronics [2].

The optical properties of MoS₂ nanodots and the traits of their electronic structure have been studied to a lesser extent. For the first time, the quantum-dimensional effect in the absorption spectra of MoS₂ nanoparticles was observed, apparently, in sols formed as a result of dissolution of MoS₂ crystalline powders in acetonitrile [3]. Later, other methods for obtaining MoS₂ nanoparticles were developed [4] and the applicability of using MoS₂ nanodots for catalysis, in energy storage devices and optoelectronics were investigated (see review [5]).

The fundamental task of studying the photophysical properties of MoS₂ nanodots is to establish the properties of the radiative states in these objects. Optical absorption and luminescence spectra of MoS₂ nanodots consist of broad bands. An effective method of studying the properties of emissive states forming broadband spectra is to study the influence of external factors (temperature, polarization and intensity of optical excitation) on their luminescent properties. In particular, the method of polarized luminescence [6, 7] allows obtaining information about the properties of elementary emitters, their interaction with each other and with the environment, even in the case of broadband spectra. The aim of this work was to study thermally induced effects in the polarized luminescence of MoS₂ nanodots dispersed in liquid matrices of different viscosity and temperature. It was found that increasing the temperature as well as decreasing the viscosity of colloidal solutions leads to depolarization of luminescence (under conditions of linearly polarized excitation). The depolarization of the emission is shown to be described by the Levshin-Perrin equation, which relates the depolarization of the radiation of elementary emitters to their rotation.

Within the framework of the Levshin-Perrin model, the size of the luminous nanoparticles was estimated, which is in satisfactory agreement with the results of the analysis of the emission spectrum of MoS₂ nanodots, taking into account the quantum size effect.

Materials and Methods

MoS₂ nanoparticles were obtained by chemical exfoliation and dispersion of massive MoS₂ (the “top-down” method) in alkali solutions under the action of ultrasound [8]. Molybdenum disulfide powder (MoS₂, particle size < 2 μm, 98%, Aldrich) weighing 1.5 g was placed in a 10M aqueous solution of LiOH and NaOH (molar ratio 1:2). The resulting suspension was subjected to ultrasonic treatment at 30 °C for 80 hours with constant stirring. MoS₂ nanoparticles were separated from coarse fractions by centrifugation on a Sigma 6–16 centrifuge, after which the target fraction was precipitated at 12000g for 1 hour. To remove Na⁺ and Li⁺ ions, the nanoparticles were redispersed three times in deionized water followed by centrifugation. Thereafter, the MoS₂ nanoparticles were dried at 70 °C. and dispersed in n-methylpyrrolidone (NMP, Aldrich, spectrophotometric purity, ≥ 99%) containing 0.2 M NaOH. The concentration of MoS₂ nanoparticles in NMP

was 1 mg/ml. Two batches of nanoparticles (E92 and E98) were prepared. The first of them was used to prepare a colloidal solution of nanodots in NMP, and the second was used to prepare nanodot solutions in NMP-glycerol mixtures. The glycerol content in the glycerol-NMP mixtures varied from 10% to 80% wt%, with the viscosity of the mixture changing by almost two orders of magnitude.

For optical studies, synthesized samples were placed in thin-walled quartz cuvettes. The luminescence of colloidal MoS₂ solutions was excited by CW laser radiation with a wavelength $\lambda_{\text{exc}} = 405 \text{ nm}$ ($h\nu_{\text{exc}} = 3.061 \text{ eV}$). The excitation power was $\sim 0.1 \text{ W}$. The degree of luminescence polarization was measured using a quartz modulator [9] and a linear polarizer in combination with a two-channel photon counting system. Exciting light polarized with $E \parallel z$ propagated along the y axis, the radiation of the sample was recorded at right angle, in the direction of the x axis. The spectra were recorded using a grating spectrometer.

Results and Discussion

Room-temperature luminescence spectra of MoS₂ nanodots upon excitation by light with $h\nu_{\text{exc}} = 3.061 \text{ eV}$ are shown in figure 1. The luminescence spectra of E92 and E98 samples consist of broad bands with maxima at $\sim 2.8 \text{ eV}$ and $\sim 2.3 \text{ eV}$, respectively. Both are significantly shifted towards shorter wavelength relative to the emission spectrum of bulk molybdenum disulfide crystals [10]. The shift of MoS₂ nanodots emission toward shorter wavelengths can be explained by the quantum-size effect in the electronic spectra of the nanodots. A decrease in the size of a semiconductor nanocrystal is accompanied by an increase in its energy band gap, which entails a shift of the edge emission of the nanocrystal to the shorter wavelength side. The effect is noticeable when nanocrystal sizes are comparable to or smaller than the Bohr exciton radius in the bulk crystal.

When excited by linearly polarized light, the emission of MoS₂ nanodot solutions turns out to be linearly polarized in the same plane as the exciting light. The state of linear polarization of the emission can be characterized by the emission anisotropy r , associated with the degree of linear polarization P by the ratio:

$$r = \frac{I_z - I_y}{I_z + 2I_y} = \frac{2P}{3 - P}, \quad (1)$$

where I_z and I_y are the intensities of the emission components polarized with $E \parallel z$ and $E \parallel y$, respectively. Increasing the temperature of the colloidal solution, as well as decreasing its viscosity at a constant temperature, leads to depolarization of the emission.

The features of the polarized luminescence of nanodots can be explained in the framework of an oscillator model [6]. Within this model, the ensemble of photoexcited nanodots is considered as a system of linear completely anisotropic dipole oscillators randomly oriented in space. Linearly polarized light excites mainly oscillators with their dipole moments oriented parallel to the

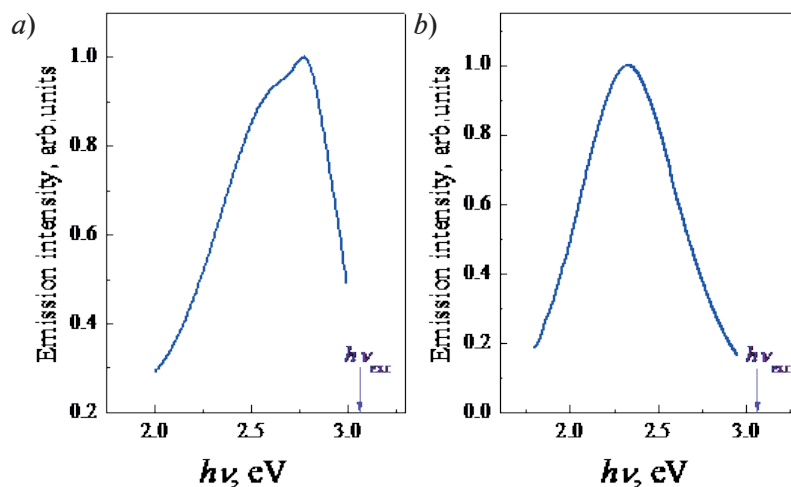


Fig. 1. Emission spectra of colloidal solutions of MoS₂ nanodots of different batches E92 (a) and E98 (b) in NMP. $h\nu_{\text{exc}} = 3.061 \text{ eV}$. $T = 298 \text{ K}$

vector E of the light. If the orientations of the dipole moments do not change significantly during the lifetime of the emissive state, the emission of the oscillator system will be predominantly polarized in the same plane as the exciting light.

The Brownian rotation of the nanoparticles in a solution disturbs the photoinduced anisotropic distribution of the directions of oscillator dipole moments. The degree of depolarization is determined by the angle of rotation of the luminous nanoparticle, which depends on its size, lifetime of the emissive state, temperature and viscosity of the solution. The dependence of the emission anisotropy of nanoparticles in the form of a rigid sphere (or an oblate ellipsoid [11]) on the above parameters is described by the Levshin-Perrin equation [7]:

$$\frac{1}{r(T)} = \frac{1}{r_0} + \frac{kT\tau(T)}{r_0\eta(T)V} = \frac{1}{r_0} + \frac{x}{r_0V}, \quad (2)$$

where k is the Boltzmann constant, T is the temperature of the solution, $\tau(T)$ is the lifetime of the emissive state, $\eta(T)$ is the dynamic viscosity of the solvent, V is the volume of the nanoparticle, $x \equiv kT\tau/\eta$, r_0 is the limit value of anisotropy (at $\eta \rightarrow \infty$). With random orientation of nanoparticles in solution, the maximum value of r_0 is equal to 0.4. An increase in temperature, as well as a decrease in the viscosity of the solution at constant temperature promotes the Brownian rotation, which, in accordance with (2), leads to a decrease in the emission anisotropy. The experimental dependences of the reciprocal emission anisotropy on the parameter x , $r^{-1}(x)$, with a change in the temperature of the colloidal solution (in the case of the E92 sample) or its viscosity at a constant temperature (in the case of the E98 sample) are shown in figure 2. (The data in figure 2 are related to the light emission in the region of the maxima of the corresponding bands.)

The values of x in figure 2 were calculated using the known dependences of the solution viscosity on temperature for pure NMP [12] and on composition for the NMP-glycerol mixture [13]. The value τ in the studied temperature range 254 K – 323 K was assumed to be independent on the temperature $\tau \approx 5.5$ ns [14]. The independence is consistent with a very weak change in the emission intensity in the temperature range studied. As can be seen from figure 2, the experimental dependences $r^{-1}(x)$ are well described by equation (2), which proves the “rotational” mechanism of depolarization of nanodot emission. The theoretical dependences in figure 2 are obtained for the following parameters: $V_{E92} = 1.8$ nm³ ($h\nu_{\text{emis}} = 2.8$ eV) and $V_{E98} = 3.5$ nm³ ($h\nu_{\text{emis}} = 2.3$ eV). Note that the given values of V characterize the volumes of nanodots that emit light in the region of the band maxima in figure 1. For a given sample the parameter V depends on the emission wavelength: the longer the wavelength, the greater V .

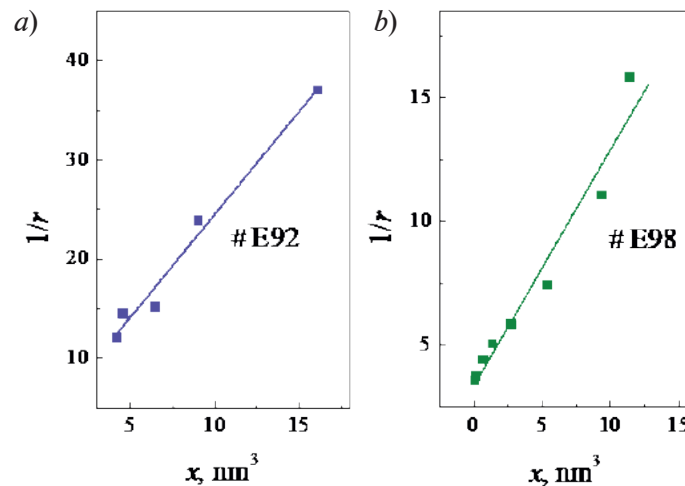


Fig. 2. The experimental dependences $r^{-1}(x)$ induced by changes in the temperature of the colloidal MoS₂ solutions (a) and their viscosity at room temperature (b). $h\nu_{\text{exc}} = 3.061$ eV. Points are experimental values, the solid lines are the fits of the experimental points by Eq. (2)

Considering that the unit cell volume of hexagonal molybdenum disulfide is $v_0 = 0.106$ nm³ [15], a nanodot with $V = 3.5$ nm³ includes ~ 30 unit cells (or ~ 60 MoS₂ molecules). For spherical MoS₂ nanodots, the sizes (diameters) of nanodots emitting in the region $h\nu_{\text{emis}} = 2.8$ eV (E92) and

$h\nu_{\text{emis}} = 2.3 \text{ eV}$ (E98) are $d = 2R = 1.5 \pm 0.3 \text{ nm}$ and $d = 2R \approx 1.9 \pm 0.2 \text{ nm}$, respectively.

The parameters r_0 used to calculate the theoretical dependencies in figure 2 are close in magnitude: $r_0 \approx 0.3$. The values of $r_0 > 0.1$ suggest that the polarization properties of the corresponding optical transitions really have the properties of a linear oscillator. Radiative transitions in two-dimensional MoS_2 structures are usually associated [5] with direct electronic transitions between states corresponding in bulk crystals to the conduction band (K_5) and the valence bands (K_4, K_1 [16]) at the K-point of the Brillouin zone. Radiative transitions $K_5 \rightarrow K_{1,4}$ are allowed for the light polarization $\mathbf{E} \perp c$ (c is the optical axis of the crystal) [17] and are equally probable for any orientation of the vector \mathbf{E} in the plane of the layer (“plane oscillator”). For such transitions, the value of r_0 for nanodot ensemble cannot exceed 0.1 [18]. Obviously, the values of $r_0 \leq 0.1$ do not agree with the experimental ones. On the other hand, it is known that in the bulk MoS_2 , the band gap at the K-point (E_{gK0}) is very close to that at the H-point of the Brillouin zone (E_{gH0}): $E_{gH0} - E_{gK0} \approx 50 \text{ meV}$ [19]. The optical transitions at the H-point $H_3 \rightarrow H_3$ [16] are polarized with $\mathbf{E} \parallel c$ and their polarization properties can be described in terms of linear oscillators, the ensemble of which is characterized by $r_0 \leq 0.4$. In this regard, it can be assumed that the transition from bulk molybdenum disulfide to a nanocrystal is accompanied by a modification of its electronic spectrum, leading to a dominant contribution to the radiative transitions of states at the H-point (transitions of the type $H_3 \rightarrow H_3$).

It is reasonable to associate the noted correlation between the energy of emitted photons and the size of nanodots with the quantum size effect in the electronic spectrum of nanodots, which leads to the dependence of the energy band gap of nanodots on their size.

Under conditions of strong quantum confinement, the band gap of a spherical semiconductor nanodot of radius R is determined by the expression [20]:

$$E_{gND}(R) = E_{g0} + \frac{\hbar^2 \pi^2}{2\mu R^2} - 1.786 \frac{e^2}{4\pi\epsilon_0\epsilon R} - 0.248 E_{Ry}, \quad (3)$$

where μ is the reduced exciton mass, \hbar is Planck's constant, e is the electron charge, ϵ_0 is the electric constant, ϵ is the dielectric constant of the nanodot material, and E_{Ry} is the exciton Rydberg. At room temperature, the energies of the radiative transitions responsible for the luminescence bands in MoS_2 bulk crystals [10] are close to E_{g0} : $h\nu_{\text{emis}} \leq E_{g0}$. Using equation (3) and assuming for simplicity that for nanodots $h\nu_{\text{emis}}(R) \approx E_{gND}(R)$, it is possible to estimate the sizes of nanodots d that form different regions of their emission spectra. For emission of nanodots in the region of band maxima in figure 1 the calculations give $d = 2R = 1.6 \text{ nm}$ (E92) and $d = 2.0 \text{ nm}$ (E98), which is close to the values obtained from polarization measurements. The following MoS_2 parameters were used in the estimation: $E_{g0} = E_{gH0} = 2.0 \text{ eV}$ [21, 22], $\mu = 0.33m_0$ [23], $\epsilon = 3.3$ [24], $E_{Ry} = 0.05$ [25]. However, it should be noted that equation (3) overestimates the value of E_{gND} [26], not taking into account, in particular, the dependence of the effective mass μ [27, 28] and ϵ [29] on the size of the nanoparticle.

On the assumption that $h\nu_{\text{emis}}(R) \approx E_{gND}(R)$, relation (3) provides a way of determining the size distribution function, $N(R)$, of photoexcited nanodots. The emission intensity of the ensemble of nanodots:

$$I(E) \propto N(E)W_r(E), \quad (4)$$

where $N(E)$ is the distribution density of photoexcited nanodots over the photon energies $E \equiv h\nu_{\text{emis}}(R) \approx E_{gND}(R)$, $W_r(E)$ is the probability of radiative electron–hole recombination in a nanodot. The size distribution function of photoexcited nanodots $N(R)$ is related to $N(E)$ by $N(E)dE = N(R)dR$, from which

$$N(R) = N(E(R)) \left| \frac{dE(R)}{dR} \right| \propto I(E(R))W_r^{-1}(R) \left| \frac{dE(R)}{dR} \right|, \quad (5)$$

where $E(R)$ is described by the relation (3). With the known dependence $W_r(R)$ [30], the relation (5) allows us to determine the main features of the function $N(R)$.

The $N(2R)$ dependences calculated on the basis of (5), characterizing the size distribution of photoexcited MoS_2 (E92 and E98) nanodots, are shown in figure 3. The shapes of the distributions

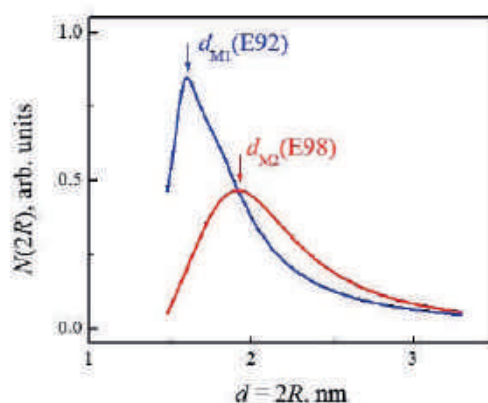


Fig. 3. Calculated size distributions of photoexcited MoS₂ nanodots (E92 and E98) in NMP. $h\nu_{\text{exc}} = 3.061$ eV

$N(2R)$ are well approximated by exponentially modified normal distribution functions with maxima at $d_{M1}(E92) = 1.6$ nm and $d_{M2}(E98) = 1.9$ nm.

Conclusion

Studies of the polarized luminescence of the nanodots demonstrate that different spectral regions of their emission spectra are formed by nanodots of different volumes. This indicates a significantly inhomogeneous broadening of the spectra. The dependence of the wavelength of nanodots emission on their size can be explained by the quantum size effect. The nanodot size estimates based on the polarized luminescence technique and on the basis of the quantum size effect are in good agreement.

REFERENCES

1. Sharon M., Sharon M., Graphene: An Introduction to the Fundamentals and Industrial Applications, Wiley – Scrivener Publishing, 2015.
2. Yang X., Li B., Monolayer MoS₂ for nanoscale photonics, Nanophotonics. 9 (7) (2020) 1557–1577.
3. Peterson M.W., Nenadovic M.T., Rajh T., Herak R., Micic O.I., Goral J.P., Nozik A.J., Quantized colloids produced by dissolution of layered semiconductors in acetonitrile, J. Phys. Chem. 92 (6) (1988) 1400–1402.
4. Gu W., Yan Y., Zhang C., Ding C., Xian Y., One-Step Synthesis of Water-Soluble MoS₂ Quantum Dots via a Hydrothermal Method as a Fluorescent Probe for Hyaluronidase Detection, ACS Appl. Mater. Interfaces. 8 (18) (2016) 11272–11279.
5. Kabel J., Sharma S., Acharya A., Zhang D., Yap Y.K., Molybdenum Disulfide Quantum Dots: Properties, Synthesis, and Applications, C-J. Carbon Research. 7 (2021) 45.
6. Feofilov P.P., The Physical Basis of Polarized Emission, New York: Consultants Bureau, 1961.
7. Lakowicz J.R., Principles of Fluorescence Spectroscopy, Springer Science & Business Media, 2006.
8. Wu P., Liu Z., Cheng Z.L., Ultrasound-Assisted Alkaline Solution Reflux for As-Exfoliated MoS₂ Nanosheets, ACS Omega. 4 (6) (2019) 9823–9827.
9. Jaspersen S.N., Schnatterly S.E., An Improved Method for High Reflectivity Ellipsometry Based on a New Polarization Modulation Technique, Rev. Sc. Instr. 40 (6) (1969) 761–767.
10. Placidi M., Dimitrievska M., Izquierdo-Roca V., Fontané X., Castellanos-Gomez A., Pérez-Tomás A., Pérez-Rodríguez A., Multiwavelength excitation Raman scattering analysis of bulk and two-dimensional MoS₂: vibrational properties of atomically thin MoS₂ layers, 2D Materials. 2 (3) (2015) 035006.
11. Weber G., Rotational Brownian Motion and Polarization of the Fluorescence of Solutions, Adv. Protein Chem. 8 (1953) 415–459.
12. Langan J.R., Salmon G.A., Physical properties of N-methylpyrrolidinone as functions of temperature, J. Chem. Eng. Data. 32 (4) (1987) 420–422.

13. **Bandarkar F., Khattab I. S., Martinez F., Kasabjafari M., Vahdati S., Jouyban A.**, Viscosity and surface tension of glycerol + N-methyl-2-pyrrolidone mixtures from 293 to 323 K, *Phys. Chem. of Liquids*. 53 (1) (2014) 104–116.
14. **Gopalakrishnan D., Damien D., Shaijumon M. M.**, MoS₂ Quantum Dot-Interspersed Exfoliated MoS₂ Nanosheets, *ACS Nano*. 8 (5) (2014) 5297–5303.
15. **Wakabayashi N., Smith H.G., Nicklow R.M.**, Lattice dynamics of hexagonal MoS₂ studied by neutron scattering, *Phys.Rev. B*. 12 (2) (1975) 659–662.
16. **Coehoorn R., Haas C., Dijkstra J., Flipse C.J.F.**, Electronic structure of MoSe₂, MoS₂, and WSe₂. I. Band-structure calculations and photoelectron spectroscopy, *Phys.Rev. B*. 35 (12) (1987) 6195–6202.
17. **Coehoorn R., Haas C., Groot R.A. de**, Electronic structure of MoSe₂, MoS₂, and WSe₂. II. The nature of the optical band gaps, *Phys.Rev. B*. 35 (12) (1987) 6203–6206.
18. **Stepanov B.I., Gribkovsky V.P.**, *Theory of Luminescence*, Iliffe Books, London, 1968.
19. **Kopaczek J., Polak M. P., Scharoch P., Wu K., Chen B., Tongay S., Kudrawiec R.**, Direct optical transitions at K- and H-point of Brillouin zone in bulk MoS₂, MoSe₂, WS₂, and WSe₂, *J. Appl. Phys.* 119 (23) (2016) 235705.
20. **Kayanuma Y.**, Quantum-size effects of interacting electrons and holes in semiconductor microcrystals with spherical shape, *Phys. Rev. B*. 38 (14) (1988) 9797–9805.
21. **Saigal N., Sugunakar V., Ghosh S.**, Exciton binding energy in bulk MoS₂: A reassessment, *Appl. Phys. Lett.* 108 (13) (2016) 132105.
22. **Evans B.L., Young P A.**, Optical absorption and dispersion in molybdenum disulphide, *Proc. Roy. Soc. A*. 284 (1398) (1965) 402–422.
23. **Goryca M., Li J., Stier A.V., Taniguchi T., Watanabe K., Courtade E., Shree S., Robert C., Urbaszek B., Marie X., Crooker S.A.**, Revealing exciton masses and dielectric properties of monolayer semiconductors with high magnetic fields, *Nature Commun.* 10 (2019) 4172.
24. Molybdenum Disulfide. Kee Hing Cheung Kee Co., Ltd: Hong Kong, <http://www.khck.hk/adgoogle/Molybdenum-Disulfide.htm>
25. **Evans B.L.**, *Optical Properties of Layer Compounds. Optical and electrical properties (Physics and chemistry of materials with layered structures Vol. 4) ed. P. A. Lee, pp. 1–143, D. Reidel Publishing Company, Dordrecht, 1976.*
26. **Woggon U.**, *Optical Properties of Semiconductor Quantum Dots*, Springer-Verlag, Berlin, Heidelberg, 1997.
27. **Pokutnyi S.I.**, Excitation states in semiconductor quantum dots in the modified effective mass approximation, *Semiconductors*. 41 (11) (2007) 1323–1328.
28. **Nishiguchi N., Yoh K.**, Energy-Dependent Effective Mass Approximation in One-Dimensional Quantum Dots, *Japan. J. Appl. Phys.* 36 (6S) (1997) 3928–3931.
29. **Abid H.A., Al-Rashid S.N.T.**, Study of the effect of nanoparticle size on the dielectric constant and concentration of charge carriers of Si and CdS materials, *Chalcogenide Letters*. 17 (12) (2020) 623–629.
30. **Driel A. F. van, Allan G., Delerue C., Lodahl P., Vos W.L., Vanmaekelbergh D.**, Frequency-Dependent Spontaneous Emission Rate from CdSe and CdTe Nanocrystals: Influence of Dark States, *Phys. Rev. Lett.* 95 (23) (2005) 236804.

THE AUTHORS

NELSON Dmitrii K.
d.nelson@mail.ioffe.ru
ORCID: 0000-0001-6391-1897

KURDYUKOV Dmitry A.
kurd@gvg.ioffe.ru
ORCID: 0000-0002-3041-9609

STARUKHIN Anatoly N.
a.starukhin@mail.ioffe.ru
ORCID: 0000-0000-0000-0000

STOVPYAGA Ekaterina Yu.
kattrof@gvg.ioffe.ru
ORCID: 0000-0003-0434-5252

Received 20.10.2022. Approved after reviewing 08.11.2022. Accepted 08.11.2022.

Conference materials

UDC 537.622.6

DOI: <https://doi.org/10.18721/JPM.161.161>

Nanoscale layers of hexaferrite $\text{BaFe}_{12}\text{O}_{19}$ grown by laser molecular beam epitaxy: growth, crystal structure and magnetic properties

B.B. Krichevtsov ¹✉, A.M. Korovin ¹, S.M. Suturin ¹, N.S. Sokolov ¹

¹Ioffe Institute, Saint Petersburg, Russia

✉ boris@mail.ioffe.ru

Abstract. Single-crystal 50 and 300 nm thick layers of BaM hexaferrite $\text{BaFe}_{12}\text{O}_{19}$ were synthesized by laser molecular beam epitaxy method on $\alpha\text{-Al}_2\text{O}_3$ (0001) substrates. Crystallization process was monitored *in situ* by RHEED and crystal structure was analyzed using three-dimensional mapping of diffraction patterns. The film surface morphology was investigated by atomic force microscopy. It was shown that the “as grown” structures exhibit hexaferrite structure but reveal violation of the long-range order, which is highly improved by the post growth annealing. Magnetic properties were studied by magneto-optical polar Kerr effect. Both the “as grown” and annealed structures were examined. After annealing, BaM hexaferrite films demonstrate square-type out-of-plane magnetic hysteresis loops indicating the presence of strong uniaxial magnetic anisotropy and remarkable pinning of domain walls.

Keywords: hexaferrite, molecular beam epitaxy, RHEED, atomic force microscopy, magneto-optical Kerr effect, magnetic properties

Funding: This study was funded by the Russian Science Foundation grant No. 22-22-00768, <https://rscf.ru/project/22-22-00768/>.

Citation: Krichevtsov B.B., Korovin A.M., Suturin S.M., Sokolov N.S., Nanoscale layers of hexaferrite $\text{BaFe}_{12}\text{O}_{19}$ grown by laser molecular beam epitaxy: growth, crystal structure and magnetic properties, St. Petersburg State Polytechnical University Journal. Physics and Mathematics. 16 (1.1) (2023) 363–368. DOI: <https://doi.org/10.18721/JPM.161.161>

This is an open access article under the CC BY-NC 4.0 license (<https://creativecommons.org/licenses/by-nc/4.0/>)

Материалы конференции

УДК 537.622.6

DOI: <https://doi.org/10.18721/JPM.161.161>

Наноразмерные слои гексаферрита $\text{BaFe}_{12}\text{O}_{19}$, выращенные методом лазерной молекулярно-лучевой эпитаксии: рост, кристаллическая структура и магнитные свойства

Б.Б. Кричевцов ¹✉, А.М. Коровин ¹, С.М. Сутурин ¹, Н.С. Соколов ¹

¹Физико-технический институт им. А.Ф. Иоффе РАН, Санкт-Петербург, Россия

✉ boris@mail.ioffe.ru

Аннотация. Монокристаллические слои гексаферрита BaM $\text{BaFe}_{12}\text{O}_{19}$ толщиной 50 и 300 нм синтезированы методом лазерной молекулярно-лучевой эпитаксии на подложках $\alpha\text{-Al}_2\text{O}_3$ (0001). Исследованы кристаллическая структура, морфология поверхности и магнитные свойства как “as grown”, так и отожженных структур.

Ключевые слова: гексаферрит, молекулярно-лучевая эпитаксия, ДБЭ, атомно-силовая микроскопия, магнитооптический эффект Керра, магнитные свойства

Финансирование: Работа выполнена при поддержке РФФ грант № 22-22-00768, <https://rscf.ru/project/22-22-00768/>.

Ссылка при цитировании: Кричевцов Б.Б., Коровин А.М., Сутурин С.М., Соколов Н.С. Наноразмерные слои гексаферрита $\text{BaFe}_{12}\text{O}_{19}$, выращенные методом лазерной

молекулярно-лучевой эпитаксии: рост, кристаллическая структура и магнитные свойства
 // Научно-технические ведомости СПбГПУ. Физико-математические науки. 2023. Т. 16.
 № 1.1. С. 363–368. DOI: <https://doi.org/10.18721/JPM.161.161>

Статья открытого доступа, распространяемая по лицензии CC BY-NC 4.0 (<https://creativecommons.org/licenses/by-nc/4.0/>)

Introduction

One of the fundamental limitations hindering the development of modern element base for information processing is the release of Joule heat during the transport of charge carriers. A possible way to solve this problem is a utilization of magnonic devices based on the use of spin waves packets propagating in magnetic nanoheterostructures [1–3]. In this regard, the problem of creating thin film materials in which it is possible to excite, control, and record weakly damping spin waves arises. For these purposes, intensive studies of nanostructures based on garnet ferrites [4–7], spinel ferrites [8–11], and orthoferrites [11–14] were carried out.

Promising for microwave applications are M-type hexaferrites, a typical representative of which is $\text{BaFe}_{12}\text{O}_{19}$ (BaM hexaferrite). The review of synthesis, properties and applications of hexaferrites can be found in Ref. [15]. Compared with the mentioned above magnetic garnets, spinels and orthoferrites, the hexaferrites have a number of advantages. Magnetization of BaM hexaferrite at RT $4\pi M_s \sim 4\text{ T}$ is higher than in yttrium iron garnet (YIG) $4\pi M_s \sim 1.7\text{ T}$ and nickel ferrite (NFO) $4\pi M_s \sim 3.3\text{ T}$. The uniaxial magnetic anisotropy field H_a in BaM hexaferrite is about 1.75 T, that is two orders of magnitude higher than in YIG and one order higher than that of NFO. Due to high value of H_a the ferromagnetic resonance frequency in BaM hexaferrite $f = \gamma(H + H_a - 4\pi M_s)$, in the absence of an external field $H = 0$ is about $f \sim 36\text{ GHz}$ and linearly increases with external magnetic field H . As a result, devices based on hexaferrites can operate at frequencies up to $f = 60\text{ GHz}$. Moreover, textured polycrystalline hexaferrites can be created with a significant residual magnetization, which in some cases makes it possible to avoid the use of external magnets.

Thin films of hexaferrites were fabricated by liquid-phase epitaxy (LPE), pulsed laser deposition (PLD), direct current magnetron sputtering, screen printing (SP), and a metallo-organic decomposition (MO) methods on different substrates (sapphire, Al_2O_3 , MgO, GdGa-garnet GGG, 6H-SiC). Comparison of films prepared by different methods, presented in [16], shows that the films of high crystal quality, prepared by PLD or LPE, show an out-of-plane orientation of c-axis and small values of FMR lines widths ($\sim 30\text{--}60\text{ Oe}$) but also small values of remanence M_r for out-of-plane hysteresis loops. For this reason, for the application of these films in microwave devices an external magnetic field is needed. Contrary to that the films of lower crystal quality, fabricated by SP [17] or MO [18], have high hysteresis loop squareness ($M_r/M_s \sim 0.9$), showing realization of self-bias effect, but large values of FMR line width. So, an obtaining a hexaferrite films with high crystal quality and high self-bias values is very desirable. Note that epitaxial films of BaM hexaferrite with in-plane orientation of easy axis and “self-bias” effect were synthesized by direct current magnetron sputtering on α -plane (11-20) of single-crystal sapphire substrates [19].

This paper reports on the growth of single-crystalline layers of hexaferrite ($\text{BaFe}_{12}\text{O}_{19}$) by laser molecular beam epitaxy on sapphire $\alpha\text{-Al}_2\text{O}_3$ (0001) substrates and the study of their structural and magnetic properties.

Materials and Methods

Thin films (thickness $d \sim 50\text{ nm}$ and 300 nm) were grown using laser molecular beam epitaxy (MBE) method on $\alpha\text{-Al}_2\text{O}_3$ (0001) substrates with an installation produced by “Surface, GmbH”. The films were grown in an oxygen atmosphere at a pressure of $P = 0.04\text{--}0.06\text{ mBar}$ at growth temperatures of $T_{\text{gr}} = 750\text{--}1000\text{ }^\circ\text{C}$. The flow of matter onto the substrate was created by ablation of a stoichiometric $\text{BaFe}_{12}\text{O}_{19}$ (Ba-hexaferrite M-type) target by a KrF excimer laser with a wavelength of 248 nm. The growth process was continuously monitored by reflection high-energy electron diffraction (RHEED). To analyze the RHEED patterns, the method of three-

dimensional mapping of diffraction patterns was applied. As a result of φ - 2φ scanning with a step of 0.01 degrees in φ , a series of 900 images was measured, from which a 3D map of the reciprocal space was obtained using the software. For our study we used both the as-grown structures and structures after annealing procedure. For post growth annealing, after preparation the samples were removed from the growth chamber and annealed up to 2 hours in air at the temperature of 1000 °C. Table 1 shows some parameters of presented in this work structures.

Table 1

Sample number, thickness of hexaferrite layer, growth temperature T_{gr} , oxygen pressure P , annealing time t_{ann} , and annealing temperature T_{ann} of presented in this work BaM hexaferrite structures

Sample, №	Thickness, nm	T_{gr} , °C	Oxygen pressure P , mBar	Annealing time, min., and T_{ann} , °C
8940A	50	850	0.004	No
8940B	50	850	0.004	120, 1000
8944	50	950	0.06	No
8947	50	1000	0.06	No
8948A	50	750	0.06	No
8948B	50	750	0.06	10, 1000
8948B+	50	750	0.06	20, 1000
8948C	50	750	0.06	60, 1000
8948C+	50	750	0.06	120, 1000
8949	50	925	0.06	No
8954A	300	750	0.06	No
8954B	300	750	0.06	60, 1000

Magnetic hysteresis loops for out-of-plane orientation of magnetic field H (up to ± 20 kOe) were studied using magneto-optical polar Kerr effect by measuring the polarization plane rotation ϕ of linearly polarized light ($\lambda = 405$ nm) practically normally reflected from the film surface. Polarization modulation with Faraday cell was used to increase the measurements sensitivity ($\delta\phi \sim 1$ sec. of arc).

Results and Discussion

BaM hexaferrite layers grown at temperatures of 700–850 °C show RHEED images corresponding well to the bulk-BaM structure (Fig. 1, left). However, the enlarged width of the streaks and chaotic distribution of the streak intensity in these patterns indicate relatively low crystalline quality of the grown films. It is also seen that every second streak has a much higher intensity, which indicates a strong violation of the long-range order. In addition, it is worth noting that the RHEED patterns do not strongly depend on the O_2 pressure in the range of 0.005–0.05 mbar.

In contrast to that, the films grown at 700–850 °C and then annealed in air at 1000 °C show the RHEED images perfectly modeled by the bulk BaM lattice (Fig. 1, center). It can be seen that the number of reflections and the signal-to-background ratio are much better compared to the non-annealed samples. All streaks have the same intensity, which indicates the presence of good long-range order.

It was found that the samples grown at temperatures of 900–1000 °C are very different as compared to those grown at lower temperatures. RHEED patterns from such samples are well modeled by the α - Fe_2O_3 lattice (Fig. 1, right). The formation of α - Fe_2O_3 is most likely associated with resputtering (desorption induced by impinging particles) of Ba ions at high temperatures. The account of resputtering process can explain the effect of 1000 °C annealing on crystal quality of films grown at low temperatures. In films grown at $T_{gr} = 700$ –850 °C the resputtering is small and Ba ions are distributed more or less homogeneously inside of hexaferrite film. The annealing results in redistribution of Ba positions and occupation by Ba ions of places corresponding to BaM crystal structure that leads to formation of high crystal quality BaM layer with improved magnetic properties (see below). The growth of films at 1000 °C is followed to disappearance of

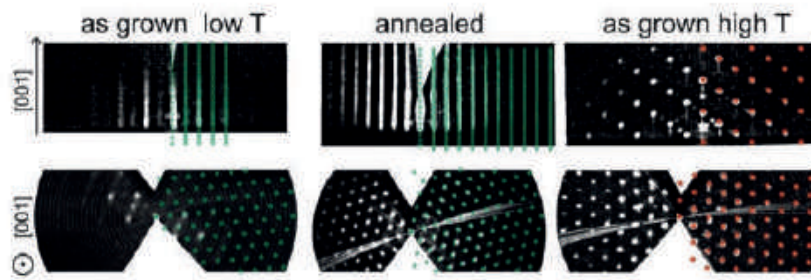


Fig. 1. 3D reconstruction of RHEED data for BaM films N8954A grown at 800 °C (left), N8954B grown at 800 °C and annealed for 1 hour at 1000 °C (center) and N 8947 grown at 1000 °C (right) in the same scale; green and red dots are a model lattice calculated using parameters of bulk BaM crystal. Films in left and central panels have thickness ~ 300 nm and in left panel ~ 50 nm

Ba ions from film and to formation of α -Fe₂O₃ structure.

Most of “as-grown” BaM films do not reveal any hysteresis magnetic loops in out-of-plane magnetic field. Only structures N 8944 and 8949 grown at $T_{gr} = 950$ and 925 °C shows small and wide ($H_c \sim 7$ kOe) hysteresis loops (Fig.2, a).

Annealing leads to a sharp change in the hysteresis loops. Fig 2, b illustrates this fact on example of the “as grown” (N 8940A) and annealed (N 8940B) at 1000 °C during 120 min parts of the same film. After annealing, an almost rectangular loop ($M_r/M_s \sim 1$, M_r and M_s are remnant and saturated magnetization correspondingly) is observed with a coercive field $H_c = 2.5$ kOe. The effect of annealing on the magnetic properties of the films was observed in all structures grown at $T_{gr} = 700$ – 850 °C. The effect of annealing time t_{ann} on shape of hysteresis loops is presented in Fig.2, c. Even 10 minutes annealing results in the appearance of a hysteresis loop. An increase of t_{ann} leads to an increase of both the magnitude of PMOKE in saturation and M_r/M_s ratio (Fig. 2, d), but does not change the coercive field value $H_c = 2.5$ kOe. The jumps in the magnetization at $H = \pm H_c$ are obviously caused by the formation of domains with the opposite orientation of the magnetization and the motion of the domain walls.

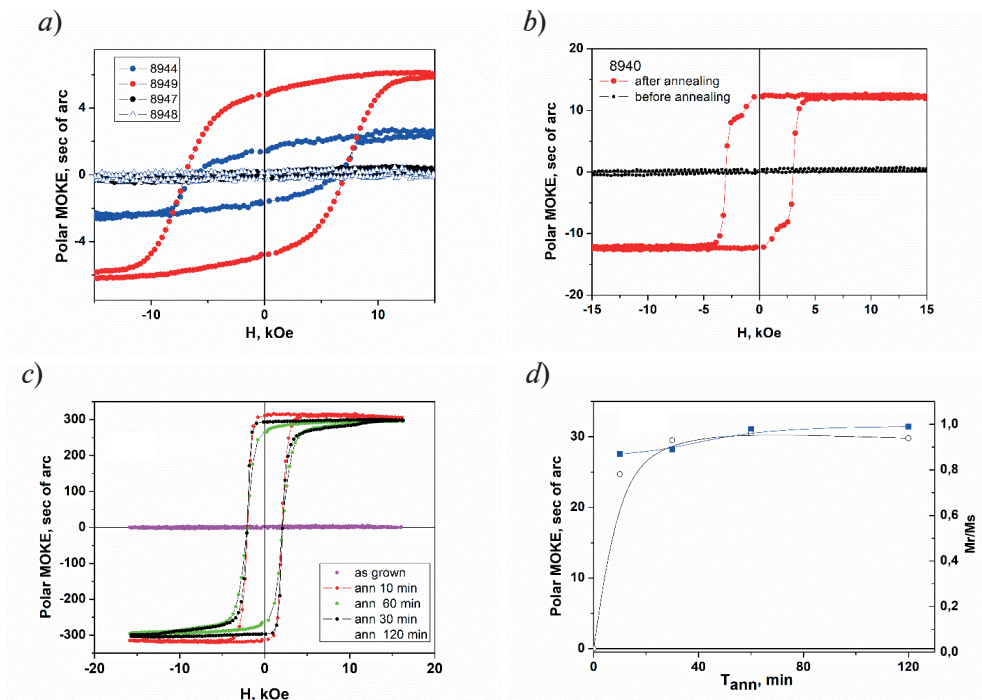


Fig. 2. Magnetic hysteresis loops measured by MOKE in “as grown” films N 8944, 8947, 4948, 8949 (a). Effect of 120 min 1000 °C annealing in 8940 film (b). Effect of annealing time t_{ann} on hysteresis loops in film N 8948 (c, d)



Relatively high values of H_c in our structures indicate that domains in BaM layers are pinned on defects in contrast to films prepared in [16].

Conclusion

The study showed that thin layers of BaM hexaferrite obtained by laser molecular beam epitaxy on sapphire (0001) substrates demonstrate well-ordered BaM crystal structure after post-growth annealing in air at 1000 °C of the samples grown at $T_{gr} = 700\text{--}850$ °C. The observation of rectangular loops in the fabricated BaM structures indicates the presence of a strong out-of-plane uniaxial magnetic anisotropy, which makes it possible to realize a saturated magnetic state with an out-of-plane orientation of magnetization in the absence of an external magnetic field H . This may be of interest for the creation of UHF microwave devices that use bulk spin waves for the operation. Future studies of these structures will focus on XRD crystal structure measurements, VSM magnetization studies, and FMR spectroscopy.

Acknowledgments

Authors thank Dr. K. Mashkov for help with carrying out MOKE experiments.

REFERENCES

1. Kruglyak V.V., Demokritov S.O., Grundler D., *Magnonics*, J. Phys. D. Appl. Phys. 43 (2010) 264001 (14pp).
2. Nikitov S.A., Kalyabin D.V., Lisenkov I.V., Slavin A.N., Barabanenkov Yu.N., Osokin S.A., Sadovnikov A.V., Beginin E.N., Morozova M.A., Sharaevsky Yu.P., Filimonov Yu.A., Khivintsev Yu.V., Vysotsky S.L., Sakharov V.K., Pavlova E.S., *Magnonics: a new research area in spintronics and spin wave electronics*, Physics-Uspekhi. 58 (2015) 1002–1028.
3. Grundler D., *Nanomagnonocs*, J. Phys. D. Appl. Phys. 49 (2016) 2014–2017.
4. Serga A.A., Chumak A.V., Hillebrands B., *YIG magnonocs*, J. Phys. D. Appl. Phys. 43 (2010) 264002.
5. Howe B.M., Emori S., Jeon H., Oxholm T.M., Jones J.G., Mahalingam K., Zhuang Y., Sun N.X., Brown G.J., *Pseudomorphic Yttrium Iron Garnet Thin Films with Low Damping and Inhomogeneous Linewidth Broadening*, IEEE Magn. Lett. 6 (2015), 2013–2016.
6. Sokolov N.S., Fedorov V.V., Korovin A.M., Suturin S.M., Baranov D.A., Gastev S.V., Krichevtsov B.B., Maksimova K.Yu., Grunin A.I., Bursian V.E., Lutsev L.V., Tabuchi M., *Thin yttrium iron garnet films grown by pulsed laser deposition: Crystal structure, static, and dynamic magnetic properties*, J. Appl. Phys., 119 (2016) 023903.
7. Chang H., Li P., Zhang W., Liu T., Hoffmann A., Deng L., Wu M., *Thin yttrium iron garnet films grown by pulsed laser deposition: Crystal structure, static, and dynamic magnetic properties*, IEEE Magn. Lett. 5 (2014) 10–13.
8. Chinnasamy C.N., Yoon S.D., Yang A., Baraskar A., Vittoria C., Harris V. G., *Effect of growth temperature on the magnetic, microwave, and cation inversion properties on NiFe₂O₄ thin films deposited by pulsed laser ablation deposition*, J. Appl. Phys. 101 (2007) 09M517.
9. Singh A. V., Khodadadi B., Mohammadi J.B., Keshavarz S., Mewes T, Negi D.S., Ranjan Datta, Galazka Z., Uecker R., Gupta A., *Bulk Single Crystal-Like Structural and Magnetic Characteristics of Epitaxial Spinel Ferrite Thin Films with Elimination of Antiphase Boundaries*, Adv. Mater. 29 (2017) 1701222.
10. Krichevtsov B., Gastev S., Mashkov K., Kaveev A., Korovin A., Lutsev L., Suturin S., Lobov I., Telegin A., Lomov A. Sokolov N., *Magnetization reversal in NiFe₂O₄/SrTiO₃ nanoheterostructures grown by laser molecular beam epitaxy*, J. Phys. Conf. Ser. 1389 (2019), 012106.
11. Bursian V.E., Kaveev A.R., Alexander, Korovin A.M., Krichevtsov B.B., Lutsev L.V., Suturin S.M., Sawada M., Sokolov N.S., *Bulk-Like Dynamic Magnetic Properties of Nickel Ferrite Epitaxial Thin Films Grown on SrTiO₃(001) Substrates*, IEEE Magn. Lett. 10 (2019) 6104505.
12. Ning S., Kumar A., Klyukin K., Cho E., Kim J. H., Su T., Kim H.-S., LeBeau J.M., Bilge Yildiz B., Ross C.A., *An antisite defect mechanism for room temperature ferroelectricity in orthoferrites*, Nature Communications. (2021) 12:4298.
13. Jeong Y.K. , Lee J.-H., Ahn S.-J., Song S.-W., Jang H.M., Choi H., Scott J.F., *Structurally*

Tailored Hexagonal Ferroelectricity and Multiferroism in Epitaxial YbFeO₃ Thin-Film Heterostructures, *J. Am. Chem.Soc.* 134 (2012) 1450–1453.

14. **Seo J.W., Fullerton E.E., Nolting F., Scholl A., Fompeyrine J., Locquet J-P.**, Antiferromagnetic LaFeO₃ thin films and their effect on exchange bias, *J. Phys.: Condens. Matter.* 20 (2008) 264014.

15. **Pullar R.C.**, *Progress in Materials Science.* 57 (2012) 1191–1334.

16. **Su Z., Bennett S., Hu B., Yajie Chen Y., Harris V.G.** Magnetic and microwave properties of U-type hexaferrite films with high remanence and low ferromagnetic resonance linewidth, *J. Appl. Phys.* 99 (2006) 08M911.

17. **Nie Y., Harward I., Balin K., Beaubien A., Celinski Z.**, Preparation and characterization of barium hexagonal ferrite thin films on a Pt template, *J. Appl. Phys.* 107 (2010) 073903.

18. **Chen Y., Sakai T., Chen T., Yoon S.D., Geiler A.L., Vittoria C., Harris V.G.** *Appl. Phys. Lett* 88 (2006) 062516.

19. **Zhang X., Meng S., Song D., Zhang Y., Yue Zh., Harris V.G.**, Epitaxially grown BaM hexaferrite films having uniaxial axis in the film plane for self-biased devices, *Sci. Rep.* 7 (2017) 44193.

THE AUTHORS

KRICHEVTSOV Boris B.

boris@mail.ioffe.ru

ORCID: 0000-0003-4032-8708

SUTURIN Sergey M.

Suturin@mail.ioffe.ru

ORCID: 0000-0002-3662-2384

KOROVIN Alexander M.

Amkorovin@mail.ioffe.ru

ORCID: 0000-0002-3255-9808

SOKOLOV Nikolai S.

Nsokolov@fl.ioffe.ru

ORCID: 0000-0002-8763-3489

Received 24.10.2022. Approved after reviewing 09.11.2022. Accepted 15.11.2022.

Conference materials

UDC 621.327.53

DOI: <https://doi.org/10.18721/JPM.161.162>

Application of cesium lamps for indoor lighting and preventive ultraviolet irradiation

A.A. Bogdanov¹✉, S.V. Gavrish², A.M. Martsinovsky¹, I.I. Stolyarov¹

¹Ioffe Institute, St. Petersburg, Russia;

²Scientific and Industrial Enterprise "Melitta" Ltd, Moscow, Russia

✉ a.bogdanov@mail.ioffe.ru

Abstract. An analysis of the radiation from cesium lamps has shown that the spectrum of such lamps is determined by the recombination continuum. This spectrum is close to the spectrum of the Sun not only in the visible, but also in the ultraviolet in the A and B ranges. This makes it possible to create environmentally friendly energy-efficient lighting systems with constant UV radiation based on these lamps to compensate for the lack of ultraviolet radiation at high latitudes and when working indoors without natural light. The advantages of such systems are considered in comparison with existing dual systems using conventional visible light sources and special erythemic fluorescent mercury lamps.

Keywords: gas discharge lamps, cesium pulse-periodic discharge, luminous efficacy, ultraviolet irradiation

Citation: Bogdanov A.A., Gavrish S.V., Martsinovsky A.M., Stolyarov I.I., Application of cesium lamps for indoor lighting and preventive ultraviolet irradiation, St. Petersburg State Polytechnical University Journal. Physics and Mathematics. 16 (1.1) (2023) 369–373. DOI: <https://doi.org/10.18721/JPM.161.162>

This is an open access article under the CC BY-NC 4.0 license (<https://creativecommons.org/licenses/by-nc/4.0/>)

Материалы конференции

УДК 621.327.53

DOI: <https://doi.org/10.18721/JPM.161.162>

Использование цезиевых ламп для внутреннего освещения и профилактического ультрафиолетового облучения

А.А. Богданов¹✉, С.В. Гавриш², А.М. Марциновский¹, И.И. Столяров¹

¹Физико-технический институт им. А.Ф. Иоффе РАН, Санкт-Петербург, Россия;

²ООО «НПП «Мелитта». Москва, Россия

✉ a.bogdanov@mail.ioffe.ru

Аннотация. Анализ излучения цезиевых ламп показал, что спектр таких ламп определяется рекомбинационным континуумом. Этот спектр близок к спектру Солнца не только в видимой, но и в ультрафиолетовой области в диапазонах А и В. Это позволяет на основе этих ламп создавать экологически чистые энергоэффективные системы освещения с постоянной УФ радиацией, восполняющие недостаток ультрафиолета в высоких широтах и при работах в помещениях без естественного освещения. Рассмотрены преимущества таких систем по сравнению с существующими двойными системами с использованием обычных источников видимого света и специальных эритемных люминесцентных ртутных ламп.

Ключевые слова: газоразрядные лампы, цезиевый импульсно-периодический разряд, светоотдача, ультрафиолетовое излучение

Ссылка при цитировании: Богданов А.А., Гавриш С.В., Марциновский А.М., Столяров И.И. Использование цезиевых ламп для внутреннего освещения и

профилактического ультрафиолетового облучения // Научно-технические ведомости СПбГПУ. Физико-математические науки. 2023. Т. 16. № 1.1. С. 369–373. DOI: <https://doi.org/10.18721/JPM.161.162>

Статья открытого доступа, распространяемая по лицензии CC BY-NC 4.0 (<https://creativecommons.org/licenses/by-nc/4.0/>)

Mercury-free lighting lamps of a high-current pulse-periodic discharge (PPD) with cesium filling at high pressure have been developed and studied in recent years [1–10]. The radiation output in such lamps occurs mainly in the recombination continuum (6P and 5D). The pulsed mode with a low duty cycle makes it possible to realize for a short pulse time a discharge plasma concentration of 10^{17} – 10^{18} cm⁻³, which is necessary for efficient continuum radiation, at a relatively low average discharge power and an allowable thermal load on the discharge tube.

These lamps have a very successful combination of characteristics. The large scattering cross sections of electrons and ions on the Cs atom make it possible to abandon the buffer gas, mercury, which makes cesium lamps environmentally friendly. The cross sections for the excitation of electronic levels and the cross sections for recombination at the 6P and 5D levels are almost an order of magnitude higher than those for other alkali metals, Cs has a minimum atomic ionization potential ($E_i = 3.89$ eV). All this provides the high luminous efficacy η of 60–70 lm/W, as can be seen in figure 1, which shows the dependence of the luminous efficacy of a cesium lamp on average power W . The average power varied due to the pulse repetition frequency f . The figure 1 shows the experimental points for pulses with different current amplitudes I_m . The indicated value of η is approximately 5 times higher than the luminous efficacy of incandescent lamps and twice that of xenon lamps, although it is inferior to LEDs. The recombination continuum with a brightness temperature of 4000–6000 K covers almost the entire visible region of the spectrum, which provides excellent “solar” quality of light: the color rendering index is $R_a = 95$ – 97 [1, 2]. The high vapour pressure of cesium provides operating currents of tens of amperes without the appearance of cathode spots, which makes it possible to count on service life even longer than that of high pressure sodium arc lamps (HPSL), which is about 15–25 thousand hours. The cost of cesium lamps should be as relatively low as that of HPSL, since the technology for the production of both lamps is practically the same, and cesium lamps can be produced on equipment for the production of sodium lamps with minimal adaptation.

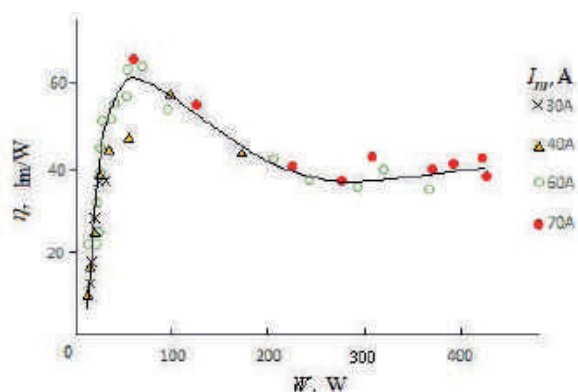


Fig. 1. The luminous efficacy η of a cesium lamp on the average power. The discharge tube radius 2.5 mm, the interelectrode distance 22 mm

The recombination continuum in the Cs lamp also generates weak continuous ultraviolet radiation. (Unlike conventional UV mercury and xenon lamps, which produce powerful monochromatic radiation in intense lines [10], and xenon flash lamps, which provide continuous but extremely intense UV radiation [11]). At the same time, in terms of spectral composition and intensity, this radiation is very close to solar radiation, which is clearly seen from figure 2. This figure shows the short-wavelength part of the standard spectrum of the Sun near the Earth's

surface, which, outside the atmosphere, corresponds to the radiation of a black body with a temperature of 5900 K [12, 13]. For comparison, a typical cesium PPD spectrum with a similar plasma temperature on the discharge axis (about 6000 K) is shown, normalized to the solar spectrum at $\lambda = 550$ nm. The lamp spectrum was not recorded in the short-wavelength region (less than 350 nm), but in this region the lamp radiation is determined by the recombination continuum. Therefore, it is possible to model the radiation of a lamp in the short-wavelength region by the functional dependence of the continuum on the wavelength. The result is shown by a smooth blue curve 3. It can be seen that the spectra are close in the visible region and coincide well in the ultraviolet A region (400–320 nm), worse – for the B region (320–280 nm).

The spectra of the Sun and a cesium lamp depend on external conditions. So for the Sun, with a decrease in its height above the horizon, the short-wave part of the radiation is absorbed more than the long-wave part, therefore, the relative fraction of UV radiation drops especially for regions B and C. For a cesium lamp, the fraction of ultraviolet depends on the discharge mode, increasing with increasing temperature of the discharge plasma. In this case, the UV spectrum of the lamp, as can be seen from figure 2, is significantly affected by the transmission of the lamp bulb. So, in general, and for region B, it is always possible to achieve a general similarity of the spectra. This means that cesium lamps can simultaneously provide high-quality indoor lighting and the necessary dose of “sunny” UV during ultraviolet deficiency in winter at high latitudes (> 60 degrees [14, 15]).

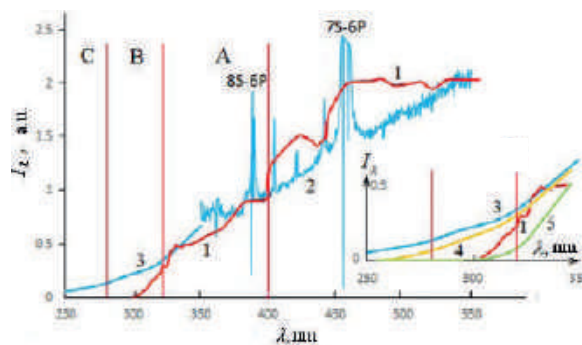


Fig. 2. Comparison of the spectra of the Sun and a cesium lighting lamp (the inset: short-wave region of the spectra). 1 — the Sun at sea level at its zenith, 2 — lamp, 3 — extrapolation to the short-wavelength region of the lamp spectrum in a quartz bulb, 4 and 5 — the same for bulbs made of different UV-glasses

It is known that UV radiation is a vital factor, and its prolonged lack leads to the development of a kind of symptom complex called “light starvation” or “UV deficiency”. Those experiencing “UV deficiency” include workers in mines, metro, people working in workshops without access to daylight, engine rooms and, most importantly, residents of the Far North. To compensate for UV deficiency, at present, as the most effective means for industrial, educational, office premises, combined lighting systems are used with parallel switching on of special fluorescent mercury erythema lamps (LE, LA, LAR), emitting a relatively weak flux of ultraviolet radiation in areas A and B. Placement and the power of the lamps is calculated in such a way that during the stay in the room (4–8 hours) a person receives at least 1/8 (prophylactic dose) and no more than 3/4 of the erythemic radiation dose. The medical erythema dose is determined experimentally by the reddening of the skin from exposure to UV radiation. It is individual, but on average it is assumed to be approximately 200 J/m^2 [15].

Figure 3 shows a typical discharge spectrum in the near UV and part of the visible region in absolute energy units for a mode with the luminous efficacy of 55 lm/W , which is close to the maximum in figure 1. The spectrum was recorded at the end of the current pulse (the pulse duration $30 \mu\text{s}$) at a maximum current value of 60 A, $W = 107 \text{ W}$, $f = 1310 \text{ Hz}$. The plasma temperature (8000 K) in this mode is higher than for the mode in figure 2. Therefore, the radiation here decays more slowly to the short-wavelength range of the spectrum. Based on the data in Figure 3, it is possible to estimate the dose of UV radiation in the B range, which is given by a cesium lamp that provides standard lighting in the room, with a constant stay with this lighting

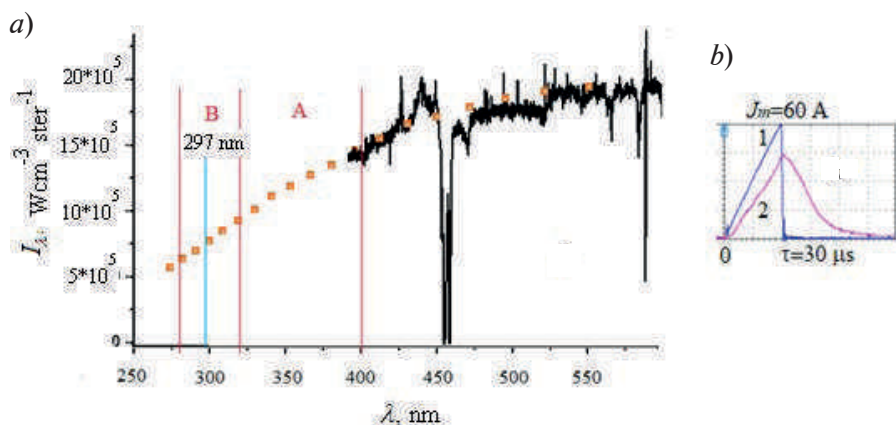


Fig. 3. The spectrum of a lamp with the interelectrode distance 22 mm and a quartz bulb. Squares — recombination continuum in the short-wavelength region (a); oscillogram of current 1 and luminous flux 2 (b)

($t = 8\text{--}16$ hours). Regulatory lighting usually varies in the range of 100–500 lx, depending on the purpose of the premises, on average 250 lx. The flux of visible radiation in this mode is 5800 lm. For an occupancy time of 8 hours, the resulting UV dose would be 100 J/m². This value is in the middle between the prophylactic and erythema doses, i.e. the ratio of the intensity of the visible and UV parts of the spectrum of cesium lamp is really close to optimal. This ratio can be changed by changing the mode of the lamps.

Thus, cesium lamps with their own UV radiation will have an advantage over combined lighting in all major parameters. First of all, eliminating the need to create a parallel UV irradiating system makes it easier and cheaper to switch to UV-enriched light. It should be especially noted that even when LEDs are used in the combined lighting system as the most efficient sources of visible light, the resulting luminous efficacy of the entire system will be at the level of the luminous efficacy of cesium lamps. This can be shown with a specific example. In [16], a calculation of the UV system for combined lighting for a room with an area of 50 m² is given, according to which it requires 8 LE-30 lamps with a total power of 240 W. To achieve lighting of 300 lx by LED sources in such a room, a luminous flux of ~ 25000 lm is required. At the current maximum the luminous efficacy of 150 lm/W (cylindrical LED sources from Philips), such a flux will require a power of 160 W, and the resulting luminous efficacy will be 60 lm/W.

In addition, the spectrum of UV radiation close to the sun should be the most favorable for the body. This ensures high quality of visible light. Rejection of mercury-containing erythema lamps in accordance with the Minamata Convention on Mercury (2013) addresses the issue of environmental safety. Guaranteed safety against an overdose of UV radiation will make it possible to switch to ultraviolet enriched lighting without additional difficulties, simply by replacing conventional light sources with cesium lamps, and to widely use it not only in industrial and public premises, but also in domestic conditions.

It should be emphasized that a necessary condition for the transition to lighting with cesium lamps should be the development of their power line in the range of 10–30 W with electronic ballasts in the base, which is realistic with modern element base. For lamps of high power ($P > 30$ W), it will be essential to develop compact electronic ballast. But, of course, the positive results of relevant biomedical studies of their radiation on the human body should play the main role in the implementation of using cesium lighting lamps. These studies can be carried out on the basis of already developed experimental samples of such lamps. Only such studies will make it possible to optimize the ratio of the visible and UV parts of the lamp spectrum and select the appropriate discharge modes.

REFERENCES

1. Baksht F.G., Lapshin V.F., Pulsed-Periodic Discharge in Cesium as an Effective Source of Light, Technical Physics, 47 (2002) 894–99.

2. **Baksht F.G., Gavrish S.V., Kaplan V.B., Korotkov S.V., Lapshin V.F., Martsinovskii A.M., Stolyarov I.I., Khristyuk D.V.**, Visible emission spectrum of pulse-periodic discharge in high-pressure cesium vapor, *Tech. Phys. Lett.*, 34 (2008) 1066–1068.
3. **Baksht F.G., Lapshin V.F.**, Generatsiya vidimogo izlucheniya s nepreryvnym spektrom impulsno-periodicheskim razryadom vysokogo davleniya v tsezii [Generation of visible radiation with the continua spectrum in conditions of a pulse-periodical high pressure cesium discharge], *Usp. Prikl. Fiz.*, 5 (6) (2017) 525–533.
4. **Bogdanov A.A., Gavrish S.V., Koval' V.V., Martsinovskiy A.M., Stolyarov I.I.**, Features of a High-Current Pulse-Periodic Cesium Discharge as a Source of Visible Radiation, *Plasma Phys. Rep.*, 47 (2021) 627–631.
5. **Bogdanov A.A., Gavrish S.V., Martsinovskiy A.M., Stolyarov I.I.**, J. Influence of contraction of a cesium pulse-periodic discharge on its luminous efficacy and spectral properties, *Phys.: Conf. Ser.* 2103 (2021) 012220.
6. **Gu H., Muzeroll M.E. Chamberlain J.C., Maya J.**, Pulse modulated high-pressure caesium discharge lamp, *Plasma Sources Sci. Technol.*, 10 (2001) 1–9.
7. **Pichler G., Živčec V., Beuc R., Mrzljak Ž., Ban T., Skenderović H., Gunther K., Liu J.**, UV, Visible and IR Spectrum of the Cs High Pressure Lamp, *Phys. Scr.*, 105 (2003) 98–100.
8. **Rakic M., Pichler G.**, Comparison of visible and infrared spectrum of light sources, *Optics Communications*, 284 (2011) 2881–2885.
9. **Rakic M., Pichler G.**, Time evolution of the spectrum of the cesium high pressure discharge light source, *J. Quant. Spectrosc. Radiat. Transf.*, 151 (2015) 169–173.
10. **Rokhlin G.N.**, *Razryadnye istochniki sveta [Discharge Light Sources]*, Energoatomizdat, Moscow, 1991
11. **Arhipov V.P., Kamrukov A.S., Kozlov N.P., Makarchuc A.A.**, Distantionnoye obezzarazhivaniye obyektov napravlenym impulsnym shirokopolosnym UF-izlucheniyem [Remote decontamination of objects by pulsed broadband UV radiation], *Prikl. Fiz.*, 6 (2016) 102–108 (in Russian).
12. **Hall E.S.**, Ground-based measurement of solar ultraviolet radiation, <https://www.accessscience.com/content/ground-based-measurement-of-solar-ultraviolet-radiation/YB090147>.
13. <https://www.newport.com/t/introduction-to-solar-radiation>.
14. **Wacker M., Holick M.F.**, Sunlight and Vitamin D. A global perspective for health, *Dermato-endocrinology*, 5 (2013) 51–108.
15. **Nenahova E.V., Nikolaeva L.A.**, Ultrafioletovoe izluchenie. Vliyanie ultrafioletovogo izlucheniya na organism cheloveka, IGMU, Irkutsk, (in Russian) 2020.
16. **Shumilin V.K., Lyoghkiy N.M., Kriventsov C.M.**, Poryadok organizatsii sistemy eritemnogo osveshcheniya v pomeshcheniyakh dlya kompensatsii ultrafioletovoy nedostatochnosti organizma [The procedure for organizing an erythematous lighting system in rooms to compensate for ultraviolet insufficiency of the body], *Simvol nauki*, 12-1 (2020) 81–85 (in Russian).

THE AUTHORS

BOGDANOV Alexander A.
a.bogdanov@mail.ioffe.ru

MARTSINOVSKY Artemiy M.
amartsinovskiy@gmail.com

GAVRISH Sergey V.
svgavr@list.ru

STOLYAROV Igor' I.
igor-stolyarov@yandex.ru

Received 26.10.2022. Approved after reviewing 08.11.2022. Accepted 10.11.2022.

Conference materials

UDC 538.97

DOI: <https://doi.org/10.18721/JPM.161.163>

Pesticides detection by SERS using dendritic structures grown in glass

E.A. Lubyankina^{1,2}✉, E.S. Babich^{1,2}, A.A. Lipovskii¹

¹ Alferov Saint Petersburg National Research Academic University of the RAS, St. Petersburg, Russia;

² Peter the Great St. Petersburg Polytechnic University, St. Petersburg, Russia

✉ lubyankina_e_st@spbau.ru

Abstract. We demonstrate that dendritic structures formed in glass by electrolysis of silver ions-enriched glass allow detection of low concentration of pesticide thiram using surface-enhanced Raman scattering spectroscopy. Thiram detection is an important issue due to its toxicity for humans. Silver ions were embedded in glass using $\text{Ag}^+ \leftrightarrow \text{Na}^+$ ion exchange procedure. Electrolysis was performed at 250 °C under 600 V and resulted in formation of silver dendrites under the glass surface. To remove the surface glass layer and ensure the access of pesticide to the dendritic structures for Raman spectroscopy we etched the glass in low-concentrated HF solution. Pesticide was adsorbed on the surface of the dendrites via drying a droplet of its aqueous solution. The detection limit and Raman enhancement were estimated, being $4.6 \cdot 10^{-10}$ g/mm² (about a monolayer) and $\sim 4 \cdot 10^5$, respectively. The influence of the morphology of the dendritic structures on Raman signal distribution and enhancement were also studied.

Keywords: surface enhanced Raman scattering spectroscopy, dendrites, electrolysis

Funding: The authors thank the Ministry of science and higher education of the Russian Federation for financial support (project FSRM-2023-0009).

Citation: Lubyankina E.A., Babich E.S., Lipovskii A.A., Pesticides detection by SERS using dendritic structures grown in glass. St. Petersburg State Polytechnical University Journal. Physics and Mathematics. 16 (1.1) (2023) 374–379. DOI: <https://doi.org/10.18721/JPM.161.163>

This is an open access article under the CC BY-NC 4.0 license (<https://creativecommons.org/licenses/by-nc/4.0/>)

Материалы конференции

УДК 538.97

DOI: <https://doi.org/10.18721/JPM.161.163>

Дендритные структуры для обнаружения пестицидов методом гигантского комбинационного рассеяния

Е.А. Лубянкина^{1,2}✉, Е.С. Бабич^{1,2}, А.А. Липовский¹

¹ Академический университет им. Ж.И. Алферова, Санкт-Петербург, Россия;

² Санкт-Петербургский Политехнический Университет Петра Великого, Санкт-Петербург, Россия

✉ lubyankina_e_st@spbau.ru

Аннотация. Мы продемонстрировали, что металлические дендритные структуры, сформированные методом электролиза в обогащенном ионами серебра стекле, позволяют детектировать малые концентрации пестицида тиурама методом гигантского комбинационного рассеяния. В рамках работы были установлены предел обнаружения пестицида и коэффициент усиления комбинационного рассеяния дендритами, а также изучено влияние морфологии дендритов на пространственное распределение сигнала гигантского комбинационного рассеяния.

Ключевые слова: гигантское комбинационное рассеяние, дендриты, электролиз

Финансирование: Работа выполнена при поддержке Министерства науки и высшего образования РФ (код темы FSRM-2023-0009).

Ссылка при цитировании: Лубянкина Е.А., Бабич Е.С., Липовский А.А. Дендритные структуры для обнаружения пестицидов методом гигантского комбинационного рассеяния // Научно-технические ведомости СПбГПУ. Физико-математические науки. 2023. Т. 16. № 1.1. С. 374–379. DOI: <https://doi.org/10.18721/JPM.161.163>

Статья открытого доступа, распространяемая по лицензии CC BY-NC 4.0 (<https://creativecommons.org/licenses/by-nc/4.0/>)

Introduction

Raman scattering is an inelastic scattering of light by vibrational modes of a molecule [1]. The frequency of scattered light depends on a vibration mode and, since sets of modes are unique for each specific molecule, one can identify various species using their Raman spectra. Since one of a million photons is involved in this type of inelastic scattering, Raman spectroscopy cannot detect low concentration of molecules. Surface-enhanced Raman spectroscopy (SERS) allows the essential increase in detection limit of the Raman scattering by using metal nanostructures. Metal nanostructures enhance scattering efficiency [2], which allows ultra-sensitive detection and identification of low concentration of molecules [3]. The applicability of metallic nanoparticles [4], dendrites [5] and nano-island films [6] in SERS has been demonstrated. Using dendrites in SERS is very promising due to numerous “hot spots” (areas of electric field maximum) at the edges and tips of the trunk and branches of the dendrites [7].

One of the important SERS applications is monitoring pesticides in food [8], since pesticides are widely used in modern agriculture [9]. In comparison with the classical methods of pesticide detection, such as gas chromatography, mass spectrometry, and high-performance liquid chromatography, SERS offers faster detection time, simpler sample preparation, portability and reduced cost [10]. Substrates with dendritic structures on the surface can be applied in SERS for the detection of low concentration of pesticide, down to 10^{-10} M [11]. For example, one can use SERS for the detection of thiram ($C_6H_{12}N_2S_4$), which is sulfur fungicide widely used in agriculture [12, 13]. Thiram is toxic for humans when both consumed and in contact with the skin, and effective techniques for its detection in food are highly needed [14]. In this paper, we present the approach to the detection of low concentration of thiram by SERS using dendritic structures on the glass surface.

Materials and Methods

Silver dendritic structures were formed by the electrolysis of a silver-enriched glass followed by chemical etching [15]. We used $Ag^+ \leftrightarrow Na^+$ ion exchange to introduce silver ions in soda-lime glass slide “Menzel”: the slide was immersed in the melt of 5 wt.% $AgNO_3$ and 95 wt.% $NaNO_3$ for 20 min at the temperature of 325 °C. Then we deposited aluminum electrodes (thickness of 200 nm) on the opposite sides of the glass slide and applied DC voltage (600V) to the glass at the elevated temperature (250 °C). Dendritic structures were formed via the reduction of silver ions by electrons and clustering of silver atoms near the cathode surface of the slide. The passed charge during the electrolysis was 1.1 C. After the electrolysis, we immersed the slide in the etchant (5 g NH_4F :40 g H_2O :5 μ l HF) for 10 min to remove the surface glass layer and ensure the access of pesticide to the dendritic structures for SERS experiments. The passed charge and the duration of the etching were chosen to provide maximum of Raman enhancement [15].

Dendritic structures were characterized using the atomic-force microscope (AFM, Veeco Dimension 3100, Bruker). The images were analyzed using Gwyddion software [16].

Dendritic structures were tested as a SERS-active substrate for pesticide thiram detection. SERS measurements were performed using the confocal Raman microscope (LabRAM HR800, Horiba, Japan) with 100x objective and 784.19 nm excitation laser. Laser wavelength was chosen to avoid photoluminescence of thiram. We deposited 2 μ l droplets of $1 \cdot 10^{-4}$ M aqueous solution of thiram on the surface of the pristine glass slide and the slide with formed dendritic structures, and let droplets dry in air at room temperature. Note, the drying of the droplet on the surface of the pristine glass resulted in the crystallization of thiram. To measure the size of the formed crystals we used the optical profilometer (NewView 6000, Zygo, Middlefield, CT, USA). We also

tested lower concentrations of thiram in SERS. The $1 \cdot 10^{-4}$ M solution of thiram was subsequently diluted with water to reach $1 \cdot 10^{-6}$ and $1 \cdot 10^{-8}$ M concentrations, 2 μl droplets of these solutions were deposited and dried on the surface of the dendrites. SERS (from thiram on dendrites) and Raman (on glass) spectra were collected for 2 and 20 s, respectively, in the spectral range of $230\text{--}1560\text{ cm}^{-1}$. The laser power was the same for SERS and Raman measurements. The SERS spectra were measured in 100 points over the area of $5 \times 5\ \mu\text{m}^2$.

Results and Discussion

In figure 1 we present optical and 3D AFM images of the formed dendrite structures. One can see, the surface consists of microstructures with lateral size of several micrometers and nanostructures with size of about $100\text{--}250\text{ nm}$. The average height of the nanostructures is $\sim 1\ \mu\text{m}$, while the microstructures' height is $\sim 10\ \mu\text{m}$.

Raman spectra of thiram acquired from the virgin glass slide and the slide with dendritic structures in frequency regions $500\text{--}900\text{ cm}^{-1}$ and $1000\text{--}1560\text{ cm}^{-1}$ are demonstrated in figures 2, *a* and *b*, respectively. One can see, the band at 1386 cm^{-1} , which is assigned to CH_3 symmetric bending, is the most intense one in the SERS spectra measured using the dendritic structures, whereas for the spectra measured from the glass slide the band around 560 cm^{-1} is the most intense one [17].

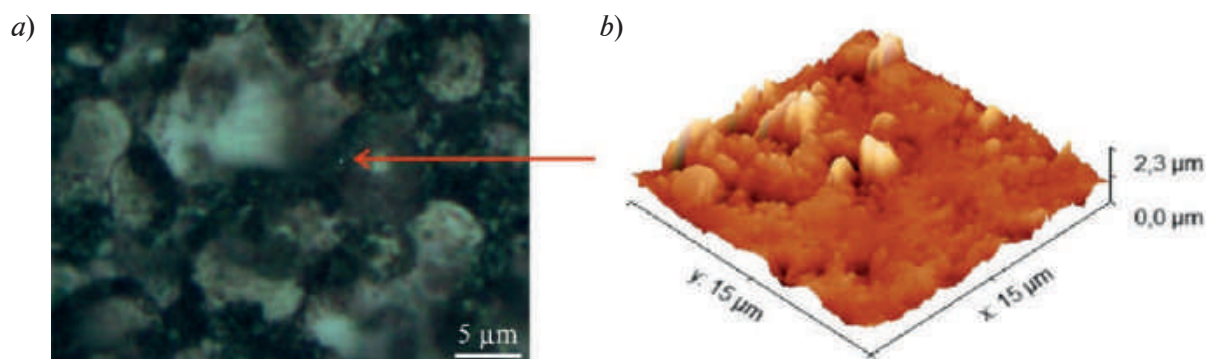


Fig. 1. Optical (*a*) and AFM (*b*) images of the dendritic structures on the glass surface

The decrease in S-S bond (560 cm^{-1}) intensity is due to thiram interaction with the metallic surface of dendrites following the bond cleavage of thiram [18]. Therefore, a relative standard deviation (RSD) of the SERS signal and enhancement factor were evaluated using 1386 cm^{-1} band.

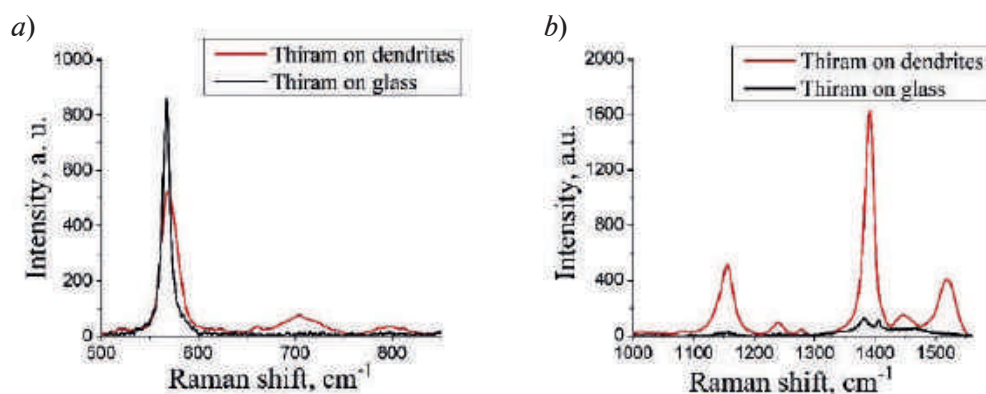


Fig. 2. Raman and SERS spectra of thiram acquired from the virgin glass slide and from the slide with dendrites in different spectral range (*a*, *b*)

To study the influence of the dendrites' morphology on the enhancement of Raman signal we measured the SERS spectra in the areas containing nanostructures and microstructures covered with thiram (area of dried droplet of $1 \cdot 10^{-4}$ M aqueous solution). The results are presented in figure 3. The signal collected in the area of the microstructure (point 1) has low intensity, while the nanostructures (point 2) demonstrate a high-intense SERS signal. The signals differ tenfold.

We attribute the observed difference in the signals to the non-uniform distribution of thiram molecules. Supposedly, the most of the thiram molecules are located between the microstructures (on the nanostructures).

To calculate the surface concentration of thiram molecules on the nanostructures we evaluated the area between microstructures using the optical image of the $1 \cdot 10^{-4}$ M droplet dried on the dendrites' surface. The area of the droplet was 1.4 cm^2 , the ratio of the areas occupied by microstructures and nanostructures was 0.74, the mass of thiram contained in the droplet was $4.8 \cdot 10^{-8} \text{ g}$.

Thus, the surface concentration of thiram on the nanostructures was about $N_{\text{SERS}} \sim 4.6 \cdot 10^{10} \text{ g/mm}^2$, which corresponds to the monolayer of thiram. Note that drying of the same droplet on the surface of the pristine glass resulted in the crystallization of thiram. We measured the height of the crystals using optical profilometer ($h \sim 1.1 \mu\text{m}$) and estimated the concentration of thiram in the crystal according to $N_{\text{RS}} = \rho \cdot h = 1.6 \cdot 10^{-6} \text{ g/mm}^2$, where ρ is thiram density ($\sim 1.3 \text{ g/cm}^3$).

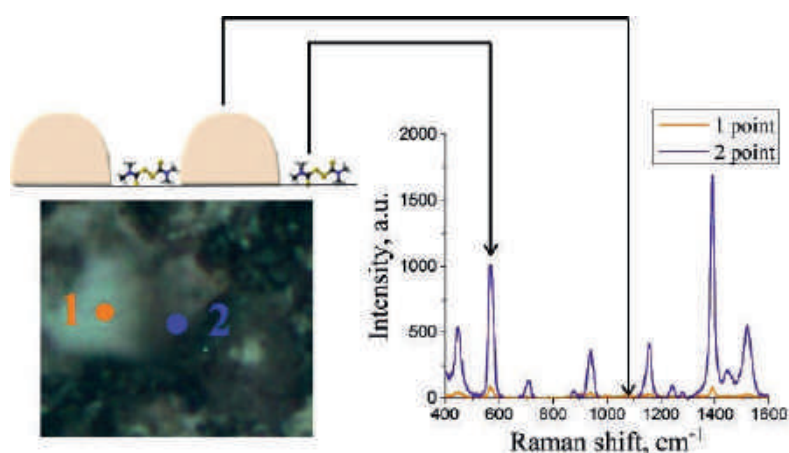


Fig. 3. Optical image of the dendritic structures and SERS spectra of thiram collected from the area of a microstructure (1 point) and nanostructures (point 2)

We calculated Raman enhancement factor (EF) provided by the nanostructures using the calculated concentrations:

$$EF = \frac{I_{\text{SERS}}}{I_{\text{RS}}} \cdot \frac{N_{\text{RS}}}{N_{\text{SERS}}} \cdot \frac{t_{\text{RS}}}{t_{\text{SERS}}}, \quad (1)$$

where I_{SERS} , N_{SERS} , t_{SERS} are the integral intensity of 1386 cm^{-1} peak ($1380\text{--}1400 \text{ cm}^{-1}$) averaged over ~ 100 SERS spectra, thiram surface concentration and the acquisition time in SERS measurements, respectively. I_{RS} , N_{RS} , t_{RS} are the integral intensity of the same peak averaged over ~ 10 Raman spectra, the concentration of thiram in crystals and acquisition time, respectively, for Raman measurements. The ratio of integral intensities was $I_{\text{SERS}}/I_{\text{RS}} \sim 13$, the ratio of the acquisition times was $t_{\text{RS}}/t_{\text{SERS}} = 10$ and the ratio of concentrations was $N_{\text{RS}}/N_{\text{SERS}} = 3 \cdot 10^3$ in our measurements. Thus, the enhancement factor of the dendritic nanostructures is $\sim 4 \cdot 10^5$.

Note, we could not detect any signal in the case of the SERS measurements using droplets of 10^{-6} and 10^{-8} M aqueous solutions of thiram. These droplets were strongly spreading out across the sample during the drying, which resulted in extra low, less than a monolayer, surface concentration of thiram.

Finally, we obtained the spatial distribution of SERS signal across the sample with the dendrites. Figure 4 presents the distribution of integral intensity of the 1386 cm^{-1} peak and the corresponding optical image. The SERS map demonstrates non-uniform SERS signal distribution which is supposedly due to the non-uniform distribution of thiram. As we discussed above, most of the thiram molecules are located between the microstructures. Therefore, RSD of the SERS signal is 99.5%.

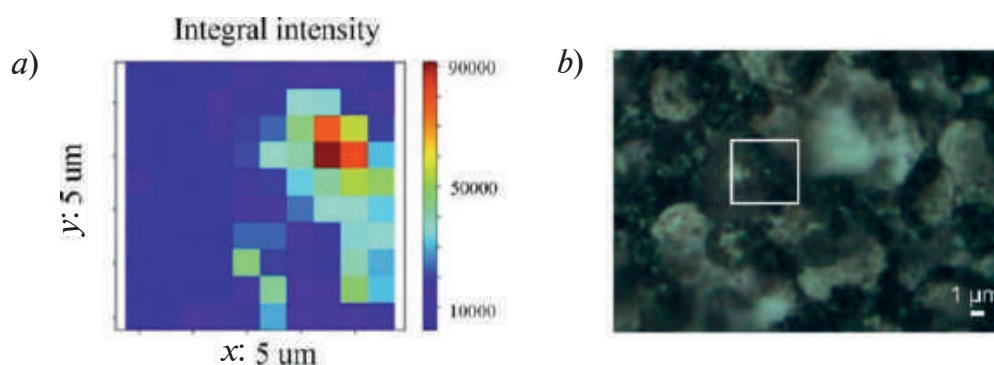


Fig. 4. Spatial distribution of integral intensity of 1386 cm^{-1} peak across the surface with dendrites (a) and corresponding optical image (b)

Conclusion

We demonstrated that SERS can be applied for the detection of low concentration of pesticide thiram using dendrite structures. Dendrites were fabricated by the electrolysis of the glass slide enriched with silver ions, and “opened” with subsequent chemical etching. The detection of thiram in surface concentration of $4.6 \cdot 10^{-10}\text{ g/mm}^2$ (a monolayer) is demonstrated. The Raman enhancement provided by the dendrites is $4 \cdot 10^5$.

Acknowledgments

The authors thank the Ministry of science and higher education of the Russian Federation for financial support (project FSRM-2023-0009).

REFERENCES

1. Wang X., Huang S. C., Hu S., Yan S., Ren B., Fundamental understanding and applications of plasmon-enhanced Raman spectroscopy, *Nature Reviews Physics*. 2 (5) (2020) 253–271.
2. Páirez-Jiménez A.I., Lyu D., Lu Z., Liu G., Ren B., Surface-enhanced Raman spectroscopy: Benefits, trade-offs and future developments, *Chemical Science*. 11 (18) (2020) 4563–4577.
3. Sharma B., Frontiera R.R., Henry A.I., Ringe E., Van Duyne R.P., SERS: Materials, applications, and the future, *Material Today*. 15 (1–2) (2012) 16–25.
4. Ju J., Liu W., Perlaki C.M., Chen K., Feng C., Liu Q., Sustained and Cost Effective Silver Substrate for Surface Enhanced Raman Spectroscopy Based Biosensing, *Science Report*. 7 (1) (2017) 1–11.
5. Wang P., Pang S., Chen J., McLandsborough L., Nugen S., Fan M., He L., Label-free mapping of single bacterial cells using surface-enhanced Raman spectroscopy, *Analyst*. 141 (4) (2016) 1356–1362.
6. Zhurikhina V.V., Brunkov P.N., Melehin V.G., Kaplas T., Svirko Y., Rutckaia V.V., Lipovskii A.A., Self-assembled silver nanoislands formed on glass surface via out-diffusion for multiple usages in SERS applications, *Nanoscale Research Letters*. 7 (1) (2012) 1–5.
7. Pham T.B., Hoang T.H.C., Pham V.H., Nguyen V.C., Vu D.C., Pham V.H., Bui H., Detection of Permethrin pesticide using silver nano-dendrites SERS on optical fibre fabricated by laser-assisted photochemical method, *Scientific Reports*. 9 (1) (2019) 1–10.
8. Pang S., Labuza T.P., He L., Development of a single aptamer-based surface enhanced Raman scattering method for rapid detection of multiple pesticides, *Analyst*. 139 (8) (2014) 1895–1901.
9. Liu K., Li Y., Iqbal M., Tang Z., Zhang H., Thiram exposure in environment: A critical review on cytotoxicity, *Chemosphere*. 295 (2022) 133928.
10. Pang S., Yang T., He L., Review of surface enhanced Raman spectroscopic (SERS) detection of synthetic chemical pesticides, *TrAC Trends in Analytical Chemistry*. 85 (2016) 73–82.
11. Liu H., Zhao P., Xiu W., Zhang L., Zhu P., Ge S., Yu J., SERS paper slip based on 3D dendritic gold nanomaterials coupling with urchin-like nanoparticles for rapid detection of thiram. *Sensors and Actuators B: Chemical*. 355 (2022) 131264.
12. Mbaye M., Diaw P. A., Mbaye O.M.A., Oturan N., Seye M.D.G., Trelu C., Coly A., Tine A., Aaron J.-J., Oturan M.A., Rapid removal of fungicide thiram in aqueous medium by electro-Fenton process with Pt and BDD anodes, *Separation and Purification Technology*. 281 (2022) 119837.

13. **Oliveira M.J.S., Martin C.S., Rubira R.J.G., Batagin-Neto A., Constantino C.J.L., Aroca R.F.**, Surface-enhanced Raman scattering of thiram: Quantitative and theoretical analyses, *Journal of Raman Spectroscopy*. 52 (12) (2021) 2557–2571.
14. **Sun Y., Zhai X., Xu Y., Liu C., Zou X., Li Z., Shi J., Huang X.**, Facile fabrication of three-dimensional gold nanodendrites decorated by silver nanoparticles as hybrid SERS-active substrate for the detection of food contaminants, *Food Control*. 122 (2021) 107772.
15. **Lubyankina E.A., Babich E.S., Lipovskii A.A., Kryzhanovskaya N.V.**, Control of the morphology of silver dendrites formed by glass electrolysis, *Journal of Physics: Conference Series*. 2227 (1) 012024.
16. **He L., Lin M., Li H., Kim N. J.**, Surface-enhanced Raman spectroscopy coupled with dendritic silver nanosubstrate for detection of restricted antibiotics, *Journal of Raman Spectroscopy*. 41 (7) (2010) 739–744.
17. **Zhu J., Chen Q., Kutsanedzie F.Y.H., Yang M., Ouyang Q., Jiang H.**, Highly sensitive and label-free determination of thiram residue using surface-enhanced Raman spectroscopy (SERS) coupled with paper-based microfluidics, *Analytical Methods*. 9 (43) (2017) 6186–6193.

THE AUTHORS

LUBYANKINA Ekaterina A.

lubjankina_e_st@spbau.ru

ORCID: 0000-0003-0210-1780

LIPOVSKII Andrey A.

lipovsky@spbau.ru

ORCID: 0000-0001-9472-9190

BABICH Ekaterina S.

babich_es@spbstu.ru

ORCID: 0000-0003-4970-2591

Received 26.10.2022. Approved after reviewing 08.11.2022. Accepted 10.11.2022.

Conference materials
UDC 621.315.592
DOI: <https://doi.org/10.18721/JPM.161.164>

2DEG-based multilayer AlGaIn/GaN heterostructures with lowered sheet resistance

D.S. Arteev ¹✉, A.V. Sakharov ¹, A.E. Nikolaev ¹, E.E. Zavarin ¹, A.F. Tsatsulnikov ²

¹Ioffe Institute, St. Petersburg, Russia;

²Submicron Heterostructures for Microelectronics, Research & Engineering Center, RAS, St. Petersburg, Russia

✉ ArteevDS@mail.ioffe.ru

Abstract. The influence of n-type doping of the AlGaIn barrier layer in AlGaIn/AlN/GaN single- and triple-channel heterostructures on their electrical properties was studied. It was found that the optimal thickness of i-AlGaIn spacer is 3 nm, and the Si concentration in n-AlGaIn is $7 \cdot 10^{18} \text{ cm}^{-3}$. The lowest predicted sheet resistance at room temperature for the triple-channel structure of the optimal design is $\sim 90 \text{ } \Omega \text{ sq}^{-1}$, three times lower than that of the single-channel structure.

Keywords: GaN, AlGaIn, HEMT, 2DEG, multichannel

Citation: Arteev D.S., Sakharov A.V., Nikolaev A.E., Zavarin E.E., Tsatsulnikov A.F., 2DEG-based multilayer AlGaIn/GaN heterostructures with lowered sheet resistance. St. Petersburg State Polytechnical University Journal. Physics and Mathematics. 16 (1.1) (2023) 380–384. DOI: <https://doi.org/10.18721/JPM.161.164>

This is an open access article under the CC BY-NC 4.0 license (<https://creativecommons.org/licenses/by-nc/4.0/>)

Материалы конференции
УДК 621.315.592
DOI: <https://doi.org/10.18721/JPM.161.164>

Многослойные AlGaIn/GaN гетероструктуры с низким слоевым сопротивлением на основе двумерного электронного газа

Д.С. Артеев ¹✉, А.В. Сахаров ¹, А.Е. Николаев ¹, Е.Е. Заварин ¹, А.Ф. Цацульников ²

¹Физико-технический институт им. А. Ф. Иоффе РАН, Санкт-Петербург, Россия;

²НТЦ микроэлектроники РАН, Санкт-Петербург, Россия

✉ ArteevDS@mail.ioffe.ru

Аннотация. В данной работе было исследовано влияние легирования барьерного слоя AlGaIn примесью n-типа в одно- и трёхканальных AlGaIn/AlN/GaN гетероструктурах на их электрические свойства. Установлено, что оптимальная толщина i-AlGaIn спейсера составляет 3 нм, а оптимальная концентрация Si примеси в n-AlGaIn составляет $7 \cdot 10^{18} \text{ см}^{-3}$. Наименьшее рассчитанное слоевое сопротивление трёхканальной структуры при комнатной температуре $\sim 90 \text{ Ом/квadrat}$, что в три раза меньше, чем у одноканальной структуры.

Ключевые слова: GaN, AlGaIn, транзистор с высокой подвижностью электронов, двумерный электронный газ, многоканальный

Для цитирования: Артеев Д.С., Сахаров А.В., Николаев А.Е., Заварин Е.Е., Цацульников А.Ф. Многослойные AlGaIn/GaN гетероструктуры с низким слоевым сопротивлением на основе двумерного электронного газа // Научно-технические ведомости СПбГПУ. Физико-математические науки. 2023. Т. 16. № 1.1. С. 380–384. DOI: <https://doi.org/10.18721/JPM.161.164>

Статья открытого доступа, распространяемая по лицензии CC BY-NC 4.0 (<https://creativecommons.org/licenses/by-nc/4.0/>)

Introduction

AlGa_N/Ga_N-based heterostructures allow the fabrication of devices, i.e., high-electron mobility transistors and Schottky barrier diodes with high current (> 1 A/mm [1, 2]) and power (> 40 W/mm [1]) due to the unique properties of the III-N material system. The typical values of the two-dimensional electron gas (2DEG) concentration in such structure are $N_s = 1.0\text{--}1.3 \cdot 10^{13} \text{ cm}^{-2}$ with electron mobility $\mu \sim 2000 \text{ cm}^2 \text{ V}^{-1} \text{ s}^{-1}$. A further increase of the concentration by increasing the Al mole fraction in the barrier layer is hindered by the strain relaxation [3]. Moreover, the 2DEG mobility is usually strongly decreases when the 2DEG density increases [4], so the conductivity remains unchanged or even becomes lower. The use of the structures with multichannel design with multiple 2DEGs could be an alternative approach to achieve higher conductivity [5, 6]. For more details on progress, benefits and drawbacks of Ga_N multi-channel power devices, the reader is referred to the recent review article [6]. Such design enables increasing the total electron concentration without degrading the mobility. However, strong internal polarization electric fields lead to a significant modification of the conduction band energy profile, so some channels of unintentionally doped structures could be completely depleted, and the total conductivity turns out to be significantly lower than expected. On the other hand, introducing too much dopants to the barrier layers may result in the forming of parasitic conduction channels. Therefore, design optimization is required.

In this paper, we investigated the influence of the design of single- and triple-channel AlGa_N/Al_N/Ga_N heterostructures on their electrical properties.

Model description and experimental details

A single channel heterostructure consisted of 23 nm Al_{0.23}Ga_{0.77}N barrier layer, 1 nm Al_N interlayer and 50 nm Ga_N channel and thick Ga_N buffer layer. In a triple channel structure, first three layers (i.e., AlGa_N, Al_N and Ga_N channel) were repeated three times. Python programming language was used to solve 1D Schrödinger-Poisson equation system [7].

Three samples were grown by metalorganic chemical vapor deposition on c-face sapphire substrates in our in-house Dragon-125 epitaxial system using trimethylgallium, trimethylaluminum, ammonia precursor gases; monosilane was used as a source of Si atoms for n-type doping. The electrical parameters of the structures were measured at several points using contactless eddy current and the van der Pauw methods.

Results and Discussion

It is known that ionized donors can scatter electrons, resulting in a lower mobility. Modulation doping technique could be used to reduce the impurity scattering. A simple expression for the scattering rate of a perfect 2DEG associated with spatially separated donors could be derived [8]:

$$\frac{1}{\tau} = N_{imp} \frac{m}{2\pi\hbar^3 k_F} \left(\frac{e^2}{2\epsilon_s \epsilon_0} \right)^2 \int_0^{2k_F} \frac{e^{-2qd_0} - e^{-2q(d_0+d_{Si})}}{2(q+q_{TF})^2} \frac{q dq}{\sqrt{1 - \left(\frac{q}{2k_F} \right)^2}}, \quad (1)$$

where N_{imp} is a 3D concentration of donors, d_0 is the thickness of i-AlGa_N spacer and d_{Si} is the thickness of the n-doped AlGa_N layer. Other symbols are used in their conventional meaning in the context of carrier scattering, i.e. q is the wavevector, k_F is the Fermi wavevector, q_{TF} is the Thomas-Fermi screening wavevector for 2DEG, m and ϵ_s are electron effective mass and relative static dielectric constant, respectively. The dependencies of the 2DEG mobility limited by ionized donor scattering and the 2DEG density versus Si concentration in the n-AlGa_N for the structures with different thickness of i-AlGa_N spacer are shown in figure 1. As one can see, the mobility associated with modulation doping could be as low as $\sim 2 \cdot 10^4 \text{ cm}^2 \text{ V}^{-1} \text{ s}^{-1}$ for entirely doped AlGa_N barrier. We chose 3 nm of unintentionally doped i-AlGa_N spacer to ensure almost negligible impurity scattering not only at room temperature but at low temperatures as well. The 2DEG density monotonically increases with increased doping concentration. One should note that very

high Si concentrations $> 7 \cdot 10^{18} \text{ cm}^{-3}$ result in a parasitic conduction channel in the AlGaN barrier. For moderate Si concentrations, the 2DEG density depends weakly on the thickness of the i-AlGaN spacer.

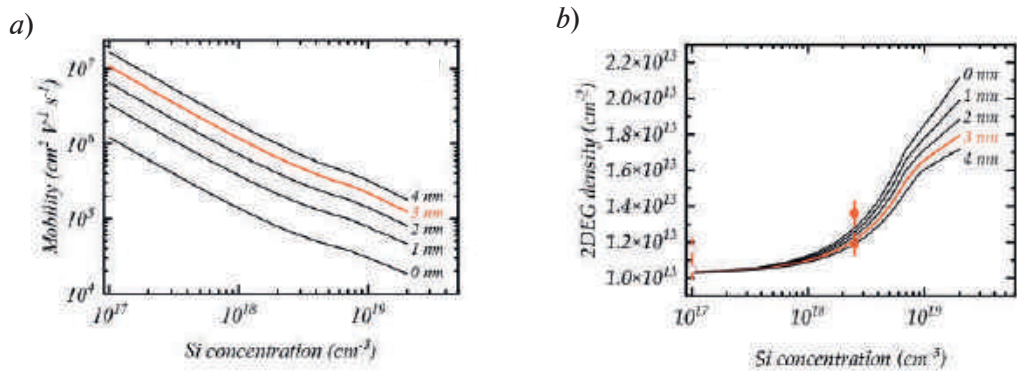


Fig. 1. The 2DEG mobility limited by remote ionized impurity scattering (a) and the 2DEG density (b) versus Si concentration in the n-AlGaN barrier in a single channel structure with different thickness of i-AlGaN spacer. Symbols are experimentally measured 2DEG density

Next, we simulated triple channel structures with the thickness of undoped i-AlGaN spacer of 3 nm. The dependence of the 2DEG density in each channel on the Si concentration is shown in Fig. 2, a. Interestingly, that the middle channel is almost depleted for moderate doping concentrations, and the total 2DEG density is almost the same as for single-channel structures. The finding is consistent with the results of [5]. For the high Si concentration, the 2DEG densities in all channels become the same, but, similarly to the single channel structures, an undesirable conduction channel appears in the AlGaN barrier layer. The calculated band diagrams for the cases of unintentionally doped (10^{17} cm^{-3}) and heavily doped (10^{19} cm^{-3}) barrier are shown in Fig. 2, b. Therefore, the optimal Si concentration in the AlGaN barrier layer is $\sim 7\text{--}8 \cdot 10^{18} \text{ cm}^{-3}$.

It is also interesting to predict the sheet resistance R_s . In order to avoid computationally intensive calculations of the 2DEG mobility including all the relevant carrier scattering mechanisms (which, however, cannot *a priori* reproduce experimentally observed strong decrease of the

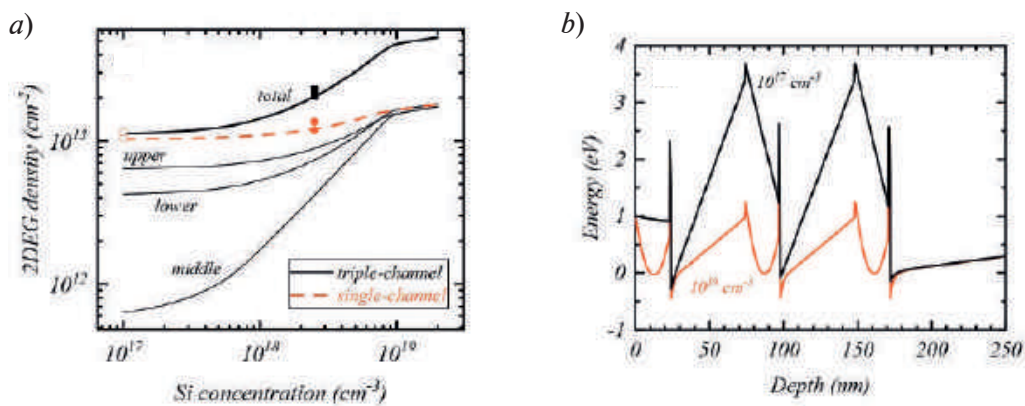


Fig. 2. The 2DEG density in upper, middle and lower channels versus Si concentration in n-AlGaN barrier layer (a) and conduction band energy (b). Dashed line is the 2DEG density in the single-channel structure. Symbols are the experimentally measured 2DEG density in unintentionally doped (open circles) and Si-doped (solid circles) single-channel and Si-doped triple-channel (squares) structures

mobility with increased 2DEG density; see [4]), we took the mobility values of the best single-channel samples grown for our previous study [9] (the inset of figure 3), fitted the data and used the obtained dependence $\mu(N_s)$ to estimate the sheet resistance of the single and triple channel structures. As one can see in figure 3, R_s for the single channel structure is almost independent on doping concentration due to reduced mobility for high 2DEG densities and $260\text{--}280 \text{ } \Omega \text{ sq}^{-1}$.

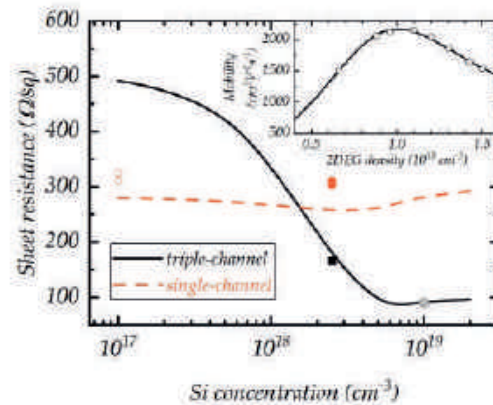


Fig. 3. The estimated sheet resistance versus Si concentration in n-AlGaIn barrier layer. Symbols are experimentally measured data in unintentionally doped (open circles) and Si-doped (solid circles) single-channel and Si-doped triple-channel (squares) structures; gray hexagon is the value from [10].

The inset shows the mobility model used in the calculations (see text for more details).

A reasonable agreement with the experimental values is observed. For the triple channel one, the lowest predicted R_s is $< 90 \Omega \text{ sq}^{-1}$ for Si concentration of $7 \cdot 10^{18} \text{ cm}^{-3}$. The measured R_s of our triple-channel structure is $\sim 160 \Omega \text{ sq}^{-1}$ due to lower Si concentration $\sim 2.5 \cdot 10^{18} \text{ cm}^{-3}$ in the barrier layers. However, R_s of triple-channel structure with similar design from [10] is $\sim 80 \Omega \text{ sq}^{-1}$ (gray hexagon in figure 3), which is in a very good agreement with our predictions. Therefore, a simple empirical mobility fit could be effectively used to optimize the design (including automated optimization using, for example, genetic algorithm) and predict R_s of different multichannel structures at low computational cost.

Conclusion

The influence of the design of the AlGaIn barrier layer on the electrical properties of single- and triple-channel AlGaIn/GaN-based heterostructures was investigated. It was found that the optimal thickness of i-AlGaIn spacer is 3 nm, and the Si concentration in n-AlGaIn is $7 \cdot 10^{18} \text{ cm}^{-3}$. The lowest predicted sheet resistance at room temperature for the triple-channel structure of the optimal design is $\sim 90 \Omega \text{ sq}^{-1}$, three times lower than that of the single-channel structure.

REFERENCES

1. Mishra U. K., Likun S., Kazior T. E., Wu Y.-F., GaN-based RF power devices and amplifiers, Proc. IEEE 96 (2) (2008) 287–305.
2. Ma J., Santoruvo G., Tandon P., Matioli E., Enhanced electrical performance and heat dissipation in AlGaIn/GaN Schottky barrier diodes using hybrid tri-anode structure, IEEE Trans. Electron Devices 69 (9) (2016) 3614–3619.
3. Ambacher O., Foutz B., Smart J., Shealy J.R., Weimann N.G., Chu K., Murphy M., Sierakowski A.J., Schaff W.J., Eastman L.F., Dimitrov R., Mitchell A., Stutzmann M. Two dimensional electron gases induced by spontaneous and piezoelectric polarization in undoped and doped AlGaIn/GaN Heterostructures, J. Appl. Phys. 87 (1) (2000) 334–44.
4. Farvacque J.-L., Bougrioua Z., Carosella F., Moerman I., Free carrier mobility in AlGaIn/GaN Quantum Wells, J. Phys.: Condens. Matter 14 (48) (2002) 13319–28.
5. Li A., Wang C., Xu S., Zheng X., He Y., Ma X., Lu X., Zhang J., Liu K., Zhao Y., Hao Y., Lattice-matched AlInN/GaN multi-channel heterostructure and hemts with low on-resistance, Appl. Phys. Lett. 119 (12) (2021) 122104.

¹ Actually, the structure is four-channel: it has three main upper channels which contribute the most of the 2DEG and one lower channel with much thinner barrier with lower doping concentration, so the authors referred it as having three channels; see figures 1 and 2, c and the note in figure 2, c in the original paper [10].

6. Nela L., Xiao M., Zhang Y., Matioli E., A perspective on multi-channel technology for the next-generation of GaN Power Devices, Appl. Phys. Lett. 120 (19) (2022) 190501.

7. Arteev D.S., Sakharov A.V., Lundin W.V., Zavarin E.E., Tsatsulnikov A.F., Influence of AlN/GaN interfacial non-idealities on the properties of two-dimensional electron gas in AlGa_N/AlN/GaN Heterostructures, J. Phys.: Conf. Ser. 2103 (2021) 012202.

8. Davies J.H., The physics of low-dimensional semiconductors: An introduction, Cambridge University Press, Cambridge, 1998.

9. Arteev D.S., Sakharov A.V., Lundin W.V., Zakheim D.A., Zavarin E.E., Tsatsulnikov A.F., Carrier mobility in the channel of AlGa_N/(AlN)/Ga_N and InAlN/(AlN)/Ga_N heterostructures, limited by different scattering mechanisms: Experiment and calculation, J. Phys.: Conf. Ser. 1400 (7) (2019) 077009.

10. Ma J., Erine C., Zhu M., Luca N., Xiang P., Cheng K, Matioli E., 1200 V multi-channel power devices with 2.8 Ω·mm on-resistance 2019 IEEE International Electron Devices Meeting (IEDM) (2019) 4.1.1–4.1.4.

THE AUTHORS

ARTEEV Dmitri S.

ArteevDS@mail.ioffe.ru

ORCID: 0000-0003-4447-8789

SAKHAROV Alexei V.

Val@beam.ioffe.ru

NIKOLAEV Andrey E.

Aen@mail.ioffe.ru

ZAVARIN Evgenii E.

EZavarin@mail.ioffe.ru

ORCID: 0000-0001-8380-3172

TSATSULNIKOV Andrei F.

Andrew@beam.ioffe.ru

ORCID: 0000-0002-5078-8946

Received 31.10.2022. Approved after reviewing 08.11.2022. Accepted 09.11.2022.

Conference materials

UDC 538.975

DOI: <https://doi.org/10.18721/JPM.161.165>

Study of ion transport in single solid state nanopores formed by optical and ion lithography

N.V. Vaulin ¹✉, P.K. Afonicheva ², D.V. Lebedev ^{1,2,3},
A.S. Bukatin ^{1,2}, I.S. Mukhin ^{1,4}

¹ St. Petersburg Academic University, St. Petersburg, Russia;

² Institute for Analytical Instrumentation RAS, St. Petersburg, Russia;

³ Saint Petersburg State University, St. Petersburg, Russia;

⁴ ITMO University, St. Petersburg, Russia

✉ nikitavaylin@mail.ru

Abstract. This work studies the transport properties of solid-state nanopores. Nanopores with a diameter of 35–40 nm formed in a thin “free-standing” silicon nitride membrane of 300 nm thick. An experimental setup has been developed to study the transport characteristics of single nanopores. Based on the results of electrical measurements, the pore conductivity was calculated for concentrations of KCl electrolyte in the range of 10^{-4} –1M. An increase of nanopore conductivity was observed with an increase of the electrolyte concentration above 10^{-2} M. This dependence can be explained by the electrical double layer overlapping that leads to appearance of a charged region inside the nanopore.

Keywords: nanopores, solid state nanopores, microfluidic, ion transport, optical lithography, ion lithography

Funding: The work was supported by Russian Science Foundation (Project No. 20-74-10117).

Citation: Vaulin N.V., Afonicheva P.K., Lebedev D.V., Bukatin A.S., Mukhin I.S., Study of ion transport in single solid state nanopores formed by optical and ion lithography, St. Petersburg State Polytechnical University Journal. Physics and Mathematics. 16 (1.1) (2023) 385–388. DOI: <https://doi.org/10.18721/JPM.161.165>

This is an open access article under the CC BY-NC 4.0 license (<https://creativecommons.org/licenses/by-nc/4.0/>)

Материалы конференции

УДК 538.975

DOI: <https://doi.org/10.18721/JPM.161.165>

Ионный транспорт в единичных твердотельных нанопорах, сформированных методами оптической и ионной литографии

Н.В. Ваулин ¹✉, П.К. Афоничева ², Д.В. Лебедев ^{1,2,3},
А.С. Букатин ^{1,2}, И.С. Мухин ^{1,4}

¹ Академический университет им. Ж.И. Алфёрова, Санкт-Петербург, Россия;

² Институт аналитического приборостроения РАН, Санкт-Петербург, Россия;

³ СПбГУ, Санкт-Петербург, Россия;

⁴ Университет ИТМО, Санкт-Петербург, Россия

✉ nikitavaylin@mail.ru

Аннотация. Данная работа посвящена изучению транспортных свойств твердотельных нанопор. Нанопоры диаметром 35–40 нм были сформированы в тонкой «свободностоящей» мембране из нитрида кремния толщиной 300 нм. Была разработана экспериментальная установка для изучения транспортных характеристик одиночных нанопор.

На основании результатов электрических измерений была рассчитана проводимость нанопор для концентраций электролита KCl в диапазоне 10^{-4} –1 М. Увеличение проводимости нанопор наблюдается при увеличении концентрации электролита выше 10^{-2} М. Эта зависимость может быть объяснена перекрытием двойного электрического слоя, что приводит к появлению заряженной области внутри нанопор.

Ключевые слова: нанопоры, твердотельные нанопоры, микрофлюидика, ионный транспорт, оптическая литография, ионная литография

Финансирование: Работа выполнена при поддержке Российского Научного Фонда (Грант РФФ № 20-74-10117).

Ссылка при цитировании: Ваулин Н.В., Афоничева П.К., Лебедев Д.В., Букатин А.С., Мухин И.С. Ионный транспорт в единичных твердотельных нанопорах, сформированных методами оптической и ионной литографии // Научно-технические ведомости СПбГПУ. Физико-математические науки. 2023. Т. 16. № 1.1. С. 385–388. DOI: <https://doi.org/10.18721/JPM.161.165>

Статья открытого доступа, распространяемая по лицензии CC BY-NC 4.0 (<https://creativecommons.org/licenses/by-nc/4.0/>)

Introduction

Nowadays, the development of microfluidic technologies makes it possible to manipulate small volumes (μl , nL, pL, fL) of liquids. The use of nanostructures in microfluidics, such as nanosized channels and pores, opens up opportunities for selective transport and separation of substances [1], energy conversion [2], and detection of particles in solutions [3]. The last one is especially useful for biology and medicine, because it allows studying small concentrations of biological molecules, proteins and DNA. Thus, microfluidic technologies are promising for such devices as lab-on-a-chip, molecular sensors [4] and DNA sequencers [5].

The principle of detection and analysis of small concentrations of dissolved substances (typically biological molecules) is to pass them through nanopores. When a molecule passes through the nanopore, a change in current can be observed. Therefore, the measurement of the current change allows one to detect and analyze the molecules dissolved in the solution. For better detection, the inner diameter of the nanopore should be as small as possible. There are two main types of nanopores: biological and solid-state. Biological nanopores are composed of transmembrane proteins embedded in lipid membranes. Their main advantages are small pore diameter (2nm for α -hemolysin [6] and 1,2nm for MspA [7]), size reproducibility, and low translocation velocity. Their disadvantages include sensitivity to pH, physical influences, temperature, and electrolyte concentration. Solid-state nanopores are thin membranes, such as a monolayer of graphene [8] or a thin film of SiNx [9], in which pores of the required diameter are created using lithography methods. Such nanopores are distinguished by the ease of fabrication, resistance to external conditions and longevity. Solid-state nanopores also have great potential for surface modification [10], which is promising for the study of selective transport.

Since the walls of nanopores are electrically charged, as the molecules under study are, characteristics such as pore conductivity, surface charge, and wall geometry affect the transport through the nanopore. Accordingly, the purpose of this work is to study ion transport of solid-state nanopores.

Experiment

For this work, we employed SiNx as the nanopore material because the formation of pores in thin semiconductor films is a well-established process [11]. First, a Si substrate with a thin 300 nm layer of SiN was formed. Then, using optical lithography, the Si substrate was partially etched, leaving a “free-standing” SiNx membrane with dimensions of $80 \times 80 \mu\text{m}$. After that, pores with a diameter of 35–40 nm were created in the SiNx membrane by ion beam milling (see scanning electron microscopy (SEM) image in Fig. 1).

The experimental setup (Fig. 2) for studying the transport characteristics consists of 2 tanks with KCl electrolyte, connected by a membrane with a nanopore using elastic gaskets. The tanks have several openings for the inlet and outlet of electrolyte and for the installation of electrodes. AgCl wires were used as electrodes. The assembled setup with a nanopore and electrodes were placed in a Faraday cage to minimize the effect of electrical noise on measurement results. Electrical measurements were made using a Keithley 2636b SourceMeter. Before each measurements, nanopores and containers were treated in oxygen plasma to impart hydrophilic properties to the surfaces.

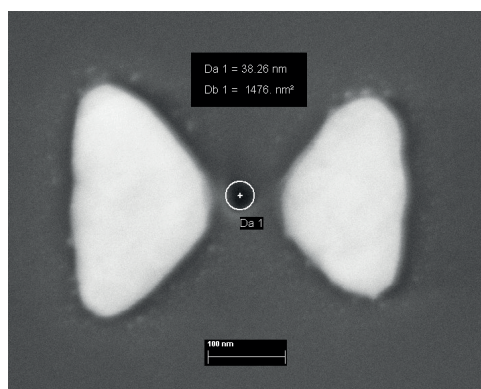


Fig. 1. SEM image of a SiN_x nanopore with diameter of 38 nm

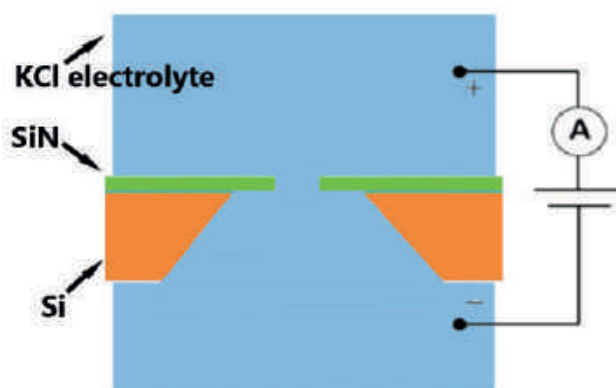


Fig. 2. Scheme of the experimental setup

Results and discussion

Nanopore transport measurements were carried out in an aqueous solution of KCl at concentrations from 10^{-4} to 1M. To determine the ionic conductivity of the pore, the current-voltage characteristics of the system were measured in the potentiostatic two-electrode mode. The applied voltage was varied from -0.3 to 0.3 V. The current was measured for 8 minutes at a given voltage. Further, according to the obtained data, the values of nanopore conductivity were obtained for the broad range of electrolyte concentrations (Fig. 3).

According to the results, in the concentrations range of 10^{-4} – 10^{-2} M, the conductivity practically does not change and remains at the level of $4.5 \cdot 10^{-11}$ S. At a concentration of 10^{-2} –1M, the conductivity increases with concentration, and at 1M, the conductivity is $1.5 \cdot 10^{-10}$ S. This behavior can be explained by the overlap of electrical double layers (EDL). EDL of opposite walls can overlap the transport channel, creating a continuous charged region in the nanopore, thereby affecting its transport properties.

Conclusion

In this work, solid-state SiN_x nanopores were fabricated. Nanopores with a diameter of 35–40 nm were formed in a “free-standing” membrane of 300 nm thick by focused ion beam milling. Then, the values of the current passing through the nanopore were measured for a KCl solution at concentrations of 10^{-4} –1M. According to the measurement results, with an increase in the concentration of KCl above 10^{-2} M, the conductivity of the nanopore increases and reaches the value of $1.5 \cdot 10^{-10}$ S at a concentration of 1M. Such dependence can be explained by the mutual the electrical double layer overlapping of opposite pore walls. Thus, the overlap of the electric double layer creates a continuous charged region in the nanopore, which affects the transport properties of the nanopore.

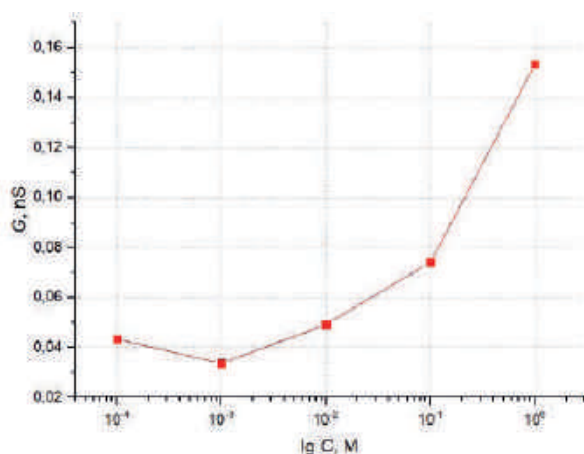


Fig. 3. Dependence of nanopore conductivity on KCl electrolyte concentration

Acknowledgments

The work was supported by Russian Science Foundation (Project No. 20-74-10117).

REFERENCES

1. Xue L., Yamazaki H., Ren R., Wanunu M., Ivanov A.P., & Edel J.B., Solid-state nanopore sensors, *Nature Reviews Materials*. 5 (12) (2020) 931–51.
2. Sparreboom W., van den Berg A., & Eijkel J.C., Principles and applications of nanofluidic transport, *Nature nanotechnology*. 4 (11) (2009) 713–20.
3. Spitzberg J.D., Zrehen A., van Kooten X.F., & Meller A., Plasmonic-nanopore biosensors for superior single-molecule detection, *Advanced Materials*. 31(23) (2019) 1900422.
4. Wei R., Gatterdam V., Wieneke R., Tampé R., & Rant U., Stochastic sensing of proteins with receptor-modified solid-state nanopores, *Nature nanotechnology*. 7 (4) (2012) 257–63.
5. Noakes M.T., Brinkerhoff H., Laszlo A.H., Derrington I.M., Langford K.W., Mount J.W., Gundlach J.H., Increasing the accuracy of nanopore DNA sequencing using a time-varying cross membrane voltage, *Nature biotechnology*. 37 (6) (2019) 651–6.
6. Vu T., Borgesi J., Soyring J., D'Alia M., Davidson S.L., Shim J., Employing LiCl salt gradient in the wild-type α -hemolysin nanopore to slow down DNA translocation and detect methylated cytosine, *Nanoscale*. 11 (21) (2019) 10536–45.
7. Manrao E.A., Derrington I.M., Laszlo A.H., Langford K.W., Hopper M.K., Gillgren N., Gundlach J.H., Reading DNA at single-nucleotide resolution with a mutant MspA nanopore and phi29 DNA polymerase, *Nature biotechnology*. 30 (4) (2012) 349–53.
8. Rollings R.C., Kuan A.T., Golovchenko J.A., Ion selectivity of graphene nanopores, *Nature communications*. 7 (1) (2016) 1–7.
9. Verschueren D.V., Yang W., Dekker C., Lithography-based fabrication of nanopore arrays in freestanding SiN and graphene membranes, *Nanotechnology*. 29 (14) (2018) 145302.
10. Emilsson G., Sakiyama Y., Malekian B., Xiong K., Adali-Kaya Z., Lim R.Y., Dahlin A.B., Gating protein transport in solid state nanopores by single molecule recognition, *ACS central science*. 4 (8) (2018) 1007–14.
11. Kudr J., Skalickova S., Nejdil L., Moulick A., Ruttikay-Nedecky B., Adam V., Kizek R., Fabrication of solid-state nanopores and its perspectives, *Electrophoresis*. 36(19) (2015) 2367–79.

THE AUTHORS

VAULIN Nikita V.
nikitavaylin@mail.ru
ORCID: 0000-0001-6080-0729

BUKATIN Anton S.
antbuk.fiztek@gmail.com
ORCID: 0000-0002-5459-1438

AFONICHEVA Polina K.
polina.afonicheva@gmail.com
ORCID: 0000-0002-0003-8477

MUKHIN Ivan S.
imukhin@yandex.ru
ORCID: 0000-0001-9792-045X

LEBEDEV Denis V.
denis.v.lebedev@gmail.com
ORCID: 0000-0001-5389-2899

Received 26.10.2022. Approved after reviewing 06.12.2022. Accepted 07.12.2022.

Conference materials

UDC 538.975

DOI: <https://doi.org/10.18721/JPM.161.166>

Investigation of ion transport in solid-state nanopores upon optical radiation

P.K. Afonicheva ¹✉, N.V. Vaulin ^{1,2}, D.V. Lebedev ^{1,2,3},

A.S. Bukatin ^{1,2}, I.S. Mukhin ^{2,4}, A.A. Evstrapov ¹

¹ Institute for Analytical Instrumentation RAS, Saint Petersburg, Russia;

² Alferov Saint Petersburg National Research Academic University of the RAS, Saint Petersburg, Russia;

³ St. Petersburg State University, Saint Petersburg, Russia;

⁴ ITMO University, Saint Petersburg, Russia

✉ polina.afonicheva@gmail.com

Abstract. We developed a technique for the fabrication of single nanopores with gold bow-tie nanoantennas in a free-standing SiN membrane of arbitrary thickness. Single pores with a diameter of 30–50 nm and a length of 300 nm were fabricated. Studies of ion transport in solid-state nanopores upon optical radiation showed that the enhancement of an electromagnetic field by plasmon structures near nanopores leads to the increase in nanochannel conductivity.

Keywords: ion transport, nanopore, nanochannel, SiN membrane, plasmon structure, gold nanoantennas

Funding: The work was supported by the Ministry of Science and Higher Education of the Russian Federation (project 075-15-2021-1057).

Citation: Afonicheva P.K., Vaulin N.V., Lebedev D.V., Bukatin A.S., Mukhin I.S., Evstrapov A.A., Investigation of ion transport in solid-state nanopores upon optical radiation, St. Petersburg State Polytechnical University Journal. Physics and Mathematics. 16 (1.1) (2023) 389–392. DOI: <https://doi.org/10.18721/JPM.161.166>

This is an open access article under the CC BY-NC 4.0 license (<https://creativecommons.org/licenses/by-nc/4.0/>)

Материалы конференции

УДК 538.975

DOI: <https://doi.org/10.18721/JPM.161.166>

Влияние оптического излучения на ионный транспорт в твердотельных нанопорах, содержащих плазмонные структуры

П.А. Афоничева ¹✉, Н.В. Ваулин ^{1,2}, Д.В. Лебедев ^{1,2,3},

А.С. Букатин ^{1,2}, И.С. Мухин ^{2,4}, А.А. Евstrapов ¹

¹ Институт аналитического приборостроения РАН, Санкт-Петербург, Россия;

² Академический университет им. Ж.И. Алферова, Санкт-Петербург, Россия

³ СПбГУ, Санкт-Петербург, Россия;

⁴ Университет ИТМО, Санкт-Петербург, Россия

✉ polina.afonicheva@gmail.com

Аннотация. Разработана методика изготовления одиночных нанопор с золотыми наноантеннами в тонкой мембране SiN. Получены одиночные поры диаметром 30–50 нм и длиной 300 нм. Исследования переноса ионов в твердотельных нанопорах под действием оптического излучения показали, что усиление электромагнитного поля плазмонными структурами вблизи нанопор приводит к увеличению проводимости наноканалов.

Ключевые слова: ионный транспорт, нанопора, наноканал, SiN мембрана, плазмонная структура, золотые наноантенны

Финансирование: Работа выполнена при поддержке Министерства науки и высшего образования Российской Федерации (проект 075-15-2021-1057).

Ссылка при цитировании: Афоничева П.К., Ваулин Н.В., Лебедев Д.В., Букатин А.С., Мухин И.С., Евстапов А.А. Влияние оптического излучения на ионный транспорт в твердотельных нанопорах, содержащих плазмонные структуры // Научно-технические ведомости СПбГПУ. Физико-математические науки. 2023. Т. 16. № 1.1. С. 389–392. DOI: <https://doi.org/10.18721/JPM.161.166>

Статья открытого доступа, распространяемая по лицензии CC BY-NC 4.0 (<https://creativecommons.org/licenses/by-nc/4.0/>)

Introduction

Experimental and theoretical research of transport in micro- and nanochannels not only has fundamental interest, but also carries great significance for applications in various fields of science and technology. These include the separation of solution, purification of substances [1] and development of biochemical sensors [2]. Nowadays, the study of molecular and ion transport in biomimetic microfluidic systems containing nanopores and nanochannels is of increased interest [3–5].

Microfluidic devices with integrated micro- and nanoscale structures can be used to develop devices for the analysis of individual molecules, pre-concentration/separation of samples and single-molecular DNA/RNA sequencing [6]. Nanofluidics-based approach has a number of unique advantages, such as an ultra-high surface-to-volume ratio and scales comparable to a range of different surface/interfacial forces and sizes of biomolecules (DNA, RNA, proteins) [7]. This allows us to explore new transport phenomena that occur only at the nanoscale.

Earlier, our research group developed a method for the formation of microfluidic chips containing a nanopore array [8].

The aim of the current study is to investigate ion transport in solid-state nanopores upon optical radiation. The methods of electron and ion lithography make it possible to create nanopores with a given geometry and specified conductive properties. Such structures are an optimal model system for the study of ion transport.

Materials and Methods

To obtain samples the technique of nanopore formation in a suspended semiconductor membrane was used. This method can be divided into two stages. At the first stage, it is necessary to form a free-standing semiconductor membrane in a silicon substrate. For this, SiN_x layer with a thickness of ~300 nm was deposited onto the double-sided polished Si (100) plate by low-pressure chemical vapor deposition (LPCVD). The thickness of this layer determines the length of the future pores. Then, using photolithography, windows were formed in the SiN_x layer for further anisotropic etching of Si substrate. As a result, a free-standing silicon-based SiN_x membrane was obtained. The membrane had a square shape with a side of 65 microns.

To study the effect of optical radiation on the transport properties of nanopores (nanochannels), a plasmonic bow-tie nanoantenna made of gold were formed (Fig. 1, *a*). The bow-tie structure consists of two triangular platforms pointed at each other by the vertices of triangles. At the second stage, nanopores were formed in the fabricated SiN_x membrane within bow-tie antennas by focused ion beam (FIB) milling. The diameter of the synthesized pores was approximately 30 nm (see scanning electron microscopy (SEM) image in Fig. 1, *a*).

Results and Discussion

When the plasmon structure is exposed by optical radiation at a resonant wavelength, the energy of an optical beam is localized within antennas via near field component of electromagnetic field. Thus, by nanopore located between gold plasmon structures, it is possible to study the effect of

optical radiation on the ion transport. Figure 1, *b* shows two spectra: the yellow one refers to gold plasmon structure located on the membrane without pore, while blue one refers to plasmon structures with the drilled nanopore. Thus, the presence of pore does not affect the spectrum. The peak of the scattering spectra is located in the wavelength range of 500–700 nm.

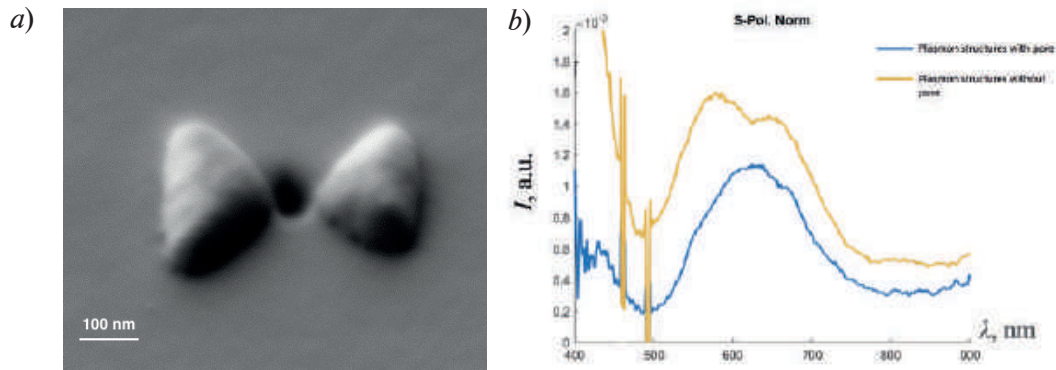


Fig. 1. SEM image of nanopore (nanochannel) modified with plasmon bow-tie nanoantenna on the surface of SiNx membrane (*a*), dark-field scattering spectra of plasmon bow-tie nanoantennas with and without nanopores on the surface of SiNx membrane (*b*)

A measuring cell with optical access (Fig. 2, *a*) was developed for the further experiments. The cell consists of two electrolyte reservoirs separated by an impermeable SiNx membrane with a single nanopore. An optical window was made at the bottom of the lower half of the cell to place on the microscope slide. Thus, laser beam can be focused in the center between the plasmon antennas using a 50x lens. A 532 nm laser with a power of 6.5 mW was used for the measurements.

To study the effect of optical radiation on the ion transport through the pore, the cell reservoirs were filled with a KCl solution with a concentration of 10 mM and the ion conductivity of the nanopore was studied by measuring the current-voltage (*I-V*) characteristics (Fig.2, *b*) without laser radiation and with the laser turned on. One can see that the laser irradiation enhances the channel conductivity. This can be explained by the enhancing of local temperature within nanopore, which provides the increase of ion transport.

Silver-chloride electrodes were used for the measuring. It is worth mentioning that the surface of the silver electrodes was refreshed by chlorinating the silver wires in 1M KCl solution before each experiment.

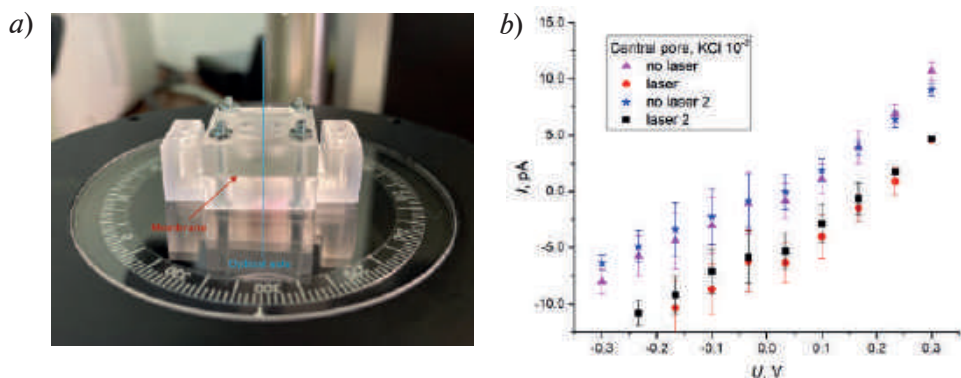


Fig. 1. SEM image of nanopore (nanochannel) modified with plasmon bow-tie nanoantenna on the surface of SiNx membrane (*a*), dark-field scattering spectra of plasmon bow-tie nanoantennas with and without nanopores on the surface of SiNx membrane (*b*)

Conclusion

The conductivity values for two measurement modes without and with laser radiation are 3 nS and 3.5 nS, respectively. We can conclude that the enhancement of an electromagnetic field by plasmon structures near nanopores leads to the increase in conductivity. It is worth mentioning that the conductivity values restore to the initial value while switching the measurement mode.

Such effect can be explained by the local heating of the solution near the pore and a temperature gradient, which, causing Brownian motion of ions, affecting the conductivity. The proposed technology makes it possible to create pores of a controlled size in a free-standing SiN membrane. The manufactured cell with optical access allows us to study ion transport upon optical radiation. However, during the experiments, we encountered difficulties in filling the cell and pores with a solution. To overcome these obstacles surface treatment for hydrophilization was carried out using oxygen plasma.

Acknowledgments

The work was supported by the Ministry of Science and Higher Education of the Russian Federation (project 075-15-2021-1057).

REFERENCES

1. **Strathmann H.**, Ion-Exchange Membrane Separation Processes, Elsevier, Amsterdam, 2004.
2. **Banica F. G.**, Chemical Sensors and Biosensors: Fundamentals and Applications, John Wiley & Sons, Chichester, UK, 2012.
3. **Hou X., Guo W., Jiang L.**, Biomimetic smart nanopores and nanochannels, Chemical Society Reviews. 40 (5) (2011) 2385.
4. **Evstrapov A.A., Mukhin I.S., Bukatin A.S., Kukhtevich I.V.**, Ion and electron beam assisted fabrication of nanostructures integrated in microfluidic chips, Nucl. Instrum. Methods Phys. Res., B. 282 (2012) 145–8.
5. **Zhu Z., Wang D., Tian Y., Jiang L.**, Ion/Molecule Transportation in Nanopores and Nanochannels: From Critical Principles to Diverse Functions, JACS. 141 (22) 2(019) 8658–69.
6. **Goto Y., Akahori R., Yanagi I., Takeda K.I.**, Solid-state nanopores towards single-molecule DNA sequencing, Journal of human genetics. 65 (1) (2020) 69–77.
7. **He Y., Tsutsui M., Zhou Y., Miao X.S.**, Solid-state nanopore systems: from materials to applications, NPG Asia Materials. 13 (1) (2021) 1–26.
8. **Lebedev D., Malyshev G., Ryzhkov I.**, Focused ion beam milling based formation of nanochannels in silicon-glass microfluidic chips for the study of ion transport. Microfluidics and Nanofluidics. 25 (6) (2021) 1–10.

THE AUTHORS

AFONICHEVA Polina K.
 polina.afonicheva@gmail.com
 ORCID: 0000-0002-0003-8477

BUKATIN Anton S.
 antbuk.fiztek@gmail.com
 ORCID: 0000-0002-5459-1438

VAULIN Nikita V.
 nikitavaylin@mail.ru
 ORCID: 0000-0001-6080-0729

MUKHIN Ivan S.
 e-mail@e-mail.ru
 ORCID: 0000-0001-9792-045X

LEBEDEV Denis V.
 denis.v.lebedev@gmail.com
 ORCID: 0000-0001-5389-2899

EVSTRAPOV Anatoly A.
 an_evs@mail.ru
 ORCID: 0000-0003-4495-8096

Received 26.10.2022. Approved after reviewing 06.12.2022. Accepted 07.12.2022.

Conference materials

UDC 620.22

DOI: <https://doi.org/10.18721/JPM.161.167>

Compositions based on porous silicon and nickel oxide obtained by cooperative synthesis

K. Khalugarova ¹✉, V.M. Kondratev ^{2,3}, Yu.M. Spivak ¹,
Z.V. Shomakhov ⁴, V.A. Moshnikov ¹

¹ Saint Petersburg Electrotechnical University "LETI", Saint Petersburg, Russia;

² Alferov University, Saint Petersburg, Russia;

³ Moscow Institute of Physics and Technology, Dolgoprudny, Russia;

⁴ Kabardino-Balkarian State University, Nalchik, Russia

✉ kamilya_kh@mail.ru

Abstract. In this work, nanocompositions based on porous silicon and nickel oxide were obtained by cooperative synthesis with and without the addition of alcohol. The XPS method was used to study the surface of the samples, and nickel oxide particles were also studied by the SEM method. The results showed the effect of the difference in synthesis on the ratio of elements in the composition of the resulting NiO-porSi samples.

Keywords: nickel oxide, porous silicon, X-ray photoelectron spectroscopy, scanning electron microscopy, energy-dispersive X-ray spectroscopy

Funding: This research was funded by the "Development program of ETU "LETI" within the framework of the program of strategic academic leadership" Priority-2030 No 075-15-2021-1318 on 29 September 2021 and by the Ministry of Science and Higher Education of the Russian Federation (agreement 075-03-2023-106, project FSMG-2021-0005).

Citation: Khalugarova K., Kondratev V.M., Spivak Yu.M., Shomakhov Z.V., Moshnikov V.A., Compositions based on porous silicon and nickel oxide obtained by cooperative synthesis, St. Petersburg State Polytechnical University Journal. Physics and Mathematics. 16 (1.1) (2023) 393–397. DOI: <https://doi.org/10.18721/JPM.161.167>

This is an open access article under the CC BY-NC 4.0 license (<https://creativecommons.org/licenses/by-nc/4.0/>)

Материалы конференции

УДК 620.22

DOI: <https://doi.org/10.18721/JPM.161.167>

Композиции на основе пористого кремния и оксида никеля, полученные совместным синтезом

К. Халугарова ¹✉, В.М. Кондратьев ^{2,3}, Ю.М. Спивак ¹,
З.В. Шомахов ⁴, В.А. Мошников ¹

¹ Санкт-Петербургский государственный электротехнический университет «ЛЭТИ» им. В.И. Ульянова (Ленина), Санкт-Петербург, Россия;

² Академический университет им. Ж.И. Алфёрова, Санкт-Петербург, Россия;

³ Центр фотоники и 2D материалов, Московский институт физики и технологии, г. Долгoprудный, Россия;

⁴ Кабардино-Балкарский Государственный университет им. Х.М. Бербекова, г. Нальчик, Россия

✉ kamilya_kh@mail.ru

Аннотация. В этой работе наноконпозиции на основе пористого кремния и оксида никеля были получены совместным синтезом с добавлением спирта и без него. Для исследования поверхности образцов использовался метод XPS, а частицы оксида никеля

также изучались методом SEM. Результаты исследования показали влияние разницы в синтезе на соотношение элементов в составе полученных образцов NiO-porSi.

Ключевые слова: оксид никеля, пористый кремний, рентгеновская фотоэлектронная спектроскопия, сканирующая электронная микроскопия, энергодисперсионная рентгеновская спектроскопия

Финансирование: Исследование выполнено при поддержке «Программы развития СПбГЭТУ «ЛЭТИ» в рамках программы стратегического академического лидерства» Приоритет-2030 № 075-15-2021-1318 от 29 сентября 2021 г. и Министерства науки и высшего образования Российской Федерации (075-03-2023-106 от 13.01.2023).

Ссылка при цитировании: Халугарова К., Кондратьев В.М., Спивак Ю.М., Шомахов З.В., Мошников В.А. Композиции на основе пористого кремния и оксида никеля, полученные совместным синтезом // Научно-технические ведомости СПбГПУ. Физико-математические науки. 2023. Т. 16. № 1.1. С. 393–397. DOI: <https://doi.org/10.18721/JPM.161.167>

Статья открытого доступа, распространяемая по лицензии CC BY-NC 4.0 (<https://creativecommons.org/licenses/by-nc/4.0/>)

Introduction

Due to the large surface area and the presence of nanopores, porous silicon (porSi) is a promising material for applications in micro- and optoelectronics, photovoltaics, sensors, as well as for medical problems [1, 2].

Composite materials based on porous matrices with incorporated particles are of great interest for the creation of new devices with improved characteristics for sensors, catalysis, and alternative energy. Varying the technological parameters of the syntheses used to obtain such substances makes it possible to obtain a wide range of certain characteristics of the final materials.

One suitable material for the porous matrix is porous silicon. Porous silicon has a large surface area, and the method of electrochemical etching used to obtain it makes it possible to obtain porous developed structures with a pore diameter from nm to μm . Thus, it is possible to create a suitable structure for incorporating particles of different sizes to obtain new compositions.

According to studies [3, 4], nickel oxide removes changes in the properties of porous silicon, including optical ones. These NiO-porSi structures show the best sensitivity for gases in gas sensors based on such structures. Thus, the aim of the work was to study the possibility of using the method of X-ray photoelectron spectroscopy to study NiO-porSi systems obtained by joint synthesis.

One of the most common methods for obtaining porous silicon is electrochemical synthesis, varying the parameters of which makes it possible to obtain samples with the possibility of controlling the formation of various porous structures and pore sizes (from nm to microns). The possibility of creating matrices with a multiporous structure makes it possible to use porous silicon in gas sensors. Interest in the use of this material is also due to the high surface to volume ratio, ease of formation, compatibility with modern technologies for the manufacture of silicon microelectronics [5].

The main field of application of composites based on porSi matrices with metals and metal oxides is gas sensing. The use of such composites makes it possible to increase the selectivity of gas sensors and reduce the reaction and relaxation times [6–8]. They are also used, for example, to create self-cleaning coatings [9].

In this work, we study porSi-NiO samples obtained by the method of chemical co-deposition of nickel oxide [10] directly in the porous silicon substrate itself. The codeposition method is a simple and inexpensive way to obtain nanoparticles. In the course of the work, the possibility of synthesizing NiO particles inside a porous silicon matrix is studied in order to simplify their incorporation.

Materials and Methods

Porous silicon

Porous silicon was obtained by electrochemical etching of single-crystal silicon with (111) orientation and n-type electrical conductivity [11–13]. Hydrofluoric acid diluted with water was used

as the electrolyte. The resulting porous matrices were washed in alcohol to purify electrolyte residues.

NiO-porSi composition

To obtain NiO-porSi compositions, the synthesis method of NiO by chemical deposition in the presence of a porous substrate was used. For the synthesis, solutions of nickel chloride hexahydrate ($\text{NiCl}_2 \cdot 6\text{H}_2\text{O}$) and sodium hydroxide (NaOH) were used [10].

The porous silicon substrate was preliminarily soaked in a NiCl solution for two days. Sodium hydroxide solution was added dropwise to the solution with the substrate and mixed with a magnetic stirrer. Next, the substrate was air-dried for two days at room temperature and then annealed in a muffle furnace for 3 hours at 500 °C.

Thus, several NiO-porSi samples were obtained: with the addition of a small amount of alcohol in the synthesis (sample 1) and with the use of water (sample 2).

The morphology of porous silicon used in this work was investigated in previous work [12].

The NiO-porSi samples obtained in this work were studied by X-ray photoelectron spectroscopy (XPS). The XPS method is widely used for chemical analysis of the surface of samples. It is used to detect contamination and analyze the presence of certain substances on the surface, as well as to control processes occurring from the volume to the surface and vice versa. The essence of the method is to measure the energy of photoelectrons knocked out from different energy levels of atoms when a substance is irradiated with X-rays [14]. In the work, the XPS study was carried out using the K-Alpha equipment.

Nickel oxide powders, also obtained during the synthesis of NiO-porSi compositions, were also additionally studied by electron microscopy (SEM) and energy dispersive X-ray spectroscopy (X-ray diffraction microanalysis) (EDX) using a Zeiss Supra25 scanning electron microscope (Carl Zeiss, Germany).

Results and Discussion

Fig. 1 and 2 show the overview XPS spectra for two samples.

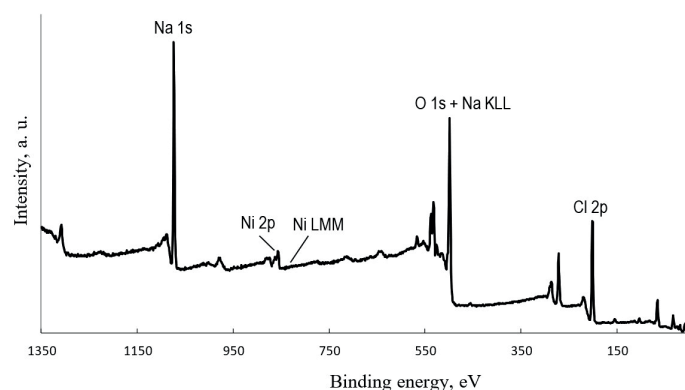


Fig. 1. Overview XPS spectrum for the sample 1 (NiO-porSi composition with the addition of alcohol during synthesis)

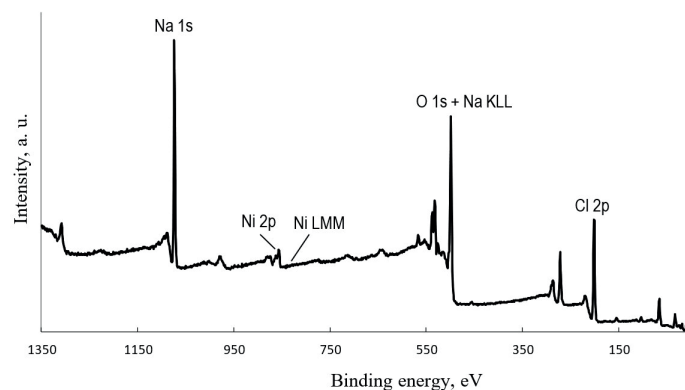


Fig. 2. Overview XPS spectrum for the sample 2 (NiO-porSi composition with the addition of water during synthesis)

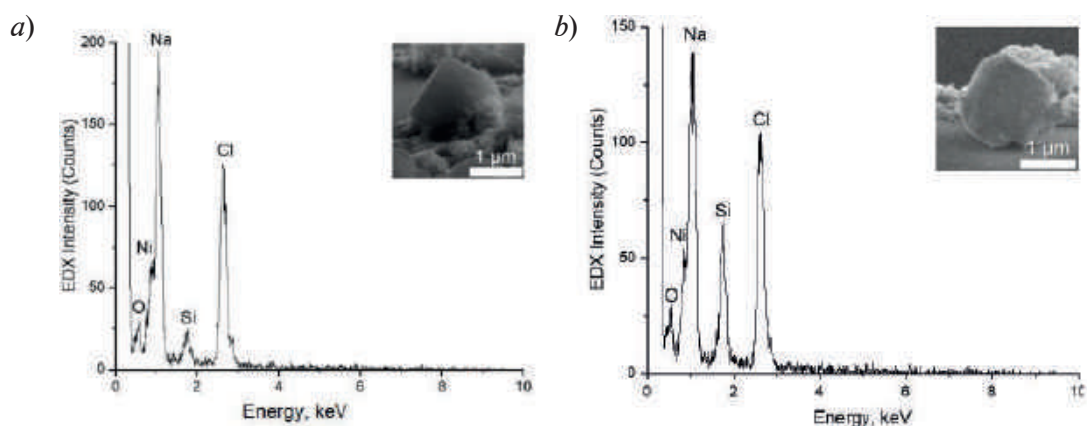


Fig 3. EDX and SEM spectra of obtained nickel oxide powders: sample 1 (a); sample 2 (b)

The results of the study of nickel oxide powders are shown in Fig. 3.

It can be seen from the survey spectra that the surface contains the formed nickel Ni 2p (856 eV) and Ni LMM (843 eV, Fig. 1). From the spectrum in Fig. 1 it can be seen that there are residues of reaction components Cl 2p (202 eV), Na 1s (1074 eV), O 1s (533 eV) on the surface of the sample with an overlapping Na KLL region. The O 1s peak with an energy of 533 eV in both spectra indicates the presence of metal hydroxide on the surface [15], which indicates that the reaction of nickel oxide formation by heating at high temperatures of nickel hydroxide obtained during synthesis was partially incompletely completed. The presence of sodium and chlorine also indicate the presence of NaCl reaction products, which can be removed by thoroughly washing the samples before annealing. Since carbon-containing substances did not participate in the synthesis reaction, it can be assumed that the C 1s peak (284 eV) in Fig. 2 is associated with carbon contamination, as most samples exposed to the atmosphere will have a detectable amount of incidental carbon contamination.

Analysis of SEM images made it possible to estimate the size of the synthesized powder particles: from 200 nm to 2 μm, typical SEM images of powder particles with a size of about 2 μm are shown in Fig. 3. An analysis of the EDX spectra showed the presence of Ni and O peaks associated with the synthesized nickel oxide; in addition, there are also Na and Cl peaks, the procurators of synthesis, as well as a Si peak (the powder was transferred to an auxiliary silicon substrate). The EDX data fully correlate with the results of the study of porSi-NiO samples by the XPS method (XPS), however, allow us to estimate the mass concentrations of nickel and oxygen for the synthesized samples as 17.4 and 22.8% (mass) for (a), as well as 19.1 and 15.8% for (b), respectively.

Conclusion

According to the obtained research results, it can be concluded that the addition of a small amount of alcohol affects the ratio of elements in the composition of the obtained NiO-porSi samples. The presence of Na and Cl elements can be explained by the residual precursors and reaction products, which can be reduced by washing the samples.

REFERENCES

1. Spivak Y.M., Belorus A.O., Somov P.A., Tulenin S.S., Beshpalova K.A., Moshnikov V.A., Porous silicon nanoparticles for target drug delivery: structure and morphology, Journal of Physics: Conference Series, IOP Publishing. 643 (1) (2015) 012022.
2. Spivak Y.M., Bukina Ya.V., Khabibulina V.R., Chistyakova L.V., Somov P.A., Isachenko A.D., Moshnikov V.A., Issledovanie vliyaniya parametrov nanochastich por-Si na ih toksichnost in vitro, In: Sovremennye sinteticheskie metodologii dlya sozdaniya lekarstvennykh preparatov i funktsionalnykh materialov (MOSM2019), Yekaterinburg, Russia, 13-16 November 2019. (2019) 219 (in Russian).
3. M'hammedi K., Haine N., Bourenane N., Gabouze N., Macroporous Silicon (MPS) with Embedded NiO Thin Film for CO₂ Gas Sensing, Arabian Journal for Science and Engineering. 44 (1) (2019) 521–529.

4. **Salih E.Y., Bashir M.B.A., Rajpar A.H., Badruddin I.A., Bahmanrokh G.**, Rapid fabrication of NiO/porous Si film for ultra-violet photodetector: The effect of laser energy, *Microelectronic Engineering*. 258 (2022) 111758.
5. **Aroutiounian V.M.**, Porous silicon gas sensors, *Semiconductor gas sensors*, Woodhead Publishing. (2013) 408–430.
6. **Soboleva E., Geydt P., Zakharchuk I., Spivak Y., Moshnikov V., Lähderanta E.**, Properties of porous silicon precipitated with nickel for gas sensors, *Sensor Letters*. 16 (9) (2018) 672–676.
7. **Bobkov A., Luchinin V., Moshnikov V., Nalimova S., Spivak Y.**, Impedance Spectroscopy of Hierarchical Porous Nanomaterials Based on por-Si, por-Si Incorporated by Ni and Metal Oxides for Gas Sensors, *Sensors*. 22 (4) (2022) 1530.
8. **Moshnikov V.A., Gracheva I., Lenshin A.S., Spivak Y.M., Anchkov M.G., Kuznetsov V.V., Olchowik J.M.**, Porous silicon with embedded metal oxides for gas sensing applications, *Journal of non-crystalline solids*. 358 (3) (2012) 590–595.
9. **Jabbar A.A., Haider A.J., Haider M.J., Al-azawi K.F.**, Preparation and characterization of NiO/PSi as self-cleaning surface, *Journal of Materials Research and Technology*. 9 (6) (2020) 15123–15131.
10. **Rahal H.T., Awad R., Abdel-Gaber A.M., Bakeer D.**, Synthesis, characterization, and magnetic properties of pure and EDTA-capped NiO nanosized particles. *Journal of Nanomaterials*. 2017 (2017).
11. **Afanasev A.V., Ilin V.A., Lebedev A.O., Luchinin V.V., Tairov Yu.M.**, Karbid kremniyananorazmernii almazopodobnii shirokozonnii poluprovodnikovii material i pribori na ego osnove, *Biotehnosfera*. (in Russian) 1-2 (13-14) (2011) 11–19.
12. **Spivak Y.M., Mjakin S.V., Moshnikov V.A., Panov M.F., Belorus A.O., Bobkov A.A.**, Surface functionality features of porous silicon prepared and treated in different conditions. *Journal of Nanomaterials*, (2016) 2016.
13. **Moshnikov V.A., Spivak Yu.M.**, Elektrohimicheskie metodi polucheniya poristih materialov dlya toplivnih elementov, In *Osnovi vodorodnoi energetiki*. (in Russian) (2010) 103–140.
14. **Bagus P.S., Ilton E.S., Nelin C.J.**, The interpretation of XPS spectra: Insights into materials properties, *Surface Science Reports*. 68 (2) (2013) 273–304.
15. **Nohira H., Tsai W., Besling W., Young E., Pétry J., Conard T., Tuominen M.**, Characterization of ALCVD-Al₂O₃ and ZrO₂ layer using X-ray photoelectron spectroscopy, *Journal of non-crystalline solids*. 303 (1) (2002) 83–87.

THE AUTHORS

KHALUGAROVA Kamilya
kamilya_kh@mail.ru
ORCID: 0000-0001-9569-7821

SHOMAKHOV Zamir V.
shozamir@yandex.ru
ORCID: 0000-0001-5738-2626

KONDRATEV Valeriy M.
kvm_96@mail.ru
ORCID: 0000-0002-3469-5897

MOSHNIKOV Vyacheslav A.
vamoshnikov@mail.ru
ORCID: 0000-0001-6500-5492

SPIVAK Yuliya M.
ymkanageeva@yandex.ru
ORCID: 0000-0002-5852-999X

Received 27.10.2022. Approved after reviewing 15.11.2022. Accepted 15.11.2022.

Conference materials

UDC 538.971

DOI: <https://doi.org/10.18721/JPM.161.168>

Electron-stimulated desorption of lithium and potassium atoms in the adsorption of lithium and potassium atoms on gold

I.A. Gromov, T.E. Kuleshova, Yu.A. Kuznetsov, M.N. Lapushkin , N.S. Samsonova

Ioffe institute, St.Petersburg, Russia

 lapushkin@ms.ioffe.ru

Abstract. The electron-stimulated desorption of lithium and potassium atoms from Li_xAu_y and K_xAu_y layers on the surface of gold adsorbed on W(100) has been studied. The yield of electron-stimulated desorption of Li and K atoms was measured by a direct method as a function of the electron energy, the concentration of Li and K atoms, and the thickness of the Au film. The formation of semiconductor intermetallic compounds Li_xAu_y and K_xAu_y is considered.

Keywords: electron-stimulated desorption, intermetallic, 2D-layers

Funding: This study was funded by RFBR grant number 20-02-00370.

Citation: Gromov I.A., Kuleshova T.E., Kuznetsov Yu.A., Lapushkin M.N., Samsonova N.S., Electron-stimulated desorption of lithium and potassium atoms in the adsorption of lithium and potassium atoms on gold, St. Petersburg State Polytechnical University Journal. Physics and Mathematics. 16 (1.1) (2023) 398–403. DOI: <https://doi.org/10.18721/JPM.161.168>

This is an open access article under the CC BY-NC 4.0 license (<https://creativecommons.org/licenses/by-nc/4.0/>)

Материалы конференции

УДК 538.971

DOI: <https://doi.org/10.18721/JPM.161.168>

Электронно-стимулированная десорбция атомов лития и калия при адсорбции атомов лития и калия на золото

И.А. Громов, Т.Э. Кулешова, Ю.А. Кузнецов, М.Н. Лапушкин , Н.С. Самсонова

Физико-технический институт им. А.Ф. Иоффе РАН, Санкт-Петербург, Россия

 lapushkin@ms.ioffe.ru

Аннотация. Исследована электронно-стимулированная десорбция атомов лития и калия из слоев Li_xAu_y и K_xAu_y на поверхности золота, адсорбированного на W(100). Выход электронно-стимулированной десорбции атомов Li и K измерялся прямым методом в зависимости от энергии электронов, концентрации атомов Li и K и толщины пленки Au. Рассмотрено образование полупроводниковых интерметаллидов Li_xAu_y и K_xAu_y .

Ключевые слова: электронно-стимулированная десорбция, интерметаллид, 2D-слои

Финансирование: Работа поддержана РФФИ, грант № 20-02-00370.

Ссылка при цитировании: Громов И.А., Кулешова Т.Э., Кузнецов Ю.А., Лапушкин М.Н., Самсонова Н.С. Электронно-стимулированная десорбция атомов лития и калия при адсорбции атомов лития и калия на золото // Научно-технические ведомости СПбГПУ. Физико-математические науки. 2023. Т. 16. № 1.1. С. 398–403. DOI: <https://doi.org/10.18721/JPM.161.168>

Статья открытого доступа, распространяемая по лицензии CC BY-NC 4.0 (<https://creativecommons.org/licenses/by-nc/4.0/>)

Introduction

Compounds of two metals are called intermetallic compounds. Intermetallic compounds can and do have properties different from the metals of which they are composed. Bronze is the first intermetallic compound known to mankind. Gold-alkali metal intermetallic compounds are of particular interest, since in them gold is an anion [1], while in the vast majority of compounds gold is a cation. Studies of intermetallic compounds gold-alkali metal started in the middle of the last century [2]. Interest in gold-alkali metal compounds is associated with the rapid growth of Au chemistry [3], the use of Au nanoparticles in various fields from catalysis [4] and medicine [5] to the creation of various sensors and detectors. [6].

2D layers of gold intermetallic compounds with alkali metals (AM) Li_xAu_y , Na_xAu_y , K_xAu_y , and Cs_xAu_y are semiconductors, in contrast to bulk samples (Li_xAu_y , Na_xAu_y and K_xAu_y), which exhibit metallic properties. Only CsAu is a semiconductor regardless of its size.

The formation of the intermetallic compound gold-alkali metal at temperatures close to room temperature can be divided into two stages. At the first stage, an adsorbed alkali metal monolayer is formed on the gold surface and no intermetallic compound is formed. At the second stage, an increase in the dose of deposited alkali metal on the gold surface leads to the diffusion of alkali metal atoms into the depth of the gold substrate with the formation of a gold-alkali metal intermetallic compound. In this case, a monolayer of alkali metal will remain on the surface. The stoichiometry of the gold-alkali metal intermetallic compound depends on the number of gold and alkali metal atoms that have reacted. Note that the Au layer closest to W does not participate in the formation of an alkali metal-Au compound, and as a result, a four-layer system is obtained: an alkali metal monolayer/an AMAu intermetallic compound/a monolayer of Au atoms/W(100) [7].

Electronic-stimulated desorption (ESD) is observed only from the surface of semiconductors and dielectrics, and it is not observed from the surface of metals, since excited states rapidly relax in metals (see review, for example [8]). In semiconductors, the lifetime of excited states is sufficient for the process of ESD of atoms [8].

The purpose of this work was a detailed consideration of the processes occurring during the electron irradiation of the $\text{Li}/\text{Li}_x\text{Au}_y/\text{Au}/\text{W}$ and $\text{K}/\text{K}_x\text{Au}_y/\text{Au}/\text{W}$ system and to compare the processes of formation of intermetallic compounds Li_xAu_y and K_xAu_y , which will allow us to highlight the commonality and differences in the formation of intermetallic compounds of 2D layers of Li_xAu_y and K_xAu_y .

Materials and Methods

The studies proposed in this work were carried out in an “ESD Spectrometer” ultrahigh vacuum setup; the design of the experiment and the structure of the sample are shown in Figure 1. The pressure of the residual gas in the installation did not exceed $5 \cdot 10^{-10}$ Torr. Textured W(100) ribbon were used as a substrate for the samples, which were cleaned by heating at 1800 K in an oxygen atmosphere at a pressure of $1 \cdot 10^{-6}$ Torr for 3 hours. Gold was deposited on a tungsten ribbon at 300 K from a straight-heated tungsten tube, into which pieces of gold foil with a purity of 99.99% were placed. Lithium was deposited on a gold-coated tungsten ribbon from a Knudsen cell by thermal reduction of lithium oxide with aluminum. Potassium was also deposited onto the tape at 300 K from a Knudsen cell by thermal decomposition of potassium chromates. The potassium concentration on the surface was determined from the deposition time with a constant flux, the intensity of which was measured from the surface ionization current on the tungsten W ribbon. The Li concentration on the surface was determined from the time of deposition by a constant flux, the intensity of which was measured by the current during surface ionization on an iridium ribbon. 1 monolayer (ML) corresponds to a close-packed monolayer of Li atoms with a hexagonal structure and is equal to $1.0 \cdot 10^{15}$ atom/cm². The surface concentration in the potassium monolayer was $5.0 \cdot 10^{14}$ at/cm². The concentration of deposited gold was determined by the time of deposition and was $1.0 \cdot 10^{15}$ atm/cm² in the monolayer [11]. The measurements were carried out at $T = 300$ K at the energy of bombarding electrons in the range of 0–300 eV.

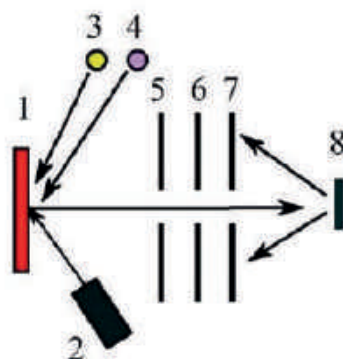


Fig. 1. Experiment scheme: 1 — sample, 2 — electron source, 3 and 4 — evaporators of Au and Li(K), 5 — ion collector, 6 — ion-retention electrode, 7 — ionic collector, 8 — surface ionization ribbon

Results and Discussion

First, two monolayers of gold were deposited on the tungsten surface. After that, Li (K) coverage was deposited to the surface of the gold film. The yield (q) of desorbing Li (K) atoms was recorded. Figure 2, a shows that ESD of Li (K) atoms are not observed when Li (K) is less than one monolayer. At a dose of deposited Li (K) atoms greater than 1 MLs, ESD of Li (K) atoms begins to be detected, which indicates the formation of intermetallic compounds of 2D Li_xAu_y (K_xAu_y) layers under the monolayer Li (K) film. Since ESD of Li (K) atoms is observed, it can be argued that Li_xAu_y (K_xAu_y) semiconductor compounds are formed. Further deposition of Li (K) atoms leads to a linear increase in the ESD yield of Li (K) atoms. The maximum value of the ESD yield of Li (K) atoms is achieved by deposition of a dose of Li (K) atoms equal to 2 MLs. A subsequent increase in the dose of deposited Li atoms leads to a sharp decrease in the ESD yield of Li atoms. However, further increase in the dose of deposited K atoms does not change the ESD yield of K atoms.

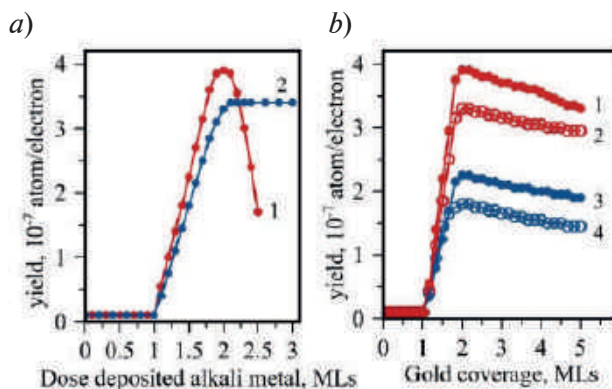


Fig. 2. Yield q of Li (K) atoms during ESD from tungsten covered with two gold monolayers at $T = 300$ K as a function of the dose of deposited Li (1) and K (2) atoms for an energy of bombarding electrons of 64 eV (a). Yield q of Li (K) atoms in ESD from gold-covered tungsten at $T = 300$ K as a function of gold deposition time for two doses of deposited Li (1,2) and K (3,4) atoms: 1,3—1.5 MLs and 2,4—2.0 MLs (b). The energy of the bombarding electrons is 64 eV

Let us consider the possible Li_xAu_y (K_xAu_y) compounds obtained and the differences in the formation of 2D layers of Li_xAu_y (K_xAu_y) upon deposition of Li (K) atoms. It can be assumed that LiAu is formed upon deposition of 2 MLs of Li atoms (corresponds to the maximum ESD yield of Li atoms) and KAu upon deposition of 3 MLs of K atoms (corresponds to the plateau of the ESD yield of K atoms). Note that the indicated stoichiometry of intermetallic compounds is an estimate and is directly related to the number of Li (K) atoms in the monolayer. The difference in the formation of 2D layers of Li_xAu_y (K_xAu_y) during deposition of Li (K) atoms is as follows: when the dose deposited of Li atoms more than 2 MLs atoms, Li atoms do not diffuse deep into the film, but Li atoms accumulate on the surface with the formation of a second monolayer on

the surface, which screens the exit of lithium atoms through the adsorbed layer of Li atoms. When the dose deposited of K atoms more than 2 MLs atoms, K atoms diffuse deep into the film and the K_xAu_y intermetallic compound continues to form.

In the next experiment, a different number of Au atoms were deposited, which was no more than 5 MLs. For each Au coverage, a fixed dose of Li (K) atoms was deposited, equal to the deposition dose of 1.5 and 2.0 MLs of Li (K) atoms. After each measurement of the ESD yield of Li (K) atoms, the deposited material on W was removed from the surface, and Au and then Li (K) were deposited again.

Figure 2, *b* shows the ESD yield of Li (K) atoms as a function of the amount of deposited Au on W for two deposition doses of Li (K) atoms: 1.5 and 2.0 MLs. As can be seen, upon deposition of less than 1 MLs of gold followed by deposition of Li (K) atoms, no ESD of Li (K) atoms is observed and no formation of Li_xAu_y (K_xAu_y) occurs. Let us consider how the ESD of Li (K) atoms changes with an increase in the thickness of the deposited gold film. Thus, in the gold coverage range from 1 to 1.8 MLs, the ESD of Li (K) atoms increases linearly, reaching its maximum value at a gold film 2 MLs thick. A further increase in the thickness of the gold film leads to a decrease in the ESD of Li (K) atoms. This indicates the formation of a 2D semiconductor layer of Li_xAu_y (K_xAu_y) between the upper monolayer of Li (K) atoms and the Au monolayer closest to the W surface.

Let us consider the possible stoichiometry of the formed Li_xAu_y (K_xAu_y) intermetallic compounds. Thus, at the maximum ESD yield of Li atoms, we can assume the formation of $LiAu_2$ at a Li deposition dose of 1.5 MLs and the formation of $LiAu$ at a Li deposition dose of 2.0 MLs. With an increase in the thickness of the deposited gold film over 2 MLs, an insignificant decrease in the ESD yield of Li atoms occurs by only 15%, which can mean either slow diffusion of lithium atoms deep into the gold layer, or a weak dependence of the probability of the ESD yield of Li atoms for Li_xAu_y , which depends on the ratio x/y with increasing y . It is possible to propose the formation of KAu by deposition of 1.5 MLs of potassium onto a gold film 1.25 MLs thick and by deposition of 2 MLs of potassium onto a gold film 1.5 MLs thick. Thus, at the maximum ESD yield of K atoms, we can assume the formation of KAu_4 at a deposition dose K of 1.5 MLs and the formation of KAu_2 at a deposition dose of K equal to 2.0 MLs. With an increase in the thickness of the deposited gold film over 2 MLs, an insignificant decrease in the ESD yield of K atoms occurs by only 15%, which can mean either slow diffusion of K atoms deep into the gold layer, or a weak dependence of the ESD yield of K atoms for K_xAu_y , which depends on the ratio x/y with increasing y .

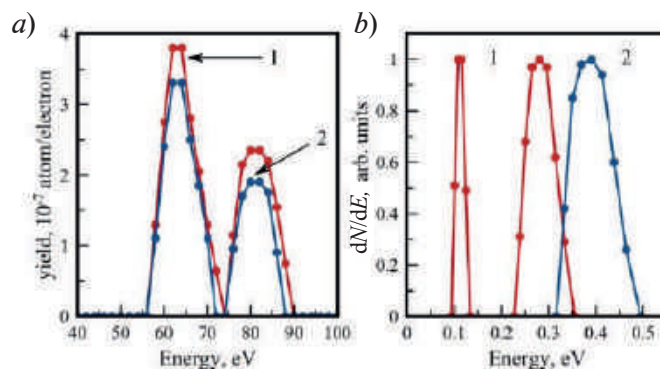


Fig. 3. Yield of Li and K atoms upon ESD from tungsten coated with two monolayers of gold and two monolayers of Li (1) and K (2) at $T = 300$ K as a function of the bombarding electron energy (*a*). Kinetic energy distribution of desorbed Li (1) and K (2) atoms during ESD from tungsten covered with two Au and two Li (K) monolayers (*b*). The energy of exciting electrons is 64 eV

Figure 3 shows the dependence of the yield of lithium (potassium) atoms q of the ESD on the energy of exciting electrons (E_e), in which two resonance peaks are observed with maxima at 63.5 and 81.4 eV, corresponding to the ionization energies of the Au levels $Au 5p_{3/2}$ and $5p_{1/2}$. The full width at half maximum of the peak is 8.8 and 9.6 eV, respectively, for the $Au 5p_{3/2}$ and $5p_{1/2}$ levels upon ESD of Li atoms. In the case of the ESD of K atoms, these values are slightly smaller:

8.6 and 8.2 eV, respectively, for the Au $5p_{3/2}$ and $5p_{1/2}$ levels. The ratio of the areas under the peaks coincides with the theoretical spin-orbit value of 0.5 for the ESD of K atoms and is much larger than the theoretical spin-orbit value of 0.70 for the ESD of Li atoms. Such a deviation may be due to the fact that the Li $1s$ level with the binding energy $E_b = 54.7$ eV is not excited by the electrons bombarding the surface and forms a channel that partially suppresses the ESD of lithium atoms. This effect is similar to the ESD of Cs atoms, when only one peak is observed in the dependence of the yield of cesium atoms $q(E_e)$ of ESD on the energy of exciting electrons at $E_b = 63.5$ eV [11]. The presence of one peak was explained by the fact that the excitation of the Au $5p_{1/2}$ level ($E_b = 74.2$ eV) is completely quenched by its resonance with the Cs $4d_{5/2}$ level ($E_b = 77.5$ eV). In the case of the ESD of lithium atoms, the Au $5p_{3/2}$ state with $E_b = 57.2$ eV partially delocalizes, and the probability of its excitation decreases, which leads to a decrease in the ESD of lithium atoms.

Figure 3, *b* shows the kinetic energy distribution (KED) of desorbing Li (K) atoms in ESD from tungsten covered with two Au monolayers and two Li (K) monolayers. It can be seen that E_{kin} has two peaks for desorbing Li atoms: a low energy peak (LE) at energy of 0.11 eV and a high energy peak (HE) at energy of 0.28 eV. The HE peak is associated with the excitation of the ESD of Li atoms from the upper monolayer of Li atoms, and the LE peak is associated with the excitation of the ESD of Li atoms from the 2D layers of Li_xAu_y intermetallide. For the ESD of K atoms, KED has only one peak for desorbing K atoms: a HE peak at energy of 0.39 eV, which is associated with the excitation of the ESD of K atoms from the upper monolayer of K atoms. Most likely, the presence of one peak is associated with the formation of an intermetallic compound with deficiency of potassium atoms – KAu_y . We assume that the LE peak in KED is observed only in intermetallic compounds Li_xAu_y when the content of alkali metal atoms is greater than or close to the content of gold atoms.

The results obtained show that the ESD process captures atoms located at the interface between the adsorbed layer of Li (K) atoms and the 2D layer of Li_xAu_y (K_xAu_y). Lithium atoms are 1.6 times smaller than potassium atoms and are the same size as Au atoms. Consequently, there are more lithium atoms on the surface in the monolayer than potassium atoms. However, this leads to the fact that to form, for example, intermetallic compounds Li_xAu_y and K_xAu_y of the same stoichiometry, it is required to deposit two times fewer monolayers of Li atoms than K atoms. It would seem that lithium and potassium atoms differ only in the size of the atoms and the size of the formed crystal cell. $LiAu$ and KAu form a more compact CsCl-type crystal cell (with cell parameter $a = 0.31$ nm for $LiAu$ and $a = 0.39$ nm for KAu). However, the ESD process of Li and K atoms is also affected by the difference in the electronic structure of Li and K atoms: the proximity of the Li $1s$ levels with $E_b = 54.7$ eV and Au $5p_{3/2}$ with $E_b = 57.2$ eV leads to partial suppression of the ESD process of Li atoms associated with excitation level Au $5p_{3/2}$.

Conclusion

It has been found that the adsorption of lithium and potassium atoms on thin gold films leads to the formation of 2D intermetallic films Li_xAu_y and K_xAu_y , which can be considered 2D semiconductor films. Intermetallic compounds are formed between the upper alkali metal monolayer and the gold monolayer closest to the W surface. As a result of the interaction of alkali metal and gold atoms, intermetallic compounds of various stoichiometries are formed, depending on the number of atoms of deposited gold and alkali metal. It is assumed the formation of $LiAu_2$ at a Li deposition dose of 1.5 MLs and the formation of $LiAu$ at a Li deposition dose of 2.0 MLs onto a gold film with a thickness of 2 MLs. It is assumed the formation of KAu_4 at a deposition dose K of 1.5 MLs and the formation of KAu_2 at a deposition dose of K equal to 2.0 MLs. onto a gold film with a thickness of 2 MLs. A resonant dependence of the yield of Li and K atoms on the energy of exciting electrons is observed, which is related to the excitation of the Au $5p_{3/2}$ and $5p_{1/2}$ core levels. A difference was found in the kinetic energy distribution of desorbed Li and K atoms: a high-energy one, which is associated with the excitation of the ESD process of Li and K atoms in the upper monolayer of Li and K, and a low-energy one, which is associated with the excitation of the ESD process of Li atoms in the Li_xAu_y intermetallic compound. The ESD process captures atoms located at the interface adsorbed layer of Li (K) atoms: 2D layer of Li_xAu_y (K_xAu_y).

Acknowledgments

This study has been funded by RFBR according to the research project No. 20-02-00370.

REFERENCES

1. **Jansen M.**, The chemistry of gold as an anion, *Chemical Society Review*. 9 (37) (2008) 1826–1835.
2. **Spicer W.E., Sommer A.H., White J.G.**, Studies of the Semiconducting Properties of the Compound CsAu, *Physical Review*. 1 (115) (1959) 57–62.
3. **Priecel P., Salami H.A., Padilla R.H., Zhong Z., Lopez-Sanchez J.A.**, Anisotropic gold nanoparticles: Preparation and applications in catalysis, *Chinese Journal of Catalysis* 10 (37) (2016) 1619–1650.
4. **Ciriminna R., Falletta E., Pina C.D., Teles J.H., Pagliaro M.**, Industrial Applications of Gold Catalysis, *Angewandte Chemie*, 46 (55) (2016) 14210–14217.
5. **Dykman L.A., Khlebtsov N.G.**, Gold Nanoparticles in Biology and Medicine: Recent Advances and Prospects, *Acta Naturae*, 2 (3) (2011) 34–55.
6. **Priyadarshini E., Pradhana N.**, Gold nanoparticles as efficient sensors in colorimetric detection of toxic metal ions: A review, *Sensors and Actuators B: Chemical*, (238) (2017) 888–902.
7. **Ageev V.N., Afanas'eva E.Yu.**, Initial stages of the interaction of sodium and cesium with gold, *Physics of the Solid State*, 12 (48) (2006) 2347–2353.
8. **Ageev V.N.**, Desorption induced by electronic transitions, *Progress in Surface Science*, 1-2 (47) (1994) 55–203.

THE AUTHORS

GROMOV Ivan A.

gromov-24-2@yandex.ru

ORCID: 0000-0001-9269-2259

LAPUSHKIN Mikhail N.

lapushkin@ms.ioffe.ru

ORCID: 0000-0002-9042-7889

KULESHOVA Tatiana E.

www.piter.ru@bk.ru

ORCID: 0000-0003-3802-2494

SAMSONOVA Natalia S.

kolomna.88@mail.ru

ORCID: 0000-0002-5965-0767

KUZNETSOV Yurii A.

kuznets@ms.ioffe.ru

ORCID: 0000-0003-2560-2182

Received 31.10.2022. Approved after reviewing 08.11.2022. Accepted 08.11.2022.

Conference materials

UDC 532.64.08

DOI: <https://doi.org/10.18721/JPM.161.169>

Wettability of transparent conductive nanostructured ITO and ITO/Al₂O₃ coatings

V.V. Aksenova^{1,2✉}, I.P. Smirnova², L.K. Markov², A.S. Pavlyuchenko²,
D.S. Kolokolov³, D.Yu. Volkov³

¹ Peter the Great St. Petersburg Polytechnic University, St. Petersburg, Russia;

² Ioffe Institute, St. Petersburg, Russia;

³ JSC Koltsov's Design Bureau, St. Petersburg, Russia

✉ valeriya11-12@mail.ru

Abstract. In this paper, the water wettability of nanostructured ITO films, including those with Al₂O₃ protective layers, was studied. Nanostructured ITO films were deposited by magnetron sputtering and electron beam evaporation on the preheated surface of a glass substrate, after which they were additionally annealed in a nitrogen atmosphere for 10 min. Some samples were covered with an aluminium oxide layer with various thicknesses. The Al₂O₃ protective coating was fabricated by atomic layer deposition. To estimate the wettability, we measured the contact angles of water drops on the horizontal surface of the films. The results show that, depending on the deposition method and thickness, structured ITO films can be characterized both by hydrophilic and by hydrophobic properties. In the case of covering of the nanostructured ITO film deposited by the electron beam evaporation with a protective coating of aluminium oxide, the hydrophobic properties of structured ITO films can be significantly improved and a superhydrophobic coating can be obtained.

Keywords: transparent conductive films, indium-tin oxide, wettability, atomic layer deposition, aluminium oxide

Citation: Aksenova V.V., Smirnova I.P., Markov L.K., Pavlyuchenko A.S., Kolokolov D.S., Volkov D.Yu., Wettability of transparent conductive nanostructured ITO and ITO/Al₂O₃ coatings, St. Petersburg State Polytechnical University Journal. Physics and Mathematics. 16 (1.1) (2023) 404–410. DOI: <https://doi.org/10.18721/JPM.161.169>

This is an open access article under the CC BY-NC 4.0 license (<https://creativecommons.org/licenses/by-nc/4.0/>)

Материалы конференции

УДК 532.64.08

DOI: <https://doi.org/10.18721/JPM.161.169>

Смачиваемость прозрачных проводящих наноструктурированных покрытий ИТО и ИТО/Al₂O₃

В.В. Аксенова^{1,2✉}, И.П. Смирнова², Л.К. Марков², А.С. Павлюченко²,
Д.С. Колоколов³, Д.Ю. Волков³

¹ Санкт-Петербургский политехнический университет Петра Великого, Санкт-Петербург, Россия;

² Физико-технический институт им. А.Ф. Иоффе РАН, Санкт-Петербург, Россия;

³ АО «СКТБ Кольцова», Санкт-Петербург, Россия

✉ valeriya11-12@mail.ru

Аннотация. Вданной работе исследовалась смачиваемость водой наноструктурированных пленок ИТО, в том числе с защитными слоями Al₂O₃. Пленки структурированного ИТО наносились методами магнетронного распыления и электронно-лучевого испарения на предварительно нагретую поверхность стеклянной подложки, после чего дополнительно отжигались в атмосфере азота в течение 10 мин. Сверху часть образцов была покрыта

слоем оксида алюминия различной толщины. Защитное покрытие Al_2O_3 наносилось методом атомно-слоевого осаждения. Для оценки смачиваемости измерялись краевые углы капель воды на горизонтальной поверхности пленок. Результаты показывают, что в зависимости от метода нанесения и толщины пленки структурированного ИТО могут обладать как гидрофильными, так и гидрофобными свойствами. В случае нанесения на пленку структурированного ИТО, нанесенного методом электронно-лучевого испарения, защитного покрытия из оксида алюминия можно значительно улучшить гидрофобные свойства структурированного ИТО и получить супергидрофобное покрытие.

Ключевые слова: прозрачные проводящие пленки, оксид индия-олова, влагостойкость, атомно-слоевое осаждение, оксид алюминия

Ссылка при цитировании: Аксенова В.В., Смирнова И.П., Марков Л.К., Павлюченко А.С., Колоколов Д.С., Волков Д.Ю. Смачиваемость прозрачных проводящих наноструктурированных покрытий ИТО и ИТО/ Al_2O_3 // Научно-технические ведомости СПбГПУ. Физико-математические науки. 2023. Т. 16. № 1.1. С. 404–410. DOI: <https://doi.org/10.18721/JPM.161.169>

Статья открытого доступа, распространяемая по лицензии CC BY-NC 4.0 (<https://creativecommons.org/licenses/by-nc/4.0/>)

Introduction

Nanostructured coatings based on indium-tin oxide (ITO) [1, 2] can be used to produce displays and optical contacts of LEDs, which makes it possible to reduce reflection and the effect of display backlighting and to increase the quantum yield of LEDs. However, the rough surface of these films leads to a greater susceptibility to the chemical action of the environment [3], especially under conditions of high humidity or in contact with water, so the fabrication of hydrophobic nanostructured coatings would solve the problem of chemical degradation of the surface.

Generally, studies of wettability of different surfaces are of great interest due to the possibility of wide use in various fields. The wettability may vary depending on the properties of the surface, such as surface structuring, surface energy, porosity. Currently, depending on the field of application, numerous studies are being carried out in the field of manufacturing both hydrophilic and hydrophobic surfaces [4]. In [5], the possibility of modifying the surface of copper pipes coated with a copper oxide layer was studied to improve the efficiency of moisture collection, which is especially important for solving the global problem of drinking water shortage, especially in arid regions. In the paper [6], the authors consider the fabrication of a nanoporous material from iron with a controlled transition of wettability from superhydrophilic to superhydrophobic for the separation of oil and water for the water purification. Superhydrophobic surfaces are important components in many fields of cleaning applications and protective coatings; such coatings can be produced, e.g., from nanostructured ZnO films [7]. As can be seen from [8], the formation of a rough nanostructure on the material surface makes it possible to significantly change the material wettability, including imparting hydrophobic properties, which can be used to improve the chemical resistance of the material.

Materials and Methods

ITO films were deposited using a specialized combined electron-beam and magnetron sputtering system manufactured by Torr Int., USA. The formation of nanostructured self-organized ITO films formed by nanowhiskers was carried out by two methods: electron-beam evaporation and magnetron sputtering, in both cases, on a substrate preheated to 500 °C. The deposition rate in both cases was about 10 nm/min. After deposition, without turning off the heating, the chamber was filled with high-purity nitrogen to almost atmospheric pressure (800 mbar), and the samples were annealed for 10 min. Under these deposition conditions, the coating layer is formed according to the vapor-liquid-crystal (VLC) mechanism. The nature of the self-organization and shape of nanocrystals depend on the deposition mode and duration. Film formation begins with a denser layer, the refractive index of which is close to the refractive index of dense ITO,

then separate whisker nanocrystals are formed, the effective refractive index of which decreases as the distance from the substrate increases. A more detailed description of the method and characteristics of the films are presented in [3]. Samples of unstructured ITO were obtained by magnetron sputtering; their thickness was ~ 170 nm. To form a protective coating on structured ITO films, an Al_2O_3 layer was deposited by atomic layer deposition using a PICOSUN P300B setup. This method consists in successive alternate treatment of the substrate with vapors of materials, namely, trimethylaluminum (TMA) and water, which react on the substrate surface.

The thickness of the films obtained by electron beam evaporation was 50 nm in an equivalent of dense film, the thickness of the films grown by magnetron sputtering was 150 nm in an equivalent of dense film. The phrase “thickness x in an equivalent of dense film” should be understood that the mass of deposited material in the nanostructured film is the same as for a dense film with thickness x . This term was introduced because the calibration of a quartz sensor used to control the film thickness can only be carried out when a dense ITO film is deposited.

Drops were formed using a mechanical dispenser from Sartorius, the drop size was $3 \mu\text{l}$. The drops were imaged using a Supereyes B011 digital optical microscope, the illumination was located on the side of the microscope. The substrate was placed horizontally, perpendicular to the camera direction, which resulted in the image of the drop from the side. SEM images of the films were obtained with a JEOL JSM-7001F scanning electron microscope.

Results and Discussion

The experimental results show that the unstructured ITO film (Film 1) (Fig. 1, *a*) are hydrophobic, the contact angle $\alpha = 100^\circ$ (Fig. 1, *b*). The film was deposited by magnetron sputtering on a cold substrate. As a protective coating for the ITO layer, an aluminium oxide layer obtained by atomic layer deposition can be used. For planar Al_2O_3 film (Film 2) deposited on a glass substrate, the contact angle is $\alpha = 95^\circ$ (Fig. 2). In the case of depositing a protective layer of Al_2O_3 on the planar surface of the dense ITO layer (Film 3) (Fig. 3, *a*), the results show no significant changes in the properties, the contact angle $\alpha = 100^\circ$ (Fig. 3, *b*).

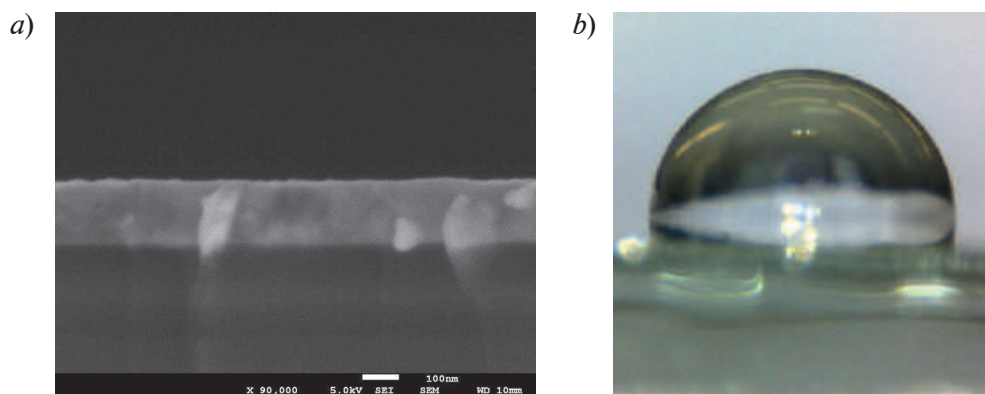


Fig. 1. SEM image of a planar dense 170 nm thick ITO film. (Film 1) (*a*). Drop profile on the film 1. Contact angle $\alpha = 100^\circ$ (*b*)



Fig. 2. Drop profile on an Al_2O_3 film 20 nm thick (Film 2). Contact angle $\alpha = 95^\circ$

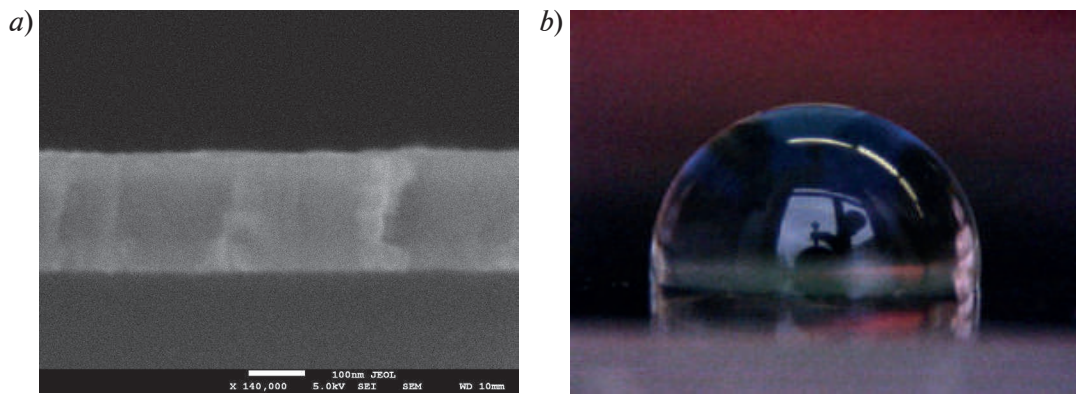


Fig. 3. SEM image of a planar ITO film coated with a 20 nm Al_2O_3 layer (Film 3) (a). Drop profile on the film 3. Contact angle $\alpha = 100^\circ$ (b)

At the same time, the nanostructured ITO film, also deposited by magnetron sputtering but on a heated substrate with subsequent annealing in a chamber (Film 4), shows hydrophilic properties, and its contact angle $\alpha = 10^\circ$ (Fig. 4, b). The SEM image of this nanostructured film shows a pronounced crystalline structure (Fig. 4, a).

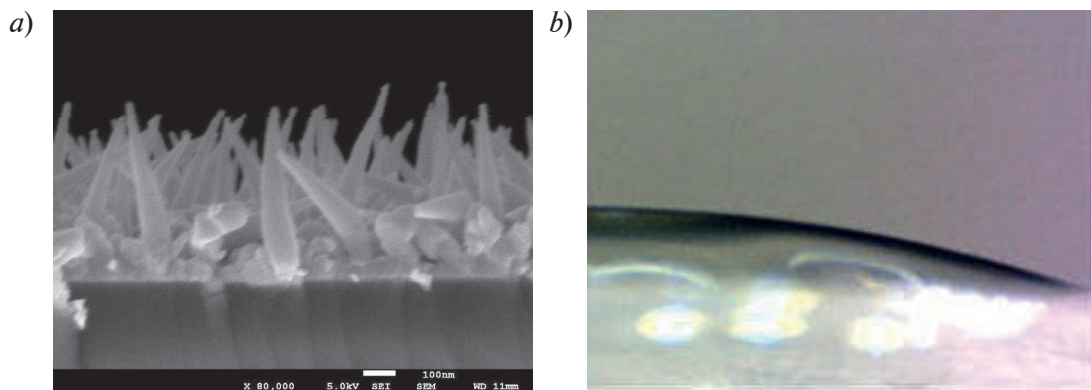


Fig. 4. SEM image of an ITO film (150 nm in equivalent of dense film) deposited on glass by magnetron sputtering on a heated substrate followed by annealing in a nitrogen atmosphere (Film 4) (a). Drop profile on film 4. Contact angle $\alpha = 10^\circ$ (b)

If the deposition method of nanostructured ITO films is changed to electron beam evaporation on a heated substrate followed by annealing in a chamber, the wettability measurements turn out to be like planar ITO films. The film thickness in equivalent of dense film is 50 nm (Film 5) (Fig. 5, a). The contact angle of the film $\alpha = 101^\circ$ (Fig. 5, b).

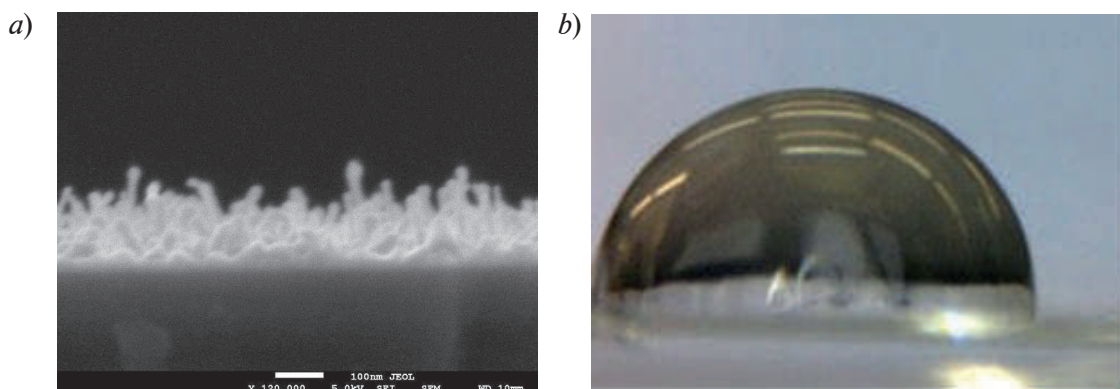


Fig. 5. SEM image of an ITO film (50 nm in equivalent of dense film) deposited on glass by electron beam evaporation followed by annealing in a nitrogen atmosphere (Film 5) (a). Drop profile on the film 5. Contact angle $\alpha = 101^\circ$ (b)

In the case of nanostructured ITO film covered with a layer of aluminium oxide 1 nm thick (Film 6) (Fig. 6, *a*) used to improve the chemical resistance of the coating, the contact angle was $\alpha = 152^\circ$ (Fig. 6, *b*), i.e., the film was superhydrophobic. Thus, the results show a significant enhancement of the hydrophobic properties compared to the structured and planar ITO films.

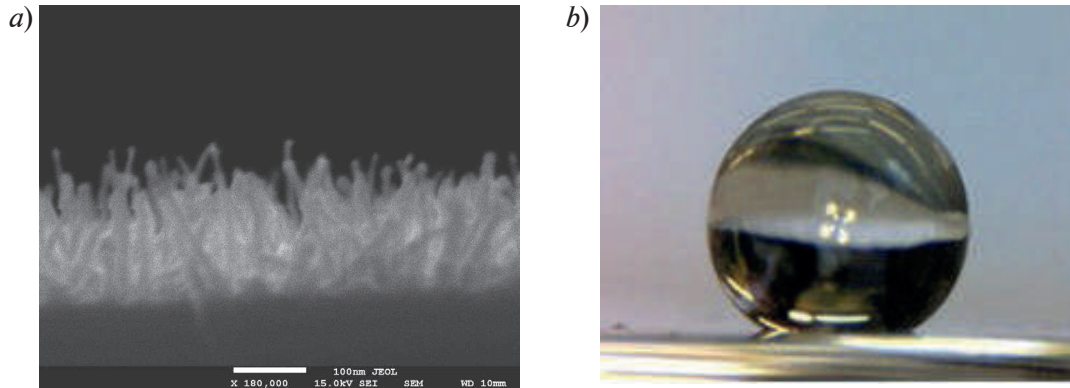


Fig. 6. SEM image of an ITO film (50 nm in equivalent of dense film) deposited on glass by electron beam evaporation on a heated substrate followed by annealing in a nitrogen atmosphere coated with 1 nm Al₂O₃ (Film 6) (*a*). Drop profile on the film 6. Contact angle $\alpha = 152^\circ$ (*b*)

To study the dependence of contact angle on the thickness of the aluminium oxide layer deposited on the nanostructured ITO film, a nanostructured ITO film with a 10 nm thick aluminium oxide coating was fabricated (Film 7) (Fig. 7, *a*). The contact angle of contact of the film was $\alpha = 128^\circ$ (Fig. 7, *b*),

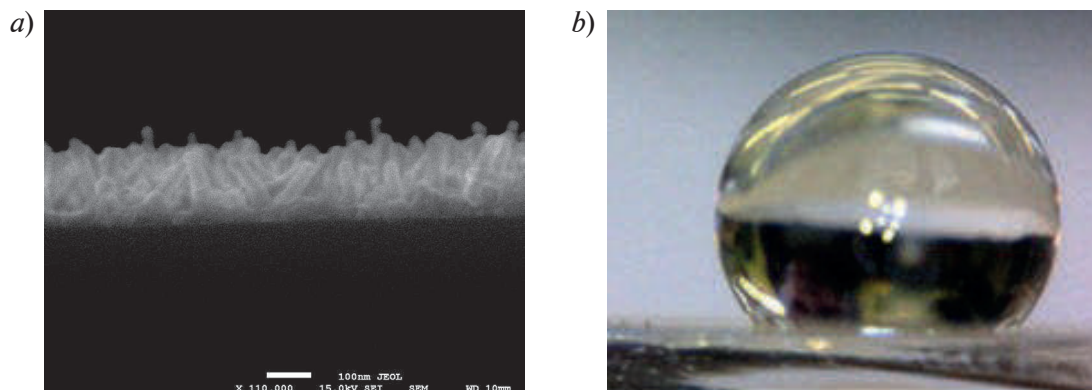


Fig. 7. SEM image of an ITO film (50 nm in equivalent of dense film) deposited on glass by electron beam evaporation on a heated substrate followed by annealing in a nitrogen atmosphere coated with 10 nm Al₂O₃ (Film 7) (*a*). Drop profile on the film 7. Contact angle $\alpha = 128^\circ$ (*b*)

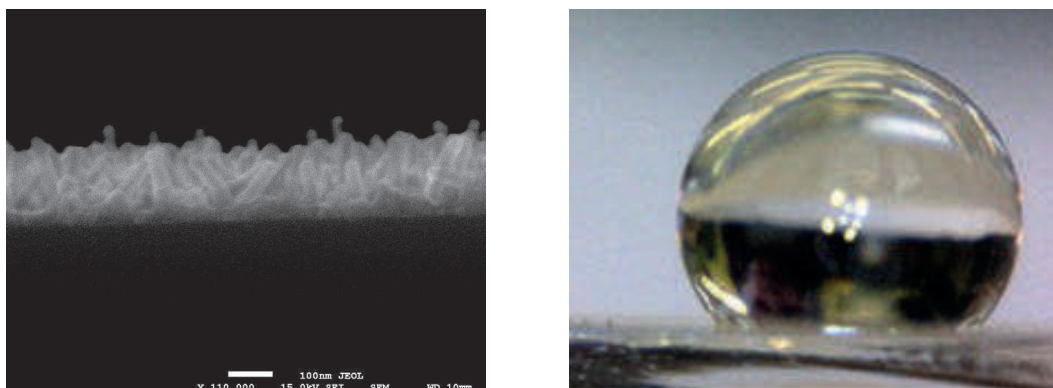


Fig. 8. SEM image of an ITO film (50 nm in equivalent of dense film) deposited on glass by electron beam evaporation on a heated substrate followed by annealing in a nitrogen atmosphere coated with 20 nm Al₂O₃ (Film 8) (*a*). Drop profile on the film 8. Contact angle $\alpha = 127^\circ$ (*b*)



i.e., the film was hydrophobic. An increase in the Al_2O_3 layer thickness did not improve the hydrophobic properties of the combined film of nanostructured ITO and aluminium oxide; on the contrary, they deteriorated.

A nanostructured ITO film with a 20 nm thick aluminium oxide coating was also fabricated (Fig. 8, *a*). The contact angle of the film was $\alpha = 127^\circ$ (Film 8) (Fig. 8, *b*), i.e., the film was hydrophobic. Thus, with an increase in the thickness of the Al_2O_3 layer, the hydrophobic properties of the combined structured ITO with an Al_2O_3 coating deteriorate, but a change in the Al_2O_3 layer from 10 nm to 20 nm had little effect on the contact angle.

Conclusion

In this work, we have studied the water wettability of nanostructured ITO films in various combinations with Al_2O_3 protective layers. ITO films were deposited by magnetron sputtering and electron beam evaporation on the preheated surface of a glass substrate, after which they were additionally annealed in a nitrogen atmosphere for 10 min. A protective Al_2O_3 coatings with various thicknesses were deposited by atomic layer deposition. To estimate the wettability, we measured the contact angles of water drops on the horizontal films surface. The experimental results show that it is possible to obtain coatings with pronounced hydrophilic properties ($\theta < 10^\circ$), moderately hydrophobic coatings ($\theta \approx 130^\circ$) as well as superhydrophobic coatings ($\theta > 150^\circ$) by changing the deposition method of nanostructured ITO films and forming a protective Al_2O_3 layer.

REFERENCES

1. Gong Z., Li Q., Li Y., Xiong H., Liu H., Wang S., Zhang Y., Guo M., Yun F., Polystyrene-catalytic indium–tin–oxide nanorods grown on green light-emitting diodes for enhancing light extraction, *Applied Physics Express*. 9 (8) (2016) 082102.
2. Park M.J., Kim C.U., Kang S.B., Won S.H., Kwak J.S., Kim C.M., Choi K.J., 3D hierarchical indium tin oxide nanotrees for enhancement of light extraction in gan-based light-emitting diodes, *Advanced Optical Materials*. 5 (2) (2017) 1600684.
3. Markov L.K., Pavlyuchenko A.S., Smirnova I.P., Mesh M.V., Kolokolov D.S., Application of atomic layer deposition for the formation of nanostructured ITO/ Al_2O_3 Coatings, *Semiconductors*. 55 (4) (2021) 438–445.
4. Otitoju T.A., Ahmad A.L., Ooi B.S., Superhydrophilic (superwetting) surfaces: A review on fabrication and application, *Journal of industrial and engineering chemistry*. 47 (2017) 19–40.
5. Seo D., Lee J., Lee C., Nam Y., The effects of surface wettability on the fog and dew moisture harvesting performance on tubular surfaces, *Scientific reports*. 6 (1) (2016) 1–11.
6. Liu Y., Zhan B., Zhang K., Kaya C., Stegmaier T., Han Z., Ren L., On-demand oil/water separation of 3D Fe foam by controllable wettability, *Chemical Engineering Journal*. 331 (2018) 278–289.
7. Mardosaitė R., Jurkevičiūtė A., Rackauskas S., Superhydrophobic ZnO nanowires: wettability mechanisms and functional applications, *Crystal Growth & Design*. 21(8) (2021) 4765–4779.
8. Cao L., Luo B., Gao H., Miao M., Wang T., Deng Y., Structure induced wide range wettability: Controlled surface of micro-nano/nano structured copper films for enhanced interface, *Journal of Materials Science & Technology*. 84 (2021) 147–158.

THE AUTHORS

AKSENOVA Valeriya V.
valeriya11-12@mail.ru
ORCID: 0000-0002-9202-6165

SMIRNOVA Irina P.
irina@quantum.ioffe.ru
ORCID: 0000-0001-5313-0640

MARKOV Lev K.
l.markov@mail.ioffe.ru
ORCID: 0000-0001-7293-1320

PAVLYUCHENKO Alexey S.
alexey.pavluchenko@gmail.com
ORCID: 0000-0001-5390-276X

KOLOKOLOV Daniil S.
k.d@koltsov-kb.ru
ORCID: 0000-0002-9624-6579

VOLKOV Dmirtiy Yu.
diman15656@gmail.com

Received 28.10.2022. Approved after reviewing 08.11.2022. Accepted 08.11.2022.

Conference materials

UDC 620.3, 620.9, 539.23, 621.315.592

DOI: <https://doi.org/10.18721/JPM.161.170>

Influence of GaP compensating layers on the characteristics of GaAs photovoltaic converters with InGaAs quantum dot arrays

R.A. Saliy¹✉, M.A. Mintairov¹, S.A. Mintairov¹,
M.V. Nakhimovich¹, M.Z. Shvarts¹, N.A. Kalyuzhnyy¹

¹Ioffe Institute, Saint-Petersburg, Russia

✉ r.saliy@mail.ioffe.ru

Abstract. In this work, we studied the influence of GaP compensating layers on the characteristics of GaAs solar cells with InGaAs quantum dot arrays. An increase in the overall level of quantum efficiency in the absorption range of quantum dots (870–1000 nm) by more than 10% has been demonstrated when GaP layers are embedded in GaAs intermediate layer (spacer) of a quantum dot array. It was also shown that in this case a noticeable increase in the open-circuit voltage can be achieved at high solar concentration.

Keywords: GaAs, InGaAs, GaP, solar cell, quantum dots, MOVPE

Citation: Saliy R.A., Mintairov M.A., Mintairov S.A., Nakhimovich M.V., Shvarts M.Z., Kalyuzhnyy N.A., Influence of GaP compensating layers on the characteristics of GaAs photovoltaic converters with InGaAs quantum dot arrays. St. Petersburg State Polytechnical University Journal. Physics and Mathematics. 16 (1.1) (2023) 411–415. DOI: <https://doi.org/10.18721/JPM.161.170>

This is an open access article under the CC BY-NC 4.0 license (<https://creativecommons.org/licenses/by-nc/4.0/>)

Материалы конференции

УДК 620.3, 620.9, 539.23, 621.315.592

DOI: <https://doi.org/10.18721/JPM.161.170>

Влияние компенсирующих слоев GaP на характеристики фотопреобразователей GaAs со встроенными массивами квантовых точек InGaAs

Р.А. Салий¹✉, М.А. Минтаиров¹, С.А. Минтаиров¹,
М.В. Нахимович¹, М.З. Шварц¹, Н.А. Калюжный¹

¹Физико-технический институт им. А.Ф. Иоффе РАН, Санкт-Петербург, Россия

✉ r.saliy@mail.ioffe.ru

Аннотация. В настоящей работе было исследовано влияние параметров компенсирующих слоев GaP на фотоэлектрические характеристики фотопреобразователей на GaAs с квантовыми точками InGaAs. Продемонстрировано увеличение общего уровня квантовой эффективности в области поглощения квантовых точек (870–1000 нм) более чем на 10% при встраивании слоев GaP в промежуточные слои массива квантовых точек. Также показано, что в этом случае при высоких кратностях солнечного излучения может быть достигнуто заметное увеличение напряжения холостого хода.

Ключевые слова: GaAs, InGaAs, GaP, фотопреобразователь, квантовые точки, МОГФЭ

Ссылка при цитировании: Салий Р.А., Минтаиров М.А., Минтаиров С.А., Нахимович М.В., Шварц М.З., Калюжный Н.А. Влияние компенсирующих слоев GaP на характеристики фотопреобразователей GaAs со встроенными массивами квантовых точек InGaAs // Научно-технические ведомости СПбГПУ. Физико-математические науки. 2023. Т. 16. № 1.1. С. 411–415. DOI: <https://doi.org/10.18721/JPM.161.170>

Статья открытого доступа, распространяемая по лицензии CC BY-NC 4.0 (<https://creativecommons.org/licenses/by-nc/4.0/>)

Introduction

Today, quantum dots (QDs) based on InAs-InGaAs materials are of great interest for various fields of semiconductor electronics. They have already shown their efficiency for lasers [1–3] and are being actively studied in the context of their application in III-V solar cells (SCs) to increase the photocurrent [4, 5]. One of the main problems when embedding arrays of QDs in a SC is the voltage (in particular, open circuit voltage (V_{oc})) drop appearing in the photovoltaic device [6]. The main reason for this drop is the additional recombination levels which are created by QDs in the band gap of the SC matrix material [7]. This leads to a decrease in average “effective” band gap in p-n junction area and, consequently, the dark saturation currents of the p-n-junction increase, on which the voltage directly depends. In addition, it is well known that in order to increase the absorption efficiency of QDs, it is necessary to grow a large number of QD rows in an QD array. In case of SC dozens of QD rows usually embedded in i-region of a device. This creates structural stresses (tensile stresses) in the semiconductor crystal lattice and local defects can be formed. At low photogenerated current (low solar radiation concentration) structural imperfection additionally leads to a decrease in device voltage due to the appearance of a tunnel current flow mechanism in the p-n junction of the structure.

In the present work we studied the effect of V_{oc} drop in single-junction GaAs SC with embedded InGaAs QDs. We used an approach of the incorporation of thin (up to 1 nm) wide-gap GaP layers into each layer of QD array. Interleaving layers of InGaAs QDs through an intermediate GaAs layer (spacer), in which GaP layers are embedded should allow compensating the increase in the effective band gap near the p-n junction. Thus, the main goal of embedding these layers between QD layers is to reduce the value of dark saturation currents, on which the value of V_{oc} strictly depends. These layers also are intended for compensating the tensile stresses created by the QD layers and eliminating of a tunneling current flow mechanism, which can additionally lead to a decrease in V_{oc} . The influence of the parameters of the GaP compensating layers on the photoelectric and spectral characteristics of GaAs SCs with QDs is studied on experimental structures described.

Materials and Methods

Four SC structures with different configuration of the QD array were grown by metalorganic vapor-phase epitaxy. The QD arrays in all SC samples contained 15 rows of QDs. Excluding the i-region design, the sequence of growth operations was the same for all experimental structures. Back surface field n-Al_{0.3}Ga_{0.7}As layer, n-GaAs base, and a part of GaAs i-region were grown at 700 °C. Then the reactor was cooled down to 520 °C for QD array deposition. The In_{0.8}Ga_{0.2}As material was deposited and coherent islands were formed in the Stranski-Krastanov mode with a wetting layer formation. The growth rate was 0.167 ML/sec [8]. Then the epitaxial growth was stopped for a post-growth interruption step. At this step, the temperature was stabilized for several seconds. After that, the completely formed QDs were covered with GaAs capping layer at the same temperature in order to protect islands from degradation during the subsequent reactor heating up to 600 °C for GaAs spacer layer growth. The value of the standard thickness of the spacer layer used for such QDs in our earlier works is about 40 nm [9]. In the framework of this work, we used both 40 nm spacer layer and a thinner one. Four structures were grown, differing in the parameters of spacer layers: a reference sample without compensating GaP layers with a spacer layer thickness of 13 nm; two samples with 5 and 10 Å GaP layers, embedded in 13 nm GaAs spacer layers; and a sample with 10 Å thick GaP layers embedded in a 40 nm GaAs spacer layer. The total thickness of the i-region was 1000 nm. The schematic structure of samples with GaP compensating layers embedded in GaAs spacer of QD arrays shown in figure 1.

For all structures, the described sequence was repeated 15 times, in accordance with the number of QD rows in the array. Then the rest of i-GaAs layer, p-GaAs emitter, p-Al_{0.8}Ga_{0.2}As “window” and p-GaAs contact layer were grown at 700 °C. The amount of In_{0.8}Ga_{0.2}As material for the QDs formation was 2 ML (~0.6 nm), since this is the optimal amount of material determined for the composition [8]. For measuring the quantum yield and photovoltaic parameters the method described elsewhere [10] has been used.

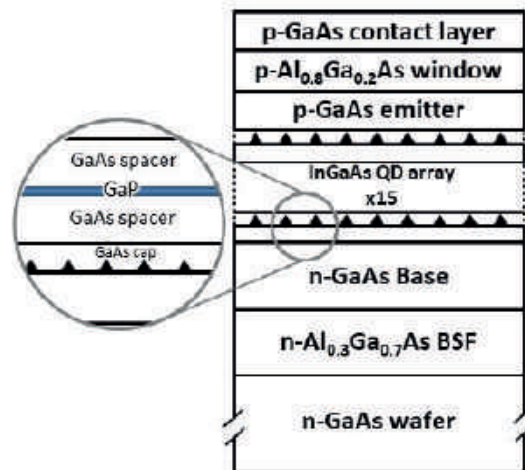


Fig. 1. The schematic structure of GaAs SC with GaP compensating layers in QD arrays

Results and Discussion

Internal quantum yield (Q_{int}) spectra have been obtained for AM1.5D spectral conditions. The obtained Q_{int} dependences showed that the use of compensating GaP layers makes it possible increasing the overall level of quantum efficiency by more than 10% in the GaAs absorption range (Fig. 2). This indicates a general improvement in the quality of the QD array.

The spectral dependences demonstrate broadening of the photosensitivity and Q_{int} increasing over the GaAs absorption edge due to sub-bandgap photon absorption (Fig. 2, on inset). In this case, the best effect of the embedding of GaP layers is demonstrated by a sample with a GaAs spacer and GaP layer thicknesses of 40 nm and 10 Å, respectively. Presumably, the combination of relatively thick GaAs spacer and GaP compensating layer makes it possible maintaining the high quality of the QD array and ensure efficient separation of carriers generated via sub-bandgap photon absorption.

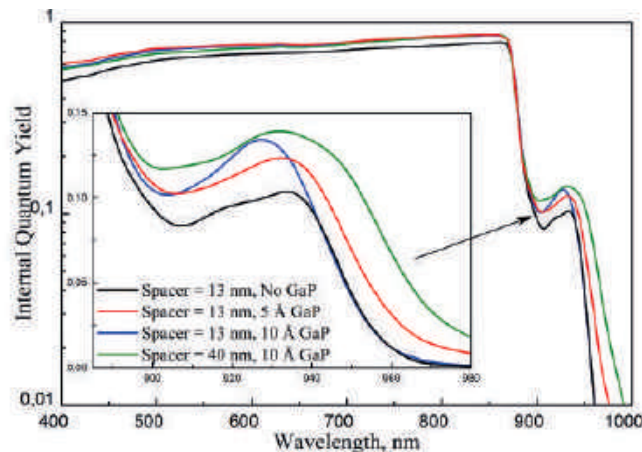


Fig. 2. Spectral characteristics of the internal quantum yield of experimental SC, as well as scaled spectral characteristics in the absorption region of embedded $In_{0.8}Ga_{0.2}As$ QDs (on inset)

At different values of the concentration of solar radiation V_{OC} value was measured (Fig. 3). For all samples V_{OC} increases uniformly with concentrations of solar radiation. The V_{OC} value for SC with GaP compensating layer thickness of 10 Å and GaAs spacer layer thickness of 13 nm is ~ 0.06 V greater, which is 7% more than for reference QD SC without GaP compensating layers. At the same time the separation of GaP layers by a wider spacer layer (40 nm) in the QD array also levels out the compensating effect (Fig. 3, *b*) from voltage point of view, in spite of that such an array design showed the best photoresponse (inset in Fig. 2).

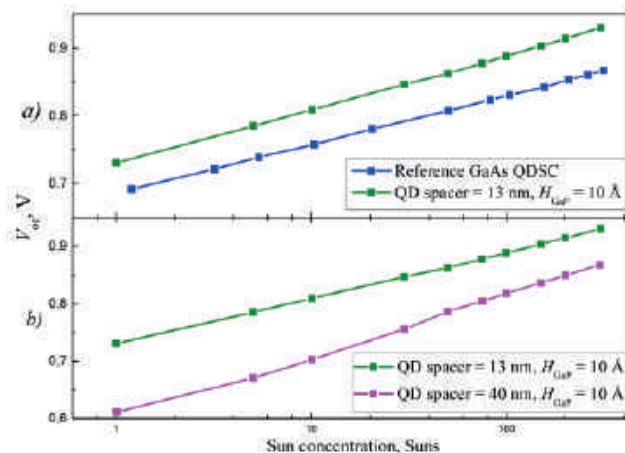


Fig. 3. V_{OC} at different values of the concentration of solar radiation

Conclusion

It was shown that thin GaP layers embedded in the GaAs SCs with InGaAs QD arrays can be used for both compensating local tensile stresses in the semiconductor crystal lattice and compensating the voltage drop (dark saturation currents increase) caused by decrease in average “effective” band gap in p-n junction area with QDs. Indeed, GaP layers embedded in QD arrays via 13 nm thick GaAs spacer layers, improve the average effective band gap and demonstrate more than 7% increase in V_{OC} in comparisons with samples without compensating layers. From the structural quality point of view, the GaAs SCs with compensating GaP layers showed increasing the overall level of quantum efficiency by more than 10% in the GaAs absorption range and quantum efficiency increasing as well as spectral broadening over the GaAs absorption edge. Wherein, the best spectral improving was demonstrated by SC with a 40 nm GaAs spacer. To further improve the parameters of the SCs with QDs by embedding compensating layers, it is necessary to optimize the GaP parameters and determine their position relative to the center of the GaAs spacer layer.

REFERENCES

1. Mintairov S.A., Kalyuzhnyy N.A., Maximov M.V., Nadtochiy A.M., Rouvimov S., Zhukov A.E., GaAs quantum well-dots solar cells with spectral response extended to 1100 nm, *Electronic Letters* 51 (20) (2015) 1602–1604.
2. Mikhrin S.S., Zhukov A.E., Kovsh A.R., Maleev N.A., Vasil'ev A.P., Semenova E.S., Ustinov V.M., Kulagina M.M., Nikitina E.V., Soshnikov I.P., Shernyakov Yu.M., Livshits D.A., Kryjanovskaya N.V., Sizov D.S., Maksimov M.V., Tsatsul'nikov A.F., Ledentsov N.N., Bimberg D., Alferov Zh.I., High efficiency ($\eta_D > 80\%$) long wavelength ($\lambda > 1.25 \mu\text{m}$) quantum dot diode lasers on GaAs substrates, *Semiconductors* 36 (11) (2002) 1315–1321.
3. Kovsh A., Krestnikov I., Livshits D., Mikhrin S., Weimert J., Zhukov A., Quantum dot laser with 75nm broad spectrum of emission, *Optics Letters*, 32(7) (2007) 793–795.
4. López N., Martí A., Luque A., Stanley C., Farmer C., Diaz P., Experimental analysis of the operation of quantum dot intermediate band solar cells, *Journal of Solar Energy Engineering*, 129 (3) (2007) 319–322.
5. Kalyuzhnyy N.A., Mintairov S.A., Salii R.A., Nadtochiy A.M., Payusov A.S., Brunkov P.N., Nevedomsky V.N., Shvarts M.Z., Marti A., Andreev V.M., Luque A., Increasing the quantum efficiency of InAs/GaAs QD arrays for solar cells grown by MOVPE without using strain-balance technology, *Progress in Photovoltaics* 24 (9) (2016) 1261–1271.
6. Nadtochiy A.M., Blokhin S.A., Kuz'menkov A.G., Maksimov M.V., Maleev N.A., Troshkov S.I., Ledentsov N.N., Ustinov V.M., Mutig A., Bimberg D., Decreasing parasitic capacitance in vertical-cavity surface-emitting laser with selectively oxidized aperture, *Technical Physics Letters* 38 (2012) 106–109.

7. **Sogabe T., Shen Q., Yamaguchi K.**, Recent progress on quantum dot solar cells: A review, *Journal of Photonics for Energy* 6 (4) (2016).
8. **Salii R.A., Mintairov S.A., Nadtochiy A.M., Nevedomsky V.N., Shvarts M.Z., Kalyuzhnyy N.A.**, Comparative Analysis of the Optical and Physical Properties of InAs and $\text{In}_{0.8}\text{Ga}_{0.2}\text{As}$ Quantum Dots and Solar Cells Based on them, *Semiconductors* 54 (10) (2020) 1267–1275.
9. **Salii R.A., Mintairov M.A., Mintairov S.A., Nakhimovich M.V., Shvarts M.Z., Kalyuzhnyy N.A.**, Influence of QD array positioning in GaAs solar cell p-n junction on their photoelectric characteristics, *Journal of Physics: Conference Series* 2103 (2021).
10. **Levina S.A., Emelyanov V.M., Filimonov E.D., Mintairov M.A., Shvarts M.Z., Andreev V.M.**, Cascade optical coupling and quantum efficiency measurements of MJ SCs, *Solar Energy Materials and Solar Cells* 213 (2020).

THE AUTHORS

SALII Roman A.
r.saliy@mail.ioffe.ru

NAKHIMOVICH Maria V.
nmar@mail.ioffe.ru

MINTAIROV Mikhail A.
mamint@mail.ioffe.ru
ORCID: 0000-0002-3481-477X

SHVARTS Maxim Z.
shvarts@scell.ioffe.ru
ORCID: 0000-0002-2230-7770

MINTAIROV Sergey A.
mintairov@scell.ioffe.ru
ORCID: 0000-0002-6176-6291

KALYUZHNYI Nikolay A.
nickk@mail.ioffe.ru
ORCID: 0000-0001-8443-4663

Received 28.10.2022. Approved after reviewing 14.11.2022. Accepted 16.11.2022.

Conference materials

UDC 539.1.074.55

DOI: <https://doi.org/10.18721/JPM.161.171>

Bragg peak effect on the electrical characteristics of Si detectors irradiated with medium energy ^{40}Ar ions

M.D. Mitina , V.E. Verbitskaya, N.N. Fadeeva, I.V. Eremin

Ioffe Institute, St Petersburg, Russia

 daria.mitina@mail.ioffe.ru

Abstract. The investigation is focused on the simulation of the I-V characteristics of Si p^+-n-n^+ diodes irradiated with medium-energy ^{40}Ar ions whose range is less than the detector thickness. The characteristics were simulated by considering the distribution of the current generating defects related to the profile of primary vacancies with a sharply rising density at the end of the ion track, which was defined by using the TRIM software. The defects involved in the simulation were two radiation-induced acceptors, the one positioned at $E_c - 0.42$ eV and the other in the lower half of the bandgap at $E_c - 0.65$ eV, responsible for the bulk current generation and the electric field distribution, respectively. With the adjusted characteristics of the defects, I-V characteristics in the fluence range $(1-4) \times 10^9 \text{ cm}^{-2}$ demonstrated a quantitative agreement with the experimental curves and a strict proportionality of the maximum current to the fluence. The electric field evolution with ion fluence was calculated and discussed as information complementary to the I-V data.

Keywords: defects, silicon detectors, ion irradiation, radiation hardness, current simulation

Citation: Mitina M.D., Verbitskaya V.E., Fadeeva N.N., Eremin I.V., Bragg peak effect on the electrical characteristics of Si detectors irradiated with medium energy ^{40}Ar ions, St. Petersburg State Polytechnical University Journal. Physics and Mathematics. 16 (1.1) (2023) 416–421. DOI: <https://doi.org/10.18721/JPM.161.171>


This is an open access article under the CC BY-NC 4.0 license (<https://creativecommons.org/licenses/by-nc/4.0/>)

Материалы конференции

УДК 539.1.074.55

DOI: <https://doi.org/10.18721/JPM.161.171>

Влияние пика Брэгга на электрические характеристики кремниевых детекторов, облученных ионами ^{40}Ar средней энергии

Д.Д. Митина , Е.М. Вербицкая, Н.Н. Фадеева, И.В. Еремин

Физико-технический институт им. Иоффе РАН, Санкт-Петербург, Россия

 daria.mitina@mail.ioffe.ru

Аннотация. Работа посвящена моделированию генерационного тока кремниевых детекторов, облученных ионами ^{40}Ar средней энергией, формирующих в структуре пик Брэгга. Продемонстрированы моделирование распределения первичных дефектов в среде TRIM, распределения электрического поля при различных дозах облучения, а также сравнение экспериментальных вольт-амперных характеристик и построенных на основе моделирования. В качестве основы для расчетов принята двухуровневая модель генерации

Ключевые слова: дефекты, кремниевые детекторы, облучение ионами, радиационная стойкость, симуляция тока

Ссылка при цитировании: Митина Д.Д., Вербицкая Е.М., Фадеева Н.Н., Еремин И.В. Влияние пика Брэгга на электрические характеристики кремниевых детекторов, облученных ионами ^{40}Ar средней энергии // Научно-технические ведомости СПбГПУ.

Физико-математические науки. 2023. Т. 16. № 1.1. С. 416–421. DOI: <https://doi.org/10.18721/JPM.161.171>

Статья открытого доступа, распространяемая по лицензии CC BY-NC 4.0 (<https://creativecommons.org/licenses/by-nc/4.0/>)

Introduction

Silicon detectors are currently a central element of the largest detection systems in accelerator complexes such as Large Hadron Collider, CERN, and GSI, Darmstadt. One of the main features of such facilities is the huge energy of accelerated particles, reaching hundreds of GeV. Under these conditions, particles traverse the total detector depth and create a uniform defect distribution throughout the device, and the detector properties in the entire bulk degrade uniformly. The model of Si detector degradation with uniformly damaged volume was developed in many studies and successfully applied for an explanation of the detector radiation degradation under the influence of light particles of high energies [1].

Nuclear physics where the study of exotic ions is one of the focuses of interest, is also exploiting the beams of larger and larger intensity. A specific feature of such experiments is that the ranges of the ion mass and the energy are wide enough, and thus detected ions can pass through the detectors creating an almost uniformly distributed damage in the detector bulk or stop inside it. The results of recent study on the comparison of radiation effects of high-energy protons and ^{40}Ar ions on Si detectors [2] demonstrated the applicability of the parameterization of the irradiated silicon properties, namely, the introduction rates of radiation-induced defects, by using scaling coefficients, and thus extend them for the modeling of heavy ion effects on Si detectors.

In the case of short-range ions (the range is less than the detector thickness), another important issue arises. The rate of energy loss increases with the energy reduction, and thus at the ion stopping point the primary defect density might be up to several orders of magnitude larger than at the beginning of the ion range, thus forming the Bragg peak. This adds to the detector degradation a new factor, a vastly non-uniform distribution of radiation defects along the ion paths.

The impact of the Bragg peak region (BPR) on the electrical characteristics has already been observed in the recent study of Si diodes irradiated with short-range ions [3]. In the current work, this line of investigation is continued and focused on the practical issue, the analysis of I-V characteristics of $p^+n\text{-}n^+$ diodes irradiated with medium energy ^{40}Ar ions forming the BPR in the silicon bulk. The goal of the work is to propose parameterization of the silicon properties, which allows calculating I-V characteristics of irradiated diodes. For this, simulations of the I-V characteristics and the distribution of the electric field across the diode depth x , $E(x)$, were carried out. The obtained results can be considered as a first step in the physics of radiation degradation of Si detector exposed to short-range ion irradiation.

Experimental

The samples were processed on the n-type Czochralski silicon wafer with a resistivity of 60 Ωcm , which allows precise profiling the effective space charge concentration N_{eff} in the damaged region by increasing the range of bias voltage needed for its depletion. The diode thickness and the p^+n junction area were 300 μm and 23 mm^2 , respectively. All samples contained a guard rings structure surrounding the p^+ contact and stabilizing I-V characteristics of the diodes. Three samples were irradiated with 53.4 MeV ^{40}Ar ions to the fluences $\Phi_1 = 1 \times 10^9$, $\Phi_2 = 2 \times 10^9$ and $\Phi_3 = 4 \times 10^9 \text{ cm}^{-2}$.

The I-V measurements were carried out at room temperature (RT) in the voltage range 0–100 V using Keithley 487 picoammeter with the diode guard ring grounded. The dependences of the bulk current on voltage after irradiation and beneficial annealing of the samples are shown in Fig. 1, *a*. The shapes of the characteristics are similar for all fluences.

Simulations of primary defect distribution using TRIM

The distribution of primary defects in silicon irradiated with 53.4 MeV ^{40}Ar ions was calculated by using Transport of Ions in Matter (TRIM) software [4]. Fig. 1, *b* shows the amount of primary vacancies $N_v(x)$ defined as their number generated in the layer at the depth x over a length of 1 \AA per 1 ion and distributed across the ion range r_p of about 15 μm .

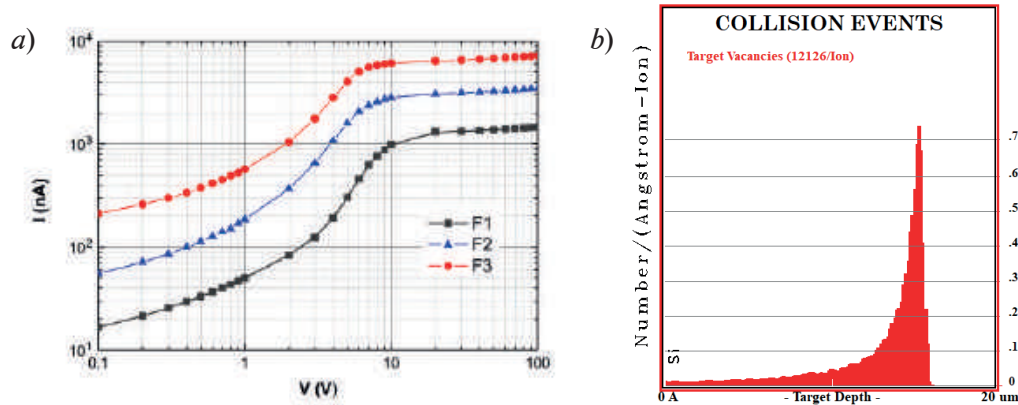


Fig. 1. Experimental I-V characteristics of Si diode irradiated with 53.4 MeV ^{40}Ar ions vs (a) primary defect distribution in silicon irradiated with 53.4 MeV ^{40}Ar ions calculated by using TRIM (b)

Obviously, subsequent interactions of the vacancies with the target atoms, the contaminations and with each other cannot be determined using simulations in TRIM, but it can be assumed that some fraction of the vacancies will contribute to the formation of electrically active defects with deep energy levels acting as the current generation centers and/or the levels responsible for the electric field distribution in the depleted region in the reverse biased diode.

Simulation of I-V characteristics and $E(x)$ profiles along the track of short-range ^{40}Ar ions

In the I-V characteristics the current shows a gradual and then a sharp rise (the latter identified with the BPR), and the following tendency to the current saturation at V about 10 V. This value is related to the depletion of the damaged region: the higher the fluence, the higher the saturated current.

Given the capabilities of the program used for simulating the electrical characteristics of p+-n-n⁺ Si diodes described in [5], the N_v dependence on the coordinate x normal to the diode surface was tabulated within the ion range. Accordingly, the concentration of electrically active defects affecting the diode I-V characteristics was assumed to be proportional to the concentration N_v . The proportionality coefficient K was an adjustable parameter, the same along the entire ion tracks, but individual for a particular type of defects.

An approach to describing the characteristics of radiation-induced defects was similar to that previously used to analyze the degradation processes in Si detectors irradiated with high-energy protons, in which the set of numerous electrically active radiation defects was replaced by a minimal number of effective defects with adjustable parameters [6]. Each of them is associated with a certain process, which enables an independent fit to the diode characteristics.

In the modeling the I-V characteristics of diodes irradiated with short-range particles, the parametrization of radiation effects should take into account the following factors:

- the rate of thermal generation of electrons and holes in the depleted region and its nonuniformity over the thickness of the diode in accordance with a vacancy profile taken from the TRIM data,
- compensation of positive charge of shallow impurities (phosphorus shallow donors in the n-type silicon) by negatively charged acceptors induced by ions, which determines the distribution of the electric field in the diode.

In the study, these processes were described by introducing into the model two effective acceptor energy levels, one of which, DA1, determined the rate of the current generation in the depleted region of the structure, while the second, DA2, compensated shallow donors, thus forming the distribution of the electric field.

The DA1 was considered as the acceptor acting as an electron trap positioned at $E_c - 0.42$ eV. This energy level does not affect the space charge concentration since it is located in the upper half of the bandgap and remains electrically neutral in the electric field region. The rate of the current generation via this energy level is determined by the activation energy $E_g - 0.42 = 0.7$ eV (where E_g is the silicon bandgap equal to 1.12 eV at RT). The second acceptor DA2 is the effective energy level located in the lower half of the bandgap at $E_c - 0.65$ eV and capable of compensating the charge of shallow donors; thereby it determines the electric field distribution in the diode. It

should be noted that both levels, DA1 and DA2, are current generation centers since they have close activation energies of 0.7 and 0.65 eV, respectively; however, their concentrations are rather different. The parameters of the levels are the electron and hole capture cross-sections set to be the same and equal to $1 \times 10^{-13} \text{ cm}^2$.

The experimental I-V characteristics and simulated curves are compared in Fig. 2. Qualitative agreement is observed for all fluences. It should be noted that the common feature of the current rise shape is the decrease in voltage at which the rate of the rise with the bias is maximal. This indicates that the material in the LDR becomes more compensated with increasing dose, which results in a lower depletion voltage of the whole damaged region. The maximum agreement between the calculated and the experimental curves is observed for the diode irradiated to $\Phi 3$. Therefore, the deviations of the current rise profile with voltage for lower fluences should be attributed to the impact of the p^+-n junction periphery on the current rather than to the factors related to the mechanisms of the silicon bulk deterioration under irradiation. The same applies to the slow increase in current observed in all I-V characteristics after depletion of the entire damaged region, which can be related to the surface properties of the structure. All simulated I-V characteristics show a smoother transition from the current rise to its saturation than the experimental ones. The reason may be the channeling of some fraction of impinging ions, which blurs the border of the damaged region and increases the width of the BPR, creating a damaged layer at a depth greater than r_p .

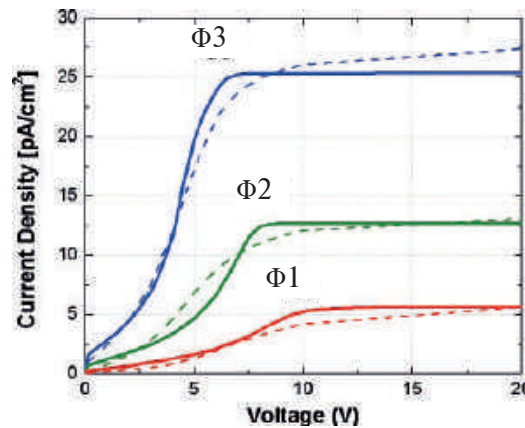


Fig.2. Comparison of the simulated and experimental I-V characteristics of irradiated

Figures 3, *a* and *b* show the simulated distributions of the effective acceptor concentrations over the depth of the damaged layer, along with the concentration of shallow donors $N_{SD} = 7 \times 10^{13} \text{ cm}^{-3}$. The DA1 and DA2 distributions correspond to the introduction coefficients $K_{DA1} = 0.4$ and $K_{DA2} = 0.007$ per vacancy obtained from the fitting and are presented for the minimum and maximum fluences. At $\Phi = 4 \times 10^9 \text{ cm}^{-2}$, the concentration of DA2 exceeds the concentration of shallow donors in the most of the Bragg peak region (13–15 μm), i.e., this bulk is overcompensated.

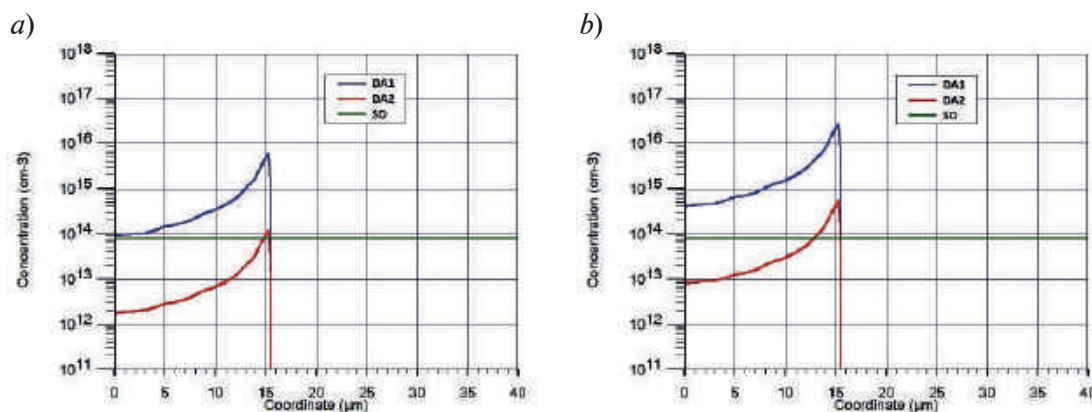


Fig. 3. Simulated distributions of the DA1 and DA2 concentrations in irradiated diodes. Φ (cm^{-2}): 1×10^9 (*a*) and 4×10^9 (*b*). For comparison, concentration of shallow donors is shown

The important data obtained as a result of the I-V characteristics simulation are shown in Fig. 4, which presents the distribution of the electric field $E(x)$ in the diodes at various bias voltages. The $E(x)$ profiles in Fig. 4, *a* correspond to the minimum Φ . In this case, according to Fig. 3, *a*, the DA2 concentration is below the concentration of shallow donors even at the Bragg peak maximum, and the arising structure can be considered as a p^+-n junction in silicon with a nonuniform negative concentration $N_{eff} = \text{abs}(N_{SD} - N_{DA2})$. Accordingly, the width of the depleted region increases gradually when propagating into the damaged region. A feature of the $E(x)$ profile in the region of the Bragg peak is that after its depletion, the electric field gradient increases (Fig. 4, *a*) and corresponds to the concentration of donors in the nonirradiated silicon.

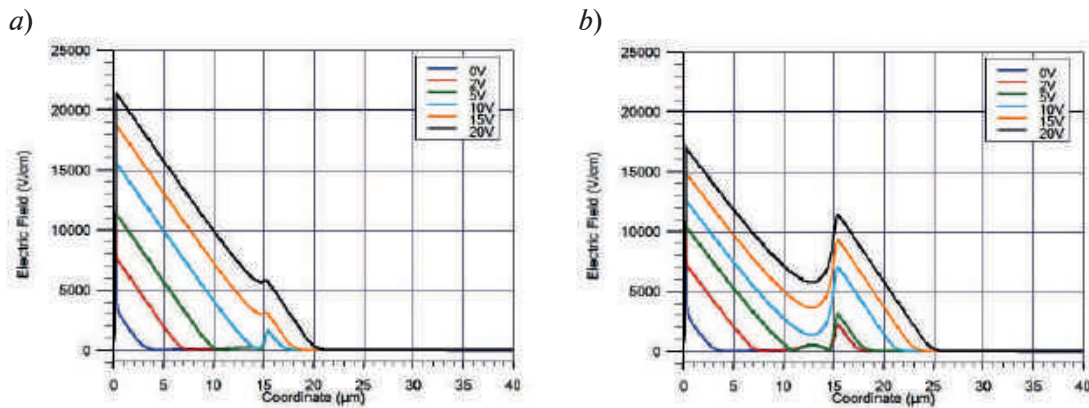


Fig.4. Distribution of the electric field across the diode thickness. Φ (cm⁻²): *a*) 1×10^9 , and *b*) 4×10^9

At the maximum fluence, the appearance of a built-in field in the range 0–5 V is clearly visible at both sides of the border between the BPR and a nondamaged region (Fig. 4, *b*). At higher bias, the electric field region is propagating outside the BPR, starting from a depth $x = 15 \mu\text{m}$, and at $V = 10 \text{ V}$ the BPR is fully depleted. Such a change in the electric field with increasing voltage is a direct consequence of the silicon overcompensation by the DA2 acceptors inside a part of the damaged region and the appearance of a narrow region of the p-type silicon forming an internal p-n junction at the BPR border with a nonirradiated silicon bulk. However, since this feature is associated with the DA2 defect, whose concentration is less than that of the DA1, it does not affect the linear rise of the bulk current vs. fluence.

Calculations show that further increase in fluence leads to the qualitative changes in the shapes of I-V characteristics, which requires separate experiments and is beyond the scope of the present study.

Conclusion

The performed simulation of I-V characteristics of the diodes irradiated with short-range 40Ar ions showed that they can be described by two acceptors: an acceptor in the upper half of the bandgap $E_C - 0.42 \text{ eV}$ and an acceptor in the lower half at $E_C - 0.65 \text{ eV}$ responsible for the bulk current generation and the electric field distribution, respectively. The proposed system of defects allows proportional scaling of the current in Si diodes irradiated with ions in the range $\Phi \leq 4 \times 10^9 \text{ cm}^{-2}$, which does not yield a significant excess of the induced acceptor concentration over the concentration of initial shallow donors in the raw n-type Si. This value is apparently the threshold fluence above which the current vs. fluence proportionality might be disturbed. The developed approach and the proposed parameterization of the concentration of acceptors induced by radiation allows their application to predict the impact of any short-range ions basing on the primary defect profile obtained via a program like TRIM.

REFERENCES

1. Moll M., Displacement Damage in Silicon Detectors for High Energy Physics, IEEE Transactions on Nuclear Science. 8 (65) (2018) 1561–1582.



2. Eremin V., Mitina D., Fomichev A., Kiselev O., Egorov N., Eremin I., Shepelev A., Verbitskaya E., A comparative study of silicon detector degradation under irradiation by heavy ions and relativistic protons, *Journal of Instrumentation*, 13 (2018) P01019.

3. Mitina D., Eremin V., Verbitskaya E., Eremin I., DLTS spectra of radiation-induced defects in silicon detectors with heavily damaged Bragg peak region, *Journal of Physics: Conference Series*, 1 (1697) (2020) 012071.

4. Mitina D., Verbitskaya E., Eremin V., Issues of TRIM program as a tool for developing a silicon detectors radiation degradation scenario, *Journal of Physics: Conference Series*, 4 (1400) (2019) 044014.

5. Eremin V., Fadeeva N., Verbitskaya E., The impact of active base on the bulk current in silicon heavily irradiated detectors, *Journal of Instrumentation*, 12 (2018) P09005.

6. Verbitskaya E., Eremin V., Ilyashenko I., Li Z., Carrier generation in irradiated Si detectors and its impact on the electric field profile, *Nuclear Instruments and Methods in Physics Research A*, 754 (2014) 63–70.

THE AUTHORS

MITINA Daria M.

daria.mitina@mail.ioffe.ru

ORCID: 0000-0001-9817-8525

FADEEVA Nadezhda N.

fadeevanadezda@gmail.com

ORCID: 0000-0002-8004-6978

VERBITSKAYA Elena V.

elena.verbitskaia@cern.ch

ORCID: 0000-0002-2313-1789

EREMIN Igor V.

ereminpti@hotmail.com

ORCID: 0000-0002-1420-2776

Received 31.10.2022. Approved after reviewing 08.11.2022. Accepted 08.11.2022.

Conference materials

UDC 621.383.51

DOI: <https://doi.org/10.18721/JPM.161.172>

New inorganic materials for electron transport layers in perovskite solar cells

A.B. Nikolskaia ¹✉, S.S. Kozlov ¹, O.V. Alexeeva ¹,
M.F. Vildanova ¹, O.K. Karyagina ¹, O.V. Almjasheva ^{2,3},
V.V. Gusarov ^{2,3}, O.I. Shevaleevskiy ¹

¹ Emanuel Institute of Biochemical Physics, RAS, Moscow, Russia;

² St. Petersburg State Electrotechnical University "LETI", St. Petersburg, Russia;

³ Ioffe Institute, St. Petersburg, Russia

✉ anickolskaya@mail.ru

Abstract. Ternary complex oxides with cubic pyrochlore structure $\text{Bi}_x\text{Fe}_y\text{WO}_q$ (BFWO) were obtained by hydrothermal synthesis at different pH values of hydrothermal fluid and were first used as electron transport layers in perovskite solar cells (PSCs). The analysis of photovoltaic parameters measured for BFWO-based PSCs demonstrated that BFWO materials obtained at pH 2 allow improving the PSC performance by ~4% (rel.) in comparison with state-of-the-art PSCs. In addition, BFWO-based PSCs exhibited higher tolerance to the degradation under continuous illumination.

Keywords: ternary complex oxides, electron transport layer, perovskite solar cells, solar photovoltaics

Funding: This work was supported by the Russian Science Foundation (RSF) under grant No. 20-69-47124.

Citation: Nikolskaia A.B., Kozlov S.S., Alexeeva O.V., Vildanova M.F., Karyagina O.K., Almjasheva O.V., Gusarov V.V., Shevaleevskiy O.I., New inorganic materials for electron transport layers in perovskite solar cells, St. Petersburg State Polytechnical University Journal. Physics and Mathematics. 16 (1.1) (2023) 422–427. DOI: <https://doi.org/10.18721/JPM.161.172>

This is an open access article under the CC BY-NC 4.0 license (<https://creativecommons.org/licenses/by-nc/4.0/>)

Материалы конференции

УДК 621.383.51

DOI: <https://doi.org/10.18721/JPM.161.172>

Новые неорганические материалы для электронно-транспортных слоев в перовскитных солнечных элементах

А.Б. Никольская ¹✉, С.С. Козлов ¹, О.В. Алексеева ¹,
М.Ф. Вильданова ¹, О.К. Карягина ¹, О.В. Альмяшева ^{2,3},
В.В. Гусаров ^{2,3}, О.И. Шевалеевский ¹

¹ Институт биохимической физики им. Н.М. Эмануэля РАН, Москва, Россия;

² Санкт-Петербургский государственный электротехнический университет «ЛЭТИ» им. В.И. Ульянова (Ленина), Санкт-Петербург, Россия;

³ Физико-технический институт им. А.Ф. Иоффе РАН, Санкт-Петербург, Россия

✉ anickolskaya@mail.ru

Аннотация. В данной работе в качестве электронно-транспортных слоев в перовскитных солнечных элементах (ПСЭ) впервые были использованы тонкие пленки тройных сложных оксидов со структурой пирохлора вида $\text{Bi}_x\text{Fe}_y\text{WO}_q$ (BFWO). Анализ фотоэлектрических параметров сконструированных ПСЭ показал, что эффективность

образца со слоем BFWO на 4% выше, чем у ПСЭ на основе стандартно используемого слоя TiO_2 . Кроме того, ПСЭ с материалом BFWO демонстрировали повышенную устойчивость к непрерывному освещению.

Ключевые слова: тройные сложные оксиды, электронно-транспортный слой, перовскитные солнечные элементы, солнечная фотовольтаика

Финансирование: Исследование выполнено за счет гранта Российского научного фонда (проект № 20-69-47124).

Ссылка при цитировании: Никольская А.Б., Козлов С.С., Алексеева О.В., Вильданова М.Ф., Карягина О.К., Альмяшева О.В., Гусаров В.В., Шевалеевский О.И. Новые неорганические материалы для электронно-транспортных слоев в перовскитных солнечных элементах // Научно-технические ведомости СПбГПУ. Физико-математические науки. 2023. Т. 16. № 1.1. С. 422–427. DOI: <https://doi.org/10.18721/JPM.161.172>

Статья открытого доступа, распространяемая по лицензии CC BY-NC 4.0 (<https://creativecommons.org/licenses/by-nc/4.0/>)

Introduction

In the last decade, perovskite solar cells (PSCs) based on hybrid materials with perovskite-like structure with the general formula ABX_3 (A — CH_3NH_3^+ , $\text{HC}(\text{NH}_2)^{2+}$, B — Pb^{2+} , Sn^{2+} , X — I⁻, Br⁻ or Cl⁻) became a major alternative to conventional crystalline silicon solar cells [1, 2, 3]. In hybrid perovskite materials organic and inorganic components alternate with each other. Due to this perovskite compounds used in PSCs exhibit unique electrical and optical properties, while the power conversion efficiency (PCE) for PSCs exceeds 25% [4, 5]. The photovoltaic characteristics (PV) and long-term stability of PSCs are significantly affected by the electron transport layer (ETL) on the surface of which perovskite material is deposited [6, 7].

The semiconductor material for the ETL layer must show high transmittance characteristics and provide good band alignment with contact. At the same time, ETL should effectively block photogenerated holes to reduce the recombination processes at the perovskite/ETL interface [8, 9]. Generally mesoscopic layer based on titanium dioxide (TiO_2) with a band gap of $E_g = 3.2$ eV is used as ETL [6]. TiO_2 -based PSCs demonstrate high PCE, but degrade significantly over time [10]. The degradation processes in PSCs are partially explained by the instability of the TiO_2 material under UV radiation where the continuous illumination causes desorption of oxygen molecules from TiO_2 layer thus initiating degradation of the perovskite layer [10, 11]. In this regard, the search of new materials with increased resistance to the UV radiation for ETLs in PSCs is an important issue for perovskite photovoltaics. For this purpose, ternary complex oxides are of great interest [12]. These materials are characterized by high electron mobility, high density of chemical sites, tunable band structures and high chemical stability even under extreme conditions [6, 13].

In this work, complex oxides formed in the ternary system Bi_2O_3 – Fe_2O_3 – WO_3 were obtained by hydrothermal synthesis at different pH values of hydrothermal fluid. The synthesized $\text{Bi}_x\text{Fe}_y\text{WO}_z$ powders (BFWO) were examined by X-ray and optical methods and used to fabricate ETLs for PSCs. PV properties of the PSCs based on BFWO layers were investigated under standard illumination conditions (AM1.5G, 1000 W/m²). The comparative analysis of the results obtained revealed a new approach to develop efficient PV devices with high tolerance to the degradation under continuous illumination.

Materials and Methods

The BFWO powders were obtained by hydrothermal synthesis at hydrothermal fluid pH values of 2, 5 and 7 according to procedure described in [14] and were mixed with acetic acid, terpeneol, ethyl cellulose and ethanol to obtain thick pastes as specified in [15]. These pastes were diluted in ethanol (1:5), sonicated in ultrasonic bath several times and were deposited by spin coating (3000 rpm, 30 s) onto FTO (fluorine doped SnO_2) conductive glass substrates (Solaronix, 2×2 cm) with subsequent annealing at 500 °C for 1 hr [16]. Thus, the mesoporous ETL thin films based on BFWO were obtained. State-of-the-art TiO_2 -based ETL thin film was fabricated using the same technique for comparative analysis.

PSCs were fabricated under ambient conditions at relatively high humidity (~ 50–60%) according to the procedure described in detail earlier [17]. Perovskite ($\text{CH}_3\text{NH}_3\text{PbI}_3$) layer was formed on ETL surface using a conventional one-step deposition method [18]. A layer of Spiro-MeOTAD hole transport material was spin-coated onto the surface of the perovskite layers. The final stage of PSC fabrication was the deposition of ~ 50-nm thick Au contacts by vacuum thermal evaporation using the VUP-4 vacuum post.

The X-ray diffraction (XRD) study of BFWO powders was performed by a DRON-3M X-ray diffractometer with Cu $K\alpha$ radiation ($\lambda = 1.5405 \text{ \AA}$) as the X-ray source. The optoelectronic properties of BFWO powders were characterized using UV-vis spectroscopy (Shimadzu UV-3600 spectrophotometer with an ISR-3100 integrating sphere in the wavelength range of 300–1200 nm). The PV measurements for PSCs fabricated were provided under standard illumination conditions of 1000 W/m^2 (AM1.5G) using Abet 10500 solar simulator (Abet Technologies, USA). The current density–voltage ($J-V$) characteristics were measured by Semiconductor Characterization System 4200-SCS (Keithley, USA). PSCs were masked to obtain working area of 0.08 cm^2 .

Results and Discussion

The chemical composition of BFWO powders obtained by hydrothermal synthesis at different pH values of hydrothermal fluid was determined by energy dispersive X-ray microanalysis (EDXMA) and is listed in Table 1 (more detailed information in [14]). The samples obtained at pH 2 and 5 have a similar composition. With an increase in pH from 5 to 7, the samples become more enriched with W and Fe ions. According to [14] BFWO particles with the average size of 30–35 nm tend to form spherical aggregates of crystallites. The room temperature XRD patterns of BFWO powders are shown in Fig. 1. The peaks indicate that all samples are single-phase, and their crystal structure corresponds to that of cubic pyrochlore. The samples contain no impurities. Obtained data are in good agreement with literature data.

The optical band gaps E_g of the BFWO powders obtained were calculated from the diffusion reflectance UV-vis spectra after Kubelka-Munk conversion and Tauc plot treatment for indirect transition (Fig. 2, a) [19]. It was found to be 2.60 eV for pH = 2, 2.35 eV for pH = 5 and 2.48 eV for pH = 7. These results indicate that the BFWO materials have the properties of semiconductors and can be used for PSCs development. It is also shown that the optoelectronic characteristics of BFWO samples are significantly influenced by hydrothermal synthesis conditions, especially pH value of hydrothermal fluid.

Table 1

The composition of BFWO powders [14]

pH	Formula
2	$\text{Bi}_{0.50}\text{Fe}_{0.34}\text{WO}_q$
5	$\text{Bi}_{0.51}\text{Fe}_{0.36}\text{WO}_q$
7	$\text{Bi}_{0.70}\text{Fe}_{0.45}\text{WO}_q$

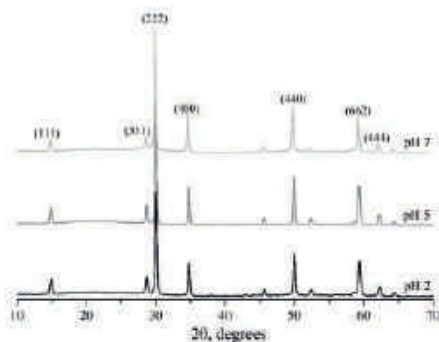


Fig. 1. XRD patterns of BFWO samples obtained at different pH values of hydrothermal fluid

The BFWO ETLs were fabricated on the surface of FTO conductive glasses by spin coating of thick pastes made by mixing BFWO powders with organic binders. PSCs with the cell architecture of FTO/BFWO/ $\text{CH}_3\text{NH}_3\text{PbI}_3$ /Spiro-OMeTAD/Au were fabricated using these ETLs under ambient conditions. State-of-the-art PSC based on TiO_2 mesoporous layer was also constructed for comparison.

$J-V$ curves recorded under standard illumination (1000 W/m^2 , AM1.5G) for PSCs with BFWO ETLs

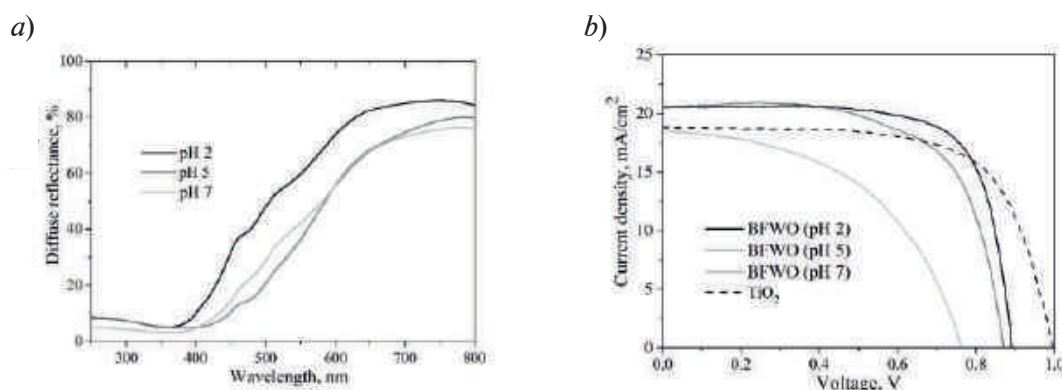


Fig. 2. Reflectance spectra of the BFWO samples at different pH values of hydrothermal fluid (a), J - V curves for the PSC devices based on different ETLs (b)

Table 1

The PV characteristics of PSC devices based on different ETLs

ETL	J_{SC} , mA/cm ²	V_{OC} , V	FF, a.u.	PCE, %
TiO ₂	18.8 ± 0.18	1.00 ± 0.02	0.69 ± 0.02	12.8 ± 0.17
BFWO pH=2	20.5 ± 0.17	0.89 ± 0.01	0.73 ± 0.01	13.3 ± 0.15
BFWO pH=5	20.5 ± 0.21	0.87 ± 0.02	0.66 ± 0.02	11.8 ± 0.23
BFWO pH=7	18.5 ± 0.17	0.77 ± 0.02	0.49 ± 0.03	7.0 ± 0.17

obtained at different pH values of hydrothermal fluid and with TiO₂ ETL are shown in Fig. 2, b. The PV parameters for all PSCs including short circuit current density (J_{SC}), open circuit voltage (V_{OC}), fill factor (FF) and power conversion efficiency (PCE) are listed in Table 2. It can be seen that the PSCs based on the BFWO compounds obtained at pH = 2 (Bi_{0.50}Fe_{0.34}WO_q) and 5 (Bi_{0.51}Fe_{0.36}WO_q) showed PCE values of 13.3% and 11.8%, respectively, which is comparable to the efficiency obtained for state-of-the-art PSCs (Table 2). PSC based on the BFWO compound obtained at pH = 7 (Bi_{0.70}Fe_{0.45}WO_q) showed poor PV performance, which was manifested in the decreased V_{OC} and FF values. The highest PCE is demonstrated in the PSC samples with BFWO-based ETLs obtained at hydrothermal fluid pH 2 and it is ~ 4% (rel.) higher than for TiO₂-based device. The data obtained confirms that BFWO materials can be used as a prospective ETL alternative in the efficient and stable PSCs.

It should be noted that for the BFWO-based PSCs the PV characteristics were obtained for the voltage sweep during J - V curve measurements started from 3 V. Previously, similar effects were observed for solar cells based on ferroelectric transition-metal oxides and were explained by the electromigration of charged defects (oxygen vacancies) and switching the ferroelectric polarization [20]. Also in contrast to state-of-the-art PSCs with TiO₂ ETL there is no compact layer in BFWO-based samples what indicates good blocking properties of BFWO thin films.

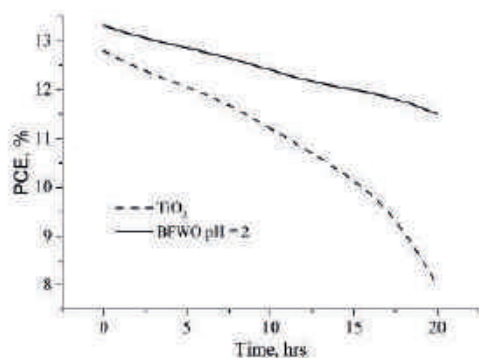


Fig. 3. Stability test of the PSCs under continuous illumination (AM1.5, 1000 W/m²)

PV parameters of PSCs with BFWO and TiO₂ ETLs were investigated under continuous standard illumination conditions (AM1.5, 1000 W/m²) and under ambient conditions. The appropriate results are presented in Fig. 3. The data obtained revealed that BFWO-based samples demonstrate more stable behavior than TiO₂-based devices.

We have shown that ternary complex oxides such as Bi_xFe_yWO_q with cubic pyrochlore structure demonstrate semiconductor properties and can be successfully used as ETL materials for the fabrication of high efficient and stable PSCs. These new inorganic materials have shown the better resistance to the degradation under continuous UV radiation than state-of-the-art ETLs. More of it their optical and photoelectrical properties can be easily tuned by synthetic conditions, especially by changing pH value of hydrothermal fluid.

Conclusion

In this paper complex oxide phases formed in the ternary system Bi₂O₃–Fe₂O₃–WO₃ were obtained by hydrothermal synthesis at different pH values of hydrothermal fluid and were used to fabricate the ETLs for PSCs. The Bi_xFe_yWO_q powders (BFWO) were examined by X-ray and optical methods. Energy bandgaps values were calculated and were found to be 2.3–2.6 eV depending on pH value of hydrothermal fluid. PSCs with the cell architecture of FTO/BFWO/CH₃NH₃PbI₃/Spiro-OMeTAD/Au were fabricated under ambient conditions. The highest PCE value was demonstrated by the PSC samples with BFWO ETL obtained at hydrothermal fluid pH 2 and it was ~ 4% (rel.) higher than for TiO₂-based device. We have shown that BFWO-based PSCs possessed higher tolerance to the degradation under continuous illumination conditions (AM1.5G, 1000 W/m²) in comparison with conventional PSCs. The obtained results revealed a new approach to develop efficient PV devices with the increased resistance to UV radiation.

REFERENCES

1. Wang R., Mujahid M., Duan Y., Wang Z.K., Xue J., Yang Y., A review of perovskites solar cell stability, *Adv. Funct. Mater.* 29 (47) (2019) 1808843.
2. Tejada A., Choy W.C.H., Deleporte E., Graetzel M., Special issue on hybrid perovskites for photovoltaics and optoelectronics, *J. Phys. D: Appl. Phys.* 53 (7) (2020) 070201.
3. Green M., Photovoltaic technology and visions for the future, *Prog. Energ.* 1 (1) (2019) 013001.
4. Park N.G., Research direction toward scalable, stable, and high efficiency perovskite solar cells, *Adv. Energ. Mater.* 10 (13) (2020) 1903106.
5. Green M.A., Dunlop E.D., Hohl-Ebinger J., Yoshita M., Kopidakis N., Hao X., Solar cell efficiency tables (version 57), *Prog. Photovolt.: Res. Appl.* 29 (1) (2021) 3–15.
6. Wang K., Olthof S., Subhani W.S., Jiang X., Cao Y., Duan L., Wang H., Du M., Liu S., Novel inorganic electron transport layers for planar perovskite solar cells: progress and prospective, *Nano Energy.* 68 (2020) 104289.
7. Mahmood K., Sarwar S., Mehran M.T., Current status of electron transport layers in perovskite solar cells: materials and properties, *RSC Adv.* 7 (28) (2017) 17044–17062.
8. Noh M. F. M., Teh C.H., Daik R., Lim E.L., Yap C.C., Ibrahim M.A., Ludin N.A., Yusoff A.R., Jang J., Teridi M.A.M., The architecture of the electron transport layer for a perovskite solar cell, *J. Mater. Chem. C.* 6 (4) (2018) 682–712.
9. Yang G., Tao H., Qin P., Kea W., Fang G., Recent progress in electron transport layers for efficient perovskite solar cells, *J. Mater. Chem. A.* 4 (11) (2016) 3970–3990.
10. Leijtens T., Eperon G.E., Pathak S., Abate A., Lee M.M., Snaith H., Overcoming ultraviolet light instability of sensitized TiO₂ with meso-superstructured organometal tri-halide perovskite solar cells, *Nat. Comm.* 4 (1) (2013) 1–8.
11. Yuan Y., Ji Z., Yan G., Li Z., Li J., Kuang M., Jiang B., Zeng L., Pan L., Mai W., TiO₂ electron transport bilayer for all-inorganic perovskite photodetectors with remarkably improved UV stability toward imaging applications, *J. Mater. Sci. Tech.* 75 (2021) 39–47.
12. Zhou Y., Li X., Lin H., To be higher and stronger—metal oxide electron transport materials for perovskite solar cells, *Small.* 16 (15) (2020) 1902579.
13. Thambidurai M., Shini F., Harikesh P.C., Mathews N., Dang C., Highly stable and efficient planar perovskite solar cells using ternary metal oxide electron transport layers, *J. Power Sourc.* 448 (2020) 227362.

14. Proskurina O.V., Sergeev A.A., Buryanenko I.V., Semenov V.G., Voznesenskiy S.S., Gusarov V.V., Crystal structure and optical properties of the Bi-Fe-W-O pyrochlore phase synthesized via a hydrothermal method, *J. Alloy. Comp.* 889 (2022) 161598.
15. Ito S., Chen P., Comte P., Nazeeruddin M.K., Liska P., Pechy P., Gratzel M., Fabrication of screen-printing pastes from TiO₂ powders for dye-sensitised solar cells, *Prog. Photovolt: Res. Appl.* 15 (7) (2007) 603–612.
16. Nikolskaia A., Vildanova M., Kozlov S., Tsvetkov N., Larina L., Shevaleevskiy O., Charge transfer in mixed-phase TiO₂ photoelectrodes for perovskite solar cells, *Sustainability.* 12 (3) (2020) 788.
17. Vildanova M.F., Nikolskaia A.B., Kozlov S.S., Shevaleevskiy O.I., Almjasheva O.V., Gusarov V.V., Group IV oxides for perovskite solar cells, *Dokl. Phys. Chem.* 496 (2) 2021 13–19.
18. Kozlov S.S., Larina L.L., Nikolskaia A.B., Almjasheva O.V., Proskurina O.V., Shevaleevskiy O.I., Solar cells based on complex oxides, *Tech. Phys. Lett.* 47 (4) (2021) 283–286.
19. Tauc J., Grigorovici R., Vancu A., Optical properties and electronic structure of amorphous germanium, *Phys. Status Solidi.* 15 (2) (1966) 627–637.
20. Wang L., Ma C., Wu T., Ma H., Yuan G., Chang L., Wang J., Ferroelectric BiFeO₃ as an oxide dye in highly tunable mesoporous all-oxide photovoltaic heterojunctions, *Small.* 13 (1) (2017) 1602355.

THE AUTHORS

NIKOLSKAIA Anna B.
 anickolskaya@mail.ru
 ORCID: 0000-0002-7430-4133

KARYAGINA Olga K.
 olgakar07@mail.ru
 ORCID: 0000-0002-6702-5195

KOZLOV Sergey S.
 sergeykozlov1@gmail.com
 ORCID: 0000-0002-8660-5646

ALMJASHEVA Oksana V.
 almjasheva@mail.ru
 ORCID: 0000-0002-6132-4178

ALEXEEVA Olga V.
 alexol@yandex.ru
 ORCID: 0000-0001-8982-3959

GUSAROV Victor V.
 victor.v.gusarov@gmail.com
 ORCID: 0000-0003-4375-6388

VILDANOVA Marina F.
 mvildanova@sky.chph.ras.ru
 ORCID: 0000-0002-5720-6048

SHEVALEEVSKIY Oleg I.
 shevale2006@yahoo.com
 ORCID: 0000-0002-8593-3023

Received 28.10.2022. Approved after reviewing 08.11.2022. Accepted 08.11.2022.

EXPERIMENTAL TECHNIQUE AND DEVICES

Conference materials

UDC 62-932.2

DOI: <https://doi.org/10.18721/JPM.161.173>

Temperature effect on spectral irradiance blurring of solar radiation by Fresnel lens sunlight concentrators

E.D. Filimonov ¹✉, S.A. Levina ¹, M.Z. Shvarts ¹

¹ Ioffe Institute, St. Petersburg, Russia

✉ efilimonov@mail.ioffe.ru

Abstract. This work is devoted to the study of the effect of temperature on the spectral irradiance blurring (concentrated in the focal plane of a Fresnel lens) arising due to the inherent chromatic aberration (CA) of the lens. This paper presents equipment for recording both irradiance distribution and spectral irradiance redistribution for the radiation concentrated by a small-sized energy concentrator adapted to temperature measurements, as well as the results of a study of Fresnel lenses.

Keywords: Fresnel lens, chromatic aberration, solar simulator, photovoltaic concentrator

Citation: Filimonov E.D., Levina S.A., Shvarts M.Z., Temperature effect on spectral irradiance blurring of solar radiation by Fresnel lens sunlight concentrators. St. Petersburg State Polytechnical University Journal. Physics and Mathematics. 16 (1.1) (2023) 428–432. DOI: <https://doi.org/10.18721/JPM.161.173>

This is an open access article under the CC BY-NC 4.0 license (<https://creativecommons.org/licenses/by-nc/4.0/>)

Материалы конференции

УДК 62-932.2

DOI: <https://doi.org/10.18721/JPM.161.173>

Влияние температуры на спектральную «деформацию» солнечного излучения в фокусе линзы Френеля

Е.Д. Филимонов ¹✉, С.А. Левина ¹, М.З. Шварц ¹

¹ Физико-технический институт им. А.Ф. Иоффе РАН, Санкт-Петербург, Россия

✉ efilimonov@mail.ioffe.ru

Аннотация. В данной работе описывается методика и оборудование для регистрации пространственно-спектрального распределения сконцентрированного линзой Френеля излучения при различных температурах. Функционал экспериментального комплекса позволяет сканировать профиль освещенности на различном расстоянии от концентратора, а используемая процедура обработки регистрируемых сигналов обеспечивает получение совокупности данных, достаточных для расчета и оценки фотоэлектрических параметров линзовых концентраторов и прогнозирования энергетических характеристик пары «линза-солнечный элемент».

Ключевые слова: линза Френеля, хроматическая aberrация, имитатор солнечного излучения, фотоэлектрический концентратор

Ссылка при цитировании: Филимонов Е.Д., Левина С.А., Шварц М.З. Влияние температуры на спектральную «деформацию» солнечного излучения в фокусе линзы Френеля // Научно-технические ведомости СПбГПУ. Физико-математические науки. 2023. Т. 16. № 1.1. С. 428–432. DOI: <https://doi.org/10.18721/JPM.161.173>

Статья открытого доступа, распространяемая по лицензии CC BY-NC 4.0 (<https://creativecommons.org/licenses/by-nc/4.0/>)

Introduction

In state-of-the-art high performance photovoltaic modules for concentrating solar radiation, the use of Fresnel lenses (FL) has already become a standard. To date, FL with two configurations are usually used: monolithic, made of polymethyl methacrylate (PMMA) by hot pressing [1]; and composite, made of a pair of different materials glued together (“silicone on glass”, SiOG) [2]. The second type of FL is preferable. It has a number of advantages (high profile accuracy, high accuracy in reproducing the teeth angles, a decrease in the inactive area between the faces, as well as increased lens rigidity and profile protection due to glass). However, the characteristics of SiOG lenses are more susceptible to change under the temperature influence. There are two main reasons for this. First, the coefficient of linear thermal expansion (CLTE) of glass and silicone can differ by an order of magnitude (depending on the chosen brand of glass and silicone). Secondly, the refractive index of silicone changes significantly [3] with temperature (Fig. 1). The change in the refractive index shifts the focal length of the lens. A difference in CLTE causes the lens teeth deformation and increase in the tilt angle error. As a result, the refracted rays will be displaced [4–6]. Eventually, in the solar cell plane, the concentrated spot enhances. The spatial and spectral distributions of the radiation energy in the spot are also changed.

Depending on the region and the time of a year, photovoltaic modules are forced to operate in highly variable temperature conditions. The ambient temperature can be below zero in winter and exceed 40 °C in summer (the temperature of photovoltaic modules can rise even higher). The influence of temperature on the solar cells efficiency is well studied, while the influence on the FL optical characteristics requires further exploration. The first issue to be determined is the effect of temperature on the light flux spatial and spectral distribution in the focus. As a consequence, one can establish the temperature dependence of the FL efficiency.

The paper presents an approach to register the spatial-spectral distribution of concentrated radiation energy using a method developed in the Ioffe Institute PV laboratory. Experimental setup [7] was adapted for temperature measurements of small-sized concentrators. The measurement technique proposed in the paper is based on precision three-dimensional scanning of the “focal space” (the region between the FL and the double focus) with a fiber-optic spectrometer with an entrance aperture diameter of 100 μm. At each scanned point, the spectrum (350–1100 nm) is recorded with subsequent splitting into spectral sensitivity ranges of subcells of a multijunction solar cell (MJ SC). Further, by integrating and combining data, it is possible to obtain the spectral-spatial distribution (in a 3D image) of energy at a certain distance from the concentrator.

The lens under study was placed in an optical thermal chamber, which provides precise control of the FL temperature conditions. The resulting “spectral patterns” allow to trace the dynamics of changes in illumination profiles in strictly defined spectral ranges corresponding to the subcells sensitivity ranges.

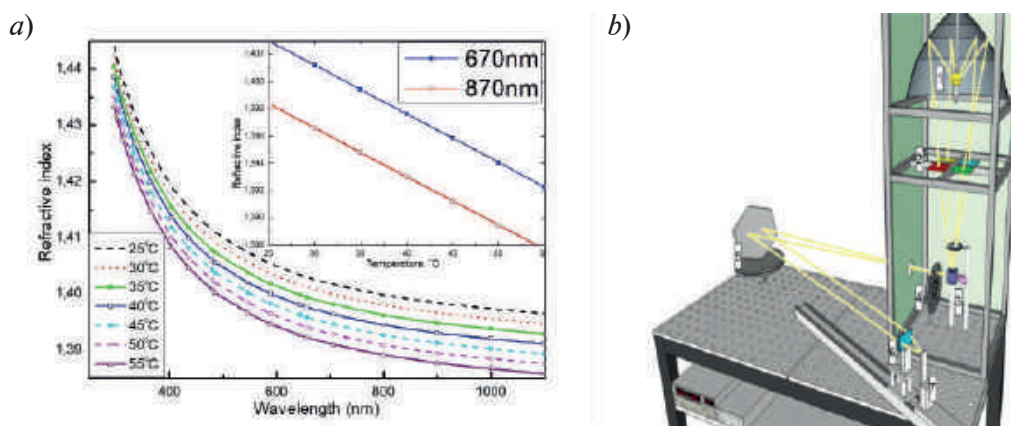


Fig. 1. Refractive index of silicone profile of Fresnel lenses (a). Optical scheme of experimental setup (b)

Experimental setup

The optical scheme of the measuring part of the setup for recording the spatial distribution of illumination is shown in Figure 2. Collimated light flux with a radiation divergence of 32 arcsec. min (which corresponds to the angular divergence of solar radiation) is directed to the studied FL. The lens is mounted on the $XYZ-\alpha\beta$ platform and oriented perpendicular to the light flux. The lens with the platform is placed in the thermal chamber. Several thermistors inside the chamber directly measure the current temperature of the FL during optical measurements and work as a feedback to maintain the set conditions. The chamber can maintain temperatures up to 60 degrees for a long time measurement. An optical fiber with an aperture of 100 μm plays the role of a receiver that scans the focal spot area. The second end of the fiber is connected to AvaSpec 2048 spectrometer. The position of the receiver is set by a precision XYZ automated coordinate device (controlled from a computer), which makes it possible to detect a radiation distribution profile with a high spatial resolution.

Measurement methodology

The measurement process begins with the determination of the light spot center focused by the lens in the design focus (105 mm) according to the developed technique [7]. Next, a scanning of the field along the XY axes (the size is determined by the spot diameter) of the focused radiation by the fiber receiver is performed. Spectral irradiance is recorded at each point in the wavelength range of 350–1100 nm, due to the sensitivity range of the spectrometer. Then the measuring fiber with the selected pitch (1 mm) is shifted along the optical axis (Z axis) relative to the design focus. In the new position, the field (slice) is also scanned along the XY axes. The operation is repeated for all selected points on the optical axis (approximately ± 10 mm relative to the design focus). Thus, we obtain a 3D representation of the radiation concentrated by the FL. The data enable to get complete analysis of the spatial-spectral distribution of the radiation above and below the focal plane relative to the design focus. Then the next temperature is set in the thermal chamber and after the lens temperature is stabilized, the registration of the “focal volume” is repeated.

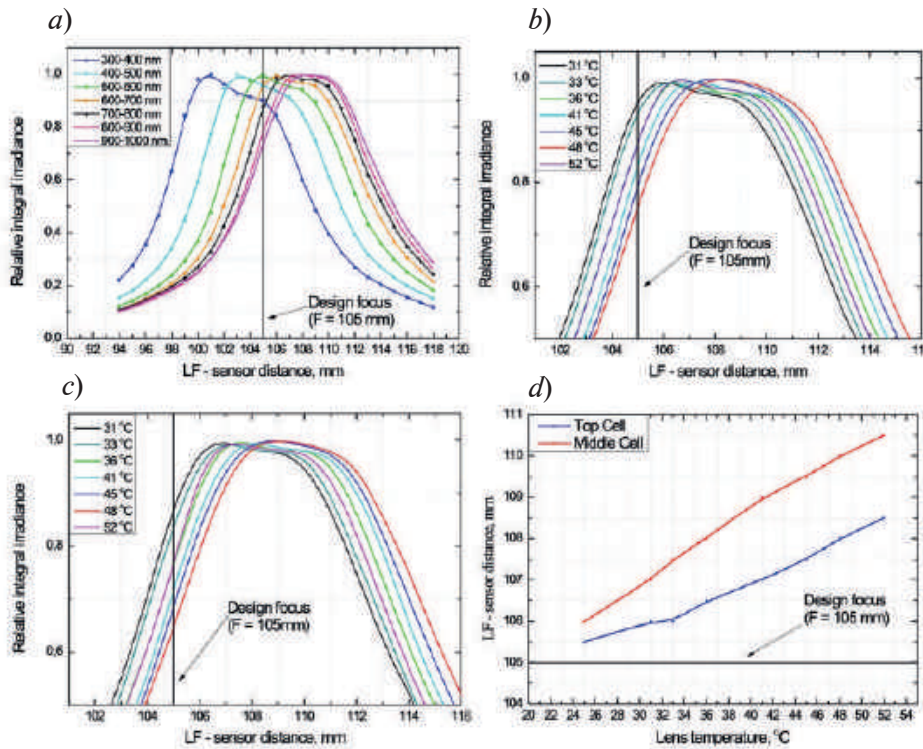


Fig. 2. The dependence of relative integral irradiance on the focal length for different spectral ranges. The temperature dependence of relative integral irradiance for spectral ranges corresponds to top GaInP (a) and middle GaAs (b) subcells sensitivities (c). The temperature dependence of focus distance for top (blue line) and middle (red line) subcells (d)



The measurement at each temperature turns out to be quite lengthy (approx. 10 000 points, each of which contains a spectrum in the range of 350–1100 nm). In order to facilitate data analysis, the spectral composition distribution recorded during the scanning process was integrated in several wavelength ranges (integration step is determined by the scanning task). Such a procedure makes it possible to form “color” energy patterns for the corresponding wavelength ranges typical for subcells of MJ SC.

The dependence of relative integral irradiance on the focal length (Fig. 3, *a*) for different spectral ranges (integration step 100 nm, registration point $X=0$, $Y=0$) occurs due to the effect of spectral blurring of light energy in the focal spot arising from chromatic aberrations. Experimentally recorded light energy blurring shows the real distances at which the maximum light focusing is provided for the selected energy ranges of solar radiation.

To make graphics readable, we take the ranges of the subcells maximum spectral sensitivity (top junction GaInP — 670 nm, middle junction GaAs — 870 nm). It can be seen from Fig. 3, *b* (GaInP) and Fig. 3, *c* (GaAs) that the main effect with increasing temperature is the displacement of the focal plane from the concentrating surface. It could be assumed that this happens because of the change in the refractive index (from Fig. 1, *b* it can be seen that the refractive index of silicone changes linearly and the rate of change is constant for the selected wavelengths). However, Fig. 3, *d* clearly shows that for the measured FL the linearity is preserved, but the rate of the focal length shift is higher for the longer wavelength spectrum (red line Fig. 3, *d*). It can be concluded that the second factor, CLTE, is involved in the focal length shifting. The change in the geometry of the refractive profile amplifies with the temperature rise and results in the displacement enhancing of the focal length from the surface of the concentrator.

Conclusion

The paper has presented the technique and equipment for recording the spatial-spectral radiation distribution of concentrated FL at various temperatures. The functionality of the experimental setup allows scanning the illumination profile at different distances from the concentrator. The procedure used for processing the recorded signals has provided a set of data sufficient to calculate and evaluate the photoelectric parameters of lens concentrators and predict the energy characteristics of the lens-solar cell pair.

It is known that temperature affects the characteristics of FL due to two main mechanisms: changes in the refractive index and deformation of the profile caused by CLTE. An increase in temperature has been shown to cause approximately linear shift of FL focal lengths for each wavelength. However, the temperature dependence of focal length shift for shorter wavelengths is slower than for longer ones. For a concentrated module, different rates of the focal length shifts depending on the wavelengths that cause an increase in focal spot size. As a result, optical efficiency will be reduced due to light scattering outside the active region of the solar cell. Therefore, when designing SiOG concentrators, it is necessary to take into account the operating temperature of the module and optimize parameters of the lens and the secondary optics, as well as, the photoconverter.

REFERENCES

1. Fassbender B., Ackermann J., Battenhausen P., Colburn P., Luffler U., Marks P.A., Reliability of PMMA for CPV lens applications, Materials Science Published, 10 (2011) 1808.
2. Shvarts M.Z., Andreev V.M., Gorohov V.S., Grilikhes V.A., Petrenko A.E., Soluyanov A.A., Timoshina N.H., Vlasova E.V., Zaharevich E.M., Flat-plate Fresnel lenses with improved concentrating capabilities: designing, manufacturing and testing, Proceedings of the 33rd IEEE Photovoltaic Specialists Conference, 2008, paper 403.
3. Schult T., Neubauer M., Bessler Y., Nitz P., Gombert A., Temperature Dependence of Fresnel Lenses for Concentrating Photovoltaics, Proc. of 2nd International Workshop on Concentrating Photovoltaic Optics and Power, 2009.
4. Rumyantsev V.D., Davidyuk N.Yu., Ionova E.A., Pokrovskiy P.V., Sadchikov N.A., Andreev V.M., Thermal Regimes of Fresnel Lenses and Cells in “All-Glass” HCPV Modules, AIP Conference Proceedings, 1277 (2010) 89–92.

5. **Büyükoşkun M., Annen H.P., González Mucoz L.F.**, Thermal deformation impacts on SOG Fresnel lens performance, AIP Conference Proceedings, 1477 (2012) 89–93.

6. **Hornung T., Kiefel P., Nitz P.**, The distance temperature map as method to analyze the optical properties of Fresnel lenses and their interaction with multi-junction solar cells, AIP Conference Proceedings, 1679 (2015) 070001.

7. **Filimonov E.D., Levina S.A., Shvarts M.Z.**, Experimental Equipment for Optical Characterization of Fresnel Lens Concentrators, AIP Conference Proceedings, 2012 (2018) 030005.

THE AUTHORS

FILIMONOV Evgeniy
efilimonov@mail.ioffe.ru
ORCID: 0000-0002-7711-2188

SHVARTS Maxim
shvarts@scell.ioffe.ru
ORCID: 0000-0002-2230-7770

LEVINA Svetlana
levina@mail.ioffe.ru
ORCID: 0000-0003-4554-3300

Received 20.10.2022. Approved after reviewing 09.11.2022. Accepted 05.12.2022.

Conference materials

UDC 533.9.08

DOI: <https://doi.org/10.18721/JPM.161.174>

Determination of discharge gas temperature with liquid non-metallic electrodes using the BOS method

Yu.A. Barinov ¹✉

¹Ioffe Institute, St Petersburg, Russia

✉ yury@mail.ioffe.ru

Abstract. Gas temperature is an important parameter in the study of atmospheric pressure plasma objects. The paper shows the possibility of determining the gas temperature of a discharge with liquid electrodes using the Background Oriented Schlieren (BOS) method. The discharge burns in an open air atmosphere between a liquid cathode and a metal anode. Tap water is used as the cathode, and a molybdenum rod is used as the anode. Based on the features of the BOS method and the geometry of the optical scheme, the main sources of errors are noted. The obtained temperatures are compared with the previously obtained results. It is shown that, taking into account the chosen geometry of the optical scheme, the results are in good agreement.

Keywords: background oriented schlieren, schlieren method, plasma diagnostics, non-equilibrium air plasma

Citation: Barinov Yu.A., Determination of discharge gas temperature with liquid non-metallic electrodes using the BOS method, St. Petersburg State Polytechnical University Journal. Physics and Mathematics. 16 (1.1) (2023) 433–437. DOI: <https://doi.org/10.18721/JPM.161.174>

This is an open access article under the CC BY-NC 4.0 license (<https://creativecommons.org/licenses/by-nc/4.0/>)

Материалы конференции

УДК 533.9.08

DOI: <https://doi.org/10.18721/JPM.161.174>

Определение температуры газа разряда с жидкими неметаллическими электродами с помощью BOS метода

Ю.А. Баринов ¹✉

¹Физико-технический институт им. А.Ф. Иоффе РАН, Санкт-Петербург, Россия

✉ yury@mail.ioffe.ru

Аннотация. Газовая температура — важный параметр при исследовании плазменных объектов атмосферного давления. В работе показана возможность определения газовой температуры разряда с жидкими электродами с помощью *фоново-ориентированного шлирен метода* (Background Oriented Schlieren – BOS). Исходя из особенностей BOS метода и геометрии оптической схемы, отмечены основные источники ошибок. Выполнено сравнение определенных температур с ранее полученными результатами. Показано, что с учетом выбранной геометрии оптической схемы результаты имеют хорошее согласие.

Ключевые слова: шлирен метод, диагностика плазмы, неравновесная плазма воздуха

Ссылка при цитировании: Баринов Ю.А. Определение температуры газа разряда с жидкими неметаллическими электродами с помощью BOS метода // Научно-технические ведомости СПбГПУ. Физико-математические науки. 2023. Т. 16. № 1.1. С. 433–437. DOI: <https://doi.org/10.18721/JPM.161.174>

Статья открытого доступа, распространяемая по лицензии CC BY-NC 4.0 (<https://creativecommons.org/licenses/by-nc/4.0/>)

Introduction

The heavy component temperature or gas temperature is an important parameter in the study of atmospheric pressure plasma objects. For example, for generators of low-temperature nonequilibrium plasma, the ratio of gas temperature to electron temperature is of interest. If the gas temperature reaches several thousand degrees, then non-contact methods, such as spectroscopic methods, are most often used for diagnostics. Among non-contact methods, the schlieren method can be noted. This method has been known for a long time, but due to difficulty of the organization, it is used mainly for the study of shock waves. Recently, because of the development of software and photo/video recording equipment, this method has received a new impetus. The new method is based on the principles of the schlieren method [1, 2], but due to computer processing of the obtained images, it has become much easier to the experiment organization. The new method has a well-established name Background Oriented Schlieren (BOS) method. To implement the method, the object under study is placed in front of the background screen. The background screen is, for example, a sheet of paper filled with dots. The rays reflected from the background screen pass through the object under study and are deflected under the action of density nonhomogeneity. This is registered as a background screen dot shift. The software used [3] determines the amount of shift. After that, using the geometry of the optical scheme, the deflection angle of the rays is calculated, and hence the refractive index of the medium n . In the case of neutral gas, such as air, the density has a simple relationship with the refractive index n_{air} through the well-known Gladstone-Dale equation: $n_{air} - 1 = G\rho$, where n_{air} is the refractive index of air, G is the Gladstone-Dale constant, and ρ is the density of the medium. The constant G depends on the properties of the medium and the wavelength used. If the ideal gas law is satisfied for the object of study, it allows us to determine the temperature. The method is also applicable to the study of weakly ionized plasma. The contribution to the refractive index is made by both free and bound electrons. In this case, the effect of free electrons on the refractive index is much stronger. If the degree of ionization is not too high (< 0.001), then this influence can be neglected. If the discharge burns in air atmosphere, then various NO, OH, etc. radicals, O, H atoms, and also water vapor can be present in the plasma. Significant concentrations of these particles can affect the refractive index.

In [4, 5], the possibility of using the BOS method to determine the temperature of the discharge gas with liquid non-metallic electrodes was considered. This discharge in various configurations was studied earlier [6–8] The gas temperature was determined using spectroscopic methods. It is of interest to determine the temperature by an alternative method. In this paper, an attempt was made to determine the gas temperature using the BOS method.

Experimental setup

Discharge configuration with liquid cathode and metal anode is selected. The anode is a molybdenum rod 3 mm in diameter. The cathode is tap water. To avoid water overheating, a small duct is organized in the anode tank. The discharge burns in open air atmosphere. A photograph of the discharge is shown in Fig. 1.

In this configuration, the discharge has axial symmetry, which makes it possible to use the inverse Abel transform in processing [5]. In Fig. 2 the optical scheme of the experimental setup is shown.

The discharge is powered through a ballast resistance from a DC source with an adjustable output voltage of up to 4000 V. The discharge current can vary over a wide range from 20 mA to 200 mA. The experiment was carried out at a fixed current of 60 mA and an interelectrode gap of 6–7 mm. The image was recorded by a camera with a matrix size of 17.3×13 mm² and a lens with a focal length of. The 150 mm minimum focusing distance for this lens is 900 mm. A background screen with a regular arrangement of dots (background patterns) was used. Such a background screen simplifies image computer processing. The background screen was illuminated by a flash. Distance $A = 745$ mm, $B = 187$ mm.

Data treatment

The resulting images were processed by a developed python program. The program was written specifically for this experiment. At the moment, there are several programs for image processing

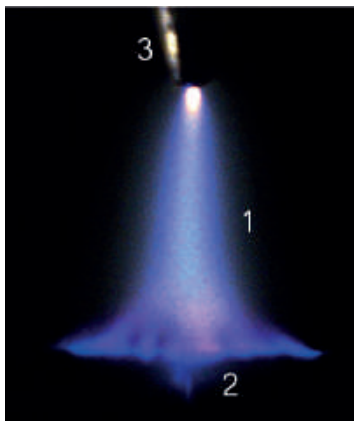


Fig. 1. Photo of discharge with a metal anode and a cathode from tap water in a stationary air atmosphere. 1 — discharge, 2 — water cathode, 3 — metal anode

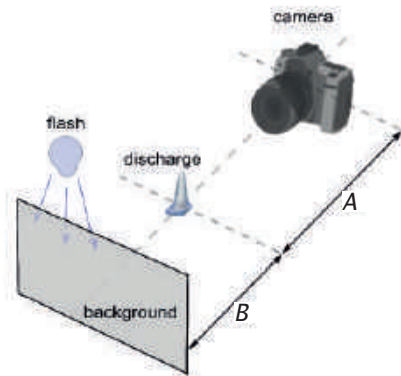


Fig. 2. Optical scheme of the experimental setup, $A = 745$ mm, $B = 187$ mm

using the BOS method, the most famous of them is PIVLAB [9]. As shown by preliminary studies [4, 5] for the chosen geometry, these programs can give a noticeable error. The developed program uses a different method for shift calculating and allows you to control the processing process.

Let us consider the main sources of errors. This, as it was found in [4], is blurring of the point contour. Disturbance of the axial symmetry of the plasma channel caused by convection and instability of the surface of the water electrode. Insufficient spatial resolution, due to the peculiarities of the BOS method. Since the camera focuses on the background screen, and not on the study object. It can also be noted the weak dependence of the refractive index on temperature at high temperatures of the medium (more than 1500 K). For processing, a region approximately 1–1.5 mm above the water electrode was cut out from the obtained images. The area close by to the water electrode, due to the presence of water vapor, has a noticeable effect on the refractive index, which leads to a distortion of the temperature profile. The treatment area was divided into 6 equal sections of ≈ 0.8 mm size. The temperature was calculated for each area. To minimize the processing error, the experiment was repeated many times. The most symmetrical ones were selected from the data set. The point shift contour obtained at the first processing step was divided into two halves, and then the halves were processed independently. Fig. 3 shows a typical view of the point shift contour. The obtained data were filtered, distant points were removed, and smoothing was performed.

As a result, the variation of temperature along the radius was calculated. The calculation is described in more detail in [5]. An example of the calculation result for the middle of the interelectrode gap is shown in Fig. 4.

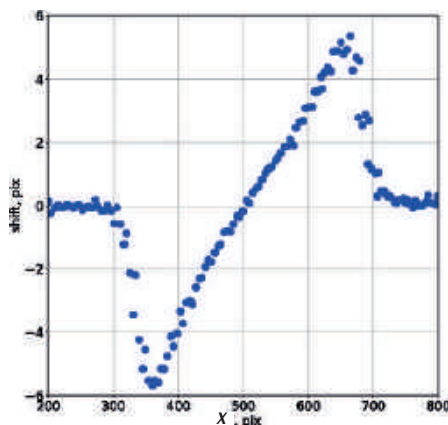


Fig. 3. Point shift contour

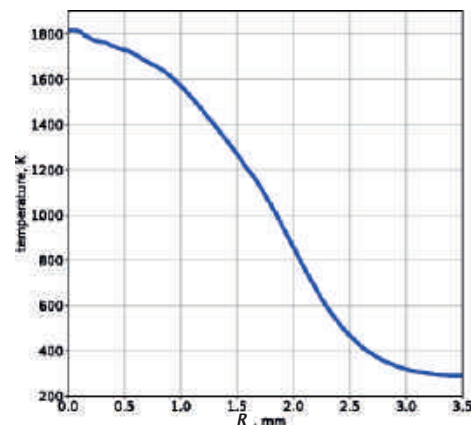


Fig. 4. Radial temperature distribution

It can be seen that the maximum temperature is reached on the discharge axis. It should be noted that due to insufficient spatial resolution, the values of spatial coordinates should be considered as approximate. An estimate of the spatial resolution gives a value of about 0.7–0.8 mm. Temperature calculations were performed for six sections of the interelectrode gap (Fig. 5).

The result of the temperature distribution in the interelectrode gap on the discharge axis is shown in Fig. 6. Starting from the cathode, the temperature rises slightly, and then slowly drops towards the anode.

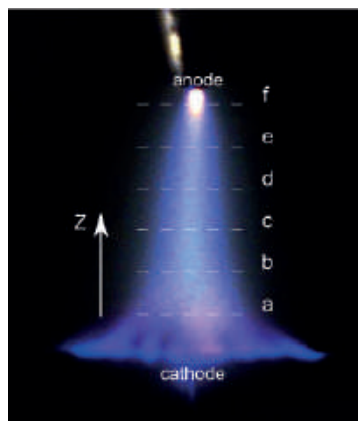


Fig. 5. Photo of discharge with measurement points

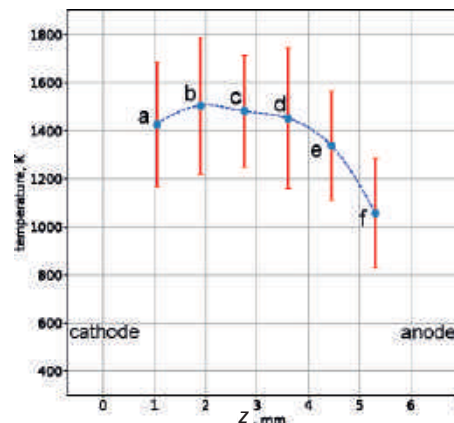


Fig. 6. Temperature distribution in the interelectrode gap

Conclusion

Let us compare the obtained temperature values with the results obtained using spectroscopic methods. In [6], the gas temperature of the discharge with liquid nonmetallic electrodes was determined. The temperature on the discharge axis reached a value of 2000 K. This value is noticeably higher than the value obtained in this work. This can be explained by the low spatial resolution. In [10], it was shown that the brightest region is on the axis of the discharge. At currents of 100–300 mA, the area has a diameter of 0.7–0.9 mm. This area can be considered the highest temperature. Thus, a rather narrow region on the discharge axis is averaged with the neighboring region where the temperature is lower, which results in a lower overall temperature. In view of the foregoing, the result obtained is in good agreement with experiment [6]. In the future, it is planned to carry out measurements with high currents. In addition, one can try to improve the spatial resolution by deconvolution of the result with a hardware function. The BOS method is interesting for its simplicity of organization and at the same time it allows obtaining not only qualitative, but also quantitative results. At the same time, depending on the geometry of the optical scheme, there may be problems with spatial resolution. Since this is a feature of the BOS method, unfortunately this influence can not always be minimized.

REFERENCES

1. Richard H., Raffel M., Measurement Science and Technology. 12 (2001) 1576–1585.
2. Raffel M., Exp. Fluids 56, (2015).
3. Raffel M., (ed), Particle image velocimetry: a practical guide 2nd ed, (Springer), 2007.
4. Barinov Y.A., Technical Physics Letters. 45 (2019) 632–634.
5. Barinov Y.A., Journal of Visualization. 24 (2021) 1131–1139.
6. Andre P., Barinov Y., Faure G., Kaplan V., Lefort A., Shkol'nik S., Vacher D., J. Phys. D: Appl. Phys. 34 (2001) 3456–3465.
7. Andre P., Aubreton J., Barinov Y., Elchinger M. F., Fauchais P., Faure G., Kaplan V., Lefort A., Rat V., Shkol'nik S., J. Phys. D: Appl. Phys. 35 (2002) 1846–1854.
8. André P., Barinov Y.A., Faure G., Shkol'nik S.M., J. Phys. D: Appl. Phys. 51 (2018) 1361–6463.
9. Thielicke W. and Stamhuis E.J., Pivlab - time-resolved digital particle image velocimetry tool for



matlab. URL: https://figshare.com/articles/online_resource/PIVlab_version_1_35/1092508. Accessed Oct. 19, 2022.

10. **Barinov Y.A., Shkol'nik S.M.**, Technical Physics. 61 (2016) 1760–1763.

THE AUTHORS

BARINOV Yury

yury@mail.ioffe.ru

ORCID: 0000-0002-0329-5743

Received 25.10.2022. Approved after reviewing 08.11.2022. Accepted 08.11.2022.

Conference materials

UDC 539.1.08

DOI: <https://doi.org/10.18721/JPM.161.175>

Shaping amplifier for soft X-ray spectrometer with a silicon drift detector

Yu.V. Tuboltsev ¹✉, Yu.V. Chichagov ¹, A. A. Bogdanov ¹, M.Yu. Kantor ¹, A.V. Sidorov ¹

¹Ioffe Institute, St. Petersburg, Russia

✉ tuboltsev@mail.ioffe.ru

Abstract. The paper presents a shaping amplifier developed to boost the count rate of a soft X-ray spectrometer AMPTEK based on a fast silicon drift detector (SDD). The amplifier differentiates step-like signals from the charge sensitive preamplifier of the SDD and gains the output signals for digitizing. The rise time of the output signals is reduced in regards with that of the AMPTEK shaping amplifier whereas the noise of these amplifiers is kept at the same level. The shorter rise time allows better resolution of closely overlapped output pulses and reduces the pile-up effects at high input count rates. The design of the amplifier is presented in the paper as well as its tests for noise, linearity and resolution of close overlapped pulses.

Keywords: shaping amplifier, VGA, PX-5, SDD

Funding: The design and construction of the shaping amplifier described in Section 2 were supported by Ioffe Institute under State Contract No. 0034-2021-0001 and data analysis in Section 3 was supported by Ioffe Institute under State Contract No. 0040-2019-0023.

Citation: Tuboltsev Yu.V., Chichagov Yu.V., Bogdanov A.A., Kantor M.Yu., Sidorov A.V., Shaping amplifier for soft X-ray spectrometer with a silicon drift detector. St. Petersburg State Polytechnical University Journal. Physics and Mathematics. 16 (1.1) (2023) 438–443. DOI: <https://doi.org/10.18721/JPM.161.175>

This is an open access article under the CC BY-NC 4.0 license (<https://creativecommons.org/licenses/by-nc/4.0/>)

Материалы конференции

УДК 539.1.08

DOI: <https://doi.org/10.18721/JPM.161.175>

Усилитель-формирователь для рентгеновского спектрометра с кремниевым дрейфовым детектором

Ю.В. Тубольцев ¹✉, Ю.В. Чичагов ¹, А.А. Богданов ¹, М.Ю. Кантор ¹, А.В. Сидоров ¹

¹Физико-технический институт им. А.Ф. Иоффе РАН, Россия

✉ tuboltsev@mail.ioffe.ru

Аннотация. В статье описывается усилитель-формирователь, разработанный для увеличения скорости счета спектрометра мягкого рентгеновского излучения AMPTEK на основе быстрого кремниевого дрейфового детектора (SDD). Усилитель дифференцирует ступенчатые сигналы с зарядочувствительного предусилителя SDD и усиливает выходные сигналы для последующей оцифровки. Усилитель-формирователь обеспечивает меньшее время нарастания выходных сигналов по сравнению с усилителем-формирователем AMPTEK, в то время как шум этих усилителей остается на прежнем уровне. Уменьшение времени нарастания позволяет лучше разрешать наложенные выходные импульсы и уменьшает эффект возрастания общего уровня при высокой скорости счета входных сигналов. В статье представлена структура усилителя, а также его испытания на шум, линейность и разрешение наложенных импульсов.

Ключевые слова: усилитель-формирователь, VGA, PX-5, SDD

Финансирование: Проект и устройство усилителя-формирователя, описанные в



Секции 2, были поддержаны ФТИ им. А.Ф. Иоффе в рамках Государственного контракта № 0034-2021-0001. Анализ данных в Секции 3 поддержаны ФТИ им. А.Ф. Иоффе в рамках Государственного контракта № 0040-2019-0023.

Ссылка при цитировании: Тубольцев Ю.В., Чичагов Ю.В., Богданов А.А., Кантор М.Ю., Сидоров А.В. Усилитель-формирователь для рентгеновского спектрометра с кремниевым дрейфовым детектором // Научно-технические ведомости СПбГПУ. Физико-математические науки. 2023. Т. 16. № 1.1. С. 438–443. DOI: <https://doi.org/10.18721/JPM.161.175>

Статья открытого доступа, распространяемая по лицензии CC BY-NC 4.0 (<https://creativecommons.org/licenses/by-nc/4.0/>)

Introduction

A soft X-ray spectrometer is developed in the Ioffe Institute for measurements of the Bremsstrahlung emission from plasma of the FT-2 tokamak [1] with the use an AMPTEK spectrometer based on a silicon drift detector (SDD) 70 mm² FASTSDD [2] and digital pulse processor (DPP) PX-5 [3]. The spectrometer is designed for high-resolution spectral measurements up to count rates 10⁶ 1/s in the energy range of photons from 0.5 to 30 keV. Higher energies are also detectable, but at less efficiency. A charge sensitive preamplifier integrated in the detector provides a step-like response on the detected photons with sensitivity 3.2 mV/keV. The detector window was collimated to 17 mm² for better energy resolution. The photon impact points in the collimated depleted region are close to the anode and the rise time of the step signals vary in the narrowest range from 15 ns to 65 ns. The rise time of pulses here and further is measured between 20% and 80% levels to the pulse amplitude. The step amplitude ranges from 2 mV to 1.7 V in the energy measurement range. The step-like signals are shaped in the PX-5 module to pulses with rise time ~ 65 ns and falling exponential tail with characteristic time 3.2 μs. The shaped pulses are digitized at 80 MHz sampling rate and processed in PX-5. The selected rise time is a tradeoff between the highest count rate and the best energy resolution of the spectrometer.

The measurements in the FT-2 tokamak require higher count rate at the same energy resolution. For that, another shaping amplifier with shorter rise time and the same output noise is designed to provide better detection of overlapped pulses. The shaped output will be digitized and processed outside the PX-5 with the use of the same or special algorithms [4–6].

Design of shaping amplifier

The schematic layout of the amplifier is presented in Fig. 1. The 1 kΩ input of the amplifier is connected to the output of the charge sensitive preamplifier of the detector. The input signal is doubled by operation amplifier DA1, differentiated in RC circuit with switchable resistors (R2...R5) and buffered by DA2. The RC circuit determines the exponential falling time of the output pulses in the range from 2 μs to 17 μs. Resistors (R2...R5) are grounded through analog switches (S1...S4) to avoid extra inductance and capacitance in the circuit. The analog switches are installed on the printed circuit board and activated by toggle switches (T1...T4) on the case of the device. The buffered signal splits in channel A and channel B having different gains to expand the measurement range of photon energies. The channels have variable gain amplifiers (VGA) DA3 and DA4. The gain in channel A and B varies from 5 to 40 and from 1 to 6 correspondingly. The gain is controlled by multi-turn potentiometers R6 and R7 connected to the reference voltage 1.225 V. Amplifiers DA5 and DA6 doubles the signals and match them to the 50 Ω inputs of digitizers.

The gain of channel A is set in the range from 10 to 80 for measurements of photon energies up to 50 keV. The gain of channel B is set from 2 to 12 for measurements of photons with energies more than 30 keV. The output pulses are formed with the least rise time providing the output noise ~ 45 eV at the level of the shaping amplifier in PX-5 module.

Test of the shaping amplifier

The amplifier has been tested with FASTSDD detector of AMPTEK and a ⁵⁵Fe isotope source radiating at ~ 25000 photon/s on the detector area. A generator of rectangular pulses with a sharp

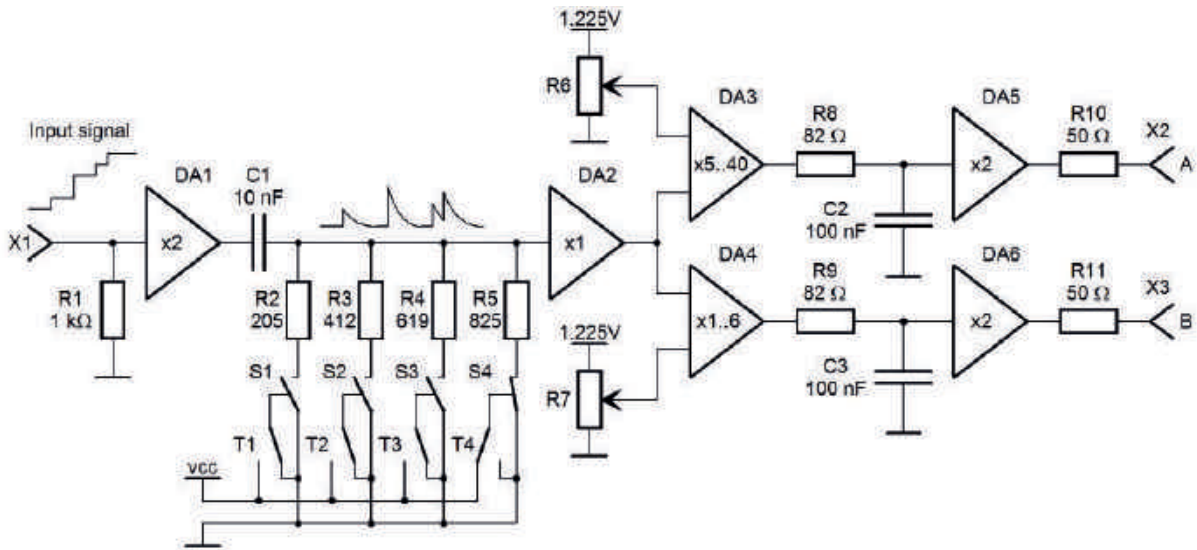


Fig. 1. Schematic layout of the amplifier

rise time of 20 ns and of switchable accurate standard amplitudes was also used for testing the amplifier. The output signals of the amplifier and PX-5 were recorded by an ADC at 250 MHz, 14 bits resolution produced by InSys [7] or a digital scope Agilent Technologies MSO9440A with 10 bits resolution and analog bandwidth 4 GHz. The recorded signals were smoothed with a digital low pass RC filter with a cut-off frequency 40 MHz. The filter dumps the noise dominated part of the spectra and does not affect the spectrum and shape of the output pulses from the PX-5 and amplifier units.

Output noises of the PX-5 and amplifier were measured in the whole gain range with the use of InSys ADC 250 MHz and plotted in Fig. 2, *a*, in eV units. Noise of the PX-5 amplifier increases from 45 eV to 130 eV when its gain reduces from 12 to 2. Channel B of the amplifier shows a similar behavior with the excess noise factor ~ 1.5 . In spite of higher absolute values, the relative noise in channel B is much less than 1% because the channel is designed for a high energy range 30–500 keV. Channel A exhibits lower absolute noise from 40 eV to 55 eV.

Amplitude spectra of the noises and output signals of PX-5 and amplifier are shown in Fig. 2, *b*. The spectra decay linearly with the frequency up to 2.4 MHz and 6.4 MHz for PX-5 and amplifier signals correspondingly. These cut-offs are inversely proportional to the rise time of the output pulses [5].

The front edges of the PX-5 and amplifier pulses along with the step-like detector signals measured with the digital scope are presented in Fig. 3, *a*. The shown detector response has the rise time 35 ns which is the mean rise time of the steps. The detector noise is 1.2 mV or 380 eV rms. The response pulses from PX-5 and amplifier shown by dashed traces have the rise times 83 ns

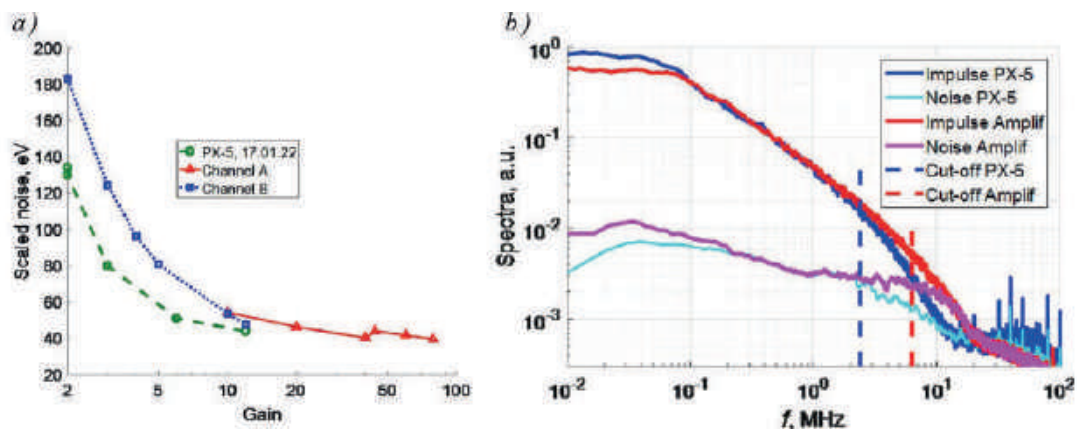


Fig. 2. Diagrams of output noise of PX-5 and amplifier on the gain (*a*), amplitude spectra of noise and signals (*b*)

and 46 ns correspondingly. The noise of the both responses is 45 eV rms. The amplifier pulse was recorded from channel A at gain 20 and reduced to the PX-5 pulse with coefficient 0.15. A solid green trace represents a step pulse from the pulse generator with a shorter rise time 19 ns and less noise 25 eV. This pulse is shaped to a pulse represented with a green dotted trace with rise time 34 ns and noise 23 eV rms. These low noises generator with variable amplitudes is used for calibration of the spectrometer in the whole energy range.

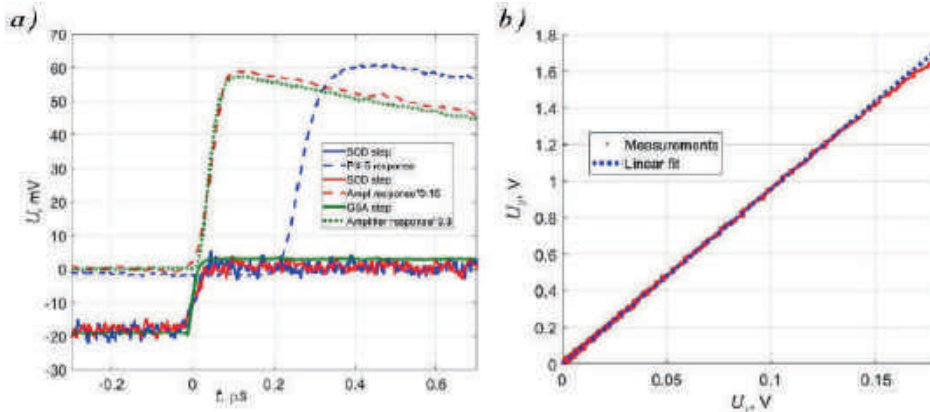


Fig. 3. Front edges of impulse responses on a photon of 5.9 keV (a), linearity of amplifier (b)

The output pulses of the amplifier maintain the shape and linearity in a wide range of output voltage. Linearity of the amplifier is shown in Fig. 3, b, by the dependence between the instant voltages of two synchronized output pulses U_1 and U_2 measured at the minimal and maximal gains in channel A, red dots. The measurements correspond to the linear fit shown by a dashed blue line up to 1.5 V of the output voltage. The signals are saturated at 1.8 V.

Low noise and short rising time of the amplifier provide better resolution of two overlapped pulses. This advantage is illustrated in Fig. 4, a, which shows two overlaps of two identical pulses. The first pulses in the overlaps were taken from PX-5 and amplifier outputs with noises and normalized to their amplitudes. The normalized pulses were delayed by 100 ns and sum to the first ones. The pulses from PX-5 and amplifier are shown in blue and red solid traces. The both overlaps do not have any peaks corresponding to the single pulses. The peaks appear in the overlaps after digital filtering. Usually, trapezoidal filtering [8] is applied in pulse detection algorithms [4].

The overlapped signals of PX-5 and amplifier filtered by a trapezoidal filter with a peaking time 50 ns and flat top 20 ns are plotted in blue and red dashed traces. The peaking time 50 ns is used in the fast channel of DPP PX-5. The trapezoidal pulse from PX-5 has an asymmetrical shape with an extended tail, whereas the shape of the trapezoidal pulse from the amplifier keeps a symmetrical form. This difference is accounted by a larger rise time of the PX-5 pulses [5].

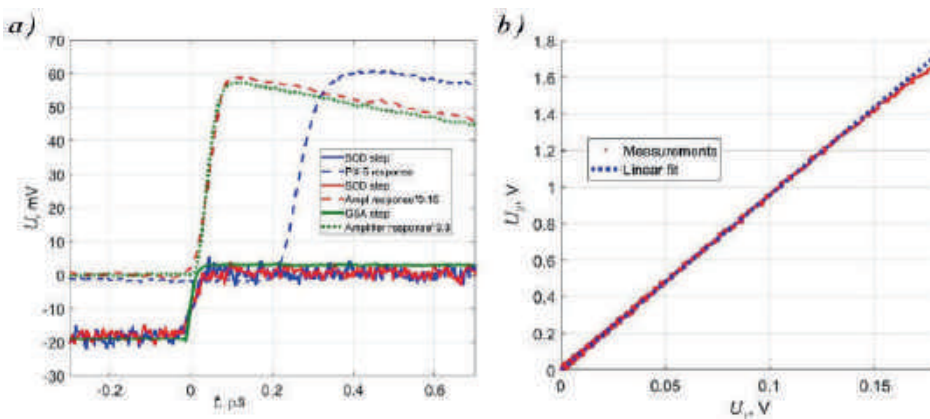


Fig. 4. Overlapped pulses from PX-5 and amplifier and overlapped trapezoidal pulses (a), peak amplitudes of two overlapped trapezoidal pulses (b)

The peak amplitudes of two overlapped trapezoidal pulses depend on the lag time between them, see Fig. 4, *b*. At large lags, the peaks from overlapped trapezoidal pulses are detected with biasing-free unit amplitudes. At lags shorter than 200 ns the amplitude of second peaks from PX-5 gets higher than the first one because of asymmetry of the trapezoidal pulses. The difference in the peak amplitudes increases while the lag is decreasing to 80 ns. At this lag the only peak remains in the overlapped signal. A blue dashed vertical line defines a threshold when the deepness of the valley between two peaks is less than 10% of the peak height.

Thus, two peaks of identical trapezoidal pulses from PX-5 are detected with their correct amplitudes while the lag is greater than ~ 170 ns. The amplitude of the second peak is biasing up to 15% when lag is decreasing to 90 ns. On the other hand, two peaks of the trapezoidal pulses from the amplifier are detected without biasing down to ~ 80 ns lag, which is close to the threshold lag of detection of overlapped pulses from the amplifier.

Conclusion

The designed shaping amplifier allows better resolution of overlapped impulse responses of Silicon Drift Detector FASTSDD than does Digital Pulse Processor PX-5 of AMPTEK Inc. This advantage is provided by a shorter rise time of output pulses and similar noise of the amplifier in regards with those of the internal amplifier in PX-5 module of AMPTEK spectrometer. The rise time affects significantly the distortion of trapezoidal pulses which restricts the least lag between the detected pulses.

The developed amplifier provides two parallel outputs with identical pulse forms and independently controlled gains. One channel with higher gain intentionally measures spectra in lower energy region up to 50 keV. The second channel with lower gain operates in a higher energy region up to 500 keV.

Better resolution of overlapped pulses provided by the shaping amplifier allows a higher count rate of the spectrometer. This possibility is presented, discussed and tested in [9].

Acknowledgment

The design and construction of the shaping amplifier described in Section 2 were supported by Ioffe Institute under State Contract No. 0034-2021-0001 and data analysis in Section 3 was supported by Ioffe Institute under State Contract No. 0040-2019-0023.

REFERENCES

1. **Lashkul S. I., et al.**, Effect of the radial electric field on lower hybrid plasma heating in the FT-2 tokamak, *Plasma Phys. Rep.* 27 (2001) 1001.
2. **Kantor M.Yu., Sidorov A.V.**, Shaping pulses of radiation detectors into a true Gaussian form, *JINST* 14 (2019) P01004.
3. **Kantor M.Yu., Sidorov A.V.**, Detection of true Gaussian shaped pulses at high count rates. *JINST* 15 (2020) P06015.
4. **Jordanov V.T., Knoll G.F. et al.**, Digital techniques for real-time pulse shaping in radiation measurements, *Nucl. Instrum. Meth. A* 353 (1994) 261.
5. **Kantor M.Yu., Sidorov A.V., Bogdanov A.A., Tuboltsev Yu.V., Chichagov Yu.V.**, A soft X-ray spectrometer with enhanced output count rate, *St.Petersburg State Polytechnical University Journal. Physics and Mathematics.* 16 (1.1) (2023) 484–490. DOI: <https://doi.org/10.18721/JPM.161.182>
6. **Redus R.**, *Digital Pulse Processors, Theory of Operation* (Amptek Inc), 2009.
7. AMPTEK 70 mm² FAST SDD, URL: <https://www.amptek.com/-/media/ametekamptek/documents/products/specs/amptek-fastsdd-70-mm-detector.pdf>
8. AMPTEK digital pulse processor, URL: <https://www.amptek.com/products/digital-pulse-processors/px5-digital-pulse-processor>
9. InSys Corp. ADC module FM814x250M, URL: <https://www.insys.ru/mezzanine/fm814x250m>



THE AUTHORS

TUBOLTSEV Yuriy V.

tuboltsev@mail.ioffe.ru

ORCID: 0000-0001-9770-0158

CHICHAGOV Yuriy V.

chichagov@mail.ioffe.ru

ORCID: 0000-0002-2679-6380

BOGDANOV Alexander A.

Alexander.A.Bogdanov@mail.ioffe.ru

ORCID: 0000-0002-5275-5603

KANTOR Michael Yu.

m.kantor@mail.ioffe.ru

ORCID: 0000-0001-9512-2155

SIDOROV Anton V.

sidorov@mail.ioffe.ru

ORCID: 0000-0002-6509-2781

Received 24.10.2022. Approved after reviewing 09.11.2022. Accepted 25.11.2022.

Conference materials

UDC 536.629.7

DOI: <https://doi.org/10.18721/JPM.161.176>

Analysis of thermal and thermoelectric processes in heat flux sensors based on layered metal structures

P.A. Popov¹✉, N.A. Monakhov¹

¹Ioffe Institute, Saint-Petersburg, Russia

✉ pavel.popov@mail.ioffe.ru

Abstract. The results of calculating the temperature and electric potential in the sensitive element of a heat flux sensor based on a layered metal structure of chromel-alumel and copper-nickel pairs in a stationary thermal regime using a two-dimensional and one-dimensional model are presented. The influence of the effective thermal conductivity of the structure on the temperature distribution and the generated thermoelectric power is shown. The possibility of using a one-dimensional homogeneous model with effective properties for describing thermal and thermoelectric processes in the sensitive element of the sensor is considered.

Keywords: layered metal structure, heat flux sensor, measurements

Citation: Popov P.A., Monakhov N.A. Analysis of thermal and thermoelectric processes in heat flux sensors based on layered metal structures, St. Petersburg State Polytechnical University Journal. Physics and Mathematics. 16 (1.1) (2023) 444–449. DOI: <https://doi.org/10.18721/JPM.161.176>

This is an open access article under the CC BY-NC 4.0 license (<https://creativecommons.org/licenses/by-nc/4.0/>)

Материалы конференции

УДК 536.629.7

DOI: <https://doi.org/10.18721/JPM.161.176>

Анализ тепловых и термоэлектрических процессов в датчиках теплового потока на основе слоистых металлических структур

П.А. Попов¹✉, Н.А. Монахов¹

¹Физико-технический институт им. А.Ф. Иоффе РАН, Санкт-Петербург, Россия

✉ pavel.popov@mail.ioffe.ru

Аннотация. Представлены результаты расчета температуры и электрического потенциала в чувствительном элементе датчика теплового потока на основе слоистой металлической структуры из пар хромель-алюмель и медь-никель в стационарном тепловом режиме с помощью двумерной и одномерной модели. Показано влияние эффективной теплопроводности структуры на распределение температуры и генерируемую термоэдс. Рассмотрена возможность применения одномерной однородной модели с эффективными свойствами для описания тепловых и термоэлектрических процессов в чувствительном элементе датчика.

Ключевые слова: слоистые металлические структуры, датчик теплового потока, измерения

Ссылка при цитировании: Попов П.А., Монахов Н.А. Анализ тепловых и термоэлектрических процессов в датчиках теплового потока на основе слоистых металлических структур // Научно-технические ведомости СПбГПУ. Физико-математические науки. 2023. Т. 16. № 1.1. С. 444–449. DOI: <https://doi.org/10.18721/JPM.161.176>

Статья открытого доступа, распространяемая по лицензии CC BY-NC 4.0 (<https://creativecommons.org/licenses/by-nc/4.0/>)



Introduction

One of the main tasks of modern experimental gas dynamics is the diagnostics of the heat flux to the surface of a body in a high-velocity gas flow. Of greatest interest are high enthalpy regimes, when the properties of a real gas are manifested and dissociation and ionization reactions begin to occur in the shock layer [1]. Under the conditions of a ground-based experiment, the creation of a high-enthalpy gas flow is possible only on short duration facilities. Therefore, the heat flux sensors used must have response time $\sim 10 \mu\text{s}$ with a measurement duration $\sim 10 \text{ ms}$, a wide dynamic range from $\sim 100 \text{ kW/m}^2$ to $\sim 10 \text{ MW/m}^2$ and sufficient mechanical strength.

In experiments on shock tubes, thin-film resistance sensors [2] and various thermoelectric sensors such as: coaxial thermocouples [3] based on anisotropic bismuth thermoelements and layered structures (GHFS, HGHFS and ALTP) [4, 5] are widely used. To the greatest extent, the above requirements are met by coaxial thermocouples and sensors based on layered metal structures (HGHFS). They have comparable sensitivity and speed. As experimental experience shows, the mechanical impact of the gas flow leads to a violation of the electrical contact in coaxial thermocouples and necessity of periodic recalibration. The metal layers in the HGHFS are connected to each other by diffusion welding; therefore, they have a significantly higher mechanical strength and the sensor parameters do not change during the experiments.

The key element in developing a methodology for processing measurement results is a correct mathematical model of thermal and thermoelectric processes in the sensitive element of the sensor. In the case of sensors based on anisotropic thermoelements and layered structures, when the ratio of the length to the thickness of the sensitive element $l/h \gg 1$ widely used approach is one-dimensional thermal and thermoelectric model [6]. It allows you to get a simple relationship between the electrical signal and the temperature difference between the working and back surfaces. This model is used for processing ALTP [5] and GHFS [7] signal. The sensing element of the HGHFS is a multilayer plate of a pair of metals with different thermal properties. This can lead to a difference in the temperature distribution from one-dimensional. Also, for a typical HGHFS, with $l/h \approx 10$ it requires an analysis of the applicability of the homogeneous medium model [8] for calculating the thermoelectric power.

The main objective of this work is to analyze thermal and thermoelectric processes in HGHFS and to evaluate the applicability of a one-dimensional model in a stationary thermal regime, when the effect of a layered structure on the temperature field is maximum. This will make it possible to obtain an upper estimate of the influence of the considered factors on the distribution of temperature and thermoelectric power. This is necessary to analyze the applicability of the technique [7] for processing the results of measuring the unsteady heat flux using the HGHFS.

Construction of heat flux sensor

The sensitive element of the HGHFS is a plate of alternating layers of metals (1) and (2) with a thickness δ_1 и δ_2 and with different Seebeck coefficient α_1 and α_2 oriented at an angle θ to the working surface (Fig. 1). The layers are connected to each other by diffusion welding. The plate is fixed on an electrically insulating substrate (3). Wires are soldered to the points *A* and *B* to register an electrical signal. For the manufacture of the sensitive element, metal pairs with the most different Seebeck coefficient are used: chromel-alumel, copper-nickel, steel-nickel, etc. [4]. The principle of operation of the HGHFS is based on the generation of a thermoelectric field in a structure with thermopower anisotropy when a temperature gradient appears [6].

Mathematical models

Consider two typical sensors with a sensitive element of chromel-alumel and copper-nickel pairs with length $l = 3 \text{ mm}$, width $w = 3 \text{ mm}$ and thickness $h = 0.5 \text{ mm}$. To analyze the influence of the thickness of metal layers on the temperature field and thermoelectric power, we consider the following typical values: $\delta_1 = \delta_2 = 0.10 \text{ mm}$, 0.15 mm , 0.20 mm with the total number of layers $N = 23, 18, 12$. The angle of inclination of the layers relative to the working surface of the sensor is $\theta = 45^\circ$.

Further, we will consider two models of thermal and thermoelectric processes in the sensitive element of the sensor. The first model takes into account the layered structure of the sensing

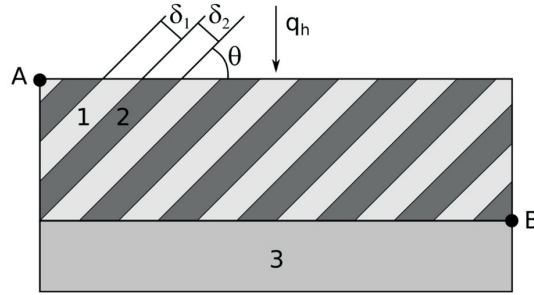


Fig. 1. The structure of the thermal sensor based on layered metal structure

element shown in Fig. 1. The computational domain is two-dimensional and is formed by a vertical section of the sensor and the substrate. We assume that ideal thermal and electrical contact is made between the metal layers. The stationary distribution of temperature $T(x, y)$ and electric potential $\varphi(x, y)$ is found from the solution of the system of equations [6]:

$$\begin{aligned} \operatorname{div} \mathbf{q} &= 0 \\ \operatorname{div} \mathbf{j} &= 0 \end{aligned}$$

where $\mathbf{q} = -\lambda \nabla T$, $\mathbf{j} = -\sigma \nabla \varphi - \sigma \alpha \nabla T$ are the heat flux and electric current density, λ , σ , α are the thermal conductivity, electrical conductivity and Seebeck coefficients. A constant heat flux $q_h = 1 \text{ MW/m}^2$ passes through the working surface of the sensor. The side faces are thermally insulated. A convective heat flux is set on the rear surface of the substrate to minimize the distortion of the temperature field in the sensing element. All surfaces of the sensing element are electrically insulated. The generated thermoelectric power $\Delta \varphi$ is registered between the points A and B . The numerical solution of the system of equations was carried out in the COMSOL Multiphysics package.

The second one-dimensional model uses the approximation of a homogeneous medium with effective properties. This assumption is applicable when the thickness of each layer is much less than the characteristic dimensions of the sensitive element [6]. It is assumed that the plate is sufficiently long and the temperature distribution can be considered one-dimensional, and the main contribution to the thermopower is made by the transverse component of the thermoelectric field. In this case, the thermoelectric power can be calculated by the formula [8]:

$$U = q_h l \frac{\alpha_1 - \alpha_2}{\lambda_1} \left(\frac{k_\delta}{k_\delta + k_p} - \frac{k_\delta}{k_\delta + k_\lambda} \right) \frac{1}{k_\xi \operatorname{tg} \theta + k_\eta \operatorname{ctg} \theta},$$

where α_1, α_2 are the Seebeck coefficients, $k_\delta = \delta_1/\delta_2$, $k_p = \rho_1/\rho_2$, $k_\lambda = \lambda_1/\lambda_2$ are the ratio of thicknesses, electrical resistivity and thermal conductivity of metals, $k_\xi = (1+k_\delta k_\lambda)/(1+k_\delta)$, $k_\eta = (1+k_\delta)/(1+k_\delta k_\lambda)$. This formula is an analogue of the Thomson formula $U = \alpha \Delta T/h$, which is used to calculate the thermoelectric power of anisotropic thermoelements [6] and underlies the method for calculating the heat flux from the signal of thermoelectric sensors GHFS [7] and ALTP [5].

Table 1 shows the physical properties of the materials of the considered sensor options. The effective thermal conductivity of the cross-layer structure in the transverse direction is calculated by the formula [8]:

$$\lambda_y = \lambda_1 (k_\xi \sin^2 \theta + k_\eta \cos^2 \theta),$$

where λ_1 is the thermal conductivity of the first metal. Since λ_y is close to the minimum and maximum values for metals, these pairs can be considered as limiting cases.

Results

Fig. 2 shows the field of temperature (Fig.2, *a, b*) and electric potential (Fig. 2, *c, d*) in the sensitive element of HGHS based on a pair of chromel–alumel (Fig. 2, *a, c*) and copper–nickel (Fig. 2, *b, d*) with layer thickness $\delta = 0.15 \text{ mm}$. The rotation of the isotherms in the direction of the slope of the layers and their kink is due to a change in the thermal conductivity at the

Table 1

Physical properties

Physical property	Sensor 1		Sensor 2	
	Chromel	Alumel	Copper	Nickel
Heat conductivity λ , W/m·K	17.6	33	395	90
Effective heat conductivity λ_y , W/m·K	25		216	
Electrical conductivity σ , 1/Ohm·m	$1.5 \cdot 10^6$	$3.5 \cdot 10^6$	$5.9 \cdot 10^7$	$1.1 \cdot 10^7$
Electrical resistance ρ , Ohm·m	$6.7 \cdot 10^{-7}$	$2.9 \cdot 10^{-7}$	$7.7 \cdot 10^{-8}$	$9.1 \cdot 10^{-8}$
Seebeck coefficient α , $\cdot 10^{-6}$ V/K	24	-17.3	3.2	-20.8

interface between metal pairs. The presence of a longitudinal and transverse temperature gradient leads to the appearance of the corresponding components of the thermoelectric field. For this reason, the isopotential lines also have a slope relative to the working surface of the sensor. It can be seen that in the case of a chromel-alumel pair, due to the lower effective thermal conductivity, the temperature difference between the working and back surfaces is greater than in the case of a copper-nickel pair. A larger temperature gradient and a larger difference in the Seebeck coefficients ($\alpha_1 - \alpha_2$) lead to a significantly larger value of the generated thermoelectric power. The difference in the polarity of the thermoelectric power is caused by the different sign ($\alpha_1 - \alpha_2$) of the metals under consideration. Despite the isotropic thermal and electrical conductivity of metals, the slope of alternating layers creates a temperature and electric potential distribution similar to the fields in bismuth thermoelements, where the anisotropy of properties is caused by the crystal structure [9].

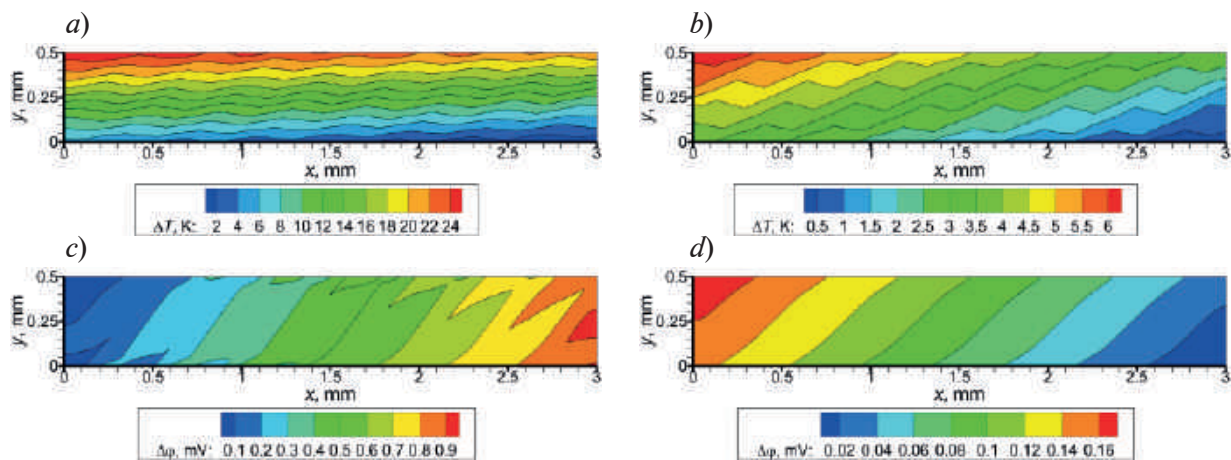


Fig. 2. Field of temperature (a), (b) and electric potential (c), (d) in the sensitive element of the sensor from a pair of chromel-alumel (a), (c) and a pair of copper-nickel (b), (d) with layer thickness $\delta = 0.15$ m

Fig. 3 shows the distribution of temperature and electric potential in the horizontal section $y = h/2$ of the HGHFS sensing element. The position of the break in the curves corresponds to the contacts of the metal layers. The linear distribution of the potential over the thickness of each layer is a consequence of the fact that the thermopower generation occurs only at the interface of dissimilar metals. It can be seen that with a decrease in the layer thickness, the temperature difference between its boundaries decreases proportionally and, accordingly, the potential difference. In this case, the total value of the thermoelectric power remains practically unchanged.

The generated thermoelectric power is an integral value that makes it possible to evaluate the influence of the physical properties of metals, the size and number of layers in the sensitive element on the distribution of temperature and electric potential (Table 2). Calculation using a

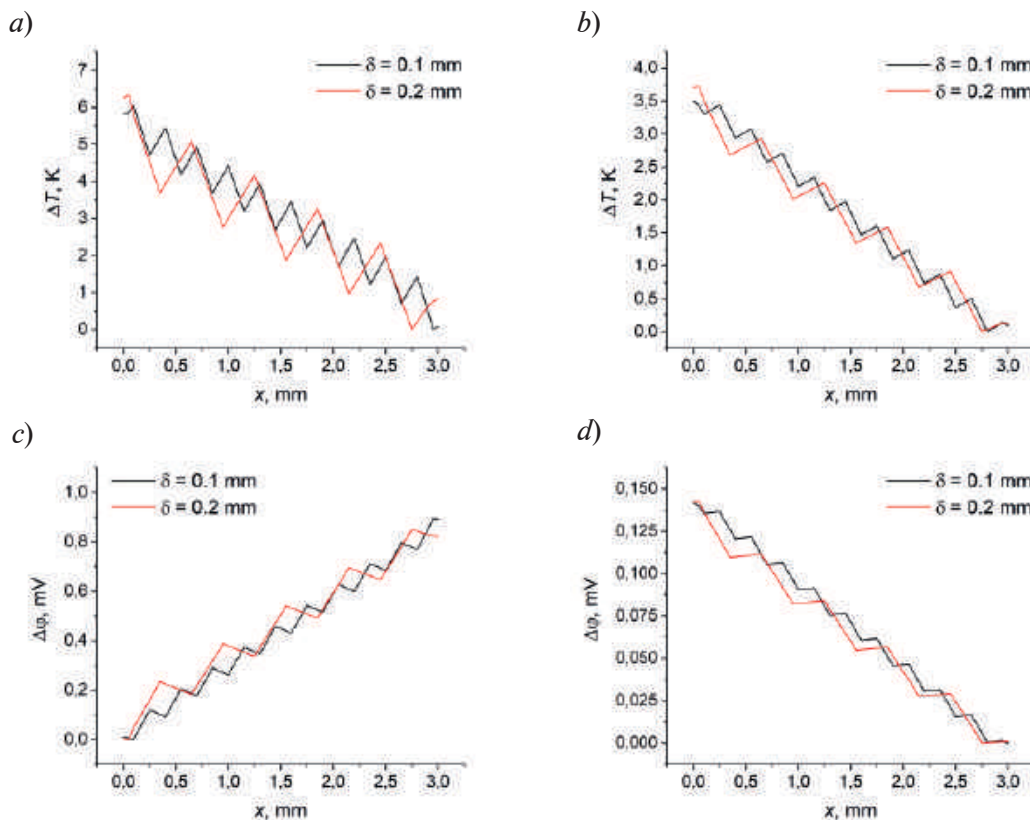


Fig. 3. Distribution of temperature (a, b) and electrical potential (c, d) in the horizontal cross section $y = h/2$ of the sensitive element of the sensor from a pair of chromel-alumel (a, c) and a pair of copper-nickel (b, d)

two-dimensional model showed that in the case of a chromel-alumel pair, with an increase in thickness and a decrease in the number of layers, an insignificant decrease in the thermoelectric power is observed; for a copper-nickel pair, it does not change. The change in thermoelectric power can be caused by edge effects, given the small ratio of the length of the sensing element to the thickness $l/h = 6$.

With the help of calibration by the reflected shock wave [10], the volt-watt coefficient $S_0 = 15 \mu V/K$ of the sensor was determined based on a copper-nickel pair with a sensitive element width $w = 3$ mm, length $l = 3$ mm, thickness $h = 0.5$ mm and layer thickness $\delta = 0.15$ mm. Accordingly, for a stationary heat flux $q_h = 1$ MW/m², the electrical signal will be $\Delta \varphi = S_0 q_h l/w = 0.14$ mV. It can be seen that the relative difference between the value obtained from the two-dimensional model $\Delta \varphi = 0.18$ mV and that calculated from the experimental value S_0 does not exceed 20%. This allows us to state that the two-dimensional model correctly reproduces the features of the distribution of temperature and electric potential in the layered structure of HGHS.

The use of a one-dimensional model for calculating the thermoelectric power leads to a significant difference from the results of calculations using a two-dimensional model and experimental data.

Table 2

The thermopower of the sensor in a stationary thermal regime calculated from the volt-watt coefficient and calculated using the exact and approximate models

Sensor	Sensor 1 (chromel-alumel)			Sensor 2 (cuprum-nickel)		
Layer thickness	0.1 mm	0.15 mm	0.2 mm	0.1 mm	0.15 mm	0.2 mm
2D model	1.01 mV	0.94 mV	0.90 mV	0.17 mV	0.18 mV	0.17 mV
1D model	1.69 mV			0.028 mV		



Conclusion

The results of calculating the temperature fields and electric potential in the sensitive element of the sensor based on layered metal structures in a stationary thermal regime are presented. A significant effect of the effective thermal conductivities of the layered structure on the temperature distribution and the generated thermoelectric power is shown. In the case of a copper-nickel pair sensor, the difference between the thermoelectric power calculated by the two-dimensional model and the experimental value does not exceed 20%. This confirms the correctness of the used model of thermal and thermoelectric processes in the sensitive element of the sensor. The use of a one-dimensional model leads to a significant difference between the calculation results and the two-dimensional model.

REFERENCES

1. **Hollis B.R., Prabhu D.K., Maclean M., Dufrene A.**, Blunt-Body Aerothermodynamic Database from High-Enthalpy Carbon-Dioxide Testing in an Expansion Tunnel, *Journal of Thermophysics and Heat Transfer*. 3 (31) (2017) 712–731.
2. **Alam T., Kumar R.**, A review on thin film fast response heat transfer gauges, *Review of Scientific Instruments*. 3 (92) (2021) 031501-01–27.
3. **Buttsworth D.R.**, Assessment of effective thermal product of surface junction thermocouples on millisecond and microsecond time scales, *Experimental Thermal and Fluid Science*. 6 (25) (2001) 409–420.
4. **Sapozhnikov S.Z., Mityakov V.Yu., Mityakov A.V.**, *Heatmetry: The Science and Practice of Heat Flux Measurement*, Springer International Publishing, 2020.
5. **Knauss H., Roediger T., Bountin D.A., Smorodsky B.V., Maslov A.A., Srulijes J.**, Novel Sensor for Fast Heat Flux Measurements, *Journal of Spacecrafts and Rockets*. 2 (46) 2009 255–265.
6. **Rowe D.M.**, *Thermoelectrics Handbook: Macro to Nano*, CRC Press, 2006.
7. **Popov P.A., Bobashev S.V., Reznikov B.I., Sakharov V.A.**, A Method of Nonstationary Heat Flux Calculation Using the Signal of a Sensor Based on Anisotropic Bismuth Single-Crystal Thermoelements, *Technical Physics Letters*. 4 (44) (2018) 316–319.
8. **Gerashenko O.A.**, *Osnovi teplometrii*, Naukova Dumka, Kiev, 1971.
9. **Bobashev S.V., Popov P.A., Reznikov B.I., Sakharov V.A.**, The influence of thermophysical properties of an anisotropic heat-element substrate on the value of thermal emf in the stationary thermal mode, *Technical Physics Letters*. 5 (42) (2016) 460–463.
10. **Popov P.A., Monakhov N.A., Lapushkina T.A., Poniaev S.A., Kurakin R.O.**, Calibration of thermal sensors based on anisotropic thermoelements and heterogeneous metal structures using a reflected shock wave, *Technical Physics Letters*. (2022) in press.

THE AUTHORS

POPOV Pavel A.
pavel.popov@mail.ioffe.ru
ORCID: 0000-0002-3843-3616

MONAKHOV Nikolai A.
nikolay.monakhov@mail.ioffe.ru

Received 30.10.2022. Approved after reviewing 14.11.2022. Accepted 16.11.2022.

Conference materials

UDC 533.6.071.3

DOI: <https://doi.org/10.18721/JPM.161.177>

Heat flux measurements of high speed flow around an axisymmetric body using sensors based on anisotropic thermoelements

N.A. Monakhov¹✉, V.A. Sakharov¹, P.A. Popov¹

¹Ioffe Institute, Saint-Petersburg, Russia

✉ nikolay.monakhov@mail.ioffe.ru

Abstract. The study is devoted to measurements of heat flux with an external high speed gas flow around the axisymmetric model. Sensors based on bismuth anisotropic thermoelements were used. Experiments were carried out using Big Shock Tube. The models used for experiments were the combinations of a cone with an opening angle of 60 degrees and a cylinder. The models with heat flux sensors were placed in the outer section of the flat supersonic nozzle. The results were compared with theoretical estimates made using the effective length method. The data obtained demonstrate the applicability of sensors in gas-dynamic experiments with test times about 1 ms.

Keywords: heat flux, shock tube, high speed flow, heat flux sensor based on anisotropic thermoelements, gradient heat flux sensor

Citation: Monakhov N.A., Sakharov V.A., Popov P.A., Heat flux measurements of high speed flow around an axisymmetric body using sensors based on anisotropic thermoelements. St. Petersburg State Polytechnical University Journal. Physics and Mathematics. 16 (1.1) (2023) 450–455. DOI: <https://doi.org/10.18721/JPM.161.177>

This is an open access article under the CC BY-NC 4.0 license (<https://creativecommons.org/licenses/by-nc/4.0/>)

Материалы конференции

УДК 533.6.071.3

DOI: <https://doi.org/10.18721/JPM.161.177>

Измерение теплового потока при высокоскоростном обтекании осесимметричного тела с помощью датчиков на анизотропных термоэлементах

Н.А. Монахов¹✉, В.А. Сахаров¹, П.А. Попов¹

¹Физико-технический институт им. А.Ф. Иоффе РАН, Санкт-Петербург, Россия

✉ nikolay.monakhov@mail.ioffe.ru

Аннотация. Представлены результаты измерения теплового потока с помощью датчиков на анизотропных термоэлементах при внешнем обтекании модели высокоскоростным потоком аргона. Эксперименты выполнены на большой ударной трубе ФТИ им. Иоффе. Обтекаемые модели представляли собой комбинацию конуса с углом раскрытия 60 градусов и цилиндра и устанавливались в рабочей камере, отделенной от ударной трубы тонкой диафрагмой, закрывающей вход в плоское сверхзвуковое сопло, находящееся в рабочей камере. Модели с тепловыми датчиками на основе анизотропных термоэлементов из висмута размещались в выходном сечении сопла. Сравнение экспериментальных результатов с теоретическими оценками теплового потока, выполненными на основе метода эффективной длины, демонстрирует корректность используемой методики обработки электрического сигнала датчиков на анизотропных термоэлементах и их перспективность в качестве диагностического средства для измерений тепловых потоков при обтекании моделей.

Ключевые слова: тепловой поток, ударная труба, высокоскоростное течение, датчик теплового потока на анизотропных термоэлементах, градиентный датчик теплового потока

Ссылка при цитировании: Монахов Н.А., Сахаров В.А., Попов П.А. Измерение теплового потока при высокоскоростном обтекании осесимметричного тела с помощью датчиков на анизотропных термоэлементах // Научно-технические ведомости СПбГПУ. Физико-математические науки. 2023. Т. 16. № 1.1. С. 450–455. DOI: <https://doi.org/10.18721/JPM.161.177>

Статья открытого доступа, распространяемая по лицензии CC BY-NC 4.0 (<https://creativecommons.org/licenses/by-nc/4.0/>)

Introduction

Studies of high speed flows around various models are usually carried out using pulsed gas-dynamic facilities, for example, shock tubes with a nozzle. The characteristic stationary flow time (“test time”) in this case is 0.1–10 ms. The heat flux to the body surface is an important measured parameter in a gas-dynamic experiment. Serious requirements are imposed on heat flux sensors in terms of dimensions, mechanical and thermal stability, sensitivity, speed, and noise immunity. Usually, thin-film resistance sensors and coaxial thermocouples are used for such measurements. St. Petersburg Polytechnic University has developed heat flux sensors based on anisotropic thermoelements called “gradient heat flux sensor” (GHFS) [1–3]. Experiments on shock tubes of Ioffe Institute demonstrated their high speed performance, sufficient mechanical strength, and reliability of the obtained results [4–6]. The method for calculating the heat flux from an electrical signal of a single anisotropic thermoelement under non-stationary thermal conditions was proposed at [7]. This method is based on a one-dimensional model of thermal and thermoelectric processes in thermoelements. The main objective of this work is to experimentally verify method proposed in [7] and analysis of its applicability in experiments on shock tubes. As a test problem, a classical gas-dynamic problem of heat transfer on the conical surface of an axisymmetric body in a high-speed gas flow was chosen, which has a well-known theoretical solution.

Sensor description

Figure 1 shows schematically the structure of the sensor based on anisotropic thermoelements. The sensitive element of these sensors is a battery of anisotropic thermoelements made of a single crystal of bismuth, fixed on a mica substrate (2) and separated from each other by lavsan strips (3) (Fig. 1, *a*). The ends of adjacent thermoelements are connected by soldering (4). Wires (5) are soldered to the outside thermoelements for connection to an oscilloscope. The anisotropic thermoelement is a bismuth parallelepiped cut at angle $\theta \approx 45^\circ$ to the crystallographic axes (Fig. 1, *b*). This leads to the appearance of off-diagonal elements of the thermopower tensor. When the thermoelement is heated and a temperature gradient appears, the longitudinal and transverse components of the thermoelectric field vector arise. The generated voltage is determined from the contacts located on the side faces.

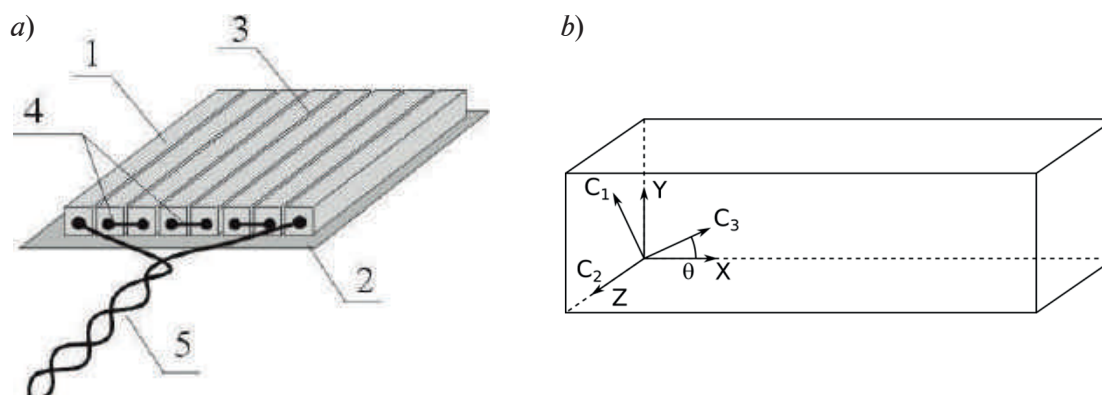


Fig. 1. Scheme of sensor based on anisotropic thermoelements (*a*); Anisotropic thermoelement in two coordinate systems: laboratory (x - y - z), crystallographic (C_1 - C_2 - C_3) (*b*)

A short response time of ~ 10 ns [8] makes it possible to use these sensors in shock tube experiments with characteristic times of 1 ms. The thickness of the sensor anisotropic thermoelements used in this work was 0.2 mm; therefore, the time to establish the stationary thermal regime ~ 100 ms significantly exceeded the characteristic gas dynamic time ~ 1 ms, and the temperature distribution over the thermoelement was nonlinear [9]. In this case, the heat flux ceases to be proportional to the sensor signal and mathematical processing of its signal is required [7]. The temperature distribution in the two-layer structure “thermoelement-substrate” was calculated using the one-dimensional non-stationary heat conduction equation:

$$C\rho \frac{\partial T}{\partial t} = \frac{\partial}{\partial x} \left(\lambda \frac{\partial T}{\partial x} \right), \quad (1)$$

with the boundary condition relating the change in the temperature of the working surface of the sensor $T_h(t)$ to the electrical signal $U(t)$, recorded in the experiment:

$$T_h^{i+1}(t) = T_0^i(t) + \frac{h}{k\lambda n l w} U(t), \quad (2)$$

where T_0 is the temperature of the back surface of the thermoelement, k is the stationary calibration coefficient of the sensor, n is the number of thermoelements in the sensitive element of the sensor, l and w are the length and thickness of the thermoelements. Further, using the known temperature distribution $T(x, t)$, we calculated the heat flux $q_h(t) = \lambda \left. \frac{\partial T}{\partial x} \right|_{x=h}$ passing through the working surface of the sensor. As shown at [7], the relative error of this method is mainly determined by length to thickness ratio of anisotropic thermoelement, and it doesn't exceed 10% even for rather short thermoelements with $l/h = 10$. Calibration coefficient k can be determined using method described at [3] and the uncertainty of its determination doesn't exceed 3%.

Experimental setup

The experiments described in this paper were carried out on the Big Shock Tube (BST) [10]. The total length of the BST is 16 m, the pressure chamber is 3 m, and its inner diameter is 100 mm. The models used for experiments were the combinations of a cone with an opening angle of 60 degrees and a cylinder. They were installed in a working chamber separated from the shock tube by a thin diaphragm that closed the entrance to a flat supersonic nozzle located in the working chamber. The model with heat flux sensors was placed in the outer section of the nozzle.

Figure 2 shows the models with thermal sensors 2.2×2.2 mm in size and 0.2 mm thick anisotropic thermoelements installed along the generatrix. The volt-watt ratio of the sensors used was in the range of 12–15 mV/W. In the first series of experiments, a plexiglass model with 6 sensors based on anisotropic thermoelements was used. The distances from the top of the cone to three sensors on the conical surface were 6, 18, and 30 mm, respectively. In the second series of experiments, a metal model with two sensors was used. The distance from the top of the cone to heat flux sensor at the cone generatrix was 15 mm.

In these experiments, hydrogen was used as driver gas, and argon was used as driven gas. The Mach number at the nozzle exit $M = 5$ was calculated from the ratio of the areas of the nozzle

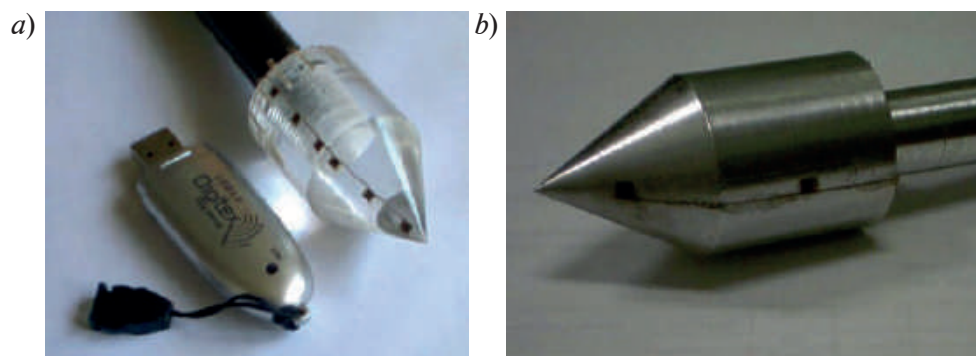


Fig. 2. Plexiglass model with six heat flux sensors (a) and the metal model with two heat flux sensors (b)



inlet and outlet. Table 1 lists the parameters of experiment. The incident shock wave velocity was measured using piezoelectric pressure transducers mounted flush to the inner surface of the driven tube at a distance of 230 mm from each other. The pressure transducer signals were recorded with a digital oscilloscope Tektronix TDS 2024C with a step of 0.2 μ s. Shock velocity was calculated by measured time interval of the shock wave passing the distance between the pressure transducers. Further, the parameters of the argon behind the reflected shock wave were determined from the known Mach number and initial pressure in the driven tube using Cantera which is an open-source suite of tools for problems involving chemical kinetics, thermodynamics, and transport processes [11]. Free stream parameters at the nozzle outlet were calculated using the model of one-dimensional stationary expansion in the nozzle.

Table 1

Gas parameters in driven tube and in free stream

Gas	Driven tube					Free stream parameters		
	Incident parameters		Parameters behind reflected shock wave					
	P_1 , mbar	M_1	P_5 , kPa	ρ_5 , kg/m ³	T_5 , K	P , kPa	ρ , kg/m ³	T , K
Ar	47	4.32	543	0.664	3972	2.052	0.024	423

During the experiments, it was found that in the case of a plexiglass model, spontaneous “splashes” occur in the electrical signal of the sensor (Fig. 3). The performed analysis showed that this phenomenon is a consequence of the accumulation of static electricity on the model surface, which occurs when a gas flows around the model [12]. The cause of this charge may be small fragments of a plastic diaphragm that at the initial moment closes the supersonic nozzle inlet. During the test time, these fragments become electrified and transfer part of the charge to the model surface upon contact with the model. In some cases, the charge drains along the measuring circuits of the heat flux sensor, causing the appearance of impulse pickups. It was found that the conical surface of the model is most often affected by this effect. The cylindrical surface of the model is much less susceptible to such splashes and the noise level turned out to be within the measurement errors, despite the fact that the signal level of the heat flux sensors located on the cylindrical surface is approximately an order of magnitude lower. When the sensors were installed on a grounded metal model, no such features were observed. Therefore, further results were obtained using a metal model.

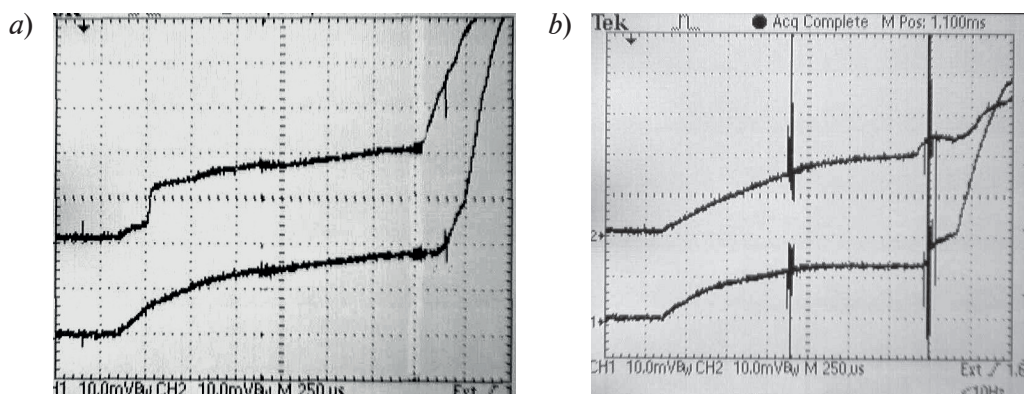


Fig. 3. Typical oscillograms of the heat flux sensor (installed on the conical surface) signal distorted by impulse noise

Results

Fig. 4a shows the electrical signals of the sensors prepared for heat flux calculation. In these experiments, the signal-to-noise ratio is much higher than in previous experiments on measuring the heat flux upon the shock wave reflection [4]. Fig. 4, b shows the heat fluxes calculated from the electrical signal of the sensors. The vertical dotted lines show the test time which corresponds to the stationary flow around the model. Due to the fig. 4, b, an increase in the heat flux during

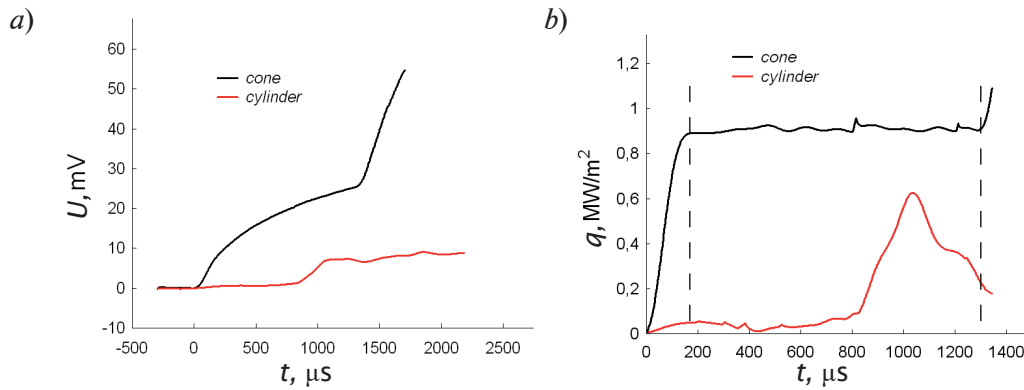


Fig. 4. Electrical signals of heat flux sensors on metal model (a); Heat fluxes calculated from sensor signals on metal model (b)

the first 200 μs corresponds to the stage of establishing a stationary flow around model and the formation of thermal boundary layer. Further, the period of quasi-stationary flow around the model is about 1000 μs . The heat flux to a cylindrical surface is much less than to a conical one.

The heat flux to the conical surface of the model was estimated using the effective length method. The main idea of this method is that the heat flux at any point on the body surface of arbitrary shape is determined by the thickness of the boundary layer and the shape of the temperature profile in a given section. The effective length is the length of a flat plate, on which, with an external flow with the same parameters as at the considered point of the body, the same thermal boundary layer is formed. Then, for bodies of simple geometry, the expression for the heat flux density is reduced to the expression for the heat flux density on the plate surface in a high-speed flow:

$$q = 0.332 \sqrt{\frac{\mu_w \rho_w u_1}{x}} C_p (T_e - T_w) \text{Pr}^{-2/3}. \quad (3)$$

Here μ_w , ρ_w are gas viscosity and density near the body surface, u_1 is longitudinal component of the flow velocity outside the boundary layer, C_p is argon specific heat, T_e is flow stagnation temperature, T_w is wall temperature, Pr is Prandtl number, x is longitudinal coordinate. Avduevsky [13] shows that for cones with a high-speed flow around at zero angle of attack, the heat flux can be calculated using relation (3), if we replace the value x in it with $x_{\text{eff}} = x/3$, that is, the value of the local heat flux density on the cone is $\sqrt{3}$ times greater than on a plate of the same length and with the same flow parameters outside the boundary layer:

$$q_{\text{cone}} = 0.332 \sqrt{\frac{\mu_w \rho_w u_1}{x/3}} C_p (T_e - T_w) \text{Pr}^{-2/3}. \quad (4)$$

In calculations of the heat flux using formula (4), the specific heat of argon and the Prandtl number were considered constant, since the stagnation temperature does not exceed 4500 K. The surface temperature of the model $T_w = 290$ K was considered constant during the flow test time, the viscosity of argon at this temperature is $2.23 \cdot 10^{-5}$ Pa·s. Heat flux calculation using relation (4) gives us the value $q_{\text{cone}} = 763$ kW/m^2 , while the averaged over the test time measured heat flux value is $q_{\text{cone}}^{\text{exp}} = 910$ kW/m^2 . The difference between these values may be due to the uncertainty of the stationary calibration of heat flux sensors (according to [3], it does not exceed 3%), the error in calculating the heat flux using a one-dimensional model of anisotropic thermoelements (according to [7], it does not exceed 10%), as well as the error in determining the parameters of high-speed flow near the model.

Conclusion

The results of measuring the heat flux by sensors based on anisotropic thermoelements with an external high-speed argon flow around a conical model are presented. The experimental results are compared with the theoretical estimates of the heat flux made on the basis of the effective length method [13]. The relative difference between the measured and calculated heat fluxes,



which does not exceed 15%, demonstrates the correctness of the electrical signal processing technique used and the prospects of a sensor based on anisotropic bismuth thermoelements as a diagnostic tool for measuring heat fluxes in high-speed flows around models.

REFERENCES

1. Sapozhnikov S.Z., Mityakov V.Y., Mityakov A.V., Gradient heat flux sensors for high temperature environments, 2004 High Temperature. (2004) 629–638.
2. Mityakov A.V., Sapozhnikov S.Z., Mityakov V.Yu., et al., Gradient heat flux sensors for high temperature environments, Sens. and Act. A: Phys. 176 (11) (2012) 1–9.
3. Sapozhnikov S.Z., Mityakov V.Yu., Mityakov A.V., Heatmetry: The Science and Practice of Heat Flux Measurement, Springer International Publishing, 2020.
4. Popov P.A., Sakharov V.A., Poniaev S.A., et al., Heat flux measurement at the initial phase of normal shock wave reflection using the sensor on anisotropic thermoelements, J. Phys. Conf. Ser.1697 (2020) 012225.
5. Popov P.A., Monakhov N.A., Kotov M.A., Poniaev S.A., Experimental investigation of the thermal loads upon electrodynamic modification of supersonic flow around axisymmetrical body, IOP Conf. Ser.: Mater. Sci. Eng. 927 (2020) 012084.
6. Kotov M.A., Shemyakin A.N., Solovyov N.G., et al., Performance assessment of thermoelectric detector for heat flux measurement behind a reflected shock of low intensity, Appl. Therm. Eng. 195 (2020) 117143.
7. Popov P.A., Bobashev S.V., Reznikov B.I., Sakharov V.A., A Method of Nonstationary Heat Flux Calculation Using the Signal of a Sensor Based on Anisotropic Bismuth Single-Crystal Thermoelements, Tech.Phys.Letters 44 (2018) 316–319.
8. Bobashev S.V., Mende N.P., Sakharov V.A., Sapozhnikov S.Z., Mityakov V.Yu., Mityakov A.V., Van Wie D.V., Application of Gradient Heat Flux Sensor in Shock Tube Experiments, Proc. 43rd AIAA Aerosp. Sci. Meeting and Exhibit (Reno) (2005).
9. Popov P.A., Bobashev S.V., Reznikov B.I., Sakharov V.A., The influence of thermophysical substrate properties of an anisotropic thermoelement on thermopower in the nonstationary thermal regime, Tech. Phys. Lett. 43 (4) (2017) 334–337.
10. Maslennikov V.G., Sakharov V.A., Double-diaphragm shock tube at the Ioffe Physicotechnical Institute, Tech. Phys. 42 (1997) 1322–1328.
11. Cantera – open-source suite of tools for problems involving chemical kinetics, thermodynamics, and transport processes. <https://cantera.org/>. Accessed Aug. 14, 2022.
12. Kuribayashi T., Ohtani K., Takayama K., et al., Heat flux measurement over a cone in a shock tube flow, Shock Waves 16 (2007) 275–285.
13. Avduevsky V.S. et al., Osnovy teploperedachi v aviatsionnoi i raketno-kosmicheskoi tekhnike, Mashinostroenie, Moscow, 1992. (in Russian).

THE AUTHORS

MONAKHOV Nikolay A.
nikolay.monakhov@mail.ioffe.ru
ORCID: 0000-0003-0585-3320

POPOV Pavel A.
Pavel.popov@mail.ioffe.ru
ORCID: 0000-0002-3843-3616

SAKHAROV Valerii A.
v.sakharov@mail.ioffe.ru

Received 26.10.2022. Approved after reviewing 08.11.2022. Accepted 08.11.2022.

Conference materials

UDC 621.373.826

DOI: <https://doi.org/10.18721/JPM.161.178>

1550 nm high-speed VCSELS based on compressively strained In(Al)GaAs QWs

S.S. Rochas¹✉, S.A. Blokhin², A.V. Babichev¹, L.Ya. Karachinsky¹, I.I. Novikov¹,
A.A. Blokhin², M.A. Bobrov², N.A. Maleev², V.V. Andryushkin¹, V.E. Bougrov¹,
A.G. Gladyshev³, I.A. Melnichenko⁴, K.O. Voropaev⁵, I.O. Zhumaeva⁵, V.M. Ustinov⁶,
H. Li⁷, S. Tian^{8,9}, S.Y. Han^{8,9}, G.A. Sapunov^{8,9}, A.Yu. Egorov^{3,10}, D.H. Bimberg^{8,9}

¹ ITMO University, St. Petersburg, Russia;

² Ioffe Institute, RAS, St. Petersburg, Russia;

³ Connector Optics LLC, St. Petersburg, Russia;

⁴ National Research University Higher School of Economics, St. Petersburg, Russia;

⁵ JSC OKB-Planeta, V. Novgorod, Russia;

⁶ Submicron Heterostructures for Microelectronics Research and Engineering Center, RAS, St. Petersburg, Russia;

⁷ College of Mathematical and Physical Sciences, Qingdao University of Science and Technology, Qingdao, China;

⁸ Bimberg Chinese-German Center for Green Photonics, Changchun Institute of Optics, Fine Mechanics and Physics (CIOMP), Chinese Academy of Sciences (CAS), Changchun, China;

⁹ Center of Nanophotonics, Institute of Solid State Physics, Technische Universität Berlin, Berlin, Germany;

¹⁰ Alferov University, St. Petersburg, Russia

✉ stanislav_rochas@itmo.ru

Abstract. High-speed vertical-cavity surface-emitting lasers of 1550 nm spectral range based on ten compressively strained In(Al)GaAs QWs were fabricated by molecular-beam epitaxy and direct double wafer-fusion technique. The devices demonstrate threshold current of 2 mA and maximum output optical power of 4.8 mW. The effect of saturable absorber was observed at a temperature above 50 °C. Small signal analysis revealed that modulation bandwidth f_{-3dB} and the resonant frequency f_R of 8 GHz and 12 GHz, respectively, can be reached for presented VCSELS design. The NRZ-mode data rate up to 20 Gbps at 20 °C across the distance of 1000 meters was demonstrated.

Keywords: VCSEL, molecular-beam epitaxy, wafer fusion, data transmission, tunnel junction, strained quantum wells

Funding: The authors from ITMO University acknowledge support in part by the Ministry of Science and Higher Education of the Russian Federation (project no. 2019-1442) for the static characteristics measurements and in part by the Government of the Russian Federation (Priority 2030 program) for the small signal modulation experiments. I.A. Melnichenko thanks the Basic Research Program of the National Research University Higher School of Economics for support of lasing spectra measurements. S.A. Blokhin acknowledges the support of the CAS PIFI program for the part of large-signal modulation experiments.

Citation: Rochas S.S., Blokhin S.A., Babichev A.V., Karachinsky L.Ya., Novikov I.I., Blokhin A.A., Bobrov M.A., Maleev N.A., Andryushkin V.V., Bougrov V.E., Gladyshev A.G., Melnichenko I.A., Voropaev K.O., Zhumaeva I.O., Ustinov V.M., Li H., Tian S., Han S.Y., Sapunov G.A., Egorov A.Yu., Bimberg D.H., 1550 nm high-speed VCSELS based on compressively strained In(Al)GaAs QWs. St. Petersburg State Polytechnical University Journal. Physics and Mathematics. 16 (1.1) (2023) 456–462. DOI: <https://doi.org/10.18721/JPM.161.178>

This is an open access article under the CC BY-NC 4.0 license (<https://creativecommons.org/licenses/by-nc/4.0/>)

Материалы конференции

УДК 621.373.826

DOI: <https://doi.org/10.18721/JPM.161.178>

Высокоскоростные вертикально излучающие лазеры 1550 нм на основе напряженных In(Al)GaAs КЯ

С.С. Рочас¹✉, С.А. Блохин², А.В. Бабичев¹, Л.Я. Карачинский¹, И.И. Новиков¹,
А.А. Блохин², М.А. Бобров², Н.А. Малеев², В.В. Андрюшкин¹, В.Е. Бугров¹,
А.Г. Гладышев³, И.А. Мельниченко⁴, К.О. Воропаев⁵, И.О. Жумаева⁵, В.М. Устинов⁶,
Н. Li⁷, S. Tian^{8,9}, S.Y. Han^{8,9}, Г.А. Сапунов^{8,9}, А.Ю. Егоров^{3,10}, D.H. Bimberg^{8,9}

¹ Университет ИТМО, Санкт-Петербург, Россия;

² Физико-технический институт им. А.Ф. Иоффе РАН, Санкт-Петербург, Россия;

³ ООО Коннектор Оптикс, Санкт-Петербург, Россия;

⁴ Национальный исследовательский университет «Высшая школа экономики», Санкт-Петербург, Россия;

⁵ АО ОКБ Планета, г. Великий Новгород, Россия;

⁶ НТЦ микроэлектроники РАН, Санкт-Петербург, Россия;

⁷ College of Mathematical and Physical Sciences, Qingdao University of Science and Technology, Qingdao, China;

⁸ Bimberg Chinese-German Center for Green Photonics, Changchun Institute of Optics, Fine Mechanics and Physics (CIOMP), Chinese Academy of Sciences (CAS), Changchun, China;

⁹ Center of Nanophotonics, Institute of Solid State Physics, Technische Universität Berlin, Berlin, Germany;

¹⁰ Академический университет им. Ж.И. Алфёрова, Санкт-Петербург, Россия

✉ stanislav_rochas@itmo.ru

Аннотация. Были изготовлены высокоскоростные вертикально излучающие лазеры (ВИЛ) спектрального диапазона 1550 нм на основе 10 напряженных In(Al)GaAs КЯ с использованием метода молекулярно-пучковой эпитаксии и двойного прямого молекулярного спекания эпитаксиальных пластин. Приборы демонстрируют пороговый ток 2 мА и максимальную выходную оптическую мощность 4,8 мВт. Эффект насыщающегося поглотителя наблюдался при температуре выше 50 °С. Малосигнальный анализ показал значения ширины полосы модуляции f_{-3dB} и резонансной частоты f_R 8 ГГц и 12 ГГц, соответственно. Была продемонстрирована скорость передачи данных до 20 Гбит/с в режиме NRZ при 20 °С на расстояние 1000 метров.

Ключевые слова: ВИЛ, молекулярно-пучковая эпитаксия, спекание пластин, передача данных, туннельный переход, напряженные квантовые ямы

Финансирование: Работа авторов из Университета ИТМО выполнена при поддержке Министерства науки и высшего образования Российской Федерации, проект тематики научных исследований № 2019-1442, в части исследований статических характеристик, при финансовой поддержке программы «Приоритет 2030» в части экспериментов по исследованию малосигнальной модуляции. И. А. Мельниченко благодарит Программу фундаментальных исследований НИУ ВШЭ за поддержку в части измерений спектров генерации. С.А. Блохин выражает благодарность программе CAS RIFI в части экспериментов по прямой модуляции лазеров большим сигналом.

Ссылка при цитировании: Рочас С.С., Блохин С.А., Бабичев А.В., Карачинский Л.Я., Новиков И.И., Блохин А.А., Бобров М.А., Малеев Н.А., Андрюшкин В.В., Бугров В.Е., Гладышев А.Г., Мельниченко И.А., Воропаев К.О., Жумаева И.О., Устинов В.М., Ли Х., Тиан С., Хан С., Сапунов Г.А., Егоров А.Ю., Бимберг Д.Х. Высокоскоростные вертикально излучающие лазеры 1550 нм на основе напряженных In(Al)GaAs КЯ // Научно-технические ведомости СПбГПУ. Физико-математические науки. 2023. Т. 16. № 1.1. С. 456–462. DOI: <https://doi.org/10.18721/JPM.161.178>

Статья открытого доступа, распространяемая по лицензии CC BY-NC 4.0 (<https://creativecommons.org/licenses/by-nc/4.0/>)

Introduction

To date, the growing needs for data storage, processing centers, information and computing systems require new light sources that can increase the bandwidth of fiber optic communication links [1]. Long-wavelength vertical-cavity surface-emitting lasers suitable for single-mode operations are among the most promising laser sources due to their relatively low threshold currents and the possibility of implementing high-frequency signal modulation [2]. Of great importance is the possibility to form 1D and 2D arrays based on VCSELs, as well as the possibility of integration with silicon, which is of interest for silicon-based radio photonics devices and their hybrid integration [3].

There are two main approaches to the creation of single-mode long-wavelength 1300–1550 nm VCSELs. The first approach uses an active region on an InP substrate with dielectric distributed Bragg reflectors (DBR) [4] formed by magnetron sputtering and requires specific materials (AlF_3 , ZnS , CaF_2) to form hybrid DBR mirrors and removal of the InP substrate before sputtering. This approach has limitations such as relatively low obtained single-mode maximal output optical power at room temperature, as well as increased requirements for the optical uniformity and roughness of dielectric DBRs interfaces [4–6].

The second approach uses the wafer fusion technology to bond the active region based on InP and DBRs based on GaAs [7]. This approach effectively combines the advantages of the active region on the InP substrate and the high reflectivity DBR on GaAs substrates based on AlGaAs/GaAs materials. Recently, we have demonstrated the successful application and adjustment of the wafer fusion technique for a long-wavelength VCSELs fabrication [8–10]. Within this approach the current and optical confinement were ensured by a tunnel junction (TJ) [11] with a following overgrowth with an InP layer. One of the main advantages of this approach is the stability of the devices to meet the requirements of the GR-468-CORE Telcordia standard [12]. Previously, we proposed an original design of the buried tunnel junction (BTJ) $n^{++}\text{-InGaAs/p}^{++}\text{-InGaAs/p}^{++}\text{-InAlGaAs}$ using the molecular-beam epitaxy (MBE) method both for the creation of active-region and DBRs heterostructures and for the overgrowth of the TJ [13].

In this paper, we present the results on fabrication and study of 1550 nm single-mode VCSELs formed by molecular-beam epitaxy and a direct dry double wafer fusion of an active region based on compressively strained In(Al)GaAs quantum wells (QWs) with a $n^{++}\text{-InGaAs/p}^{++}\text{-InGaAs/p}^{++}\text{-InAlGaAs}$ BTJ and GaAs DBRs.

Materials and methods

The schematic cross-section of the 1550 nm VCSEL is shown in Fig. 1. The heterostructure of the In(Al)GaAs/InP active region on InP substrate, including a microcavity, as well as heterostructures of distributed Bragg reflectors on GaAs substrates, were formed by the MBE method using an Riber 49 [14]. Each technical step of a direct dry double wafer fusion was performed with a modified EVG 501 wafer bonding system.

The In(Al)GaAs/InP optical cavity consisted of an active region with ten compressively strained $\text{In}_{0.74}\text{Ga}_{0.26}\text{As}/\text{In}_{0.53}\text{Al}_{0.26}\text{Ga}_{0.21}\text{As}$ QWs/barriers of 2.6 nm and 7 nm-thick, respectively, sandwiched by bottom intra-cavity (IC) layer with a heavily doped InGaAs contact layer from one side and a p-InAlAs emitter, a composite BTJ $n^{++}\text{-InGaAs/p}^{++}\text{-InGaAs/p}^{++}\text{-InAlGaAs}$ with layers doped up to $5 \times 10^{19} \text{ cm}^{-3}$ and a top IC from the other side. The optical resonator was geometrically constructed to place $\text{In}_{0.74}\text{Ga}_{0.26}\text{As}$ QWs with a lattice mismatch parameter of $\sim 1.4\%$ and the composite BTJ in the maximum and minimum of the calculated electromagnetic field distribution, respectively (Fig. 2). The total thickness of microcavity was 3λ . The top and bottom DBRs consisted of 22.5 and 35.5 pairs of $\text{Al}_{0.9}\text{Ga}_{0.1}\text{As}/\text{GaAs}$ layers, respectively. Note that gain-to-cavity detuning was performed to red shift microcavity resonance on the value of $\sim 25 \text{ nm}$.

The composite BTJ mesa with a diameter of $6 \mu\text{m}$ was formed by a chemical etching, the first mesa was formed by a dry etching and inductively coupled plasma, the second mesa was formed by a two-step selective wet etching, the dielectric passivation was performed by a plasma enhanced chemical vapor deposition of Si_3N_4 and metallization of Ti/Pt/Au contacts was performed by a lift-off process to form ground-source-ground contacts topology.

Results and Discussion

Fig. 3 shows light-current-voltage (L-I-V) characteristics for the 1550 nm VCSEL based on compressively strained In(Al)GaAs in the temperature range of 20 to 90 °C. Temperature change

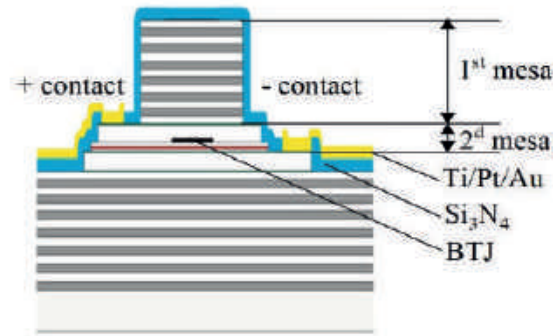


Fig. 1. Cross-section of the 1550 nm VCSEL based on compressively strained In(Al)GaAs QWs

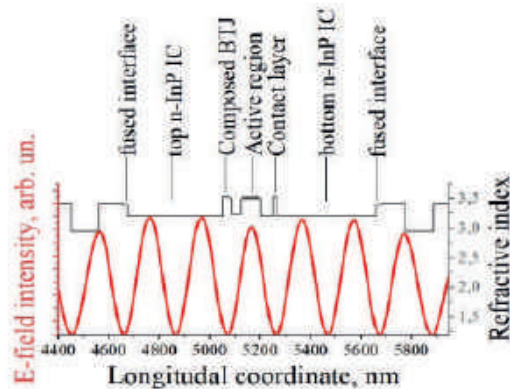


Fig. 2. Vertical distribution of electromagnetic field intensity along the refractive index of the 1550 nm VCSEL based on compressively strained In(Al)GaAs QWs

was carried out with a Peltier module. The studied devices at 20 °C demonstrated threshold current of ~ 2 mA with a slope efficiency of ~ 0.47 W/A and a maximum output optical power of ~ 4.8 W at the thermal roll-over current of ~ 18 mA. Raising the temperature resulted in reducing of the maximum output optical power with a disproportionate increase in the threshold current and a sharp increase in the optical power value at the beginning of the lasing, which can be explained by the effect of so-called saturable absorber, which we earlier observed in 1300 nm and 1550 nm VCSELs with a diameter of BTJ mesa lower than critical value [15]. Thus, rising temperature up to 60 °C leads to a rise in threshold current up to ~ 4.6 mA and at the temperature of 90 °C the threshold current reaches the value of 10.2 mA. Note that despite of the non-linearity of L-I-V characteristics for the all bias currents the single-mode operation is observed (inset to Fig. 2) which eliminates the possibility of the effect of a saturable absorber due to mode competition. According to lasing spectra fabricated VCSELs are suitable for 1550 nm window (also called third window) of optical fiber, namely for L band.

The estimation of the dynamic performance of the 1550 nm VCSEL based on compressively strained In(Al)GaAs QWs was carried out with a small signal modulation analysis $S_{21}(f)$ at a various forward bias currents using Rodhe & Schwarz ZVA 40 network analyzer and a 25 GHz New Focus 1434 photodetector. The classical method of three-pole transfer function was used to determine laser response to sinusoidal pump current modulation.

Fig. 4 shows the -3dB modulation bandwidth (f_{3dB}) at the temperature of 20 °C. At the bias current of 3 mA the f_{3dB} reaches 5 GHz and at the bias current of 6 mA the f_{3dB} reaches 7.6 GHz and then saturates at the level of ~ 8 GHz with higher currents.

The corresponding to the f_{3dB} saturation point modulation current efficiency factor is of ~ 3.6 GHz/mA^{0.5} (Fig. 5). The D -factor which demonstrates the rise of the resonant frequency (f_R) with a current and the differential gain level is at the level of 3.2 GHz/mA^{0.5}. One can see that at high bias currents relaxation resonance frequency f_R reaches more than ~ 12 GHz (Fig. 5).

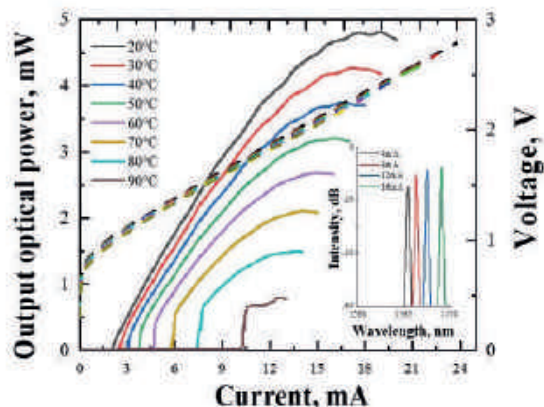


Fig. 3. L - I - V characteristics of the 1550 nm VCSEL based on compressively strained In(Al) GaAs QWs, inset shows lasing spectra at the temperature of 20 °C

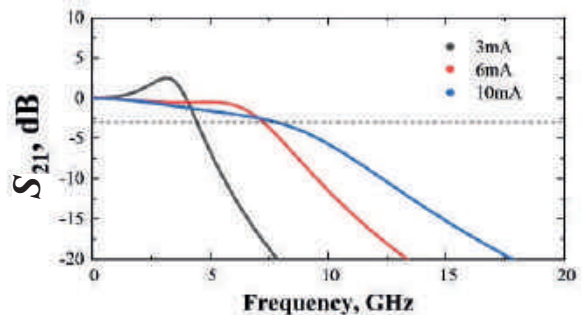


Fig. 4. Small signal modulation analysis $S_{21}(f)$ of the 1550 nm VCSEL based on compressively strained In(Al)GaAs QWs

The estimation of large signal modulation of the 1550 nm VCSEL was carried out with a SHF 12105A bit pattern generator, a 33 GHz Tektronix DPO70E1 optical probe and Tektronix 59 GHz real time oscilloscope DPO75902SX. The data transmission was carried out in the non-return-to-zero (NRZ)-mode with a pseudo-random binary sequence (PRBS) of 2^7-1 using back-to-back (B2B) configurations over single-mode fiber (SMF) at a distance of 1000 meters.

Fig. 6 shows clear open eye diagram for the studied devices at data rate of 20 Gbps at 20 °C. The jitter value extracted from the bit error rate (BER) = 10^{-12} was 23 ps (~ 0.31 UI) at the 16 mA bias current and 300 mV modulation voltage.

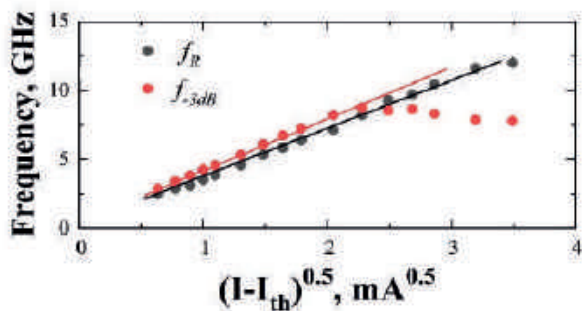


Fig. 5. The -3dB modulation bandwidth (f_{3dB}) and the extracted relaxation resonance frequency (f_R) versus current at the temperature of 20 °C of the 1550 nm VCSEL based on compressively strained In(Al)GaAs QWs

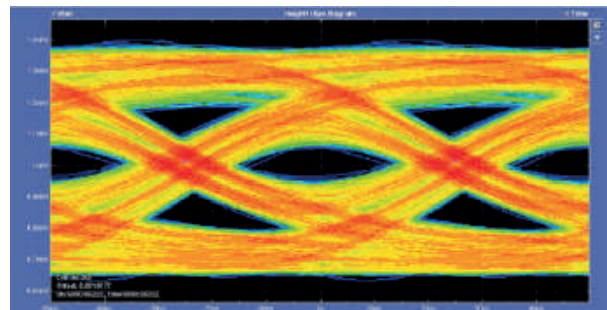


Fig. 6. Eye diagram of the 1550 nm VCSEL at the 16 mA bias current and 300 mV modulation voltage at 20 °C across 1000 meters SMF

Conclusion

We presented the results on fabrication and investigation of MBE-grown wafer-fused 1550 nm VCSELs based on compressively strained In(Al)GaAs QWs. The devices demonstrated the threshold current of about 2 mA and the maximum output optical power of 4.8 mW at 20 °C while increase in the influence of the saturable absorber effect [15] was observed at higher temperatures. According to the small signal modulation analysis $S_{21}(f)$ the -3dB modulation bandwidth f_{3dB} and the relaxation resonance frequency f_R were 8 GHz and 12 GHz, respectively. The data rate up to 20 Gbit/s was achieved for VCSELs with BTJ mesa diameter 6 μ m which is of interest of data transmissions for a large distance across single-mode fibers (e.g. 1000 meters).

We believe that the further improvement of the mesas geometric parameters and temperature stability of the devices (e.g. increase of QW barriers band gap), which is related with suppression of thermal escape of carriers from the QWs, as well as reducing parasitic capacitance to increase the -3dB modulation bandwidth, will lead to a better devices performance.



REFERENCES

1. Zhang Y., Chowdhury P., Tornatore M., Mukherjee B., Energy efficiency in telecom optical networks, *IEEE Communications Surveys & Tutorials*. 12 (4) (2010) 441–458.
2. Markou S., Dris S., Kalavrouziotis D., Avramopoulos H., Pleros N., Tsiokos D.M., 1550 nm VCSEL-based 0.48 Tb/s transmission scheme employing PAM-4 and WDM for active optical cables, *Semiconductor Lasers and Laser Dynamics VI. – SPIE*. 9134 (2014) 454–460.
3. Heck M.J., Bauters J.F., Davenport M.L., Doylend J.K., Jain S., Kurczveil G., Srinivasan S., Tang Y., Bowers J.E., Hybrid silicon photonic integrated circuit technology, *IEEE Journal of Selected Topics in Quantum Electronics*. 19 (4) (2012) 6100117–6100117.
4. Spiga S., Soenen W., Andrejew A., Schoke D. M., Yin X., Bauwelinck J., Boehm G., Amann M.C., Single-mode high-speed 1.5- μm VCSELs, *Journal of Lightwave Technology*. 35 (4) (2016) 727–733.
5. Muller M., Hofmann W., Grundl T., Horn M., Wolf P., Nagel R.D., Ronneberg E., Bohm G., Bimberg D., Amann M.C., 1550-nm high-speed short-cavity VCSELs, *IEEE Journal of selected topics in Quantum Electronics*. 17 (5) (2011) 1158–1166.
6. Malacarne A., Soriano V., Daly A., Kögel B., Ortsiefer M., Neumeier C., Romagnoli M., Bogoni A., Performance analysis of 40-Gb/s transmission based on directly modulated high-speed 1530-nm VCSEL, *IEEE Photonics Technology Letters*. 28 (16) (2016) 1735–1738.
7. Mereuta A., Caliman A., Sirbu A., Iakovlev V., Ellafi D., Rudra A., Bimberg D., Kapon E., Recent progress in 1.3- and 1.5- μm waveband wafer-fused VCSELs, *Semiconductor Lasers and Applications VII. – SPIE*. 10017 (2016) 1001702.
8. Rochas S.S., Novikov I.I., Karachinsky L.Y., Babichev A.V., Blokhin S.A., Nevedomskii V.N., Voropaev K.O., Egorov A.Yu., Wafer fusion technique features for near-IR laser sources, *Journal of Physics: Conference Series. – IOP Publishing*. 2103 (1) (2021) 012107.
9. Blokhin S.A., Nevedomsky S.N., Bobrov M.A., Maleev N.A., Blokhin A.A., Kuzmenkov A.G., Vasil'ev A.P., Rochas S.S., Babichev A.V., Gladyshev A.G., Novikov I.I., Karachinsky L.Ya., Denisov D.V., Voropaev K.O., Ionov A.S., Egorov A.Yu., Ustinov V.M., 1.55- μm -Range Vertical-Cavity Surface-Emitting Lasers, Manufactured by Wafer Fusion of Heterostructures Grown by Solid-Source Molecular-Beam Epitaxy, *Semiconductors*. 54 (10) (2020) 1276–1283.
10. Blokhin S.A., Ledentsov Jr.N., Rochas S.S., Babichev A.V., Gladyshev A.G., Chorchos L., Makarov O.Yu., Karachinsky L.Ya., Novikov I.I., Blokhin A.A., Bobrov M.A., Maleev N.A., Andryushkin V.V., Voropaev K.O., Zhumaeva I.O., Ustinov V.M., Egorov A.Yu., Ledentsov N.N., 1300-nm wafer-fused VCSELs with InGaAs/InAlGaAs superlattice-based active region, *Vertical-Cavity Surface-Emitting Lasers XXVI. – SPIE*. 12020 (2022) 132–140.
11. Nishiyama N., Caneau C.G., Zah C.E., Long-wavelength VCSELs on InP grown by MOCVD, *Active and Passive Optical Components for WDM Communications III. SPIE*. 5246 (2003) 10–17.
12. Sirbu A., Suruceanu G., Iakovlev V., Mereuta A., Mickovic Z., Caliman A., Kapon E., Reliability of 1310 nm wafer fused VCSELs, *IEEE Photonics Technology Letters*. 25 (16) (2013) 1555–1558.
13. Blokhin S.A., Bobrov M.A., Maleev N.A., Blokhin A.A., Kuz'menkov A.G., Vasil'ev A.P., Rochas S.S., Gladyshev A.G., Babichev A.V., Novikov I.I., Karachinsky L.Ya., Denisov D.V., Voropaev K.O., Ionov A.S., Egorov A.Yu., Ustinov V.M., A Vertical-Cavity Surface-Emitting Laser for the 1.55- μm Spectral Range with Tunnel Junction Based on n^{++} -InGaAs/ p^{++} -InGaAs/ p^{++} -InAlGaAs Layers, *Technical Physics Letters*. 46 (9) (2020) 854–858.
14. Babichev A., Blokhin S., Gladyshev A., Karachinsky L., Novikov I., Blokhin A., Bobrov M., Maleev N., Andryushkin V., Kolodeznyi E., Denisov D., Kryzhanovskaya N., Voropaev K., Ustinov V., Egorov A., Li H., Tian S-C., Han S., Sapunov G., Bimberg D., *IEEE Photonics Technology Letters*. 35 (6) (2023) 297–300.
15. Blokhin S.A., Bobrov, M.A., Blokhin, A.A., Vasil'ev, A.P., Kuz'menkov, A.G., Maleev N.A., Rochas S.S., Gladyshev A.G., Babichev A.V., Novikov I.I., Karachinsky L.Ya., Denisov D.V., Voropaev K.O., Ionov A.S., Egorov A.Yu., Ustinov V.M., The effect of a saturable absorber in long-wavelength vertical-cavity surface-emitting lasers fabricated by wafer fusion technology, *Technical Physics Letters*. 46 (12) (2020) 1257–1262.

THE AUTHORS

ROCHAS Stanislav S.

stanislav_rochas@itmo.ru
ORCID: 0000-0002-6519-2897

BLOKHIN Sergei A.

blokh@mail.ioffe.ru
ORCID: 0000-0002-5962-5529

BABICHEV Andrey V.

a.babichev@itmo.ru
ORCID: 0000-0002-3463-4744

KARACHINSKY Leonid Ya.

lkarachinsky@itmo.ru
ORCID: 0000-0002-5634-8183

NOVIKOV Innokenty I.

innokenty.novikov@itmo.ru
ORCID: 0000-0003-1983-0242

BLOKHIN Aleksey A.

Aleksey.Blokhin@mail.ioffe.ru
ORCID: 0000-0002-3449-8711

BOBROV Mikhail A.

bobrov.mikh@gmail.com
ORCID: 0000-0001-7271-5644

MALEEV Nikolai A.

maleev@beam.ioffe.rssi.ru
ORCID: 0000-0003-2500-1715

ANDRYUSHKIN Vladislav V.

vvandriushkin@itmo.ru
ORCID: 0000-0002-7471-8627

BOUGROV Vladislav E.

Vladislav.bougrov@niuitmo.ru
ORCID: 0000-0002-1365-9184

GLADYSHEV Andrey G.

andrey.gladyshev@connector-optics.com
ORCID: 0000-0002-9448-2471

MELNICHENKO Ivan A.

Ivankomel550@gmail.com
ORCID: 0000-0003-3542-6776

VOROPAEV Kirill O.

kirill.voropaev@novsu.ru
ORCID: 0000-0002-6159-8902

ZHUMAEVA Irina O.

zhumaevaio@okbplaneta.ru
ORCID: 0000-0003-4182-8616

USTINOV Victor M.

info@ntcm-ras.ru
ORCID: 0000-0002-6401-5522

LI Hui

lihui6526@qust.edu.cn
ORCID: 0000-0002-5590-7019

TIAN Si-Cong

tiansicong@ciomp.ac.cn

HAN Saiyi

hansaiyi@163.com

SAPUNOV Georgiy A.

sapunovgeorgiy@gmail.com
ORCID: 0000-0002-4314-2178

EGOROV Anton Yu.

anton.egorov@connector-optics.com
ORCID: 0000-0002-0789-4241

BIMBERG Dieter H.

bimberg@physik.tu-berlin.de
ORCID: 0000-0003-0364-6897

Received 26.10.2022. Approved after reviewing 08.11.2022. Accepted 08.11.2022.

Conference materials

UDC 533.6.071.3

DOI: <https://doi.org/10.18721/JPM.161.179>

Application of temperature-sensitive paint with two channels for studying thermal processes in short duration gas dynamic facilities

V.E. Mosharov¹, V.N. Radchenko¹, I.V. Senuev¹, M.A. Kotov²✉

¹ Central Aerohydrodynamic Institute, TsAGI, Zhukovsky, Moscow Region, Russia;

² Ishlinsky Institute for Problems in Mechanics of RAS, Moscow, Russia

✉ kotov@ipmnet.ru

Abstract. Specialists from TsAGI have developed a unique two-channel luminescent transducer, a temperature-sensitive paint that allows the measurement of full-field surface heat transfer rates in short-duration wind tunnels. The paper contains a description of the features of the method, its advantages, as well as a brief review of several main results obtained in the study of complex heat transfer structures under high gas flow velocities.

Keywords: wind tunnel, shock tube, heat flux, TSP

Funding: This work was supported by the Government contract (No. AAAA-A20-120011690135-5).

Citation: Mosharov V.E., Radchenko V.N., Senuev I.V., Kotov M.A., Application of temperature-sensitive paint with two channels for studying thermal processes in short duration gas dynamic facilities. St. Petersburg State Polytechnical University Journal. Physics and Mathematics. 16 (1.1) (2023) 463–471. DOI: <https://doi.org/10.18721/JPM.161.179>

This is an open access article under the CC BY-NC 4.0 license (<https://creativecommons.org/licenses/by-nc/4.0/>)

Материалы конференции

УДК 533.6.071.3

DOI: <https://doi.org/10.18721/JPM.161.179>

Применение двухканальных люминесцентных преобразователей температуры для исследований тепловых процессов в трубах кратковременного действия

В.Е. Мошаров¹, В.Н. Радченко¹, И.В. Сенюев¹, М.А. Котов²✉

¹ Центральный аэрогидродинамический институт, Московская область, ЦАГИ, Россия;

² Институт проблем механики им. А.Ю. Ишлинского РАН, г. Москва, Россия

✉ kotov@ipmnet.ru

Аннотация. Специалисты ЦАГИ разработали уникальный двухканальный люминесцентный преобразователь температуры — термочувствительную краску, которая позволяет измерять тепловые потоки к поверхности модели в аэродинамических трубах кратковременного действия. Статья содержит описание особенностей метода, его преимуществ, а также краткий обзор нескольких основных результатов, полученных при исследовании сложной структуры течений в условиях высоких скоростей набегающего газового потока.

Ключевые слова: аэродинамическая труба, ударная труба, тепловые потоки, ЛПТ

Финансирование: Работа выполнена в рамках Государственного задания № AAAA-A20-120011690135-5.

Ссылка при цитировании: Мошаров В.Е., Радченко В.Н., Сенюев И.В., Котов М.А., Применение двухканальных люминесцентных преобразователей температуры для исследований тепловых процессов в трубах кратковременного действия // Научно-

технические ведомости СПбГПУ. Физико-математические науки. 2023. Т. 16. № 1.1. С. 463–471. DOI: <https://doi.org/10.18721/JPM.161.179>

Статья открытого доступа, распространяемая по лицензии CC BY-NC 4.0 (<https://creativecommons.org/licenses/by-nc/4.0/>)

Introduction

Luminescent temperature transducers, which are used in aerodynamic experiments to determine thermal characteristics, are of two types: those based on organic phosphors and those based on crystal phosphors. In the literature, the first ones are called TSP (temperature-sensitive paint), and the second TGP (thermographic phosphors). TSPs emerged and developed in parallel with luminescent pressure transducers (Pressure Sensitive Paint, PSP) as a “co-product”. Sensors based on crystal phosphors appeared earlier; their scope is not limited to aerodynamics [1].

TSPs are used to study the laminar-turbulent transition of the boundary layer and measure heat fluxes [2]. In the first case, TSP compete with the thermal imaging method [3, 4], and when measuring the heat flux, they also compete with thermal melting indicators [5–7]. The sensitivity of modern thermographic cameras is higher than TSP with a larger dynamic range; it also does not require the application of a sensitive coating on the model and the organization of model lighting. However, the spatial resolution of camera matrices is still significantly inferior to CCD and CMOS matrices. Another disadvantage of the thermal imaging method (as well as pyrometry) is the influence of external thermal illumination, which can penetrate, for example, from the test section of a wind tunnel (the metal walls of the nozzle and the working part are mirror for IR radiation). Also in cryogenic installations (large Reynolds numbers) [8–10] the surface temperature of the model is 110–140 K, the thermal imager cannot measure such temperatures. Finally, most thermal imagers use matrices of bolometers, the information from which is read sequentially. The non-simultaneity of temperature measurement must be taken into account when studying fast processes – if the heating time is comparable to the time of reading the matrix, then the use of a thermal imager is impossible.

Simultaneity of temperature measurement is an important advantage of TSP over melting temperature indicators. In contrast, TSPs do not absorb energy for phase transition and can be thinner, which also reduces their heat capacity and allows them to be used in short duration shock tubes. Also TSP is a reversible sensor, i.e. it is enough to apply TSP only once for the entire cycle of thermal testing of the model.

This work contains a description of a two-channel TSP developed by TsAGI specialists and which makes it possible to register the thermal features of short duration high-speed gas-dynamic flows with particular accuracy. A brief overview of some of the studies performed with this tool is also provided. There are works where TSP based on organic phosphors are used to measure heat fluxes and study the transition of the boundary layer in short duration facilities [11–13]. However, in all works, single-channel (single-color) TSPs are used, which lose in accuracy to two-channel transducers.

Creation of two channel TSP

The temperature transducer should not feel pressure; the excited state time should be very small. It is necessary either to provide short-lived fluorescence or to place the phosphor molecules in a polymer matrix that is impermeable to oxygen [14]. Or, it is necessary to use molecules with deep-lying transitions that are inaccessible for oxygen quenching. It is desirable to have a high luminous intensity of the sensor coating with high sensitivity, which means that temperature quenching should occur in a limited, given temperature range. For short duration shock tubes, the temperature range of 10–150 °C is of interest. The mechanism of temperature dependence of fluorescence (internal conversion) can be described as:

$$I = h\nu_f \Omega k_f \frac{k_{ex} I_{ex} n_{S0}}{k_f + k_{ms}} = \frac{I_0}{1 + b \cdot \exp\left(-\frac{\Delta E_m}{kT}\right)}. \quad (1)$$

Where ν_f is the frequency of luminescence light, k_{ex} is the rate constant of excitation of luminophore molecules, k_f is the fluorescence emission rate constant, n_{s0} is the concentration of luminophore molecules in the ground state, I_0 is luminescence intensity in the absence of oxygen or at absolute zero temperature, Ω is luminescent sensor volume, k_{ms} is the rate constant of nonradiative transitions, I_{ex} is the intensity of the exciting radiation, b is distortion factor, ΔE_m is the activation energy of internal conversion, I_0 is the luminescence intensity in the absence of temperature quenching at $T=0$ K. The sensitivity is described by the expression:

$$\frac{dI}{I} = -\frac{b \cdot \exp\left(-\frac{\Delta E_m}{kT}\right)}{1 + b \cdot \exp\left(-\frac{\Delta E_m}{kT}\right)} \frac{\Delta E}{kT} \frac{dT}{T}. \quad (2)$$

If the quantum yield is not optimized, then the sensitivity can be written as:

$$\frac{dI}{IdT} = -\frac{\Delta E_m}{kT^2}. \quad (3)$$

The activation energy cannot be greater than the energy of the excited state $-\Delta E_m \ll h\nu_f = hc/\lambda_f$. I.e. under normal conditions, it is impossible to obtain a high sensitivity of the luminescence intensity to temperature in a limited temperature range. It is necessary to look for other mechanisms. Such mechanisms may include concentration quenching or intermolecular energy transfer, if these processes are controlled by the mobility of molecules in the polymer matrix and, therefore, are determined by temperature.

The lanthanide ions Ln^{3+} have a rather bright luminescence due to radiative transitions inside the 4-f shells, and these transitions are inaccessible for oxygen quenching. Good results can be obtained with the cluster luminescence of one of the Europium complexes ($Eu(dbm)_3phen$). Its molecules practically do not luminesce either in solution or in crystals, but clusters consisting of several molecules have bright luminescence that is not quenched by molecular oxygen. The temperature dependence of this luminescence is determined by the mobility of molecules of Europium complex in the polymer. This allows one to adjust the temperature sensitivity, but all the imperfections of the polymer (relaxation after polymerization, temperature hysteresis) affect the calibration characteristic. It means that TSP needs to be calibrated.

Epoxy resin E-41 without polymerization turned out to be the optimal polymer for creating a converter based on the Europium complex. At temperatures up to 100 °C, the resin remains solid. The calibration characteristic of such a sensor is shown in Fig. 1, a. Temperature sensitivity can be changed by adding a plasticizer.

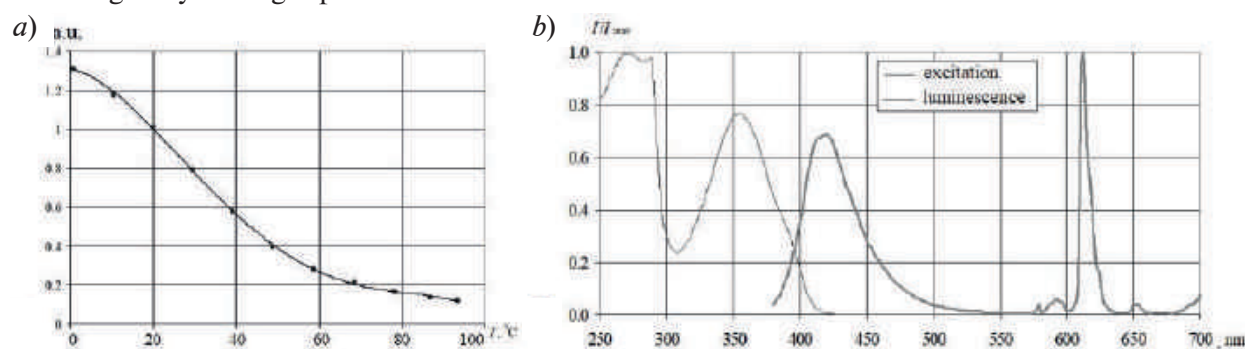


Fig. 1. TSP calibration curve (a); excitation and luminescence spectra (b)

Many recipes for TSP have been proposed, including the complexes of Europium and Terbium lanthanides [15–17]. The application methods of TSP and PSP are very close, with the only difference being that TSP are temperature sensitive and not pressure sensitive, while PSPs sense both. For accurate temperature measurement, two-channel TSP must be used.

TsAGI specialists developed a two-color TSP containing an additional reference phosphor, the luminescence of which does not depend on temperature, the Coumarin-7 laser dye. Its luminescence is used for pixel-by-pixel correction of changes in the intensity of the exciting radiation. Both phosphors are excited simultaneously from the same light source, but emit light

in different spectral regions and can be easily separated (see Fig. 1, *b*). The two-channel TSP does not exclude a normalization frame at a known temperature of the model to eliminate the inhomogeneity of the ratio of active and reference phosphors on the surface under study. In this case, it is necessary to ensure the isothermality of the model and measure its temperature. It is interesting that the TGP application technique also uses registration in two spectral regions [18]. However, no other two-channel (two-color) TSP have been developed.

As with the PSP, markers must be applied to the surface of the model to match the images with and without flow from each luminophore. They (with known 3D coordinates) are also used to transfer the measurement results to the 3D surface of the model.

The central point of the thermal experiment is the choice of the model material. It must be heat-insulating, homogeneous in terms of thermophysical properties and technologically advanced. The use of optical methods also imposes additional conditions: optical uniformity of the surface, light color and opacity. TSP is applied to the surface of the model with a spray gun like ordinary paint. The layer thickness after drying is 3–5 microns, which makes it practically invisible and significantly complicates the application process. However, control of the thickness and uniformity of the coating can be carried out in ultraviolet light. After applying TSP, markers (black dots) are applied to the surface of the model. More detailed information about the features of the experiment, the method of application and post-processing of the results can be found in [19, 20].

Application of TSP at different facilities

1. Wind tunnel UT-1M TsAGI

In this installation, operating on the principle of the Ludwig tube, a series of experimental studies of heat transfer on the surface of sharp and blunt plates near a single wedge and near a pair of wedges was carried out at Mach numbers $M = 5-10$ and several values of the Reynolds number corresponding to laminar, transitional and turbulent boundary layer states in front of the wedge. The research results are presented in [21–24]. The possibilities of TSP are illustrated in Fig. 2, *a*, which shows the heat flux distribution on a flat plate between two wedges for two bluntness radii of the leading edge of the plate at $M = 6$ and $Re = 1.5 \cdot 10^6$. It is very difficult to obtain heat flux information with such a spatial resolution by any other method. Studies of the transition of the boundary layer on blunt cones were also carried out (Fig. 2, *b*).

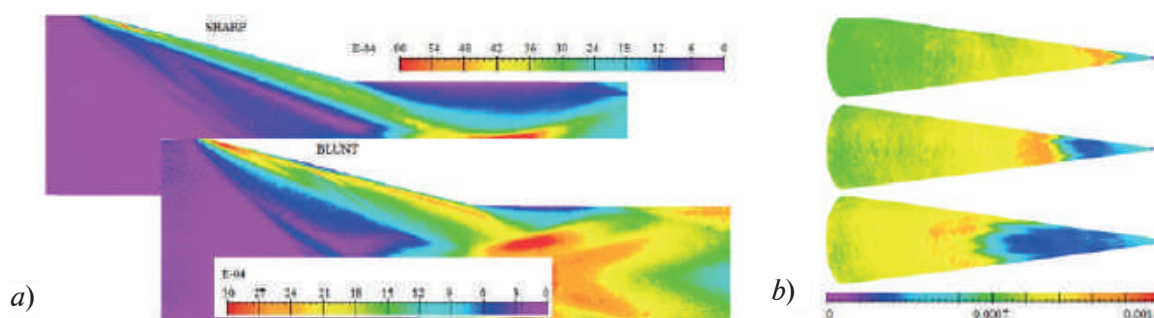


Fig. 2. Excitation and luminescence spectra of a two-color TSP (*a*); boundary layer transition on a cone depending on bluntness (*b*)

2. Wind tunnel AT-303 ITAM SB RAS

Here, TSP was used to study the transition of the boundary layer on a model of a hypersonic demonstrator. In the studied modes ($M = 5.73; 7.75$), in comparison with UT-1M, the AT-303 wind tunnel has high stagnation temperatures. Some of the results obtained are shown in Fig. 3, where the fields of the conditional Stanton number are shown in color. In all launches at $M = 5.73$ (Fig. 3, *a*), the heat flux increased approximately twice immediately behind the bow, which can be interpreted as a transition of the boundary layer. Decreasing Re from $13.8 \cdot 10^6$ to $9.2 \cdot 10^6$ results in a slight downstream shift of the transition. The level of values of the Stanton number on the line of symmetry in turbulent flow agrees in order of magnitude with the calculated values for a flat plate. At the Mach number $M = 7.75$ (Fig. 3, *b*) at $Re = 6.1 \cdot 10^6$, a natural transition is also observed. The experiment in AT-303 is described in more detail in [25].

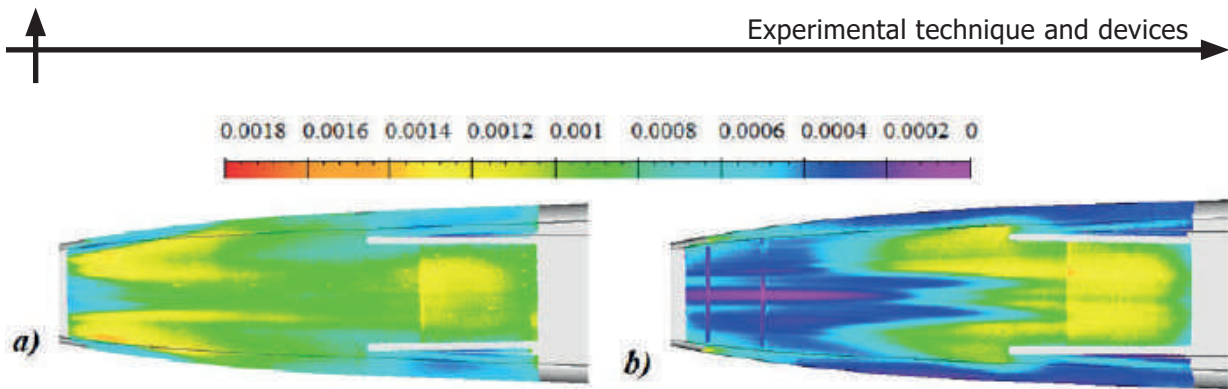


Fig. 3. St distributions at $M = 5.73$ (a); 7.75 (b) [25]

3. HAST IPMech RAS

Experiments with TSP have been prepared and carried out to visualize the temperature field on the surface of models at the HAST IPMech RAS, which functions as shock tube with aerodynamic section. Results with triple angle semi-wedge imitating scramjet air intake are shown in Fig. 4.

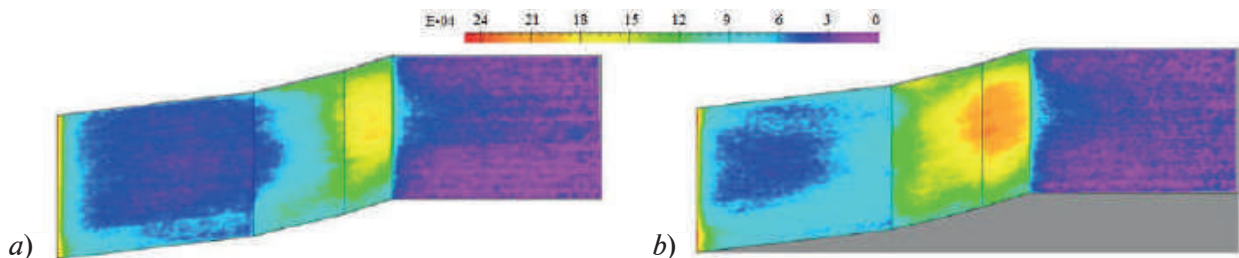


Fig. 4. Model surface temperature processed data at $M = 5.3$ (a); 5.5 (b) [26]

Heat transfer structures

Influence of entropy layer generated by blunt plate leading edge on the flow over different wedge configurations was studied experimentally by means of TSP [27]. It was shown that even a small bluntness of the plate leading edge considerably changes the heat transfer distributions at shock wave/boundary layer interaction (Fig. 5, a), and under certain conditions it results in the change of flow structure (Fig. 5, b, c).

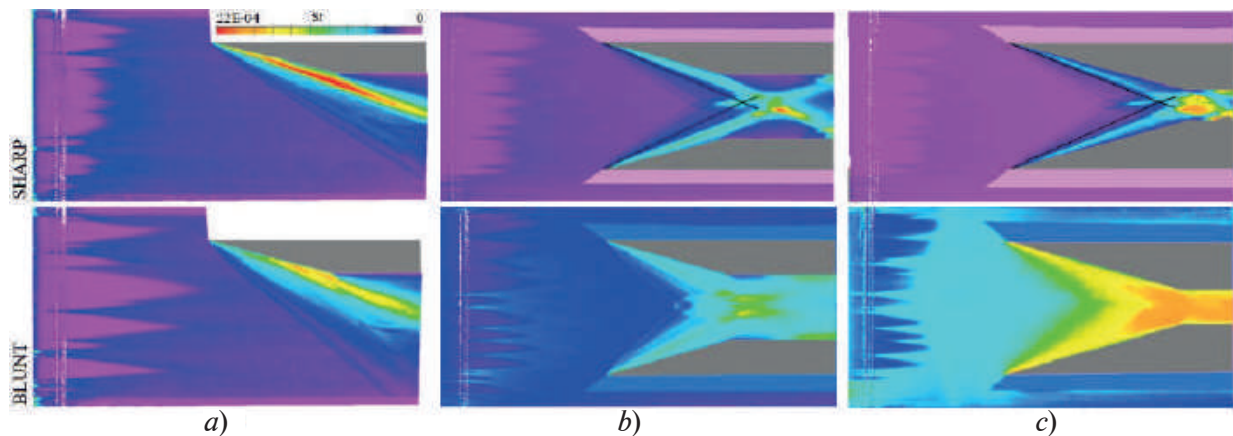


Fig. 5. St distributions at $M = 5$ gas flow on the sharp and blunt plates with 15° wedge configurations [27]

In [28, 29] a generic inlet with flat walls and rectangular cross section was considered (Fig. 6, 7). Also the data about an influence of upper cowl on heat transfer and flow structure inside an inlet are obtained (Fig. 6, 7, b).

The flow around a cylinder mounted on a sharp or blunted plate is experimentally studied in [30, 31]. The results on the flow structure and heat transfer on the plate surface ahead of the cylinder and in its vicinity are described (Fig. 8). It was founded that heat-transfer coefficient peak values in interference regions decrease with increases in plate bluntness and distance from cylinder to leading edge.

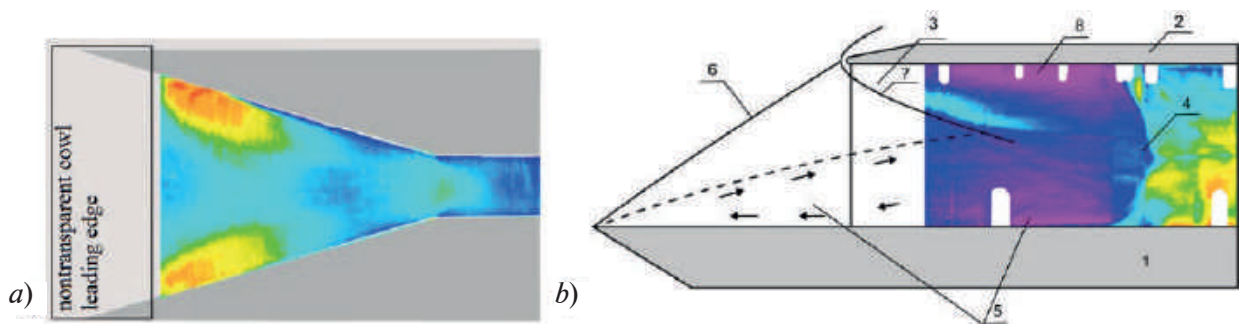


Fig. 6. St distributions on the cowl (a) and flow structure on a wedge in the inlet with blunted cowl (b) [28]

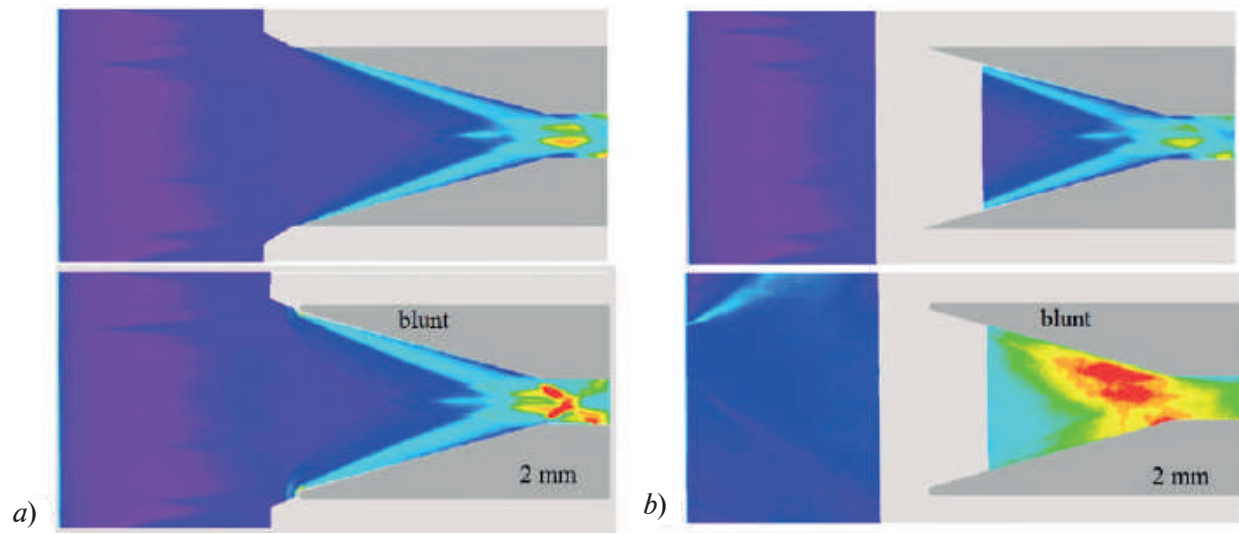


Fig. 7. Results of $M = 5$ on the plate with (b) and without a cowl (a) [28]

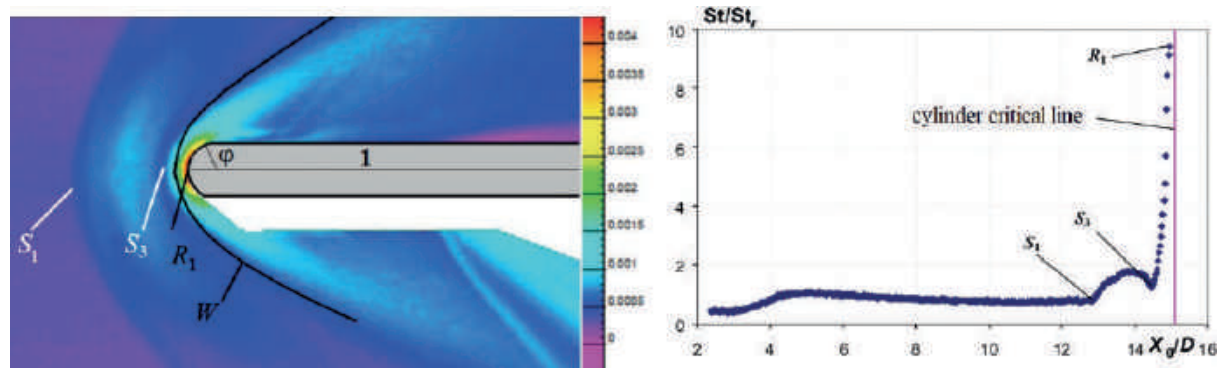


Fig. 8. Heat transfer picture and the distribution of St along the line of symmetry [30]

Heat transfer over 15° compression corner flow affected by reattachment vortices of controllable intensity are carried out in [32]. The intensity of the vortices was varied by accurate controlling the height of a spanwise rake of cylindrical pins placed on the plate. It helped to determine the state of boundary layers at reattachment as close to laminar or transitional (Fig. 9).

The influence of flow parameters and nose radius of blunt cone on the location of laminar–turbulent transition is investigated in [33]. It is shown that transition reversal can occur either in the absence of turbulent wedges or at a constant level of freestream disturbances. Both increasing and decreasing branches of $Re_{\infty,t}$ ($Re_{\infty,R}$) dependency were observed at constant nose radius while varying only the unit Reynolds number (Fig. 10).

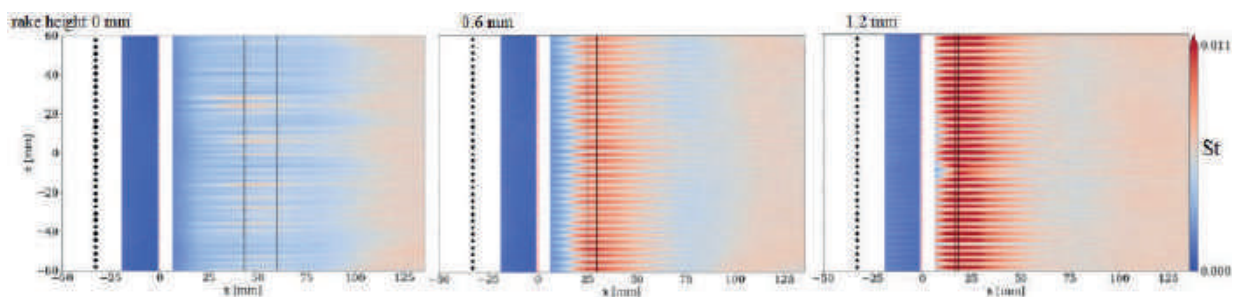


Fig. 9. Example distributions of St over compression corner surface showing appearance of reattachment vortices at rake height growth [32]

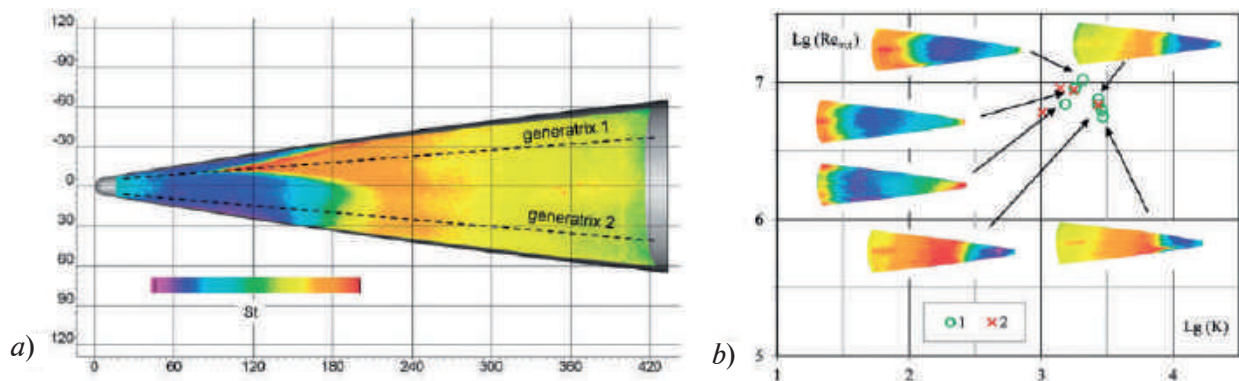


Fig. 10. Transition location determination by St distribution (a); Panoramic St distributions and its correspondence to points of $Lg(Re_{\infty,t})$ [33] (b)

Conclusion

TsAGI scientists have created two-channel TSP, which can significantly improve the accuracy of temperature measurement. On the basis of digital technologies for recording and processing images, the measurement of thermal parameters of gas on the surface of bodies has been worked out. A technique has been developed for measuring heat flux fields in short duration gas dynamic facilities. A brief analysis of some of the results obtained in recent years and demonstrating a wide range of applications of the developed methodology is presented.

Acknowledgement

This work was supported by the Government contract (No. AAAA-A20-120011690135-5).

REFERENCES

1. Khalid A.H., Kontis K., Thermographic Phosphors for High Temperature Measurements: Principles, Current State of the Art and Recent Applications 2008 Sensors 8.
2. Tianshu Liu, et al., Pressure and Temperature Sensitive Paints Springer Cham 2021.
3. Carlomango G.M., et al., Infrared Thermography as a Tool for Thermal Surface Flow Visualization 1998 Journal of Visualization 1 1.
4. De Luca L., et al., Flow Visualization and Heat Transfer Measurement in a Hypersonic Wind Tunnel 1992 Experimental Heat Transfer 5 65–78.
5. Ardasheva M.M., et al., Primenenie plavyashikhshya termoindikatorov dlya izmereniya teplovykh potokov k modelyam v aerodinamicheskikh trubakh 1972 Uch. Zap. TsAGI 1 (in Russian).
6. Ardasheva M.M., et al., Primenenie termoindikatornykh pokrytij v issledovaniyakh teploobmena 1975 Trudy TsAGI 1162 14-17 (in Russian).
7. Ardasheva M.M., et al., Primenenie termoindikatornykh pokrytij v issledovaniyakh teploobmena 1975 Trudy TsAGI 1692 (in Russian).
8. Asai K., et al., 1996 Detection of Boundary-Layer Transition in a Cryogenic Wind Tunnel by Using Luminescent Paint AIAA Paper 1996–2185.

9. **Iijima Y., et al.**, 2003 Optimization of Temperature Sensitive Paint Formulation for Large-Scale Cryogenic Wind Tunnels 20th ICIASF Aug 25–29.
10. **Fey U., et al.**, 2003 Transition detection using temperature sensitive paint at Cryogenic Temperatures in the European Transonic Wind Tunnel (ETW) 20th ICIASF, Aug 25-29.
11. **Hubner J.P., et al.**, 2002 Heat Transfer Measurements in Hypersonic Flow Using Luminescent Coating Techniques AIAA Paper 2002–0741.
12. **Popernack T.G., et al.**, 1997 Application of temperature sensitive paint for detection of boundary layer transition 17th International Congress on Instrumentation in Aerospace Simulation Facilities Sep 29–Oct 2 77–83.
13. **McLachlan B.G., et al.**, 1993 Boundary layer transition detection by luminescence imaging AIAA Paper 1993. – 0177.
14. **Borovoy V.Ya.**, Techenie gaza i teploobmen v zonakh vzaimodeystviya udarnykh voln s pogranychnym sloem Mashinostroenie, 1983
15. **Liu T., Sullivan J.P.**, Pressure and temperature sensitive paints Springer-Verl 2005.
16. **Campbell B., et al.**, Temperature measurement using fluorescent molecules 6th International Symposium on Applications of Laser Techniques to Fluid Mechanics Portugal Lisbon. 1992.
17. **Shinya Katagiri, et al.**, New strategy for thermo-sensing dye based on the back energy transfer in photosensitized luminescence Proceedings of International Workshop on Molecular Imaging for Interdisciplinary research Japan Sendai Nov 8–9, 2004
18. **Buck G.M.**, An Imaging System for Quantitative Surface Temperature Mapping Using Two-Color Thermographic Phosphors 34th International Instrumentation Symposium NM Albuquerque, 1988.
19. **Mosharov V., et al.**, Temperature sensitive paint (TSP) for heat transfer measurement in short duration wind tunnels 20th ICIASF, 2003, 351–356.
20. **Mosharov V.E., Radchenko V.N.**, Izmerenie polej teplovykh potokov v trubakh kratrovremennogo dejstviya s pomoshyu lyuminiscentnykh preobrazovatelej temperatury, 2007 Uch. Zap. TsAGI 1 2 (in Russian).
21. **Borovoy V.Y., et al.**, Laminar-turbulent flow over wedges mounted on sharp and blunt plates 2009 Fluid Dyn 44 382–396.
22. **Borovoy V., et al.**, Three-Dimensional Shock-Wave/Boundary-Layer Interaction at the Presence of Entropy Layer EUCASS St. Petersburg Jul 4–8, 2011.
23. **Borovoy V., et al.**, Temperature sensitive paint application for investigation of boundary layer transition in short-duration wind tunnels Flight Physics book of EUCASS 2011, 109–118.
24. **Mosharov V., et al.**, Hypersonic turbulent heating of sharp and blunt plates near a wedge 2011 Visualization of Mechanical Processes 1.
25. **Borovoy V., et al.**, Issledovanie perekhoda pogranychnogo sloya s pomoshyu lyuminiscentnykh preobrazovatelej temperatury v aerodinamicheskoy trube impulsnogo dejstviya AT-303 Proc. of ICMAR 2010 Novosibirsk Nov 1–6 (in Russian)
26. **Mosharov V.E., et al.**, 2018 J. Phys.: Conf. Ser. 1009 012036.
27. **Borovoy V., et al.**, 2014 Influence of entropy layer on the airflow over a wedge and a pair of wedges on the plate AIAA Paper 2014–1139.
28. **Borovoy V., et al.**, 2015 Gas Flow in a Generic Inlet with Blunted Leading Edges AIAA Paper 2015–1061.
29. **Borovoy V., et al.**, Influence of leading edge bluntness on hypersonic flow in a generic internal-compression inlet 2015 Progress in Flight Physics 7 419–436.
30. **Borovoy V.Y. et al.**, Shock Wave Interaction Near a Cylinder Aligned Normal to a Bluntedge-Part I: Gas Flow and Heat Transfer on a Plate Near a Cylinder 2018 TsAGI Science Journal 49 2.
31. **Borovoy V.Y. et al.**, Interaction of Shock Waves Near a Cylinder Perpendicular to a Blunt Plate, Part II: Heat Transfer on a Cylinder 2018 TsAGI Science Journal 49 6.
32. **Chuvakhov P.V., Radchenko V.N.**, Effect of Gurtler-like vortices of various intensity on heat transfer in supersonic compression corner flows 2020 Int J Heat Mass Transf 150 119310.
33. **Vaganov A. et al.**, 2020 Laminar–turbulent transition reversal on blunt ogive body of revolution at hypersonic speeds Proc. of the Institution of Mechanical Engineers, Part G: Journal of Aerospace Engineering 234 1 102–108.



THE AUTHORS

MOSHAROV Vladimir E.
vladimir.mosharov@tsagi.ru

SENUEV Ivan V.
senyuev_ivan@mail.ru

RADCHENKO Vladimir N.
vradchenko@yandex.ru

KOTOV Mikhail A.
kotov@ipmnet.ru
ORCID: 0000-0002-5523-0300

Received 26.10.2022. Approved after reviewing 15.11.2022. Accepted 15.11.2022.

Conference materials

UDC 533.6.071.3

DOI: <https://doi.org/10.18721/JPM.161.180>

Pulse thermal load for thermoelectric detector calibration

M.A. Kotov ¹✉, N.G. Solovyev ¹, V.N. Glebov ², G.A. Dubrova ², A.M. Malyutin ²

¹ Ishlinsky Institute for Problems in Mechanics of the RAS, Moscow, Russia;

² Institute on Laser and Information Technologies - Branch of the Federal Scientific Research Centre "Crystallography and Photonics" of RAS, Moscow Region, Russia

✉ kotov@ipmnet.ru

Abstract. The work is devoted to the calibration of the developed thermoelectric detectors with different sensitive elements. A pulsed laser diode with a power of 5 W was used as a radiation source. A lamp with a tungsten filament was also used to set the combined thermal load and assess the overall level of sensor sensitivity. The performed calibration procedures made it possible to obtain volt-watt characteristics for thermoelectric detectors of a new type, which will help to better describe the thermal processes of high-intensity shock-wave interactions occurring in a pulsed gas-dynamic experiment.

Keywords: heat flux, shock tube, laser heating, calibration

Funding: This work was supported by the Ministry of Science and Higher Education within the Russian State Contracts No. AAAA-A20-120011690135-5 and the State assignment FSRC "Crystallography and Photonics" RAS.

Citation: Kotov M.A., Solovyev N.G., Glebov V.N., Dubrova G.A., Malyutin A.M., Pulse thermal load for thermoelectric detector calibration, St. Petersburg State Polytechnical University Journal. Physics and Mathematics. 16 (1.1) (2023) 472–477. DOI: <https://doi.org/10.18721/JPM.161.180>

This is an open access article under the CC BY-NC 4.0 license (<https://creativecommons.org/licenses/by-nc/4.0/>)

Материалы конференции

УДК 533.6.071.3

DOI: <https://doi.org/10.18721/JPM.161.180>

Импульсная тепловая нагрузка для калибровки термоэлектрического детектора

М.А. Котов ¹✉, Н.Г. Соловьев ¹, В.Н. Глебов ², Г.А. Дуброва ², А.М. Малютин ²

¹ Институт проблем механики им. А.Ю. Ишлинского РАН, Москва, Россия;

² Институт проблем лазерных и информационных технологий РАН – филиал ФНИЦ «Кристаллография и фотоника» РАН, Московская область, Россия

✉ kotov@ipmnet.ru

Аннотация. Работа посвящена калибровке разработанных термоэлектрических детекторов с различными чувствительными элементами. В качестве источника излучения использовался импульсный лазерный диод мощностью 5 Вт. Лампа с вольфрамовой нитью также использовалась для установки комбинированной тепловой нагрузки и оценки общего уровня чувствительности датчика. Выполненные калибровочные процедуры позволили получить вольт-ваттные характеристики термоэлектрических детекторов нового типа, которые помогут лучше описывать тепловые процессы высокоинтенсивных ударно-волновых взаимодействий, происходящих в импульсном газодинамическом эксперименте.

Ключевые слова: фазовый тепловой поток, ударная труба, лазерный нагрев, калибровка

Финансирование: Работа выполнена в рамках Государственных заданий № АААА-А20-120011690135-5 и ФИЦ «Кристаллография и Фотоника» РАН.

Ссылка при цитировании: Котов М.А., Соловьев Н.Г., Глебов В.Н., Дуброва Г.А., Малютин А.М., Некоторые аспекты импульсной тепловой нагрузки для калибровки термоэлектрического детектора // Научно-технические ведомости СПбГПУ. Физико-математические науки. 2023. Т. 16. № 1.1. С. 472–477. DOI: <https://doi.org/10.18721/JPM.161.180>

Статья открытого доступа, распространяемая по лицензии CC BY-NC 4.0 (<https://creativecommons.org/licenses/by-nc/4.0/>)

Introduction

Surface temperature and heat flux measurements play a very important role in heat transfer studies. Registration of changes in heat fluxes in a gas-dynamic experiment during ultra-short time periods is one of the most significant factors in setting up and conducting studies of heat transfer in pulse supersonic and hypersonic flows. Typical time values in such gas dynamic experiments range from hundreds of microseconds to several milliseconds. In shock tube experiments [1–4], the model is subjected to a sudden high thermal load on a very short measurement time scale. To calibrate the thermal sensors for such free flow conditions, experiments are carried out by applying a thermal load from a laser beam with a known output power [4–6]. For pulsed gas dynamic processes, the laser calibration method is the most suitable, since it allows the desired value of the heat flux to be applied to the sensor very quickly. The emitted power value used is fixed and can change rapidly during the calibration process. The resulting volt-watt characteristic of the sensor is used for its subsequent application under the considered gas flow regimes – short time intervals and high temperature loads.

This work is devoted to the calibration of thermoelectric detectors [7–9] with different sensitive elements. A laser diode (975 nm) were used as a radiation source in the calibration stand. A pulsed operation mode was set at a radiation power of 5 W. Solution of issues related to radiation homogenization makes it possible to obtain reliable calibration dependences. To control the response time of the sensor and signal rise fronts, a high-speed photodiode with a time resolution of less than 20 ns was placed in the optical scheme of the stand. In addition to laser devices, a lamp with a tungsten filament was also used to set the combined thermal load and assess the overall level of sensor sensitivity.

The performed calibration procedures made it possible to obtain volt-watt characteristics for thermoelectric detectors of a new type, which will help to better describe the thermal processes of high-intensity shock-wave interactions occurring in a pulsed gas-dynamic experiment.

Creation of two types of thermoelectric detector

The principle of operation of thermoelectric detectors is based on the generation of thermo-EMF when a temperature gradient occurs in the sensitive element with anisotropy of the coefficient. The method used under the conditions described above for measuring transient temperature with surface transient sensors should have a fast response time and be adequate for rapidly changing flow conditions. As a surface heat flux sensor, these devices are suitable for measuring high power transient heat flux. In [7, 8], such sensors showed good results in measuring heat fluxes in shock tubes with shock waves of low and high intensity. The obtained values reached more than 45 MW/m² for 1 μs with a registration frequency of 10⁷ Hz and a high signal-to-noise ratio, and the environments of the sensors were quite aggressive.

For this work, two sets of sensors with different sensitive elements were manufactured. They were based on a silicon layer 0.4 mm thick, thermally oxidized on both sides and having a high resistance. A film of an oblique anisotropic layer 0.3 μm thick in the form of an inclined columnar structure is deposited on the front side of the sensor by vacuum deposition. For the first set, this was the Cr layer. The second set used the GeTe alloy. On the sides of the sensing element there were contact pads through which the thermo-EMF was taken.

Lamp calibration

In this method, heat transfer occurs due to broadband thermal radiation. The purpose of the procedure was to evaluate the overall level of sensitivity of the manufactured sensors. The sensitive elements were placed on an Al substrate. To ensure heat dissipation, a layer of thermal paste is applied between the sensor and the substrate. A constant heat flux to the plane of the sensitive element was provided by a tungsten lamp. To register the sensor readings, a V7-40 microvoltmeter was used. After turning on the lamp, the readings of the microvoltmeter were set to a certain maximum value for the sensor under test. The time to reach the maximum value was approximately 1 s. Then the lamp was turned off, the heat flux sensor was replaced by the next one (Cr and GeTe, 6 sensors in each set) and the procedure was repeated. Table 1 shows the obtained values. The sensitivity level of GeTe sensors exceeds Cr by several orders of magnitude. At the same time, the sensitivity of elements in one set can differ by dozens (more than 40 times for Cr and more than 8 times for GeTe, see Table 1). It depends on the deposition density of the sensitive element.

Table 1

Lamp calibration results for Cr and GeTe sets

r	#1	30 μ V	x_1	GeTe	#1	10 mV	x_2
	#2	40 μ V	$1.2 \cdot x_1$		#2	18 mV	$1.8 \cdot x_2$
	#3	50 μ V	$1.6 \cdot x_1$		#3	42 mV	$4.2 \cdot x_2$
	#4	200 μ V	$6.6 \cdot x_1$		#4	45 mV	$4.5 \cdot x_2$
	#5	280 μ V	$9.3 \cdot x_1$		#5	48 mV	$4.8 \cdot x_2$
	#6	580 μ V	$19.3 \cdot x_1$		#6	64 mV	$6.4 \cdot x_2$
	#7	1.25 mV	$41.6 \cdot x_1$		#7	81 mV	$8.1 \cdot x_2$

Laser diode pulses

The stand for measuring sensors is shown in Fig. 1, *a*. A laser diode PLD-10 975 nm with optical fiber of 0.13 NA was used as a radiation source. The fiber output is set at a distance of 40 mm from the sensor. The sensor was located at the bottom of the stand and covered with a special Al mask (0.7 mm thick with 3 mm hole at center) for thermal load set directly on sensitive element and to ensure that there was no thermal effect on the contact pads (Fig. 1, *b*). Hantek DSO5202P digital oscilloscope was used for data registration.

The sensor is mounted on a 2 mm thick duralumin heat-removing plate through a thin layer of thermal paste. The signal to the oscilloscope was taken directly from the sensor, the probe resistance is 1 MOhm (the standard probe for this oscilloscope), a 1 kOhm resistor is installed in parallel with the sensor. To evaluate the speed of the laser diode, an SFH203P photodiode with a rise and fall time of 5 ns in the voltage generation mode was used. The result is shown in Fig. 2. The rise and fall time of the laser diode is approximately 1 μ s.

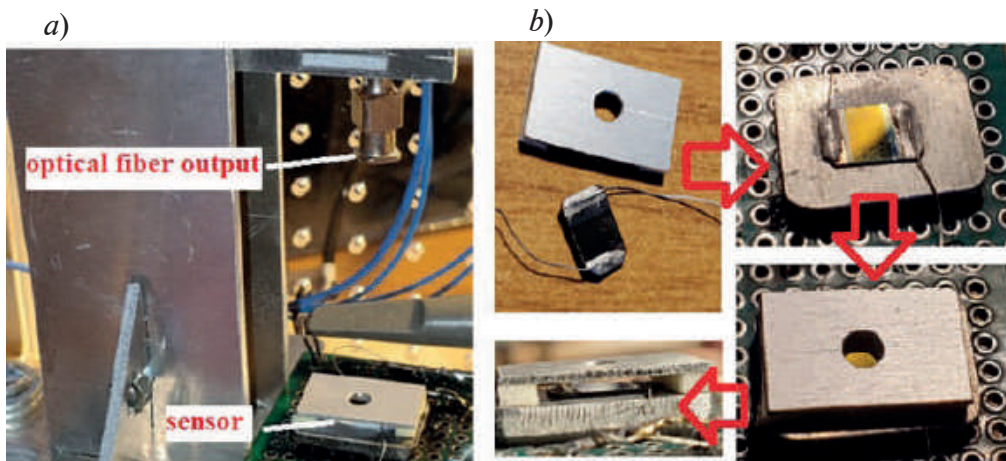


Fig. 1. Laser diode stand (*a*); The procedure for installing the sensor with Al mask (*b*)

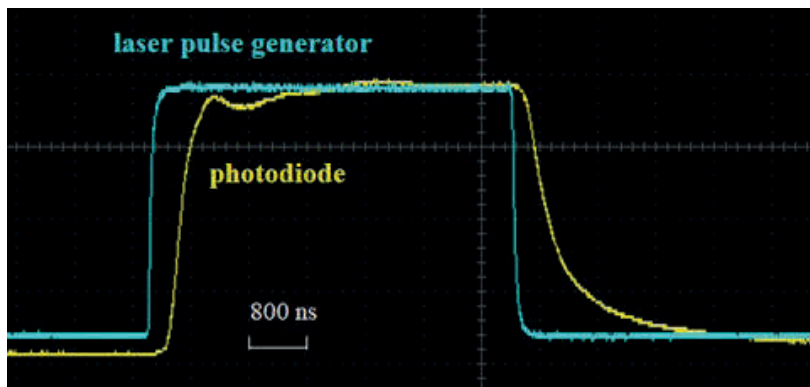


Fig. 2. Data (a.u.) from laser pulse generator (blue) and photodiode at sensor plate (yellow)

To comply with the conditions for correct calibration by laser radiation, it is important to ensure its instantaneous and uniform absorption directly on the sensitive element of the sensor being calibrated. It is also necessary to ensure that radiation does not pass through the sensitive element due to its possible absorption/dissipation in other places of the sensor. For these purposes, a thin layer ($\sim 20 \mu\text{m}$) of black matte nitro paint was applied. The radiation absorption coefficient was considered equal to 0.9, which can be set as valid for a wavelength of 975 nm and such environmental conditions. Some results obtained with a laser pulse duration of 500 μs and a repetition rate of 100 Hz are shown in Fig. 3.

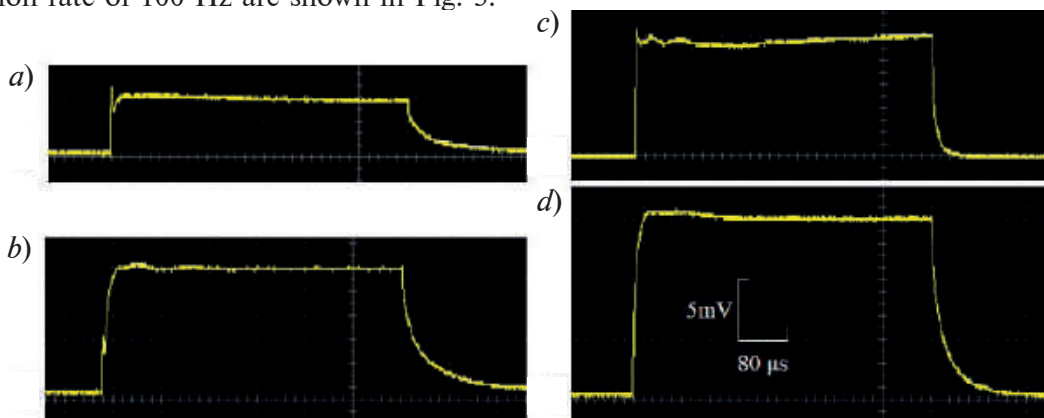


Fig. 3. Signals for #1 (a), #2 (b), #4 (c) and #7 (d) GeTe sensors from 500 μs laser pulse heat load

Cr-based sensors have a significantly lower sensitivity; therefore, to study their characteristics, an amplifier with a voltage amplification factor of 50 was used. The performance of the amplifier was tested using the GK101 pulse generator at 1–100 kHz rate.

The value of the power coming to the sensor can be estimated as follows. Let's assume that the distribution profile of the radiation intensity of the multi-mode fiber is uniform. Knowing the numerical aperture (0.13) and the distance to the sensor mask (40 mm), we can calculate the laser spot diameter – 10.5 mm. The power of the radiation incident on the sensor through the mask is approximately equal to the ratio of the output power from the optical fiber (5 W) to the ratio of the areas of the laser spot and the mask hole (3) – 1.66 W. Estimates of the calibration coefficient for manufactured sensors are given in Table 2.

Fig. 3 shows that the exposure time of the laser diode is sufficient to establish a quasi-constant value in the sensor readings. The long rising and falling fronts of signals can be explained by the heating and cooling time of the black paint layer that absorbs radiation. The discrepancy between the coefficients at tables 2 and 1 is up to 5 times for cases with sensors that show the largest signal. The reasons explaining that may be the following:

- The lamp has a broadband spectrum in contrast to the monochromatic radiation of a laser diode. The principle of sensors operation is based on the occurrence of thermal emf, however, radiation at different wavelengths can heat the sensitive element in different ways.

Table 2

Laser pulse calibration results for Cr and GeTe sets

Cr	#1	0.28 mV	x_1	GeTe	#1	5 mV	x_2
	#2	0.3 mV	$1.1 \cdot x_1$		#2	9 mV	$1.8 \cdot x_2$
	#3	0.67 mV	$2.4 \cdot x_1$		#3	11 mV	$2.2 \cdot x_2$
	#4	0.98 mV	$3.5 \cdot x_1$		#4	11.5 mV	$2.3 \cdot x_2$
	#5	1.37 mV	$4.9 \cdot x_1$		#5	12 mV	$2.4 \cdot x_2$
	#6	2.43 mV	$8.7 \cdot x_1$		#6	14.5 mV	$2.9 \cdot x_2$
	#7	4.87 mV	$17.4 \cdot x_1$		#7	17 mV	$3.4 \cdot x_2$

• No absorbent paint was applied in procedure with the lamp (Section 3), so readings are slightly high.

• On the other hand, the action with a laser diode is limited to a round spot with a diameter of ~ 3 mm instead of no limitation in the case of a lamp, which affects the signal in the direction of decreasing. Typical values for the areas of sensitive elements of manufactured sensors lie in the range from 3.5×3.5 mm² to 4.5×4.5 mm². Those, the areas of thermal impact can differ by 1.5–2.5 times. At the same time, this difference can be neglected, because the full heating of the black paint layer is still carried out, and this rather affects the growth of the readings, but not their steady value.

• The same can be said about the possible uneven distribution of radiation power in the laser spot and other inhomogeneities.

• Despite the high signal-to-noise ratio, the presence of noise contributes to the error in the readings of the sensors. This is especially true in the case of Cr sensors and laser heating, when an amplifier was used due to small values and the noise level was high.

The heat flux density in mask experiments is approximately 8.3 W/cm² with an average sensing element area of 20 mm². The values of x_1 and x_2 for Table 2 can be estimated at $3.3 \cdot 10^{-9}$ V·m²/W and $6 \cdot 10^{-8}$ V·m²/W, respectively, which looks similar to the data obtained in [7] during shock tube calibration. It can be said that this procedure is suitable for calibration of thermoelectric detectors for the purpose of their further application in the pulse gas-dynamic experiment. However, there are several points that may affect the differences in the resulting calibration rates:

• The radiation power value of 5 W was set with high accuracy at the input to the optical fiber of the laser diode. It was assumed that there was no absorption of radiation in fiber, however, with long fibers it can be up to several percent.

• Fiber multimode, inhomogeneity of the power profile distribution in the laser spot, other peculiarities also affect the values of the radiation power directly at the input of the sensor.

• The generation of thermo emf with such short structures may have a non-linearity as the heat flux increases/decreases. At tens of W/cm², a good agreement is observed, but for higher/lower thermal loads, it is advisable to perform separate calibrations.

Conclusion

Cr-based thermoelectric detectors have been manufactured, which have shown their effectiveness in measuring the heat flux in a pulsed gas-dynamic experiment in [7–9]. A new type of sensors based on GeTe has been developed. The calibration procedures (lamp calibration and laser pulse) carried out in this work made it possible to obtain reliable estimates of the volt-watt dependencies. The data obtained for different types of sensors and calibration procedures are in good agreement both with each other and with previous experiments. This allows one to speak about the suitability of such procedures for obtaining calibration characteristics. Aspects that may affect the discrepancy in the received data are described.

Acknowledgment

This work was supported by the Ministry of Science and Higher Education within the Russian State Contracts No. AAAA-A20-120011690135-5 and the State assignment FSRC “Crystallography and Photonics” RAS.



REFERENCES

1. **Zel'dovich Y.B., Raizer Y.P.**, Physics of Shock Waves and High-Temperature Hydrodynamic Phenomena, Academic Press, 1967.
2. **Kotov M.A., et al.**, 2018 J. Phys.: Conf. Ser. 1009 012038.
3. **Surzhikov S.T.**, 2017 J. Phys.: Conf. Ser. 815 012023.
4. **Kumar R., Sahoo N., Kulkarni V.**, Conduction based calibration of handmade platinum thin film heat transfer gauges for transient measurements, International journal of heat and mass transfer. 55 9-10 (2012) 2707–2713.
5. **Kumar R., Sahoo N.**, Dynamic calibration of a coaxial thermocouples for short duration transient measurements, journal of heat transfer. 135 (12) (2013).
6. **Sapozhnikov S.Z., Mityakov V.Yu., Mityakov A.V.**, Heatmetry: The Science and Practice of Heat Flux Measurement, Springer International Publishing, 2020, p. 209.
7. **Kotov M.A., et al.**, 2021 Performance assessment of thermoelectric detector for heat flux measurement behind a reflected shock of low intensity, Applied Thermal Engineering, 195 117143.
8. **Kotov M.A., et al.**, 2021 J. Phys.: Conf. Ser. 2103 012218.
9. **Kotov M.A., et al.**, 2022 Registration of the Ignition of A Combustible Mixture in a Shock Tube Using a Thermoelectric Detector, Russ. J. Phys. Chem. B 16 (4).

THE AUTHORS

KOTOV Mikhail A.

kotov@ipmnet.ru

ORCID: 0000-0002-5523-0300

SOLOVYEV Nickolay G.

lantan.ltd@mail.ru

GLEBOV Vladislav N.

jorik14@mail.ru

DUBROVA Galina A.

dgala@list.ru

MALYUTIN Andrey M.

ammaliutin@rambler.ru

Received 26.10.2022. Approved after reviewing 14.11.2022. Accepted 15.11.2022.

Conference materials

UDC 53.083.9

DOI: <https://doi.org/10.18721/JPM.161.181>

Estimation of optical diffuse properties of Fresnel lenses

M.Z. Shvarts ¹✉, D.A. Malevskiy ¹, M.V. Nakhimovich ¹, P.V. Pokrovskiy ¹,
N.A. Sadchikov ¹, A.A. Soluyanov ¹

¹Ioffe Institute, St. Petersburg, Russia

✉ shvarts@scell.ioffe.ru

Abstract. This paper proposes a method for determining the diffuse properties of sunlight concentrators such as Fresnel lens. The decrease in Fresnel lens concentrating ability is usually associated with imperfectness in optical refractive surfaces, where some part of the direct light, which comes along the normal to the surface of the Fresnel lens and intended to be concentrated, is getting scattered and directing off a highly efficient concentrator solar cell. The diffuse light flux generated propagates inside the volume of the combined photovoltaic module. This flux undergoes multiple reflections from the structural elements, partially absorbed and ultimately reaches the photoconverters of the planar circuit.

Keywords: Fresnel lens, photoconverters, diffuse light

Citation: Shvarts M.Z., Malevskiy D.A., Nakhimovich M.V., Pokrovskiy P.V., Sadchikov N.A., Soluyanov A.A., Estimation of optical diffuse properties of Fresnel lenses, St. Petersburg State Polytechnical University Journal. Physics and Mathematics. 16 (1.1) (2023) 478–483. DOI: <https://doi.org/10.18721/JPM.161.181>

This is an open access article under the CC BY-NC 4.0 license (<https://creativecommons.org/licenses/by-nc/4.0/>)

Материалы конференции

УДК 53.083.9

DOI: <https://doi.org/10.18721/JPM.161.181>

Определение диффузных свойств линз Френеля

М.З. Шварц ¹✉, Д. А. Малевский ¹, М.В. Нахимович ¹, П.В. Покровский ¹,
Н.А. Садчиков ¹, А.А. Солюянов ¹

¹Физико-технический институт им. А.Ф. Иоффе РАН, Санкт-Петербург, Россия

✉ shvarts@scell.ioffe.ru

Аннотация. В данной работе предложена методика определения диффузных свойств концентраторов солнечного излучения типа линза Френеля. Снижение концентрирующей способности линз Френеля обычно связывают с несовершенством оптических преломляющих поверхностей, когда часть прямого (поступающего по нормали к поверхности линзы Френеля и подлежащего концентрированию) излучения рассеивается и не направляется на высокоэффективный концентраторный солнечный элемент. Формируемый при этом поток диффузного излучения, распространяясь внутри объема фотоэлектрического модуля, претерпевает многократные отражения от элементов конструкции, частично поглощается и в конечном итоге попадает на фотопреобразователи планарного контура.

Ключевые слова: линза Френеля, фотопреобразователь, диффузное излучение

Ссылка при цитировании: Шварц М.З., Малевский Д.А., Нахимович М.В., Покровский П.В., Садчиков Н.А., Солюянов А.А. Определение диффузных свойств линз Френеля // Научно-технические ведомости СПбГПУ. Физико-математические науки. 2023. Т. 16. № 1.1. С. 478–483. DOI: <https://doi.org/10.18721/JPM.161.181>



Статья открытого доступа, распространяемая по лицензии CC BY-NC 4.0 (<https://creativecommons.org/licenses/by-nc/4.0/>)

Introduction

Designing the photovoltaic modules with lens sunlight concentrator is a promising solution for increasing solar energy conversion efficiency. However, despite the use of highly efficient multi-junction (MJ) solar cells (SCs) in such modules, the efficiency of which exceeds 44% (at concentration ratio of 100X and more), the overall efficiency of the modules hardly reaches 40% [1–4], particularly due to “weak” optical characteristics of Fresnel lenses.

The main reason for decrease concentrating power ability and optical efficiency of Fresnel lenses (FLs) is chromatic aberration, which leads to spectral and spatial redistribution (smearing) of the focused radiation over the MJ SC. Additional optical losses are associated with absorption of radiation in the material and its reflection on the front surface of the FL and losses on the refractive faces. Since a FL concentrates only direct light (coming normally to its surface), the imperfection of the optical surfaces leads to its diffuse scattering and/or reflection [5–8].

Up-to-date combine modules designed in terms of both concentrator photovoltaic circuit and planar one [9–13] provides energy conversion of both direct solar light by concentrator MJ SCs and scattered (diffuse) solar light by planar photoconverters. The diffuse light flux coming from FL is converted photoelectrically by a planar cell. The proportion of the direct light transformed by FL into the diffuse one is determined by the quality of the optical surfaces and the parameters of the refractive profile, namely, the technological rounding of the profile teeth’s peaks and valleys, local geometric errors in working faces and diffuse characteristics of the optical material [7, 8]. It is obvious that when fabricating an FL by copying methods, the quality of optical surfaces varies depending on the type of matrix used: whether it is the primary master matrix or its working copy [14]. Accordingly, when controlling FL quality, in addition to its concentrating ability estimation, it is also necessary to evaluate the fraction of the light being diffused. Such quantification is an experimental problem, which is both important and nontrivial.

This paper presents the percentage component estimating results for diffuse light using a simulation model for calculating the optical-energy characteristics (OPC) of Fresnel lenses based on the method of tracing the direct path of light rays coming from the source through the FL to the SC (Fig. 1). The direct light flux is simulated by a large number of conical beams with a spatial angle corresponding to the angular size of the radiation source. The proportion of diffuse light is estimated from the level of energy reduction in a concentrated flux when modeling errors in the shape of the FL profile. When experimentally detecting the proportion of the diffuse component in the total flux transmitted through the FL, the developed dual-level optical-photovoltaic system is used. Here the concentrated light is directed into an aperture formed in a full-size planar photoconverter (the first level receiver) and then, while passing through the aperture, it is captured by a receiver fixed in the certain distance below (the second level receiver). The diffuse component is recorded by the planar photoconverter itself. Thus, in the experimental installation, the conditions for the propagation and PV conversion of the diffuse flux formed by the FL turn out to be almost identical to the conditions of the combined module.

A comparison was made for the “silicone-on-glass” FLs that had been fabricated: *a*) by direct copying from a negative nickel master matrix (precision diamond micro-turning method); *b*) by the procedure of double copying to obtain a working negative matrix of polyurethane [14]. An increase (by ~4% abs.) in the level of scattered FL radiation for the FL sample with a profile formed from the working matrix has been found, which indicates sufficient sensitivity of the proposed method for estimating the diffuse properties of FL.

Theoretical part

When designing the Fresnel profile and calculating OPC of FLs that performs the function of sunlight concentrating, the method based on tracing the great number of rays coming from the light source through the concentrating system to the solar cell is used. The concentrating system is represented as a set of flat or curved refractive surfaces of a given size and optical

media separating them. The model enables taking into account the influence of the set of factors (accurately described in [6, 7]) on the concentrating ability and optical efficiency of lens.

In mathematical description of ray passage from one surface of a concentrating system to another through optical media with certain refractive indices, the approaches of geometric optics, equations of analytical geometry, and vector algebra are used. Accounting for local geometric inaccuracies of the lens profile is carried out by introducing corrections to the components of the normal vector to the working faces of the teeth. When the ray hits the non-working faces, the rounding of the profile teeth tops and valleys, the ray is considered “lost”, and its further tracing to the focus of the lens discontinues. Thus, the energy of diffusely scattered radiation is considered lost for the process of photovoltaic conversion of concentrated radiation.

It should be assumed that these “lost” rays form a diffuse radiation flux from the lens propagating inside the volume of the photovoltaic module. By varying in the model the effective width of zones associated with the peaks and valleys of the teeth, it is possible to estimate the proportion of diffuse radiation in the total light flux that has passed through the Fresnel lens. Thus, the calculation model makes it possible to predict FL “efficiency” in terms of converting the direct radiation flux into diffuse-scattered (Fig. 1, *b*).

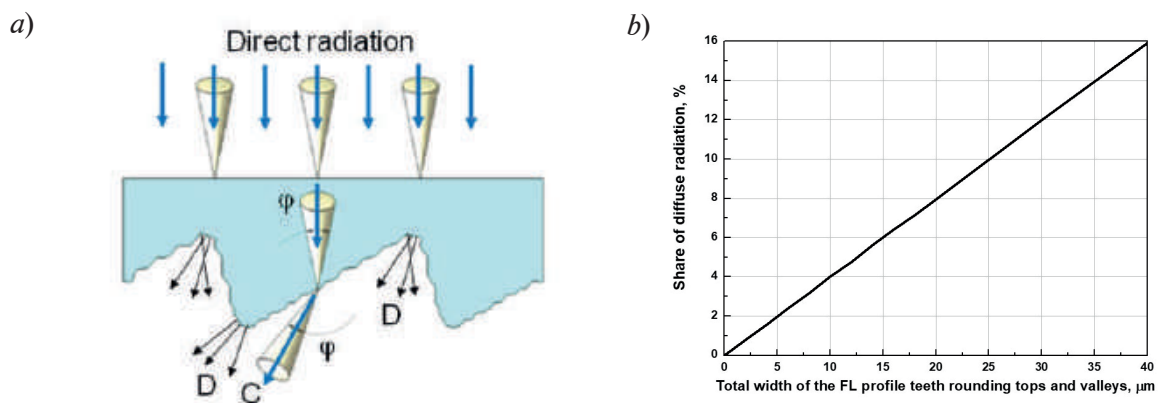


Fig. 1. Transformation of the direct (normal incident) radiation at the passage through the FL refractive surfaces with the formation of spilled direct (scattered, diffuse D) light and of the flux being concentrating in lens focus (C) (*a*). Share of diffuse radiation in the total light flux passing through the FL, depending on the width of the non-working zones (peaks and valleys) of the FL refractive teeth (*b*)

The results of mathematical modeling of the characteristics of circular Fresnel lenses with flat working surfaces show that in order to increase their energy efficiency, it is necessary to reduce the pitch of the profile teeth, and hence increase their number for a given lens size [7, 8]. In this case, a positive effect is achieved due to a more accurate approximation of the surface of the original plano-convex lens by a large number of sections of the conical surfaces of the working faces (the generatrices of the faces are straight lines). However, an increase in the number of profile teeth leads to an increase in optical losses in the non-working (dead) zones of the teeth (technological rounding of their tops and valleys).

Experimental estimations of diffuse light productivity by Fresnel lenses

FLs comparison in terms of direct radiation “conversion efficiency” into diffuse radiation was carried out using a specially designed device, the optical scheme and general view of which are shown in Fig. 2. The collimated beam flux (1) from the pulse simulator [17, 18] is directed perpendicular to FL input aperture (2). The main portion the flux that has passed through the FL is concentrated in the focal spot (F) at a given focal length from the lens, while the rest is scattered forming a diffuse flux (D). A full-size silicon SC (photosensor “A”) was mounted in the plane of the focal spot with a hole in the center for transmitting radiation concentrated in the focal spot F. By means of XYZ adjustments for the FL, such a position was chosen in which the focused light completely passes through the hole and hits the photosensor “B”, which is completely similar to the photosensor “A” in terms of the structure and design of the contact grid. In this configuration, the photocurrent of the photosensor “B” made it possible to estimate (in relative units) the

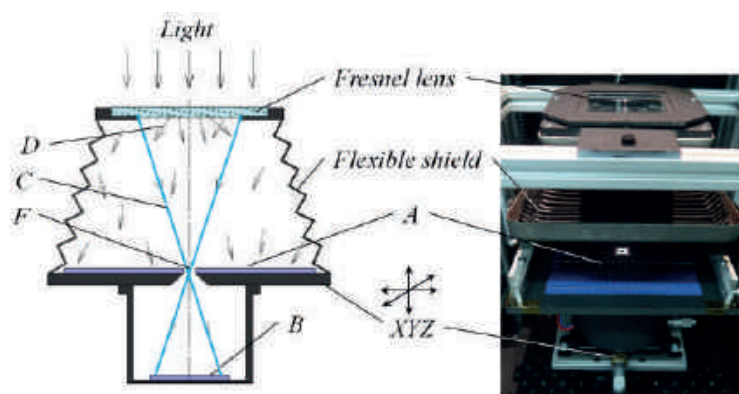


Fig. 2. The optical scheme (left) and general view (right) of the device for examination of FL in terms of scattered light productivity. On the right image, the “accordion-like” light-shield is half-lifted to show the silicon photosensor “A” with a hole (around the hole a light halo of radiation is visible, since in the photo the photosensor “A” is placed a little closer to the lens compared to the its exact focal distance)

power of the concentrated flux through FL, and the photosensor “A” – scattered (diffuse) flux propagating downward (it should be taken into account that diffuse flux is isotropic and in the presented device cannot be completely intercepted by a photosensor “A”).

To eliminate the influence of radiation reflected from the surrounding infrastructure on the current signal of the photosensor “A”, a light-shield housing of the “accordion-like” type was used, the flexibility of which ensured the unhindered movement of the receiver within ± 10 mm in the XY plane and ± 20 mm along the vertical axis Z. The inner matte (absorbing) surface of the protective housing excluded uncontrolled re-reflection of diffuse light.

The reference value when comparing FLs produced by different technological methods was the photocurrent of the photosensor “A”, which was recorded when the lens was placed directly on its surface. The value of the photocurrent obtained in this way reflects the total radiation flux passing through the lens. For all the lenses studied in the work, this value differed by no more than 0.5%, which means the equality of the integral values for the optical transmission of the studied FLs.

The procedure for adjusting the FL position was to find such a position, at which the photosensors “A” and “B” would show the minimum and maximum possible values of photocurrents, respectively. Upon completion of the necessary tuning actions for each experimental sample of the FL, the ratio of the concentrated and diffusely scattered energy of solar radiation is defined. Obviously, when changing the configuration of the refractive faces, due to technological factors in FL manufacturing, the balance of concentrated and diffused fluxes will change, and for the most part in favor of the latter one. Registration of photocurrents of the photosensors 3 and 4 is carried out during the flat part of the light flash (variation of the irradiation level within $\pm 1.5\%$ with duration of 1.2 ms, [15, 16]).

Comparison of experimental Fresnel lenses

A comparison has been made for the “silicone-on-glass” FLs that had been fabricated: *a*) by direct copying from a negative nickel master matrix (precision diamond micro-turning method); *b*) by the procedure of double-stage copying with obtaining an “intermediate” negative matrix of polyurethane. The FL design parameters are: aperture $60 \text{ mm} \times 60 \text{ mm}$, focal length 105 mm, profile step 0.25 mm. We also studied the FL made of poly(methyl methacrylate) with an aperture of $63 \text{ mm} \times 63 \text{ mm}$, a focal length of 125 mm, and a profile step of 0.125 mm.

For the photosensors “A” and “B”, their photocurrent absolute values measurement results are presented in Table 1. As was expected, a lens made by the direct copying method scatters radiation less. For radiation passed through the optical elements of the FL (glass, refractive profile), only 6% is diffusely scattered, while when using double copying technology, this figure reaches 10%. Accordingly, the optical efficiency of the FL, as a radiation concentrator, is higher by 4% for the FL made by direct copying. The FL made of PMMA has the highest diffuseness

coefficient – almost 21% of the radiation transmitted through the lens is diffuse. It should be noted that all the samples under study are close to each other in terms of the total transmission coefficient of radiation (within 0.2% rel.), which indicates comparable losses in the reflection of radiation from the front and surface and from the refractive elements of the profile (data were recorded when FL is positioned directly over the photosensor “A”, see column 2 of Table 1).

The summation of the values of the photocurrents of the photosensors “A” and “B” (column 5) makes it possible to estimate (qualitatively) the fraction of diffuse radiation absorbed by the elements of the installation structure. It is clearly seen that the smaller the fraction of scattered radiation, the smaller the difference between the obtained data and the photocurrent of the photosensor “A” operating in the mode of total optical transmission record (column 2).

Table 1

Photocurrent absolute values measurement results

1	Photosensor current, mA				
	2	3	4	5	6
FL type	“A” (Total radiation)	“B” (Direct radiation)	“A”(Diffuse radiation)	Direct+Diffuse radiation	% of Diffused radiation
SOG Direct copy	957.8	901.6	57.5	959.1	5.9
SOG Double copy	957.4	861.9	86.5	948.4	10.0
PMMA	954.6	753.8	179.4	933.2	20.9

Conclusion

A method for determining the diffuse properties of solar radiation concentrators such as Fresnel lens was proposed. A comparison was made for the “silicone-on-glass” FLs that had been fabricated: a) by direct copying from a negative nickel master matrix (precision diamond micro-turning method); b) by the procedure of double-stage copying with obtaining a negative matrix of polyurethane. An increase (by ~ 4% abs.) in the level of scattered FL radiation for the FL sample with a profile formed from a polyurethane matrix was defined, which indicates sufficient sensitivity of the proposed method for estimating the FL diffuse properties.

REFERENCES

1. Green M., Dunlop E., Hohl-Ebinger J., Yoshita M., Kopidakis N., Hao X., Solar cell efficiency tables (version 59). Prog Photovolt Res Appl. 30 (1) (2022) 3–12.
2. Riesen S., Neubauer M., Boos A., Rico M., Gourdel C., Wanka S., Krause R., Guernard P., Gombert A., New module design with 4-junction solar cells for high efficiencies, Conf. Proc., 1679 (2015) 100006.
3. Rey-Stolle I., Handbook on Concentrator Photovoltaic Technology, John Wiley & Sons, 2016.
4. Wiesenfarth M., Anton I., Bett A.W., Challenges in the design of concentrator photovoltaic (CPV) modules to achieve highest efficiencies, Appl Phys Rev, 2018, Vol.5. p. 41601.
5. Victoria M., Askins S., Herrero R., Antyn I., Sala G., Assessment of the optical efficiency of a primary lens to be used in a CPV system, Solar Energy, 134 (2016) 406–415.
6. Shvarts M.Z., Andreev V.M., Gorohov V.S., Grilikhes V.A., Petrenko A.E., Soluyanov A.A., Timoshina N.H., Vlasova E.V., Zaharevich E.M., Flat-plate Fresnel lenses with improved concentrating capabilities: designing, manufacturing and testing, 33rd IEEE PVSC, 2 (2008) 1–6.
7. Shvarts M.Z., Soluyanov A.A., Improved Concentration Capabilities of Flat-plate Fresnel Lenses, Adv. Sci. Technol, 74 (2010) 185–195.
8. Shvarts M.Z., Emelyanov V.M., Nakhimovich M.V., Soluyanov A.A., Andreev V.M., Compromise solutions for design and technology of Fresnel lenses as sunlight concentrators, AIP Conf. Proc. 2149 (2019) 070011.
9. Yamada N., Okamoto K., Experimental measurements of a prototype high concentration Fresnel lens CPV module for the harvesting of diffuse solar radiation, Optics Express, 22/S1 (2014) A28–A34.



10. Yamada N., Hirai D., Maximization of conversion efficiency based on global normal irradiance using hybrid concentrator photovoltaic architecture, Prog Photovolt Res Appl. 2016; Vol.24 (6), pp. 846–854.
11. Martínez J.F., Steiner M., Wiesenfarth M., Siefer G., Glunz S. W., Dimroth F., Hybrid Bifacial CPV Power Output Beyond 350W/m², IEEE PVSC 47th, 2020, pp. 2708–2711.
12. Martínez J.F., Steiner M., Wiesenfarth M., Development and outdoor characterization of a hybrid bifacial HCPV module. Prog Photovolt Res Appl. 28 (2020) 349–357.
13. Martínez J.F., Steiner M., Wiesenfarth M., Siefer G., Glunz S. W., Dimroth F., Power rating procedure of hybrid concentrator/flat-plate photovoltaic bifacial modules, Progress in Photovoltaics, 29/6 (2021) 614–629.
14. Alferov Z.I., Andreev V.M., Rumyantsev V.D., Sadchikov N.A., Lovygin I.V., Method for producing a composite concentrator lens panel for photovoltaic modules, RU patent application publication,” Pub. No.: RU02359291, 2007.
15. Larionov V.R., Malevskiy D.A., Pokrovskiy P.V., Rumyantsev V.D., Measuring complex for studying cascade solar photovoltaic cells and concentrator modules on their basis, Tech. Phys. 60 (2015) 891–896.
16. Shvarts M.Z., Larionov V.R., Malevskiy D.A., Nakhimovich M.V., Pokrovskiy P.V., Multi-Lamp Concepts for Spectrally Adjustable Pulsed Solar Simulators, AIP Conf. Proc., 2550 (2022) 020010.

THE AUTHORS

SHVARTS Maxim Z.

shvarts@scell.ioffe.ru

ORCID: 0000-0002-2230-7770

MALEVSKIY Dmitriy A.

dmalevsky@scell.ioffe.ru

ORCID: 0000-0002-9337-4137

NAKHIMOVICH Mariia V.

nmar@mail.ioffe.ru

ORCID: 0000-0002-7711-2188

POKROVSKIY Pavel V.

p.pokrovskiy@mail.ioffe.ru

ORCID: 0000-0001-7442-2052

SADCHIKOV Nikolai A.

N.A.Sadchikov@mail.ioffe.ru

ORCID: 0000-0001-6173-0654

SOLUYANOV Andrey A.

vinivka442@yandex.ru

Received 09.11.2022. Approved after reviewing 06.12.2022. Accepted 06.12.2022.

Conference materials
UDC 539.1.08, 539.1.074.9
DOI: <https://doi.org/10.18721/JPM.161.182>

A soft X-ray spectrometer with enhanced output count rate

M.Yu. Kantor ¹✉, A.V. Sidorov ¹, A.A. Bogdanov ¹, Yu.V. Tuboltsev ¹, Yu.V. Chichagov ¹

¹ Ioffe Institute, Saint-Petersburg, Russia

✉ m.kantor@mail.ioffe.ru

Abstract. An upgrade of an AMPTEK soft X-ray spectrometer with a silicon drift detector (SDD) to boost the output count rate is presented in the paper. Enhanced count rate is provided by a shaping electronic amplifier which forms pulses with a short rise time from step-wise impulse responses of SDD charge sensitive preamplifier. The rise time of the amplifier pulses is about a half of that used in the AMPTEK amplifier. The output noise of the amplifier equals the noise of the AMPTEK amplifier. The spectrometer is tested with the developed amplifier and amplifier in its digital pulse processing (DPP) unit and SDD radiated by an isotope ⁵⁵Fe source. The results of the test are compared in terms of the rise time and amplitudes of the response pulses as well as trapezoidal pulses at various peaking and flat top times. The developed amplifier is capable to provide the count rate of output pulses increased by a factor of 1.5 in regards with the standard methods at the same energy resolution.

Keywords: soft X-ray spectrometers, pulse counting, amplitude spectra, digital filters

Funding: The design and construction of the soft X-ray diagnostic system in the FT-2 tokamak described in the Introduction were supported by Ioffe Institute under State Contract No. 0034-2021-0001. Data analysis in other sections was supported by Ioffe Institute under State Contract No. 0040-2019-0023.

Citation: Kantor M.Yu., Sidorov A.V., Bogdanov A.A., Tuboltsev Yu.V., Chichagov Yu.V., A soft X-ray spectrometer with enhanced output count rate, St. Petersburg State Polytechnical University Journal. Physics and Mathematics. 16 (1.1) (2023) 484–490. DOI: <https://doi.org/10.18721/JPM.161.182>

This is an open access article under the CC BY-NC 4.0 license (<https://creativecommons.org/licenses/by-nc/4.0/>)

Материалы конференции
УДК 539.1.08, 539.1.074.9
DOI: <https://doi.org/10.18721/JPM.161.182>

Спектрометр мягкого рентгеновского излучения с повышенной скоростью счета фотонов

М.Ю. Кантор ¹✉, А.В. Сидоров ¹, А.А. Богданов ¹, Ю.В. Тубольцев ¹, Ю.В. Чичагов ¹

¹ Физико-технический институт им. А.Ф.Иоффе РАН, Санкт-Петербург, Россия

✉ m.kantor@mail.ioffe.ru

Аннотация. В работе представлена модернизация спектрометра мягкого рентгеновского излучения AMPTEK с дрейфовым кремниевым детектором (SSD) с целью повышения его выходной скорости счета квантов. Повышение скорости обеспечивается электронным усилителем-формирователем, который формирует импульсы с коротким фронтом нарастания из ступенчатых импульсов отклика зарядо-чувствительного усилителя сигнала SDD. Время нарастания импульсов усилителя примерно половина времени нарастания выходного импульса усилителя в AMPTEK. Выходные шумы этих усилителей одинаковы. Спектрометр испытывался с разработанным усилителем и усилителем в модуле счета квантов (DPP) с использованием источника излучения от изотопа ⁵⁵Fe. Проводится сравнение тестирования времени нарастания и амплитуды импульсов усилителей, а также трапецеидальных импульсов, полученных цифровой фильтрацией, при их разных



длительностях пикирования и плоской вершины. Разработанный усилитель способен обеспечить рост скорости счета в 1.5 раза по сравнению со стандартным методом при сохранении энергетического разрешения спектрометра.

Ключевые слова: спектрометры мягкого рентгеновского излучения, счет импульсов, амплитудные спектры, цифровые фильтры

Финансирование: Проект и изготовление диагностики мягкого рентгеновского излучения на токамаке ФТ-2, описанные в Введении, были поддержаны ФТИ им. А.Ф.Иоффе в рамках Государственного контракта № 0034-2021-0001. Анализ данных в остальных разделах статьи поддержаны ФТИ им. А.Ф.Иоффе в рамках Государственного контракта № 0040-2019-0023.

Ссылка при цитировании: Кантор М.Ю., Сидоров А.В., Богданов А.А., Тубольцев Ю.В., Чичагов Ю.В., Спектрометр мягкого рентгеновского излучения с повышенной скоростью счета фотонов // Научно-технические ведомости СПбГПУ. Физико-математические науки. 2023. Т. 16. № 1.1. С. 484–490. DOI: <https://doi.org/10.18721/JPM.161.182>

Статья открытого доступа, распространяемая по лицензии CC BY-NC 4.0 (<https://creativecommons.org/licenses/by-nc/4.0/>)

Introduction

High count rate spectrometers of soft X-ray emission employ silicon drift detectors (SDD) [1] and digital pulse processors for counting the detected pulses and measurements of their amplitudes [2, 3]. One of the main factors which restrict the output count rate of the spectrometers is the rise time of the impulse response on photons. It is set from a trade-off between the highest count rate and the best energy resolution determined by noise and ballistic effects in the detector [4] as well as pile-up of pulse processing [3]. Advanced modern spectrometers are capable to operate at output count rates up to $4 \cdot 10^5$ 1/s with energy resolution 200 eV [4, 5]. The resolution strongly degrades with increasing the count rate.

A study of fast dynamics of electrons in plasma of the FT-2 tokamak [6] requires measurements of soft X-ray Bremsstrahlung emission at higher count rates and high energy resolution. The enhanced count rate can be achieved with modified algorithms of pulse counting [7, 8] or/and hardware upgrades of spectrometers. The second way is presented in the paper. A commercially available soft X-ray spectrometer of AMPTEK Inc. has been upgraded with a shaping electronic amplifier [9] and a 14 bits digitizer operating at a sampling rate up to 250 MHz [10]. The digitized pulses are shaped to shorter pulses of trapezoidal [11] form which are processed with pulse counting algorithms [3, 12].

The spectrometer is equipped with a 70 mm² FASTSDD detector [13] and digital pulse processor (DPP) PX-5 [14]. A charge sensitive preamplifier integrated in the detector delivers step-wise responses on detected photons with sensitivity 3.2 mV per 1 keV of photon energy. The step-wise signals are reshaped in PX-5 to pulses which are digitized by an internal ADC at sampling rate 80 MHz. Further in the paper the pulses from the developed amplifier are referred as A-pulses and pulses from the internal amplifier in PX-5 are referred as P-pulses.

The rise time of the step-wise signals increase with the distance of the photon impact point in the depleted region to the detector anode [15]. This effect results in variations of the rise time of the step-wise signals in AMPTEK charge sensitive preamplifier in the range from 15 ns to 110 ns, see Section 2 of the paper.

Hereafter the rise time of pulses is defined as the time interval between 20% and 80% levels of the pulse amplitude.

The rise time of P-pulses was set about a twice of that of the step signals to optimize the count rate and energy resolution of the spectrometer. This is the rise time which restricts the highest count rate of the spectrometer.

A key unit of the upgraded system is a shaping amplifier which transforms the step-wise signals to A-pulses with shorter rise time and the same noise as in PX-5 unit. The amplifier was

described and tested in [9]. The formed pulses are digitized at a sampling rate up to 250 MHz and 14 bits resolution with ADC FM814×250M produced by InSys AO [10]. The recorded signals are numerically shaped to trapezoidal pulses and processed for amplitude measurements. A higher sampling rate and resolution of the employed ADC are advantageous for accurate digitizing short leading edges of the pulses from the amplifier outputs.

The shaping amplifier has been tested with 70 mm² FASTSDD AMPTEK detector exposed to photons of 5.9 keV and 6.5 keV energy radiated by an isotope source ⁵⁵Fe. The developed shaping amplifier and amplifier in PX-5 have been tested for rise times and amplitudes changing with the rise time of the step-wise signals. Changing the amplitudes and rise times of trapezoidal pulses obtained from the amplifier outputs at various peaking times have been tested as well. The amplifier signals were recorded in the test by a digital scope Agilent Technologies MSO9440A with 10 bits resolution and analogue bandwidth 4 GHz at sampling frequency 1 GHz. The recorded signals were smoothed with a digital low pass RC filter with a cut-off frequency 40 MHz.

Rise Time of Reshaped Pulses

Sample pulses measured in the outputs of charge sensitive preamplifier of SDD, external and PX-5 amplifiers are presented in Fig. 1. The amplitudes of five pulses correspond to photon energy 5.9 keV, the second pulse is the response on a photon 6.5 keV and the highest pulse is an overlap of two pulses. The shapes of A- and P-pulses are compared in a larger scale in Fig. 4 in [9]. The rms noises of the signals in terms of photon energy are 300 eV, 44 eV and 46 eV correspondingly.

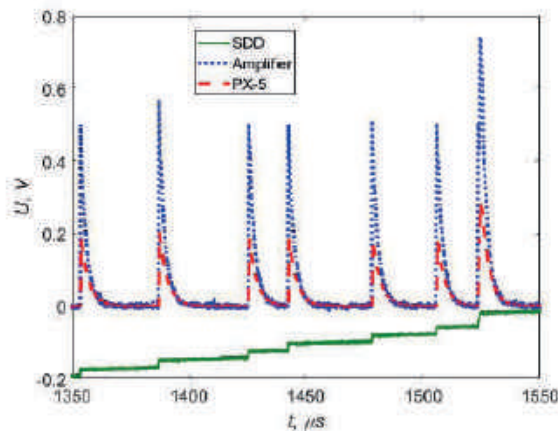


Fig. 1. Impulse responses of amplifies on detected photons

A set of about 1000 pulses measured at the mean input count rate $\sim 2 \cdot 10^4$ photons per second were collected and analyzed. Some traces were measured with fully opened 50 mm² actual aperture of the detector, the others were recorded with restricted aperture 17 mm² collimated by AMPTEK collimator EML-3. The amplitude of a pulse was found from polynomial fitting the measurements around its peak with taking into account the background from preceding pulses. The rise time amounts a time interval between 20% and 80% levels of the amplitudes in the leading edge of the pulse.

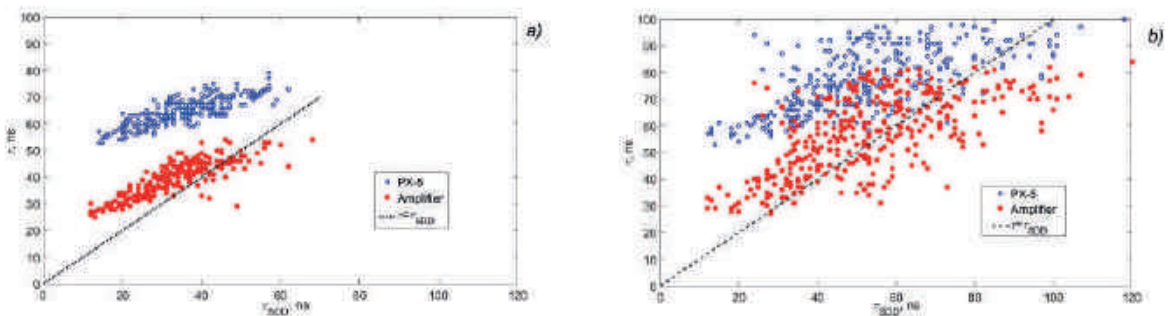


Fig. 2. Rise times of PX-5 and amplifier pulses with (a) and without (b) collimator

Fig. 2 shows the rise times of pulses from both amplifiers measured with collimated (a) and not collimated (b) detectors at various rise times of the step-wise pulses. One can see that the developed amplifier provides considerable shortening the front edges of A-pulses which amount 0.5–0.8 of that of P-pulses in the range from the shortest to longest fronts of the step-wise detector responses.

The pulse amplitudes versus their rise times are presented in figure 3 for collimated (a) and open aperture (b) detector. The spectral peaks of the ⁵⁵Fe radiation source at 5.9 keV and 6.5 keV are clearly resolved in the plots. The energy resolutions of the K α peak measured from the amplitude distribution of A- and P-pulses are 255 eV and 315 eV at FWHM correspondingly. The amplitude resolution of A-pulses is close to the specified resolution of SuperSDD 25 mm² AMPTEK detector measured for trapezoidal pulses at peaking time 200 ns [5]. Resolution of P-pulses used in the PX-5 unit is 20% worse. Digital trapezoidal shaping is normally used to improve energy resolution and count rate of spectrometers. Trapezoidal shaping of A- and P-pulses is considered in the next section in terms of distortion of their trapezoidal form and variation of their amplitudes with the rise time.

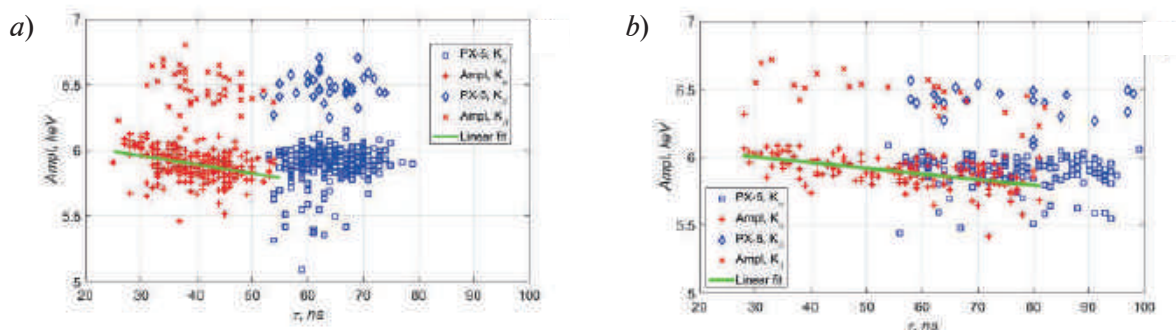


Fig. 3. Amplitudes of reshaped pulses with collimated (a) and open area (b) detectors

Trapezoidal Shaping of Output Amplifier Pulses

The digitized signals are digitally shaped to trapezoidal pulses which are used in processing algorithms for counting and measuring pulse amplitudes. The algorithms are most efficient with trapezoidal pulses of ideal symmetrical forms. Real pulses tend to this form when their width is much larger than the rise time of input pulses. Wide symmetrical trapezoidal pulses may be not consistent with high count rate measurements because a large rise time of digitized pulses. Distortion of short trapezoidal pulses weaken detection of overlapped pulses [8, 9]. The external amplifier with shorter rise time output addressed to these problems.

Fig. 4 represents digitized normalized P- and A-pulses responded on a step voltage in the output of the charge sensitive preamplifier of 17 ns (Fig. 4, a) and 107 ns (Fig. 4, b) rise time. They are plotted in the figure with dashed-dotted and solid black curves indicated by letters P and A. The other curves in the figure are trapezoidal pulses shaped from the P- and A-pulse. They

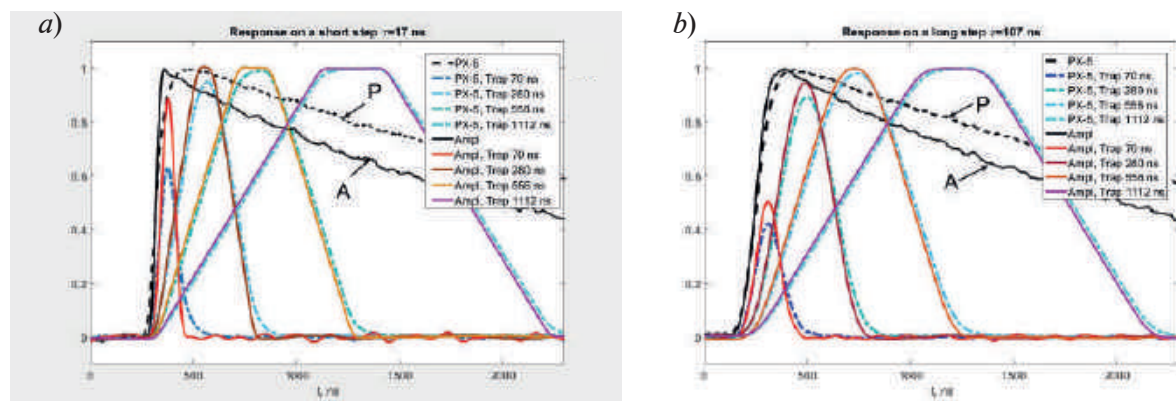


Fig. 4. Shapes of trapezoidal pulses responding short (a) and long (b) step input pulses

are plotted with colour dashed-dotted and solid curves correspondingly. The trapezoidal pulses have Gaussian-like form [7], [8], i.e. their width and slope at FWHM equal the width and slope of a Gaussian pulse of the same amplitude. The widths of the trapezoidal pulses at FWHM shown in legends correspond to their peaking times 50, 200, 400 and 800 ns. The trapezoidal pulses are calculated using [11] and then divided by the set peaking time and normalized to the amplitude of the longest trapezoidal pulse.

One can see that the longest trapezoidal pulses shaped from the A-pulse exhibit the best form in Fig. 4, *a*. Trapezoidal A-pulses calculated at smaller peaking time have smoothed but symmetrical form within 0.5% of their amplitude. Trapezoidal pulses shaped from the P-pulse are far from the ideal trapezoidal form at all peaking times. The biggest asymmetrical distortions at the tail of short trapezoidal pulses restrict detection of overlapped pulses and, hence, limit the count rate of the spectrometer, see example in [9].

Amplitude of Trapezoidal Pulses

Fig. 4 shows that the normalized amplitude of trapezoidal pulses strongly depends on the rise time of step-wise signals at small peaking time of trapezoidal filter. Thus, the amplitude of trapezoidal pulses should depend on the rise time of trapezoidal pulses. Note that the rise time of an ideal trapezoidal is 60% of its peaking time, but it does not hold for actual trapezoidal pulses. Fig. 5 presents the dependence of amplitudes on the rise time of trapezoidal pulses determined with an accuracy of 1 ns. The mean amplitudes versus the rise times for trapezoidal pulses shaped from P- and A-pulses are plotted in the figure 5 for peaking times 50 ns, 100 ns, 200 ns and 400 ns. The error bars are the standard deviation of the amplitude measured at the corresponding rise times of trapezoidal pulses. The amplitude of trapezoidal pulses decreases linearly with the rise time (Fig. 5, *a*, *b*). The measured amplitudes scan in the range which is consistent with a model developed in [7] for KETEK H7 SDD of 7 mm² sensitive area [16].

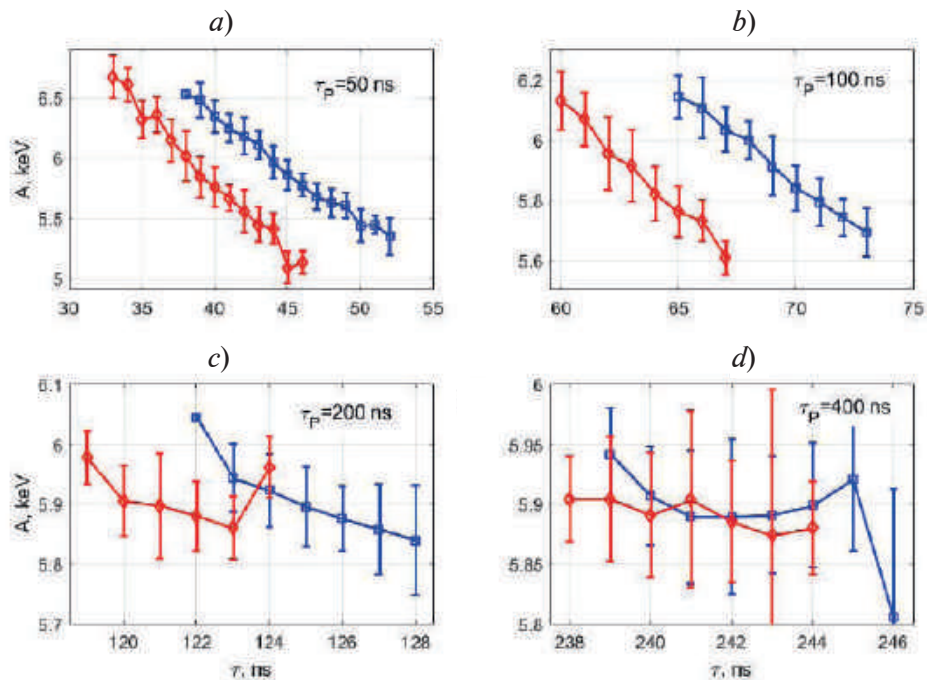


Fig. 5. Amplitude versus rise time of trapezoidal pulses at peaking times τ_p of 50 (*a*), 100 (*b*), 200 (*c*), and 400 (*d*) ns

Thus, the inferred amplitudes were corrected for measured rise time of pulses for better amplitude spectral resolution. The effect of the correction on the spectral resolution is presented in Fig. 6.

The spectral width of $K\alpha$ peaks at FWHM in various measurements with collimated detector and the technical specifications of the spectrometer are plotted versus the peaking time of trapezoidal pulses. The range of the peaking times is separated in two plots for better reading.



A black dashed line shows the spectral width of $K\alpha$ measured with DPP PX-5 which collected more than 10^6 photons. The measurements are conducted at four peaking times and count rate $2 \cdot 10^4$ 1/s. Blue diamonds and red crosses represent the widths of the $K\alpha$ peak calculated from the amplitude distribution of about 250 P- and A-pulses correspondingly. Some difference between the distributions measured by PX-5 and from P-pulses is accounted for a small statistic of P-pulses.

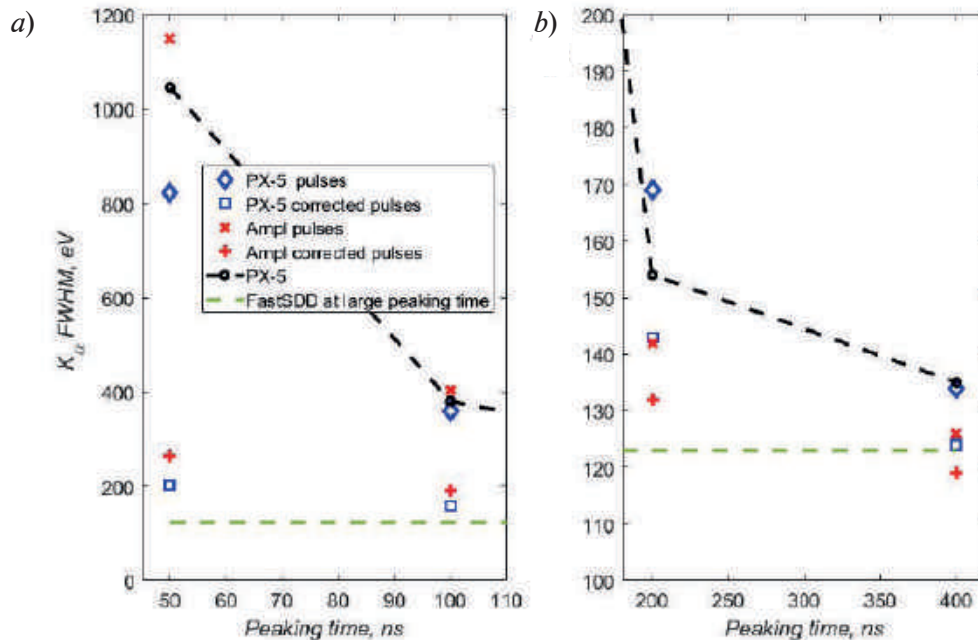


Fig. 6. The width of $K\alpha$ peak measured at short (a) and long (b) peaking times

Blue squares and red pluses represent the peak width of P- and A-pulse amplitudes corrected for their rise time. The correction is most pronounced at small rise times - spectral resolution improves by factors of 5 and 2 for 50 ns and 100 ns peaking times. The spectral resolution considerably improves at larger peaking times and achieves the specification of the AMPTEK spectrometer 123 eV. This level is actually available with DPP PX-5 at peaking times of a few microseconds, see [5].

Conclusion

Shaping step-wise signals from a charge sensitive preamplifier of AMPTEK FASTSDD and recording the shaped pulses at a high sampling rate allows more accurate measurements of their amplitude at shorter rise times. The shorter rise time provides better resolution of amplitudes of strongly overlapped pulses and reduction of the dead and resolving time of spectrometers [8]. A two-fold reduction of the rise time of shaped pulses should increase the count rate of the spectrometer at least by a factor 1.5–2. Algorithms for counting and amplitude measurements of recorded pulses with taking into account their rise time are under development.

Acknowledgment

The design and construction of the soft X-ray diagnostic system in the FT-2 tokamak described in the Introduction were supported by Ioffe Institute under State Contract No. 0034-2021-0001. Data analysis in other sections was supported by Ioffe Institute under State Contract No. 0040-2019-0023.

REFERENCES

1. Lechner P., Pahlke A. and Soltau H., Novel high-resolution silicon drift detectors, X-Ray Spectrometry, 33 (2004) 256–261.
2. Knoll G.F., Radiation detection and measurement, 4th edition John Wiley and Sons Inc., USA (2010).

3. **Nakhostin M.**, Signal processing for radiation detectors, John Wiley and Sons Inc., USA (2018).
4. **Gatti E., Longoni A., Sampietro M. and Rehak P.**, Dynamics of Electrons in Drift Detectors, Nucl. Instrum. Meth. A253, 393–399 (1987).
5. AMPTEK Understanding Amptek’s Silicon Drift Detectors. URL: <https://www.amptek.com/-/media/ametekamptek/documents/resources/application-notes/understanding-amptek-silicon-drift-detectors.pdf?la=en&revision=48f9d4e1-81f7-4c1d-b702-d36f4fd3aa48>. Accessed: May 05, 2023.
6. **Lashkul S.I. et al.**, Effect of the radial electric field on lower hybrid plasma heating in the FT-2 tokamak, Plasma Phys. Rep. 27 1001–1010 (2001).
7. **Kantor M.Yu. and Sidorov A.V.**, Shaping pulses of radiation detectors into a true Gaussian form, JINST 14 P01004, (2019), URL: <https://doi.org/10.1088/1748-0221/14/01/P01004> Accessed: May 05, 2023.
8. **Kantor M.Yu. and Sidorov A.V.**, Detection of true Gaussian shaped pulses at high count rates JINST 15 P06015 (2020), URL: <https://doi.org/10.1088/1748-0221/15/06/P06015> Accessed Oct. 20, 2022.
9. **Tuboltsev Yu.V., Chichagov Yu.V., Bodganov A.A., Kantor M.Yu., Sidorov A.V.**, Shaping amplifier for soft X-ray spectrometer with a silicon drift detector. St. Petersburg State Polytechnical University Journal. Physics and Mathematics. 16 (1.1) (2023) 438–443. DOI: <https://doi.org/10.18721/JPM.161.175>
10. InSys Corp. ADC module FM814x2 URL: <https://www.insys.ru/mezzanine/fm814x250m> Accessed: May 05, 2023.
11. **Jordanov V.T., Knoll G.F. et al.**, Digital techniques for real-time pulse shaping in radiation measurements, Nucl. Instrum. Meth. A 353, 261–264 (1994).
12. **Redus R.**, Digital Pulse Processors, Theory of Operation (Amptek Inc) URL: https://www.amptek.com/-/media/ametekamptek/documents/resources/dpp_theory.pdf Accessed: May 05, 2023.
13. AMPTEK 70 mm² FAST SDD URL: <https://www.amptek.com/internal-products/70-mm2-fast-sdd> Accessed: May 05, 2023.
14. AMPTEK digital pulse processor URL: <https://www.amptek.com/products/digital-pulse-processors/px5-digital-pulse-processor> Accessed: May 05, 2023.
15. **Metzger W., Engdahl J. et al.**, Large-Area Silicon Drift Detectors for New Applications in Nuclear Medicine Imaging IEEE Trans. on Nucl. Science 51, 4, 1631–1635, (2004).
16. KETEK GmbH VITUS H7 - Silicon Drift Detector (SDD) URL: <https://www.ketek.net/sdd/vitus-sdd-modules/vitus-h7/> Accessed: May 05, 2023.

THE AUTHORS

KANTOR Mikhail Yu.
m.kantor@mail.ioffe.ru
ORCID: 0000-0001-9512-2155

TUBOLTSEV Yury V.
Tuboltsev@mail.ioffe.ru
ORCID: 0000-0001-9770-0158

SIDOROV Anton V.
sidorov@mail.ioffe.ru
ORCID: 0000-0002-6509-2781

CHICHAGOV Yury V.
Chichagov@mail.ioffe.ru
ORCID: 0000-0002-2679-6380

BOGDANOV Alexandr A.
alexander.a.bogdanov@mail.ioffe.ru
ORCID: 0000-0002-5275-5603

Received 27.10.2022. Approved after reviewing 13.12.2022. Accepted 13.12.2022.

Conference materials

UDC 54.07

DOI: <https://doi.org/10.18721/JPM.161.183>

Application of a liquid electrode for collecting products of chemical reactions carried out in charged microdroplets of an electrospray torch

D.O. Kuleshov¹✉, A.V. Solovieva¹, I. A. Gromov², I.I. Pikovskoi³,
N.V. Ul'yanovskii³, A.V. Belesov³, S.A. Sypalov³, D.M. Mazur⁴

¹Institute for Analytical Instrumentation of the RAS, St. Petersburg, Russia;

²Ioffe Institute, St. Petersburg, Russia;

³Core Facility Center "Arctica", Northern (Arctic) Federal University, Arkhangelsk, Russia;

⁴Lomonosov Moscow State University, Moscow, Russia

✉ hellchemist@yandex.ru

Abstract. The experimental device for carrying out chemical reactions in charged microdroplets with the accumulation of reaction products and reactants in a liquid electrode was developed. The fundamental possibility of electrospraying a liquid onto the surface of a polar liquid (using acetonitrile as an example) in the modes of both positively and negatively charged microdroplets generation has been shown. In the mode of positively charged microdroplets generation, acidified acetonitrile was used as a sprayed solution; in the mode of negatively charged microdroplets generation, pure acetonitrile was used. In both cases, a stable electrospray mode was obtained over a wide range of the spraying voltage U (from 2.2 kV to 5 kV), the distance from the spraying capillary to the surface of the liquid electrode L (from 3 mm to 23 mm) and the sprayed solution feed rate Q (from 25 $\mu\text{l}/\text{min}$ to 200 $\mu\text{l}/\text{min}$). It was shown on the example of the reaction of phenylhydrazine with anisic aldehyde that the products of reactions occurring in charged microdroplets, as well as the reactants, accumulate in the volume of the liquid electrode.

Keywords: charged microdroplets, electrospray, condensation reactions, liquid electrode, mass spectrometry, high-performance liquid chromatography

Citation: Kuleshov D.O., Solovieva A.V., Gromov I.A., Pikovskoi I.I., Ul'yanovskii N.V., Belesov A.V., Sypalov S.A., Mazur D.M., Application of a liquid electrode for collecting products of chemical reactions carried out in charged microdroplets of an electrospray torch. St. Petersburg State Polytechnical University Journal. Physics and Mathematics. 16 (1.1) (2023) 491–497. DOI: <https://doi.org/10.18721/JPM.161.183>

This is an open access article under the CC BY-NC 4.0 license (<https://creativecommons.org/licenses/by-nc/4.0/>)

Материалы конференции

УДК 54.07

DOI: <https://doi.org/10.18721/JPM.161.183>

Применение жидкого электрода для сбора продуктов химических реакций, проводимых в заряженных микрокаплях факела электроспрея

Д.О. Кулешов¹✉, А.В. Соловьева¹, И.А. Громов², И.И. Пиковской³,
Н.В. Ульяновский³, А.В. Белесов³, С.А. Сыпалов³, Д.М. Мазур⁴

¹Институт аналитического приборостроения РАН, Санкт-Петербург, Россия;

²Физико-технический институт им. А.Ф. Иоффе РАН, Санкт-Петербург, Россия;

³ЦКП НО "Арктика", Северный (Арктический) федеральный университет им. М.В. Ломоносова, г. Архангельск, Россия;

⁴Московский государственный университет им. М. В. Ломоносова, г. Москва, Россия

✉ hellchemist@yandex.ru

Аннотация. Разработано экспериментальное устройство для проведения химических реакций в заряженных микрокаплях с возможностью накопления продуктов реакции и реагирующих веществ в жидком электроде. Показана принципиальная возможность электрораспыления жидкости на поверхность полярной жидкости (на примере ацетонитрила) в режимах генерации как положительно, так и отрицательно заряженных микрокапель. В режиме генерации положительно заряженных микрокапель в качестве распыляемого раствора использовали подкисленный ацетонитрил; в режиме генерации отрицательно заряженных микрокапель использовали чистый ацетонитрил. В обоих случаях был получен стабильный режим электрораспыления в широком диапазоне напряжения распыления U (от 2,2 кВ до 5 кВ), расстояния от капилляра распыления до поверхности жидкого электрода L (от 3 мм до 23 мм) и скорости подачи распыляемого раствора Q (от 25 мкл/мин до 200 мкл/мин). На примере реакции фенилгидразина с анисовым альдегидом было показано, что продукты реакций, протекающих в заряженных микрокаплях, и исходные реагирующие вещества накапливаются в объеме жидкого электрода.

Ключевые слова: заряженные микрокапли, электрораспылительная ионизация, реакции конденсации, жидкий электрод, масс-спектрометрия, высокоэффективная жидкостная хроматография

Ссылка при цитировании: Кулешов Д.О., Соловьева А.В., Громов И.А., Пиковской И.И., Ульяновский Н.В., Белесов А.В., Сыпалов С.А., Мазур Д.М. Применение жидкого электрода для сбора продуктов химических реакций, проводимых в заряженных микрокаплях факела электроспрея // Научно-технические ведомости СПбГПУ. Физико-математические науки. 2023. Т. 16. № 1.1. С. 491–497. DOI: <https://doi.org/10.18721/JPM.161.183>

Статья открытого доступа, распространяемая по лицензии CC BY-NC 4.0 (<https://creativecommons.org/licenses/by-nc/4.0/>)

Introduction

To date, a new direction in chemistry known as microdroplet chemistry which involves carrying out chemical reactions in micro- and nanodroplets generated by various methods, has been formed and is actively developing [1]. One of the most promising approaches to this synthesis method is to carry out chemical reactions in micro- and nanodroplets of an electrospray torch. In the course of mass spectrometric experiments, it was found that both simple and complex multi-stage chemical reactions can take place in micro- and nanodroplets of an electrospray torch, sometimes with a significant acceleration compared to their occurrence in the bulk phase [2]. Reactants and products of chemical reactions are collected using solid absorbers in most studies devoted to the study of chemical reactions in charged microdroplets of an electrospray torch. This approach requires a subsequent procedure for extracting the accumulated reactants and reaction products by washing the sample collector with an extractant, which is not convenient and increases time costs. A much more suitable option is the accumulation of chemical reaction products and reacting substances in a liquid sample collector. This approach will greatly simplify the further use of the accumulated reaction products for analytical and preparative purposes. In addition, the use of a suitable liquid in the liquid electrode will make it possible to realize the multiple-repeated electrospraying of reaction mixtures in a continuous mode, which in some cases should increase the yield of the reaction product. Thus, the objectives of this work were: 1) to study the fundamental possibility of electrospraying to the surface of a liquid, 2) to study the possibility of collection of reacting substances and reaction products in the volume of a liquid electrode.

Equipment and methods of HPLC-MS analysis

HPLC-MS analysis of the obtained samples was performed using a Nexera HPLC system (Shimadzu, Japan) equipped with a DGU-20A degasser, two LC-30AD chromatographic pumps, an SPD-M20A diode array detector, an LC-30AC autosampler, a CTO-20A thermostat. HPLC

© Кулешов Д.О., Соловьева А.В., Громов И.А., Пиковской И.И., Ульяновский Н.В., Белесов А.В., Сыпалов С.А., Мазур Д.М., 2023. Издатель: Санкт-Петербургский политехнический университет Петра Великого.

system was connected with a high-resolution mass spectrometer Orbitrap QExactive Plus (Thermo Scientific, USA) with a mass analyzer based on an orbital ion trap. Chromatographic separation was carried out on a Nucleodur PFP column (2×150 mm, 1.8 μm, Macherey-Nagel, Germany) in the gradient elution mode. Acetonitrile grade 0 (A) and water (B) with the addition of formic acid (0.1%) were used as the mobile phase. The gradient elution was set as follows: 0–1 min 20% A, then a linear gradient from 20% to 100% A from 1 to 17 minutes, keeping at 100% A from 17 to 18 minutes, then returning to the original ratios (20% A) for 1 minute and hold for 2 minutes at 20% A. The flow rate was set at 0.45 ml/min. The total analysis time was 21 minutes. The column temperature control was carried out at 40 °C. The sample injection volume was 5 μl. Ultrapure water (Type I) was used in all experiments, obtained using the Milli-Q system (Millipore, France). The high-resolution mass spectrometer system operated in the mode of detecting positively charged ions during electrospray ionization. The optimal parameters of the ion source, which ensured the maximum intensity of the mass spectra of the analytes, were used during ionization.

Experimental device

Previously, we made an experimental device [3] for studying the course of chemical reactions in micro- and nanodroplets of an electrospray torch. It used a solid absorber of reaction products, which greatly complicates their further use for preparative or analytical purposes. In this work, a modified version of the device was used. Its scheme is shown in Fig. 1. In the modernized device for collecting reaction products, a liquid electrode (LE) was proposed and implemented. The sample collector of the reaction products is a cylindrical glass cell (1) with an internal diameter of 45 mm and a height of 29.5 mm, on the bottom of which is placed a metal tantalum or copper plate, completely covering the bottom of the cell, with an electrical output, which has the Earth's potential. The cuvette is placed in a fluoroplastic cup (2) and filled with the test liquid, i.e. element (1) is actually a LE. The spray unit of the experimental device (5) consists of a spray capillary (1) made of stainless steel and having an inner diameter of 0.4 mm; walls of the main air duct (2) and capillary for gas supply (3), made of stainless steel and having an inner diameter of 0.6 mm (see Fig. 2). Electro spraying is carried out as follows: using a syringe pump (4), the solution is fed through the inlet capillary to the spray unit (5). From the end of the inner needle, the solution is electro sprayed onto the surface of the liquid electrode. The power supply (7) supplies voltage to the spray unit (6). The spraying current (on the needle) is measured with digital multimeter № 1 (8), and the current on the liquid in the sample collector is measured with multimeter № 2 (9). Changing the polarity of the voltage (Earth potential on the spray capillary, spray potential on the metal plate) makes it possible to create both positively charged and negatively charged microdroplets.

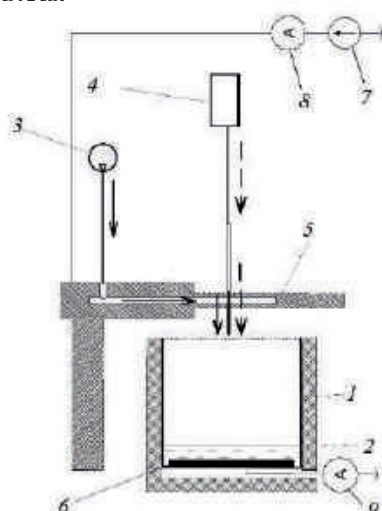


Fig. 1. 1 – glass cuvette, 2 – fluoroplastic cup, 3 – gas supply device, 4 – syringe dispenser, 5 – spray unit, 6 – metal plate, 7 – high-voltage power supply, 8 – digital multimeter № 1, 9 – digital multimeter № 2

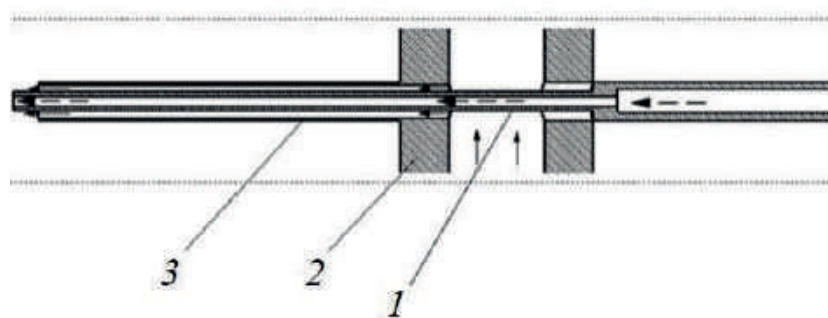


Fig. 2. 1 – spray capillary, 2 – main duct wall, 3 – capillary for gas supply

Investigation of the possibility of electro-spraying to the surface of a liquid

The possibility of obtaining a stable mode of electro-spraying to a liquid electrode was studied using an experimental device. For this purpose, the dependences of the electro-spray current on the spraying voltage U , the distance from the spraying capillary to the surface of the liquid electrode L , and the sprayed solution feed rate Q were determined. Acetonitrile with a volume of 40 ml was used as a liquid electrode. The experiments were carried out both in the mode of positively charged microdroplets generation and in the mode of negatively charged microdroplets generation. The presence/absence of electro-spraying was detected visually and with a multimeter (according to the stability of the spray current). Acidified acetonitrile was used as a spray solution in the mode of positively charged microdroplets generation. Pure acetonitrile was used in the mode of negatively charged microdroplets generation. Electro-spraying was carried out without using a spray gas flow. In both cases, a stable electro-spray mode was obtained. The ranges of the electro-spraying potential difference, which provide a stable electro-spray mode, are presented in tables 1 and 2. It should be noted that the current on the liquid electrode was equal to the electro-spray current both in the mode of generating positively charged microdroplets and in the mode of generating negatively charged microdroplets in all experiments.

Investigation of the possibility of collecting reacting substances and products of chemical reactions occurring in charged microdroplets of an electro-spray torch in the volume of a liquid electrode

The possibility of reaction products accumulation occurring in charged microdroplets of an electro-spray torch in the volume of a liquid electrode was studied using the example of the

Table 1

Voltage ranges (in kV) that provide a stable electro-spray mode for different flow rates of the sprayed solution and different distances between the spray capillary and the surface of the liquid electrode, in the mode of generating positively charged microdroplets

Sprayed solution feed rate Q , $\mu\text{l}/\text{min}$	Distance from spray electrode to liquid electrode L , mm				
	3	8	13	18	23
25	2,3 (13) – 4 (210)	3,1 (10) – 4,9 (106)	3,8(15) – 5(123)	4,2(18) – 5(95)	4,7(12) – 5(29)
50	No measurements taken	2,5(17) – 4,9(360)	3,3(22) – 4,9(171)	3,7(14) – 4,9(120)	4,4(11) – 5(56)
75		2,7(17) – 4,9(360)	3,4(14) – 4,9(174)	3,8(11) – 4,9(110)	4,4(14) – 5(78)
100		2,9(28) – 5(276)	3,6(19) – 5(168)	4,2(19) – 5(95)	4,5(21) – 5(52)
200		2,7(20) – 4,5(453)	3,3 (12) – 4,9 (229)	3,9 (16) – 4,9(124)	4,4 (12) – 5(72)

The current values in nA corresponding to the specified voltage are given in brackets.

Table 2

Voltage ranges (in kV) that provide a stable electrospray mode for different flow rates of the sprayed solution and different distances between the spray capillary and the surface of the LE, in the mode of generating negatively charged microdroplets

Sprayed solution feed rate Q , $\mu\text{l}/\text{min}$	Distance from spray electrode to liquid electrode L , mm				
	3	8	13	18	23
25	2,2 (17) – 2,9 (253)	2,8 (23) – 3,9 (186)	3,6 (23) – 5 (204)	4,3 (19) – 4,9 (90)	4,8 (18) – 5 (30)
50	No measurements taken	3,1 (16) – 3,9 (193)	3,7 (26) – 5 (180)	4,2 (16) – 5 (101)	4,6 (11) – 5 (26)
75		2,7 (11) – 4 (273)	3,5 (13) – 5 (168)	4,2 (18) – 5 (90)	4,9 (12) – 5 (23)
100		3,6 (70) – 5 (455)	4,1(45) – 5(201)	Electrospraying is absent in the voltage range from 0 to 5 kV	

The current values in nA corresponding to the specified voltage are given in brackets.

condensation reaction of phenylhydrazine with anisic aldehyde with the formation of anisaldehyde phenylhydrazone. For this, a reaction mixture was prepared. The mixture was a solution of 10 μl phenylhydrazine and 10 μl anisaldehyde in 5 ml of a 0.1% acetic acid in methanol solution. Immediately after preparation, a 200 μl aliquot of the reaction mixture was sprayed onto the liquid electrode (40 ml methanol) for 2 minutes. The electrospraying of the freshly prepared reaction mixture was carried out in the mode of positively charged microdroplets generation. Q was 100 $\mu\text{l}/\text{min}$ and U was 4.2 kV. The distance between the spray capillary and the surface of the liquid electrode L was 8 mm. A HPLC-MS analysis of the LE composition was performed immediately after electrospraying. The initial reaction mixture was kept at room temperature for 3 hours and was also subjected to HPLC-MS analysis (initial reaction mixture was preliminarily diluted 200 times with methanol). The main expected reaction product is anisaldehyde phenylhydrazone. Chromatograms for total ion current, as well as extracted chromatograms for exact masses, obtained as a result of HPLC-MS analysis, are shown in Fig. 3 and 4. In all figures, 1 is chromatogram for total ion current, 2 is extracted chromatogram for exact mass for the ion m/z 94.0652 (protonated aniline molecule); 3 is extracted chromatogram by exact mass

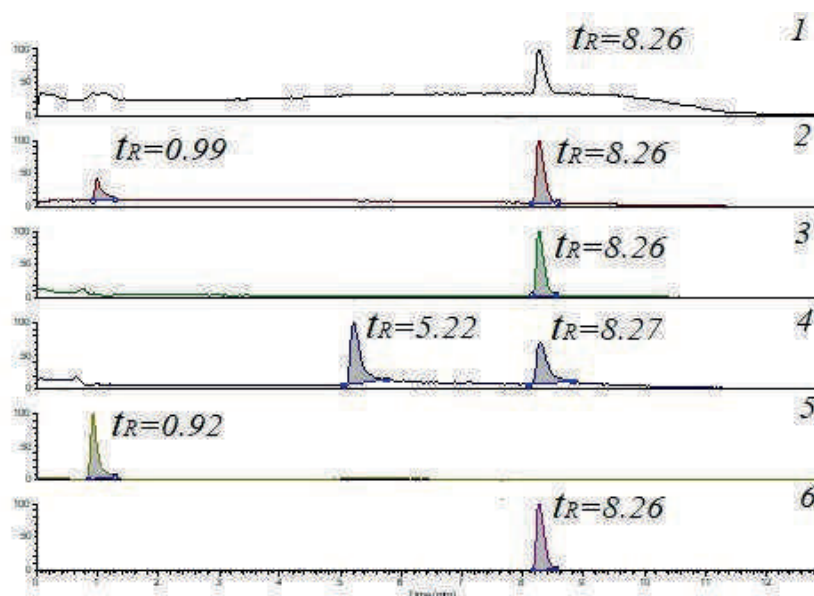


Fig. 3. Chromatograms obtained as a result of the initial reaction mixture HPLC-MS analysis

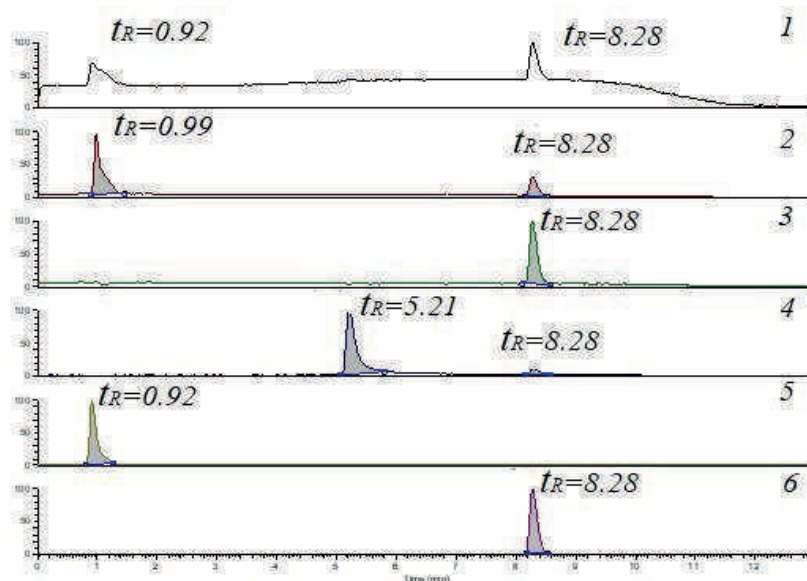


Fig. 4. Chromatograms obtained as a result of the LE HPLC-MS analysis after electro spraying the reaction mixture on it in the mode of positively charged microdroplets generation

for an ion with m/z 119.0607 (protonated 1H-indazole molecule); 4 is extracted chromatogram by exact mass for an ion with m/z 137.0603 (protonated anisaldehyde molecule); 5 is extracted chromatogram by exact mass for an ion with m/z 109.0764 (protonated phenylhydrazine molecule); 6 is extracted exact mass chromatogram for an ion with m/z 227.1181 (a protonated anisaldehyde phenylhydrazone molecule).

As can be seen from the obtained chromatograms, both the reactants phenylhydrazine ($t_R = 0.92$ min) and anisic aldehyde ($t_R = 5.21$ min) and the product of their reaction phenylhydrazone anisic aldehyde ($t_R = 8.28$ min) are accumulated in the volume of liquid electrode. The presence of chromatographic peaks with a retention time $t_R = 8.28$ min on the extracted chromatograms by exact mass for ions different from the ion with m/z 109.0764 allows us to conclude that chemical reactions occur in the ion source of the mass spectrometer with the participation of anisaldehyde phenylhydrazone, contained in the analyzed samples. As a result of these reactions, anisaldehyde (an ion with m/z 137.0603 is protonated anisaldehyde molecule), aniline (an ion with m/z 94.0652 – protonated aniline molecule) and, presumably, 1H-indazole (an ion with m/z 119.0607 is protonated 1H-indazole molecule) are formed.

Conclusion

The experimental device for carrying out chemical reactions in charged microdroplets with the accumulation of reaction products and reactants in a liquid electrode was developed. In the course of the studies carried out, the fundamental possibility of electro spraying a liquid onto the surface of a polar liquid (using acetonitrile as an example) in the modes of both positively and negatively charged microdroplets generation has been shown. In the mode of positively charged microdroplets generation, acidified acetonitrile was used as a sprayed solution; in the mode of negatively charged microdroplets generation, pure acetonitrile was used. In both cases, a stable electro spray mode was obtained over a wide range of U (from 2.2 kV to 5 kV), L (from 3 mm to 23 mm) and Q (from 25 $\mu\text{l}/\text{min}$ to 200 $\mu\text{l}/\text{min}$). It was shown on the example of the reaction of phenylhydrazine with anisic aldehyde that the products of reactions occurring in charged microdroplets, as well as the reactants, accumulate in the volume of the liquid electrode.

REFERENCES

1. Yan X., Emerging microdroplet chemistry for synthesis and analysis, International Journal of Mass Spectrometry. 468 (2021) 116639.



2. **Banerjee S., Gnanamani E., Yan X., Zare R.N.**, Can all bulk-phase reactions be accelerated in microdroplets, *Analyst*. 142(9) (2017) 1399–1402.

3. **Kuleshov D.O., Mazur D.M., Gromov I.A., Alekseyuk E.N., Gall N.R., Polyakova O.V., Lebedev A.T., Gall L.N.**, Study of the Aniline and Acetone Condensation Reaction under Electrospray Ionization Conditions, *Journal of Analytical Chemistry*. 75 (13) (2020) 1647–1652.

THE AUTHORS

KULESHOV Denis O.

hellchemist@yandex.ru

ORCID: 0000-0002-4484-8308

SOLOVIEVA Anna V.

ancka.solov@ya.ru

ORCID: 0000-0001-5876-9734

GROMOV Ivan A.

gromov-24-2@yandex.ru

ORCID: 0000-0001-9269-2259

PIKOVSKOI Ilya I.

pikowskoy@yandex.ru

ORCID: 0000-0002-6149-6770

UL'YANOVSKII Nikolay V.

uluanovskii_n@mail.ru

ORCID: 0000-0003-4796-9313

BELESOV Artem V.

a.belesov@narfu.ru

ORCID: 0000-0002-9857-4373

SYPALOV Sergey A.

sypych.one@yandex.ru

ORCID: 0000-0002-2947-5099

MAZUR Dmitriy M.

neodmitrii@gmail.com

ORCID: 0000-0002-9780-1490

Received 30.10.2022. Approved after reviewing 21.11.2022. Accepted 22.11.2022.

Journal

**ST. PETERSBURG STATE POLYTECHNICAL UNIVERSITY
JOURNAL: PHYSICS AND MATHEMATICS**

Vol. 16, No. 1.1, 2023

Founder and publisher: Peter the Great St. Petersburg Polytechnic University

The journal is registered with the Federal Service for Supervision of Communications,
Information Technology and Mass Media (Roskomnadzor).
Certificate ПИИ ФС77-51457 issued 19.10.2012.

Editorial Office

Dr. Prof. *V.K. Ivanov*, Editor-in-Chief
Dr. Prof. *A.E. Fotiadi*, Deputy Editor-in-Chief
Dr. Prof. *V.V. Dubov*
Dr. Prof. *P.A. Karaseov*
Dr. Assoc. Prof. *V.M. Kapralova*
A.S. Kolgatina, translator
N.A. Bushmanova, editorial manager

*All papers presented are final author versions
Peer review is under responsibility of the Organizing Committee*

Phone 8 (812) 294-22-85

Website <https://physmath.spbstu.ru/>

E-mail: physics@spbstu.ru

Typesetting by *A.S. Kolgatina*

Published 30.04.2023. Format 60x84/8. Digital print.

Printer's sheets

Print circulation 1000. Order ID .
